GEOLOGICAL SURVEY OF CANADA
COMMISSION GÉOLOGIQUE DU CANADA

**PAPER/ÉTUDE
92-1E**

# CURRENT RESEARCH, PART E

# RECHERCHES EN COURS, PARTIE E

**1992**

Energy, Mines and Resources Canada
Énergie, Mines et Ressources Canada

Canada

THE ENERGY OF OUR RESOURCES - THE POWER OF OUR IDEAS

L'ÉNERGIE DE NOS RESSOURCES - NOTRE FORCE CRÉATRICE

## NOTE TO CONTRIBUTORS

Submissions to the Discussion section of Current Research are welcome from both the staff of the Geological Survey of Canada and from the public. Discussions are limited to 6 double-spaced typewritten pages (about 1500 words) and are subject to review by the Chief Scientific Editor. Discussions are restricted to the scientific content of Geological Survey reports. General discussions concerning sector or government policy will not be accepted. All manuscripts must be computer word-processed on an IBM compatible system and must be submitted with a diskette using WordPerfect 5.0 or 5.1. Illustrations will be accepted only if, in the opinion of the editor, they are considered essential. In any case no redrafting will be undertaken and reproducible copy must accompany the original submissions. Discussion is limited to recent reports (not more than 2 years old) and may be in either English or French. Every effort is made to include both Discussion and Reply in the same issue. Current Research is published in January and July. Submissions should be sent to the Chief Scientific Editor, Geological Survey of Canada, 601 Booth Street, Ottawa, Canada, K1A 0E8.

## AVIS AUX AUTEURS D'ARTICLES

Nous encourageons tant le personnel de la Commission géologique que le grand public à nous faire parvenir des articles destinés à la section discussion de la publication Recherches en cours. Le texte doit comprendre au plus six pages dactylographiées à double interligne (environ 1500 mots), texte qui peut faire l'objet d'un réexamen par le rédacteur scientifique en chef. Les discussions doivent se limiter au contenu scientifique des rapports de la Commission géologique. Les discussions générales sur le Secteur ou les politiques gouvernementales ne seront pas acceptées. Le texte doit être soumis à un traitement de texte informatisé par un système IBM compatible et enregistré sur disquette WordPerfect 5.0 ou 5.1. Les illustrations ne seront acceptées que dans la mesure où, selon l'opinion du rédacteur, elles seront considérées comme essentielles. Aucune retouche ne sera faite au texte et dans tous les cas, une copie qui puisse être reproduite doit accompagner le texte original. Les discussions en français ou en anglais doivent se limiter aux rapports récents (au plus de 2 ans). On s'efforcera de faire coïncider les articles destinés aux rubriques discussions et réponses dans le même numéro. La publication Recherches en cours paraît en janvier et en juillet. Les articles doivent être envoyés au rédacteur en chef scientifique, Commission géologique du Canada, 601, rue Booth, Ottawa, Canada, K1A 0E8.


GEOLOGICAL SURVEY OF CANADA
COMMISSION GÉOLOGIQUE DU CANADA

**PAPER / ÉTUDE**
**92-1E**

# CURRENT RESEARCH, PART E
# RECHERCHES EN COURS, PARTIE E

**Includes/comprend:**

**Cordillera and Pacific Margin**
**Cordillère et marge du Pacifique**

**Interior Plains and Arctic Canada**
**Plaines intérieures et région arctique du Canada**

**Canadian Shield**
**Bouclier canadien**

**Eastern Canada and National and General Programs**
**Est du Canada et programmes nationaux et généraux**

**1992**

Available in Canada through authorized
bookstore agents and other bookstores

or by mail from

Canada Communication Group — Publishing
Ottawa, Canada K1A 0S9

and from

Geological Survey of Canada offices:

601 Booth Street
Ottawa, Canada K1A 0E8

3303-33rd Street N.W.,
Calgary, Alberta T2L 2A7

100 West Pender Street
Vancouver, B.C. V6B 1R8

A deposit copy of this publication is also available for
reference in public libraries across Canada

Cat. No. M44-92/1E
ISBN 0-660-57437-3

Price subject to change without notice

**Cover description**

Geologist walking back to camp along the east shore of Axel Heiberg Island, Northwest Territories. Photo by B. Beauchamp.

Géologue s'en retournant à son camp le long de la côte orientale de l'île Axel Heiberg, dans les Territoires du Nord-Ouest. Photo prise par Benoît Beauchamp.

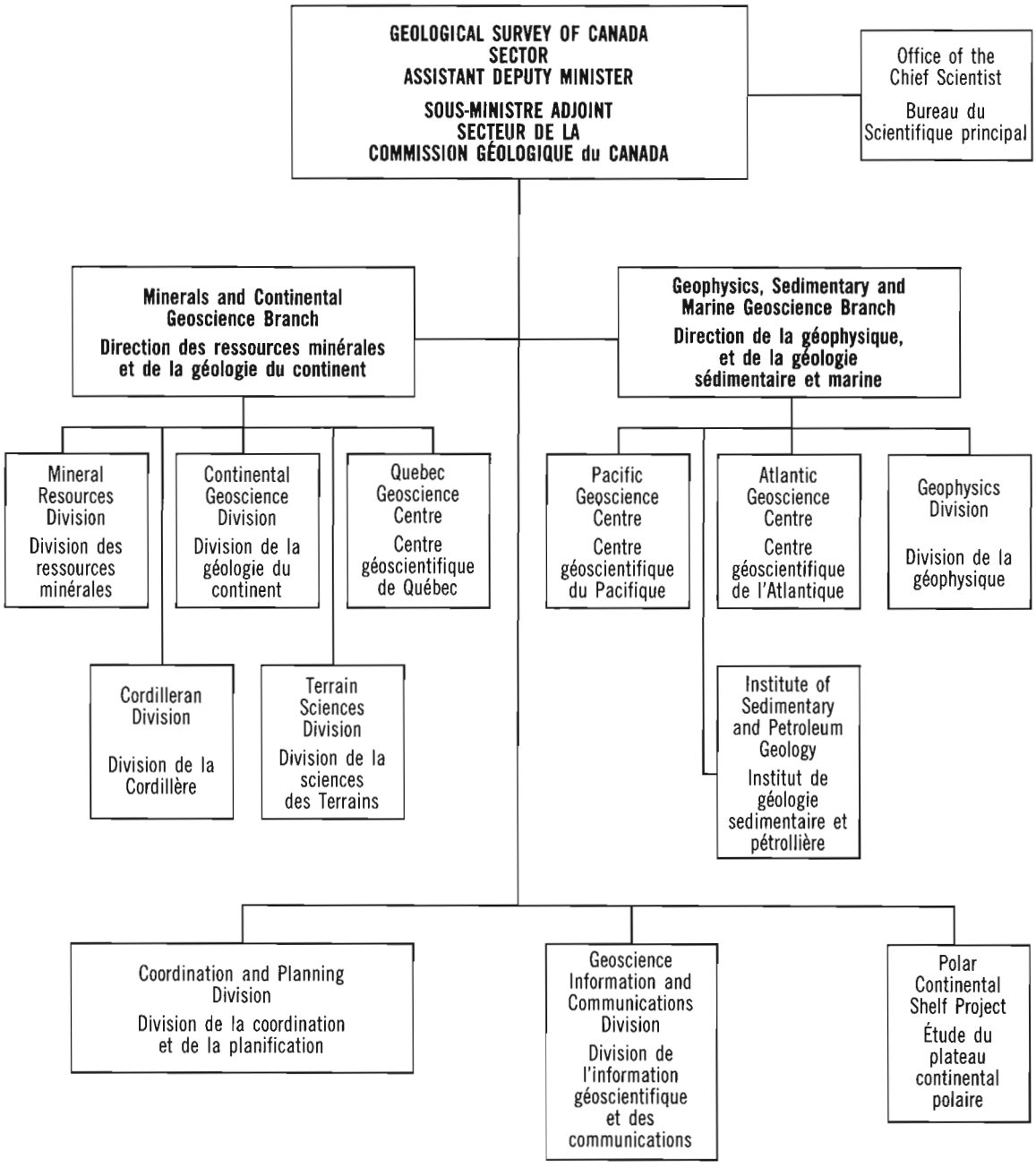
GEOLOGICAL SURVEY OF CANADA
SECTOR
ASSISTANT DEPUTY MINISTER
SOUS-MINISTRE ADJOINT
SECTEUR DE LA
COMMISSION GÉOLOGIQUE du CANADA
Office of the Chief Scientist
Bureau du Scientifique principal
Minerals and Continental Geoscience Branch
Direction des ressources minérales et de la géologie du continent
Geophysics, Sedimentary and Marine Geoscience Branch
Direction de la géophysique, et de la géologie sédimentaire et marine
Mineral Resources Division
Division des ressources minérales
Continental Geoscience Division
Division de la géologie du continent
Quebec Geoscience Centre
Centre géoscientifique de Québec
Pacific Geoscience Centre
Centre géoscientifique du Pacifique
Atlantic Geoscience Centre
Centre géoscientifique de l'Atlantique
Geophysics Division
Division de la géophysique
Cordilleran Division
Division de la Cordillère
Terrain Sciences Division
Division de la sciences des Terrains
Institute of Sedimentary and Petroleum Geology
Institut de géologie sedimentaire et pétrollière
Coordination and Planning Division
Division de la coordination et de la planification
Geoscience Information and Communications Division
Division de l'information géoscientifique et des communications
Polar Continental Shelf Project
Étude du plateau continental polaire

## Separates

A limited number of separates of the papers that appear in this volume are available by direct request to the individual authors. The addresses of the Geological Survey of Canada offices follow:

601 Booth Street
OTTAWA, Ontario
K1A 0E8
(FAX: 613-996-9990)

Institute of Sedimentary and Petroleum Geology
3303-33rd Street N.W.
CALGARY, Alberta
T2L 2A7
(FAX: 403-292-5377)

Cordilleran Division
100 West Pender Street
VANCOUVER, B.C.
V6B 1R8
(FAX: 604-666-1124)

Pacific Geoscience Centre
P.O. Box 6000
9860 Saanich Road
SIDNEY, B.C.
V8L 4B2
(Fax: 604-363-6565)

Atlantic Geoscience Centre
Bedford Institute of Oceanography
P.O. Box 1006
DARTMOUTH, N.S.
B2Y 4A2
(FAX: 902-426-2256)

Québec Geoscience Centre
2700, rue Einstein
C.P. 7500
Ste-Foy (Québec)
G1V 4C7
(FAX: 418-654-2615)

When no location accompanies an author's name in the title of a paper, the Ottawa address should be used.

## Tirés à part

On peut obtenir un nombre limité de «tirés à part» des articles qui paraissent dans cette publication en s'adressant directement à chaque auteur. Les adresses des différents bureaux de la Commission géologique du Canada sont les suivantes:

601, rue Booth
OTTAWA, Ontario
K1A 0E8
(facsimilé : 613-996-9990)

Institut de géologie sédimentaire et pétrolière
3303-33rd St. N.W.,
CALGARY, Alberta
T2L 2A7
(facsimilé : 403-292-5377)

Division de la Cordillère
100 West Pender Street
VANCOUVER, British Columbia
V6B 1R8
(facsimilé : 604-666-1124)

Centre géoscientifique du Pacifique
P.O. Box 6000
9860 Saanich Road
SIDNEY, British Columbia
V8L 4B2
(facsimilé : 604-363-6565)

Centre géoscientifique de l'Atlantique
Institut océanographique Bedford
B.P. 1006
DARTMOUTH, Nova Scotia
B2Y 4A2
(facsimilé : 902-426-2256)

Centre géoscientifique de Québec
2700, rue Einstein
C.P. 7500
Ste-Foy (Québec)
G1V 4C7
(facsimilé : 418-654-2615)

Lorsque l'adresse de l'auteur ne figure pas sous le titre d'un document, on doit alors utiliser l'adresse d'Ottawa.

# CONTENTS

## CORDILLERA AND PACIFIC MARGIN
## CORDILLÈRE ET MARGE DU PACIFIQUE

## INTERIOR PLAINS AND ARCTIC CANADA
## PLAINES INTÉRIEURES ET RÉGION ARCTIQUE DU CANADA



## CANADIAN SHIELD
## BOUCLIER CANADIEN

## EASTERN CANADA AND NATIONAL AND GENERAL PROGRAMS
## EST DU CANADA ET PROGRAMMES NATIONAUX ET GÉNÉRAUX

# Cordillera and Pacific Margin

# Cordillère et marge du Pacifique

# Paleomagnetic evidence for rotation in the Neoproterozoic Mount Harper volcanic complex, Ogilvie Mountains, Yukon Territory

**John K. Park[1], Charles F. Roots[2], and Normand Brunet[3]**

*Park, J.K., Roots, C.F., and Brunet, N., 1992: Paleomagnetic evidence for rotation in the Neoproterozoic Mount Harper volcanic complex, Ogilvie Mountains, Yukon Territory; in Current Research, Part E; Geological Survey of Canada, Paper 92-1E, p. 1-10.*

***Abstract***

*In the Cordillera of northwestern Canada, the Mount Harper volcanics (751 +26/-18 Ma) of the Ogilvie Mountains may have formed coevally with the Little Dal basalts and the diabase intrusions (777.7 +2.5/-1.8 Ma) of the Mackenzie Mountains. Comparison of the Mount Harper primary pole with reference poles from the Mackenzie Mountains and the Canadian Shield, suggests that the Mount Harper region has rotated by at least 60°.*

*Basaltic flows of the Mount Harper volcanic complex contain at least three stable magnetic components. The primary component in hematite and probable magnetite has a pole roughly estimated at 140°W, 29°S ($\underline{N}$=6; $\underline{A}_{95}$=12°). One secondary component, attributed to synfolding burial heating or hematite formation, yields a steeply directed pole (166°W, 74°N; $\underline{N}$=8 sites; $\underline{A}_{95}$=22°) similar in direction to a postfolding pole (178°W, 78°N; $\underline{N}$=4 sites; $\underline{A}_{95}$=9°) derived from hematitic siltstone elsewhere in the complex.*

***Résumé***

*Dans la Cordillère de la partie nord-ouest du Canada, les roches volcaniques de Mount Harper (751 +26/-18 Ma), observées dans les monts Ogilvie, se sont peut-être formées à la même époque que les basaltes de Little Dal et les intrusions de diabase (777,7 +2,5/-1,8 Ma) des monts Mackenzie. Une comparaison entre le pôle primaire du mont Harper et les pôles de référence des monts Mackenzie et du Bouclier canadien suggère que la première région a subi une rotation d'au moins 60°.*

*Les coulées basaltiques du complexe volcanique de Mount Harper contiennent au moins trois composantes magnétiques stables. La composante primaire dans l'hématite et probablement dans la magnétite possède un pôle dont la position estimée approximativement est 140°W, 29°S ($\underline{N}$=6; $\underline{A}_{95}$=12°). Une composante secondaire, attribuée soit à un réchauffement dû à un enfouissement contemporain du plissement, soit à la formation d'hématite, possède un pôle secondaire de direction fortement inclinée (166°W, 74°N; $\underline{N}$=8 sites; $\underline{A}_{95}$=22°), à peu près semblable à celle d'un pôle ultérieur au plissement (178°W, 78°N; $\underline{N}$=4 sites; $\underline{A}_{95}$=9°) qui a été déterminé à partir d'un siltstone hématitique présent ailleurs dans le complexe.*

[1] Continental Geoscience Division
[2] Cordilleran Division, Vancouver
[3] 1850 Simard St., Orleans, Ont. K1C 1R8

## INTRODUCTION

Paleomagnetic studies of ancient rocks can help unravel the tectonic history of a region. For example, where two coeval rock units yield paleopoles that are significantly different, it could mean that one unit has been tectonically displaced relative to the other. If this is the reason, the type of displacement, whether translational or rotational, and its amount may be inferred if one pole can be used as a reference for comparing the other.

The Mount Harper volcanic complex of the Ogilvie Mountains has a markedly dissimilar paleopole from poles of broadly similar age reported from the well-exposed Neoproterozoic succession in the Mackenzie Mountains, 500 km to the east (see Park and Jefferson, 1991 for list of poles and references). Among the Mackenzie Mountains paleopoles is a well-dated and well-determined pole from diabase intrusions, which may be part of the same magmatic event as the Mount Harper volcanic complex. To reconcile the primary pole from Mount Harper with that of the diabase intrusions requires an 80° clockwise rotation of the Mount Harper pole. The discrepancy is thought to reflect tectonic displacement, perhaps rotation, between the southern Ogilvie Mountains and the Mackenzie Mountains.

This paper reports paleomagnetic data for the volcanics and sediments of the Mount Harper group. The study incorporates paleomagnetic results from a B.Sc. honours thesis (Brunet, 1986). Further sampling is required to confirm the result and understand regional structures occurring between the Ogilvie and Mackenzie mountains that might account for the apparently rotated paleopole.

## GEOLOGY

### *Setting*

From Middle Proterozoic until early Triassic time the western (present day coordinates) edge of cratonic North America remained a passive margin, acquiring a nearly continuous sedimentary record. Periods of stable shelf deposition (300-400 Ma) were separated by intervals of more active tectonism characterized by block faulting, clastic sedimentation, and magmatism (Thompson and Eisbacher, 1984; Thompson et al., 1987). These intervals occurred around 1.2 Ga and between 780-600 Ma in the northern Cordillera. During the latter interval, a westward thickening, clastic apron was formed along the margin from Alaska to California; these sedimentary rocks are now collectively known as the Windermere Supergroup (e.g. Stewart, 1972). In the Yukon the Windermere Supergroup is represented by two northwest-trending belts of exposed rock; both have been shortened by northward and eastward folding and thrusting during the Mesozoic (Fig. 1). The outer belt includes the Mount Harper group in the northwest, as well as the Little Dal flows and similar-aged igneous intrusions in the Mackenzie Mountains. The inner belt, on the southwest side of the outer belt, includes the grit unit (Gabrielse, 1972), more recently known as the Hyland Group (Gordey, in press).

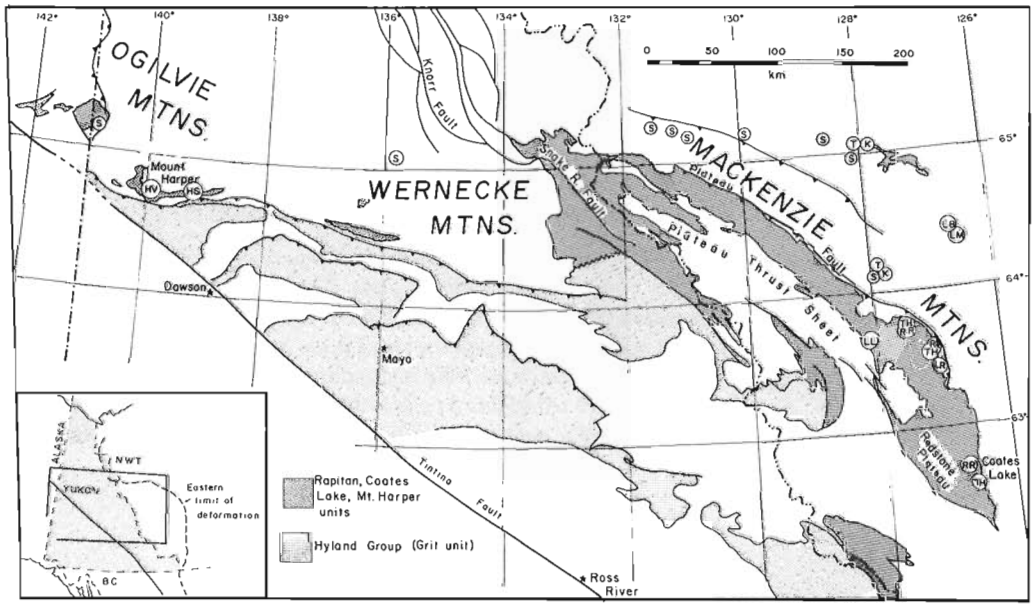


**Figure 1.** Location map and paleomagnetic sampling localities of Late Proterozoic clastic and igneous rocks in the northern Cordillera. Rocks belonging mainly to the Windermere Supergroup are patterned. In Mackenzie Mountains region, Plateau Fault separates Outer Fold Belt to northeast from Plateau Thrust Sheet. Symbols refer to Harper volcanics (HV); Mount Harper sedimentary rocks (HS); Katherine Group (K); Little Dal Group: Basinal sequence (LB), basalts (LL), Mudcracked formation (LM), Rusty Shale formation (LR); Coates Lake Group, Redstone River Formation (RR); diabase sills and dykes (S); Tsezotene Formation (T); Coates Lake Group, Thundercloud Formation (TH). See Figure 3 for stratigraphic relationships.

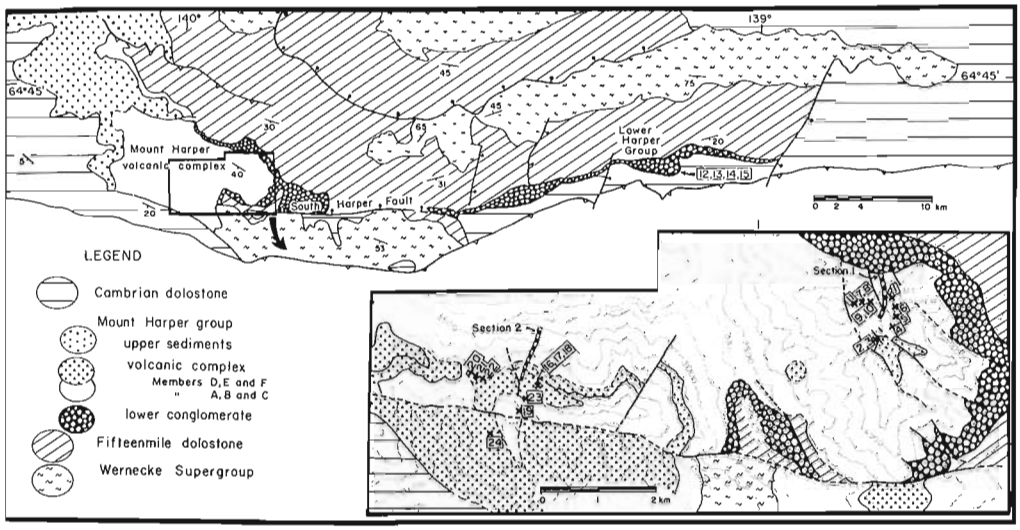


**Figure 2.** Geology of the southern part of the Coal Creek inlier, Ogilvie Mountains (from Thompson and Roots, 1982). Numbers with crosses in volcanic complex (inset) indicate paleomagnetic site locations.

In the Southern Ogilvie Mountains the Mount Harper volcanic complex is the uppermost unit of the Proterozoic shelf strata (Thompson and Roots, 1982) in a structural culmination referred to as the Coal Creek inlier (Fig. 2). In this erosional window the Mount Harper group overlies a 3.5 km thick shallow-water carbonate unit informally called the Fifteenmile group (Fig. 3). Another shallow water carbonate of Cambrian through Devonian age overlies the Mount Harper group. It is referred to as the Mackenzie Platform and covers much of northern Yukon.

### *Mount Harper group*

The Mount Harper group consists of a lower conglomerate-siltstone wedge, a lenticular volcanic complex (105 km$^2$), and an upper sandstone-mudstone succession. The lower unit was shed northward from adjacent fault scarps. The overlapping volcanic rocks are divided into six lithostratigraphic members (Fig. 4). Pillow flows (Member A) overstepped the conglomerate and a nearby fault scarp, and are covered by shallow water breccias and hematitized flows (Member B). Pyroclastic and epiclastic breccias (Member C) record the explosive activity, erosion, and subsidence of the northern part of this early edifice. In the southern part, subaerially erupted rhyolite flows (Member D) and coeval andesitic flows (Member E) unconformably overlie Members A and B. Basaltic tuff and sills (Member F) are intercalated with sediments of the overlying upper unit.

Samples were collected from one sedimentary and two volcanic members of the Mount Harper group: 1) hematitic siltstone of the distal facies in the lower unit located 35 km to the east of Mount Harper (sites 12-15); 2) Member B, on Mount Harper (sites 1-11) and at West Harper (sites 20-22); and 3) Members B and E, at West Harper (sites 16-18, 23, 24) (Fig. 2).

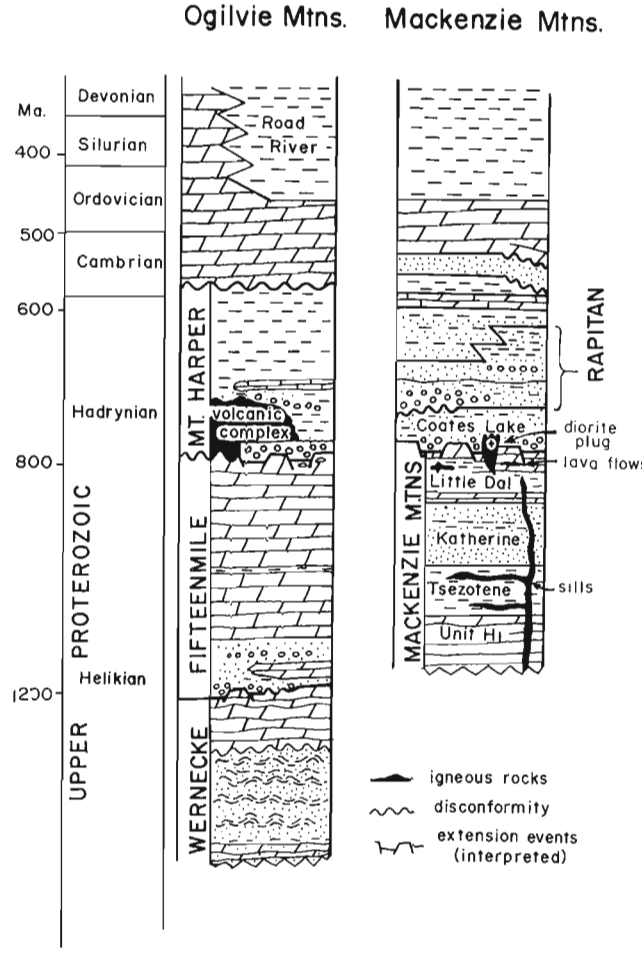


**Figure 3.** Schematic stratigraphic sections from the Ogilvie and Mackenzie mountains.

# METHODS

## Sample preparation

Block samples were collected in the field, 3 to 8 per site, and oriented by sun and magnetic compasses. Samples were drilled in the laboratory and several specimens, 2.2 cm in height and 2.5 cm in diameter, were cut from each core.

## Demagnetization

Natural remanent magnetizations (NRMs) were measured using Schonstedt DSM-1A and Geofyzika JR-4 spinner magnetometers. Specimens were demagnetized by several different methods. Thermal demagnetization was performed using an in-house instrument (Roy et al., 1972) and a Schonstedt TSM-1 furnace; specimens were heated in steps and measured after each step. Alternating field (AF) treatment was performed on an in-house instrument with 3-axis tumbler (Roy et al., 1973). Specimens were measured after each step of field increase; some were taken up to a maximum field of 290 mT. Residual fields in the in-house instruments were generally less than 2 nT and in the Schonstedt furnace, less than 10 nT. Sometimes a combination of alternating field followed by thermal treatment was used. For the sediments, acid leaching using concentrated HCl was also employed. Specimens were put in acid following the procedures of Park (1970) and Park and Aitken (1986a) and periodically measured. Treatment ended when specimens either crumbled or acquired a significant induced component after a maximum of about 400 hours in acid.

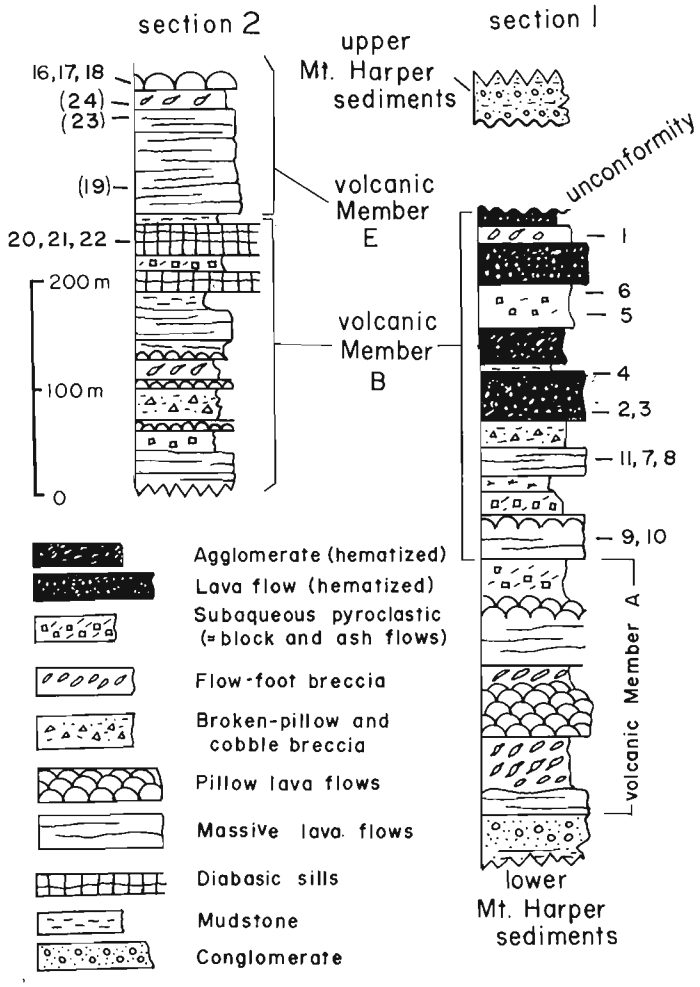


**Figure 4.** Measured stratigraphic sections with positions of paleomagnetic sites. Parentheses indicate sites interpolated within section.

## Analysis of directions

Paleomagnetic directions were determined with the aid of computer programs LINEFIND (Kent et al., 1983) and Linear Spectrum Analysis (Schmidt, 1982). Specimen directions were combined within samples and site mean directions calculated using sample unit weight.

## Correction for attitude

The present orientation of paleohorizontal (at the time of volcanism) was estimated or interpolated from map data, estimated from flow top data where it is consistent with sedimentary attitudes in the area (sites 7-10), or determined from the attitude of adjacent sedimentary rocks (Table 1).

**Table 1.** Bedding corrections

| Site | Tilt data DDA°,DIP° | Description | Reference |
|---|---|---|---|
| 1 | 212,55 | ca. 70 m from site | Roots (1987) |
| 2,3 | 224,17 | at site 2, 2 m above 3 | this sludy |
| 4 | 208,50 | ca. 160 m from site | Roots (1987) |
| 5,6 | 210,52 | mean of data used for 1 and 4; sites from same flow, between measurements ca. 300-400 m away | Roots (1987) |
| 7,8 | 212,40 | flow top data, consistent with tilt data in area | Roots (1987) |
| 9,10 | 212,40 | flow top data, ca. 120 m from sites; consistent with tilt data in area | Roots (1987) |
| 11 | 232,35 | ca. 60 m from site | Roots (1987) |
| 12-15 | 179,19 | mean of tilt data at sites | this study |
| 16-18 | 084,18 | ca. 240 m from site to SW | Roots (1987) |
| 19 | 090,12 | tuff? layer at site; like data 270 m away (084,15) | this study |
| 20 | 326,22 | tuff? layer at site | this study |
| 21,22 | 293,16 | tuff? layer at site 21; 22 at same level, 25 m away | this study |
| 23 | 197,11 | tuff? layer at site | this study |
| 24 | 196,32 | at site; like data ca. 70 m away (181,35; Roots, 1987) | this study |

NOTE: DDA refers to down dip azimuth.

## RESULTS AND ANALYSES

Natural remanent magnetization directions from the volcanics appear to be randomly scattered; those from the sediments are steeply inclined, close to the present Earth's field direction (PEF) in the region.

### *Volcanic units*

Analysis of the natural remanent magnetization using alternating field and thermal treatments revealed a resolvable magnetization in 13 of the 20 sites, with as many as four components. The first component removed ($HV_D$) in alternating fields generally <20 mT (e.g. Fig. 5b) and temperatures <300°C (e.g. Fig. 6a) is scattered in direction and probably viscous in origin. Its ranges of removal overlapped those of the major components, $HV_A$ and $HV_C$. Out of 69 samples, $HV_A$ and $HV_C$ were each resolved from 26 (38%), sometimes from the same sample, and a minor component, $HV_B$, from only 7 (10%).

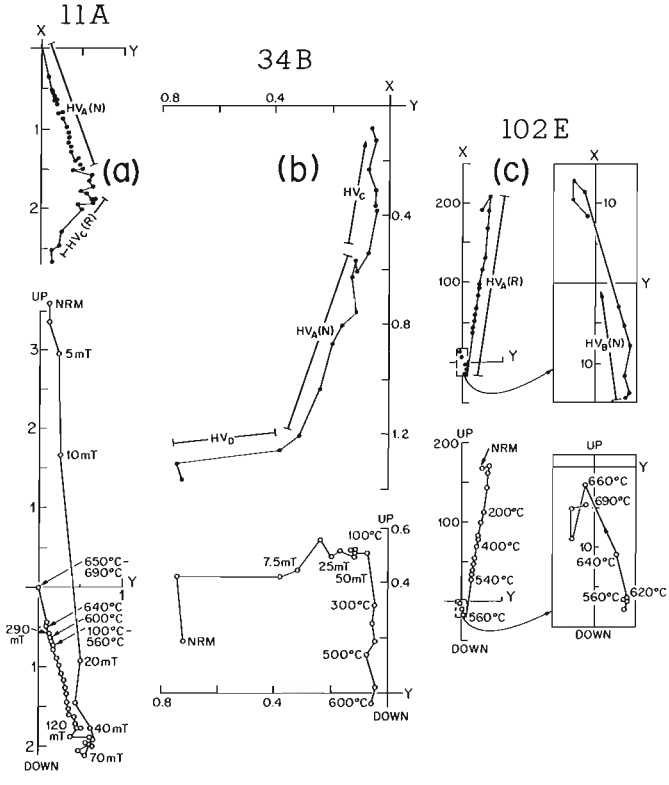


**Figure 5.** Vector diagrams showing alternating field and thermal demagnetization of volcanic specimens from sites (**a**)1, (**b**)3, and (**c**)10 in the Mount Harper area. X-Y projections show the magnetization plotted in the horizontal plane and UP-Y projections, the magnetization plotted in the vertical plane. All projections are with respect to the present horizontal and true north. All scales are in A/m. The ranges over which different magnetic components are largely removed are indicated. N and R in parentheses refer to normal and reverse.

### $HV_C$ component

$HV_C$ is generally the first major component demagnetized, with resistive coercive forces up to at least 120 mT and unblocking temperatures ($T_{UB}$s) to 550° or 600°C (Table 2; Fig. 5a,b, and 6a). Its direction has predominantly reverse polarity compared to the PEF, with moderate to steep inclinations (Table 2) when plotted with respect to the present horizontal. A fold test (McFadden, 1990) suggests that $HV_C$ is synfolding at the 95% confidence level (test statistic $\xi_2$ = 2.38 in situ and 2.88 after tilt correction for $N$ = 5, with the minimum $\xi_2$ = 0.56 occurring at 56% unfolding).

### $HV_A$ component

$HV_A$ has $T_{UB}$s similar to $HV_C$ and higher, with some in the hematite range (400-690°C) (Fig. 5a-c; Table 3). Resistive coercive forces are also generally higher (Table 3). Its direction is normal or reverse, with shallow to moderate inclination. There is a definite correlation of this component with the presence of large hematite grains at Mount Harper. It occurs in hematite and probable magnetite at site 10 (Fig. 5c) and possible magnetite at site 24 (Fig. 6b,c). A fold test on $HV_A$ directions is inconclusive, but indicates a slight increase in precision after correction for tilt.

### $HV_B$ component

A fourth component $HV_B$, occasionally resolved, correlates with sites having abundant hematite pigmentation (5, 8, 11) but no large hematite grains. Sites 6 and 7, also with abundant pigment, probably have this component, but averaging of sample directions gives a random result.

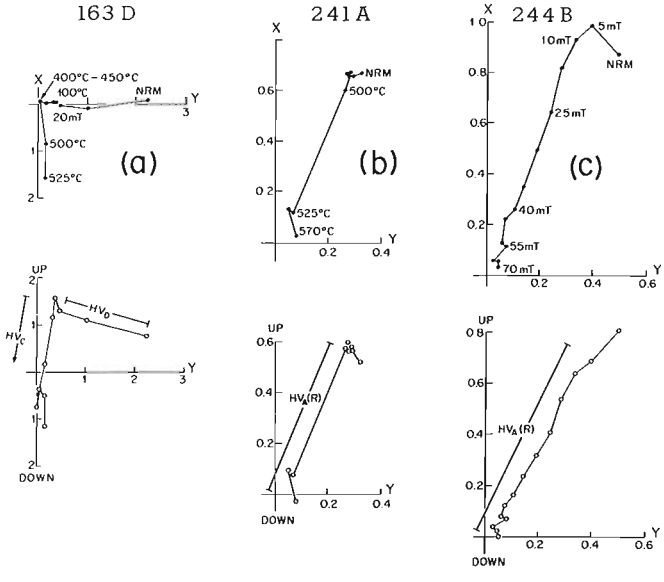


**Figure 6.** Vector diagrams showing alternating field and thermal demagnetization of volcanic specimens from sites (**a**)16 and (**b, c**)24 in the West Harper area. See Figure 5 for explanations.

**Table 2.** $HV_C$ in situ directions from Harper volcanic rocks

| Si | N | Treatment AF (mT), TH (°C) | D°,I° | R | k | $\alpha_{95}$° |
|---|---|---|---|---|---|---|
| | | **Mount Harper** | | | | |
| 1 | 2 | 3- 70, 100-525 | 238,-68 | 1.94 | - | - |
| 2 | 3 | - , 100-550 | 185,-79 | 2.79 | 10 | 42 |
| 3 | 5 | - , 100-550 | 171,-55 | 4.51 | 8 | 28 |
| 11 | 2 | - , NRM-600 | 206,-55 | 1.95 | - | - |
| *Mean* in situ *direction* | | | *199,-66* | *3.87* | *23* | *19* |
| *Mean tilt-corrected dir.* | | | *088,-87* | *3.73* | *11* | *29* |
| | | **West Harper** | | | | |
| 16 | 3 | 18- 35, 100-300 | 060,-65 | 2.69 | 6 | 53 |
| 18 | 2 | 30-110, - | 023,+81[1] | 1.99 | - | - |
| 21 | 5 | 30-120, 100-400 | 299,-84 | 4.81 | 21 | 17 |
| 22 | 4 | NRM-90,100-400 | 105,-75 | 3.93 | 45 | 14 |
| *Mean* in situ *direction* | | | *084,-83* | *3.88* | *25* | *19* |
| *Mean tilt-corrected dir.* | | | *114,-82* | *3.78* | *14* | *15* |
| *Grand mean* in situ, *8 sites* | | | *181,-79* | *7.54* | *15* | *15* |
| *Grand mean tilt-corrected* | | | *098,-80* | *7.50* | *14* | *15* |

NOTES: Si is site; *N* is the number of samples; AF is alternating field and TH is thermal treatment; *D°,I°* are the declination and inclination of the paleomagnetic direction; *R* is the vector resultant; *k* is Fisher's (1953) measure of precision; and $\alpha_{95}$° is the semi-angle of the 95% cone of confidence about the direction. Apparent $HV_C$ data from sites 4, 6, 7, and 9 were random (Vincenz and Bruckshaw, 1960). No $HV_C$ directions were analyzed from sites 5, 8, 10, 17, 19, 20, 23, and 24. [1]Reversed before averaging.

**Table 3.** $HV_A$ and $HV_B$ till-corrected directions from Harper volcanic rocks

| Si | N | Treatment AF (mT), TH (°C) | D°,I° | R | k | $\alpha_{95}$° |
|---|---|---|---|---|---|---|
| | | **Mount Harper** | | | | |
| 1 | 2 | - , 400- 690 | 190,-02[1] | 2.00 | - | - |
| 2 | 1 | 50-200, - | 151,-07 | - | - | - |
| 3 | 4 | 10- 50, 400->540 | 169,-12[1] | 3.79 | 14 | 25 |
| 4 | 3 | - , 400- 650 | 167,-30[1] | 2.68 | 6 | 54 |
| 5 | 3 | 30- 90, 300- 690 | 228,+10[2] | 2.87 | 15 | 33 |
| 7 | 1 | - , >670 | 029,+72 | - | - | - |
| 8 | 2 | 30-220, 100- 525 | 237,-15[2] | 1.95 | - | - |
| 10[3] | 4 | 18-120, NRM- 580 | 178,-19[1,4] | 3.70 | 10 | 31 |
| 10[3] | 5 | 60-280, 525- 690 | 179,+13[1,4] | 4.88 | 32 | 14 |
| 11 | 2 | 30-200, >500 | 216,-34[2] | 1.93 | - | - |
| | | **West Harper** | | | | |
| 22 | 1 | 50->130, - | 032,-30 | - | - | - |
| 24 | 8 | 5- 70, 475- 560 | 017,-13[1,5] | 7.84 | 45 | 8 |
| $HV_A$ in situ *mean, 6 sites* | | | *177,+27* | *5.59* | *12* | *20* |
| $HV_A$ *tilt-corrected mean* | | | *180,-06* | *5.67* | *15* | *18* |
| $HV_B$ in situ *mean, 3 sites* | | | *232,+26* | *2.70* | *7* | *52* |
| $HV_B$ *tilt-corrected mean* | | | *228,-13* | *2.82* | *11* | *38* |

NOTES: Individual samples or sites have been excluded from the analysis if the direction of respective specimens or samples are random (site 6). In the case of two specimens or samples, a sample or site is rejected if R<1.88 (40° separation) (site 17). See Table 2 for explanation of symbols. [1]Component $HV_A$. [2]Component $HV_B$. [3]Magnetile (entry one) and hematite (entry two) directions of site 10 are considered to be separate determinations of $HV_A$. [4]Mixed directions. [5]Reversed before averaging.

## Opaque mineralogy

There is a major difference between the magnetic minerals in the two volcanic sampling areas. Members B and E at West Harper (sites 16-24) contain reduced iron, chiefly as pyrite, and only site 24 contains identifiable hematite as large grains and fine grained pigment. In contrast, Member B flows at Mount Harper have abundant, fine grained hematite as staining, microlite overgrowths (sites 1, 8, 10), and microscopic veins (sites 2, 3, 5, 6). Large hematite grains, the oxidized products of original magnetite, were observed at four Member B sites (1, 3, 4, 10). Most sites also have amygdules in which hematite occurs as an initial deposit, as later discontinuous layers, and as veinlets. Secondary rutile is often abundant, replacing to some extent all magnetic phases in the volcanic sites. One sample from Member B contains a partially-filled vesicle with a vein cutting the infilling minerals, the vesicle wall, and the enclosing rock. Inside the vesicle, hematite constitutes the inner layer and the vein material; outside the vesicle, rutile constitutes the vein material. Clearly, rutile postdates formation of the vesicular hematite. At West Harper, sulfides sometimes replace hematite that occur as veins, overgrowths, and as initial deposits in vesicles.

**Table 4.** $HS_C$ in situ directions from Mount Harper sedimentary rocks

| Si | N | Treatment TH (°C), CH (h) | D°,I° | R | k | $\alpha_{95}$° |
|---|---|---|---|---|---|---|
| 12 | 4 | 300-540, 121-328 | 352,+82 | 3.97 | 118 | 8 |
| 13 | 5 | 100-600, NRM-207 | 352,+78 | 4.96 | 115 | 7 |
| 14 | 4 | 100-640, NRM-255 | 309,+79 | 3.97 | 106 | 9 |
| 15 | 5 | 300-680, 26-255 | 324,+81 | 4.97 | 139 | 7 |
| *Mean* in situ *direction, 4 sites* | | | *334,+81* | *3.99* | *384* | *5* |
| *Mean tilt-corrected direction* | | | *200,+79* | *3.99* | *259* | *6* |
| *Mean* in situ *CH dir., 14 specimens* | | | *327,+83* | *12.82* | *65* | *5* |
| *Mean tilt-corrected CH direction* | | | *199,+78* | *12.74* | *46* | *6* |
| *Mean* in situ *TH dir., 28 specimens* | | | *334,+81* | *27.45* | *49* | *4* |
| *Mean tilt-corrected TH direction* | | | *201,+79* | *27.39* | *44* | *4* |

NOTES: CH is chemical leaching in hours (h). See Table 2 for explanation of symbols.

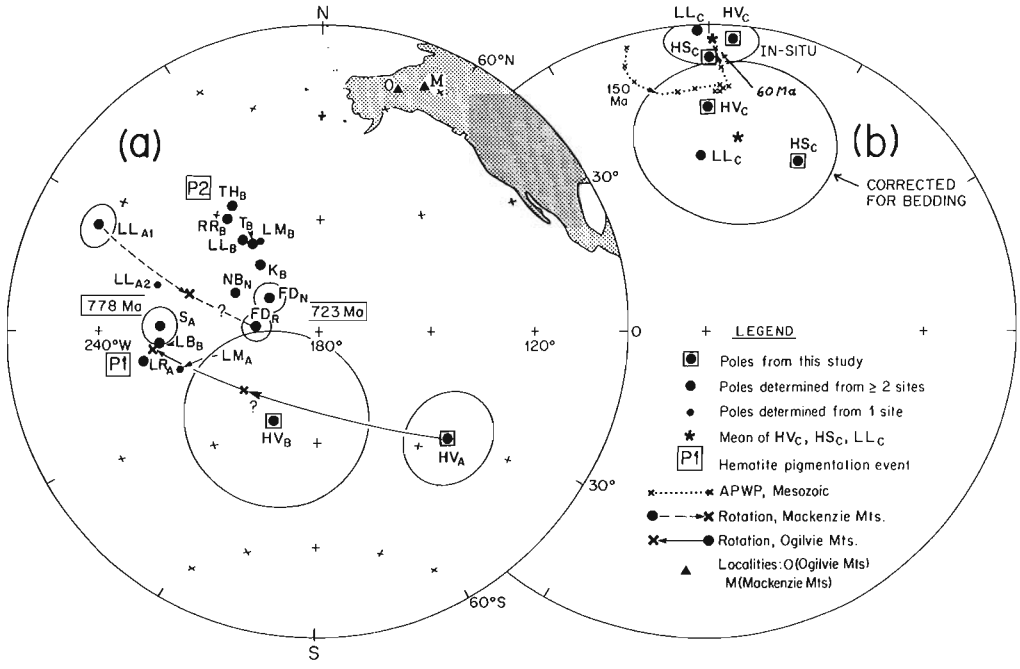


**Figure 7.** Paleopoles from the Mackenzie Arc. Ellipses represent the error of 95% confidence ($A_{95}$°) calculated from (**a**) site poles or (**b**) rock unit poles. Poles are as follows: $FD_N$, $FD_R$, Franklin diabases, normal (27 sites) and reverse (51 sites) (see Park and Jefferson, 1991 for references); $HS_C$, sedimentary poles (this study); $HV_A$, $HV_B$, and $HV_C$, volcanic poles (this study); $K_B$, Katherine Group (Park and Aitken, 1986a); $LB_B$, Basinal Sequence, Little Dal Group (Park, 1981a); $LL_{A1}$, basalts, Little Dal Group (Morris and Aitken, 1982); $LL_{A2}$, basalt site, Little Dal Group (J. Park, unpub. data, 1991); $LL_B$, $LL_C$, basalts, Little Dal Group (one site of Park, unpublished data combined with sites of Morris and Aitken, 1982); $LM_A$, $LM_B$, Mudcracked formation, Little Dal Group (Park, 1984); $LR_A$, Rusty Shale formation; Little Dal Group (Park and Jefferson, 1991); $NB_N$, Natkusiak basalts, normal (Palmer and Hayatsu, 1975; Palmer et al., 1983); $RR_B$, Redstone River Formation (Park and Jefferson, 1991); $S_A$, diabase sills and dykes (Park, 1981b; Park et al., 1989); $TH_B$, Thundercloud Formation (Park and Jefferson, 1991); $T_B$, Tsezotene Formation (Park and Aitken, 1986b). Reference poles of part (b) after Irving and Irving (1982). See text for discussion.

### *Sedimentary rocks*

Magnetic components in the oxidized siltstone were resolved with the use of thermal and chemical treatment. Two stable components, $HS_C$ and $HS_B$, were analyzed, but only $HS_C$ was consistently resolved. $HS_C$ has a steeply-inclined positive direction, either with respect to the present horizontal or the paleohorizontal (Table 4). Where both $HS_B$ and $HS_C$ are resolved, $HS_C$ is removed prior to $HS_B$ with either thermal treatment or chemical leaching. $HS_B$ has mainly directions with positive intermediate inclinations; but there are too few data to make a reliable determination. Application of the fold test (McFadden, 1990) to $HS_C$ directions shows them to be postfolding at the 95% confidence level (test statistic $\xi_2 = 0.50$ in situ and 2.46 on correction for tilt with $N = 4$, with the minimum $\xi_2$ occurring at 0% unfolding).

The sedimentary samples contain patchy to abundant pigmental hematite and sparse to common detrital hematite, with grains up to 75 μm in diameter. The leaching results suggest that $HS_C$ is associated with the pigmental hematite and $HS_B$ with the detrital hematite. Some of the detrital hematite grains are martite and some have been altered to rutile.

## DISCUSSION AND CONCLUSIONS

### *Interpretation of magnetic components*

Volcanic samples contain three stable magnetic components $HV_A$, $HV_B$, and $HV_C$. $HV_A$ is interpreted to be a primary magnetization because of two observations. First, it seems to reside in both the large hematite grains and unobserved magnetite: a condition either indicative of primary magnetization or of remagnetization through reheating. The former option is favoured, because the latter, possible through burial heating, would have affected only magnetic grains with $T_{UB}$s ranging to 550°C (Pullaiah et al., 1975). Second, the $HV_A$ component in possible magnetite contains reversals, which together with the first observation, tends to corroborate $HV_A$ as primary. The mixed magnetization at site 10 is

difficult to explain, but may indicate remagnetization in a reverse field following reheating caused by the extrusion of an adjacent flow. $HV_B$ resides in fine grained hematite found as a general staining and possibly in overgrowths and veins. $HV_C$ may reside in magnetite and represent a late thermal overprint due to the burial heating. Alternatively, or in addition, it could reside in late-forming diagenetic hematite or iron oxyhydroxides as a chemical remanent magnetization.

The sedimentary samples contain two stable magnetic components, $HS_B$ and $HS_C$. Only $HS_C$ could be reliably analyzed. $HS_B$ seems related to detrital hematite grains that have either a primary or secondary origin. If the hematite is secondary, an earlier $HS_A$ component may have existed in primary magnetite. $HS_C$, which seems to postdate $HS_B$, resides in the hematite pigment and has a direction similar to $HV_C$. Its direction is closer to $HV_C$ if uncorrected for tilt, and corroborates that $HV_C$ and $HS_C$ are syn- or postfolding.

### *Significance of paleomagnetic poles*

Poles calculated from Mount Harper group directions are plotted in Figure 7. Pole $HV_A$ (140°W, 29°S; $\underline{N}$=6 sites; $\underline{A}_{95}$=12°), attributed to primary magnetization in the Mount Harper volcanics (751 +26/-18 Ma U-Pb zircon age; Roots, 1987; Roots and Parrish, 1988), differs in direction by about 80° from pole $S_A$ (Park et al., 1989) of the diabase intrusions of the Mackenzie Mountains (777.7 +2.5/-1.8 Ma U-Pb zircon age, Jefferson and Parrish, 1989). It also differs by about 60° from poles $FD_N$, $FD_R$, and $NB_N$ of the Franklin igneous episode (723 ± 3 Ma U-Pb baddeleyite/zircon age, Heaman et al., 1992).

Likewise, secondary pole $HV_B$ (192°W, 24°S; $\underline{N}$=3 sites; $\underline{A}_{95}$=24°) differs in direction, in the same sense as $HV_A$, from possible counterparts in the Mackenzie Mountains (Fig. 7). It may correlate with one of the hematitization events recorded in the Mackenzie Mountains, either P1 or P2. If $HV_B$ correlates with P1, it may relate to the igneous episode, represented by $S_A$ from the diabase intrusions and $LL_{A1}/LL_{A2}$ from the Little Dal lavas, that possibly gave rise to P1 in the Mackenzie Mountains. Alternatively, if $HV_B$ correlates with P2, like its apparent counterpart $LL_B$ from the Little Dal lavas, it relates to a separate, later event. It is likely, in view of the argument for rotation given below, that $HV_B$ correlates with P1. The later pole $HV_C$ (in situ: 166°W, 74°N; $\underline{N}$ = 8; $\underline{A}_{95}$ = 22°) may be equivalent to the Little Dal lava pole $LL_C$, which is also postfolding (Morris and Aitken, 1982; Park and Jefferson, 1991).

Pole $HV_A$ appears to be a primary magnetization, yet diverges from poles $S_A$, $FD_N$, and $FD_R$, and poles of the Mackenzie Mountains of broadly similar age (Fig. 7a). There are no compelling reasons to attribute this discrepant direction to apparent polar wander (APW). The only other explanations for the position of $HV_A$ are (1) that improper tilt corrections have been applied to sites, or (2) that relative rotation has occurred between the Ogilvie and Mackenzie mountains. These possibities are considered below.

### Tilt corrections

Precise tilt corrections are difficult to determine. Sampled flows may have been deposited on slopes as steep as 30°; thus, a misinterpretation of paleohorizontal could significantly increase the scatter of magnetization directions and associated paleopoles acquired prior to deformation.

Only one locality (sites 2 and 3) yielding $HV_A$ has an associated paleohorizontal determination; all others use measurements made at distances ranging from 60 to 240 m away (Table 1). However, bedding determinations are reasonably consistent within each sampling area (Table 1), consistent with their location on the south-dipping flank of a structural uplift. Also, the $HV_A$ direction ($D,I$ = 169°, -12°) at site 3 is coincident within error with the mean $HV_A$ direction ($D,I$ = 183°, -05°; $\alpha_{95}$ = 22°) determined from all other sites. Because of the uncertainties involved, we consider the $HV_A$ determination to be a rough estimate.

Because down-dip azimuths of beds are mostly south (Table 1) in accord with Cretaceous tilting, any errors in dip determination would result in an $HV_A$ pole displaced north or south of its present position rather than east as would be required for rotating the pole into coincidence with the $S_A$ or $FD_N/FD_R$ paleopoles (Fig. 7a). Therefore, in view of (1) the evidence for the approximate $HV_A$ direction at site 3, (2) the consistent bedding attitudes that allow reasonable estimates of bedding to be made and that likely preclude errors greater than about 20°, and (3) the orientation of down-dip azimuths perpendicular to the required corrective direction, it is unlikely that the difference in poles can be explained by errors in dip determination.

Although additional sampling is warranted to confirm the Mount Harper results, we accept the present data, and proceed to consider the possibility of rotation about a vertical axis.

### Rotational corrections

Tectonic block rotations take place along curving fault systems. They may be inferred from geological structures but are difficult to quantify. Paleomagnetism of contemporaneous sites can be used where reference poles are available. For this study the well-dated poles $S_A$ for Mackenzie Mountains diabase and $FD_N/FD_R$ for the Franklin diabase, together with the secondary pole $T_B$ for the Tsezotene Formation, are used (Fig. 7) (see Park and Jefferson, 1991 for background).

There is paleomagnetic evidence for clockwise rotations within the Plateau Thrust sheet (inner fold belt) of the Mackenzie Mountains (Park and Jefferson, 1991). These appear to be related to a late Proterozoic event, possibly to incipient rifting. Not enough is known about Windermere structures in the northern Cordillera to determine large-scale tectonism, or the structural linkage between exposures in the Mackenzie and Ogilvie mountains.

There is no present geological evidence for rotation of the region including the Mount Harper group. Paleomagnetic evidence for rotation relies on a demonstrated time equivalence of $HV_A$ with reference poles from the Mackenzie Mountains and the Canadian Shield. If $HV_A$ is dated by the age of the Mount Harper volcanics (751 +26/-18 Ma), it should lie between reference poles $S_A$ (777.7 +2.5/-1.8 Ma) and $FD_N/FD_R$ (723 ± 3 Ma), suggesting that rotation has occurred.

### *High-latitude poles*

High-latitude poles $LL_C$, $HV_C$, and $HS_C$ have been shown to be either syn- or postfolding in origin. A second fold test (McFadden, 1990) on mean directions of the three poles, showing that they are postfolding at the 99% confidence level (test statistic $\xi_2 = 1.45$ in situ and 2.70 corrected for tilt, with a minimum $\xi_2$ occurring at 0% unfolding), implies that they represent the same event (Fig. 7b). Their postfolding position, close to the 60 Ma reference pole for North America, suggests that their magnetizations relate to the Cretaceous Laramide Orogeny.

In summary, although evidence for rotation of $HV_A$ is not conclusive, it is highly suggestive. A possible net tectonic rotation of 60 to 80° between the Ogilvie and Mackenzie mountains should provoke additional research in the large scale structural linkage between them.

## ACKNOWLEDGMENTS

Samples were collected with logistical support and advice of Bob Thompson and Peter Mustard. Azad Rafeek drafted the illustrations. Earlier versions were typed by Diane Regimbald, commented on by Randy Parrish, and critically read by B. Thompson and an anonymous reviewer. The present version was reviewed by Ken Buchan.

## REFERENCES

**Brunet, N.**
1986: Paleomagnetism of the Mt. Harper Volcanic Complex, Yukon, and its geological relationships; B.Sc. honours thesis, University of Ottawa, Ottawa, Ontario.

**Fisher, R.A.**
1953: Dispersion on a sphere; Proceedings of the Royal Society of London, Series A: Mathematical and Physical Sciences, v. 217, p. 295-305.

**Gabrielse, H.**
1972: Younger Precambrian of the Canadian Cordillera; American Journal of Science, v. 272, p. 521-536.

**Gordey, S.P.**
in press: Evolution of the northern Cordilleran miogeocline: Geology of Nahanni map-area (105I), Yukon Territory and District of Mackenzie; Geological Survey of Canada, Memoir 428.

**Heaman, C.M., LeCheminant, A.N., and Rainbird, R.H.**
1992: Nature and timing of Franklin igneous events, Canada: implications for a Late Proterozoic mantle plume and the break-up of Laurentia; Earth and Planetary Science Letters, v. 109, p. 117-131.

**Irving, E. and Irving, G.A.**
1982: Apparent polar wander paths Carboniferous through Cenozoic and the assembly of Gondwana; Geophysical Surveys, v. 5, p. 141-188.

**Jefferson, C.W. and Parrish, R.R.**
1989: Late Proterozoic stratigraphy, U-Pb zircon ages and rift tectonics, Mackenzie Mountains, Northwestern Canada; Canadian Journal of Earth Sciences, v. 26, p. 1784-1801.

**Kent, J.T., Briden, J.C., and Mardia, K.V.**
1983: Linear and planar structure in ordered multivariate data as applied to progressive demagnetization of paleomagnetic remanence; Geophysical Journal of the Royal Astronomical Society, v. 75, p. 593-621.

**McFadden, P.L.**
1990: A new fold test for palaeomagnetic studies; Geophysical Journal International, v. 103, p. 163-169.

**Morris, W.A. and Aitken, J.D.**
1982: Paleomagnetism of the Little Dal lavas, Mackenzie Mountains, Northwest Territories, Canada; Canadian Journal of Earth Sciences, v. 19, p. 2020-2027.

**Palmer, H.C. and Hayatsu, A.**
1975: Paleomagnetism and K-Ar dating of some Franklin lavas and diabases, Victoria Island; Canadian Journal of Earth Sciences, v. 12, p. 1439-1447.

**Palmer, H.C., Baragar, W.R.A., Fortier, M., and Foster, J.H.**
1983: Paleomagnetism of Late Proterozoic rocks, Victoria Island, Northwest Territories, Canada; Canadian Journal of Earth Sciences, v. 20, p. 1456-1469.

**Park, J.K.**
1970: Acid leaching of red beds and the relative stability of the red and black magnetic components; Canadian Journal of Earth Sciences, v. 7, p. 1086-1092.
1981a: Analysis of the multicomponent magnetization of the Little Dal Group, Mackenzie Mountains, Northwest Territories, Canada; Journal of Geophysical Research, v. 86, p. 5134-5146.
1981b: Paleomagnetism of the Late Proterozoic sills in the Tsezotene Formation, Mackenzie Mountains, Northwest Territories, Canada; Canadian Journal of Earth Sciences, v. 18, p. 1572-1580.
1984: Paleomagnetism of Mudcracked formation of the Precambrian Little Dal Group, Mackenzie Mountains, Northwest Territories; Canadian Journal of Earth Sciences, v. 21, p. 371-375.

**Park, J.K. and Aitken, J.D.**
1986a: Paleomagnetism of the Katherine Group in the Mackenzie Mountains: Implications for post-Grenville (Hadrynian) polar wander; Canadian Journal of Earth Sciences, v. 23, p. 308-323.
1986b: Paleomagnetism of the late Proterozoic Tsezotene Formation of the Mackenzie Mountains, Northwestern Canada; Journal of Geophysical Research, v. 91, p. 4955-4970.

**Park, J.K. and Jefferson, C.W.**
1991: Magnetic and Tectonic History of the Late Proterozoic Upper Little Dal and Coates Lake Groups of northwestern Canada; Precambrian Research, v. 52, p. 1-35.

**Park, J.K., Norris, D.K., and Larochelle, A.**
1989: Paleomagnetism and the origin of the Mackenzie Arc of northwestern Canada; Canadian Journal of Earth Sciences, v. 26, p. 2194-2203.

**Pullaiah, G., Irving, E., Buchan, K.L., and Dunlop, D.J.**
1975: Magnetization changes caused by burial and uplift; Earth and Planetary Science Letters, v. 28, p. 133-143.

**Roots, C.F.**
1987: Regional tectonic setting and evolution of the Late Proterozoic Mount Harper volcanic complex, Ogilvie Mountains, Yukon; Ph.D. thesis, Carleton University, Ottawa, Canada, 218 p.

**Roots, C.F. and Parrish, R.R.**
1988: Age of the Mount Harper volcanic complex, southern Ogilvie Mountains, Yukon; in Radiogenic age and isotope studies: report 2, Geological Survey of Canada, Paper 88-2, p. 29-35.

**Roy, J.L., Reynolds, J., and Sanders, E.**
1973: An alternating field demagnetizer for rock magnetism studies; Publications of the Earth Physics Branch, no. 44(3), p. 37-45.

**Roy, J.L., Sanders, E., and Reynolds, J.**
1972: Un four électrique pour l'étude de propriétés magnetiques des roches; Publication de la Direction de la Physique du Globe, v. 42, p. 229-237.

**Schmidt, P.W.**
1982: Linearity spectrum analysis of multicomponent magnetizations and its application to some igneous rocks from south-eastern Australia; Geological Journal of the Royal Astronomical Society, v. 70, p. 647-665.

**Stewart, J.H.**
1972: Initial deposits of the Cordilleran geosyncline: evidence of Late Precambrian (<850 my) continental separation; Geological Society of America Bulletin, v. 83, p. 1345-1360.
**Thompson, R.I. and Eisbacher, G.H.**
1984: Late Proterozoic rift assemblages, northern Canadian Cordillera; Geological Society of America, Cordilleran Section, Abstracts with Program, v. 16, p. 336.
**Thompson, R.I. and Roots, C.F.**
1982: Ogilvie Mountains project, Yukon: Part A: A new regional mapping program; Geological Survey of Canada, Paper 82-1A, p. 405-411.
**Thompson, B., Mercier, E., and Roots, C.**
1987: Extension and its influence on Canadian Cordilleran passive margin evolution; in Continental Extensional Tectonics, (ed.) M.P. Coward, J.F. Dewey, and P.L. Hancock, Geological Society of London Special Publication 28, p. 409-418.
**Vincenz, S.A. and Bruckshaw, J. McG.**
1960: Note on the probability distribution of a small number of vectors; Proceedings of the Cambridge Philosophical Society, v. 56, p. 21-26.

---

Geological Survey of Canada Project 870002

# Did Laurentia pass over the south pole during earliest Cambrian time?

**John K. Park**
**Continental Geoscience Division**

*Park, J.K., 1992: Did Laurentia pass over the south pole during earliest Cambrian time?; in Current Research, Part E; Geological Survey of Canada, Paper 92-1E, p. 11-22.*

***Abstract***

*A reconnaissance paleomagnetic study of the Ingta and Backbone Ranges formations just above the Cambrian-Precambrian boundary in the Selwyn Basin of the northwestern Cordillera revealed steeply-inclined, normal and reverse magnetic directions. Magnetizations of the Ingta sites are complex and not fully understood, but those of the Backbone Ranges, though complex, indicate a simple reversal stratigraphy. Because the units have similar directions and probably similar ages, 7 direction determinations from 4 sites are averaged together to yield a pole at 91°E, 59°S ($\delta p, \delta m$ = 10°,11°) and a paleolatitude of 69 ± 11°S.*

*The pole extends a trend of Early Cambrian poles to high southern latitudes. A natural extension of this path connects with Neoproterozoic poles, about 180° from Late Cambrian poles, and suggests that North America passed over the south pole during Neoproterozoic-Early Cambrian time.*

***Résumé***

*Une étude paléomagnétique de reconnaissance des formations d'Ingta et de Backbone Ranges, observées immédiatement au-dessus de la limite du Cambrien et du Précambrien dans le bassin de Selwyn de la partie nord-ouest de la Cordillère, a révélé l'existence de directions magnétiques normales et inverses fortement inclinées. Les magnétisations obtenues aux sites de la Formation d'Ingta sont complexes et encore incomplètement comprises, mais celles des sites de la Formation de Backbone Ranges, bien que complexes, indiquent une simple inversion de la stratigraphie. Les unités ayant des directions et probablement des âges similaires, la moyenne de 7 directions mesurées à 4 sites a permis de déterminer un pôle à 91°E, 59°S ($\delta p, \delta m$ = 10°, 11°) et une paléolatitude de 69 ± 11°S.*

*Ce pôle prolonge une tendance des pôles du Cambrien précoce à se situer aux latitudes méridionales élevées. Un prolongement naturel de cette trajectoire rejoint les pôles du Néoprotérozoïque, à environ 180° des pôles du Cambrien tardif, et semble indiquer que l'Amérique du Nord est passée au-dessus du pôle Sud pendant le Néoprotérozoïque-Cambrien précoce.*

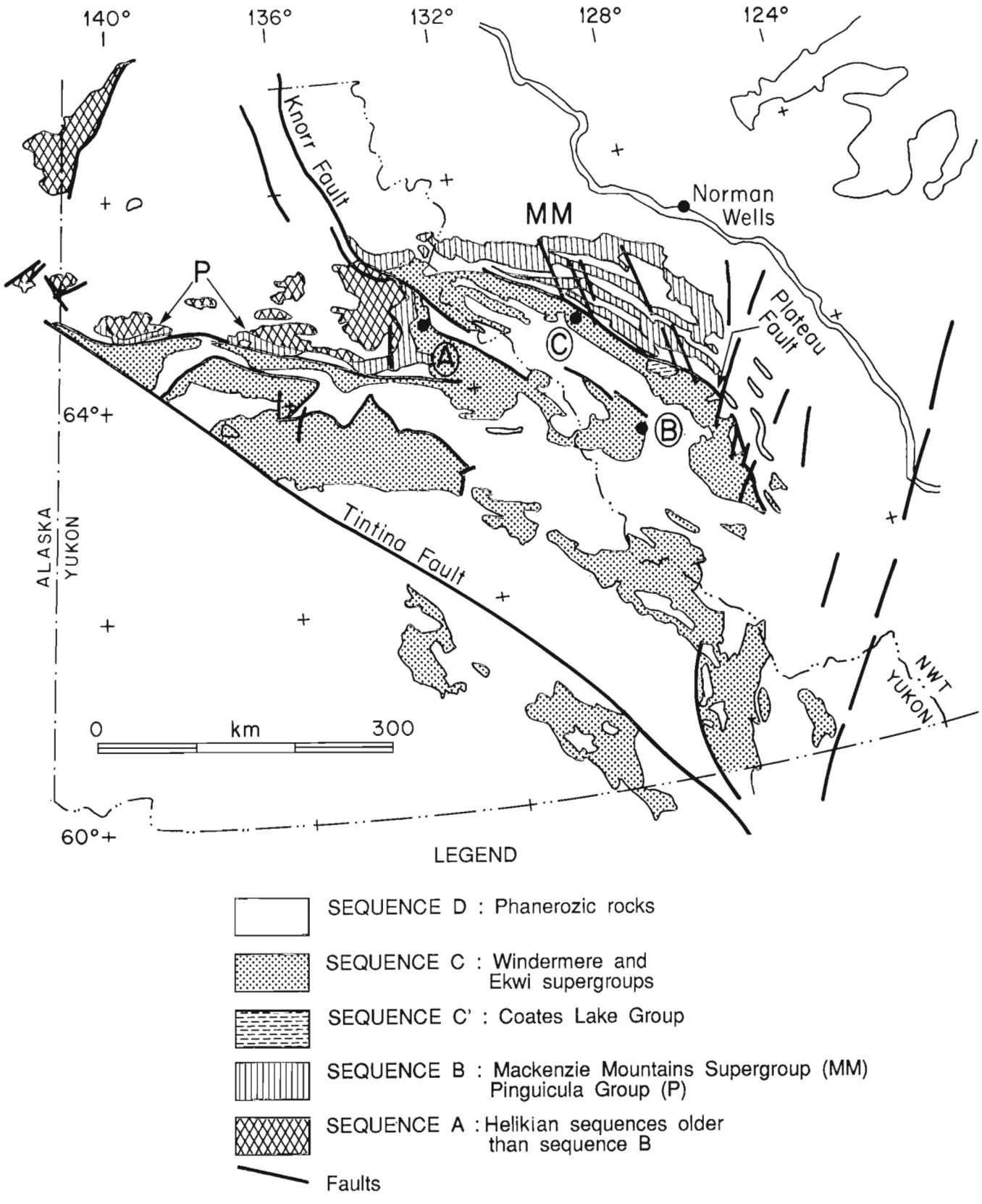


**Figure 1.** Locality map of sampled sections: **A**, Backbone Ranges Formation (section 9, Fritz et al., 1983; sites 22-24; 132°55′W, 64°39′N); **B**, Ingta Formation (section 81AC-15, Aitken, 1989; sites 14-17; 128°38′00″W, 63°21′10″N) (sites 18, 19; 128°41′00″W, 63°22′30″N); **C**, Sekwi Formation (sites 41-43; 129°34′W, 64°29′N). Sequence distribution after Young et al. (1979) and Jefferson (1983).

## INTRODUCTION

Most paleomagnetic studies of North American Cambrian and Late Proterozoic (Neoproterozoic) rock units have revealed low-latitude poles suggesting that North America was situated in equatorial latitudes between about 900 and 500 Ma ago. A few studies have suggested the existence of a Hadrynian (Neoproterozoic) apparent polar wander (APW) path passing over the north pole between ca. 950 and 670 Ma ago (Roy and Robertson, 1978; Morris and Park, 1981); but the high-latitude (above 60°) poles were derived from undated secondary magnetizations. High-latitude poles have usually been assumed to represent late magnetizations acquired during Cretaceous to Recent times. However, evidence has been accumulating from secondary overprint magnetizations of Neoproterozoic units of the Mackenzie Mountains for high-latitude poles possibly relating to Neoproterozoic or Early Cambrian time (Park and Jefferson, 1991). The possibility of such poles is supported by a trend of Late to Early Cambrian poles from low to mid latitudes (Symons and Chiasson, 1991).

The present study reports a high-latitude pole from the Backbone Ranges and Ingta formations, located just above the Cambrian-Precambrian boundary in the Mackenzie and Wernecke mountains of northwestern Canada. It extends the apparent trend of some Early Cambrian poles to higher latitudes and suggests that Laurentia was over the south pole during earliest Cambrian time. It also suggests the possibility of a Late Precambrian apparent polar wander path as proposed in earlier studies (Roy and Robertson, 1978; Morris and Park, 1981), but a path that is better constrained in time and which passes near the south rather than the north pole. Further evidence for this path will be presented in a future paper.

## GEOLOGY

The Mackenzie and Wernecke mountains include some of the best preserved Late Proterozoic strata in North America. These strata are located on the stable platform, which has the oldest rocks (Sequence B units occurring northeast of Plateau Fault; Fig. 1), and in the adjacent Selwyn Basin, which has the youngest (Sequence C). Units of this study, the Ingta and Backbone Ranges formations, are located in the Selwyn Basin (localities A-C, Fig. 1).

There is some controversy regarding the correlation of Neoproterozoic strata in the Selwyn Basin. Fritz (1991) interpreted the Risky and Ingta formations to be part of, or equivalent to, the upper part of the Backbone Ranges Group (Fig. 2). Aitken (1989), on the other hand, considered these formations as being older than the Backbone Ranges Group. However, he did indicate that the Ingta could be a facies-equivalent of the basal Backbone Ranges. The Cambrian-Precambrian boundary had been placed between Ingta and Backbone Ranges formations (Aitken, 1989), but a more likely level is at the contact between the Risky and Ingta formations (Narbonne and Aitken, in press).

The Backbone Ranges Formation is well exposed in the Mackenzie Mountains where the type section is located (Gabrielse et al., 1973). The laterally equivalent Vampire-Backbone Ranges occurs in the Wernecke Mountains where it was sampled below the Sekwi transition from the middle third of the formation (section 9, Fritz et al., 1983). In its type section the Backbone Ranges is thick bedded and consists of two clastic units sandwiching a unit of dolomites (Gabrielse et al., 1973; Fritz, 1982). In some areas a tongue of the Vampire Formation lies between the Backbone Ranges and the Sekwi formations (Fritz, 1982). In the Wernecke Mountains, an unconformity separates Vampire-Backbone Ranges Formation from the underlying Risky Formation. The upper Vampire-Backbone Ranges passes gradationally into carbonates of the overlying Sekwi Formation (locality A, Fig. 1). Three sites were collected from the 224 m thick Vampire-Backbone Ranges unit at locality A: site 22, at the base of the hematitic facies (Osborne et al., 1986), and sites 22 and 23, 1.5 and 28 m below the base, respectively. At these sites beds dip about 19° east-southeast.

Fritz (1991, p. 153) proposes that the Ingta may be a tongue of the Narchilla Formation and that it is equivalent to the lower part of an unnamed formation within the upper portion of the Backbone Ranges Group (Fig. 2). At its type section the Ingta Formation mainly consists of interbedded shale and sandstone (section 81AC-15; Aitken, 1989). Here, Aitken reports an erosional contact with the overlying Backbone Ranges Formation and here and elsewhere there is evidence for erosion at the top of the underlying Risky

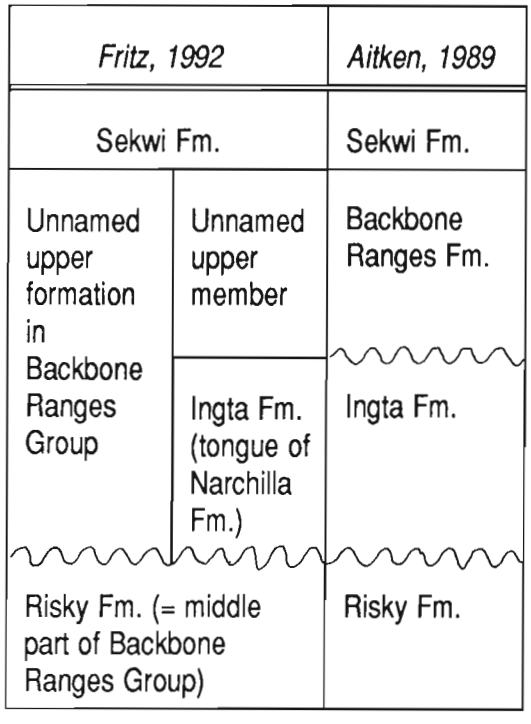


**Figure 2.** Correlation chart.

Formation. Four sites were collected from the type section (locality B), 250 km southeast of the mentioned Vampire-Backbone sites, within the overturned east limb (dipping 105°) of an anticline: site 14, 23.9 m above the base of the Ingta; site 15, 66 m above the base; site 16, 74.7 m above the base; and site 17, 148.5 m above the base. Two sites were obtained from the west limb (dipping 54° west-southwest): site 19 and 18, 15 and 48 m above the base, respectively. All sites are from shale except 17, which is from maroon sandstone.

Additional sites were collected from carbonates of the Sekwi Formation that lie above quartzite of the Backbone Ranges Formation near Palmer Lake (locality C, Fig. 1). Sites 41-43 are located, respectively, about 14 m, 20 m, and 26.5 m above the quartzite, and beds dip 23° south-southeast.

## METHODS

Three to six block samples were obtained at all sites; cores, 2.5 cm in diameter, were drilled from each of these and cut into 2 to 6 specimens, 2.2 cm long, in the laboratory. Block orientations were measured with sun and magnetic compasses.

Experimental work to analyze magnetic components of specimens began with initial measurement of the natural remanent magnetization (NRM) using a Geofyzika Instruments JR-4 fast spinner magnetometer. Specimens were then selected for alternating field (AF), thermal (TH), and chemical (CH) treatments. Alternating field demagnetization was done using an in-house 3-axis tumbler in zero field (±2 nT) (Roy et al., 1973). Specimens were usually demagnetized in incremental steps of 5 to 10 mT and measured after each step. Thermal demagnetization was carried out in near zero field in a large in-house oven (Roy et al., 1972) and in small Schonstedt Instruments TSM-1 ovens. Specimens were heated in incremental steps ranging from 5 to 50°C and measured after each step. Chemical treatment was carried out using the techniques of Park (1970), Roy and Park (1974), and Park and Jefferson (1991). Only 2 specimens from site 17 of the Ingta and 3 from site 22 of the Backbone Ranges Formation were chemically leached. Most leached specimens were thermally demagnetized after leaching was essentially complete.

Magnetic components were determined using vector diagrams, contour plots of directions, and the computer programs LINEFIND (Kent et al., 1983) and Linear Spectrum

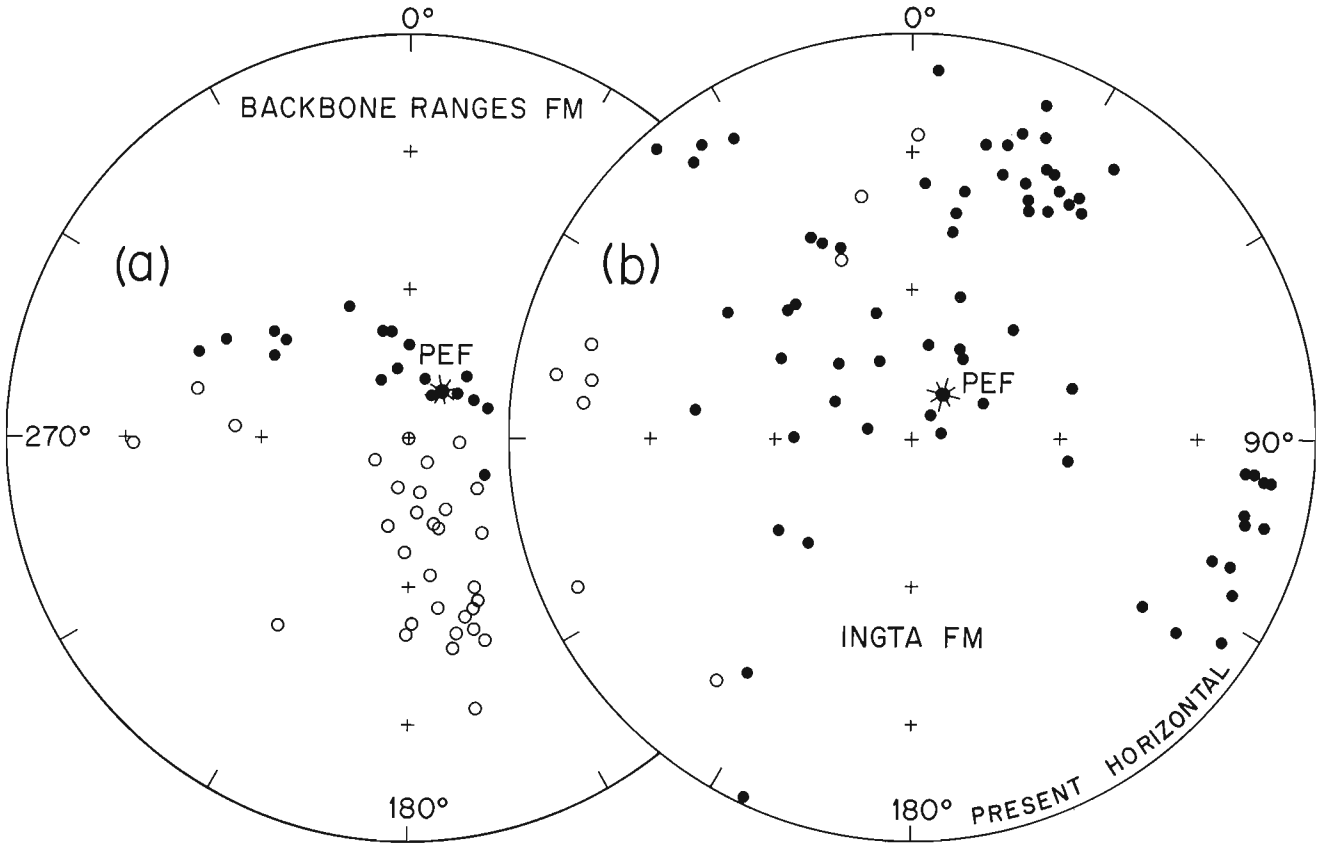


**Figure 3.** Natural remanent magnetization directions of specimens for (a) Backbone Ranges Formation and (b) Ingta Formation. PEF is the present Earth's field direction at the time of sampling in the region. Solid (open) circles are directions plotted on the lower (upper) hemisphere of an equal area projection.

Analysis (Schmidt, 1982). Concentrations of directions on contour plots (DIPS program of Hoek and Diederichs, 1989) indicate the approximate position of a component.

Magnetic minerals were identified by means of standard microscopic identification, scanning electron microscope analysis of elemental compositions, and X-ray analysis. For X-ray work, heavy minerals were concentrated with heavy liquids and the use of a magnetic separator.

## RESULTS AND ANALYSIS

### *Backbone Ranges Formation*

Natural remanent magnetizations of the Backbone Ranges are generally grouped in steeply-inclined, downward and upward directions (Fig. 3a). Upon demagnetization most samples, both before and after tilt-correction, yielded steeply-inclined downward and upward components that are designated A (Table 1). Two other components have low-dipping westerly directions. One of these in site 24 has unblocking temperatures ($T_{UB}$s) less than 100°C and is resistant to alternating fields of at least 50 mT, the other in site 23 has $T_{UB}$s greater than 670°C (Table 1); the magnetic characteristics are indicative of goethite and hematite, respectively. The latter component and the steeply-inclined A components are illustrated in one specimen from site 23 (Fig. 4a). A companion specimen suggests that all components are removed quickly by chemical treatment (Fig. 4b). All three chemically treated specimens from site 23 indicated the removal of a downward-directed A component in under 2 hours of leaching; this probably corresponds to the downward-directed A component removed from thermally treated specimens between 300 and 570°C (Table 1)

**Table 1.** Magnetic directions

| Si | N | Treatment | | | D°,I° | D°,I° | R | k | $\alpha_{95}$° | Co |
|---|---|---|---|---|---|---|---|---|---|---|
| | | AF (mT) | TH (°C) | CH (h) | in-situ | bedding | | | | |
| **Backbone Ranges Formation** | | | | | | | | | | |
| 22 | 4 | - | N-550 | N-125 | 333,+70 | 041,+76 | 2.91 | 23 | 26 | A |
| | 1 | - | 500-580 | - | 284,+40 | 280,+60 | - | - | - | A |
| | 1 | 5->290 | 150-540 | N-245 | 161,-54 | 191,-63 | - | - | - | A |
| | 1 | - | 100-700 | - | 162,-19 | 170,-31 | - | - | - | A |
| 23 | 3 | - | 300-570 | - | 333,+85 | 118,+75 | 2.99 | 250 | 8 | A |
| | 1 | - | 540-580 | - | 089,-87 | 313,-73 | - | - | - | A |
| | 3 | - | N-495 | 2-127 | 153,-79 | 279,-80 | 3.98 | 123 | 8 | A |
| | 6 | - | 550-670 | - | 163,-76 | 260,-79 | 5.89 | 45 | 10 | A |
| | 1 | - | 670-680 | - | 298,+14 | 297,+33 | - | - | - | - |
| 24 | 2 | - | N-100 | - | 271,-33 | 274,-16 | 2.00 | - | - | - |
| | 4 | 5->50 | 100-450 | - | 318,+82 | 095,+78 | 3.74 | 11 | 28 | A |
| | 2 | - | 620-640 | - | 199,-77 | 255,-69 | 1.99 | - | - | A |
| **Ingta Formation** | | | | | | | | | | |
| 14 | 3 | 8-045 | N-450 | - | 279,-02 | 087,+75 | 2.84 | 12 | 37 | A? |
| 15 | 3 | - | N-450 | - | 320,+48 | 078,+26 | 2.93 | 28 | 23 | B? |
| 16 | 4 | 8-020 | 100-560 | - | 103,+17 | 287,-87 | 3.87 | 22 | 20 | A |
| 17 | 5 | N-027 | 100-300 | - | 031,+00 | 000,-23 | 4.81 | 21 | 17 | D |
| | 4 | - | 225-575 | | 011,+37 | 043,-12 | 3.99 | 283 | 6 | C |
| | 5 | - | 300-680 | - | 316,+74 | 087,-02 | 4.87 | 31 | 14 | B |
| 18, 19 no consistent direction in more than 2 samples | | | | | | | | | | |
| *mean A, 7 directions* | | | | | *315,+71* | - | *5.86* | *5* | *29* | |
| | | | | | - | *085,+79* | *6.95* | *116* | *6* | |
| mean A, 3 down directions | | | | | | 088,+79 | 2.98 | 84 | 13 | |
| mean A, 4 up directions | | | | | | 264,-79 | 3.97 | 107 | 9 | |
| **Sekwi Formation** | | | | | | | | | | |
| 41 | 4 | 20-035 | 200-400 | - | 185,+87 | 299,+65 | 3.99 | 314 | 5 | - |
| 42 | 4 | N-050 | 25-400 | - | 056,+86 | 277,+78 | 3.98 | 171 | 7 | - |
| 43 | 2 | - | 250-400 | - | 049,+88 | 258,+67 | 1.98 | - | - | - |
| *mean of 3 in-situ directions* | | | | | *085,+88* | - | *3.00* | *496* | *6* | |
| *mean of 3 bedding directions* | | | | | - | *279,+71* | *2.97* | *58* | *16* | |

Notes: Si, site; *N*, samples; *D°,I°*, declination and inclination of direction with respect to present horizontal (in-situ) and paleohorizontal (bedding); *R*, vector resultant; *k*, precision; $\alpha_{95}$°, half-angle of the circle of 95% confidence about the direction; Co, magnetic component. h, hours in acid. Under 'Backbone Ranges Formation', entries under each site represent different magnetic mineral phases. One-sample determinations not used in mean calculations.

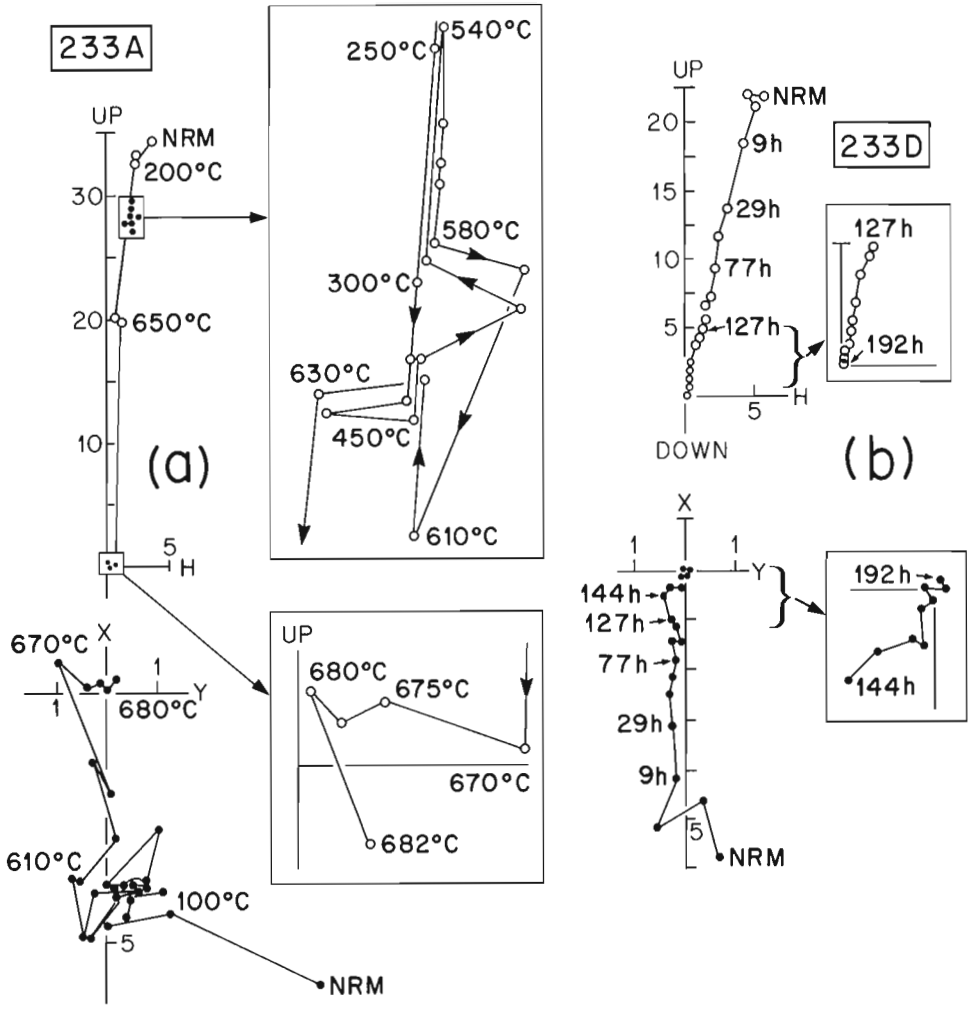


**Figure 4.** Vector diagrams depicting the respective thermal and chemical demagnetization of companion specimens of site 23 of the Backbone Ranges Formation. The regularity of distances between some of the points in the top blow-up of (a) relates to accuracy of measurement. Directions with respect to the present horizontal are plotted on the horizontal (X-Y, solid symbols) and vertical (UP-H, open symbols) planes, where $H = (X^2 + Y^2)^{1/2}$.

(e.g. Fig. 4a). Magnetic characteristics indicate that the upward A components could reside in both magnetite and hematite. A final component in one sample of site 22 is anomalous; it had a lower inclination than the upward A component and an extremely high magnetization of 5 to 10 A/m that did not disappear until between 680 and 700°C.

### *Ingta Formation*

In contrast to the Backbone Ranges Formation, natural remanent magnetizations of the Ingta are generally scattered (Fig. 3b). On thermal and alternating field treatment a variety of magnetic components were revealed (Fig. 5, Table 1). Site 16, alone, revealed only one stable component A under all treatments (alternating field, thermal, thermal after alternating field) (Fig. 5a), and this is steeply-inclined upward after correction for tilt (Table 1). Site 14 appears to yield a similar but downward-directed component; however, because magnetizations are complex, it is not used in the final results. Component A from both sites resides in two major magnetic phases with unblocking temperatures respectively, between about 100-350°C and 350-550°C. Site 15, indicating only the first phase, yielded a component with an entirely different direction than site 16. Site 17, the only red sediment, shows three well-defined components (B, C, D; Fig. 5b, Table 1). Component C is revealed by thermal demagnetization both before and after chemical treatment, suggesting by its magnetic characteristics that it resides in largely insoluble magnetite. Component B is removed between 1700 and 3700 hours of chemical treatment.

Contour plots can be used to support a pre- or postfolding age for directions. Component B corresponds to the main concentration of directions on east-limb plots (sites 14-17; Fig. 6a, b) and may correspond to a concentration of directions on west-limb plots (sites 18, 19; Fig. 6c, d), though individual directions were not directly resolved. On the in situ contour plots of each limb (Fig. 6a, c), the similarity of the steeply-inclined concentration of directions, corresponding

to B, strongly suggests that this component is postfolding. It has $T_{UB}$s into the hematite range. Another concentration, especially prominent from east-limb sites, only has $T_{UB}$s characteristic of magnetite; this corresponds to component A (Fig. 6a, b). The direction of this concentration is similar to the direction of a less-prominent concentration from the west-limb (Fig. 6d) when both limbs are corrected for tilt, although this direction was not defined by vector analysis in west-limb sites. This relation suggests that A is prefolding (see below).

### *Sekwi Formation*

Sites from this unit are very weakly magnetized. Analysis of the natural remanent magnetizations revealed a characteristic steeply-inclined normal component with $T_{UB}$s between 200 and 500°C and resistive coercive forces of 20 to >50 mT, and a probably-viscous, less-stable component. Comparison of in situ and tilt-corrected directions (Table 1) suggests that the major component is syn- or postfolding at the 99% level of the fold test (test statistic $\xi_2 = 1.54$ in situ and 2.92 after tilt correction for $N = 3$, with a minimum $\xi_2$ occurring at 9% unfolding) (McFadden, 1990).

### *Opaque mineral study*

Backbone Ranges sites 23 and 24 show evidence of recent weathering: sulphides occurring in fractures have been mostly altered to limonite and limonite spots are common. One occurrence was found in site 24 of a close association of 1-5 μm cubic pyrite and rutile grains, with pyrite rimmed by goethite. The goethite was identified magnetically (Table 1). Primary (?) detrital hematite and secondary hematite phases are abundant at site 22, but decrease through site 23 to become rare in site 24; these phases are identified with component A. Site 22 is also characterized by detrital hematite clasts containing quartz inclusions. The fine secondary phases include interstitial hematite and pyrite (site 24) associated with quartz, chlorite, and carbonate, and occasional hematite overgrowths (site 22) on silicates, carbonates, and hematite clasts.

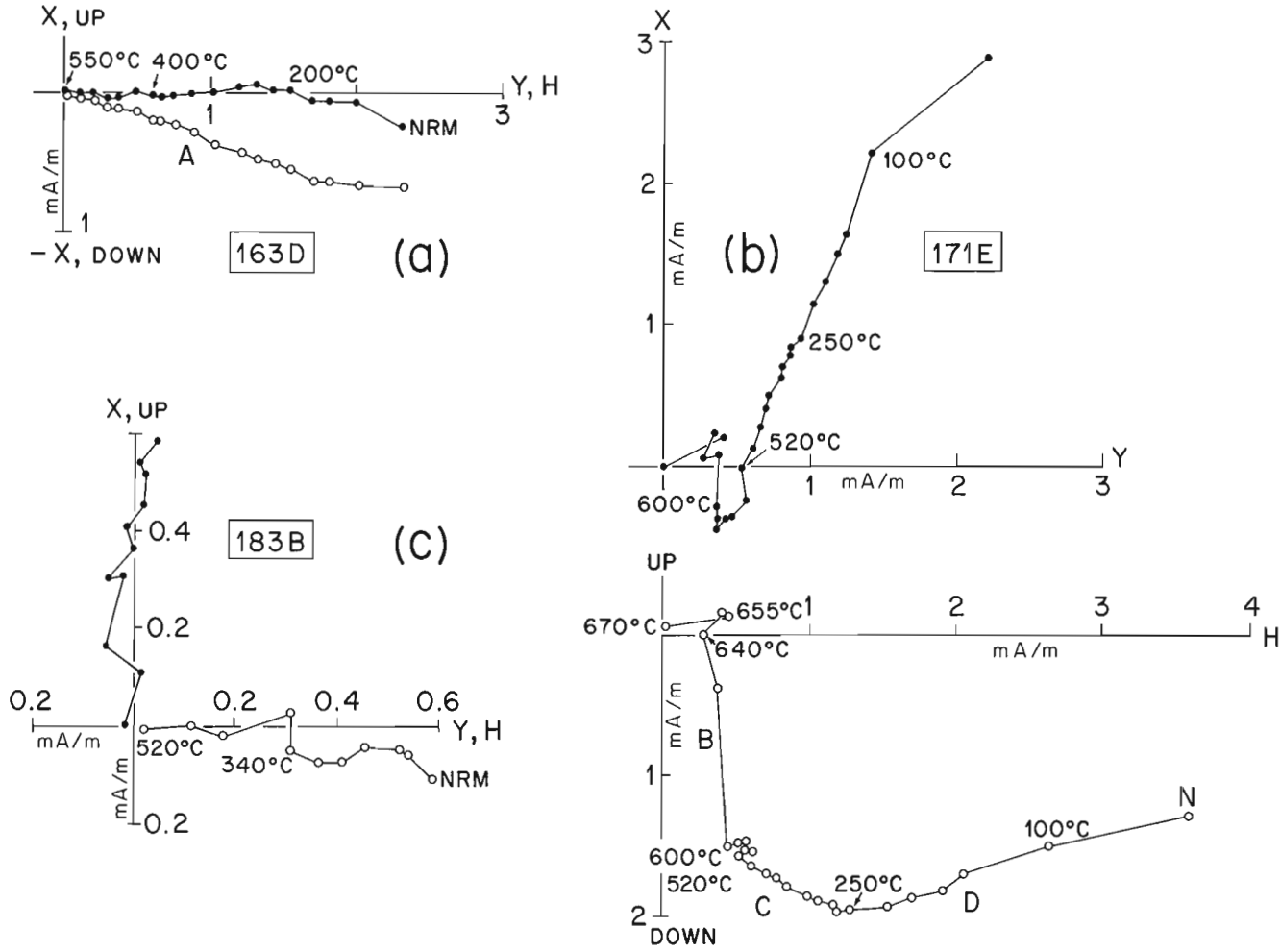


**Figure 5.** Vector diagrams depicting the thermal demagnetization of specimens from sites (a) 16, (b) 17, and (c) 18 of the Ingta Formation. Other explanations given in Figure 4.

In general, except at site 17, primary opaque minerals in the Ingta Formation are sparsely distributed and almost totally altered. As with Backbone Ranges sites, recent weathering is evident, with pyrite altering to goethite and hematite (site 17). The latter may harbour the postfolding B component. Ti-rich opaque phases have changed to rutile in varying degree, with alteration affecting detrital grains, overgrowths, inclusions in chlorite (original biotite?), and interstitial minerals. No hematite was identified by reflection microscopy except in site 17, and none was identified by X-ray analysis except in site 16. Unaltered iron oxide grains (<5 μm), some with minor Ti, were found by scanning electron microscopy to occur in chlorite, albite, and quartz; these may include some of the 'magnetite' grains that harbour A. Finer phases of probable secondary hematite occur as overgrowths and as interstitial material with carbonate; both may contain traces of manganese. Other sulfides found beside pyrite include galena, chalcocite, and chalcopyrite.

## DISCUSSION

### *Evidence for primary magnetization*

Sites from the Backbone Ranges Formation evidence a convincing reversal stratigraphy (Fig. 7). Detrital hematite grains in site 23 record an upward-directed A magnetization but in site 22, depending on the sample, either an upward- or downward-directed A magnetization. Although no detrital hematite grains were detected in site 24, the magnetic characteristics are consistent with an upward-directed A magnetization in hematite. Though rarely resolved, the probable magnetite directions in sites 22 and 23 conform to

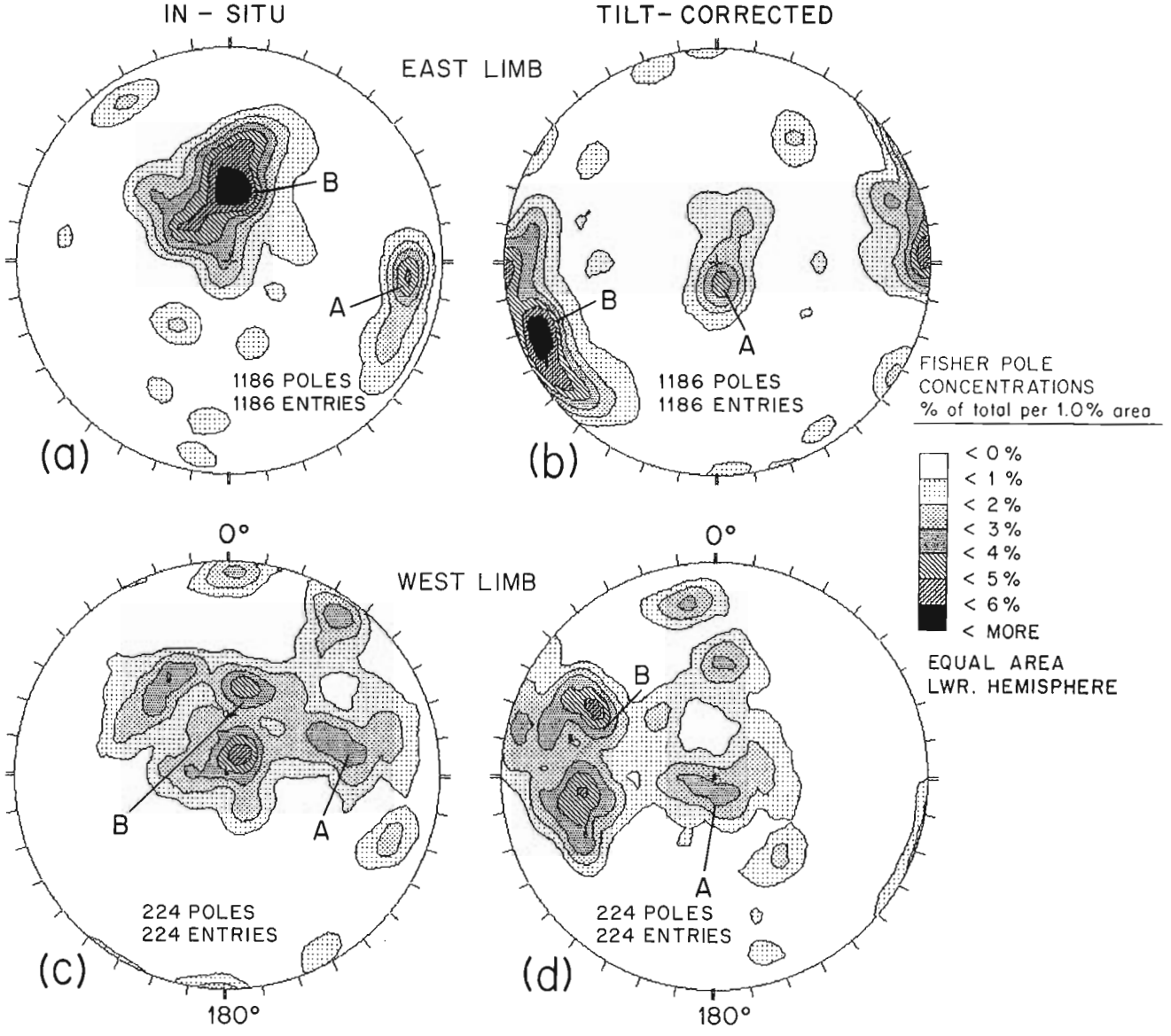


**Figure 6.** Contour plots of all directional data from the Ingta Formation: (a) and (b), east-limb sites 14-17; (c) and (d), west-limb sites 18 and 19. Probable magnetic components are labelled.

the interpreted detrital hematite directions (Fig. 4a, Fig. 7) and suggest that the hematite was formed before or very shortly after deposition.

Besides detrital hematite, sites 22 and 23 also have abundant secondary hematite pigment. Within-sample directions in the secondary hematite pigment conform to those of the detrital hematite (e.g. Table 1: compare N-495°C entry with 550-670°C entry, site 23). Superimposed on the upward-directed magnetic signatures of sites 22 and 23 is a minor downward-directed component, probably indicative of secondary hematite development after the field reversal. Its probable initial removal by chemical treatment indicates that it formed later than the bulk of the hematite pigment. This magnetization is consistent with a reversal of the Earth's field during deposition of site 22, although the stratigraphic relation between samples was not recorded. Development of secondary hematite closely follows deposition of the beds, and is probably coeval with formation of the hematite facies.

Magnetic characteristics of Ingta sites 14 and 16 suggest that component A is carried by magnetite, although only hematite was identified by X-ray analysis at site 16. Other components documented in the Ingta Formation do not agree between sites and probably reflect the extensive alteration.

| Site | Polarity | Magnetic mineral phases | | | |
|---|---|---|---|---|---|
| | | Magnetite | Detrital hematite | Secondary hematite | |
| | | | | before reversal | after reversal |
| 22 | R | ⇓ 500-580 | ? | | ⇓ N-550 |
| | N | | ⇑ 600-660 | ⇑ 150-540 | ⇓ 300-550 |
| 23 | N | ⇑ 540-580 | ⇑ 550-670 | ⇑ 100-495 | ⇓ 300-570 |
| 24 | N | | ⇑ 620-640 | | ⇓ 100-450 |

**Figure 7.** Reversal stratigraphy at the top of the Backbone Ranges Formation. Polarities and unblocking temperatures (°C) of magnetic directions related to the magnetic mineral phases are shown. Owing to the interpretation of a south polar location for Laurentia, a downward-directed (upward-directed) magnetization indicates reverse (normal) polarity. Each block under 'magnetic mineral phases' relates to a different time interval.

Although the site 14 'A' direction is not used in calculating the mean, its reverse polarity to that of site 16 resembles the reverse polarity exhibited in Backbone Ranges sites.

### *Structural control*

A fold test performed on the identified Ingta A direction from contour plots (Fig. 6) supports evidence that A is a primary magnetization by indicating that the direction is prefolding at the 99% level of the test (test statistic $\xi_2 = 2.00$ in situ and 1.88 after tilt correction for $N = 2$, with a minimum $\xi_2$ occurring at 96% unfolding) (McFadden, 1990). A similar test performed on the A directions from both Ingta and Backbone Ranges sites confirms that the direction is prefolding at the 99% level (test statistic $\xi_2 = 3.84$ in situ and 1.78 after tilt correction for $N = 4$, with a minimum $\xi_2$ occurring at 100% unfolding), although only the site 16 result was used from the Ingta. The latter test indicates that the evidence of a possible synfold magnetization in the former is probably not significant.

Structural tilt is relatively easy to account for, but structural rotation is not. An important question is: Have the Ingta and Backbone Ranges localities, and paleopoles derived therefrom, been rotated relative to the stable craton? There is no direct geological evidence for such movement. First, the arcuate shape of the Mackenzie Foldbelt, which includes localities A-C (Fig. 1), does not result from secondary bending during the Cretaceous and early Tertiary Laramide Orogeny, but is, rather, a largely inherited geometry conforming to the arcuate foreland margin (Norris, 1972; Aitken and Long, 1978). This thesis was confirmed by a paleomagnetic study of diabase intruding Neoproterozoic units along the Outer Foldbelt, northeast of the Plateau Fault (Park et al., 1989). Thus, arcuate folds and thrust faults relate to the original geometry (Norris, 1972; Aitken and Long, 1978) and do not imply local rotation took place. Second, minor rotations caused by thrusting along the curved arcs of the original foreland margin may be present but have not been detected.

Proof that structural rotations of sampling localities relative to the craton are negligible or minor comes from an argument involving paleomagnetism. First, no relative rotational movements have been recorded by primary or secondary paleomagnetic directions resolved from widespread units within the Outer Foldbelt, northeast of the Plateau Fault (Park and Aitken, 1986a, b; Park et al., 1989). Second, good agreement between poles of the Little Dal Group of the Outer Foldbelt and the geologically-correlated Reynolds Point Formation of Victoria Island revealed that the Outer Foldbelt as a whole had not rotated relative to the craton (Park and Aitken, 1986a). Third, although it was shown that the Plateau Thrust Sheet, immediately southwest of the stable platform and the Plateau Fault, had been subject to local block rotations during incipient rifting close to 780 Ma ago, comparison of secondary hematitization directions from units on either side of the fault indicated that rotations virtually ended shortly thereafter (Park and Jefferson, 1991), long before deposition of the Ingta and Backbone Ranges units. It would be expected, then, that localities A and B would only

be subject to effects of the Laramide Orogeny. These effects appear to be minimal because, fourth, though localities A and B are located some 250 km apart, A directions from both agree exceptionally well. And, fifth, this agreement is supported by correspondence between prefolding secondary directions in the Risky Formation, below the Backbone Ranges Formation at locality A ($N = 7$; $D,I = 070°, +70°$; $\alpha_{95} = 11°$) and the Blueflower Formation, near locality B ($N = 13$; $D,I = 069°, +69°$; $\alpha_{95} = 4°$) (J. Park, unpub. data, 1992). It should also be noted that because the magnetizations are steeply-directed any minor rotations will have virtually no effect on the results.

### *Relationship between Ingta and Backbone Ranges formations*

The similarity of A directions suggests that the Ingta and Backbone Ranges formations are not separated by a significant time interval, as suggested by Aitken (1989); but more results are required to confirm this. This agreement between directions supports the interpretation that the Ingta is part of the Backbone Ranges Group. Because directions are similar, there are few results, and possible secular variation effects need to be minimized, they are combined. Calculation of the pole ($BR_A$) involves combining 7 determinations from 4 sites (mean pole 91°E, 59°S; $N = 7$; $\delta p,\delta m = 10°,11°$; Fig. 8).

### *Apparent polar wander path*

Symons and Chiasson (1991) recently reviewed the existing Cambrian paleomagnetic data base of North America, selecting poles that met certain criteria. Their selections, less the Sept-Îles complex B pole, which is considered by Tanczyk et al. (1987) to be secondary, are plotted in Figure 8. These poles trend to mid-southern latitudes from the equator, and a great circle through them passes close to $BR_A$ of this study.

I suggest that the simplest apparent polar wander path that can be drawn between Early Cambrian and Neoproterozoic poles passes through high southern latitudes along a near great circle route to meet the well-determined Franklin diabase pole (FD), which is almost reversed from the Late Cambrian mean pole (1Є) of Symons and Chiasson (1991). Most people have considered that FD, dated at 723 ± 3 Ma, and other Neoproterozoic poles of the Cryogenian Period (850-650 Ma) of North America are properly plotted in the vicinity of 1C rather than 180° reversed as in this paper, and that, therefore, there has been little latitudinal movement of the North American craton for at least 300 Ma. Earlier studies interpreted an apparent polar wander path passing over the north pole for a slightly earlier period (ca. 900-700 Ma) (Morris and Roy, 1977; Roy and Robertson, 1978); though this interpretation does not agree with paleomagnetic results from the Mackenzie Mountains Supergroup (e.g. Park and Jefferson, 1991), which appears to fit this time frame. However, some poles cited in the earlier studies and in Park and Jefferson (1991) may relate to the Early Cambrian-Late Precambrian path proposed in this paper. A corollary of this apparent polar wander path is that Laurentia was located over

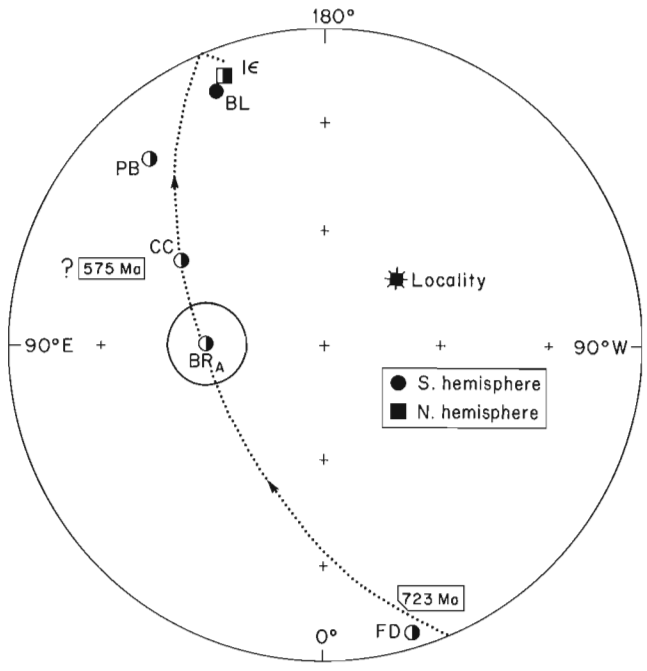


**Figure 8.** Possible Early Cambrian-Late Precambrian apparent polar wander path plotted on a south polar projection. Poles used are $BR_A$, combined Backbone Ranges and Ingta formations (this study); FD, combined normal and reverse pole from Franklin diabases (see Park and Jefferson, 1991 for references); and selected poles of Symons and Chiasson (1991) BL, Buckingham latites (Dankers and Lapointe, 1981); CC, Callander Complex (Symons and Chiasson, 1991); 1Є, Late Cambrian poles, average (see Symons and Chiasson, 1991); and PB, Puerto Blanco volcanoclastics (Barr and Kirschvink, 1983). For PB, Symons and Chiasson (1991) have combined together 11 directions from groups I, II, and III of Dankers and Lapointe (1981). Solid symbols represent normal poles; open symbols, reverse poles; and half-solid symbols, mixed poles. The oval of 95% confidence is shown for pole $BR_A$.

the south pole during Early Cambrian and latest Precambrian time. Pole $BR_A$ indicates that the Mackenzie and Wernecke Mountains were at 69 ± 11°S.

## CONCLUSIONS

1. The Ingta Formation and the unnamed formation (called Backbone Ranges Formation in this paper) within the Backbone Range Group contain prefolding paleomagnetic directions that appear to be primary. Paleomagnetic evidence suggests that site localities have suffered little if any rotation relative to one another or to the craton.
2. The similarity of directions supports the concept that the Ingta Formation and locally overlying Backbone Ranges map units are closely related in time. If an unconformity separates these units, it represents a short duration of time.

3. Mackenzie and Wernecke mountains were at 69 ± 11°S at the time of deposition of the Ingta and Backbone Ranges units.

4. A pole from the combined Ingta and Backbone Ranges formations suggests a continuation of a proposed Early Cambrian apparent polar wander path to higher latitudes and suggests the possibility that Laurentia passed over the south pole in the Early Cambrian.

## ACKNOWLEDGMENTS

I would like to thank J.D. Aitken (now retired from the Geological Survey of Canada) for arranging field trips in 1976 and 1988, for camp facilities and logistical support, for selecting geological sections to sample, and for geological advice. Some of the measurements were made by Y. Bouchard in 1984 and W. Lewis in 1989. R. Langridge of Queen's University was responsible for improvements to measuring and analysis software. A. Rafeek drafted the illustrations. Crushing of rock samples and subsequent heavy mineral separation was done by B. Machin (Mineral Resources Division). X-ray analysis of powders was carried out by R. Dilabio (Terrain Sciences Division). Identification of opaque mineral phases was aided by L. Radburn (Mineral Resources Division) on the scanning electron microscope. I thank W.H. Fritz (Institute of Sedimentary and Petroleum Geology), who checked the geological discussion; G.M. Narbonne (Queen's University), who supplied some geological information; and K.L. Buchan of my division, who reviewed the manuscript.

## REFERENCES

**Aitken, J.D.**
1989: Uppermost Proterozoic formations in central Mackenzie Mountains, Northwest Territories; Geological Survey of Canada, Bulletin 368, p. 1-26.

**Aitken, J.D. and Long, D.G.F.**
1978: Mackenzie tectonic arc - reflection of early basin configuration; Geology, v. 6, p. 626-629.

**Barr, T.D. and Kirschvink, J.L.**
1983: The paleoposition of North America in the early Paleozoic: new data from the Carborca sequence in Sonora, New Mexico; Eos, v. 64, p. 689-690.

**Dankers, P. and Lapointe, P.**
1981: Paleomagnetism of Lower Cambrian volcanics and a cross-cutting Cambro-Ordovician diabase dike from Buckingham (Quebec); Canadian Journal of Earth Sciences, v. 7, p. 1174-1186.

**Fritz, W.H.**
1982: Vampire Formation, a new Upper Precambrian (?)/Lower Cambrian Formation, Mackenzie Mountains, Yukon and Northwest Territories; in Current Research, Part B; Geological Survey of Canada, Paper 82-1B, p. 83-92.
1991: Cambrian assemblages; in Geology of the Cordilleran Orogen in Canada, (ed.) H. Gabrielse and C.J. Yorath; Geological Survey of Canada, no. 4, p. 155-183 (*also* Geological Society of America, The Geology of North America, v. G-2).

**Fritz, W.H., Narbonne, G.M., and Gordey, S.P.**
1983: Strata and trace fossils near the Precambrian-Cambrian boundary, Mackenzie, Selwyn, and Wernecke Mountains, Yukon and Northwest Territories; in Current Research, Part B; Geological Survey of Canada, Paper 83-1B, p. 365-375.

**Gabrielse, H., Blusson, S.L., and Roddick, J.A.**
1973: Geology of Flat River, Glacier Lake, and Wrigley Lake map-areas, District of Mackenzie and Yukon Territory; Geological Survey of Canada, Memoir 366, p. 1-153.

**Hoek, E. and Diederichs, M.**
1989: DIPS, version 2.2; Users Manual, advanced version, Rock Engineering Group, Department of Civil Engineering, University of Toronto, Toronto, Canada.

**Jefferson, C.W.**
1983: The Upper Proterozoic Redstone Copper Belt, Mackenzie Mountains, N.W.T; Ph.D Thesis, The University of Western Ontario, London, Ontario, 445 p.

**Kent, J.T., Briden, J.C., and Mardia, K.V.**
1983: Linear and planar structure in ordered multivariate data as applied to progressive demagnetization of palaeomagnetic remanence; Geophysical Journal of the Royal Astronomical Society, v. 75, p. 593-621.

**McFadden, P.L.**
1990: A new fold test for palaeomagnetic studies; Geophysical Journal International, v. 103, p. 163-169.

**Morris, W.A., and Park, J.K.**
1981: Correlation of Upper Proterozoic strata in the Cordillera: paleomagnetism of the Tsezotene sills and the Little Dal lavas; in Proterozoic Basins of Canada, (ed.) F.H.A. Campbell; Geological Survey of Canada, Paper 81-10, p. 73-78.

**Morris, W.A. and Roy, J.L.**
1977: Discovery of the Hadrynian polar track and further study of the Grenville problem; Nature, v. 266, p. 689-692.

**Narbonne, G.M. and Aitken, J.D.**
in press: Neoproterozoic of the Mackenzie Mountains, northwestern Canada; Proceedings of the 29th International Geological Congress, Kyoto, Japan.

**Norris, D.K.**
1972: *En échelon* folding in the northern Cordillera of Canada; Bulletin of Canadian Petroleum Geology, v. 20, p. 634-642.

**Osborne, D.T., Narbonne, G.M., and Carrick, J.**
1986: Stratigraphy and economic potential of Cambrian-Precambrian boundary strata, Wernecke Mountains, east-central Yukon; in Yukon Geology, v. 1, Exploration and Geological Services Division, Indian and Northern Affairs Canada, p. 131-138.

**Park, J.K.**
1970: Acid leaching of red beds and the relative stability of the red and black components; Canadian Journal of Earth Sciences, v. 7, p. 1086-1092.

**Park, J.K. and Aitken, J.D.**
1986a: Paleomagnetism of the Katherine Group in the Mackenzie Mountains: implications for post-Grenville (Hadrynian) apparent polar wander; Canadian Journal of Earth Sciences, v. 23, p. 308-323.
1986b: Paleomagnetism of the Late Proterozoic Tsezotene Formation of northwestern Canada; Journal of Geophysical Research, v. 91, p. 4955-4970.

**Park, J.K. and Jefferson, C.W.**
1991: Magnetic and tectonic history of the Late Proterozoic Upper Little Dal and Coates Lake Groups of Northwestern Canada; Precambrian Research, v. 52, p. 1-35.

**Park, J.K., Norris, D.K., and Larochelle, A.**
1989: Paleomagnetism and the origin of the Mackenzie Arc of northwestern Canada; Canadian Journal of Earth Sciences, v. 26, p. 2194-2203.

**Roy, J.L. and Park, J.K.**
1974: The magnetization process of certain red beds: vector analysis of chemical and thermal results; Canadian Journal of Earth Sciences, v. 11, p. 437-471.

**Roy, J.L. and Robertson, W.A.**
1978: Paleomagnetism of the Jacobsville Formation and the apparent polar path for the interval -1100 to -670 m.y. for North America; Journal of Geophysical Research, v. 83, p. 1289-1304.

**Roy, J.L., Reynolds, J., and Sanders, E.**
1973: An alternating demagnetizer for rock magnetism studies; Publications of the Earth Physics Branch, Canada; no. 44(3), p. 37-45.

**Roy, J.L., Sanders, E., and Reynolds, J.**
1972: Un four électrique pour l'étude des propriétés magnétiques des roches; Publication de la direction de la physique du globe; no. 42, p. 229-237.

**Schmidt, P.W.**
1982: Linearity spectrum analysis of multicomponent magnetizations and its application to some igneous rocks from southeastern Australia; Geological Journal of the Royal Astronomical Society, v. 70, p. 647-665.

**Symons, D.T.A. and Chiasson, A.D.**
1991: Paleomagnetism of the Callander Complex and the Cambrian apparent polar wander path for North America; Canadian Journal of Earth Sciences, v. 28, p. 355-363.

**Tanczyk, E.I., Lapointe, P., Morris, W.A., and Schmidt, P.W.**
1987: A paleomagnetic study of the layered mafic intrusion at Sept-Îles, Quebec; Canadian Journal of Earth Sciences, v. 24, p. 1431-1438.

**Young, G.M., Jefferson, C.W., Delaney, G.D., and Yeo, G.M.**
1979: Middle and Late Proterozoic evolution of the northern Canadian Cordillera and Shield; Geology, v. 7, p. 125-128.

Geological Survey of Canada Project 870002

# Petrography, geochemistry and utilization potential of the Division Mountain coal occurrence, Yukon Territory

**A.P. Beaton[1], A.R. Cameron, and F. Goodarzi**
**Institute of Sedimentary and Petroleum Geology, Calgary**

*Beaton, A.P., Cameron, A.R., and Goodarzi, F., 1992: Petrography, geochemistry and utilization potential of the Division Mountain coal occurrence, Yukon Territory; in Current Research, Part E; Geological Survey of Canada, Paper 92-1E, p. 23-32.*

***Abstract***

*Laberge Group rocks (Jurassic) exposed near Division Mountain in Yukon contain a thick coal zone with economic potential. The main seam was sampled in detail from a shallow trench and analyzed for petrographic and geochemical composition as well as utilization potential, including coalbed methane and "oil from coal" possibilities. The main seam (Cairnes Seam) is 15.6 m thick, and contains two partings, 92 and 54 cm thick. Coal rank is high volatile bituminous C ($R_{o\,max}$ 0.60-0.64%). Petrographically, on a mineral-matter-free basis, the coals average 54% vitrinite, which is predominantly desmocollinite. Liptinites average 10% and inertinites average 36%. Sulphur content is low (<0.46%), and overall ash content averages 20%, although thick units within the seam contain less ash. Most elements are associated with high-ash coal and mineral matter; however, Ca, Sr, and Zn show elevated concentrations in low-ash samples. Rock-Eval pyrolysis suggests low hydrocarbon potential, although this may be misleading owing to the weathered nature of the samples.*

***Résumé***

*Les roches du Groupe de Laberge (Jurassique) affleurant près du mont Division au Yukon contiennent une épaisse zone charbonnière qui pourrait être exploitable. Un échantillonnage détaillé à partir d'une tranchée peu profonde a été effectué dans la principale couche de charbon; le matériel a ensuite été analysé pour déterminer la composition pétrographique et géochimique des échantillons ainsi que les possibilités d'exploitation du gisement, y compris l'extraction du méthane des couches de charbon et la production de «pétrole à partir du charbon». La principale couche de charbon (couche de Cairnes) a 15,6 m d'épaisseur et présente deux minces intercalations stériles, l'une de 92 cm et l'autre de 54 cm d'épaisseur. Le charbon est de rang «bitumineux C très volatil» ($R_{o\,max}$ 0,60–0,64 %). La pétrographie des charbons, établie sur une base exempte de matières minérales, indique qu'ils contiennent en moyenne 54 % de vitrinite, principalement sous forme de desmocollinite. Les liptinites représentent en moyenne 10 % du contenu et les inertinites, 36 %. La proportion de soufre est faible (<0,46 %) et la teneur globale en cendres se situe en moyenne à 20 %, bien que d'épaisses unités de la couche renferment moins de cendres. La plupart des éléments sont associés au charbon riche en cendres et aux matières minérales; les éléments Ca, Sr et Zn sont toutefois présents en concentrations élevées dans les échantillons à faible teneur en cendres. Les résultats de la pyrolyse Rock-Eval suggèrent un faible potentiel en hydrocarbures, mais ceci n'est peut-être pas le cas, compte tenu de la forte altération des échantillons.*

[1] Department of Geology, University of Western Ontario, London, Ontario

## INTRODUCTION

Coal deposits of the Jurassic-Cretaceous Whitehorse Trough (Fig. 1) are currently under investigation to assess coal quality, geochemistry, mineralogy, and alternative fuel potential (i.e., coalbed methane and "oil from coal").

Coal of the Jurassic Laberge Group outcrops at two localities above the Nordenskiold River Valley in the Braeburn-Kynocks coal district (Cairnes, 1910). This report describes the petrography, rank, inorganic geochemistry, mineralogy, and Rock-Eval characteristics of one of these outcrops, which occurs approximately 4 km north of Division Mountain along Teslin Creek (Fig. 2, 3). On the basis of six drillholes and extensive bulldozer trenching by Arjay Kirker Resources Ltd. in 1972, it was estimated that the Cairnes Seam and overlying and underlying seams contain 2.8 million tons of bituminous coal in place (Phillips, 1973). The Cairnes Seam dips 65 to 70° southwest, but becomes less steep along strike toward the south. Standard coal tests (ash, sulphur, volatile matter, fixed carbon, and moisture) were performed as a part of the 1972-1973 work; however, reflectance, petrography, and elemental composition were not investigated.

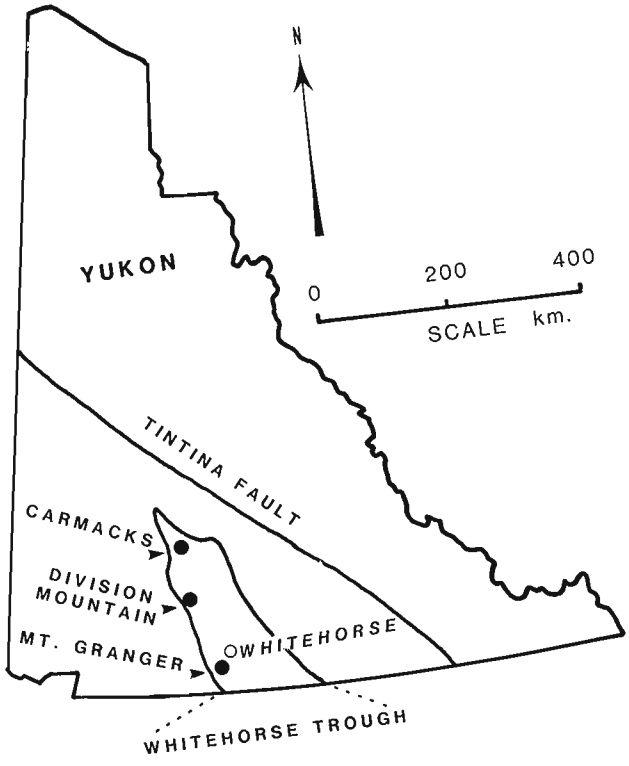


**Figure 1.** Location map, showing the Whitehorse Trough, the town of Whitehorse, and three major coal deposit sites: Mt. Granger, Carmacks, and Division Mountain.

## GENERAL GEOLOGY

Thick coal seams occur throughout the Whitehorse Trough in strata of the Jurassic Laberge Group and the overlying Lower Cretaceous Tantalus Formation. The Laberge Group consists primarily of sandstone and conglomerate; however, Cairnes (1910) noted that, in the Division Mountain area, the upper portion of the Laberge Group consists of coarse sand, with shaly beds and coal-bearing sequences. At this locality, the coal-bearing strata occur approximately 500 m below the base of the Tantalus Formation. Dickie and Hein (1988) described the facies within the Laberge Group conglomerates around Braeburn as alluvial fan progradation deposits and braided channel deposits. Mid-Cretaceous deformation has folded and faulted the Laberge Group along northwest-southeast-trending axes. The Cairnes Seam occurs

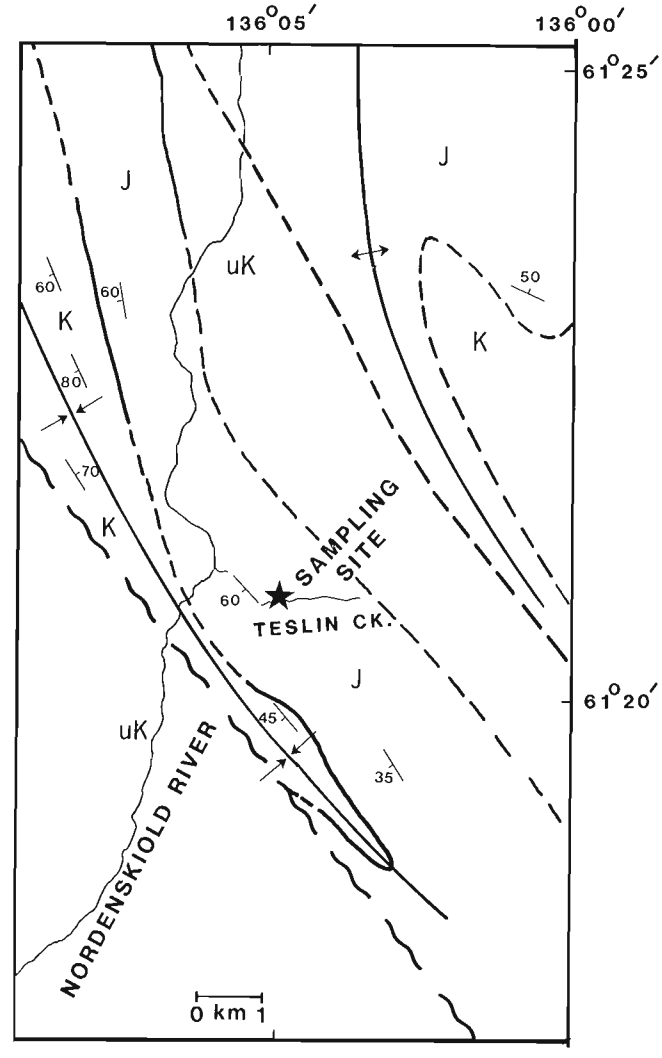


**Figure 2.** Sample location and general geology of the Division Mountain coal deposit. J, Jurassic Laberge Group; uK, Middle to Upper Cretaceous igneous rocks; K, Lower Cretaceous Tantalus Formation. (Geology compiled from Cairnes, 1910; Templeman-Kluit, 1974; and Carne, 1990.)

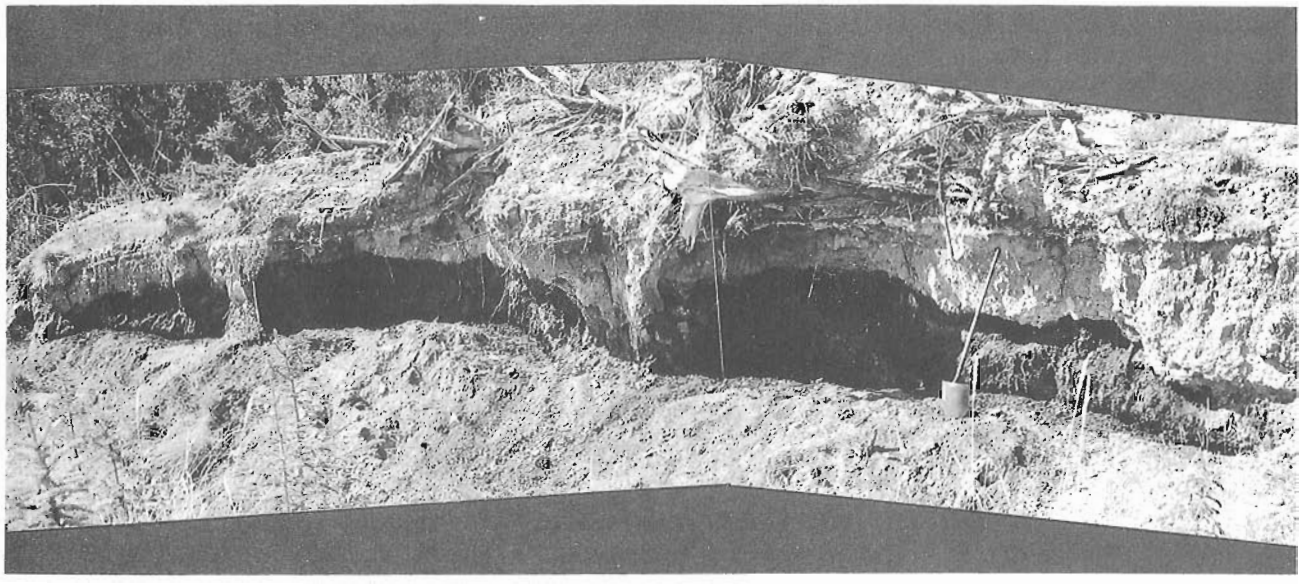

**Figure 3.** Photograph of the trench in the Cairnes Seam at Division Mountain, from which the coal samples were obtained.

in the Laberge Group and is exposed near Teslin Creek, along the eastern limb of a syncline. Phillips (1973) reported Cretaceous Hutshi Group andesite dykes and sills intruding the Laberge Group, both parallel to and cutting across the coal and shale units. Intrusive rocks were not observed in the trench or in Laberge Group strata near the trench. The bedrock in the area is overlain by 2 to 3 m of till, and an ash layer 8 to 12 cm thick (Cairnes, 1910).

## SAMPLING AND ANALYTICAL METHODS

In 1990, GSC personnel collected a series of samples from a trench that exposed coals of the Cairnes Seam at Division Mountain. The samples were collected either as channel samples, with breaks based on changes in apparent lithology, or, in zones of uniform lithology, at 50 cm intervals. Roof, floor, and parting rocks were sampled individually. A total of 41 samples was collected (each sample stored in a sealed plastic bag), representing a continuous profile of the coal zone which is 15.6 m thick (Fig. 4).

Individual samples were crushed to -20 mesh (850 μm) and a 10 g representative split was removed for petrographic examination. A 35 g representative split was crushed to -100 mesh (150 μm) for chemical (elemental and proximate) and Rock-Eval analyses.

Petrographic composition was determined by counting 500 points on the -20 mesh splits, each mounted as an epoxy pellet and polished, using both white and ultraviolet reflected light examination and oil immersion techniques (Bustin et al., 1985). Average maximum vitrinite reflectance was determined, based on 50 points on vitrinite type 1 from selected samples under standard conditions (monochromatic light, 546 nm., $n_0$ immersion oil = 1.52; Stach et al., 1982).

The -100 mesh samples were analyzed for ash content by combustion at 750°C as per A.S.T.M.(1979) standards; sulphur contents were determined utilizing a LECO[1] sulphur analyser. Elemental composition was determined by Instrumental Neutron Activation analysis (INAA), Atomic Absorption, and DC plasma spectrometry techniques. Rock-Eval pyrolysis was performed on a 10 mg sample split according to the method outlined by Fowler et al. (1991).

Six composites were made, representing the main coal benches within the coal zone (Fig. 4, Table 1). A -100 mesh portion was analyzed for "proximate" composition (i.e., moisture, sulphur, ash, fixed carbon, and volatile matter). These composites were also low-temperature-ashed in an International Plasma Corporation LFE RF oxygen plasma asher, at 100°C. The ash was then analyzed in a Phillips PW 1700 automated powder X-ray diffractometer for mineralogical composition.

## RESULTS

### *Petrography*

A detailed maceral composition of the complete column sample of the Cairnes Seam is presented in Table 1. Maceral group abundances [on a mineral-matter-free basis (mmf)] and ash composition are shown in Figure 4. Photomicrographs of maceral types and associations typical of the Division Mountain deposit are shown in Figure 5.

[1] registered trademark

Vitrinite (mmf) comprises 54% of the seam. Three varieties of vitrinite were distinguished, based on morphology and reflectance. These are identified as vitrinite A (telocollinite), vitrinite B (desmocollinite), and vitrodetrinite. Vitrinite B occurs as a groundmass, commonly hosting liptinite, inertodetrinite, vitrodetrinite, and mineral matter. Vitrinite A occurs in relatively homogeneous bands and lenses and has a higher overall reflectance than vitrinite B. In this study, two types of vitrinite A were distinguished, one shows very faint remnant cell structure while the other is structureless. The unstructured vitrinite (type 1) commonly showed a slightly higher reflectance than its structured counterpart (type 2). Vitrodetrinite consists of variably sized fragments of vitrinite, commonly angular, which were probably derived from plant material physically comminuted in the peat swamp. Vitrodetrinite, inertodetrinite, and liptodetrinite associated with vitrinite B may have originated in a plant community with a significant proportion of grasses and reeds with little structural material and, therefore, could be indicative of low-lying wetland (marsh) flora.

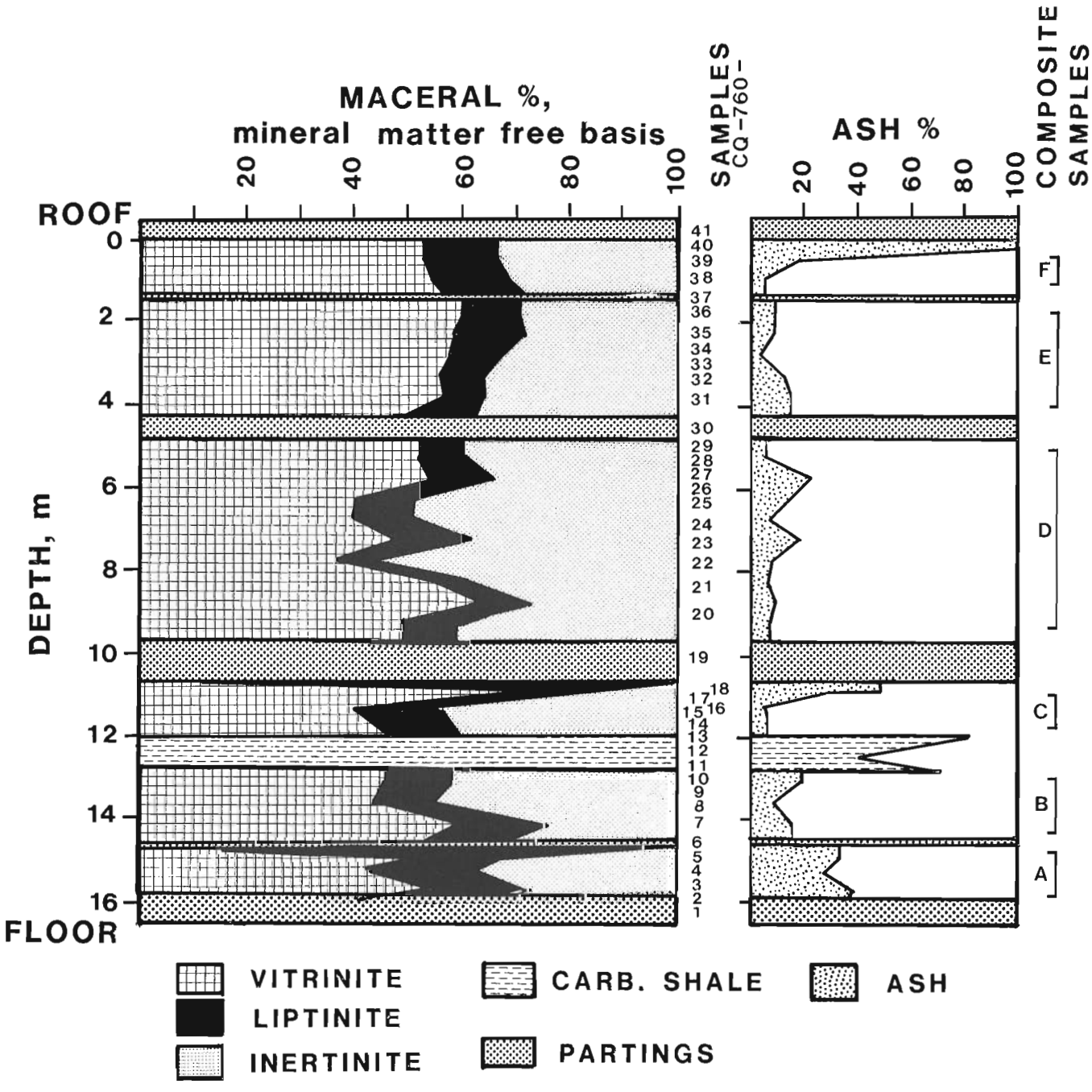


**Figure 4.** Maceral group profile (mineral-matter-free basis) and ash contents for the Cairnes Seam. Composite samples are also shown (samples 760-A to F).

**Table 1.** Petrographic composition (volume %) of the Cairnes Seam, on an 'as received' basis. The asterisks (*****) delineate the bottoms and tops of the coal benches, based on major partings

| | | Vitrinite Group (Vol. %) | | | | | Liptinite Group (Vol. %) | | | | | | | | Inertinite Group (Vol. %) | | | | | |
|---|---|---|---|---|---|---|---|---|---|---|---|---|---|---|---|---|---|---|---|---|
| Thickness (cm) | Sample CQ-760- | VIT. A type 1 | VIT. A type 2 | VIT. B | V. DET | TOT. V | SPOR | CUT | RESIN | L. DET | Bt | Al | Exs | TOT. L | SEMIFUS | FUS. | I. DET | TOT. I | MIN. (vol. %) | ASH % (as. rec.) |
| ***** | 41 Roof | | | | | | | | | | | | | | | | | | | 83.7 |
| 29 | 40 | 19.8 | 5.6 | 13.8 | 3.6 | 42.8 | 3.8 | 2.4 | 1.2 | 2.6 | 1.4 | tr | | 11.4 | 5.0 | 18.0 | 4.2 | 27.2 | 18.6 | 8.3 |
| 50 | 39 | 20.2 | 4.0 | 25.2 | 1.6 | 51.0 | 6.0 | 2.8 | 1.4 | 3.4 | 0.6 | | | 14.2 | 5.0 | 20.0 | 4.2 | 29.2 | 5.6 | 15.9 |
| 50 | 38 | 27.0 | 4.0 | 21.2 | 1.0 | 53.2 | 5.8 | 0.8 | 4.4 | 3.6 | 0.4 | tr | tr | 15.0 | 4.0 | 18.0 | 2.6 | 24.6 | 7.2 | 16.6 |
| 3 | 37 Ptg. | | | | | | | | | | | | | | | | | | | 83.6 |
| 27 | 36 | 19.2 | 2.6 | 32.4 | 0.8 | 55.0 | 5.8 | 0.8 | 1.2 | 1.8 | 0.4 | | | 10.0 | 5.0 | 19.6 | 1.8 | 26.4 | 8.6 | 13.9 |
| 50 | 35 | 18.6 | 3.8 | 30.6 | 0.8 | 53.8 | 4.8 | 1.8 | 3.0 | 2.8 | tr | | tr | 12.4 | 2.8 | 20.6 | 2.2 | 25.6 | 8.2 | 16.7 |
| 50 | 34 | 17.4 | 4.0 | 32.8 | 0.8 | 55.0 | 5.0 | 1.2 | 0.8 | 3.4 | tr | | | 10.4 | 12.8 | 16.6 | 1.4 | 30.8 | 3.8 | 13.5 |
| 50 | 33 | 19.8 | 2.6 | 24.6 | 1.8 | 48.8 | 4.4 | 0.0 | 1.2 | 1.4 | 0.4 | | | 7.4 | 11.2 | 17.0 | 3.2 | 31.4 | 12.4 | 20.3 |
| 50 | 32 | 20.6 | 3.0 | 23.0 | 1.6 | 48.2 | 3.8 | 0.8 | 1.2 | 1.4 | tr | tr | | 7.2 | 6.0 | 22.6 | 1.6 | 30.2 | 14.4 | 20.2 |
| 50 | 31 | 22.7 | 4.7 | 14.7 | 2.7 | 44.8 | 5.5 | 1.7 | 3.0 | 1.7 | tr | tr | | 11.9 | 5.5 | 27.0 | 1.5 | 34.0 | 9.3 | 18.0 |
| *****54 | 30 Ptg. | | | | | | | | | | | | | | | | | | | 84.8 |
| 43 | 29 | 22.0 | 3.5 | 22.0 | 1.7 | 49.2 | 5.5 | 0.7 | 1.5 | 1.2 | | | | 8.9 | 6.7 | 28.2 | 1.7 | 36.6 | 5.3 | 14.8 |
| 50 | 28 | 14.2 | 2.7 | 24.7 | 1.0 | 42.6 | 4.5 | 0.5 | 2.5 | 2.2 | tr | | | 9.7 | 1.5 | 21.5 | 3.2 | 26.2 | 21.5 | 30.6 |
| 50 | 27 | 11.2 | 2.2 | 21.2 | 0.2 | 34.8 | 5.0 | 1.0 | 2.7 | 1.0 | | | | 9.7 | 5.5 | 33.0 | 2.5 | 41.0 | 14.5 | 23.2 |
| 50 | 26 | 8.7 | 1.2 | 26.5 | 0.5 | 36.9 | 6.5 | 0.7 | 1.7 | 2.0 | | | | 10.9 | 6.7 | 36.0 | 2.0 | 44.7 | 7.5 | 14.0 |
| 50 | 25 | 14.5 | 2.7 | 22.2 | 0.0 | 39.4 | 7.7 | 1.5 | 1.2 | 1.2 | tr | | | 11.6 | 3.0 | 26.5 | 1.7 | 31.2 | 17.8 | 18.4 |
| 50 | 24 | 11.5 | 1.5 | 21.7 | 0.0 | 34.7 | 4.0 | 0.7 | 2.0 | 0.7 | | | | 7.4 | 10.5 | 38.5 | 1.2 | 50.2 | 7.7 | 14.2 |
| 50 | 23 | 15.5 | 8.2 | 26.5 | 1.5 | 51.7 | 3.2 | 1.0 | 1.2 | 1.2 | | | | 6.6 | 6.0 | 24.7 | 4.7 | 35.4 | 6.3 | 11.8 |
| 50 | 22 | 25.2 | 12.7 | 19.7 | 0.2 | 57.8 | 4.2 | 1.7 | 1.5 | 1.2 | | | | 8.6 | 3.0 | 18.2 | 2.7 | 23.9 | 9.7 | 22.7 |
| 50 | 21 | 15.0 | 5.2 | 25.2 | 0.7 | 46.1 | 5.5 | 0.2 | 2.2 | 1.0 | | | | 8.9 | 6.0 | 30.2 | 2.0 | 38.2 | 6.8 | 16.8 |
| 50 | 20 | 16.7 | 3.2 | 29.2 | 0.5 | 49.6 | 5.5 | 0.7 | 1.0 | 1.7 | | | | 8.9 | 8.7 | 21.2 | 1.5 | 31.4 | 10.1 | 20.6 |
| *****92 | 19 Ptg. | | | | | | | | | | | | | | | | | | | 88.0 |
| 24 | 18 | 8.0 | 5.2 | 9.2 | 3.0 | 25.4 | 7.5 | 1.0 | 1.0 | 3.7 | | | | 13.2 | 1.7 | 10.5 | 2.0 | 14.2 | 47.2 | 47.2 |
| 3 | 17 | 33.2 | 4.2 | 15.0 | 0.0 | 52.4 | 3.2 | 0.0 | 0.2 | 0.5 | | | | 3.9 | 3.7 | 9.2 | 1.0 | 13.9 | 29.8 | 31.9 |
| 36 | 16 | 24.0 | 3.5 | 17.2 | 1.0 | 45.7 | 3.5 | 0.5 | 1.0 | 1.5 | | | | 6.5 | 3.7 | 37.5 | 1.7 | 42.9 | 4.9 | 13.8 |
| 10 | 15 | 15.0 | 2.2 | 20.7 | 0.0 | 37.9 | 10.0 | 1.7 | 1.7 | 2.2 | | | | 15.6 | 6.5 | 32.0 | 1.7 | 40.2 | 6.3 | 19.5 |
| 54 | 14 | 15.0 | 2.0 | 24.2 | 1.2 | 42.4 | 7.5 | 1.2 | 1.2 | 2.5 | | | | 12.4 | 4.7 | 27.5 | 4.2 | 36.4 | 8.8 | 19.4 |
| 10 | 13 C. sh | | | | | | | | | | | | | | | | | | | 82.9 |
| 40 | 12 C. sh | | | | | | | | | | | | | | | | | | | 41.6 |
| 25 | 11 C. sh | | | | | | | | | | | | | | | | | | | 69.7 |
| 40 | 10 | 16.7 | 1.5 | 19.7 | 0.2 | 38.1 | 6.7 | 1.0 | 1.0 | 1.2 | | | | 9.9 | 2.0 | 30.2 | 2.0 | 34.2 | 17.8 | 19.0 |
| 50 | 09 | 7.0 | 4.5 | 29.5 | 0.0 | 41.0 | 6.5 | 0.0 | 2.2 | 1.0 | | | | 9.7 | 2.7 | 36.7 | 1.0 | 40.4 | 8.9 | 13.3 |
| 50 | 08 | 19.2 | 7.2 | 24.2 | 0.0 | 50.6 | 7.5 | 0.2 | 2.5 | 3.6 | 0.4 | | | 14.2 | 2.2 | 14.2 | 3.0 | 19.4 | 15.8 | 24.2 |
| 50 | 07 | 7.2 | 8.2 | 23.7 | 0.5 | 39.6 | 8.7 | 1.7 | 1.2 | 0.3 | 0.4 | | | 12.3 | 3.5 | 15.5 | 4.7 | 23.7 | 24.4 | 31.1 |
| 3 | 06 Ptg. | | | | | | | | | | | | | | | | | | | 80.5 |
| 32 | 05 | 8.7 | 10.5 | 15.0 | 1.2 | 35.4 | 5.5 | 0.7 | 0.7 | 2.9 | 0.6 | tr | | 10.4 | 2.2 | 18.0 | 1.5 | 21.7 | 32.5 | 41.4 |
| 28 | 04 | 6.2 | 6.2 | 16.5 | 2.2 | 31.1 | 9.7 | 2.7 | 0.7 | 2.0 | tr | | | 15.1 | 3.2 | 20.0 | 2.5 | 25.7 | 28.1 | 37.7 |
| 44 | 03 | 7.5 | 9.5 | 14.5 | 3.2 | 34.7 | 7.5 | 0.7 | 1.0 | 2.0 | tr | | | 11.2 | 3.0 | 11.7 | 1.7 | 16.4 | 37.7 | 40.9 |
| 30 | 02 | 3.7 | 10.5 | 10.0 | 2.0 | 26.2 | 10.0 | 0.5 | 1.5 | 1.0 | 1.2 | | | 14.2 | 1.7 | 18.0 | 3.5 | 23.2 | 36.4 | 33.5 |
| ***** | 01 Floor | | | | | | | | | | | | | | | | | | | 90.1 |

**Vitrinite Group Macerals**
VIT. A type 1 - bright homogeneous vitrinite; see text
VIT. A type 2 - darker vitrinite, showing faint structure; see text
VIT. B - Desmocollinite; groundmass vitrinite, containing liptinite and intertinite
V. DET - vitrodetrinite
TOT. V. - total amount of vitrinite group macerals

**Liptinite Group Macerals**
SPOR - sporinite
CUT - cutinite
RESIN - resinite
L. DET - liptodetrinite
Bt - bituminite
Al - alginite
Exs - exsudatinite
TOT. L - total amount of liptinite group macerals

**Inertinite Group Macerals**
SEMIFUS - semifusinite
FUS. - fusinite
I. DET - inertodetrinite
TOT. I - total amount of inertinite group macerals

MIN. - mineral matter
ASH % - ash content determined at 750°C
tr - trace amounts

(cm) - centimetres
Ptg. - parting
C. sh. - carbonaceous shale

The dominant vitrinite maceral is vitrinite B. It accounts for up to two-thirds of the total vitrinite content. Samples with a higher ash content usually contain greater amounts of vitrinite B, whereas cleaner samples with a lower ash content contain relatively greater amounts of vitrinite A.

Macerals of the liptinite group (mmf) comprise, on average, 10% of the Cairnes Seam. Liptinite macerals are easily identified by their fluorescent properties under ultraviolet irradiation. Sporinite accounts for approximately 50% of the liptinite present, although high concentrations of resinite are present in some samples. Liptodetrinite and cutinite constitute the remainder of the liptinite; however, traces of alginite, bituminite, and exsudatinite are present within the upper and lower coal benches (Table 1).

Average total inertinite content (mmf) is 36%. The most important inertinite macerals are fusinite (average 24%) and semifusinite (average 5%). The inertinite group present in these coals represents a continuous series from slightly oxidized (low-reflecting) semifusinite to highly oxidized (high-reflecting) fusinite. Furthermore, some anisotropic fusinite (pyrolytic carbon) is present, the wood char derived from peat fires.

Mineral matter content varies throughout the seam, ranging from 4 to 47%, and closely follows ash contents. The most frequently observed minerals are clays and quartz, with minor amounts of carbonate (probably calcite). Large radial masses of siderite are scattered throughout the seam. Mineral matter typically occurs as finely disseminated particles within desmocollinite rather than discrete lenses or large masses.

Maceral distribution within the seam profile is fairly constant (Fig. 4). On an "as received" basis (Table 1), there is a slight decrease in vitrinite toward the base of the Cairnes Seam, and a slight increase in inertinite in the middle part of the seam. Liptinite concentrations show a slight decrease in the middle part of the seam. Mineral matter and ash content show a progressive increase toward the base of the seam.

## *Reflectance analysis*

Maximum reflectance ($R_{o\,max}$) values for the composite samples (CQ-760-A to F) are presented in Table 2. The $R_{o\,max}$ average of 0.62% identifies the coal rank as high volatile C bituminous. The coals show weathering effects,

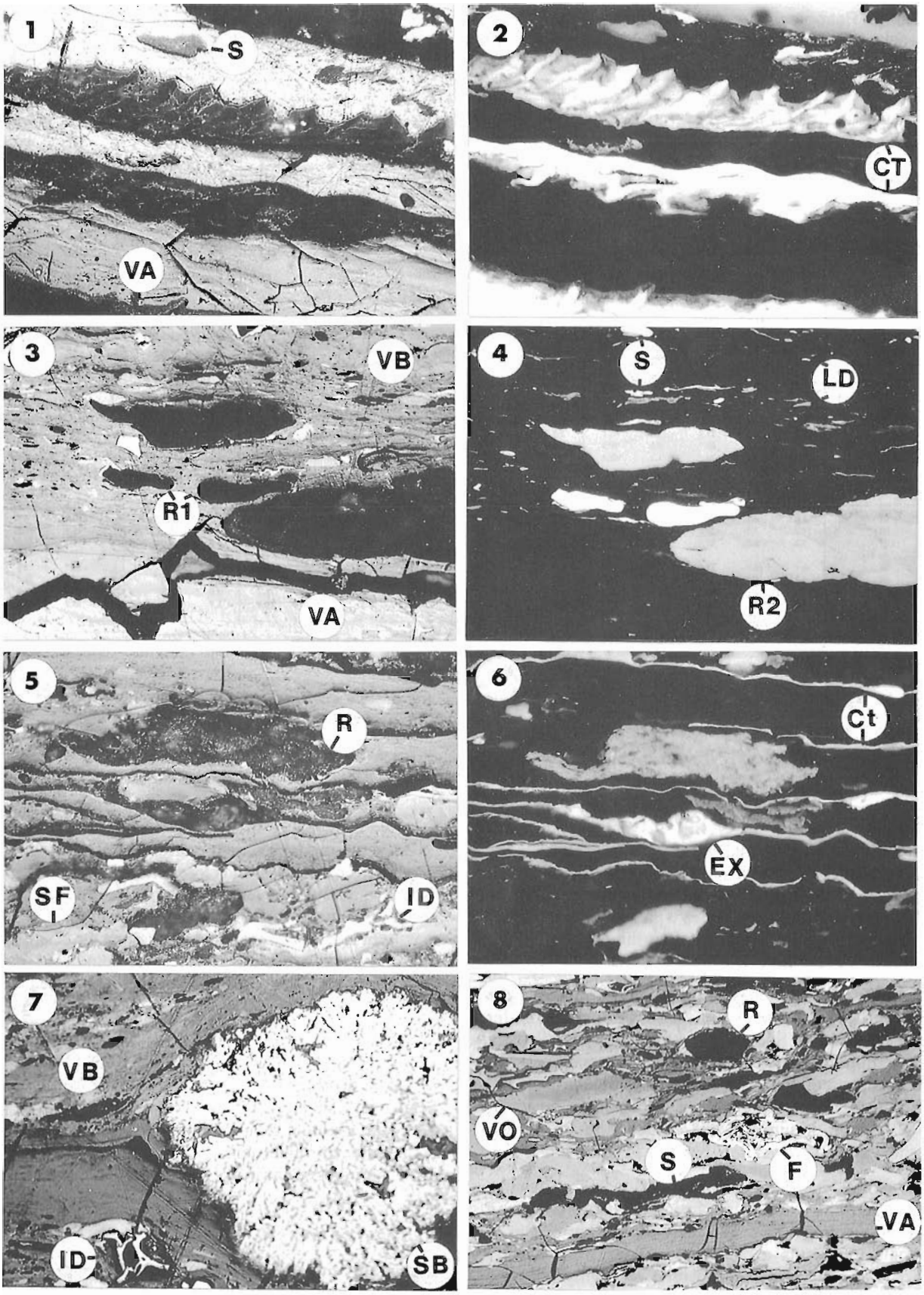
1
S
VA
2
CT
3
VB
R1
VA
4
S
LD
R2
5
R
SF
ID
6
Ct
EX
7
VB
ID
SB
8
R
VO
S
F
VA

such as variation in reflectance (standard deviation up to 0.06) and microporosity; therefore, the reflectance values may differ slightly from those for unweathered samples (Marchioni, 1983).

### *Proximate analysis*

Ash and sulphur contents were determined for all samples. Ash content varies significantly throughout the seam profile (Fig. 4); sulphur content, however, was uniformly low in all samples (average 0.40%, dry basis) and never exceeded 0.46%. The partings and high-ash samples contained <0.2% sulphur. Table 2 shows proximate data for the composite samples. Moisture content is moderately high (13% average), and ash content averages 20% for the upper two main coal benches. Coal from the lower coal bench (samples 1-18, composites A-C) contains greater ash contents. Volatile matter and fixed carbon average 45% and 55%, respectively, on a dry, ash-free basis (daf), which is in agreement with the high volatile C bituminous rank indicated by reflectance analysis.

**Table 2.** Average reflectance and results of proximate analysis for the composite samples from the Cairnes Seam. Ash and sulphur on a weight per cent, dry basis. Volatile matter and fixed carbon on a weight per cent, dry, ash-free basis.

| | 760-A | 760-B | 760-C | 760-D | 760-E | 760-F |
|---|---|---|---|---|---|---|
| $R_{o\,max}$ % | 0.62 | 0.62 | 0.62 | 0.60 | 0.60 | 0.61 |
| Moisture % | 11.7 | 14.1 | 12.1 | 12.4 | 16.2 | 15.3 |
| Ash % | 42.13 | 24.56 | 20.25 | 21.11 | 19.45 | 19.13 |
| Volatile Matter % | 51.1 | 45.5 | 44.2 | 44.4 | 45.2 | 44.8 |
| Fixed Carbon % | 48.9 | 54.5 | 55.8 | 55.6 | 54.8 | 55.2 |
| Total Sulphur % | 0.43 | 0.44 | 0.38 | 0.40 | 0.37 | 0.40 |

**Figure 5.** Maceral assemblages typical of the Cairnes Seam, Division Mountain coal deposit. Long axis of all photomicrographs is 240 μm.

**1, 2.** White and fluorescent light photomicrograph of thick-walled cutinite (CT) and sporinite (S) in vitrinite A (VA).

**3, 4.** White and fluorescent light photomicrograph showing strong (R1) and weaker (R2) fluorescing resinite, associated with sporinite (S) and liptodetrinite (LD) in a vitrinite B matrix. A band of vitrinite A (VA) is present in the lower part of the photomicrograph.

**5, 6.** White and fluorescent light photomicrographs of resinite (R), thin-walled cutinite (Ct), semifusinite (SF), and inertodetrinite (ID). Possible occurrence of exsudatinite (EX) associated with mineral matter.

**7.** Siderite bloom (SB) and inertodetrinite (ID) associated with vitrinite B (VB).

**8.** Typical associations of macerals within the Cairnes Seam, suggestive of the hypautochthonous nature of the coals. Resinite (R), sporinite (S), inertinite (?pyrofusinite, F), and a band of vitrinite A (VA) in a matrix composed primarily of vitrinite B, semifusinite, and inertodetrinite. Note the slight oxidation rim on the vitrinite A particle (VO), suggestive of paleo-oxidation.

### *Mineralogy*

Semiquantitative mineralogy, as determined by X-ray diffraction (XRD) analysis of the low-temperature ash from the composite samples, is presented in Table 3. Quartz dominates the mineral assemblage followed by kaolinite. Lesser amounts of calcite are present, with feldspars, gypsum, and weddelite occurring in minor to trace amounts. Siderite, observed in the coal under optical microscopy and scanning electron microscopy/energy dispersive X-ray analysis (SEM-EDX), was not detected in the low-temperature ash during XRD analysis, probably due to the low concentrations in which it occurs overall.

### *Elemental composition*

Elemental composition was determined for each sample. The weighted elemental average for the entire seam (excluding partings), and the elemental average and range for coal, carbonaceous shale, and partings are presented in Table 4. Data from individual samples are not presented. Most elements are more abundant in the shale and partings, although Ca, S, and Sr are present in greater concentrations in the coals (<35% ash), and Mg, Na, and As show greater concentrations in the carbonaceous shale (35-70% ash). Anomalously high levels of Zn are present in coal samples 20, 25, and 38, at concentrations of 980, 400, and 520 ppm, respectively. These values contrast with much lower values (3-26 ppm) for other coal samples in the series, and bias the weighted seam average for Zn in Table 4. No other elements correlate with these Zn anomalies and, furthermore, SEM-EDX examination of the coal and XRD analysis of the coal ash failed to reveal zinc minerals.

Compared to the whole coal weighted seam average, most elements are present in concentrations less than the Clarke values (average Earth's crust composition). The elements Se, Sb, As, and B do occur in concentrations greater than the Clarke values; however, the content of these elements is comparable to that found in coals worldwide (Swaine, 1990).

### *Rock-Eval analysis*

Rock-Eval pyrolysis was conducted on all samples to determine the hydrocarbon potential for the seam, and average data for the composite samples are presented in Table 5. The S1 values (hydrocarbons present) are very low, <0.35 mg HC/g coal. The amount of generated hydrocarbon

**Table 3.** Semiquantitative mineralogy, determined for low-temperature ash of the composite samples from the Cairnes Seam

| | 760-A | 760-B | 760-C | 760-D | 760-E | 760-F |
|---|---|---|---|---|---|---|
| Kaolinite | 19 | 30 | 22 | 33 | 21 | 26 |
| Quartz | 74 | 60 | 57 | 53 | 42 | 51 |
| Calcite | 0 | 10 | 7 | 5 | 18 | 14 |
| Feldspar | 7 | 0 | 8 | 5 | 5 | 3 |
| Gypsum | tr | 2 | 4 | 8 | 3 | 3 |
| Weddelite | tr | 6 | tr | 6 | 3 | 2 |

(S2) is also low, ranging from 4 to 26 mg HC/g coal. The Hydrogen Index (HI) is very low (8-38) and, as expected, the Oxygen Index (OI) is relatively high but within the range for coals (30-46).

**Table 4.** Weighted average elemental composition of the entire seam, on a whole coal basis, with Clarke values, and the elemental averages and ranges of the coal, carbonaceous shale and partings.

| | WHOLE COAL AVERAGE | CLARKE VALUES * | COALS [< 35% ash] average (range) | CARB. SHALE [35-70% ash] average (range) | PARTINGS (> 70 % ash) average and (range) |
|---|---|---|---|---|---|
| ASH % | 21.8 | | 19.15 | 46.40 | 84.81 |
| S % | 0.4 | | 0.34 (.25-.46) | 0.28 (.19-.39) | 0.04 (.01-.06) |
| Al % | 3.94 | 8.10 | 3.27 (1.10-8.7) | 7.71 (5.5-9.4) | 15.06 (13.0-18.1) |
| Ba % | 0.03 | 0.04 | 0.03 (.05-.05) | 0.04 (.03-.08) | 0.08 (.03-.14) |
| Ca % | 2.18 | 3.60 | 2.71 (1.1-13.4) | 1.30 (.6-2.0) | 0.34 (.14-.80) |
| Fe % | 0.79 | 5.00 | 0.83 (.37-1.73) | 0.80 (.5-1.7) | 1.47 (.47-5.62) |
| Mg % | 0.26 | 2.10 | 0.27 (.11-.53) | 0.33 (.13-.81) | 0.18 (.14-.25) |
| K % | 0.12 | 3.00 | 0.11 (.03-.32) | 0.35 (.17-1.0) | 1.09 (.4-2.0) |
| Na % | 0.08 | 2.80 | 0.08 (.04-.25) | 0.32 (.07-1.4) | 0.17 (.06-.29) |
| Ti % | 0.23 | 0.44 | 0.19 (.06-.36) | 0.50 (.30-.74) | 0.57 (.43-1.0) |
| Sb | 0.5 | 0.2 | 0.5 (.2-1.4) | 1 (.6-1.5) | 0.6 (.4-.8) |
| As | 3 | 1.8 | 2 (1-6) | 8 (3-15) | 5 (4-7) |
| B | 49 | 10 | 46 (23-73) | 58 (31-76) | 72 (49-106) |
| Be | 1 | - | 0.8 (.5-2) | 2 (1-2) | 2 (1-2) |
| Br | 2 | 3 | 2 (1-4) | 2 (1-4) | 0.7 (.4-1.2) |
| Cs | 0.3 | 3 | 0.3 (.1-1.4) | 0.7 (.4-1.3) | 2 (.4-2.7) |
| Cl | 22 | 130 | 22 (9-43) | 22 (10-67) | 27 (17-73) |
| Cr | 12 | 100 | 11 (4-31) | 29 (9-80) | 84 (13-204) |
| Co | 3 | 25 | 3 (2-5) | 4 (2-7) | 5 (1-12) |
| Cu | 25 | 55 | 21 (11-43) | 33 (20-61) | 41 (18-62) |
| Hf | 2 | 3 | 1 (.6-3) | 5 (3-7) | 6 (3-9) |
| Pb | 8 | - | 6 (3-13) | 13 (9-16) | 21 (16-24) |
| Li | 9 | - | 6 (2-20) | 19 (15-23) | 29 (18-38) |
| Mn | 130 | 950 | 140 (18-374) | 124 (36-349) | 207 (13-1090) |
| Mo | 0.5 | 1.5 | 0.5 (.3-3) | 0.7 (.6-1.1) | 8 (.6-22) |
| Ni | 6 | 75 | 4 (2-8) | 9 (2-26) | 69 (3-306) |
| Nb | 10 | 20 | 8 (2-19) | 19 (4-33) | 28 (15-47) |
| Rb | 7 | 90 | 6 (3-15) | 15 (8-39) | 39 (16-59) |
| Sc | 8 | 22 | 7 (4-13) | 14 (9-21) | 13 (5-21) |
| Se | 0.6 | 0.1 | 0.6 (.3-1) | 0.7 (.5-.9) | 0.8 (.5-1) |
| Sr | 350 | 375 | 408 (97-1189) | 211 (75-400) | 201 (112-383) |
| Ta | 0.2 | 2 | 0.2 (.02-.6) | 0.6 (.3-.7) | 1 (.4-1.65) |
| Th | 2 | 7 | 1.8 (.2-5) | 5 (3-7) | 7 (3-13) |
| W | 0.5 | 1.5 | 0.5 (.1-2) | 1 (.7-2) | 2 (.7-3) |
| U | 1 | 1.8 | 1 (.4-3) | 2.4 (1.5-3.7) | 4 (2-5) |
| V | 47 | 135 | 43 (14-117) | 90 (39-252) | 89 (18-179) |
| Zn | 72 | - | 5 (3-26)** | 8 (5-19) | 28 (3-70) |
| Ce | 18 | 60 | 16 (6-32) | 31 (17-49) | 40 (20-57) |
| Dy | 3 | 3 | 3 (1-6) | 5 (3-6) | 4 (1-7) |
| Eu | 0.5 | 1.2 | 0.5 (.2-.9) | 1 (.7-1.2) | 1 (.5-1.6) |
| Ho | 0.5 | 1.2 | 0.4 (.1-1) | 1 (.4-1.3) | 1 (.5-1.6) |
| La | 9 | 3 | 8 (3-17) | 16 (7-34) | 19 (11-25) |
| Lu | 0.2 | 0.5 | 0.2 (.08-.5) | 0.4 (.2-.6) | 0.3 (.2-.5) |
| Nd | 8 | 28 | 7 (3-15) | 14 (9-19) | 18 (8-31) |
| Pr | 2 | - | 2 (1-4) | 5 (2-13) | 9 (6-17) |
| Sm | 2 | 6 | 2 (.7-3) | 4 (3-5) | 4 (2-8) |
| Tb | 0.3 | - | 0.3 (.09-.6) | 0.6 (.3-.8) | 0.5 (.2-.8) |
| Tm | 0.2 | 0.5 | 0.2 (.08-.5) | 0.4 (.2-.6) | 0.3 (.2-.5) |
| Yb | 1.3 | 3.5 | 1 (.4-3) | 2 (1-3) | 2 (.9-2.7) |

- values in parts per million unless otherwise stated.
* from Mason and Moore, 1982.
** Zn values do not include samples 20, 25 and 38 - see text.

Table 5 also includes Rock-Eval data for medium volatile bituminous coals with gas potential from the Mist Mountain Formation, Elk Valley Coalfield (Dawson and Clow, 1992). The Elk Valley coals are relatively unoxidized and were collected immediately upon core retrieval. Compared to coals in the Cairnes Seam exposure at Division Mountain, the Elk Valley coals have higher S1, S2, and HI values, and significantly higher Tmax values (as expected).

## DISCUSSION

The Cairnes Seam exposed at Division Mountain contains three, main, thick coal "benches" separated by two partings of clastic material. The maceral composition of the coal in the benches is very similar, with moderately high amounts of inertinites (36%), and an average of 10% liptinites. The ash content is variable and averages 20%; however, there are zones, 2 to 3 m thick, in the upper two benches which contain low-ash coal (8-16% ash). The dominance of desmocollinite, which contains much liptinite and inertinite, coupled with the presence of vitrodetrinite, and the high overall concentrations of inertinite suggest a high-energy depositional environment with frequent water-level fluctuations. This environment produced a hypautochthonous peat/coal (Hacquebard and Donaldson, 1969). This is consistent with the inferred geological setting for the Laberge Group.

Volatile matter content and calorific values determined for these coals by other workers indicate a rank of high volatile C-B bituminous (Phillips, 1973), based on A.S.T.M. standards. A reflectance average of 0.62% $R_{o\,max}$ and a volatile matter content average of 45% (daf), determined in this study, indicate a high volatile C bituminous rank.

Unfortunately, the coals sampled were close to surface and weathered. Weathering can modify proximate values, so that true rank may not be readily apparent. Reflectance may be the best indicator of rank, as it has been shown, for coals of similar rank, that weathering only suppresses reflectance values slightly (Marchioni, 1983). The heating effect of

**Table 5.** Rock-Eval pyrolysis data and ash contents (weight per cent, dry basis). Samples 760-A to F are the Cairnes Seam composites; samples 1-4 and 1-5 are from Seam 1, Greenhills Mine, Elk Valley Coalfield; samples 7-1 and 10-1 are from seams 7 and 10, respectively, Greenhills Mine (Dawson and Clow, 1992).

| SAMPLE | Tmax | S 1 | S 2 | S 3 | TOC | H I | O I | ASH % (dry basis) |
|---|---|---|---|---|---|---|---|---|
| 760-A | 445 | 0.10 | 12.89 | 17.70 | 48.73 | 26 | 36 | 42.13 |
| 760-B | 445 | 0.12 | 20.97 | 24.18 | 64.89 | 32 | 37 | 24.56 |
| 760-C | 446 | 0.11 | 19.67 | 22.67 | 67.20 | 29 | 33 | 20.25 |
| 760-D | 443 | 0.10 | 14.68 | 25.36 | 66.85 | 22 | 38 | 21.11 |
| 760-E | 448 | 0.07 | 17.21 | 28.44 | 66.56 | 25 | 42 | 19.45 |
| 760-F | 447 | 0.00 | 17.19 | 27.73 | 67.00 | 26 | 41 | 19.13 |
| 1-4 | 470 | 9.28 | 112.3 | 0.71 | 41.28 | 271 | 1 | 11.99 |
| 1-5 | 470 | 8.92 | 121.8 | 1.54 | 41.38 | 294 | 3 | 23.13 |
| 7-1 | 464 | 3.83 | 143.7 | 1.66 | 48.10 | 298 | 3 | 7.21 |
| 10-1 | 461 | 2.58 | 159.5 | 1.57 | 54.71 | 291 | 2 | 3.66 |

intrusions can increase reflectance; however, intrusive rocks were not observed in or near the trench sampled and, furthermore, there were no signs of heating (such as high-reflecting rims around macerals, or strong anisotropy).

Coals with an average $R_{o\ max}$ of 0.62% should produce Tmax values within the 430 to 440°C range (Teichmüller and Durand, 1983; Snowdon and Fowler, 1991), and yet the Tmax values (440-450°C) obtained by analysis of samples from the Division Mountain coal deposit suggest ranks up to high volatile A bituminous. It is as yet uncertain if weathering or the high contents of ash and inertinite have affected the Tmax values of these samples.

In the Division Mountain coal deposit, most elements are found in concentrations lower than their Clarke values, but certainly within the range of "typical" coals worldwide (Swaine, 1990). Most elements are likely associated with mineral matter, particularly clays. The coals exhibit low levels of hazardous elements such as U, Th, As, B, Pb, and Se. Furthermore, elements of economic interest; for example, Cu, Ni, and Pb, occur in low concentrations. The exception to this is the elevated level of Zn in three samples. The possibility of mineralizing fluids travelling along shear planes or along coal/sediment interfaces may be indicative of mineralization from nearby intrusions. The possibility of Zn having been leached from the overlying till and volcanic ash strata cannot be discounted. Initial results do not suggest the presence of economic concentrations of elements in the coal ash, but the concentrations of some rare-earth elements within the ash may be worth investigating.

## HYDROCARBON AND UTILIZATION POTENTIAL

Rock-Eval results indicate a low hydrocarbon generation potential for these coals. Coals having significant generation potential typically have a high Hydrogen Index (>200), much greater than that shown for the Division Mountain samples. Furthermore, the low HI and high OI may be indicative of the weathered nature of the samples, high inertinite content or low hydrocarbon saturation. Aside from the Rock-Eval parameters, the coals exhibit moderate liptinite contents (10%), and there are indications of hydrocarbon production (exsudatinite) within the samples. Fresh samples should be examined to assess the hydrocarbon potential accurately.

The coalbed methane potential of the deposit is difficult to assess at this stage. In general, high rank, vitrinite-rich coal (approximately 1.2% $R_{o\ max}$) is likely to have the greatest potential for gas generation, based on the degree of saturation; however, any coal approaching the first coalification jump (approximately 0.65% $R_{o\ max}$) has the potential to produce significant amounts of gas (Teichmüller and Durand, 1983). Additionally, a combination of various compositional, geological, structural, physical, and hydrological factors are required for a good gas potential. The coals are moderately high in ash, which adversely affects gas potential. Furthermore, the coal showed only very minor shearing and no cleat development. The Laberge Group strata are folded into a syncline, and the coal measures may show increases in rank with depth if they are continous within the sequence. A syncline is not the ideal gas-trapping structure; however, hydrological conditions beneath the Nordenskiold River valley may assist in methane retention (if any was generated, and if the coal seams are continuous throughout the syncline).

Additionally, there may be differences in maceral composition due to in-seam facies variations; these would locally enhance hydrocarbon and coalbed methane potential. If the Rock-Eval data obtained from the Elk Valley coals are indeed indicative of requirements for gas potential, then the Cairnes Seam may have a limited potential.

The coals may have their greatest utilization potential in thermal applications. The coal as observed in outcrop has too low a rank for coking applications, and the rank and petrographic composition are not ideal for coal liquefaction processes. Thermal use of the coal is favoured by the low sulphur concentrations and the overall low concentrations of undesirable elements.

Ash contents vary within the seam. The mineral matter is intimately associated with desmocollinite and, therefore, may be difficult to remove or reduce prior to coal utilization. The lower coal bench contains significantly higher amounts of ash. The thick middle and upper coal benches show the greatest thermal utilization potential at present.

## CONCLUSIONS

The Division Mountain coal deposit contains a thick sequence of high volatile C bituminous coal. The coals have moderately high ash but low sulphur contents. The rank and maceral assemblage suggest that the coal may be best suited for combustion; however, the potential for coalbed methane and hydrocarbon generation exists in deeper, unweathered parts of the deposit. The elemental and mineral composition of the coals fall within the range of coals worldwide; however, the influence of nearby intrusions and overlying till and ash may have influenced the elemental composition of the coals. Further exploration in deeper regions of the syncline is required in order to outline the extent, rank, and composition of the coal, in order to assess the full potential of the deposit.

## ACKNOWLEDGMENTS

We thank Archer Cathro Ltd. for allowing access to their property at Division Mountain. B.L. Gorham, J.N.Y. Wong, and B.C. Rutley, Geological Survey of Canada, provided assistance in analytical and technical aspects of this report. J. Potter contributed useful comments and suggestions in a thoughtful review of this paper.

## REFERENCES

**A.S.T.M. Annual book of A.S.T.M. standards**

1979: American Society for Testing and Materials, Part 26 — Gaseous fuels; coal and coke; atmospheric analysis, A.S.T.M., Philadelphia, Pennsylvania.

**Bustin, R.M., Cameron, A.R., Grieve, D.A., and Kalkreuth, W.D.**
1985: Coal petrology — its principles, methods and applications; Geological Association of Canada, Short Course Notes, v. 3, 230 p.

**Cairnes, D.D.**
1910: Lewes and Nordenskiold Rivers coal district; Canada Department of Mines, Geological Survey Branch, Memoir 5, 70 p.

**Carne, R.C.**
1990: Summary report on the Division Mountain coal prospect, southern Yukon; Archer Cathro Ltd., 5 p.

**Dawson, F.M. and Clow, J.T.**
1992: Coalbed methane research — Elk Valley Coalfield; Proceedings, The Canadian Coal and Coalbed Methane Geoscience Forum, Parksville, British Columbia, p. 57–71.

**Dickie, J.R. and Hein, F.J.**
1988: Facies and depositional setting of Laberge conglomerates (Jurassic), Whitehorse Trough; Exploration and Geological Services Division, Indian and Northern Affairs Canada, Yukon Geology, v. 2, p. 26-32.

**Fowler, M.G., Gentzis, T., Goodarzi, F., and Foscolos, A.E.**
1991: The petroleum potential of some Tertiary lignites from northern Greece, as determined using pyrolysis and organic petrological techniques; Organic Geochemistry, v. 17, p. 805-826.

**Hacquebard, P.A. and Donaldson, J.R.**
1969: Carboniferous coal deposition associated with floodplain and limnic environments in Nova Scotia; in Environments of Coal Deposition, (ed.) E.C. Dapples and M.E. Hopkins; Geological Society of America, Special Paper 114, p. 1157-1169.

**Marchioni, D.L.**
1983: The detection of weathering in coal by petrographic, rheological and chemical methods; International Journal of Coal Geology, v. 2, p. 231-259.

**Mason, B and Moore, C.**
1982: Principles of Geochemistry; (Fourth edition) John Wiley and Sons, New York, 344 p.

**Phillips, M.P.**
1973: Report on 1972 diamond drilling and trenching program, Nordenskiold coal area, Yukon; Archer Cathro Ltd., 10 p.

**Snowdon, L.R and Fowler, M.G.**
1991: Interpretation of organic geochemical data; Canadian Society of Petroleum Geologists, Short Course SC-2, Calgary, Alberta, 86 p.

**Stach, E., Mackowsky, M.-Th., Teichmüller, M., Taylor, G.H., Chandra, D., and Teichmüller, R.**
1982: Stach's Textbook of Coal Petrology; (Third Edition) Gebruder Borntraeger, Berlin and Stuttgart, 428 p.

**Swaine, D.J.**
1990: Trace Elements in Coal; Butterworths, London, 278 p.

**Teichmüller, M. and Durand, B.**
1983: Fluorescence microscopical rank studies on liptinites and vitrinites in peat and coals, and comparison with results of the Rock-Eval pyrolysis; International Journal of Coal Geology, v. 2, p. 197-230.

**Templman-Kluit, D.J.**
1974: Reconnaissance geology of Aishihik Lake, Snag and part of Stewart River map areas, west-central Yukon; Geological Survey of Canada, Paper 73-41, 97 p.

# An airgun seismic survey of the Fraser Delta slope, British Columbia

**B.S. Hart, G. Horel[1], H.W. Olynyk[2], and I. Frydecky**
**Pacific Geoscience Centre, Sidney**

*Hart, B.S., Horel, G., Olynyk, H.W., and Frydecky, I., 1992: An airgun seismic survey of the Fraser Delta slope, offshore British Columbia; in Current Research, Part E; Geological Survey of Canada, Paper 92-1E, p. 33-39.*

***Abstract***

*An airgun seismic survey of the Fraser Delta slope was conducted in November 1991. Data collection parameters were chosen to provide the best possible images of the internal structure of the upper portion of the sediment column. The delta slope adjacent to Sturgeon Bank appears to be comprised of offshore-dipping reflectors, representing undisturbed Holocene deltaic sediments. Much of the south central portion of the Roberts Bank slope is comprised of a downslope tapering "wedge" of Holocene sediment, the upper portions of which appear to be failure deposits. The Foreslope Hills, an area of elongate hills and troughs at the base of the central part of the slope, consist of a series of discrete blocks in which stratification dips landward. Efforts are currently under way to map and interpret the origin of these features.*

***Résumé***

*On a réalisé un levé sismique par la méthode du canon à air, sur le talus du delta du Fraser, en novembre 1991. Le choix des paramètres de collecte des données s'est fait de façon à obtenir les meilleures images possibles relatives à la structure interne de la partie supérieure de la colonne sédimentaire. Le talus du delta à proximité du banc Sturgeon paraît composé de réflecteurs inclinés vers le large, qui correspondent à des sédiments deltaïques non dérangés d'âge holocène. Une grande partie du centre sud du talus du banc Roberts se compose d'un «biseau» de sédiments holocènes qui s'amincit en aval-pente, et dont les portions supérieures semblent être des éboulis. Les collines d'avant-pente (Foreslope Hills), région de collines et dépressions allongées à la base de la partie centrale du talus, sont constituées par une série de blocs discrets dans lesquels la stratification est inclinée vers l'intérieur des terres. On cherche actuellement à cartographier ces structures et à donner une interprétation sur leur origine.*

[1] The Capstan Group, Victoria, British Columbia
[2] Terra Surveys Ltd., Sidney, British Columbia

## INTRODUCTION

The Fraser Delta is the largest delta on Canada's west coast, and is adjacent to the rapidly growing greater Vancouver region. Several previous studies have discussed the stability of the Fraser Delta slope and adjacent Strait of Georgia (e.g. Hamilton and Luternauer, 1983; Luternauer and Finn, 1983) and some have suggested that massive failure complexes may be present (e.g. Tiffin et al., 1971; Hamilton and Wigen, 1987). The results of these studies and the developmental pressures on the delta have stimulated the Geological Survey of Canada to intensify its research efforts on the submarine portions of the delta (Hart et al., 1991). Furthermore, the concerns of BC Hydro for its foreshore installations and submarine cables have resulted in a program of cooperative research between the Survey and BC Hydro.

Two field programs (PGC91-01 and PGC91-04) were undertaken by the GSC in early 1991 to investigate the internal structure and surface morphology of the submarine Fraser Delta slope and adjacent Strait of Georgia. Geophysical systems utilized on those surveys consisted of a Huntec Deep Tow Seismic Profiler (frequency bandwidth of 800 Hz - 5 kHz) and a 100 kHz, fully corrected side-scan sonar (using horizontal ranges of 150 and 200 m). As noted by Hart et al. (1991), interstitial gas (observed as "acoustic turbidity") adversely affected the penetration of the Huntec system, often limiting direct observation of the internal structure of the sediment column to the upper few metres. Hart and Hamilton (in press) mapped the distribution of the acoustically detectable interstitial gas from analysis of 3.5 kHz records.

The Foreslope Hills are an area of elongate hills and troughs at the base of the delta slope which previous studies (e.g. Mathews and Shepard, 1962; Tiffin et al., 1971; Hamilton and Wigen, 1987) have suggested may be the product of massive submarine failures. An additional concern is that a failure of the magnitude implied could be tsunamigenic (Hamilton and Wigen, 1987). The two surveys of early 1991 provided little new evidence as to the origin of the hills, as interstitial gas prevented their internal structure from being resolved by the Huntec system.

The Roberts Bank foreshore is the landing site of the high voltage cables which connect Vancouver Island to the mainland, as well as the site of a ferry terminal which links the island to the mainland (over 6.5 million passengers used this facility in 1991), and Canada's largest coal export terminal (250 X $10^6$ tonnes of coal loaded in the first 21 years of operation). High resolution seismic data collected from this part of the slope during early 1991 suggested that a significant portion of it may consist of failure deposits (Terra Surveys Ltd., 1991; Hart et al., in press). Discontinuous, "contorted" reflectors are found at the top of the slope, whereas chaotic reflection configurations are found at the base of the slope. The sandy and gassy nature of the slope material in this area reduced penetration of the Huntec signal, preventing determination of the thickness of these deposits, or the relation of the chaotic and contorted units.

Because of the limitations of the Huntec data collected earlier in the year, a marine geophysical survey (PGC91-08) was planned specifically to collect airgun seismic data from the Fraser Delta. The objective was to obtain the best possible resolution of the internal structure of the upper part of the sediment column from those areas of the delta slope where the Huntec data proved inadequate. For a variety of reasons (including ship speed, source/receiver depths, filter settings, hydrophone length, etc.), airgun seismic data collected in the previous decade (Hamilton et al., 1987; Hamilton, 1991) did not adequately resolve the internal structure of the portions of the delta of interest here.

In this paper, we report on the details of the data acquisition system, and present a preliminary geological analysis of the results obtained on cruise PGC91-08. Results of detailed stratigraphic and structural analyses, and mapping will form the basis of subsequent studies.

## DATA ACQUISITION METHODS

The survey was conducted between November 20-28, 1991 aboard the C.S.S. R.B. Young. Approximately 460 km of survey lines were shot during these 9 days (Fig. 1). Internav 408 Loran C and Trimble Pathfinder GPS receivers were employed to obtain navigation data. Bathymetry data were recorded with a Raytheon DSF6000 100 kHz survey echosounder.

The survey was conducted with an 82 $cm^3$ (5 $in^3$) airgun fired at 1 second intervals. Combined with an average ship speed of 5 knots, this firing rate provided a nominal shot

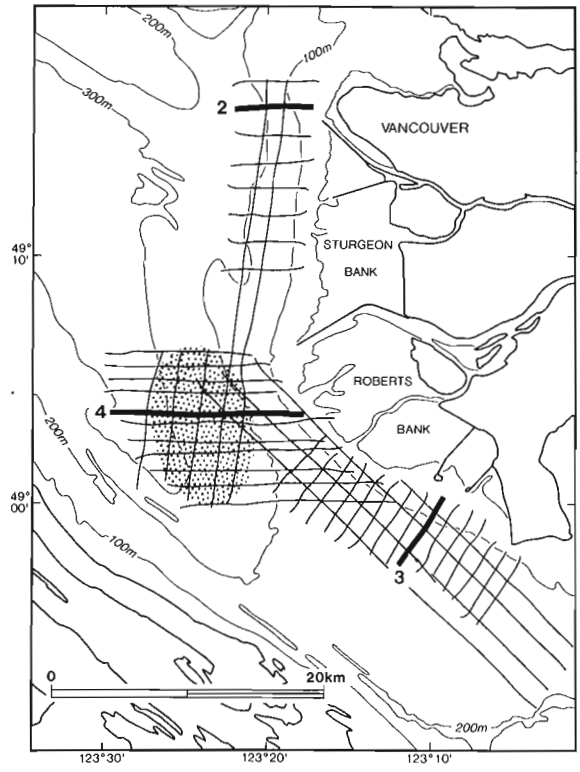


**Figure 1.** Study area showing tracklines and location of cross-sections illustrated in Figures 2-4. Stipple shows approximate extent of the Foreslope Hills.

The survey was conducted with an 82 $cm^3$ (5 $in^3$) airgun fired at 1 second intervals. Combined with an average ship speed of 5 knots, this firing rate provided a nominal shot spacing of 2.5 m. The airgun was suspended below a tow bar which was buoyed at either end by a 1 metre long cylindrical fenders each approximately 0.2 m in diameter. With this arrangement, the gun was towed at a consistent, shallow (<0.5 m) depth, even during periods of substantial (>1.5 m) seas. On-board analyses of the outgoing pulse with the Vista(tm) software package showed excellent shot to shot coherency during a variety of sea states. The data are of high enough quality to be amenable to subsequent digital processing techniques.

Hydrophones employed included 7.6 m Benthos and Nova Scotia Research Foundation streamers, and a 30 m array (built at the Pacific Geoscience Centre). With the longer hydrophone it was possible to obtain clearer images of the deeper structure of the sediment column in the deep water portion of the axis of the Strait, however the internal structure of the slope was "smeared" in the shallower water of the delta

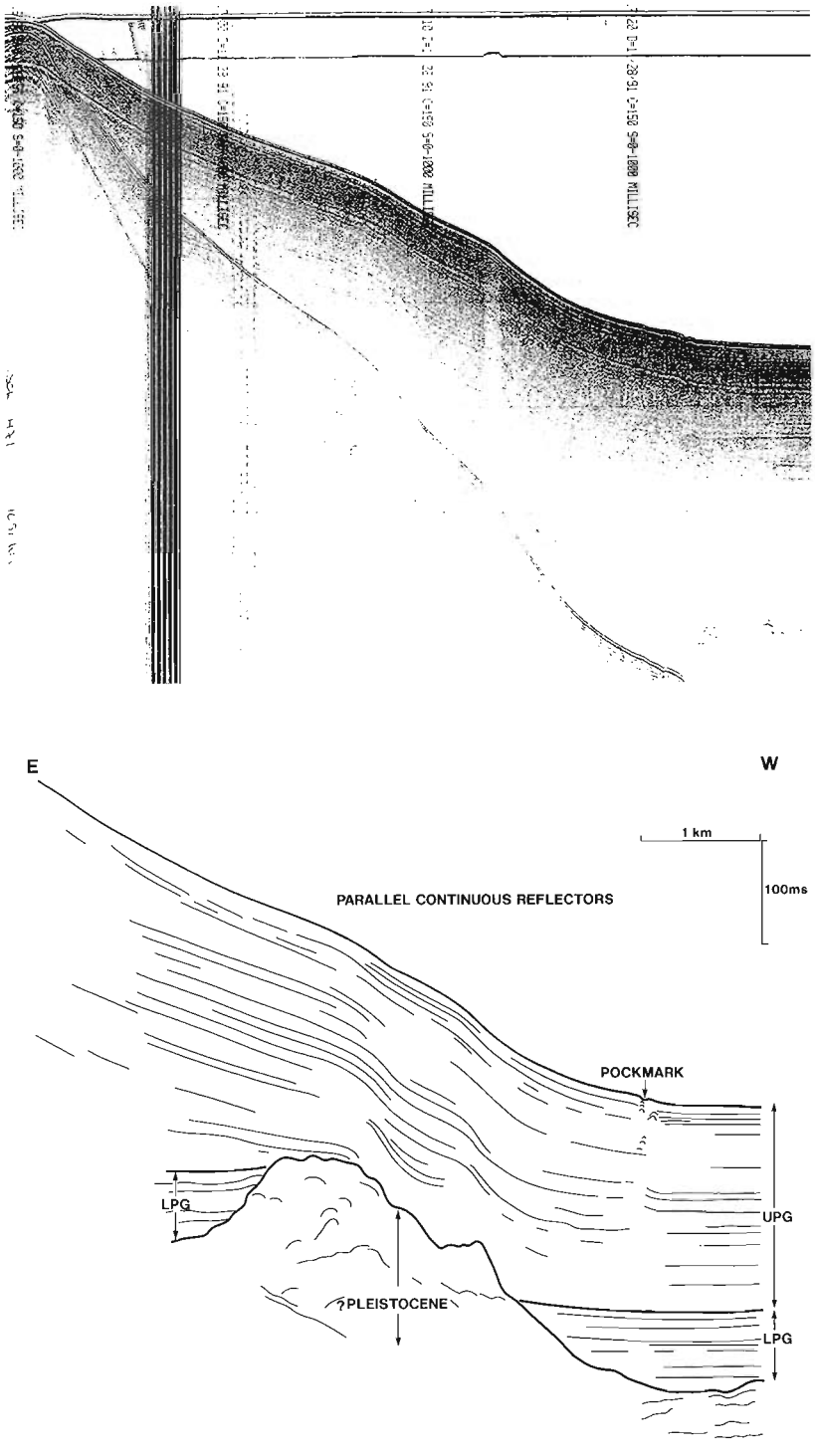


**Figure 2.**

Airgun seismic profile and interpretation of delta slope adjacent to Sturgeon Bank. Reflectors are generally parallel, continuous and dip in downslope direction. Depth scale assumes water velocity of 1485 m/s.

slope. Seismic data logging was done simultaneously on an EPC 9701 thermal recorder and an EPC 4800 recorder. Digital logging was done both on a 9 track recorder (with data acquisition software developed at PGC) and a GeoAcoustics SE880 system on loan from the Atlantic Geoscience Centre.

Several different filter settings were tried. The low-pass filter was typically set at 100 Hz. By keeping the high-pass filter open to 5 kHz, we hoped to resolve the fine details of the internal structure of the subsurface in gas-free areas. In gassy areas, it was found that by cutting the high-pass filter back to 2 kHz, slightly less "acoustic turbidity" was apparent on the records, allowing better definition of the internal structure of these areas. This is because the effect of interstitial gas is frequency dependant, with higher frequency acoustic signals suffering greater attenuation by scattering than lower frequency pulses (Anderson and Bryant, 1990). By filtering out some of the high frequency "noise", the lower frequency "signal" (less affected by gas) became clearer.

The presence of interstitial gas also affects the dominant frequency of prodelta/delta slope deposits measureable on the analogue records. Reflection frequency describes the number of reflections per unit time and is a function of sediment characteristics, such as bed spacing and the frequency of the seismic signal (Badley, 1985). In areas along the western margin of the Strait (at the base of the delta slope) without acoustically detectable gas, the sediments are characterized by a dominant frequency of about 500 Hz on records from the EPC 9701 thermal recorder. Adjacent gassy areas have a dominant frequency close to 170 Hz at the same stratigraphic level. It seems probable that these differences are attributable to attenuation of the higher frequencies by gas, rather than to differences of lithology.

In gas-free areas, it was often possible to obtain high quality images of the subbottom structure over 400 ms two-way travel time (TWT) below the seafloor. However, effective penetration was sometimes reduced to less than 100 ms (TWT) in gassy areas.

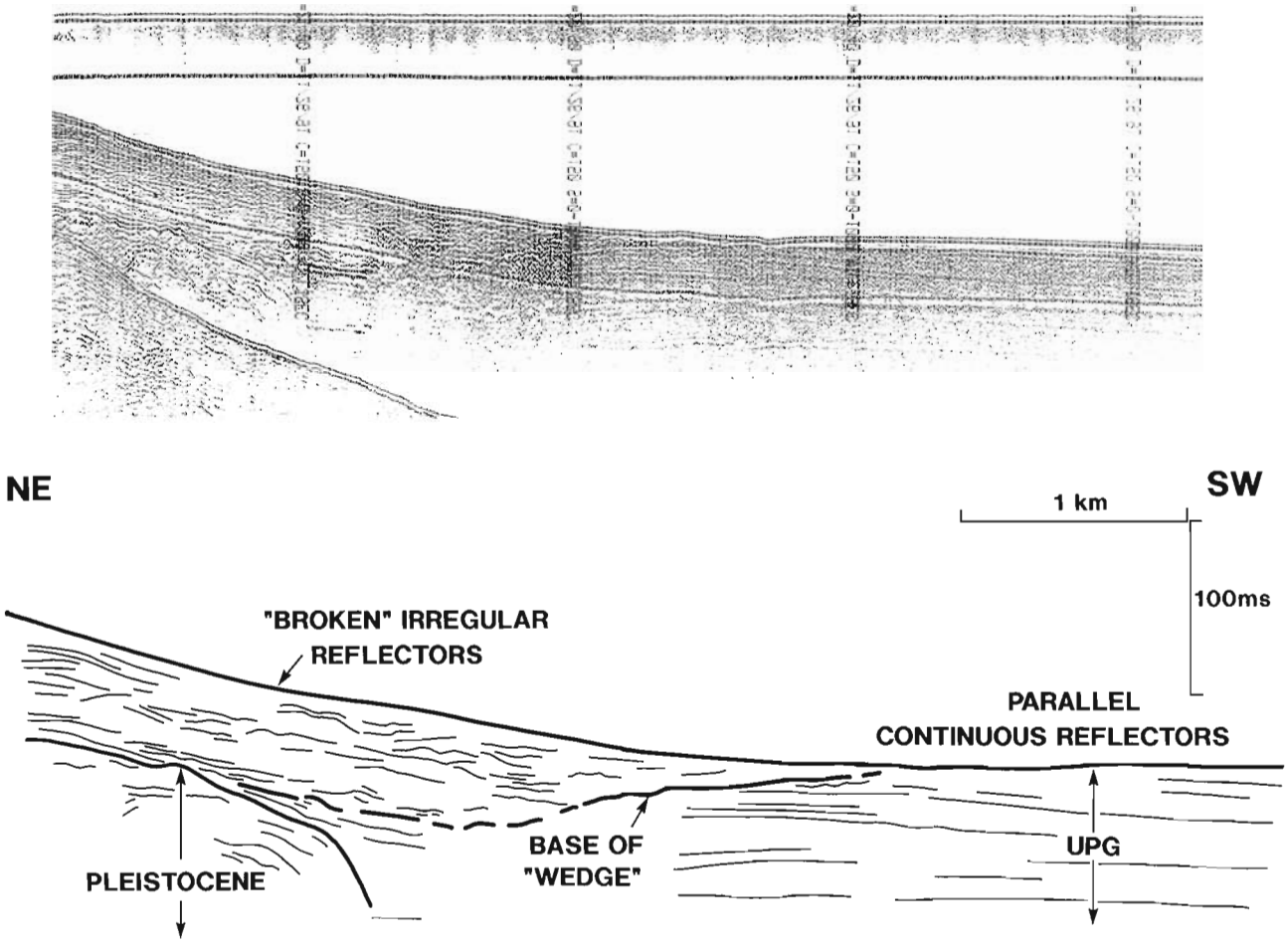


**Figure 3.** Airgun seismic profile and interpretation of delta slope adjacent to Roberts Bank. Much of the slope is comprised of a downslope tapering "wedge" of discontinuous, wavy reflectors. The wedge overlies undisturbed Holocene deposits which themselves overlie a mound of Pleistocene material. Depth scale assumes water velocity of 1485 m/s.

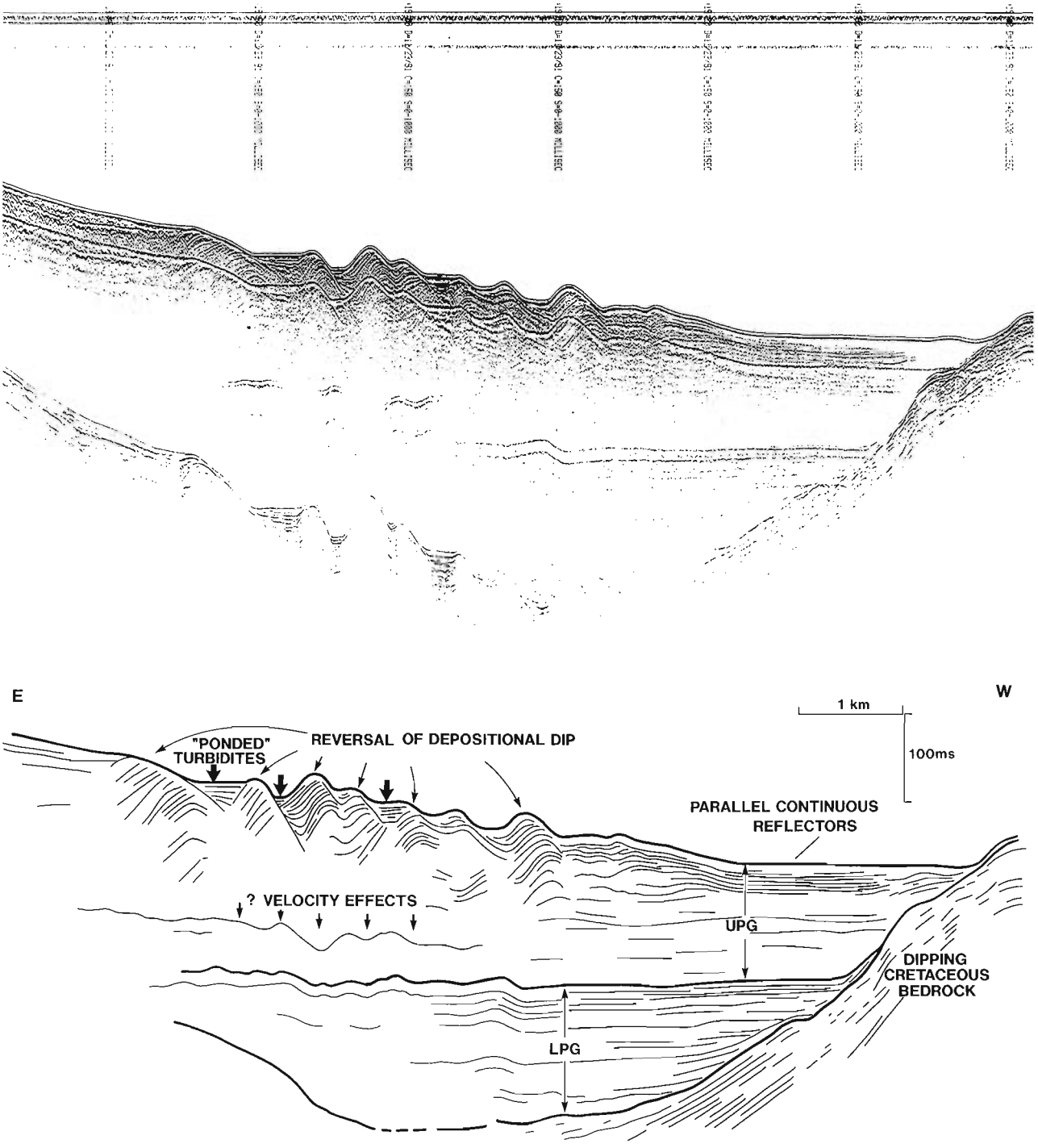


**Figure 4.** Airgun seismic record and interpretation of profile through central portion of Foreslope Hills. Line crosses hill crests at approximately right angle. Hills consist of discrete blocks, within which stratification dips upslope. Depth scale assumes water velocity of 1485 m/s. See text for further description.

the sediment's internal structure at depth. It is hoped that further testing will identify means of reducing the amplitude of this secondary bubble pulse.

## RESULTS

Surveying lines were divided into three groupings, each designed to examine a specific portion of the delta slope with both strike and dip lines (Fig. 1). These areas are: a) the Sturgeon Bank slope, b) the Roberts Bank slope, and c) the Foreslope Hills. In this section we will briefly describe the characteristics of the data acquired from each of these zones. Seismostratigraphic units employed in the text and figures are those described by Hamilton (1991) and include: a) Tertiary and older bedrock, b) ice-sculpted Pleistocene deposits, c) "Lower postglacial" (LPG) stratified glaciomarine sediments deposited during deglaciation, and d) "Upper postglacial" (UPG) deltaic and prodeltaic sediments deposited during the Holocene progradation of the Fraser Delta.

### *Sturgeon Bank slope*

Airgun records from this part of the delta slope indicate that the Holocene sediments here are comprised principally of (sub-) parallel continuous reflectors which drape relief on underlying (?Pleistocene) sediments (Fig. 2). Signal attenuation by gas obscures the base of the deltaic sediments over much of this area, especially below the middle to upper portions of the slope. Locally however, the thickness of the deltaic sediments exceeds 300 ms (TWT). The reflection patterns observed on the seismic records suggest that this part of the slope has not been significantly disturbed in Holocene times.

### *Roberts Bank slope*

As noted earlier, mapping of this area based on Huntec and side-scan sonar data collected earlier in 1991 suggested that failure deposits may form a significant portion of the south central part of this slope. Integration of airgun data collected in 1982 suggested that the failure deposits may form part of a "wedge" which pinches out downslope and along slope to the southeast. The dimensions of this wedge were difficult to evaluate with these data, as its base was poorly imaged on the earlier airgun data and only imaged at the toe of the slope where the wedge thins to less than 10 m on Huntec records.

The newly acquired airgun data confirm the existence of a wedge of sediment (locally over 50 ms thick) along the Roberts Bank slope. Reflectors within this package are "wavy" (or "hummocky") and discontinuous. The internal structure appears homogeneous from the base of the slope (chaotic reflectors on Huntec records) to its top (discontinuous, contorted reflectors on Huntec records). Delineation of the upslope and northwestern limits of the wedge will require detailed mapping, whereas the southeastern limit can be clearly defined and roughly corresponds to the base of the delta slope. The base of the wedge is clearly imaged on most airgun records (e.g. Fig. 3), and the stratigraphic relationships suggest that this feature is Holocene in age. This interpretation is consistent with the results of on-land seismic surveys along the causeway to the coal port (Luternauer et al., 1986) which show that the neighbouring intertidal portion of Roberts Bank is comprised of Holocene sediments (exceeding 200 ms thick in places) overlying an irregular erosion surface on Pleistocene deposits.

### *Foreslope Hills*

The origin of the Foreslope Hills has been the subject of considerable controversy. An historical review of the debate will not be presented here, instead the reader is referred to Tiffin et al. (1971) and Hamilton and Wigen (1987).

The Foreslope Hills form a series of hills and troughs, each of which extends for several kilometres in a north to north-northeast direction (Hamilton and Wigen, 1987). The primary survey lines for this study were therefore oriented in a east-west direction: this direction would give the least distorted images of the internal structure of the hills, assuming that they represent features generated by forces acting at right angles to hill crestlines, and reduce the occurrence of "side-echoes" from seafloor structures normal to the acoustic pulse.

A sample airgun record from cruise PGC91-08 and interpretation are presented in Figure 4. This profile, representative of others through the centre of the Foreslope Hills, suggests that each hill is comprised of a distinct "block" of sediment, some of which appear to be fault bounded. Stratification within each block dips landward, in direct contrast to reflection patterns observed on undisturbed portions of the delta slope, such as Sturgeon Bank (see above and Fig. 2). The blocks can be over 100 ms thick, and comprise the middle to upper portion of the Upper Postglacial (i.e. Holocene) deltaic deposits. Some type of in situ failure and rotation of the Holocene section, possibly due to downslope extension (e.g. Wernicke and Burchfiel, 1982) appears consistent with the newly acquired data.

Note the apparent relief on reflectors below the Foreslope Hills in Figure 4. The "phase" of the relief on these two markers is opposite that of the seafloor relief, so that they are "depressed" below hill tops. Previous interpretations (e.g. Luternauer and Finn, 1983) suggested that the relief on the lower markers may be due to "previous" phases of deformation. An alternative explanation, presented below, is that these horizons may be planar, and the apparent relief may in fact be a velocity effect.

The hills are known to be comprised of gassy, muddy sediments. Previous studies have shown that interstitial gas can reduce sound speed velocity by 15 to 50 per cent in sediments with respect to water saturated values (Anderson and Bryant, 1990). Hart and Hamilton (in press) have found velocity reductions of about 20 per cent due to interstitial gas in the Strait of Georgia. If the sound wave velocity is 1600 m/s for non-gassy muds, 20% reduction due to gas would result in a velocity of 1280 m/s. This is about 200 m/s slower than the velocity of the ambient seawater (1485 m/s). The result is

that planar features below the hills would appear distorted, with velocity effects "pulling" them down below gas-charged hill crests to produce a geometry similar to that observed here.

## SUMMARY

We conducted an airgun seismic survey to obtain high resolution images of the internal structure of the upper portion of the submarine Fraser Delta slope. The details of this structure were obscured by interstitial gas on Huntec high-resolution seismic records from this area collected earlier in 1991. Although the effects of the gas also adversely affected the airgun records we collected, these records provide the best images yet obtained of the slope's internal structure.

At least three different structural styles can be identified. The slope adjacent to Sturgeon Bank is comprised of parallel reflectors which dip offshore, in the direction of the slope. They represent apparently largely undisturbed sediments deposited during the progradation of the Fraser Delta in Holocene time. The south central part of the Roberts Bank slope is cored by a downslope tapering wedge of Holocene sediment which is locally over 50 ms thick. Previously collected Huntec high-resolution seismic records from this area suggest that the surficial portion of the wedge is comprised of failure deposits; the newly acquired data presented here indicates that the wedge is acoustically homogeneous through most of its extent. The Foreslope Hills are comprised of discrete blocks of Holocene sediment within which the stratification dips upslope; some type of in situ rotational failure appears to represent the most probable explanation for their origin.

Much further work will be needed to test the hypotheses presented in this paper regarding the origin of specific components of the Fraser Delta slope. This work will include: a) mapping of the internal structure of the deposits in three dimensions; b) dating of core material to help constrain the age of features observed on seismic records; c) measurement of geomechanical properties of the slope sediments in order to constrain the types of failure which are likely to occur on the slope, and the nature of the forces required to initiate failure. The results of this work will form the basis of subsequent publications.

## ACKNOWLEDGMENTS

We thank Kay Gimbel (Master) and the crew of the R.B. Young for their efforts during (the sometimes stormy) cruise PGC91-08, BC Hydro for their involvement and support, and Ralph Currie for his helpful suggestions on the manuscript.

## REFERENCES

**Anderson, A.L. and Bryant, W.R.**
1990: Gassy sediment occurrence and properties: northern Gulf of Mexico; Geo-Marine Letters, v. 10, p. 209-220.

**Badley, M.E.**
1985: Practical Seismic Interpretation; International Human Resources Development Corporation, Boston, 266 p.

**Hamilton, T.S.**
1991: Seismic Stratigraphy of Unconsolidated Sediments in the Central Strait of Georgia: Hornby Island to Roberts Bank; Geological Survey of Canada, Open File 2350.

**Hamilton, T.S. and Luternauer, J.L.**
1983: Evidence of seafloor instability in the south-central Strait of Georgia, British Columbia: a preliminary compilation; in Current Research, Part A; Geological Survey of Canada, Paper 83-1A, p. 417-421.

**Hamilton, T.S. and Wigen, S.O.**
1987: The Foreslope Hills of the Fraser Delta: Implications for tsunamis in Georgia Strait; International Journal of the Tsunami Society, v. 5, p. 15-33.

**Hamilton, T.S., Jewsbury, G. and Frydecky, I.I.**
1987: Single channel seismic data, for the Strait of Georgia: British Columbia, Canada and Washington, U.S.A.; Geological Survey of Canada, Open File 1514.

**Hart, B.S. and Hamilton, T.S.**
in press: High resolution acoustic mapping of shallow gas in unconsolidated sediments beneath the Strait of Georgia, British Columbia; Geo-Marine Letters.

**Hart, B.S., Barrie, J.V., Currie, R.G., Luternauer, J.L., Prior, D.B., and Macdonald, R.D.**
1991: High resolution seismic and side-scan sonar mapping of the Fraser Delta front and adjacent Strait of Georgia, British Columbia; in Current Research, Part E; Geological Survey of Canada, Paper 91-1E, p. 19-23.

**Hart, B.S., Prior, D.B., Hamilton, T.S., Barrie, J.V., and Currie, R.G.**
in press: Patterns and styles of sedimentation, erosion and failure, Fraser Delta slope, British Columbia; Proceedings of Geohazards '92, Canadian Geotechnical Society.

**Luternauer, J.L. and Finn, W.D.L.**
1983: Stability of the Fraser River delta front; Canadian Geotechnical Journal, v. 20, p. 606-613.

**Luternauer, J.L., Clague, J.J., Hamilton, T.S., Hunter, J.A., Pullan, S.E., and Roberts, M.C.**
1986: Structure and stratigraphy of the southwestern Fraser River delta: a trial shallow seismic profiling and coring survey; in Current Research, Part B; Geological Survey of Canada, Paper 86-1B, p. 707-714.

**Mathews, W.H. and Shepard, F.P.**
1962: Sedimentation of the Fraser River delta, British Columbia; American Association of Petroleum Geologists Bulletin, v. 46, p. 1416-1438.

**Terra Surveys Ltd.**
1991: Interpretation of marine geophysical data from PGC Cruises 91-01 & 91-04, south Roberts Bank detailed grid area; Report submitted to Seaconsult Marine Research, November 1991, 33 p.

**Tiffin, D.L., Murray, J.W., Mayers, I.R., and Garrison, R.E.**
1971: Structure and origin of Foreslope Hills, Fraser Delta, British Columbia; Bulletin of Canadian Petroleum Geology, v. 19, p. 589-600.

**Wernicke, B. and Burchfiel, B.C.**
1982: Modes of extensional tectonics; Journal of Structural Geology, v. 4, p. 105-115.

---

Geological Survey of Canada Project 890052

# Permian and Triassic radiolarian ages from the Cache Creek Complex, Dog Creek and Alkali Lake areas, southwestern British Columbia[1]

**Fabrice Cordey and Peter B. Read[2]**
**Cordilleran Division, Vancouver**

*Cordey, F. and Read, P.B., 1992: Permian and Triassic radiolarian ages from the Cache Creek Complex, Dog Creek and Alkali Lake areas, southwestern British Columbia; in Current Research, Part E; Geological Survey of Canada, Paper 92-1E, p. 41-51.*

***Abstract***

*Ten radiolarian chert localities from the Cache Creek Complex on both sides of the Fraser Fault in Dog Creek and Alkali Lake areas range in age from Early Permian (late Asselian-late Sakmarian) through Middle Triassic (late Anisian-early Ladinian) to Late Triassic (Early Carnian, Early-Middle Norian, Late Norian). This age range is similar to that of the Cache Creek cherts in their type locality, 150 km to the south. The newly discovered localities come from one or more slices of the complex which were thrust northeastward over Early Jurassic rocks. Chert-bearing units underlie undated clastic rocks that may represent a regional(?) overlap assemblage.*

***Résumé***

*Les associations de radiolaires provenant de dix localités de radiolarites dans le complexe de Cache Creek de part et d'autre de la faille Fraser, zones de Dog Creek et d'Alkali Lake, ont un âge qui s'étend du Permien précoce (fin de l'Asselien à fin du Sakmarien), au Trias moyen (fin de l'Anisien au début du Ladinien) et Trias supérieur (Carnien précoce, Norien précoce ou moyen, Norien tardif). Cet intervalle de temps est semblable à celui obtenu sur les radiolarites du complexe de Cache Creek dans leur localité-type, soit 150 km au sud. Les localités sont réparties sur une ou plusieurs écailles tectoniques charriées vers le nord-est, chevauchant ainsi des roches du Jurassique précoce. Sur les unités à radiolarites reposent des couches détritiques non datées qui pourraient représenter une unité de recouvrement régionale(?).*

---

[1] Contribution to the Frontier Geoscience Program Chilcotin-Nechako Hydrocarbon Province
[2] Geotex Consultants Limited, #1200 - 100 West Pender Street, Vancouver, British Columbia V6B 1R8

## INTRODUCTION

This paper gives the faunal associations, ages and structural setting of major areas of ribbon chert in the Riske Creek (92O/15) and Alkali Lake (92O/16) map areas. The results are part of the continuing study of Jurassic and older rocks which underlie the northeast corner of the Taseko Lakes map area (92O) (Hickson et al., 1991; Read, 1992). The discovery of moderately to well preserved radiolaria in the ribbon cherts of this area, which straddles the major dextral strike-slip Fraser Fault, provides critical support for the correlation of the Cache Creek Complex across the fault. Both authors sampled the chert-rich successions of units shown in Figures 1 and 2, but Cordey is responsible for the paleontology and Read, the geological mapping.

West of the fault, Early Permian to Late Triassic grey to green ribbon chert, siliceous phyllite and phyllite of unit **PTcctp** dated by radiolarians are part of the Cache Creek Complex. South of Ross Gulch (Fig. 2) a light to medium grey, locally bedded limestone (**PTccc**) up to 140 m thick outlines an isoclinal fold in the upper part of the ribbon chert succession. These rocks structurally overlie unnamed Early Jurassic flows and tuffs (**lJv**) which range from dacite to andesite and aphanitic to porphyritic. Grey siltstone and poorly bedded dacite lapilli tuff form layers and lenses of unit **lJvs** and a few medium grey limestone lenses up to 5 m thick of unit **lJc** are scattered through the volcanics. In the absence of fossils and radiometric dating, the rocks are tentatively correlated with dated Early Jurassic (late Toarcian) rocks 12 km southwest of Ross Gulch (Fig. 1) based on the presence of dacite tuffs and the good preservation of primary textures.

The contact between the Cache Creek Complex and underlying rocks is poorly exposed. At the head of Ross Gulch, knobs of dark grey ribbon chert (**tp**), grey limestone (**c**) and greenstone (**v**) dot the meadows, and in a few creeks outcrops of slickensided black serpentinite (**us**) form extensive banks. This area of fault-bounded blocks in a serpentinite matrix exposes the mélange unit **PTccmx** that forms between thrust slices of the complex west of Fraser Fault.

The metadiorite (**JKdi**) is part of Farwell Pluton, which immediately south of the map area (Fig. 1), intrudes the Early Jurassic volcanics on the west bank of the Fraser River. Although a mid-Permian zircon age of 258±5 Ma for the pluton (Friedman and van der Heyden, 1992) would require the intruded volcanics to be pre-mid-Permian, a lithologically similar pluton exposed 12 km to the south in Word Creek yields radiometric ages of 135.5±1.6 Ma and 161.1±2.6 Ma from hornblende for integrated $^{40}Ar$-$^{39}Ar$ and K-Ar respectively (unpublished data) and would permit intruded wall rocks of Early Jurassic age. On the basis of two radiometric dates, Farwell Pluton may be composite as presently named and include rocks of Permian and Jura-Cretaceous ages.

East of Fraser Fault, the Cache Creek Complex encompasses rocks of mid-Pennsylvanian to Middle(?) Jurassic age (Monger, 1989). In the northeast corner of Taseko Lakes, the massive limestone of the Marble Canyon Formation forms the eastern edge of the area. West of it, and probably structurally higher, lies a tightly folded but upright succession of marble, grey phyllite, ribbon chert and basic metavolcanic rocks of Permo-Triassic age. Parts of this consist of fault-slivered marble, grey phyllite, ribbon chert, metabasalt flows of unit **PTccmx** (Fig. 2). Structurally above this unit is a thick sequence (**PTccpw**) of poorly bedded grey siltstone, with less shale and lithic greywacke, and no chert (Fig. 1, 2). The unit is locally tuffaceous.

## RADIOLARIAN ASSOCIATIONS AND AGES

### *Permian*

Early Permian radiolarians were obtained from a disrupted grey radiolarian chert sequence (loc. 1, Fig. 1, Table 1). Although the preservation of the siliceous skeletons is moderate to poor, the association (Table 2) reliably correlates with the *Pseudoalbaillella lomentaria* Assemblage zone of Japan (Ishiga, 1990) in the interval late Asselian to late Sakmarian (Tables 2, 3).

### *Middle Triassic*

The radiolarian association (Table 2) found at loc. 6 (Fig. 2; Table 1) is correlative with the *Triassocampe deweveri* Assemblage zone of Yao (1982), Middle Triassic in age (Tables 2, 3) previously reported in many different part of the world, including North America (Cordey, 1986; Blome et al., 1988), Japan (Yao, 1982; Matsuda and Isozaki, 1982; Kido, 1982), and Europe (Dumitrica et al., 1980; De Wever, 1979; Gorican and Buser, 1990). The closest faunal resemblance with our association is obtained from chert of the Mino belt of southwest Japan (Yao et al., 1982) which includes *Triassocampe* sp. G. (pl. 1, fig. 16-18), *Eptingium* sp. cf. *manfredi* Dumitrica 1978 *sensu* Yao 1982 similar to our *Eptingium* (?) sp. A. (pl. 1, fig. 20). In the present knowledge of Middle Triassic radiolarian faunas in the world, it is premature to assess if this similarity is due to similar paleogeographic distribution factors or if they represent coeval stratigraphic levels. However, our association also contain taxa reported in the Tethyan realm as in the chert/limestone sequence of Zaklanec, Bohinj, and Vojsko, Slovenia (Gorican and Buser, 1990) including *Pseudostylosphaera longispinosa* (De Wever) 1979 (pl. 1, fig. 7), *Ps. tenuis* (Nakaseko and Nishimura) 1979 (pl. 1, fig. 9), *Sepsagon*? *robustus* Lahm 1984 and *Silicarmiger* sp. (pl. 1, fig. 12).

Poor radiolarian preservation prevented dating of four chert localities more precisely than Ladinian-Carnian (loc. 2, 3, and 7; Tables 2, 3) and Ladinian-Early Carnian (loc. 8).

### *Late Triassic*

#### Carnian

Locality 5 (Fig. 2; Table 1) released an Early Carnian radiolarian association (Table 2), including *Pseudostylosphaera nazarovi* Kozur and Mostler 1979 which occurs also in the Middle Triassic of the Harrison Lake

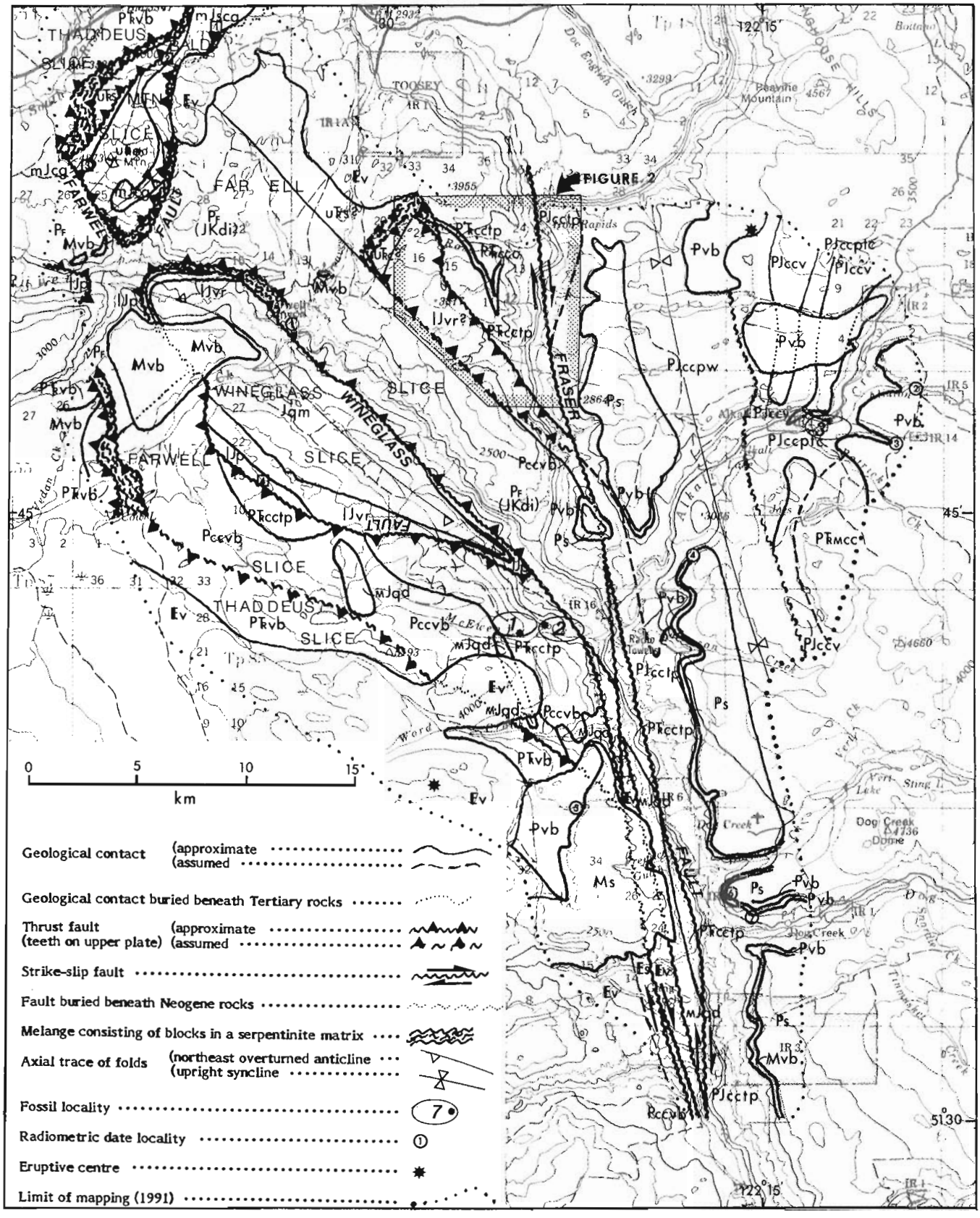


**Figure 1.** Preliminary geological map of parts of Riske Creek (92O/15) and Alkali Lake (92O/16) map areas showing radiolarian-bearing ribbon chert localities 1, 2 (west of Fraser Fault) and 3 (east of Fraser Fault), and emplacement of Figure 2.

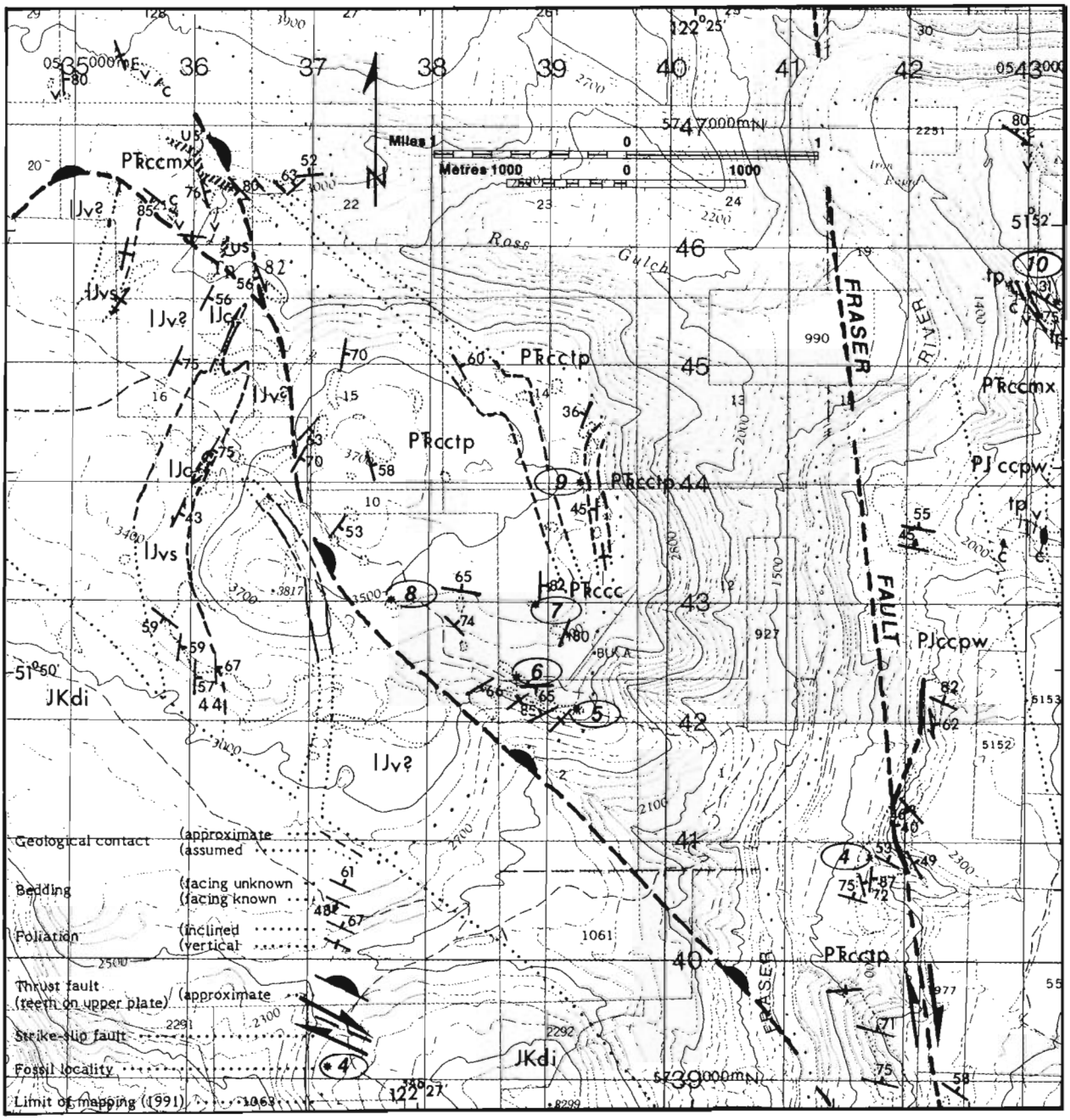


MESOZOIC
Jurassic or Cretaceous
Middle Jurassic or Early Cretaceous

JKdi — Chloritized and locally foliated metadiorite; minor quartz metadiorite and metagranodiorite

Jurassic
Lower Jurassic

IJv — Grey-green aphanitic and porphyritic (plagioclase, quartz) dacite and (plagioclase) andesite flows and tuffs

IJvs — Grey noncalcareous siltstone and coarsely bedded dacite lapilli tuff

IJc — Medium grey unbedded limestone

PALEOZOIC AND MESOZOIC
Permian to Jurassic
Lower Permian to Middle(?) Jurassic
CACHE CREEK COMPLEX (PJccpw to PTrccmx)

PJccpw — Grey siltstone, shale; minor grey lithic wacke

PTrcctp — Grey to green ribbon chert, siliceous phyllite and phyllite

PTrccc — Light to medium grey, locally bedded limestone

PTrccmx — Tectonic(?) lenses of greenstone, limestone and chert in a serpentinite (us) or grey phyllite (gp) matrix. The matrix is hachured and the lithology of the blocks is given by c = limestone, tp = grey phyllite and ribbon chert, v = greenstone.

**Figure 2.** Geological setting of the radiolarian-bearing ribbon chert localities 4-10 on both sides of the Fraser Fault south of Ross Gulch.

## LEGEND
## Figure 2

CENOZOIC
Quaternary and Tertiary
Pleistocene

**CHILCOTIN GROUP (Pvb to Ms)**

Pvb — Grey olivine- and/or plagioclase-phyric subaerial basalt flows

Tertiary
Pliocene

Pvb — Grey olivine- and/or plagioclase-phyric subaerial basalt flows

Ps — Unconsolidated fluviatile sandstone and pebble to boulder conglomerate

Miocene

Mvb — Grey olivine- and/or plagioclase-phyric subaerial basalt flows

Ms — Unconsolidated fluviatile sediments; minor rhyolite ash and diatomaceous earth

Eocene

Es — Conglomerate, sandstone; minor siltstone and bentonitic shale; rare coal

Ev — Hornblende-plagioclase-phyric dacite and hornblende-biotite-quartz-phyric rhyolite flows and tuff; rare basalt

MESOZOIC
Jurassic
Middle to Upper Jurassic

mJcg — South of Bald Mountain: Red sparsely plagioclase-phyric volcanic conglomerate overlying nonbedded quartz-bearing feldspathic sandstone

mJscg — North of Bald Mountain: Interbedded grey-green volcanic chip conglomerate and nonbedded quartz-bearing feldspathic sandstone

Jqm — Chloritized leucoquartz monzonite, leucoquartz diorite; rare metagabbro. Hypabyssal dacite and felsite intrusions occur marginally

mJqd — Chloritized hornblende diorite and quartz diorite

Lower Jurassic

lJp — Grey noncalcareous siltstone with thin sandstone laminae; minor thin limestone

lJvr — Grey-green and locally maroon porphyritic (plagioclase, quartz) dacite and rhyolite flows and tuffs, felsite- and quartz-feldspar porphyry-bearing tuff; minor green metabasalt flows

Triassic
Middle to Upper Triassic

uTrs — Grey nonlimy siltstone and minor interbedded thin calcareous sandstone

uTrc — Nonbedded light to medium grey micritic limestone

PALEOZOIC
Permian
Late Permian

**FARWELL PLUTON**

Pf — Chloritized and locally foliated metadiorite; minor quartz metadiorite and metagranodiorite

Permian to Jurassic
Lower Permian to Middle(?) Jurassic

**CACHE CREEK COMPLEX (PJccpw to Pccvb)**

PJccpw — Western Belt: Grey siltstone, shale; minor grey lithic wacke

PJccv — Western Belt: Meta-andesite and metabasalt breccia and flows

PJcctpc — Western Belt: Tectonic(?) lenses of greenstone, limestone and chert in a grey phyllite matrix

PJcctp — Western Belt: Grey phyllite, siliceous phyllite, and grey to green ribbon chert

**Marble Canyon Formation**

PTrMcc — Grey unbedded micritic limestone

Permian to Triassic

PTrvb — Green and grey-green aphanitic basic metatuff and minor flows

PTrcctp — Grey, grey-green and minor light green chert, ribbon chert and phyllite

PTrccc — Light grey unbedded limestone

Permian and(?) older
Lower Permian and(?) older

Pccvb — Grey-green and green greenstone

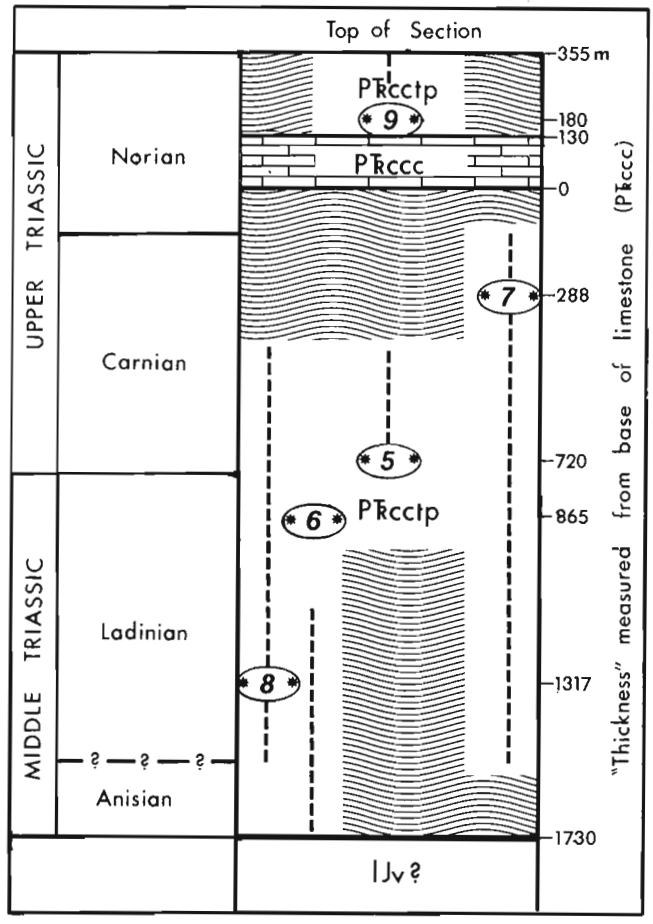


**Figure 3.** A "stratigraphic column" showing the positions of the fossil localities relative to the base of limestone (**PTccc**) on the right side of the column and to the age of each locality (Table 3) given on the left side of the column. The limestone unit is at present undated.

package (Cordey et al., 1988). At locality 10, the association is Late Carnian or Early Norian in age; it contains *Capnodoce anapetes* De Wever 1979 and *Capnuchosphaera theloides* De Wever 1979, described in the western Tethyan realm but reported also in Japan and North America by numerous workers.

### Norian

Early-Middle Norian radiolarians were found at locality 4 (Fig. 2; Tables 1, 2), including taxa of *Xipha striata* and *Latium paucum* subzones of Blome (1984).

The first Late Norian chert of British Columbia found so far at locality 9 contains Gen. nov. C (*in* Carter, 1990) previously reported in the Queen Charlotte Islands and possibly in "Rhaetian" strata of eastern former-USSR (in Bragin, 1991: "*Hagiastrum* sp.", broken specimen, pl. 7, fig. 2). Our association is possibly correlative with Assemblage 3 of Carter (1990), the youngest of the Late Norian.

## DISCUSSION

### *Stratigraphic and structural significance*

On the west side of Fraser Fault, the ribbon chert sequences range from Early Permian to latest Triassic. Five of the localities (5-9) are in an area south of Ross Gulch (Fig. 2) and come from a 2100 m "thick" sequence of grey-green ribbon chert with a 140 m thick limestone immediately beneath loc. 9 (Fig. 2, 3). This steep easterly dipping sequence spans time from the late Anisian or early Ladinian (loc. 6) to Late Norian (loc. 9), and based on the distribution of the dated samples, the sequence is upright. The "thickness" of nearly 2100 m for the sequence probably results from intense folding and faulting replicating the section but still retaining its overall original facing. A folded thrust forms the base of the section and sets it over structurally deeper Jurassic(?) rocks.

A 2.5 km wide belt of ribbon chert outcrops along the lower parts of Word and McEwen creeks and locally in the intervening area (Fig. 1). Although several collections from it were extensively recrystallized, localities 1 and 2 show that the sequence ranges in age from Early Permian to Middle or Late Triassic. The Early Permian locality (1) lies near the western edge of the belt close to the metavolcanic rocks of unit **PTvb**, and the Ladinian or Carnian locality (2) is near the eastern margin of the belt adjacent to Fraser Fault. Because these intensely deformed rocks likely dip and face easterly, the metavolcanic rocks west of the belt probably stratigraphically underlie the ribbon chert sequence.

The combined stratigraphy from these two areas west of the Fraser Fault indicates that ribbon chert was the dominant sediment deposited from Early Permian to Late Norian time. The absence of Late Permian and Early Triassic dates may reflect the degree of recrystallization of the radiolarians and difficulties of sampling rather than the absence of rocks of this interval.

West of the Fraser Fault, the Cache Creek Complex and Jurassic rocks form three or more northeasterly directed thrust slices (Fig. 1). Between the Chilcotin River and Bald Mountain, the slices from bottom to top are: (a) Wineglass Slice composed of dated but unnamed Early Jurassic stratified rocks and younger intrusions, all of which may be autochtonous, (b) Farwell Slice containing Farwell Pluton and probably the metavolcanics and dated ribbon cherts of the Cache Creek Complex; (c) Bald Mountain Slice consisting of Middle to Late Triassic limestone of the Cache Creek Complex and unnamed Middle to Late Jurassic sediments; and (d) Thaddeus Slice made of undated volcanics. The ribbon cherts south of Ross Gulch and along McEwen Creek belong either to Farwell Slice or a new unnamed slice. Because the complex west of Fraser Fault is a collage of slices, it provides an explanation as to why the deposition of Permo-Triassic ribbon chert along Ross Gulch and McEwen

**Table 1.** Radiolarian localities in the study area. 1-10 correspond to localities in Figures 1 and 2

| TEXT LOC. | GSC LOC. | SAMPLE No. COLLECTOR | UTM | | COORDINATES | | LOCATION | LITHOLOGY |
|---|---|---|---|---|---|---|---|---|
| | | | E. | N. | Lat. | Long. | | |
| 1. | C-177598 | FC91-CHIL6 F. Cordey | 540930 | 5727750 | 51°42'02" | 122°24'25" | Elev. 3340', 3.5 km at 273° from the mouth of McEwen Ck | light green ribbon chert |
| 2. | C-177597 | FC91-CHIL3 F. Cordey | 541800 | 5728250 | 51°42'20" | 122°23'40" | Elev. 2900', 2.8 km at 283° from the mouth of McEwen Ck | light grey ribbon chert |
| 3. | C-081597 | C91-3F P.B. Read | 554970 | 5737800 | 51°47'25" | 122°12'11" | Elev. 2650', 1.2 km at 081° from Patrick & Alkali Ck junct. | grey and green ribbon chert |
| 4. | C-176161 | C91-15F P.B. Read | 541710 | 5740860 | 51°49'08" | 122°23'42" | Elev. 1600', 6.65 km at 177° from the mouth of Riske Creek | grey and green ribbon chert |
| 5. | C-081571 | C91-34F P.B. Read | 539250 | 5742080 | 51°49'48" | 122°25'50" | Elev. 3075', 5.8 km at 201° from the mouth of Riske Creek | light green ribbon chert |
| 6. | C-081570 | C91-33F P.B. Read | 538730 | 5742350 | 51°49'57" | 122°26'17" | Elev. 3200', 5.75 km at 207° from the mouth of Riske Creek | light green ribbon chert |
| 7. | C-081572 | C91-35F P.B. Read | 538880 | 5742930 | 51°50'16" | 122°26'08" | Elev. 3375', 5.2 km at 209° from the mouth of Riske Creek | light green ribbon chert |
| 8. | C-081574 | C91-37F P.B. Read | 537700 | 5743000 | 51°50'18" | 122°27'10" | Elev. 3450', 5.75 km at 219° from the mouth of Riske Creek | red to grey-green r.c. |
| 9. | C-081573 | C91-36F P.B. Read | 539250 | 5744000 | 51°50'50" | 122°25'49" | Elev. 3425', 4.07 km at 210° from the mouth of Riske Creek | light green ribbon chert |
| 10. | C-176164 | C91-18F P.B. Read | 543170 | 5745550 | 51°51'40" | 122°22'40" | Elev., 2150', 2.8 km at 135° from the mouth of Riske Creek | grey and green ribbon chert |

**Table 2.** Radiolarian determinations and age assignments

| TEXT LOC. | GSC LOC. | FAUNA | AGE |
|---|---|---|---|
| **1.** | C-177598 | *Pseudoalbaillella sakmarensis* (Kozur) 1981<br>*Ps.* sp. cf. *longicornis* Ishiga & Imoto 1980<br>*Ps.* sp. cf. *scalprata* m. *scalprata* Holdsworth & Jones 1980<br>*Ps.* sp. cf. *scalprata* m. *postscalprata* Ishiga | Early Permian,<br>late Asselian to late Sakmarian |
| **2.** | C-177597 | *Pseudostylosphaera* sp.<br>*Triassocampe* sp. | Middle or Late Triassic,<br>e.Ladinian to L.Carnian |
| **3.** | C-081597 | ?*Pseudostylosphaera* sp.<br>Oertlispongid-related spines<br>Conical nassellarian shells | Triassic,<br>possibly early Ladinian to Late Carnian |
| **4.** | C-176161 | *Capnodoce extenta* Blome 1984<br>*Capnuchosphaera deweveri* Kozur & Mostler 1979<br>*Corum* sp. cf. *regium* Blome 1984<br>*Loffa* sp.<br>*Napora* sp. cf. *robusta* Nakaseko & Nishimura 1979<br>*Palaeosaturnalis vigrassi* (Blome) 1984 | Late Triassic,<br>Early or Middle Norian |
| **5.** | C-081571 | *Capnuchosphaera* sp.<br>*Plafkerium* sp.<br>*Pseudostylosphaera hellenica* (De Wever) 1979<br>*Ps. nazarovi* (Kozur & Mostler) 1979<br>*Ps.* sp. cf. *compacta* (Nakaseko & Nishimura) 1979<br>?*Vinassaspongus subsphaericus* Kozur & Mostler 1979 | Late Triassic,<br>Early Carnian |
| **6.** | C-081570 | *Plafkerium* sp.<br>*Pseudostylosphaera longispinosa* Kozur & Mostler 1981<br>*Ps. tenuis* (Nakaseko & Nishimura) 1979<br>*Ps.* sp. aff. *tenuis* (Nakaseko & Nishimura) 1979<br>*Ps.* sp. A<br>*Sepsagon*? *robustus* Lahm 1984<br>*Silicarmiger* sp.<br>*Triassocampe* sp. G<br>*Yeharaia* sp. aff. *elegans* Nakaseko & Nishimura 1979 | Middle Triassic,<br>late Anisian or early Ladinian |
| **7.** | C-081572 | ? *Eptingium manfredi* Dumitrica 1978<br>*Pseudostylosphaera compacta* (Nakaseko & Nishim.) 1979<br>? *Staurodoras variabilis* Nakaseko & Nishimura 1979<br>*Triassocampe* sp. | Triassic,<br>Ladinian-Carnian |
| **8.** | C-081574 | *Eptingium manfredi* Dumitrica 1978<br>*Pseudostylosphaera japonica* (Nakaseko & Nishim.) 1979<br>*Ps. spinulosa* (Nakaseko & Nishimura) 1979 | Triassic,<br>early Ladinian to Early Carnian |
| **9.** | C-081573 | *Betraccium* sp.<br>*Cantalum* sp. cf.*inornatum* Blome 1984<br>*Podocapsa* sp.<br>Gen. nov. C sp. 1 Carter 1990 | Late Triassic,<br>Late Norian |
| **10.** | C-176164 | *Canesium lentum* Blome 1984<br>*Capnodoce anapetes* De Wever 1979<br>*Capnuchosphaera theloides* De Wever 1979 | Late Triassic,<br>Late Carnian or Early Norian |

Creek in the Farwell or an unnamed slice is absent from the several hundred metre thick Bald Mountain limestone of Middle to Late Triassic age only 12 km away, in the Bald Mountain Slice. Apparently the collage consists of stratigraphic elements which were formerly widely separated.

East of the Fraser Fault, ribbon chert combined with basic metavolcanics, grey phyllite and limestone to form two zones each up to a few hundred metres in thickness. The western of these two zones first appears north of Dog Creek and outcrops sporadically within a few kilometres of the fault trace for 31 km northward to and beyond locality 10 where an eastward dipping ribbon chert yields a Late Carnian or Early Norian radiolarian age. Exposures around the locality show that the rock units are extensively faulted along their boundaries. Here the zone is treated as a melange rather than a stratigraphic succession, but farther south exposures are insufficient to allow an interpretation.

The eastern zone dips gently westerly and crosses Alkali Creek at the Alkali Lake Indian Reservation. The limestones and some of the metavolcanics are lenticular, the ribbon chert is intensely crumpled, and the phyllite has a good sheen on the foliation. These characteristics contrast to the unfolded, bedded siltstone and shale of the overlying and upward-facing rocks of unit **PJccpw** which separate the eastern and western ribbon chert zones and fill the core of a northerly trending syncline. Although the Ladinian or Carnian age of the poorly preserved fauna of locality 3 on the eastern limb of the syncline is less precise than the Late Carnian or Early Norian range from locality 10 on the western limb, the ranges allow a correlation of the limbs in a sequence which may have been partly dismembered.

### *Correlation with other chert-bearing units in the region*

The ten new radiolarian ages (Table 3) substantiate earlier correlations of the ribbon chert-greenstone assemblages on the west side of Fraser Fault to the Cache Creek Complex on the east side (Hickson et al., 1991; Read, 1992). In particular, cherts in the eastern belt of the complex also range from Early Permian (*Pseudoalbaillella scalprata* Assemblage zone of

**Table 3.** Ages of radiolarian associations at localities 1 to 10. Each vertical bar shows the age interval for one radiolarian association in one sample (isotopic ages for stage boundary based on DNAG time scale; Palmer, 1983)

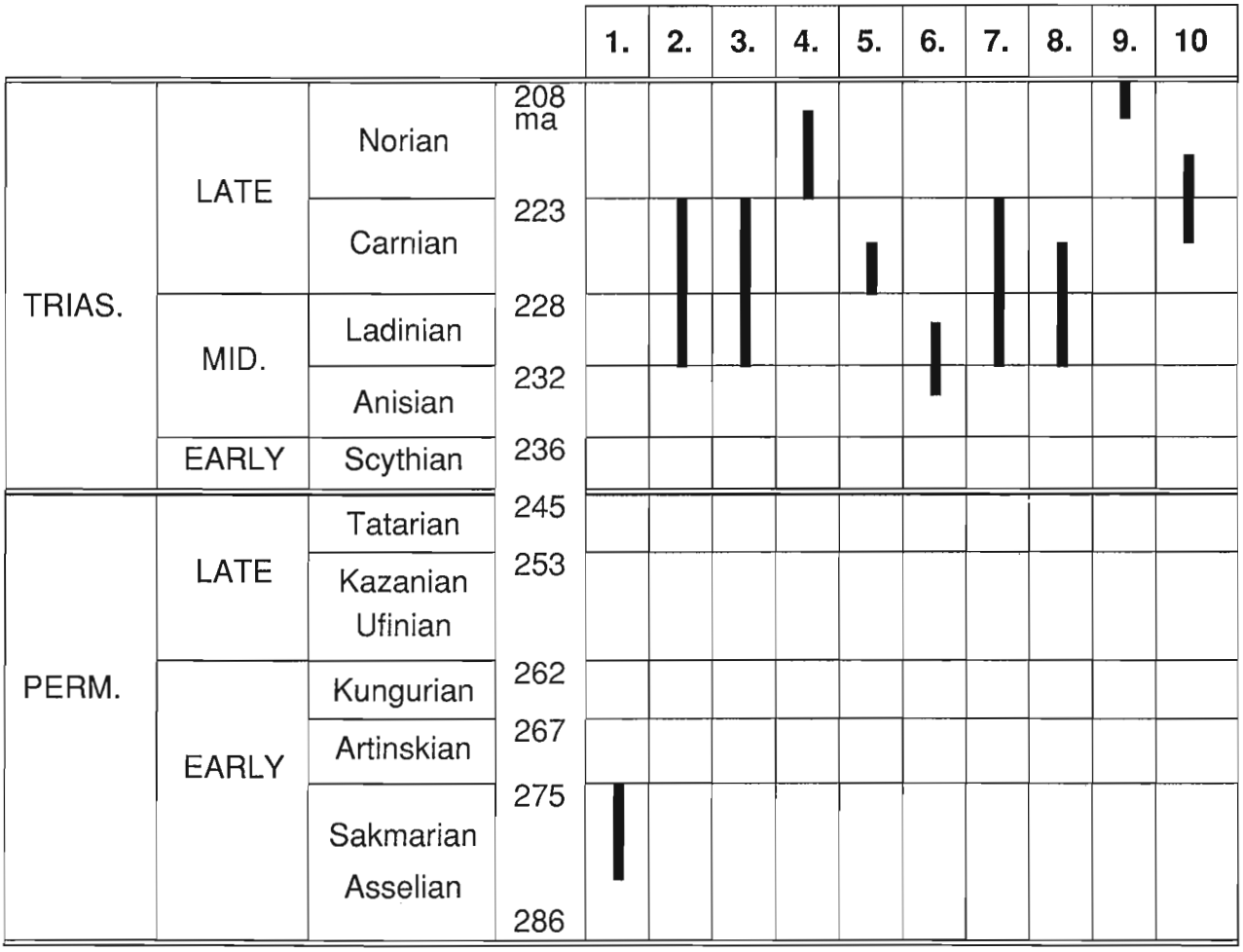

Ishiga, 1990) near Carquile (Cordey, 1986) to the Late Triassic (Orchard, 1984; Cordey, 1986, *Capnodoce* Zone of Blome, 1984, in the matrix of the mélange zone). Although Late Norian is absent in the type locality, it does occur in the Northern Cache Creek Complex in southern Yukon (Cordey et al., 1991). In contrast to the Cache Creek Complex, the Bridge River Complex contains not only Permian and Triassic, but also Mississippian, Early Jurassic, lower Middle and late Middle Jurassic radiolarian cherts (Cordey and Schiarizza, in prep.). The apparent sparsity of Jurassic rocks in the study area may result from a lack of Jurassic ribbon cherts, not a lack of Jurassic rocks. For example, in the Cache Creek Complex east of Fraser Fault and near Alkali Lake, the structurally highest rocks within the map area are grey shale-siltstone-greywacke turbidites of unit **PJccpw**, which are devoid of chert, undated, upward-facing, and probably younger than the radiolarian chert dated Ladinian or Carnian (loc. 3) to Late Carnian or Early Norian (loc. 10) that they overlie. These rocks could be correlative with the Early or Middle Jurassic radiolarian-bearing clastic rocks from the western belt of the Cache Creek Complex near Kelly Lake (Cordey et al., 1987). East of Alkali Lake, the abrupt upward passage from a grey siliceous phyllite and ribbon chert sequence containing lenses (tectonic ?) of limestone and greenstone into a thick succession of grey slate and siltstone with no chert across a few hundred metre wide gap in outcrop parallels the transition described by Journeay and Northcote (1992) from the eastern Bridge River Complex into the overlying but undated grey turbidites of the Cayoosh Assemblage. If the dating of unit **PJccpw** and the Cayoosh Assemblage were to substantiate such a correlation, it could suggest that they form a regional overlap assemblage across the eastern Bridge River and the Cache Creek complexes.

## ACKNOWLEDGMENTS

Funding by the Geological Survey of Canada project 810028, a post-doctoral fellowship administrated by the National Sciences and Engineering Research Council of Canada to Cordey, and C.J. Hickson's financial support through the Chilcotin-Nechako Hydrocarbon Province Project under contract #23254-1-01-0146/01-XSB to Read permitted the unravelling of a small area of the Cache Creek Complex along lines that may be more widely applicable. We are grateful to Susan Cannon and Hillary Taylor who picked a large part of the samples residues. Special thanks to Steve Irwin, Peter Krauss, Jim Monger and Mike Orchard for their support for radiolarian dating. Bev Vanlier and Jim Monger edited and improved the manuscript.

## REFERENCES

**Blome, C.D.**
1984: Upper Triassic Radiolaria and radiolarian zonation from western North America; Bulletin of American Paleontology, v. 85, n° 318, 88 p.

**Blome, C.D., Reed, K.M., and Tailleur, I.L.**
1988: Radiolarian biostratigraphy of the Otuk Formation in and near the national petroleum reserve in Alaska; United States Geological Survey, Professional Paper 1399, p. 725-774.

**Bragin, N.**
1991: Radiolaria and Lower Mesozoic units of the USSR east regions; Academy of Sciences of the USSR, Transactions, v. 469, 125 p. (In Russian with English abstract)

**Carter, E.S.**
1990: New biostratigraphic elements for dating upper Norian strata from the Sandilands Formation, Queen Charlotte Islands, British Columbia, Canada; Marine Micropaleontology, v. 15, p. 313-328.

**Cordey, F.**
1986: Radiolarian ages from the Cache Creek and Bridge River complexes and from chert pebbles in Cretaceous conglomerates, southwestern British Columbia; in Current Research, Part A; Geological Survey of Canada, Paper 86-1A, p. 595-602.

**Cordey, F., Mortimer, N., De Wever, P., and Monger, J.W.H.**
1987: Significance of Jurassic radiolarians from the Cache Creek terrane, British Columbia; Geology, v. 15, p. 1151-1154.

**Cordey, F., De Wever, P., Dumitrica, P., Danelian, T., Kito, N., and Vrielynck, B.**
1988: Description of some new Middle Triassic radiolarians from the Camp Cove Formation, Southern British Columbia, Canada; Revue de Micropaléontologie, v. 31, n°1, p. 30-37.

**Cordey, F., Gordey, S.P., and Orchard, M.J.**
1991: New biostratigraphic data for the northern Cache Creek Terrane, Teslin map area, southern Yukon; in Current Research, Part E; Geological Survey of Canada, Paper 91-1E, p. 67-76.

**De Wever. P.**
1979: Systematic section; in Triassic Radiolarians from Greece, Sicily and Turkey, (ed.) P. De Wever, A. Sanfilippo, W.R. Riedel, and B. Gruber; Micropaleontology, v. 25, n° 1, p. 75-110.

**Dumitrica, P.**
1978: Family Eptingiidae n. fam., extinct Nassellaria (Radiolaria) with sagital ring; Dari de Seama, Institutul de Geologie si Geofizicà, Bucuresti, v. 64, n° 3, p. 27-38.

**Dumitrica, P., Kozur, H., and Mostler, H.**
1980: Contribution to the radiolarian fauna of the Middle Triassic of the Southern Alps; Geologische Palaontologische Mitteilungen, v. 10, p. 1-46.

**Friedman, R.M. and van der Heyden, P.**
1992: Late Permian U-Pb dates for Farwell and Northern Mount Lytton plutonic bodies, Intermontane Belt, British Columbia; in Current Research, Part A; Geological Survey of Canada, Paper 92-1A, p. 137-144.

**Gorican, S. and Buser, S.**
1990: Middle Triassic radiolarians from Slovenia (Yugoslavia); Geologija, v. 32, p. 133-197.

**Hickson, C.J., Read, P., Mathews, W.H., Hunt, J.A., Johansson, G., and Rouse, G.E.**
1991: Revised geological mapping of northeastern Taseko Lakes map area, British Columbia; in Current Research, Part A; Geological Survey of Canada, Paper 90-1A, p. 207-217.

**Holdsworth, B.K. and Jones, D.L.**
1980: Preliminary zonation for Late Devonian through Permian time; Geology, v. 8, n° 6, p. 281-285.

**Ishiga, H.**
1983: Morphological change in the Permian radiolaria *Pseudoalbaillella scalprata* in Japan; Earth Sciences (Chikyu Kagahu), v. 36, p. 333-339.
1990: Paleozoic Radiolarians; in Pre-Cretaceous Terranes of Japan, (ed.) K. Ichikawa, S. Mizutani, I. Hara, and A. Yao, International Geological Correlation Program Project no. 224, Osaka, p. 285-295.

**Ishiga, H. and Imoto, N.**
1980: Some Permian radiolarians in the Tamba district, southwest Japan; Earth Sciences (Chikyu Kagaku), v. 34, n° 6, p. 333-345.

**Journeay, J.M. and Northcote, B.R.**
1992: Tectonic assemblages of the Eastern Coast Belt, southwest British Columbia; in Current Research, Part A; Geological Survey of Canada, Paper 92-1A, p. 215-224.

**Kido, S.**
1982: Occurrence of Triassic chert and Jurassic siliceous shale at Kamiaso, Gifu Prefecture, Central Japan; News of Osaka Micropaleontologists, Special Volume n° 5, p. 135-152. (In Japanese with English abstract)

**Kozur, H.**
1981: Albaillellidea (Radiolaria) aus dem Unterperm des Vorurals; Geologisch Paläontologisch Mitteilungen, Innsbruck, v. 10, p. 263-274.

**Kozur, H. and Mostler, H.**
1979: Beiträge zur Erforschung der mesozoischen Radiolarien. Teil III: Die Oberfamilie Actinommacea Haeckel 1862 emend., Artiscacea Haeckel 1882, Multiarcusellacea nov. der Spumellaria and triassische Nassellaria; Geologisch Paläontologisch Mitteilungen, Innsbruck, v. 9, p. 1-132.
1981: Beiträge zur Erforschung der mesozoischen Radiolarien. Teil IV: Thalassosphaeracea Haeckel, 1862, Hexastylacea Haeckel, 1882 emend. Petrusevskaja, 1979, Sponguracea Haeckel, 1862 emend. und weitere triassische Lithocycliacea, Trematodiscacea, Actinommacea and Nassellaria; Geologisch Paläontologisch Mitteilungen, Innsbruck, p. 1-208.

**Lahm, B.**
1984: Spumellarienfaunen (Radiolaria) aus den mitteltriassischen Buchensteiner-Schichten von Recoaro (Norditalien) und den obertriassischen Reiflingerkelken von Grossreifling (Osterreich). Systematik, Stratigraphie; München Geoswiss. Abh., v. 1, 161 p.

**Matsuda, T. and Isozaki, Y.**
1982: Radiolarians around the Triassic-Jurassic boundary from the bedded chert in the Kamiaso area, Southwest Japan. Appendix: Anisian radiolarians; News of Osaka Micropaleontologists, Special Volume n° 5, p. 93-102. (In Japanese with English abstract)

**Monger, J.W.H.**
1989: Geology of Hope and Ashcroft map areas, British Columbia; Geological Survey of Canada, Maps 41-1989 and 42-1989.

**Nakaseko, K. and Nishimura, A.**
1979: Upper Triassic radiolarians from southwest Japan; Science Reports, College of General Education, Osaka University, v. 28, n° 2, p. 61-109.

**Orchard, M.J.**
1984: Pennsylvanian, Permian, and Triassic conodonts from the Cache Creek Group, southern British Columbia; in Current Research, Part B; Geological Survey of Canada, Paper 84-1B, p. 197-206.

**Palmer, A.R.**
1983: The Decade of North American Geology 1983 Time Scale; Geology, v. 11, p. 503-504.

**Read, P.B.**
1992: Geology of parts of Riske Creek and Alkali Lake areas, British Columbia; in Current Research, Part A; Geological Survey of Canada, Paper 92-1A, p. 105-112.

**Yao, A.**
1982: Middle Triassic and Jurassic radiolarians from the Inuyama Area, Central Japan; Journal of Geosciences, Osaka University, v. 25, p. 53-70.

**Yao, A., Matsuoka A., and Nakatani, T.**
1982: Triassic and Jurassic assemblages from southwest Japan; News of Osaka Micropaleontologists, Special Volume n° 5, p. 27-44. (In Japanese with English abstract)

Geological Survey of Canada Project 810028

## Plate 1

Scanning electron micrographs of Permian (fig. 1-4) and Triassic (fig. 5-22) radiolarians from the Cache Creek Complex, Dog Creek and Alkali Lake map area, southwestern British Columbia. The following are indicated for each figure: identification, locality (cf. text-Fig. 1, 2), GSC locality no., field sample no., GSC specimen no., and magnification.

fig. 1. *Pseudoalbaillella sakmarensis* (Kozur) 1981, Loc. 1, GSC C-177598, FC91-CHIL6, GSC 101453, x 170.

fig. 2. *Pseudoalbaillella* sp., Loc. 1, GSC C-177598, FC91-CHIL6, GSC 101454, x 170.

fig. 3. *Ps.* sp. cf. *scalprata* m. *postscalprata* Ishiga 1983, Loc. 1, GSC C-177598, FC91-CHIL6, GSC 101455, x 130.

fig. 4. *Ps.* sp. cf. *longicornis* Ishiga & Imoto 1980, Loc. 1, GSC C-177598, FC91-CHIL6, GSC 101456, x 250.

fig. 5, 6. *Pseudostylosphaera* sp. A, Loc. 6, GSC C-081570, C91-33F, 5: GSC 101457, x 130, 6: GSC 101458, x 130.

fig. 7. *Pseudostylosphaera longispinosa* Kozur & Mostler 1981, Loc. 6, GSC C-081570, C91-33F, GSC 101459, x 110.

fig. 8. *Ps.* sp. aff. *tenuis* (Nakaseko & Nishimura) 1979, Loc. 6, GSC C-081570, C91-33F, GSC 101460, x 105.

fig. 9. *Ps. tenuis* (Nakaseko & Nishimura) 1979, Loc. 6, GSC C-081570, C91-33F, GSC 101461, x 115.

fig. 10. *Ps. nazarovi* (Kozur & Mostler) 1979, Loc. 5, GSC C-081571, C91-34F, GSC 101462, x 110.

fig. 11. *Plafkerium* sp. , Loc. 6., GSC C-081570, C91-33F, GSC 101463, x 130.

fig. 12. *Silicarmiger* sp., Loc. 6., GSC C-081570, C91-33F, GSC 101464, x 190.

fig. 13. *Yeharaia* sp. aff. *elegans* Nakaseko & Nishimura 1979, Loc. 6., GSC C-081570, C91-33F, GSC 101465, x 215.

fig. 14. *Yeharaia* sp., Loc. 6, GSC C-081570, C91-33F, GSC 101466, x 200.

fig. 15. *Triassocampe* sp., Loc. 6, GSC C-081570, C91-33F, GSC 101467, x 200.

fig. 16, 17, 18: *Triassocampe* sp. G, Loc. 6, GSC C-081570, C91-33F, 16: GSC 101468, x 200. 17: GSC 101469, x 200, 18: x 500 (enlargement of fig. 17 outlining shape of cephalo-thorax).

fig. 19. gen. sp. indet, Loc. 6, GSC C-081570, C91-33F, GSC 101470, x 170.

fig. 20. *Eptingium* (?) sp. A, Loc. 6, GSC C-081570, C91-33F, GSC 101471, x 150.

fig. 21. *Capnodoce extenta* Blome 1984, Loc. 4, GSC C-176161, C91-15F, GSC 101472, x 140.

fig. 22. *Palaeosaturnalis vigrassi* (Blome) 1984 , Loc. 4, GSC C-176161, C91-15F, GSC 101473, x 150.

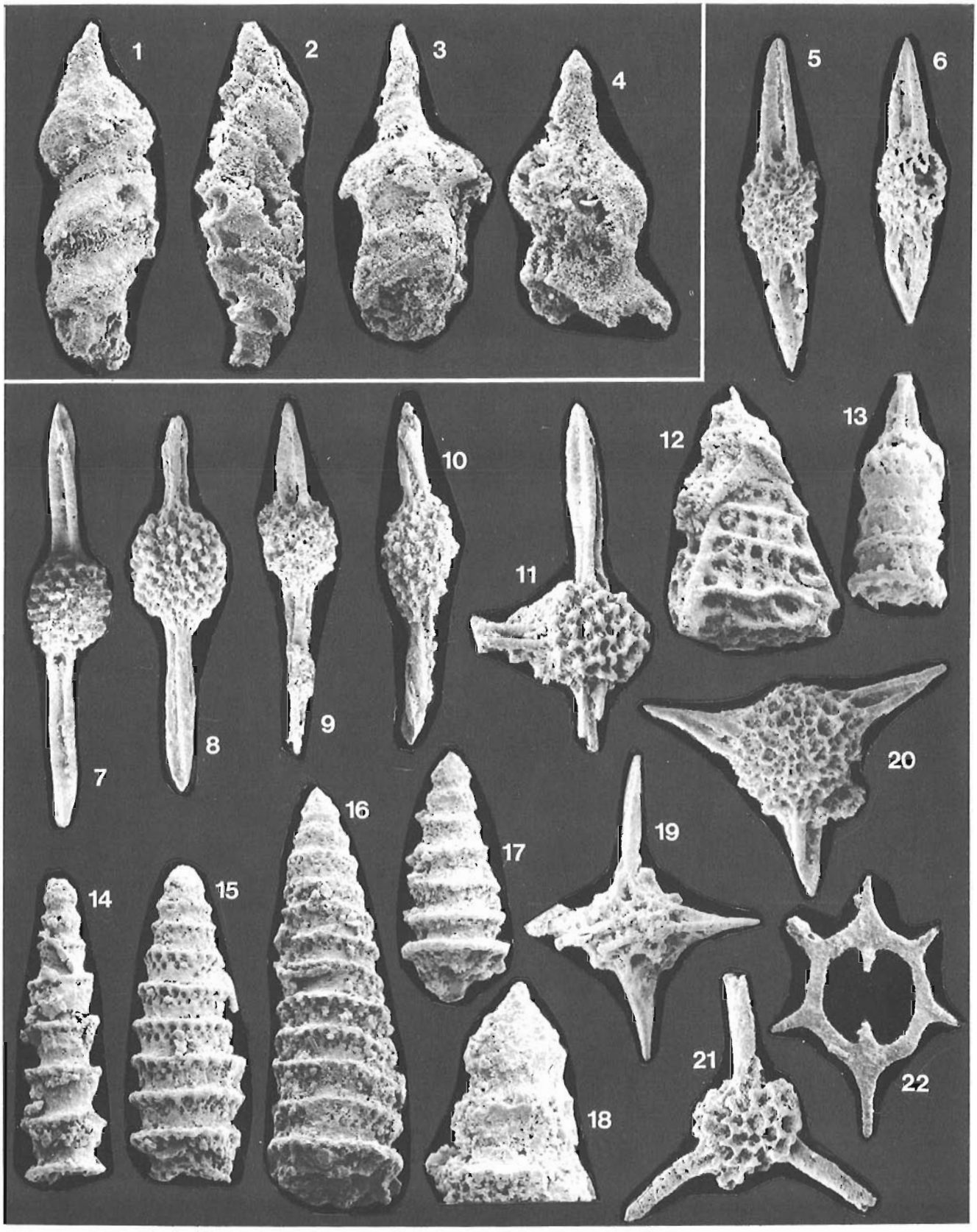
1
2
3
4
5
6
7
8
9
10
11
12
13
14
15
16
17
18
19
20
21
22

# Radiolarian ages from chert pebbles of the Tantalus Formation, Carmacks area, Yukon Territory

**Fabrice Cordey**
**Cordilleran Division, Vancouver**

*Cordey, F., 1992: Radiolarian ages from chert pebbles of the Tantalus Formation, Carmacks area, Yukon Territory; in Current Research, Part E; Geological Survey of Canada, Paper 92-1E, p. 53-59.*

***Abstract***

*Eighteen chert pebbles from three levels of the Late Jurassic-Cretaceous Tantalus Formation conglomerate near Carmacks contain radiolaria of Triassic (Ladinian-Carnian, Late Carnian-Middle Norian, Middle Norian, Late Norian) age. The known ages of chert pebbles from the Tantalus Formation near Whitehorse and Carmacks, which range from the Early Permian to the latest Triassic, differ from the age of Paleozoic chert-bearing units located to the northeast of the Tintina Fault. They more closely resemble the age of ribbon cherts of the northeastern part of the Northern Cache Creek Terrane (Teslin Plateau) in southern Yukon.*

***Résumé***

*Près de Carmacks, dix-huit cailloux de chert provenant de trois niveaux conglomératiques de la Formation de Tantalus du Jurassique tardif-Crétacé contiennent des radiolaires triasiques (Ladinien-Carnien, Carnien tardif-Norien moyen, Norien moyen, Norien tardif). L'âge connu des cailloux de chert de la Formation de Tantalus près de Whitehorse et de Carmacks, qui varie du Permien précoce au Trias terminal, diffère de celui des unités du Paléozoïque observées au nord-est de la faille de Tintina. Il correspond plus à celui des cherts rubanés de la partie nord-est du terrane de Cache Creek (plateau Teslin), dans le Yukon méridional.*

## INTRODUCTION

The Tantalus Formation (Fig. 1A) is a scattered chert pebble conglomerate unit of the south-central Yukon Territory, an overlap assemblage lying unconformably on the Lower and Middle Jurassic Laberge Group, the upper part of the pre-Cretaceous succession of the Whitehorse Trough (Fig. 1A). First described by Cairnes (1912, "Tantalus Conglomerates"), it has also been mapped near Carmacks by Bostock (1936) and Tempelman-Kluit (1974, 1984). The Tantalus Formation also outcrops to the south in Whitehorse area (Fig. 1A), where Wheeler (1961) was the first to recognize radiolaria in chert clasts. Recent work on the Tantalus includes sedimentological studies by Lowey and Hills (1988), and mapping by Hart and Radloff (1990).

The Tantalus Formation consists mainly of massive beds of conglomerate, along with sandstone, shale, and coal seams. As first indicated by Cairnes (1912), these conglomerates are distinctive from others in the Yukon region, as the clasts consist almost entirely of chert, quartz, or slate. The age of the Tantalus Formation is Upper Jurassic to Early Cretaceous, possibly Late Cretaceous (Hart and Radloff, 1990, and references therein) based on palynomorphs.

Two previous ages are known from pebbles of the Tantalus conglomerate: a black chert pebble collected in Indian River area near Dawson (Fig. 1A) released pyritized radiolarians identified as Late Triassic in age by B. Murchey (U.S. Geological Survey) (Orchard, 1986; Lowey and Hills, 1988). A grey chert pebble collected near Whitehorse (C. Hart, pers. comm., 1989) has released Permian radiolarians identified by the writer (unpub. data).

Near the town of Carmacks, the Tantalus Formation outcrops along a north-trending belt crossed by the Lewes River (Fig. 1B). Good exposures occur on the south-facing slopes of Tantalus Butte where the formation dips 40° to the west. There, a conglomeratic sequence approximately 150 m thick contains abundant chert clasts of relatively uniform size, varying from 0.5 to 5 cm with an average diameter of 2 to 3 cm. The chert is a variety of colours, including green, grey, brown, black, and pink.

## TECHNIQUE

The search for radiolarian-bearing chert pebbles was done at three different stratigraphic levels of the Tantalus Butte slope (GSC locality C-177599, Fig. 1B). Six pebbles were selected at each level (Fig. 1B, 2A; pebbles A1 to A6: elevation 640 m (2100 ft.); B1 to B6: 670 m (2200 ft.); C1 to C6: 700 m (2300 ft.)). These eighteen pebbles range in diameter from 0.6 cm to 5 cm with an average of 1.8 cm, and are either slightly angular or well-rounded (Fig. 2A). Colour of the chert is mostly green or grey-green, but some of the pebbles are pink, brown-black, and black (Tables 1-3). Processing (Cordey, 1986) included mechanically removing residual matrix surrounding parts of a pebble, and further chemical cleaning with highly concentrated (50%) hydrofluoric acid (HF). Each pebble was then separately etched several times in a low-concentration (5%) HF solution, each etching ranging from 4 to 24 hours.

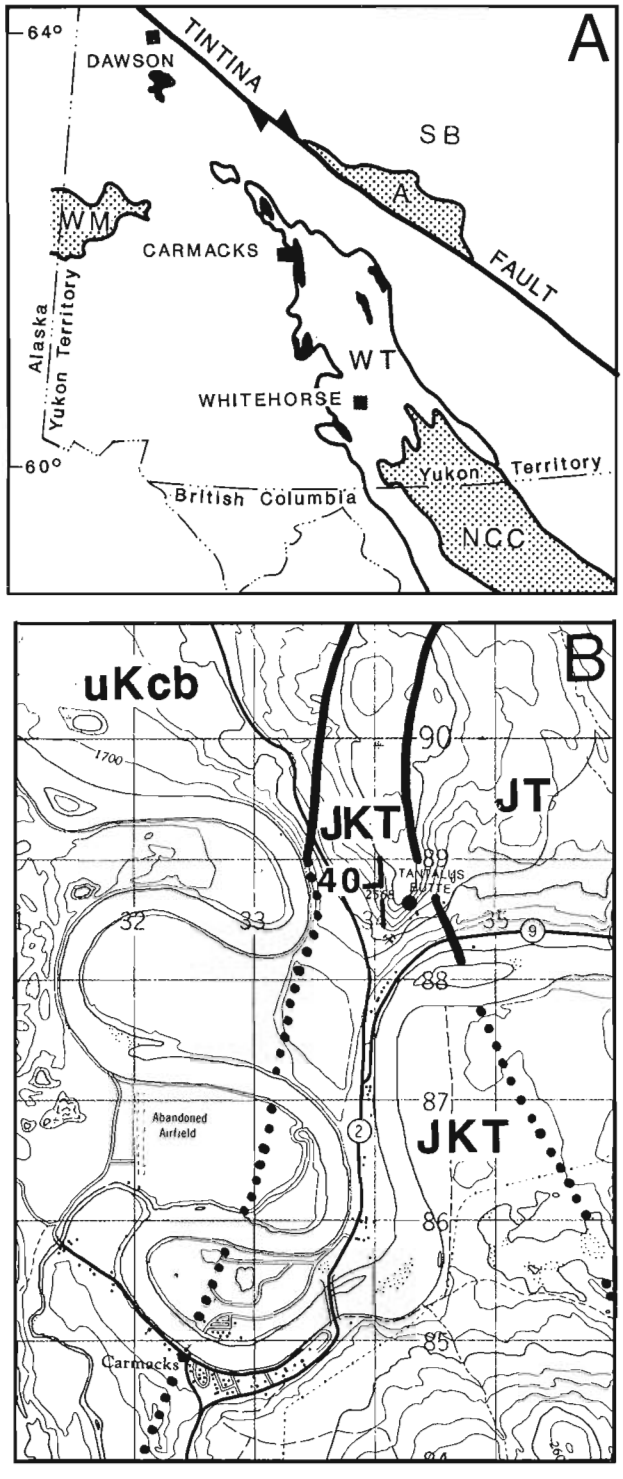


**Figure 1A.** Geographic extent of the Tantalus Formation, Yukon Territory (shown in black). WT: Whitehorse Trough (Lewes River and Laberge groups) (grey pattern). Main chert-bearing terranes of the region (dots pattern): NCC = Northern Cache Creek Terrane; WM = Windy-McKinley Terrane; A = Anvil; SB = Selwyn Basin). Modified from Lowey and Hills (1988). **B.** Location map of the Tantalus Butte near Carmacks (from Carmacks map area 115 I/1), and locality GSC C-177599 (black dot; X = 136°16′33″, Y = 62°07′29″). Transposed geology from Tempelman-Kluit (1984). JKT = Tantalus Formation; JT = Laberge Group; uKcb = Carmacks Group (stratigraphic contacts).

The duration of etching required to release well-preserved radiolaria is a function of (1) radiolarian/matrix silica composition differences, and (2) the decrease in HF concentration during etching process. This duration varies from one pebble to another. Recovery frequency of radiolarian-bearing residues must be high because of the small size of samples (Fig. 2A, B). Under these conditions, a clast as small as pea-size has the potential to release an identifiable faunal association.

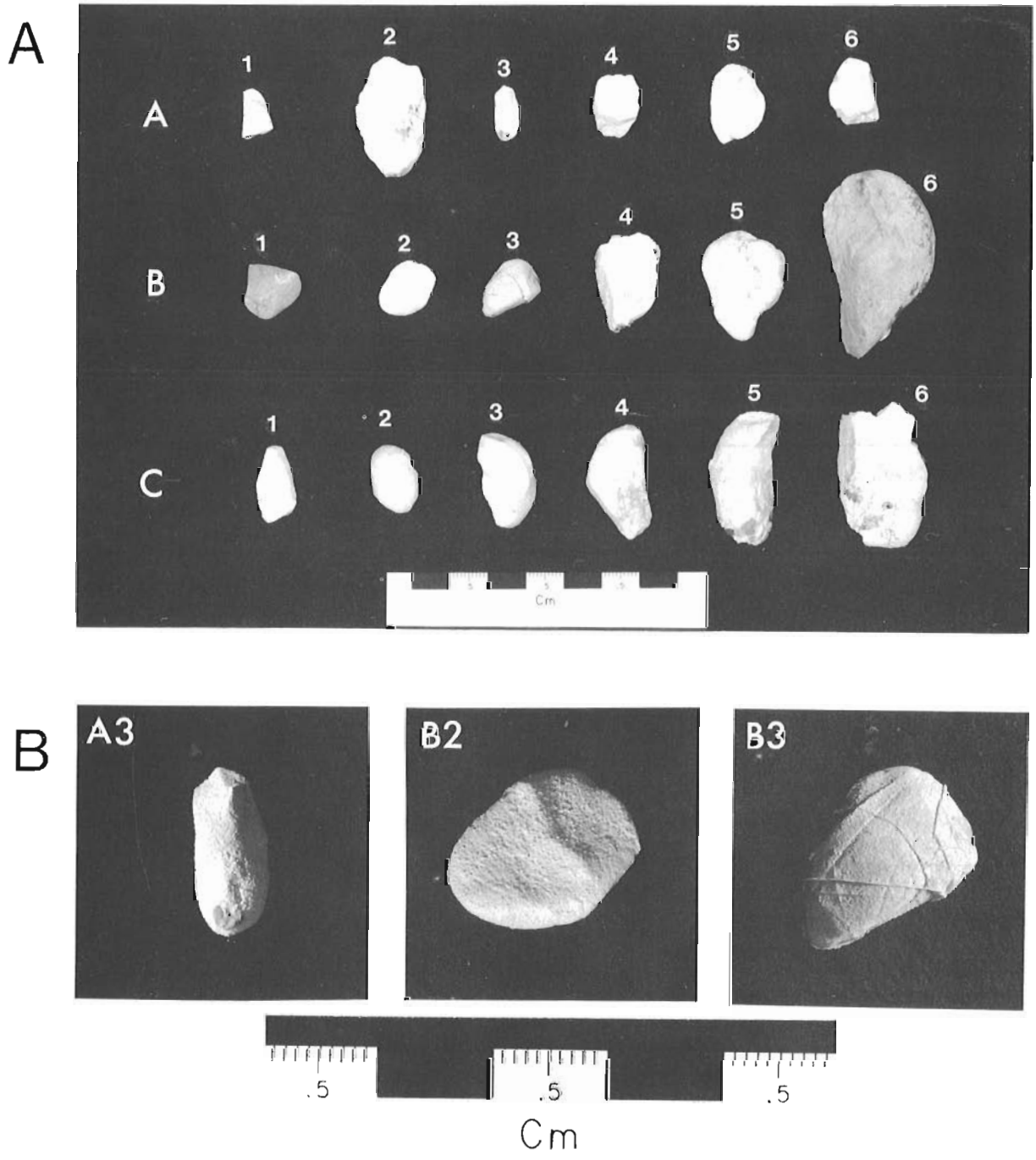


**Figure 2A.** Chert pebbles from levels A, B and C after 24 hours of 5% hydrofluoric acid (HF) processing. **B.** Pebbles A3, B2, and B3. Occurrence of radiolarians skeletons partly removed from the matrix on the pebble surface is outlined by tangential lighting. Thin silica joints visible on B3 are commonly observed in Cordilleran ribbon cherts.

**Table 1.** Radiolarian determinations and age assignments, pebbles A1 to A6 (Fig. 2A)

| PEBBLE N° LITHOLOGY | RADIOLARIAN ASSOCIATION | AGE |
|---|---|---|
| 91FC-TAN-A1 grey-green chert | *Capnodoce* sp.<br>*Latium* sp.<br>*Squinabolella* sp. | Late Triassic, Late Carnian-Middle Norian |
| 91FC-TAN-A2 grey chert | *Sarla* sp. | Late Triassic |
| 91FC-TAN-A3 green chert | *Palaeosaturnalis* sp.<br>*Sarla* sp. | Late Triassic |
| 91FC-TAN-A4 brown-green chert | *Betraccium* sp.<br>*Canoptum* sp.<br>*Canesium lentum* Blome 1984<br>*Corum* sp. | Late Triassic, Middle Norian |
| 91FC-TAN-A5 green chert | *Plafkerium* sp. cf. *cochleatum* (Nakaseko and Nishimura) 1979<br>*Pseudostylosphaera compacta* (Nakaseko and Nishimura) 1979<br>*Triassocampe* sp. | Triassic, Ladinian-Carnian |
| 91FC-TAN-A6 brown-black chert | *Pseudostylosphaera* sp.<br>*Triassocampe* sp. | Triassic, Ladinian-Carnian |

**Table 2.** Radiolarian determinations and age assignments, pebbles B1 to B6 (Fig. 2A)

| PEBBLE N° LITHOLOGY | RADIOLARIAN ASSOCIATION | AGE |
|---|---|---|
| 91FC-TAN-B1 brown-black chert | *Capnodoce* sp. aff. *anapetes* DeWever (in Blome 1984)<br>*Palaeosaturnalis* sp. | Late Triassic, Late Carnian-Middle Norian |
| 91FC-TAN-B2 grey chert | *Capnodoce* sp. cf. *antiqua* Blome<br>*Pseudosaturniforma* sp.<br>*Xipha striata* Blome | Late Triassic, Lower-Middle Norian |
| 91FC-TAN-B3 pink chert | *Canoptum* sp.<br>*Ferresium* sp. | Late Triassic, Late Norian |
| 91FC-TAN-B4 green chert | *Pseudostylosphaera* sp.<br>*Triassocampe* sp. | Triassic, Ladinian-Carnian |
| 91FC-TAN-B5 grey chert | ?*Ferresium* sp. | Triassic, possibly Late Norian |
| 91FC-TAN-B6 black chert | *Capnodoce* sp. cf *traversi* Pessagno 1979 | Late Triassic, Late Carnian-Middle Norian |

**Table 3.** Radiolarian determinations and age assignments, pebbles C1 to C6 (Fig. 2A)

| PEBBLE N° LITHOLOGY | RADIOLARIAN ASSOCIATION | AGE |
|---|---|---|
| 91FC-TAN-C1 green chert | *Ferresium* sp.<br>*Livarella* sp.<br>Gen sp. indet. C Carter 1990 | Late Triassic, Late Norian |
| 91FC-TAN-C2 dark grey chert | *Canoptum* sp.<br>*Ferresium* sp.<br>Gen sp. indet. C Carter 1990 | Late Triassic, Late Norian |
| 91FC-TAN-C3 grey-green ch. | torsaded spines | Middle or Late Triassic |
| 91FC-TAN-C4 grey chert | ?*Betraccium* sp.<br>*Canoptum* sp.<br>*Ferresium* sp. | Late Triassic, Late Norian |
| 91FC-TAN-C5 grey-green ch. | *Betraccium* sp.<br>*Ferresium* sp. | Late Triassic, Late Norian |
| 91FC-TAN-C6 grey-green ch. | *Pseudoheliodiscus* sp. | Late Triassic |

**Table 4.** Pebble ages grouped by levels (A, B, and C). Each vertical bar shows the age assignment for each pebble (Tables 1-3). Isotopic ages for stage boundaries based on DNAG time scale (Palmer, 1983)

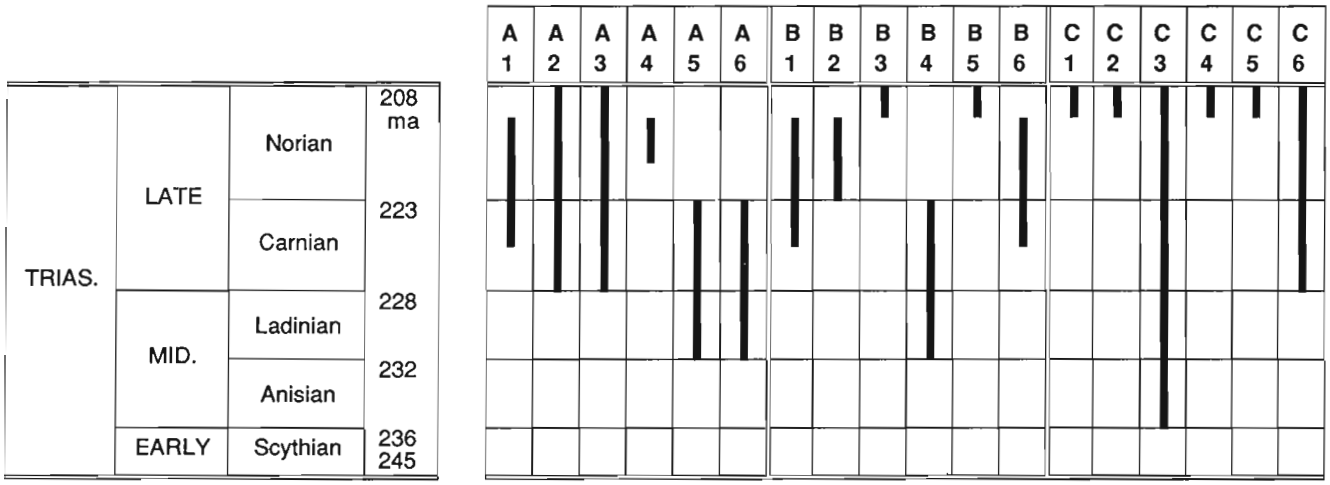

**Table 5.** Pebble ages displayed in order of age. Chert colours: gy = grey; gg = grey-green; gr = green; bg = brown-green; bb = brown-black; b = black; p = pink

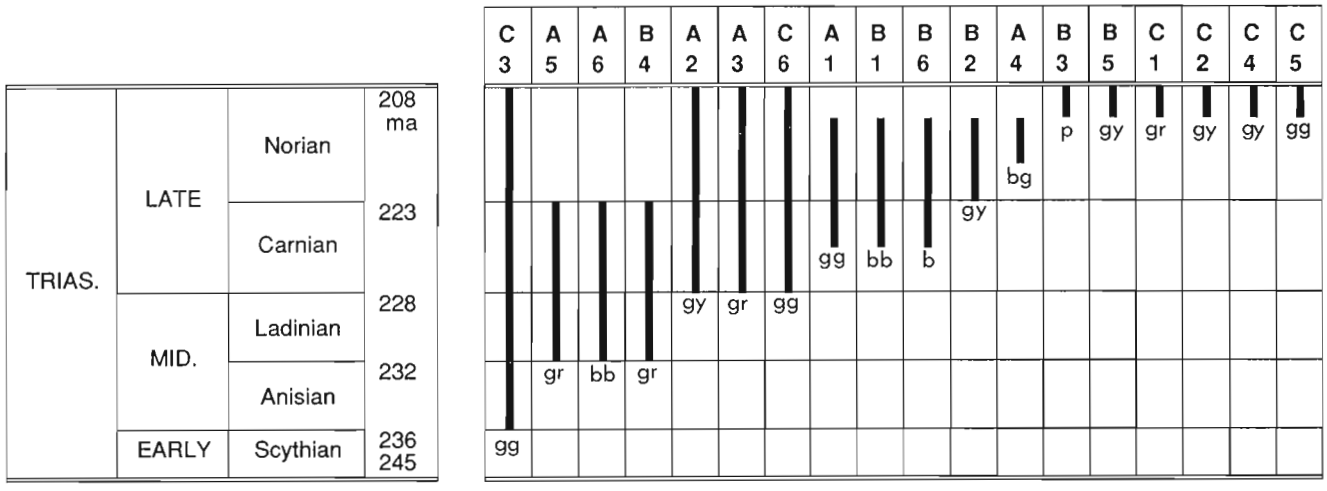


## DISCUSSION

### *Age of pebbles*

All pebbles released identifiable Triassic radiolarians (Tables 1-3). Occurrence of radiolarians of Middle Triassic age in pebbles A5, A6, B4, and C3 is uncertain as the association may be Ladinian or Carnian (Table 1-3). Remaining pebbles are Late Triassic in age, with five or six pebbles being of Late Norian age. Pebbles of level A (Table 1) range in age from Middle-Late Triassic (Ladinian-Carnian) to Late Triassic (Middle Norian; *Latium paucum* - *Pantanellium silberlingi* Subzones of Blome, 1984). Pebbles of level B (Table 2), are younger on average and include Late Norian fauna (*Betraccium deweveri* Subzone of Blome, 1984) in B3 and possibly in B5. Radiolarian ages in C (Table 3) are predominantly Late Norian (*Betraccium deweveri* Subzone; pebbles C1, C2, C4, C5).

Although the age data hint that the erosion that yielded the pebbles affected progressively younger chert strata (Tables 4, 5), the confirmation of this hypothesis requires further detailed sampling. Occurrence of pebbles exclusively of Triassic age over a stratigraphic interval of 60 m at the Tantalus Butte suggests that clastics were derived from a large volume of Triassic chert. At a maximum "sedimentation rate" of 5 m/Ma (on average 1 or 2 m/Ma, circum-Pacific regions; Matsuda and Isozaki, 1991), a continuous Triassic chert sequence would represent a thickness of only 200 m. Erosion must therefore have affected tectonically disrupted, structurally thickened Triassic radiolarian chert sequences. Such structure is commonly observed in the main accreted oceanic terranes, for instance the Northern Cache Creek Terrane in southern Yukon where exposures of exclusively Triassic radiolarian chert cover wide areas (Cordey et al., 1991; Gordey, 1992).

### *Potential source terranes*

This study shows that Paleozoic chert-bearing units of south-central and eastern Yukon such as the Anvil Range Group (Fig. 1A) or the Road River Group of the Selwyn Basin (Lowey and Hills, 1988) represent unlikely potential source rocks for the Tantalus chert pebbles, at least in Carmacks area. The Paleozoic-Mesozoic Windy McKinley Terrane (Fig. 1A) possesses chert strata which are poorly exposed in Canada, but which are predominantly Pennsylvanian and Permian in age in Alaska (Jones et al., 1981). Referring to radiolarian occurrences, Wheeler (1961) suggested that chert clasts may be derived from the Cache Creek Group (called "Taku Group"). Wheeler illustrated (p. 28) a radiolarian chert thin section that possibly includes specimens of *Capnodoce* sp., *Capnuchosphaera* sp. (Late Triassic; Late Carnian-Middle Norian), or *Livarella* sp. (Late Triassic; Late Norian). More recently, Hart and Radloff (1990) have correlated the chert clasts of the Tantalus Formation with the western belt of the Northern Cache Creek Terrane (Kedahda Formation; Monger, 1975). This study shows that the strongest age similarity lies with the northeast belt of the Northern Cache Creek Terrane (Teslin Plateau) which contains chert of Permian (from blocks in melange, unpub. data by the writer), Middle Triassic, and Late Triassic age (Cordey et al., 1991) including Late Norian chert which is rare in the Canadian Cordillera. Chert colours occurring in the Tantalus pebbles are observable in place in Teslin Plateau exposures. Early Jurassic sediments (chert and siliceous argillite/greywacke) occur in a few localities in the Teslin Plateau (Cordey et al., 1991). If, as suggested by this study, the northeast belt of the Cache Creek Terrane is a source area, Jurassic chert pebbles may yet be found in Tantalus conglomerate, possibly at higher stratigraphic levels.

## ACKNOWLEDGMENTS

The writer wishes to thank Craig Hart and Dirk Tempelman-Kluit for outlining occurrences of radiolarian chert pebbles in the Tantalus. This study is supported by the

Geological Survey of Canada - Cordilleran Division project 810028, while the writer benefits from a visiting fellowship administrated by the National Sciences and Engineering Research Council of Canada. Baron M.J. Orchard is thanked for his support and corrections of the manuscript. Tonia Oliveric did the drafting and Peter Krauss the pictures of this paper. Bev Vanlier and Steve Gordey edited and improved the manuscript.

## REFERENCES

**Blome, C.D.**
1984: Upper Triassic Radiolaria and radiolarian zonation from western North America; Bulletin of American Paleontology, v. 85, no. 318, 88 p.

**Bostock, H.S.**
1936: Carmacks District, Yukon; Geological Survey of Canada, Memoir 189, 67 p.

**Cairnes, D.D.**
1912: Wheaton District, Yukon Territory; Geological Survey of Canada, Memoir 31.

**Carter, E.S.**
1990: New biostratigraphic elements for dating upper Norian strata from the Sandilands Formation, Queen Charlotte Islands, British Columbia, Canada; Marine Micropaleontology, v. 15, p. 313-328.

**Cordey, F.**
1986: Radiolarian ages from the Cache Creek and Bridge River complexes and from chert pebbles in Cretaceous conglomerates, southwestern British Columbia; in Current Research, Part A; Geological Survey of Canada, Paper 86-1A, p. 595-602.

**Cordey, F., Gordey, S.P., and Orchard, M.J.**
1991: New biostratigraphic data for the northern Cache Creek Terrane, Teslin map area, southern Yukon; in Current Research, Part E; Geological Survey of Canada, Paper 91-1E, p. 67-76.

**Gordey, S.P.**
1992: Geological fieldwork in Teslin map area, southern Yukon Territory; in Current Research, Part A; Geological Survey of Canada, Paper 92-1A, p. 279-286.

**Hart, C.J.R. and Radloff, J.K.**
1990: Geology of Whitehorse, Alligator Lake, Fenwick Creek, Carcross and part of Robinson map areas (105D/11, 6, 3, 2 & 7); Indian and Northern Affairs Canada, Northern Affairs: Yukon Region, Open-File 1990-4, 113 p.

**Jones, D.L., Silberling, N.J., Berg, H.C., and Plafker, G.**
1981: Tectonostratigraphic terrane map of Alaska; U.S. Geological Survey, Open-File Report 81-792.

**Lowey, G.W. and Hills, L.V.**
1988: Lithofacies, petrography and environments of deposition, Tantalus Formation (Lower Cretaceous), Indian River area, west-central Yukon; Canadian Society of Petroleum Geologists, v. 36, no. 3, p. 296-310.

**Matsuda, T. and Isozaki, Y.**
1991: Well-documented travel history of Mesozoic pelagic chert in Japan: from remote ocean to subduction zone; Tectonics, v. 10, no. 2, p. 475-499.

**Monger, J.W.H.**
1975: Upper Paleozoic rocks of the Atlin Terrane, northwestern B.C. and south-central Yukon; Geological Survey of Canada, Paper 74-47, 63 p.

**Nakaseko, K. and Nishimura, A.**
1979: Upper Triassic radiolarians from southwest Japan; Science Reports, College of General Education, Osaka University, v. 28, no. 2, p. 61-109.

**Orchard, M.J.**
1986: Conodonts from western Canadian chert: their nature, distribution and stratigraphic application; in Investigative Techniques and Applications, (ed.) R.H. Austin; Ellis Horwood Limited, Chichester, p. 94-119.

**Palmer, A.R.**
1983: The Decade of North American Geology 1983 Time Scale; Geology, v. 11, p. 503-504.

**Pessagno, E.A., Jr.**
1979: Systematic Paleontology; in Upper Triassic Radiolaria from the San Hipolito Formation, Baja California, (ed.) E.A. Pessagno, Jr., W. Finch, and P.L. Abbott; Micropaleontology, v. 25, no. 2, p. 160-197.

**Tempelman-Kluit, D.J.**
1974: Reconnaissance geology of Aishihik Lake, Snag and part of Stewart River map-areas, west-central Yukon; Geological Survey of Canada, Paper 73-41.
1984: Maps of Laberge (105E) and Carmacks (115I) map sheets, with legends; Geological Survey of Canada, Open File 1101.

**Wheeler, J.O.**
1961: Whitehorse map-area, Yukon Territory; Geological Survey of Canada, Memoir 312, 156 p.

---

Geological Survey of Canada Project 810028

# Preliminary field and petrographic studies of the sulphide-bearing network underlying the western orebody, Sullivan stratiform sediment-hosted Zn-Pb deposit, British Columbia

**Craig H.B. Leitch and R.J.W. Turner**
**Mineral Resources Division, Vancouver**

*Leitch, C.H.B. and Turner, R.J.W., 1992: Preliminary field and petrographic studies of the sulphide-bearing network underlying the western orebody, Sullivan stratiform sediment-hosted Zn-Pb deposit, British Columbia; in Current Research, Part E; Geological Survey of Canada, Paper 92-1E, p. 61-70.*

***Abstract***

*The western massive sulphide portion of the Sullivan deposit is underlain by an extensive, in places intensely developed, pyrrhotite ± quartz-Fe carbonate stringer network in tourmalinite. This probably represents the major fluid upflow zone that formed the deposit. The network ranges from wispy, irregular veinlets that appear to have been emplaced in unindurated sediments at relatively early stages, to planar veins with increasingly abundant quartz and carbonate that appear to have formed at later stages of the development of the feeder zone. A crescent-shaped zone around the margins of this pipe is characterized by the presence of sphalerite and galena in the veinlets, with associated tourmaline-destructive muscovite alteration. This may represent the site of late-stage fluid flow after sealing of the main central conduit. Chlorite-dominant veins and alteration envelopes in the footwall and albite-chlorite-pyrite alteration in the hangingwall may be later, related to hydrothermal flow generated by the emplacement of mafic magma at depth below Moyie sills and dykes that are unusually abundant in the footwall of the deposit.*

***Résumé***

*Un vaste réseau parfois très dense de filons à pyrrhotine ± quartz et carbonates de Fe dans une tourmalinite est observé au-dessous des sulfures massifs de la portion occidentale du gisement de Sullivan. Il représente probablement la zone principale de remontée des fluides qui a donné naissance au gisement. Le réseau se compose tantôt de veinules très fines qui ont apparemment été mises en place dans des sédiments non indurés à des étapes relativement précoces de l'établissement de la zone nourricière, tantôt de veines planaires contenant des quantités de plus en plus abondantes de quartz et de carbonates qui se seraient formées à des étapes ultérieures de ce processus. Une zone en croissant autour des marges de cette colonne minéralisée se caractérise par la présence de sphalérite et de galène dans les veinules, accompagnée d'une altération en muscovite qui a détruit la tourmaline. Ceci pourrait correspondre au site de l'écoulement des fluides tardifs après l'obturation du principal conduit central. Les veines à chlorite dominante et les enveloppes d'altération de l'éponte inférieure de même que l'altération en albite-chlorite-pyrite de l'éponte supérieure pourraient être ultérieures et associées à l'écoulement hydrothermal généré par l'intrusion de magma mafique en profondeur, au-dessous des filons-couches et des dykes de Moyie qui sont particulièrement abondants dans l'éponte inférieure du gisement.*

## INTRODUCTION

Stratiform sediment-hosted (SEDEX) Zn-Pb deposits are characterized by bedded zinc and lead sulphides formed as hydrothermal sediments on the seafloor. Some stratiform deposits include a vent complex representing the zone of hydrothermal fluid upflow and discharge at the seafloor during formation of the sulphide sediments, though relatively few studies of such vent complexes are known (e.g. Hamilton et al., 1982; Goodfellow and Rhodes, 1990; Turner, 1990). As a consequence, little is known about the chemistry and temperature of fluids that formed stratiform Zn-Pb deposits. Studies in this regard include the Jason (Gardner and Hutcheon, 1985; Turner, 1990), Tom (Ansdell et al., 1989; Goodfellow and Rhodes, 1990) and Vulcan (Mako and Shanks, 1984) deposits in Yukon and Northwest Territories, and Silvermines (Samson and Russell, 1983) in Ireland.

The Sullivan deposit in southeastern British Columbia is a classic example of a stratiform deposit composed of a vent complex flanked by bedded sulphides. This deposit offers a unique opportunity to study the interaction of ore-forming fluids of a SEDEX deposit with the host rocks and bedded sulphides, because of its well-developed vent complex, relatively undeformed state, moderate metamorphic grade and extensive data from underground development and drilling. The vent complex includes a massive pyrrhotite replacement body within the bedded ores, an underlying tourmalinite pipe consisting of breccia, altered and fragmented strata and disseminated or veinlet sulphides, and albite-chlorite altered sediments in the hangingwall. Work to date on the tourmalinite pipe includes description (Hamilton et al., 1982), a study of the character of footwall veins (McAdam, 1978) and unpublished studies of alteration (summarized in Shaw and Hodgson, 1980; 1986). Interpretation of tourmalinite formation temperatures, based on oxygen isotope studies, range from <100°C (Nesbitt et al., 1984) to 200-250°C (Beaty et al., 1988). Ongoing studies by Leitch (1992b) suggest that ore-forming fluids were of moderate to high salinity (15-27 wt% NaCl equivalent but containing significant $CaCl_2$ and possibly $MgCl_2$). Regional

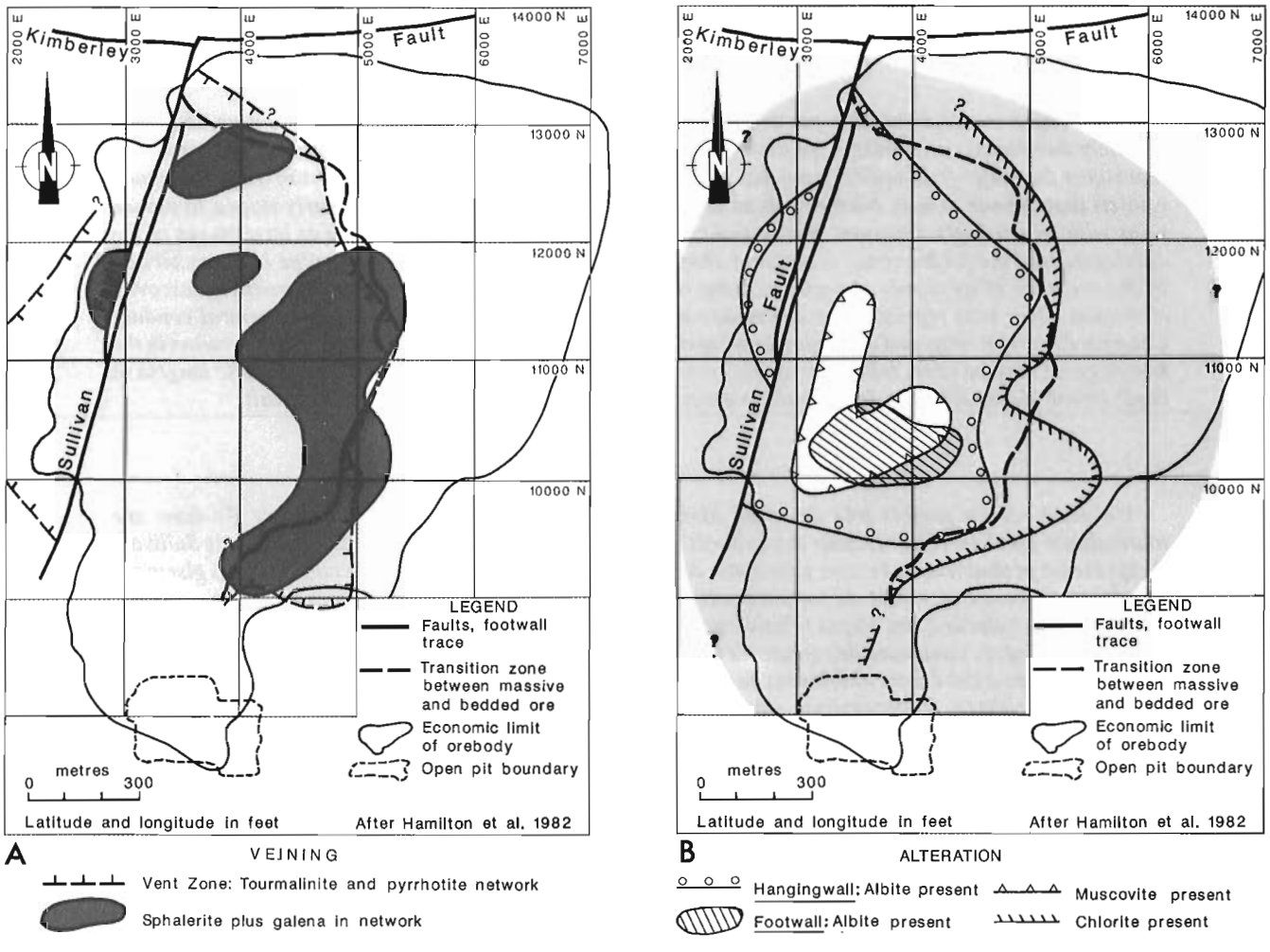


**Figure 1.** Plan views of Sullivan deposit showing **A**) distribution of pyrrhotite-rich and sphalerite-galena-rich footwall mineralization, and **B**) distribution of albite and muscovite alteration in the hangingwall, albite and chlorite in the footwall (after Shaw, written communication, and data of this study). Regional context is shown in Figure 1 of Turner and Leitch (1992).

metamorphism is biotite-Mn garnet middle greenschist facies at 400°C (McMechan and Price, 1982) and 2.0 kb (5.8-7.6 km depth of burial: Edmunds, 1977).

This study focuses on the nature of veining within the tourmalinite pipe, and is based on 3 weeks of core logging at the Sullivan mine by Leitch and Turner, and petrographic studies by Leitch. It adds to petrographic and fluid inclusion studies of the Sullivan deposit (Leitch, 1991; Leitch and Turner, 1991), and complements petrographic studies of district-scale alteration in the Sullivan-North Star area (Leitch et al., 1991). Locations of all samples and drill holes referred to in the discussions following are shown in plan view in Figure 4 of Turner and Leitch (1992) and in cross section in Figures 1 and 2 of Leitch (1992a), and will not be referred to individually. Study of the massive pyrrhotite body, associated altered rocks of the Sullivan vent complex, and veining footwall to the massive pyrrhotite body by Leitch and Turner is a subproject of the Sullivan Project.

## FOOTWALL VEINLETS, VEINS

A number of veinlet types of varying texture and mineralogy occur within the tourmalinite pipe. These are grouped primarily by mineralogy of vein envelopes (sulphide only, tourmalinite altered to muscovite, or tourmalinite altered to chlorite) and secondly by irregular or planar character. The envelope mineralogy reflects chemistry of the hydrothermal fluid, whereas the character relects the degree of induration of the sediment at the time of veining. The term veinlet is used for irregular, thin, discontinuous features; vein is used for throughgoing features generally greater than several mm thick. Orientations of veins are unknown because observations are restricted to drill core.

### *Tourmalinite-stable sulphide veinlets (lacking silicate envelopes)*

The most abundant veins and veinlets in the tourmalinite pipe are sulphide-rich and lack an alteration envelope overprinting the tourmalinite wall rock. Thus tourmaline is stable within the sulphidic envelopes, unlike other veinlets where tourmaline is altered to muscovite or chlorite.

### *(A1) Pyrrhotite-chalcopyrite veinlets*

Veins and veinlets of pyrrhotite, with minor chalcopyrite, are widespread and abundant throughout most of the shallow tourmalinite zone, close to the footwall of the orebody (Fig. 1A). The veinlets range from discontinuous sulphide blebs along microfractures (Fig. 2A) to narrow (generally less than 1 mm) wispy replacements either cross-cutting or along bedding planes, to veins or semi-massive replacement of the rock (Fig. 2B). Pyrrhotite veinlets are centred on indistinct or narrow fractures but the bulk of the pyrrhotite occurs in adjacent envelopes resulting in irregular, diffuse or wispy texture. Locally, pyrrhotite forms intense networks of irregular veins (Fig. 2C). Within conglomerate or breccia, pyrrhotite occurs as a disseminated or massive cement to fragments, the latter forming a "pyrrhotite matrix breccia" (Leitch and Turner, 1991, Fig. 5A). The abundance of pyrrhotite veinlets and replacement generally increases upward toward the base of the massive pyrrhotite body. This relation and the widespread occurrence of veinlets underlying the body suggest that formation of the massive pyrrhotite was related to the veinlets.

A good example of pyrrhotite veinlets occurs in diamond drill hole (DD) 280, 120-185 feet below the central portion of the western orebody. Immediately below the massive sulphide body, abundant pyrrhotite occurs as lacey net veinlets, intergranular disseminations and 1-2 cm diffuse irregular veins derived by replacement along hairline fractures. Also present are planar veins with quartz selvages and pyrrhotite centres, and thick massive pyrrhotite veins with rounded quartz fragments. Common coincidence of, and gradation among, these vein types suggests they are related. Irregular veinlets may represent early hydrothermal flow prior to lithifaction whereas relatively planar veins reflect progressive lithification during continued hydrothermal induration.

### *(A2) Planar quartz-carbonate-sulphide veins*

Planar veins contain significant amounts of quartz and carbonate in addition to sulphides. An increase in quartz-carbonate content is correlated with increasingly planar character in the gradation from irregular, sulphide-rich veinlets to planar veins. Planar veins are commonly sharp walled and zoned from outer selvages of inward terminating euhedral coarse quartz to an inner Fe carbonate zone, to a central pyrrhotite ± sphalerite-galena zone (e.g. DD280 120-163'). A second type, referred to as "quartz-pebble pyrrhotite veins", contains rounded fragments of coarse quartz floating in a pyrrhotite-rich sulphide matrix (also in DD280 120-163'). Another example is in DD3158 (211-213'), where a 0.6 m massive pyrrhotite vein containing coarse rounded quartz fragments cuts tourmalinite with pyrrhotite veinlets. These veins are interpreted as zoned veins which have been disrupted by displacement on the fracture.

No alteration envelope is typically associated with planar veins within tourmalinite. However, in some cases these veins contain chlorite and have pyritic envelopes (e.g. DD1141 140') or have muscovite envelopes (DD202 40'), suggesting this vein type is transitional to chlorite-pyrite or muscovite stable assemblages.

### *(A3) Pyrrhotite-galena-sphalerite-quartz-calcite veinlets*

In the marginal portions of the footwall network zone, principally underlying the transition zone, irregular pyrrhotite veinlets contain significant sphalerite, galena, quartz and carbonate (Fig. 1A). This relationship has been noted previously by D. Shaw (written comm., 1991). For instance, the interval 0-19 feet in DD296 is marked by irregular veinlets of quartz-carbonate-pyrrhotite-sphalerite-galena-trace arsenopyrite-minor sphene and chlorite, cutting tourmalinite. Some veinlets are associated with extremely fine (<1 to 10 μm) intimately intergrown pyrrhotite, galena

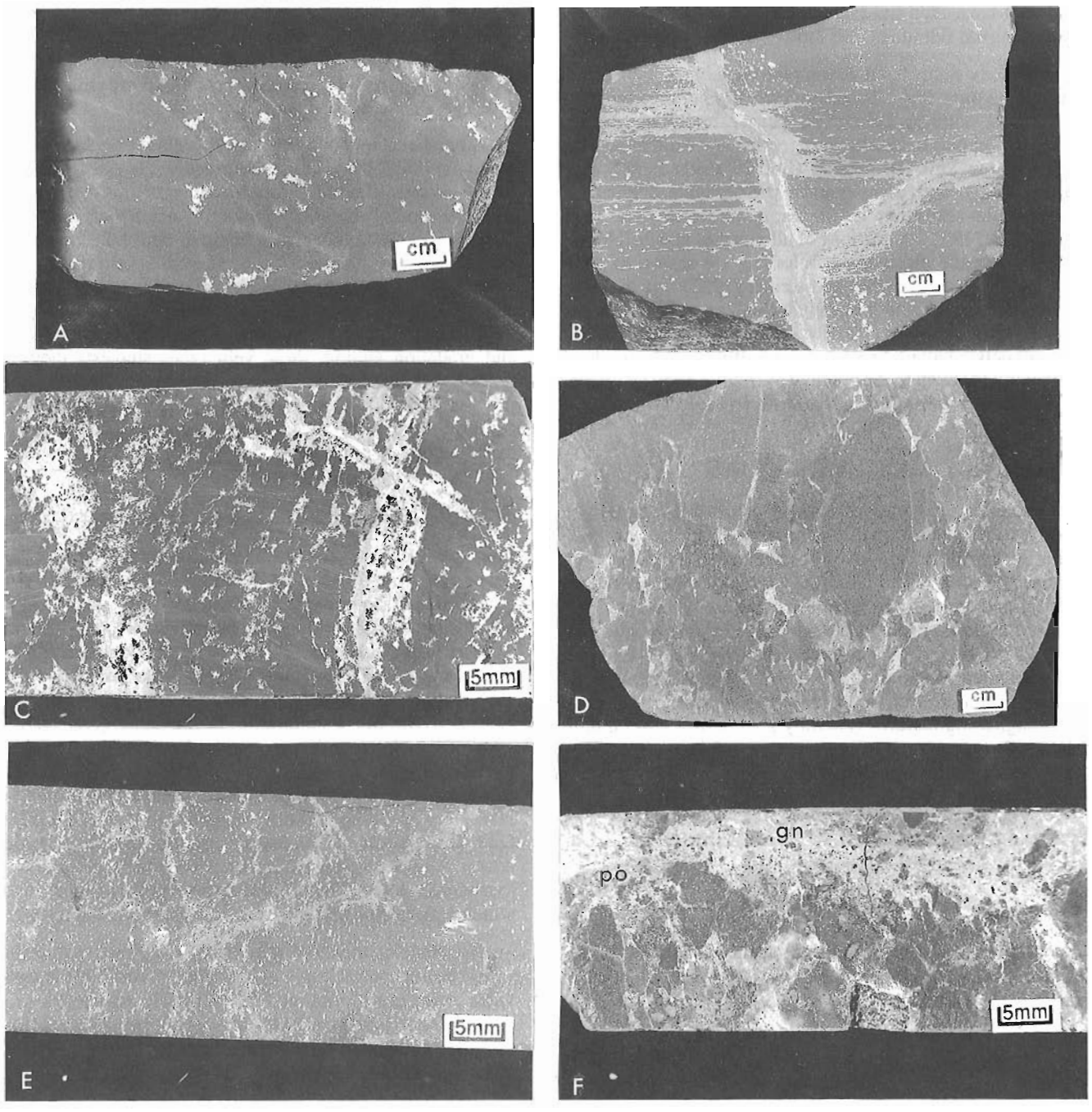


**A.** Blebs of pyrrhotite along partially healed microfractures in tourmalinite (sample 90SVT12).

**B.** Thicker, bedding-perpendicular veins and wispy bedding-parallel replacements in tourmalinite (sample 85SVT3).

**C.** Typical pyrrhotite networks in tourmalinite (DD4483-16.5').

**D.** Intraclast network or breccia cement underlying the transition zone, containing significant sphalerite and galena (sample 83SVH5).

**E.** Diffuse style pyrrhotite veinlets in tourmalinite (DD1141-110').

**F.** Galena (gn)-pyrrhotite (po) vein in fragmental (DD1041-83').

**Figure 2.** Macroscopic views of pyrrhotite network underlying the vent zone, Sullivan orebody.

and tourmaline between the detrital quartz grains of the wallrock and may tie sulphide deposition to tourmaline deposition.

The sphalerite-galena-bearing network, as with the pyrrhotite network, grades into cement between tourmalinized clasts in fragmental units (Fig. 2D). In DD1141 (95-150 feet), quartz-pyrrhotite ± chalcopyrite, galena, sphalerite cements tourmalinized wallrock fragments. The preferential development within a fragmental unit suggests hydrothermal fluids utilized the existing higher permeability of the fragmental unit. Locally diffuse veinlets (e.g. at 143', or 110': Fig. 2E) suggest fluid flow was intergranular adjacent to the fractures and therefore occurred prior to lithification.

In certain areas of the transition zone, a more diverse sulphide assemblage accompanies the pyrrhotite and zinc-lead sulphide bearing veinlets. This assemblage includes some or all of: arsenopyrite, chalcopyrite; boulangerite, bismuthian boulangerite and jamesonite; native Bi-Sb alloy, gudmundite (FeSbS), possible bismuthinite; freibergite (argentian tetrahedrite), stannite; ± pyrite, marcasite, quartz and cassiterite (Leitch, 1992a). Less commonly, such polymetallic assemblages occur within the central tourmalinite, e.g. arsenopyrite-chalcopyrite-galena-native Bi, or arsenopyrite, chalcopyrite, boulangerite, pyrite, marcasite in samples 85SVT3 and G79SL4 respectively (Turner and Leitch, 1992, Fig. 4).

### *Veins/veinlets with muscovite alteration envelopes*

An important set of veins and veinlets are associated with muscovite alteration of tourmalinite, and are concentrated in the transition zone at the base of the pyrrhotite body. Turbidite beds and hangingwall sediments are preferentially altered to muscovite in the area overlying this zone (Fig. 1B).

### *(B1) Pyrrhotite-sphalerite-galena ± Fe carbonate, garnet veinlets with muscovite-pyrrhotite envelopes*

Within the crescent-shaped transition zone (Fig. 1A), veins and veinlets of pyrrhotite-sphalerite-galena ± chalcopyrite, stannite-freibergite are associated with discrete envelopes of medium- to coarse-grained quartz, muscovite, Fe carbonate, chlorite and fine grained sulphides as found in the vein (Fig. 2F). These veins occur within broad zones of sericitic alteration. The similarity of muscovite-bearing envelopes to extensive sericitic alteration suggests that both are associated with formation of these veins. In DD3973 57-131 feet (Fig. 3A) immediately below the massive pyrrhotite body, a 2 m massive sulphide vein fault contains fragments of tourmalinite, variably altered to sericite, chlorite, quartz, and Fe carbonate, in a pyrrhotite-muscovite cement. In the hangingwall of the vein fault is a broad network alteration zone composed of abundant pyrrhotite-sphalerite-galena veinlets in similarly altered tourmalinite. A clear link between formation of pyrrhotite-sphalerite-galena veinlets and sericitic alteration is also displayed in DD1141, (150-208') immediately below the massive pyrrhotite body within the transition zone. Patches of pyrrhotite-sphalerite-medium grained sericite and garnet occur within sericite-chlorite-quartz altered tourmalinite surrounded by a pale-grey, bleached and weakly sericitized halo. Sericitic alteration is most strongly developed at the immediate base of the massive pyrrhotite body, forming a "detourmalinized" zone. This sericite-quartz assemblage appears to be one of the few areas in the altered footwall with significant secondary quartz. Such addition occurs only as part of this later quartz-sericite alteration and is not associated with tourmalinization.

A good example of a well developed portion of such a veinlet network is found in DD4483 from 0-31 feet (Fig. 2C; schematic section in Fig. 3B). In this interval, tourmalinized interbedded footwall conglomerate and siltite cut by a pyrrhotite-muscovite-sphalerite ± galena, chalcopyrite network grades to "pyrrhotite-cemented breccia", with abundant pyrrhotite ± sphalerite-galena and muscovite interstitial to tourmalinized conglomerate fragments. This is gradational upward into a 1.5 m zone of intense (10-20%) pyrrhotite ± sphalerite-muscovite-dravite-calcite replacement of tourmalinized sediment immediately below the base of massive pyrrhotite body. The mineralogy of this replacement is similar to cement in Figure 4D of Leitch and Turner (1991). In DD202 from 0-14 feet, sphalerite-pyrrhotite-galena-cassiterite ± arsenopyrite-chalcopyrite-bismuthian boulangerite and jamesonite, quartz-muscovite-Mn calcite veinlets occur immediately below massive pyrrhotite in sericitized tourmalinite of the transition zone.

There is thus an intense pyrrhotite network and replacement of sedimentary rocks immediately below a 50 m thick massive pyrrhotite body, implying proximity to a centre of intense hydrothermal discharge. The entire overlying massive sulphide body is highly pyrrhotized. There also appears to be a high sphalerite to galena ratio in the footwall veinlets (approximately 100:1 in a sample from 15'in DD4483) but a low sphalerite to galena ratio in the overlying massive pyrrhotite body (two samples at 177' and 207' are 1.25 and 0.5 respectively).

### *(B2) Planar veins with muscovite envelopes*

Planar veins rarely have muscovite envelopes. However, in DD202 at 40 feet within the immediate hangingwall of the transition zone, a planar 8 mm thick vein zoned as described above for type A2 has an envelope of muscovite-dolomite-chlorite after formerly tourmalinized rock. In DD4092 at 209 feet, one wall of a quartz fragment pyrrhotite vein consists of an intense net of pyrrhotite veinlets within sericitic altered rock containing abundant disseminated pyrrhotite and sphalerite.

### *Veins/veinlets with chlorite alteration envelopes*

A third major group of veins/veinlets is distinguished by chlorite as the dominant silicate in alteration envelopes and within veinlets. Muscovite and chlorite co-exist in some envelopes, and muscovite-dominant veins may be transitional to chlorite-dominant veins.

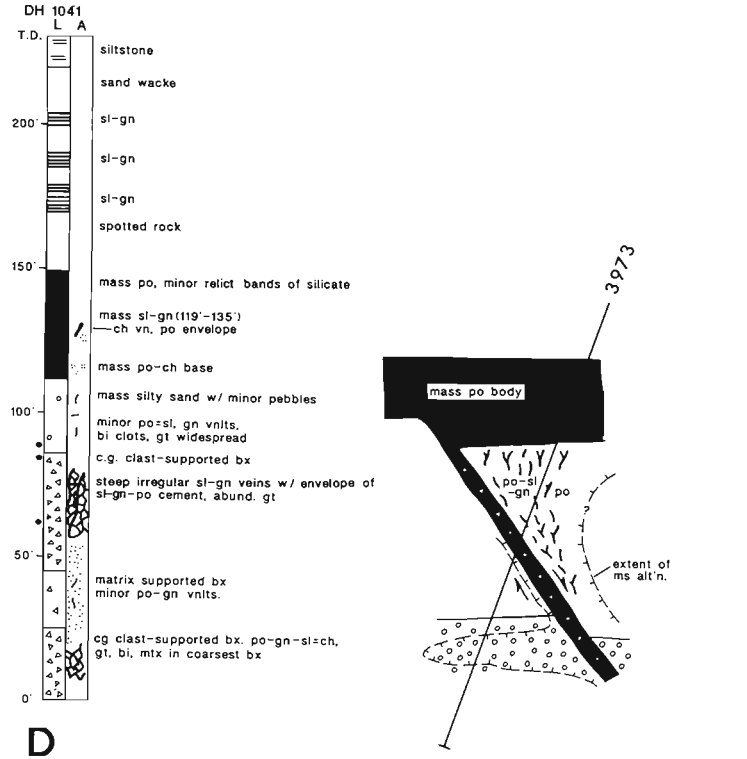


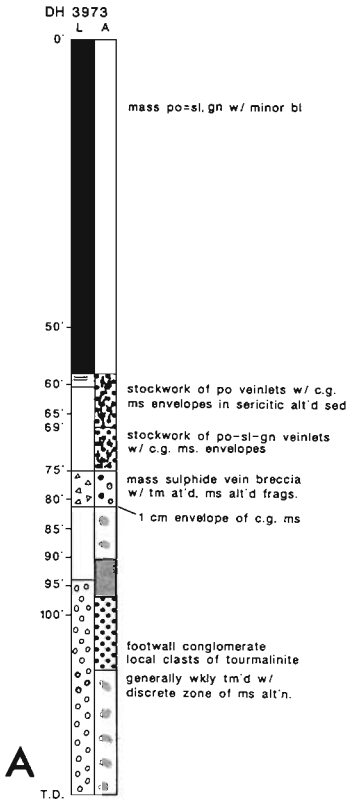


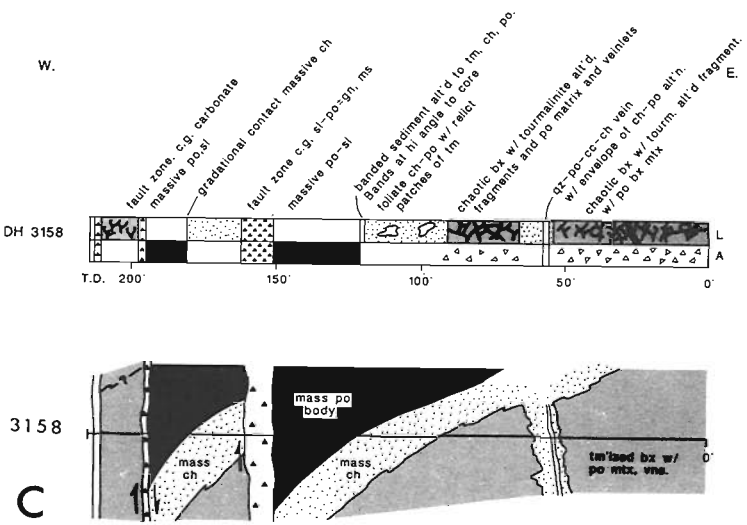


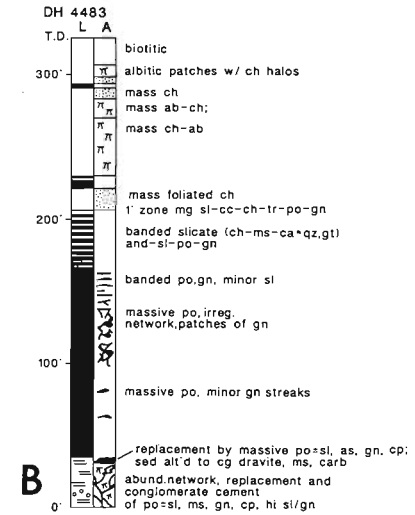


LITHOLOGY (L)

- interbedded siltstone, mudstone, sandstone
- conglomerate
- breccia
- massive sulphide – po, sl, gn, py
- sulphide veinlets/veins
- interbedded po laminae, siltstone, mudstone, sandstone
- gabbro; chlorite altered hornblende

ALTERATION (A)

- granophyric biotite hornfels
- muscovite = chlorite, dolomite
- chlorite rock
- chlorite – pyrite
- massive pyrite = chlorite
- albite – chlorite – pyrite
- tourmalinite

- fault zone
- • thin section

do = dolomite
cp = chalcopyrite
ms = muscovite
py = pyrite
po = pyrrhotite
gn = galena
sl = sphalerite
ru = rutile
gt = garnet

ab = albite
al = allanite
ch = chlorite
sp = sphene
tm = tourmaline
cz = clinozoisite
bi = biotite
qz = quartz

**Figure 3.**

**A.** Schematic log and interpretation of DD3973 through massive sulphide vein and adjacent sulphide network below massive sulphide body, on fringe of tourmalinite body in a zone of sericitic alteration. Sericitic alteration is linked to the sulphide vein and network as all veins have muscovite-rich envelopes.

**B.** Schematic log of DD4483 through thick massive pyrrhotite orebody underlain by zone of pyrrhotite replacement of footwall tourmalinite and pyrrhotite-sphalerite network. Sphalerite-rich footwall veins likely reflect lower solubility of zinc relative to lead in ore solutions; galena-rich pyrrhotized bedded ores reflect the preferential replacement of sphalerite rather than galena, due to Fe in sphalerite.

**C.** Schematic reconstruction of DD3158 drilled parallel to the base of the pyrrhotite body through several "keels". It cuts pyrrhotite matrix breccia in bleached tourmalinite rock ("chaotic breccia"), crosscutting a quartz-pyrrhotite-calcite-chlorite vein zone with envelope of massive foliate chlorite-pyrrhotite replacement of tourmalinite. Sulphide keels are asymmetric drags along west-side-down faults.

**D.** Schematic log of DD1041 illustrating sulphide-chlorite networks within footwall fragmental units. This relation suggests hydrothermal fluids followed the higher permeability of footwall fragmentals.

### *(C1) Pyrrhotite(±pyrite)-chalcopyrite-quartz-calcite-chlorite veinlets with chlorite envelopes*

Patchy to irregular veinlets of pyrrhotite(±pyrite)-chalcopyrite-quartz-calcite-chlorite surrounded by broad chloritic-sericitic haloes that alter ("detourmalinize") the wall rock under the massive pyrrhotite body (e.g. DD1141 49-66'). In DD3158 from 0-214 feet immediately below the massive pyrrhotite body, quartz-pyrrhotite-calcite-chlorite vein zones up to 1 m wide are surrounded by 0.6 to 2 m envelopes of massive foliate chlorite-pyrrhotite-calcite-minor albite and sphene, ± muscovite, hydrobiotite, garnet. This grades outward to a pale bleached distal envelope, that overprints hard, pale brown tourmalinite (Fig. 3C). The entire interval in this hole, drilled parallel to the base of the massive pyrrhotite body on section 11600N, consists of alternating zones of 1) pervasively brecciated tourmalinite (intermediate dravitic tourmaline, biotite and possible quartz) with an abundant pyrrhotite network that contains quartz, chlorite and rare chalcopyrite, crosscut by 2) major chlorite vein zones flanked by chlorite altered envelopes replacing tourmaline and biotite. This hole is interpreted to be in tourmalinized "chaotic breccia" of the footwall cut by "keel zones" of chlorite-pyrrhotite (Fig. 3C).

### *(C2) Pyrrhotite-sphalerite-galena-chlorite veins*

Chlorite-bearing veins also occur in the transition zone, where they tend to be enriched in sphalerite and galena relative to pyrrhotite-rich veins found in the core of the alteration pipe. These veins occur in the same area but tend to have lower sphalerite+galena to pyrrhotite ratios than pyrrhotite-sphalerite-galena veinlets with muscovite envelopes discussed above. However, chlorite alteration may be later (see below) and has merely utilized pre-existing conduits. Thus there is not necessarily any link between the galena-sphalerite veinlets and chlorite alteration. In DD1041 from 10-25 feet, two clast-supported fragmental units have central zones flooded by a cement of pyrrhotite-galena-sphalerite ± chlorite (Fig. 3D). Adjacent matrix-rich fragmentals lack significant sulphides suggesting the hydrothermal fluids were guided along the higher permeability zones of coarse clast-supported fragmentals. Clasts in the sulphide cemented breccia are variably altered to chlorite and muscovite (after biotite and garnet), plus possible secondary quartz. This softer, paler sericitic altered rock associated with sulphide veinlets grades outwards to intense chlorite alteration; concentrations of garnet seem associated with the veinlets.

A sample from DD2001 from 107.5 feet consists of coarse grained Mn calcite, garnet, Mg chlorite with pyrrhotite-sphalerite-galena-arsenopyrite-chalcopyrite-stannite-cassiterite-bismuthian jamesonite (Leitch, 1992a). Mg chlorite refers to a pale green, length-fast chlorite lacking pleochroism and anomalous birefringence; microprobe analysis shows that Fe approximately equals Mg (90NSH4A, Table 2 of Leitch, 1992a).

### *(C3) "Keel" fault zones (chlorite-muscovite-sphalerite ± carbonate)*

In DD3158 (Fig. 3C) between 152 and 163 feet, a 3 m breccia with chlorite-muscovite-sphalerite cement forms a fault zone on the west side of a sulphide "keel". Keel zones are structures at the base of the orebody along which massive sulphides extend down into the footwall for several metres (Hamilton et al., 1982). Two keels intersected in this hole each have an eastern conformable limb and a western faulted contact indicating that the keels form by east-side down movement on steep faults coincident with a curious rotation of the base of the sulphide on the east side. Other faults in this hole are composed of a massive coarse grained carbonate vein (e.g. 196-197 feet) or massive pyrrhotite with coarse grained quartz fragments (212-214'). Some keel zones are associated with semi-massive pyrrhotite or pass downward into sulphide veins (Hamilton et al., 1982).

### *(C4) Sulphosalt-rich veinlets*

An example of a bedding-parallel sulphosalt-rich vein occurs at the base of the massive orebody, along the contact between a turbidite bed and massive replacement pyrrhotite. This vein (sample 90SVL2, Fig. 4 of Turner and Leitch, 1992) consists of bismuthian boulangerite and jamesonite, lesser pyrrhotite, muscovite and quartz with minor arsenopyrite, chalcopyrite, gudmundite, stannite, freibergite, and native Bi-Sb alloys (Leitch, 1992a). In the adjacent turbidite bed, a needle-like mineral that resembles stibnite is also boulangerite (sample 91SVL6: Leitch, 1992a).

## COMPARISON TO VEINLETS ASSOCIATED WITH THE STEMWINDER DEPOSIT

The Stemwinder is a steeply dipping vein and vein breccia of primarily pyrrhotite, 2 km southwest of the Sullivan deposit. Many similarities exist between the two deposits. The Stemwinder is a northerly trending vein zone up to 30 m thick, subparallel to the chaotic breccia zones that underlie the Sullivan deposit. A small sphaleritic lens in the footwall of the vein contained 150 000 tonnes of 82g/t Ag, 3.1% Pb and 16.6% Zn (Hamilton et al., 1982). This high sphalerite to galena ratio is like that of the footwall veinlets at Sullivan. Tourmalinite alteration accompanied by sulphide stringer networks forms an envelope up to 50 m wide around the vein zone. At the Stemwinder deposit, several types of veins may be distinguished:

1. Abundant "Stemwinder-type" veinlets, composed of pyrrhotite ± sphalerite- galena as irregular veins, pods and breccia cement that comprise the bulk of the 1 million tonne deposit.
2. Rare irregular pyrrhotite-poddy quartz, or poddy quartz ± pyrrhotite, chlorite, and ferroan carbonate veins that are cut by planar pyrrhotite vein breccia (4, below).
3. "Quantrell-type" planar quartz-Fe carbonate-sphalerite ± galena- chlorite veins that locally have chlorite selvages and broad envelopes of pervasive chloritic alteration of biotite. They are characterized by high chalcopyrite to sphalerite + galena and high chalcopyrite + sphalerite + galena to pyrrhotite + pyrite ratios.
4. Planar pyrrhotite-quartz-sphalerite ± chlorite breccia veins cut quartz-carbonate-sulphide veins (e.g. DD5439-718'); these may merely represent remobilization along faults.
5. Planar quartz veins which grade to (4) above.

Both Sullivan and Stemwinder share similar early pyrrhotite and pyrrhotite-quartz vein sets. Early pyrrhotite veins post-date formation of pebbly siltstone and some slump breccias. The dominant type (1) veins are associated with more disrupted strata, suggesting that fragmentation and hydrothermal fluid flow were related. Vein types (1) to (3) could all be of the same major episode, as suggested by mutual occurrence and gradation from type (1) to (3); this is similar to relations seen at the Sullivan deposit. Similarly, types (4) and (5) may also be roughly contemporaneous; fluid inclusions in quartz in these veins from a Quantrell dump sample are similar to those seen in the Sullivan veins (Leitch, 1992b).

## DISCUSSION

### *Timing of veinlets*

Textural criteria for early veinlet formation include their irregular to poddy shape, suggesting that the host was not lithified at time of hydrothermal activity. Also, a preferential development within early fragmental rocks would be expected if hydrothermal fluids utilized these higher permeability zones. The matrix position of sulphides within early sedimentary breccias suggests that hydrothermal fluids were flowing through permeable clastic rock, therefore prior to loss of this permeability. The diffuse appearance of many thin veinlets appears to be caused by an irregular sulphidic envelope on a hairline fracture rather than open-space filling of a fracture. This suggests a weakly indurated sediment that could not support open fractures, with high intergranular permeability and porosity allowing invasion by hydrothermal fluids and partial replacement or cementing by sulphides.

Textural criteria for later veinlet formation are principally the planar form of veins and veinlets, implying brittle fracture of a more indurated rock. Cross-cutting relationships are observed, but are not consistent from place to place in the deposit, suggesting broad contemporaneity of veining.

Within a vent complex, induration would be expected to be variable, and the induration history complex. Hydrothermally altered sediments might be expected to be partially or fully indurated during hydrothermal activity (cf. Middle Valley on the Juan de Fuca Ridge or the Escanaba Trough). A progression from early irregular veinlets to later more planar veinlets would be expected.

### *Paragenesis among vein types*

The spatial association of pyrrhotite veinlets with tourmalinite and the lack of alteration envelopes around the veins suggests that the fluids depositing these veins were in

equilibrium with tourmaline. Thus pyrrhotite veining was either synchronous with tourmalinization or followed it closely. However, tourmaline is not seen in the pyrrhotite veins except where it forms a cement to breccia. Muscovite and chlorite both destroy tourmaline and therefore post-date it; there appears to be a gradation between muscovite and chlorite. Transition zone veins are enriched in sphalerite, galena and variable amounts of sulphosalts regardless of alteration envelope, but are most commonly associated with muscovite. Muscovite alteration, focused on the transition zone, predominates above the footwall, suggesting it is a later event. Lack of muscovite alteration in the core of the vent complex (muscovite absent area, Fig. 1B) suggests that this later discharge was focused at the periphery of the system. Chlorite in the footwall, associated with pyrrhotite, is approximately co-extensive with the tourmalinite pipe. This is probably distinct from the chlorite associated with the late albite event, because the latter is associated with pyrite rather than pyrrhotite. Thus the timing of footwall chlorite may be late-stage hydrothermal, prior to albite-chlorite-pyrite associated with sill intrusion (see below).

Evolution of the hydrothermal system is postulated to have taken place along the following lines (Fig. 4):

1. main stage hydrothermal, high temperature discharge with pyrrhotite precipitation/replacement in the subsurface, and base metals remobilized or flushed through (black smoker discharge) and deposited as sediments on the overlying seafloor. It is possible that the bulk of the pervasive tourmalinite alteration took place at this pre-brittle stage, contemporaneous with the irregular to planar pyrrhotite (± increasing gangue proportion) veining. Continuation of this process converted previously deposited laminated sulphides to massive pyrrhotite over the main vent zone.

2. In late stage hydrothermal, physical plugging of the vent complex may have taken place by tourmaline, quartz and pyrrhotite precipitation. Continued leakage of fluids at ?higher or lower temperature in a crescent-shaped zone along the eastern margin of the indurated zone caused precipitation of base metals in footwall veinlets with muscovite selvages in a brittle fracture, muscovite stable, tourmalinite unstable event. The Sn, ± As (?high-temperature) assemblage precipitated in the footwall portions of this zone, while the Sb-Bi-Ag (?low temperature) assemblage precipitated in the sulphide body. This would have been represented by white smoker discharge. It is not clear whether (1) and (2) represent (a) a zoned vent complex with high-temperature pyrrhotite (+tourmalinite?) in core, and lower temperature sphalerite-galena (+muscovite-chlorite) on periphery; or (b) later stage sphalerite-galena veins and sericite, then chlorite alteration in transition area related to late-stage hydrothermal activity. The crescent shape of the sphalerite-galena rich zone appears to favour the first model, but concentration of sphalerite-galena ± sulphosalt along cross-cutting structures suggests late stage hydrothermal activity.

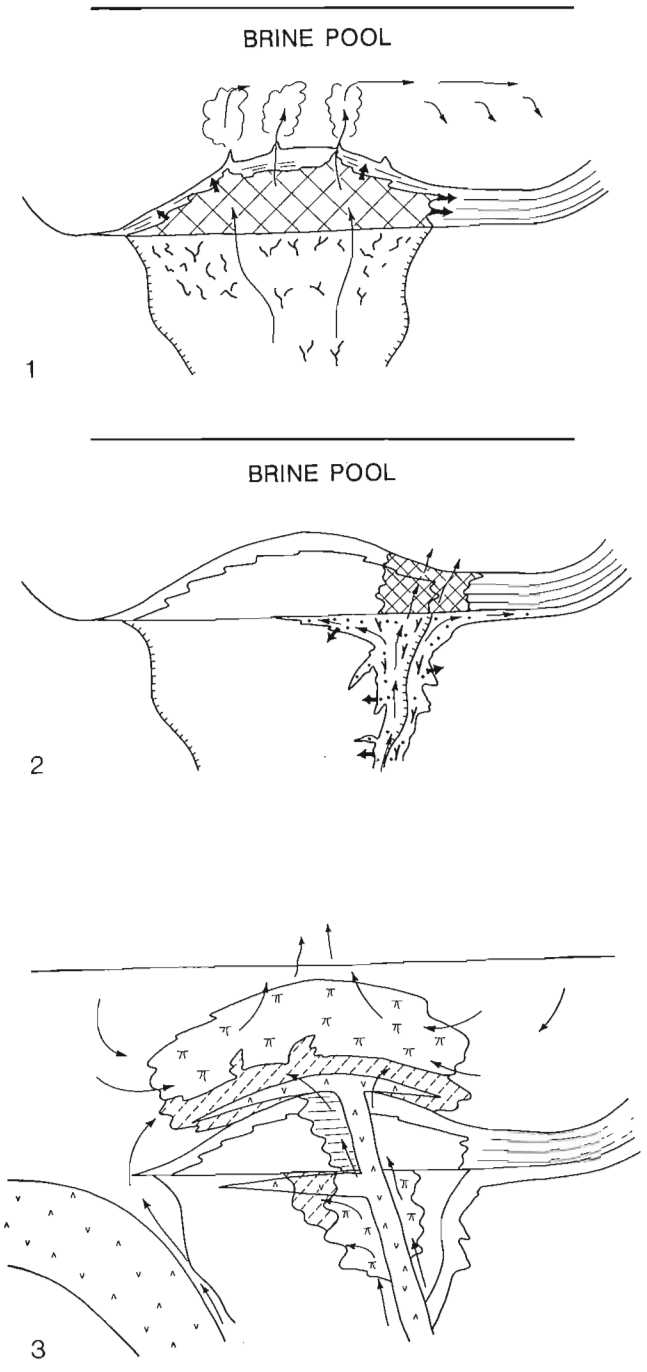


**Figure 4.** Postulated evolution of the hydrothermal system, Sullivan deposit (legend in Fig. 3). (**1**) Main stage hydrothermal flow results in sulphide sedimentation in a brine pool, with progressive replacement of sulphides by massive pyrrhotite and underlying pyrrhotite network/tourmalinite alteration. (**2**) Late-stage hydrothermal flow is concentrated at the periphery of the main vent zone giving rise to pyrrhotite-sphalerite-galena-sulphosalt veinlets in the transition zone, accompanied by muscovite and ?later chlorite. (**3**) Post-mineral fluid flow set up by magma body feeding Moyie sills and focused by vertical structures results in albite-chlorite-pyrite alteration (see Turner and Leitch 1992).

3. Finally, sills and dykes, were emplaced controlled by the density interface at the top of the ore body (Hamilton et al., 1982; see Turner and Leitch, 1992). In this stage, albite-chlorite alteration of sediments, chlorite-pyrite alteration of pyrrhotite body, and intense chlorite alteration of some sills took place. This may have been a long-lived process spanning the pre-, syn-, and post-mineralization period. Emplacement, and especially alteration, were probably controlled by vertical fracturing to allow access of hydrothermal fluids heated by a magma body at depth (cf. Guaymas Basin, Escanaba Trough, or Middle Valley, where observed sills do not have sufficient heat to cause such strong alteration: Turner and Leitch, 1992).

### *Sulphide-rich nature of footwall veins*

The footwall veins mimic the sulphide rich (pyrrhotite-dominant) nature of metasomatized hydrothermal sediments in the overlying concordant body of laminated massive sulphides. There is a very low gangue (quartz, carbonate, muscovite, chlorite) component in the veins as in the massive sulphides. Also, the sulphide mineralogy of vein sets mimics the sulphide mineralogy of the overlying orebody. Pyrrhotite veinlets and networks in tourmalinite are dominant under the massive pyrrhotite body; sphalerite and galena-rich veinlets in sericite-chlorite altered rock are common in the transition zone. The relatively high sphalerite to galena nature of veins, opposite to the low sphalerite to galena ratio observed in the overlying massive pyrrhotite body, is similar to that of the Jason deposit (Turner, 1990), where high sphalerite to galena ratios are observed in the footwall to metasomatized hydrothermal sediments which have low sphalerite to galena ratio.

## ACKNOWLEDGMENTS

We thank Marcia Knapp and Norris del Bel Belluz of Cominco's Sullivan mine, and George Wanuk of Kimberley, for assistance in the field. Photography and polishing of slabs used to illustrate this paper are courtesy of Richard Lancaster. Critical reviews by John Hamilton and Don Sangster are appreciated.

## REFERENCES

**Ansdell, K.M., Nesbitt, B.D., and Longstaffe, F.J.**
1989: A fluid inclusion and stable isotope study of the Tom Ba-Pb-Zn deposit, Yukon Territory, Canada; Economic Geology, v. 84, p. 841-856.

**Beaty, D.W., Hahn, G.A., and Threlkeld, W.E.**
1988: Field, isotopic, and chemical studies of tourmaline-bearing rocks in the Belt - Purcell Supergroup: genetic constraints and exploration significance for Sullivan type ore deposits; Canadian Journal of Earth Science, v. 25, p. 392-402.

**Edmunds, F.R.**
1977: The Aldridge Formation, B.C., Canada; Ph.D. thesis, Pennsylvania State University, University Park, Pennsylvania, 368 p.

**Gardner, H.D. and Hutcheon, I.**
1985: Geochemistry, mineralogy, and geology of the Jason Pb-Zn deposits, MacMillan Pass, Yukon, Canada; Economic Geology, v. 80, p. 1257-1276.

**Goodfellow, W.D., and Rhodes, D.**
1990: Geological setting, geochemistry and origin of the Tom Zn-Pb-Ag-barite deposits, in Mineral deposits of the northern Canadian Cordillera, Yukon-northeastern British Columbia, (ed.) J.G. Abbot, and R.J.W. Turner; IAGOD Field Guide, Excursion 14; Geological Survey of Canada, Open File 2169, p. 177-241.

**Hamilton, J.M., Bishop, D.T., Morris, H.C. and Owens, O.E.**
1982: Geology of the Sullivan orebody, Canada, in Precambrian Sulphide Deposits, H.S. Robinson Memorial volume, (ed.) R.W. Hutchinson, C.D. Spence, and J.M. Franklin; Geological Association of Canada, Special Paper 25, p. 597-665.

**Leitch, C.H.B.**
1991: Preliminary fluid inclusion and petrographic studies of the Sullivan sedimentary exhalitive Pb-Zn deposit, southeastern B.C.; in Current Research, Part A; Geological Survey of Canada, Paper 91-1A, p. 91-101.
1992a: Mineral chemistry of selected silicates, carbonates, and sulphides in the Sullivan and North Star stratiform Zn-Pb deposits, British Columbia, and in district-scale altered and unaltered sediments; in Current Research, Part E; Geological Survey of Canada, Paper 92-1E.
1992b: A progress report of fluid inclusion studies of veins from the vent zone, Sullivan stratiform sediment-hosted Zn-Pb deposit, British Columbia; in Current Research, Part E; Geological Survey of Canada, Paper 92-1E.

**Leitch, C.H.B. and Turner, R.J.W.**
1991: The vent complex of the Sullivan stratiform sediment-hosted Zn-Pb deposit, B.C.: preliminary petrographic and fluid inclusion studies; in Current Research, Part E, Geological Survey of Canada, Paper 91-1E, p. 33-44.

**Leitch, C.H.B., Turner, R.J.W. and Höy, T.**
1991: The district-scale Sullivan-North Star alteration zone, Sullivan mine area, British Columbia: a preliminary petrographic study; in Current Research, Part B; Geological Survey of Canada, Paper 91-1E, p. 45-57.

**Mako, D.A. and Shanks, W.C. III.**
1984: Stratiform sulphide and barite - fluorite mineralization of the Vulcan prospect, Northwest Territories: exhalation of basinal brines along a faulted continental margin; Canadian Journal of Earth Sciences, v. 21, p. 78-91.

**McAdam, J.H.**
1978: A preliminary study of footwall mineralization at the Sullivan mine, Kimberley, B.C.; B.Sc. Thesis, Queen's University, Kingston, 71 p.

**McMechan, M.E. and Price, R.A.**
1982: Superimposed low-grade metamorphism in the Mount Fisher area, southeastern British Columbia--implications for the East Kootenay orogeny; Canadian Journal of Earth Science, v. 19, p. 476-489.

**Nesbitt, B.E., Longstaffe, F.J. and Muehlenbachs, K.**
1984: Oxygen isotopic geochemistry of the Sullivan massive sulphide deposit, Kimberley, British Columbia; Economic Geology, v. 79, p. 933-946.

**Samson, I.M. and Russell, M.J.**
1983: Fluid inclusion data from Silvermines base-metal - baryte deposits, Ireland; Transactions of the Institution of Mining and Metallurgy (Section B: Applied earth science), v. 92, p. 67-71.

**Shaw, D.R. and Hodgson, C.J.**
1980: Wall-rock alteration at the Sullivan mine, Kimberley, British Columbia; Preprint presented at 5th Annual District 6 Meeting of Canadian Institute of MIning and Metallurgy, Kimberley, B.C., October 23-25, 1980, 14 p.
1986: Wall-rock alteration at the Sullivan mine, Kimberley, B.C.; in The genesis of stratiform sediment-hosted lead and zinc deposits: conference proceedings (ed.) R.J.W. Turner and M.T. Einaudi; Stanford University Publications, School of Earth Sciences, v. XX, p. 13-21.

**Turner, R.J.W.**
1990: Jason stratiform Zn-Pb-barite deposit, Selwyn Basin, Canada (NTS 105-O-1): geological setting, hydrothermal facies and genesis; in Mineral deposits of the northern Canadian Cordillera, Yukon-northeastern British Columbia, (ed.) J.G. Abbot, and R.J.W. Turner; IAGOD Field Guide, Excursion 14; Geological Survey of Canada, Open File 2169, p. 137-175.

**Turner, R.J.W. and Leitch, C.H.B.**
1992: Relationship of albitic and chloritic alteration to gabbro dykes and sills in the Sullivan mine and nearby area, British Columbia; in Current Research, Part E; Geological Survey of Canada, Paper 92-1E.

Geological Survey of Canada Project 900020
(Contribution No. 6, Sullivan-Aldridge project)

# A progress report of fluid inclusion studies of veins from the vent zone, Sullivan stratiform sediment-hosted Zn-Pb deposit, British Columbia

**Craig H.B. Leitch**
**Mineral Resources Division, Vancouver**

*Leitch, C.H.B., 1992: A progress report of fluid inclusion studies of veins from the vent zone, Sullivan stratiform sediment-hosted Zn-Pb deposit, British Columbia; in Current Research, Part E; Geological Survey of Canada, Paper 92-1E, p. 71-82.*

***Abstract***

*The western portion of the Sullivan orebody is underlain by an extensive network of pyrrhotite ± quartz-Fe carbonate veins in tourmalinite that probably represents the feeder zone of the deposit. Quartz, and to a lesser extent sphalerite and carbonate, in these veins contain abundant secondary or pseudosecondary fluid inclusions. Inclusions are not seen in wallrock detrital quartz grains that do not appear significantly recrystallized by greenschist metamorphism at 350-400°C and 2 kbar. Fluids trapped in the inclusions are probably samples of the mineralizing fluids, in places diluted and/or reset by metamorphism. Mineralizing fluids are characterized as moderately saline 15-27 wt.% ($NaCl+CaCl_2+?MgCl_2$) brines; homogenization temperatures (Th) range from 200-300°C, but may reflect metamorphism. Similar fluids are found at other prospects (North Star, Quantrell, and Kidstar) in Aldridge rocks. Dilution of these brines to < 5wt.% NaCl, with mainly low but variable $CO_2+CH_4$, is suspected in several generations of secondary inclusions with Th 200-350°C. Low temperature secondary inclusions range from 3 to 20 wt.% NaCl, Th 90-150°C.*

***Résumé***

*Un vaste réseau de veines carbonatées à pyrrhotine ± quartz et carbonates de Fe dans une tourmalinite est observé au-dessous de la portion occidentale du corps minéralisé de Sullivan; il représente probablement la zone nourricière du gisement. Le quartz et, dans une moindre mesure, la sphalérite et les carbonates de ces veines contiennent d'abondantes inclusions fluides secondaires ou pseudosecondaires. Il n'y a pas d'inclusions dans les grains de quartz détritique de la roche encaissante, lesquels ne paraissent pas recristallisés de façon significative par le métamorphisme du faciès des schistes verts qui a eu lieu à une température de 350 à 400 °C et à une pression de 2 kb. Les fluides piégés dans les inclusions sont probablement des échantillons des fluides minéralisateurs, par endroits dilués ou représentatifs du métamorphisme. Les fluides minéralisateurs sont considérés comme étant des saumures de salinité moyenne avec 15 à 27 % de $NaCl+CaCl_2+?MgCl_2$ en poids; les températures d'homogénéisation (Th) se situent entre 200 et 300 °C, mais pourraient être associées au métamorphisme. Des fluides similaires sont décrits dans le cas d'autres gîtes (North Star, Quantrell et Kidstar) des roches d'Aldridge. Une dilution de ces saumures jusqu'à < 5 % de NaCl en poids (quantités généralement faibles mais variables de $CO_2+CH_4$) est jugée plausible dans le cas de plusieurs générations d'inclusions secondaires à des Th de 200 à 350 °C. Les inclusions secondaires de basse température sont caractérisées par des pourcentages en poids de NaCl de 3 à 20 % et par des Th de 90 à 150 °C.*

## INTRODUCTION

Sullivan is a stratiform, sediment-hosted (SEDEX) Zn-Pb deposit with a vent complex representing the zone of fluid upflow during formation of the overlying bedded sulphides. Relatively little is known about the chemistry and temperature of fluids that formed stratiform Pb-Zn deposits. Known studies include the Jason (Gardner and Hutcheon, 1985), Tom (Ansdell et al., 1989) and Vulcan (Mako and Shanks, 1984) deposits in Yukon and Northwest Territories, and Silvermines (Samson and Russell, 1983) in Ireland.

The Sullivan deposit offers an opportunity to study the ore-forming fluids of a SEDEX deposit because of its well-developed vent complex, which comprises a massive pyrrhotite replacement body within the bedded ores, an underlying tourmalinite pipe of brecciated and altered strata and disseminated or veinlet sulphides, and albite-chlorite altered sediments in the hanging wall (Hamilton et al., 1982). Interpretation of tourmalinite formation, based on oxygen isotope studies, varies from <100°C (Nesbitt et al., 1984) to 200-250°C (Beaty et al., 1988). Limited fluid inclusion studies by Shaw and Hodgson (1986) suggested temperatures of 200-250°C and salinities of 22-29 wt.% for albite-chlorite alteration. Leitch (1991) and Leitch and Turner (1991) suggested saline ore-forming fluids (15-27 wt.% NaCl with significant dissolved Ca and possibly Mg). The homogenization temperatures of 200-300°C observed in this study may have been re-set by biotite-Mn garnet middle greenschist metamorphism at 350-400°C (McMechan and Price, 1982). Such an overprinting of mineralizing temperatures by metamorphism has been proposed for the Tom deposit (Ansdell et al., 1989). The 100-150°C difference between metamorphic and homogenization temperatures implies a "pressure correction" of 1.5-2.2 kbar (Roedder, 1984); this is supported by the 5.8-7.6 km depth of burial (Edmunds, 1977) that indicates 1.5-2.0 kbar.

This study of fluid inclusions in veins of the Sullivan footwall vent complex adds to previous studies (Leitch, 1991; Leitch and Turner, 1991). Sixteen samples of diamond drill (DD) core from the vent zone of the Sullivan mine (Table 1) and 4 surface samples from the North Star and Quantrell deposits 3-4 km southwest of Sullivan, and the Horn and Kidstar prospects 25 km southwest and 40 km south of Sullivan (Table 2) were used in this study. The latter were intended to determine if similar fluids were present in other mineralized rocks in Aldridge strata. Sample locations in discussions following are in Figure 4 of Turner and Leitch (1992) and Figures 1 and 2 of Leitch (1992). Analytical methods are in Leitch (1991).

## SULLIVAN DEPOSIT: FOOTWALL VEINLETS, VEINS

The footwall vent zone of the Sullivan deposit (Leitch and Turner, 1992) contains an extensive network of pyrrhotite ± quartz, Fe carbonate, sphalerite and galena as irregular veinlets and planar veins that grade in places to breccia cement or local massive pyrrhotite. The proportion of quartz and carbonate increases with planar character of the veins; gradation from one to the other and co-occurrence suggests broadly contemporary formation. However, the occurrence in planar veins of minor chlorite and muscovite, minerals common in altered tourmalinite, suggests a transition to late-stage hydrothermal flow in the planar veins. This is supported by their planar character, which suggests they formed in more indurated rocks than the irregular veins. Pyrrhotite veins containing rounded fragments of coarse grained quartz may represent planar veins affected by fault movement. Fluid inclusions are generally more abundant in the planar veins. Wall rocks adjacent to veins are mainly tourmalinite, which in places is altered to muscovite, chlorite, or albite. Inclusions associated with each of these alteration types were studied (Fig. 1: tourmalinite; Fig. 2: muscovite and chlorite).

## DESCRIPTION OF FLUID INCLUSIONS

Fluid inclusions are present mainly in vein quartz, and to a lesser extent in sphalerite and carbonate. Inclusions were seen (but not subjected to microthermometry) in coarse tourmaline crystals where tourmalinite has been overprinted by albite alteration (Leitch and Turner, 1992). Inclusions rarely occur along primary mineral growth zones (Fig. 2C). Most inclusions occur in groups or along planar healed fractures. Where these fractures do not cross boundaries of relatively large, optically continuous crystals up to 1 cm across, they are classed as pseudosecondary (Fig. 1A-C). Inclusions along fractures that cross these earlier fractures and grain boundaries are classed as secondary.

Fluid inclusions are most abundant in coarse grained quartz that has not undergone significant recrystallization. This is most apparent where such quartz is adjacent to finer grained, strained quartz, which typically contains few or no inclusions. This suggests that any fluid inclusions originally in the fine grained quartz were destroyed by recrystallization. Inclusions are only found in coarse grained sphalerite, or in smaller crystals occurring in veins. No inclusions are found in the fine grained sphalerite which typically comprises the bulk of the orebody. This may be due to extensive dynamic deformation of sphalerite (McClay, 1983). The coarse sphalerite may have formed by hydrothermal recrystallization, as suggested by the inclusions in vein sphalerite, or by metamorphic recrystallization. All inclusions in sphalerite and most in carbonate are secondary and thus were trapped after recrystallization.

Only rare, 1-3 μm secondary inclusions are observed in wall rock detrital quartz grains. Most of this quartz does not appear to be significantly recrystallized by metamorphism, although in places it does show minor overgrowths that may be hydrothermal or metamorphic. The abundance of inclusions in quartz veins clearly associated with mineralization, and relative absence of inclusions in wall rock quartz, suggests the inclusions in vein quartz were trapped from mineralizing fluids. The absence of inclusions and lack of recrystallization in wall rock quartz suggests this quartz has not trapped metamorphic fluids. However, it is possible some inclusions in vein quartz have been fractured during metamorphism, causing them to leak and/or be diluted by variable amounts of metamorphic fluids.

**Table 1.** Summary of fluid inclusion data, Sullivan deposit

| Sample | Zone | Mineral (n) | Paragenesis | Type | Tr (Ts) | Te | $Tm_1$ ($Tm_c$) | $Tm_2$ | $Tm_f$ | Th |
|---|---|---|---|---|---|---|---|---|---|---|
| **Quartz-pyrrhotite veins in tourmalinite** | | | | | | | | | | |
| DD 118- 174.0 | FW (W) | qz (24) | cse qz planar vein in **tmite**; py,Bi,sp | 1,2 (PS,S) | -74 +276 | -44 -70 | -31 -45 | -21 -28 | -6.4 -21 | +161 +233 |
| DD 202- 4.0 | FW (TZ) | qz (9) | fine qz,ca irreg vein in **tmite**; sl,as,po,gn | 1,2 (PS,S) 5 | -73 +205 | -44 -64 -45 | -48 -37 | -22 -25 -24 | -9.0 -11 -11 | +167 +246 + 87 |
| DD 296- 14.0 | FW (TZ) | qz (17) | fine qz irreg vein in **tmite**; po,sl,gn,as,sp | 1,2 (PS) | -75 | -37 -61 | -36 -45 | -22 -27 | -9.2 -19 | +194 +282 |
| DD 367- 1.0 | FW (C) | qz, ca (24) | qz-Fe ca-py planar vein in **tmite**; gn,cp,sp,sl ($Tm_{CO2}$=-58.4 to -62.0; $Th_{CO2}$=-11.2 to 11.4; $Tm_c$=7.5 to 10.3 | 2 (PS,S) | | -31 -47 | | | -3.5 -12 | +255 +290 |
| DD 1141- 85.0 | FW (C) | qz (32) | qz-po planar vein in **tm-ite**; po,cp,gn,sl,ru,ch | 1,2 (PS) | -78 +240 | -36 -65 | -39 -48 | -23 -28 | -4.0 -17 | +148 +293 |
| 137.0 | | qz (23) | qz-po wispy vein in **tm-ite**; py,gn,cp,Bi,as,ru ($Tm_{CO2}$=-58.9; $Th_{CO2}$=1.9; $Tm_c$=4.9 to 10.5) | 2 (PS,S) | | -34 -53 | | -24 | -3.6 -20 | +175 +442 |
| DD 3158- 212.5 | FW (C) | qz (18) | qz-po planar vein in **tmite**-po breccia | 2 (PS,S) | -67 | -55 -68 | (11) | -21 -26 | -9.8 -29 | +119 +211 |
| 90SVL4 #2Cutout | FW TZ | qz (26) | thin qz-ca-po-cp-gn (±ch-ru) veinlets | 1,2 (PS,S) | -75 | -23 -37 | (7.5) | -21 -23 | -7.5 -22 | +186 +280 |
| 90SVL5A P-10-4 | FW (C) | qz (24) | thin qz-po-as-cp-sp-il-ru(±ms) veinlets | 2 (PS,S) | -75 | -23 -50 | | -22 -25 | -4.2 -22 | +166 +274 |
| G79SL4 P-10-4 | FW (C) | qz (63) | thin irreg qz-as-po-cp gn-bl-Bi-il-ru-sp veinlets (±py,mc) cut | 1,2 (PS,S) | -70 +295 | -23 -58 | -35 -40 (8) | -20 -29 | -10 -29 | +160 +445 |
| | | (7) | by qz-ch fractures | 5 | | -34 | | | -15 | +100 |
| **Quartz-pyrrhotite veins with muscovite** | | | | | | | | | | |
| DD 2429- 45.0 | HW (TZ) | qz (17) | qz-po-sl-gn stringers in **ms**-po alteration | 1,2 (PS) | +274 | -47 -69 | -31 -46 | -21 -28 | -5.4 -21 | +235 +370 |
| **Quartz-pyrrhotite (±pyrite) veins with chlorite** | | | | | | | | | | |
| DD 270- 324.0 | HW (TZ) | ca (0) | cse ca-py planar vein in **ch-ab-ms-sp**(tmite) | ?5 (S) | Inclusions all too small for microthermometry | | | | | |
| DD 280- 124.0 | FW (C) | qz (29) | cse qz planar vein in **ch** (tmite); po,cp,Bi | 2 (PS) | | -36 -53 | | (7.0) | -7.6 -20 | +137 +254 |
| DD 313- 384.0 | HW (TZ) | qz (19) | qz-sl-po irreg vein in **ab-ch-sp-ca**; po,gn,cp | 2 (PS,S) | -75 | -37 -64 | -28 -42 | -25 (6.7) | -6.2 -27 | +159 +289 |
| | | sl (8) | cse sl looks recrystal-lized in hand specimen | ?3 (S) | -63 | -51 -57 | | -26 (6.3) | -8.6 -12 | +183 +299 |
| DD 338- 150.0 | FW (C) | qz (30) | **ab-qz-ca** planar vein in gabbro; py,po,cp,as,**ch** | 1,2 (PS) | -75 +250 | -39 -69 | -40 -52 | -23 -30 | -5.4 -20 | +165 +275 |
| | | ca (15) | qz-ca stringers cut ab vein | 2 (S) | -65 | -41 -57 | | | -5.0 (6.5) | +197 -12 +268 |
| DD 2579- 56.0 | FW (W) | qz (49) | qz-py-ch planar vein, **ch** altered tmite ($Tm_{CO2}$=-71.8; $Th_{CO2}$=16.6; $Tm_c$=3.2 to 21.6; Th(v)=+375-450) | 1,2 (PS,S) | -72 +209 | -42 -69 | | -21 -25 | -3.2 -21 | +138 +312 |
| DD 3900- 105.0 | HW (E) | qz (14) | qz-Fe ca-py irreg vein, **ab-ch-ms** alteration ($Tm_{CO2}$=-60.0, -72.7; $Th_{CO2}$=-0.8 to 4.2; $Tm_c$=4.7 to 9.4) | 2 (PS,S) | -74 | ? -70 | | | -22 -23 | -7.3 +95 -16 +355 |
| DD 5085- 75.5 | FW (C) | qz (12) | sl-qz-**ch** irreg vein in **ab-ch**-py alteration | 2 (PS,S) | | -24 -38 | | | -3.5 -9.4 | +104 +315 |
| 87.0 | FW (C) | qz (8) | qz-**ch**-py-gn±po,cp planar vein in **ch** alteration | 2 (PS/S) | | -48 -72 | | -24 (5.4) | -1.7 -14 | +137 +230 |
| SULIV2 | HW (?) | qz (44) | qz with py in ab-ch±ca alteration | 2 (PS,S) | | -29 -55 | -29 -32 | -21 -25 | -3.0 -21 | +169 +305 |
| | | ab (6) | | 5 (S) | | -25 -35 | | -21 -24 | -14 -17 | +124 +141 |
| 89SVT9 R-10-30 | OZ (C) | qz (20) | qz ?veins in massive ch below massive po-sl | 2 (PS,S) | | -29 -35 | (7.4) | -20 -23 | -8.9 -13 | +150 +259 |
| **Massive sulphides** | | | | | | | | | | |
| 91SVL8 | OZ (SE) | ca (19) | ca, py inclusions in massive po±sl-gn-bl-as | 2 (PS/S) | -72 | -52 -60 | -26 -41 | | -8.0 -38 | +276 +381 |
| 83SVT6 | OZ (?) | ca (8) | ca, py inclusions in massive po±sl-gn-cp | 2 (PS) | | -29 -52 | -29 (9.2) | -20 -26 | -2.9 -17 | +224 +306 |
| SULIV4 | OZ (SE) | qz (92) | qz, ca, py inclusions in massive po-gn-sl-cp ($Tm_{CO2}$=-56.6 to -58.5; $Th_{CO2}$=7.8 to 18 or 24 to 31; $Tm_c$=7.3 to 10.5) | 2,3,4 (PS) | | -23 -49 | | | -1.9 -12 | +184 +425 |
| | | ca (10) | (±qz-ms-ch-gt-ru-il) ($Tm_{CO2}$=-56.6; $Th_{CO2}$=26 to 31; $Tm_c$=9.5) | 2,4 (PS) | | -29 | | | -7 -13 | +165 +290 |

Samples are located by drill hole number and footage (DD 118-174.0') or as underground locations (e.g. 91SVL8). FW=footwall, HW= hangingwall, OZ=ore zone; C=central; W=west; E=east; S=south; TZ=transition zone. Minerals are ab=albite, as=arsenopyrite, Bi=native Bi, bl=boulangerite, ca=calcite, ch=chlorite, cp=chalcopyrite, gn=galena, gt=garnet, il=ilmenite, ms=muscovite, po=pyrrhotite, py=pyrite, qz=quartz, ru=rutile, sl=sphalerite, sp=sphene; tmite=tourmalinite, cse=coarse, irreg= irregular. (n)= number of inclusions studied in the section. Temperatures: Tr=recrystallization, Te=eutectic, $Tm_1$=first melting event, $Tm_2$= second melting event, $Tm_f$=final melting, $Tm_c$=clathrate melting, $Tm_{CO2}$=melting of $CO_2/CH_4$, $Th_{CO2}$=homogenization of carbonic phase, Ts=dissolution of halite, Th= final homogenization (to liquid unless noted). All temperatures given as total range (minimum over maximum). See text for description of type; S=secondary, PS=pseudosecondary.

Fluid inclusions are classified in Leitch (1991) except for Type 2c which now includes those Type 2a and 2b that have relatively low salinities (3-10 wt.%) and immature shapes.

**Type 1:** saline brine containing daughter halite crystal and vapour bubble, each representing 10 volume per cent of the inclusion.

**Type 2(a,b):** saline brine and vapour bubble about 10-15 volume per cent of the inclusion.

**Type 2(c):** as for 2a,b but dilute aqueous solution; vapour bubble contains minor carbonic (CO2+CH4) fluid.

**Type 3:** dilute aqueous solution and vapour bubble up to 50% by volume of the inclusion containing carbonic fluid.

**Type 4:** vapour-rich, up to 90% by volume containing major carbonic fluid and minor dilute aqueous fluid.

**Type 5:** moderately saline brine, vapour bubble about 5% by volume.

Inclusions selected for measurement in this study range from 3 to 85 μm in size, although most are between 5 and 15 μm. Inclusion shapes in quartz vary from regular (mature: Bodnar et al., 1985) shapes in Type 1 and 2a,b to irregular (immature) in 2c. Type 3 and 4 inclusions are characterized by larger, tear-drop or ovoid shapes. Type 5 secondary inclusions tend to be small, with regular, rounded shapes. Most inclusions in carbonate and sphalerite have negative crystal shapes.

Type 1 and 2 inclusions tend to occur in separate healed fractures and have different habits (Fig. 1A, B). Type 1 inclusions (Fig. 1E) are generally small, regular-shaped, and have low relief against the host; they occur along relatively short fractures that do not cross grain boundaries (Fig. 1B). Type 2a inclusions have bolder outlines, regular shapes, and occur in longer fractures that cross Type 1 fractures and in places grain boundaries; Type 2c inclusions are similar to 2a but have irregular outlines and occur on fractures that cross all grain boundaries. Rare Type 1 inclusions have irregular outlines similar to those of Type 2c, and possibly represent Type 1 inclusions that have been broken during metamorphism and re-trapped. Similarly, Type 2 inclusions that are isolated or occur along short fractures that do not cross grain boundaries generally have higher salinities than inclusions in adjacent quartz along throughgoing fractures, although homogenization temperatures are similar (Fig. 2B).

## FLUID INCLUSION MICROTHERMOMETRY

Microthermometric data for inclusions studied are summarized in Table 1 for Sullivan and Table 2 for regional samples. Most inclusions except for Type 3/4 homogenized to liquid. Temperature of homogenization (Th) or decrepitation (Td) data are presented in histogram form for all samples in Figure 3. Decrepitation data are presented because their distribution clearly mimics that of Th (Fig. 3), and in some samples almost all inclusions decrepitated.

Most Type 1 and 2a, b inclusions froze to a clear or brown glassy solid at temperatures between -50 and -100°C; some more saline examples froze only on warming to the range -95 to -85°C. Some of the most saline could not be frozen at all. Most of these saline inclusions showed a distinct "recrystallization" (Tr) event, in which the glassy solid became crystalline, generally below -70°C. This may represent metastable melting, indicating the presence of metastable salt hydrates such as Mg/CaCl2.4-8H2O (Davis et al., 1989). Less saline inclusions recrystallized immediately after freezing to a brown mixture of ice and these Ca-Mg hydrates. Inclusions of less saline Type 2c froze between -30 and -50°C, many with double freezing (clathrate followed by ice) indicating the presence of minor carbonic fluid not detectable optically as a separate phase.

Eutectic temperatures (Te, first distinct melting) range from -24 to -72°C but cluster around -35 and -55°C and indicate that the divalent salts $MgCl_2$ and $CaCl_2$,

**Table 2.** Summary of fluid inclusion data, 1991 samples, regional prospects

| Sample | Mineral (n) | Paragenesis | Type | Tr (Ts) | Te | $Tm_1$ | $Tm_2$ ($Tm_c$) | $Tm_f$ | Th |
|---|---|---|---|---|---|---|---|---|---|
| | | **Quartz-pyrrhotite veins in tourmalinite** | | | | | | | |
| KIDSTAR | qz | thin planar qz veins in | 1,2 | -69 | -33 | -28 | -21 | -15 | +224 |
| 91ALL11 | (25) | **tmite**; po | (PS,S) | +295 | -63 | -32 | -25 | -25 | +451 |
| N.STAR | qz | coarse planar qz vein in | 1,2 | -68 | -52 | -27 | -22 | -19 | +203 |
| 91NSL3 | (30) | **tmite**; po | (PS) | ?+390 | -69 | -49 | -29 | -35 | +443 |
| | | **Quartz-sphalerite veins with chlorite** | | | | | | | |
| QUANTRELL | qz | coarse qz-sl-**ch** planar | 1,2 | -71 | -53 | -36 | -24 | -23 | +176 |
| 91ALT17 | (16) | vein in **ch** alteration | (PS,S) | +325 | -62 | -41 | -29 | -27 | +348 |
| | | **Quartz veins in unmineralized Moyie sills** | | | | | | | |
| HORN | qz | Coarse qz-ms-fuchsite in | 2 | | -37 | | | -5.6 | +230 |
| 91ALL4 | (7) | altered gabbro | (PS) | | -49 | | | -16 | +291 |

Symbols, abbreviations as in Table 1.

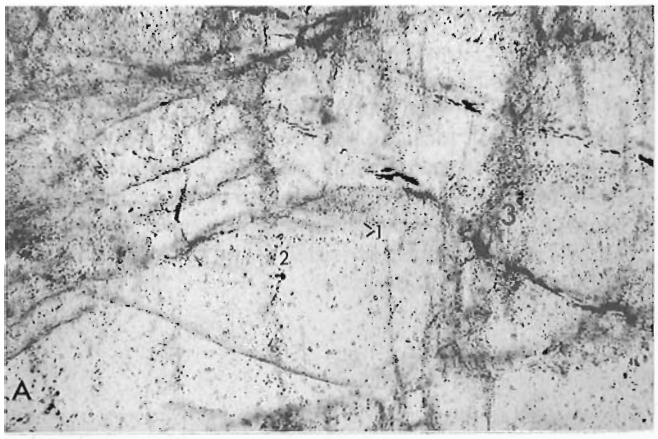


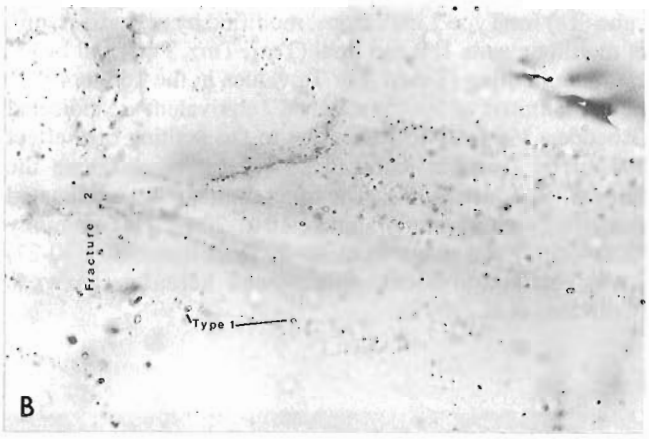


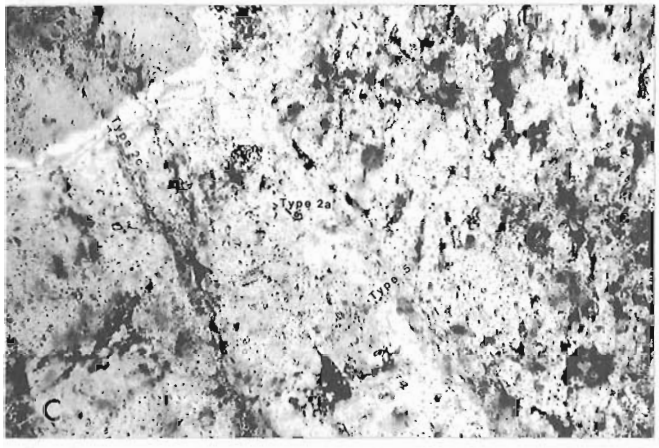


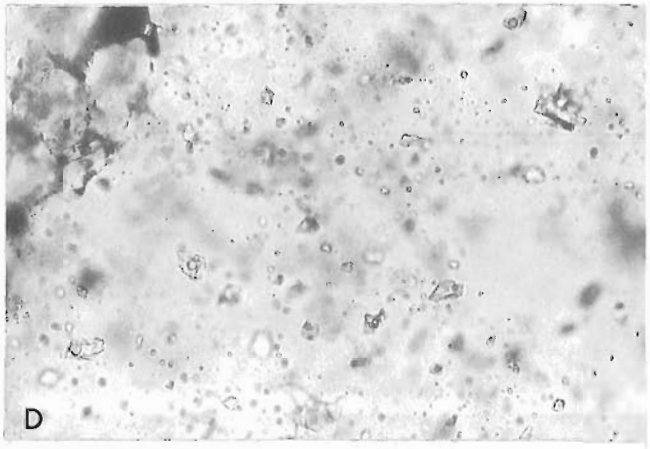


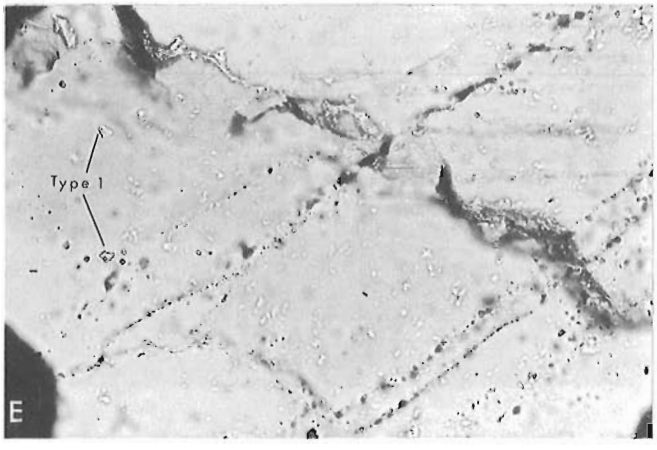


**A.** Short fractures (1) containing Type 1 inclusions, crossed by longer fractures (2,3) containing Type 2 inclusions (118-174; 1.3 mm).

**B.** Close-up of central portion of A) showing Type 1 inclusions (370 μm).

**C.** Overview of abundant Type 2 inclusions with different orientations in three crystals of quartz; inclusions on throughgoing fractures are Type 2c, mainly dark due to autodecrepitation, and Type 5 (280-124; 1.3 mm).

**D.** Enlargement of central portion of C) showing Type 2 inclusions (370 μm).

**E.** Isolated Type 1 fluid inclusions with halite cube and vapour bubble in vein quartz, cut by trails of secondary inclusions (296-14'; 370 μm)

**Figure 1.** Fluid inclusions in quartz veins and veinlets in Sullivan footwall tourmalinite (transmitted light, uncrossed polars except partially crossed in C, sample number; width of view).

respectively, are present in addition to NaCl (and possible KCl reflected by Te≈-24). Salinities of the inclusion fluids were estimated by (1) temperature of dissolution of halite cube (Ts) for Type 1 inclusions, modified by (2) temperature of melting events 1, 2 and final ($Tm_1$, $Tm_2$, Tmf) and by (3) clathrate melting (Tmc). For Ts values in the 160 to 405°C range, salinities of 30-45 wt.% NaCl equivalent are indicated (Roedder, 1984) . However, due to the "salting out" effect caused by divalent salts, these values overestimate the salinity (Roedder, 1984). The true saliniies can be estimated from final melting temperatures (-10 to -20°C; less commonly -5 to -35°C) and range from 15-20 (less commonly 10-27) wt.% NaCl equivalent, abbreviated hereafter as wt.% (Crawford et al., 1979).

Clathrate melting is common in Type 2c inclusions but rare in Type 2a or 2b; it is not seen in Type 1 inclusions. Clathrate melting temperatures from 3.2 to 21.6°C but mainly in the 6-7°C range indicate salinities up to 15 wt.% but mainly <10 wt.%, variably affected by the presence of $CH_4$ in addition to $CO_2$ (Fig. 8-22 of Roedder, 1984). Minor $CH_4$ is confirmed by rare observations of $CO_2$ freezing and melting in the -58.4 to -60.0°C range indicating less than 5 mole per cent $CH_4$ in the carbonic fluid (rarely to -72.7°C indicates up to 50% $CH_4$). Carbon dioxide homogenization temperatures in the -11.2 to 16.6°C range indicate densities of the carbonic fluid in the 0.93 to 0.84 g/cm3 range.

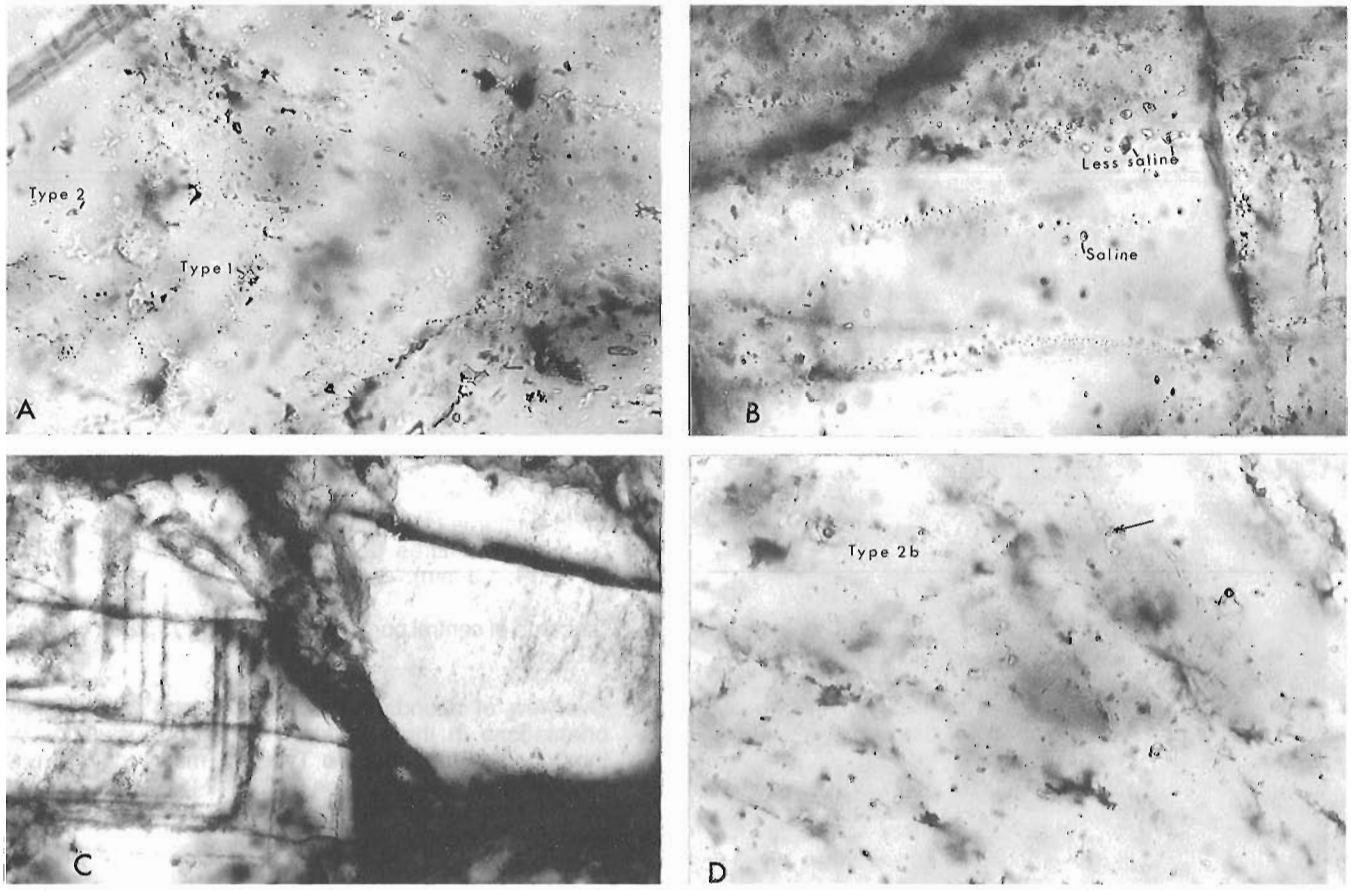


**A.** Scattered groups of Type 1 and 2 inclusions in small areas of less recrystallized quartz associated with muscovite alteration (2429-45; 370 μm).

**B.** Saline (>20 wt.%) inclusions isolated or on short fractures and less saline (9-14 wt.%) inclusions along fractures that cross grain boundaries, although both have similar Th values (chlorite-albite alteration, 313-384; 370 μm).

**C.** Growth zones of 1-2 μm inclusions in quartz-chlorite veins; adjacent quartz contains no growth zones (2579-56; 2.5 mm).

**D.** Large, saline Type 2b inclusions (10-20 wt.%, Th 200-230°C) except for arrowed inclusion that is dilute and low temperature (3 wt.%, 137°C), apparently opened by a fracture passing through it (5085-87; 370 μm).

**Figure 2.** Fluid inclusions in quartz veins associated with muscovite and chlorite alteration (transmitted light, uncrossed polars, sample number; width of view).

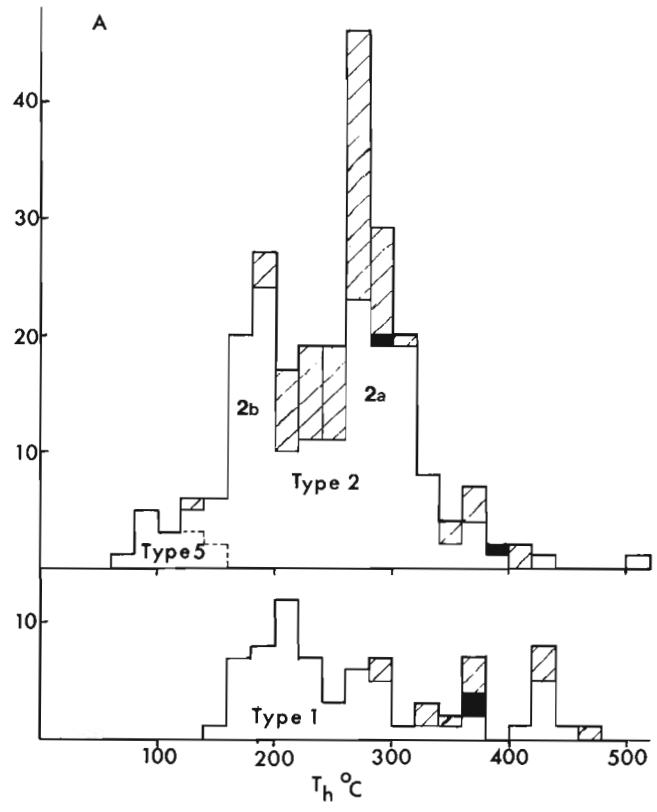


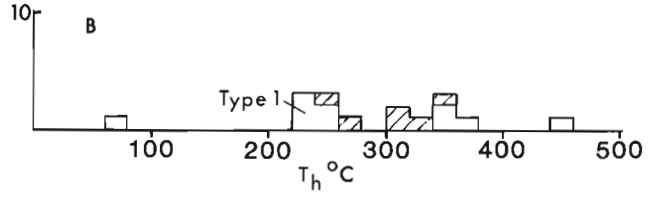


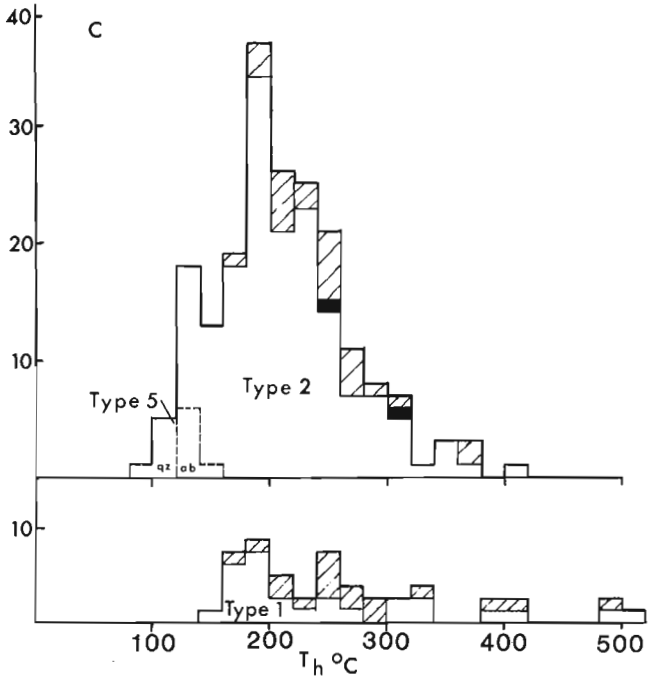


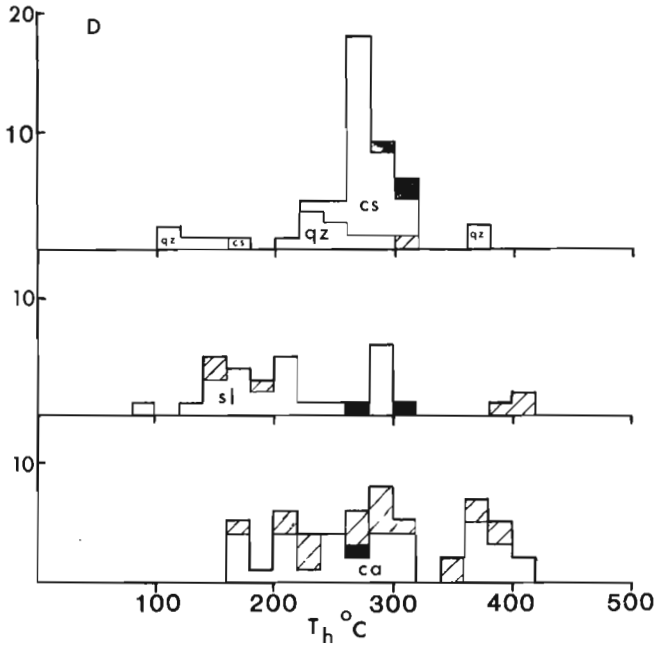


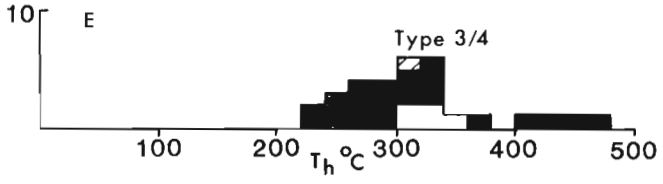


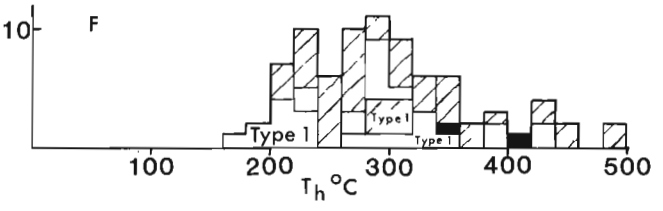


**A.** in quartz associated with tourmalinite;

**B.** in quartz associated with muscovite alteration;

**C.** in quartz (qz) and albite (ab) associated with chlorite (±albite) alteration;

**D.** in other minerals: carbonate (ca), sphalerite (sl), and cassiterite (cs) plus quartz associated with cassiterite (qz);

**E.** Type 3/4, mainly in quartz and calcite of the ore zone; data partly from Leitch (1991);

**F.** in quartz from regional samples.

**Figure 3.** Histograms of homogenization temperatures for Type 1-5 inclusions. Cross-hatched areas are decrepitation measurements, which overestimate Th by 3 to 132°C; dark squares are for inclusions homogenizing to vapour.

### *Inclusions in quartz-pyrrhotite veins with tourmalinite*

In the footwall vent zone of the Sullivan orebody, quartz in thin irregular pyrrhotitic veins in tourmalinite may best represent the main mineralizing stage (Leitch and Turner, 1992). Samples of this type include core samples DD202-4', 296-14', and 1141-137', and previous underground samples 90SVL4, 5A, and G79SL4. Vein mineralogy includes major pyrrhotite or arsenopyrite, minor chalcopyrite, sphalerite, galena, and rare sulphosalt, native Bi, sphene, and rutile, with variable quartz, carbonate, and rare chlorite or muscovite.

Fluid inclusions in the veinlet quartz in DD296-14' and DD202-4' are Type 1 and 2a (Fig. 1E). The two types have different Th, with Type 1 mainly from 167-246°C and Type 2 from 230 to 282°C (Fig. 3A). Wispy veinlet quartz of DD1141-137' contains Type 2a inclusions that have high Th (267-442°C) and salinities (10-20 wt.% by ice melting or 10 wt.% by clathrate melting; minor CO2/CH4 present). Less saline, lower temperature Type 2b inclusions (10-17 wt.% by ice melting or 7 wt.% by clathrate melting; Th 175-213°C) occur on separate fractures.

Planar quartz-carbonate-pyrrhotite veins occur throughout the tourmalinite pipe of the footwall vent zone but are less abundant than irregular pyrrhotite veinlets. Studied examples of planar veins in tourmalinite include DD118-174', 367-1', and 1141-85'. At the extreme west edge of the orebody, footwall tourmalinite above a gabbro sill in DD118-174' contains planar quartz veins with inclusions of Type 1 (16-27 wt.% $NaCl+CaCl_2$; Th 179-221°C) and Type 2a (salinity 10-24 wt.% $NaCl+CaCl_2$, Th 161 to 233°C). In DD367-1', quartz and calcite in a planar vein contain Type 2 inclusions of low to moderate salinity (5-10 wt.% by clathrate melting) with minor $CO_2/CH_4$. A 2 cm thick planar quartz vein in DD1141 at 85' contains inclusions distinct from those in wispy veinlets at 137': abundant Type 1 (Th 148-274°C, Ts 190-263°C) and Type 2 along separate fractures (Th 175-309°C, 5-15 wt.% by ice melting or 4-10 wt.% by clathrate melting).

### *Inclusions in quartz-pyrrhotite-sphalerite-galena veins with muscovite*

Only one sample of veinlets with muscovite envelopes was studied, from DD2429-45' (others containing muscovite also contained chlorite). In this sample, a network of 1-2 mm milky white quartz-sphalerite-galena cuts intensely muscovite altered sediment. Quartz is recrystallized, causing stretching near Th. However, in relatively unstrained crystals (Fig. 2A), Th is higher than in tourmalinite for both Type 1 (225-250°C) and Type 2 (up to 360°C) inclusions (Fig. 3B). Several adjacent, large, irregular inclusions contain moderately saline (8-22 wt.%) fluids similar to the other Type 2 inclusions, but low Th in the 35-71°C range suggests breaking and re-trapping of these inclusions without dilution.

### *Inclusions in quartz-pyrrhotite(±pyrite) veins with chlorite (±albite)*

Most quartz-pyrrhotite veins with associated chlorite alteration are planar, and include variable carbonate; albite may occur in the altered envelope. Examples include DD270-324, 280-124', 338-150', 2579-56', 3158-212.5', and 5085-87'. Two samples collected underground and reported previously (89SVT9, from quartz in massive pyrrhotite-chlorite immediately under the orebody, and 90SVL3, from a quartz-sphalerite-chlorite±albite pod in the southeast fringe zone: Leitch and Turner, 1991) have similar inclusions.

Quartz in planar veins in chloritized tourmalinite of DD280-124' contains abundant large fluid inclusions (Fig. 1D) that are mainly Type 2c containing minor CO2, with salinities of 6-8 wt.% estimated from clathrate melting and Th 137-192°C, or Type 2a, with greater salinity of 10-20 wt.% estimated from ice melting and Th around 250°C, although many decrepitate between 237-288°C: Fig. 3C). In the quartz-fragment pyrrhotite veins (e.g. 3158-212.5'), coarse quartz contains similar abundant, large, immature secondary Type 2c inclusions with Th (119-152°C) similar to Type 5 and compositions gradational to Type 2a, plus less common Type 2b (Th 196-211°C). A planar quartz-chlorite-pyrite-galena±pyrrhotite vein from 87' in DD5085 contains inclusions that vary from Type 2a (Tmf -24 to -14°C, Th 202-230°C) to Type 2c (-1.7°C, Th 137°C). The latter are found along late fractures (Fig. 2D) and appear to have been opened and diluted (cf. Simmons, 1991).

Carbonate in planar veins contains secondary inclusions too small for microthermometry, e.g. Type 5 in DD270-324', or along fractures that terminate in adjacent minerals (Type 2a, 10-15 wt%, Th 197-268°C in DD338-150'). Inclusions in quartz of 338-150' contain fluids similar to those in the carbonate. The histogram for inclusions in carbonate (Fig. 3D) also includes data from 3158-212.5' (planar quartz-fragment pyrrhotite vein), 91SVL8 and SULLIV-4 (massive sulphides of the southeast fringe of the deposit), and 83SVT6 (massive pyrrhotite body: Leitch, 1991).

Quartz from a large pyrite-quartz-chlorite vein with chloritic envelopes in DD2579-56' contains Type 2a and 2b inclusions (23 and 15 wt.% and Th 186-400 and 137-182°C respectively). Several crystals contain 1-2 μm inclusions aligned along growth zones (Fig. 2C). However, the only measureable Type 2a/b inclusions occur between growth zones, and are indistinguishable from inclusions found along fractures. In other crystals large Type 2 (Th 186-400°C) and Type 1 (Th 153-202°C; Ts 170-240°C, but halite did not recrystallize on cooling) inclusions occur in the same fracture with vapour-rich inclusions, two of which contain daughter halite. Other vapour-rich inclusions are Type 4 with Th to vapour at temperatures of 375-450°C (Fig. 3E).

Irregular quartz-sphalerite-chlorite-pyrrhotite±pyrite, calcite veins cut variably chlorite-albite or chlorite-muscovite altered wall rocks. Such a veinlet in

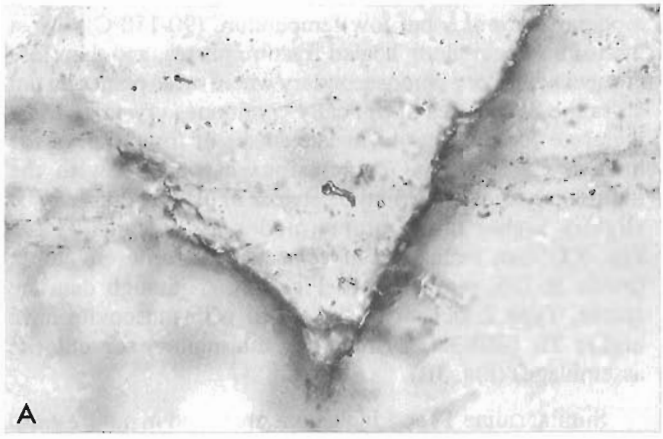


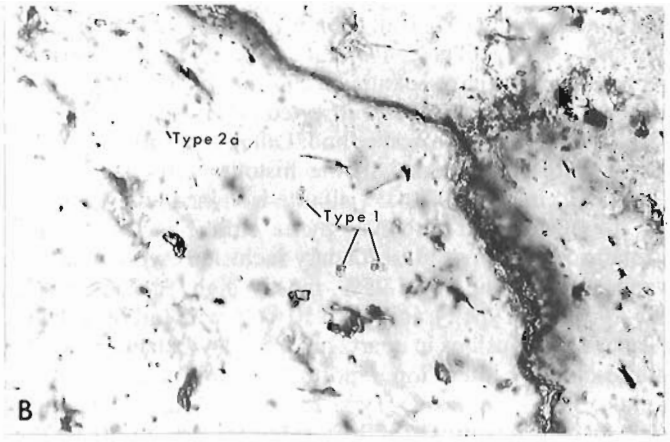


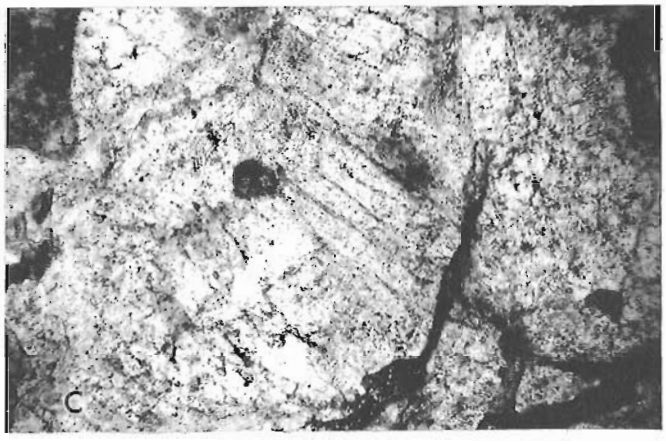


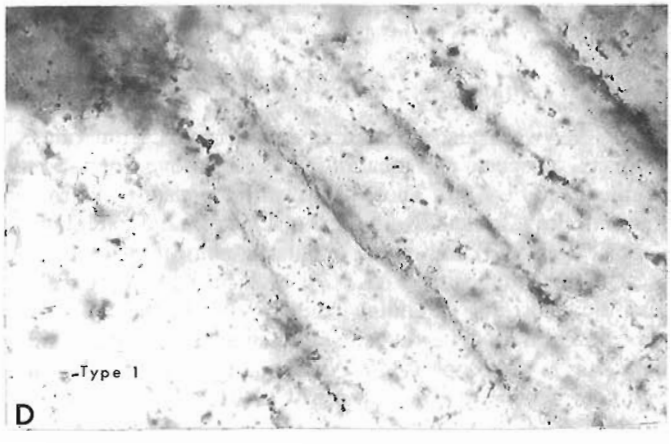


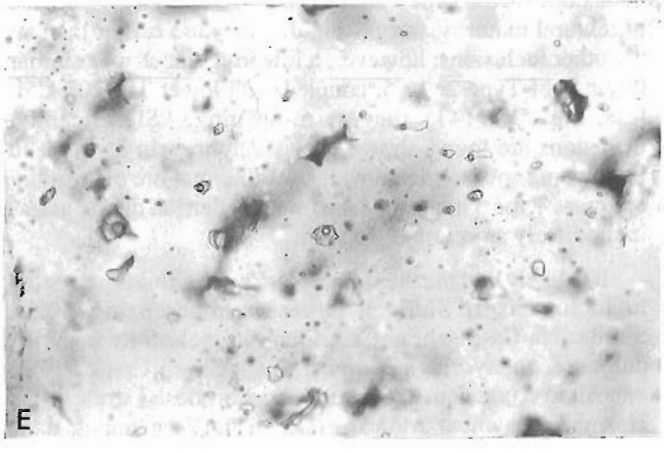


**A.** Secondary Type 2 inclusions on fractures crossing grain boundaries in quartz cutting tourmalinite (Star prospect; 370 μm).

**B.** Scattered Type 1 and 2a inclusions in 1 cm planar vein cutting tourmalinite (North Star; 370 μm).

**C.** Distribution of Type 2 inclusions along planes (Quantrell quartz-sphalerite-chlorite vein; 1.3 mm).

**D.** Enlargement of center of C) showing Type 1 inclusions in clear area (370 μm).

**E.** Large, relatively mature Type 2 inclusions from unmineralized area (Moyie sill 25 km southwest of Sullivan; 370 μm).

**Figure 4.** Fluid inclusions in quartz veins found in regional samples (transmitted light, uncrossed polars; sample number and width of view).

DD5085-75.5' in the central footwall contains Type 2 (5-15 wt.%, Th 225-315°C) plus Type 5 (similar salinity, 104-116°C) inclusions (Fig. 3C). In the hanging wall, quartz and sphalerite in DD313-384 contain inclusions with similar Th and salinity (Table 1). Fluids in sphalerite from a recrystallized quartz-sphalerite-chlorite pod in southeast fringe bedded ore (90SVL3) reported previously are similar (20-25 wt.%, minor carbonic fluid: Leitch and Turner, 1991). These data are included in the histogram for sphalerite (Fig. 3E). In DD3900-105', albitite is veined and replaced by irregular quartz-carbonate-pyrite stringers. The quartz contains unusual pseudosecondary inclusions with variable vapour/liquid ratios of 5-95%, mostly high Th 250-355°C (95-195°C for Type 5), and about 10 wt.% with carbonic fluid (Table 1). Inclusions in quartz associated with hanging wall albite-chlorite alteration reported previously (SULIV-2; Leitch, 1991) are mostly Type 2b with Th 165-237°C plus rare Type 2a with Th 250°C; salinities are 15-20 wt.% NaCl+?KCl.

### *Regional samples*

Inclusions were also studied in quartz veins from other deposits, prospects and locations in the Aldridge Formation (Table 2 and Fig. 3F). These samples are, respectively, from tourmalinite associated with the North Star massive sulphide deposit (91NSL3) and quartz-sphalerite-chlorite veins from the Quantrell deposit (91ALT17), both in the district-scale alteration corridor extending southwest from the Sullivan deposit; quartz-calcite-fuchsite veins in a Moyie gabbro sill near the Horn property (91ALL4); and quartz veins in tourmalinite from the Kidstar prospect (91ALL11).

Tourmalinite from the Kidstar prospect is cut by 1-3 mm clear quartz veinlets that contain inclusions mainly where crosscut by later 0.5 mm quartz fractures. These healed fractures cross grain boundaries (Fig. 4A) and are Type 2a with Th 265-400°C. Rare Type 1 inclusions not obviously related to any fracture also have high Th around 430°C. Planar veins cutting the North Star tourmalinite also contain Type 1 (Th 210°C) and 2a (Th 280-443°C) inclusions in quartz (Fig. 4B). The Quantrell quartz-sphalerite-chlorite veins contain abundant saline (25 wt.%) Type 2a inclusions along fractures (Fig. 4C) that decrepitate largely between 265 and 355°C, and Type 1 inclusions in adjacent clear areas (Fig. 4D) with Th 275-348°C. Similar quartz-chlorite-sphalerite veins are seen at the nearby Stemwinder deposit (Leitch and Turner, 1992). Sample 91ALL4 (Fig. 4E), containing only Type 2 (Th 230-291°C) and lacking Type 1 inclusions, is unrelated to mineralization.

## DISCUSSION

Fluids trapped in quartz veins cutting tourmalinite beneath the Sullivan deposit are mainly saline, 15-27 wt.% NaCl plus significant $CaCl_2$ and possible $MgCl_2$ but range down to 5 wt.%. Inclusions are divisible into several principal groups (Fig. 3): Type 1, halite-saturated, bimodal with Th modes at 210 and 275°C but in places 160-200°C; Type 2a and 2b, with lower salinities and Th 230-320°C and 160-230°C respectively; Type 2c, 3, and 4 with much lower salinities, Th principally between 160 and 300°C, and increasing vapour/liquid ratios and carbonic fluid contents; and Type 5, moderate salinities but low temperature (90-150°C). Most inclusions occur along healed fracture planes, and therefore are secondary, or pseudosecondary where these planes do not cross the boundaries of optically continuous crystals. Most therefore formed after or in late stages of formation of the host crystals. Type 2 inclusions associated with the tourmalinite stable pyrrhotite network or planar veins may be slightly higher temperature (modes at 200 and 275°C: Fig. 3A) than inclusions in veins with chlorite envelopes (mode at 195, mean 210°C: Fig. 3C). Although data are sparse, Type 2 inclusions associated with muscovite have higher Th (240-380°C) than for tourmalinite or chlorite assemblages (Fig. 3B).

Similar saline Type 1 inclusions are found in quartz veins at other deposits and prospects in the Aldridge Formation such as the North Star massive sulphide, the Quantrell vein, and the Star tourmalinite; only Type 2 inclusions are found in quartz associated with a Moyie sill. This supports a relation between saline fluids and mineralization in the Aldridge Formation, but more work is needed on samples unrelated to mineralization. A search has been made for such samples, but to date, fluid inclusions have not been found except in vein quartz related to either mineralization or Moyie sills.

As implied by the classification numbers, Type 1 appear to be the earliest inclusions (found on short fractures that are crossed by other fractures; most saline). Type 1 inclusions are distinctive, with low relief against the enclosing quartz compared to high relief (dark outlines) shown by the Type 2 inclusions. Most Type 1 inclusions also display a high degree of textural maturity, suggesting that they are earlier than all the other inclusions; however, a few irregular shapes similar to those of Type 2c or 5, coupled with lower Th (200°C or less, e.g. DD1141) suggest re-opening. Significantly, inclusions are found almost exclusively in vein quartz, and these veins are associated with hydrothermal ore deposition; only rare Type 5 inclusions are found in detrital quartz grains immediately adjacent to the veins.

It is likely that the the saline, Na-Ca-?Mg fluids preserved in inclusions at Sullivan represent mineralizing fluids. Similar Na-Ca-Mg brines are found in inclusions in barite, dolomite, andhydrite and quartz at the Sheep Creek Cu-Co deposit in equivalent age but unmetamorphosed strata of the Helena Embayment, Montana (Leitch and Zieg, unpub. data, 1992). At Sullivan, possible re-setting of homogenization temperatures during biotite metamorphism may have occurred to variable degrees. The low Th recorded for some inclusions, notably Type 5 and some 2c (e.g. DD4483), suggests they were trapped under retrograde conditions. They may thus represent samples of the mineralizing fluids that have been variably diluted by opening and re-healing, possibly during metamorphism. This is supported by a correlation between salinity and Th in Type 2a-c (Leitch, 1991) suggesting lower salinity inclusions represent increasing degrees of mixing with metamorphic water as temperature fell.

### *Brine pool model*

The extensive, in places up to several metre thick pyrrhotite veins found in the footwall tourmalinite pipe appear to be main feeders to the Sullivan deposit, and show similarities to the Stemwinder vein (Leitch and Turner, 1992). The high ratio of sulphide to gangue in the feeder veins directly underlying the Sullivan deposit and in the massive sulphides suggest a concentrated, strong flow of fluid rich in metals combined with a minimal input of detrital material to the basin where sulphide precipitation and deposition was occurring. An analagous situation is the Red Sea Deeps, where a brine pool develops because fluids exhaled on the bottom in restricted basins do not mix with overlying seawater (Ramboz et al., 1988). Instead, they form one or two density-stratified brine layers that cool by conduction to normal seawater without significant loss of salinity. This is a key point, allowing hot, saline exhaled fluids at up to 300°C and therefore lower density than seawater, to form brine pools; regardless of the buoyancy of such fluids, the empirical observation is that mixing does not occur and pools form. Surface waters are at 30°C and bottom water is at 22°C in such a restricted sea, compared to open ocean bottom temperatures of 4°C. Temperatures of Red Sea exiting fluids are not known, but inclusions in anhydrite, veins beneath the central portion of the deeps show that boiling occurred, at up to 420°C (Ramboz et al., 1988). It is possible that the first discharge of the hydrothermal system would be cooler than main stage discharge due to conductive cooling, giving rise to a higher density fluid and initiation of the brine pool, which could then not be perturbed by later, hotter, more buoyant fluids (McDougall, 1984).

Such a model for the Sullivan deposit is supported by two key observations. The extremely finely laminated nature of the major portion of the bedded ores, in which details of stratigraphy can be followed for up to 2 km (Hamilton et al., 1982) is suggestive of dewatered Red Sea muds (although plume fallout could also account for the laterally continuous nature of the laminae). If Type 1 and 2 fluids represent the mineralizing fluids, the 15-27 wt.% salinities are like those in anhydrite veins underlying the Red Sea brine pools, and similar to the salinity of the brine pools (13.5-25.6%: Ramboz et al., 1988). Although evaporites are not known in the Belt Basin, they may have been present at the base of the section, and dissolved during metamorphism (as postulated in the Broken Hill district of Australia: J. Slack et al., unpub. manuscript). Dilute fluids containing a variable carbonic component are likely a metamorphic overprint.

## ACKNOWLEDGMENTS

Critical reviews of this manuscript by Jan Peter and John Hamilton are appreciated.

## REFERENCES

**Ansdell, K.M., Nesbitt, B.D., and Longstaffe, F.J.**
1989: A fluid inclusion and stable isotope study of the Tom Ba-Pb-Zn deposit, Yukon Territory, Canada; Economic Geology, v. 84, p. 841-856.

**Beaty, D.W., Hahn, G.A., and Threlkeld, W.E.**
1988: Field, isotopic, and chemical studies of tourmaline-bearing rocks in the Belt-Purcell Supergroup: genetic constraints and exploration significance for Sullivan type ore deposits; Canadian Journal of Earth Sciences, v. 25, p. 392-402.

**Bodnar, R.J., Reynolds, T.J., and Kuehn, C.A.**
1985: Fluid inclusion systematics in epithermal systems; in Geology and Geochemistry of Epithermal Systems (ed.) B.R. Berger and P.M. Bethke; Reviews in Economic Geology, v. 2, p. 73-97.

**Crawford, M.L., Kraus, D.W., and Hollister, L.S.**
1979: Petrologic and fluid inclusion study of calc-silicate rocks, Prince Rupert, British Columbia; American Journal of Science, v. 279, p. 1135-1159.

**Davis, D.W., Lowenstein, T.K., and Spencer, R.J.**
1989: Melting behavior of fluid inclusions in laboratory-grown halite crystals in the systems NaCl-$H_2O$, NaCl-$H_2O$, NaCl-$MgCl_2$-$H_2O$, and NaCl-$CaCl_2$-$H_2O$; Geochimica et Cosmochimica Acta, v. 54, p. 591-601.

**Edmunds, F.R.**
1977: The Aldridge Formation, B.C., Canada; Ph.D. thesis, Pennsylvania State University, University Park, Pennsylvania, 368 p.

**Gardner, H.D. and Hutcheon, I.**
1985: Geochemistry, mineralogy, and geology of the Jason Pb-Zn deposits, MacMillan Pass, Yukon, Canada; Economic Geology, v. 80, p. 1257-1276.

**Hamilton, J.M., Bishop, D.T., Morris, H.C., and Owens, O.E.**
1982: Geology of the Sullivan orebody, Canada; in Precambrian Sulphide Deposits; H.S. Robinson Memorial volume, (ed.) R.W. Hutchinson, C.D. Spence, and J.M. Franklin; Geological Association of Canada, Special Paper 25, p. 597-665.

**Leitch, C.H.B.**
1991: Preliminary fluid inclusion and petrographic studies of the Sullivan sedimentary exhalitive Pb-Zn deposit, southeastern British Columbia; in Current Research, Part A; Geological Survey of Canada, Paper 91-1A, p. 91-101.
1992: Mineral chemistry of selected silicates, carbonates, and sulphides in the Sullivan and North Star stratiform Zn-Pb deposit, British Columbia, and in district-scale altered and unaltered sediments; in Current Research, Part E; Geological Survey of Canada, Paper 92-1E.

**Leitch, C.H.B. and Turner, R.J.W.**
1991: The vent complex of the Sullivan stratiform sediment-hosted Zn-Pb deposit, B.C.: preliminary petrographic and fluid inclusion studies; in Current Research, Part E; Geological Survey of Canada, Paper 91-1E, p. 33-44.
1992: Preliminary field and petrographic studies of the sulphide-bearing network underlying the western orebody, Sullivan stratiform sediment-hosted Zn-Pb deposit, British Columbia; in Current Research, Part E; Geological Survey of Canada, Paper 92-1E.

**Mako, D.A. and Shanks, W.C. III**
1984: Stratiform sulfide and barite-fluorite mineralization of the Vulcan prospect, Northwest Territories: exhalation of basinal brines along a faulted continental margin; Canadian Journal of Earth Sciences, v. 21, p. 78-91.

**McClay, K.R.**
1983: Structural evolution of the Sullivan Fe-Pb-Zn-Ag orebody, Kimberley, British Columbia, Canada; Economic Geology, v. 78, p. 1398-1424.

**McDougall, J.**
1984: Fluid dynamic implications for massive sulphide deposits flowing into a submarine depression from below; Deep Sea Research, v. 2, p. 145-170.

**McMechan, M.E. and Price, R.A.**
1982: Superimposed low-grade metamorphism in the Mount Fisher area, southeastern British Columbia--implications for the East Kootenay orogeny; Canadian Journal of Earth Sciences, v. 19, p. 476-489.
**Nesbitt, B.E., Longstaffe, F.J., and Muehlenbachs, K.**
1984: Oxygen isotopic geochemistry of the Sullivan massive sulfide deposit, Kimberley, British Columbia; Economic Geology, v. 79, p. 933-946.
**Ramboz, C., Oudin, E., and Thisse, Y.**
1988: Geyser-type discharge in Atlantis II deep, Red Sea: evidence of boiling from fluid inclusions in epigenetic anhydrite; Canadian Mineralogist, v. 26, p. 765-786.
**Roedder, E.**
1984: Fluid Inclusions: Mineralogical Society of America, Reviews in Mineralogy, v. 12, 644 p.
**Samson, I.M. and Russell, M.J.**
1983: Fluid inclusion data from Silvermines base-metal-baryte deposits, Ireland; Transactions of the Institution of Mining and Metallurgy (Section B: Applied earth science), v. 92, p. 67-71.
**Shaw, D.R. and Hodgson, C.J.**
1986: Wall-rock alteration at the Sullivan mine, Kimberley, B.C.; in The genesis of stratiform sediment-hosted lead and zinc deposits: conference proceedings (ed.) R.J.W. Turner and M.T. Einaudi; Stanford University Publications, School of Earth Sciences, v. XX, p. 13-21.
**Simmons, S.F.**
1991: Hydrologic implications of alteration and fluid inclusion studies in the Fresnillo district, Mexico: evidence for a brine reservoir and a descending water table during the formation of hydrothermal Ag-Pb-Zn orebodies; Economic Geology, v. 86, p. 1579-1601.
**Turner, R.J.W. and Leitch, C.H.B.**
1992: Relationship of albitic and chloritic alteration to gabbro dykes and sills in the Sullivan mine and nearby area, B.C.; in Current Research, Part E; Geological Survey of Canada, Paper 92-1E.

Geological Survey of Canada Project 900020
(Contribution No. 10, Sullivan-Aldridge project)

# Mineral chemistry of selected silicates, carbonates, and sulphides in the Sullivan and North Star stratiform Zn-Pb deposits, British Columbia, and in district-scale altered and unaltered sediments

**Craig H.B. Leitch**
**Mineral Resources Division, Vancouver**

*Leitch, C.H.B., 1992: Mineral chemistry of selected silicates, carbonates, and sulphides in the Sullivan and North Star stratiform Zn-Pb deposits, British Columbia, and in district-scale altered and unaltered sediments; in Current Research, Part E; Geological Survey of Canada, Paper 92-1E, p. 83-93.*

***Abstract***

*At the Sullivan deposit, bedded sulphides are separated from a lens of massive sulphides by the arcuate transition zone around the eastern margin of the major footwall tourmalinite-pyrrhotite vent zone. Several minor minerals (cassiterite, stannite, freibergite, arsenopyrite, bismuthian boulangerite and jamesonite, gudmundite, ?bismuthinite, Bi-Sb alloy) rich in Sn, Ag, and the semi-metals As, Sb, and Bi appear concentrated in the transition zone in late-stage veins with associated muscovite alteration. Preliminary analyses from limited numbers of samples suggest zoning of mineral compositions that give several vectors of potential use to exploration: sphalerite to higher Fe inside the transition zone, and both carbonate and garnet to higher Mn toward the fringes of the Sullivan deposit. Plagioclase remaining in tourmalinized rocks is anorthite (up to $An_{92}$) compared to andesine ($An_{38}$) in regionally unaltered rocks. Clinozoisite, found regionally, is more Fe-rich (epidote) near the deposits, and the Fe content of chlorites also appears to be highest in massive sulphides.*

***Résumé***

*Dans le gisement de Sullivan, les sulfures lités sont séparés d'une lentille de sulfures massifs par une zone de transition arquée, laquelle entoure la marge orientale de la principale zone de griffon à pyrrhotine dans de la tourmalinite, observée dans l'éponte inférieure. Plusieurs minéraux accessoires (cassitérite, stannite, freibergite, arsénopyrite, boulangérite et jamesonite bismuthifères, gudmundite, bismuthinite ?, alliage de Bi-Sb) riches en Sn et en Ag ainsi que les métalloïdes As, Sb et Bi paraissent se concentrer dans la zone de transition, dans les veines de phase tardive accompagnées d'une altération en muscovite. L'analyse préliminaire d'un nombre limité d'échantillons semble indiquer une zonation des compositions minérales qui peut orienter l'exploration dans plusieurs directions, notamment vers la sphalérite qui passe à des concentrations plus élevées en Fe dans la zone de transition, mais aussi vers les carbonates et les grenats qui sont de plus en plus riches en Mn à mesure qu'on approche des bords du gisement de Sullivan. Le plagioclase qui subsiste dans les roches tourmalinisées est l'anorthite (jusqu'à $An_{92}$) alors que celui présent dans les roches non altérées de la région est l'andésine ($An_{38}$). La clinozoïsite, observée à l'échelle régionale, est plus riche en Fe (épidote) près des gisements; quant à la teneur en Fe des chlorites, elle semble atteindre son maximum dans les sulfures massifs.*

## INTRODUCTION

The Sullivan and North Star stratiform sediment-hosted Zn-Pb deposits occur in a corridor of district-scale alteration (Höy, 1984). Minerals in these deposits, the enclosing alteration assemblages, and in the regional unaltered rocks have been investigated petrographically (Leitch and Turner, 1991; Leitch et al., 1991). Minerals with varying solid solution chemistry are important in characterizing alteration trends, thereby helping to define pathways of mineralizing fluids; these are the subject of this contribution.

Previous work on the compositions of minerals in the Sullivan deposit includes albite and chlorite compositions in Hamilton et al. (1982), and studies of allanite (Campbell and Ethier, 1984; Schandl and Gorton, 1992). Elevated Mn at the base and around the margins of the orebody is due mainly to Mn contents of garnet (R.L. Barnett, unpub. manuscript, 1982), but is also influenced by Mn in carbonate (Hamilton et al., 1982). In this study, the main focus is on (1) sulphide and sulphosalt minerals mainly in the transition zone between distal bedded sulphides and massive sulphides overlying the vent zone, and (2) comparison of silicate and carbonate alteration minerals on and around the sulphide deposits, with similar minerals in unaltered regional strata.

Locations of the studied samples from underground workings and drill holes are shown in cross-section (Fig. 1, 2) and in plan (Fig. 4 of Turner and Leitch, 1992) and will not be individually referenced to figures hereafter. Geological settings of these samples are described in Leitch and Turner (1991) for underground samples, and in Leitch and Turner (1992) for drill core samples.

Average mill feed from the Sullivan mine over 20 years contained Cu 0.033%, As 0.083%, Sb 0.026%, Bi 0.0036%, Sn 0.031%, Ag 0.068% or 75 g/t, Mn 0.244%, Cd 0.0142%, In 0.00146% and Tl 0.00097% (Hamilton et al., 1982).

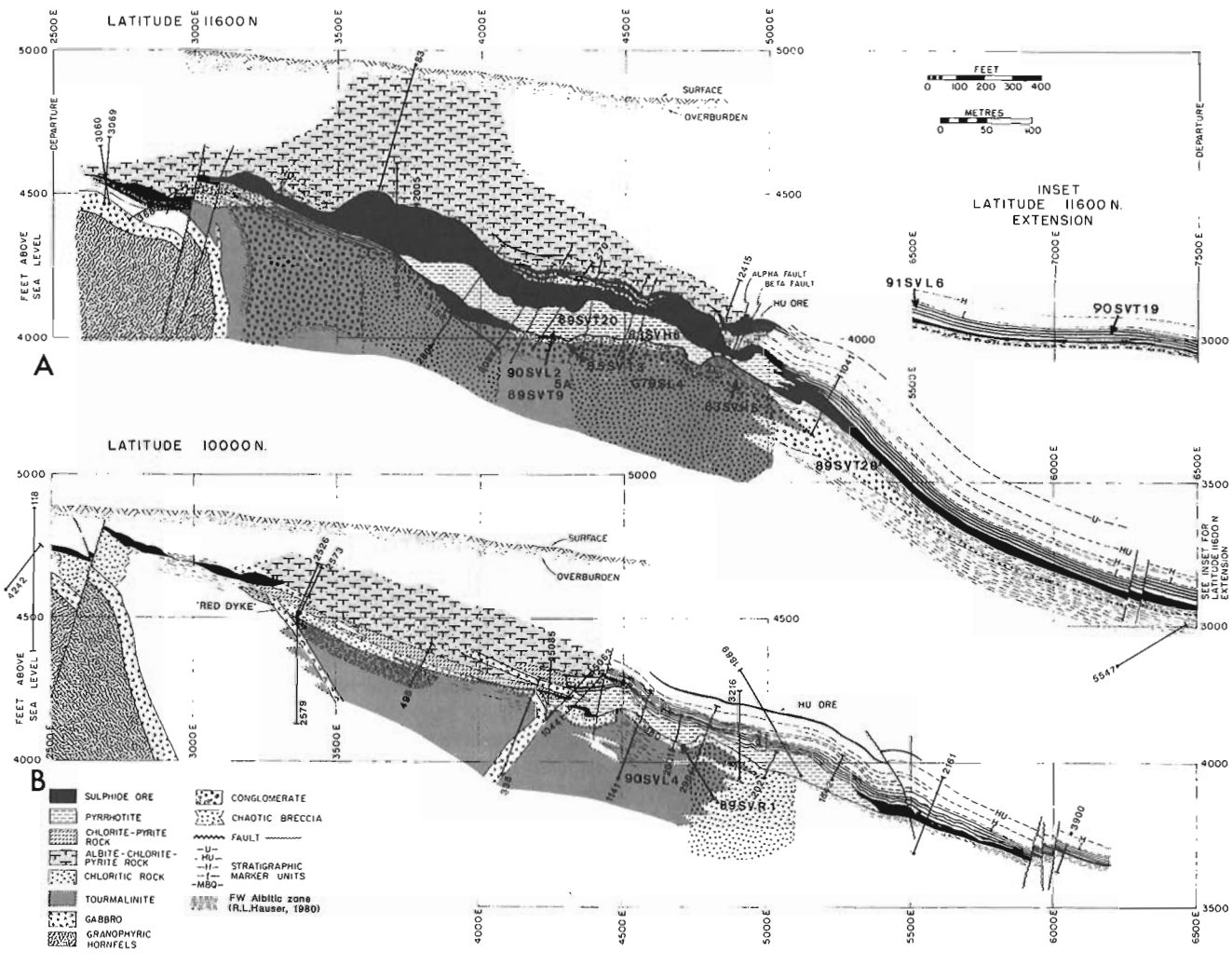


**Figure 1.** East-west cross-sections showing geology and alteration (after Hamilton et al., 1982), and location of diamond drill holes logged and sampled in this study **A)** 11600N, and **B)** 10000N. Locations of underground samples are approximate, and are projected to the 11600 section. Sections are located in plan view in Figure 4 of Turner and Leitch (1992).

Freeze (1966) ascribed copper to widespread but not abundant chalcopyrite, and lesser tetrahedrite and stannite. Arsenic occurs in arsenopyrite, which also is widespread, and slightly more common than chalcopyrite. Both minerals occur as traces in the vent zone and massive pyrrhotite replacement body, with minor amounts in bedded ores. Arsenic is concentrated, to 0.6%, immediately south of the so-called central Fe (pyrite-chlorite-calcite) zone.

Freeze (1966) also described the distribution of Sb and Sn in the deposit, and Hamilton et al. (1982) outlined the distribution of Mn and Tl. Higher concentrations of Ag (Ransom, 1977), found in tetrahedrite and possibly pyrargyrite, are coincident with the vent zone as outlined by the transition zone or the underlying chaotic breccias (Hamilton et al., 1982). Manganese, found in carbonate and garnet, is most abundant in the southwest portion of the deposit in the open pit area where it attains concentrations of 1.0% in the ore (Hamilton et al., 1982). Thallium is concentrated up to 0.02% on the east fringe of the deposit in ore in which sphalerite predominates over galena (Hamilton et al., 1982).

There are no data concerning the distribution of Bi, In, Cd, or Cu in the ore. Also, the mineralogical sites for some trace elements have not been fully explained. Earlier reports (Leitch, 1991; Leitch and Turner, 1991) proposed the existence of discrete Bi phases such as native Bi. This study confirms the presence of Bi as the native metal (alloyed with Sb) and in bismuthian boulangerite and jamesonite, plus possible rare bismuthinite. Analyses of minerals were conducted at the laboratories of the Geological Survey of Canada in Ottawa using a Cameca SX-50 microprobe at 15 kv/10 na and 10 sec peak counting times.

## (Bi, Sb, Ag, Sn) SULPHOSALTS

Although found elsewhere in and near the Sullivan and North Star deposits in trace amounts, several minor minerals containing the semi-metals Sb, Bi, and As (boulangerite, bismuthian boulangerite and jamesonite, gudmundite, native Bi-Sb alloys, and possible bismuthinite), and others including freibergite, stannite, and cassiterite containing Ag, Sb, and Sn appear to be concentrated in and near the transition zone. Analyses of these minerals (Table 1) are referred to below by sample number.

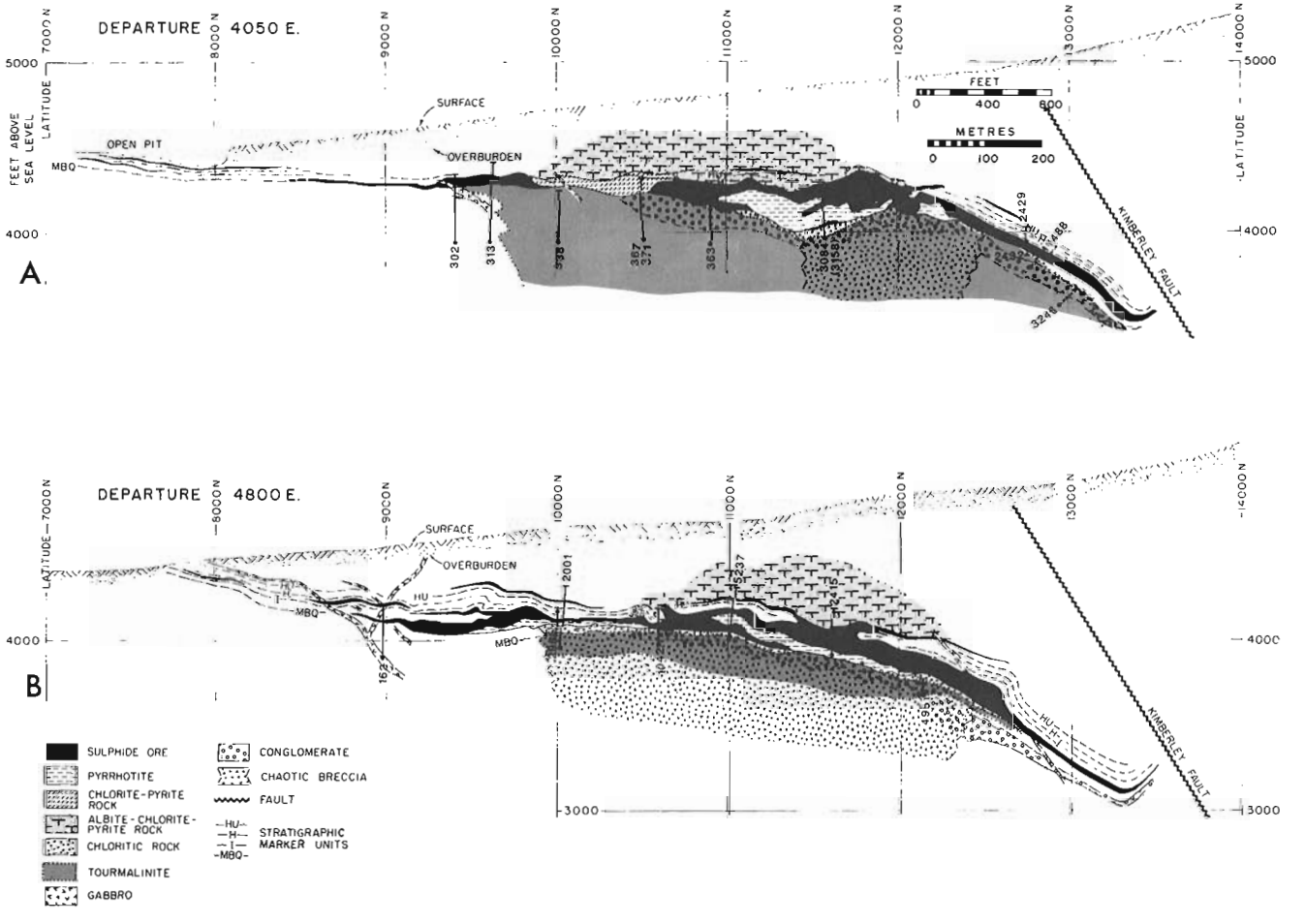


**Figure 2.** North-south longitudinal sections **A**) 4050E, and **B**) 4800E (details as for Fig. 1).

**Table 1.** Microprobe analyses of Bi-, Ag- and Sn-sulfosalts, Sullivan deposit

| | Boulangerite | | | | Bi-boulangerite | | | | | |
|---|---|---|---|---|---|---|---|---|---|---|
| Sample | 83SVH5 | 89SVT28 | 1842-16 | 1488-83 | 90SVL2 | 90SVL2 | 202-13 | 89SVR1 | 89SVR1 | 296161 |
| (n) | (2) | (1) | (2) | (1) | (1) | (1) | (2) | (2) | (2) | (2) |
| Pb | 61.39 | 56.34 | 54.57 | 54.43 | 53.28 | 59.47 | 49.13 | 48.17 | 49.33 | 47.74 |
| Ag | ND | 0.12 | 0.07 | 0.05 | ND | ND | 0.44 | 1.09 | 0.64 | 0.41 |
| Sb | 19.35 | 25.51 | 25.97 | 26.49 | 23.96 | 17.52 | 11.57 | 8.62 | 6.90 | 5.48 |
| Bi | 0.15 | 0.19 | 0.09 | ND | 4.93 | 6.35 | 20.05 | 24.96 | 26.67 | 28.87 |
| As | 0.37 | 0.18 | 0.10 | 0.07 | ND | ND | ND | ND | ND | ND |
| S | 17.57 | 18.49 | 19.18 | 19.35 | 18.82 | 18.07 | 17.78 | 17.35 | 17.20 | 17.11 |
| Total | 98.83 | 100.83 | 99.98 | 100.39 | 100.99 | 101.41 | 98.97 | 100.19 | 100.74 | 99.61 |

Approximate formulae: 83SVH5 $Pb_{5.9}(Sb,Bi,As)_{3.3}S_{11}$ 89SVT28 $Pb_{5.2}(Sb,Bi,As)_{4.0}S_{11}$ 1842-16.5 $Pb_{4.8}(Sb,Bi)_{3.9}S_{11}$ 1488-83 $Pb_{4.8}(Sb,Bi)_{4.0}S_{11}$ 90SVL2 $(Pb,Ag)_{4.9\text{-}5.6}(Bi_{0.4\text{-}0.6}Sb_{3.7\text{-}2.8})S_{11}$ 202-13.2 $(Pb,Ag)_{4.8}(Sb_{1.9}Bi_{1.9})S_{11}$ 89SVR1 $(Pb,Ag)_{5.0}(Sb_{1.2\text{-}1.4}Bi_{2.7\text{-}2.5})S_{11}$ 296-161 $(Pb,Ag)_{4.8}(Sb_{0.9}Bi_{2.8})S_{11}$

| | Bi-jamesonite | | | Gd'ite | Bs'ite | Bi-Sb alloy | | | | |
|---|---|---|---|---|---|---|---|---|---|---|
| Sample | 90SVL2 | 2001107 | 202-13 | 90SVL2 | 89SVR1 | 85SVT3 | 296161 | 89SVR1 | 90SVL2 | |
| (n) | (1) | (1) | (2) | (2) | (2) | (2) | (2) | (1) | (2) | (1) |
| Pb | 41.17 | 36.30 | 36.82 | | | 0.22 | ND | 0.11 | ND | ND |
| Sb | 30.19 | 26.84 | 22.64 | 59.59 | 5 | 0.95 | 3.57 | 7.87 | 22-30 | 80.87 |
| Bi | 9.64 | 12.54 | 16.64 | 0.17 | 72 | 96.63 | 98.21 | 91.42 | 78-70 | 20.27 |
| Fe | 2.81 | 1.69 | 2.27 | 26.96 | 2 | 0.30 | ND | 0.19 | 0.3 | ND |
| S | 21.17 | 20.81 | 20.49 | 15.76 | 14 | ND | ND | ND | ND | ND |
| Total | 104.98 | 98.18 | 98.86 | 102.47 | 93 | 98.10 | 101.78 | 99.59 | 100 | 101.14 |

Approximate formulae: **Bi-jamesonite**, 90SVL2 $Pb_{4.2}Fe_{1.0}(Sb_{5.2}Bi_{1.0})S_{14}$ 2001-107.5 $Pb_{3.8}Fe_{0.7}(Sb_{4.8}Bi_{1.3})S_{14}$ 202-13.2 $Pb_{3.9}Fe_{0.9}(Sb_{4.1}Bi_{1.8})S_{14}$. **Gd'ite** (Gudmundite): FeSbS. **Bs'ite** (?Bismuthinite): $(Bi,Sb)_{2.5}S_3$. Native **Bi-Sb alloys**: range from $Bi_{98}Sb_2$ through $Bi_{92}Sb_8$ to $Bi_{78}Sb_{22}$, $Bi_{70}Sb_{30}$ to $Sb_{80}Bi_{20}$. Ag, As not detected.

| | Ag-Tetrahedrite | | | Freibergite | | | | Stannite | | | |
|---|---|---|---|---|---|---|---|---|---|---|---|
| Sample | 83SVH5 | 90SVL2 | 91NSL2 | 3084-225 | | 83SVH6 | | 83SVH6 | | 90SVL2 | 296161 |
| (n) | (2) | (1) | (2) | (3) | (1) | (3) | | (2) | (1) | (2) | (1) |
| Sb | 30.21 | 28.57 | 28.35 | 28.92 | 28.25 | 26.12 | Sn* | 25 | 20 | 25 | 23 |
| As | 0.08 | 0.22 | 0.07 | 0.14 | 0.06 | 0.07 | As | ND | ND | ND | ND |
| Ag | 5.93 | 10.30 | 15.38 | 13.00 | 17.00 | 28.10 | Ag | ND | ND | ND | ND |
| Cu | 32.44 | 30.75 | 26.24 | 28.68 | 25.70 | 16.31 | Cu | 30 | 24 | 27 | 31 |
| Fe | 5.14 | 6.55 | 5.88 | 5.65 | 5.18 | 6.71 | Fe | 12 | 23 | 16 | 11 |
| Zn | 1.69 | 0.18 | 0.95 | 1.31 | 0.87 | 0.54 | Zn | 1 | <1 | <1 | 2 |
| S | 24.42 | 24.90 | 23.49 | 24.05 | 23.61 | 21.54 | S | 31 | 33 | 31 | 32 |
| Total | 99.91 | 101.47 | 100.36 | 101.75 | 100.67 | 99.39 | | 99 | 100 | 99 | 99 |

**Argentiferous tetrahedrite:** $(Cu, Ag)_{9.7\text{-}10.0}(Fe,Zn)_{2.0\text{-}2.8}(Sb,As,Bi)_{4.0\text{-}4.2}S_{13}$
**Stannite:** $Cu_2SnFeS_4$; Sn* by SEM-EDS analysis.

(c't'd). Microprobe analyses of sphalerites, Sullivan and North Star deposits.

**Sphalerite**

| Sample | 90SVL2 | 89SVT28 | 2001107 | 1842-16 | 1488-83 | 270-277 | 202-13 | 3084-225 | 91NSL2 |
|---|---|---|---|---|---|---|---|---|---|
| (n) | (1) | (1) | (4) | (2) | (2) | (2) | (3) | (4) | (2) |
| Zn | 56.33 | 59.32 | 57.70 | 57.10 | 60.75 | 59.34 | 59.65 | 57.92 | 58.08 |
| Fe | 7.56 | 6.86 | 7.22 | 7.79 | 5.56 | 6.77 | 6.06 | 8.10 | 7.31 |
| Mn | | | 1.22 | 0.91 | 0.25 | 0.31 | 0.21 | 0.30 | 0.17 |
| Cd | | | | | | | 0.16 | | 0.25 |
| Hg | | | | | | | 0.37 | | 0.21 |
| In | | | | | | | 0.05 | | 0.08 |
| S | 34.46 | 34.49 | 33.72 | 33.95 | 33.88 | 33.71 | 33.29 | 33.95 | 33.53 |
| Total | 98.35 | 100.67 | 99.86 | 99.75 | 100.44 | 100.13 | 99.79 | 100.27 | 99.63 |

| Location | Rim | Core | | | | | | | Rim |
|---|---|---|---|---|---|---|---|---|---|
| Sample | | 3084-225 | | | | | | | |
| (n) | (1) | (1) | (1) | (1) | (1) | (1) | (1) | (1) | (1) |
| Zn | 58.57 | 57.98 | 57.53 | 56.94 | 56.93 | 57.13 | 56.99 | 56.81 | 58.09 |
| Fe | 7.15 | 7.72 | 8.26 | 8.36 | 8.38 | 8.50 | 8.19 | 8.17 | 7.51 |
| Mn | 0.24 | 0.30 | 0.28 | 0.28 | 0.30 | 0.33 | 0.29 | 0.30 | 0.21 |
| Cd | 0.27 | 0.23 | 0.22 | 0.30 | 0.31 | 0.22 | 0.21 | 0.19 | 0.16 |
| Hg | 0.16 | 0.14 | 0.32 | 0.20 | 0.30 | 0.35 | 0.29 | 0.16 | 0.31 |
| In | 0.07 | ND | ND | 0.05 | ND | ND | 0.08 | 0.08 | 0.06 |
| S | 33.22 | 33.62 | 33.07 | 33.22 | 33.20 | 33.22 | 33.45 | 33.49 | 33.16 |
| Total | 99.68 | 100.02 | 99.68 | 99.35 | 99.42 | 99.75 | 99.50 | 99.20 | 99.50 |

ND= not detected; blank indicates not analysed.

**Goethite and limonite** (primary, intergrown with sphalerite in 3084-225)

| | Goethite | Limonite |
|---|---|---|
| Sample | 3084225 | 3084225 |
| (n) | (4) | (2) |
| FeO | 86.29 | 75.80 |
| $SiO_2$ | 2.83 | 1.03 |
| $Al_2O_3$ | 0.03 | 0.01 |
| MnO | 0.50 | 0.05 |
| MgO | 0.08 | 1.31 |
| NiO | 0.15 | 0.21 |
| ZnO | 0.64 | 0.82 |
| Total | 90.49 | 79.23 |

($H_2O$ in goethite, αFeO.OH, about 10%; in limonite variable, up to 20%)

Boulangerite $Pb_6(Sb,Bi,As)_4S_{11}$ is the predominant Sb-bearing mineral in the deposit; jamesonite, tetrahedrite, gudmundite and chalcostibite have also been reported (Freeze, 1966). Antimonian boulangerite is widespread in bedded ores where it occurs as rounded blebs up to 0.5 mm, commonly in galena (sample 89SVT28). The blebs appear to be concentrated in certain layers parallel to the bedding. It is also common in the footwall vent zone of the deposit where it occurs 1) as grains up to 0.7 mm in galena (83SVH5: Fig. 2G of Leitch, 1991); 2) in quartz-arsenopyrite-pyrrhotite veins (G79SL4); 3) in bedding-parallel layers up to 1.5 cm thick in massive pyrrhotite (90SVL2: Fig. 6 of Leitch and Turner, 1991); or 4) euhedral needles previously identified as stibnite at the base of this massive pyrrhotite (91SVL4, 15 cm below 90SVL2). This is similar to the description of Freeze (1966, p. 276) "as spectacular felt-like masses of fine flexible needles on the walls or in openings associated with the fractures". A more common occurrence in drill core, however, is irregular blebs up to 1 cm in massive pyrrhotite or massive ore, particularly in the transition zone. Here both pure antimonian (1488-83', 1842-16.5') and bismuthian (202-13.2', Fig. 3A; 296-161', Fig. 3E; 89SVR1, Fig. 2D of Leitch, 1991) varieties occur, mainly in quartz-pyrrhotite-arsenopyrite-sphaleritecassiterite veins cutting muscovite ± quartz-carbonate altered sedimentary rock in massive pyrrhotite.

All jamesonite $Pb_4Fe(Sb,Bi)_6S_{14}$ analysed is bismuthian, with a direct substitution of Bi for Sb (Table 1). It typically occurs as slender prismatic crystals distinguished from boulangerite only by the presence of Fe in microprobe analysis (e.g. 202-13.2, in association with bismuthian boulangerite: Fig. 3A). In sample 2001-107.5 it occurs with a cassiterite-stannite rich, pyrrhotite-sphalerite-galena-arsenopyrite-garnet-Mn calcite-muscovite assemblage (Fig. 3B); in 90SVL2, it is intergrown with bismuthian boulangerite (Fig. 3C).

Gudmundite FeSbS was only found in one sample, 90SVL2. It occurs as small (100μm) intergrowths with galena, native Bi-Sb alloys, and stannite in the host bismuthian boulangerite and jamesonite (Fig. 3C) or in microveinlets with pyrrhotite and carbonate cutting boulangerite.

Native Bi-Sb alloys are widespread in the central, particularly footwall, portion of the Sullivan deposit, and also occur as traces in massive sulphides of the North Star deposit and altered rocks around it. Native Bi-Sb has not been previously identified at Sullivan, but is probably the "small bits of a white mineral...thought to be native silver" described by Freeze (1966). Analyses in Table 1 show that compositions range from nearly pure Bi (97%) with 3% Sb through intermediate alloys containing 70-90% Bi, 30-10% Sb, to native Sb (80%) with 20% Bi. The alloy typically occurs as 1-25μm blebs in either boulangerite (89SVR1: Fig. 2D of Leitch and Turner, 1991; 90SVL2: Fig. 3C, D; 296-161: Fig. 3E) or galena (85SVT3: Fig. 3F). Other samples containing the Bi-Sb alloy (identified optically) include DD4242-174' in the extreme western footwall tourmalinite, DD280-124' and 1141-85', -137' in the central footwall tourmalinite, and DD3973-30' in massive pyrrhotite of the transition zone.

One grain of bismuthinite was tentatively identified in sample 89SVR1 (Table 1). The analysis is poor because of contamination by, and a sloped surface near, hard pyrrhotite adjacent to the grain which lies within softer boulangerite.

The sulphosalt optically identified as tetrahedrite (darker grey, Fig. 2H of Leitch, 1991; see also Fig. 6 of Leitch and Turner, 1991) proved to be stannite ($Cu_2SnFeS_2$). It was also analyzed in samples 296-161 and 2001-107.5, both from the transition zone, and identified optically in other samples. The lighter grey sulphosalt in Figure 2H of Leitch (1991), tentatively identified as pearceite-polybasite, proved to be argentian tetrahedrite. All tetrahedrite analyzed is variably argentiferous, ranging from 6 to 28 wt.% Ag (Table 1). Most of this material could be called freibergite; arsenic is virtually absent (maximum 0.22%). There is a normal substitution of Ag for Cu, and possibly a concomitant decrease in Sb with increasing Ag. Iron is fairly constant, whereas Zn shows wide variations, independent of Ag. Bismuth ranged from nondetectable to 0.2% (possibly due to contamination); mercury was not analyzed.

## SPHALERITE COMPOSITIONS

Previous analyses of bedded ores suggest that there is no statistically significant variation in the Fe compositions of sphalerite laterally between different sample locations, or vertically between different ore bands (Ethier et al., 1976). However, Ethier et al. (1976) note that where sphalerite coexists only with pyrite, Fe contents are lower. Also, a large gap exists between sample locations over the eastern part of the vent zone in data of Ethier et al. (1976). A reconnaissance of this gap was attempted in sphalerite from holes 2415, 270, and 3084 and extended to a few other samples (Fig. 1A; Table 1). Results suggest that sphalerites in massive ore within the transition zone are lower in Zn and higher in Fe compared to bedded sphalerites outside the zone. This supports the contention that higher Fe contents are found where sphalerite coexists only with pyrrhotite (90SVL2, 2001-107.5, 1842-16.5, 3084-225) whereas sphalerite in bedded sulphides (89SVT28, 1488-83, 270-277) or footwall rocks (202-13.2) have lower Fe contents. Partial data were also acquired for other elements in the sphalerite structure, especially Mn, Cd, Hg, and In. Two samples with Mn contents around 1% stand out from the rest at about 0.25%; both are from the massive pyrrhotite body near the transition zone. In order to investigate zoning within a crystal, a reconnaissance traverse was made across a single 1 mm grain (Table 1). Results suggest zoning is from rims enriched in Zn and possibly In, to cores with slightly more Fe, Mn, Cd, and possibly Hg. These data are contrary to the opinion of Ethier et al. (1976) who found no consistent pattern in Fe content. Contents of Hg and In are questionable until further analytical work confirms their validity.

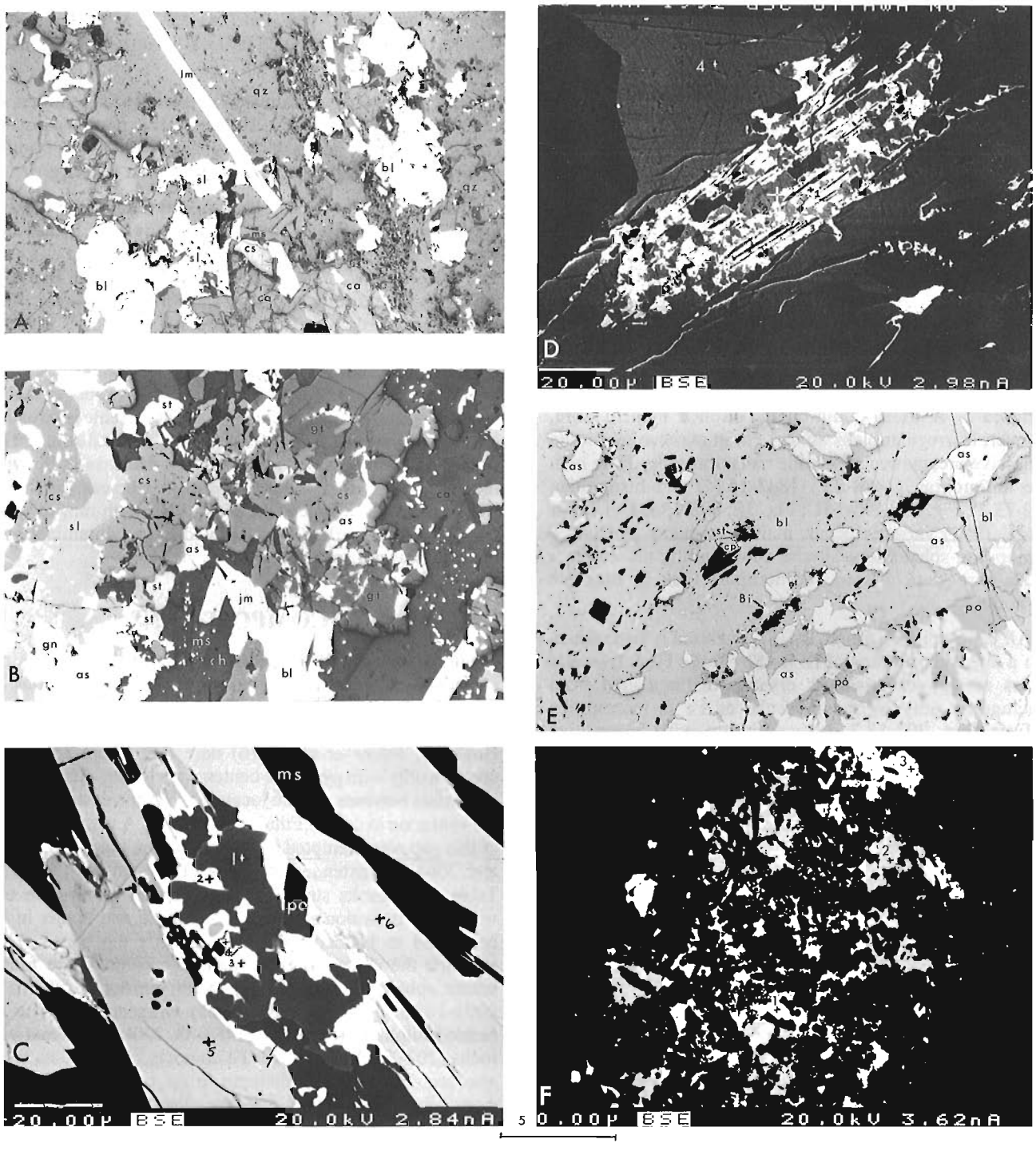


**Figure 3.** Photomicrographs of Bi-, Sb-, Sn-, and Ag-bearing minerals in Sullivan ore (reflected light, uncrossed polars, width of view 1.3 mm in A, B, and E). **A**) Needle-like Bi-jamesonite (jm), Bi-boulangerite (bl) (202-13.2, transition zone). **B**) Bismuthian jamesonite and boulangerite; stannite (st), cassiterite (cs); sphalerite (sl), pyrrhotite (po), arsenopyrite (as), galena (gn); muscovite (ms), chlorite (ch), garnet (gt), Mn calcite (ca) (2001-107.5, transition zone). **C**) Backscattered electron (BSE) image of composite grain with analyzed spots of (1) gudmundite; (2) galena; (3) and (4) native Bi-Sb alloy; (7) stannite, in host of (5) Bi-jamesonite and (6) Bi-boulangerite (po=pyrrhotite, ms=muscovite). Sample 90SVL2, central basal massive pyrrhotite (reflected light view in Fig. 6 of Leitch and Turner, 1991). **D**) BSE image of another composite grain in 90SVL2, with analysed spots of (1) galena and (3) native Sb-Bi alloy in host Bi-boulangerite (2 and 4). **E**) Massive Bi-boulangerite containing native Bi and trace chalcopyrite (cp), stannite in massive pyrrhotite-arsenopyrite (296-161, transition zone). **F**) BSE image of fine intergrowth of native Bi(±Sb) alloy (1, 3) in galena (2), in tourmalinite (dark; 85SVT3, central pipe).

The oxide minerals goethite and limonite are rare, but occur as minor primary phases intergrown with sphalerite in one sample (3084-225) from massive bedded ores over the center of the deposit. These hypogene phases have been tentatively identified optically in a few other samples, e.g. in nearby massive pyrrhotite (89SVT20). Magnetite is more common, e.g. in the massive pyrrhotite body (89SVT15, 83SVT6 near 90SVL2) and particularly around the southeast fringes (SUL13, 90SVT16-19, 91SVL6). Such occurrences may preserve remnants of originally more widespread oxide phases, if an analogy is drawn with a sulphide-oxide deposit such as the Red Sea deeps. During metamorphism, such oxides may have become unstable and the elements in them re-quilibrated into sulphides and gangue minerals (e.g., Fe into magnetite and sulphides; Mn into sphalerite, carbonate or silicates).

## MANGANIFEROUS GANGUE MINERALS

Carbonates, including calcite, ankerite, and siderite intergrown with massive sulphides at the Sullivan and nearby North Star deposit, are manganiferous (Table 2). Although based on few samples, an increase in Mn content toward the fringes of the Sullivan deposit is apparent. Manganese contents range from 2 mole per cent $MnCO_3$ in massive pyrrhotite (83SVH6) to 3-10% in the transition zone, 7-13% in bedded ores (89SVT28) and up to 35 mole per cent in manganosiderite from the southeastern fringe zone (90SVT19). Two poorly located samples of manganiferous siderite from the North Star deposit contain 70-75 mole per cent $FeCO_3$ and 15-28 mole per cent $MnCO_3$.

Garnets in the Sullivan and North Star deposits are also Mn-rich, ranging from 45 to 79% end-member spessartine (Table 2). Two 1-2 mm garnets from the Sullivan deposit analyzed in detail suggest normal zonation, with slight Mn enrichment and Fe depletion in the cores. Although garnet from the B band triplet near the southeast fringe zone (91SVL6) has lower Mn content than garnet from the transition zone (2001-107.5), the latter is from massive pyrrhotite near the base of the Main band where garnets have the highest Mn contents in the deposit (R.L. Barnett, unpub. manuscript, 1982). Thus lateral variations in Mn content of garnet are only seen if samples are constrained to a particular horizon in the deposit, such as the lower B band triplet, where "average MnO content of garnet increases from lowest values in the region of maximum sulphide thickness to highest values at the fringe in the northern, eastern, and southern margins of layered ore" (R.L. Barnett, unpub. manuscript, 1982, p. i).

Garnet from the North Star deposit has higher MnO values in massive ore (samples K38-33B and 91NSL2) than garnet in tourmalinite (samples K38-34B, 90NSH4A and 4B). No significant zoning was found within individual crystals.

Other minerals found in and near the Sullivan and North Star deposits with anomalous Mn contents (Deer et al., 1963) include tremolite, diopside, chlorite, and biotite. Ilmenite found in regional Aldridge sedimentary rocks is also anomalous, containing enough MnO (7%) to class it as a manganese ilmenite compared to normal 0.4-1.4% levels. Sphene found both regionally and in altered rocks is not anomalous in MnO (Table 2). Tremolite is a Ca-Mg silicate found locally in the Sullivan deposit (e.g. 83SVH6, massive pyrrhotite) and in Aldridge strata hosting the North Star deposit (90NSH4A) or near certain Moyie sills (e.g. to the west of the North Star deposit; Leitch et al., 1991). The MnO contents in these tremolites (0.5-0.6%) are above normal (<0.3%). Diopside found in the same sample (83SVH6) is also enriched, containing 0.4-1.0% MnO compared to <0.24% in normal diopsides. For both these calc-silicates, similar MnO contents are found only in skarns or ore deposits in analyses listed in Deer et al. (1963).

The MnO content of chlorites from the Sullivan and North Star deposits (0.4-1.4%) is consistently higher than MnO values listed for the most closely corresponding chlorite analyses in Deer et al. (1963; see DHZ#, Table 2). However, chlorite in an unaltered Middle Aldridge marker (90ALT1) contains higher than normal MnO. Chlorites, classified according to the scheme of Hey (1954), plot (Fig. 4) as pycnochlorite for regional (unaltered) chlorite developed after biotite, clinochlore to ripidolite from the district-scale alteration zone surrounding the Sullivan and North Star deposits, and Fe-rich ripidolite (approaching aphrosiderite) and rare chamosite for chlorites intergrown with massive sulphides at the deposits. Thus there is a general trend of increasing Fe:Mg and slight decrease in Si from background chlorites to chlorites in ore zones. Most chlorite associated with ore can best be described as Fe-rich ripidolite (averaging 28.4% FeO, Hamilton et al., 1982). Fe-rich chamosite (40% FeO) found in massive sulphides of sample 91NSL2 with a distinctive Fe-rich green biotite is relatively rare.

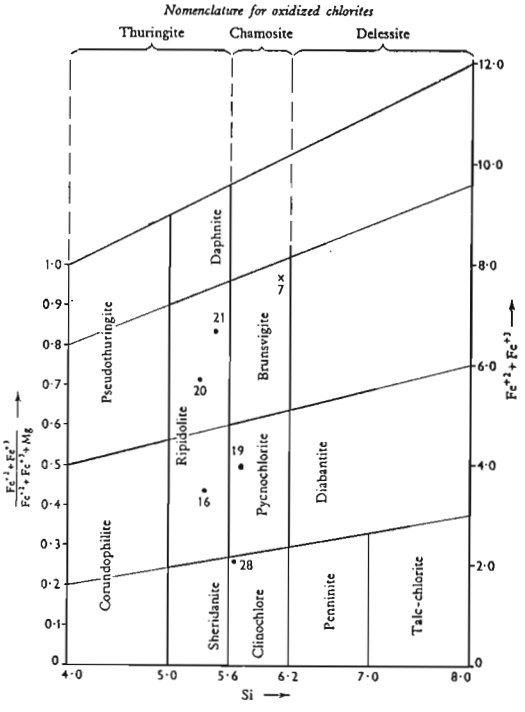


**Figure 4.** Classification of chlorites (after Hey, 1954, in Deer et al., 1963). Analyzed chlorites are plotted by DHZ# from Table 2; filled circle = ortho-chlorite, x = oxidized chlorite.

**Table 2.** Microprobe analyses of gangue minerals, Sullivan-North Star deposits

**Carbonates**

| Location | Ore zone-Sullivan | | | | | | | | North Star | | | |
|---|---|---|---|---|---|---|---|---|---|---|---|---|
| Sample | 83SVH6 | 202-13 | | 2001107 | 89SVT28 | | 90SVT19 | | 91NSL2 | | K38-33B | |
| (n) | (3) | (2) | (1) | (2) | (2) | (2) | (1) | (1) | (1) | (3) | (2) | (2) |
| $CaCO_3$ | 96.9 | 96.1 | 86.9 | 93.7 | 53.7 | 51.7 | 3.0 | 2.0 | 5.0 | 5.5 | 5.3 | 9.4 |
| $MgCO_3$ | 0.2 | 0.1 | 0.7 | 0.2 | 32.8 | 24.4 | 23.0 | 15.8 | 0.2 | 0.3 | 0.2 | 0.2 |
| $FeCO_3$ | ND | 0.3 | 1.8 | 0.2 | 6.5 | 10.4 | 38.5 | 49.1 | 66.3 | 75.1 | 68.8 | 75.9 |
| $MnCO_3$ | 2.0 | 3.4 | 10.5 | 5.9 | 7.0 | 13.4 | 35.4 | 33.0 | 28.1 | 19.0 | 25.5 | 14.4 |
| $Ba,SrCO_3$ | 0.4 | 0.1 | ND | ND | ND | 0.2 | 0.1 | ND | 0.3 | 0.1 | 0.2 | ND |
| Total | 99.5 | 100.0 | 99.9 | 100.1 | 100.0 | 100.1 | 100.0 | 99.9 | 99.9 | 100. | 100. | 99.9 |
| Type | CALCITE | Mn-CALCITE | | | ANKERITE | | | Mn-SIDERITE | | | | |

**Plagioclase** — **Clinozoisite** — **Epidote** — **Allanite**

| Location | Regional | Altered (North Star) | | | Regional | Alt'd (North Star) | | Regional | |
|---|---|---|---|---|---|---|---|---|---|
| Sample | 90ALT1 | 90NSH4A | K38-34B | | 90ALT1 | 90NSH4A | 90NSH4B | 90ALT1 | ALT7 |
| (n) | (1) | (3) | (1) | | (1) | (2) | (2) | (1) | (2) |
| $SiO_2$ | 55.97 | 42.67 | 44.94 | $SiO_2$ | 38.13 | 37.73 | 37.29 | 32.68 | 35.95 |
| $Al_2O_3$ | 26.44 | 34.54 | 34.02 | $Al_2O_3$ | 28.68 | 26.95 | 26.58 | 21.26 | 17.57 |
| $Na_2O$ | 7.05 | 0.86 | 1.56 | $TiO_2$ | 0.25 | 0.08 | ND | 0.98 | 0.11 |
| CaO | 8.07 | 18.89 | 17.46 | CaO | 23.98 | 23.14 | 23.28 | 15.03 | 12.06 |
| $K_2O$ | 0.31 | ND | ND | MnO | 0.16 | 0.32 | 0.54 | 0.43 | 0.58 |
| FeO | 0.28 | 0.33 | 0.16 | FeO | NA | 0.18 | ND | 10.11 | 9.51 |
| | | | | $Fe_2O_3$ | 7.10 | 9.19 | 9.92 | NA | NA |
| Total | 98.12 | 97.29 | 98.15 | MgO | 0.01 | 0.03 | 0.03 | 0.24 | 0.18 |
| Ab | 60.2 | 7.8 | 13.9 | SrO | 0.26 | 0.25 | 0.17 | 0.26 | 0.21 |
| An | 38.1 | 92.2 | 86.1 | $P_2O_5$ | ND | ND | 0.18 | 0.51 | 0.29 |
| Or | 1.7 | -- | -- | $Ce_2O_3$ | -- | -- | -- | 7.0* | 11.0* |
| | | | | $La_2O_3$ | -- | -- | -- | 4.0* | 5.0* |
| | | | | | 98.32 | 97.87 | 97.99 | 92.50 | 92.46 |

($H_2O$ in epidotes about 1.5 % (2.5 % in allanites; *rare earths estimated by EDS, $Nd_2O_3$ also possibly present.)

**Garnet**

| Location | North Star | Alt'd | Ore zone | | | | Sullivan | | | |
|---|---|---|---|---|---|---|---|---|---|---|
| Sample | 90NSH4A | 90NSH4B | 91NSL2 | | K38-33B | K38-34B | 91SVL6 | | 2001-107 | |
| (n) | (2) | (2) | (2) | (2) | (2) | (1) | Rim(2) | Core(2) | Rim | Core |
| $SiO_2$ | 37.15 | 36.76 | 35.40 | 35.34 | 35.74 | 36.71 | 35.83 | 35.91 | 36.64 | 36.43 |
| $Al_2O_3$ | 21.00 | 21.06 | 20.14 | 19.96 | 20.40 | 21.11 | 20.74 | 20.77 | 21.48 | 21.14 |
| $Fe_2O_3$ | 1.37 | 2.22 | | | | | | | | |
| FeO* | 14.12 | 11.16 | **15.93** | **14.26** | **16.91** | **15.49** | **18.38** | **17.02** | **3.06** | **2.48** |
| MgO | 1.19 | 1.03 | 0.26 | 0.23 | 0.32 | 1.34 | 0.60 | 0.45 | 0.84 | 0.73 |
| MnO | 20.02 | 22.08 | 23.90 | 26.08 | 23.07 | 18.96 | 20.66 | 21.95 | 33.39 | 33.97 |
| CaO | 6.27 | 6.80 | 3.37 | 3.18 | 3.04 | 5.52 | 3.75 | 3.80 | 4.15 | 4.17 |
| Total | 101.12 | 101.11 | 99.00 | 99.05 | 99.48 | 99.13 | 99.96 | 99.90 | 99.56 | 98.92 |
| Sps(Mn) | 46 | 51 | 55 | 60 | 53 | 45 | 47 | 50 | 77 | 79 |
| Alm($Fe2^+$) | 32 | 26 | **37** | **32** | **39** | **36** | **43** | **40** | **9** | **8** |
| Gro(Ca) | 13 | 13 | 7 | 7 | 7 | 12 | 8 | 8 | 9 | 9 |
| And($Fe3^+$) | 4 | 7 | | | | | | | | |
| Pyr(Mg) | 5 | 4 | 1 | 1 | 1 | 7 | 2 | 2 | 4 | 4 |

(FeO* in bold figures is total Fe)

**Chlorites**

| Location | Regional | North Star | | | | | Sullivan |
|---|---|---|---|---|---|---|---|
| | | Altered | | Ore zone | | | Ore zone |
| Sample | 90ALT1 | 90NSH4A | 90NSL3A | K38-33B | 91NSL2 | | 91SVL6 |
| (n) | (1) | (1) | (1) | (2) | (2) | (2) | (4) |
| $SiO_2$ | 28.97 | 27.30 | 28.14 | 24.43 | 25.05 | 26.72 | 23.74 |
| $Al_2O_3$ | 23.33 | 21.01 | 19.26 | 19.14 | 18.92 | 11.29 | 22.75 |
| $TiO_2$ | 0.23 | 0.08 | 0.44 | 0.06 | 0.12 | 0.97 | ND |
| FeO | 18.30 | 19.36 | 11.89 | 34.02 | 29.68 | 40.99 | 28.16 |
| MnO | 0.75 | 0.68 | 0.63 | 1.39 | 1.11 | 0.58 | 0.42 |
| MgO | 15.99 | 19.91 | 22.90 | 9.09 | 12.01 | 5.79 | 12.91 |
| CaO | 0.10 | 0.02 | 0.03 | ND | 0.02 | 0.09 | ND |
| $Na_2O$ | ND | ND | 0.04 | ND | 0.05 | 0.21 | ND |
| $K_2O$ | 3.18 | 0.05 | 0.45 | ND | 0.03 | 0.54 | 0.04 |
| F | ND | ND | ND | ND | ND | 0.20 | ND |
| Cl | 0.08 | 0.06 | 0.01 | ND | 0.03 | 0.14 | 0.03 |
| Total | 90.93 | 88.53 | 84.00 | 88.13 | 87.02 | 87.52 | 88.05 |
| Fe/(Fe+Mg) | 0.39 | 0.35 | 0.18 | 0.70 | 0.60 | 0.75 | 0.58 |
| Type | pycno | ripid | clino | Fe-rip | Fe-rip | cham | Fe-rip |
| DHZ # | 19 | 16 | 28 | 21 | 20 | 7 | 20 |

($K_2O$ partly from contamination by biotite; $H_2O$ about 10-14 %). Chlorite type from Hey, 1954, in Deer, Howie and Zussman (DHZ) 1963. DHZ# refers to analyses on pages 138-145.

**Micas:** **Biotite** **Lepidomelane** **Muscovite** **Tourmaline**

| Location | Regional | North Star | | Sullivan-ore zone | | Regional | North Star |
|---|---|---|---|---|---|---|---|
| Sample | 90ALT1 | 90NSH4B | 91NSL2 | 90SVT28 | 202-13.2 | 90ALT1 | 90NSH4B |
| (n) | (1) | (2) | (1) | (2) | (2) | (1) | (1)† |
| $SiO_2$ | 36.37 | 37.18 | 33.50 | 45.41 | 47.72 | 36.25 | 43.31 |
| $Al_2O_3$ | 19.45 | 18.35 | 13.58 | 35.44 | 33.19 | 35.62 | 16.57 |
| $TiO_2$ | 0.63 | 1.34 | 1.23 | 0.5* | 0.52 | 0.52 | 0.11 |
| FeO | 15.03 | 15.46 | 29.52 | 0.39* | 0.72 | 7.16 | 6.25 |
| MnO | 0.40 | 0.39 | 0.85 | 0.1* | 0.04 | 0.04 | 0.06 |
| MgO | 13.00 | 13.07 | 7.22 | 1.8* | 1.80 | 5.12 | 6.46 |
| CaO | 0.05 | 0.02 | 0.02 | ND | 0.07 | 0.52 | 0.45 |
| $Na_2O$ | 0.01 | ND | 0.11 | 1.41 | 0.45 | 1.49 | 1.72 |
| $K_2O$ | 10.01 | 10.51 | 8.69 | 9.09 | 10.88 | 0.04 | 0.02 |
| BaO | 0.06 | 0.09 | 0.17 | **1.27** | 0.08 | ND | 0.11 |
| F | 0.34 | 0.33 | 0.28 | NA | 0.35 | ND | 0.20 |
| Cl | 0.04 | 0.07 | 0.14 | NA | 0.03 | ND | 0.03 |
| $P_2O_5$ | 0.17 | 0.09 | 0.16 | NA | 0.05 | ND | ND |
| Total | 95.56 | 96.90 | 95.63 | 95.41 | 95.90 | 86.77 | 75.30 |
| DHZ # | 8,p.63 | 8,p.63 | 10,p.59 | Ba-ms | 4,p.16 | | |

(*indicates estimate; $H_2O$ about 3.0-4.5 %). DHZ # = analysis number, page of Deer, Howie and Zussman, 1963. † Analysis contaminated by quartz due to fine-grained nature of the alteration tourmaline; included to give Fe-Mg ratios. ($B_2O_3$ about 11% in tourmaline).

**Tremolite** — **Diopside** — **Sphene** — **Ilmenite**

| Location | North Star | Sullivan | | Sullivan | | | Regional | North Star | Regional |
|---|---|---|---|---|---|---|---|---|---|
| Sample | 90NSH4A | 83SVH6 | | 83SVH6 | | | 90ALT1 | 90NSL3A | 90ALT7 |
| (n) | (1) | (2) | (2) | (2) | (2) | | (1) | (1) | (2) |
| $SiO_2$ | 54.83 | 57.71 | 54.12 | 54.70 | 55.00 | | 30.00 | 30.48 | 0.21 |
| $Al_2O_3$ | 1.70 | 2.23 | 0.38 | 0.38 | 0.38 | | 1.49 | 3.98 | 0.21 |
| $TiO_2$ | ND | 0.02 | 0.04 | 0.02 | ND | | 37.55 | 35.90 | 51.00 |
| FeO | 11.82 | 0.30 | 0.46 | 2.49 | 0.21 | | 0.08 | 0.12 | 40.12 |
| MnO | 0.63 | 0.55 | 1.03 | 1.02 | 0.39 | | 0.04 | 0.16 | 6.76 |
| MgO | 16.66 | 23.79 | 18.13 | 16.62 | 18.50 | | ND | 0.10 | 0.04 |
| CaO | 13.11 | 13.49 | 25.12 | 25.10 | 25.85 | | 28.91 | 27.39 | 0.04 |
| $Na_2O$ | 0.05 | 0.20 | 0.05 | 0.04 | 0.03 | BaO | 0.22 | 0.32 | 0.25 |
| $K_2O$ | 0.06 | 0.16 | 0.02 | 0.02 | 0.02 | $V_2O_3$ | 0.19 | 0.11 | 0.23 |
| Total | 98.86 | 98.45 | 99.35 | 100.39 | 100.38 | | 98.48 | 98.56 | 98.82 |

($H_2O$ about 1.5% in tremolite).

Biotite in both regional unaltered samples and the deposits is brown, non-distinctive, indistinguishable chemically (Table 2) and comparable to metamorphic biotite (Deer et al., 1963); it probably formed during regional metamorphism. It also contains anomalous MnO (0.4% compared to normal <0.2%). Unusual Fe-rich green biotite (29% FeO) found with massive sulphides of the North Star deposit (91NSL2) is similar to lepidomelane (Deer et al., 1963); it is also found rarely in the Sullivan deposit, e.g. in massive pyrrhotite (83SVT6) and the southeast fringe zone (90SVT19). A similar, although brown, Fe-rich biotite with 30% FeO is described by Connor (1990) in stratiform "biotitites" associated with stratabound Cu-Co mineralization and tourmalinite in Middle Proterozoic, possibly lower Belt equivalent Yellowjacket Formation in the Lemhi County, Idaho, Cobalt Belt.

Muscovite analyses included in Table 2 for comparison with published analyses do not show any enrichment in MnO. However, one from Sullivan bedded ore (90SVT28) is anomalous in BaO (1.3%).

## OTHER ALTERATION MINERALS

Plagioclase throughout the Sullivan deposit is uniformly albite ($An_7$ determined optically; $An_{0-2.5}$ quoted in Hamilton et al., 1982). Although optical determination of An content of plagioclase is difficult in the fine (0.1 to 0.2 mm) anhedral grains, results based mainly on refractive indices indicate calcic plagioclase is present in district scale alteration surrounding the Sullivan and North Star deposits (Leitch et al., 1991). Plagioclase in unaltered Aldridge rocks has been described as albite or albite-oligoclase by Edmunds (1977), based on optical determination of a single grain large enough to permit it and work by D.T. Bishop in Idaho (pers. comm. to Edmunds, 1970) that reports oligoclase generally $>An_{13}$. However, a single sample from regional Middle Aldridge strata (90ALT1) contains andesine, $An_{38}$. Even more startling is the relict plagioclase, almost pure anorthite ($An_{86-92}$), in variably tourmalinized rocks near the North Star deposit. This is based on only four analyses, of small grains, but the results are consistent.

Tourmaline associated with the North Star deposit may be slightly higher in Mg and lower in Fe compared to the ?detrital tourmaline found regionally throughout Aldridge rocks (Table 2). Leitch et al. (1991) described these two types of tourmaline. Only two analyses were done, and the analysis of fine grained (1-2 by 5-10μm) hydrothermal tourmaline is contaminated by quartz. Nevertheless, analyses give an indication of the Fe:Fe+Mg ratio, which is 0.44 in regional ?detrital tourmaline and 0.35 in hydrothermal tourmaline. These are both intermediate schorl-dravite compositions (group II of Fig. 4, Ethier and Campbell, 1977). However, the fine hydrothermal tourmaline plots close to the boundary with their group III: coarse grained, yellowish dravite closely associated with Sullivan ore, 10-11% MgO. At the Sullivan deposit, this coarse grained, pale coloured tourmaline (not anlayzed in this study) is also found in tourmalinized rocks, but only where they have been overprinted by albitic alteration.

The composition of epidote-group minerals also appears to change with proximity to the Sullivan-North Star deposits. Clinozoisite (Fe-poor epidote with 7% $Fe_2O_3$, <0.2% MnO) is found regionally (90ALT1, Table 2). Clinozoisite and possible zoisite are also found in calc-silicate altered samples 38-2, 38-7b, 38-23 near Moyie sills to the west of the North Star deposit (Leitch et al., 1991). Epidote with 9-10% $Fe_2O_3$ and up to 0.5% MnO occurs in the North Star tourmalinite (90NSH4A and B) and is identified optically within the Sullivan and North Star deposits.

Rare radioactive minerals, enclosed by pleochroic haloes in biotite and chlorite, appear to be largely allanite in both regional Aldridge rocks and altered rocks in the Sullivan-North Star corridor. Allanite has been described at the Sullivan deposit in footwall veins (Campbell and Ethier, 1984) and in chlorite alteration (Schandl and Gorton, 1992). All the radioactive minerals analyzed in this study (90ALT1 and 7, in regional Aldridge rocks), previously identified as monazite (Leitch et al., 1991; cf. Huebschman, 1973) are allanite. Based on these results, monazite previously identified in chlorite altered rocks at the Sullivan deposit (Leitch and Turner, 1991) is probably also allanite; if zircon is present it is not common. Analyses presented here are semi-quantitative, but suggest allanite in the footwall of the deposit is enriched in Fe compared to regional allanite, although both appear to contain the same rare-earth elements, in about the same proportions.

## DISCUSSION AND EXPLORATION SIGNIFICANCE

The distribution of Sb which is peripheral to that of As and Sn (Freeze, 1966; Fig. 5) may be explained by the abundance of boulangerite and lesser jamesonite in and near the

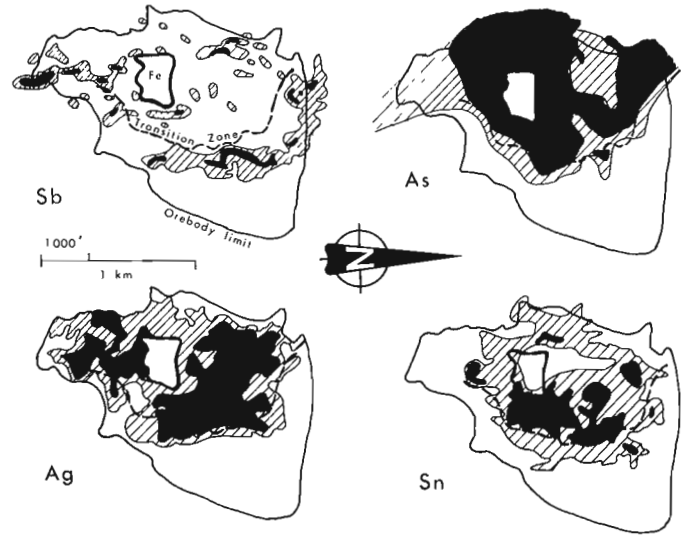


**Figure 5.** Distribution of minor metals in the Sullivan deposit (after Ransom, 1977 and Freeze, 1966). White, hachured, and dark areas indicate increasing levels of each element; Fe=central pyrite-chlorite-calcite zone.

transition zone. Tetrahedrite probably broadens the Sb distribution as it is more common and widespread than boulangerite and jamesonite. Tetrahedrite (freibergite) also controls the distribution of Ag in the orebody: Ag is concentrated over the footwall vent zone inside the transition zone. In this study, Ag was found only in freibergite. Microprobe analyses of galena do not support the contention by Freeze (1966) and Hamilton et al. (1982) that significant Ag is present as a solid solution in galena. Ag was detected in trace amounts only (up to 0.32 wt.%) in galena, notably in galena adjacent to or containing discrete sulphosalt inclusions.

The distribution of Bi probably lies roughly inside that of Sb, since it is found in bismuthian boulangerite and jamesonite, and native Bi-Sb alloy, within the area delimited by the transition zone. It thus mimics the distribution of arsenic (Fig. 5); the occurrence of the Bi-Sb alloy with arsenopyrite supports this hypothesis.

Tin, dependent primarily on the distribution of cassiterite, is concentrated in an annular zone inside the transition zone coincident with higher arsenic concentrations (Freeze, 1966; Fig. 5). Most tin is associated with the pyrrhotite-rich zone at the base of the orebody; values decrease toward the hanging wall (Freeze, 1966). In this study both cassiterite and stannite were observed near the base of the deposit in footwall rocks or massive pyrrhotite, within an area bounded by the transition zone. The association of tin-bearing minerals with muscovite- or arsenopyrite-bearing crosscutting structures suggests that Sn, along with As, Bi, and possibly Sb, is related to late-stage upflow of hydrothermal fluids in the transition zone (Leitch and Turner, 1992). The association of Ag with this process is less clear, although Ag appears to be primarily controlled by the distribution of tetrahedrite that also contains significant amounts of Sb.

Cadmium, indium, thallium, possibly mercury and a portion of the manganese in the Sullivan deposit are probably contained within and controlled by distribution of sphalerite. Cadmium up to 0.3 wt.% was detected in sphalerite; further work is required to determine if the 0.05-0.08% In and 0.4% Hg levels are real. Coincidence of maximum concentrations of Tl with Zn-rich areas suggests Tl occurs in sphalerite. Gallium and germanium recovered in minor quantities at the Trail smelter probably are also hosted in sphalerite, although this was not tested in this study. These elements are likely at levels too low to be detected except by the most rigorous microprobe analysis employing high beam currents and long counting times.

Several minerals in the Sullivan and North Star deposits are anomalous in Mn, particularly around the periphery of the Sullivan deposit. Manganese enrichment occurs peripheral to other stratiform sediment-hosted Zn-Pb deposits, such as Meggen in Germany (Gwosdz and Krebs, 1977) or Tynagh in Ireland (Russell, 1974), and is known to concentrate distally in the Red Sea muds (Zierenberg and Shanks, 1988). This suggests elevated Mn content peripheral to the Sullivan and North Star deposits is due to Mn-rich exhalations. Metamorphic recrystallization has concentrated the Mn into certain preferred phases such as garnet and carbonate, and to a lesser extent tremolite, diopside, chlorite, biotite, and epidote. Garnet formed preferentially during metamorphism in the Sullivan-North Star altered corridor because of elevated Mn content of the altered strata (Leitch et al., 1991). Thus the simple picture of a manganese "halo" surrounding the Sullivan deposit has been modified and blurred, mainly by widespread exhalation from several centers surrounding the deposit, and by local metamorphic redistribution. Whole-rock analyses for Mn around the Sullivan deposit and in the Aldridge show complex trends possibly due to mobilization of Mn into variable minor carbonates (J. Hamilton, pers. comm., 1991).

Trends are also apparent in Fe content of minerals such as chlorite, epidote, and possibly biotite in the Sullivan-North Star deposits and surrounding altered rocks. The Fe content of epidote increases slightly from regional unaltered rocks to the altered corridor. Also, Fe contents in chlorites are highest in massive sulphide samples, associated with minor occurrences of Fe-rich chlorite (chamosite) and biotite (lepidomelane). This is in contrast to the observed decrease in the Fe content of most silicates toward the center of other metamorphosed massive sulphide deposits, predicted by the greater affinity of sulphides for Fe in the competition between sulphides and silicates (Nesbitt, 1986).

The occurrence of anorthite in tourmalinized rocks near North Star compared to regional andesine or oligoclase is difficult to explain. The process of tourmalinization may remove $Na_2O$, resulting in feldspar enriched in CaO. Widespread albite in altered rocks in the hanging wall and less commonly the footwall at Sullivan appears to be related to hot fluids mobilized by intrusion of Moyie sills and dykes and focused along vertical structures, after emplacement of the orebody (Turner and Leitch, 1992).

Tourmaline as both regionally distributed, coarse, possibly detrital grains and fine hydrothermal needles is intermediate in composition between schorl and dravite. Coarse, pale yellow-brown tourmaline probably closer to dravite in composition (10% MgO: Ethier and Campbell, 1977) is found in (1) matrix to breccia clasts at the base of the massive pyrrhotite body and (2) where albitization has recrystallized tourmalinite in both footwall and hanging wall. These relations suggest that recrystallization of early formed tourmaline was by ongoing hydrothermal alteration and heat flow generated by Moyie sills (Turner and Leitch, 1992) rather than "related to uneven heat flow during metamorphism" (Ethier and Campbell, 1977, p. 2348). Tourmalines related to massive sulphides are distinctly Mg-rich, approaching end-member dravite, and are not thought to be greatly altered by subsequent metamorphism due to the refractory nature of tourmaline (Taylor and Slack, 1984). The compositions of regional and hydrothermal tourmaline are also similar, respectively, to sulphide-free tourmaline of the Broken Hill Group tourmalinites and sulphide-rich tourmalines of the Globe mine tourmalinite at the northern end of the Broken Hill lode, Australia (J. Slack et al., unpub. manuscript).

# REFERENCES


**Campbell, F.A. and Ethier, V.G.**
1984: Composition of allanite in the footwall of the Sullivan orebody, British Columbia; Canadian Mineralogist, v. 22, pt. 3, p. 507-511.

**Connor, J.J.**
1990: Geochemical stratigraphy of the Yellowjacket Formation (Middle Proterozoic) in the area of the Idaho Cobalt Belt, Lemhi County, Idaho; United States Geological Survey, Open-File Report 90-0234A, 30 p.

**Deer, W.A., Howie, R.A., and Zussman, J.**
1963: Rock-forming minerals, v. 1-5; Longmans, London.

**Edmunds, F.R.**
1977: The Aldridge Formation, B.C., Canada; Ph.D. thesis, Pennsylvania State University, University Park, Pennsylvania, 368 p.

**Ethier, V.G. and Campbell, F.A.**
1977: Tourmaline concentrations in Proterozoic sediments of the southern Cordillera of Canada and their economic significance; Canadian Journal of Earth Science, v. 14, p. 2348-2363.

**Ethier, V.G., Campbell, F.A., Both, R.A., and Krouse, H.R.**
1976: Geological setting of the Sullivan orebody and estimates of temperature and pressure of metamorphism; Economic Geology, v. 71, p. 1570-1588.

**Freeze, A.C.**
1966: On the origin of the Sullivan orebody, Kimberley, B.C.; in Tectonic History and Mineral Deposits of the Western Cordillera, Canadian Institute of Mining and Metallurgy, Special Volume 8, p. 263-294.

**Gwosdz, W. and Krebs, W.**
1977: Manganese halo surrounding Meggen ore deposit, Germany; Transactions Institution of Mining and Metallurgy (Sect. B: Applied earth science), v. 86, p. 73-77.

**Hamilton, J.M., Bishop, D.T., Morris, H.C., and Owens, O.E.**
1982: Geology of the Sullivan orebody, Canada; in Precambrian Sulphide Deposits, H.S. Robinson Memorial volume, (ed.) R.W. Hutchinson, C.D. Spence, and J.M. Franklin; Geological Association of Canada, Special Paper 25, p. 597-665.

**Hey, M.H.**
1954: A new review of the chlorites; Mineralogic Magazine, v. 30, p. 277-292.

**Höy, T.**
1984: Structural setting, mineral deposits, and associated alteration and magmatism, Sullivan Camp, southeastern British Columbia (82 F,G); British Columbia Ministry of Energy, Mines and Petroleum Resources, Geological Fieldwork 1983, Paper 1984-1, p. 25-35.

**Huebschmann, R.P.**
1973: Correlation of fine carbonaceous bands across a Precambrian stagnant basin; Journal of Sedimentary Petrology, v. 43, p. 688-699.

**Leitch, C.H.B.**
1991: Preliminary fluid inclusion and petrographic studies of the Sullivan sedimentary exhalitive Pb-Zn deposit, southeastern British Columbia; in Current Research, Part A; Geological Survey of Canada, Paper 91-1A, p. 91-101.

**Leitch, C.H.B. and Turner, R.J.W.**
1991: The vent complex of the Sullivan stratiform sediment-hosted Zn-Pb deposit, British Columbia: preliminary petrographic and fluid inclusion studies; in Current Research, Part E; Geological Survey of Canada, Paper 91-1E, p. 33-44.
1992: Preliminary field and petrographic studies of the sulphide-bearing network underlying the western orebody, Sullivan stratiform sediment-hosted Zn-Pb deposit, British Columbia; in Current Research, Part E; Geological Survey of Canada, Paper 92-1E.

**Leitch, C.H.B., Turner, R.J.W., and Höy, T.**
1991: The district-scale Sullivan-North Star alteration zone, Sullivan mine area, British Columbia: a preliminary petrographic study; in Current Research, Part E; Geological Survey of Canada, Paper 91-1E, p. 45-57.

**Nesbitt, B.E.**
1986: Oxide-sulfide-silicate equilibria associated with metamorphosed ore deposits. Part II: pelitic and felsic volcanic terrains; Economic Geology, v. 81, p. 841-856.

**Ransom, P.W.**
1977: Geology of the Sullivan orebody; in Fieldtrip Guidebook, Trip 1 (Lead-zinc deposits of southeastern British Columbia); Geological Association of Canada Annual Meeting, Vancouver, April 1977, p. 7-21.

**Russell, M.J.**
1974: Manganese halo surrounding the Tynagh ore deposit, Ireland: a preliminary note; Transactions Institution of Mining and Metallurgy (Sect. B: Applied earth science), v. 83, p. 65-66.

**Schandl, E.S. and Gorton, M.P.**
1992: Rare-earth element geochemistry of selected samples from the Sullivan Pb-Zn sedex deposit: the role of allanite in mobilizing rare-earth elements in the chlorite-rich footwall (82G/12); in Geological Fieldwork, 1991, British Columbia Ministry of Energy, Mines and Peteroleum Resources, Paper 1992-1, p. 273-279.

**Taylor, B.E. and Slack, J.F.**
1984: Tourmalines from Appalachian-Caledonia massive sulfide deposits: textural, chemical, and isotopic relationships; Economic Geology, v. 79, p. 1703-1726.

**Turner, R.J.W. and Leitch, C.H.B.**
1992: Relationship of albitic and chloritic alteration to gabbro dykes and sills in the Sullivan mine and nearby area, British Columbia; in Current Research, Part E; Geological Survey of Canada, Paper 92-1E.

**Zierenberg, R.A. and Shanks, W.C.III.**
1988: Isotopic studies of epigenetic features in metalliferous sediment, Atlantis II Deep, Red Sea; Canadian Mineralogist, v. 26, p. 737-753.


---


Geological Survey of Canada Project 900020
(Contribution No. 9, Sullivan-Aldridge project)

# Relationship of albitic and chloritic alteration to gabbro dykes and sills at the Sullivan deposit and nearby area, southeastern British Columbia

**Robert J.W. Turner and Craig H.B. Leitch**
**Mineral Resources Division, Vancouver**

*Turner, R.J.W. and Leitch, C.H.B., 1992: Relationship of albitic and chloritic alteration to gabbro dykes and sills at the Sullivan deposit and nearby area, southeastern British Columbia; in Current Research, Part E; Geological Survey of Canada, Paper 92-1E, p. 95-105.*

***Abstract***

*Chlorite-albite-pyrite alteration cuts the tourmalinite pipe, Sullivan orebody and overlying strata. The root zone of this alteration coincides with a set of dykes and sills, apophyses of the larger footwall gabbro sill. Alteration postdates intrusion as dykes and sills are locally altered. Altered sedimentary rocks adjacent to gabbro are zoned from proximal albite-chlorite to chlorite-pyrite. The ascent of Na-rich, Mg-depleted hydrothermal fluids followed dykes in the Sullivan orebody localizing albitic alteration. Fluids may be related to deep gabbro intrusions below the Moyie sill complex. Mixing with Mg-rich seawater caused peripheral chloritic alteration, and late collapse of the hydrothermal system caused chloritic alteration to overprint earlier-formed albitite. Southwest of the Sullivan mine, albite-chlorite alteration extends 200 m above the contact of a gabbro sill. The absence of base metals suggests albite-chlorite-pyrite alteration is not directly related to ore-forming processes.*

***Résumé***

*L'altération en chlorite-albite-pyrite traverse la cheminée de tourmalinite, le corps minéralisé de Sullivan et les strates sus-jacentes. La zone d'origine de cette altération coïncide avec un groupe de dykes et de filons-couches qui sont des apophyses du filon-couche de gabbro de plus grande taille, présent dans l'éponte inférieure du gisement. L'altération est ultérieure à l'épisode d'intrusion, puisque les dykes et les filons-couches sont localement altérés. Les roches sédimentaires altérées adjacentes au gabbro présentent une zonation; en position proximale, elles contiennent de l'albite et de la chlorite tandis que plus loin, il y a passage à de la chlorite et de la pyrite. La montée de fluides hydrothermaux riches en Na et pauvres en Mg est postérieure aux dykes du corps minéralisé de Sullivan et a confiné l'albitisation. Les fluides peuvent être associés à des intrusions de gabbro au-dessous du complexe de filons-couches de Moyie. Le brassage avec de l'eau de mer riche en Mg est à l'origine de la chloritisation périphérique et l'effondrement tardif du réseau hydrothermal a permis à la chloritisation de se surimposer à l'albitite formée auparavant. Au sud-ouest de la mine Sullivan, l'altération en albite-chlorite se prolonge à 200 m au-dessus du contact avec un filon-couche de gabbro. L'absence de métaux communs semble indiquer que l'altération en albite-chlorite-pyrite n'est pas directement liée aux processus de minéralisation.*

## INTRODUCTION

Various bodies of altered rock are associated with the Sullivan orebody. These alteration types, which include tourmalinite, chlorite-albite-pyrite, and muscovite alteration, occur immediately adjacent to the orebody (Shaw and Hodgson, 1980; Hamilton et al., 1982; Leitch and Turner, 1991; Leitch and Turner, 1992), and as discrete bodies within a 5 km zone of altered, mineralized and fragmented strata south of the Sullivan mine (Hoy, 1984; Leitch et al., 1991; Leitch, 1992). Because similar altered bodies elsewhere in the Aldridge Formation have attracted exploration interest as possible Sullivan-type targets, it is important to understand the relationship of these alteration types to the ore forming process. This paper focuses on chlorite-albite-pyrite alteration and its relationship to gabbro intrusions in the mine area.

The western part of the Sullivan orebody is interpreted as the vent complex for a seafloor hydrothermal system during formation of the bedded sulphide ores (Shaw and Hodgson, 1980; Hamilton et al., 1982). This vent complex includes a massive pyrrhotite body that formed as a replacement of bedded zinc and lead sulphides, an underlying tourmalinite pipe, and a body of chlorite-albite-pyrite alteration that extends from below to as much as 150 m above the orebody (Shaw and Hodgson, 1980; Hamilton et al., 1982). Such extensive hanging wall alteration is not known to be associated with other stratiform sediment-hosted lead-zinc deposits. Does chlorite-albite-pyrite alteration reflect the latest stages of the hydrologic system that formed the orebody, or a hydrologic regime related to intrusion of the Moyie sill complex interpreted to be penecontemporaneous with deposition of the Aldridge Formation (Hamilton, 1984; Hoy, 1989)? As albite-chlorite-pyrite alteration occurs sporadically throughout the Aldridge Formation, this question is critical to establishing the value of these altered rocks as an exploration guide for Sullivan-type orebodies.

## MOYIE SILL COMPLEX IN THE VICINITY OF THE SULLIVAN MINE

Moyie intrusions of gabbro comprise 30-40% of the Lower and lower Middle Aldridge Formation (Hamilton et al., 1982; Hoy, 1989). Intrusions are most commonly sills and slightly discordant sheets up to several hundred metres thick. Textures and contact relationships have led Hoy (1989) to suggest emplacement of sills into partly consolidated wet Aldridge sediments.

Aldridge strata are well exposed southwest of the Sullivan mine (Leech, 1957). Gabbro intrusions occur as two sill complexes at separate stratigraphic levels. The lower sill complex occurs throughout the exposed 3000 m of Lower Aldridge and the exposed strata has a combined thickness of 1000 m. The stratigraphically highest sills in this complex are just below the contact with the overlying Middle Aldridge Formation, the stratigraphic level of the Sullivan orebody. A second, smaller sill complex occurs near the middle of the Middle Aldridge Formation.

At the Sullivan mine, the uppermost sill (Fig. 1, 2) occurs about 500 m below the eastern edge of the orebody (Hamilton et al., 1982). This sill becomes discordant and cuts upsection to meet the footwall of the western margin of the orebody (Fig. 2). Further west, the gabbro transgresses down-section to regain its sill-like form. This anomalous "gabbro arch" can be traced south along a south-southeast-trend that is roughly coincident but slightly oblique to the zone of altered and fragmented Lower Aldridge strata that hosts the Stemwinder, North Star and Quantrell deposits and appears controlled by synsedimentary faults (Fig. 1).

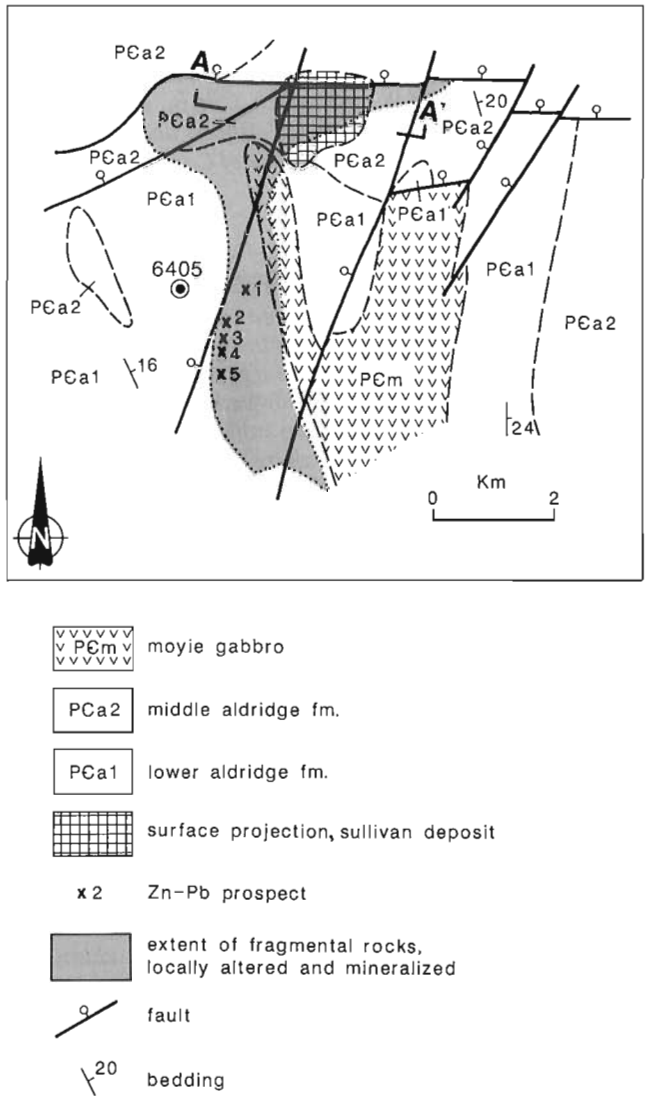


**Figure 1.** Geological map of Sullivan mine area (modified after Hoy, 1984). Extent of fragmental, altered, and mineralized rocks from unpublished company report by A.S. Hagen (Cominco Ltd., 1985). Location of drill hole 6405 and section A-A' (Fig. 2) is shown. Zn-Pb prospects are: 1) Stemwinder; 2) Quantrell; 3) Midnight; 4) Kellogg; and 5) North Star.

Within the western part of the Sullivan orebody and adjacent to the eastern flank of the gabbro arch, a set of thin northwest-trending dykes and sills cuts the orebody and underlying tourmalinite (Fig. 3A). According to unpublished maps by O.E. Owens (Cominco Ltd., 1959), dykes dip steeply northeast and to a lesser extent southwest, and are aphophyses of the footwall gabbro sill (Fig. 4). Most of the dykes terminate upward within the orebody or flare out to form stubby sills (Fig. 3A,B) that are elongate to the northwest, parallel to the trend of the dyke set (Fig. 4). Rarely, dykes intrude strata overlying the orebody (Fig. 3B).

The cores of dykes and sills are commonly least altered and are composed of amphibole altered to chlorite and plagioclase altered to albite (Fig. 5F). Gabbro-sediment contacts are typically gradational and obscure because of intensely altered margins.

## ALBITE-CHLORITE-PYRITE ALTERATION

In the Sullivan mine area, albite-chlorite-pyrite alteration occurs in two distinct altered bodies: a zone that transgresses the Sullivan orebody altering tourmalinite, massive sulphide and hanging wall strata over 200 m of vertical distance; and a separate body of similar extent immediately overlying the gabbro sill 3 km southwest of the Sullivan Mine (DH 6405, Fig. 1). Two distinct mineral assemblages are recognized in both bodies. Massive albite with lesser intergrown chlorite is a distinctive white-coloured albitite rock that includes albite-chlorite-sphene ± pyrite (Fig. 5B). A second chlorite-pyrite assemblage (chlorite-pyrite ± albite, carbonate, sphene, apatite, quartz) typically occurs peripheral to a core of albitite, or as veinlets and breccia matrix that cut albitite (Fig. 5B, D, E).

### *Albite-chlorite body southwest of Sullivan mine*

Drill hole 6405 collared 1.5 km west of the Stemwinder deposit and 2 km west of the gabbro arch (Fig. 1) intersected 190 m of altered rock overlying the gabbro contact (Fig. 6). Adjacent to the gabbro is 20 m of massive albitite that obscures original bedding. Albitite is transitional upward into mixed albite-chlorite-biotite composed of patches, "beds", and subvertical veins of albite, biotite hornfels, chlorite veins and patches, and spots of biotite-sphene-rutile or quartz-pyrrhotite-chlorite-muscovite. The stratigraphically highest alteration includes biotitized and bleached silt wacke beds cut by vertical albitic fractures. The size and mineralogy of this alteration zone is similar to the albite-chlorite-pyrite alteration overlying the Sullivan orebody, but is distinct because it is not associated with base metal mineralization.

### *Alteration associated with dykes below orebody*

Chlorite-albite-pyrite alteration at the Sullivan deposit is rooted in a narrow zone below the orebody, transgresses the orebody as a pyrite-chlorite-calcite zone, and flares outward and upward within overlying turbidite strata (Shaw and Hodgson, 1980; Hamilton et al., 1982). Within this alteration zone, proportions of albite, chlorite, and pyrite vary markedly, to some extent reflecting the chemistry of the different altered protoliths (e.g. massive sulphide, gabbro, feldspathic turbidite, mudrock).

Unpublished mapping by R.L. Hauser (Cominco Ltd., 1980) indicates that albite-chlorite-pyrite alteration underlying the Sullivan orebody extends over an irregular 300 by 500 m footwall zone within the volume containing the highest density of gabbro dykes underlying the orebody (Fig. 4). Within this volume, crosscutting albite-chlorite-pyrite alteration coalesces upward to form a stratabound alteration zone at the base of the orebody, and albitite occurs along faults and fractures, and as veins, large masses, and breccias within chloritic rock (Shaw and Hodgson, 1980; Hamilton et al., 1982). A typical alteration zone cutting tourmalinite is zoned from a core of albitite-pyrite outward to chlorite-pyrite and distal tourmalinite with pyrite after pyrrhotite (Shaw and Hodgson, 1980; Hamilton et al., 1982).

Drill hole 2579 on the southwestern margin of the footwall albitic alteration (Fig. 3A, 4) illustrates the close association of this alteration to the contacts of gabbro dykes. Albite-chlorite-pyrite occurs as a 70 m wide alteration envelope that cuts across altered tourmalinite rock and is zoned with respect to the contacts of a 10 m thick dyke (Fig. 7). With increasing distance from the gabbro contact these alteration assemblages are: (1) proximal albite-chlorite ± biotite; (2) intermediate chlorite-pyrite-albite; and (3) distal pyrite replacement of pyrrhotite in tourmalinite. This alteration overprints earlier tourmalinite-pyrrhotite and has resulted in "detourmalinization" of this portion of footwall strata. Crosscutting relationships suggest that early formed

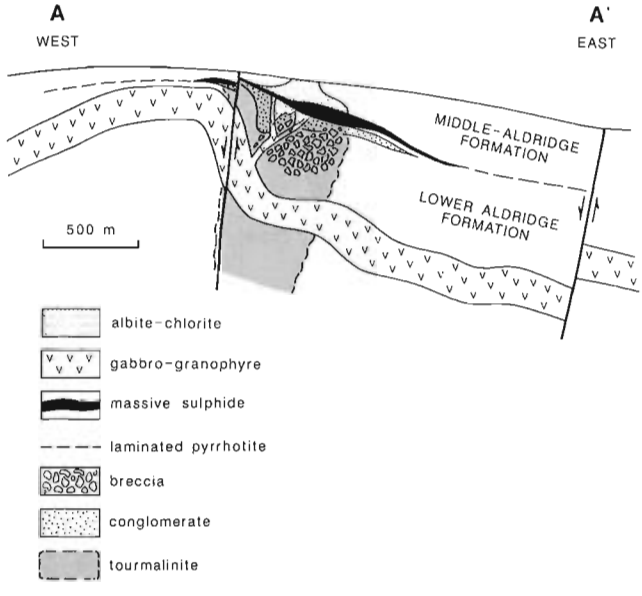


**Figure 2.** Schematic east-west geological cross-sections illustrating the relationship of the gabbro arch to the Sullivan orebody (modified after Hamilton, 1984). Location of section on Fig. 1.

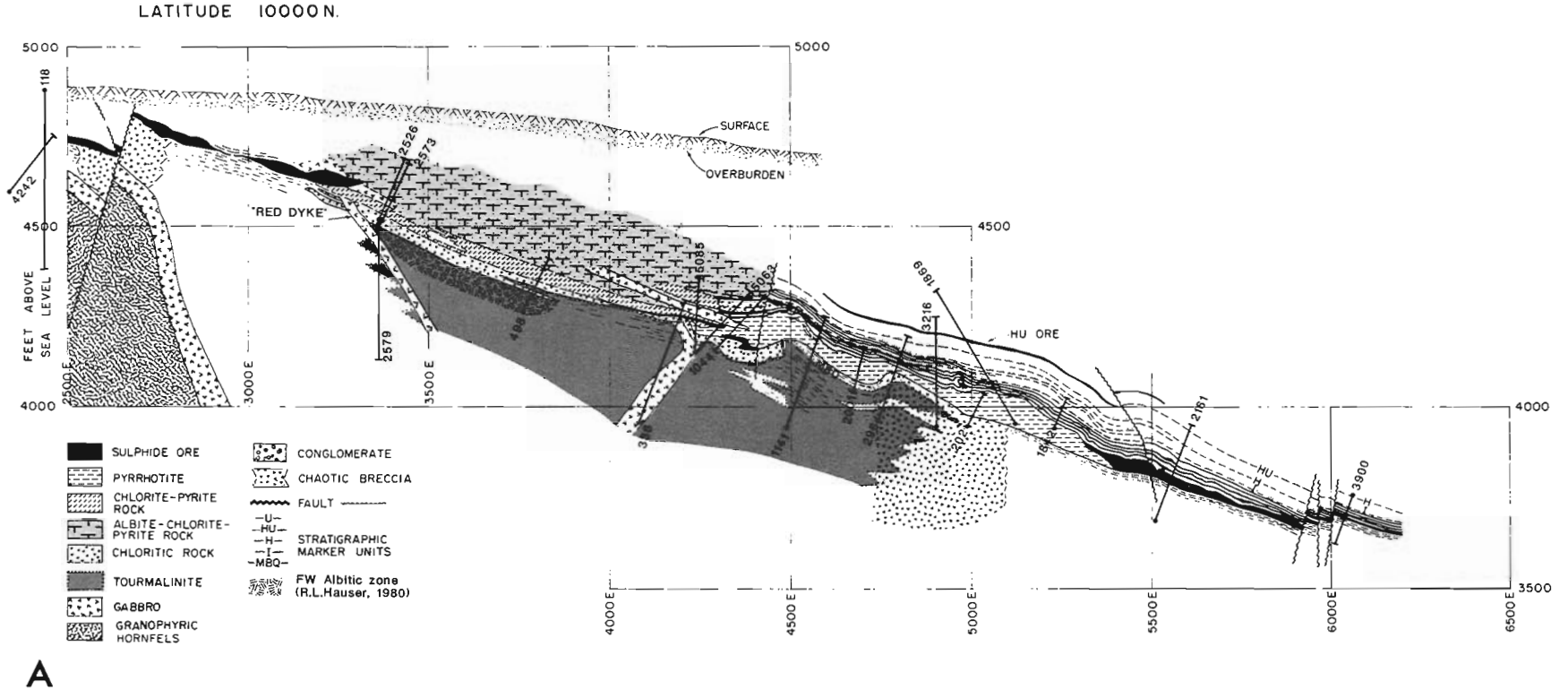
LATITUDE 10000 N.
FEET ABOVE SEA LEVEL
SURFACE
OVERBURDEN
"RED DYKE"
HU ORE
SULPHIDE ORE
PYRRHOTITE
CHLORITE-PYRITE ROCK
ALBITE-CHLORITE-PYRITE ROCK
CHLORITIC ROCK
TOURMALINITE
GABBRO
GRANOPHYRIC HORNFELS
CONGLOMERATE
CHAOTIC BRECCIA
FAULT
STRATIGRAPHIC MARKER UNITS
FW Albitic zone (R.L.Hauser, 1980)

A

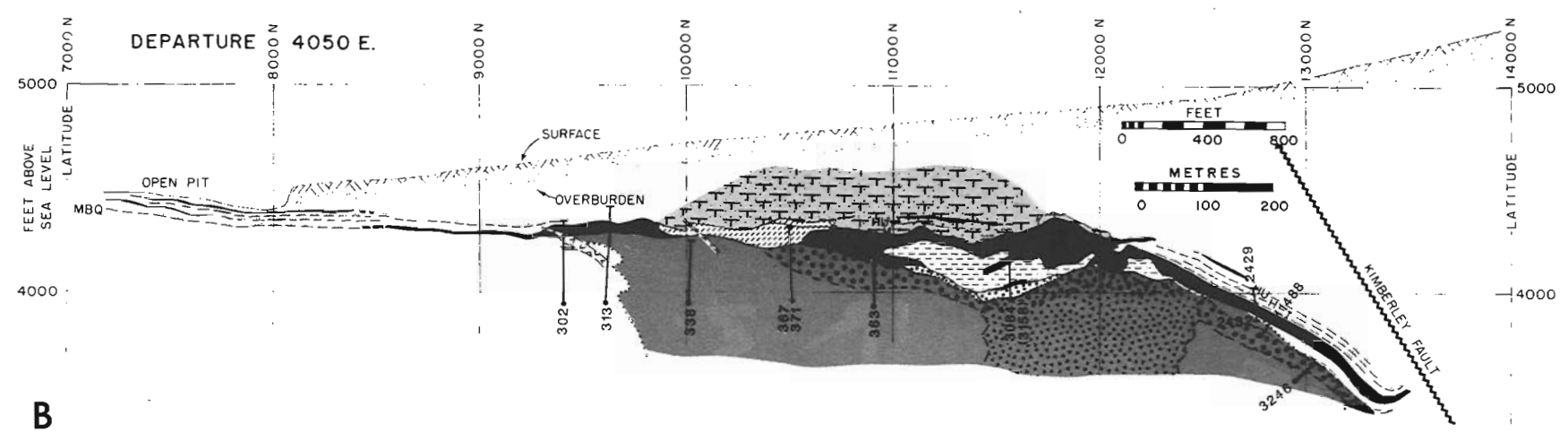
DEPARTURE 4050 E.
LATITUDE
FEET ABOVE SEA LEVEL
SURFACE
OVERBURDEN
OPEN PIT
MBQ
FEET
METRES
KIMBERLEY FAULT

B

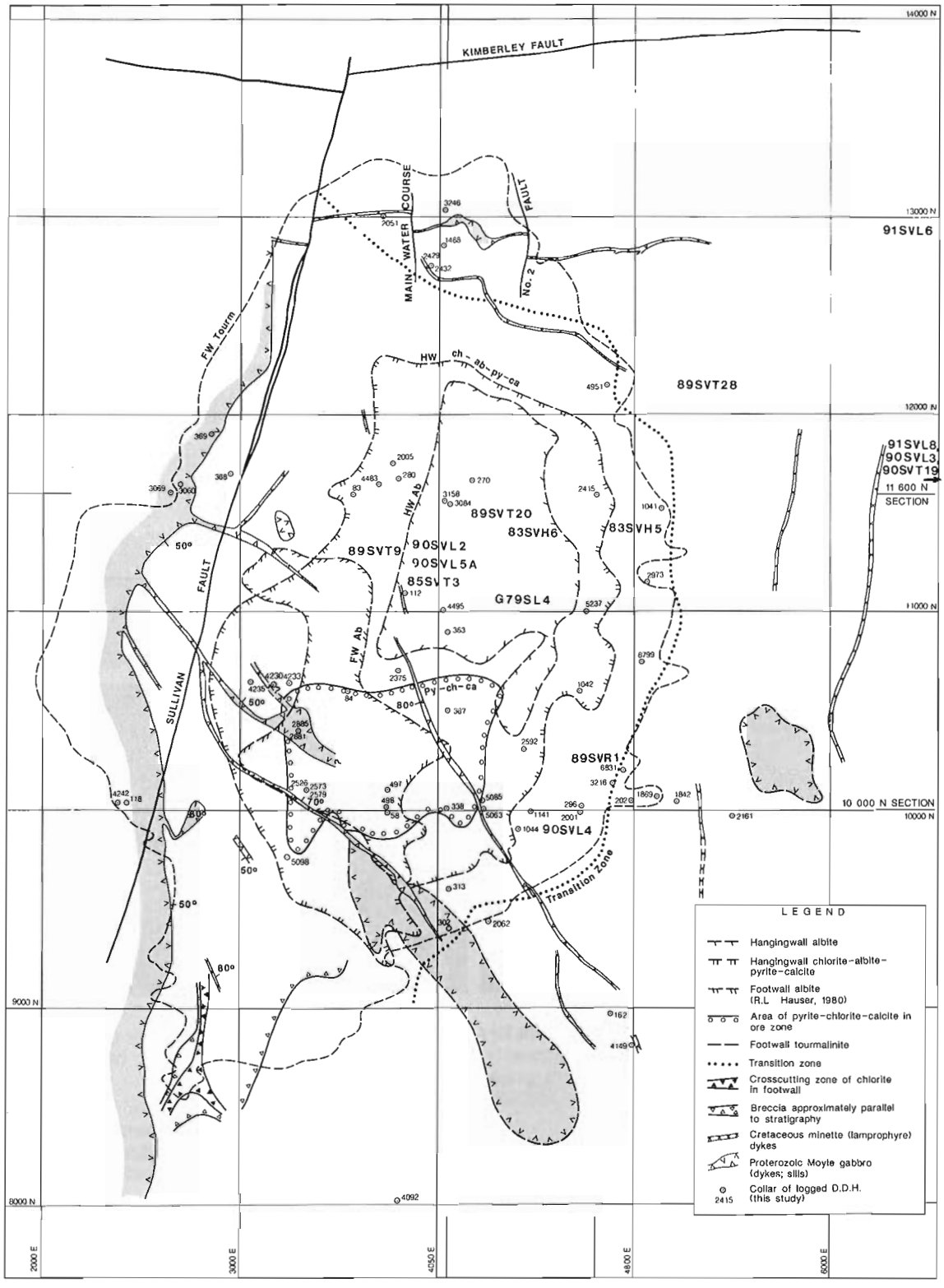


**Figure 4.** Plan view of the Sullivan ore body illustrating distribution of gabbro dykes and sills, and albitic and chloritic alteration. Grid is in feet. Tourmalinite and transition zone are shown for reference. Dykes are shown where they intersect the base of the massive sulphide body. Eastern limit of concordant domain of footwall gabbro sill is shown (approx. 2500 E); to the west sill becomes discordant. Sources for the map include unpublished mapping of dykes and sills by O.E. Owens (Cominco Ltd., 1960), unpublished mapping of footwall albitic alteration by R.L. Hauser (Cominco Ltd., 1980) and chlorite-pyrite, and hanging wall albite alteration from Hamilton et al. (1982). Note that dykes are offshoots of the footwall gabbro sill, and the spatial relationship among dykes and sills, footwall albite alteration, chlorite-pyrite-calcite alteration in the orebody, and hanging-wall albitic alteration.

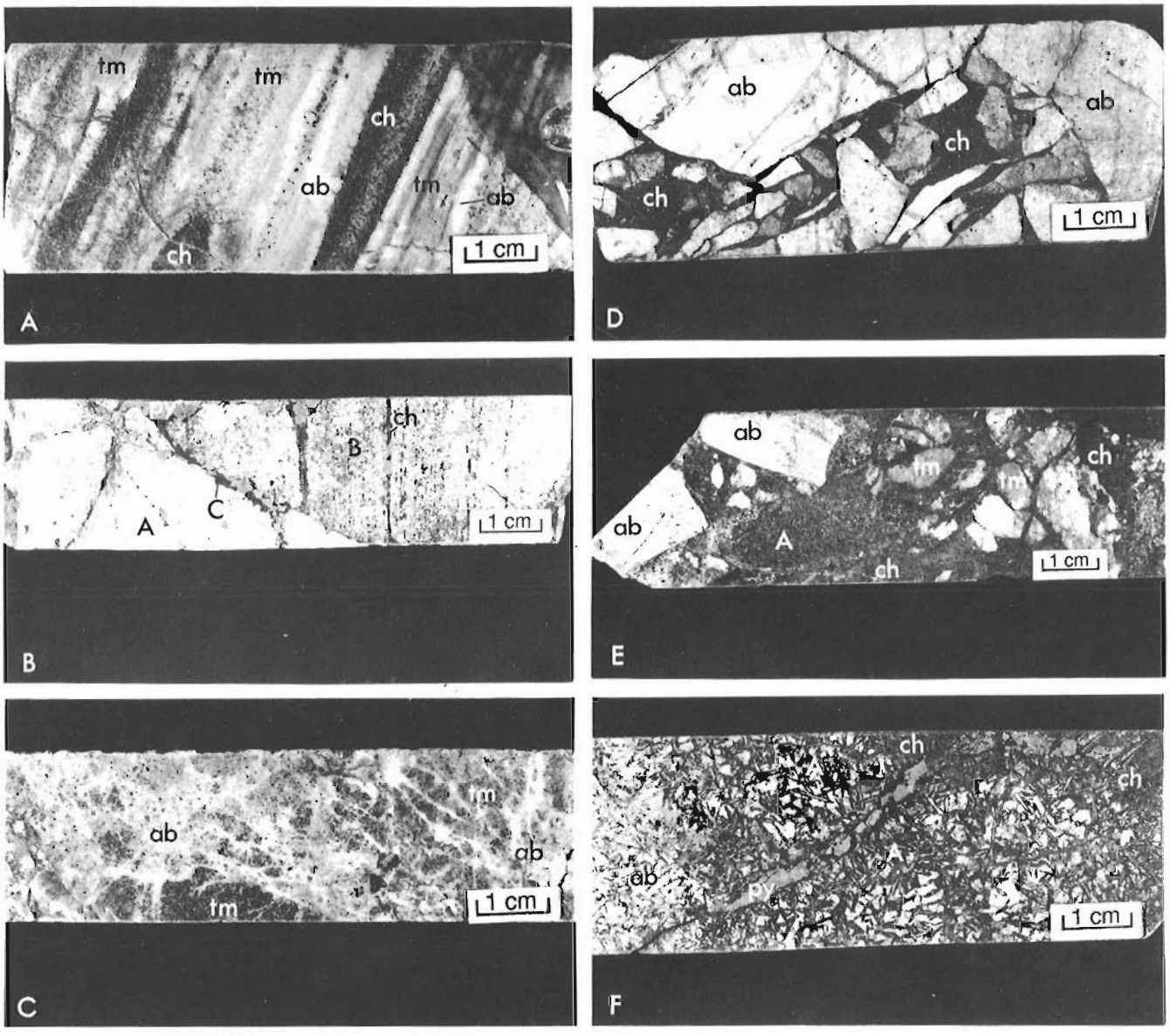


**A.** Detourmalinized albite-chlorite altered bedded sedimentary rock. Relict brown recrystallized tourmalinite (tm) altered by white albite-chlorite (ab) and bands of dark green chlorite-albite (ch). Drill hole 5098-185', footwall albite-chlorite zone (Fig. 4).

**B.** Laminated sandstone altered to massive albite (A) and albite-chlorite (B). Massive albite obscurs original bedding. Chlorite (ch) occurs preferentially along bedding, possibly after mudrock laminae. Cut by chlorite-pyrite veinlets (C). Drill hole 2526-113', western hanging wall albite zone (Fig. 3A, 4).

**C.** Brown recrystallized and partly albitized tourmalinite (tm) cut by stockwork of albite veinlets (ab). Drill hole 2415-220', hanging wall to orebody, transition zone area (Fig. 4).

**D.** Albite (ab) breccia cemented by chlorite-pyrite (ch). Drill hole 5085-164', base of eastern hanging wall albite zone (Fig. 3A, 4).

**E.** Mixed fragments of albite (ab), tourmalinite (tm), and chlorite altered rock (A) in breccia cemented by chlorite (ch). Tourmalinite is brown, recrystallized and partly replaced by albite. Drill hole 5098-193', footwall albite-chlorite zone (Fig. 4).

**F.** Coarse grained gabbro altered to albite-chlorite along margin of sill (DH 5063, Fig. 7). Massive albite alteration (ab) transitional to albite replacement of plagioclase phenocrysts and hornblende phenocrysts rimmed by chlorite (A). Late chlorite-pyrite vein. Drill hole 5063-123' (Fig. 3A, 4).

**Figure 5.** Photographs of albite-chlorite-pyrite alteration.

proximal albite graded outward to tourmalinite, and that albite was subsequently overprinted by chlorite ± albite veins, and tourmalinite by chlorite-pyrite alteration.

The gabbro dyke in drill hole 2579 is albitized, particularly along its margins (Fig. 7). The grain size of the gabbro decreases toward contacts, but the extensive alteration obscures the gabbro-turbidite contact. Similar relations occur in hole 5063 (Fig. 7) that intersects the upper contact of a footwall dyke near its termination at the base of the orebody (Fig. 3A). Again, the marginal portion of the dyke is albitized, and albitic alteration extends 10 m into the adjacent siliciclastic rocks. Alteration of the dyke indicates that alteration occurred after intrusion of the gabbro and argues against dykes intruding along previously altered faults or fractures.

### *Alteration associated with sills within orebody*

Footwall dykes tend to sill out or terminate abruptly within the Sullivan orebody. Sills within or in contact with the Sullivan orebody are variably altered to chlorite, albite, and pyrite and associated with similarily altered siliciclastic beds. Hole 5063 drilled in the transition zone area (Fig. 3A) intersects a gabbro sill intruded along the upper contact of the orebody. The sill is chloritized, and locally altered to patchy albite-chlorite (Fig. 5F), massive chlorite, massive albite, and quartz-chlorite-pyrite-galena pods. Thin massive albite zones occur along both sill margins, with the lower albitite within a thin siliciclastic bed separating the sill from the orebody. This albitite is separated from the massive sulphide body by a thin chlorite-pyrite zone with poddy quartz-chlorite-galena. Sedimentary rocks overlying the sill are altered to massive chlorite-pyrite that extends up to the base of the hanging-wall albitite body where chlorite veins cut earlier albitite.

Drill holes 2881 and 2885 intersect altered sediment and gabbro sills on the western margin of a pyrite-chlorite-calcite pipe that transgresses the sulphide orebody (Fig. 4). This pipe roughly overlies the footwall albite zone and is therefore coincident with a cluster of footwall dykes (Fig. 4). Gabbro sills or dykes are in part altered to massive albite or massive chlorite (Fig. 7). Adjacent siliciclastic sedimentary rocks are altered to albitite or biotite hornfels.

### *Extensive alteration overlying the Sullivan orebody*

An extensive body of albite-chlorite-pyrite altered siliciclastic strata overlying the western part of the orebody was described by Shaw and Hodgson (1980) and Hamilton et al. (1982). Overlying the alteration zone cutting the orebody and extending outward along the top of the orebody is massive chlorite up to 30 m thick. Above this is a core of massive albitite as much as 60 m thick that is transitional laterally and upward into chlorite-albite-pyrite that extends as much as 150 m above the orebody.

Hole 84 was drilled from surface close to the area of maximum hanging-wall alteration (Fig. 6). With increasing depth, the following alteration types were intersected (Fig. 6): massive sericitic altered siltstone (0-40 m), massive albite-chlorite-biotite (40-50 m), chlorite-albite with albite cut by chlorite veins and breccias (50-80 m), massive chlorite (80-100 m) and massive chlorite-pyrite-iron dolomite just above the orebody (100-150 m). Throughout this drill hole, relict tourmaline was recrystallized by albite alteration. The upper sericite-altered zone may form part of an envelope around albite-chlorite as suggested by Hamilton et al. (1982). Alternatively, this sericitic alteration may be related to muscovite-dolomite alteration in the transition zone that alters tourmalinite and unaltered sediments (Leitch and Turner, 1992).

## DISCUSSION

### *Timing of intrusion of sills and dykes in and near the Sullivan orebody*

Hoy (1989) suggested that the Moyie sills were intruded into unconsolidated Aldridge sediment and proposed the Guaymas sedimented rift basin as a modern analogy. Basalt

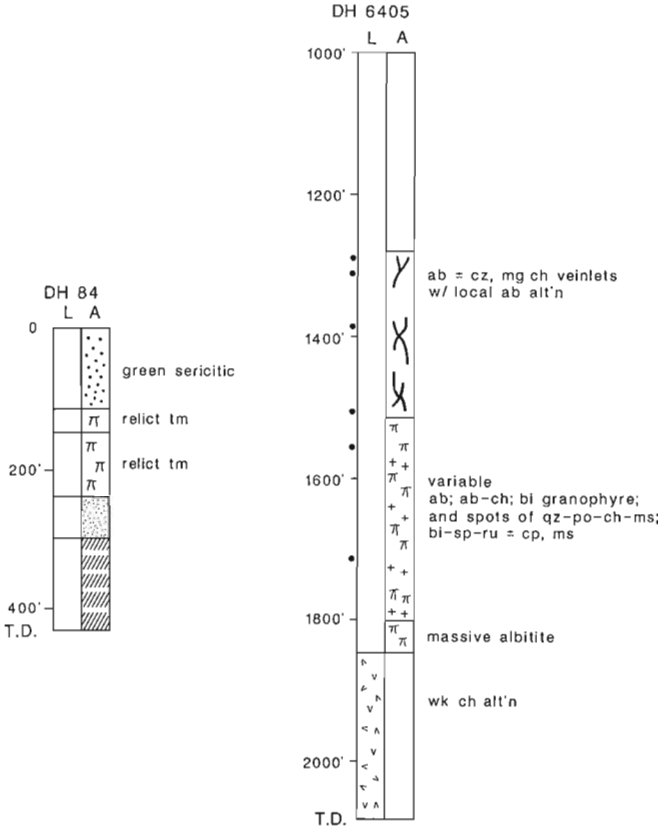


**Figure 6.** Schematic summaries of drill logs illustrating protolith (L) and alteration type (A). See Figure 7 for legend. Drill hole 84 extends from surface to just above the Sullivan ore body through 150 m of altered rock. Alteration is zoned (with increasing depth) from sericitic to albite-chlorite-biotite, chlorite-albite, and chlorite-pyrite-Fe dolomite. Drill hole 6405, 3 km southwest of the Sullivan Mine (Fig. 1) illustrates decreasing intensity of albite-chlorite-pyrite alteration away from the upper margin of a gabbro sill.

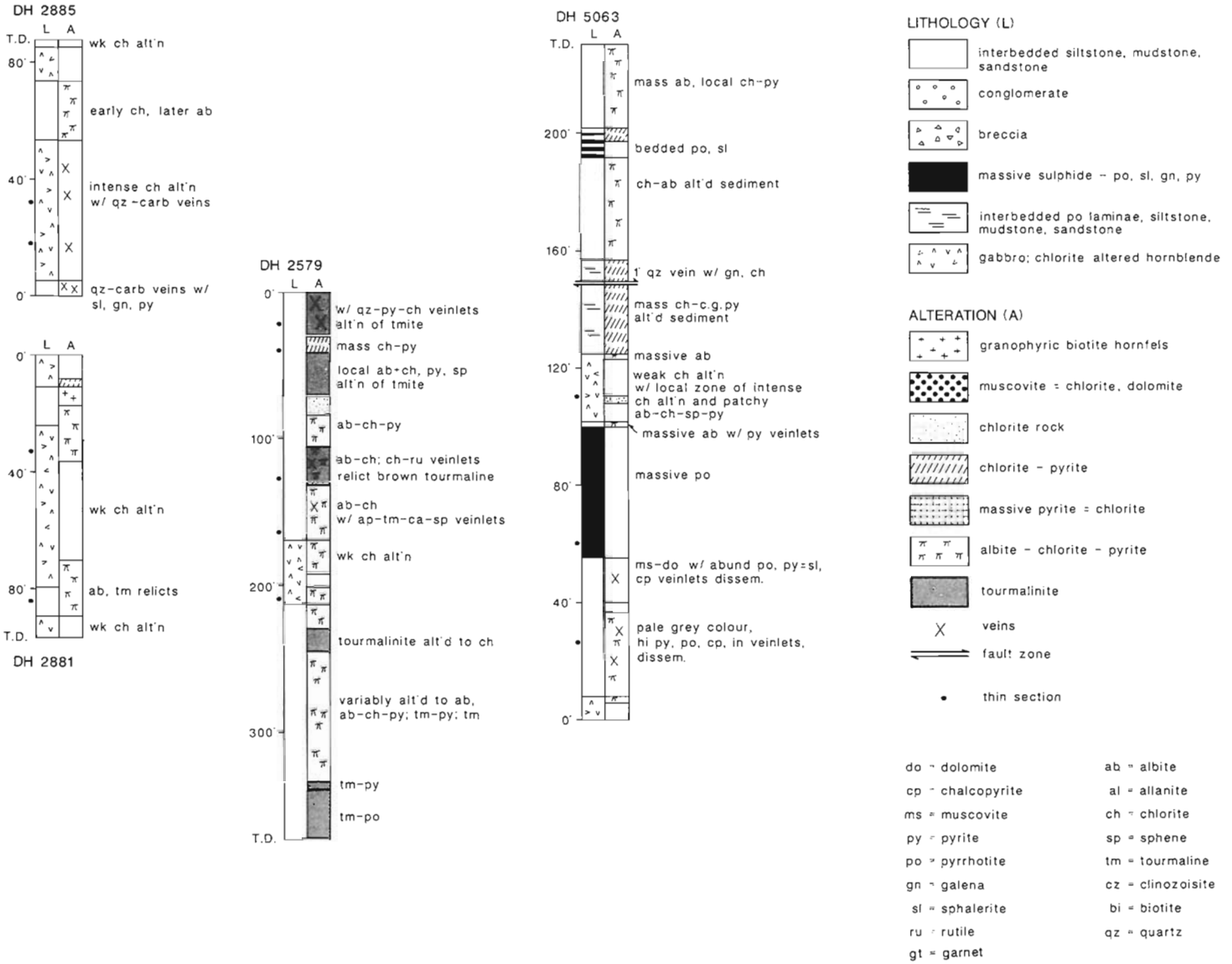


**Figure 7.** Schematic summaries of drill logs illustrating protolith (L) and alteration type (A). Drill hole 2579 (Fig. 3A) illustrates zoned alteration associated with a gabbro dyke cutting tourmalinized sedimentary rocks footwall to the Sullivan ore body. With increasing distance away from the gabbro contact, alteration is zoned from albite to intermediate chlorite-pyrite, and to distal pyritization of pyrrhotite in tourmalinite. Drill hole 5063 (Fig. 3A) drilled upwards successively through tourmalinized footwall sediments and gabbro, the massive sulphide body, a gabbro sill, chlorite rock, and hanging wall albite rock. Drill holes 2885 and 2881 (Fig. 4) are a transect through the margin of the pyrite-chlorite-carbonate zone that cuts through the orebody and intersects gabbros and altered sedimentary rocks.

sill complexes are known to intrude modern sediments to within tens of metres of the present seafloor (Einsele, 1982; Gieskes et al., 1982; Zierenberg et al., in press). A model for intrusion by Einsele (1982) assumes upward-younging sills as each subsequent magma injection rises to the top of previously altered sediment, achieves neutral bouyancy and spreads laterally. Such sills are only slightly younger than the sediments they intrude. One might speculate therefore, that the minimum age of the two gabbro sill complexes exposed southwest of the Sullivan Mine (Leech, 1957) can be dated by the stratigraphic level of the uppermost sill of each complex: an older intrusive event up to the time of formation of the Sullivan deposit, and a younger event during middle Middle Aldridge time. Such a scenario raises the larger question of the role of the source magma for the Moyie sills as a heat engine of fluids that formed the Sullivan orebody, as suggested by Hamilton (1984). Here we restrict ourselves to the possible relationship of intrusions to albite-chlorite-pyrite alteration.

The upward termination or "silling out" of small gabbro dykes within or immediately above the Sullivan orebody, and the intrusion of the footwall sill up to the base of the orebody suggests that local gabbro intrusion took place when the Sullivan sulphide body was only buried a short distance below the seafloor, as suggested by Hamilton et al., (1982). During early burial, the indurated footwall sediments and thick sulphide mass of the Sullivan deposit would have had a significantly higher density than overlying turbidite sediments. Magma rising through the indurated tourmalinized footwall sediments and massive sulphide body achieved neutral bouyancy at the base of overlying partly lithified silts and muds and did not rise further.

### *Timing of albite-chlorite alteration*

Many of the small dykes and sills within the Sullivan mine are altered in part to an albite-chlorite or chlorite-pyrite assemblage and this alteration clearly postdates these intrusions. Zoned envelopes of albite-chlorite-pyrite alteration in sedimentary rocks adjacent to dyke and sill contacts suggest either alteration occurred during gabbro intrusion, or that later flow of hydrothermal fluids was localized along intrusion contacts. It is considered unlikely that alteration occurred during intrusion given the small size of the dykes, the significant addition and removal of components during alteration, the absence of such albite-chlorite alteration associated with most Moyie intrusive contacts throughout the Aldridge Formation, and the minimal alteration associated with modern sills intruded into wet sediments (see below). Albite-chlorite alteration is superimposed on tourmalinite, the massive sulphide body and siliciclastic strata up to the present erosional surface 150 m above the Sullivan orebody. Alteration must be at least as young as these youngest altered rocks. Using modern rates of deposition of 100 to 2000 cm/1000 years for active turbidite depocentres (e.g. Luternauer et al., 1983), the 150 m of thick-bedded turbidites overlying the Sullivan deposit might represent between 7500 and 150 000 years of deposition. This suggests that the youngest albite-chlorite alteration is no less than 10 000-150 000 years younger than ore formation.

### *Significance of spatial association of alteration and gabbro intrusions*

Footwall albite-chlorite altered rock, the root of the alteration zone that transgresses the Sullivan sulphide deposit and hanging wall, is centered on the cluster of gabbro dykes and sills. The position of the dyke set appears to have localized the plume of rising hydrothermal fluids. Zoned alteration envelopes noted on individual dykes indicate fluid flow was channeled along intrusion margins. We presume that these dykes would connect with the steeply dipping discordant limb of the footwall sill at depth and that hydrothermal fluids ascended along this discordant intrusive contact (Fig. 8).

It is worth comparing these relationships with studies within the Guaymas Basin, a modern sedimented submarine rift zone intruded to shallow levels by sills and plugs where

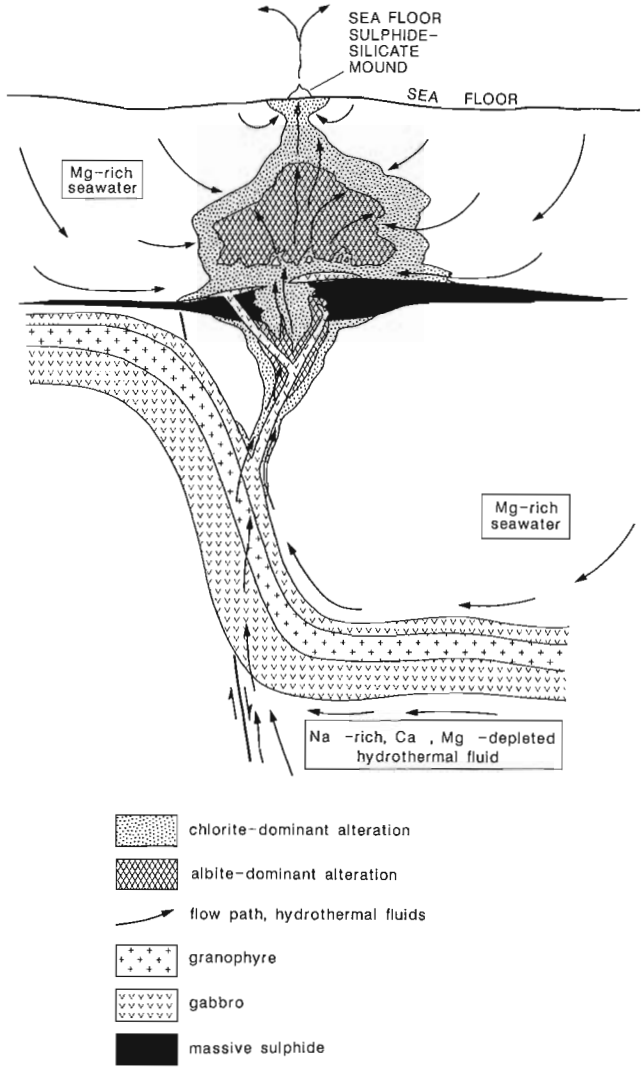


**Figure 8.** Schematic interpretation of geological environment during formation of albite-chlorite-pyrite alteration. Sodium-rich brines rise along syndepositional fault and discordant gabbros causing alteration across and above recently formed sulphide body; mixing with Mg-rich seawater creates peripheral chloritic alteration.

two types of hydrothermal system are recognized (Gieskes et al., 1982). Shallow sills emplaced in the Guaymas Basin unconsolidated sediments produce relatively low-temperature (<200°C), short-duration hydrothermal cells created by expulsion of ambient pore water (Einsele, 1982) and minor alteration of adjacent sediments (Gieskes et al., 1982). However, sedimentary rocks altered to a greenschist-facies metamorphic assemblage were intersected below 190 m depth in a hole drilled to 250 m (Kelts, 1982; Gieskes et al., 1982). With increasing depth, turbidite sediment is progressively lithified and altered to anhydrite-dolomite, illite-chlorite-pyrite, chlorite-pyrite- calcite, and chlorite-epidote-quartz-albite-pyrrhotite-sphene (Kelts, 1982). This alteration is interpreted to reflect the upflow zone of a second much larger hydrothermal circulation system (>300°C) driven by large magmatic intrusions at depth and recharged by deeply circulating seawater (Gieskes et al., 1982). Sills can act as a lid on such deeper fluid flow, and lead to lateral channelling of fluids to zones of cross-stratal permeability such as faults, fractures, and sill margins (Einsele, 1982; Geiskes et al., 1982). Discordant intrusive margins disrupt the natural lateral permeability of strata, and are zones of cross-stratal permeability (Einsele, 1982), as indicated by the abundance of submarine hydrothermal deposits along the margins of seafloor hills underlain by shallow level sills (e.g. Zierenberg et al., in press).

During emplacement of the Moyie syn-rift intrusive complex, hydrothermal circulation driven by intrusions below those presently exposed (sedimentary rocks adjacent to most sills in the Aldridge Formation are not significantly altered) are interpreted to have moved laterally at the base of overlying sill sheets, and ascended along fault zones such as the west side of the Sullivan subbasin. At Sullivan, these fluids appear to have followed the steep contacts of the footwall sill and branching dyke apophyses, resulting in the hydrothermal plume focusing upwards on the orebody and overlying strata.

What localized the large albitite-chlorite alteration body immediately overlying the footwall sill in drill hole 6405 is unclear. Maximum alteration occurs at the sill contact and diminishes away from it, suggesting fluid flow along and upward from the contact. Steeply dipping albite veinlets in the altered body indicate that subvertical fluid flow was important, possibly related to an unrecognized fault that breached the sill and allowed heated fluids from below the sill to rise into overlying sediments.

### *Geochemistry of alteration and evolution of the hydrothermal system*

Albite-chlorite alteration is distinguished by elevated $Na_2O$ (>7%); chlorite-pyrite by elevated MgO (>13%) and total Fe (>29%). Both alteration types are significantly depleted in $SiO_2$, $K_2O$ and CaO relative to unaltered Aldridge strata (Hamilton et al., 1982).

Formation of Mg-silicates in seafloor hydrothermal systems relate to high temperature mixing of Mg-bearing seawater and Mg-depleted silica-rich hydrothermal fluids (Seyfried et al., 1988). Magnesium uptake by secondary phases makes it unlikely that seawater-derived Mg will penetrate significantly into the high temperature regions of submarine geothermal systems. The chloritic alteration at Sullivan therefore likely was produced by a seawater dominant system.

Experiments by Bischoff et al. (1981) monitored the reaction of greywacke with seawater and brines at 350°C and 500 bars and indicate that an assemblage of chlorite-smectite +albite can form from heated seawater. However, the formation of extensive bodies of massive albite (i.e. albitite) with little chlorite likely requires brines enriched in sodium (Bischoff et al., 1981) and significantly depleted in Mg and Ca, unlike seawater (Seyfried et al., 1988). Sodium fixing through albitization is expected in upflow zones of seafloor hydrothermal systems in which Si-rich, Mg-free, and Ca-depleted fluids form during high-temperature reactions at depth to form epidote-quartz-chlorite assemblages (Seyfried et al., 1988).

Early formed proximal albite occurs along hydrothermal conduits surrounded by chlorite-rich assemblages, and is locally overprinted by late chlorite veins. This suggests albitic alteration refects the core of the upflow zone of high Na/(Mg+Ca) brines (Fig. 8). On the margins of this hydrothermal plume, mixing with entrained Mg-rich seawater-derived intersitial fluids resulted in chlorite-dominant alteration. During the late stages, collapse of the hydrothermal plume allowed penetration of Mg-rich seawaters into the altered rock body along fractures, particularily at the base of the massive albite causing chloritic alteration to overprint albite.

### *Relevance to the exploration for Sullivan-type Pb-Zn deposits*

This work is preliminary and speculation regarding relevance to exploration may be premature. However, our interpreted association of albite-chlorite alteration with a hydrothermal system related to gabbro intrusion rather than related to late stage ore formation downplays the importance of this alteration type as a pathfinder for Sullivan-type deposits. However, to the extent that younger hydrothermal systems discharge along structures previously used by an ore forming hydrothermal system (e.g Sullivan), these altered bodies may have value as guides.

## ACKNOWLEDGMENTS

We thank Cominco Ltd. for access to materials, company data and reports, and Doug Anderson, Norris del bel Belluz, Marcia Knapp, and Paul Ransom for their assistance during our field studies. Discussions with Wayne Goodfellow, John Hamilton, Trygve Hoy, Dave Shaw, John Slack, and Bruce Taylor were helpful in focusing on this problem. Glenn Woodsworth, John Hamilton and Trygve Hoy provided helpful criticism of the manuscript. We thank George Wanuk for his cheerful assistance moving, sawing and strapping core, and Richard Lancaster for polishing and photographing core samples used in this paper.

# REFERENCES


**Bischoff, J.L., Radke, A.S., and Rosenbauer, R.J.**
1981: Hydrothermal alteration of graywacke by brine and seawater: roles of alteration and chloride complexing on metal solubilization at 200°C and 350°C; Economic Geology, v. 76, p. 659-676.

**Einsele, G.**
1982: Mechanism of sill intrusion into soft sediment and explusion of pore water; Initial Report of the Deep Sea Drilling Project (Part II), v. 64, p. 1169-1176.

**Gieskes, J.M., Kastner, M., Einsele, G., Kelts, K., and Niemitz, J.**
1982: Hydrothermal activity in the Guaymas Basin, Gulf of California: a synthesis; Initial Report of the Deep Sea Drilling Project (Part II), v. 64, p. 1159-1167.

**Hamilton, J.M.**
1984: The Sullivan deposit, Kimberley, British Columbia – a magmatic component to genesis? in The Belt; Montana Bureau of Mines and Geology, Special Publication 90, p. 58-60.

**Hamilton, J.M., Bishop, D.T., Morris, H.C., and Owens, O.E.**
1982: Geology of the Sullivan orebody, Canada; in Precambrian sulphide deposits, (ed.) Hutchinson, R.W., Spence, C.D., and Franklin, J.M.; Geological Association of Canada, Special Paper 25, p. 597-665.

**Hoy, T.**
1984: Structural setting, mineral deposits, and associated alteration and magmatism, Sullivan camp, southeastern British Columbia (82 F,G); in Geological Fieldwork, 1983, British Columbia Ministry of Energy, Mines and Petroleum Resources, Paper 1984-1, p. 24-35.
1989: The age, chemistry, and tectonic setting of the Middle Proterozoic Moyie sills, Purcell Supergroup, southeastern British Columbia; Canadian Journal of Earth Sciences, v. 26, p. 2305-2317.

**Kelts, K.R.**
1982: Petrology of hydrothermally metamorphosed sediments at DSDP Site 477, southern Guaymas Rift, Gulf of California; Initial Reports of the Deep Sea Drilling Project (Part II), v. 64, p. 1123-1136.

**Leech, G.B.**
1957: St. Mary Lake, Kootenay District, British Columbia (82F/9); Geological Survey of Canada, Map 15-1957.

**Leitch, C.H.B.**
1992: Mineral chemistry of selected silicates, carbonates, and sulphides in the Sullivan and North Star stratiform Zn-Pb deposits, British Columbia, and in district-scale altered and unaltered sediments; in Current Research, Part E; Geological Survey of Canada, Paper 92-1E.

**Leitch, C.H.B. and Turner, R.J.W.**
1991: The vent complex of the Sullivan stratiform sediment-hosted Zn-Pb deposit, British Columbia: preliminary petrographic and fluid inclusion studies; in Current Research, Part E; Geological Survey of Canada, Paper 91-1E, p. 33-43.
1992: Preliminary field and petrographic studies of the sulphide-bearing network underlying the western orebody, Sullivan stratiform sediment-hosted Zn-Pb deposit, British Columbia; in Current Research, Part E; Geological Survey of Canada, Paper 92-1E.

**Leitch, C.H.B., Turner, R.J.W., and Hoy, T.**
1991: The district-scale Sullivan-North Star alteration zone, Sullivan mine area, British Columbia: a preliminary petrographic study; in Current Research, Part E; Geological Survey of Canada, Paper 91-1E, p. 45-57.

**Luternauer, J.L., Clague, J.J., and Pharo, C.H.**
1983: Substrates of the Strait of Georgia, British Columbia; Canadian Journal of Fisheries and Aquatic Sciences, v. 40, p. 1026-1032.

**Seyfried, W.E., Jr., Berndt, M.E., and Seewald, J.S.**
1988: Hydrothermal alteration processes at mid-ocean ridges: constraints from diabase alteration experiments, hot-spring fluids and composition of the oceanic crust; Canadian Mineralogist, v. 26, p. 787-804.

**Shaw, D.R. and Hodgson, C.J.**
1980: Wall-rock alteration at the Sullivan mine, Kimberley, British Columbia (abstract); in Canadian Institute Mining Metallurgy, Bulletin 73, no. 821, p. 75.

**Zierenberg, R.A., Morton, J.L., Koski, R.A., Ross, S.L., and Holmes, M.L.**
in press: Geologic setting of massive sulfide mineralization in the Escanaba Trough; U.S. Geological Survey Bulletin.


---


Geological Survey of Canada Project 900020
(Contribution no. 7, Sullivan-Aldridge project)

# Permian, Triassic, and Middle Jurassic microfaunal associations, Stikine terrane, Oweegee and Kinskuch areas, northwestern British Columbia

**F. Cordey, C.J. Greig[1], and M.J. Orchard**
**Cordilleran Division, Vancouver**

*Cordey, F., Greig, C.J., and Orchard, M.J., 1992: Permian, Triassic, and Middle Jurassic microfaunal associations, Stikine terrane, Oweegee and Kinskuch areas, northwestern British Columbia; in Current Research, Part E; Geological Survey of Canada, Paper 92-1E, p. 107-116.*

***Abstract***

*Nine age-diagnostic microfossil collections from the Stikine terrane in northwestern British Columbia confirm the presence and extend the distribution of several regionally mappable geological units; they also place constraints on the timing of early Mesozoic deformation affecting western Stikine terrane. Radiolarians are Early Permian, Late Triassic, and Middle Jurassic in age, spanning a large part of the stratigraphic range of Stikine terrane, and are found in various lithologies, including siliceous siltstone, limestone, and bedded chert. Conodonts are from carbonate and are Late Triassic (Late Carnian, Late Norian) in age.*

***Résumé***

*L'échantillonnage de neuf microfossiles caractéristiques du terrane de Stikine dans le nord-ouest de la Colombie-Britannique confirme la présence de plusieurs unités géologiques régionales et en étend la répartition. Il permet aussi de préciser l'âge de la déformation du Mésozoïque précoce qui a eu lieu dans la partie occidentale du terrane de Stikine. Les radiolaires, qui datent du Permien précoce, du Trias tardif et du Jurassique moyen, couvrent une part importante de la stratigraphie du terrane de Stikine; ils proviennent de lithologies variées, dont notamment de siltstones siliceux, de calcaires et de cherts zonés. Les conodontes ont été échantillonnés dans des carbonates et sont d'âge triasique tardif (Carnien tardif, Norien tardif).*

[1] Department of Geosciences, University of Arizona, Building #77, Tucson, Arizona 85721, U.S.A.

## INTRODUCTION

This paper reports radiolarian and conodont occurrences and preliminary age assignments for nine samples from western Stikine terrane, in the Oweegee and Kinskuch areas of northwestern British Columbia (Fig. 1). Age assignments and discussions of faunal associations are by Cordey (radiolarians) and Orchard (conodonts) for samples collected by Greig in the course of Ph.D. thesis mapping along the west-central margin of the Bowser Basin. Stratigraphic and structural relationships within and between basement and cover rocks provide the focus for mapping, which is described in detail in Greig (1991, 1992). Although age interpretations are provided for two samples collected in 1991, processing of most 1991 samples is still underway.

## HOST ROCKS AND FIELD RELATIONS

### *Oweegee Range*

Three samples from the Oweegee area yielded microfossils. A well-preserved Middle Jurassic radiolarian fauna was extracted from dark grey, thin-bedded to laminated siliceous siltstone of the Spatsizi Group near the northern margin of Oweegee dome (Fig. 2, loc. 1, Table 1). Radiolarians were restricted to 1 cm darker, more argillaceous layers within the siltstone. It is notable that the fauna was well-preserved, despite its occurrence in a tightly folded, locally sheared section with abundant calcite veinlets. The Spatsizi Group forms the base of the Bowser basin sedimentary "cover" to the Oweegee dome, and at the sample locality is exposed over a thickness of approximately 20 m. Constituent lithologies are typical of the rusty weathering, thinly bedded Spatsizi Group in the Oweegee area and include siliceous siltstone, silty limestone (commonly as lenses), siliceous dust tuff, cherty argillite, chert, and distinctive pale grey, centimetre-scale, clay-rich dust tuff (?). The early Bajocian to late Bathonian age assignment (see below) supports a correlation with the lithologically-similar Quock Formation in the type area of the Spatsizi Group to the northeast (Thomson et al., 1986).

The two other productive samples from the Oweegee area yielded Late Triassic microfossils (Fig. 2, loc. 2 = radiolarians, Table 2; loc. 3 = conodonts, Table 3), confirming the presence in Oweegee dome of Late Triassic rocks of the Stuhini Group. Previous age-control for the unit consisted only of Late Triassic belemnites (Monger, 1977). Although yielding different microfossils, the samples were collected from similar decimetre to metre thick lenses of silty carbonate mudstone. The carbonate lenses are uncommon and are found interbedded with black siliceous siltstone within a sequence dominated by dark green, metre-scale turbiditic arkose. The Triassic rocks are imbricated with Paleozoic Stikine assemblage rocks and together they are unconformably overlain by Lower Jurassic Hazelton Group rocks which were not involved in the imbrication. The microfossils therefore provide an older limit to the deformation.

### *Kinskuch Lake*

Six samples collected from the Kinskuch Lake area (Fig. 3) yielded microfossils. Distinctive bedded radiolarian chert, commonly pale green, yielded an Early Permian fauna (loc. 5, Table 2). Five other samples, from either limestone or limy to siliceous siltstone, yielded Late Triassic radiolarian or conodont faunas. Prior to this work, Paleozoic rocks had not been mapped in the Kinskuch region, although Orchard

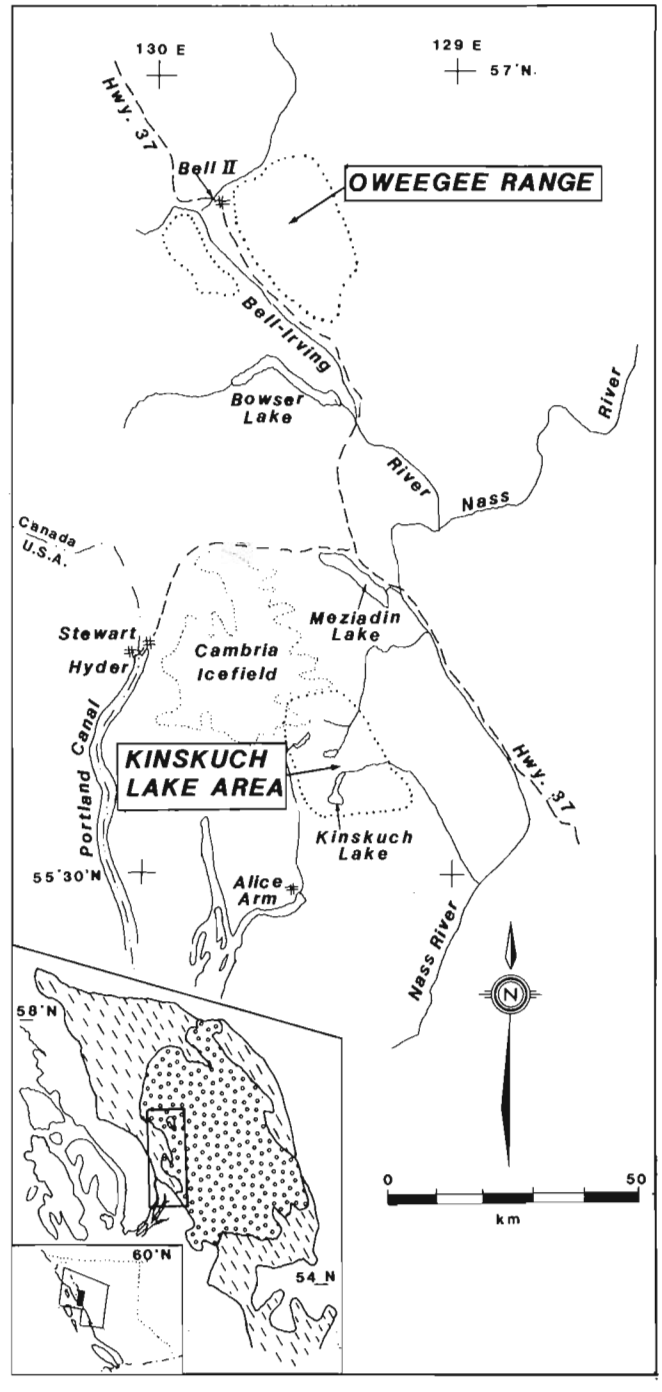


**Figure 1.** Location map of the Oweegee and Kinskuch area (after Greig, 1992).

(1991b) reported Early Permian conodonts from collections made during a proprietary mapping project in the valley of the Kitsault River, less than 10 km south-southwest of the area shown in Figure 3.

The Permian and four of the Triassic collections come from a unit of fine grained, clastic rocks and chert previously without age-control. Greig (1992) tentatively assigned the unit to the Stuhini Group on the basis of its unconformable contact with the overlying and relatively undeformed Hazelton Group rocks. Triassic microfossils from the lower package are Late Carnian (loc. 9, Table 3), Norian (loc. 4, Table 3), Late? Norian (loc. 6, Table 3), and Early or Middle Norian (loc. 7, Table 2), and occur in metre-scale silty limestone lenses (conodonts) or in siliceous argillite (radiolarians). A single Triassic collection from the lowermost part of the sequence overlying the unconformity (loc. 8, Table 3) yielded Late Norian conodonts. It was collected from a pale grey and hackly weathering, dark grey, fetid, locally tuffaceous limestone. The limestone is at least 50 m in length, several metres thick, and unconformably overlies bedded radiolarian chert of probable Paleozoic age. If the conodonts from locality 8 are not reworked (several additional collections are being processed to test this possibility), they bracket tightly the timing of deformation to the Norian, and possibly to the Late Norian, and suggest that the Hazelton Group in the Kinskuch area is as old as latest Triassic. Siliceous argillite at locality 6, which yielded Late? Norian conodonts, may provide an older limit to the deformation, and has been recollected in an attempt to obtain more diverse and diagnostic faunal assemblage.

## RADIOLARIAN ASSOCIATIONS

### *Permian*

Well-preserved radiolarians were obtained from the bedded chert unit from Kinskuch Lake described above (loc. 5). The association (Table 2) correlates with the *Pseudoalbaillella lomentaria* Assemblage zone (Ishiga, 1990) of Early Permian, late Asselian to late Sakmarian age (Tables 2, 4). *Pseudoalbaillella* sp. 1 (Plate 1, fig. 8) and Genre 1 sp. (Plate 1, fig. 10, 12) were first reported from southwest Japan within the Shimomidani Formation (Caridroit, 1986). Radiolarians of the same Assemblage zone (unpub. data; GSC C-088125) were reported previously from Telegraph Creek area (104G), from a siliceous unit of uncertain correlation (C.A. Evenchick, pers. comm., 1992); this association contains *Pseudoalbaillella asymmetrica* Ishiga and Imoto, which ranges within the upper part of the *Ps. lomentaria* Assemblage zone (Ishiga, 1990).

**Table 1.** Radiolarian and conodont localities

| TEXT LOC. | GSC LOC. | SAMPLE No. | UTM COORD. | | NTS | LOCATION | GEOLOGICAL UNIT |
|---|---|---|---|---|---|---|---|
| | | | E. | N. | | | |
| 1. | C-177761 | 90-EPC-48C | 460640 | 6283960 | 104A/12E | Owegee dome, 150 m SSE of Mount Skowill | Spatsizi Gp |
| 2. | C-177776 | 90-EPC-143 | 464160 | 6280900 | 104A/12E | Owegee dome, 1.3 km NW of Owegee Peak | Stuhini Gp |
| 3. | C-177800 | 90-EPC-207A | 466580 | 6279740 | 104A/12E | Owegee dome, 1.7 km NE of Delta Peak | Stuhini Gp |
| 4. | C-175166 | 90-EPC-297 | 470560 | 6173400 | 103P/11 | Kitsault area, 5.0 km SW of Jade Lake | Stuhini Gp |
| 5. | C-175177 | 90-EPC-340 | 476120 | 6173530 | 103P/11 | Kitsault area, 1.5 km NW of Kinskuch Lake | Stikine Assemblage |
| 6. | C-175179 | 90-EPC-343 | 476500 | 6173660 | 103P/11 | Kitsault area, 1.2 km NW of Kinskuch Lake | Stuhini Gp |
| 7. | C-175182 | 90-EPC-355 | 476790 | 6173220 | 103P/11 | Kitsault area, 0.8 km NW of Kinskuch Lake | Stuhini Gp |
| 8. | C-178198 | 91-EPC-202-1 | 476770 | 6172180 | 103P/11 | NW edge of Kinskuch Lake | Hazelton Gp |
| 9. | C-178200 | 91-EPC-208-2 | 477900 | 6173510 | 103P/11 | North end of Kinskuch Lake | Stuhini Gp |

### *Late Triassic*

Radiolarians from locality 2 and 7 are Late Triassic in age (Tables 2, 4). At locality 7, the radiolarian association is correlative with the *Capnodoce* Zone (Blome, 1984). The joint occurrence of *Canesium lentum* Blome, *Latium* sp., and *Pachus* sp. cf. *luculentus* Blome more likely relates to the *Xipha striata* or *Latium paucum* Subzones of Blome (1984), which are of Early or Middle Norian age.

### *Middle Jurassic*

Well-preserved Middle Jurassic radiolarians were recovered from a siliceous siltstone of the Spatsizi Group (loc. 1). The association is correlative with early Bajocian fauna of the Yakoun Formation in the Queen Charlotte Islands (Carter, 1988), e.g., *Parvicingula preaculeata* Carter (Plate 1, fig. 19) and *Emiluvia* sp. A (Plate 1, fig. 17) which is possibly related to the broken specimen of *E. oldmassetensis* Carter (1988, Plate 16, fig. 6). Other species from locality 1 appear younger, like *P. profunda* Pessagno & Whalen (Plate 1, fig. 23) which is reported in the late Bathonian of the Snowshoe Formation of east-central Oregon (Pessagno and Whalen, 1982) but not earlier. The youngest strata exposed in the Yakoun Formation are early Bajocian in age, meaning that the radiolarians described by Carter (1988) could occur later, e.g., in the late Bajocian and ?Bathonian. Although *Parvicingula burnsensis* Pessagno & Whalen (Plate 1, fig. 22) does not occur later than the late Bajocian, our determination is uncertain because of a lack of well-defined morphological characterization of that species. The age of the fauna at loc. 1 is therefore regarded as early Bajocian to late Bathonian (Tables 2, 4).

In the Canadian Cordillera, Middle Jurassic radiolarians are known in the Bridge River Complex, an oceanic terrane in southwestern British Columbia. A recent study (Cordey and Schiarizza, in prep.) suggests that late Middle Jurassic chert of the Bridge River Complex contains radiolarian associations closely similar (taxa, assemblage) to those of some Japanese terranes, for example, the *Dictyomitrella*(?) *kamoensis* - *Pantanellium foveatum* assemblage (Mizutani and Kido, 1983). In contrast, Middle Jurassic radiolarians of the Spatsizi Group have more affinities with radiolarian associations of the Yakoun Formation of the Queen Charlotte Islands (Carter, 1988) and the Snowshoe Formation of

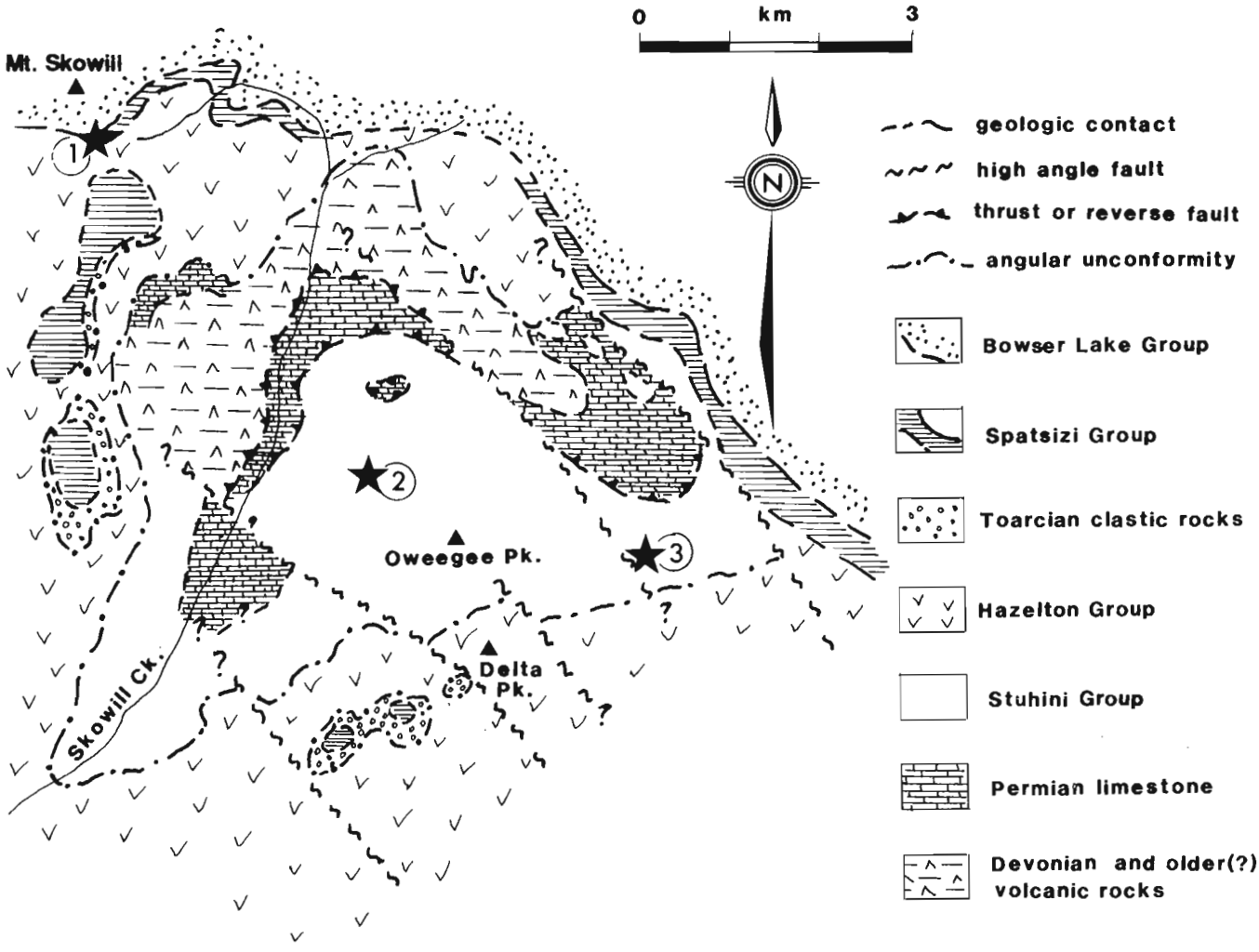


**Figure 2.** Fossil localities 1-3 and geology, northern Oweegee Range.

east-central Oregon (Pessagno and Whalen, 1982). Pessagno et al. (1987) have interpreted these radiolarian assemblages to be characteristic of a Boreal realm, reflecting the translation of Wrangell terrane to the north in the Middle Jurassic, the differentiation being attributed to a change from Tethyan to Boreal paleolatitudes. The apparent faunal radiolarian differentiation between the Spatsizi Group and the Bridge River Complex may reflect differences in paleolatitude or, as suggested by Baumgartner (1987), may represent the influence of paleoceanographic factors (bathymetry, currents) along the margins of Cordilleran terranes during the Middle Jurassic. This may be reflected by differences in lithology (organic-rich siliceous siltstone in the Spatsizi, well-oxygenated ribbon chert in the Bridge River).

Faunal correlations may signify that the Wrangell and Stikine terranes experienced similar Middle Jurassic low-fertility paleoceanographic conditions, different from those of chert-rich terranes like the Bridge River Complex.

## CONODONT ASSOCIATIONS

Five conodont collections have been recovered from within the area under discussion, details of which are provided in Tables 1, 3, and 4. At least two different associations are present: an older Late Carnian fauna from carbonates of the Stuhini Group, and a younger one from unnamed carbonate of Late Norian age. One other collection is poorly preserved and can only be determined as Norian.

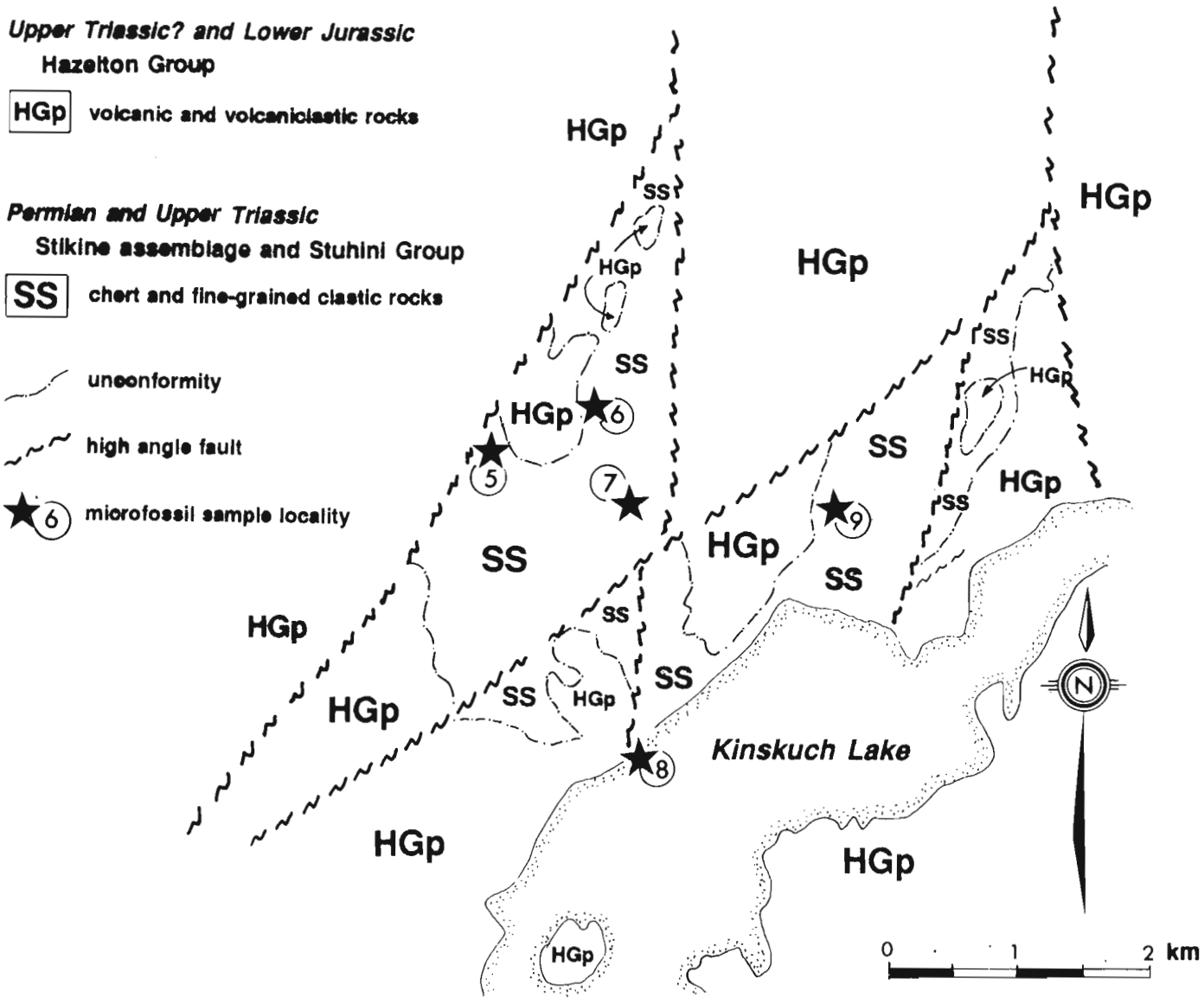


**Figure 3.** Fossil localities 5-9 and geology, northern Kinskuch Lake.

The Late Carnian collection is known from both the Oweegee Dome (loc. 3, Table 3) and Kinskuch Lake (loc. 9, Table 3) areas, where the association of *Metapolygnathus nodosus* (Hayashi) and the shorter ranging *M. lindae* Orchard define a position low in the *nodosus* Zone (Orchard, 1991a, 1991c). Although both species range throughout that zone, they are particularly diagnostic of the Lower *nodosus* Zone, which has been shown to correlate with the Welleri Zone of the ammonoid chronology (Tozer, 1967; Orchard, 1991c). This fauna has been reported from both northeastern British Columbia and from the Peril Formation of Queen Charlotte Islands (Orchard, 1991a).

**Table 2.** Radiolarian fauna and age assignments

| TEXT LOC. | GSC LOC. SAMPLE No. | RADIOLARIAN FAUNA | AGE |
|---|---|---|---|
| 1. | C-177761<br>90-EPC-48C | *Emiluvia* sp. A<br>?*Parvicingula burnsensis* Pessagno & Whalen 1982<br>*P. preaculeata* Carter 1988<br>*P. profunda* Pessagno & Whalen 1982<br>*Ristola* sp. aff. *decora* Pessagno & Whalen 1982<br>?*Triversus* sp.<br>gen. sp. indet. A | Middle Jurassic, early Bajocian - late Bathonian |
| 2. | C-177776<br>90-EPC-143 | *Capnuchosphaera*? sp.<br>*Kahlerosphaera* sp.<br>*Plafkerium* sp. | Late Triassic, Carnian-Norian. |
| 5. | C-175177<br>90-EPC-340 | *Quadricaulis* sp. aff. *femoris* Caridroit & De Wever<br>*Quinqueremis* sp. 1986<br>*Pseudoalbaillella longicornis* Ishiga & Imoto 1980<br>*Ps. sakmarensis* (Kozur) 1981<br>*Ps.* sp. aff. *scalprata* Holdsworth & Jones 1980<br>*Ps.* sp. 1 in Caridroit 1986<br>Genre 1 sp. in Caridroit 1986 | Early Permian, late Asselian to late Sakmarian |
| 7. | C-175182<br>90-EPC-355 | *Canesium lentum* Blome 1984<br>*Capnodoce* sp.<br>*Corum* sp.<br>*Latium* sp.<br>*Pachus* sp. cf. *luculentus* Blome 1984 | Late Triassic, Early-Middle Norian |

**Table 3.** Conodont fauna and age assignments

| TEXT LOC. | GSC LOC. SAMPLE No. | CONODONT FAUNA | AGE |
|---|---|---|---|
| 3. | C-177800<br>90-EPC-207A | *Metapolygnathus nodosus* (Hayashi)<br>*M.* cf. *lindae* Orchard | Late Triassic, Late Carnian |
| 4. | C-175166<br>90-EPC-297 | *Epigondolella* sp. | Late Triassic, Norian |
| 6. | C-175179<br>90-EPC-343 | *Epigondolella bidentata* Mosher<br>*Parvigondolella*? sp. | Late Triassic, Late? Norian |
| 8. | C-178198<br>91-EPC-202-1 | *Epigondolella mosheri* Kozur & Mostler | Late Triassic, Late Norian |
| 9. | C-178200<br>91-EPC-208-2 | *Metapolygnathus nodosus* (Hayashi)<br>*M. lindae* Orchard | Late Triassic, Late Carnian |

The Late Norian association is known only from the Kinskuch Lake area (loc. 8, Table 3). Late Norian conodont faunas are widespread in western Canada (Orchard, 1991b), where they are invariably characterized by *Epigondolella bidentata* Mosher. As can be demonstrated in both the Kunga Group of Queen Charlotte Islands (Wrangell terrane), the Tyaughton Group of south-central British Columbia (Cadwallader terrane), and the Gabbs Formation of central Nevada, *E. bidentata* is gradually replaced by *E. mosheri*, accompanied by *Parvigondolella*, in the middle part of the Late Norian; this defines an Upper *bidentata* Zone which corresponds to the Ameonum Zone and part of the overlying

**Table 4.** Ages of faunal associations at localities 1-9. Each vertical bar shows the age range at given locality; Isotopic ages for stage boundaries from DNAG time scale (Palmer, 1983)

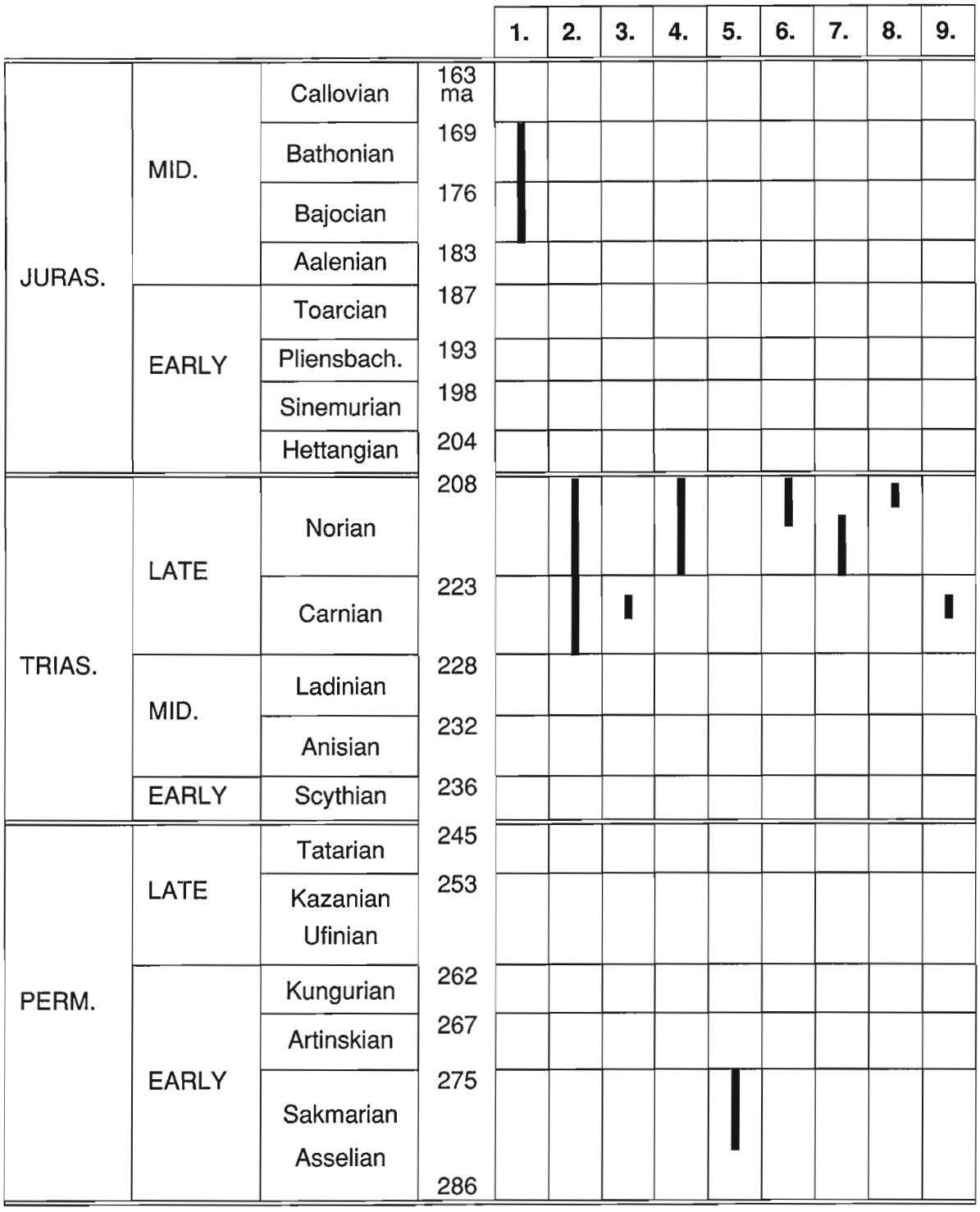

## Plate 1

Scanning electron micrographs of Triassic conodonts (fig. 1-6), Permian radiolarians (fig. 7-12), and Triassic and Jurassic radiolarians (fig. 13-23) from the Oweegee range and Kinskuch Lake area, northwestern British Columbia. The following are indicated for each figure: identification, locality (Table 1), GSC locality no., field sample no., GSC specimen no., and magnification.

fig. 1. *Epigondolella mosheri* Kozur & Mostler, loc. 8, GSC C-178198, 91-EPC-202-1, GSC 95363, x 80.

fig. 2-4. *Metapolygnathus lindae* Orchard, loc. 9, GSC C-178200, 91-EPC-208-2, 2: GSC 95364, x 80, 3: GSC 95365, x 80, 4: GSC 95366, x 80.

fig. 5, 6. *Metapolygnathus nodosus* (Hayashi), loc. 9, GSC C-178200, 91-EPC-208-2, 5: GSC 95367, x 80, 6: GSC 95368, x 80.

fig. 7. *Pseudoalbaillella sakmarensis* (Kozur) 1981, loc. 5, GSC C-175177, 90-EPC-340, GSC 101436, x 160.

fig. 8. *Ps.* sp. 1 in Caridroit 1986, loc. 5, GSC C-175177, 90-EPC-340, GSC 101437, x 175.

fig. 9. *Ps.* sp. aff. *scalprata* Holdsworth & Jones 1980, loc. 5, GSC C-175177, 90-EPC-340, GSC 101438, x 175.

fig. 10, 12. Genre 1 sp. in Caridroit 1986, loc. 5, GSC C-175177, 90-EPC-340, 10: GSC 101439, 12: GSC 101441, 10, 12: x 115.

fig. 11. *Quadricaulis* sp. aff. *femoris* Caridroit & De Wever 1986, loc. 5, GSC C-175177, 90-EPC-340, GSC 101440, x 115.

fig. 13. *Latium* sp., loc. 7, GSC C-175182, 90-EPC-355, GSC 101442, x 200.

fig. 14. *Latium* sp., loc. 7, GSC C-175182, 90-EPC-355, GSC 101443, x 200.

fig. 15. *Canesium lentum* Blome 1984, loc. 7, GSC C-175182, 90-EPC-355, GSC 101444, x 250.

fig. 16. *Corum* sp., loc. 7, GSC C-175182, 90-EPC-355, GSC 101445, x 150.

fig. 17. *Emiluvia* sp. A, loc. 1, GSC C-177761, 90-EPC-48C, GSC 101446, x 130.

fig. 18. ?*Triversus* sp., loc. 1, GSC C-177761, 90-EPC-48C, GSC 101447, x 160.

fig. 19. *Parvicingula preaculeata* Carter 1988, loc. 1, GSC C-177761, 90-EPC-48C, GSC 101448, x 200.

fig. 20. *Ristola* sp. aff. *decora* Pessagno and Whalen 1982, loc. 1, GSC C-177761, 90-EPC-48C, GSC 101449, x 185.

fig. 21. gen. sp. indet. A, loc. 1, GSC C-177761, GSC 90-EPC-48C, GSC 101450, x 220.

fig. 22. ?*Parvicingula burnsensis* Pessagno and Whalen 1982, loc. 1, GSC C-177761, 90-EPC-48C, GSC 101451, x 174.

fig. 23. *Parvicingula profunda* Pessagno and Whalen 1982, loc. 1, GSC C-177761, 90-EPC-48C, GSC 101452, x 200.

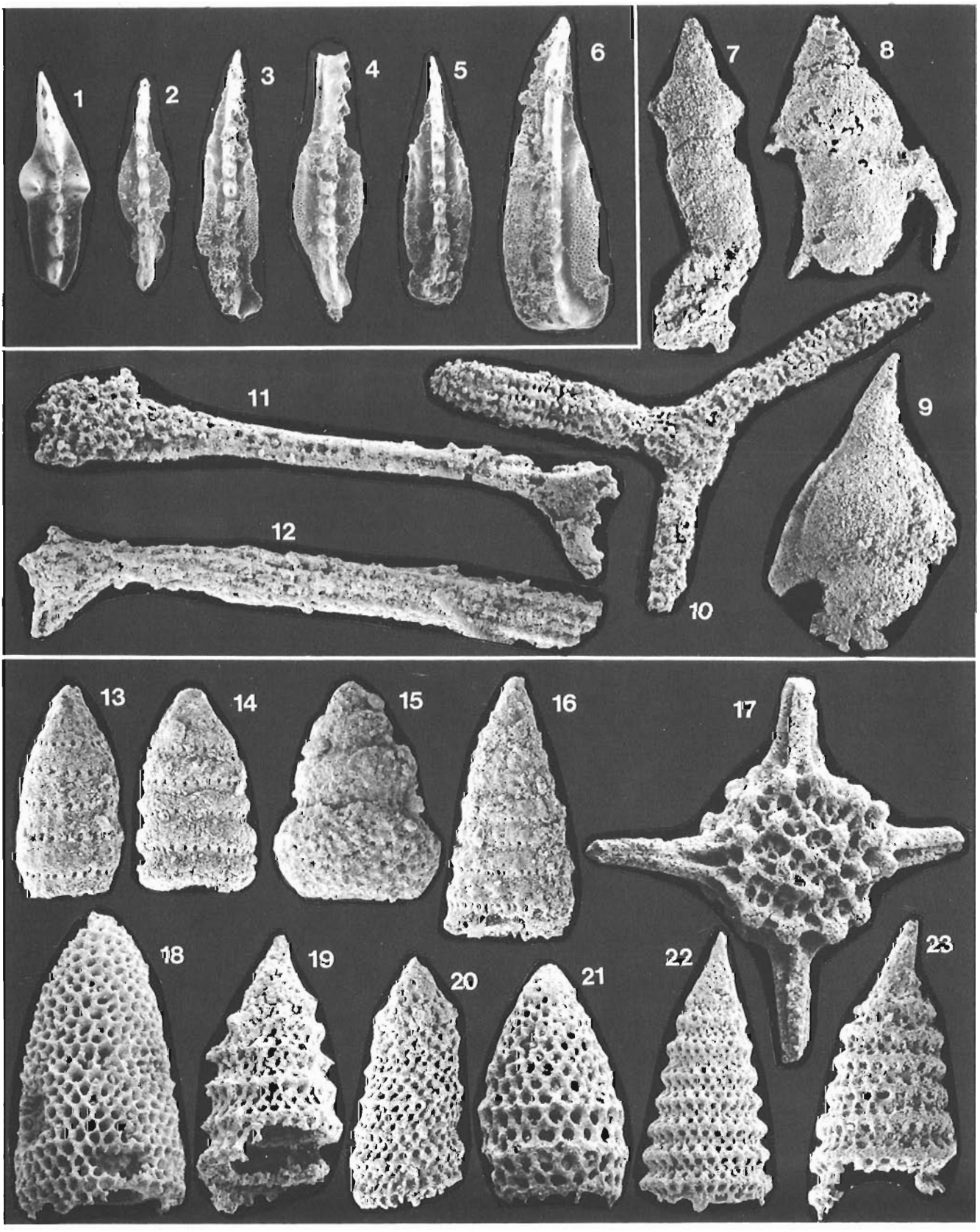
1
2
3
4
5
6
7
8
9
10
11
12
13
14
15
16
17
18
19
20
21
22
23

Crickmayi Zone of the ammonoid chronology (Tozer, 1967; Orchard, 1991c). *E. mosheri* is also known from the Bocock Limestone of northeastern British Columbia, and the Lewes River Group of Whitehorse Trough. A second small collection from Kinskuch Lake area (loc. 6, Table 3) contains both *E. bidentata* and a questionable *Parvigondolella*. Both of these may be early growth stages of older *Epigondolella* species, and so the collection is only tentatively assigned to the Late Norian.

## ACKNOWLEDGMENTS

Funding by the Geological Survey of Canada project 810028 and a post-doctoral fellowship administrated by the National Sciences and Engineering Research Council of Canada to Cordey. Susan Cannon and Hillary Taylor completed the picking of samples residues. We thank Tonia Oliveric and Peter Krauss for respective drafting and photographic help. Thanks also to Carol Evenchick for her review and to Bev Vanlier who edited the manuscript.

## REFERENCES

**Baumgartner, P.O.**
1987: Tethyan Jurassic Radiolarites; Eclogae geologicae Helveticae, v. 80, no. 3, p. 831-879.

**Blome, C.D.**
1984: Upper Triassic Radiolaria and radiolarian zonation from western North America; Bulletin of American Paleontology, v. 85, no. 318, 88 p.

**Caridroit, M.**
1986: Contribution à l'étude géologique du Japon du Sud-Ouest dans l'île de Honshu; 2ème partie: Paléontologie de la faune de radiolaires permiens; Thèse de Doctorat de l'Université d'Orléans, 500 p.

**Caridroit, M. and De Wever, P.**
1986: Some Late Permian radiolarians from pelitic rocks of the Tatsuno Formation (Hyogo Prefecture), southwest Japan; in Eurorad IV, (ed.) P. De Wever; Marine Micropaleontology, v. 11, no. 3-4, p. 55-90.

**Carter, E.S.**
1988: Systematic paleontology; in Lower and Middle Jurassic Radiolarian Biostratigraphy and Systematic Paleontology, Queen Charlotte Islands, British Columbia, (ed.) E.S. Carter, B.E.B. Cameron, and P.L. Smith; Geological Survey of Canada, Bulletin 386, 109 p.

**Greig, C.J.**
1991: Stratigraphic and structural relations along the west-central margin of the Bowser Basin, Oweegee and Kinskuch areas, northwestern British Columbia; in Current Research, Part A; Geological Survey of Canada, Paper 91-1A, p. 197-205.
1992: Fieldwork in the Oweegee and Snowslide ranges and Kinskuch Lake area, northwestern British Columbia; in Current Research, Part A; Geological Survey of Canada, Paper 92-1A, p. 145-155.

**Holdsworth, B.K. and Jones, D.L.**
1980: Preliminary zonation for Late Devonian through Permian time; Geology, v. 8, no. 6, p. 281-285.

**Ishiga, H.**
1990: Paleozoic Radiolarians; in Pre-Cretaceous Terranes of Japan, (ed.) K. Ichikawa, S. Mizutani, I. Hara, and A. Yao; International Geological Correlation Program Project no. 224, Osaka, p. 285-295.

**Ishiga, H. and Imoto, N.**
1980: Some Permian radiolarians in the Tamba district, southwest Japan; Earth Sciences (Chikyu Kagaku), v. 34, no. 6, p. 333-345.

**Kozur, H.**
1981: Albaillellidea (Radiolaria) aus dem Unterperm des Vorurals; Geologisch Paläontologisch Mitteilungen, Innsbruck, v. 10, p. 263-274.

**Mizutani, S. and Kido, S.**
1983: Radiolarians in Middle Jurassic siliceous shale from Kamiaso, Gifu Prefecture, Central Japan: Transactions and Proceedings of Palaeontologic Society of Japan, no. 132, p. 253-262.

**Monger, J.W.H.**
1977: Upper Paleozoic rocks of northwestern British Columbia; in Report of Activities, Part A; Geological Survey of Canada, Paper 77-1A, p. 255-262.

**Orchard, M.J.**
1991a: Late Triassic conodont biochronology and biostratigraphy of the Kunga Group, Queen Charlotte Islands, British Columbia; in Evolution and Hydrocarbon Potential of the Queen Charlotte Basin, British Columbia, (ed.) G.J. Woodsworth; Geological Survey of Canada, Paper 90-10, p. 173-193.
1991b: Conodonts, time and terranes: an overview of the biostratigraphic record in the western Canadian Cordillera; in Ordovician to Triassic Conodont Paleontology of the Canadian Cordillera, (ed.) M.J. Orchard and A.D. McCracken; Geological Survey of Canada, Bulletin 417, p. 1-26.
1991c: Upper Triassic conodont biochronology and new index species from the Canadian Cordillera; in Ordovician to Triassic Conodont Paleontology of the Canadian Cordillera, (ed.) M.J. Orchard and A.D. McCracken; Geological Survey of Canada, Bulletin 417, p. 299-335.

**Palmer, A.R.**
1983: The Decade of North American Geology 1983 Time Scale; Geology, v. 11, p. 503-504.

**Pessagno, E.A. Jr. and Whalen, P.A.**
1982: Lower and Middle Jurassic radiolaria (multicyrtid Nassellariina) from California, east-central Oregon and the Queen Charlotte Islands, B.C.; Micropaleontology, v. 28, no. 2, p. 111-169.

**Pessagno, E.A. Jr., Blome, C.D., Carter, E.S., MacLeod, N., Whalen, P.A., and Yeh, K.**
1987: Preliminary Radiolarian zonation for the Jurassic of North America, Studies of North American Jurassic Radiolaria; Cushman Foundation Special Publication no. 23, p. 1-18.

**Thomson, R.C., Smith, P.L., and Tipper, H.W.**
1986: Lower to Middle Jurassic (Pliensbachian to Bajocian) stratigraphy of the northern Spatsizi area, north-central British Columbia; Canadian Journal of Earth Sciences, v. 23, p. 1963-1973.

**Tozer, E.T.**
1967: A Standard for Triassic Time; Geological Survey of Canada, Bulletin 156.

Geological Survey of Canada Project 810028

# Progress in mapping of Jurassic and Tertiary plutonic styles, Queen Charlotte Islands, British Columbia[1]

**R.G. Anderson, M.H. Gunning[2], and S. Porter[3]**
**Cordilleran Division, Vancouver, B.C.**

*Anderson, R.G., Gunning, M.H., and Porter, S., 1992: Progress in mapping of Jurassic and Tertiary plutonic styles, Queen Charlotte Islands, British Columbia; in Current Research, Part E; Geological Survey of Canada, Paper 92-1E, p. 117-123.*

***Abstract***

*Mapping resumed along parts of the Graham, Moresby, and Lyell islands to refine the distributions and plutonic styles of Middle to Late Jurassic and Tertiary plutons.*

*The northern segment of the San Christoval plutonic suite in Van Inlet extends farther east than previously known. A 0.5-1.5 km foliated zone along the eastern margin of the San Christoval plutonic suite between Bigsby Point and Haswell Bay parallels the intrusive contact with the Karmutsen Formation. Foliation decreases in intensity away from the contact; syn-intrusion strain may account for the deformation.*

*The Eocene or early Oligocene Lyell Island porphyry plutonic complex in the southeastern third of Lyell Island comprises aphyric clinopyroxene basalt, feldsparphyric andesite, dacite and syenite, and late amygdaloidal, layered andesite phases sequentially intruded into intermediate composition, Tertiary volcaniclastic rocks. Subvertical, north-northwest- to north-northeast-trending intraphase contacts, synplutonic dykes, joints, and fracture and gouge zones are abundant and distinctive.*

***Résumé***

*La cartographie de certaines zones des îles Graham, Moresby et Lyell a été entreprise afin d'y préciser la répartition et le style des plutons de Jurassique moyen-tardif et du tertiaire.*

*Dans la région de l'inlet Van, le segment septentrional de la suite plutonique de San Christoval possède une extension orientale plus importante qu'il ne l'a été établi auparavant. Une zone à foliations de 0,5-1,5 km, observée le long de la marge orientale de la suite plutonique de San Christoval entre la pointe Bigsby et la baie Haswell, est parallèle au contact intrusif avec la Formation de Karmutsen. La foliation s'estompe en s'éloignant du contact et le régime de contraintes contemporain de l'intrusion expliquerait la déformation.*

*Le complexe plutonique de type porphyrique de l'Éocène ou de l'Oligocène précoce observé dans le tiers sud-est de l'île Lyell comprend du basalte à clinopyroxène aphyrique, de l'andésite à phénocristaux de feldspath, de la dacite et de la syénite, ainsi que des phases stratifiées d'andésite tardive amygdaloïdes, en intrusion séquentielle dans des volcanoclastites tertiaires de composition intermédiaire. Diverses structures subverticales de direction nord-nord-ouest à nord-nord-est sont abondantes et distinctives, en l'occurrence les contacts intraphases, les dykes synplutoniques, les diaclases ainsi que les zones de fracturation et de trituration.*

---

[1] Contribution to Frontier Geoscience Program

[2] Department of Geology, University of Western Ontario, London, Ontario N6A 5B7

[3] Department of Geology and Geophysics, University of Calgary, 2500 University Drive N.W., Calgary, Alberta T2N 1N4

## INTRODUCTION

Recent mapping in the Queen Charlotte Islands and geochronometric studies have defined Middle to Late Jurassic and middle to late Paleogene plutonic suites (Sutherland Brown, 1968; Young, 1981; Anderson and Greig, 1989; Anderson and Reichenbach, 1991; Lewis et al., 1991). Geological setting, finer grain size, unfoliated and homogeneous character of individual plutons, small size (commonly á 20 $km^2$), orthopyroxene, common miarolitic cavities, seriate texture, intrusive relations, and age distinguish the Tertiary Kano plutonic suite (KPS) from the Jurassic San Christoval (SCPS) and Burnaby Island plutonic suites (Anderson and Greig, 1989; Anderson and Reichenbach, 1991; Lewis et al., 1991). Mapping in 1991 sought to: 1) further examine parts of the eastern margins of the San Christoval plutonic suite in Graham and Moresby islands; and 2) map the nature and distribution of suspected Tertiary igneous rocks in southeastern Lyell Island (Fig. 1). Extensive exposures along coastlines and logging roads facilitated mapping on Lyell Island. The work was prompted by the imminent infill of the logging roads and loss of these critical exposures.

## EASTERN MARGINS OF SAN CHRISTOVAL PLUTONIC SUITE (SCPS)

The eastern margin of San Christoval plutonic suite was examined along Van Inlet in southwestern Graham Island and between Bigsby Point and Haswell Bay in eastern Moresby Island. The Graham Island locality indicates the San Christoval plutonic suite extends farther east than previously recognized. A 0.5-1.5 km zone of well-foliated plutonic rock and narrower, more discontinuous zone of deformed Karmutsen Formation volcanic country rock extend along much of the eastern margin of San Christoval plutonic suite in eastern Moresby Island.

Along the shores of Van Inlet, the contact between the northern part of San Christoval plutonic suite and the Tertiary Kano pluton is well bracketed but not exposed. Lack of foliation in the biotite-hornblende (quartz) monzodiorite of San Christoval plutonic suite along Van Inlet distinguishes it from San Christoval plutonic suite in Rennell Sound which contains widespread but scattered north-trending mineral foliation (Anderson and Greig, 1989). An exception is rare subvertical, north-trending mafic schlieren at the mouth of Van Inlet which may be related to the heterogeneous Hunter Point-Kindakun Point diorite complex (Anderson and Greig, 1989).

Reconnaissance of the Van Inlet shoreline confirms the speculation by Anderson and Greig (1989) that the San Christoval plutonic suite-Kano plutonic suite contact in Van Inlet occurs about 3 km farther east than that inferred by Sutherland Brown (1968). The Kano plutonic suite-San Christoval plutonic suite contact continues northwest to the eastern shore of Givenchy Anchorage. However, the marginal phases of the Tertiary Kano pluton differ at the two localities. At Van Inlet, an unaltered, fine- to medium-grained, leucocratic hornblende-biotite quartz monzonite occurs along the margin of the Kano pluton. At Givenchy Anchorage, heterogenous fine- to medium-grained equigranular hornblende-biotite quartz monzodiorite and diorite with acicular hornblende form the marginal phases for the Tertiary pluton.

The eastern margin of San Christoval plutonic suite between Bigsby Point and Haswell Bay is typical of the structural and plutonic styles developed along much of the pluton's margin in eastern Moresby Island and Woodruff Bay (Anderson, 1988; Anderson and Greig, 1989). Two varieties of intrusive contact occur.

Most commonly, San Christoval plutonic suite at the contact consists of unfoliated quartz diorite containing 5% or less oblate to prolate mafic inclusions (20 cm or less in size) which have flattening ratios as great as 10:1:1. The flattened inclusions defined a closely spaced foliation which is concordant with the intrusive contact with massive Karmutsen Formation basalt. Foliation decreases in intensity within 1.5 km of the contact along the De La Beche Inlet transect.

At least one segment of the contact is faulted. A northwest-trending fault extends from an unnamed bay north of De la Beche Island to Stevenson Bay; well foliated San Christoval plutonic suite quartz diorite shows no increase in

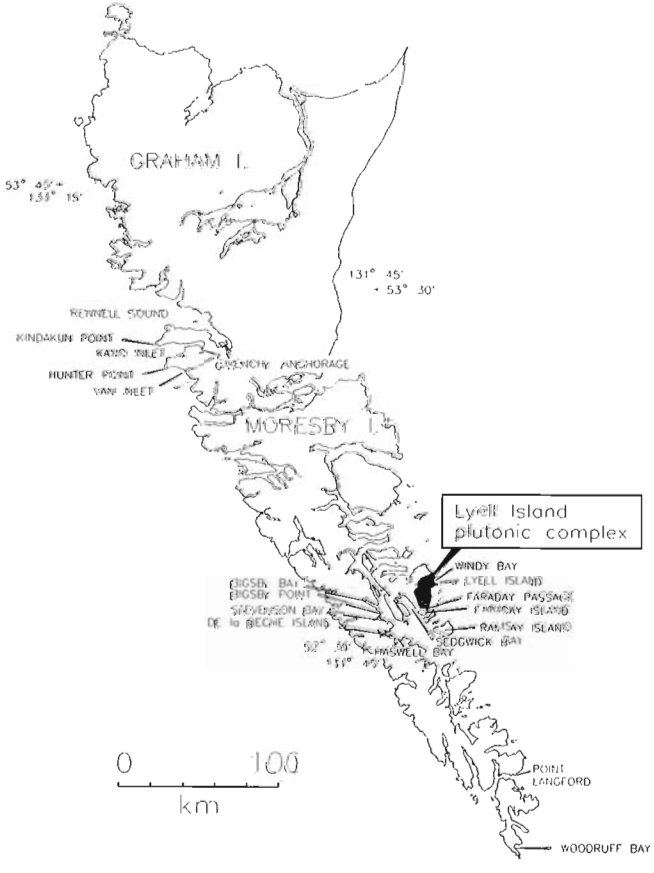


**Figure 1.** Location map for localities and study area discussed in text.

foliation intensity towards the inferred fault contact with apparently unaltered pillowed lava breccia of the Karmutsen Formation. The fault diminishes in importance to the north-northwest in Stevenson Bay where only brittle calcite-, quartz-, and epidote-filled fracture zones were developed in the Karmutsen Formation and no apparent juxtaposition of units occurred across the lineament.

Another variety of intrusive contact features 100-250 m wide migmatite zones developed between weakly foliated, inclusion-poor San Christoval plutonic suite quartz diorite at the intrusion's margin and Karmutsen Formation amphibolite. The migmatite comprises alternating, thin and irregular, leucodiorite and amphibolite layers. Rare, coarse agmatite is developed near Bigsby Point. Commonly the amphibolite will preserve a well-developed foliation which extends at least 200 m from the contact to form a structural as well as metamorphic aureole concordant with the contact.

## TERTIARY LYELL ISLAND PLUTONIC COMPLEX (LIPC) OF THE KANO PLUTONIC SUITE

The distribution of Lyell Island plutonic complex sketched by Anderson and Greig (1989) and Souther and Jessop (1991) refined the previous mapping by Sutherland Brown (1968) that indicated that the eastern half of the island was dominated by porphyritic hypabyssal equivalents of the Masset Formation (Sutherland Brown's unit TMd). The largely porphyritic, heterogeneous mafic to felsic igneous complex underlies at least 20 km$^2$ in southeastern Lyell Island and probably represents a high level, porphyritic plutonic root to the mantling Tertiary volcanics (Sutherland Brown, 1968; Anderson and Greig, 1989; Souther and Jessop, 1991; Souther, 1992).

### *Distribution and composition*

At least three extensive (Fig. 2) and three locally important phases make up the complex (Fig. 3). In decreasing order of area the mappable phases are: greenish-grey (hornblende-) plagioclase andesitic porphyry; buff to white dacitic quartz-plagioclase-porphyry; and dark greenish-grey aphyric basaltic andesitic intrusions. Flow-layered rhyolitic, syenitic alkali-feldspar porphyritic and flow-layered amygdaloidal andesitic dyke phases are locally important but are not mappable.

Figure 3 indicates where the phases are most common and dominant. However, the map oversimplifies the heterogeneity of the complex; everywhere dykes and small intrusions of other phases uncommonly to commonly occur within the main outcrop area of a given phase.

Andesitic porphyry is common in the southeastern and northeastern parts of the Lyell Island plutonic complex. It is typically dark greenish-grey, phenocryst-rich (locally the

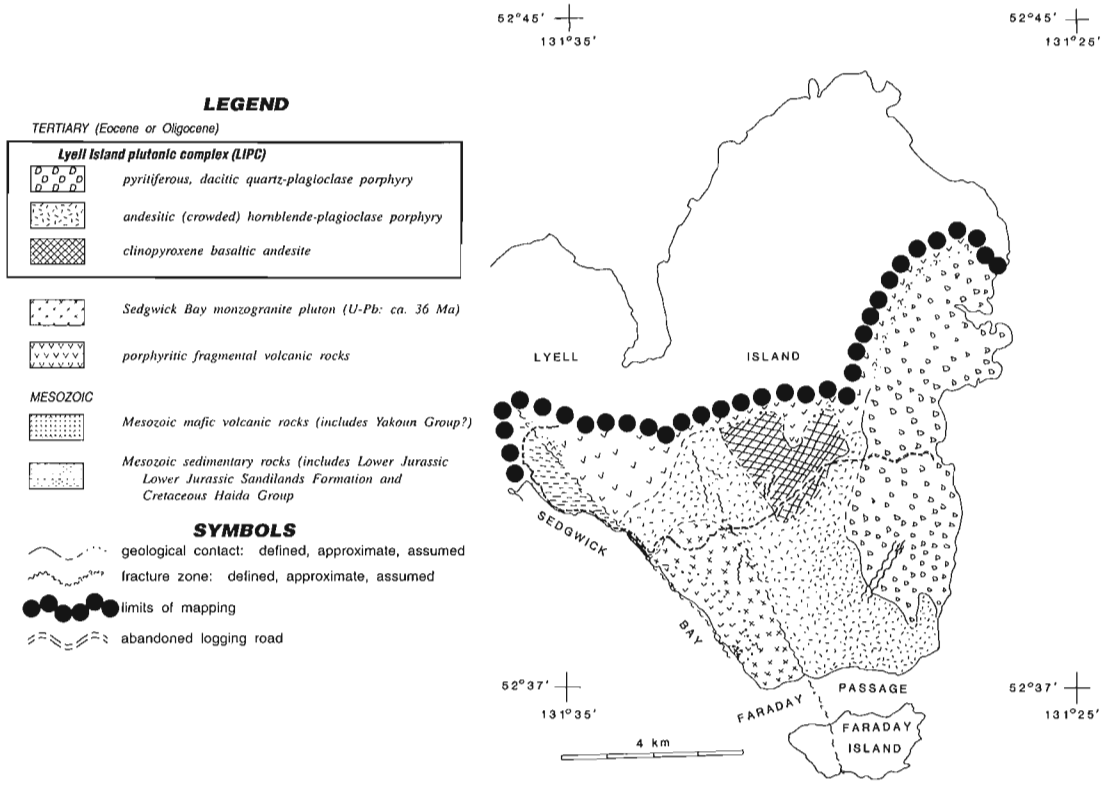


**Figure 2.** Distribution of plutonic phases in the Lyell Island plutonic complex (LIPC).

andesite is a "crowded" porphyry) and xenolith-poor. Plagioclase dominates hornblende in phenocryst abundance. Rare melanocratic inclusions appear to be fine grained, mafic analogues of the host porphyry.

Dacitic plagioclase-quartz porphyry is common in the southeastern part of Lyell Island plutonic complex and is well exposed along the southeastern shoreline of Lyell Island, south of Windy Bay. It is characterized by buff weathering, common pyrite content, and siliceous nature; aphyric varieties are common. Hornblende is a rare phenocryst phase. Pyrite is disseminated and occurs (rarely with bornite) along fractures in the dacite. Oxidation of the pyrite results in a locally characteristic and extensive rusty brown discolouration. Epidote alteration of the unit is widespread and distinctive.

Dark green, aphanitic basaltic andesite is most common in the northwestern part of the complex but also occurs as small intrusions in the southern part of the intrusion. Locally it is clinopyroxene-phyric but aphyric varieties dominate yet characteristically retain groundmass clinopyroxene.

Locally important but areally insignificant dyke phases include: white aphanitic to flow-layered rhyolitic dykes; flow-layered and amygdaloidal, pale green andesitic dykes; and syenitic alkali-feldspar porphyry. The pale green, amygdaloidal, and flow-layered andesite is the most widespread of these dyke phases but the syenitic alkali-feldspar porphyry is the phase which most resembles a nearby, well-dated phaneritic plutonic member of Kano plutonic suite, the Sedgwick Bay monzogranite pluton to the southwest of Lyell Island plutonic complex.

## *Intrusive relations*

### External intrusive relations

Mesozoic and Tertiary strata host phases of Lyell Island plutonic complex. At one locality along the eastern coast of Sedgwick Bay, green, epidotized plagioclase porphyry (Yakoun Group?) is intruded by fresh hornblende-plagioclase porphyry resembling the andesitic porphyry phase. Highly fractured, thin-bedded, limy shale (Sandilands Formation?) east of the Sedgwick Bay fracture zone is intruded locally by white, felsic, aphanitic dykes which may be related to the late rhyolitic phases of Lyell Island plutonic complex.

Tertiary country rock is most common along the northwestern and northern limits to the map area and at the highest elevations mapped; the contact probably marks the roof of the intrusion. Volcanic-block breccia and conglomerate characterized by pale mauve volcanic groundmass and pale green or maroon porphyry fragments are the most common hosts. The country rocks are distinctive from porphyritic intrusive phases and are intruded by two of

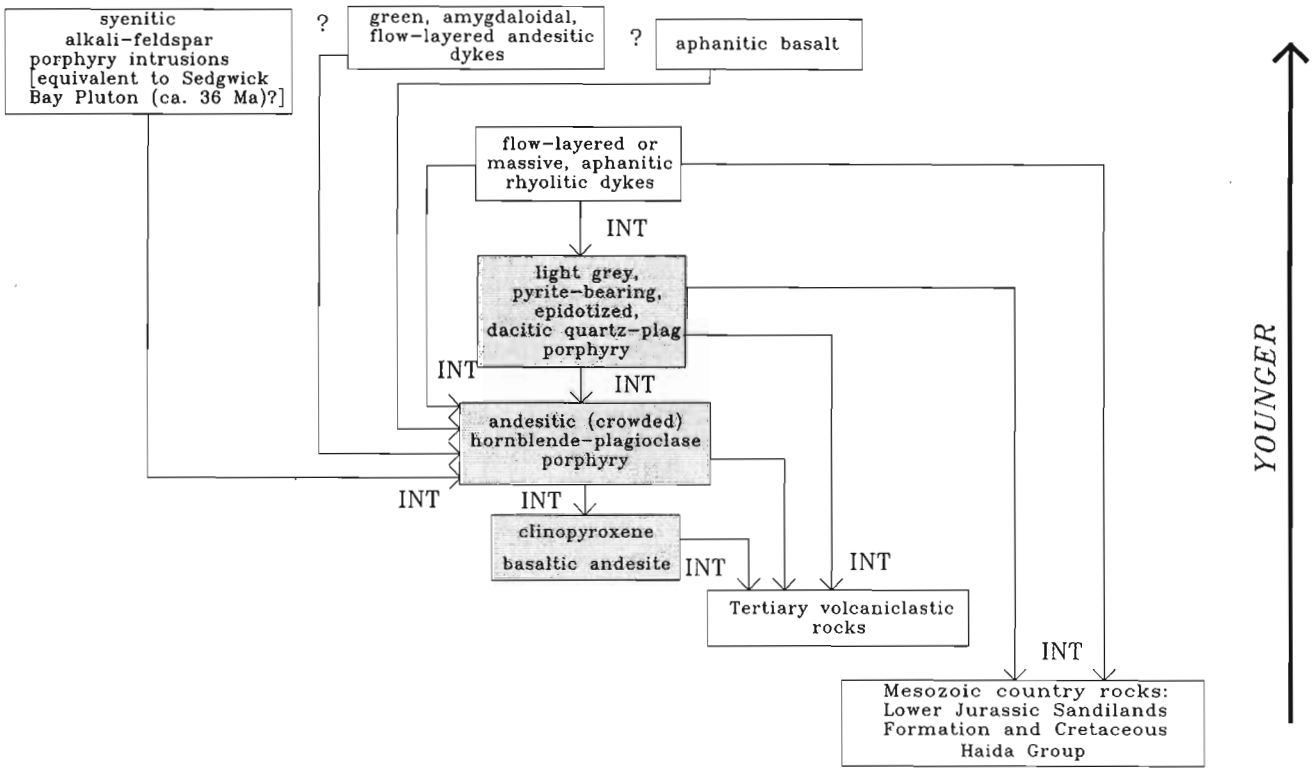


**Figure 3.** Summary of intrusive relations in the Lyell Island plutonic complex. Arrows extend from youngest to oldest geological unit; apparent anomalies in mafic to felsic intrusive sequence suggest contemporaneity of intrusive pulses. Shaded boxes indicate mappable plutonic phases (see Fig. 2).

the three mappable phases (Fig. 3). Potassium-argon dates for Tertiary volcanic whole rocks to the south on Ramsay Island range in age from 41 to 36 Ma (Hyndman and Hamilton, 1991).

### Intraplutonic intrusive relations

The mappable phases of Lyell Island plutonic complex most commonly, but not invariably, intruded in a mafic to felsic sequence (Fig. 4). Narrow (2-5 cm) selvedges, apophyses and rarely, inclusions of host rock define the relative intrusive sequence. Internal contacts are subvertical and commonly trend northeast or north-northeast (Fig. 4). As with the distribution map (Fig. 2) of the plutonic phases, the intrusive sequence shown in Figure 3 oversimplifies the complex intrusive relations; rare contradictory intrusive relations are seen. These anomalies indicate contemporaneity or error in correlation among mappable phases that are difficult to discriminate at some localities.

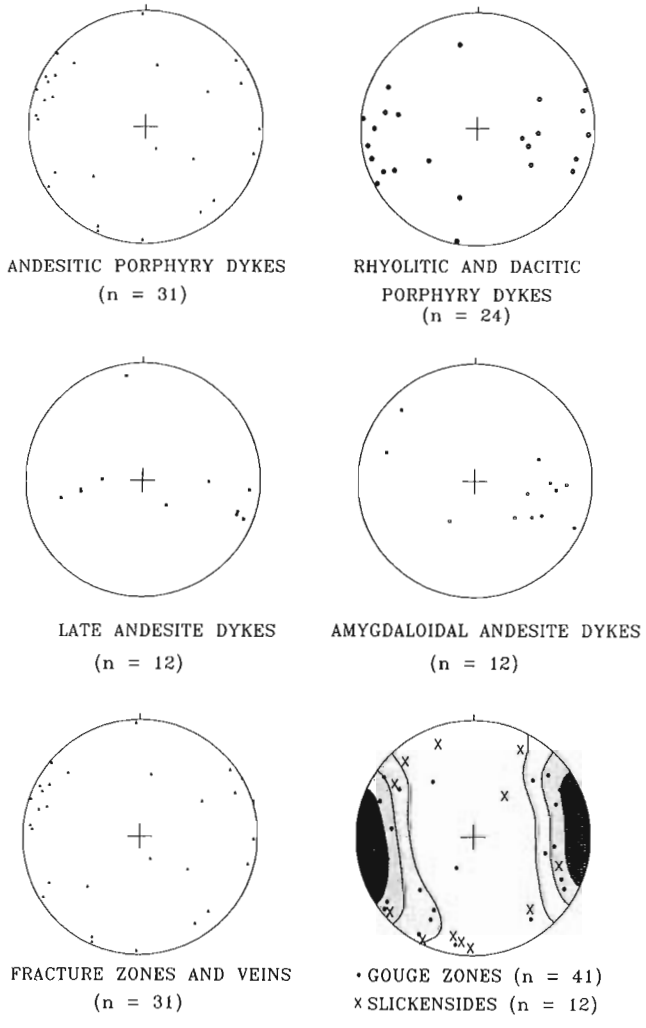


**Figure 4.** Equal area stereonet plots of internal intraphase contacts, dykes, fracture and gouge zones, and slickensides in Lyell Island plutonic complex.

Intraphase intrusive breccias are uncommon but are important to distinguish from the Tertiary volcaniclastic country rock of Lyell Island plutonic complex. Close similarity of monolithic fragments with groundmass for the intrusive breccias and steep contacts of the breccias with unbrecciated host are the best criteria. Formation of intrusive breccia was an important component in the evolution of Lyell Island plutonic complex.

### *Structure*

A striking characteristic of Lyell Island plutonic complex is the abundance and concordance of subvertical, north-northwest- to north-northeast-trending intraphase contacts, synplutonic dykes, joints, and fracture and gouge zones (Fig. 4). This structural style is analogous to that of intraphase contacts in the Eocene Carpenter Bay pluton at Point Langford (Anderson, 1988) and of the trend of Eocene porphyry dykes (Souther and Jessop, 1991; Anderson and Reichenbach, 1991).

Fracture and gouge zones are common throughout Lyell Island plutonic complex, are not restricted to a particular phase but are most abundant in the northwest corner of the complex. They locally developed along interphase contacts to the extent that intrusive relations are obscured. Well-developed fracture zones comprise closely-spaced fractures that are either unfilled or sealed by calcite or quartz veins. One fracture zone on Lyell Island north of the northeastern tip of Faraday Island is a fossil hydrothermal zone (Souther and Jessop, 1991) containing botryoidal quartz partly filling the north-northeast-trending and east-trending fracture sets. Gouge zones are 0.2 to 30 m thick, are traceable along strike up to 0.5 km, and are most common in the northwestern part of the complex. Slickensides are rare and of variable trend but everywhere subhorizontal or gently plunging (Fig. 4).

### Relationship of plutonism to Faraday Passage and Sedgwick Bay fracture zones

Two regional, north-northwest-trending fracture zones, the Sedgwick Bay fracture zone to the west and the Faraday Passage fracture zone to the east follow obvious lineaments on southeastern Lyell Island east of Sedgwick Bay and on Faraday Island. Typically the topographic depressions marking these lineaments are the locus for anastomosing subvertical fractures; few slickensides or other kinematic indicators occur. Both fracture zones involve the early Oligocene (Anderson and Reichenbach, 1991) Sedgwick Bay pluton and the Sedgwick Bay fracture zone appears to be part of the complex boundary between the Lyell Island plutonic complex and Sedgwick Bay pluton. The greater abundance of the gouge and fracture zones in northwest Lyell Island plutonic complex may mark the northwestern extent of the Faraday Passage fracture zone which bounds the eastern margin of the Sedgwick Bay pluton (Fig. 2).

### *Age*

Structural and geological relations and possible lithological similarities between the syenitic alkali-feldspar porphyry and the early Oligocene Sedgwick Bay pluton (ca. 36 Ma; Anderson and Reichenbach, 1991) suggest an Eocene and/or early Oligocene age for the complex. The north-northwest to north-northeast trend of Lyell Island plutonic complex internal contacts, faults and gouge zones and synplutonic dykes are nearly concordant with, and analogous to, the Carpenter Bay plutonic complex. North-trending dykes (Souther and Jessop, 1991), dated at ca. 41-55 Ma (Anderson and Reichenbach, 1989; Souther and Jessop, 1991), and parallel internal contacts of co-spatial phases of the Carpenter Bay pluton at Point Langford (ca. 46 Ma; Anderson and Reichenbach, 1991) suggest an Eocene age for easterly directed extension in southeastern Moresby Island.

If the syenitic alkali-feldspar porphyry phase of Lyell Island plutonic complex is a hypabyssal equivalent of the early Oligocene Sedgwick Bay monzogranite pluton, the youngest phases of Lyell Island plutonic complex may be post-Eocene. Potassium-argon studies (by J.G. Souther and J.C. Roddick) and U-Pb analyses on zircon (part of the present study) are underway to refine the age of Lyell Island plutonic complex.

## DISCUSSION

New mapping extends the distribution of Middle Jurassic San Christoval plutonic suite eastward to the eastern end of Van Inlet, suggests the foliated eastern margin of San Christoval plutonic suite (and deformed Karmutsen Formation country rocks) continues south from Bigsby Point to Haswell Bay and permits the first description of a heterogeneous, porphyritic plutonic complex in southeastern Lyell Island.

A 0.5-2 km wide foliated and rarely migmatitic zone marking the eastern margin of the San Christoval Range segment of San Christoval plutonic suite is traceable from Bigsby Inlet south to the Woodruff Bay segment of San Christoval plutonic suite and is concordant with the orientation of the pluton-country rocks contact. These features apparently do not occur in the northern segment of San Christoval plutonic suite in the Rennell Sound and Kano and Van inlets area where a more widespread and consistently north-trending but less intensely developed mineral foliation is characteristic. In the two southern segments, strain may have developed within the eastern marginal phase of San Christoval plutonic suite as intrusion continued in the interior, medial part of the batholith. The strain is recorded in the flattened mafic inclusions which rest in a massive, equigranular hornblende quartz diorite groundmass. Deformation along the eastern margin of San Christoval plutonic suite apparently developed subsequent to intrusion and incorporation of mafic inclusions but before the magma was of sufficient crystallinity to sustain and preserve mineral fabric.

The Tertiary Lyell Island plutonic complex is unusual among the Kano plutonic suite in comprising entirely porphyritic (rarely seriate) rocks; it is devoid of equigranular, coarser grained plutonic phases. Lyell Island plutonic complex is unlike the Carpenter Bay plutonic complex, a dyke and plutonic complex farther south where porphyritic dykes are co-spatial and coeval with the large (12 $km^2$) equigranular Carpenter Bay pluton. Also unlike the Carpenter Bay plutonic complex, Lyell Island plutonic complex is flanked to the north, east and south by slightly older but probable Tertiary volcanic rocks (see Souther, 1992) and is bounded along its western margin by fracture zones. The Lyell Island plutonic complex probably represents the magmatism at an intermediate crustal level between deeper seated Kano plutonic suite plutonism and the Tertiary volcanic rocks at surface and marks the centre for this localized Tertiary volcanism. If the porphyry complex is Eocene, the regional fracture zones, later reactivated and partly annealed during intrusion of the 36 Ma Sedgwick Bay pluton, may have facilitated down-to-the-east fault displacements during localized Eocene extension which preserved the porphyry complex.

## SUMMARY

The eastern margin of Middle Jurassic San Christoval plutonic suite (SCPS) is shown to extend farther east in the northern segment of the suite. The southern segments of the eastern margin of San Christoval plutonic suite from Bigsby Bay to Woodruff Bay, is characterized by a deformed zone (0.5-2 km wide) comprising planar fabric in the plutonic and country rocks and probably records syn-intrusion strain.

An extensive Eocene to early Oligocene? porphyry plutonic complex, the Lyell Island plutonic complex (LIPC), consists of sequentially intruded mafic, intermediate and felsic phases which crosscut texturally and compositionally similar Tertiary volcaniclastic rocks. Abundant and concordant subvertical, north-northwest- to north-northeast-trending intraphase contacts, synplutonic dykes, joints, and fracture and gouge zones are distinctive. Lyell Island plutonic complex may have been preserved by northwest-trending, synvolcanic extension faults which were partly annealed by intrusion of the late Oligocene Sedgwick Bay pluton and re-activated as regional fracture zones involving that pluton.

## ACKNOWLEDGMENTS

Jim Haggart is thanked for laying on the superb logistical support which greatly expedited our work; his project 870070 funded the field work reported herein. Audrey Putterill, our expediter, conscientiously stood by the radio through good signals and bad to keep us in touch with the outside world. Bryan Pullman ably piloted us through shoals and schools of dolphins during the latter stages of the project. Tracy Feeney accurately produced the AutoCAD image for the outline of the Queen Charlotte Islands.

# REFERENCES


**Anderson, R.G.**
1988: Jurassic and Cretaceous-Tertiary plutonic rocks on the Queen Charlotte Islands, British Columbia; in Current Research, Part E; Geological Survey of Canada, Paper 88-1E, p. 213-216.

**Anderson, R.G. and Greig, C.J.**
1989: Jurassic and Tertiary plutonism in the Queen Charlotte Islands, British Columbia; in Current Research, Part H; Geological Survey of Canada, Paper 89-1H, p. 95-104.

**Anderson, R.G. and Reichenbach, I.**
1989: A note on the geochronometry of Late Jurassic and Tertiary plutonism in the Queen Charlotte Islands, British Columbia; in Current Research, Part H; Geological Survey of Canada, Paper 89-1H, p. 105-112.
1991: U-Pb and K-Ar framework for Middle to Late Jurassic (172-≥158 Ma) and Tertiary (46-27 Ma) plutons in Queen Charlotte Islands, British Columbia; in Evolution and Hydrocarbon Potential of the Queen Charlotte Basin, British Columbia, (ed.) G.J. Woodsworth; Geological Survey of Canada, Paper 90-10, p. 59-87.

**Hyndman, R.D. and Hamilton, T.S.**
1991: Cenozoic relative plate motions along the northeastern Pacific margin and their association with Queen Charlotte area tectonics and volcanism; in Evolution and Hydrocarbon Potential of the Queen Charlotte Basin, British Columbia, (ed.) G.J. Woodsworth; Geological Survey of Canada, Paper 90-10, p. 107-126.

**Lewis, P.D., Haggart, J.W., Anderson, R.G., Hickson, C.J., Thompson, R.I., Dietrich, J.R., and Rohr, K.M.M.**
1991: Triassic to Neogene geological evolution of the Queen Charlotte region; Canadian Journal of Earth Sciences, v. 28, no. 6, p. 854-869.

**Souther, J.G.**
1992: Geology of central Lyell Island, Queen Charlotte Islands, British Columbia (103B); in Current Research, Part A; Geological Survey of Canada, Paper 92-1A, p. 343-350.

**Souther, J.G. and Jessop, A.M.**
1991: Dyke swarms in the Queen Charlotte Islands, British Columbia, and implications for hydrocarbon exploration; in Evolution and Hydrocarbon Potential of the Queen Charlotte Basin, British Columbia, (ed.) G.J. Woodsworth; Geological Survey of Canada, Paper 90-10, p. 465-487.

**Sutherland Brown, A.**
1968: Geology of the Queen Charlotte Islands, British Columbia; British Columbia Department of Mines and Petroleum Resources, Bulletin 54, 226 p.

**Young, I.F.**
1981: Structure of the western margin of the Queen Charlotte Basin, British Columbia; M.Sc. thesis, University of British Columbia, Vancouver, British Columbia.


---

Geological Survey of Canada Project 870070

# A kinematic analysis of the Beresford Inlet fault zone, Lyell Island, Queen Charlotte Islands, British Columbia[1]

**Ian J. Foreman[2]**
**Cordilleran Division, Vancouver**

*Foreman, I.J., 1992: A kinematic analysis of the Beresford Inlet fault zone, Lyell Island, Queen Charlotte Islands, British Columbia; in Current Research, Part E; Geological Survey of Canada, Paper 92-1E, p. 125-131.*

***Abstract***

*Beresford Inlet is a north-northwest striking lineament that cuts the southwest peninsula of Lyell Island and is created by the Beresford Inlet fault zone. It has been interpreted as a main splay of the Louscoone Inlet fault zone. Within the Beresford Inlet fault zone, two distinct schistosity trends have been recognized: the Beresford trend, parallel with the inlet, and an earlier trend that is oblique to the inlet. Three separate phases of movement have been documented, but the magnitude of offsets along the Beresford Inlet fault zone could not be determined, because offset markers in the immediate area of the inlet were not found. The presence of kinematic indicators with opposing movement sense in several outcrops suggest that the Beresford Inlet fault zone has undergone a history of multiple deformation.*

***Résumé***

*L'anse de Beresford est un linéament de direction nord-nord-ouest qui recoupe la péninsule du sud-ouest de l'île de Lyell et qui correspond à la zone de failles de Beresford Inlet. On la considère comme un segment divergent majeur de la zone de failles de Louscoone Inlet. Au sein de la zone de failles de Beresford Inlet, deux orientations de la schistosité ont été reconnues: la direction de Beresford, parallèle à l'anse, et une direction antérieure oblique à l'anse. Trois phases de mouvement distinctes ont été relevées, mais l'ampleur des rejets le long de la zone de failles de Beresford Inlet n'a pu être determinée, en raison de l'absence de marqueurs dans la zone proche de l'anse. La présence d'indices cinématiques à sens de mouvement opposés au sein de plusieurs affleurements porte à croire que cette zone de failles a subi plusieurs phases de déformation.*

---

[1] Contribution to Frontier Geoscience Program

[2] Department of Geological Sciences, Queens University, Kingston, Ontario, K7L 3N6

## INTRODUCTION

Beresford Inlet is a north-northwest striking 6 km long lineament that dominates the southwest peninsula of Lyell Island, Queen Charlotte Islands (Fig. 1). Within the inlet is the Beresford Inlet fault zone (BIFZ).

Sutherland Brown (1968) interpreted the Beresford Inlet fault zone as a main splay of the Louscoone Inlet fault zone (LIFZ) (Fig. 1), which he linked with the Rennell Sound fault zone (Fig. 1). He suggested that approximately 10 km of right-lateral movement had occurred on the Beresford splay and that the vertical displacement could be several hundred metres. He interpreted the region between Beresford Inlet and the main strand of the Lousconne Inlet fault zone, located 5 km to the east, as a graben, implying that the displacement along the Beresford splay should be east-side down.

Yorath and Chase (1981) re-interpreted the tectonic history of the Queen Charlotte Islands by treating the Rennell Sound and Louscoone Inlet fault zones as separate entities and suggesting that the Sandspit fault (Fig. 1) is an offset continuation of the Louscoone Inlet fault zone. More recently, on the basis of detailed mapping, Lewis (1991) modified Yorath and Chase's model and subdivided the region immediately to the south of Lyell Island into three domains based on structural styles. Beresford Inlet would loosely fit into domain B of this classification, which contains similar trends within the Karmutsen Formation, and has few offset markers. According to Lewis (1991), the Louscoone Inlet fault system has dextral strike-slip offsets of at least 10-20 km in its southern portion, but this amount decreases to zero towards the north, at the intersection with the Rennell Sound fault zone.

As a result of this work, the present project was designed to investigate the kinematic significance of fault-related structures in Beresford Inlet and to determine the sense and , if possible, the magnitude of offset within the fault zone. This was done by collecting structural and petrographic data from outcrops along the shoreline of the inlet while the author was a attached to the field party of M. Sanborn-Barrie (see Sanborn-Barrie, 1992).

## REGIONAL GEOLOGY

The southern Darwin Sound and western Lyell Island area (Fig. 1) was mapped previously on a regional scale by Sutherland Brown (1968). Approximately 30% of the southern

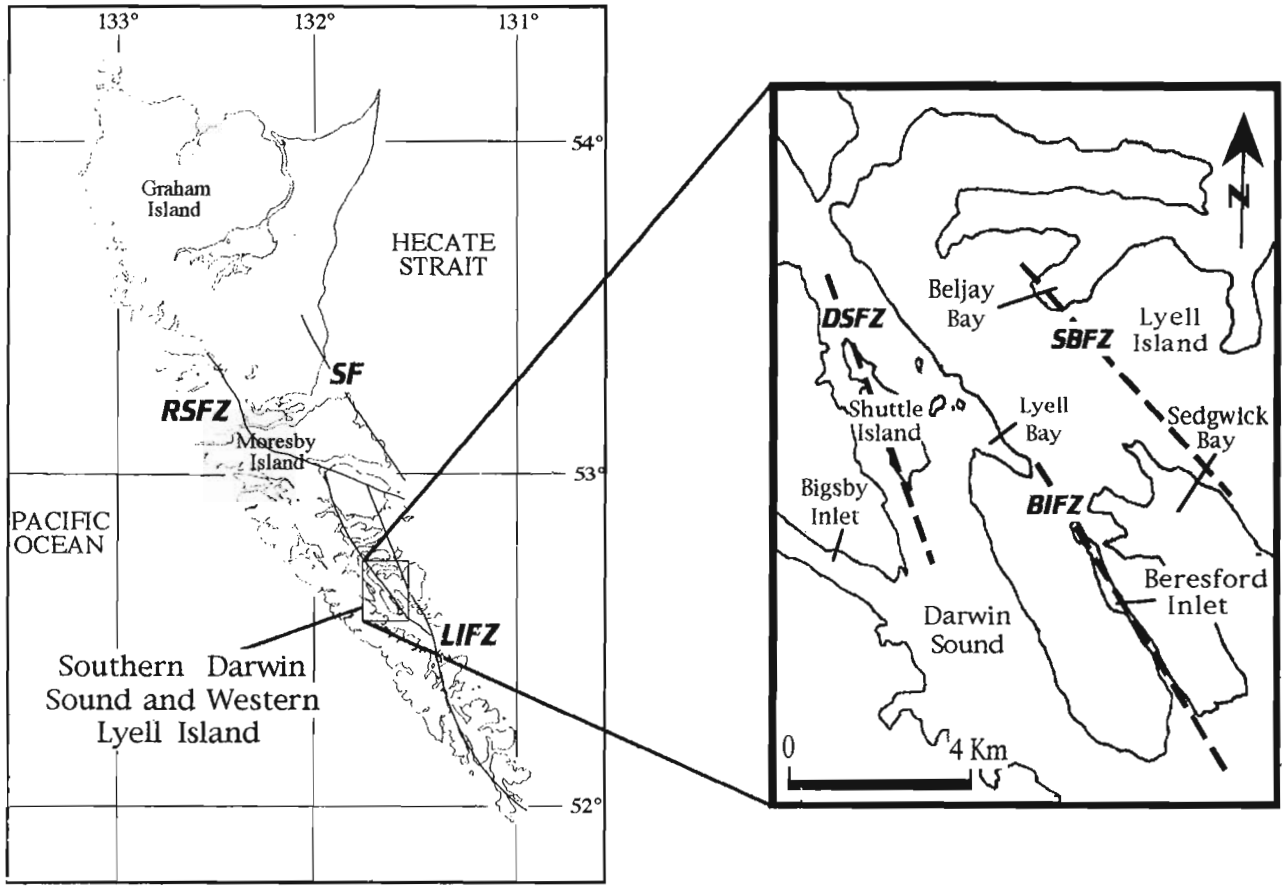


**Figure 1.** Location map of the southern Darwin Sound and western Lyell Island area. The faults shown are: RSFZ = Rennell Sound fault zone; SF = Sandspit fault; LIFZ = Louscoone Inlet fault zone; DSFZ = deformation zone in southern Darwin Sound; BIFZ = Beresford Inlet fault zone; and SBFZ = Sedgwick Bay fault zone.

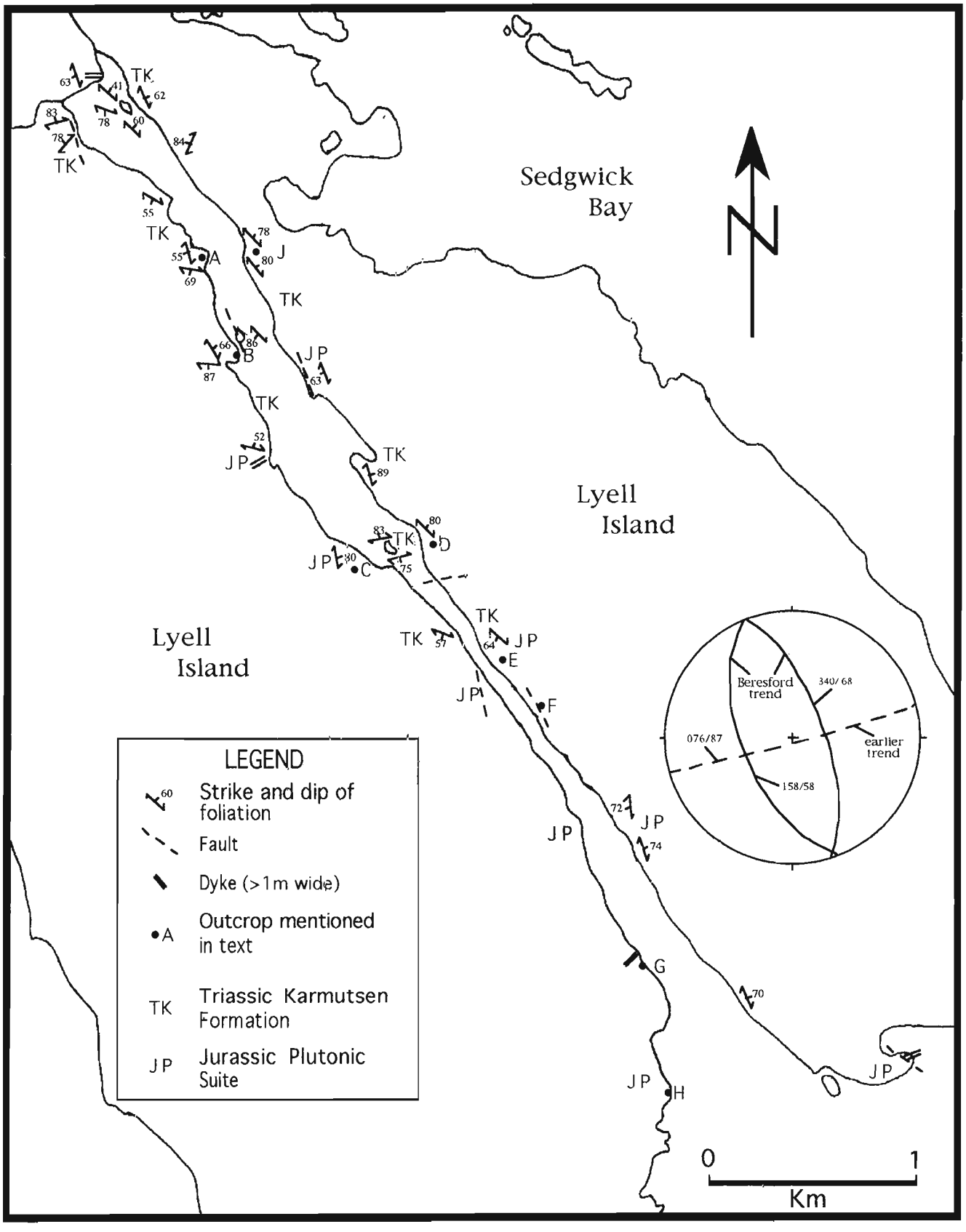


**Figure 2.** Detailed geological map of Beresford Inlet, SW Lyell Island, Queen Charlotte Islands. The stereonet shows the two dominant structural trends termed the Beresford trend and the earlier trend.

Darwin Sound and western Lyell Island area is underlain by plutonic rocks (Sanborn-Barrie, 1992). These are primarily diorites and quartz diorites of Middle to Late Jurassic age and minor felsic intrusions of Cretaceous age (Sanborn-Barrie, 1992). Tertiary dykes and sills are common throughout the southern Darwin Sound and western Lyell Island area.

On the west side of Darwin Sound, within Bigsby Inlet (Fig. 1), spectacularly exposed pillowed basalts of the Karmutsen Formation are preserved at prehnite-pumpellyite grade of regional metamorphism. Younging and regional dip of the Karmutsen Formation are both to the west. In contrast, highly deformed Triassic and Lower Jurassic sedimentary strata on the east side of Darwin Sound young consistently to the east (Sanborn-Barrie, 1992). On the west point of Lyell Bay (Fig. 1), rocks of the Karmutsen Formation are at greenschist grade.

During detailed mapping, mylonitic rocks and shear zones have been identified in Beljay Bay (Fig. 1) and western Lyell Island (Sanborn-Barrie, 1992 and Souther, 1992). These are inferred to be related to a structural zone extending southeast to Sedgwick Bay (Fig. 1) (Sanborn-Barrie, 1992) that has been termed the Sedgwick Bay fault zone (Souther, 1992). Souther (1992) concluded that major transcurrent movement has occurred within the up to half a kilometre wide Sedgwick Bay fault zone.

In addition, Sanborn-Barrie (1992) found evidence for a major ductile deformation zone through Darwin Sound. Movement within this zone is thought to be responsible for the juxtaposition of differing metamorphic grades and younging directions of the Karmutsen Formation and the Triassic and Lower Jurassic sedimentary strata across Darwin Sound. On Shuttle Island (Fig. 1), the deformation zone consists of low-angle, reverse shear zones with local normal and transcurrent structures also observed (Sanborn-Barrie, 1992). Sanborn-Barrie (1992) suggested that this zone may be part of the Louscoone Inlet fault system, although structures throughout the sound appear to represent earlier oblique-slip movement rather than the major extensional faulting seen to the south, in the Burnaby Island area (Lewis, 1991).

Beresford Inlet lies between the Sedgwick Bay fault zone and the major ductile deformation zone in Darwin Sound. The recognition of these structural zones suggest that the region has undergone a complex structural history.

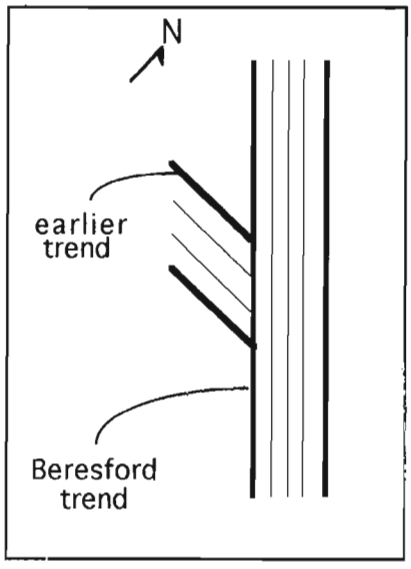


**Figure 3.** Schematic diagram showing the two dominant structural trends in Beresford Inlet.

## STRATIGRAPHY WITHIN BERESFORD INLET

The study area (Fig. 2) is underlain by two principle rock types: Triassic (Carnian) Karmutsen Formation and Jurassic plutonic rocks. Sedimentary rocks are found in minor amounts. All of the foliated rocks in the study area have a generic green appearance due to their deformation and weathering, and rock types are difficult to differentiate.

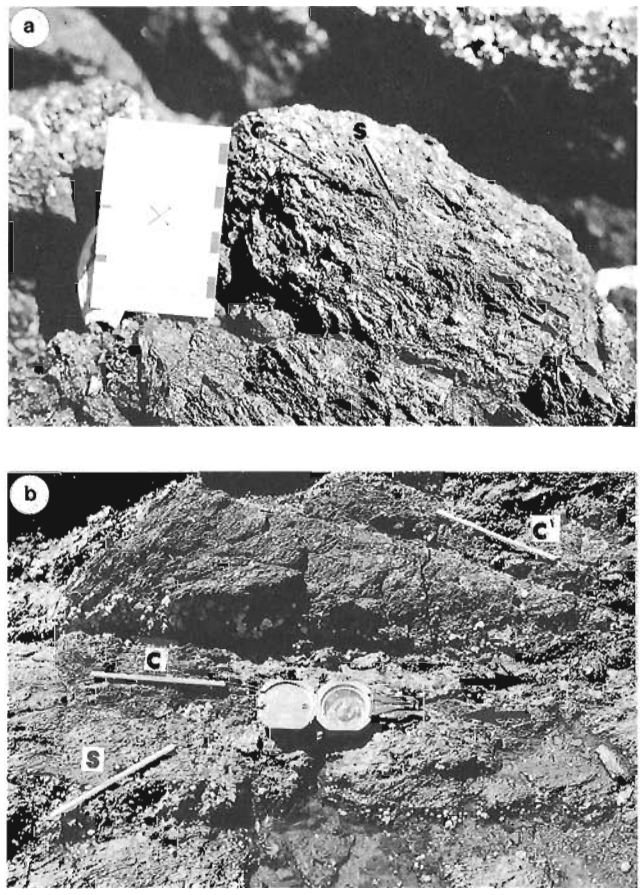


**Figure 4.** Mesoscopic kinematic indicators preserved in the Karmutsen Formation. **a)** S-C fabrics showing a sinistral sense of displacement (view to NE). **b)** S-C-C' fabrics showing dextral movement (view to SE). The pencils are approximately 16 cm long.

Exposure is excellent in the southern half of the inlet. North of the thinnest portion of inlet (Fig. 2), exposure is poor; fortunately, exposure improves towards the end of the inlet.

### Triassic Karmutsen Formation

In the field, the Karmutsen Formation was identified primarily by its colour index. Within the southern Darwin Sound area, the Karmutsen volcanic package is consistently mafic in composition, with colour index ranging from 35-50. All outcrops of the Karmutsen Formation in the study area show varying signs of strain and are predominantly schistose. The rocks are fine to medium grained with no more than 10% plagioclase phenocrysts up to 3 mm in length. In thin-section, plagioclase, chlorite, and epidote are the dominant minerals. A majority of the plagioclase phenocrysts have been sericitized, and chlorite makes up much of the groundmass. Epidote phenocrysts appear to have formed prior to deformation.

Many outcrops contain minor secondary calcite. Samples examined in thin section show pervasive silicification as evidenced by the anomalously high quartz content. Textures and mineralogy within the Karmutsen Formation suggest that the area has undergone greenschist grade metamorphism.

#### *Jurassic pluton*

The plutonic rocks within Beresford Inlet belong to the Beresford Complex of the Burnaby Island Plutonic Suite (BIPS) (Anderson and Greig, 1989; Anderson and Reichenbach, 1991). They have been dated by Anderson and Reichenbach (1991) as 158 ± 4 Ma. The most common rock type is a distinctive hornblende diorite. Where best preserved (outcrop C, Fig. 2), west of the southernmost island, the diorite contains 8-10 mm hornblende phenocrysts comprising about 5% of the rock. The medium grained groundmass has a colour index of 25.

The plutonic rocks are commonly deformed and can be distinguished from the Karmutsen Formation by their lower colour index and larger average grain size. Many samples have more than 5% quartz and should therefore be named quartz diorites.

At outcrop G (Fig. 2), the quartz diorite exhibits gneissic bands of alternating feldspar-rich and mafic layers. This was previously mapped by Sutherland Brown (1968) as syntectonic Jurassic migmatite but has now been grouped with the Jurassic plutonic suite which is consistent with mapping by Anderson and Greig (1989) and Sanborn-Barrie (1992).

#### *Triassic(?) sedimentary rocks*

Within the narrowest part of the inlet (outcrops E and F, Fig. 2), 20-50 cm xenoliths and 1-2 m slivers of sedimentary rock were found within diorite. These consist of limestone and graphitic argillaceous limestone and possibly represent altered fragments of the Sadler and Peril formations, respectively.

#### *Dykes*

Dykes of intermediate composition and varying greatly in orientation have intruded the foliated country rock throughout the inlet. They are probably of Tertiary age.

## STRUCTURES WITHIN BERESFORD INLET

All structures within Beresford Inlet appear to be fault-related and are associated with the Beresford Inlet fault zone, a narrow region of heterogeneous strain containing the Beresford fault.

Overall trends of the schistose planar fabric vary more than 100° throughout the inlet (Fig. 2) but two distinct trends can be identified: one between 310°-340°, parallel with the inlet, and the other between 70°-117°. For convenience, these have been termed the Beresford trend and the earlier trend, respectively (Fig. 3).

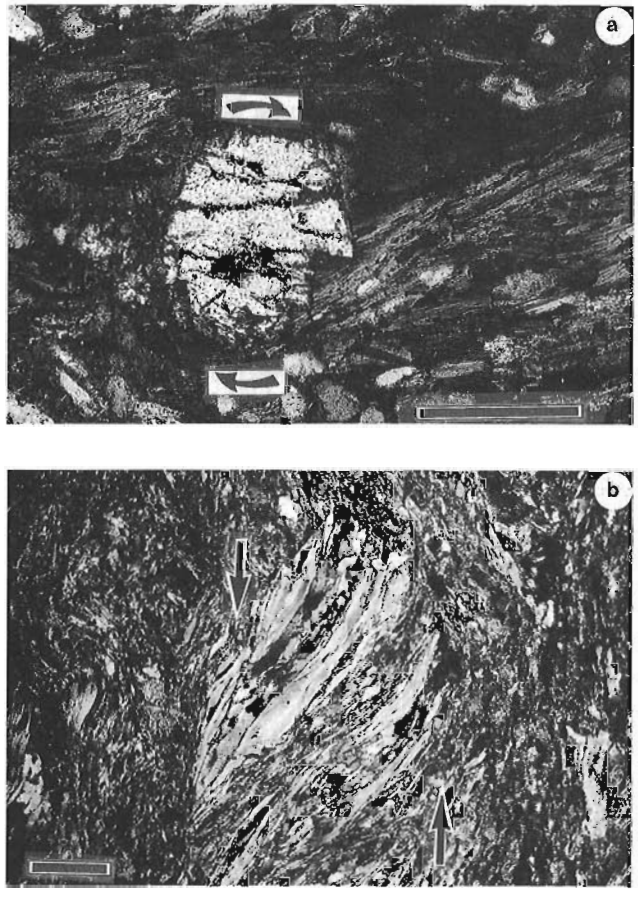


**Figure 5.** Microscopic kinematic indicators in thin sections of Karmutsen Formation samples. **a)** Rotated epidote phenocryst with chlorite forming 'delta' shape, indicating clockwise rotation. **b)** S fabrics preserved as muscovite showing left-side up. The scale bars are 0.5 mm.

The Beresford trend, which dominates the northeastern shore of the inlet, is represented by a very well developed, closely spaced schistosity that, in places, may have reworked (transposed) the earlier trend. Planar fabrics of the earlier trend are less well developed than those in the Beresford trend, and at several localities show a spaced cleavage with thin anastomosing shear zones surrounding blocks of massive fine grained diorite.

The earlier trend is also characterized by a steeply southeast plunging (66°-73°) weak to moderate mineral lineation. Locally, stretched quartz grains reach several millimetres in length while usually less than a millimetre wide. In contrast, the Beresford trend does not have a well preserved mineral lineation, and this may indicate that there has been more of a flattening component than previously thought (M. Sanborn-Barrie, pers. comm., 1991). Lineations observed vary both in trend (290°-020°) and plunge (17°-61°).

At two key localities (outcrops A and B, Fig. 2), the two contrasting trends can be seen in the same outcrop. In both cases, the earlier trend is preserved south of the Beresford trend and, where the two intersect, the later bends and even crosscuts the earlier trend. These crosscutting relationships confirm that the earlier trend predates the Beresford trend (Fig. 3).

Throughout the inlet mesoscopic fabrics provide kinematic indicators. These consist of well preserved S-C fabrics, asymmetric folds and kinks. S-C fabrics (and S-C-C' fabrics) tend to be best preserved in the Karmutsen Formation (Fig. 4a,b). At several different localities (i.e. outcrop D, Fig. 2), fabrics indicate opposite senses of ductile movement within the same outcrop, suggesting that there has been more than one phase of movement within the Bereford Inlet fault zone. In these cases, determination of the relative timing of movement is difficult. Dextral indicators are far more common and tend to be better preserved. This, combined with the fact that the earlier trend may have been deflected by dextral deformation (Fig. 3), would suggest that the sinistral movement was earlier and possibly of lesser significance.

**Figure 6.** An example of brittle dextral overprinting of a shear zone within the Jurassic plutonic rocks.

Microscopically, the fabrics are very similar. The best kinematic indicators are also found in the mafic volcanic Karmutsen Formation (outcrop J) and consist of rotated epidote phenocrysts which consistently have delta shapes (Fig. 5a). In other thin sections S-C fabrics are seen, as muscovite tends to be preserved as S fabrics (Fig. 5b). At two localities, well preserved microscopic indicators show opposite senses of vertical movement. Outcrop J (Fig. 2) indicates that movement was east-side down while micro S fabrics in outcrop B (Fig. 2) suggest that movement was west-side down.

Evidence of brittle overprinting is seen in almost every outcrop in the study area. The brittle faults consistently have a dextral sense of displacement (Fig. 6). At outcrop H (Fig. 2), brittle shear planes strike 290°-330° (Beresford trend) and dip 50° to the east. In the same outcrop, well developed extension fractures striking 000°-010° are pervasive. If these are associated with the brittle overprinting, they would imply dextral movement (H. Helmstaedt, pers. comm., 1991).

## DISCUSSION AND CONCLUSIONS

At two localities (outcrops A and B, Fig. 2) in Beresford Inlet, contrasting structural trends are seen in close proximity, indicating multiple phases of activity have occurred within the area. The earlier fabric has been locally deflected by, and even transposed into, the younger Beresford trend.

The northeast side of the inlet shows the most consistent strong fabrics of the Beresford trend and this may suggest that the Beresford fault may be traced along the northeast side of the inlet rather than along its centre as has been interpreted (Sutherland Brown, 1968). In support of this, the southernmost island within the inlet shows fabrics that are almost perpendicular to the inlet, while undeformed diorite outcrops nearby (outcrop C, Fig. 2) on the southwest shore of the inlet.

The magnitude of total offset along the Beresford Inlet fault zone cannot be determined, due to the lack of offset markers within the study area. A comparison of fabrics within the inlet suggests a greater flattening (NE-SW) component within the fault zone than previously considered.

Sanborn-Barrie (1992) has attributed the conspicuous topographic lineament that defines Beresford Inlet to competency contrasts of the Karmutsen Formation and the surrounding Jurassic plutonic rocks. This is mimicked north of the study area, western Lyell Island, where topographic highs appear to coincide with mapped plutonic rocks.

A possible scenario of the three distinct phases of movement documented within the Beresford Inlet fault zone would involve ductile sinistral, followed by ductile dextral movement and, finally, brittle dextral faulting. Kinematic indicators at two localities show that contrasting directions of vertical movement may have occurred within the fault zone.

The multiple phases of deformation within the Beresford Inlet fault zone are thought to reflect the complex structural history of the southern Darwin Sound and western Lyell

Island area. The discovery of a major ductile deformation zone in Darwin Sound and it's subsequent association with the Lousconne Inlet fault zone (Sanborn-Barrie, 1992) and the major movement within the Sedgwick Bay fault zone (Souther, 1992) may change the role of the Beresford Inlet fault zone in the regional faulting history of the area.

## ACKNOWLEDGMENTS

This project is a contribution to the Frontier Geoscience Program and part of an ongoing mapping program of the Queen Charlotte Islands under the supervision of J.W. Haggart. I thank Jim Haggart for initiating this project, designed as the core of a BSc.H thesis at Queen's University, and for his support throughout the field season. Mary Sanborn-Barrie is thanked for her field supervision and for many great days of fieldwork. Mark Hamilton proved to be great company and a welcome change of pace. I wish to thank Herb Helmstaedt for his visit during the field season and all his continuing help and support. Careful reviews and conversations with H. Helmstaedt and J. Haggart greatly improved the paper.

## REFERENCES

**Anderson, R.G. and Greig, C.J.**
1989: Jurassic and Tertiary plutonism in the Queen Charlotte Islands, British Columbia; in Current Research, Part H; Geological Survey of Canada, Paper 89-1H, p. 95-104.

**Anderson, R.G. and Reichenbach, I.**
1991: U-PB and K-Ar framework for the Middle to Late Jurassic (172-≥158 Ma) and Tertiary (46-27 Ma) plutons in Queen Charlotte Islands, British Columbia; in Evolution and Hydrocarbon Potential of the Queen Charlotte Basin, British Columbia, (ed.) G.J. Woodsworth; Geological Survey of Canada, Paper 90-10, p. 59-87.

**Lewis, P.D.**
1991: Dextral strike-slip faulting and associated extension along the southern portion of the Louscoone Inlet fault system, southern Queen Charlotte Islands, British Columbia; in Current Research, Part A; Geological Survey of Canada, Paper 91-1A, p. 383-391.

**Sanborn-Barrie, M.**
1992: Geology of the Darwin Sound area, Queen Charlotte Islands, British Columbia; in Current Research, Part A; Geological Survey of Canada, Paper 92-1A, p. 351-360.

**Souther, J.G.**
1992: Geology of central Lyell Island, Queen Charlotte Islands, British Columbia; in Current Research, Part A; Geological Survey of Canada, Paper 92-1A, p. 343-350.

**Sutherland Brown, A.**
1968: Geology of the Queen Charlotte Islands, British Columbia; British Columbia Department of Mines and Petroleum Resources, Bulletin 54, 226 p.

**Yorath, C.J. and Chase, R.L.**
1981: Tectonic history of the Queen Charlotte Islands and adjacent areas – a model; Canadian Journal of Earth Sciences, v. 18, p. 1717-1739.

---

Geological Survey of Canada Project 870070

# Conodont-ammonoid intercalibration around the Lower-Middle Triassic boundary: Nevadan clocks help tell British Columbian time

**Mike J. Orchard and Hugo Bucher**
**Cordilleran Division, Vancouver**

*Orchard, M.J. and Bucher, H., 1992: Conodont-ammonoid intercalibration around the Lower-Middle Triassic boundary: Nevadan clocks help tell British Columbian time; in Current Research, Part E; Geological Survey of Canada, Paper 92-1E, p. 133-140.*

***Abstract***

*The range of key conodont elements with respect to ammonoid biochronology of the late Spathian and Early Anisian of Nevada and British Columbia, representing Triassic low- and mid-latitudes, are presented. The resulting intercalibration provides an enhanced biochronological tool that is applied in the western Cordillera to identify and precisely date strata in four accreted terranes. Late Spathian strata of Cache Creek Terrane include algal laminated limestones that contrast markedly with coeval, fine grained siliciclastics in Stikinia. Similar sedimentary strata associated with volcaniclastics characterize the Early Anisian of Quesnellia, Stikinia, and Taku terranes. Conodont faunas of this age from at least Stikinia and Quesnellia give a low-latitude signal.*

***Résumé***

*Le présent travail fait état de la répartition biochronologique des conodontes par rapport aux zones d'ammonites standard de la fin du Spathien et de l'Anisien précoce. La Colombie-Britannique et l'État du Nevada fournissent respectivement les échelles de référence pour les moyennes et basses latitudes. La calibration entre eux des ammonites et des conodontes, et les corrélations établies au niveau de la Colombie-Britannique et du Nevada, constituent un outil performant utile à la datation et à la paléogéographie. Cet outil est utilisé à ces fins dans quatre terranes de l'ouest de la Cordillère. Les couches datant de la fin du Spathien et appartenant au terrane de Cache Creek, contiennent des calcaires laminés d'origine algaire qui se distinguent fortement des roches contemporaines et silicoclastiques de la Stikinie. Des séries sédimentaires silicoclastiques, associées à des roches volcanoclastiques, caractérisent l'Anisien précoce des terranes suivants: Quesnellie, Stikinie et Taku. Les faunes de condontes de l'Anisien précoce provenant de la Stikinie et de la Quesnellie se distinguent par leur cachet de basse latitude.*

## INTRODUCTION

The establishment and intercalibration of Canadian Triassic conodont and ammonoid biochronologies has been the focus of research undertaken in the Cordilleran Division for many years (Tozer, 1967, in press; Orchard, 1983, 1991b). Recently, this work has been extended to the western United States, particularly Nevada, through collaboration with the second author who is currently studying at the GSC through support provided by the Swiss National Science Foundation.

The importance of the Nevadan work to GSC programs is two-fold. First, it improves the Triassic biochronological scale by filling gaps evident in the Canadian zonal sequence, and secondly it provides a low-latitude, craton-bound (Tozer, 1982) standard against which biogeographic comparisons may be made. The enhanced zonation helps in dating isolated occurrences of Triassic strata, whereas biogeographic data provides the potential to resolve questions of provinciality and allochthoneity of accreted terranes of the western Cordillera.

This report summarizes progress on the study of conodont successions of the upper part of the Lower Triassic (Spathian) and lower Middle Triassic (Anisian) in Nevada, and the less complete record for the interval from the mid- to high-latitude Canadian autochthon. Conodont occurrences of this age are also reported from four Cordilleran terranes: Quesnellia, Cache Creek, Stikinia, and (in southeast Alaska) Taku. Precise dating of these strata is possible because of the intercalibration of ammonoid and conodont fauna recently established in Nevada (Table 1; Bucher, 1989; Orchard, in press).

## NEVADA: LOW-LATITUDE SUCCESSION

The Nevada sequence has two Spathian ammonoid faunas, that of the *Prohungarites-Subcolumbites* beds followed by the faunas of the Haugi Zone. These are followed by a Lower Anisian sequence first described by Silberling and Wallace (1969) and Silberling and Nichols (1982). Bucher (1989) has presented the most recent account, and a significant refinement of the Lower Anisian succession, which was formerly correlated with the Caurus Zone by Silberling and Tozer (1968). A four-fold subdivision of the interval is now recognized by Bucher (1989): *Japonites welteri* beds, overlain by *Pseudokeyserlingites guexi* beds, *Silberlingites mulleri* Zone, and then the restricted *Lenotropites caurus* Zone (Table 1).

Large conodont collections have been recovered from the matrix of each of these ammonoid levels, although intervening samples have yet to be studied. The

**Table 1.** Ranges of key conodonts with respect to ammonoid zones of Nevada and British Columbia. The central column shows the inferred ages of conodont collections from the four named terranes.

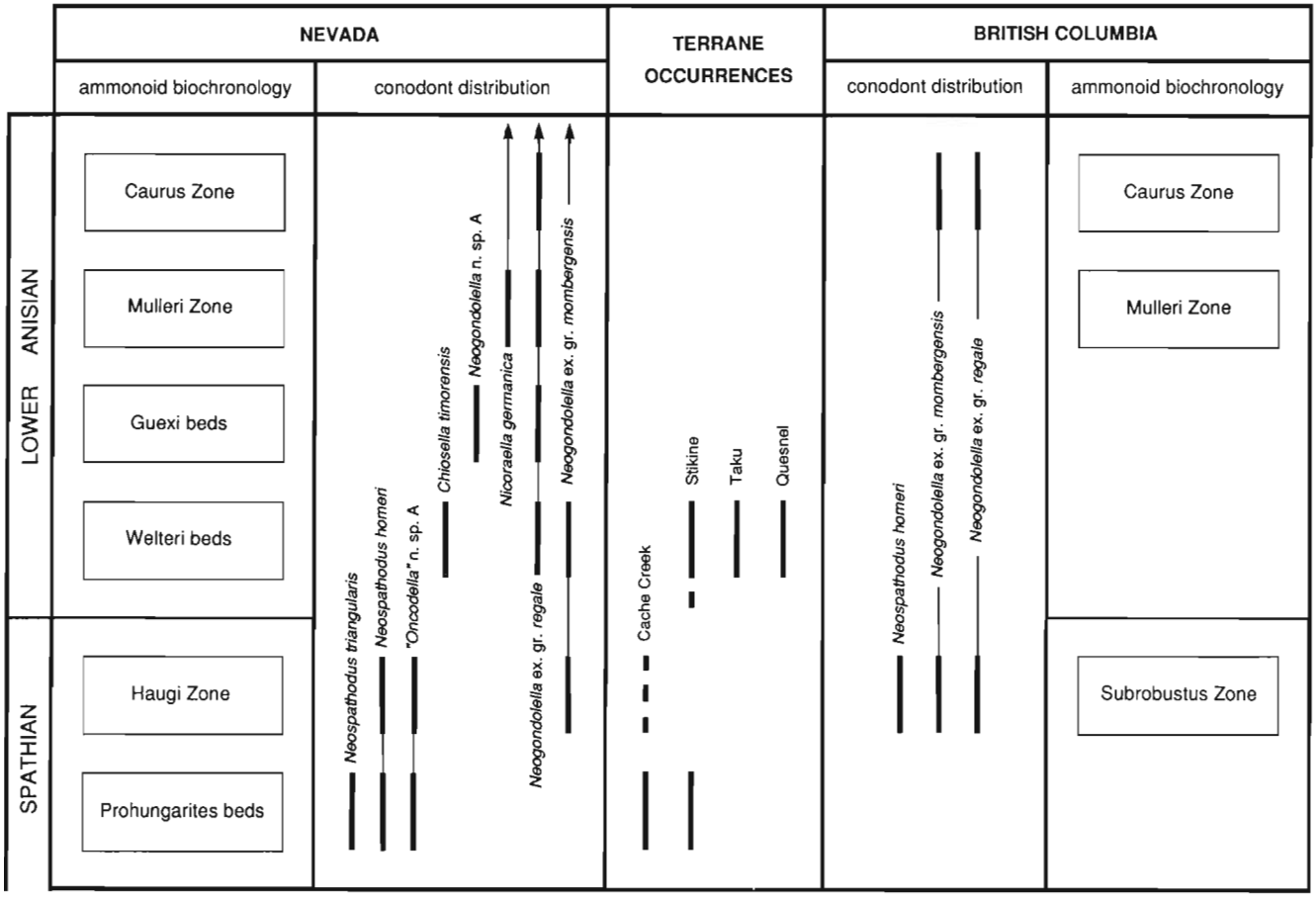

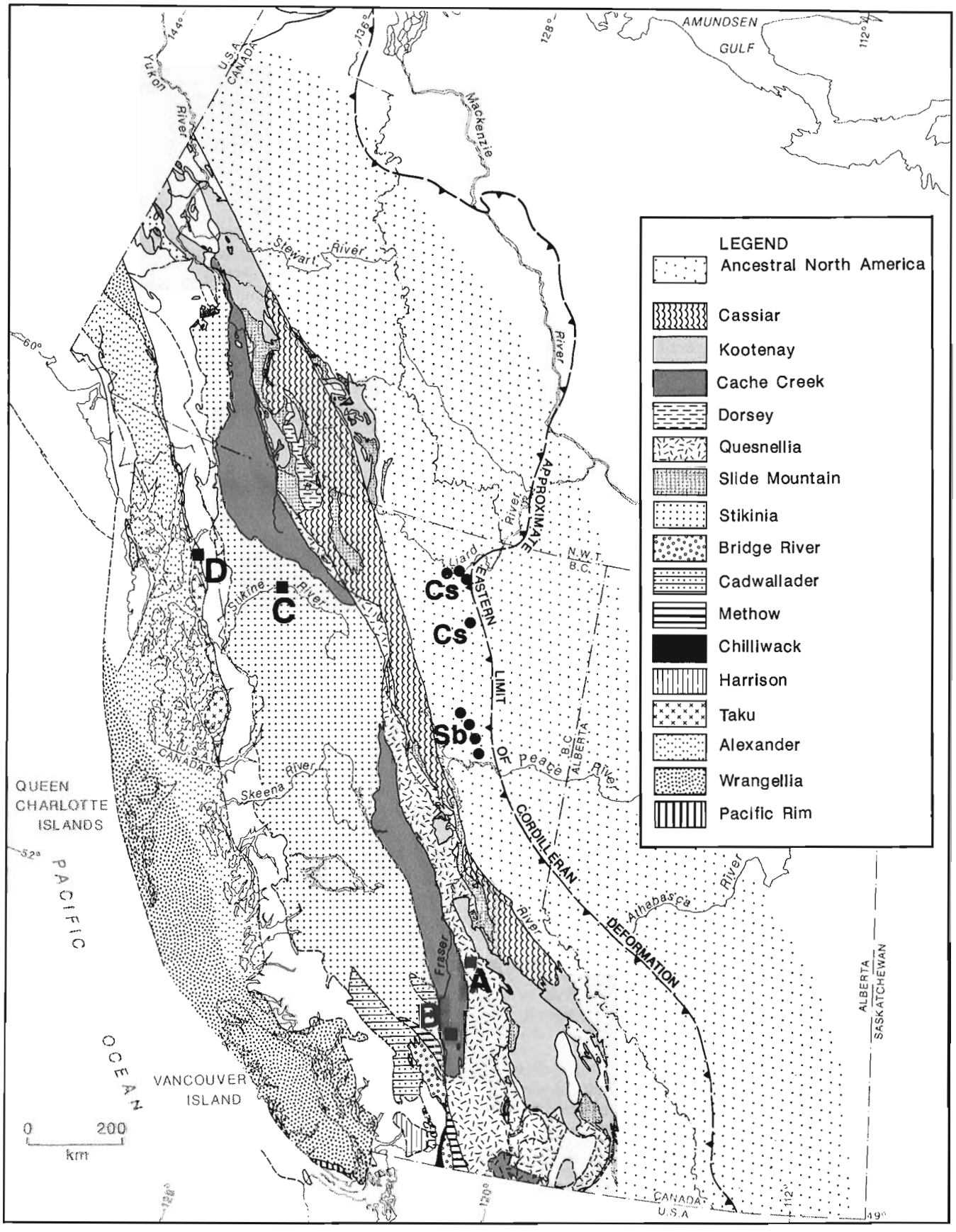


**Figure 1.** Map of western Canada showing location of conodont locations discussed in text in relation to terranes and the cratonal margin: Sb = Subrobustus Zone, Cs = Caurus Zone; A = Quesnellia, B = Cache Creek, C = Stikinia, D = Taku.

*Prohungarites* fauna contains the conodonts *Neospathodus homeri* Bender, *N. triangularis* Bender, '*Oncodella*' n. sp. A, and rare *Neogondolella* sp. Limited data from older ammonoid levels in Idaho suggest that the *Prohungarites* beds may represent the lower limit for the first three of these taxa (Orchard, in press). Conodonts from the Haugi Zone in the Lower member of the Prida Formation of the Humboldt Range in Nevada have been recorded by Collinson and Hasenmueller (1978, p. 187) who reported *Neospathodus homeri* and *Chiosella timorensis* (Nogami). The latter species is unconfirmed at this level, where the author has found only *N. homeri*, and less commonly *Neogondolella* ex gr. *mombergensis* Tatge and '*Oncodella*' n. sp. A.

Lower Anisian conodonts from the Prida Formation in Nevada were first studied by Nicora (1977), but the greater ammonoid resolution developed by Bucher (1989) has revised the ranges of key conodonts as shown in Figure 1. *Chiosella timorensis* has been found only in the basal Anisian *Japonites welteri* beds. *Nicoraella*? n. sp. A characterizes one collection from the *Pseudokeyserlingites guexi* beds, and *N. germanica* (Kozur) occurs in two collections from the Mulleri Zone. Both the low-bladed *Neogondolella* ex gr. *mombergensis* and far less common, high-bladed *N.* ex gr. *regale* Mosher also occur in the *J. welteri* beds, whereas all other Lower Anisian collections are dominated by *N.* ex gr. *regale* (Orchard, in press).

## NORTHEAST BRITISH COLUMBIA: MID-LATITUDE SUCCESSION

The Canadian ammonoid biochronology has been developed by Tozer (1967, in press) who recognized two Spathian and two Lower Anisian zones, in ascending order: the Pilaticus, Subrobustus, Mulleri, and Caurus zones (Table 1). The Pilaticus and Mulleri zones have not yielded conodont fauna, but the others have produced many collections from craton-bound successions in British Columbia (Fig. 1).

Both Mosher (1973) and Orchard (in press) recorded conodonts from the Subrobustus Zone of British Columbia. The collections are characterized by *Neospathodus homeri*, *Neogondolella* ex gr. *regale*, and *N.* ex gr. *mombergensis*. The presence of *N. homeri* establishes a link with the Haugi Zone of Nevada although *Neogondolella* is rare in that zone, possibly due to environmental (latitudinal?) differences. The common occurrence of Anisian-like neogondolellids in the Subrobustus Zone suggests that the scope of this zone may be broader compared with the Haugi Zone.

The Lower Anisian strata of Canada, all formerly classed as the Caurus Zone (Tozer, 1967), are divided into the Mulleri Zone and an overlying Caurus Zone of restricted scope (Tozer, in press). No certain equivalents of the *J. welteri* and *P. guexi* ammonoid beds have been identified. No conodonts have as yet been found in the Mulleri Zone of Canada. The collection recorded by Mosher (1973, p. 184) from the Caurus Zone on the Alaska Highway contained equal numbers of the generalized "*Neogondolella mombergensis*" and "*N. regale*", although additional collections made by the author are generally dominated by *N.* ex gr. *regale*, as are all the collections of this zone from Nevada. *Nicoraella* has not yet been found in the Canadian faunas.

## IN SUSPECT TERRANE: EVIDENCE FOR LOWER-MIDDLE TRIASSIC BOUNDARY FAUNA

Given the foregoing biochronological framework, upper Lower and lower Middle Triassic strata can be identified on the basis of conodonts within four tectonostratigraphic terranes of the Cordillera north of the 49th parallel (Fig. 1). The broad extent of this record has been summarized by Orchard (1991a), but greater resolution is now possible through our knowledge of the succession in Nevada.

---

### PLATE 1

SEM photos are lateral views x80, unless specified otherwise.

Figures 1-8. *Chiosella timorensis* (Nogami).
- 1,2. GSC 101600. GSC loc. C-176512, Taku. Upper and lateral views.
- 3. GSC 101601. GSC loc. C-117649, Quesnellia.
- 4. GSC 101602. GSC loc. C-117649, Quesnellia.
- 5. GSC 101603. GSC loc. C-102821, Quesnellia. Upper view.
- 6. GSC 101604. GSC loc. C-102821, Quesnellia.
- 7. GSC 101605. GSC loc. C-102821, Quesnellia.
- 8. GSC 101606, x100. GSC loc. C-102770, Stikinia.

Figures 9, 10. ?*Chiosella gondolelloides* (Bender).
- 9. GSC 101607, x100. GSC loc. C-102770, Stikinia.
- 10. GSC 101608, x100. GSC loc. C-102770, Stikinia.

Figures 11, 12. *Neospathodus homeri* Bender
- 11. GSC 101609, x100. GSC loc. C-102762, Stikinia.
- 12. GSC 101610. GSC loc. C-149959, Cache Creek.

Figure 13. *Neospathodus* ex gr. *spathi* Sweet
- GSC 101611, x100. GSC loc. C-102762, Stikinia.

Figures 14, 18-20. *Neogondolella* ex gr. *regale* Mosher
- 14. GSC 101612. GSC loc. C-102821, Quesnellia. Upper view.
- 18. GSC 101613. GSC loc. C-102821, Quesnellia. Upper view.
- 19,20. GSC 101614. GSC loc. C-102821, Quesnellia. Upper and lateral views.

Figure 15, 16. *Neospathodus triangularis* Bender
- 15. GSC 101615. GSC loc. C-102762, Stikinia.
- 16. GSC 101616. GSC loc. C-149960, Cache Creek.

Figure 17. '*Oncodella*' n. sp. A
- GSC 101617. GSC loc. C-102762, Stikinia.

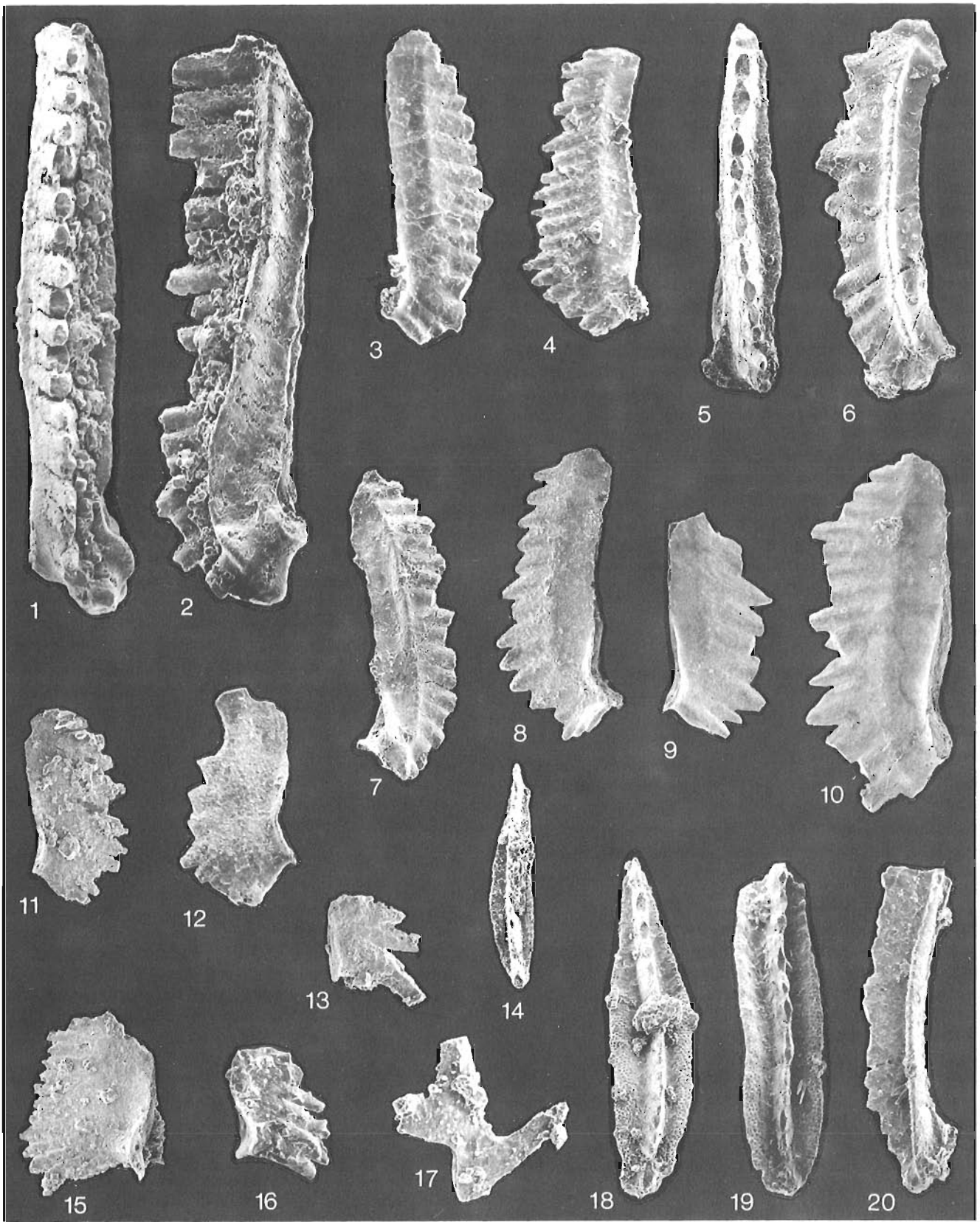
1
2
3
4
5
6
7
8
9
10
11
12
13
14
15
16
17
18
19
20

### *Quesnellia*

Quesnellia is a large composite terrane whose unifying character is an extensive Triassic volcanic island arc assemblage with a predominance of volcanics (the Nicola Group) in the west and more sedimentary equivalents ("black phyllite unit") in the east. Both structural and stratigraphic interleaving of fine grained siliciclastic sediment and volcaniclastic units is common in Quesnel Lake map area and relationships are difficult to resolve without fossil control (Struik, 1988). Most Triassic megafossils from Quesnellia are Late Triassic, but much older conodonts are known (Orchard, 1991a).

The oldest Triassic conodonts recovered from Quesnellia are known from two localities (Fig. 1, A) within small carbonate lenses associated with the informal "volcaniclastic unit" in Quesnel Lake map area (Struik, 1988). Both localities have yielded *Chiosella timorensis*, which correlates with basal Anisian *Japonites welteri* beds of Nevada. One sample (C-102821 - see Appendix) also includes other species that occur in the basal Anisian of Nevada, namely *Neogondolella* ex gr. *regale* and *N.* ex gr. *mombergensis*. A second collection (C-117649) lacks neogondolellids but contains pectiniform elements tentatively referred to *Cratognathus*? sp. and ramiform elements which resemble those associated with gladigondolellid platforms in Early Anisian Tethyan faunas (e.g., Timor, Oman; Orchard, in press). Faunas such as these have not been found in craton-bound Triassic collections from North America and their occurrence in Quesnellian strata suggests a 'Tethyan' affinity (see also Nestell and Orchard, 1991). We are unsure whether this is best explained by invoking a distant (western Pacific), low-latitude origin, or whether it arises solely from the oceanic, island arc setting envisaged for Quesnellia during the Triassic.

### *Cache Creek Terrane*

The Cache Creek Terrane includes structurally complex radiolarian chert and argillite, extensive shallow water carbonates with "Tethyan" Permian faunas, and mélange deposits (Monger and Berg, 1984). The terrane is bounded on the east by an early Mesozoic subduction complex for which the Nicola Group of Quesnellia is the corresponding volcanic arc.

In southern British Columbia, the Cache Creek complex has been divided into three belts, the central belt of which includes the Marble Canyon Formation. This formation consists primarily of bedded and massive carbonates which are well known for their Late Permian "Tethyan" verbeekinid fusulinaceans. Much of the limestone is now known to be Triassic (summarized in Beyers and Orchard, 1991). For the purpose of this paper, several collections from the north end of the Marble Range made near Jesmond in Bonaparte Lake map area are of interest (Fig. 1, B; Appendix). These are from algal-laminated, bedded limestones representative of warm, shallow water conditions. The strata yield *Neospathodus homeri* sometimes associated with *N. triangularis*. Both species are known from Spathian *Prohungarites* beds of Nevada (Orchard, in press), but *N. homeri* alone ranges up into the Haugi Zone. Correlation with one or both of these Nevada intervals is implied (Table 1).

### *Stikinia*

Stikine Terrane encompasses a large part of central British Columbia and southern Yukon. It is underlain by Paleozoic sediments as old as Early Devonian and has the large, post-accretionary Bowser Basin developed upon it, obscuring much of the Triassic and older stratigraphy. Nevertheless, Triassic conodonts establish an age range from Smithian to Norian (Orchard, 1991a).

Most Triassic strata in northern Stikinia have been included in the Stuhini Group, which comprises an extremely variable succession of basinal sedimentary and volcanic rocks of largely Late Triassic age. Early and Middle Triassic conodonts have helped to identify a lower sedimentary package, also associated with volcaniclastics, which has been assigned informally to the "Tsaybahe group" in Dease Lake (Read, 1983).

Both Spathian and Early Anisian conodont collections are known from the Stikine River section (Fig. 1, C) within thin limestones in a siliceous argillite, siltstone and chert succession. An older fauna (C-102762, from drillcore) contains *Neospathodus homeri*, *N. triangularis*, *N.* ex gr. *spathi* Sweet, '*Oncodella*' n. sp. A and other unnamed ramiform elements, all of which are also known from low-latitude Spathian strata both in the *Prohungarites* beds of Nevada and Idaho, and in 'Tethyan' faunas of Oman (Orchard, 1992, in press). A second, younger collection (C-102770) from Stikine River contains the widespread *Chiosella timorensis*, more 'primitive' elements tentatively referred to ?*C. gondolelloides* (Bender), fewer *Neogondolella* ex gr. *regale*, typical of North American Anisian strata, and other elements which are 'exotic' in relation to coeval North American craton-bound faunas. These 'exotic' elements are similar to those known from the Early Anisian fauna of Quesnellia discussed earlier, and our comments also apply here (see above).

### *Taku Terrane*

The Taku Terrane is located on the western flank of the northern Coast Mountains and is sandwiched between Stikinia on the east and Alexander-Wrangellia on the west. Originally defined in the Ketchikan area of southeast Alaska (Berg et al., 1978), a more northerly segment of the terrane has recently been studied by Gehrels et al. (in press) who defined a new unit, the Perseverance Group. This comprises a sequence of calcareous and pelitic strata containing siliceous and carbonaceous concretions and metavolcanics. Several conodont collections were recovered (op. cit., Table 1; Fig. 1, D), the oldest of which (C-176512) comprises *Chiosella timorensis* and *Neogondolella* ex gr. *regale*, here dated as Early Anisian.

## SUMMARY

The range of key conodont elements has been determined in Nevada, and to a lesser extent in British Columbia, with respect to standard ammonoid zones of the late Spathian and Early Anisian (Table 1). This intercalibration of conodont and ammonoid faunas provides an enhanced biochronological tool for assessing the age and provinciality of strata in the terranes of the western Cordillera that lack macrofossils.

Strata from one or both sides of the Lower-Middle Triassic boundary has been identified in Quesnellia, Cache Creek, Stikinia, and Taku terranes (Fig. 1, A-D, Table 1). Except for Cache Creek, each of these regions are characterized by fine grained siliciclastic sedimentary rocks associated with volcanic elements in the late Spathian and/or Early Anisian. Spathian strata of Cache Creek Terrane are algal laminated bearing limestones and contrast markedly with coeval strata of Stikinia. Although these localities lie within structurally complex regions and are often isolated outcrops lacking stratigraphic context, they nevertheless represent precisely dated, contemporaneous strata that can be directly compared - a prerequisite for terrane analysis.

Conodont faunas from all areas discussed contain some elements that are widespread, and provide no obvious biogeographic signature; Spathian *Neospathodus* species are an example. Apart from the occurrences recorded here, *Chiosella* is only known at present from low-latitude Lower Anisian, as is *Nicoraella*. Although mid-latitude, craton-bound Canadian strata of this age may not have been sampled, the relatively common occurrence of *Chiosella* in the accreted terranes may represent remnants of a fauna that was particularly widespread in low-latitudes. *Gladigondolella*, as far as is known, is a low-latitude form and the presence of *Gladigondolella*-like elements in Lower Anisian collections from apparently very similar stratigraphic successions in both Stikinia and Quesnellia implies that they share a pelagic, presumably low-latitude origin. A similar origin has long been argued for the Cache Creek Terrane, which is envisaged as a shallow, warm water carbonate atoll during the Spathian. The atoll was presumably surrounded by coeval deeper water sediments like those preserved in Stikinia.

## ACKNOWLEDGMENTS

We thank E.T. Tozer for providing ammonoid matrix samples from Canada, and P. Read and L.C. Struik for information on the stratigraphy of Stikine Canyon and Quesnel Lake respectively. J. Beyers, M.A. Bloodgood, G. Gehrels, J. Psutka, and L.C. Struik collected the conodont samples from Cordilleran terranes discussed herein. P. Krauss undertook the SEM photography. H. Bucher acknowledges the support of the Swiss National Science Foundation Fellowship 8220-030667.

## REFERENCES

**Berg, H.C., Jones, D.L., and Coney, P.J.**
1978: Map showing pre-Cenozoic tectonostratigraphic terranes of southeastern Alaska and adjacent areas; United States Geological Survey, Open-File Report 78-1085.

**Beyers, J.M. and Orchard, M.J.**
1991: Upper Permian and Triassic conodont faunas from the type area of the Cache Creek Complex, south-central British Columbia; in Ordovician to Triassic Conodont Paleontology of the Canadian Cordillera, (ed.) M.J. Orchard and A.D. McCracken; Geological Survey of Canada, Bulletin 417, p. 269-298.

**Bucher, H.**
1989: Lower Anisian Ammonoids from the northern Humboldt Range (northwestern Nevada, USA) and their bearing upon the Lower-Middle Triassic boundary; Eclogae Geologicae Helvetiae, v. 82/3, p. 945-1002.

**Collinson, J.W. and Hasenmueller, W.A.**
1978: Early Triassic paleogeography and biostratigraphy of the Cordilleran miogeosyncline; in Mesozoic Paleogeography of the Western United States, (ed.) D.G. Howell and K. McDougall; Pacific Coast Paleogeography Symposium 2, p. 175-187.

**Gehrels, G.E., McCelland, W.C., Samson, S.D., Patchett, P.J., and Orchard, M.J.**
in press: Geologic and tectonic relations along the western flank of the Coast Mountains Batholith between Cape Fanshaw and Taku Inlet, southeastern Alaska; Tectonics.

**Monger, J.W.H. and Berg, H.C.**
1984: Lithotectonic terrane map of western Canada and southeastern Alaska; in Lithotectonic Terrane Maps of the North American Cordillera, (ed.) N.J. Silberling and D.L. Jones; United States Geological Survey, Open-File Report 84-523, p. B1-B31.

**Mosher, L.C.**
1973: Triassic conodonts from British Columbia and the northern Arctic Islands; Geological Survey of Canada, Bulletin 222, p. 141-193.

**Nestell, M.K. and Orchard, M.J.**
1991: A Middle Triassic (Ladinian) tethyan conodont fauna containing *Gladigondolella tethydis* (Huckriede) from the Baker Terrane, eastern Oregon, and its paleogeographic significance (abstract); in Canadian Paleontology Conference I and the Pander Society Meeting, Vancouver, Program and Abstracts, p. 61.

**Nicora, A.**
1977: Lower Anisian platform-conodonts from the Tethys and Nevada: taxonomy and stratigraphic revision; Paleontographica, Abt. A 157/1-3, p. 88-107.

**Orchard, M.J.**
1983: *Epigondolella* populations and their phylogeny and zonation in the Norian (Upper Triassic); Fossils and Strata, no. 15, p. 177-192.
1991a: Conodonts, time and terranes: an overview of the biostratigraphic record in the western Canadian Cordillera; in Ordovician to Triassic Conodont Paleontology of the Canadian Cordillera, (ed.) M.J. Orchard and A.D. McCracken; Geological Survey of Canada, Bulletin 417, p. 1-26.
1991b: Upper Triassic conodont biochronology and new index species from the Canadian Cordillera; in Ordovician to Triassic Conodont Paleontology of the Canadian Cordillera, (ed.) M.J. Orchard and A.D. McCracken; Geological Survey of Canada, Bulletin 417, p. 299-335.
1992: Lower Triassic Conodonts from Oman (abstract); Geological Society of America, Abstracts with Programs, v. 24/3.
in press: Conodont biochronology around the Early-Middle Triassic boundary: new data from North America, Oman, and Timor; Mémoire de Géologie Université de Lausanne, Switzerland.

**Read, P.B.**
1983: Geology, Classy Creek (104J/2E) and Stikine Canyon (104J/1W), British Columbia; Geological Survey of Canada, Open File 940.

**Silberling, N.J. and Nichols, K.M.**
1982: Middle Triassic molluscan fossils of biostratigraphic significance from the Humboldt Range, Northwestern Nevada; United States Geological Survey, Professional Paper 1207.

**Silberling, N.J. and Tozer, E.T.**
1968: Biostratigraphic classification of the marine Triassic in North America; Geological Society of America, Special Paper 10.

**Silberling, N.J. and Wallace, R.E.**
1969: Stratigraphy of the Star Peak Group (Triassic) and overlying lower Mesozoic rocks, Humboldt Range, Nevada; United States Geological Survey, Professional Paper 592, p. 1-50.

**Struik, L.C.**
1988: Regional imbrication within Quesnel terrane, central British Columbia, as suggested by conodont ages; Canadian Journal of Earth Sciences, v. 25, p. 1608-1617.

**Tozer, E.T.**
1967: A Standard for Triassic Time; Geological Survey of Canada, Bulletin 156.
1982: Marine Triassic faunas of North America: their significance for assessing plate and terrane movements; Geologische Rundschau, v. 71, p. 1077-1104.
in press: Canadian Triassic ammonoid faunas; Geological Survey of Canada, Bulletin.

---

Geological Survey of Canada Project 810028

## APPENDIX

Available details on the location and stratigraphy of conodont collections described in text.

**GSC Loc. No. C-102762**

NTS: Dease Lake (104J). UTM Zone 9; 425782.40E, 6441950.07N. On the right bank of the Stikine River, 5.85 km at 117° from the mouth of Pallen Creek, at 118.8 m within drill hole DH82-Z57. From 25 cm dark-grey limestone layer in well-bedded, dark-grey to white siliceous argillite and siltstone of "Tsaybahe group"; from 79.2 m to 166.7 m succession is well bedded, black, pyritic, graphitic, siliceous argillite, gradational into (from 166.7 m to 219.7 m) uniform, massive green tuffaceous wacke; upper 79.2 m is gabbro intrusion. Collected by P. Read/J.F. Psutka (82-P-26F). See Read, 1983, no. F14c'.

**GSC Loc. No: C-102770**

NTS: Dease Lake (104J). UTM Zone 9; 424208E, 6442445N. On north bank of Stikine River, 4.3 km upstream from the mouth of Pallen Creek at elevation 1673'. From grey limestone lens (1 m x 2 m) in thick succession of medium-dark-grey argillite with thin light grey limy layers of "Tsaybahe group"; succession lies below folded thrust fault. Collected by P. Read/J.F. Psutka (82-P-64F, station P226i). See Read, 1983, no. F12g.

**GSC Loc. No: C-102821**

NTS: Quesnel Lake (93A). UTM Zone 10; 621125E, 5820925N. About 0.5 km west of Abbott Creek Recreation Site on shoreline of Quesnel Lake. Isolated spotted micritic limestone 50 cm pod in bedded andesitic lapilli tuff. Collected by L.C. Struik (84SCB-409). See Struik, 1988, p. 1617.

**GSC Loc. No: C-117649**

NTS: Quesnel Lake (93A). UTM Zone 10; 611870E, 5822960N. Spanish Mountain east. Carbonate in black pelite of "volcaniclastic unit". Collected by M.A. Bloodgood (87MB-16-02).

**GSC Loc. Nos: C-149952, -53, -59, -60, C-157238**

All collections from NTS: Bonaparte Lake (92P), Jesmond fire lookout access road. Marble Canyon Formation. Collected by J.M. Beyers.

**GSC Loc. No: C-149952**

As last. UTM Zone 10; 575775E, 5683825N. At elevation 1864 m (6150 ft). Massive, light grey, fine grained, Mn-stained, recrystallized carbonate; at 28.5 m in section 4 (86OFB-SW3-JAR-100).

**GSC Loc. No: C-149953**

As last. UTM Zone 10; 575775E, 5683825N. At elevation 1870 m (6170 ft). Ochre weathering, recrystallized, algal-laminated light grey carbonate, with Mn dendritic stain and slickensided surface; at 36.5 m in section 4 (86OFB-SW3-JAR-101); bedding attitude 168/07 NE.

**GSC Loc. No: C-149959**

As last. UTM Zone 10; 575500E, 5684575N. At bearing 346° to tower, elevation 1955 m (6450 ft). Dark grey, recrystallized carbonate with calcite pods and veins (86OFB-JFT-1).

**GSC Loc. No: C-149960**

As last. UTM Zone 10; 575475E, 5684600N. At bearing 161° to tower, elevation 1915 m (6320 ft). Grey weathering, Mn stained, medium grey, dolomitic carbonate (86OFB-JFT-2).

**GSC Loc. No: C-157238**

As last. UTM Zone 10; 575775E, 5683875N. Grey micrite, at 51.5 m in section 4 (87OFB-J-T6).

**GSC Loc. No. C-176512**

NTS: Sumdum (104F), Port Snettisham, southeast Alaska. UTM Zone 8; 564700E, 6426549N. Collected by G.E. Gehrels (89-GC-617).

# Interior Plains and Arctic Canada

# Plaines intérieures et région arctique du Canada

# Electromagnetic measurements on the Beaufort Shelf, Northwest Territories

**G.J. Palacky and L.E. Stephens[1]**
**Mineral Resources Division**

*Palacky, G.J. and Stephens, L.E., 1992: Electromagnetic measurements on the Beaufort Shelf, Northwest Territories; in Current Research, Part E; Geological Survey of Canada, Paper 92-1E, p. 143-148.*

***Abstract***

*Field experiments recently carried out on the Beaufort Shelf indicate that multifrequency horizontal-loop electromagnetic (HLEM) measurements are a fast and cost-effective means for detection of subbottom ice-bonded permafrost. Previously, refraction and high-resolution reflection seismic surveys and drilling have been used by the Geological Survey of Canada for this purpose. Horizontal-loop electromagnetic field data have been processed using ridge regression inversion techniques. The results are presented in the paper as resistivity sections. The uppermost layer, sea ice, is highly resistive (5000 Ω•m). The second layer, seawater and seawater-saturated sediments (average resistivity 1 Ω•m), is underlain by ice-bonded permafrost (5000 Ω•m). The basement is formed by conductive unfrozen sediments. A comparison with the results of drilling and seismic surveys indicates that the detection of ice-bonded permafrost using HLEM methods is reliable.*

***Résumé***

*Des expériences récemment réalisées sur la plate-forme de Beaufort indiquent que les levés électromagnétiques à bobines horizontales et fréquences multiples (levés HLEM) représentent un moyen efficace et rentable de détection du pergélisol cimenté par la glace, présent dans la subsurface du fond marin. Autrefois, la Commission géologique du Canada a employé aux mêmes fins des levés de sismique-réfraction et des levés de sismique-réflexion de haute résolution ainsi que des forages. On a traité les données de terrain HLEM en faisant appel à des techniques d'inversion à régression des crêtes. On présente dans cet article les résultats sous forme de coupes de résistivité. La couche sommitale, constituée de glace de mer, présente une forte résistivité (5 000 Ω•m). La seconde couche, composée d'eau de mer et de sédiments saturés en eau de mer (résistivité moyenne 1 Ω•m), recouvre un pergélisol cimenté par la glace (5 000 Ω•m). Le socle est composé de sédiments qui sont conducteurs, non gelés. Une comparaison avec les résultats des forages et des levés sismiques montre que la détection du pergélisol cimenté par la glace, au moyen des levés HLEM, est fiable.*

[1] Deceased.

## INTRODUCTION

Since 1985, the Terrain Sciences Division of the Geological Survey of Canada has carried out several geophysical and geological field studies in the vicinity of a proposed offshore-onshore pipeline to North Head, Richards Island, east of the Mackenzie Delta, N.W.T. Figure 1 depicts the location of a 30-km-long portion of the proposed pipeline route and nine boreholes that were drilled in the spring of 1990 (Dallimore, 1991). From 1985 to 1987, during the first phase of the project, shallow reflection and refraction surveys were carried out in several areas along the transect.

In 1989, the Electrical Methods Section of the Mineral Resources Division was asked to assess the suitability of ground electromagnetic techniques for detection of shallow subbottom ice-bonded permafrost on the Beaufort Shelf. A decision was made to carry out surveys with the frequency-domain horizontal-loop APEX MaxMin I system, which has been successfully used in Quaternary mapping programs in northeastern Ontario (Palacky and Stephens, 1990, Palacky et al., 1992a, b). The section staff carried out field surveys near the northern end of the transect. Approximate coordinates of the centre of the survey area are 69°51'N and 134°04'W (Fig. 1). To our knowledge, this MaxMin sounding survey was the first of its kind in an Arctic marine environment. However, time-domain electromagnetic sounding surveys have been previously used in permafrost investigations (Scott et al., 1990).

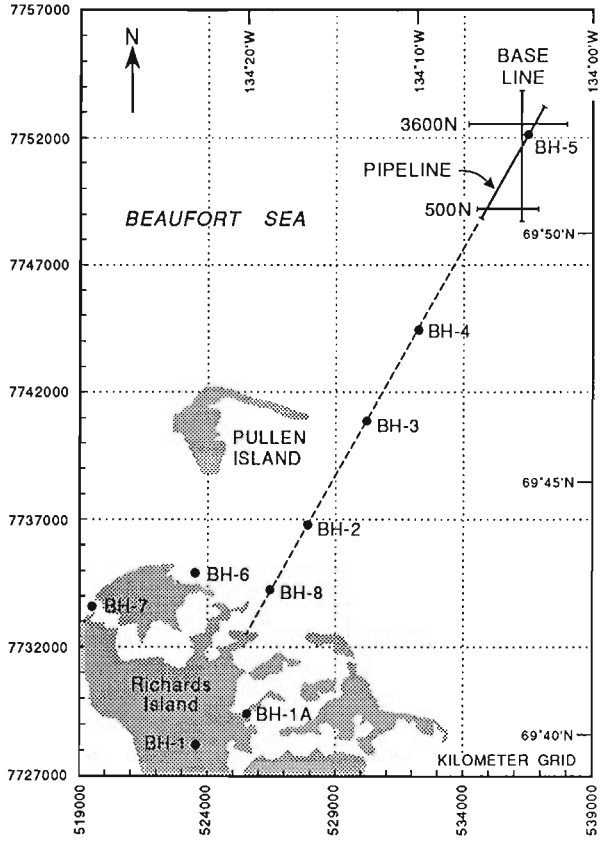


**Figure 1.** Map of the Beaufort Shelf study area. The proposed pipeline route, HLEM survey lines (near the northern end of the transect) and the location of boreholes are depicted (base and drilling information from Dallimore, 1991).

## GEOGRAPHIC SETTING AND GEOLOGY

The shelf in the transect area slopes very gently; 20 km from the shore, its depth is only 10 m. In absence of detailed drilling information, geological description is based on seismo-stratigraphy along the transect (Blasco and Lewis, 1991). The geological unit mapped on the seabottom in the transect area has been denominated Unit B. This transgressive unit deposited in a deltaic environment under high-energy conditions consists of a sequence of interbedded sand, silt, and clay. Although the thickness of this unit varies locally, it reaches up to 14 m in depressions. Unit C, which is formed by glaciofluvial sand and silty sand, rests unconformably on transgressive marine clays and silts of Unit D. Unit E (sand) is the oldest in the sequence identified on the Beaufort Shelf.

Unlike thick permafrost, which has been extensively studied in many places, the nature of near-surface frozen sediments is still poorly understood. Pockets of ice-bonded permafrost can be identified on shallow reflection profiles as high-amplitude events, but shallow gas occurrences prevent their identification in several near-shore areas. It was considered essential to test whether another geophysical technique measuring a different physical property could be used to complement seismic surveys.

## GROUND ELECTROMAGNETIC SURVEYS

In horizontal-loop electromagnetic (HLEM) measurements, the primary electromagnetic field is generated by current in a horizontal transmitting coil. Changes in the secondary magnetic field are detected by the receiver, which is another horizontal coil. The effect of the much stronger primary field is compensated for a given coil separation, which must be kept with a high degree of accuracy (e.g., ± 30 cm for a coil separation of 100 m). A failure to accurately maintain the coil distance is the most common operator error. Modern HLEM surveys are carried out at multiple frequencies in the audio range (100 Hz to 50 kHz). Details of the technique are given in Frischknecht et al. (1991).

The MaxMin I instrument, which was used in the survey, has 8 frequencies from 110 to 14080 Hz, always increasing by a factor of two. The measured parameters are in-phase and quadrature components of the ratio secondary/primary magnetic field expressed in percent. The coil separation, which can be changed from 12.5 to 400 m, remained 100 m in all surveys described here. The survey readings, taken at an interval of 50 m, were recorded automatically using a Rautaruukki KTP-84 data logger. The average daily production was 3 km with a crew of two operators, but substantial variations were reported due to unstable weather conditions common in Arctic environments. Even when the weather was favourable, the maximum daily production was limited by rapid draining of batteries in cold weather (between -15°C and -30°C).

Interpretation of the field data was carried out in Ottawa with the EMIX-MM program, which uses an inversion routine based on the ridge regression technique (Inman, 1975; Interpex Ltd., 1988). The main difficulty in using this program lies in correctly selecting a suitable interpretation model. In areas where resistivity layering is not known, an incorrect choice of the number of layers results in erroneous interpretation. Palacky (1991) suggested a procedure to evaluate whether an interpretation is geologically realistic. It is based on the observation that resistivities of individual layers change only within a narrow range which is characteristic of the geological formation in the area.

## FIELD RESULTS

Horizontal-loop electromagnetic surveys were carried out along four lines depicted in Figure 1. The baseline was 5 km long and oriented in the north-south direction. From station 3600N, two perpendicular lines 2 km long were surveyed in easterly and westerly directions. Another east-west line was surveyed at 500N. Finally, a 5 km long profile followed the proposed pipeline route.

The only borehole drilled in the area surveyed by the HLEM method is located along the pipeline route, at point 600N. Jenner and Blasco (1991) described the drill core: The sea bottom was reached at a depth of 10 m and the drilling terminated 75 m below that. The upper 10 m of sediments, which could not be cored, were water-saturated sandy clays (Unit B). The core recovery was good between 10 and 38.7 m; sediments were described as fine to medium sands of Unit C. This ice-hosting unit is underlain by silty clays of Unit D and the sand-rich Unit E. The contact between units D and E could not be established because of a lack of core recovery.

Hunter et al. (1991b) logged all holes using seismic, gamma ray and electromagnetic probes. The results of electromagnetic logging, which were obtained with the Geonics EM-39 system, are reproduced in Figure 2. The EM-39 probe, which measures electrical conductivity,

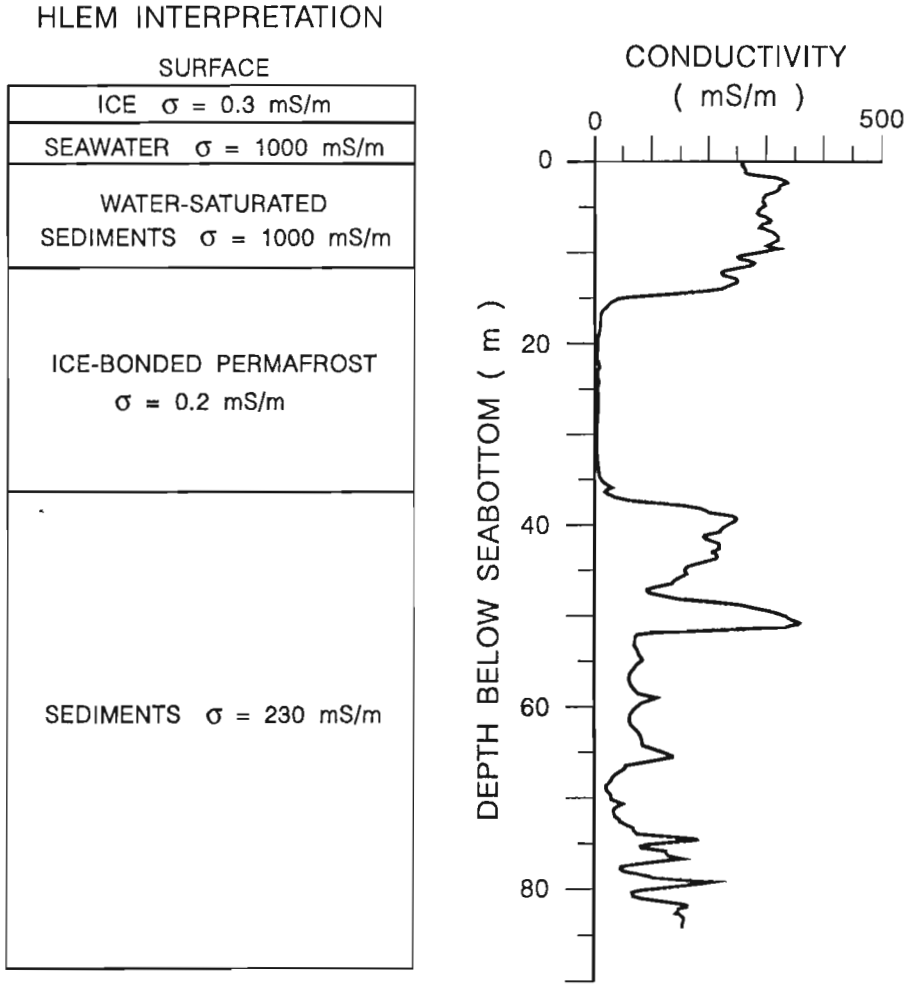


**Figure 2.** Right: Results of a logging survey at borehole 5. The Geonics EM-39 system and a probe with two coaxial coils 0.5 m apart was used in the survey (after Hunter et al., 1991b). Left: Conductivity section obtained by unconstrained inversion of HLEM data recorded at station 600N of the pipeline. (The vertical scale of the logging data has zero at the seabottom, 10 m below the ice surface.)

consists of two coaxial coils 0.5 m apart. In the specifications, the instrument manufacturer estimates the average penetration to be 1 to 1.5 m; the measurement accuracy is 5%. Conductivity values of about 300 mS/m (milliSiemens/metre), which correspond to resistivity 3.33 Ω•m, were recorded in the upper 14 m. Highly resistive material (subbottom ice-bonded permafrost) was encountered between 15 and 36 m. Conductivity of the underlying unfrozen sediments was between 25 and 360 mS/m (resistivity 2.7 to 40 Ω•m). While high conductivity values are due to silty clays of Unit D, low conductivity values characterize sand of Unit E. Unfortunately, the correlation could not be elaborated in detail because of poor core recovery.

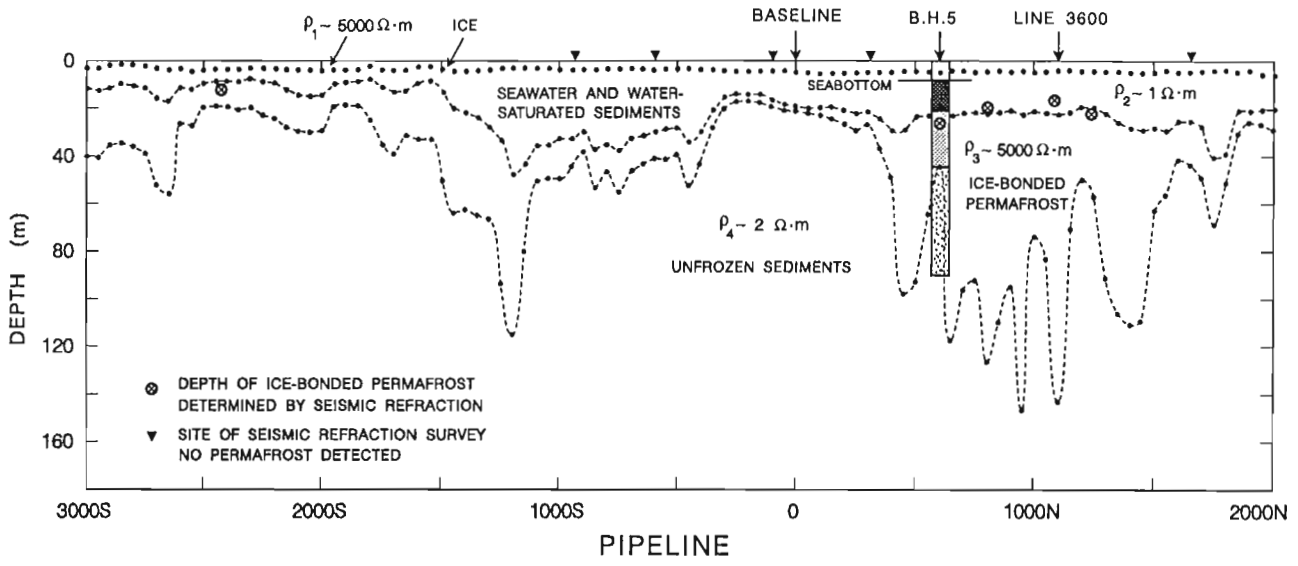


**Figure 3.** Resistivity section along the pipeline route with interpretation of individual layers and their average resistivities. Symbols used to display seismic results are in the explained in the legend. Arrows indicate intersect points with the baseline and line 3600N. Thicknesses of individual layers at station 600N were determined by logging of borehole 5.

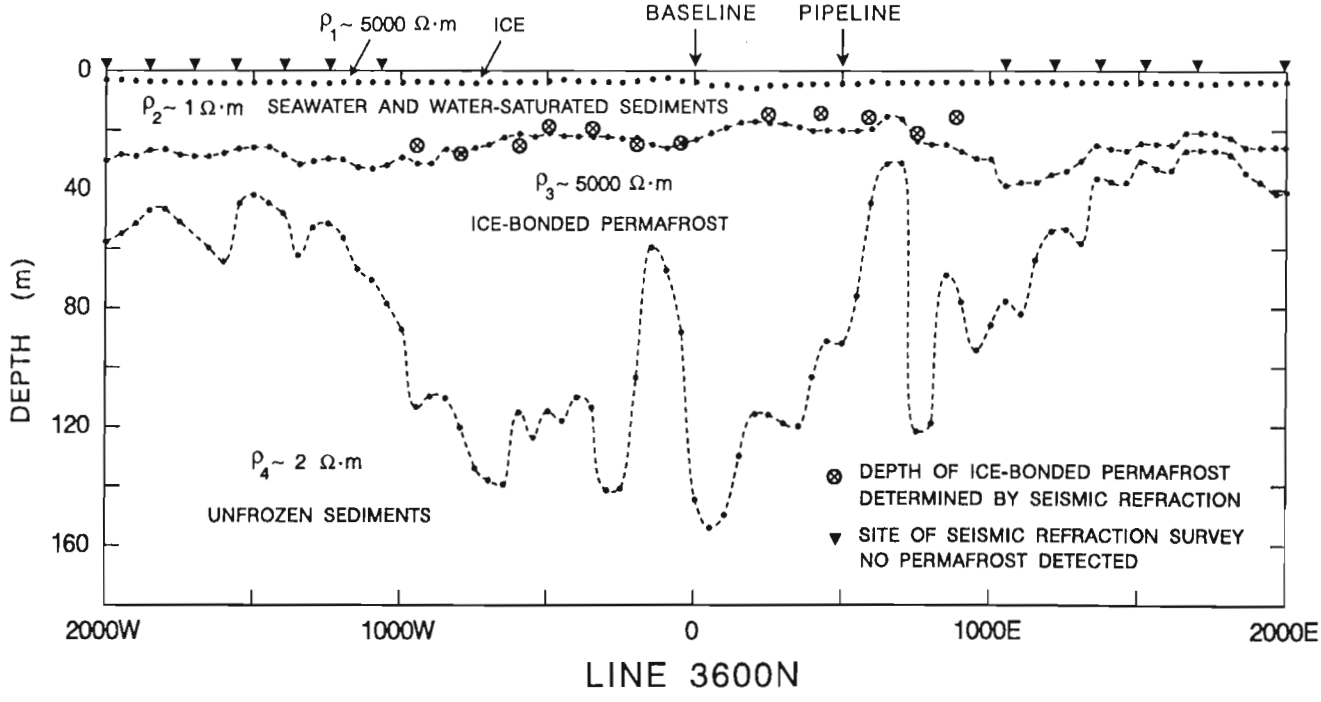


**Figure 4.** Resistivity section along line 3600N. The section layout and symbols are in the same as in Figure 3. Intersect points with the baseline and pipeline route are depicted.

The output of the EMIX-MM program is resistivity (in Ω•m) and thickness (in metres) of individual layers. Any parameter can be fixed for a given inversion. In the interpretations described here, the only assumption was the number of layers (four). All interpreted parameters could vary freely to achieve the best fit to the measured data indicated by the lowest RMS error. For an easy comparison with the logging data depicted in Figure 2, the estimated resistivities were converted to conductivities.

The results for station 600N of the pipeline are plotted as a conductivity section. Values associated with each parameter in the resolution matrix indicated that, for the given model, thickness determinations are more reliable than resistivity estimates. In highly resistive environments, electromagnetic surveys, unlike resistivity soundings, are not significantly affected by small resistivity changes.

Compared with the known thickness of sea ice (2.5 m), the estimate obtained by inversion is about twice the true value. As this discrepancy is unimportant for the detection of ice-bonded permafrost, which was the aim of the survey, no attempt was made to constrain the inversion to obtain better ice thickness estimates. Despite many attempts, it was not possible to separate seawater and water-saturated seabottom sediments by means of unconstrained inversion; the HLEM method sees them as one layer of intermediate conductivity (1000 mS/m). Hunter et al. (1991a) who measured seawater conductivity in the study area determined a range between 2000 and 2400 mS/m (corresponding to resistivities of 0.42 to 0.5 Ω•m). Because of extensive mixing of seawater and fresh water of the Mackenzie River, water salinity and consequently its conductivity are somewhat lower than typical for seawater. Conductivity of water-saturated sandy and silty clay determined by EM-39 logging (average 300 mS/m) is about three times lower that the estimate obtained by inversion of HLEM data.

The lower boundary of subbottom ice-bonded permafrost determined by HLEM interpretation is in excellent agreement with logging data (36 m below the seabottom). Conductivity estimated by inversion of HLEM data (230 mS/m) is about average of the highly variable conductivity of unfrozen sediments measured by logging.

The same four-layer model has been used in inversion of HLEM along the survey profiles. Figure 3 shows the results along the pipeline route. Inversion-determined layer thicknesses are plotted at each sounding site and average resistivity values are given for each formation. The sea ice forms a highly resistive layer (average resistivity 5000 Ω•m) at the top of the sequence. The inverted layer thickness varied between 3.5 and 5 m over the length of the profile.

The second inversion layer is seawater and water-saturated sediments of Unit B (average resistivity 1 Ω•m). From bathymetric charts, the sea depth is known to increase from 7 m in the south to about 9.5 m in the north. Conductive seabottom sediments represent a significant, but variable portion of the interpreted second layer thickness. The present knowledge of seabottom geology remains sketchy, but thinning and thickening of sea water-saturated sediments does not appear geologically unreasonable. This layer appears thicker in the centre of the pipeline route (up to 40 m), where the subbottom ice-bonded permafrost is absent or very thin. Because the seabottom is known to be shallow and flat, it can be concluded that seawater penetrates deeper in such places.

The third layer, which is highly resistive (average 5000 Ω•m), is interpreted to be subbottom ice-bonded permafrost of Unit C. Also depicted in Figure 3 are depths derived from seismic refraction surveys. Generally, they are in agreement with the results of HLEM data inversion. Where seismic surveys did not detect ice-bonded permafrost (survey locations indicated in the figure by triangles), the third layer

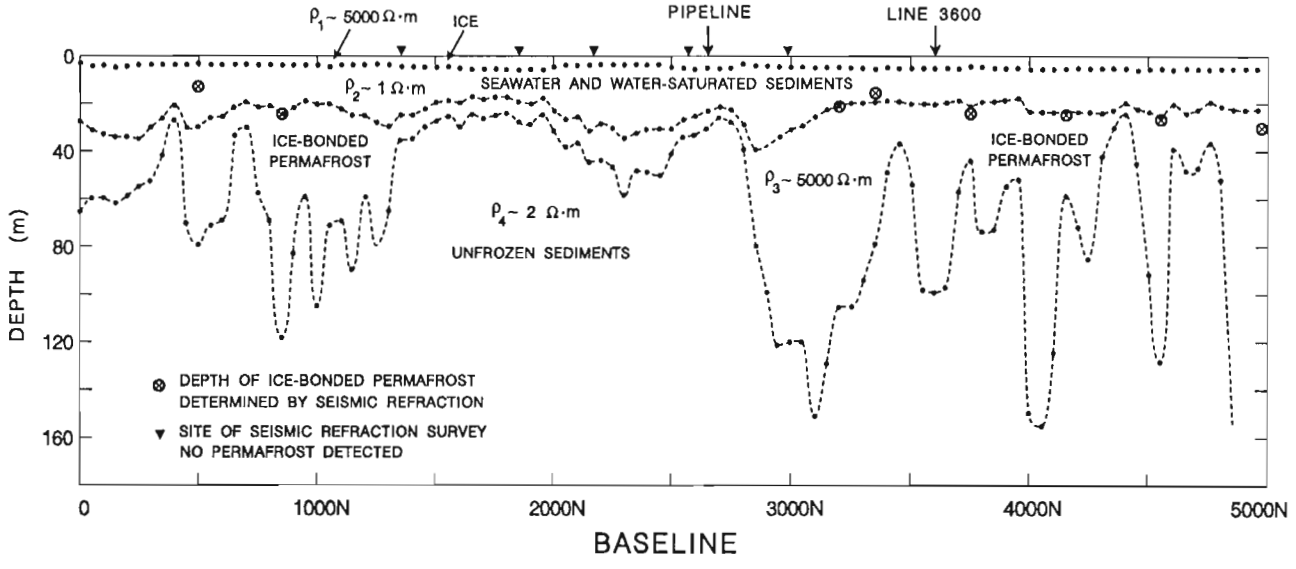


**Figure 5.** Resistivity section along the baseline. The section layout and symbols are in the same as in Figure 3. Arrows indicate intersect points with the pipeline route and line 3600N.

in the resistivity section is thin. The only segment of the line where thick ice-bonded permafrost was detected is between stations 400N and 1550N. This interpretation is in agreement with the results of refraction seismic surveys and drilling (borehole 5). The layer is thin between stations 900S and 400N and only moderately thick elsewhere. The seismic results are poor along the southern third of the profile due to the presence of gas. The last layer in HLEM inversion is conductive basement (unfrozen sediments) with an estimated average resistivity of 2 Ω•m. The true resistivity along the profile most likely varies as a function of sediment type.

Four kilometres of HLEM profiles were surveyed along an east-west line (3600N). A resistivity section derived by unconstrained inversion of HLEM data (Figure 4) indicates that the second resistive layer, interpreted as ice-bonded permafrost, is much thicker in the centre of the profile (between 900W and 1100E) than near the ends. Seismic refraction surveys detected subbottom ice-bonded permafrost between stations 1000W and 1000E. The seismic coverage was denser along this profile (every 150 m) than along any other line discussed in this paper. The difference between the permafrost depth determined by the two geophysical techniques was on average 3 m; only in one location (station 900E) was the discrepancy more than 5 m. The relative rise in the permafrost topography in the easterly direction was reflected in both surveys.

Figure 5 shows a resistivity section obtained by inversion of HLEM along the base line. Subbottom ice-bonded permafrost of variable thickness was detected between the beginning of line 1300N and again between 2800N and the end of the profile (5000N). The central portion of the profile is either permafrost free, as indicated by refraction seismic surveys, or the layer is thin (less than 10 m), as suggested by HLEM surveys. There are only two significant discrepancies between the results of interpretation of seismic and electromagnetic data: at station 500N, the permafrost appears much deeper from electromagnetic interpretation; at station 3000N, seismic surveys did not indicate permafrost, but the results of inversion suggested a thick resistive layer. As the two surveys were carried out during different field seasons, there is a possibility of error in positioning of the stations.

## CONCLUSIONS

A multifrequency horizontal-loop electromagnetic (HLEM) system (APEX MaxMin I) has been used on the Beaufort Shelf for detection of subbottom ice-bonded permafrost. Previously, refraction and high-resolution shallow reflection seismic methods have been used in the transect test area for such purpose. Horizontal-loop electromagnetic field data at individual sounding stations have been processed by means of unconstrained inversion using a four-layer model. Along the four test lines, the inversion yielded stable resistivity and thickness estimates, with small RMS errors averaging one per cent. The results, presented in the form of resistivity sections, are in good agreement with information obtained by seismic surveys and drilling. All known areas of ice-bonded permafrost have been reliably detected. Because of its speed and cost-effectiveness, the HLEM method has the potential of becoming the tool of choice of geophysicists in similar investigations elsewhere in the Arctic.

## ACKNOWLEDGMENTS

S.M. Birk of the Mineral Resources Division, Geological Survey of Canada, assisted in the measurements. The field work was funded by the Panel on Energy Research and Development, Government of Canada. Dr. J.A.M. Hunter of the Terrain Sciences Division kindly provided unpublished seismic data. Dr. P. Keating of the Geophysics Division and Dr. K.A. Richardson of the Mineral Resources Division critically read the manuscript. S.J. Davis of the Mineral Resources Division prepared all illustrations for print.

## REFERENCES

**Blasco, S.M. and Lewis, J.F.**
1991: Offshore geology; in Geological, geotechnical and geophysical studies along an onshore-offshore transect of the Beaufort Shelf, (ed.) S.R. Dallimore; Geological Survey Canada, Open File 2408, p. 26-31.

**Dallimore, S.R. (ed.)**
1991: Geological, geotechnical and geophysical studies along an onshore-offshore transect of the Beaufort Self; Geological Survey of Canada, Open File 2408.

**Frischknecht, F.C., Labson, V.F., Spies, B.R., and Anderson, W.L.**
1991: Profiling methods using small sources; in Electromagnetic Methods in Applied Geophysics, v. 2 - Applications, (ed.) M.N. Nabighian; Investigations in Geophysics, No. 3, Society of Exploration Geophysicists, p. 105-270.

**Hunter, J.A., Kurfurst, P.J., and Birk, S.M.**
1991a: Water-column temperature, salinity and conductivity measurements; in Geological, geotechnical and geophysical studies along an onshore-offshore transect of the Beaufort Shelf, (ed.) S.R. Dallimore; Geological Survey of Canada, Open File 2408, p. 79-115.

**Hunter, J.A., Kurfurst, P.J., Birk, S.M., Burns, R.A., and Good, R.L.**
1991b: Borehole geophysical logging; in Geological, geotechnical and geophysical studies along an onshore-offshore transect of the Beaufort Shelf, (ed.) S.R. Dallimore; Geological Survey of Canada, Open File 2408, p. 116-137.

**Inman, J.R.**
1975: Resistivity inversion with ridge regressions: Geophysics, v. 40, p. 798-817.

**Interpex Ltd.**
1988: EMIX-MM - User's Manual; Interpex Ltd., Golden, Colorado.

**Jenner, K.A. and Blasco, S.M.**
1991: Sedimentology; in Geological, geotechnical and geophysical studies along an onshore-offshore transect of the Beaufort Shelf, (ed.) S.R. Dallimore; Geological Survey of Canada, Open File 2408, p. 32-49.

**Palacky, G.J.**
1991: Application of the multifrequency horizontal-loop electromagnetic method in overburden investigations; Geophysical Prospecting, v. 39, p. 1061-1082.

**Palacky, G.J. and Stephens, L.E.**
1990: Mapping of Quaternary sediments in northeastern Ontario using ground electromagnetic methods; Geophysics, v. 55, p. 1596-1604.

**Palacky, G.J., Smith, S.H, and Stephens, L.E.**
1992a: Quaternary investigations in Geary, Thorburn, and Wilhelmina Townships, Ontario; in Current Research, Part E; Geological Survey of Canada, Paper 92-1E.
1992b: Use of ground electromagnetic measurements to locate sites for overburden drilling near Smoky Falls, Ontario; in Current Research, Part E; Geological Survey of Canada, Paper 92-1E.

**Scott, W.J., Sellmann, P.V., and Hunter, J.A.**
1990: Geophysics in the study of permafrost; in Geotechnical and Environmental Geophysics, v. 1 - Review and Tutorial, (ed.) S.H. Ward; Investigations in Geophysics, No. 5, Society of Exploration Geophysicists, p. 355-384.

Geological Survey of Canada Project 850058

# The Mitchell Point Fault Zone at Phillips Inlet, northern Ellesmere Island, Northwest Territories

**Yoshide Ohta[1] and Eva M. Klaper[2]**
**Institute of Sedimentary and Petroleum Geology, Calgary**

*Ohta, Y. and Klaper, E.M., 1992: The Mitchell Point Fault Zone at Phillips Inlet, northern Ellesmere Island, Northwest Territories; in Current Research, Part E; Geological Survey of Canada, Paper 92-1E, p. 149-156.*

***Abstract***

*The Mitchell Point Fault Zone separates granitic gneisses of the Mitchell Point Belt from the sedimentary and volcanogenic sequence of the Cape Alfred Ernest Belt to the northwest. The segment of the fault zone studied, north of Phillips Inlet, splits into four branches that enclose three subzones, the rocks of which differ in age and metamorphic grade. Amphibolite-grade schists in the southeastern subzone, outcropping to the northwest of the Mitchell Point Belt, are comparable to the Petersen Bay assemblage to the southeast of that belt. The middle subzone comprises a complex fault zone of rocks of Late Proterozoic-Cambrian (Cape Alfred Ernest Belt) and Late Cretaceous (Hansen Point volcanics) ages. The northwestern subzone is underlain by the Late Cretaceous Wootton intrusion. The earliest movements in this complex fault zone are of middle Paleozoic age. Reactivation of the fault zone occurred during Late Cretaceous rifting and Paleogene compression (Eurekan Orogeny).*

***Résumé***

*La zone de failles de Mitchell Point se trouve entre les gneiss granitiques de la ceinture de Mitchell Point et la séquence volcano-sédimentaire de la ceinture de Cape Alfred Ernest, au nord-ouest. Le segment étudié de la zone de failles est celui au nord de l'inlet Phillips; il se divise en quatre branches délimitant trois sous-zones de roches d'âges et de faciès métamorphiques différents. Les schistes du faciès des amphibolites de la sous-zone du sud-est, qui affleurent au nord-ouest de ceinture de Mitchell Point, sont semblables à ceux de l'assemblage de Petersen Bay; ce dernier est observé au sud-est de la ceinture de Mitchell Point. La sous-zone intermédiaire présente une zone de failles complexe composée de roches du Protérozoïque tardif-Cambrien (ceinture de Cape Alfred Ernest Belt) et de roches volcaniques du Crétacé tardif (Hansen Point). Quant à la sous-zone du nord-ouest, elle est représentée par l'intrusion de Wootton du Crétacé tardif. Les premiers mouvements de cette zone de failles complexe remontent au Paléozoïque moyen. Il y a eu une réactivation au cours du rifting du Crétacé tardif et de la compression du Paléogène (orogenèse eurékienne).*

[1] Norsk Polarinstitutt, P.O. Box 158, N-1330 Oslo Lufthavn, Norway
[2] Geologisches Institut, Universität Bern, Baltzerstrasse 1, CH-3012 Bern, Switzerland

## INTRODUCTION

Pearya, an exotic terrane of Caledonian affinity that borders the Franklinian mobile belt in northern Ellesmere Island, has been considered to have been accreted to the northern rim of Laurentia by sinistral strike slip during Late Silurian time (Trettin, 1987, 1989; Trettin and Mayr, 1990a,b) (Fig. 1).

The study area lies within Pearya, northwest of upper Phillips Inlet, in the southwestern part of the Yelverton Inlet map area (Fig. 1) (Trettin and Frisch, 1987). The rocks of this area belong to the two oldest among four major successions in Pearya (Trettin and Frisch, 1987; Bjornerud, 1989, 1991; H.P. Trettin, pers. comm., 1991). Succession I, the late Middle Proterozoic Mitchell Point Belt, represents an igneous and metasedimentary rock suite subjected to amphibolite facies metamorphism. Succession II, the Cape Alfred Ernest Belt, comprises various clastic, calcareous, and volcanogenic rocks of Late Proterozoic to earliest Ordovician age, metamorphosed mainly under greenschist and locally under amphibolite facies conditions.

The Mitchell Point Belt is bordered on the southeast by the Clements Markham Fold Belt. The latter comprises arc-type and alkaline volcanic rocks and associated carbonates of Middle or Late Ordovician to Early Silurian (middle Llandovery) age, the Kulutingwak Fiord assemblage. Schist, amphibolite, and crinoidal marble outcropping on the southeastern side of the Mitchell Point Belt, assigned to the Petersen Bay assemblage, are probably metamorphic equivalents of the Kulutingwak Fiord assemblage. These two assemblages are probably overlain conformably by upper Llandovery turbidites of the Imina Formation, in turn succeeded by mudrocks and turbidites of the Lands Lokk Formation (Wenlock to early Ludlow).

Sedimentary rocks of Sverdrup Basin, mainly Carboniferous and Permian in age, are preserved south of the Yelverton Inlet map area. A Late Cretaceous rifting event on the northwest side of the Mitchell Point Belt controlled the location of the Wootton intrusion, composed of gabbro and granitoid rocks, and the slightly younger "Hansen Point volcanics", an informal unit of formational rank that also includes sedimentary rocks. The youngest rocks in the area are coarse clastic sediments of the Paleogene Eureka Sound Group, lying unconformably on strata of the Cape Alfred Ernest Belt (Wilson, 1976).

Important in the present context are the fault zones bounding both sides of the Mitchell Point Belt, the Petersen Bay Fault Zone (Klaper, in press) on the southeast and the Mitchell Point Fault Zone on the northwest, both of which have been reactivated at different times. The Petersen Bay Fault truncates structural trends of Succession II southeast of the Mitchell Point Belt, suggesting that it originated as a transcurrent fault. Previous information on the southwestern segment of the Mitchell Point Fault Zone can be summarized as follows:

1. Analogy with the Petersen Bay Fault Zone suggests that it may also have originated as a transcurrent fault.
2. Direct contact of the Wootton intrusion with the Mitchell Point Belt on central Wootton Peninsula, suggests that this segment of the fault zone localized Late Cretaceous rifting and intrusion.
3. A late phase of compression, presumably during the Paleogene Eurekan Orogeny, has been inferred from the fact that the Mitchell Point gneiss belt has been thrust onto schists of uncertain younger age in the area east of lower Yelverton Inlet.

## STRUCTURAL OUTLINE OF THE STUDY AREA

The study area, which comprises the southwestern segment of the Mitchell Point Fault Zone, was poorly known previously. In this area the fault zone is triangular in shape, 5 km wide in the south and about 10 km long to the northeast (Fig. 2). Two marginal faults and two internal faults separate three subzones, consisting of igneous and sedimentary rocks of different age and metamorphic grade. The two internal faults coalesce in the northeastern part of the study area and the resulting fault seems to coalesce with the southeastern marginal fault of the fault zone farther northeast.

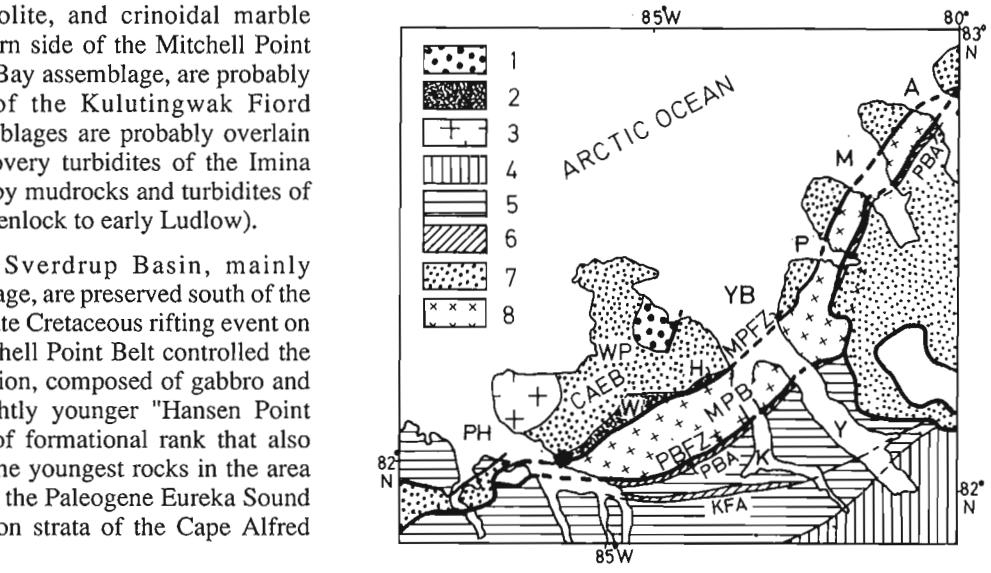


**Figure 1.** Geological map of northwestern Ellesmere Island. (Simplified after Trettin, 1989.). A, Ayles Fiord; M, Milne Fiord; P, Petersen Bay; YB, Yelverton Bay; Y, Yelverton Inlet; K, Kulutingwak Fiord; WP, Wootton Peninsula; PH, Phillips Inlet. MPB, Mitchell Point Belt; CABE, Cape Alfred Ernest Belt; MPFZ, Mitchell Point Fault Zone; PBFZ, Petersen Bay Fault Zone; PBA, Petersen Bay assemblage; KFA, Kulutingwak Fiord assemblage; W, Wootton Intrusion; H, Hansen Point volcanics. **1** – Tertiary (Eureka Sound Group); **2** – Cretaceous igneous and sedimentary rocks; **3** – Devonian granite; **4**, **5**, and **6** – Clements Markham Fold Belt; **4** – Lands Lokk Formation; **5** – Imina Formation; **6** – metamorphosed Middle–Late Ordovician and Middle Silurian rocks; **7** – Succession II, Late Proterozoic-earliest Ordovician rocks; **8** – Succession I, late Middle Proterozoic gneisses. Solid diamond, study area.

The northwestern marginal fault is a sheared contact of the Wootton intrusion with the carbonates of the Cape Alfred Ernest Belt. The carbonates form three successive units and the intrusion is in contact with all these units from south to north. The carbonates are cut by several dykes. The U-Pb zircon age of the Wootton intrusion is 92 ± 1 Ma (Trettin and Parrish, 1987; Trettin et al., 1987).

The markedly arcuate southeastern boundary fault truncates the three subzones in the south.

## DESCRIPTION OF ROCKS WITHIN THE MITCHELL POINT FAULT ZONE

### *The northwestern subzone: the Wootton intrusion*

This subzone consists entirely of rocks of the Wootton intrusion, ranging from clinopyroxene-hornblende gabbro to diorite. The diorites occur as irregular patches and networks within the gabbros, giving them a blocky appearance. The gabbros and diorites both contain numerous xenoliths of felsic gneisses, schistose amphibolites, and banded granitic gneisses. Also present is a network of coarse grained plagioclase-quartz veins. Numerous shear planes within the gabbro and diorite are accentuated by concentrations of hornblende.

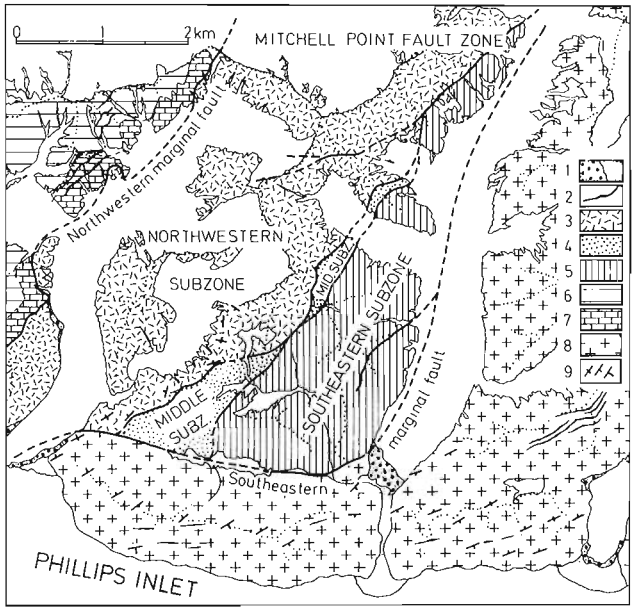


**Figure 2.** Geological map of the southwestern segment of the Mitchell Point Fault Zone. **1** – moraine and alluvial plain; **2** – diabase dyke; **3** – Wootton gabbro-diorite; **4** – various rocks of the middle subzone (see Fig. 3); **5** – schist and amphibolite; **6** – clastic rocks of the Cape Alfred Ernest Belt; **7** – carbonate rocks of the Cape Alfred Ernest Belt; **8** – gneisses of the Mitchell Point Belt; **9** – dip and strike symbols : vertical symbol = vertical bedding, dip symbol with short bar = dips steeper than 70°, dip symbol with long bar = dips of 40° to 65°.

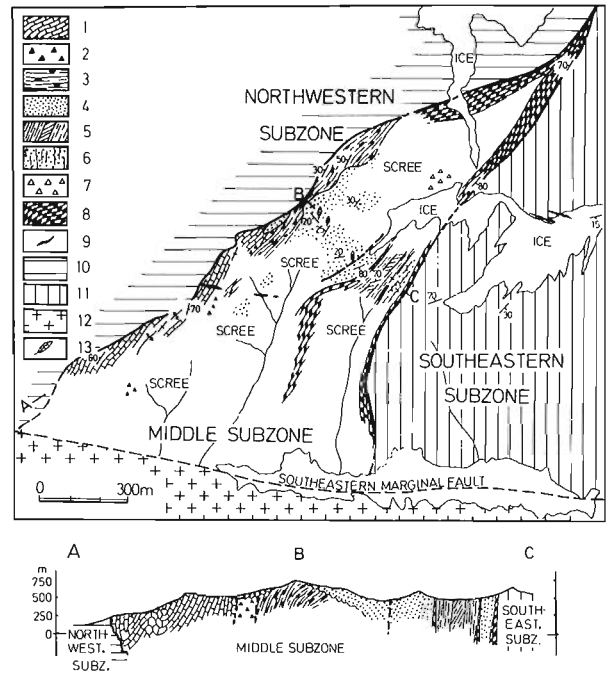


**Figure 3.** Geological sketch map of the middle subzone, southwestern segment of the Mitchell Point Fault Zone. **1** – map unit 1, dolomite; **2** – map unit 2, volcanic eruption breccia; **3** – map unit 3, conglomeratic phyllite; **4** – map unit 4, clastic sediments; **5** – map unit 5, black slate (middle) and phyllite; **6** – map unit 6, sheared sandstone; **7** – map unit 7, diamictite; **8** – map unit 8, brecciated siliceous dolomite; **9** – diabase dyke; **10** – Wootton gabbro-diorite; **11** – schists and amphibolites of the southeastern subzone; **12** – granitic gneisses of the Mitchell Point Belt; **13** – plant fossil locality. A—B—C = geological profile line.

Distinct compositional layering (5 to 10 cm thick) and indistinct flow structures are locally apparent. These structures are subparallel to the local contact between the northwestern and middle subzones.

No intrusive relationships and no thermal effects were observed at the contact between the gabbros and the rocks of the middle subzone. All observed contacts are moderately- to steeply-dipping faults that strike in northeasterly directions. They form a staircase pattern in profile that steps down toward the southeast, beneath the dolomite of the middle subzone. Two orientations of striations were often observed on fault planes. Both plunge about 30° west, but show opposing senses of movement.

### *The middle subzone*

Eight lithological units have been mapped in this triangular area (Fig. 3). The units are numbered and described from northwest to southeast; their age relationships are also discussed.

### Dolomite unit (map unit 1)

This unit, composed of dolomitic rocks, borders the Wootton intrusion on the southeast. The strata form asymmetric flexural folds without cleavage. The fold axes are oblique to the boundary with the gabbro, suggesting that the folding was earlier than the last movements on the fault zone.

A brecciated dolomite, 30 to 40 m thick, occurs in the southeastern part of map unit 1 (Fig. 3). It contains numerous dark grey chert concretions that locally form nearly continuous layers. Also abundant are silicified flat laminae and concentric structures interpreted as stromatolites. Breccia fragments, less than 15 cm in greatest dimension and not flattened, are embedded in an argillaceous carbonate matrix. The western part of map unit 1 consists of a brown, argillaceous dolomite, more than 35 m thick, which contains little chert.

### Volcanic eruption breccia (map unit 2)

An outcrop of undeformed volcanic rocks, 15 m wide, is exposed southeast of the dolomite unit. The contact is covered by a flat-lying younger conglomerate (map unit 4). The outcrop consists of dark red, rough surfaced volcanic breccias, volcanic bombs, oxidized pyroclastics, tuff, and a thin basalt flow. The surface features of the breccias indicate the influence of eruptive fumaroles. The breccia fragments, set in a carbonate-rich matrix, consist of recrystallized siliceous glass and doleritic rocks. The unit appears to be intruded by a few diabase dykes, less than 5 m thick, although the contacts are covered.

### Conglomeratic phyllite unit (map unit 3)

A phyllitic pebble conglomerate, grey-green and partly purple and more than 50 m thick, occurs southeast of the eruption breccias. The pebbles, 5 to 10 cm long and composed of shale, sandstone, and rhyolite, are completely flattened and embedded in a sandy and argillaceous matrix. The cleavage of the rocks is due to the alignment of tiny flakes of chlorite and sericite and is accentuated by opaque seams.

Two quartzite beds, each less than 5 m thick, and a brecciated carbonate bed, about 1 m thick, are interbedded with the phyllites. A shear zone, about 3 m thick and consisting of quartz and epidote, is developed along the fault between a quartzite bed and the Wootton intrusion. Striations on the fault plane plunge gently southwest and indicate sinistral strike slip.

### Clastic sediment unit (map unit 4)

A succession of interbedded conglomerate, sandstone and siltstone, about 200 m thick, outcrops to the east of map unit 3. The western contact with map unit 3 is scree-covered. Crossbedding in sandstones indicates that stratigraphic tops are to the west. The strata strike northeast and dip in northwesterly directions. Gently dipping strata in the western part of the outcrop area may be separated by a fault from steeply (>70°) dipping strata in the eastern part. The observed stratigraphy can be summarized as follows, from northwest to southeast (measurements are approximate only):

| | |
|---|---|
| Polymict pebble conglomerate, with two siltstone beds | 30 m |
| Black siltstone lenses, fossiliferous, in conglomeratic sandstone beds | 30 m |
| Covered | 50 m |
| Graded sandstones with thin lenses of conglomerate | 5 m |
| Black siltstone | 20 m |
| *(possible fault)* | |
| Mainly quartzitic sandstone with minor interbeds of conglomerate and siltstone (fossiliferous) | 30 m |
| Black siltstone | 30 m |

Conglomerates are thicker and more common in the western (i.e. uppermost) part of the outcrop area where at least four beds were counted. They are poorly sorted, impersistent channel fills. Well rounded pebbles, less than 10 cm in diameter and coated by black films, are embedded in a matrix of coarse grained sand. The pebbles are composed of varicoloured quartzite, vein quartz, sericite–chlorite phyllite, grey sandstone, shale, and brecciated carbonate rocks. Various types of microfossils are present in the clasts, including (?)foraminifers in dark grey shale, (?)algae in dense siliceous rocks, and a horn coral in a light grey limestone pebble. Plant fragments occur in four siltstone beds.

### Black slate and phyllite unit (map unit 5)

This unit comprises, from west to east; black slate (50 m), phyllitic siliceous tuff and tuff-breccia (13 m), and green phyllite (10 m). Brecciated siliceous carbonate (3 m, map unit 8) separates these rocks from adjacent units.

The strike of the slaty cleavages is oblique to the general trend of the middle subzone, while those of the phyllitic schistosities are subparallel to it.

### Sheared sandstone unit (map unit 6)

This unit is a sheared sandstone, about 50 m thick, similar to those of map unit 4. It is bounded on both sides by slices of brecciated carbonate rocks.

### Diamictite unit (map unit 7)

A distinct diamictite occurs as isolated outcrops in scree on the slope to the northwest of a brecciated carbonate unit (map unit 8). The rocks are characterized by scattered, unsorted pebbles of carbonate and clastic sediments, mainly dolomitic in composition, in a coarse grained sandy matrix with carbonate cement. No penetrative cleavage is developed in the rocks.

**Table 1.** Chemical composition of schistose rocks from the southeastern subzone of the Mitchell Point Fault Zone

A. Major element analyses of a felsic schist (88E113) and an amphibolite (88E117).

B. Trace element analysis of a felsic schist (88E113).

A

| | 88E113 | 88E117 |
|---|---|---|
| $SiO_2$ | 57.33 | 55.52 |
| $TiO_2$ | 1.03 | 1.37 |
| $Al_2O_3$ | 14.21 | 15.07 |
| $Fe_2O_3$ | 1.55 | 3.62 |
| FeO | 12.97 | 6.25 |
| MnO | 0.33 | 0.20 |
| MgO | 3.94 | 5.19 |
| CaO | 2.32 | 6.31 |
| $Na_2O$ | 1.01 | 2.39 |
| $K_2O$ | 1.35 | 1.43 |
| $P_2O_5$ | 0.14 | 0.25 |
| Ig.ls. | 3.21 | 2.73 |
| Total | 99.39 | 99.97 |

B

| | |
|---|---|
| Ba | 314.04 |
| Co | 82.72 |
| Cr | 242.64 |
| Cu | 93.02 |
| Nb | 8.68 |
| Ni | 28.84 |
| Rb | 66.90 |
| Sr | 75.48 |
| Y | 54.58 |
| Zn | 109.36 |
| Zr | 178.72 |

### Diamictite unit (map unit 7)

A distinct diamictite occurs as isolated outcrops in scree on the slope to the northwest of a brecciated carbonate unit (map unit 8). The rocks are characterized by scattered, unsorted pebbles of carbonate and clastic sediments, mainly dolomitic in composition, in a coarse grained sandy matrix with carbonate cement. No penetrative cleavage is developed in the rocks.

### Brecciated siliceous carbonate unit (map unit 8)

Brecciated carbonate rocks are in contact with several other rock units. Their thicknesses increase, up to approximately 100 m, to the southwest along the northwestern boundary of map unit 5 and to the northeast along the eastern margin of the middle subzone. In the latter area these rocks mark the boundary between gabbro of the Wootton intrusion and the schists of the southeastern subzone. There the rocks are distinctly banded, dip nearly vertically, and are cut by many basic dykes. Although similar to the dolomites of map unit 1 with respect to their brecciated structure, rocks of map unit 8 differ by their uniformly siliceous composition and lack of chert concretions.

### Age and correlation of the map units of the middle subzone

Map unit 7 is closely comparable to diamictites elsewhere in the Pearya Terrane, including the Cape Alfred Ernest Belt on northeastern Wootton Peninsula. All these rocks are comparable to glaciogenic diamictites of latest Proterozoic (Vendian) age in the North Atlantic regions (Hambrey, 1983).

The rocks of map units 3, 5, 7, and 8 are comparable to those of Succession II, the Cape Alfred Ernest Belt of the Pearya Terrane, with respect to overall composition and metamorphic grade.

Map unit 1 differs from the units discussed above by an absence of metamorphic features and may be younger, although virtually unmetamorphosed dolomites are known to occur in Succession II in other areas. Map unit 1 may be as young as late Paleozoic [Late Carboniferous-Permian Nansen Formation(?); Thorsteinsson, 1974; Mayr and Trettin, 1990a,b].

Map unit 2 can be correlated with the Hansen Point volcanics, which outcrop widely on northeastern Wootton Peninsula. The volcanics have been dated as Late Cretaceous on the basis of isotopic age determinations and spore analyses (Trettin et al., 1987; Embry and Osadetz, 1988; MacRae et al., 1990; Muecke et al., 1990). At Emma Fiord, northwestern Ellesmere Island, the unit unconformably overlies the Nansen Formation (Trettin and Frisch, 1987).

Map unit 4 has yielded carbonized plant fragments of an unspecified post-Middle Devonian age (J. Basinger, pers. comm., 1989). No palynomorphs were seen in several samples analyzed (D.J. McIntyre, pers. comm., 1988). A horn coral contained in a limestone clast has not been identified.

On Wootton Peninsula, sandy and conglomeratic sediments containing plant material occur in the Hansen Point volcanics (Embry and Osadetz, 1988; MacRae et al., 1990; Muecke, pers. comm., 1989), and in the Eureka Sound Group (Wilson, 1976). Assignment of map unit 4 to the Hansen Point volcanics is supported by the observation that the unit probably is intruded by a diabase dyke, as such dykes are generally older than the Eureka Sound Group, and also by the absence of clasts derived from Cretaceous intrusions.

## *The southeastern subzone: crystalline schists*

The southeastern subzone, 1.5 km wide and bounded by the southeastern marginal fault on the south and east, is composed of crystalline schists. The rocks are mainly felsic garnet two-mica schists with intercalated, thin, pelitic, garnet two-mica schists and schistose amphibolites.

The felsic schists are composed mainly of plagioclase and quartz in roughly equal proportions. Large, poikiloblastic hornblende crystals, centimetres in length, project from the felsic schists into adjacent pelitic layers. Brown biotite flakes in both felsic and pelitic schists are extensively chloritized, whereas muscovite flakes are fresh and show strong preferred orientation and secondary bending. Garnet grains always contain numerous inclusions, the trains of which are either

**Table 2.** Representative mineral composition of the schistose rocks from the southeastern subzone

**A.** Felsic schist (88E113)

| | ga | st | st-ga | bi | mu | ch | ep | pl |
|---|---|---|---|---|---|---|---|---|
| $SiO_2$ | 34.36 | 28.44 | 28.19 | 37.02 | 51.01 | 26.12 | 38.49 | 61.13 |
| $TiO_2$ | 0.12 | 0.74 | 0.62 | 0.04 | 0.25 | 0.08 | 0.09 | 0.00 |
| $Al_2O_3$ | 20.37 | 54.13 | 53.91 | 20.87 | 31.79 | 21.32 | 27.47 | 23.67 |
| $Fe_2O_3$ | 34.50 | 13.00 | 12.55 | 29.01 | 3.51 | 34.45 | 7.55 | 0.07 |
| MnO | 2.83 | 0.12 | 0.23 | 0.47 | 0.04 | 0.13 | 0.04 | 0.01 |
| MgO | 3.43 | 0.85 | 0.86 | 4.45 | 1.91 | 10.80 | 0.03 | 0.00 |
| CaO | 3.50 | 0.00 | 0.01 | 1.91 | 0.09 | 0.16 | 23.25 | 6.07 |
| $Na_2O$ | 0.03 | 0.01 | 0.00 | 0.00 | 0.41 | 0.02 | 0.03 | 8.30 |
| $K_2O$ | 0.00 | 0.00 | 0.00 | 2.42 | 9.36 | 0.00 | 0.01 | 0.09 |
| $Cr_2O_3$ | 0.00 | 0.01 | 0.02 | 0.00 | 0.04 | 0.00 | 0.03 | 0.00 |
| NiO | 0.02 | 0.03 | 0.03 | 0.01 | 0.00 | 0.05 | 0.02 | 0.07 |
| Total | 99.16 | 97.33 | 96.42 | 96.20 | 98.41 | 93.13 | 97.01 | 99.41 |

**B.** Amphibolite (88E117)

| | ho | ga-c | ga-m | ep | ch | pl |
|---|---|---|---|---|---|---|
| $SiO_2$ | 41.96 | 35.25 | 35.32 | 37.29 | 27.31 | 67.37 |
| $TiO_2$ | 0.45 | 0.06 | 0.02 | 0.12 | 0.05 | 0.00 |
| $Al_2O_3$ | 16.00 | 20.92 | 21.12 | 23.58 | 18.75 | 21.90 |
| $Fe_2O_3$ | 18.08 | 29.28 | 29.78 | 11.59 | 25.09 | 0.35 |
| MnO | 0.42 | 5.23 | 5.03 | 0.32 | 0.36 | 0.00 |
| MgO | 9.03 | 3.89 | 4.02 | 0.87 | 18.76 | 0.00 |
| CaO | 11.08 | 4.33 | 4.33 | 21.78 | 0.03 | 2.10 |
| $Na_2O$ | 1.57 | 0.03 | 0.04 | 0.09 | 0.00 | 10.60 |
| $K_2O$ | 0.23 | 0.00 | 0.00 | 0.00 | 0.00 | 0.10 |
| $Cr_2O_3$ | 0.07 | 0.05 | 0.08 | 0.04 | 0.13 | 0.00 |
| NiO | 0.00 | 0.00 | 0.02 | 0.00 | 0.06 | 0.01 |
| Total | 98.89 | 99.04 | 99.76 | 95.68 | 90.54 | 102.43 |

ga – garnet; ga-c – core of garnet; ga-m – margin of garnet; st – staurolite; st-ga – staurolite included in garnet; ho – hornblende; bi – biotite; mu – muscovite; ep – epidote; ch – chlorite; pl – plagioclase.

ratios between garnet and biotite indicate a peak metamorphic temperature of approximately 500°C at an estimated pressure of 5 kbar (Table 2).

The schistosity is generally parallel to the compositional layering, and small-scale isoclinal fold crests can be seen. This indicates an early event of tight and complex isoclinal folding. Measurements of schistosity and compositional layering indicate a major synform, the axis of which strikes roughly north-south and plunges about 20° to the south (Fig. 4). This fold, which postdates the formation of the schistosity, shows no axial plane cleavage. Extensive chloritization of biotite and bending of muscovite flakes also indicate a later retrogressive event that may be correlated with this folding.

Two orientations of small faults and younger dykes are recognized in the southeastern subzone: one subparallel or at small angles to the prevalent schistosity, and the other subperpendicular to the fold axis (Fig. 4). The oblique orientation of the major synform axis with respect to the overall trend of the subzone, and the orientation of the two sets of faults, probably a conjugate set, may indicate a dextral southwest-northeast transpression during the later folding episode.

The rocks of the southeastern subzone are very similar to those of the Petersen Bay assemblage, which borders the Mitchell Point Belt on the southeast along a fault contact. The Petersen Bay assemblage is probably correlative with the Kulutingwak Fiord assemblage dated as Middle (or Late) Ordovician to Early Silurian (middle Llandovery) on the basis of conodonts and a U-Pb age determination (M. Bjornerud and H.P. Trettin, pers. comm., 1991). These rocks are definitely different from the phyllites in the middle subzone.

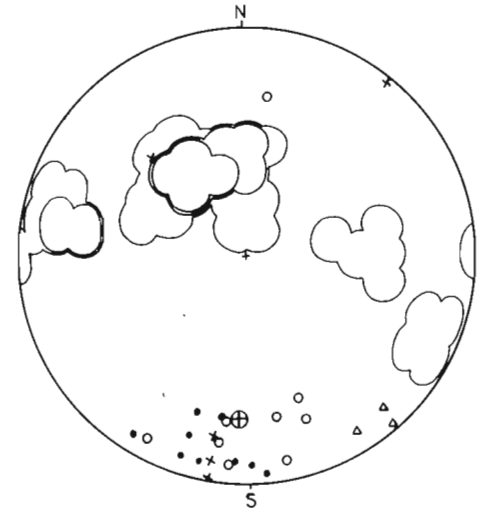


**Figure 4.** Stereographic projection (lower hemisphere) of the mesoscopic structural elements from the southeastern subzone of the Mitchell Point Fault Zone. Contour = schistosity, 38 measurements, 0 - 10 - 15 % contours. Open circle = small fold axis. Dot = striation lineation. Oblique cross = small fault. Triangle = diabase dyke. Large circle with cross = calculated fold axis for the cleavage girdle.

An occurrence of similar schists along the northwest side of the Mitchell Point gneiss belt has been reported, on the northeast side of Yelverton Inlet where the gneisses overthrust the schists from the southeast (Frisch, 1974; H.P. Trettin, pers. comm., 1991).

## THE GRANITIC GNEISSES OF THE MITCHELL POINT BELT

These rocks are exposed along the northern coast of Phillips Inlet, south and east of the Mitchell Point Fault Zone (Fig. 2). The rocks are essentially porphyritic, two-mica granites with K-feldspar phenocrysts (S-type granite of Chappell and White, 1974). The feldspar crystals are locally deformed into augen shapes, concomitantly with the development of varying degrees of gneissosity. The gneissosity strikes east-northeast, roughly parallel to the overall trend of the gneiss belt.

Small inclusions of micaceous gneisses and schists are scattered in the granitic gneisses and are especially common in the southeastern part of the mapped area. Inclusions of hornblende-bearing schists and zoned skarns are less common.

## DISCUSSION

The Mitchell Point Fault Zone in the study area is more complex than was previously known and consists of four branch faults which define three lithologically different subzones. The discovery, on the northwest side of the Mitchell Point gneiss belt, of schists and amphibolites (southeastern subzone) that are similar in lithology to the Petersen Bay assemblage on its southeastern side emphasizes the significance of the fault zone. However, the tectonic significance of the southeastern subzone is still enigmatic.

If the correlation of the southeastern subzone with the Petersen Bay assemblage is correct, then a minimum age for the metamorphism of the schists and amphibolites is given by the late Llandovery age of the Imina Formation, which was also affected by this metamorphic event in the area southeast of the Mitchell Point Belt. An $^{39}Ar$-$^{40}Ar$ plateau age of hornblende from the Petersen Bay assemblage is 428 ± 4.6 Ma (preliminary determination; J.C. Roddick, pers. comm., 1991), or early Wenlock, and is compatible with the stratigraphic relationships. Thus, the minimum age for the middle Paleozoic movements on the Mitchell Point Fault Zone may be later than Wenlock.

The sequence of variably metamorphosed strata of different ages (e.g. diamictite) in the middle subzone forms a complex zone of fault slices from the Cape Alfred Ernest Belt and from the Hansen Point volcanics. The most reasonable explanation for this association appears to be that the rocks of the middle subzone were inserted between the Cape Alfred Ernest Belt and Mitchell Point Belt during a phase of major thrusting and/or strike slip, after deposition of the Hansen Point volcanics.

The northwesternmost branch fault of the Mitchell Point Fault Zone may have originated in the Paleozoic, but must have controlled the emplacement of the Late Cretaceous Wootton intrusion. The faults bounding the gabbro body on the northwest and southeast were reactivated later, presumably during the Tertiary Eurekan Orogeny.

The overall geometry of the southeastern subzone may suggest a dextral shear sense (in map view) along the southeastern boundary fault.

## ACKNOWLEDGMENTS

The authors are grateful to H.P. Trettin for his kind invitation to participate in the field work in 1988, for constructive criticism and improvement of the manuscript. Examinations of fossils by J. Basinger and D.J. McIntyre and a preliminary radiometric age determination by J.C. Roddick are acknowledged. A travel grant to E.M.K. by the "Stiftung zur Förderung der wissenschaftlichen Forschung an der Universität Bern" is also gratefully acknowledged.

## REFERENCES

**Bjornerud, M.G.**
1989: Structural transects in northwestern Ellesmere Island, Canadian Arctic Archipelago; in Current Research, Part G; Geological Survey of Canada, Paper 89-1G, p. 125-131.
1991: Structural evolution of the Kulutingwak zone, northwestern Ellesmere Island, Northwest Territories: the northern edge of Paleozoic North America? in Current Research, Part E; Geological Survey of Canada, Paper 91-1E, p. 187-195.

**Chappell, B.W. and White, A.J.R.**
1974: Two contrasting granite types; Pacific Geology, v. 8, p. 173-174.

**Embry, A.F. and Osadetz, K.G.**
1988: Stratigraphy and tectonic significance of Cretaceous volcanism in the Queen Elizabeth Islands, Canadian Arctic Archipelago; Canadian Journal of Earth Sciences, v. 25, p. 1209-1219.

**Frisch, T.**
1974: Metamorphic and plutonic rocks of northernmost Ellesmere Island, Canadian Arctic Archipelago; Geological Survey of Canada, Bulletin 229, 87 p.

**Hambrey, M.J.**
1983: Correlation of Late Proterozoic tillites in the North Atlantic region and Europe; Geological Magazine, v. 120, p. 209-232.

**Klaper, E.M.**
in press: The Paleozoic tectonic evolution of the northern edge of North America – a structural study of northern Ellesmere Island, Canadian Arctic Archipelago; Tectonics.

**MacRae, R.A., Muecke, G.K., and Reynolds, P.H.**
1990: Palynology, stratigraphy and radiometric age of an Upper Cretaceous sedimentary–volcanic sequence, Emma Fiord, NW Ellesmere Island, Canadian Arctic; (abstract) Geological Association of Canada, Mineralogical Association of Canada, Annual Meeting, May 16-18, 1990; Program with Abstracts, v. 15, p. A80-A81.

**Mayr, U. and Trettin, H.P.**
1990a: Revised geological map, Tanquary Fiord, District of Franklin (NTS 340 D), scale 1:125 000; Geological Survey of Canada, Open File 2135.
1990b: Revised geological map, Clements Markham Inlet and Robeson Channel, District of Franklin (NTS 120 E, F, G), scale 1:125 000; Geological Survey of Canada, Open File 2138.

**Muecke, G.K., Reynolds, P.H., and Avison, H.A.**
1990: $^{40}Ar/^{39}Ar$ geochronology of episodic magmatism during the late phases of Sverdrup Basin development, Canadian Arctic Islands; (abstract) Geological Association of Canada, Mineralogical Association of Canada, Annual Meeting, May 16-18, 1990; Program with Abstracts, v. 15, p. A93.

**Thorsteinsson, R.**
1974: Carboniferous and Permian stratigraphy of Axel Heiberg and western Ellesmere Island, Canadian Arctic Archipelago; Geological Survey of Canada, Bulletin 224, 115 p.

**Trettin, H.P.**
1987: Pearya: a complex terrane with Caledonian affinities in northern Ellesmere Island; Canadian Journal of Earth Sciences, v. 24, p. 224-245.

1989: The Arctic Islands; in The Geology of North America, v. A, The Geology of North America – An Overview; Geological Society of America, p. 349-369.

**Trettin, H.P. and Frisch, T.**

1987: Bedrock geology, Yelverton Inlet map area, northern Ellesmere Island, interim report and map (340 F, 560 D); Geological Survey of Canada, Open File 1651.

**Trettin, H.P. and Mayr, U.**

1990a: Revised geological map, Lady Franklin Bay, District of Franklin (NTS 120 E, H), scale 1:125 000; Geological Survey of Canada, Open File 2136.

1990b: Revised geological map, M'Clintock Inlet, District of Franklin (NTS 340 E, H), scale 1:125 000; Geological Survey of Canada, Open File 2137.

**Trettin, H.P. and Parrish, R.**

1987: Late Cretaceous bimodal magmatism, northern Ellesmere Island: isotope age and origin; Canadian Journal of Earth Sciences, v. 24, p. 257-265.

**Trettin, H.P., Parrish, R., and Loveridge, W.D.**

1987: U–Pb age determinations on Proterozoic to Devonian rocks from northern Ellesmere Island, Arctic Canada; Canadian Journal of Earth Sciences, v. 24, p. 246-256.

**Wilson, D.G.**

1976: Eureka Sound and Beaufort formations, Yelverton Bay, Ellesmere Island, District of Franklin; in Report of Activities, Part A, Geological Survey of Canada, Paper 76-1A, p. 453-456.

Geological Survey of Canada Project 860007

# Pore structure of shales from the Beaufort-MacKenzie Basin, Northwest Territories

**T.J. Katsube and M.E. Best[1]**
**Mineral Resources Division**

*Katsube, T.J. and Best, M.E., 1992: Pore structure of shales from the Beaufort-MacKenzie Basin, Northwest Territories; in Current Research, Part E; Geological Survey of Canada, Paper 92-1E, p. 157-162.*

***Abstract***

*Pore-size distribution measurements were made on 10 shale samples from depths of 1000-4100 m in the Beaufort-MacKenzie Basin, as part of a study designed to obtain petrophysical data required for modelling hydrocarbon distribution in sedimentary basins. Results show that porosity decreases with compaction and burial depth and reaches a value of 30% at 1000 m, and then continues to decrease to 5-15% at greater depth. The pores generally show a unimodal pore-size distribution, with a mean pore-size of about 120 nm at 1000 m, decreasing to 10-20 nm at greater depth. Between depths of 2500 to 4100 m, there is an indication of a slight increase in total porosity. The mean pore-size shows a similar trend. The smaller pore-sizes seen in these samples are in the same size range as those reported for tight shales from the Venture Gas Field, offshore Nova Scotia, which are some of the smallest ever reported for rocks.*

***Résumé***

*Des mesures en vue d'établir la distribution de la dimension des pores ont été effectuées sur 10 échantillons de shale du bassin de Beaufort-Mackenzie, sur un intervalle allant de 1 000 à 4 100 m; ce travail s'inscrivait dans le cadre d'une étude conçue en vue d'acquérir les données pétrophysiques nécessaires pour modéliser la distribution des hydrocarbures dans les bassins sédimentaires. Les résultats montrent que la porosité diminue en fonction du compactage et de la profondeur d'enfouissement; elle est de 30 % à 1 000 m, puis continue de diminuer jusqu'à atteindre une valeur de 5 à 15 % plus en profondeur. La dimension des pores présente généralement une distribution unimodale, la moyenne étant d'environ 120 nm à 1 000 m, mais diminuant jusqu'à une valeur de 10 à 20 nm à plus grande profondeur. Entre 2 500 et 4 100 m, il semble qu'il y ait une légère augmentation de la porosité totale; la dimension moyenne des pores montre une tendance similaire. Quant à la dimension minimale des pores dans ces échantillons, elle se situe dans le même intervalle de dimensions que celui obtenu dans le cas des shales peu perméables du champ de gaz Venture, au large des côtes de la Nouvelle-Écosse; ces dimensions sont parmi les plus petites jamais signalées.*

[1] Pacific Geoscience Centre, Sidney, B.C.

**Table 1.** Depth of shale samples taken from the six wells located in the Beaufort-MacKenzie Basin in the Northwest Territories

| Sample Number | Direction | Well Name | Depth (m) | Rock Type |
|---|---|---|---|---|
| B-01 | v | Malik A-06 | 2639.1 | Shale |
| B-02 | v | Malik A-06 | 2827.6 | Shale |
| B-03 | v | Kadluk 0-07 | 999.3 | Silty Shale |
| B-04 | v | Koakoak 0-22 | 4106.7 | Black Shale |
| B-05 | v | Kopanoar 2J-44 | 3760.4 | Sandy Shale |
| B-06 | v | Ivik J-26 | 3116.9 | Shale |
| B-07 | h | Ivik J-26 | 3116.9 | Sandy Shale |
| B-08 | v | Ivik J-26 | 3466.3 | Shale |
| B-09 | v | Issugnak 20-61 | 2593.7 | Sandy Shale |
| B-10 | v | Issugnak 20-61 | 3283.4 | Silty Shale |

h = sample taken in horizontal direction
v = sample taken in vertical direction

**Table 2.** Pore-size distribution data for different pore-size ranges, d, obtained by mercury porosimetry for the 10 shale samples from the Beaufort-MacKenzie Basin offshore Northwest Territories.

| Sample Number | B-1 | B-2 | B-3 | B-4 | B-5 | B-6 | B-7 | B-8 | B-9 | B10 |
|---|---|---|---|---|---|---|---|---|---|---|
| d(nm) | | | | | $\phi_a$ (%) | | | | | |
| 2.5-4.0 | 0.76 | 0.66 | 0.30 | 0.51 | 0.26 | 1.08 | 0.45 | 0.63 | 0.29 | 0.79 |
| 4.0-6.3 | 1.16 | 0.89 | 0.27 | 0.96 | 0.48 | 1.73 | 1.17 | 0.93 | 0.66 | 1.10 |
| 6.3-10 | 1.95 | 1.38 | 0.38 | 1.45 | 0.79 | 2.22 | 1.99 | 1.61 | 0.84 | 1.64 |
| 10- | 0.78 | 0.89 | 0.47 | 2.20 | 0.86 | 0.94 | 1.59 | 1.98 | 0.89 | 2.38 |
| 16- | 0.35 | 0.71 | 1.20 | 6.04 | 1.80 | 0.49 | 0.74 | 5.71 | 1.64 | 3.41 |
| 25- | 0.18 | 0.49 | 1.43 | 0.98 | 2.32 | 0.20 | 0.27 | 1.02 | 2.08 | 0.75 |
| 40- | 0.20 | 0.37 | 2.47 | 0.49 | 2.08 | 0.17 | 0.17 | 0.42 | 2.57 | 0.40 |
| 63- | 0.13 | 0.27 | 2.97 | 0.14 | 0.62 | 0.05 | 0.00 | 0.19 | 1.42 | 0.19 |
| 100- | 0.10 | 0.25 | 8.31 | 0.14 | 0.48 | 0.07 | 0.00 | 0.21 | 1.26 | 0.21 |
| 160- | 0.05 | 0.07 | 8.35 | 0.07 | 0.29 | 0.02 | 0.00 | 0.19 | 0.66 | 0.09 |
| 250- | 0.08 | 0.17 | 3.80 | 0.12 | 0.41 | 0.02 | 0.00 | 0.09 | 0.53 | 0.14 |
| 400- | 0.03 | 0.07 | 0.61 | 0.14 | 0.48 | 0.00 | 0.00 | 0.19 | 0.51 | 0.00 |
| 630- | 0.00 | 0.05 | 0.27 | 0.05 | 0.10 | 0.00 | 0.00 | 0.00 | 0.22 | 0.00 |
| 1000- | 0.00 | 0.10 | 0.27 | 0.07 | 0.07 | 0.00 | 0.00 | 0.00 | 0.24 | 0.00 |
| 1585- | 0.00 | 0.20 | 0.38 | 0.07 | 0.02 | 0.00 | 0.00 | 0.00 | 0.38 | 0.00 |
| 2512- | 0.00 | 0.20 | 0.18 | 0.07 | 0.00 | 0.00 | 0.00 | 0.00 | 0.31 | 0.00 |
| $\phi_{gm}$ | 5.77 | 6.76 | 31.7 | 13.5 | 11.6 | 7.00 | 6.38 | 13.2 | 14.5 | 11.1 |
| $d_{hg}$ | 10.0 | 22.4 | 121. | 18.5 | 37.2 | 8.4 | 10.0 | 17.5 | 56.4 | 14.7 |
| $\delta_D$ | 2.64 | 2.46 | 1.79 | 2.34 | 2.39 | 2.47 | 2.48 | 2.33 | 2.22 | 2.34 |

$\phi_a$ = Partial porosity (%)
d = Pore-size range (nm)
$\phi_{gm}$ = Total porosity measured by mercury porosimetry (%)
$d_{hg}$ = Mean (geometric) pore-size (nm)
$\delta_D$ = Density (g/cc)

## INTRODUCTION

Hydrocarbon distribution in sedimentary basins is influenced by the petrophysical properties of shales. Shales play a dominant role in the development of fluid migration pathways during the geological evolution of sedimentary basins. Therefore, the acquisition of petrophysical data for shales, especially tight shales at depth, is essential (Mudford and Best, 1989) to help describe the hydrocarbon generation, migration and accumulation history in sedimentary basins (Williamson, 1992). As part of a program designed to obtain such information, a study to determine why permeabilities of tight shales are extremely low, often less than $10^{-20}$ $m^2$ (Luffel and Guidry, 1989; Brace, 1980; Morrow et al., 1984; Mudford and Best, 1989), was carried out on samples from the Scotian Shelf. The results (Katsube et al., 1991a) have suggested that the low permeability of tight shales is due to the extremely small pores, with pore-sizes of the order of 10 nm, that constitute the throats of the interconnected pore network. These pores (nano-pores) exhibit a unimodal pore-size distribution in the range of 2.5-60 nm with a mean of about 8-16 nm (Katsube et al., 1991a). Since these nano-pores play a significant role in determining the petrophysical properties of shales, a study has been carried out to obtain a better understanding of their characteristics (Katsube, 1992). This paper presents the results of pore-size distribution measurements made to study how pore-structure of shales change with compaction, finally ending up as nano-pores at depth. Ten shale core samples taken from depths in the range of 1000-4100 m in the Beaufort-MacKenzie Basin (Table 1) have been used for this study.

## METHOD OF INVESTIGATION

### *Samples and sample preparation*

This study is carried out in conjunction with measurements and analyses of formation-factor, effective porosity (by immersion), fluid permeability and mineralogical and textural analysis (Katsube et al., 1990, 1991a, 1992a). The mineralogical and texture analysis includes X-ray diffraction (XRD), scanning electron microscopy (SEM), and petrographic thin section analysis (PTA). The specimens used for the pore-size distribution measurements in this study are fragments of about 5-10 g in weight that were cut out of 10 shale samples obtained from 6 wells located in the Beaufort-MacKenzie Basin in the Northwest Territories (Table 1). Specimens for all of the other measurements were also taken from these samples.

### *Mercury porosimetry*

The pore-size distribution of these shale samples was determined by mercury intrusion porosimetry, following the procedures described in previous publications (e.g. Katsube, 1981; Katsube and Walsh, 1987; Katsube and Hume, 1987), using an equilibration time of 30 seconds for each of the high pressure steps, and 10 seconds for the low pressure (<0.7 MPa) steps. This technique was first suggested by Washburn (1921). The mercury porosimeter used for these measurements, in principle, is capable of generating pressures high enough to force mercury into all accessible pores, and measure the volume of mercury taken up by them (Rootare, 1970). If the pores in a substance are assumed to be cylindrical, the Washburn equation (Rootare, 1970) can be

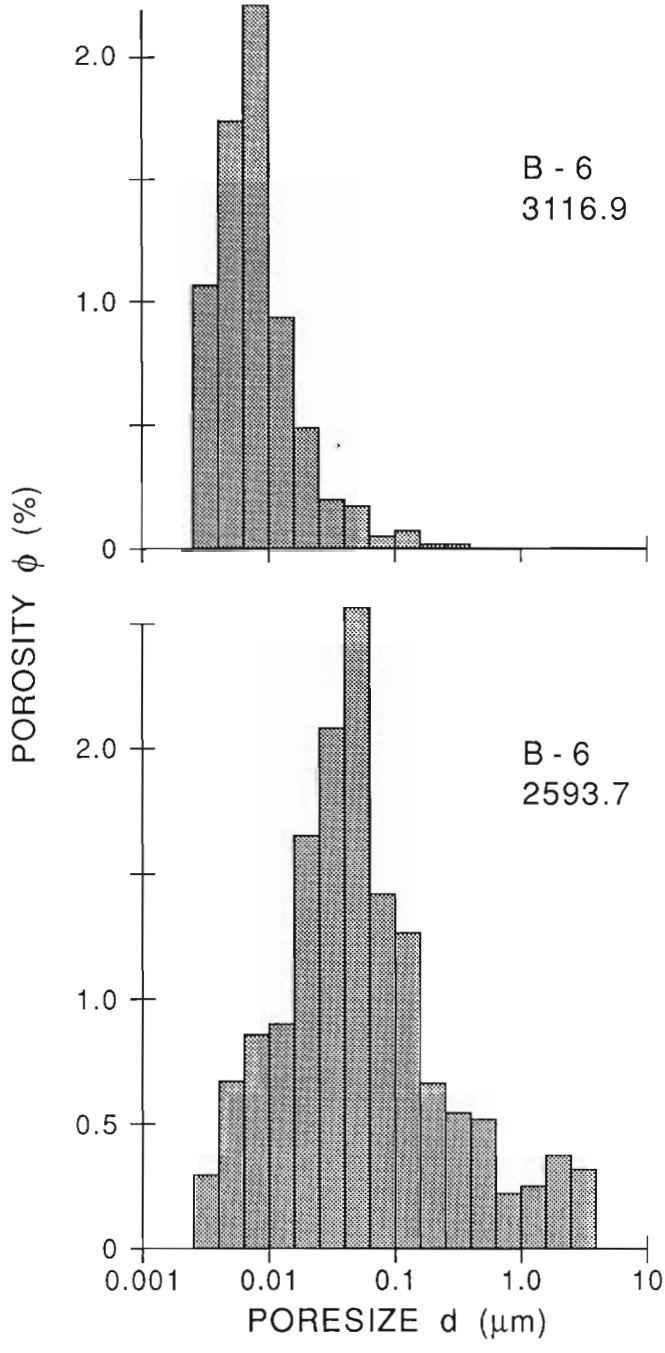


**Figure 1.** Typical pore-size distributions in terms of partial porosity ($\phi_a$) for (a) sample number B-6 (3116.9 m), and (b) sample number B-9 (2593.7 m) from the Beaufort-MacKenzie Basin. Partial porosity ($\phi_a$) is the porosity contributed by each pore-size range (e.g. 2.5-4.0 nm, 4.0-6.3 nm).

used to relate the pressure, p, required to force the mercury into pores with pore-size (diameter), d, equivalent or greater than

$$d = -4\gamma\cos(\theta)/p \quad (1)$$

where $\gamma$ is the surface tension of mercury, and $\theta$ is the contact angle. In this study, values of $\theta$=30° and =0.48 N/m have been used with equilibration times of 10 and 30 seconds for low and high pressures, respectively. These measurements were made by ORTECH (Toronto, Ontario), using a Micromeretics, Auto Pore 9200, mercury porosimeter. The pressure range available is 0.14-420 MPa with an equivalent pore-size range of 10-0.003 μm.

## EXPERIMENTAL RESULTS

Results of the pore-size distribution measurements made by mercury porosimetry are presented in Table 2. The partial porosity, $\phi_a$, which is the porosity contributed by each pore-size range (e.g. 2.5-4.0 nm, 4.0-6.3 nm), is listed in the column under each sample. The total porosity measured by mercury porosimetry, $\phi_{gm}$, listed near the bottom of the table, is the sum of the partial porosities ($\phi_a$). The total porosity ($\phi_{gm}$) is in the range of 5.8 to 32%, the largest value for the sample taken at 999 m depth, and the smaller values for samples from greater depth. Typical pore-size distributions in terms of partial porosity ($\phi_a$) shown in Figure 1 depict relatively simple unimodal populations, concentrated in the

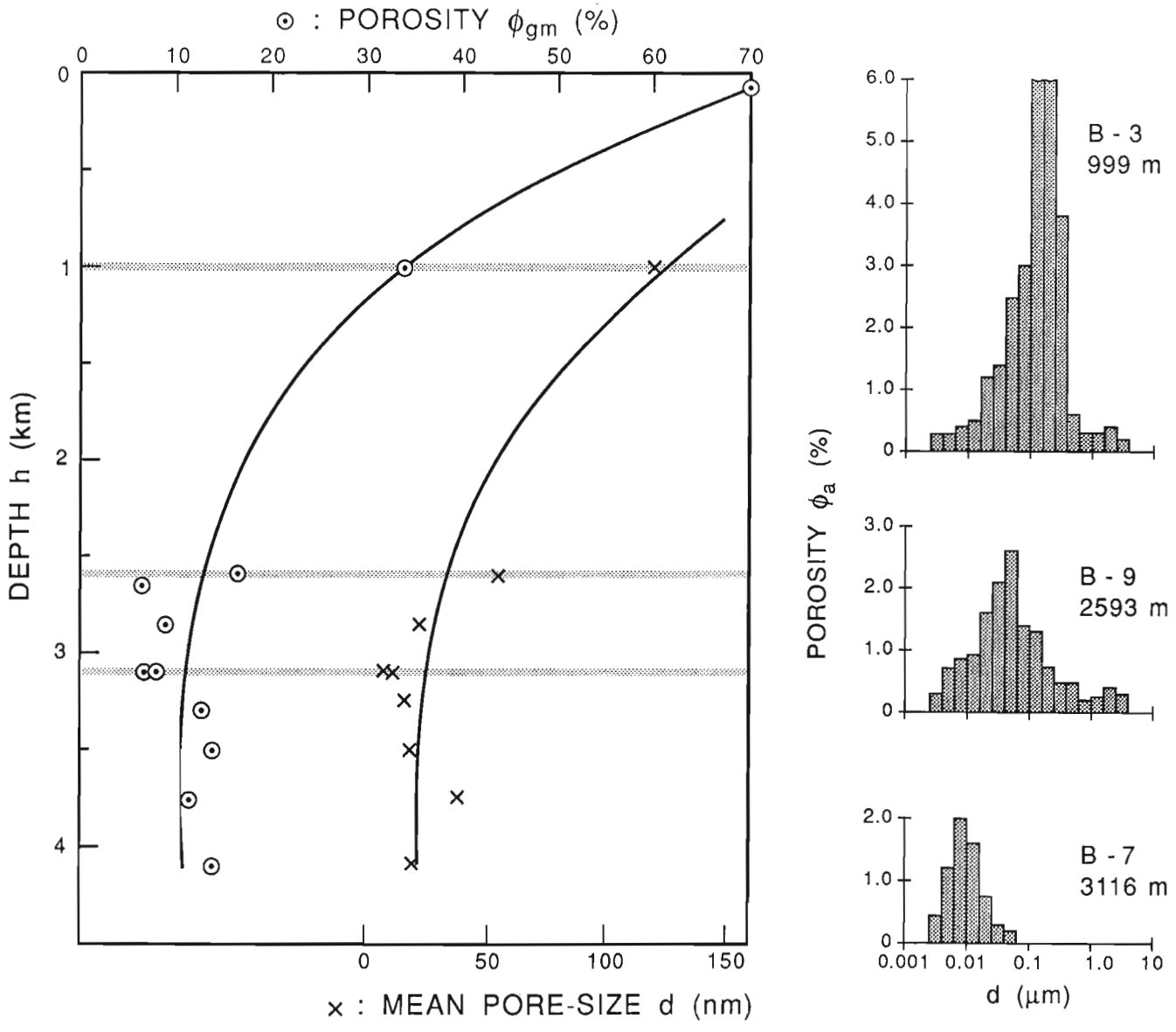


**Figure 2.** Pore-size distribution change with depth, with modes at about 200 nm at 1000 m decreasing to 10-20 nm at greater depth.

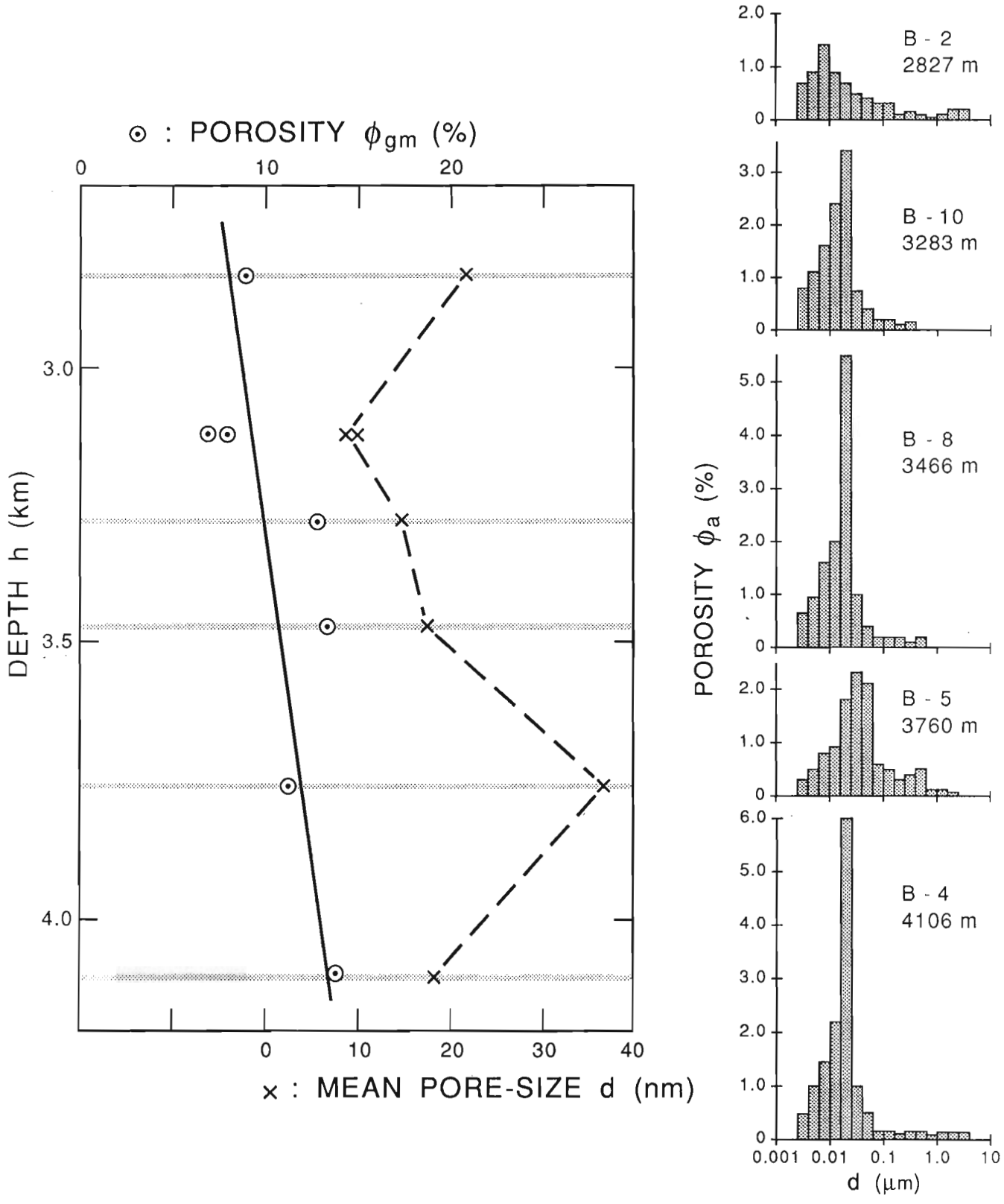


**Figure 3.** Porosity ($\phi_{gm}$) and mean pore-size (d) as a function of depth, from about 2.8 km depth.

4.0-10 nm range for a sample taken at a depth of 3116.9 m, and in the 25-60 nm range for a sample taken at a depth of 2590 m. The geometric mean pore-size ($d_{hg}$):

$$\text{Log}(d_{hg}) = (1/n)\Sigma\{\phi_{ai}\text{Log}(d_{hgi})\}/\{\Sigma\phi_{ai}\}, \; i = 1 - n \quad (2)$$

is in the range of 8.4-121 nm for these samples (Table 2). The smaller values for total porosity ($\phi_{gm}$) and geometric mean pore-sizes ($d_{hg}$) for these samples are similar to those for the tight shale samples from the Venture Gas Field, offshore Nova Scotia (Katsube et. al., 1990, 1991a).

## DISCUSSION AND CONCLUSIONS

The total porosity ($\phi_{gm}$) decreases with compaction and burial depth (Fig. 2), and reaches a value of 30% at 1000 m, and then continues to decrease to 5-15% at greater depths (2500 to 4100 m). The pore-structure generally shows a unimodal pore-size distribution, with a mean pore-size ($d_{hg}$) of about 120 nm at 1000 m, which decreases to 10-20 nm at the greater depths as shown in Figure 2. The porosity value for the minimum depth (5-10 m) in this figure is obtained from Katsube et al. (1991b).

Following the porosity ($\phi_{gm}$) decrease with depth to about 2500-2800 m, there are indications that there might be a slight increase in porosity with depth from about 2800 m to greater depth, as shown in Figure 3. Although the mean pore-size ($d_{hg}$) shows a considerable scatter at depths greater than the 2800 m, there are indications that it may also show a trend similar to that of the total porosity ($\phi_{gm}$). Although, the reason for these trends are unknown at present, interesting results are expected to emerge from relating this data to the studies of shale texture analysis and other petrophysical measurements carried out on the same samples, and from correlations with the geophysical logging data (Issler, in press) obtained from the same area.

The porosity concentration in the smaller pore-sizes seen in some of these rocks results in extremely small mean pore-size values (Katsube et al., 1991a; Katsube and Walsh, 1987) and, to our knowledge, some of the smallest ever reported for rocks. The fact that the pore-size distribution pattern of some of the samples from the Beaufort-MacKenzie Basin are very similar to those of the low permeability tight shale samples from the Venture Gas Field, offshore Nova Scotia (Katsube et al., 1991a), suggest that these Beaufort-MacKenzie samples will likely have very low permeabilities ($<10^{-20}$ m$^2$).

## ACKNOWLEDGMENTS

The authors thank K.A. Richardson (Geological Survey of Canada) for critically reviewing this paper. The authors acknowledge the efficient work carried out by B. Smith (ORTECH International, Toronto, Ontario) regarding the mercury porosimetry measurements.

## REFERENCES

**Brace, W.F.**
1980: Permeability of crystalline and argillacious rocks; International Journal of Rock Mechanics and Mining Sciences and Geomechanics Abstracts, v. 17, p. 241-251.

**Issler, D.R.**
in press: A new approach to shale compaction and stratigraphic restoration, Beaufort-MacKenzie Basin and MacKenzie Corridor, Northern Canada; American Association of Petroleum Geologists Bulletin.

**Katsube, T.J.**
1981: Pore structure and pore parameters that control the radionuclide transport in crystalline rocks; Proceedings of the Technical Program, International Powder and Bulk Solids Handling and Processing, Rosemont, Illinois, p. 394-409.
1992: Statistical analysis of pore-size distribution data for tight shales from the Scotian Shelf; in Current Research, Part E; Geological Survey of Canada, Paper 92-1E.

**Katsube, T.J. and Hume, J.P.**
1987: Pore structure characteristics of granitic rock samples from Whiteshell Research Area; in Geotechnical Studies at Whiteshell Research Area (RA-3), CANMET, Report MRL 87-52, p. 111-158.

**Katsube, T.J. and Walsh, J.B.**
1987: Effective aperture for fluid flow in microcracks; International Journal of Rock Mechanics and Mining Sciences and Geomechanics Abstracts, v. 24, p. 175-183.

**Katsube, T.J., Murphy, T.B., Best, M.E., and Mudford, B.S.**
1990: Pore structure characteristics of low permeability shales from deep formations; in Proceedings of the 1990 SCA (Society of Core Analysts) 4th Annual Technical Conference, August, 1990, Dallas, Texas, SCA-9010, p. 1-21.

**Katsube, T.J., Best, M.E., and Mudford, B.S.**
1991a: Petrophysical characteristics of shales from the Scotian shelf; Geophysics, v. 56, p. 1681-1689.

**Katsube, T.J., Wires, K., Cameron, B.I., and Franklin, J.M.**
1991b: Porosity and permeability of ocean floor sediments from the Middle Valley Zone in the northeast Pacific; Borehole PAR90-1; in Current Research, Part E; Geological Survey of Canada, Paper 91-1E, p. 91-97.

**Katsube, T.J., Scromeda, N., and Williamson, M.**
1992a: Effective porosity and irreducible water saturation of tight shales from the Venture Gas field; in Current Research, Part D; Geological Survey of Canada, Paper 92-1D, p. 111-119.

**Katsube, T.J., Williamson, M., Issler, D.R., and Best, M.E.**
1992b: Petrophysical properties of shales; Significance for modelling sedimentary basins; Poster paper presented at the "GSC Oil and Gas Forum '92", Calgary, Alberta, March 2-3, 1992.

**Luffel, D.L. and Guidry, F.K.**
1989: Reservoir rock properties of Devonian shale from core and log analysis; The Society of Core Analysts, Annual Technical Conference Preprints, Vol. I, Aug. 2-3, Paper 8910.

**Morrow, C., Shi, L., and Byerlee, J.**
1984: Permeability of fault gauge under confining pressure and shear stress; Journal of Geophysical Research, 89, p. 3193-3200.

**Mudford, B.S. and Best, M.E.**
1989: Venture Gas Field, offshore Nova Scotia; case study of overpressuring in region of low sedimentation rate; AAPG Bulletin, v. 73, p. 1383-1396.

**Rootare, H.M.**
1970: A review of mercury porosimetry; Perspectives of Power Metallurgy, v. 5, p. 225-252.

**Washburn, E.W.**
1921: Note on a method of determining the distribution of pore sizes in a porous material; Proceedings of the National Academy of Science, v. 7, p. 115-116.

**Williamson, M.A.**
1992: Hydrocarbon resource study of east coast frontier basins; past present and future (abstract); in Geological Survey of Canada, Current Activity Forum, Program with Abstracts, p. 4.

Geological Survey of Canada Project 870057

# CANADIAN SHIELD

# BOUCLIER CANADIEN

# Early Proterozoic subtidal carbonate platform evolution, Taltheilei and Utsingi formations, Great Slave Lake, Northwest Territories

**Terry T. Sami[1] and Noel P. James[1]**

*Sami, T.T. and James, N.P., 1992: Early Proterozoic subtidal carbonate platform evolution, Taltheilei and Utsingi formations, Great Slave Lake, Northwest Territories; in Current Research, Part E; Geological Survey of Canada, Paper 92-1E, p. 165-175.*

***Abstract***

*The Taltheilei and Utsingi formations form a 190 m thick sequence of shallow-water platform carbonates in the lower part of the Early Proterozoic Pethei Group in the East Arm of Great Slave Lake. The predominantly limestone sequence comprises ten lithofacies organized into four assemblages: (1) shelf biostrome; (2) ramp biostrome; (3) bioherm; and (4) cyclic. These wholly subtidal lithofacies record the development of the outer shelf, shelf margin, and upper slope of the Taltheilei-Utsingi platform. The Taltheilei rimmed shelf comprises four stages of development: (1) Siliciclastic to carbonate ramp transition; (2) Rimmed shelf growth; (3) Incipient drowning and shelf margin migration; and (4) Incipient drowning and ramp development. Three complete shallowing-upward events are represented within the transgressive Taltheilei Formation and the beginning of a fourth event is recorded within the overlying Utsingi Formation.*

***Résumé***

*Les formations de Taltheilei et d'Utsingi forment une séquence de 190 m d'épaisseur de roches carbonatées néritiques mises en place en eau peu profonde dans la partie inférieure du Groupe de Pethei (Protérozoïque précoce) situé dans le bras est du Grand lac des Esclaves. Cette séquence dominée par les calcaires comprend dix lithofaciès qui constituent les quatre assemblages suivants: 1) plate-forme biostromale, 2) glacis biostromal, 3) biohermal et, 4) cyclique. Ces lithofaciès de nature complètement infratidale correspondent aux étapes de formation de la plate-forme externe, de la marge de la plate-forme et du talus supérieur de la plate-forme de Taltheilei et d'Utsingi. La plate-forme protégée de Taltheilei comporte les quatre stades de développement suivants: 1) transition d'un glacis de nature silicoclastique à un glacis de roches carbonatées, 2) croissance de la plate-forme protégée, 3) début de la submersion et migration de la marge de la plate-forme et, 4) début de la submersion et formation du glacis. La formation transgressive de Taltheilei renferme trois épisodes complets à granoclassement normal tandis que la formation sus-jacente d'Utsingi comporte des indices de la présence d'un quatrième épisode embryonnaire.*

[1] Department of Geological Sciences, Queen's University, Kingston, Ontario K7L 3N6

## INTRODUCTION

This report is a preliminary description of the spatial and temporal distribution of facies within the Taltheilei and Utsingi formations of the lower Pethei Group, a carbonate sequence developed in the upper part of the Great Slave Lake Supergroup of northwest Canada. These wholly subtidal rocks preserve the outer shelf, shelf margin, and upper slope of the first of two carbonate platforms within the Pethei Group, a compound transtensional-transpressional-foreland basin carbonate platform (Hoffman, 1987, 1989a). Much of the stratigraphic framework for this study is based on the regional work of P.F. Hoffman (1968, 1969, 1973, 1988a, Hoffman et al., 1977) in the East Arm of Great Slave Lake.

Strata of the Early Proterozoic Pethei Group are important because, unlike other Proterozoic carbonates, most are limestone rather than dolomite, and textural preservation is generally excellent. Laterally continuous exposure allows for detailed examination of carbonate facies and assessment of platform dynamics. This study is part of a larger project aimed at gaining an increased understanding of Proterozoic carbonate systems. Such Proterozoic carbonate successions provide an excellent opportunity for the study of carbonate platform development, in that, lacking carbonate-secreting skeletal metazoans, they contains few components. This relatively simple system is conducive to the examination of the fundamental controls of platform development, which in turn can provide a key to the understanding of more complex Phanerozoic platforms.

## GEOLOGICAL SETTING AND STRATIGRAPHY

The Early Proterozoic (1.88 Ga-Paleoproterozoic) Pethei Group is preserved in a synclinorium exposed on the islands and peninsulas of the East Arm of Great Slave Lake, north of the McDonald-Wilson fault zone (Hoffman and Bowring, 1984, Hoffman, 1989a,b). Platform and slope facies examined outcrop along Pethei and Douglas peninsulas, which form the northern, autochthonous limb of the synclinorium (Fig. 1). The Pethei Group is part of the upper Great Slave Lake Supergroup (Fig. 2), which is interpreted to be the product of progressive infilling of a foredeep along the southern margin of the Slave craton (Hoffman, 1989a). The

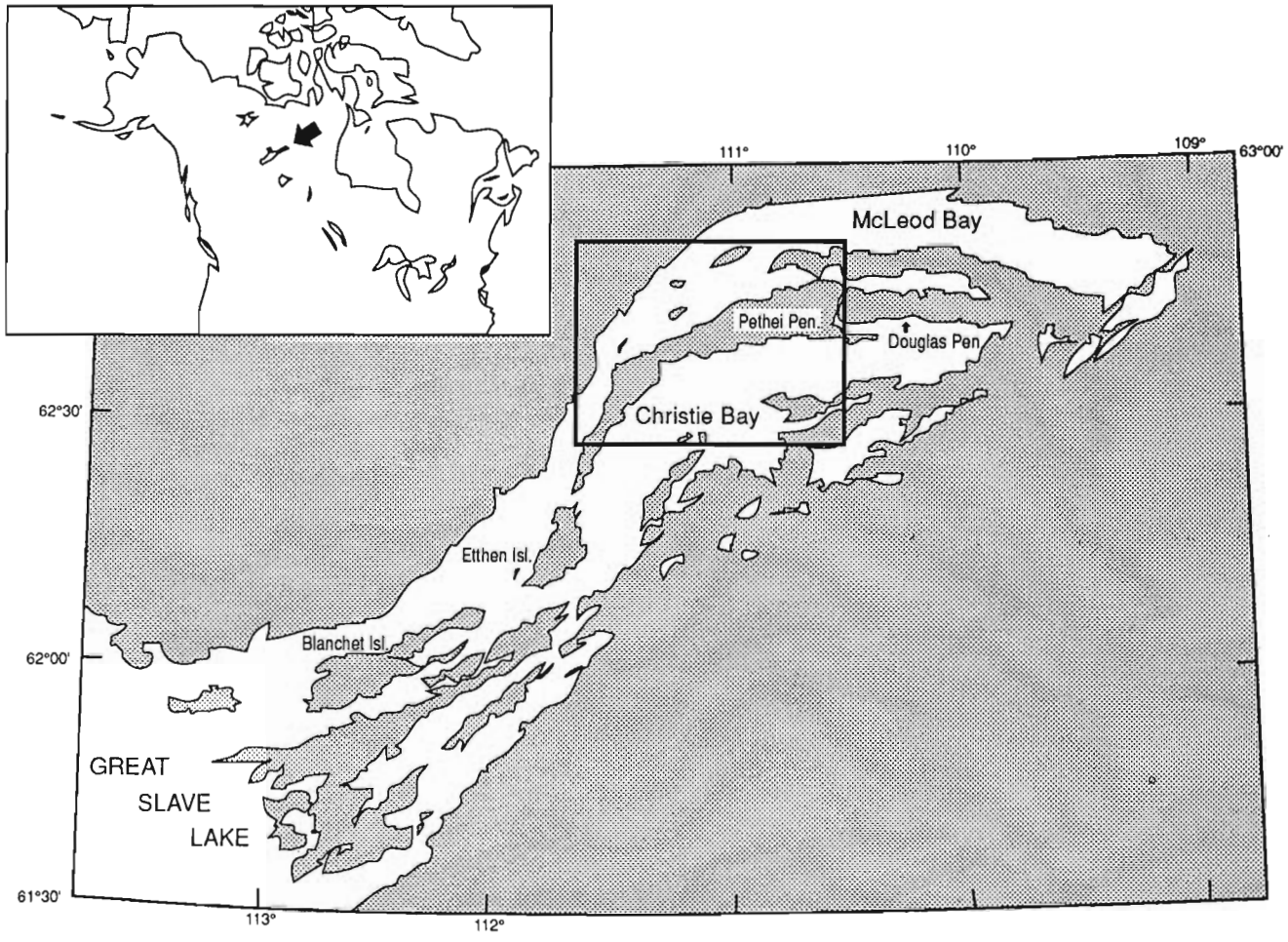


**Figure 1.** Map of East Arm of Great Slave Lake showing study area along Pethei and Douglas peninsulas.

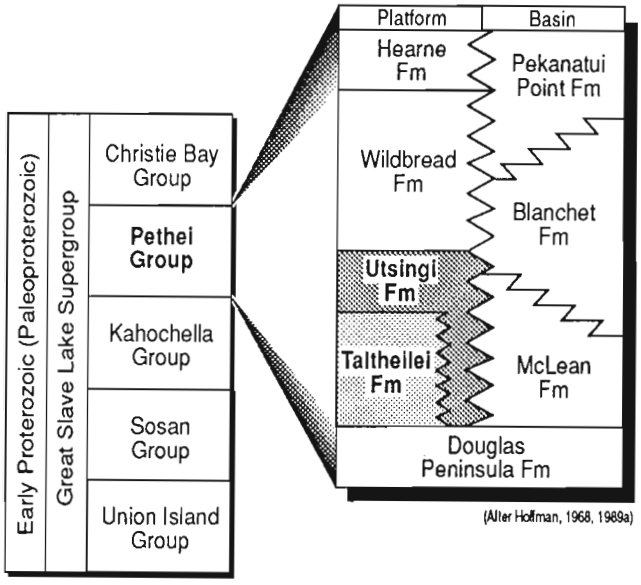


**Figure 2.** Great Slave Lake Supergroup stratigraphy, showing stratigraphic position of Taltheilei and Utsingi formations within the Pethei Group.

basin received sediment from both the Thelon Orogen (2.02-1.91 Ga) to the east and the Wopmay Orogen (1.95-1.84 Ga) to the west (Hoffman, 1988b).

The Pethei Group conformably overlies deep-marine clastic rocks of the Kahochella Group (Fig. 2) and shallow marine and nonmarine clastic, carbonate and volcanic rocks of the Sosan and Union Island groups (Hoffman, 1973; Hoffman et al., 1977; Hoffman, 1989a). It is unconformably overlain by the Stark Formation, a carbonate-redbed megabreccia of probable solution collapse origin, and the remainder of the Christie Bay Group, composed of shallow and nonmarine clastic and volcanic rocks (Hoffman et al., 1977). The whole sequence has been interpreted as a shallowing upwards sequence related to flexural subsidence and infilling of the foredeep (Hoffman, 1989a).

The Pethei Group comprises eight formations, four platformal (Taltheilei, Utsingi, Wildbread, Hearne), three basinal (McLean, Blanchet, Pekanatui Point), and the widespread basal Douglas Peninsula Formation which underlies both platformal and basinal strata (Fig. 2). Lateral platform to basin formation transitions are generally gradational and interfingering. Most of the 140-150 m thick

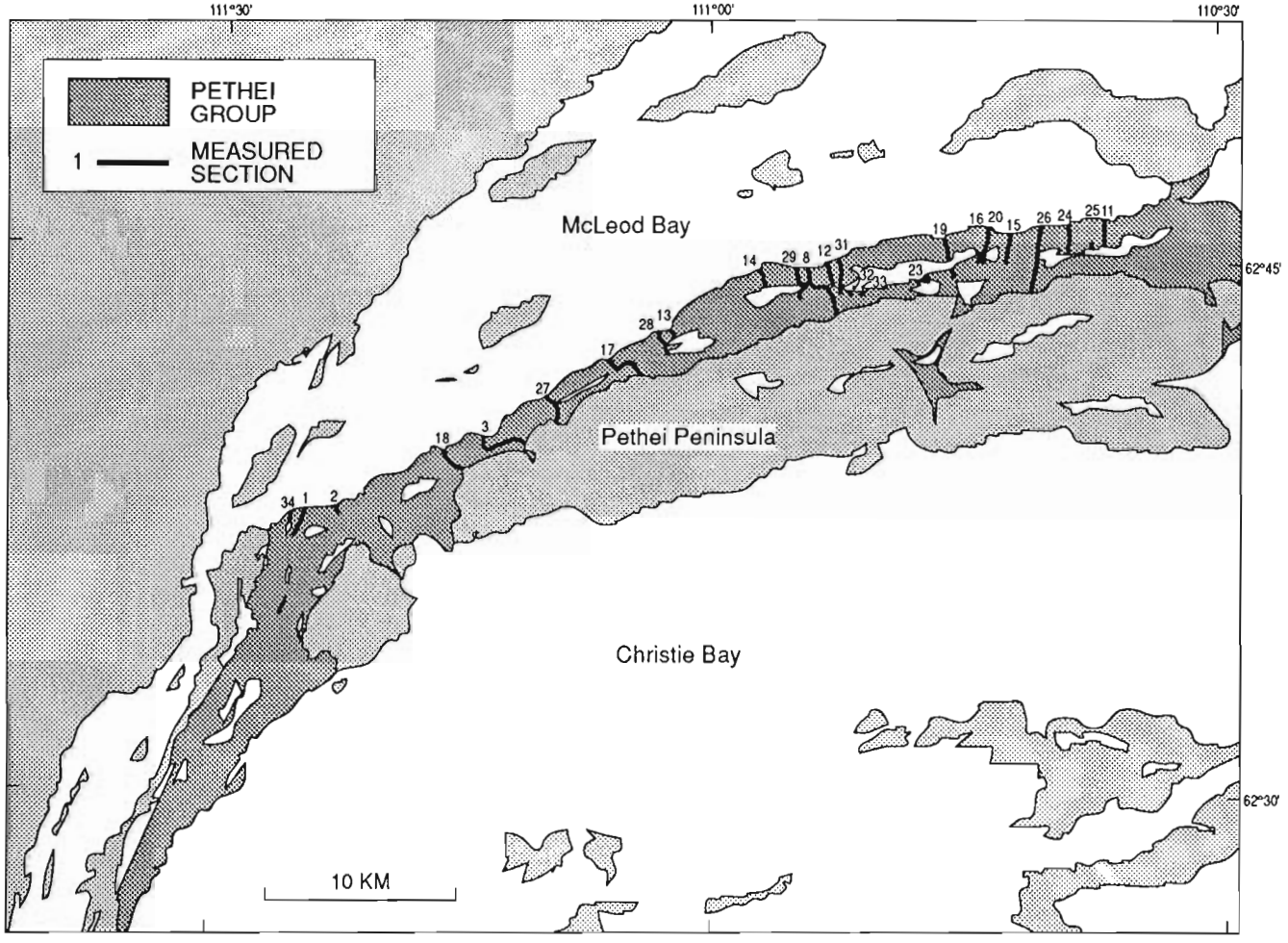


**Figure 3.** Geographic distribution of measured sections along the Pethei Peninsula.

Taltheilei Formation is dolostone, while the overlying (40-50 m) and laterally correlative (180-200 m) Utsingi Formation is limestone and dolomitic limestone. The sequence is overlain by less than 90m of the Wildbread Formation, mostly limestone, which is truncated by a gabbro sill.

The study area is approximately 80 km long and includes strata displaying a wide variety of correlative facies (Fig. 4). Shallow, platformal rocks of the Taltheilei Formation are exposed in the west, whereas ramp and slope facies of the Utsingi Formation occur primarily in the east. The thirty measured sections through the Taltheilei and Utsingi formations (Fig. 3) form an oblique transect across the presently southeast-facing platform (Hoffman, 1969). Correlation is facilitated by several well-exposed, laterally continuous ridge-forming marker units which occur throughout (Fig. 4). The datum used to correlate the cross-section is a distinctive stromatolite horizon at the base of the Wildbread Formation.

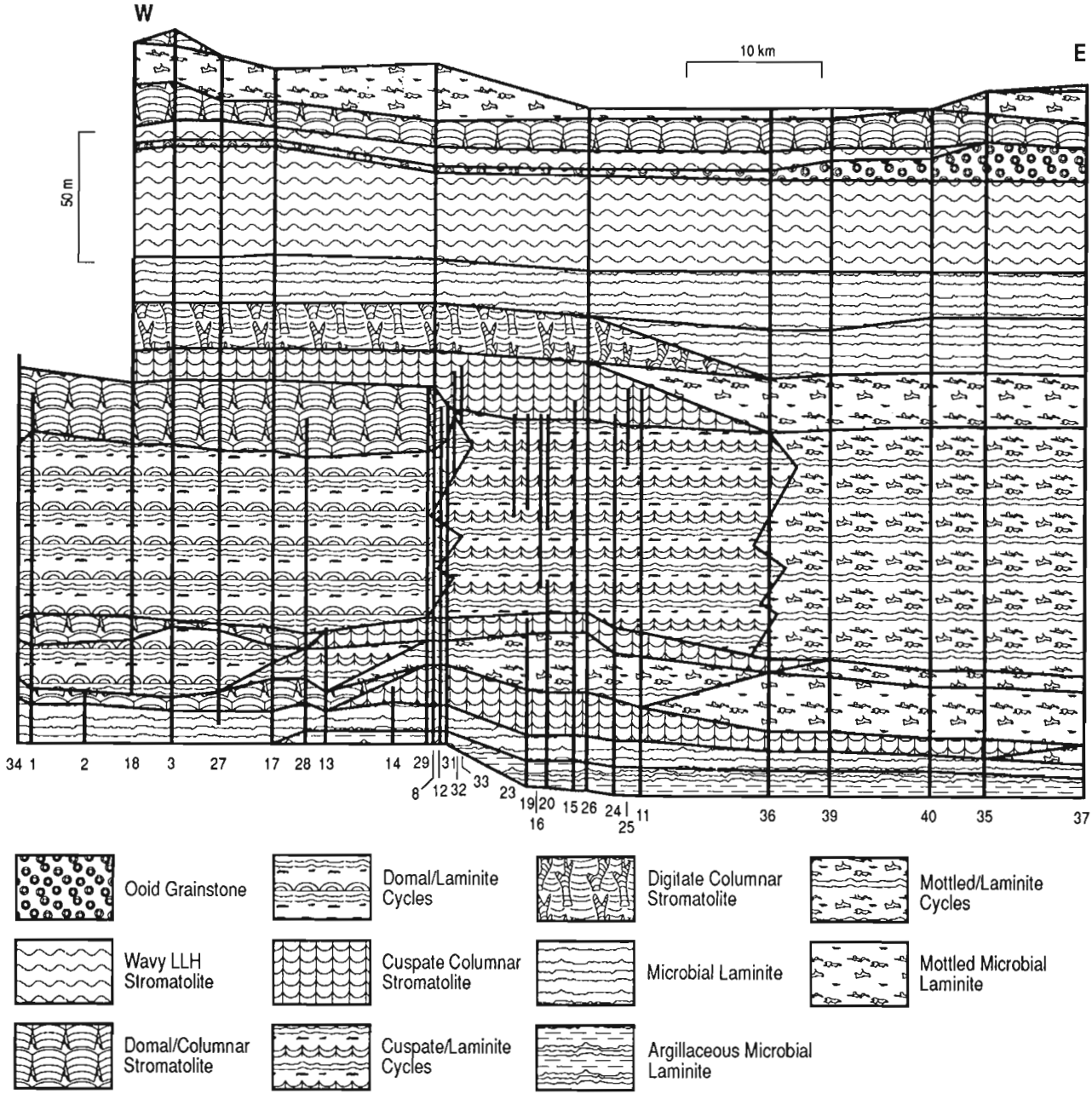


**Figure 4.** Facies correlation of measured sections.

**Table 1.** Facies descriptions

| Lithofacies | Constituents | Bedding | Sedimentary Structures | Stromatolites |
|---|---|---|---|---|
| **Microbial Laminite** | Sparite-Micrite Couplets | Flat to undulatory, to pseudocolumnar lamination, 1 to 2 mm | Large, 10 to 20 m diameter, domes with 1 to 2 m synoptic relief<br>Small intraclast lenses | Isolated hemispherical stromatolites<br>Horizontal microbial laminae |
| **Argillaceous Microbial Laminite** | Sparite-argillaceous micrite couplets | Flat to slightly undulatory lamination ,1 to 2 mm | Small intraclast lenses | Horizontal microbial laminae |
| **Mottled Microbial Laminite** | Micrite with irregular dolosparite "fenestrae" | Highly irregular, discontinous vertical and horizontal laminae | | Irregular microbial laminae? |
| **Intraclastic Grainstone** | Intraclasts, tabular to subspherical, fine to coarse-grained, micrite, grainstone, microbial laminite, and stromatolite laminae clasts<br>Oncolites, tabular, up to 20 cm in diameter<br>Sparite cement | Tabular to lenticular<br>Beds up to 40 cm thick<br>Faint lamination, 1 to 5 cm | Cross-bedding, imbrication, intraclast rosettes, grading, preferred orientation of intraclasts | Oncolites |
| **Domal/Columnar Stromatolite** | Sparite-micrite couplets<br>Laminated mudstone and intraclasts between heads | Concave to undulatory lamination, 1 to 2 mm | Intraclast rosettes | Hemispherical to turbinate, circular in plan, branching to non-branching, isolated to close spacing, erect, up to 80 cm diameter<br>Cylindrical, circular to elongate in plan, branching to non-branching, contiguous spacing, erect to inclined, 10 to 15 cm dia. |
| **Columnar Cuspate Stromatolite** | Sparite-micrite couplets | Cuspate to undulatory lamination, 1 to 2 mm | Large, 1 to 10 m diameter domes with 0.5 to 1 m synoptic relief<br>Locally inclined | Cylindrical, conical to cuspate, circular in plan, non-branching, close to contiguous spacing, erect to inclined, 5 to 10 cm in diameter |
| **Columnar Digitate Stromatolite** | Sparite-micrite couplets<br>Laminated mudstone and fibrous cement botryoids between heads | Concave lamination, <1 mm | | Digitate to mottled appearance, branching, close to open spacing, unlinked, moderate vertical continuity, < 5 cm in diameter |
| **Domal/Laminite Cycles** | Sparite-micrite couplets<br>Laminate mudstone<br>Intraclasts<br>Oncolites | Concave to undulatory lamination, 1 to 2 mm<br>Massive<br>Tabular to lenticular | Cross-bedding, imbrication, intraclast rosettes and lags, preferred orientation, tepee structures, sharp bases, truncated tops, grading | Domal and columnar<br>Isolated hemispherical<br>Oncolites<br>Microbial laminae |
| **Cuspate/Laminite Cycles** | Sparite-micrite couplets<br>Intraclasts | Cuspate to undulatory lamination, 1 to 2 mm | Sharp bases, intraclast lags | Cuspate and digitate columnar<br>Microbial laminae |
| **Mottled/Laminite Cycles** | Micrite with irregular dolosparite "fenestrae"<br>Sparite-micrite couplets | Highly irregular laminae<br>Flat to undulatory lamination, 1 to 2 mm | | Irregular and microbial laminae |

## LITHOFACIES AND ASSEMBLAGES

Ten mappable lithofacies are discernable within the rocks of the Taltheilei and Utsingi formations (Table 1). These are associated in four lithofacies assemblages representing significant differences in sedimentary environment and dynamics (Fig. 5, Table 2).

### *Biostromal shelf assemblage*

This subtidal assemblage of domal/columnar stromatolite, cuspate columnar stromatolite, and mottled microbial laminite, caps the three large-scale shallowing-upward cycles within the Taltheilei-Utsingi sequence (Fig. 4) and the facies represent, respectively, the outer shelf, shelf edge, and upper slope (Fig. 6). Facies are laterally correlative and intergradational with increasing depth and distance from the shelf. All are biostromal, display lateral continuity of up to 50 km and uniformity and range in thickness from 5-25 m. This assemblage represents the shallowest environments formed on a rimmed shelf during maximum regression.

#### Domal/columnar stromatolite facies

The domal/columnar stromatolite facies comprises both isolated, unlinked domal stromatolites and linked, columnar stromatolites in a well-defined vertical succession (Fig. 5a). Large, isolated bulbous domes, coalesce upwards into large, unlinked and linked columnar stromatolites. Increased branching and decrease in diameter upwards gives rise to medium and small, contiguous columnar stromatolites whose cross-section becomes increasingly elongate to lanceolate (cf. Grey, 1989; Hofmann, 1969). The lower two biostromes each contain a single sequence, whereas the third contains two of these shallowing-upward successions (cf. Southgate, 1989). This facies also occurs in the biohermal assemblage but can be distinguished here by the lack of mound morphology. Unlinked stromatolites are separated by laminated mudstone, microbial laminite (commonly extending into stromatolite heads), and tabular intraclasts derived from stromatolite laminae. Columnar stromatolites are elongate in a shelf-normal orientation and inclined basinward. Abundance of carbonate cements and intraclasts suggests that the stromatolites were well cemented on the sea floor. Early marine botryoidal and isopachous cement fabrics

**Table 2.** Facies assemblages

| Assemblage | Lithofacies | Bedding | Vertical Trends | Lateral Trends | Stratigraphic Range |
|---|---|---|---|---|---|
| Biostromal Shelf | Domal/columnar stromatolite<br>Cuspate columnar stromatolite<br>Mottled microbial laminite | Tabular | Stromatolite size decreases upward<br>Stromatolite elongation increases upward | Domal/columnar grades into cuspate stromatolite and microbial laminite basinward | Lower and upper Taltheilei Fm<br>Lower and middle Utsingi Fm |
| Biostromal Ramp | Microbial laminite<br>Cuspate columnar stromatolite<br>Digitate columnar stromatolite<br>Argillaceous microbial laminite | Domal to tabular | Cuspate columnar grades into digitate stromatolite and microbial laminite upward | Cuspate columnar grades into digitate stromatolite and microbial laminite basinward | Lower Taltheilei Fm<br>Lower and upper Utsingi Fm |
| Cyclical | Domal/laminite cycles,<br>Cuspate/laminite cycles,<br>Mottled/laminite cycles | Tabular, 0.5 to 12 m thick cycles<br>Interbedded stromatolite and laminite/grainstone units | Stromatolite content increases upward<br>Stromatolite columnar nature increases upward<br>Digitate stromatolite content increases upward | Columnar stromatolite content increases basinward<br>Laminated mudstone content decreases and microbial laminite content increases basinward<br>Digitater columnar stromatolite content increases basinward<br>Intraclast content decreases basinward<br>Domal/laminite cycles grade into cuspate/laminite and mottled/laminite cycles basinward | Middle Taltheilei Fm<br>Middle Utsingi Fm (laterally equivalent to Taltheilei Fm) |
| Biohermal | Domal/columnar stromatolite<br>Intraclast grainstone | Domal mounds, up to 30 m diameter and <5 m synoptic relief | Stromatolite size decreases upward<br>Stromatolite elongation increases upward | Sromatolite mounds grade into intraclast grainstone-filled channels | Lower and upper Taltheilei Fm (basinward edge of biostromes) |

indicate that the stromatolites formed primarily by direct carbonate precipitation; micrite binding/trapping was only a minor contributor to growth.

### Cuspate columnar stromatolite facies

The cuspate columnar stromatolite facies comprises well-defined cuspate laminae arranged in small vertical columns (Fig. 5b), locally inclined in a shelf-normal orientation. It is present both as a ramp facies and as a lateral, deeper water equivalent of domal/columnar stromatolites on a shelf setting (Fig. 6). These rocks occur adjacent to the inferred shelf edge in the biostromal assemblage. A conical morphology (cf. Hofmann, 1969) may be developed locally alongside true cuspate forms. Columns are generally circular in plan, yet they are locally arranged in small (0.5-2.0 m), domal, mounds which show a shelf-normal elongation.

### Mottled microbial laminite facies

The mottled microbial laminite facies is transitional between true microbial laminite, digitate columnar stromatolites, and cuspate columnar stromatolite facies. Laminae are highly irregular and exhibit poor lateral and vertical continuity due to irregular dolomite-spar-filled voids. Mottled microbial laminite is gradational and interfingers shelfward with, cuspate columnar stromatolite (Fig. 6) and is therefore interpreted as a more basinal facies.

## *Biostromal ramp assemblage*

Biostromal ramp facies, restricted to the Utsingi and Lower Taltheilei formations, are laterally continuous and intergradational across the whole study area (Fig. 4). High energy features such as intraclasts, high relief stromatolites and stromatolite elongation are absent. Lateral and vertical facies contacts are gradational. This assemblage is restricted to: (1) the basal Taltheilei Formation, where it directly overlies siliciclastic/marly ramp facies of the Douglas Peninsula Formation (Fig. 2); and (2) the Upper Utsingi Formation, where it overlies rimmed shelf facies of the Taltheilei Formation. The lower occurrence represents development of a carbonate ramp on a siliciclastic ramp and the upper occurrence represents the drowning and possible shoreward migration of a rimmed carbonate shelf.

### Cuspate columnar stromatolite facies

The cuspate columnar stromatolite facies is similar to its occurrence in the shelf assemblage but stromatolite columns are less distinct in the ramp assemblage. It onlaps shelf facies of the upper Taltheilei Formation (Fig. 6), and may have developed as a consequence of extensive backstepping of the shelf edge. The vertical transition from domal to cuspate stromatolites is abrupt but continuous, suggesting minimal interruption of sedimentation following shelf margin migration. Stromatolite diameter remains relatively constant (3-5 cm) across the contact (Fig. 5c).

### Digitate columnar stromatolite facies

The digitate columnar stromatolite facies is similar to mottled microbial laminite in the field and requires slabbing to confirm its distinct character. It consists of small (1-2 cm) diameter, unlinked digitate stromatolites separated by mudstone and small cement botryoids. Digitate columnar stromatolite occurs only above cuspate columnar stromatolite facies of the Upper Utsingi Formation, but further examination of slope mottled microbial laminite facies may extend the range of this facies. Contacts with cuspate columnar stromatolite and microbial laminite facies are gradational. Lateral and vertical facies relationships and internal features (high mud content, low column relief) suggest that deposition occurred in a low-energy subtidal ramp environment deeper than cuspate columnar stromatolites but shallower than microbial laminite facies (Fig. 6).

### Microbial laminite facies

The microbial laminite facies is the most extensive and is an integral part of many other ramp and shelf facies. It comprises both tabular (upper Taltheilei Formation) and large-scale domal (upper Utsingi Formation) bodies (Fig. 4). The laminae commonly have low relief and excellent lateral continuity. Microbial laminite grades into cuspate columnar stromatolites with increasing vertical inheritance and into mottled microbial laminite with decreasing lateral continuity (Fig. 5d). Microbial laminites are interpreted as having formed in deeper environments than cuspate columnar stromatolites and in shallower environments than mottled microbial laminites (Fig. 6), with the corresponding differences in energy levels controlling morphology of the internal laminae. The pervasiveness of carbonate cement within the laminae and the occurrence of intraclasts suggests early cementation. Microscopic fabric is indicative of precipitated cements alternating with microbial mats, with only minor muddy sediment trapping.

### Argillaceous microbial laminite facies

The argillaceous microbial laminite facies, apart from localized thin marlstone beds, marks the only significant occurrence of argillaceous material within the shallow water facies of the Pethei platform. This facies represents the gradual transition from siliciclastic to carbonate dominated environments within the basin (Fig. 4). The facies resembles both the local microbial laminite facies and the shallow water, microbially laminated rocks of the upper Douglas Peninsula Formation. Its position within the assemblage is interpreted the same as that of the microbial laminated facies (Fig. 6), but in an environment with stronger siliciclastic influence.

## *Biohermal assemblage*

The two facies occurring in this assemblage represent the highest energy environments preserved within the Taltheilei/Utsingi platform sequence. Distinct stromatolitic mounds and intervening channels are restricted to shelf edge positions during later, shallow water stages of shelf development of the Taltheilei Formation (Fig. 6). The

areal distribution of outcrop prevents a definitive determination of whether these mound and channel belts form a true barrier system or are only locally distributed along the shelf edge. There is no evidence that the mounds grew up into the intertidal zone or severely restricted shelf circulation. The scarcity of intraclasts in shelf facies deposited during periods of extensive bioherm development, in contrast to intraclast-rich facies deposited during periods lacking significant mound development, suggests that the stromatolitic mounds effectively reduced energy levels on the shelf.

### Domal/columnar stromatolite facies

This facies is similar to the domal/columnar stromatolite facies in the biostromal shelf assemblage but has more intraclasts and columnar stromatolites and lacks laminated mudstone. The same vertical shallowing-upward sequence of large, isolated domes to small, contiguous columns is present, though commonly restricted to one cycle per mound. Overall morphology of this facies is domal, with lateral edges interfingering with intraclastic grainstone (Fig. 5e). Mounds generally are not connected although several have thin stromatolitic "bridges". The mounds are slightly elongate, normal to the inferred paleoshoreline. These high energy, subtidal mounds occur at the shelf edge, gradational from domal/columnar biostromes, during all three biostromal events within the Taltheilei/Utsingi sequence.

Isolated mounds also occur basinwards within the cuspate columnar stromatolite facies but display significantly lower relief that shelf edge mounds, lack the abundant intraclastic material, and commonly include cuspate and conical stromatolites.



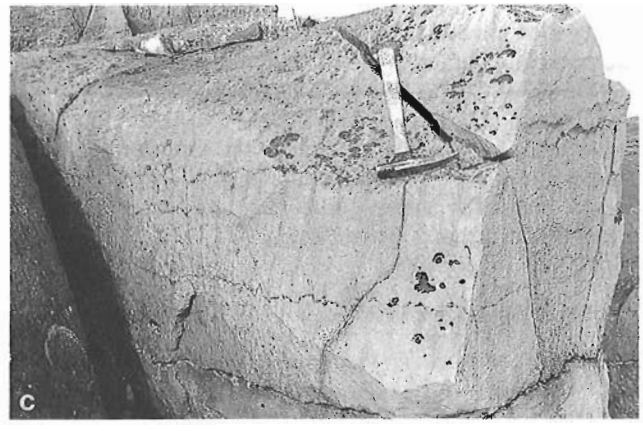


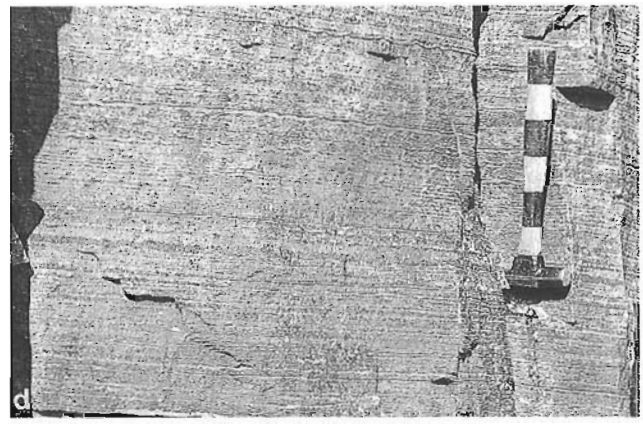


**a.** Slightly inclined, round columnar stromatolites located near the shelf edge of the third biostrome, capping the Taltheilei Formation.

**b.** Cuspate columnar stromatolites of the first biostrome at the base of the Utsingi Formation showing dolomitic pillars which help define the columns.

**c.** Cuspate columnar stromatolites of the Utsingi Formation ramp, directly overlying the Taltheilei Formation, showing small circular shape in plan view.

**d.** Slightly undulatory microbial laminite displaying good lateral continuity and pseudocolumnar laminae from the basal Utsingi Formation ramp.

**Figure 5.** Lithofacies assemblages (Hammer is 34 cm in length, pencil is 14 cm in length and staff is 1.5 m in length)

### Intraclastic grainstone facies

The intraclastic grainstone facies is composed of both spherical and tabular intraclasts (Table 1), and fills channels between the stromatolitic mounds as well as capping many mounds. Offshelf-directed (southeast) crossbedding is pervasive in the coarse channel-fill (Fig. 5f). Rosettes of edgewise stromatolitic intraclasts are common adjacent to and within the mounds. These channels could be interpreted as spur and groove with the intraclasts representing intense wave erosion and reworking of the stromatolite mounds and previous intraclastic grainstone at the shelf edge (cf. Beukes and Lowe, 1989). Basinward the grainstone becomes progressively finer and the channels less pronounced. Shelfward, channels disappear and mounds merge into a continuous domal/columnar stromatolite biostrome.

### *Cyclic assemblage*

The cyclic assemblage comprises 50-60% of the sequence, forming most of the Taltheilei Formation and its lateral equivalents within the Utsingi Formation (Fig. 4). The constituent facies, domal/laminite cycles, cuspate/laminite cycles, mottled/laminite cycles (Table 2) are broadly equivalent to the three similar shelf biostrome facies, but occur in a different dynamic setting (Fig. 6). The assemblage overlies shelf biostrome facies and is interpreted to represent periods of maximum shelf development. Incipient drowning of the shelf and subsequent repositioning of the shelf top and margin within an episodically high energy subtidal zone is responsible for the abundance of high energy features (intraclasts, columnar stromatolites) interbedded with low energy sediments (microbial laminite, laminated mudstone) in this assemblage. The repetition of shallowing-upward cycles throughout suggests fluctuating relative sea level

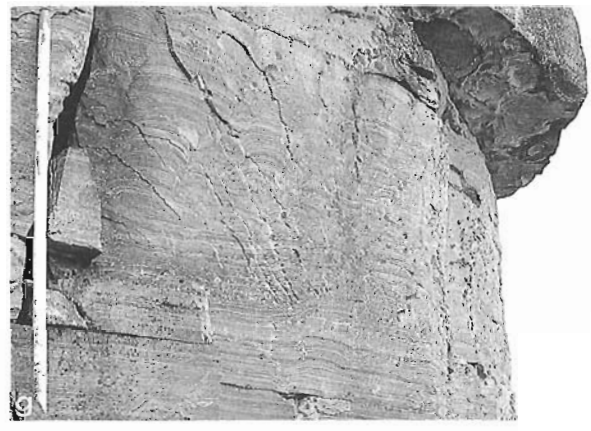

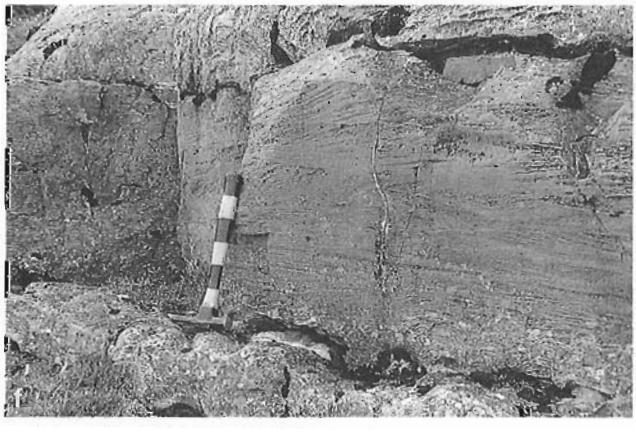

**e.** The edge of a columnar stromatolite mound showing the interfingering relationship of stromatolites and intraclastic grainstone, eastern Blanchet Island.

**f.** Tabular unit of thick, cross-bedded intraclastic grainstone, overlain and underlain by stromatolitic "bridges", making up a channel-fill between stromatolite mounds at the shelf edge of the third biostrome, eastern Blanchet Island.

**g.** Domal/laminite cycles of the middle Taltheilei Formation showing interbedded domal/columnar stromatolite and microbial laminite-intraclastic grainstone units.

**h.** Cuspate/laminite cycles, from the middle Utsingi Formation, showing interbedded cuspate columnar to mottled stromatolites and microbial laminite-intraclastic grainstone.

**Figure 5.** (cont.)

(Southgate, 1989). The magnitude of relative sea level change was not sufficient to induce ramp development or to allow a rimmed shelf edge to develop. Cycle development was terminated when the rate and amplitude of relative sea level fluctuations were no longer sufficient to induce drowning of stromatolite facies. No unequivocal evidence exists in any of the facies to suggest development within a peritidal environment. The cycles are organized into several lower-order shallowing upwards packages.

### Domal/laminite cycle facies

Domal/laminite cycles are commonly sharp-based and have truncated tops. Laminated mudstone, intraclastic grainstone, and isolated stromatolites grade up into domal/columnar stromatolites (Fig. 5g). Basinward, microbial laminite becomes more common relative to laminated mudstone and stromatolites become increasingly columnar. Intraclastic grainstone becomes increasingly abundant toward the shelf edge, reflecting a gradual increase in depositional energy. The abundance of intraclasts and common occurrence of subtidal tepee structures formed within microbial laminites suggest widespread early lithification. There are no stromatolite mounds at the shelf edge zone and most cycles can be traced into those of the cuspate/laminite cycle facies (Fig. 6). The absence of a shelf rim, together with the lack of any exclusively peritidal facies, argues against development of a peritidal barrier. These cycles are similar in style to those of the outer shelf shoal complex recognized by Grotzinger (1986a,b) in the slightly older Lower Proterozoic Rocknest Formation.

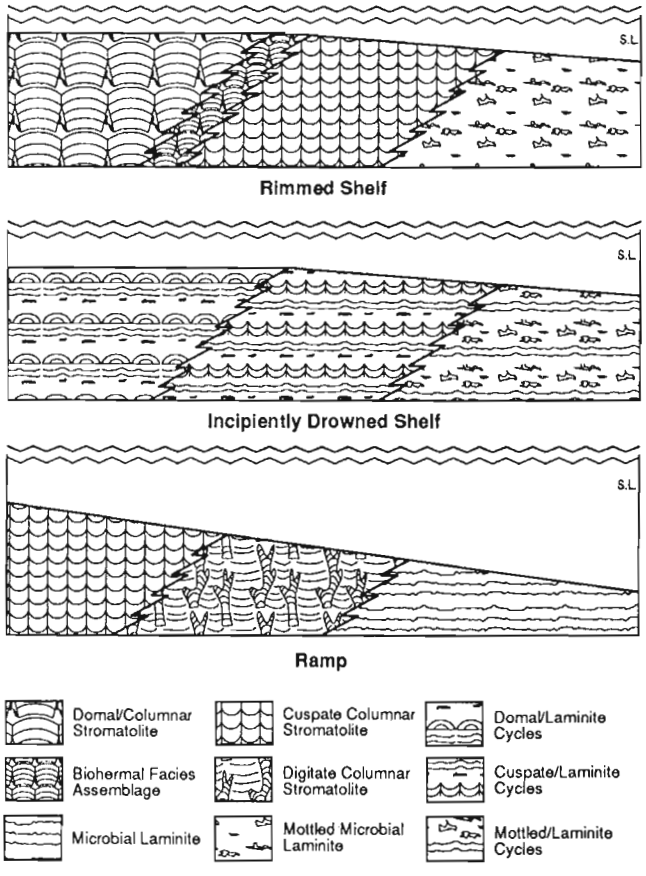


**Figure 6.** Inferred lateral facies transitions for ramp, rimmed shelf, and drowned shelf environments, with attendant relative water depths. S.L.= sea level.

### Cuspate/laminite cycle facies

Cuspate/laminite cycles are sharp-based but truncated tops are rare. Microbial laminite and intraclastic grainstone grade up into cuspate columnar stromatolites (Fig. 5h). Intraclasts decrease in abundance and cuspate stromatolites grade basinward into mottled microbial laminite. Internal contacts in cuspate/laminite cycles are gradational and less well-defined compared to domal/laminite cycles. Correlation of cycles from the shelf to basin is good, with only the thinnest cycles pinching out basinward. The decrease in high energy features and lateral continuity suggest a slightly deeper depositional environment than the domal/laminite cycles (Fig. 6).

### Mottled/laminite cycle facies

The mottled/laminite cycles are least well-developed, with sharp to gradational contacts. They comprise alternating units of microbial laminite and mottled microbial laminite with minor cuspate columnar stromatolite. Many shelf and margin cycles are incomplete or missing and correlation is restricted to thicker cycles. Mottled/ laminite cycles grade basinward into mottled microbial laminite and therefore are interpreted as representing the deepest-water cyclic facies observed within the Taltheilei shelf sequence.

## EVOLUTION OF TALTHEILEI SHELF

The Kahochella-Pethei-Christie Bay Group sequence is an overall upwards-shallowing sequence (Hoffman, 1989a). Within the Pethei Group four distinct upwards-shallowing stages have been identified (Sami and James, 1991). Three of these stages and part of the fourth can be identified within the Taltheilei and Utsingi formations. All four stages are marked by the development of a rimmed shelf, either from a ramp (first and fourth) or from an incipiently drowned shelf (second and third). Growth of the first shelf included the transition from a siliciclastic to carbonate-dominated ramp and the subsequent development of a rimmed shelf margin due to progradation of shallow water facies and the growth of small stromatolite mounds on the ramp. Evolution of the two subsequent shelf stages involved incipient drowning and re-establishment of the shelf margin. Incipient drowning of the rimmed shelf resulted in the deposition of cyclic facies on the antecedent outer shelf and shelf edge. The rimmed shelves developed when shallowing was sufficient to initiate biostrome development and the appearance of shelf edge bioherms. Development of the fourth shelf followed a more extreme incipient drowning event and the subsequent establishment of a carbonate ramp. The ramp sequence represents a transgressive event, as deep water ramp facies

onlapped shorewards. A relatively sudden sea level drop enabled shallow water subtidal and peritidal facies of the Wildbread Formation to prograde over ramp facies of the Utsingi Formation and eventual establishment of a fourth rimmed shelf outboard of the previous shelf margins.

## ACKNOWLEDGMENTS

The project was initially suggested by P.F. Hoffman, who kindly provided helpful background information and advice on logistics. R. Rainbird critically reviewed the manuscript. N.S.E.R.C. provided postgraduate scholarships to T. Sami and operating funds to N.P. James. EMR provided funds through Research Agreement # 079 4 91. Able field assistance was provided by S. Whittaker, E. Romero-Sierra, and T. Ryan. R. Stone and J. Chillebeck of the Geological Survey of Canada provided enthusiastic expediting.

## REFERENCES

**Beukes, N.J. and Lowe, D.R.**
1989: Environmental control on diverse stromatolite morphologies in the 3000 Myr Pongola Supergroup, South Africa; Sedimentology, v. 36, p. 383-397.

**Grey, K.**
1989: Handbook for the study of stromatolites and associated structures; Stromatolite Newsletter, v. 14, p. 83-140.

**Grotzinger, J.P.**
1986a: Evolution of Early Proterozoic passive-margin carbonate platform, Rocknest Formation, Wopmay Orogen, Northwest Territories, Canada; Journal of Sedimentary Petrology, v. 56, p. 831-847.

**Grotzinger, J.P.**
1986b: Cyclicity and paleoenvironmental dynamics, Rocknest platform, northwest Canada; Geological Society of America Bulletin, v. 97, p. 1208-1231.

**Hoffman, P.F.**
1968: Stratigraphy of the Great Slave Supergroup (Aphebian), east arm of Great Slave Lake, District of Mackenzie; Geological Survey of Canada, Paper 68-42.
1969: Proterozoic paleocurrents and depositional history of the East Arm fold belt, Great Slave Lake, Northwest Territories; Canadian Journal of Earth Sciences, v. 6, p. 441-462.
1973: Evolution of an early Proterozoic continental margin: the Coronation geosyncline and associated aulacogens of the northwestern Canadian shield; in Evolution of the Precambrian Crust, (ed.) J. Sutton and B.F. Windley; Philosophical Transactions of the Royal Society, London, Series A, v. 273, p. 547-581.
1987: Continental transform tectonics: Great Slave Lake shear zone (ca. 1.9 Ga), northwest Canada; Geology, v. 15, p. 785-788.
1988a: Geology and tectonics, East Arm of Great Slave Lake, Northwest Territories; Geological Survey of Canada, Map 1628A, 2 sheets.
1988b: United Plates of America, the birth of a craton: Early Proterozoic assembly and growth of Laurentia; Annual Review of Earth and Planetary Sciences, v. 16, p. 543-603.
1989a: Pethei reef complex (1.9 Ga), Great Slave Lake, N.W.T.; in Reefs, Canada and Adjacent Area, (ed.) H.H.J. Geldsetzer et al.; Canadian Society of Petroleum Geologists, Memoir 13, p. 38-48.
1989b: Precambrian geology and tectonic history of North America; in The Geology of North America–An Overview, (ed.) A.W. Bally and A.R. Palmer; Geological Society of America, The Geology of North America, v. A, p. 447-512.

**Hoffman, P.F. and Bowring, S.A.**
1984: A short-lived 1.9 Ga continental margin and its destruction, Wopmay Orogen, northwest Canada; Geology, v. 12, p. 68-72.

**Hoffman, P.F., Bell, I.R., Hildebrand, R.S., and Thorstad, L.**
1977: Geology of the Athapuscow aulacogen, East Arm of Great Slave Lake, District of Mackenzie; in Report of Activities, Part A; Geological Survey of Canada, Paper 77-1A, p. 117-129.

**Hofmann, H.J.**
1969: Attributes of stromatolites; Geological Survey of Canada, Paper 69-39, 58 p.

**Sami, T.T. and James, N.P.**
1991: An Early Proterozoic ramp to open platform; Taltheilei Formation, Great Slave Lake, Northwest Territories, Canada (abstract); in Program with Abstracts; Geological Association of Canada/Mineralogical Association of Canada Joint Annual Meeting, v. 16, p. A109.

**Southgate, P.N.**
1989: Relationships between cyclicity and stromatolite form in the Late Proterozoic Bitter Springs Formation, Australia; Sedimentology, v. 36, p. 323-339.

# Inversion of helicopter electromagnetic data along the Kapuskasing transect, Ontario[1]

**G.J. Palacky, J.S. Holladay[2], and P. Walker[3]**
**Mineral Resources Division**

*Palacky, G.J., Holladay, J.S., and Walker, P., 1992: Inversion of helicopter electromagnetic data along the Kapuskasing transect, Ontario; in Current Research, Part E; Geological Survey of Canada, Paper 92-1E, p. 177-184.*

***Abstract***

*Two data processing routines have been tested on helicopter electromagnetic (HEM) data acquired along the Kapuskasing transect in northeastern Ontario: least squares inversion based on singular value decomposition (SVD) and centroid depth algorithm (z*). The results have shown that the accuracy of SVD inversion is seriously affected even by small errors in levelling of the measured HEM data and that depth-to-bedrock estimates are often unstable. The z* algorithm is faster and more robust, and it also produces more reliable results; the 32 kHz centroid depth determinations have been found to be very close to depth-to-bedrock values from overburden drilling. Predominant Quaternary stratigraphy can be interpreted from conductivity estimates. HEM surveys can be recommended as a fast and inexpensive means of Quaternary reconnaissance.*

***Résumé***

*On a mis à l'épreuve deux programmes de traitement des données obtenues lors de levés héliportés effectués le long du transect de Kapuskasing dans le nord-est de l'Ontario: l'inversion par la méthode des moindres carrés, basée sur la décomposition des valeurs singulières, et l'algorithme de profondeur centroïde (z*). Les résultats ont montré que la précision de l'inversion basée sur la décomposition des valeurs singulières est sérieusement compromise même par de petites erreurs de nivellement des données obtenues au moyen de levés électromagnétiques héliportés, et que les estimations de la profondeur du substratum sont souvent instables. L'algorithme z* est plus rapide et plus solide, et produit aussi des résultats plus fiables; les déterminations de profondeur par l'algorithme centroïde à 32 kHz se sont avérées très proches des valeurs de la profondeur du substratum obtenues par forage des morts-terrains. On peut déterminer la stratigraphie dominante du Quaternaire d'après les profils de conductivité. On peut recommander l'emploi des levés eléctromagnétiques héliportés comme moyen rapide et peu coûteux de reconnaissance des terrains du Quaternaire.*

[1] Contribution to the Canada-Ontario Mineral Development Agreement 1985-1990. Project funded by the Geological Survey of Canada.

[2] Aerodat Ltd., 3883 Nashua Drive, Mississauga, Ontario L4V 1R3

[3] Geological Survey of Norway, P.O. Box 3006, Trondheim 7001, Norway, formerly Aerodat Ltd.

## INTRODUCTION

The staff of the Geological Survey of Canada conducts research to promote the use of geophysical techniques for mapping of Quaternary sediments. In the late 1980s, tests were carried out with two airborne electromagnetic systems and various ground techniques at the Val Gagné test site in northeastern Ontario (Pullan et al., 1987, Palacky et al., 1992a).

As part of this program, 830 line kilometres of helicopter surveys were flown in 1987 along three transects in northeastern Ontario. The Fraserdale transect followed Highway 634 from Smooth Rock Falls to Smoky Falls. The Timmins transect was carried out along logging roads west of Mattagami River between Smooth Rock Falls and Kamiskotia Lake west of Timmins. Finally, the Kapuskasing transect followed forest roads from Guerney Lake, northeast of Kapuskasing, to Lisgar Lake, south of Kapuskasing (Figure 1). After interpretation of airborne geophysical data, selected anomalies were followed up on the ground using the horizontal-loop electromagnetic method. The results of the ground surveys have been described in several papers (Palacky and Stephens, 1990, Palacky, 1991; Palacky et al., 1992b, c).

Results from 70 boreholes in the area (Smith, in press) were used to improve interpretation of electromagnetic surveys. The airborne data have been reprocessed several times using different data processing algorithms and research continued until 1992. The results of the application of two inversion techniques, one based on singular value decomposition and the other on the centroid depth algorithm, are described in this paper.

## AIRBORNE GEOPHYSICAL MEASUREMENTS

The sensors used by Aerodat Limited in the helicopter surveys included a total-field proton precession magnetometer (Geometrics G-803), a Herz Totem-2A VLF system measuring total field and quadrature component data at two frequencies (21.4 and 24 kHz), and a closely coupled, multifrequency, multicoil electromagnetic (HEM) system whose principles have been described by Palacky and West (1991). The nominal flight height of the helicopter was 60 m. The magnetometer and the VLF system were towed separately in two small birds (respective nominal terrain clearances 40 and 50 m).

The helicopter electromagnetic transmitters and receivers (spacing 6.5 m) were rigidly mounted in a bird, whose terrain clearance was kept at about 30 m. Two pairs of vertical coaxial coils were operated at frequencies of 935 and 4531 Hz; there were also two pairs of horizontal coplanar coils at 4175 Hz and 32 kHz.

Figure 2 depicts some of the measured parameters along segment KAP-2. At the top is the Hoffman HRA-100 radar altimeter trace (height of the helicopter above the ground in metres) and the total magnetic field (relative scale in nT - nanoTesla). Below is the time scale (in seconds) with hand picked fiducials. For correlation with the ground data, the extent of ground electromagnetic follow-up surveys and the location of boreholes were subsequently added. The results of Quaternary stratigraphic drilling have been published by Smith (1990) and ground electromagnetic data by Palacky and Stephens (1991). HEM data obtained at two coil configuration (coaxial and coplanar) and at four frequencies are plotted using different vertical scales. The plotted values are in-phase and quadrature components in ppm (parts per million of the ratio secondary to primary magnetic field). The data were first calibrated and levelled (Palacky and West, 1991). While the vertical coaxial coil data are more suitable for identification of small bedrock conductors, the horizontal coplanar response is better coupled to horizontal layers. In moderately conductive areas, such as the one depicted in the figure, the in-phase response at the lowest frequency are close to zero and the amplitude increases with frequency. The

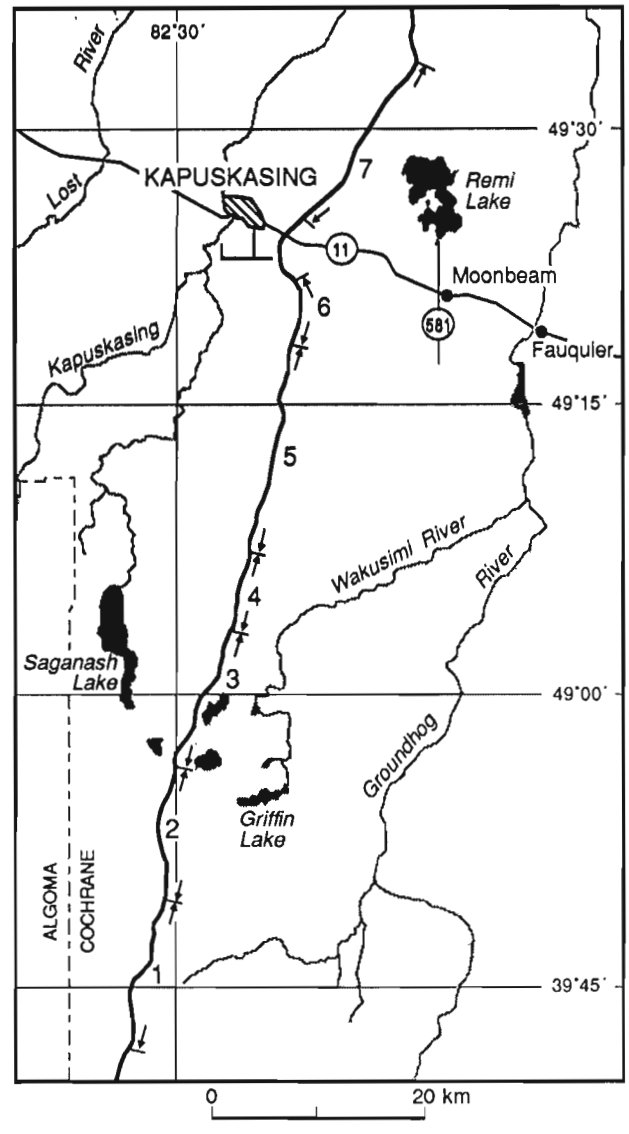


**Figure 1.** Map of the Kapuskasing area, where helicopter electromagnetic (HEM) transect surveys were carried out. Indicated is the location of seven segments, which were surveyed twice in opposite flight directions.

thicker and/or more conductive the underlying ground, the higher the HEM response. The parameter best reflecting this change is the conductance (product of conductivity and thickness).

In the original processing made as a part of the survey contract, three parameters were calculated for all four frequencies: apparent conductivity using a 200 m thick horizontal layer (essentially identical to homogenous half-space for all frequencies used), apparent depth to bedrock assuming that the overburden is lacustrine clay of conductivity 30 mS/m (milliSiemens/metre), and apparent layer conductance. In calculating the first two parameters (apparent conductivity and overburden depth), assumptions have been made that are geologically unrealistic: thick overburden with changing lithology, or homogeneous overburden of varying thickness. Examples of HEM data presented as colour bars of apparent conductivity and depth to bedrock have been published by Palacky (1989). The original objective of the survey, to simultaneously estimate overburden thickness and lithology, could not be achieved, and extensive ground follow-up was required to select suitable sites for overburden drilling.

## INVERSION OF AIRBORNE ELECTROMAGNETIC DATA

Since 1990, experiments have been conducted with two inversion techniques to obtain more reliable estimates of overburden thickness and conductivity. The Kapuskasing transect, where the results of ground electromagnetic surveys and drilling provided sufficient ground truth, was reprocessed several times to obtain satisfactory results.

Singular value decomposition (SVD) inversion technique is based on finding the best least squares fit between the calibrated and levelled HEM data and the calculated response of a layered conductive medium. The use of the ridge regression algorithm was proposed by Inman (1975). The principles of SVD inversion and its use in interpretation of

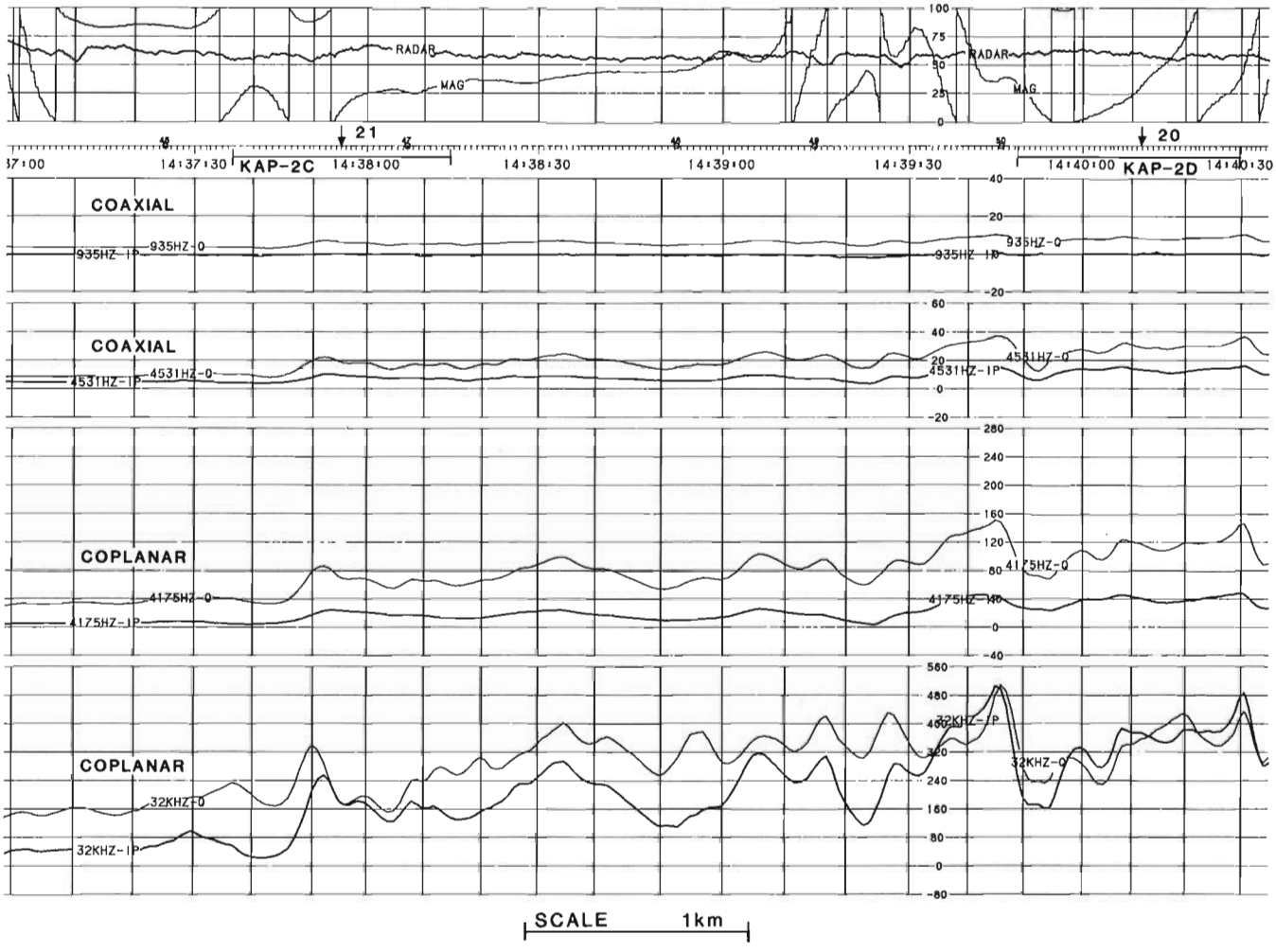


**Figure 2.** Processed airborne geophysical data along segment KAP-2 (northerly direction). From the top, total-field magnetic data and radar altimeter, time scale and location of ground follow-up profiles, four HEM channels (coil configuration and frequency are given in the figure). Thin line depicts the quadrature component data, thick line the in-phase data. Units are explained in the text.

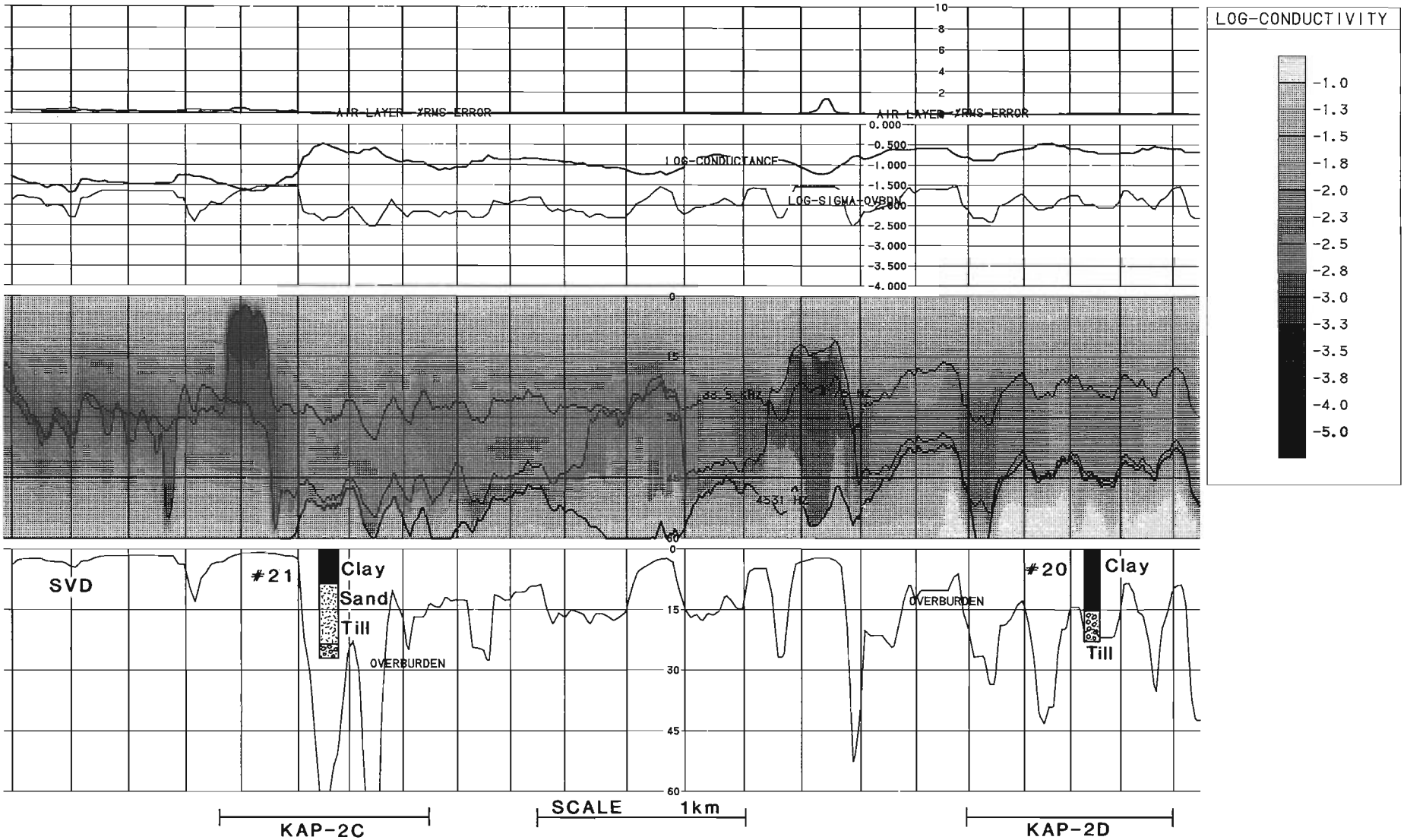


**Figure 3.** Results of inversion of HEM data along segment KAP-2 (northerly direction). From the top, in four bands: 1) RMS error and air-layer thickness, 2) conductivity and conductance of overburden, 3) three centroid depths and shaded conductivity section, 4) depth to bedrock, drill logs and the location of ground electromagnetic survey profiles. Parameters in bands 1, 2 and 4 were obtained by SVD inversion, in band 3 by centroid depth algorithm. Details and units are given in the text. Scale of grey shading key is logarithmic, units S/m.

geophysical data have been explained by Mencke (1989). Application of SVD inversion to the processing of time-domain airborne electromagnetic data has been described by Huang and Palacky (1991). Examples of processing of frequency-domain helicopter electromagnetic measurements have been published by Paterson and Reford (1986). The computer programs used in our study have been derived from software developed by Holladay (1980) for inversion of electromagnetic soundings.

For the SVD inversion of HEM data, the following constraints were introduced:

1. Conductivity of the bedrock was fixed at 0.5 mS/m.
2. Conductivity of the overburden could vary only between 3 and 30 mS/m. Using statistical analysis of resistivities of clay, till, and sand, Palacky and Stephens (1990) found this conductivity range to be typical of Quaternary sediments in northeastern Ontario.
3. Existence of an air layer with zero conductivity was assumed in areas where the tree cover caused inaccurate radar altimeter readings.

At each point along the survey profile, six measured and subsequently levelled values of in-phase and quadrature components at three frequencies (4175, 4531, and 32 000 Hz) and radar altimeter reading were used as input. These values were compared with modelled HEM data for the same frequency and component. The normalized RMS error was defined as a difference between the measured and modelled values which was squared and normalized by the datum magnitude for the given frequency. The RMS error was calculated after each iteration, which was repeated 10 times or until a preset error level was achieved.

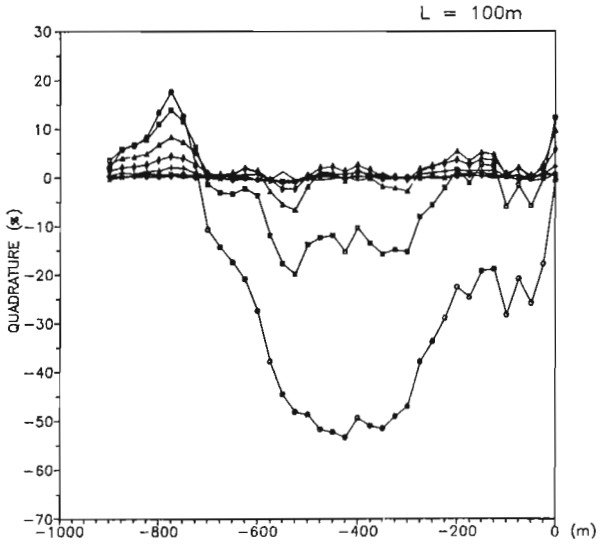


**Figure 4.** Results of horizontal-loop electromagnetic (HLEM) surveys along profile KAP-2C, quadrature component data. The rapid change in depth is reflected in inverted HEM data (Fig. 3) and ground HLEM data.

The outputs of the routine were the following quantities: 1) overburden conductivity (in S/m - Siemens/metre), 2) overburden thickness (in metres); 3) overburden conductance (in Siemens); 4) air-layer thickness (in metres); 5) RMS error (in per cent).

The centroid depth (z*) algorithm was developed by Sengpiel (1988) for interpretation of HEM surveys flown for groundwater exploration. The concept of centroid depth was originally proposed by Schmucker (1970) for inversion of magnetotelluric measurements. Data recorded at a given frequency are treated separately. This procedure adds to interpretation stability; a levelling error at one frequency will affect only one set of results, but not all as in SVD inversion. The inputs are in-phase and quadrature readings, the outputs are centroid depths z* (in metres) and ambient conductivities of the half-space below z* (in S/m). The centroid depth decreases with frequency. To map a vertical change of conductivity with depth, it is possible to combine the responses obtained with different coil configuration, because coplanar response is four times the coaxial response over the layered medium. In the survey described here, coaxial data recorded at 935 Hz had to be omitted because of low signal. Thus for each point along the survey profile, three values of z* and conductivity were available. An apparent conductivity section at a given point can be obtained by interpolating conductivities between $z^*_1$, $z^*_2$, and $z^*_3$ and extrapolating them to the surface and cut-off depth.

## PROCESSING OF HELICOPTER ELECTROMAGNETIC PROFILES

The Kapuskasing transect was flown in two directions and the results were compiled in seven segments (Fig. 1). In this paper, two segments are discussed in detail, KAP-2 and KAP-5.

Processed data using two inversion routines are given in Figure 3 for segment KAP-2 flown in the northerly direction. From the top are shown:

- RMS error (in per cent) and air-layer thickness (in metres);
- conductivity and conductance of overburden (logarithmic scale in S/m and Siemens, respectively);
- conductivity pseudosection (vertical scale in metres); conductivity is normally indicated by colour which had to be changed to shades of grey for this paper;
- overburden thickness (in metres) and the results of drilling;
- extent of ground follow-up surveys.

Along the segment, RMS error from SVD inversion is less than 0.5%. Each point has been inverted independently. The air-layer thickness is zero. The overburden conductance trace indicates two distinct patterns; the average value is 0.03 Siemens to the south of borehole 21, and about 0.1 Siemens to the north. The overburden conductivity varies relatively rapidly within the limits of constraint (0.003 to 0.03 S/m)

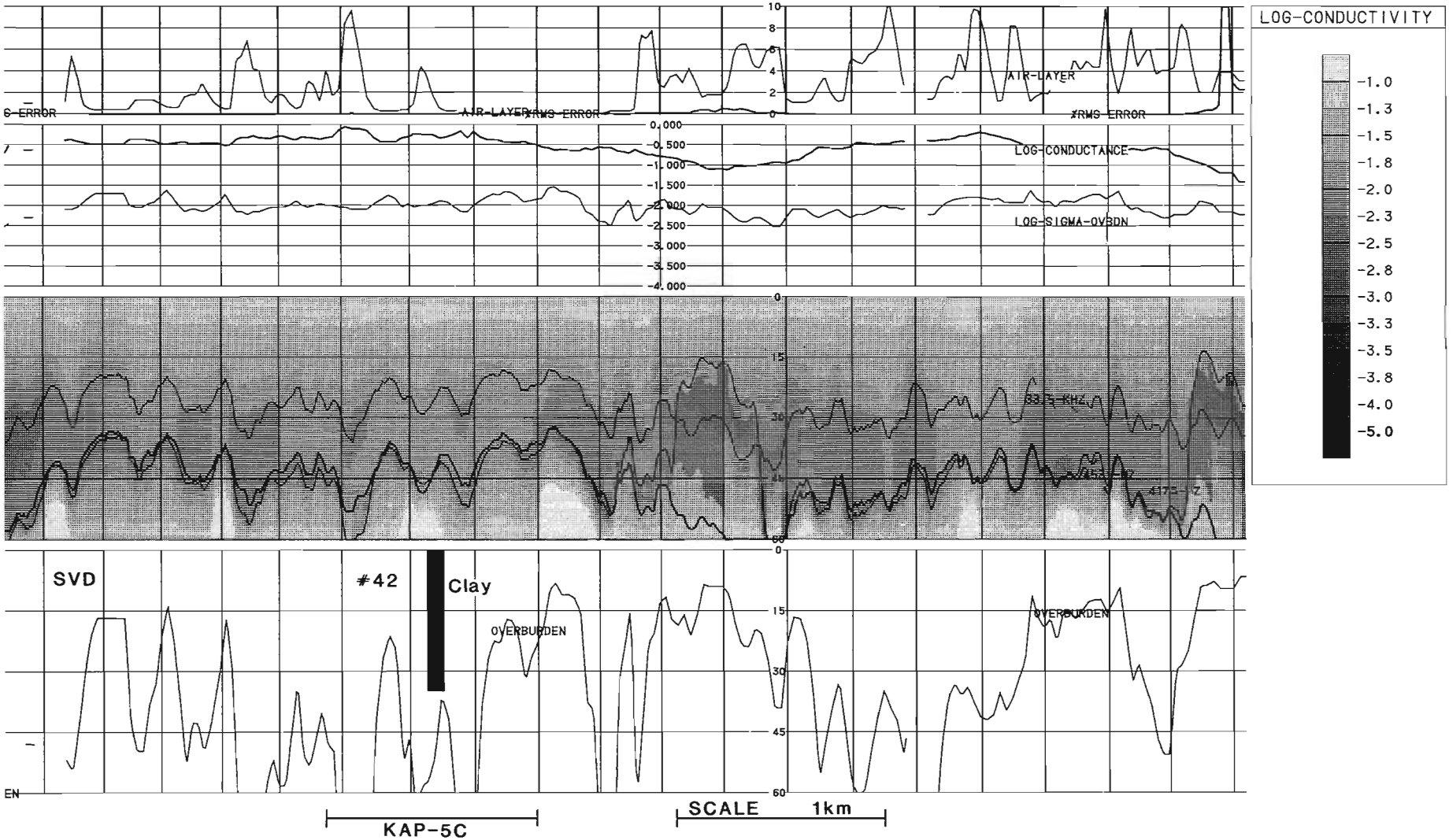


**Figure 5.** Results of inversion of HEM data along segment KAP-5 (northerly direction). The layout is the same as in Figure 3. Scale of grey shading key is logarithmic, units S/m. Details and units are given in the text.

without showing any distinct pattern. The local changes show a distinct correlation with the overburden thickness trace, which in principle should not exist. Variations in amplitudes of the measured data are attributed to changes in both conductivity and thickness, but, geologically, neither can vary so rapidly. Instability of inversion results, which is due to high correlation of parameters in the SVD matrix, is the main shortcoming of the routine.

As correlation with the drilling data shows, the depth-to-bedrock estimates cannot be considered reliable. At borehole 21, the overburden thickness has been overestimated by 100%, but at borehole 20, the estimated value proved quite accurate (Smith, 1990). Conductivity estimates at the two drill sites are meaningful, at least in the qualitative sense; at borehole 20, where 15 m of conductive clays have been intersected, the conductivity was estimated at 10 mS/m, and the value was 5 mS/m at borehole 21, where only 8 m of clay have been logged. Sand and till are significantly more resistive than clay. The actual values are low compared with the regional averages of 22 mS/m for clay and 9 mS/m for till (Palacky and Stephens, 1990). However, if the true overburden thickness were assumed at borehole 21 (28 m), conductivity would increase to 20 mS/m. This example shows that conductance estimate are realistic despite errors in individual estimates of conductivity and thickness.

Some features of bedrock topography have been correctly determined by SVD inversion, notably the sudden rise to the south of borehole 21. This feature has been confirmed by ground horizontal-loop electromagnetic measurements, which elsewhere in the area have proved to be accurate in delineating bedrock topography (Palacky et al., 1992b). The quadrature component data reflect changes in overburden thickness fairly well (Figure 4).

Conductivity pseudosection and centroid depth traces have also indicated the existence of the sudden change in bedrock topography near borehole 21. Centroid depth (z*) at 32 kHz was 30 m at borehole 21 (actual thickness of overburden is 28 m) and 23 m at borehole 20 (about the same value was found by drilling). Two other centroid depth traces (4175 and 4531 Hz) have a mean of 45 m. The penetration is significantly greater at the two frequencies, but the centroid depths do not appear to have any geological meaning. Apparent conductivity was determined 3 mS/m at borehole 21 and 10 mS/m at borehole 20; both values are rather close to the original SVD estimates.

Another segment of processed HEM data (KAP-5, northerly flight direction) is presented in Figure 5. Unlike the previous example, the air-layer thickness becomes locally significant, indicating inaccuracies in radar altimeter measurements caused by tree cover. Over the southern half of the segment, the estimated overburden conductance was more than 0.3 Siemens, significantly higher than over segment KAP-2. Higher conductance can be caused by higher conductivity (more clay) and/or greater overburden thickness. As the conductivity variation was constrained, SVD inversion resulted in much greater depth-to-bedrock estimates than along segment KAP-2. As the results of drilling show, the SVD interpretation is in the first approximation correct. At borehole 42, 35 m of conductive clay were intersected. However, the problem of rapid and unrealistic changes in SVD depth estimates is even more acute in this highly conductive area. At some points, thicknesses of over 60 m have been estimated.

The second routine, the centroid depth algorithm, indicated that conductivity along segment KAP-5 is higher than along KAP-2 (shaded conductivity section). The estimated value was 20 mS/m at borehole 42, which is very close to the regional average of 22 mS/m. The centroid depth at the drill site was 27 m; the actual depth to bedrock is 33 m. Unlike the SVD depth-to-bedrock estimates, the 32 kHz centroid depth trace is smoother and better defined; depth values between 20 and 30 m appear realistic.

## CONCLUSIONS

Helicopter electromagnetic surveys are a rapid and relatively inexpensive means of Quaternary reconnaissance. Multifrequency data from northeastern Ontario have been experimentally processed using two routines, true inversion using singular value decomposition (SVD) and centroid depth (z*) algorithm. The first routine requires more computer time and is often unstable because of highly correlated input parameters. To obtain good results, accurately levelled and calibrated data are required for consistency between frequencies. The centroid depth algorithm, which treats data measured at each frequency separately, is inherently more robust.

Evaluation of the results along the Kapuskasing transect and elsewhere in northeastern Ontario has shown that the centroid depth algorithm produces more reliable results. The 32 kHz centroid depth was remarkably close to the actual depth to bedrock at sites where drilling data were available. Both methods can be used to determine predominant composition of Quaternary sediments. If surveys are repeated with improved instrumentation that would allow more accurate levelling, the relative merits of the two techniques may have to be reassessed.

## ACKNOWLEDGMENTS

The helicopter electromagnetic survey and data processing were carried out by Aerodat Limited of Mississauga, Ontario, under contracts to Supply and Services Canada. The centroid depth algorithm was supplied by Dr. P. Sengpiel of Bundesanstalt für Geowissenschaften und Rohstoffe in Hanover, Germany. Dr. P. Keating of the Geophysics Division critically read the manuscript. S.J. Davis of the Mineral Resources Division prepared figures for final presentation. The contracts were funded by the Canada-Ontario Mineral Development Agreement 1985-1990.

# REFERENCES


**Holladay, J.S.**
1980: Interpretation of electromagnetic sounding data for a layered earth by means of nonlinear regression; Research in Applied Geophysics, v. 16, University of Toronto.

**Huang, H. and Palacky, G.J.**
1991: Damped least-squares inversion of time-domain airborne EM data based on singular value decomposition; Geophysical Prospecting, v. 39, p. 827-844.

**Inman, J.R.**
1975: Resistivity inversion with ridge regression; Geophysics, v. 40, p. 798-817.

**Mencke, W.**
1989: Geophysical data analysis: Discrete inverse theory; Academic Press.

**Palacky, G.J.**
1989: Advances in geological mapping with airborne electromagnetic systems; in Proceedings of Exploration '87: Third Decennial International Conference on Geophysical and Geochemical Exploration for Minerals and Groundwater, (ed.) G.D. Garland; Ontario Geological Survey, Special Volume 3, p. 137-152.
1991: Application of the multifrequency horizontal-loop EM method in overburden investigations; Geophysical Prospecting, v. 39, p. 1062-1082.

**Palacky, G.J. and Stephens, L.E.**
1990: Mapping of Quaternary sediments in northeastern Ontario using ground electromagnetic methods; Geophysics, v. 55, p. 1595-1604.
1991: Results of multifrequency horizontal-loop electromagnetic measurements along transects in northeastern Ontario; Geological Survey of Canada, Open File 2343.

**Palacky, G.J. and West, G.F.**
1991: Airborne electromagnetic methods; in Electromagnetic Methods in Applied Geophysics, v. 2 - Applications, Part B, (ed.) M.N. Nabighian; Investigations in Geophysics 3, Society of Exploration Geophysicists, p. 811-877.

**Palacky, G.J., Mwenifumbo, C.J., and Stephens, L.E.**
1992a: Geophysical studies at the Val Gagné test site, Ontario;. in Current Research, Part E; Geological Survey of Canada, Paper 92-1E.

**Palacky, G.J., Smith, S.H., and Stephens, L.E.**
1992b: Quaternary investigations in Geary, Thorburn and Wilhelmina Townships; in Current Research, Part E; Geological Survey of Canada, Paper 92-1E.
1992c: Use of ground electromagnetic measurements to locate sites for overburden drilling near Smoky Falls, Ontario; in Current Research, Part E; Geological Survey of Canada, Paper 92-1E.

**Paterson, N.R. and Reford, S.W.**
1986: Inversion of airborne electromagnetic data for overburden mapping and groundwater exploration; in Airborne Resistivity Mapping, (ed.) G.J. Palacky; Geological Survey of Canada, Paper 86-22, p. 39-48.

**Pullan, S.E., Hunter, J.A., Gagné, R,M., and Good, R.L.**
1987: Delineation of bedrock topography at Val Gagné, Ontario, using seismic reflection techniques; in Current Research, Part A; Geological Survey of Canada, Paper 87-1A, p. 905-912.

**Schmucker, U.**
1970: Anomalies of geomagnetic variations in the southwestern United States; Bulletin of the Scripps Institution of Oceanography 13, University of California.

**Sengpiel, P.**
1988: Approximate inversion of airborne EM data from a multilayer ground; Geophysical Prospecting, v. 36, p. 446-459.

**Smith, S.L.**
1990: Geochemical and lithological data from overburden drill cores with descriptive core logs - Timmins to Smoky Falls, Ontario; Geological Survey of Canada, Open File 2278.
in press: Quaternary stratigraphic drilling transect, Timmins to the Moose River Basin, Ontario; Geological Survey of Canada, Bulletin 415.



Geological Survey of Canada Project 850058

# Geophysical studies at the Val Gagné test site, Ontario[1]

**G.J. Palacky, C.J. Mwenifumbo and L.E. Stephens[2]**
**Mineral Resources Division**

*Palacky, G.J., Mwenifumbo, C.J., and Stephens, L.E., 1992: Geophysical studies at the Val Gagné test site, Ontario; in Current Research, Part E; Geological Survey of Canada, Paper 92-1E, p. 185-193.*

***Abstract***

*A site was established near Val Gagné, Ontario, for testing of geophysical instruments. The area is covered by 20 to 40 m of highly conductive varved clays (average resistivity 30 Ω•m). Since 1985, the following methods have been used at the site by staff of the Geological Survey of Canada: airborne electromagnetic and magnetic, high-resolution shallow seismic reflection, resistivity sounding, horizontal-loop electromagnetic with APEX MaxMin I, ground conductivity using Geonics EM-16R, EM-31, and EM-34. Seismic reflection and resistivity sounding techniques have proven to be the most effective in delineating buried bedrock valleys. Horizontal-loop electromagnetic measurements also provided satisfactory results, but of limited reliability compared with the more expensive seismic and resistivity sounding surveys. None of the ground conductivity measuring systems could effectively penetrate the thick and highly conductive overburden at the Val Gagné site.*

***Résumé***

*On a établi un site près de Val Gagné en Ontario dans le but de mettre à l'épreuve des appareils de levés géophysiques. Le secteur est couvert de 20 à 40 m d'argiles varvées fortement conductrices (résistivité moyenne de 30 Ω•m). Depuis 1985, le personnel de la Commission géologique du Canada utilise les méthodes suivantes sur le site en question: des levés électromagnétiques et magnétiques aéroportés, des levés de sismique-réflexion de haute résolution à faible profondeur, des sondages de résistivité, des levés électromagnétiques au moyen du système APEX MaxMin I à bobines horizontales, et un levé de conductivité du sol au moyen des systèmes Geonics EM-16R, EM-31 et EM-34. Les techniques de sismique-réflexion et de sondages de résistivité se sont avérées les plus efficaces pour délimiter les vallées enfouies, creusées dans le substratum. Les mesures électromagnétiques avec bobines horizontales ont également donné des résultats satisfaisants, mais de fiabilité limitée comparativement aux procédés plus coûteux de sismique-réflexion et de résistivité. Aucun des systèmes de mesure de la conductivité du sol n'a pu efficacement pénétrer les épais morts-terrains fortement conducteurs du site de Val Gagné.*

[1] Contribution to the Canada-Ontario Mineral Development Agreement 1985-1990. Project funded by Geological Survey of Canada.

[2] Deceased.

## INTRODUCTION

Thick, conductive overburden can hamper the use of electromagnetic methods in mineral exploration. In Canada, the most affected area is the Abitibi clay belt, where conductive lacustrine clays deposited in the former lakes Barlow and Ojibway can reach thicknesses of 60 m (Veillette, 1989). In the past 30 years, many electromagnetic instruments were designed to overcome the problem of conductive overburden. The manufacturers of ground and airborne instruments expressed interest in documented sites, where they could test their equipment (Palacky, 1986). The Ontario Geological Survey (OGS) developed a test site at Night Hawk Lake, approximately 50 km east of Timmins, Ontario (Barlow, 1981; Barlow et al., 1982; Pitcher et al., 1983; Pitcher, 1985). At that site, graphitic conductors are covered by 60 m of tills and clays.

After consultations with the private sector, the Ontario Geological Survey and the Geological Survey of Canada concluded that it would be desirable to establish another site, where the ability of geophysical instruments to outline bedrock topography could be tested. R.B. Barlow of the Ontario Geological Survey suggested a site east of Val Gagné, where buried bedrock valleys were known from previous geophysical surveys and drilling. A large area east of Timmins had previously been surveyed with a time-domain airborne electromagnetic system (INPUT) and selected features were followed up on surface with Geonics EM-31 and EM-34 equipment and drilled. The results of that program (denominated Black River-Matheson) have been described by Pitcher et al. (1984).

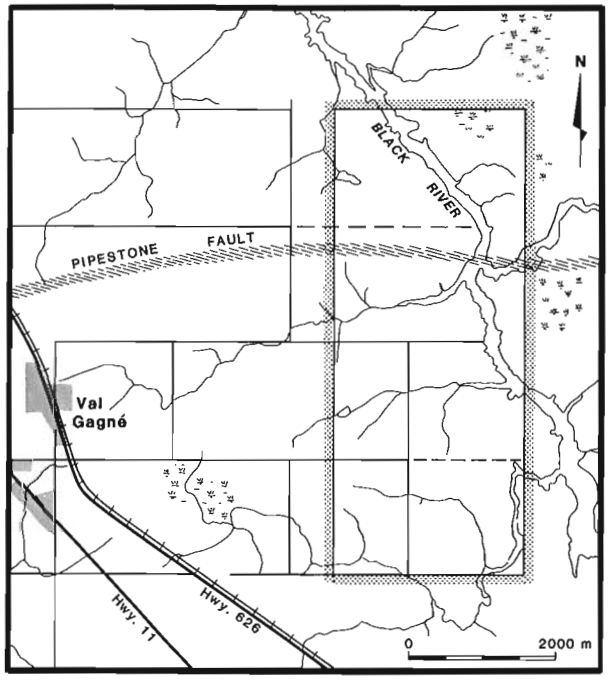


**Figure 1.** Location of the Val Gagné test site. An outline is given of the rectangular area that was surveyed with airborne geophysical systems.

The Val Gagné test site was outlined in 1985 after a reconnaissance by the staff of Geophysics and Geochemistry Section of the Ontario Geological Survey and Electrical Methods Section of the Geological Survey of Canada. Later in the year, the GSC staff carried out resistivity soundings along selected profiles and OGS geophysicists used ground time-domain electromagnetic equipment. In the following year, several geophysical techniques were used by GSC scientists; apparent conductivity of the ground was measured by the staff of Electrical Methods Section using Geonics EM-16R, EM-31, and EM-34 equipment and high-resolution optimum-offset seismic reflection surveys were carried out by the Terrain Geophysics Section (Pullan et al., 1987, Pullan and Hunter, 1990). In 1987-1988, the Electrical Methods Section surveyed the site with horizontal-loop APEX MaxMin I electromagnetic instrument. Detailed airborne electromagnetic measurements were carried out at the site in 1986 (time-domain, towed-bird GEOTEM surveys) and in 1987 (multifrequency, multicoil helicopter surveys). Interpretation of the data using a variety of data processing techniques continued until 1991.

## TOPOGRAPHY AND GEOLOGY OF THE TEST SITE

The Val Gagné test site is located 3 km east of the village of Val Gagné, approximately at latitude 48°35'N and longitude 80°35'W. Its extent is 2.7 km in the east-west direction and 6.1 km in the north-south direction (Fig. 1). The site was selected to include two distinct environments; in the south, the terrain is mostly flat and the overburden is thick; in the north, the rivers are deeply incised and the overburden is believed to be thinner. Black River flows through the area in north-northwest direction.

The most important geological feature is the Pipestone Fault which crosses the area in east-west direction. Several gold deposits are associated with this fault in the Timmins area. Bedrock geology comprises pyroclastic rocks to the north of the fault and Precambrian sedimentary rocks (mostly siltstone) in the south. Mafic volcanic flows striking east-west and north-south have been identified in the area by interpretation of aeromagnetic data (Palacky, 1992).

Overburden consists of a thick layer of varved clays deposited circa 9000 years BP on the floor of the glacial Lake Barlow. Glacial tills and glaciofluvial sands have been preserved in valleys beneath the lacustrine sediments. Quaternary stratigraphy of northeastern Ontario and western Quebec has been summarized by Veillette (1989). Two boreholes drilled in the test area by the OGS intersected in excess of 30 m of varved clay, followed 2 to 4 m of glacial till. In one borehole, sand was also found.

## AIRBORNE ELECTROMAGNETIC SURVEYS

The surveys were conducted along north-south flight lines with a spacing of 100 m. The extent of the rectangular survey area is outlined in Figure 1. In the first survey, the

time-domain GEOTEM system was tested. The electromagnetic data were recorded as 12 channels, which measure the secondary magnetic field at delay times ranging from 0.36 to 1.9 milliseconds after the transmitter switch-off. Details of the system can be found in Palacky and West (1991).

Subsequently, a helicopter electromagnetic survey was carried at the test site. Aerodat Limited used a multifrequency, multicoil system described by Palacky and West (1991). Two pairs of vertical coaxial coils were operated at frequencies of 935 and 4600 Hz, two pairs of horizontal coplanar coils at 4175 and 32 000 Hz. The measured parameters were in-phase and quadrature components at the four frequencies. The nominal terrain clearance of the bird in which the transmitting and receiving coils were mounted was 30 m. The flight height of the helicopter was 60 m. The details of airborne operations were given by Palacky (1992).

Simultaneously with electromagnetic measurements, other geophysical parameters were recorded in the course of the airborne survey. The magnetic total field was measured with a Geometrics G-803 proton precession magnetometer. A Totem-2A Herz receiver (Herz, 1986) recorded the VLF total-field and quadrature component at two frequencies. The results of the survey were presented as stacked profiles of all measured and calculated data and contour maps. A set of five contour maps at a scale 1:10 000 was released as a GSC Open File (Palacky, 1992):

- magnetic total field (contour interval 5 nT);
- VLF total field using transmitter NSS Annapolis at 21.4 kHz (contour interval 0.5%);
- VLF total field using transmitter NAA Cutler at 24 kHz (contour interval 0.5%);
- apparent conductivity calculated from electromagnetic data at 4175 Hz, horizontal coplanar coil geometry (logarithmic contour interval, 5 per decade);
- apparent conductivity calculated from electromagnetic data at 32 kHz, horizontal coplanar coil geometry (logarithmic contour interval, 5 per decade).

The magnetic map was useful for definition of bedrock geology (mafic flows), but did not yield any information on Quaternary lithology and overburden thickness. The only clear VLF anomaly was associated with the Black River. The Pipestone Fault was marginally detected on NAA data.

The most useful products of the helicopter survey for overburden mapping are apparent conductivity maps. In-phase and quadrature responses measured at four frequencies were separately fitted to precalculated responses of a 200 m thick horizontal layer. Because the penetration of the helicopter system with the frequencies used is less than 200 m, this model is equivalent to the homogenous half-space. The assumption of an unrealistically thick upper layer (overburden) results in underestimating the layer conductivity.

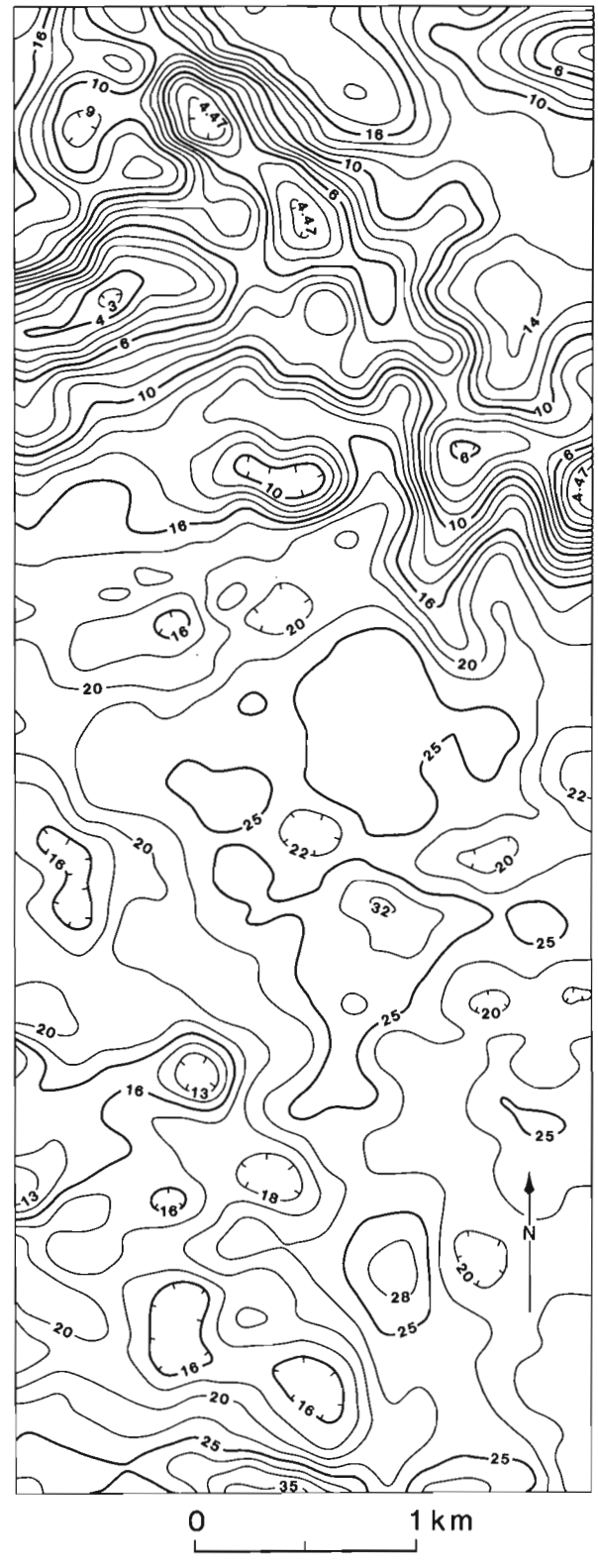


**Figure 2.** Map of apparent conductivity of the test site (contours in mS/m) compiled by computer processing of helicopter electromagnetic surveys with a horizontal coplanar coil configuration at the frequency of 4175 Hz.

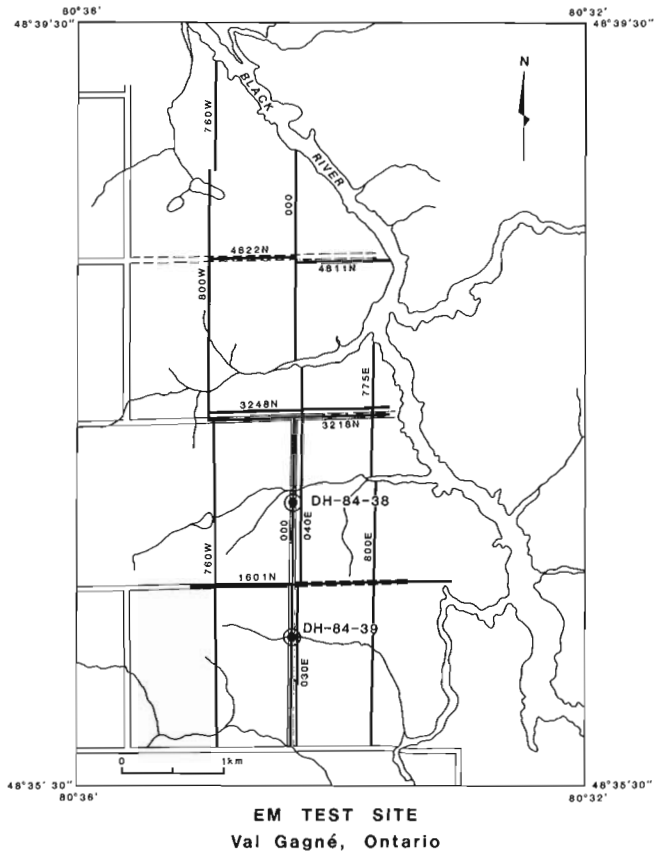


**Figure 3.** Map of the Val Gagné test site showing the location of boreholes and survey lines along which ground geophysical surveys were carried out.

Figure 2 depicts a contour map of apparent conductivity calculated from horizontal coplanar data measured at 4175 Hz. The contours are in mS/m (milliSiemens/metre) and their intervals are logarithmically spaced. Conductivity patterns over the northern third of the area (north of Pipestone Fault) are different from the rest of the area. Using a thick layer of a constant thickness for interpretation, a reduction in overburden thickness appears in the map as lower apparent conductivity. In the north, an elongated anomaly of low apparent conductivity anomaly is associated with the Black River and it is apparent that lacustrine clays are much thinner there. Apart from the river, the average apparent conductivity is about 10 mS/m north of the Pipestone Fault; it increases to about 20 mS/m in the south. These values are about 40% lower than conductivities determined by ground measurements (see below). This finding has a simple physical explanation: Apparent conductivity is smaller than the true conductivity when overburden thickness is less than the value used in the model definition. In fact, the system "sees" and integrates into apparent conductivity the more resistive basement. The true thickness of overburden at the Val Gagné test site is about 40 m, but the model thickness was assumed 200 m.

## GROUND SURVEY GRID

Ground geophysical surveys were carried out along lines depicted in Figure 3. The base line (000) runs north-south. All distances are measured from the base line (e.g., station 800E is located 800 m east of the base line) and from the dirt road, which forms the southern boundary of the area. Some of the lines follow existing dirt roads, but most of the survey lines had to be cut. Electromagnetic surveys could not be

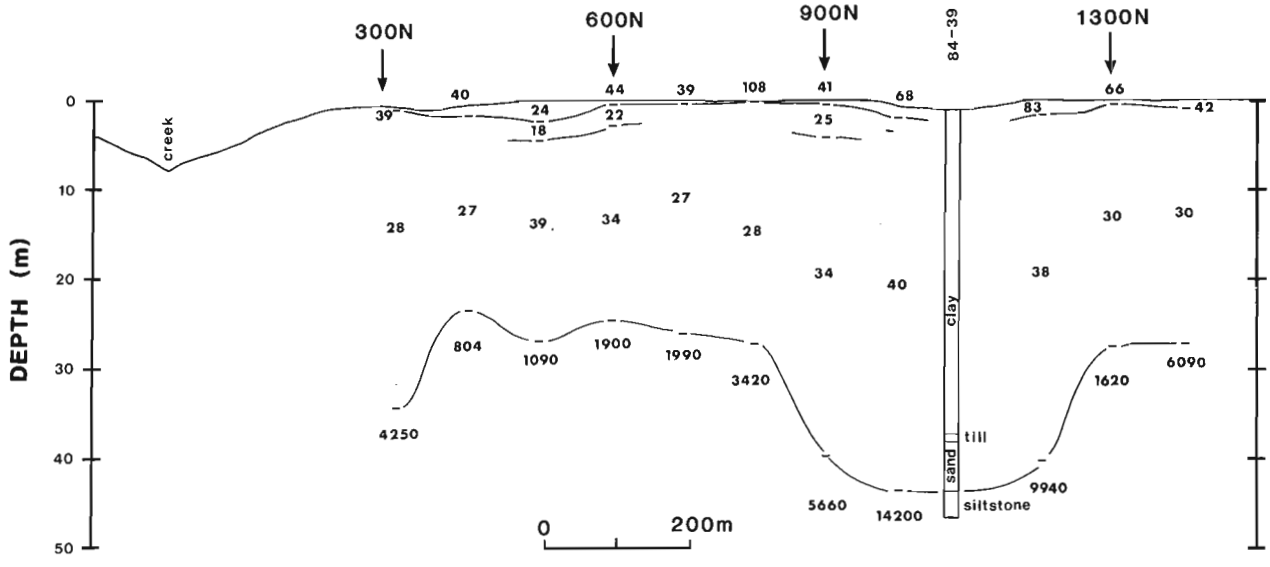


**Figure 4.** Section obtained by interpretation of Schlumberger resistivity sounding measurements along the baseline (from 300N to 1400N). Numbers indicate interpreted resistivity values in Ω•m. The log of borehole 84-39 is also plotted.

carried out along some of the existing roads because of grounded fences. For this reason, parallel lines (e.g., 030E, 3248N) had to be cut and chained. The topography is rather rough in the northern half of the test site and the coverage there was less complete. Because of access problems, no ground measurements were carried out east of the Black River. The locations of two boreholes drilled by the OGS (DH-84-38, DH-84-39) are also given in Figure 3.

## GROUND RESISTIVITY MEASUREMENTS

The first geophysical technique applied at the Val Gagné site by the GSC staff was Schlumberger resistivity/induced polarization sounding using a Huntec M-3 induced polarization transmitter and Huntec Mark IV receiver. In resistivity surveys, current is injected into the ground by means of current electrodes and electrical potential in the centre of the array is measured at two potential electrodes. Details of the technique and principles of data interpretation are given in Koefoed (1979) and Ward (1990). The spacing of current electrodes was increased in logarithmic intervals from 2 to 400 m. Readings included apparent resistivity and chargeability. Data were interpreted by curve matching in the field and by computer inversion in Ottawa. Most of the measured responses were of the three-layer type, but some could be better approximated by a four-layer model.

Field surveys were carried out along the base line from 300N to 1600N and along line 1601N, from 700W to 800E. Readings were taken every 100 m and 28 soundings were made. A section depicting interpreted soundings between 300N and 1400N is given in Figure 4. Resistivities and thicknesses were obtained by computer inversion of the field data. A near surface layer, a few metres thick, was interpreted at most sounding sites. In soundings at 500N, 600N and 900N, two near surface layers were identified. The layer resistivity varies between 18 and 108 Ω.m. There is no clear correlation between this interpreted layer and changes in Quaternary geology. Most likely, resistivity changes were caused by varying water saturation immediately below the surface. The most prominent layer has been correlated with clay. The layer resistivity is stable, between 27 and 40 Ω•m. Depth to bedrock determined by inversion of sounding data at stations 1000N and 1200N (43 m) agrees with the log of borehole 84-39. However, a thin layer of till and sand at the bottom of the valley could not be interpreted from resistivity data. The existence of the bedrock valley has been confirmed by subsequent optimum-offset seismic reflection surveys (Pullan et al., 1987). Based on interpretation of both seismic and resistivity data, depth to bedrock away from the valley has been estimated at 30 m. Seismic data provided more accurate information about the presence of till and sand in the valley.

Resistivity soundings were successful in achieving the survey objectives, detection of buried bedrock valleys, but the manpower and time requirements were deemed too high to recommend their routine use. Electromagnetic techniques are much faster and typically require only two operators (rather than four for soundings), but doubts existed about their effectiveness. At the time of the surveys, no similar investigations had been undertaken anywhere.

## GROUND CONDUCTIVITY MEASUREMENTS

The electromagnetic techniques most commonly used in engineering overburden studies measure apparent conductivity. A primary electromagnetic field is generated by the transmitting coil and the response of the conductivity of the ground is measured by a receiving coil. Instruments of this type (Geonics EM-31 and EM-34) operate at low inductions numbers, which implies special features compared with other electromagnetic techniques (McNeill, 1990):

1. Skin depth for the operating frequency is significantly greater than the coil spacing.
2. Only the quadrature component of the secondary magnetic field is measured; the reading (after calibration of the instrument by the manufacturer) is apparent conductivity in mS/m.
3. To determine variation of conductivity with depth, coil separation rather than frequency is changed (the opposite is done in horizontal-loop measurements which will be discussed later).

The EM-31 instrument was designed to be operated by one person. Two small horizontal coils are placed at the ends of a rigid boom (coil spacing 3.66 m). The operating frequency is 9.8 kHz. The EM-34 instrument consists of two coils, which can be held by operators in horizontal coplanar or vertical coplanar position. Depending on the penetration required for conductivity measurements, appropriate coil separation is chosen (10, 20, or 40 m). The corresponding frequencies are 6.4, 1.6 and 0.4 kHz. The penetration is approximately 0.75 times the coil spacing for the horizontal coplanar mode, and 1.5 times the coil spacing for the vertical coplanar mode. When conductivity and thickness of the underlying layers are to be determined, six readings (three coil separations at two coil configurations) must be taken. Computer inversion of the data is then used in interpretation.

In areas of relatively high resistivity, the in-phase component of the secondary magnetic field remains small, and the coil separation can be adjusted by using a standard procedure (distance indicator on the instrument console). In highly conductive areas, such as the Val Gagné test site, this procedure becomes inaccurate resulting in erroneous values of layer conductivity and thickness when inversion of EM-34 data is attempted.

Another technique, which can be used to measure ground conductivity, is based on the theory that resistivity can be calculated from the measured ratio of the horizontal components of the Earth's electrical and magnetic fields. Such measurements form the basis of the magnetotelluric method, but they can also be performed with VLF

transmitters as the source of the primary electromagnetic field. The EM-16R instrument measures apparent resistivity and phase angle at one VLF frequency (McNeill, 1990). Depending on the location of the survey area, the most appropriate VLF station will be chosen. In favourable conditions, it is possible to determine overburden resistivity and thickness from EM-16R measurements. However, the overburden thickness must be somewhat smaller than the skin depth in overburden (McNeill and Labson, 1991) and this condition was not satisfied at the test site.

Surveys with the three systems were carried out over most of the lines depicted in Figure 3. The standard station spacing was 20 m. Some lines in the more remote northern part were omitted. Conductivity measurements with EM-16R, EM-31, and EM-34 instruments (the latter with three coil separations and two coil configurations) showed consistent results in the whole test site area - average conductivity of approximately 30 mS/m, which corresponds to resistivity of 33 Ω•m. This value is in good agreement with the results of resistivity surveys. A sample profile (line 30E, from 0 to 1600N) obtained with the EM-34 equipment, coil separation 10 m, is reproduced in Figure 5. This profile is the same as one depicted in Figure 4 (resistivity soundings). In principle, only surveys with the largest coil separation and vertical coplanar configuration could be affected by changes in bedrock topography. However, even after careful analysis of the field data, no anomalies due to known bedrock valleys could be identified. Obviously, the systems cannot penetrate overburden of medium thickness (30 to 50 m) and high conductivity (30 mS/m).

## HORIZONTAL-LOOP ELECTROMAGNETIC SURVEYS

The horizontal-loop electromagnetic (HLEM) method was originally developed in Sweden in the 1930s. Forty years later, a Canadian company, APEX Parametrics Ltd., developed a versatile multifrequency system MaxMin, which can be operated at various coil configuration and separations. Although the system was designed for mineral exploration, it has successfully been used in other applications. Groundwater and overburden investigations with the system have been pioneered in Africa by Palacky et al. (1981). After disappointing results with the three conductivity measuring techniques, experiments were carried out with the MaxMin I system. Initial tests indicated that the horizontal-loop mode is the most suitable for the survey objective. In the APEX MaxMin system, the primary electromagnetic field is generated by current in a horizontal transmitting coil. The secondary magnetic field, which is induced by conductors in the ground, is sensed by a receiver (also a horizontal coil). Field surveys are carried out in the profiling mode; operators move with both coils along a survey line. The coil separation can be varied according to survey objectives, but must be kept constant during a given survey. Details about the technique can found in Frischknecht et al. (1991).

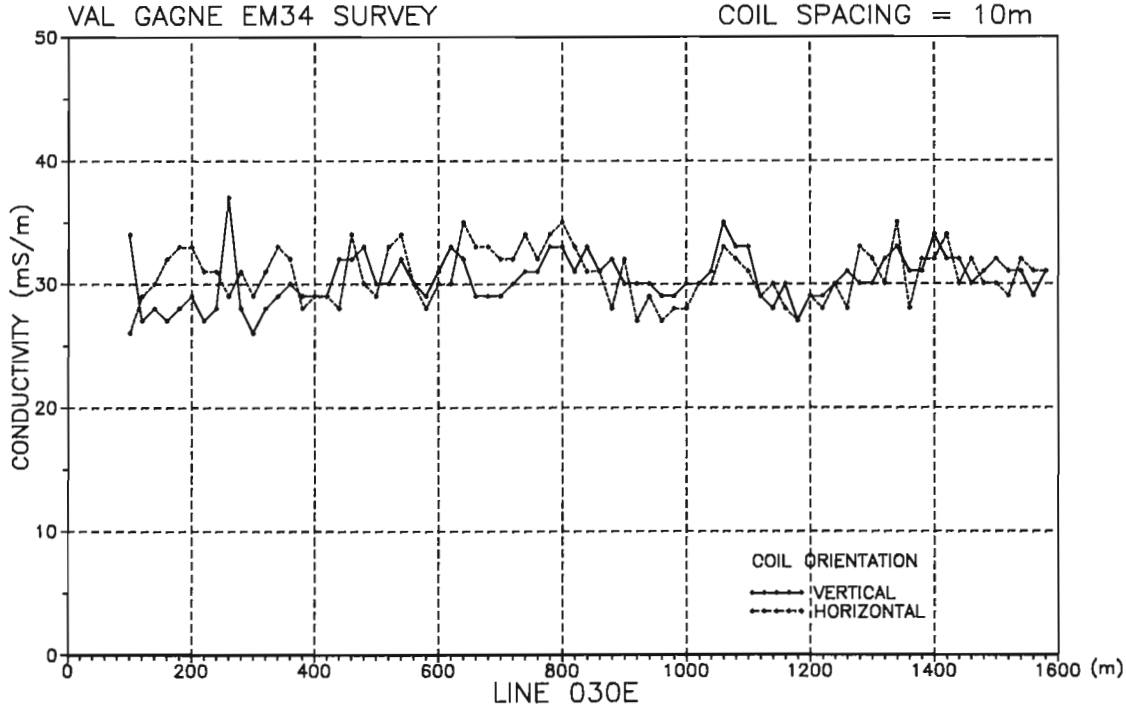


**Figure 5.** Results of ground conductivity measurements (in mS/m) along line 30E from 0 to 1600N (30 m parallel with the base line). The instrument used in the survey was Geonics EM-34 with a coil spacing of 10 m and two coil configurations (horizontal coplanar and vertical coplanar).

At the Val Gagné test site, HLEM surveys were carried out with coil separations of 60, 80, 100, and 160 m. Most of the surveys with multiple coil separations were carried out in the southern portion of the area, where resistivity sounding and reflection seismic surveys were carried out previously. The APEX MaxMin I instrument, which was used in the surveys, has 8 frequencies increasing by a factor of two from 110 to 14 080 Hz. If the results are to be interpreted as soundings, readings must be taken at all frequencies. Another requirement, which is much more stringent than in mineral exploration surveys, is the accuracy of coil separation, which must be maintained with a precision better than 0.3% of the coil distance. The measured parameters are in-phase and quadrature component of the ratio secondary/primary magnetic field; the results are given in per cent. The readings were recorded automatically using a Rautaruukki KTP-84 data logger.

Interpretation of the field data was done with the EMIX-MM Plus software (Interpex Limited, 1989). The inversion routine is based on ridge regression described in Inman (1975). As the original objective was to outline bedrock topography, a two-layer model was used in all interpretations. The upper layer is the conductive overburden, the lower layer the resistive bedrock (whose conductivity was fixed). Unconstrained inversion, which uses all measured parameters simultaneously, produces estimates of overburden conductivity and thickness.

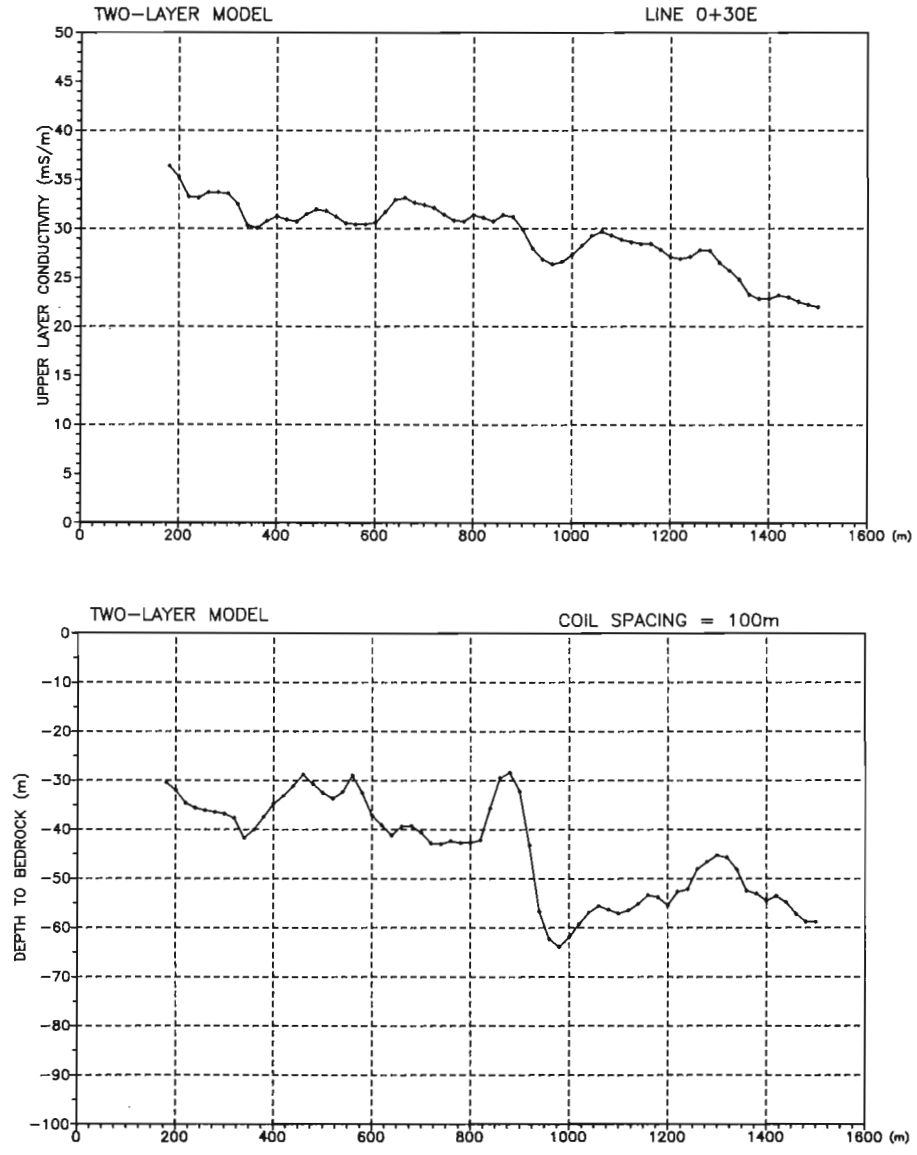


**Figure 6.** Results of unconstrained inversion of horizontal-loop electromagnetic data (8 frequencies, coil spacing 100 m): Top, overburden conductivity (in mS/m); bottom, depth to bedrock (in m). The profile shown is 30E from 0 to 1600N (the same as in Figs. 4, and 5).

A sample interpreted profile (line 30E from 0 to 1660N) is given in Figure 6. At the top is plotted the overburden conductivity, at the bottom, depth to bedrock. The conductivity values are generally in good agreement with estimates obtained by field conductivity measurements (see the previous section). While the depth to bedrock has generally been overestimated, some features of the bedrock topography (valley between 1000N and 1200N) have nevertheless been recognized. The most difficult problem in interpreting electromagnetic data is the resolution of layer thickness and conductivity. Only their product, conductance, is accurately determined. The problem of resolution is graphically illustrated in Figure 6. If the resolution were perfect, no common trend (downward slope from south to north) would exist between conductivity and depth-to-bedrock. The results could be improved by constrained inversion of the data. Assuming a constant conductivity of 30 mS/m, the northern side of the bedrock valley would appear closer to the surface. Such a result would be in agreement with seismic reflection data (Pullan et al., 1987).

## CONCLUSIONS

The original objective of establishing the Val Gagné site was to provide controlled environment for testing geophysical instruments over buried bedrock valleys. The site was intended to be typical of overburden conditions in northeastern Ontario. As subsequent investigations elsewhere have shown, the overburden at the site is significantly thicker and more conductive than elsewhere in the area. Smith (in press) described the results of an extensive overburden drilling program in northeastern Ontario. Of the 70 boreholes drilled, none intersected 40 m of highly conductive varved clay, which is typical of the Val Gagné site.

If geophysical detection of valleys buried under a thick and highly conductive clay layer is the objective, high-resolution seismic reflection and resistivity sounding surveys provide the best answers. At the Val Gagné test site, seismic measurements outlined a till layer at the bottom of the valley which was not detected by resistivity sounding. Both techniques are slow and manpower intensive. Of the four electromagnetic instruments tested (Geonics EM-16R, EM-31, EM-34, APEX MaxMin I), only the last one gave some indication of bedrock topography. The MaxMin I has subsequently been used with a considerable degree of success in routine surveys in northeastern Ontario, where the overburden is generally thinner and less conductive (Palacky and Stephens, 1990; Palacky et al., 1992a, b). Extensive surveys with electromagnetic instruments at the Val Gagné site were extremely valuable in testing the limits of all four systems.

## ACKNOWLEDGMENTS

The work was funded by the Canada-Ontario Mineral Development Agreement 1985-1990. Helicopter electromagnetic surveys were carried out by Aerodat Limited of Mississauga, Ontario, under contract to Supply and Services Canada. Staff of the Exploration Geophysics Subdivision (G.R. Bernius, S. Birk, W.G. Hyatt, and the authors) carried out ground electrical and electromagnetic surveys. They were assisted by students J. Allison, A. Cinq-Mars, C. Hyde, M. Eising, M.E. Muttes, and S. Ratté. R.B. Barlow of the Ontario Geological Survey was helpful in selecting the test site. A. Cinq-Mars and Dr. K.A. Richardson of the Mineral Resources Division critically read the manuscript. S.J. Davis of the Mineral Resources Division was responsible for final presentation of all illustrations.

## REFERENCES

**Barlow, R.B.**
1981: Night Hawk geophysical test range results using two electromagnetic systems, District of Cochrane; in Summary of Field Work 1981, (ed.) J. Wood, O.L. White, R.B. Barlow, and A.C. Colvine; Ontario Geological Survey, Miscellaneous Paper 100, p. 152-159.

**Barlow, R.B., Pitcher, D.H., and Wadge, D.R.**
1982: Night Hawk geophysical test range results, Night Hawk Lake, District of Cochrane; in Summary of Field Work 1982, (ed.) J. Wood, O.L. White, R.B. Barlow, and A.C. Colvine; Ontario Geological Survey, Miscellaneous Paper 106, p. 152-161.

**Frischknecht, F.C., Labson, V.F., Spies, B.R., and Anderson, W.L.**
1991: Profiling methods using small sources; in Electromagnetic Methods in Applied Geophysics, v. 2 - Applications, (ed.) M.N. Nabighian; Investigations in Geophysics 3, Society of Exploration Geophysicists, p. 105-270.

**Herz, A.**
1986: Airborne EM instruments operating at VLF and higher frequencies; in Airborne Resistivity Mapping, (ed.) G.J. Palacky; Geological Survey of Canada, Paper 86-22, p. 55-61.

**Inman, J.R.**
1975: Resistivity inversion with ridge regression; Geophysics, v. 40, p. 798-817.

**Interpex Limited**
1989: EMIX-MM Plus - User's Manual; Interpex Ltd., Golden, Colorado.

**Koefoed, O.**
1979: Geosounding Principles - v. 1: Resistivity Sounding Measurements; Elsevier Scientific Publishing, Amsterdam.

**McNeill, J.D.**
1990: Use of electromagnetic methods for groundwater studies; in Geotechnical and Environmental Geophysics, v. 1 - Review and Tutorial, (ed.) S.H. Ward; Investigations in Geophysics 5, Society of Exploration Geophysicists, p. 191-218.

**McNeill, J.D. and Labson, V.**
1991: Geological mapping using VLF radio signals; in Electromagnetic Methods in Applied Geophysics, v. 2 - Applications, Part B, (ed.) M.N. Nabighian; Investigations in Geophysics 3, Society of Exploration Geophysicists, p. 521-640.

**Palacky, G.J.**
1986: Panel discussion: Airborne resistivity mapping and its future; in Airborne Resistivity Mapping, (ed.) G.J. Palacky; Geological Survey of Canada, Paper 86-22, p. 181-192.
1992: Helicopter geophysical surveys at the Val Gagné test site, District of Cochrane, Ontario; Geological Survey of Canada, Open File 2503.

**Palacky, G.J. and Stephens, L.E.**
1990: Mapping of Quaternary sediments in northeastern Ontario using ground electromagnetic methods; Geophysics, v. 55, p. 1595-1604.

**Palacky, G.J. and West, G.F.**
1991: Airborne electromagnetic methods; in Electromagnetic Methods in Applied Geophysics, v. 2 - Applications, Part B, (ed.) M.N. Nabighian; Investigations in Geophysics 3, Society of Exploration Geophysicists, p. 811-877.

**Palacky, G.J., Ritsema, I.L., and de Jong S.J.**
1981: Electromagnetic prospecting for groundwater in Precambrian terrains in the Republic of Upper Volta; Geophysical Prospecting, v. 29, p. 932-955.

**Palacky, G.J., Smith, S.L., and Stephens. L.E.**
1992a: Quaternary investigations in Geary, Thorburn and Wilhelmina Townships; in Current Research, Part E; Geological Survey of Canada, Paper 92-1E.
1992b: Use of ground electromagnetic measurements to locate sites for overburden drilling near Smoky Falls, Ontario; in Current Research, Part E; Geological Survey of Canada, Paper 92-1E.

**Pitcher, D.H.**
1985: Night Hawk geophysical test range results, District of Cochrane; in Summary of Field Work and Other Activities 1985, (ed.) J. Wood, O.L. White, R.B. Barlow, and A.C. Colvine; Ontario Geological Survey, Miscellaneous Paper 126, p. 170-177.

**Pitcher, D.H., Barlow, R.B., and McNeill, J.D.**
1984: Mapping the overburden in the Black River-Matheson (BRIM) area, District of Cochrane; in Summary of Field Work and Other Activities 1984, (ed.) J. Wood, O.L. White, R.B. Barlow, and A.C. Colvine; Ontario Geological Survey, Miscellaneous Paper 119, p. 299-307.

**Pitcher, D.H., Barlow, R.B., and Wadge, D.R.**
1983: Night Hawk geophysical test range results, Night Hawk Lake, District of Cochrane; in Summary of Field Work 1982, (ed.) J. Wood, O.L. White, R.B. Barlow, and A.C. Colvine; Ontario Geological Survey, Miscellaneous Paper 116, p. 132-141.

**Pullan, S.E. and Hunter, J.A.**
1990: Delineation of buried bedrock valleys using the optimum offset shallow seismic reflection technique; in Geotechnical and Environmental Geophysics, v. 3 - Geotechnical, (ed.) S.H. Ward; Investigations in Geophysics 5, Society of Exploration Geophysicists, p. 75-87.

**Pullan, S.E., Hunter, J.A., Gagné, R.M., and Good, R.L.**
1987: Delineation of bedrock topography at Val Gagné, Ontario, using seismic reflection techniques; in Current Research, Part A; Geological Survey of Canada, Paper 87-1A, p. 905-912.

**Smith, S.E.**
in press: Quaternary stratigraphic drilling transect, Timmins to the Moose River Basin, Ontario; Geological Survey of Canada, Bulletin 415.

**Veillette, J.J.**
1989: Ice movements, till sheets and glacial transport in Abitibi-Timiskaming, Quebec and Ontario; in Drift Prospecting, (ed.) R.N.W. DiLabio, and W.B. Coker; Geological Survey of Canada, Paper 89-20, p. 139-154.

**Ward, S.H.**
1990: Resistivity and induced polarization methods; in Geotechnical and Environmental Geophysics, v. 1 - Review and Tutorial, (ed.) S.H. Ward; Investigations in Geophysics 5, Society of Exploration Geophysicists, p. 147-190.

Geological Survey of Canada Project 850058

# Use of ground electromagnetic measurements to locate sites for overburden drilling near Smoky Falls, Ontario[1]

**G.J. Palacky, S.L. Smith[2], and L.E. Stephens[3]**
**Mineral Resources Division**

*Palacky, G.J., Smith, S.L., and Stephens, L.E., 1992: Use of ground electromagnetic measurements to locate sites for overburden drilling near Smoky Falls, Ontario; in Current Research, Part E; Geological Survey of Canada, Paper 92-1E, p. 195-200.*

***Abstract***

*The results of ground electromagnetic surveys along 105 km of transects in northeastern Ontario show that the horizontal-loop technique is effective as a tool for preliminary mapping of Quaternary sediments. The use of the technique is explained on survey results from the Smoky Falls transect in northeastern Ontario. Ground electromagnetic surveys were carried out along 12.2 km of roads. After qualitative interpretation of the field data, shear zones, bedrock conductors, and areas of thick overburden were identified. The six Rotasonic boreholes drilled at sites selected on the basis of geophysical investigations intersected between 17.5 and 27 m of Quaternary sediments, mostly diamictons (till). Subsequent quantitative interpretation of ground electromagnetic data using inversion techniques yielded estimates of overburden thickness. Use of electromagnetic surveys prior to drilling can prevent investigation of sites with insufficient accumulation of Quaternary sediments.*

***Résumé***

*Les résultats de levés électromagnétiques au sol réalisés le long de 105 km de transects dans le nord-est de l'Ontario montrent que la technique des bobines horizontales est un outil efficace, utile à la réalisation de la cartographie préliminaire des sédiments du Quaternaire. L'emploi de cette technique est expliqué dans les résultats des levés effectués selon le transect réalisé à Smoky Falls dans le nord-est de l'Ontario. Les levés électromagnétiques suivent 12,2 km de routes. Après une interprétation qualitative des données de terrain, on a identifié les zones de cisaillement, les conducteurs présents dans le substratum, et les secteurs où les morts-terrains sont épais. Les six sondages effectués à l'aide d'une foreuse de type Rotasonic dans des sites choisis en fonction des études géophysiques ont recoupé entre 17,5 et 27 m de sédiments quaternaires, principalement composés de diamictons (tills). L'interprétation quantitative ultérieure des données provenant des levés électromagnétiques au sol, au moyen des techniques d'inversion, a permis d'établir des estimations de l'épaisseur des morts-terrains. L'emploi des levés électromagnétiques avant les forages permet d'éviter l'étude d'endroits où l'accumulation des sédiments quaternaires est insuffisante.*

[1] Contribution to Canada-Ontario Mineral Development Agreement 1985-1990. Project funded by the Geological Survey of Canada.

[2] Environment Canada, Environmental Impact Assessment Branch, Place Vincent Massey, 15th floor, Ottawa, Ontario K1A 0H3

[3] Deceased

## INTRODUCTION

The potential effectiveness of drift prospecting in northeastern Ontario is greatly reduced due to thick glaciolacustrine cover, particularly in the area of glacial lakes Barlow and Ojibway. To use the technique successfully, good knowledge of local Quaternary stratigraphy is required (DiLabio and Coker, 1989). To enhance the usefulness of drift prospecting in difficult areas, the Terrain Sciences Division of the Geological Survey of Canada initiated a project whose aim was to link previously unknown Quaternary stratigraphy in the area north of the Timmins mining camp with that established from abundant exposures in the Moose River drainage basin (Smith, in press). The Rotasonic drilling method, which was used in the drilling program, was developed by Hawker-Siddley of Canada Limited and applied by Midwest Drilling of Winnipeg. Drilling results of the first phase of the program were reported by Smith and Wyatt (1988).

One of the most difficult problems faced by the geologists executing the program was the selection of suitable drill sites with drift thicknesses sufficient to represent multiple stratigraphic units. As little drift thickness information could be obtained by ground reconnaissance, it was decided early in the project to use geophysical techniques for site selection. Two physical properties can be used for identification of Quaternary sediments: electrical resistivity and velocity. The former can be measured by means of galvanic resistivity sounding or using a variety of ground and airborne electromagnetic techniques. Velocity differences are detected by seismic measurements.

Since 1985, experimental geophysical surveys have been conducted at the Val Gagné test site by Electrical Methods Section of the Mineral Resources Division and by Terrain Geophysics Section of the Terrain Sciences Division (Pullan et al., 1987; Palacky et al., 1992a). Evaluation of the survey data has shown that ground electromagnetic measurements with the multifrequency horizontal-loop (HLEM) method yield the best results for identification of Quaternary sediments and estimation of overburden thickness. Since 1987, helicopter and ground electromagnetic measurements have been used for selection of overburden drill sites. Using funding provided by the Canada-Ontario Mineral Development Agreement (1984-1989), 70 holes were drilled in 1987-1988 (Smith, 1990). The location of the boreholes is given in Figure 1.

The principle of using the results of electromagnetic surveys for drill site selection has been explained in previous publications; in a given area, resistivity of clay, till and sand is sufficiently stable to allow their identification from measured resistivity patterns (Palacky and Stephens, 1990). Recognition of Quaternary sediments can be achieved by visual inspection of field data (qualitative interpretation). Careful interpretation of HLEM data by means of data inversion allows additionally an estimation of layer thicknesses even in moderately complex situation (up to three distinct layers of Quaternary sediments). Examples of the more complex quantitative interpretation of HLEM from northeastern Ontario were presented by Palacky (1991). The results of all ground electromagnetic transect measurements in northeastern Ontario (total of 105 km) were released as Open File 2343 (Palacky and Stephens, 1991).

In this paper, a case history is described of drilling based on ground electromagnetic surveys near Smoky Falls, Ontario. The ground surveys were carried out in 1988 along a 12.2 km transect. After interpretation of the results, six sites were selected for drilling (holes 36-41 in Fig. 1). A case history of more quantitative interpretation of horizontal-loop electromagnetic measurements is presented separately in this volume (Palacky et al., 1992b).

## GEOGRAPHY AND GEOLOGY OF THE SURVEY AREA

The transect under investigation follows a dirt road from Little Long Rapids to Smoky Falls and Long Rapids. The road was built to service a series of dams on the Mattagami River which lies about one kilometre to the east. The road is the only vehicular access to this remote area of northeastern Ontario. The nearest town with accommodation and service infrastructure is Kapuskasing, 120 km to the south.

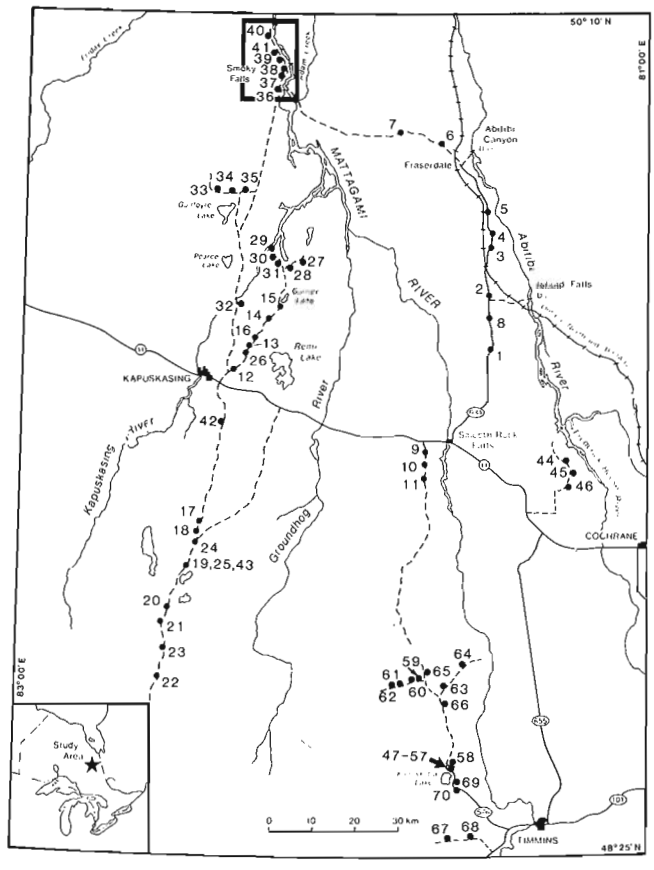


**Figure 1.** Map of the Quaternary study area in northeastern Ontario. Locations of 70 boreholes drilled in the course of the program are indicated. The study area near Smoky Falls is outlined.

Quaternary sediments have previously been described along Adam Creek, which flows parallel to the Mattagami River, about 15 km to the east (Skinner, 1973). Along the creek, three till units are more or less continuously exposed for a distance of 30 km. Figure 2 depicts logs of six cores drilled in the Smoky Falls area. The borehole locations are given in Figure 3. Accumulation of Quaternary sediments varies from 17.5 m in core 36 (the most southerly) to 27 m in core 39. In all cores, most of the Quaternary material is classed as diamicton. Well developed sand layers (over 5 m in thickness) were intersected in three boreholes (36, 37, 38). In borehole 41, a pocket of Mesozoic kaolin was identified in a bedrock depression. All boreholes were terminated in Precambrian crystalline bedrock.

Unlike other parts of northeastern Ontario, hardly any lacustrine clay was intersected in the area under investigation. The sand layers are laterally discontinuous. The diamictons interpreted as till have a clay-rich, cohesive matrix. Using Skinner's model of till units in the Moose River Basin (1973), the uppermost two till units cored in the Smoky Falls area have been correlated with Kipling Till and Adam Till from top down, respectively. Through development of regional stratigraphic profiles, the two uppermost till units in the cores seem to occupy the same relative stratigraphic positions as Cochrane and Matheson units to the south and are likely correlative.

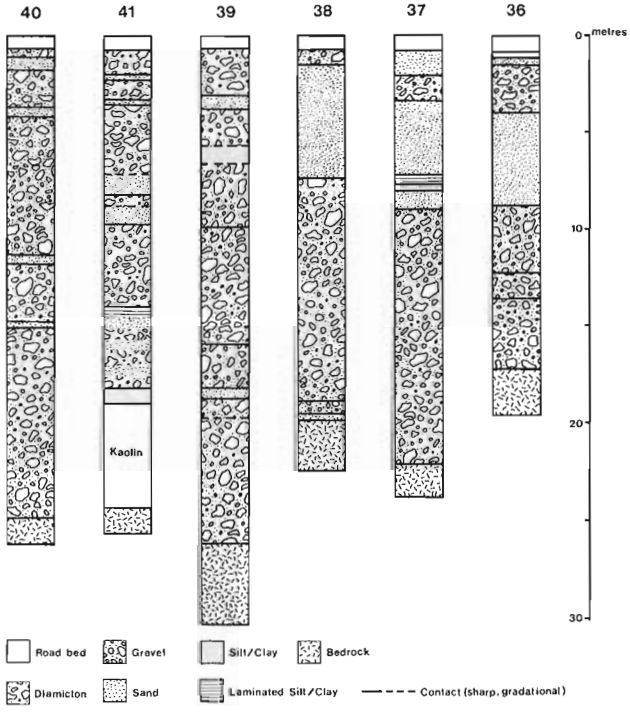


**Figure 2.** Logs of cores obtained by Rotasonic drilling. The location of boreholes is given in Figures 1 and 3.

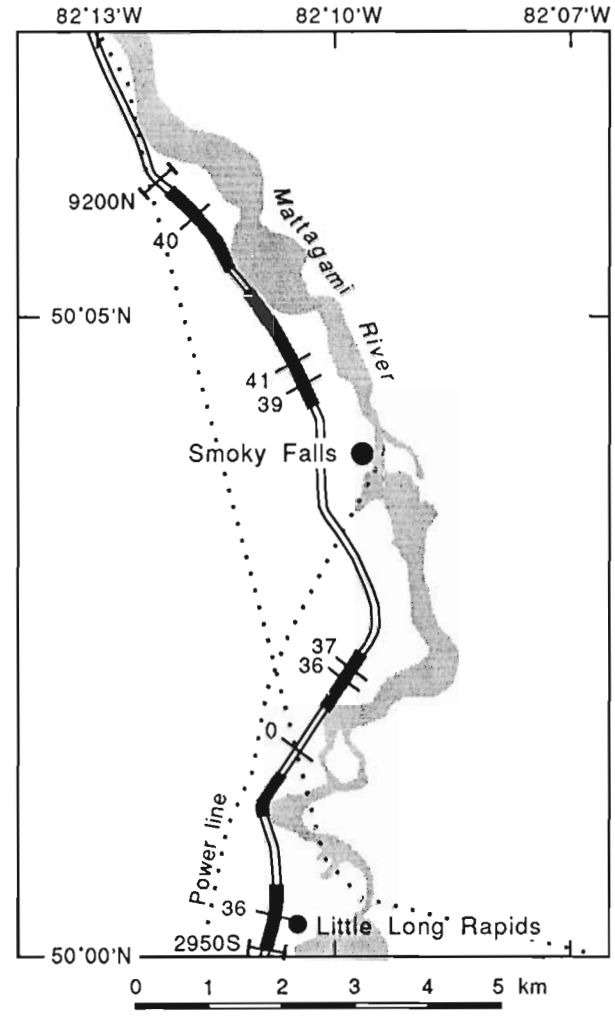


**Figure 3.** Smoky Falls transect: horizontal-loop electromagnetic survey profile (from 2950S to 9200 N) and borehole locations. Areas of thick overburden are indicated by bars.

## HORIZONTAL-LOOP ELECTROMAGNETIC SURVEYS

The horizontal-loop electromagnetic (HLEM) method has been used in mineral exploration for over 60 years. The use of the technique for the detection of shallow sediments has become possible only after the development of multifrequency equipment in the 1970s. The primary electromagnetic field is generated by current in a horizontal transmitting coil. The secondary electromagnetic field, which is induced by conductive inhomogeneities in the ground, is sensed by means of another horizontal coil. Field surveys are carried out in the profiling mode; both coils move along survey profiles. Their separation can be varied according to survey objectives, but must be kept constant during a given survey with a high degree of accuracy. If high resolution of discrete targets is necessary, the coil separation should be small (e.g., 50 m). If deep penetration is required, the separation can be extended to 400 m. After tests at the Val Gagné site, it was decided that 100 m would be used as

optimum separation for overburden mapping in northeastern Ontario. In the surveys described here, the distance between the coils was kept with a precision of 30 cm. Failure to accurately maintain the coil separation is the most common operator error. Details of the technique and data interpretation are described in Frischknecht et al. (1991).

The APEX MaxMin I instrument, which was used in the survey, has 8 frequencies from 110 to 14 080 Hz, always increasing by a factor of two. If the results are to be interpreted as soundings (as in the case described here), readings must be taken at all frequencies. The measured parameters are in-phase and quadrature components of the ratio of secondary and primary magnetic fields; the results are given in per cent. The survey readings were taken at intervals of 25 m and recorded automatically using a Rautaruukki KTP-84 data logger. The average daily production was 3 km with a field crew of two.

Preliminary interpretation and target selection was carried out in the field. Areas of thick overburden can be selected even without quantitative interpretation; the electromagnetic response is strong over such areas. Detailed interpretation was subsequently carried out in Ottawa using the EMIX-MM Plus software (Interpex Limited, 1989). The inversion routine used in the program is based on ridge regression described by Inman (1975). Unlike other areas, where the selection of the correct number of layers is critical to the success of inversion (Palacky, 1991; Palacky et al., 1992b) the layering near Smoky Falls could be approximated in most situations by a two-layer model (moderately conductive overburden and resistive bedrock).

## FIELD RESULTS

The Smoky Falls transect is depicted in Figure 3. For data presentation the transect was divided into 8 segments, each approximately 1.5 km long (Palacky and Stephens, 1991). The zero station of the transect was at the intersection of the road with an electrical transmission line. For about 100 m on each side of the power line, HLEM data were affected by interference. The survey extended 2.95 km to the south and 9.2 km to the north of the zero point. In the figure, areas of thick overburden are depicted by a bar. The location of the six boreholes is also given.

Horizontal-loop electromagnetic data are given in Figures 4 and 5 for segments F and H. In-phase component readings for 8 frequencies are plotted in the upper half of the figure, quadrature data in the lower half. Different symbols are used to depict readings at 8 frequencies. This presentation of HLEM data differs from one commonly used in mineral exploration, where in-phase and quadrature data for one frequency are plotted in the same graph. Also depicted in the figures are interpreted geological features and the location of the boreholes (39 at station 5800N, 40 at 8500N). The two examples were selected to demonstrate interpretation of HLEM data. Narrow trough-like anomalies are due to bedrock conductors or shear zones in the bedrock. Wide anomalies are caused by conductive overburden.

Quaternary sediments are thin (less than 10 m) between stations 4500N and 5500N on segment F (Fig. 4). Four shear zones were detected over a distance of 1 km: at 4750N, 5100N, 5275N, and 5500N. A typical shear zone has a strong HLEM response at high-frequency quadrature component data. On in-phase component data, the response is visible only at two or three highest frequencies. Examples of HLEM surveys to locate shear and fracture zones are given in Palacky et al. (1981) and Frischknecht et al. (1991). To the north of the shear zone at 5500N, thickness of Quaternary sediments increases to more than 25 m. Inversion of HLEM data with the EMIX-MM Plus program indicated bedrock at 32 m in the vicinity of borehole 39; the actual depth from drilling is 26 m (Fig. 2). The estimated resistivity of overburden was 107 Ω•m; resistivity remains relatively constant along the whole transect. This value falls within the range determined by interpretation of HLEM data in the

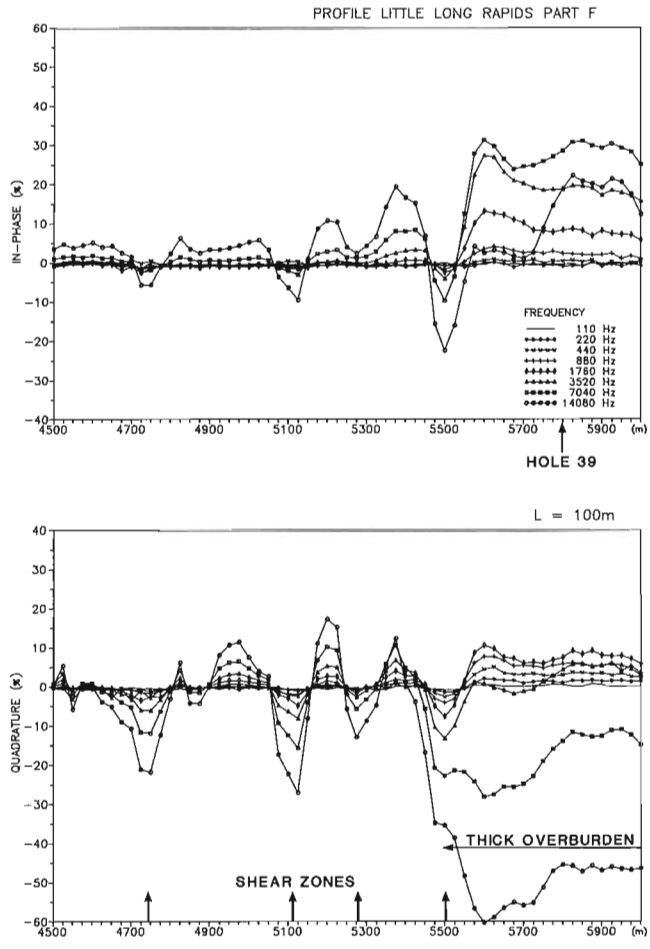


**Figure 4.** Horizontal-loop electromagnetic data along segment F (between stations 4500N and 6000N). Overburden is relatively thin (less than 10 m) between 4500N and 5500N. The survey detected four shear zones in the bedrock. Overburden is thicker than 25 m north of the shear zone at 5500N.

Kapuskasing-Timmins area (Palacky and Stephens, 1990). The average resistivity of tills was 123 Ω•m with a standard deviation of 35 Ω•m.

Horizontal-loop electromagnetic data from segment H are depicted in Figure 5. Conductive Quaternary sediments underlie most of the segment – from the southern edge of the segment to the shear zone at station 8900N. Another shear zone was detected at 7675N. Notice that the characteristics of this anomaly differ from those on segment F. The HLEM response is modified by the effect of conductive overburden. The trough-like response at 8525N was interpreted as being due to a bedrock conductor (massive sulphide or graphitic layer). Unlike the previously described shear zones, its conductance (product of conductivity and thickness) is significantly higher. This is evidenced by strong responses on the in-phase component data even at low frequencies. The reversal at the highest frequency on the quadrature data is typical of highly conductive bedrock conductors covered by moderately conductive overburden (Frischknecht et al., 1991). Inversion of HLEM data at points close to borehole 40 indicated overburden thickness of 27 m and resistivity of 111 Ω•m. The actual thickness determined by drilling (Fig. 2) is 25 m.

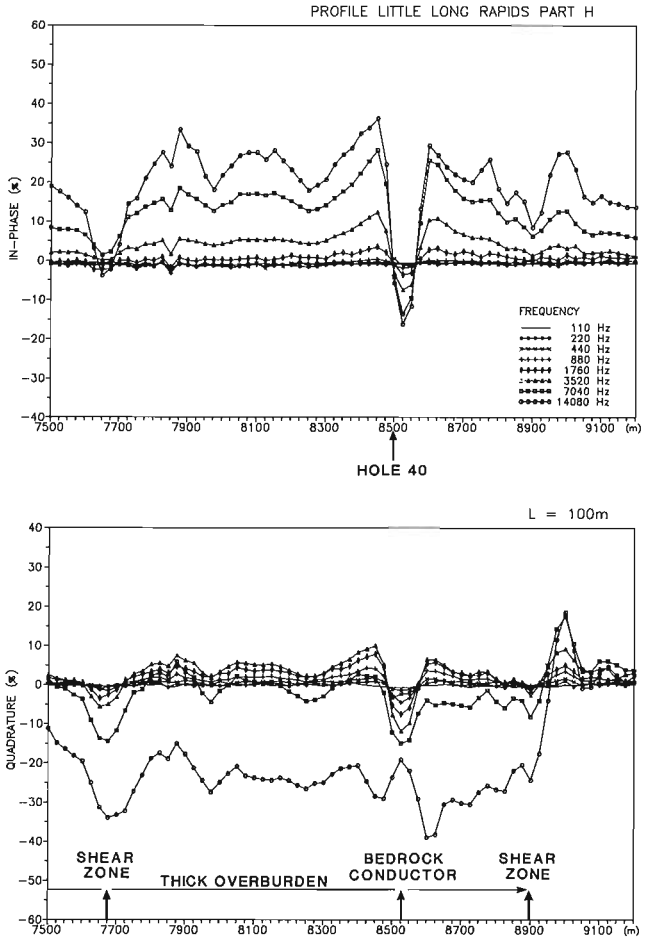


**Figure 5.** Horizontal-loop electromagnetic data along segment H (between stations 7500N and the end of the transect). Overburden is moderately thick along the segment with the exception of the last 300 m in the north, where its thickness is less than 10 m. Two shear zones and one bedrock conductor were detected in the bedrock (their locations are given in the figure).

## CONCLUSIONS

The use of ground electromagnetic measurements for preliminary mapping of Quaternary sediments has greatly enhanced the usefulness of overburden drilling and its application to drift prospecting. As Figure 2 and sample HLEM profiles illustrate, thickness of overburden varies significantly over the transect under investigation. By executing geophysical surveys first, it was possible to avoid drilling at sites where overburden thickness is small or where till units may not be present. Ground geological reconnaissance was not effective for this purpose.

Qualitative interpretation of HLEM data, which is sufficient to identify segments of deep overburden and lineaments in the bedrock, can be carried out in the field without any interpretation software. Quantitative interpretation of HLEM results by means of inversion of field data requires more skill and experience. In areas of relatively homogeneous Quaternary cover, inversion yields realistic estimates of overburden thickness using a two-layer interpretation model. In complex areas, careful analysis of resistivity distribution of Quaternary sediments and inversion results is required (Palacky, 1991; Palacky et al., 1992b).

## ACKNOWLEDGMENTS

The field work was funded by the Canada-Ontario Mineral Development Agreement, 1985-1990. Rotasonic drilling was carried out by Midwest Drilling of Winnipeg under contract to Supply and Services Canada. Ground electromagnetic surveys were performed by the staff of the Electrical Methods Section and student assistants J. Allison, M. Eising, and S. Ratté. Dr. W.W. Shilts of the Terrain Sciences Division critically read the manuscript. S.J. Davis of the Mineral Resources Division was responsible for final presentation of all figures.

## REFERENCES

**DiLabio, R.N.W. and Coker, W.B. (eds.)**
1989: Drift prospecting; Geological Survey of Canada, Paper 89-20, 169 p.

**Frischknecht, F.C., Labson, V.F., Spies, B.R., and Anderson, W.L.**
1991: Profiling methods using small sources; in Electromagnetic Methods in Applied Geophysics, v. 2 - Applications, (ed.) M.N. Nabighian; Investigations in Geophysics 3, Society of Exploration Geophysicists, p. 105-270.

**Inman, J.R.**
1975: Resistivity inversion with ridge regression; Geophysics, v. 40, p. 798-817.

**Interpex Limited**
1989: EMIX-MM Plus - User's Manual; Interpex Ltd., Golden, Colorado.

**Palacky, G.J.**
1991: Application of the multifrequency horizontal-loop EM method in overburden investigations; Geophysical Prospecting, v. 39, p. 1061-1082.

**Palacky, G.J. and Stephens, L.E.**
1990: Mapping of Quaternary sediments in northeastern Ontario using ground electromagnetic methods; Geophysics, v. 55, p. 1595-1604.
1991: Results of multifrequency horizontal-loop electromagnetic measurements along transects in northeastern Ontario; Geological Survey of Canada, Open File 2343.

**Palacky, G.J., Mwenifumbo, J., and Stephens, L.E.**
1992a: Geophysical studies at the Val Gagné test site, Ontario;. in Current Research, Part E; Geological Survey of Canada, Paper 92-1E.

**Palacky, G.J., Ritsema, I.L., and deJong, S.J.**
1981: Electromagnetic prospecting for groundwater in Precambrian terrains in the Republic of Upper Volta; Geophysical Prospecting, v. 29, p. 932-955.

**Palacky, G.J., Smith, S.L., and Stephens. L.E.**
1992b: Quaternary investigations in Geary, Thorburn and Wilhelmina Townships, Ontario; in Current Research, Part E; Geological Survey of Canada, Paper 92-1E.

**Pullan, S.E., Hunter, J.A., Gagné, R.M., and Good, R.L.**
1987: Delineation of bedrock topography at Val Gagné, Ontario, using seismic reflection techniques; in Current Research, Part A; Geological Survey of Canada, Paper 87-1A, p. 905-912.

**Skinner, R.G.**
1973: Quaternary stratigraphy of the Moose River Basin; Geological Survey of Canada, Bulletin 225, 77 p.

**Smith, S.L.**
1990: Geochemical and lithological data from overburden drill cores with descriptive core logs - Timmins to Smoky Falls, Ontario; Geological Survey of Canada, Open File 2278.

**Smith, S.L.**
in press: Quaternary stratigraphic drilling transect, Timmins to the Moose River Basin, Ontario; Geological Survey of Canada, Bulletin 415.

**Smith, S.L. and Wyatt, P.H.**
1988: Quaternary stratigraphy of overburden drill cores, Timmins to Smoky Falls, Ontario; in Current Research, Part C; Geological Survey of Canada, Paper 88-1C, p. 207-216.

---

Geological Survey of Canada Project 850058

# Quaternary investigations in Geary, Thorburn, and Wilhelmina townships, Ontario[1]

**G.J. Palacky, S.L. Smith[2], and L.E. Stephens[3]**
**Mineral Resources Division**

*Palacky, G.J., Smith, S.L., and Stephens, L.E., 1992: Quaternary investigations in Geary, Thorburn, and Wilhelmina townships, Ontario; in Current Research, Part E; Geological Survey of Canada, Paper 92-1E, p. 201-206.*

***Abstract***

*Quaternary geological studies were carried out in townships of Geary, Thorburn, and Wilhelmina, approximately 50 km northwest of Timmins, Ontario. Ground electromagnetic data obtained with the horizontal-loop method were interpreted using a two-layer model. The result was a depth-to-bedrock profile from which areas of thick overburden were selected for Rotasonic drilling. Subsequently, electromagnetic data were reinterpreted using an inversion program for three- and four-layer media. If estimated resistivity values did not fall within the resistivity range previously determined for the region, another model was selected. Using this approach, Quaternary lithology and layer thicknesses of up to three overburden layers could be determined in most situations. The technique will find application in drift prospecting as a cost-effective way to locate and select a desired lithological sequence (e.g., glacial till) for drilling.*

***Résumé***

*On a réalisé des études géologiques des dépôts Quaternaires dans les cantons de Geary, de Thorburn et de Wilhelmina, à environ 50 km au nord-ouest de Timmins en Ontario. On a interprété, à l'aide d'un modèle à deux strates, les données provenant des levés électromagnétiques effectués au sol, au moyen de la technique des bobines horizontales. On a ainsi obtenu un profil de la profondeur du substratum, à partir duquel on a choisi des zones d'épais morts-terrains en vue d'y effectuer des forages à l'aide d'une foreuse de type Rotasonic. On a ensuite réinterprété les données électromagnétiques en ayant recours à un programme d'inversion convenant aux milieux à trois et à quatre strates. Lorsque les valeurs estimées de la résistivité ne se situaient pas dans la gamme de résistivités déterminée auparavant pour cette région, on a choisi un autre modèle. Le recours à cette méthode a permis d'établir, dans la plupart des situations, la lithologie du Quaternaire et des épaisseurs de strates pouvant représenter jusqu'à trois couches de terrains de couverture. Cette technique, appliquée à la prospection glacio-sédimentaire, est un procédé rentable se prêtant bien à la localisation et à la sélection de toute séquence lithologique (par ex., un till) aux fins de forage.*

[1] Contribution to Canada-Ontario Mineral Development Agreement 1985-1990. Project funded by the Geoloical Survey of Canada.

[2] Environment Canada, Environmental Impact Assessment Branch, Place Vincent Massey, 15th floor, Ottawa, Ontario K1A 0H3

[3] Deceased

## INTRODUCTION

In 1985, the staff of the Geological Survey of Canada initiated a project whose aim was to improve the effectiveness of drift prospecting in mineral exploration programs. The principles of the technique are explained among other publications in DiLabio and Coker (1989). Research was needed to improve the knowledge of Quaternary stratigraphy and to devise a methodology that would permit fast and cost-effective recognition of thick till sequences, where drill holes would be sited (Smith, in press). Geophysical techniques have been used to solve the latter problem. Initially, test surveys with a variety of geophysical methods were conducted at the Val Gagné test site (Pullan et al., 1987; Palacky et al., 1992).

Since 1987, extensive helicopter-borne and ground electromagnetic surveys were carried out along selected transects in northeastern Ontario. Areas of thick overburden could be identified by interpreting the results of airborne surveys. The ground horizontal-loop electromagnetic method was used to follow up selected airborne anomalies on the ground. After interpretation of ground electromagnetic data, it was possible to estimate the depth to bedrock and, in simple situations, also the composition of Quaternary sediments. In 1987-1988, 70 boreholes were drilled with the Rotasonic equipment to investigate Quaternary stratigraphy. Their location is given in Figure 1. The holes were located at sites recommended by geophysicists after interpretation of ground electromagnetic surveys.

The results of helicopter-borne electromagnetic surveys along the Kapuskasing transect have been described in this volume by Palacky et al. (1992a). Ground electromagnetic data (total of 105 km) were released as an Open File (Palacky and Stephens, 1991).

In this paper, a case history is given of ground electromagnetic surveys in Geary, Thorburn, and Wilhelmina townships, Ontario. The surveys have been exceptionally successful in locating thick sequences of Quaternary tills and in determining the composition of Quaternary sediments by quantitative interpretation (inversion) of horizontal-loop electromagnetic data. In other case histories of ground electromagnetic surveys presented in this volume (Palacky et al., 1992c), the emphasis has been on qualitative interpretation of electromagnetic data and recognition of areas with significant accumulation of Quaternary sediments.

## GEOGRAPHY AND GEOLOGY OF THE SURVEY AREA

The centre of the studied area lies approximately 50 km northwest of Timmins. This swampy area forms a plateau approximately 300 m above sea level, from which creeks flow in all directions to join the Mattagami River to the east and the Groundhog River to the west. Access to the area is by a logging road leading north from Kamiskotia.

A total of 11 km of profiles was measured with the horizontal-loop electromagnetic (HLEM) system (Fig. 2). All geophysical profiles followed logging roads. Profiles SRF-2A, SFR-2B, SRF-2C, and SRF-3A were designed to follow-up airborne electromagnetic anomalies. Surveys WR1, WR2, GR1, and GR2 were carried out in the following year to better investigate this area of thick overburden. The results of all ground geophysical surveys are included in the already mentioned Open File (Palacky and Stephens, 1991). After interpretation of HLEM results, seven boreholes (59, 60, 61, 62, 63, 65, and 66) were drilled in the area.

The results of drilling have confirmed the previously made geophysical interpretation that overburden in the area is thicker than 20 m. Thickness and composition of Quaternary sediments change rapidly over relatively short distances. This variability is illustrated in Figure 3, where logs of four borehole cores are shown. The distance between the most distant boreholes, 59 and 62, is 4 km. In borehole 62, which was 32 m deep, 25 m of till with interbedded minor sand and clay were intersected. At the neighbouring site, 650 m to the east, core indicated overburden 48 m thick. While the upper till layer was of about the same thickness as in core 62, the intermediate layer was much thicker (13 m) and, in addition to sand, it contained a well developed clay sequence. Despite a considerable accumulation of overburden cored in borehole 60 (48 m), no till was encountered. Core 59, 600 m to the east, showed overburden thickness of only 24.5 m with a considerably thinner upper

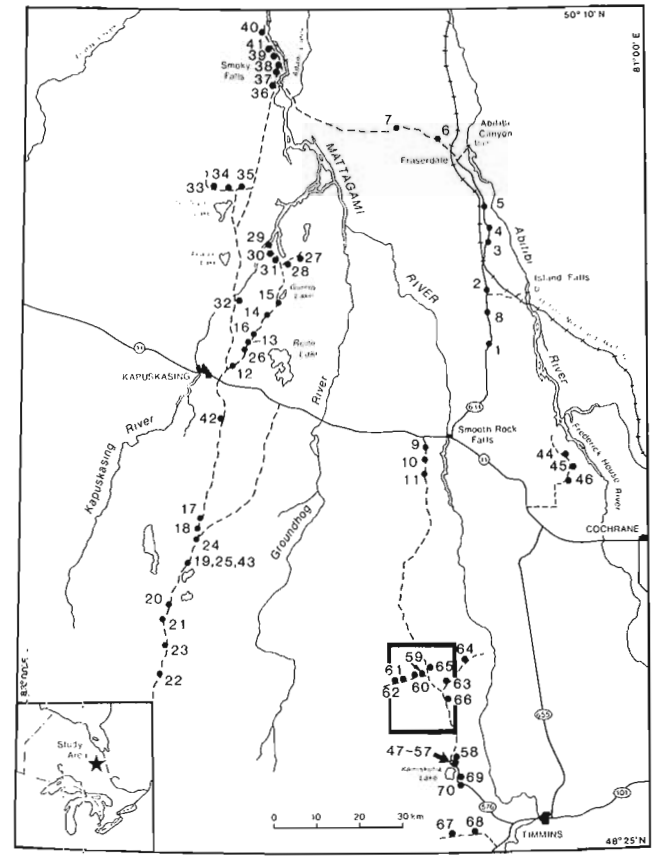


**Figure 1.** Map of the Quaternary study area in northeastern Ontario. Sites of 70 boreholes drilled in the course of the program are depicted. The area of the surveys described in the paper is outlined.

massive clay unit. Unlike the neighbouring core, where clay was underlain by a thick layer of pebbly sand, this core showed that clay was deposited after glacial till.

Original interpretation of HLEM data was carried out assuming one-layer overburden. Boreholes 60 and 61 were recommended at sites interpreted as bedrock valleys. While the interpreted bedrock relief may follow the true topography even in areas of multilayer overburden, the estimated overburden thickness will be in error. In this paper, we will examine the effect of complex Quaternary geology on the accuracy of interpretation of HLEM data and investigate how to improve it.

## HORIZONTAL-LOOP ELECTROMAGNETIC SURVEYS

The electromagnetic equipment used in the surveys described here was a MaxMin I manufactured by APEX Parametrics Ltd. of Markham, Ontario. The instrument can be operated in several modes, but only the horizontal-loop configuration was used. The primary electromagnetic field is generated by current in a horizontal transmitting coil. Another horizontal coil is used as a receiver. The measured parameters are the in-phase and quadrature components of the ratio of secondary and primary magnetic fields. The primary magnetic field is fully compensated when the two coils are held precisely at a determined distance (coil separation) and the measurement is a function of ground resistivity. Penetration of the survey depends on the ground resistivity and on the selected frequency and coil separation. Using multiple frequencies and/or coil separations, the HLEM results can be interpreted as resistivity soundings. The principle of dipole source electromagnetic techniques has been described by Frischknecht et al. (1991).

The APEX MaxMin I instrument operates at the following frequencies: 110, 220, 440, 880, 1760, 3520, 7040, and 14 080 Hz. Cables are supplied for coil separations from 12.5 to 400 m. In the surveys described here, measurements were carried out by recording the in-phase and quadrature components at all frequencies, while keeping the coil separation fixed at 100 m. To interpret the data as resistivity soundings, it is essential to maintain the coil separation with a precision better than 0.3%. The survey readings were taken at intervals of 25 m and recorded automatically using a Rautaruukki KTP-84 data logger. A crew of two operators could measure on average 3 km of profiles per day.

Interpretation of ground electromagnetic data was done in three phases. First, plots of in-phase and quadrature data were scanned visually for lateral inhomogeneities (shear zones,

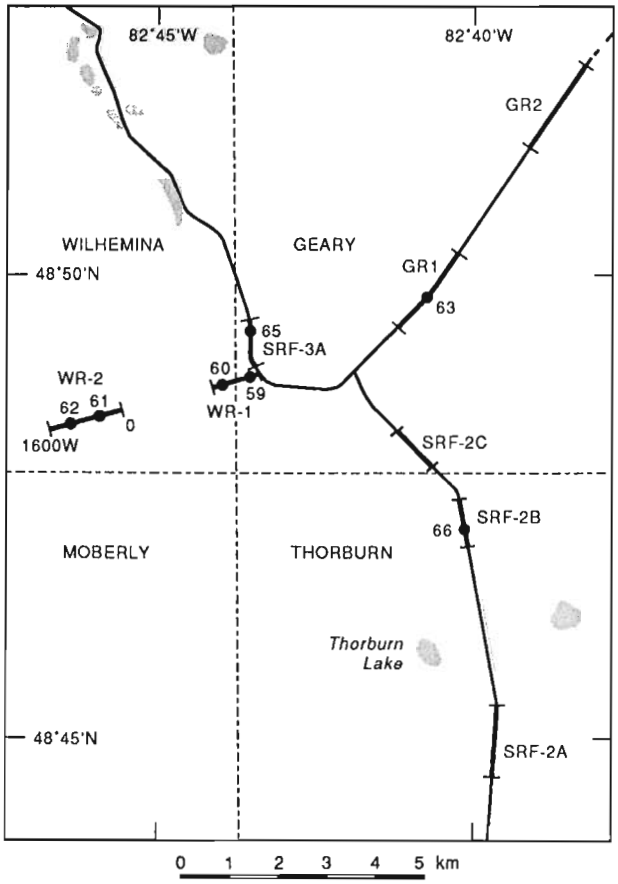


**Figure 2.** Map of portions of Geary, Thorburn, and Wilhelmina townships with the location of geophysical profiles and boreholes.

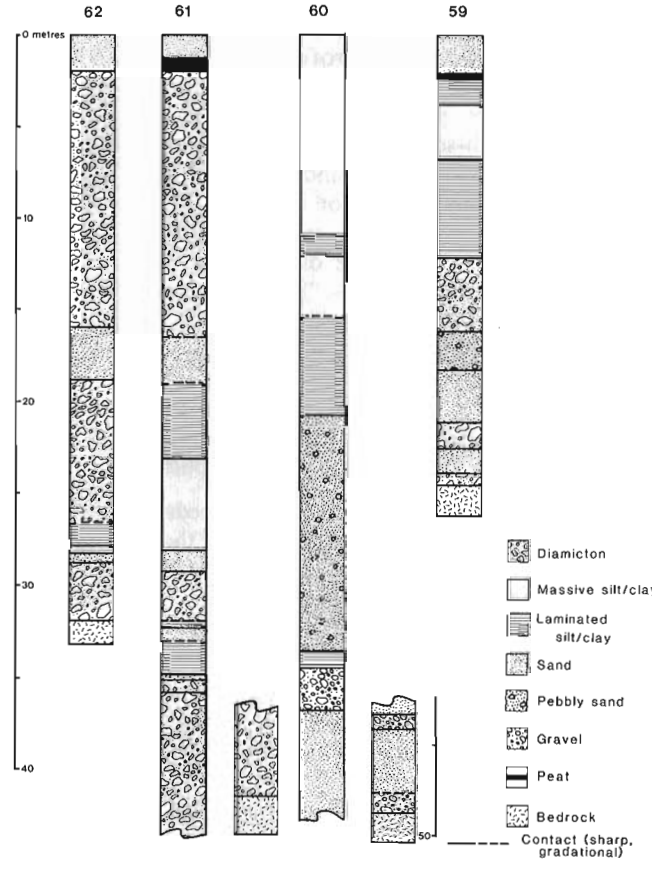


**Figure 3.** Logs of cores from boreholes located along profiles WR1 and WR2. Their location is indicated in Figure 2.

bedrock conductors). This type of interpretation, which we call qualitative, was described in detail by Palacky and al. (1992c). To obtain an outline of bedrock topography, the field data were inverted using the EMIX-MM Plus program for one horizontal layer (Interpex Limited, 1989). The result is a plot of depth to the bedrock. From the in-phase and quadrature response patterns (phasor diagrams), it is possible to determine whether the overburden consists mostly of clay, till, or sand. Boreholes were recommended at sites where bedrock was deep and the overburden contained till. This procedure has been described by Palacky and Stephens (1990).

After completion of the drilling program in 1988, the last phase of data evaluation and interpretation begun. A correlation was made of the geophysical data, resistivity measured on core samples, and drilling results. It was noticed that, in many circumstances, the previous interpretation of HLEM data was not accurate. Therefore, research continued until 1991 to develop a new approach to HLEM interpretation, which is based on statistical analysis of resistivity values determined by inversion of data using multilayer models (Palacky, 1991). An example of field data interpretation using this approach is given in this paper.

## INTERPRETATION OF HORIZONTIAL-LOOP ELECTROMAGNETIC FIELD DATA

In Figure 4, an HLEM profile and depth-to-bedrock interpretation are depicted. The zero point of the line WR2 lies in the southern part of Wilhelmina Township, 3 km west of the main north-south logging road. At the top and in the middle of the figure, in-phase and quadrature component data are plotted, respectively, for 8 frequencies. While the in-phase responses are close to zero for the four lowest frequencies, from 1760 Hz on, they increase with the frequency to more than 20%. The rise on the quadrature response starts at 220 Hz, but the values remain under 10% before changing polarity between 7040 and 14 080 Hz. This progressive change of measured amplitudes with frequency is typical of moderately thick and moderately conductive layers. Geophysicists usually examine such patterns in the form of phasor diagrams (Palacky and Stephens, 1990).

At the bottom of the figure, depth to bedrock is plotted. Originally, an unconstrained inversion of the in-phase and quadrature component data was made using the EMIX-MM Plus program (Interpex Limited, 1989). In subsequent processing of the data, the conductivity of the upper layer (overburden) was fixed as the average resistivity value found for the segment (125 Ω•m). Constrained inversion produces smoother depth-to-bedrock profiles. There is a resemblance in shape between the depth-to-bedrock trace and the quadrature response at 14 080 Hz. Thus in an area of homogeneous overburden, such as the one depicted, even raw high-frequency quadrature data give a good idea about the bedrock topography.

The depth estimated by inversion of HLEM data at station 1150W is 24 m; the borehole at this site (62 in Fig. 3) intersected 32 m of overburden. At the second drilling site at station 510W (borehole 61), the overburden is 48 m thick; inversion indicated 45 m. As Figure 3 shows, core consists of three significant layers (more than 3 m thick): from the top, till, clay, and till. Unconstrained inversion of HLEM data produced a good thickness estimate (error of about 3 m, or 6%) and a resistivity value close to the regional average for till (Palacky and Stephens, 1990).

Despite apparent success at many sites, attempts were made to use multilayer inversion with the EMIX-MM program (Interpex, Limited, 1988) at most of the surveyed profiles. In the inversion process, only the number of horizontal layers was specified; other parameters were not constrained. The results of two- and three-layer inversions at the site of borehole 66 were identical as far the overburden was concerned. The difference was in the resistive basement,

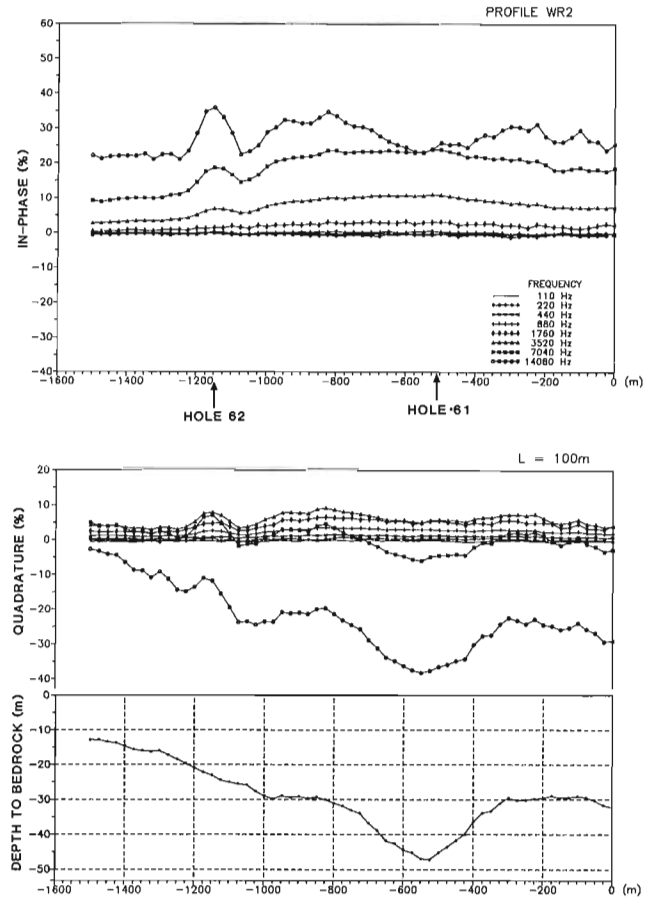


**Figure 4.** Results of horizontal-loop electromagnetic surveys along profile WR2. At the top is the in-phase component response, in the middle the quadrature component response, at the bottom depth to bedrock obtained by inversion of the data above. The symbols used in plotting data measured at 8 frequencies are explained in the figure.

where an additional layer of resistivity of 60 000 Ω•m was identified. Such a result is geologically meaningless because the MaxMin I system is not sensitive to high resistivity layers. The RMS error, which provides the best measure of the fit between the field data and the model response, remained at 0.54%.

When an inversion with a four-layer model was made, the determinations of thickness of the three overburden layers became more accurate and the RMS error decreased to 0.41% (Fig. 5). The resistivity of the clay layer was within the range determined statistically for the area under investigation (47.3 ± 6.7 Ω•m) (Palacky and Stephens, 1990). Also the resistivity of the upper till layer satisfied this criterion (123 ± 35 Ω•m), but the lower layer had a significantly higher resistivity. So far, no geological explanation for the high resistivity has been found.

Another example of the novel approach to interpretation is from borehole 66, which is located near the northern boundary of Thorburn Township, on the main north-south logging road. The original interpretation of HLEM data using unconstrained inversion for two layers yielded a thickness of 26 m and overburden resistivity of 86 Ω•m. As the simplified drill core in Figure 6 indicates, the thickness of overburden has been seriously underestimated (true value 38 m). The resistivity value is slightly smaller than the lower limit of the range expected for till and significantly higher than typical clay resistivity. Even without knowing the results of drilling, such a result would have to be examined carefully. An unusual resistivity value is an indication that the model used in the inversion is not appropriate.

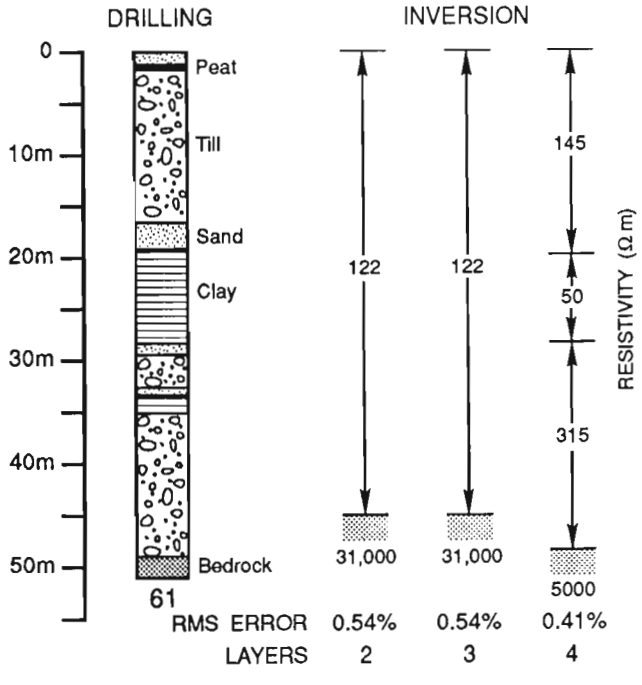


**Figure 5.** Log of core from borehole 61 and the results of inversion of horizontal-loop electromagnetic data for two-, three- and four-layer models.

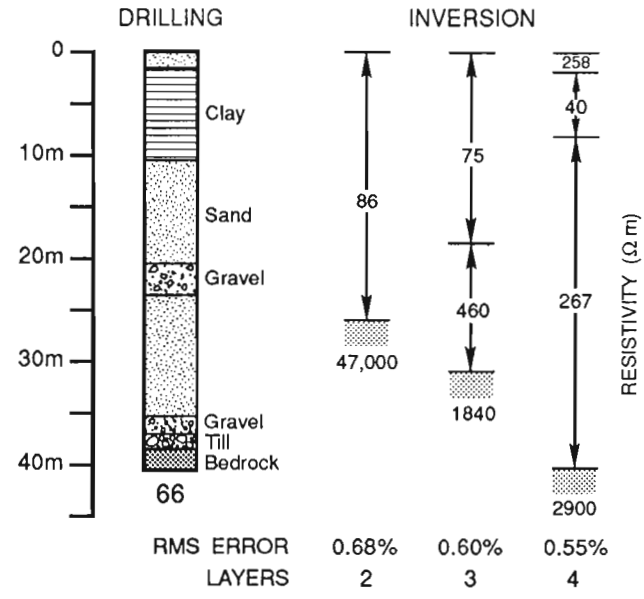


**Figure 6.** Log of core from borehole 66 and the results of inversion of horizontal-loop electromagnetic data for two-, three- and four-layer models.

Another inversion with the EMIX-MM program was made for a three-layer model. The RMS error decreased from 0.68% to 0.60%, but resistivities remained untypical: 75 Ω•m (first layer) is between the ranges of clay and till, and 460 Ω•m (second layer) is too high for any overburden material. The four-layer inversion yielded a solution, in which a 6 m thick clay layer (resistivity 40 Ω•m) is sandwiched between two sand layers. In reality, this layer is 8 m thick. The resistivities of the sand layers (258 and 267 Ω•m) are close to the mean value determined for the area (251 Ω• m). The final RMS error was 0.55%. Had detailed interpretation, such as described here, been made before selecting targets for drilling, the site would not have been recommended. It would have become apparent that the probability of intersecting tills was very small because no layer with appropriate resistivity was identified.

## CONCLUSIONS

Recommendations for overburden drilling can be made more accurate, if ground electromagnetic data are interpreted using multilayer models. Surveys in northeastern Ontario indicated that up to three overburden layers can be identified from horizontal-loop electromagnetic data. The key to reliable interpretation of field data is to carefully assess interpreted resistivities after each inversion. It was found by statistical analysis of field geophysical data and correlation with the drilling results that resistivities of clay, till, and sand stay within relatively narrow and non-overlapping ranges which are typical of a given area (Palacky and Stephens, 1990). However, these ranges could only be determined after the results of drilling became available. If resistivity values determined by inversion of HLEM data do not fall within limits typical of any Quaternary sediment, another model should be selected for interpretation. If the detection of a

certain overburden material (e.g., glacial till) is the objective, drilling funds could be deployed more efficiently by carrying out preliminary ground electromagnetic surveys and interpreting carefully the results.

## ACKNOWLEDGMENTS

The field work was funded by the Canada-Ontario Mineral Development Agreement 1985-1990. The authors were assisted in ground geophysical surveys by student assistants M. Eising and S. Ratté. Rotasonic drilling was carried out by Midwest Drilling of Winnipeg under contract to Supply and Services Canada. Dr. W.W. Shilts of the Terrain Sciences Division critically read the manuscript. S.J. Davis of the Mineral Resources Division was responsible for final presentation of all illustrations.

## REFERENCES

**DiLabio, R.N.W. and Coker, W.B. (ed.)**
1989: Drift prospecting; Geological Survey of Canada, Paper 89-20, 169 p.

**Frischknecht, F.C., Labson, V.F., Spies, B.R., and Anderson, W.L.**
1991: Profiling methods using small sources; in Electromagnetic Methods in Applied Geophysics, v. 2 – Applications, (ed.) M.N. Nabighian; Investigations in Geophysics 3, Society of Exploration Geophysicists, p. 105-270.

**Interpex Limited**
1988: EMIX-MM – User's Manual; Interpex Ltd., Golden, Colorado.
1989: EMIX-MM Plus – User's Manual; Interpex Ltd., Golden, Colorado.

**Palacky, G.J.**
1991: Application of the multifrequency horizontal-loop EM method in overburden investigations; Geophysical Prospecting, v. 39, p. 1061-1082.

**Palacky, G.J. and Stephens, L.E.**
1990: Mapping of Quaternary sediments in northeastern Ontario using ground electromagnetic methods; Geophysics, v. 55, p. 1595-1604.
1991: Results of multifrequency horizontal-loop electromagnetic measurements along transects in northeastern Ontario; Geological Survey of Canada, Open File 2343.

**Palacky, G.J., Holladay, J.S., and Walker, P.**
1992a: Inversion of helicopter electromagnetic data along the Kapuskasing transect, Ontario; in Current Research, Part E; Geological Survey of Canada, Paper 92-1E.

**Palacky, G.J., Mwenifumbo, C.J., and Stephens, L.E.**
1992b: Geophysical studies at the Val Gagné test site, Ontario; in Current Research, Part E; Geological Survey of Canada, Paper 92-1E.

**Palacky, G.J., Smith, S.H., and Stephens L.E.**
1992c: Use of ground electromagnetic measurements to locate sites for overburden drilling near Smoky Falls, Ontario; in Current Research, Part E; Geological Survey of Canada, Paper 92-1E.

**Pullan, S.E., Hunter, J.A., Gagné, R.M., and Good, R.L.**
1987: Delineation of bedrock topography at Val Gagné, Ontario, using seismic reflection techniques; in Current Research, Part A; Geological Survey of Canada, Paper 87-1A, p. 905-912.

**Smith, S.L.**
1990: Geochemical and lithological data from overburden drill cores with descriptive core logs – Timmins to Smoky Falls, Ontario; Geological Survey of Canada, Open File 2278.
in press: Quaternary stratigraphic drilling transect, Timmins to the Moose River Basin, Ontario; Geological Survey of Canada, Bulletin 415.

---

Geological Survey of Canada Project 850058

# Modélisation géophysique et caractérisation thermique du pergélisol dans les palses de Blanc-Sablon, Québec[1]

**Maurice K. Seguin et J.C. Dionne[2]**
**Division de la science des terrains**

*Seguin, M.K. et Dionne, J.C., 1992: Modélisation géophysique et caractérisation thermique du pergélisol dans les palses de Blanc-Sablon, Québec; dans Recherche en Cours, Partie E; Commission géologique du Canada, Étude 92-1E, p. 207-216.*

***Résumé***

*Des levés géophysiques (sondages de résistivité électrique, de polarisation provoquée et géothermiques) ont été effectués pour connaître la nature et la forme géométrique du pergélisol sporadique dans des palses de la région de Blanc-Sablon. L'interprétation des résultats géophysiques indique que la base du pergélisol est très variable sous une même palse. Certaines palses sont caractérisées par une faible épaisseur (3 m) de pergélisol et d'autres par une plus grande épaisseur (11 m). Les variations entre les limites minimales et maximales de l'épaisseur du pergélisol indiquent une corrélation avec le contenu en eau et en glace ainsi que la granulométrie des dépôts non consolidés. Le pergélisol est généralement plus épais dans les argiles et les limons argileux. L'amincissement de la base du pergélisol aux extrémités et les zones de taliks au centre des plus petites palses sont autant d'indices de leur état de dégradation.*

***Abstract***

*Geophysical surveys (electrical resistivity soundings, induced polarisation and geothermal) were carried out to determine the nature and geometrical shape of sporadic permafrost in palsas from the Blanc-Sablon area. The interpretation of the geophysical results indicates that the base of permafrost is variable under a specific palsa. Some palsas are characterised by a small thickness (3 m) of permafrost while others are much thicker (11 m). The variations between the minimal and maximal limits in thickness of permafrost show a correlation with the water and ice content and with the grain size of the unconsolidated deposits. Permafrost is generally thicker in clay and clayey silt. Thinning of the base of permafrost at the extremities of palsas and the presence of talik zones in the center of smaller palsas are arguments for their state of degradation.*

[1] Programme des conventions de recherche d'EMR 243-4-92
[2] Dépt. de géologie et de géographie et Centre d'études nordiques, Université Laval, Québec, G1K 7P4

## INTRODUCTION

Cette étude fait état des méthodes utilisées pour délimiter l'extension verticale du pergélisol dans les palses de Blanc-Sablon et montre la relation existant entre les paramètres physiques, la température et le contenu en glace du pergélisol.

## DESCRIPTION DU SITE

Le site étudié se trouve dans la région de Blanc-Sablon (latitude : 51° 10' W), au Québec, à la limite avec le Labrador, soit au sud de la limite méridionale du pergélisol discontinu (sporadique) établie par Brown (1978). Le site a été étudié et décrit sommairement par Dionne (1984). Les palses sont localisées dans de petites tourbières au fond d'une large vallée remblayée de sédiments fins quaternaires (fig. 1). Comme elles se trouvent au sud de la limite méridionale des palses au Canada et en Europe, on pense qu'il s'agit de formes de pergélisol résiduel (Dionne et Seguin, 1992). De 1 à 3 m de hauteur, les palses sont composées d'une couche de tourbe de 75 à 150 cm d'épaisseur et d'un coeur minéral de sable fin limoneux et argileux stratifiés contenant de la glace de ségrégation. Le site se trouve à environ 60 m d'altitude, à 6 km au nord-nord-est de l'aéroport et à une distance équivalente de la mer (baie de Brador).

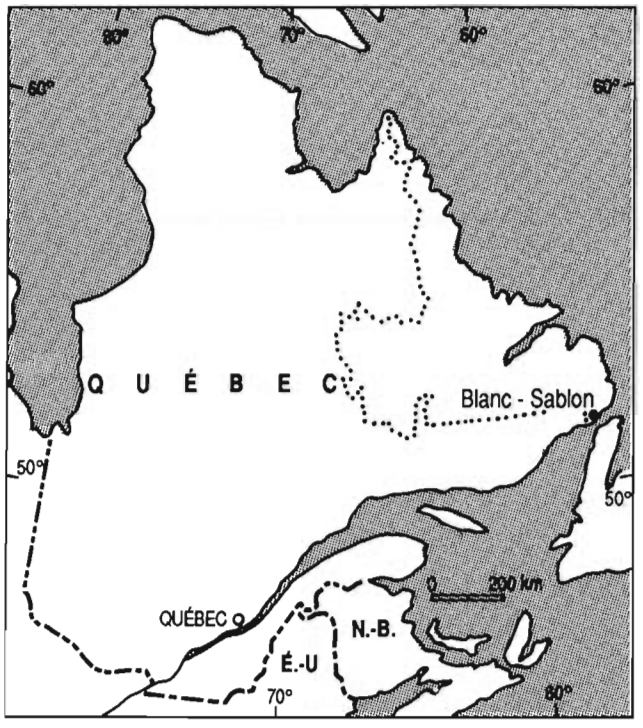


**Figure 1.** Carte de localisation des palses étudiées (d'après Dionne, 1984).

[1] Bureau de recherches géologiques et minières

## MÉTHODES

Trois types de levés ont été effectués sur le champ de palses : des sondages de résistivité électrique (RE), des sondages-profilages de polarisation provoquée (PP) et des profils géothermiques (GT). Les levés de RE et de PP ont été réalisés à l'aide d'un appareil de type SYSCAL-R2E fabriqué par le BRGM[1]. Les profils géothermiques ont été établis à l'aide d'une thermistance fixée à une tige d'acier et la résistance électrique a été lue à l'aide d'un multimètre numérique, quelques heures après les forages. Trois forages mécaniques atteignant plus de 4 m de profondeur ont été pratiqués pour mesurer le profil géothermique et obtenir des renseignements sur la stratigraphie et le contenu en glace du pergélisol. Ces forages se situent au centre des palses sur lesquels des levés de RE et de PP ont été effectués. Les trois forages coïncident avec les levés (PP1, RE1), (PP2, RE3) et (PP3, RE8) respectivement. Neuf sondages de RE ont été réalisés en faisant appel à la configuration de Schlumberger. Les sondages RE1, 3, 8 et 9 correspondent respectivement aux lignes PP1, 2, 3 et 4. Cinq levés de PP faisant appel à la configuration dipôle-dipôle ont permis d'obtenir 30 pseudo-sections. Chaque levé de PP comprend une pseudo-section de résistivité apparente et de chargeabilité apparente ($m_a$), mesurée pour quatre intervalles de temps (120, 220, 420 et 820 ms), et de chargeabilité apparente totale ($m_t$), calculée à l'aide de la formule $m_t = (120m_1 + 220m_2 + 420m_3 + 820m_4)/1580$. La pente moyenne (Pm) des chargeabilités est obtenue à l'aide de la formule suivante :

$$Pm = \frac{(m_2 - m_1}{170} + \frac{m_3 - m_2}{320} + \frac{m_4 - m_{3)}}{620} \; /3.$$

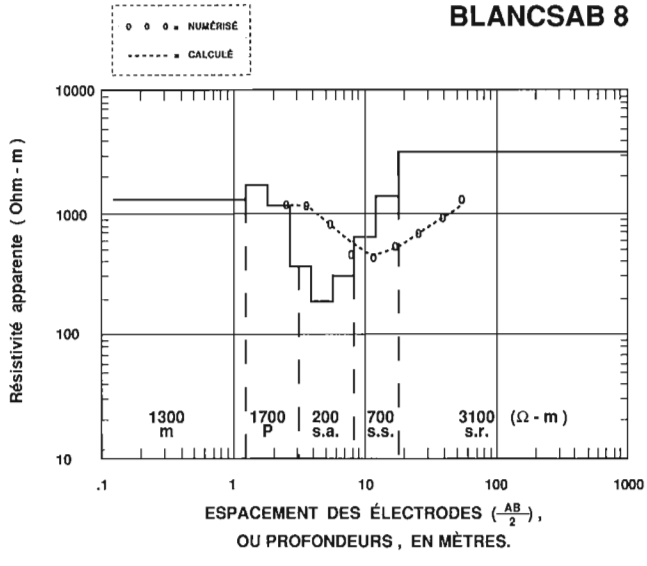


**Figure 2.** Sondage de résistivité électrique; les valeurs de résistivité vraie sont exprimées en ohm-mètres (Ω•m) et les profondeurs des divers contacts (M, P, s.a., s.s., s.r.) sont indiquées en abscisse. M = mollisol, P = pergélisol, s.a. = sable argileux, s.s. = sable limoneux, s.r. = socle rocheux.

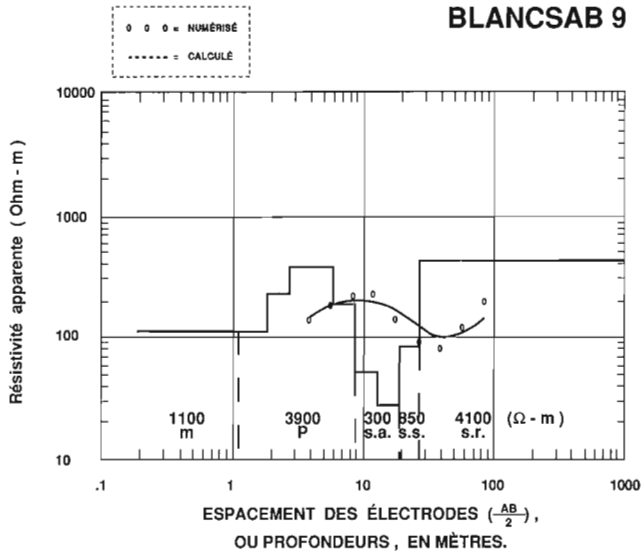


**Figure 3.** Sondage de résistivité électrique; même description qu'à la figure 2.

La séparation des électrodes (r) pour les levés PP1, PP3 et PP5 est de 3 m, tandis que celle des levés PP2 et PP4 est de 4 m. La profondeur (h) examinée à partir des pseudo-sections est approximée par la formule établie par Barker (1989), soit h = 0,25 L où L = (2 + n) r, n étant un nombre entier.

Les sondages de RE ont été traités graphiquement à l'aide d'un logiciel d'interprétation, en utilisant la configuration de Schlumberger et la mise au point apportée par Zohdy et Bisdorf (Zohdy, 1989). Les pseudo-sections de résistivité et de chargeabilité ont été réalisées à l'aide du logiciel SURFER.

## RÉSULTATS DES SONDAGES DE RÉSISTIVITÉ ÉLECTRIQUE (RE)

La figure 2 fait voir les résultats d'un sondage de résistivité sur une palse allongée et légèrement bombée (BLANCSAB 8). Le graphique bilogarithmique de la résistivité apparente en fonction de la mi-séparation des électrodes de courant (AB/2) indique les valeurs ponctuelles de résistivité observées, les valeurs de résistivité calculées et les valeurs inversées de résistivité vraie (ligne pleine discontinue). L'interprétation quantitative des résultats de ce sondage de RE permet de déterminer la stratigraphie du sous-sol ainsi que l'épaisseur du mollisol et du pergélisol.

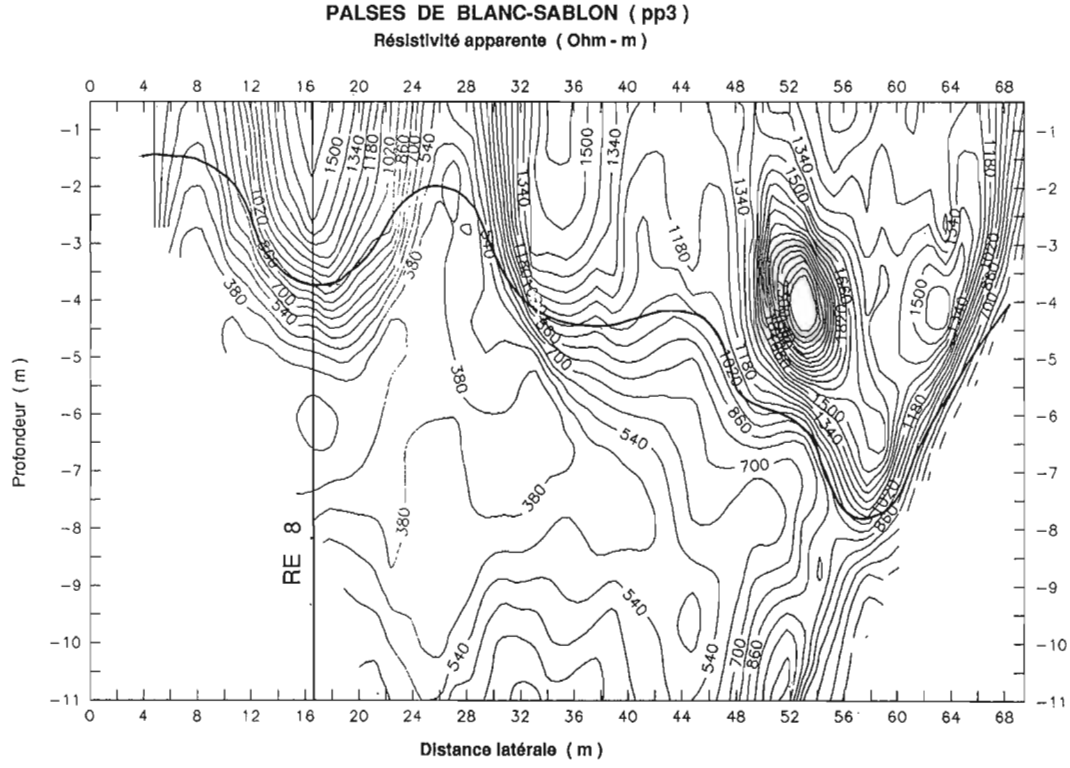


**Figure 4.** Pseudo-section de résistivité électrique apparente; les courbes d'isorésistivité sont exprimés en Ω•m. La position du sondage de résistivité RE 8 est indiquée et la base du pergélisol est représentée par le trait foncé qui recoupe les courbes d'isorésistivité.

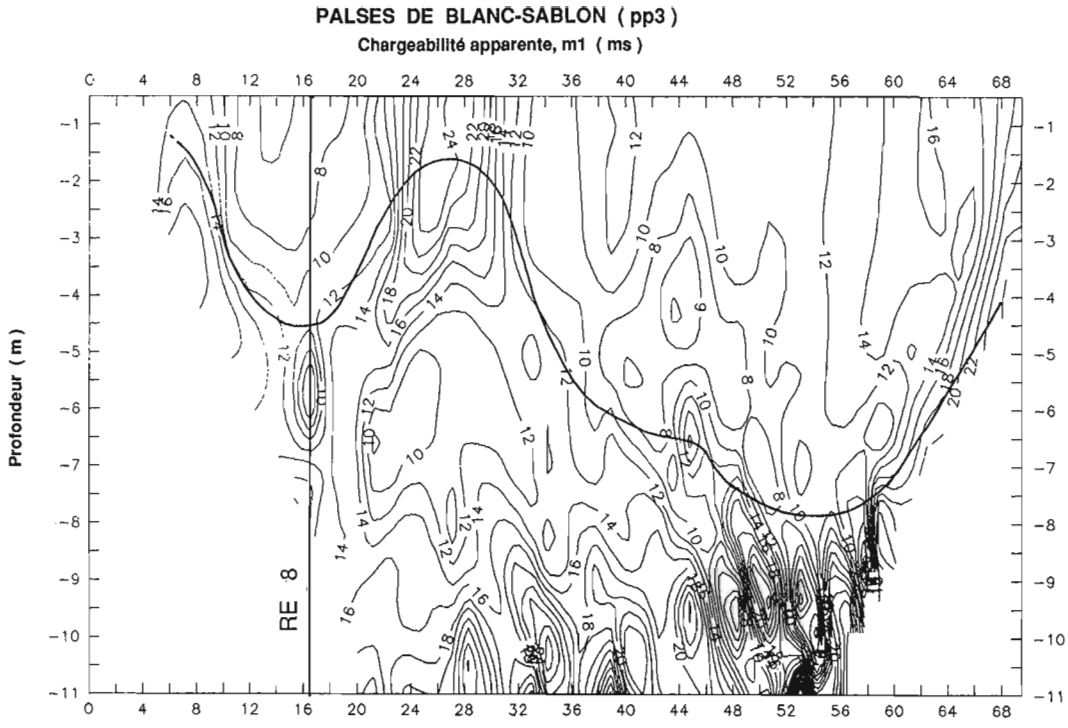


**Figure 5.** Pseudo-section de la chargeabilité apparente ($m_1$); les isocontours sont exprimés en millisecondes. Le reste de la description est identique à celle de la figure 4.

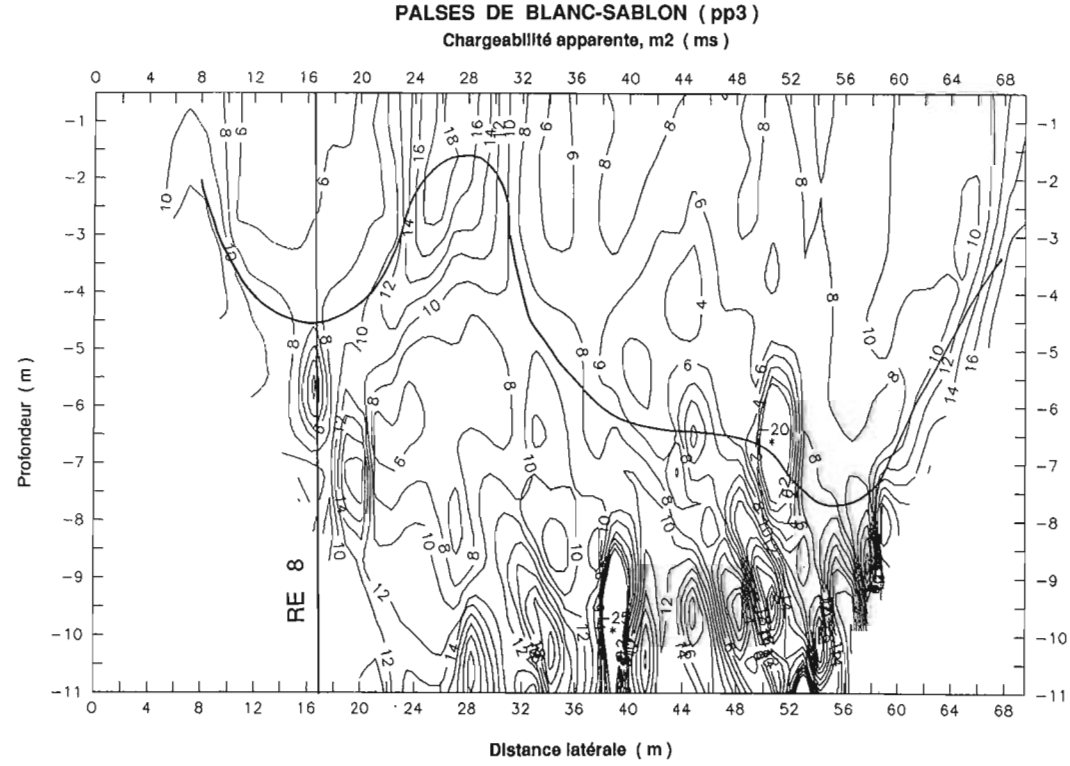


**Figure 6.** Pseudo-section de la chargeabilité apparente ($m_2$); même description qu'à la figure 5.

Dans le cas du sondage de RE BLANCSAB 8, on a déterminé une épaisseur de 1,1 m de mollisol dans de la tourbe (1300 Ω•m), de 2 m de pergélisol dans de la tourbe et du sable argileux (1700 Ω•m), de 5 m de sable argileux dégelé (200 Ω•m) et de 9 m de sable limoneux (700 Ω•m). La profondeur au socle rocheux (gneiss granitique, 3100 Ω•m) se situe à 17 m.

L'interprétation du sondage de RE BLANCSAB 9 s'est faite de la même manière (fig. 3). Le mollisol dans la tourbe (1100 Ω•m) a une épaisseur de 1,1 m. Les épaisseurs du pergélisol dans le sable argileux (3900 Ω•m), du sable argileux dégelé sous-jacent (300 Ω•m) et du sable limoneux (850 Ω•m), sont de 7, 9 et 7 m respectivement. Le socle rocheux (4100 Ω•m) se trouve à 24 m de profondeur. Les données du sondage de RE BLANCSAB 8 indiquent une faible épaisseur de pergélisol (2 m) sous le sondage de la figure 2 et une épaisseur plus importante (7 à 8 m) sous le sondage de la figure 3.

## RÉSULTATS DES SONDAGES DE POLARISATION PROVOQUÉE (PP)

La figure 4 montre une pseudo-section de résistivité électrique dont la profondeur est calibrée. La position du sondage de RE BLANCSAB 8 et la base du pergélisol (courbe plus épaisse recoupant celles représentant les isorésistivités) sont indiqués sur la figure 2. On observe que la base du pergélisol est très variable. Sa profondeur se situe à environ 3,5 m à l'aplomb du sondage de RE BLANCSAB 8 qui indique 3,1 m; la correspondance des interprétations est donc fiable.

La figure 5 fait voir une pseudo-section calibrée de la première chargeabilité ($m_1$). La base du pergélisol est interprétée de la façon suivante : le pergélisol qui a un contenu en glace plus ou moins élevé est caractérisé par une faible chargeabilité ou une chargeabilité nulle. Directement sous la base du pergélisol, les ions libres (généralement négatifs) donnent lieu à de fortes variations de chargeabilité (le plus souvent négatives). Sur la figure 5, la base du pergélisol se situe à 4 m à l'aplomb du sondage de RE BLANCSAB 8 (3,1 m).

La base du pergélisol est très irrégulière et atteint un maximum de 7 m au chaînage 56 m. La forme de la courbe indiquant la base du pergélisol sur la figure 5 est très semblable à celle de la figure 4, excepté entre les chaînages 36 et 50 m.

La figure 6 montre la pseudo-section de la seconde chargeabilité sur le même profil PP3. L'épaisseur du pergélisol sous le sondage de RE BLANCSAB 8 et la couche délimitant la base du pergélisol sont très semblables à celles de la figure 5. L'observation précédente s'applique également aux pseudo-sections de chargeabilité ($m_3$ et $m_4$) des figures 7 et 8, sauf que sur ces deux dernières pseudo-sections, les contrastes de chargeabilité négative à la base du pergélisol sont plus prononcés. La figure 9, qui représente une intégration des quatre chargeabilités

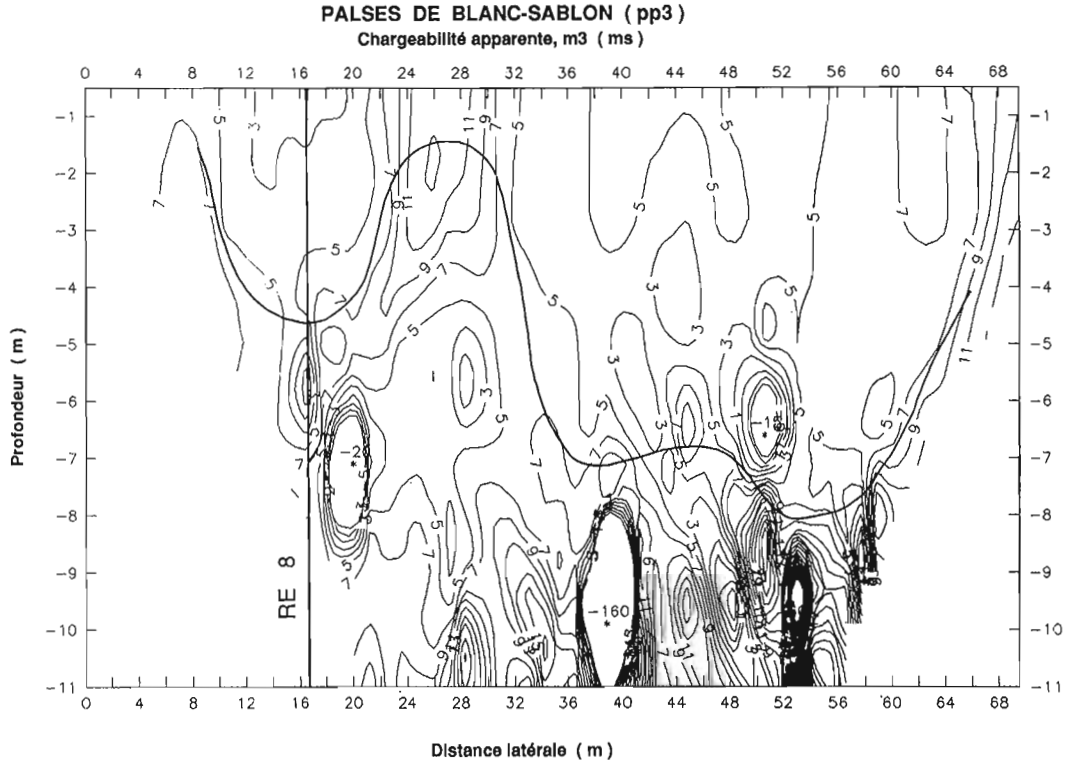


**Figure 7.** Pseudo-section de la chargeabilité apparente ($m_3$) ; même description qu'à la figure 5.

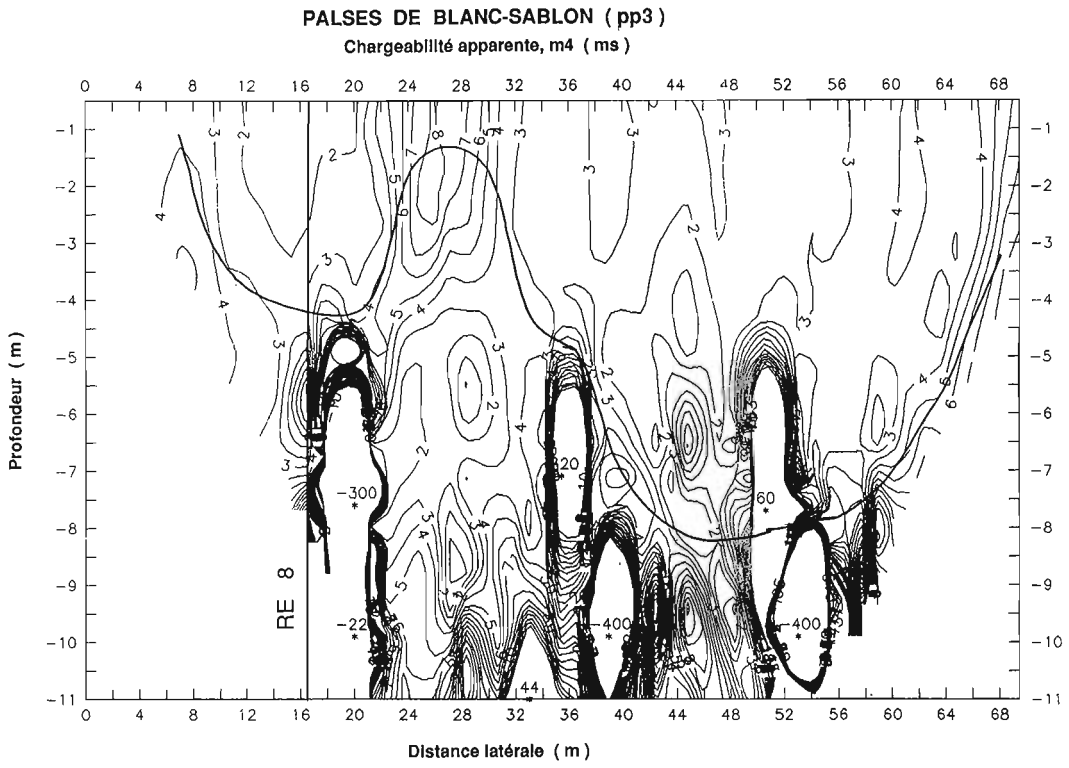


**Figure 8.** Pseudo-section de la chargeabilité apparente ($m_4$); même description qu'à la figure 5.

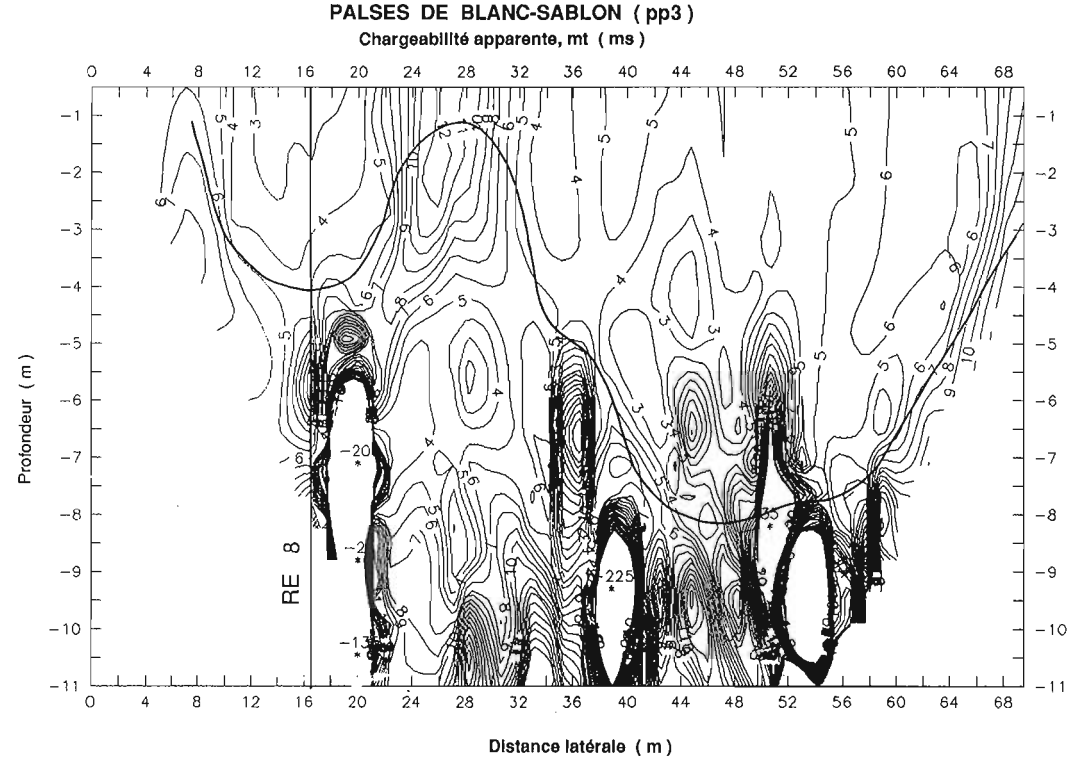


**Figure 9.** Pseudo-section de la chargeabilité apparente totale ($m_t$); même description qu'à la figure 5.

antérieures, donne une image très fidèle de la chargeabilité $m_4$ (fig. 8). Une compilation des courbes délimitant la base du pergélisol à partir des interprétations indépendantes de la résistivité électrique et des chargeabilités $m_1$, $m_2$, $m_3$, $m_4$ et $m_t$ de la pseudo-section calibrée PP3 apparaît à la figure 10. L'enveloppe de ces courbes donne une idée de la qualité de l'interprétation et du degré d'incertitude de celle-ci. Le degré de résolution le moins élevé se situe entre les chaînages 36 et 54 m.

La pseudo-section PP4 représentant les données du sondage de RE BLANCSAB 9 fait aussi voir une grande variabilité de la base du pergélisol. Sur la pseudo-section calibrée de résistivité apparente (fig. 11), on note une profondeur de 9 m à la base du pergélisol; cette profondeur correspond à une valeur similaire (8 m) obtenue à partir du sondage de RE (fig. 3). Sur la pseudo-section, la profondeur maximale de la base du pergélisol se situe à environ 10 m. La figure 12 illustre la pseudo-section calibrée de chargeabilité

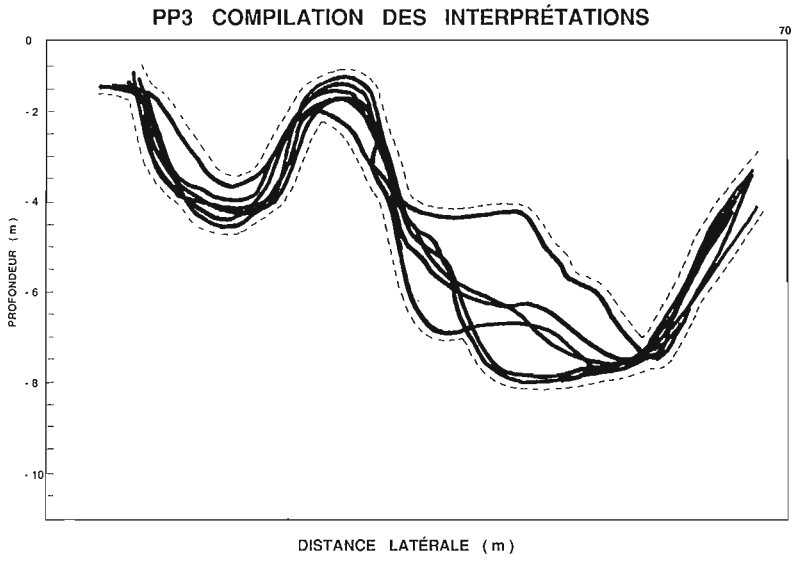


**Figure 10.**

Délimitation de la base du pergélisol sur la pseudo-section PP3 à partir de l'interprétation des données de résistivité et de chargeabilité. Les limites minimales et maximales de la base du pergélisol sont indiquées par les tirets.

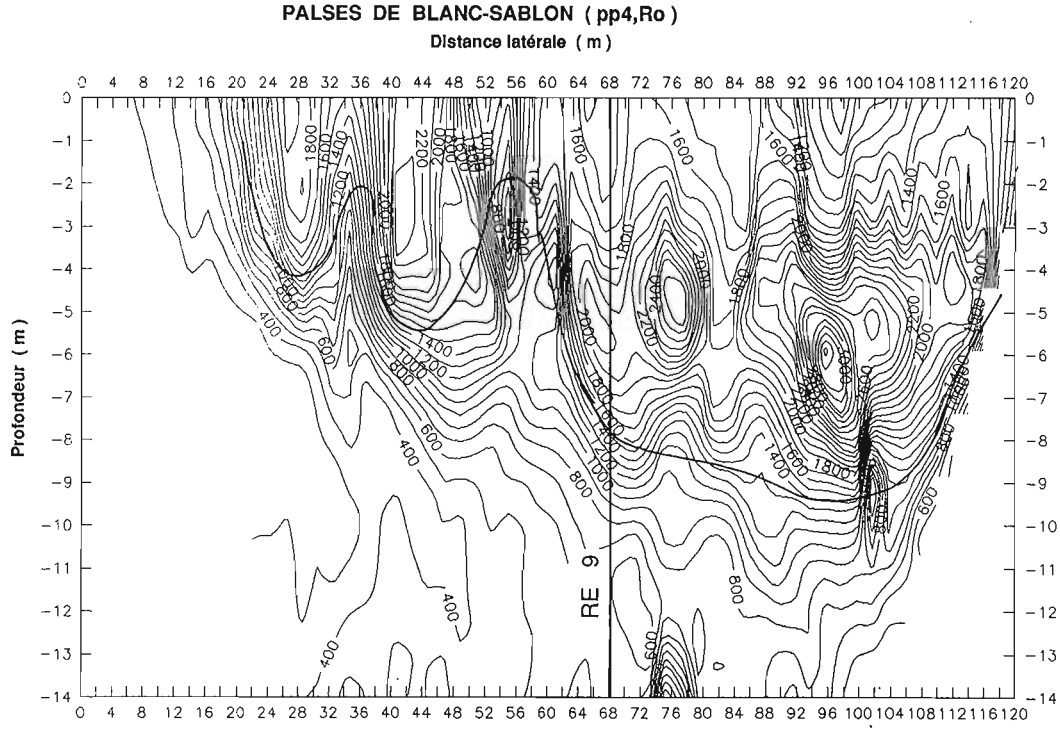


**Figure 11.** Pseudo-section de la résistivité électrique apparente; même description qu'à la figure 4. La position du sondage de résistivité RE 9 est indiquée.

apparente $m_t$. La position et la forme de la courbe qui délimite la base du pergélisol sont très semblables à celles des autres chargeabilités. À l'aplomb du sondage de RE BLANCSAB 9, la profondeur de la base du pergélisol se situe à environ 9 m. La pseudo-section calibrée de chargeabilité totale ($m_t$) du profil PP4 est montrée à la figure 12. La position et la forme de la courbe indiquant la base du pergélisol sont similaires à celles obtenues sur les pseudo-sections des chargeabilités $m_3$ et $m_4$; il existe une petite divergence entre les chaînages 32 et 44 m. Dans ce secteur, la base du pergélisol sur la figure 12 se situe à 2 m sous celle de la figure 10. La compilation des résultats obtenus à partir des pseudo-sections de RE $m_1$, $m_2$, $m_3$, $m_4$ et $m_t$ du profil PP4 apparaît à la figure 13. L'enveloppe des courbes délimitant la base du pergélisol indique une bonne convergence des solutions indépendantes, excepté dans les plages de 32 à 44 m et de 68 à 90 m.

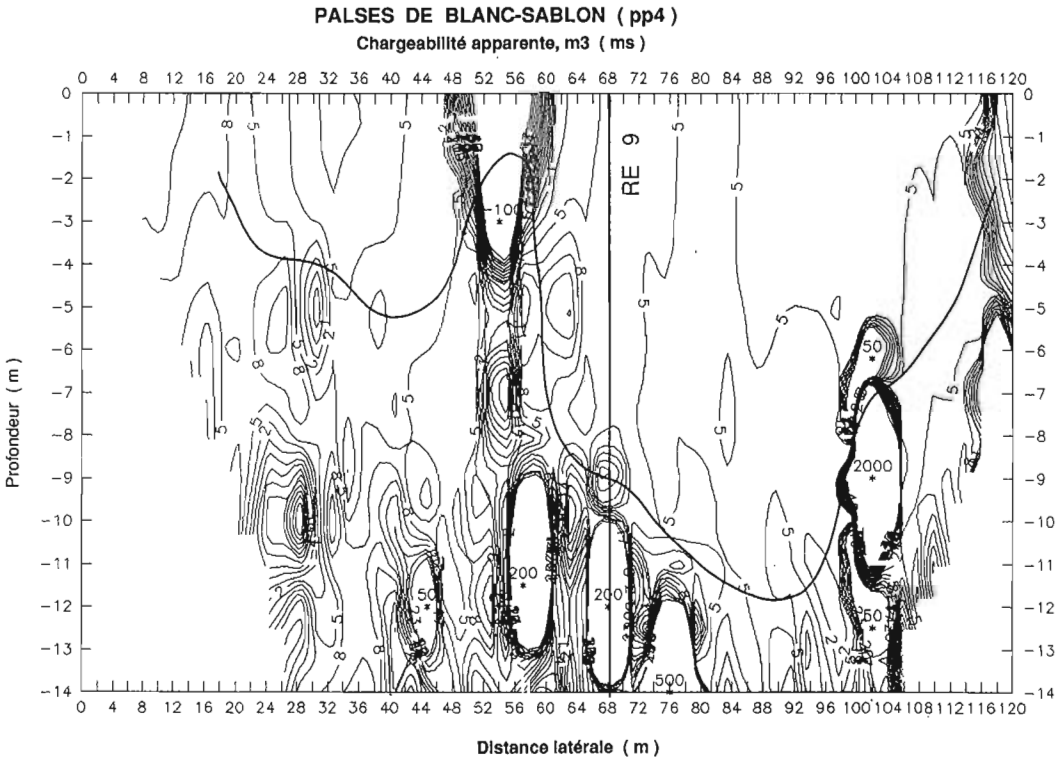


**Figure 12.** Pseudo-section de la chargeabilité apparente totale ($m_t$); même description qu'à la figure 5.

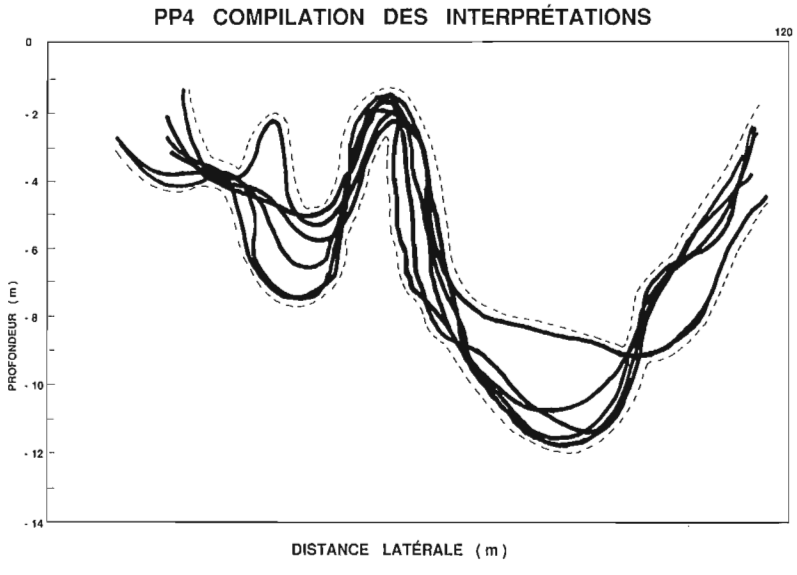


**Figure 13.**

Délimitation de la base du pergélisol sur la pseudo-section PP4; même description qu'à la figure 10.

**Tableau 1.** Corrélations : teneur en eau, température et résistivité électrique

| Profondeur (cm) | Forage 1 | | | Forage 2 | | | Forage 3 | | |
|---|---|---|---|---|---|---|---|---|---|
| | % $H_2O$ | T (°C) | p (Ω•m) | % $H_2O$ | T (°C) | p (Ω•m) | % $H_2O$ | T (°C) | p (Ω•m) |
| 60 | | 0,31 | | | | | | | |
| 65 | 504 | | | 128 | | | 328 | | |
| 85 | 733 | | | 57 | | | 248 | | |
| 105 | 1116 | | | 65 | | 755 | 672 | | |
| 108 | | | | | -0,46 | | | -0,47 | |
| 125 | 433 | | | 54 | | | 833 | | 1285 |
| 143 | | -0,51 | | | | | | | |
| 145 | 236 | | | 40 | | | 543 | | |
| 154 | | | 1267 | | | 1582 | | | |
| 165 | 52 | | | 46 | | | 30 | | |
| 179 | | | | | | | | | 1708 |
| 185 | 50 | -0,52 | | 34 | | | 46 | | |
| 188 | | | | | | | | | |
| 205 | 40 | | | 80 | | | 59 | | |
| 221 | | | | | -0,53 | | | | |
| 225 | 45 | | 1348 | 60 | | 2976 | 32 | | |
| 245 | 40 | | | 89 | | | 41 | | |
| 255 | | -0,48 | | | | | | | |
| 265 | 38 | | | 67 | | | 45 | | 1135 |
| 285 | 86 | | | 61 | | | 44 | | |
| 305 | 41 | | | 65 | | | 54 | | |
| 310 | | -0,50 | | | | | | | |
| 325 | 76 | | | 46 | | | 55 | | |
| 331 | | | 993 | | | 4382 | | | |
| 345 | 58 | | | 59 | | | 67 | | |
| 359 | | | | | -0,55 | | | -0,49 | |
| 365 | 37 | -0,59 | | | | | | | |
| 385 | | | | | | | | | 365 |
| 486 | | | 483 | | | 4343 | | | |

## RÉSULTATS DES FORAGES

Le tableau 1 résume les données des trois forages. Dans le premier, situé à l'extrémité est du champ de palses, l'épaisseur de la tourbe est de 150 cm. Au moment des travaux de terrain (fin juillet 1989), les 45 premiers centimètres étaient dégelés. Sous le couvert tourbeux, une épaisseur de 325 cm de sable fin limoneux stratifié a été traversée. Cette tranche comprend, bien entendu, la glace de ségrégation dont les couches les plus épaisses atteignent 10 mm. Les températures, mesurées quelques heures après le forage, voisinent -0,50° C; elles correspondent à peu près à la température enregistrée par la suite par le câble à thermistances installé en 1990 (Dionne et Seguin, 1992). La teneur en eau (poids) est forcément élevée dans la tourbe (236 à 1116 %), alors que dans le substrat minéral, elle varie de 37 à 86 % avec une médiane à 45 %.

Le deuxième forage, situé à peu près au centre du champ de palses, a révélé une couche tourbeuse mince (75 cm dont 50 cm étaient dégelés). Le substrat minéral est similaire à celui du forage 1, mais il est plus riche en glace de ségrégation. La teneur en eau varie de 34 à 89 %, avec une médiane de 59 %. La température du pergélisol est comparable à celle du forage 1.

Le troisième forage a été fait sur une grosse palse allongée située à la bordure ouest du champ de palses. Le couvert tourbeux fait 200 cm dont les 50 premiers étaient dégelés. Le substrat minéral est semblable à celui des deux autres forages. La teneur en eau du couvert tourbeux est élevée, allant de 248 à 833 %, alors que dans le substrat minéral, elle varie de 30 à 67 %, avec une médiane de 45 % comme dans le forage 1.

## DISCUSSION

Les sondages de RE sont utilisés pour déterminer l'épaisseur des dépôts quaternaires et délimiter l'épaisseur du mollisol et du pergélisol. La méthode de la PP est employée pour délimiter de façon plus détaillée, en deux dimensions, la base du pergélisol. L'interprétation des résultats obtenus est principalement basée sur le gradient maximal de résistivité électrique ou de chargeabilité entre les courbes ou en fonction des critères suivants : une résistivité élevée est caractérisée par une augmentation du contenu en glace ou par une faible teneur en eau (soit une plus basse température) ou les deux.

**Tableau 2.** Variations de la base du pergélisol

| Pseudo-section | Profondeur minimale (m) | Profondeur maximale (m) | Profondeur moyenne (m) |
|---|---|---|---|
| PP1 | 3,5 | 5,5 | 4,5 |
| PP2 | 3,5 | 11 | 9 |
| PP3 | 1,5 | 8 | 6 |
| PP4 | 2 | 12 | 9 |
| PP5 | 6 | 8 | 7 |

La chargeabilité tend vers zéro lorsque la quantité de glace est plus grande et elle est fortement négative sous la base du pergélisol où la concentration d'ions négatifs est élevée. La compilation de l'interprétation des diverses pseudo-sections permet d'obtenir des solutions indépendantes pour délimiter la base du pergélisol. Trois forages ont permis d'établir des corrélations entre la teneur en eau (glace), la température et la résistivité électrique (tableau 1).

## CONCLUSION

Le tableau 2 montre les profondeurs minimale, maximale et moyenne de la base du pergélisol sur cinq pseudo-sections de polarisation provoquée. Les variations entre les limites (minimale et maximale) du pergélisol (surtout sur PP2, 3 et 4) peuvent être corrélées non seulement au contenu en glace et en eau mais aussi à la granulométrie des dépôts non consolidés. Les données de RE font très bien ressortir la nature et le caractère des couches. En dernier lieu, l'étendue latérale et l'épaisseur du pergélisol indiquent que les plus petites palses sont en voie de disparition (dégradation). Les amincissements de la base du pergélisol à leurs extrémités et les zones de taliks ou de quasi-taliks en leurs centres sont autant d'indices de cet état de dégradation.

## REMERCIEMENTS

Richard Levesque, autrefois professionnel de recherche au Centre d'études nordiques et actuellement à l'emploi de POLY-GÉO (Montréal), a contribué aux travaux de terrain en 1989. Alain Hupé, du Département de géologie de l'Université Laval, a participé au traitement des données géophysiques. Leur contribution a été grandement appréciée.

## RÉFÉRENCES

**Barker, R.D.**
1989: Depth of investigation of colinear symmetrical four-electrode arrays; Geophysics, v. 54, p. 1031-1037.

**Brown, R.J.E.**
1978: Carte du pergélisol au Canada, planche 32, dans Atlas hydrologique du Canada, Ottawa, Pêches et Environnement Canada.

**Dionne, J.C.**
1984: Palses et limites méridionales du pergélisol dans l'Hémisphère Nord : le cas de Blanc-Sablon, Québec. Géographie physique et Quaternaire, vol. 38, nº 2, p. 165-184.

**Dionne, J.C. et Seguin, M.**
1992: Recherches sur le pergélisol dans la région de Blanc-Sablon, Québec; dans Recherche en cours, Partie D; Commission géologique du Canada, Étude 92-1D, p. 59-65.

**Zodhy, A.A.R.**
1989: A new method for the automatic interpretation of Schlumberger and Wenner sounding curves; Geophysics, v. 54, p. 245-253.

Projet 904267 de la Commission géologique du Canada

# High frequency reflection seismic profiling at Les Mines Selbaie, Quebec

**B. Milkereit, L. Reed[1], and A. Cinq-Mars[2]**
**Continental Geoscience Division**

*Milkereit, B., Reed, L., and Cinq-Mars, A., 1992: High frequency reflection seismic profiling at Les Mines Selbaie, Quebec; in Current Research, Part E; Geological Survey of Canada, Paper 92-1E, p. 217-224.*

***Abstract***

*Les Mines Selbaie is located in the Harricana-Turgeon belt of the Abitibi Subprovince in northern Quebec and is well known for its Cu-Zn-Au-Ag deposits. As part of the LITHOPROBE Abitibi-Grenville transect, two high frequency seismic reflection surveys were conducted around the active mine site. The main goal of the seismic surveys was to obtain an image of the east-dipping contact between the granite and the underlying andesite and volcanic rocks hosting the ore bodies. Interpretation of the seismic data, by correlation with existing borehole and surface geological data, suggests that prominent east-dipping reflections define the shape of the Brouillan pluton at depth. In addition, several east-dipping structures, parallel to the granite-andesite contact, have been imaged in the mine area beneath the limit of detailed drilling.*

***Résumé***

*Les Mines Selbaie, reconnue pour ses dépôts de Cu-Zn-Au-Ag, est située dans la zone de Harricana-Turgeon de la sous-province de l'Abitibi du nord-ouest québécois. Dans le cadre du transect Abitibi-Grenville du projet LITHOPROBE, deux levés de sismique réflexion à haute fréquence ont été réalisés sur le site de la mine en exploitation. Les roches volcaniques hôtes de la minéralisation sont délimitées à l'est par une andésite tectonique et par le granite de Brouillan. Le levé sismique avait pour but de cartographier le contact incliné vers l'est relevé entre le granite de Brouillan et les roches volcaniques sous-jacentes (andésite et roches hôtes de la minéralisation). La géophysique des sondages a permis d'identifier un contraste de densité marqué entre le granite et les roches volcaniques. L'interprétation des données sismiques corrélées avec les données géologiques recueillies en surface et en profondeur, semble indiquer que les réflexions inclinées vers l'est définissent la forme de l'intrusion de Brouillan en profondeur. D'autres réflexions parallèles aux précédentes ont été identifiées dans la région de la mine, mais à des profondeurs supérieures à la zone définie par forages.*

[1] BP Resources Canada, Ltd., Mining Division, Toronto
[2] Mineral Resources Division

## INTRODUCTION

Reflection profiling techniques are well established in hydrocarbon exploration and in recent years, have been adapted sporadically to mineral exploration (e.g. Dahle et al., 1985; Pretorius et al., 1987; Reed, 1987). An experimental high resolution reflection seismic program was carried out at Buchans, Newfoundland in 1989 with joint support from Lithoprobe and BP Canada, Mining Division. The results of this survey (Boerner et al., 1990; Thurlow et al., in press; and Spencer et al., in press) were sufficiently encouraging to cause Lithoprobe and BP to collaborate again to carry out similar surveying at Les Mines Selbaie in northern Quebec (Fig. 1). While the nature of the ore deposition is significantly different at Buchans and Les Mines Selbaie, there were enough common structural characteristics to expect that useful information could be derived from a seismic survey at Selbaie.

### *Local setting*

The zinc, copper, silver, and gold deposits at Les Mines Selbaie were discovered in 1974 following an airborne electromagnetic survey (Reed, 1981) in the Harricana-Turgeon belt of the Abitibi Subprovince in northern Quebec. Geology of the deposits has been described by Deptuck et al. (1982). An up-to-date outline of mining operations as well as recent geological considerations at Les Mines Selbaie was published recently (e.g. Bryce, 1990; Bouillon, 1990). The deposits are unlike the predominant exhalative massive sulphides found in the Abitibi (and at Buchans); at Selbaie, they occur as veins, in multiple open space fractures or breccias. These deposits occur in felsic volcanics locally described as rhyodacite breccia, welded acid tuff, and dacite tuff (Fig. 1). Volcanic rocks hosting the ore bodies are bounded on the east by structurally emplaced andesite and granite of the Brouillan Batholith whose contacts dip to the east. One of the orebodies consisting predominantly of chalcopyrite with pyrite, the B zone, is contained in a fault structure also dipping to the east. Structures controlling ore in the A1 and A2 zones are more complex, but commonly dip vertically or steeply to the south. Lenses of generally flat-lying, bedded massive pyrite are found only within the upper rhyodacite breccia unit. The A1 and the upper parts of the A2 zones make the largest contribution of ore to the mine while the smaller B zone has provided one third of the ore until recently.

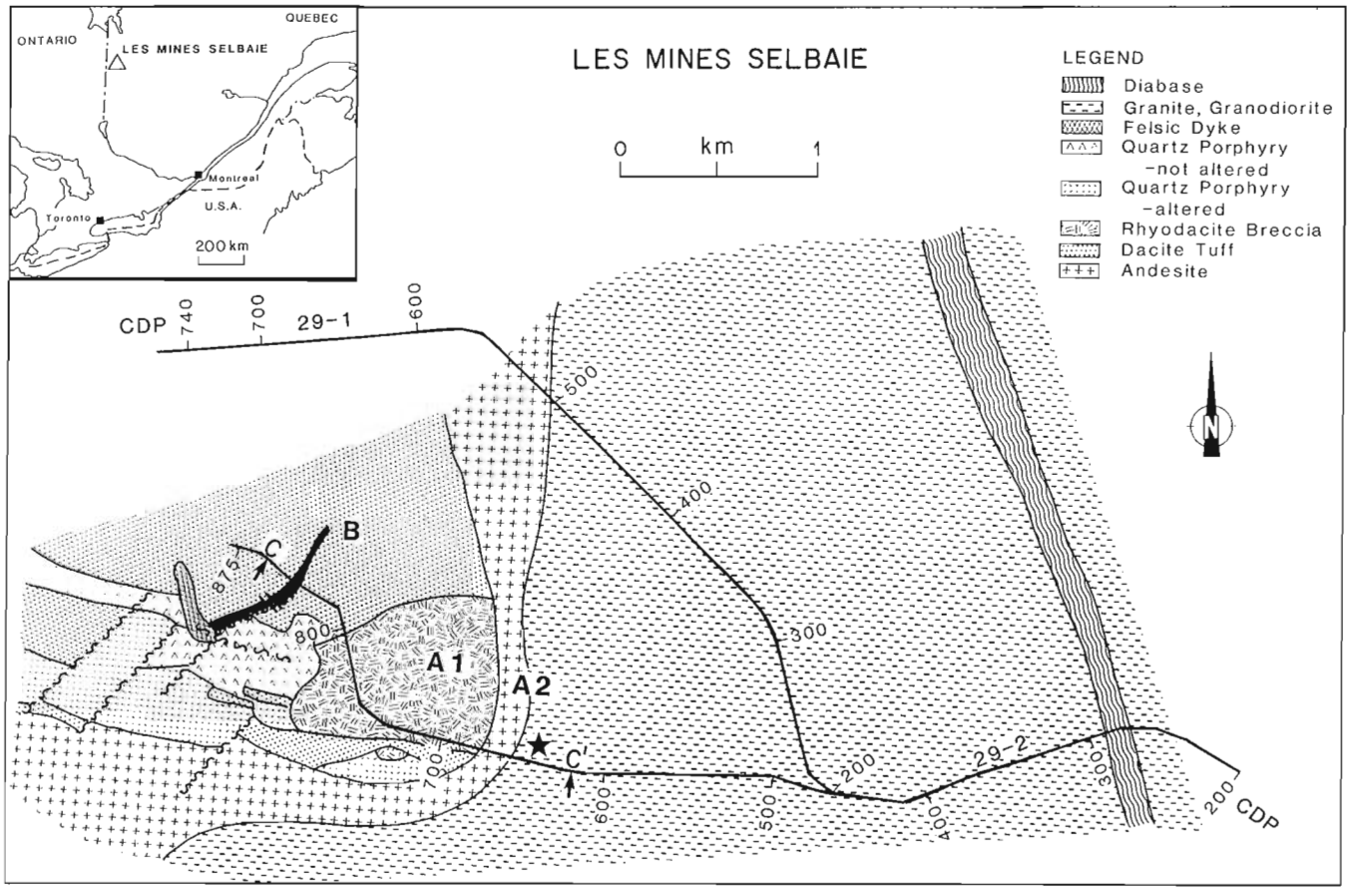


**Figure 1.** Geological map of the Les Mines Selbaie area showing main lithological units crossed by LITHOPROBE seismic reflection profiles 29-1 and 29-2. Granite and granodiorite are part of the Brouillan Batholith. Star indicates location of borehole used for geophysical logging (see Fig. 8). Geological cross-section C-C' is shown in Figure 9. Insert shows location of the survey area.

### *Objectives*

The intent and expectation of the seismic survey was not to map sulphide bodies, as these would be too small or thin to produce observable seismic reflections. Instead, using the Buchans results as a guide, it was hoped that various structures in the mine area could be mapped and their location extended to depth below current drilling. Mapping of the B zone structure could provide a guide to the location of ore at depth, while mapping of the andesite-granite contacts could develop opportunities for new ore as the mine rocks and A2 zone mineralization pass under the andesite and granite of the Brouillan Batholith. Figure 1 shows the location of the two high resolution survey lines. Line 29-1 lies along the regional access road coincident with a small part of the Lithoprobe regional transect line 29. Line 29-2 starts further east of 29-1 also on the main access road, then it branches along a local road through the mine site, over parts of the A2 and A1 zones, to finish across and to the west of the B zone.

## SEISMIC DATA ACQUISITION AND PROCESSING

Source and receiver group spacing were 20 m to give a nominal fold of 120. The receiver spread consisted of a 240-channel telemetry system. High frequency geophones with a resonant frequency of 30 Hz were used to attenuate low frequency noise. The seismic source consisted of 2 vibrator trucks sweeping four times at every station. For any individual field record, successive sweeps were recorded such that the external 60 Hertz powerline noise would be effectively cancelled in the vertical sum of four sweeps (COS filter). Further improvement of the signal-to-noise ratio during data acquisition was achieved by extending both bandwidth and sweep length (12 s linear upsweep from 30 to 140 Hz) and utilizing the equipment's diversity stack option to suppress random noise bursts. More details about data acquisition parameters are given in Milkereit et al. (1992).

Often in seismic studies ambient noise is assumed to have low amplitudes and a flat spectrum. However, a different environment was encountered at Les Mines Selbaie. Some of the data acquisition problems are illustrated by a typical 240-channel field record shown in Figure 2. These include ambient and source generated noise as well as variable recording conditions imposed by overburden variations. Important data processing steps include frequency filter and deconvolution tests to suppress high ambient noise levels, spectral balancing to suppress source generated noise (e.g. shear waves/ground roll), and first break analysis and computation of static corrections to compensate for significant variations in overburden thickness along the seismic profiles.

The field example shows a 50 ms delay (marked b in Figure 2) due to low velocity overburden at the seismic source. At Les Mines Selbaie, total static corrections of up to 100 ms were calculated. It is worth emphasizing that time shifts due to total static corrections are an order of magnitude larger than shifts due to residual stacking velocities. The near surface velocity model showed large variations in overburden thickness (glacial drift), from near basement outcrop to more than 50 m over only a few surface stations.

Source generated noise such as a strong basement refraction (c in Fig. 2), high velocity shear wave (d), and an air wave (e) are best tackled by subsequent processing steps such as muting, spectral balancing, and high-fold stacking. More difficult to deal with is the occurrence of persistent,

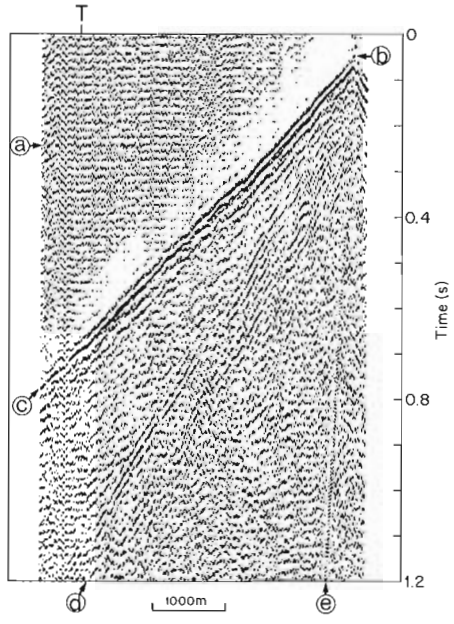


**Figure 2.** Correlated Vibroseis field record from the Les Mines Selbaie experiment highlighting several noise problems. (a) Coherent ambient noise from poorly suppressed external 60 Hz powerline signal; (b) delay times of up to 50 ms due to highly variable overburden conditions; (c) high velocity basement refraction; (d) high velocity shear wave refraction/ground roll; (e) low velocity, high frequency air wave. Location of data for filter tests shown in Figure 4 is marked "T".

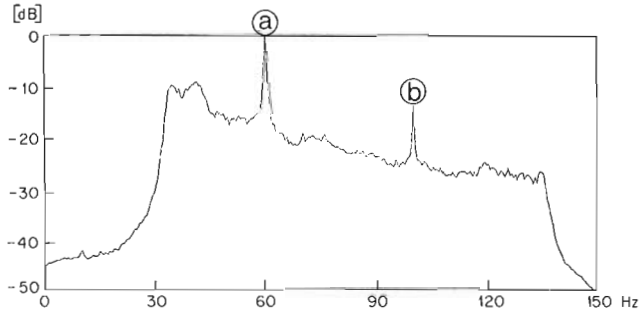


**Figure 3.** Amplitude spectrum of 240 channel field record showing high levels of noise contamination. Vibroseis sweep frequencies range from 30 to 140 Hz. (a) External powerline noise after reduction by COS filter during acquisition is about 20 dB above signal. (b) Second monochromatic noise source at 100 Hz.

monochromatic noise (marked a in Fig. 2). No single, stationary noise source could be identified and eliminated. Instead, numerous high voltage powerlines parallel and perpendicular to the seismic transects may have contributed to the noise pattern seen in Figure 2. In addition to powerlines, the west end of line 29-2 was subject to a considerable amount of man-made noise as it passed over the underground A2 workings, around the southern edge of the A1 open pit, and over the underground B zone. The strongest noise sources were observed at the B zone as the line traversed through the mine camp just south of the mill and concentrator buildings.

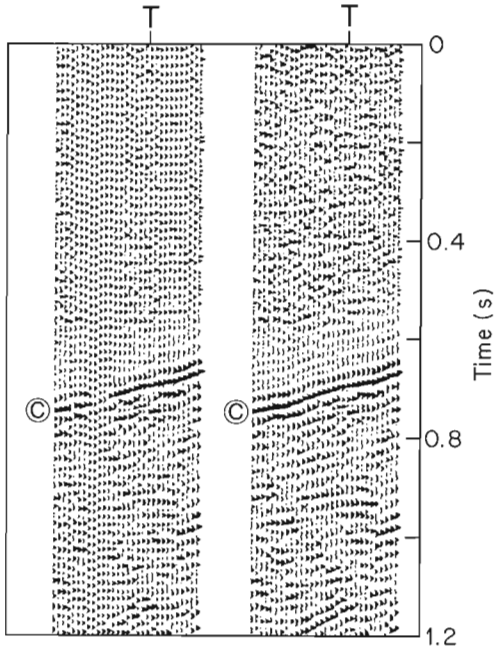


**Figure 4.** Filter test of a portion of the field record shown in Figure 2 (location marked T). Left: input data without notch filters applied. Right: broad 56-64 Hz notch filter and narrow 98-102 Hz notch filter applied. Note improved first breaks (c) and continuous reflections.

It is worth emphasizing that high 60 Hz noise levels or random noise bursts may easily saturate the dynamic range of fixed gain recording equipment often used for shallow dynamite surveys. Thus, high ambient noise levels may make the use of low fold dynamite surveys unacceptable because the recovery of hidden (weak) signal is hampered when the signal falls below the system noise or outside of the effective dynamic range of the recording system.

The amplitude spectrum of the field record with the sweep frequencies between 30 and 140 Hz and two peaks at 60 and 100 Hz is shown in Figure 3. The first peak (marked a in Fig. 3) highlights the fact that despite external 60 Hz cancellation, "dirty" 60 Hz between 56 and 64 Hz were not cancelled completely. The effective dynamic range of the acquisition equipment allows suppression of remnant 60 Hz noise during data processing. The sharp peak at 100 Hz in the amplitude spectrum points (marked b) points towards a second noise source: electric motors used in mill operations are the most likely source. Again, such monochromatic noise is best handled by carefully selected notch filters (or spectral equalization) during data processing.

Results of the application of two notch filters followed by a short-window amplitude equalization to a noisy section of the Selbaie mines data are shown in Figure 4. Continuous refracted and reflected seismic signal has been retrieved at the expense of high-energy, monochromatic noise. The drawback of using a robust processing sequence is that detailed lateral variations of the ground's reflection response are indistinguishable from lateral variations of recording conditions, and the interpreter cannot rely on the amplitudes of the stacked section to interpret the nature of reflectors.

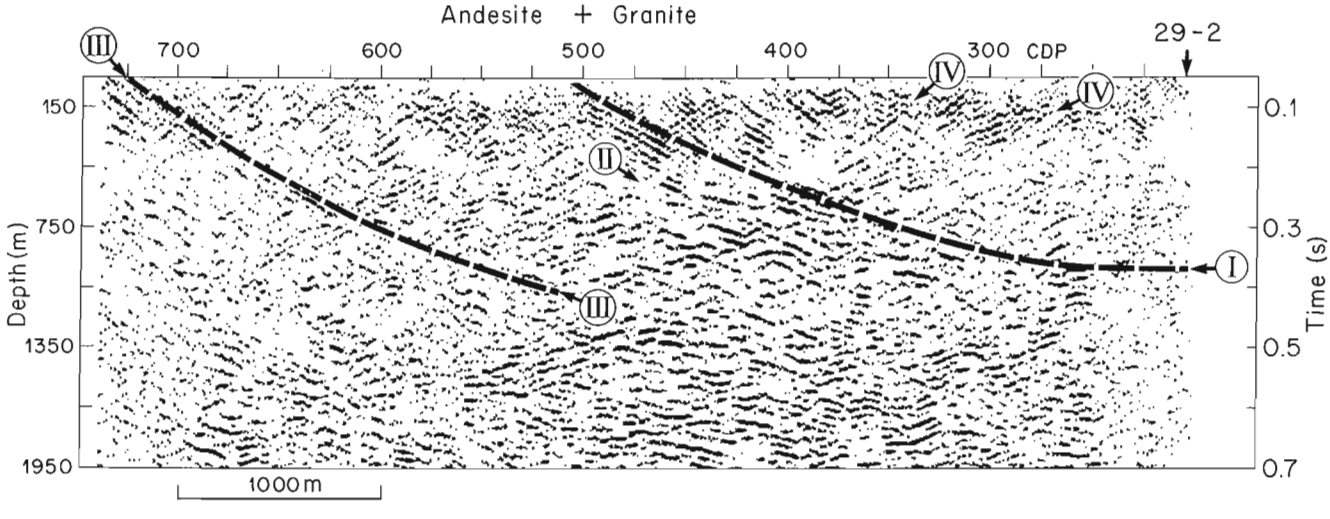


**Figure 5.** Interpreted stacked seismic section from line 29-1. Prominent reflections and groups of reflections are marked I to IV. A 6000 m/s average crustal velocity was used to convert two-way reflection times into depths. Reflection I marks the granite-andesite-dacite contacts.

## INTERPRETATION

The most prominent feature of the seismic data is a series of east-dipping reflections that can be identified on both profiles. There are four groups of reflectors (marked I, II, III, and IV) highlighted in Figure 5. Reflection I begins at the surface at CDP 550, dips to the east, and can be traced to 350 ms (approximately 900 m depth) beneath the intersection with line 29-2. The surface location of reflector I coincides with the mapped granite-andesite contact along profile 29-1. Reflection II cannot be traced to surface; it begins at 200 ms beneath CDP 500, dips to the east, and can be traced for 1.5 km as an east-dipping reflection parallel to the interpreted granite contact. Reflection III projects to the surface at CDP 725; it dips to the east and can be traced to 400 ms beneath CDP 500. Within the granite, prominent west-dipping reflections (IV) are observed. Most of the deeper reflections seen in Figure 5 cannot be tied to known surface geology.

Similar seismic images are obtained from data acquired along line 29-2. Four groups of reflectors are marked in Figure 6. Reflection I begins at the surface at CDP 670, dips to the east, can be traced to 350 ms (approximately 900 m depth) beneath the intersection with line 29-1, and reaches 500 ms (approximately 1500 m depth) beneath the eastern end of the seismic profile. Again, the surface location of reflector I coincides with the mapped granite-andesite

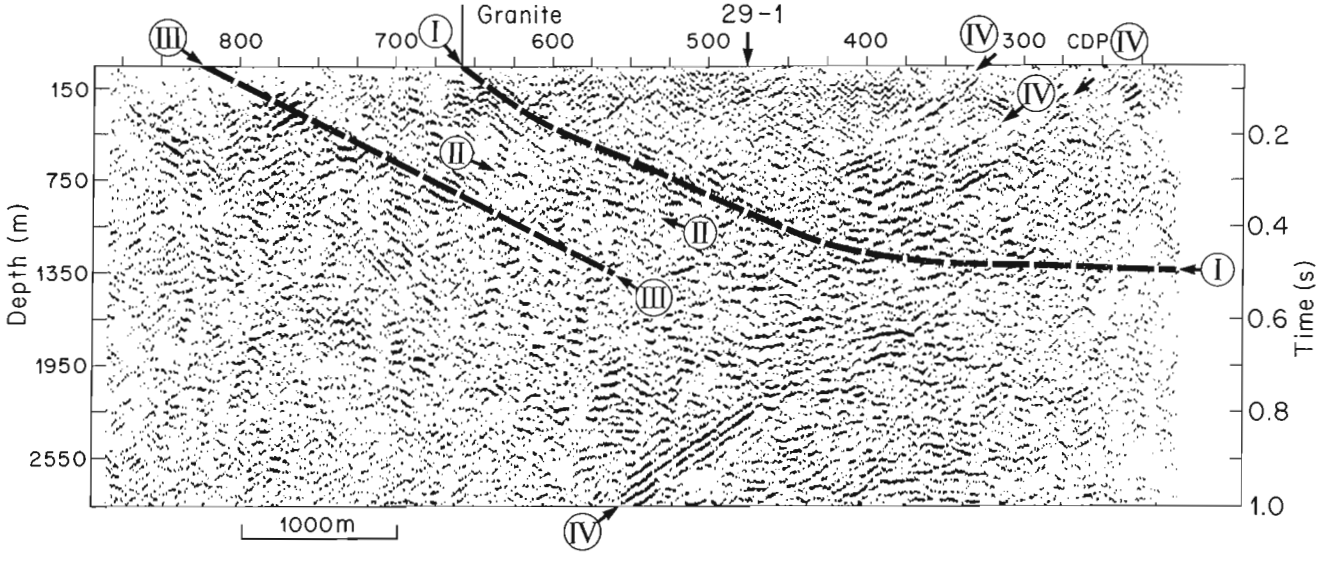


**Figure 6.** Interpreted stacked seismic section from line 29-2. Prominent reflections and groups of reflections are marked I to IV. A 6000 m/s average crustal velocity was used to convert two-way reflection times in depth estimates. Reflection I marks the granite-andesite-dacites contacts. West-dipping reflections (IV) within the Brouillan pluton may be associated with diabase dykes.

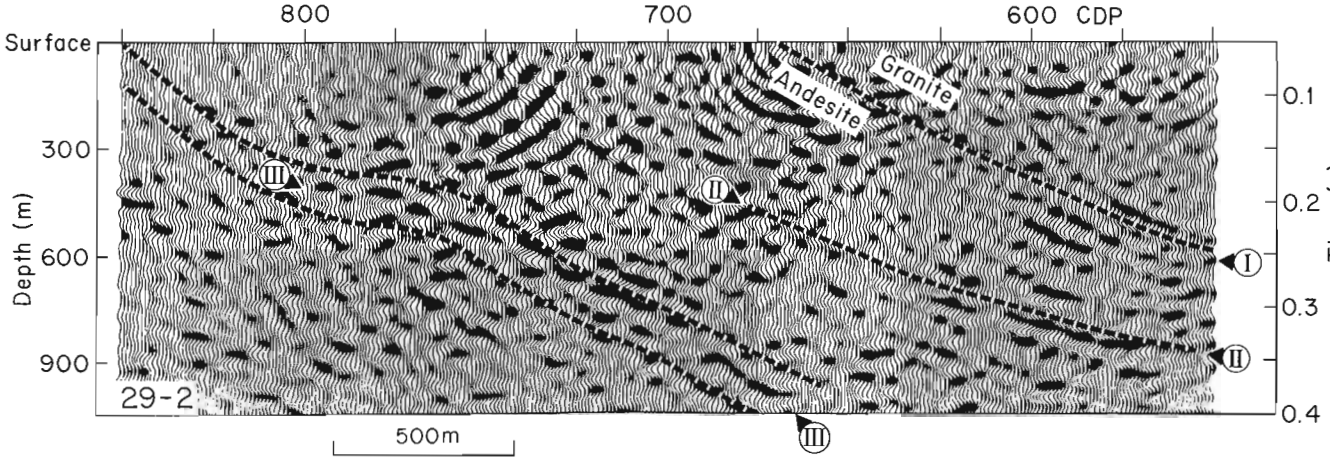


**Figure 7.** Interpretation of migrated seismic data from profile 29-2. The granite-andesite contact (I), structures parallel to the contact (II, III) have been imaged as east-dipping reflections beneath the seismic profile. The origin of the deeper reflectors requires further studies.

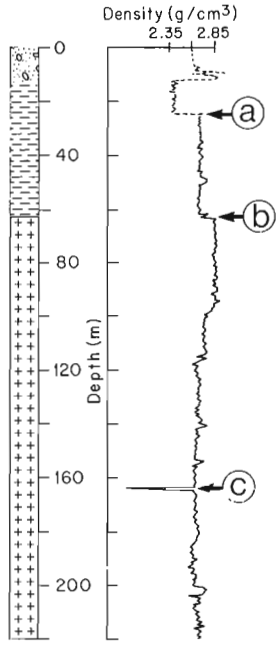


**Figure 8.** Density log (gamma-gamma) from borehole along seismic profile 29-2. For location and legend see Figure 1. Density variations are observed at the granite-andesite contact (b) at 63 m depth. Groundwater table is at 25 m (a) and an important fracture within the andesite (c) can be seen at 164 m depth.

contact. Reflection II begins at 250 ms (approximately 600 m depth) beneath CDP 650 and dips to the east. Reflection III projects to the surface at CDP 825; it dips to the east and can be traced to 500 ms (1500 m depth) beneath CDP 550. A number of prominent, west-dipping reflections (IV) are observed within the granite outside the mining camp. The most continuous west-dipping reflection observed on line 29-2 can be tied to a diabase dyke in the granite at the east end of the line (Fig. 1). A steep westerly dip is implied for this dyke.

In stacked sections, continuous dipping reflections are always defocused so their apparent lengths are frequently overestimated and their true in-line dip is underestimated. The western end of line 29-2 has been migrated to obtain improved in-line dip estimates from dipping structures (Fig. 7). Migration results are often adversely affected by properties of the seismic data such as spatial sampling, frequency content, and poor signal-to-noise ratios. A constant velocity model with 6000 m/s was used for a fk-migration. Reflection I projects into the granite-andesite contact with a dip of 25-30° to the east. The in-line dip of reflection II does not exceed 25° to the east. Migrated reflection III may be more difficult to interpret since surface geology changes strike and dip direction along the western end of line 29-2. Variable easterly dips are observed for reflection III: 30° beneath CDP 675, 40° beneath the CDP 750, and 15° beneath CDP 775.

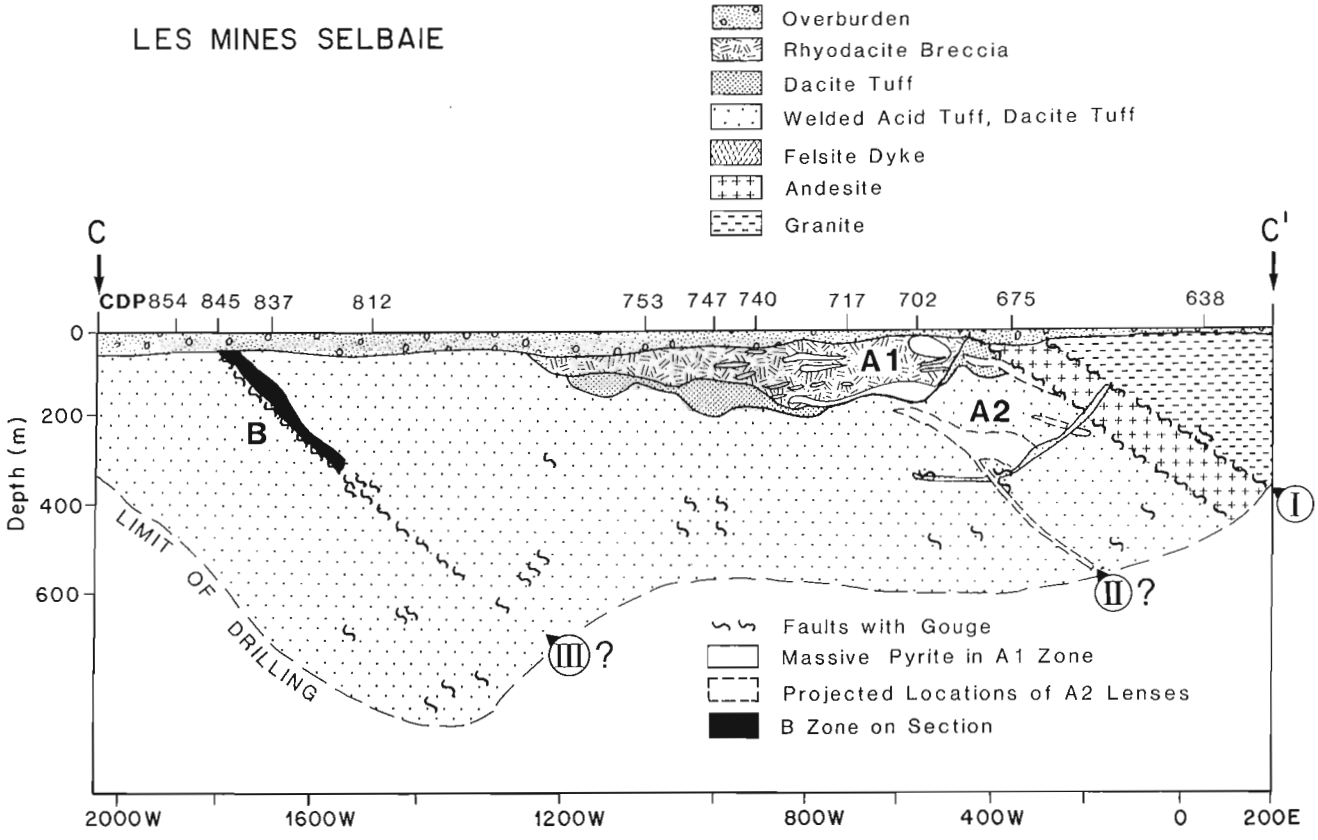


**Figure 9.** Geological cross-section along profile 29-2 based on drilling results. The granite-andesite-dacites contacts coincides with reflection group I, east-dipping reflections marked II may be related to structures parallel to the fault bounded granite-andesite-dacite contacts. East-dipping reflections marked III may image deeper structures related to the B-zone.

### *Borehole geophysical data*

In an attempt to better determine the source of shallow crustal reflectivity, borehole geophysical studies were carried out in three holes at the east end of the deposit. These holes are either on, or very close to the seismic traverse; they penetrate thick overburden, granite, andesite, and dacite, and pass through or near portions of the A2 lenses. The most important measurement made for interpreting the seismic data was density. The measured density contrast between rock units was generally small. The granite-andesite contact in two holes showed a specific density increase of between 0.04 and 0.12 $g \cdot cm^{-3}$. The most significant density variation at the granite-andesite contact is shown in Figure 8. In this hole, the upper 35 m of the andesite is more dense, showing an increase of 0.12 $g \cdot cm^{-3}$ over the granite. Small scale density variations coincide with faults (marked c in Fig. 8). Similar density lows are observed on faults in other holes on the andesite-dacite and granite-andesite contacts. Theses faults, as described in the geology, and the responses on the density logs, are too thin (at about one metre) to produce significant reflections at signal frequencies of 140 Hz or less. More studies, particularly on the seismically relevant physical properties of the rocks and minerals of the mine are required to resolve this question.

Generally, the density contrasts between the granite, andesite, and dacite are too small to produce strong, continuous reflectors. The significant increase in the density in the andesite at one location (Fig. 8) could cause strong reflections. However, the lateral and down-dip extent of this andesite unit is not known.

### *Discussion*

Figure 9 shows the generalized geology under line 29-2 through the mine site. The bottom of this section represents the limit of detailed drilling on the section. In addition, a few holes to a vertical depth of greater than 1000 m provide a limited view of the rocks at depth under the A2 and B zones. The dacite tuff unit described in Figure 1 has been differentiated to dacite tuff and welded acid tuff, and dacite tuff units in Figure 9. Further differentiation of the dacite tuffs are carried out at the mine scale which cannot be shown on these figures.

Based on the stacked and migrated sections, a series of east-dipping reflections has been imaged beneath the Les Mines Selbaie area. A number of these reflectors can be tied spatially to known geological structures, particularly faults and faulted contacts within the mine section. Depth and dip estimates of the migrated data (Fig. 7) are in good agreement with the deeper part of the geological cross-section. The granite-andesite and andesite-dacite contacts coincide with reflection group I, east-dipping reflections marked II may be related to structures parallel to the fault bounded granite-andesite contact. East-dipping reflections marked III may image deeper structures related to the B-zone. This interpretation is in agreement with drill sections and the limited borehole geophysical data base.

On the regional scale, east-dipping reflections may be related to a complex pattern of lithological contacts and fault zones associated with the east-over-west directed overthrusting of the Brouillan Batholith. However, the nature of most reflectors in the mine section remains open to question. While significant reflectors have been identified on the apparent down dip projections of the B zone fault and the faulted contacts of the granite, andesite and dacite, the cause of these reflectors requires further study.

Similar easterly-dipping reflection events have been observed on the two lines in the vicinity of the mine. If the granite-andesite contact can be taken as a marker, then both lines show reflector events at approximately the same locations with respect to this contact. The responses on line 29-1 are better defined, as the noise levels are significantly lower away from the mine. Little is known in detail about the deeper geology along line 29-1 as only a few shallow exploration holes have been drilled there. Apparently the major structures observed on line 29-2 which are tied to known geology, continue north through 29-1. There is a difficulty in correlating the reflectors at the west ends of the lines if easterly dipping reflectors on 29-2 are assigned to the B zone. As may be seen in Figure 1, the B zone strikes into the location of reflectors at the granite-andesite-dacite contact on line 29-1. It is possible that the easterly dipping events at the west end of 29-1 are independent of the B zone structure and the B zone event merges into the granite-andesite contact structures.

## CONCLUSIONS AND RECOMMENDATIONS

In this paper we reported on the preliminary findings of two high-frequency vibroseis profiles in the Les Mines Selbaie area. The use of a multichannel telemetry system, high fold data acquisition, detailed refraction static corrections, comprehensive noise and filter tests, permitted the processing of data in an area where initial seismic sections were extremely noisy.

1. An alternative (and safe) seismic data acquisition strategy could be the collection of raw (uncorrelated and unsummed) vibroseis field records for processing (e.g. Stanley, 1986). Such an approach would eliminate some of the problems associated with the unexpected high levels of ambient noise at an active mine site.
2. The high frequency reflection survey revealed the location and dip of several reflectors in a geologically complicated setting. It is important to emphasize that similar reflection patterns are observed on both profiles, but only the fault-bounded granite-andesite-dacite contacts have been positively identified. The interpreted seismic data present a crustal model where the Brouillan Batholith and andesites are thrust over the mine rocks. The contact can be traced from surface to about 900 m depth beneath the intersection of the two profiles. Thickness of the Brouillan granite is interpreted not to exceed 1500 m at the eastern end of profile 29-2. Our interpretation predicts the down-dip continuation of the

felsic tuff sequence beneath the granite. The recognition of the shallow depth extent of the structurally implaced Brouillan granite beyond the limit of detailed drilling has implications for interpretation of the structural setting and long-term exploration strategies.

3. A series of prominent east-dipping reflections underlies the Selbaie mines to a maximum depth of about 1.5 km. Some of these reflectors can be tied spatially to known geological structures, particularly faults and faulted contacts within the mine section. However, many of the deeper reflections cannot be tied to known surface geology. Interpretation of the LITHOPROBE deep seismic data from northern Abitibi may provide the necessary framework to address the regional setting and importance of deeper basement structures at Les Mines Selbaie. Alternatively, deep drilling and borehole geophysical studies could be employed to calibrate deeper reflections with lithological or structural interfaces.

4. The specific cause of many reflectors has not been clearly established. Incorporating additional geophysical data obtained from detailed borehole studies such as full waveform sonic logging, physical rock property studies, and density logging will help to constrain the interpretation of reflection seismic data from the Les Mines Selbaie area. Further analyses of seismic reflection data will be based on true amplitude processing in conjunction with rock physical studies, full waveform sonic logging, and modelling. Some of these studies are currently underway.

## ACKNOWLEDGMENTS

The seismic data for this LITHOPROBE survey was collected by JRS Exploration of Calgary and preliminary data processing was carried out by Seismic Data Processors (SDP) of Calgary. Downhole geophysical measurements were conducted by the borehole geophysics section of the Geological Survey of Canada. We thank BP Resources Canada, Ltd., Billiton Metals Canada Inc., and Les Mines Selbaie Inc. for permission to publish this case history.

## REFERENCES

**Boerner, D.E., Spencer, C.P., Wright, J.A., Carroll, P., and Reed, L.E.**
1990: Developing new methods at an old mine; Engineering and Mining Journal, July, p. 25-29.

**Bouillon, J.J.**
1990: Les Mines Selbaie Story - Geology; CIM Bulletin, v. 83, p. 79-82.

**Bryce, R.C.**
1990: Les Mines Selbaie Story - Introduction; CIM Bulletin, v. 83, p. 73-76.

**Dahle, A., Gjøystal, H., Grammeltvedt, G., and Søyland Hansen, T.**
1985: Application of seismic reflection methods for ore prospecting in crystalline rock; First Break, v. 3, p. 9-16.

**Deptuck, R., Squair, H., and Wierzbicki, V.**
1982: Geology of the Detour zinc-copper deposits, Brouillan Township, Quebec; in Precambrian Sulphide Deposits, (ed.) R.W. Hutchinson, C.D. Spence, and J.M. Franklin; Robinson Memorial Volume, Geological Association of Canada, Special Paper 25, p. 319-342.

**Milkereit, B., Adam, E., Barnes, A., Beaudry, C., Pineault, R., and Cinq-Mars, A.**
1992: An application of reflection seismology to mineral exploration in the Matagami area, Abitibi belt, Quebec; in Current Research, Part C; Geological Survey of Canada, Paper 92-1C, p. 13-18.

**Pretorius, C.C., Jamison, A.A., and Irons, C.**
1987: Seismic exploration in the Witwatersrand Basin, Republic of South Africa; in Proceedings of Exploration '87, (ed.) G.D. Garland; Ontario Geological Survey, Special Paper 3, p. 241-253.

**Reed, L.E.**
1981: The airborne electromagnetic discovery of the Detour zinc-copper-silver deposit, northwestern Quebec; Geophysics, v. 46, no. 9, p. 1278-1290.
1987: Geophysics in gold exploration - some examples; in Proceedings of Exploration '87, (ed.) G.D. Garland; Ontario Geological Survey, Special Paper 3, p. 473-485.

**Spencer, C.P., Thurlow, J.G., Wright, J.A., White, D., Carroll, P., Milkereit B., and Reed, L.E.**
in press: A vibroseis reflection survey at the Buchans mine in central Newfoundland; Geophysics.

**Stanley, P.J.**
1986: Some comments regarding ambient noise in Vibroseis surveys; First Break, v. 4, no. 7, p. 31-33.

**Thurlow, J.G., Spencer, C.P., Boerner, D.E., Reed, L.E., and Wright J.A.**
in press: Geologic interpretation of data from a high resolution seismic survey at the Buchans mine, Newfoundland; Canadian Journal of Earth Sciences.

Geological Survey of Canada Project 870046

# Electrical resistivity and porosity of crystalline rock samples from the Kapuskasing Structural Zone, Ontario

**T.J. Katsube, N. Scromeda, M. Mareschal[1], and R.C. Bailey[2]**
**Mineral Resources Division**

*Katsube, T.J., Scromeda, N., Mareschal, M., and Bailey, R.C., 1992: Electrical resistivity and porosity of crystalline rock samples from the Kapuskasing Structural Zone, Ontario; in Current Research, Part E; Geological Survey of Canada, Paper 92-1E, p. 225-236.*

***Abstract***

*Complex electrical resistivity, formation factor, effective porosity, and pore-size distribution of four surface rock samples (three containing grain-boundary graphite) from the Kapuskasing Structural Zone (Ontario) have been measured to obtain petrophysical information that might help understand the origin of deep crustal electrical conductors. The zone is considered a relict of an Archean uplift having brought to the present surface rocks formed in the intermediate to lower continental crust.*

*Results show strong directional effects, with bulk resistivities normal to the plane of foliation being $2x10^4$ to $3x10^4$ Ω·m, values slightly lower than those commonly observed for similar rocks. Bulk resistivities parallel to the foliation range from $6x10^3$ to $1.2x10^4$ Ω·m, one third to one fifth of those for the vertical direction, and values considerably smaller than those commonly observed for these rock types. Considerable evidence exists indicating that directional effects are primarily caused by low pore surface resistivities parallel to foliation.*

***Résumé***

*La distribution complexe de la résistivité électrique, du facteur de formation, de la porosité efficace et de la dimension des pores a été établie dans le cas de quatre échantillons de surface (trois contenant du graphite à la limite des grains) de la zone structurale de Kapuskasing (Ontario); l'étude visait à obtenir de l'information pétrophysique qui puisse aider à mieux comprendre l'origine des conducteurs électriques de la croûte profonde. La zone susmentionnée est considérée comme un vestige d'un soulèvement archéen qui a amené jusqu'à la surface actuelle des roches formées dans les niveaux intermédiaires à inférieurs de la croûte continentale.*

*Les résultats indiquent de forts effets directionnels et les résistivités apparentes normales au plan de foliation sont de l'ordre de $2x10^4$ à $3x10^4$ Ω·m; ces valeurs sont légèrement inférieures à celles généralement observées dans des roches similaires. Les résistivités apparentes parallèles à la foliation se situent entre $6x10^3$ et $1,2x10^4$ Ω·m, soit entre le tiers et le cinquième de celles mesurées à la verticale; ces valeurs sont considérablement plus faibles que celles habituellement notées dans ces types de roches. De très nombreux indices montrent que les effets directionnels découlent essentiellement de la faible résistivité de la surface des pores parallèlement à la foliation.*

[1] Ecole Polytechnique, C.P. 6079, Succ. A, Montreal, Quebec, Canada H3C 3A7
[2] University of Toronto, Physics Department, 60 St. George St., Toronto, Ontario M5S 1A7

# INTRODUCTION

Complex electrical resistivity, formation factor, effective porosity, and pore-size distribution for four (4) surface rock samples from the Kapuskasing Structural Zone (KSZ; Ontario, Canada) have been measured in order to obtain petrophysical information that may help explain the origin of the deep crustal electrical conductors. The zone is considered as relict of an Archean uplift (Percival and Card, 1983, 1985) having brought to the present surface rocks formed in the intermediate to lower continental crust. Although the present upper crust of the Kapuskasing Structural Zone is very resistive (100 000 Ω·m) and only includes a few zones of very weak subhorizontal electrical anomalies, some probably unrelated to the uplift itself (Bailey et al., 1989), its lower crust is characterized by a bulk resistivity of a few 100 Ω·m at the most and may show signs of electrical anisotropy (Kurtz et al., in press). Three of the four rock samples used in this study contain grain-boundary graphite (Mareschal et al., in press), therefore having a possibility of providing useful information on the subject. The purpose of this paper is to report the results of these measurements, which adds to the information provided by similar measurements (Katsube et al., 1991) on a graphitic sample obtained from the same zone.

The origin of zones of enhanced electrical conductivity in the intermediate to lower continental crust detected by surface electromagnetic methods has given rise to long-standing debates. This is because although some acceptable explanations for the source of high conduction have been offered, it has been difficult to find such evidence in rocks of deep origin that have been uplifted to the surface. This is particularly true for the shields where lower crustal electrical resistivities are of the order of a few 100 Ω·m, whereas their upper crust is often characterized by resistivities on the order of $10^5$ Ω·m (Mareschal, 1990). Some good reviews on the subject are found in the literature (e.g., Mareschal, 1990; Jones, in press). Results of these measurements will be analyzed using the "broken conductor model" introduced by Katsube and Mareschal (in press). This model uses petrophysical information recently made available for non-reservoir low-porosity rocks in an attempt to explain the electrical conductivity of the intermediate to lower crust of Precambrian shields, as well as its disappearance when the rocks are uplifted.

**Table 1.** Samples, their identification number, I.D., and rock type

| Sample Number | Sample I.D. | Rock Type | Comments |
|---|---|---|---|
| KP-2 | 80-857 | tonalitic gneiss | mafic gneiss with high Ca, Al basaltic composition |
| KP-3 | 85-16 | fault rock | seams in tonalite |
| KP-4 | 79-215 | paragneiss | graphite in outcrop |
| KP-5 | 80-604 | anorthosite | no foliation |

The sample number and I.D. for the sample used in Katsube et al. (1991) is KP-1 and PBA79-32, respectively

# METHOD OF INVESTIGATION

### *Samples and Sample Preparation*

The rock type of the samples are described in Table 1. The samples are hand picked rocks from which rectangular specimens have been cut out. The geometric characteristics of a first set of specimens are listed in Table 2a, their dimensions being of the order of (1.0-2.7)x(1.0-2.7) cm for the cross-section, and 1.0-1.5 cm in thickness. Remaining chips from each sample were prepared for effective porosity measurements. Subsequent to the measurement of these specimens, a second set of specimens was cut out from some of those of the first set. The geometric characteristics of the second set are listed in Table 2b, their dimensions generally being similar to those of the first set, except for the

**Table 2a.** Dimensions of specimens, Set #1, cut out from the Kapuskasing samples for electrical measurements

| Sample No. | $a_1$ (cm) | $a_2$ (cm) | $\ell$ (cm) | W (gm) | $K_G$ ($10^{-2}$m) | δ (g/mL) |
|---|---|---|---|---|---|---|
| KP-2/1 | 1.463 | 1.500 | 1.255 | 8.0126 | 1.749 | 2.91 |
| KP-2/2 | 1.474 | 1.478 | 1.070 | 6.8923 | 2.036 | 2.96 |
| KP-2/6 | 0.990 | 1.515 | 0.419 | 1.8365 | 3.580 | 2.92 |
| KP-2/7 | 1.008 | 1.095 | 0.575 | 1.9588 | 1.920 | 3.08 |
| KP-3/1 | 1.703 | 1.958 | 1.400 | 13.6983 | 2.381 | 2.93 |
| KP-3/2 | 1.716 | 1.589 | 1.081 | 8.4662 | 2.523 | 2.87 |
| KP-4/1 | 1.294 | 1.621 | 1.197 | 7.5052 | 1.753 | 2.99 |
| KP-4/2 | 1.546 | 1.565 | 1.279 | 9.1578 | 1.891 | 2.96 |
| KP-5/1 | 1.482 | 1.481 | 1.163 | 7.3446 | 1.887 | 2.88 |
| KP-5/2 | 2.367 | 2.676 | 1.493 | 28.5277 | 4.242 | 3.02 |

$a_1$, $a_2$: Length of the two sides of the rectangular specimen
$\ell$: Thickness of specimen
W: Weight of specimen
$K_G$: Geometric factor
δ: Bulk density

**Table 2b.** Dimensions of specimens, Set #2, cut out from specimens of Set #1.

| Sample No. | $a_1$ (cm) | $a_2$ (cm) | $\ell$ (cm) | W (gm) | $K_G$ ($10^{-2}$m) | δ (g/mL) |
|---|---|---|---|---|---|---|
| KP-2/4 | 1.454 | 1.503 | 0.570 | 3.6195 | 3.833 | 2.91 |
| KP-3/5 | 1.264 | 1.709 | 0.624 | 4.0053 | 3.462 | 2.97 |
| KP-3/6 | 1.701 | 1.386 | 0.448 | 3.3095 | 5.263 | 3.13 |
| KP-4/4 | 1.614 | 1.296 | 0.529 | 3.3654 | 3.955 | 3.04 |
| KP-5/5 | 1.490 | 1.479 | 0.440 | 2.8991 | 5.009 | 2.99 |

$a_1$, $a_2$: Length of the two sides of the rectangular specimen
$\ell$: Thickness of specimen
W: Weight of specimen
$K_G$: Geometric factor
δ: Bulk density

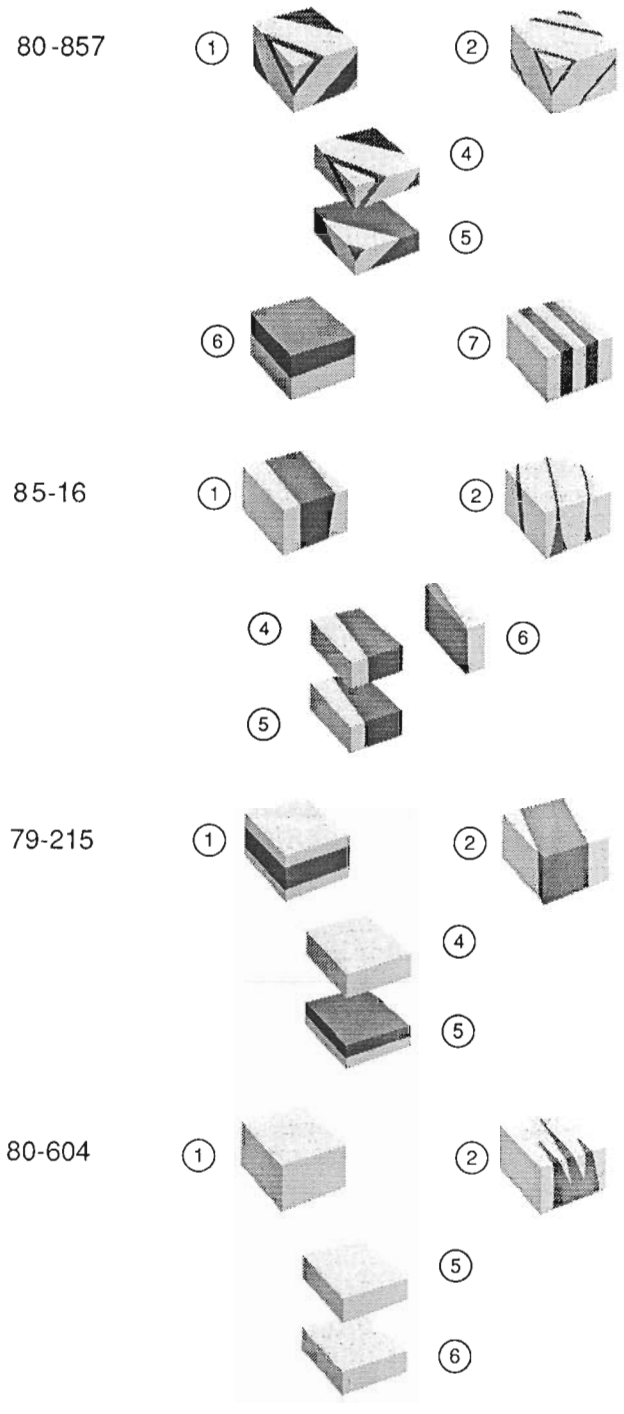


**Figure 1**. Block diagram of specimens used for complex resistivity and formation factor measurements. Sample number is listed on left hand side of the diagram. Numbers inside the circles indicate specimen number. Black stripes or bands on specimens illustrate the foliation. The I.D. numbers in the illustration are for the following sample numbers: KP-2 (80-857), KP-3 (85-16), KP-4 (79-215), and KP-5 (80-604).

thicknesses which are reduced to about one half. Generally, at least two rectangular specimens are cut out from each sample, one cut so that the electrical measurements will be parallel to the foliation, and the other vertical. The orientations of the specimens described above are shown in detail in Figure 1. The circled numbers (beside the specimens) following the identification (I.D.) numbers of the samples in the figure, appear as subscript following a slash after the sample numbers in the tables that follow. For example, the specimen following the circled 6 for sample I.D. number 80-857 in Figure 1, appears as KP-2/6 in Tables 2a, 7a, and 9.

The geometric factor, $K_G$, calculated for all of the rectangular specimens prior to the electrical measurements is derived from

$$K_0 = A/\ell$$

$$A = a_1\, a_2 \qquad (1)$$

where $a_1$ and $a_2$ are the lengths of the two sides of the rectangular specimen, and $\ell$ is its thickness.

**Table 3a.** Extent of saturation with time ($t_s$) under atmospheric pressure

| Sample/ Specimen | $t_s$ (min) | $W_r$ (g) | $\Delta W_r$ (mg) | $S_r$ (%) |
|---|---|---|---|---|
| KP-2/3 | 0 | 10.1184 | 6.4 | 15.2 |
| | 60 | 10.1531 | 41.1 | 97.6 |
| | 90 | 10.1531 | 41.1 | 97.6 |
| | 120 | 10.1533 | 41.3 | 98.1 |
| | 150 | 10.1534 | 41.4 | 98.3 |
| | 180 | 10.1534 | 41.4 | 98.3 |
| | 210 | 10.1540 | 42.0 | 99.8 |
| | 240 | 10.1540 | 42.0 | 99.8 |
| | 270 | 10.1540 | 42.0 | 99.8 |
| | 1350 | 10.1541 | 42.1 | 100.0 |
| | 1470 | 10.1541 | 42.1 | 100.0 |
| | 1770 | 10.1541 | 42.1 | 100.0 |
| | 2790 | 10.1541 | 42.1 | 100.0 |
| KP-3/3 | 0 | 13.9773 | 6.6 | 33.0 |
| | 30 | 13.9847 | 14.0 | 70.0 |
| | 60 | 13.9862 | 15.5 | 77.5 |
| | 90 | 13.9864 | 15.7 | 78.5 |
| | 150 | 13.9873 | 16.6 | 83.0 |
| | 270 | 13.9900 | 19.3 | 96.5 |
| | 390 | 13.9900 | 19.3 | 96.5 |
| | 1410 | 13.9900 | 19.3 | 96.5 |
| | 1650 | 13.9900 | 19.3 | 96.5 |
| | 1830 | 13.9900 | 19.3 | 96.5 |
| | 2860 | 13.9904 | 19.7 | 98.5 |
| | 3220 | 13.9907 | 20.0 | 100.0 |
| | 10000 | 13.9907 | 20.0 | 100.0 |

### *Effective porosity measurements*

Effective porosity in principle includes the pore volume of all interconnected pores, and is determined from the difference in weight between the oven-dried and water saturated rock specimen (Katsube, 1981). The effective porosity, $\Phi_E$, is derived using the following equation:

$$\Phi_E = \delta_r (W_M - W_D) / (\delta_W W_D) \quad (2)$$

where $W_w$, $W_D$ and $\delta_r$ are the wet weight, dry weight and bulk density of the rock sample, respectively, and $\delta_W$ is the density of the pore water. A separate study shows the porosity variation within a sample to be 10% for gneisses (Wadden and Katsube, 1982). Long duration times for saturating and oven drying have been used to determine $W_w$ and $W_D$, following the recommended practices for tight rocks described in Katsube and Scromeda (1991). The Recommended Practice for Core-Analysis Procedures (API, 1960) has generally been followed for these practices. Further details of the technique, including its advantages and limitations are described in Katsube et al. (1992). The methods used to determine bulk density, $\delta$, of regular and irregular shaped specimens for porosity measurements are also described in that paper.

The duration times for drying and degassing under vacuum, for saturating under atmospheric pressure, and for heat treatment are represented by $t_I$, $t_s$, and $t_D$, respectively, and are expressed in minutes. The weight of a specimen at any given duration time is represented by $W_r$ in grams. When $W_r$ reaches a constant value during the saturation process, the sample is considered to be fully saturated and its weight is represented by $W_W$. When $W_r$ reaches a constant value during oven drying, the sample is considered to be completely dried and its weight is represented by $W_D$. The weight difference between $W_r$ and $W_D$ is $\Delta W_r$:

$$\Delta W_r = W_r - W_D. \quad (3)$$

The degree of saturation, $S_r$, is the weight of the water content ($\Delta W_r$) at any given duration time over the weight of the maximum water content ($W_W - W_D$), and is expressed as follows:

$$S_r = \Delta W_r / (W_W - W_D). \quad (4)$$

**Table 3b.** Extent of saturation with time ($t_s$) under atmospheric pressure

| Sample/ Specimen | $t_s$ (min) | $W_r$ (g) | $\Delta W_r$ (mg) | $S_r$ (%) |
|---|---|---|---|---|
| KP-4/3 | 0 | 14.5743 | 15.1 | 48.6 |
| | 30 | 14.5853 | 26.1 | 83.9 |
| | 60 | 14.5857 | 26.5 | 85.2 |
| | 120 | 14.5863 | 27.1 | 87.1 |
| | 240 | 14.5875 | 28.3 | 91.0 |
| | 360 | 14.5881 | 28.9 | 92.9 |
| | 420 | 14.5890 | 29.8 | 95.8 |
| | 1440 | 14.5892 | 30.0 | 96.5 |
| | 1740 | 14.5903 | 31.1 | 100.0 |
| | 8580 | 14.5903 | 31.1 | 100.0 |
| KP-5/3 | 0 | 3.2319 | 2.6 | 27.7 |
| | 30 | 3.2347 | 5.4 | 57.5 |
| | 90 | 3.2353 | 6.0 | 63.8 |
| | 150 | 3.2353 | 6.0 | 63.8 |
| | 280 | 3.2355 | 6.2 | 66.0 |
| | 340 | 3.2361 | 6.8 | 72.3 |
| | 430 | 3.2362 | 6.9 | 73.4 |
| | 1450 | 3.2363 | 7.0 | 74.5 |
| | 1630 | 3.2363 | 7.0 | 74.5 |
| | 1870 | 3.2363 | 7.0 | 74.5 |
| | 3010 | 3.2367 | 7.4 | 78.7 |
| | 3250 | 3.2376 | 8.3 | 88.3 |
| | 3960 | 3.2387 | 9.4 | 100.0 |

**Table 4.** Extent of saturation with vacuum drying time ($t_I$)

| Sample/ Specimen | $t_I$ (min) | $W_r$ (g) | $\Delta W_r$ (mg) | $S_r$ (%) |
|---|---|---|---|---|
| KP-2/3 | 0 | 10.1541 | 42.1 | 100.0 |
| | 15 | 10.1238 | 11.8 | 28.0 |
| | 30 | 10.1196 | 7.6 | 18.1 |
| | 115 | 10.1161 | 4.1 | 9.7 |
| | 175 | 10.1155 | 3.5 | 8.3 |
| | 235 | 10.1148 | 2.8 | 6.7 |
| | 295 | 10.1146 | 2.6 | 6.2 |
| | 415 | 10.1142 | 2.2 | 5.2 |
| KP-3/3 | 0 | 13.9896 | 18.9 | 94.5 |
| | 15 | 13.9854 | 14.7 | 73.5 |
| | 30 | 13.9846 | 13.9 | 69.5 |
| | 60 | 13.9836 | 12.9 | 64.5 |
| | 90 | 13.9831 | 12.4 | 62.0 |
| | 120 | 13.9828 | 12.1 | 60.5 |
| | 180 | 13.9820 | 11.3 | 56.5 |
| | 260 | 13.9820 | 11.3 | 56.5 |
| | 320 | 13.9809 | 10.2 | 51.0 |
| | 410 | 13.9806 | 9.9 | 49.5 |
| KP-4/3 | 0 | 14.5838 | 24.6 | 79.1 |
| | 15 | 14.5727 | 13.5 | 43.4 |
| | 30 | 14.5709 | 11.7 | 37.6 |
| | 60 | 14.5688 | 9.6 | 30.9 |
| | 90 | 14.5681 | 8.9 | 28.6 |
| | 120 | 14.5676 | 8.4 | 27.0 |
| | 180 | 14.5663 | 7.1 | 22.8 |
| | 260 | 14.5653 | 6.1 | 19.6 |
| | 320 | 14.5647 | 5.5 | 17.7 |
| | 410 | 14.5643 | 5.1 | 16.4 |
| KP-5/3 | 0 | 3.2347 | 5.4 | 54.5 |
| | 15 | 3.2308 | 1.5 | 16.0 |
| | 30 | 3.2307 | 1.4 | 14.9 |
| | 60 | 3.2306 | 1.3 | 13.8 |
| | 120 | 3.2304 | 1.1 | 11.7 |
| | 240 | 3.2304 | 1.1 | 11.7 |
| | 300 | 3.2304 | 1.1 | 11.7 |
| | 360 | 3.2302 | 0.9 | 9.6 |

**Table 5.** Extent of saturation with oven-drying time ($t_D$) at 105°C

| Sample/ Specimen | $t_D$ (min) | $W_r$ (g) | $\Delta W_r$ (mg) | $S_r$ (%) |
|---|---|---|---|---|
| KP-2/3 | 0 | 10.1147 | 2.7 | 6.4 |
| | 30 | 10.1123 | 0.3 | 0.7 |
| | 90 | 10.1121 | 0.1 | 0.2 |
| | 150 | 10.1120 | 0.0 | 0.0 |
| | 270 | 10.1120 | 0.0 | 0.0 |
| | 330 | 10.1120 | 0.0 | 0.0 |
| KP-3/3 | 0 | 13.9785 | 7.8 | 39.0 |
| | 30 | 13.9758 | 5.1 | 25.5 |
| | 60 | 13.9752 | 4.5 | 22.5 |
| | 120 | 13.9737 | 3.0 | 15.0 |
| | 240 | 13.9728 | 2.1 | 10.5 |
| (continued | 360 | 13.9720 | 1.3 | 6.5 |
| 19 hours | 540 | 13.9712 | 0.5 | 2.5 |
| later) | 660 | 13.9707 | 0.0 | 0.0 |
| KP-4/3 | 0 | 14.5655 | 6.3 | 20.3 |
| | 30 | 14.5617 | 2.5 | 8.0 |
| | 60 | 14.5611 | 1.9 | 6.1 |
| | 120 | 14.5604 | 1.2 | 3.9 |
| | 240 | 14.5598 | 0.6 | 1.9 |
| (continued | 360 | 14.5592 | 0.0 | 0.0 |
| 19 hours | 540 | 14.5595 | 0.3 | 1.0 |
| later) | 660 | 14.5592 | 0.0 | 0.0 |
| KP-5/3 | 0 | 3.2305 | 1.2 | 12.8 |
| | 30 | 3.2294 | 0.1 | 1.1 |
| | 60 | 3.2293 | 0.0 | 0.0 |
| | 140 | 3.2293 | 0.0 | 0.0 |
| | 260 | 3.2293 | 0.0 | 0.0 |
| | 350 | 3.2293 | 0.0 | 0.0 |
| KP-5/4 | 0 | 10.2919 | 3.9 | 6.8 |
| | 30 | 10.2885 | 0.5 | 0.9 |
| | 60 | 10.2881 | 0.1 | 0.2 |
| | 140 | 10.2881 | 0.1 | 0.2 |
| | 260 | 10.2881 | 0.1 | 0.2 |
| | 350 | 10.2880 | 0.0 | 0.0 |

**Table 6.** Final results of the effective porosity measurements

| Sample/ Specimen | δ (g/cc) | $W_W$ (g) | $W_D$ (g) | $S_{ir}$ (%) | $\phi_E$ (%) |
|---|---|---|---|---|---|
| KP-2/3 | 2.91 | 10.1541 | 10.1120 | 5.2 | 1.21 |
| KP-3/3 | 2.93 | 13.9907 | 13.9707 | 49.5 | 0.42 |
| KP-4/3 | 2.99 | 14.5903 | 14.5592 | 16.4 | 0.64 |
| KP-5/3 | 2.88 | 3.2387 | 3.2293 | 9.6 | 0.84 |

**Table 7a.** Complex electrical resistivity measurements

| Sample/ Specimen* | Sample Direction | Bulk Electrical Resistivity, $\rho_r$, ($10^3$ Ωm/t) Measurement (#1) | Measurement (#2) | Mean |
|---|---|---|---|---|
| KP-2/1 | DG | 12.67 /24:00 | 14.54 /48:00 | 13.61 |
| KP-2/2 | DG | 8.99 /24:00 | 11.85 /48:00 | 0.42 |
| KP-2/6 | V | 32.24 /23:40 | 32.22 /70:55 | 32.23 |
| KP-2/7 | P | 10.66 /23:25 | 13.57 /70:50 | 12.12 |
| KP-3/1 | P | 12.48 /24:20 | 13.53 /48:20 | 13.01 |
| KP-3/2 | P | 17.82 /24:00 | 19.12 /48:00 | 18.47 |
| KP-4/1 | V | 15.14 /24:40 | 15.77 /48:40 | 15.46 |
| KP-4/2 | P | 5.63 /24:00 | 6.03 /48:00 | 5.83 |
| KP-5/1 | X | 16.24 /25:00 | 16.41 /49:15 | 16.33 |
| KP-5/2 | X | 18.51 /24:00 | 24.31 /48:00 | 21.41 |

t: Saturation time, in hours, prior to measurement.
*: Specimens 1 and 2 are cut in different directions, except for KP-3/1 and KP-3/2 which are cut in the same directions.
V: Specimen slab cut parallel with foliation plane, implying that electrical current will flow in the vertical direction to foliation.
P: Specimen slab cut normal to foliation plane, implying that electrical current will flow parallel to foliation.
DG: Specimen slab cut diagonal to foliation.
X: Foliation not observed.

Further details of the technique are described in Katsube et al. (1992).

### *Complex resistivity and formation factor measurements*

The techniques used for the complex electrical resistivity and formation-factor measurements have previously been described (Katsube, 1981; Katsube and Walsh, 1987), and more recently in Katsube et al. (1991) and Katsube and Salisbury (1991).

The complex resistivity, $\rho^*$ (Katsube, 1975):

$$\rho^* = \rho_R + i\rho_I \quad (5)$$

where $\rho_R$ is the real resistivity and $\rho_I$ is the imaginary resistivity, is derived from the impedance $Z(\Theta)$ measurements by

$$\rho^* = K_G Z(\Theta), \quad (6)$$

**Table 7b.** Complex electrical resistivity measurements

| Sample/ Specimen* | Sample Direction | Bulk Electrical Resistivity, $\rho_r$, ($10^3$ Ωm/t) Measurement (#1) | Measurement (#2) | Mean |
|---|---|---|---|---|
| KP-2/4 | DG | 15.06 /24:00 | 22.30 /48:00 | 18.68 |
| KP-3/5 | P | 10.43 /24:20 | 13.60 /48:20 | 12.02 |
| KP-3/6 | V | 28.55 /24:00 | 34.34 /48:00 | 31.45 |
| KP-4/4 | V | 27.02 /24:40 | 27.23 /48:40 | 27.13 |
| KP-5/5 | X | 28.81 /24:00 | 30.87 /48:00 | 29.84 |

t: Saturation time, in hours, prior to measurement
*: Specimens 1 and 2 are cut in different directions, except for KP-3/1 and KP-3/2 which are cut in the same directions
V: Specimen slab cut parallel with foliation plane, implying that electrical current will flow in the vertical direction to foliation
P: Specimen slab cut normal to foliation plane, implying that electrical current will flow parallel to foliation
DG: Specimen slab cut diagonal to foliation
X: Foliation not observed
KP-2/4: Sample/specimen KP-2/1 cut in approximately half thickness
KP-3/5: Sample/specimen KP-3/1 cut in approximately half thickness
KP-3/6: Sample/specimen KP-3/1 cut in different direction
KP-4/4: Sample/specimen KP-4/1 cut in approximately half thickness
KP-5/5: Sample/specimen KP-5/1 cut in approximately half thickness

**Table 8.** Results of complex electrical resistivity data analysis

| Sample | Bulk Electrical Resistivity, $\rho_r$, ($10^3$ Ωm) Vertical to Foliation | Parallel to Foliation |
|---|---|---|
| KP-2 | 32.23 | 12.1 |
| KP-3 | 31.5 | 12.0 |
| KP-4 | 27.1 | 5.8 |
| KP-5 | 21.4 - 29.8 | |

*: No foliation

where $\Theta$ is the phase angle. The bulk rock resistivity, $\rho_r$, is determined from the complex resistivity ($\rho^*$), by the method described in Katsube (1975) and Katsube and Walsh (1987), or in more recent publications (e.g., Katsube, et al., 1991; Katsube and Salisbury, 1991).

The formation factor, F, is defined by the ratio of the bulk rock resistivity ($\rho_r$) over the pore fluid resistivity, $\rho_w$ (Archie, 1942), and is a parameter representing one of the pore structure characteristics of the rock. In order to eliminate the pore surface electrical conductivity effect (Patnode and Wyllie, 1950), F is actually derived by measuring the bulk resistivity ($\rho_r$) of the rock for solutions of different salinities (NaCl: 0.02, 0.05, 0.10, 0.20 and 0.50 N), and then inserting the results into an equation derived from the Patnode and Wyllie (1950, equation 1) equation:

$$1/F_a = 1/F + \rho_w/\rho_c \quad (7)$$

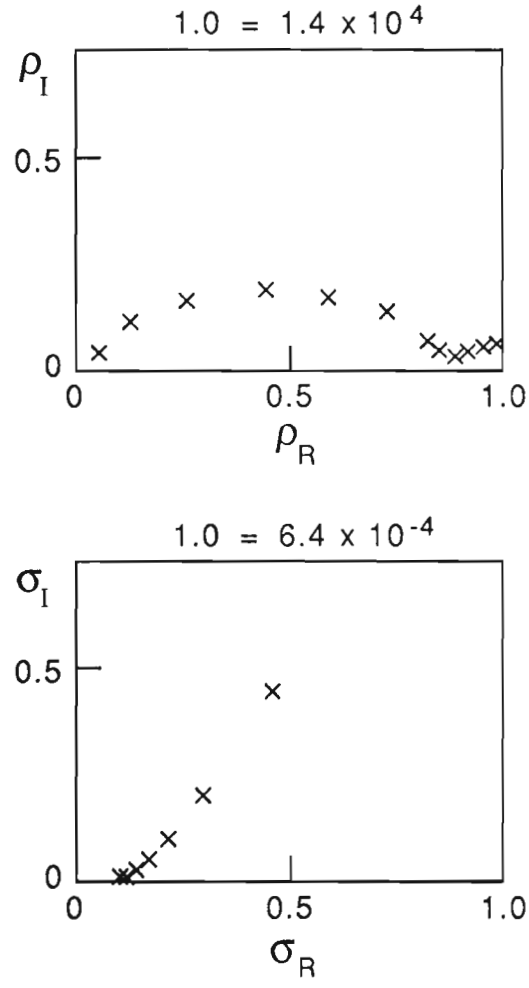


**Figure 2.** Typical example of the complex resistivity plots for sample/specimen KP-3/1 (I.D. = 85-16). The value of "1" at the top of the boxes containing the complex resistivity plots represent the full scale, and the values following the equal signs after it represents the resistivity value of the full scale in Ω·m for the upper box, and the conductivity in S/m for the lower box.

where

$F_a = \rho_r/\rho_w$

$\rho_c = F\rho_s d$

$F_a$ = apparent formation factor

$\rho_c$ = bulk surface resistivity

$\rho_s$ = surface resistivity

d = pore aperture.

Complex resistivity and formation-factor were determined at room temperature conditions. The errors for these parameters are estimated to be generally in the ranges of 10-20% and 20-40%, respectively (Wadden and Katsube, 1982; Katsube, 1981). Further details of the measuring procedures can be found elsewhere (Katsube, 1981; Katsube and Walsh, 1987; Katsube et al., 1991; Katsube and Salisbury, 1991).

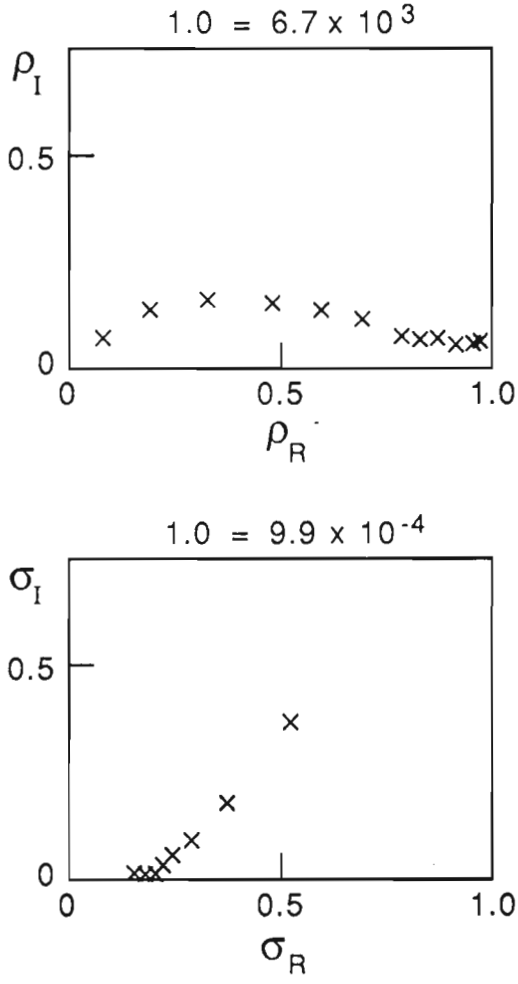


**Figure 3.** Typical example of the complex resistivity plots for sample/specimen KP-4/2 (I.D. = 79-215). The value of "1" at the top of the boxes containing the complex resistivity plots represent the full scale, and the values following the equal signs after it represents the resistivity value of the full scale in Ω·m for the upper box, and the conductivity in S/m for the lower box.

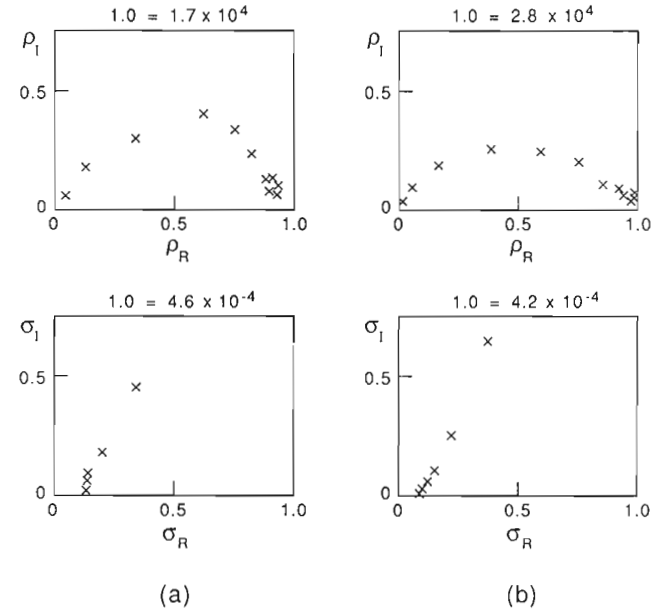


**Figure 4.** Complex resistivity plots for sample KP-4 (I.D. = 79-215) that shows an irregularly shaped arc which deviate from a semi-circle (a, sample/specimen KP-4/1). Complex resistivity plot for the same sample after the specimen thickness was reduced (b, sample/specimen KP-4/4). It now displays a regularly shaped arc. The meaning of the values at the top of the boxes are explained in Figures 2 and 3.

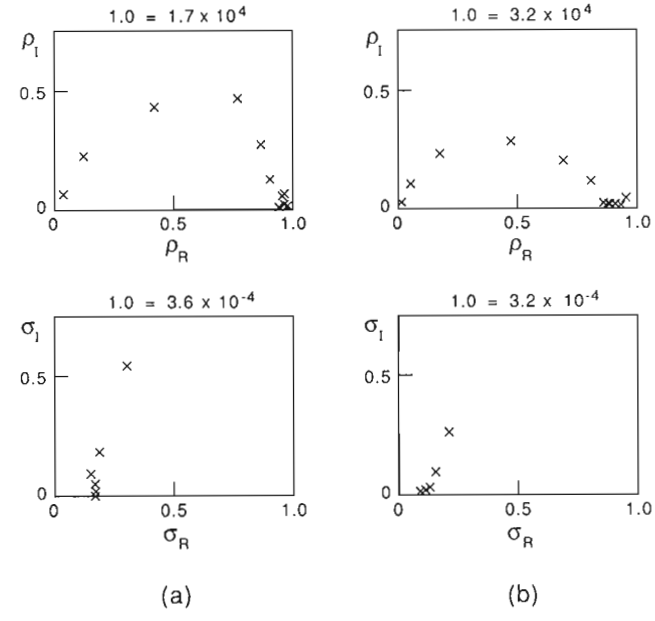


**Figure 5.** Complex resistivity plot for sample KP-5 (I.D. = 80-604) that shows an irregularly shaped arc which deviate from a semi-circle (a, sample/specimen KP-5/1). Complex resistivity plot for the same sample after the specimen thickness was reduced (b, sample/specimen KP-5/5). It now displays a regularly shaped arc. The meaning of the values at the top of the boxes are explained in Figures 2 and 3.

**Table 9.** Formation-factor, surface resistivity and bulk resistivities for different concentrations of NaCl solutions for the Kapuskasing samples

| Samples | $\rho_{rn}$ (x$10^3$ Ω–m) | | | | | F ±% (x$10^3$) | $\rho_c$ ±% (x$10^4$) (Ω–m) |
|---|---|---|---|---|---|---|---|
| $\rho_w$ (Ω–m) | 0.34 ±0.02 | 0.74 ±0.03 | 1.29 ±0.05 | 2.35 ±0.09 | 5.46 ±0.23 | | |
| NaCl (N) | 0.5 | 0.2 | 0.1 | 0.05 | 0.02 | | |
| KP-2/4,DG | 0.3 | 0.69 | 1.3 | 2.6 | 4.2 | 1.05±6.4 | 1.6 ±43.9 |
| KP-2/6,V | 0.24 | 0.92 | 1.1 | 1.8 | 3.5 | 1.05±23.6 | 0.74±67.9 |
| | | X | X | X | X | 1.20± 5.5 | 0.67±11.9 |
| | | | X | X | X | 0.93± 0.1 | 1.10± 0.5 |
| (*) | 0.21 | 0.51 | 1.1 | 2.3 | 4.2 | 0.63±13.9 | – |
| KP-2/7,P | 0.22 | 0.57 | 1.1 | 1.7 | 2.6 | 0.87±21.9 | 0.54±55.8 |
| | | X | X | X | X | 1.00± 1.8 | 0.51± 3.7 |
| (*) | 0.20 | 0.44 | 0.89 | 2.3 | 6.0 | 0.71±38.9 | 0.98±180. |
| KP-3/5,P | 1.1 | 2.5 | 4.6 | 6.8 | 8.0 | 4.6 ±3.0 | 1.2 ±3.9 |
| KP-3/6,V | 2.3 | 5.4 | 7.1 | 16. | 22. | 7.9 ± 8.7 | 4.3 ±21.3 |
| KP-4/2,P | 0.73 | 1.6 | 2.8 | 3.6 | 5.0 | 2.8 ± 1.3 | 0.72± 1.5 |
| KP-4/4,V | 1.3 | 3.3 | 6.0 | 10. | 18. | 4.8 ±5.7 | 5.6 ±31.6 |
| KP-5/2,x | 0.30 | 0.60 | 1.4 | 2.2 | 5.0 | 1.0 ± 329 | 1.8 ± 621 |
| (*) | 0.31 | 0.99 | 1.5 | 2.6 | 5.0 | 1.3 ±19.4 | 1.2 ±67.8 |
| | | X | X | X | X | 1.4 ± 0.6 | 1.5 ± 2.6 |
| KP-5/5,x | 0.29 | 0.58 | 0.95 | 1.7 | 3.7 | 0.84± 1.7 | 1.7 ±17.6 |

$\rho_w$ = pore fluid resistivity
$\rho_{rn}$ = bulk resistivity of the rock for solutions of different salinities
F = formation-factor
$\rho_c$ = surface resistivity
(*) = repeated measurements
X = data points used for formation factor determination
DG, V, P, x = direction of specimen (see Table 7 for details)

### *Mercury porosimetry*

The pore-size distribution of these samples was determined by mercury intrusion porosimetry, following the procedures described in previous publications (e.g. Katsube, 1981; Katsube and Walsh, 1987; Katsube and Hume, 1987a), but using an equilibration time of 45 seconds for each pressure step (usually 30 seconds). This technique was first suggested by Washburn (1921). The mercury porosimeter used for these measurements is capable of generating pressures high enough to force mercury into all accessible pores, and measure the volume of mercury taken up by them (Rootare, 1970). If the pores in a substance are assumed to be cylindrical, the Washburn equation (Rootare, 1970) can be used to relate the pressure, p, required to force the mercury into pores with pore-size (diameter), d, equivalent or greater than

$$d = -4\gamma \cos(\theta)/p, \qquad (8)$$

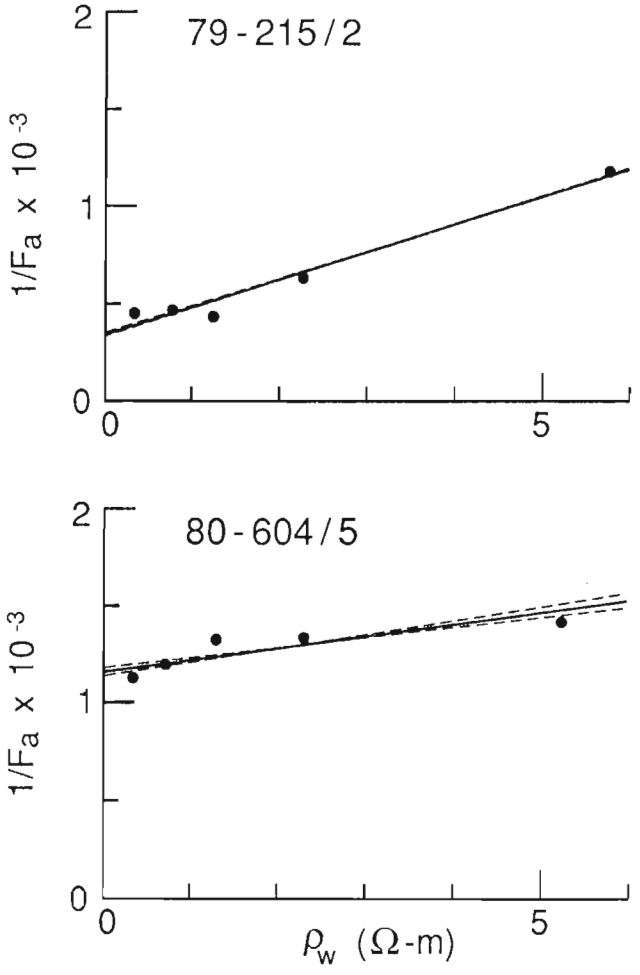


**Figure 6.** Typical examples of $1/F_a$ versus $\rho_w$ plots used for formation factor determination, for sample/specimens KP-4/2 (I.D. = 79-215) and KP-5/5 (I.D. = 80-604), with small errors for formation factor (F) and surface resistivity ($\rho_c$) values. The solid line is the reduced major axis, and the broken lines are the two normal regression lines.

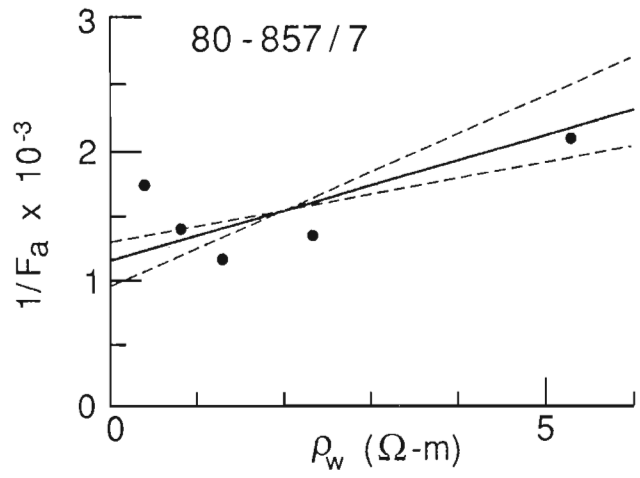


**Figure 7.** Typical examples of $1/F_a$ versus $\rho_w$ plots used for formation factor determination, for sample/specimen KP-2/7 (I.D. = 80-857), with larger errors for the formation factor (F) and surface resistivity ($\rho_c$) values. The solid line is the reduced major axis, and the broken lines are the two normal regression lines.

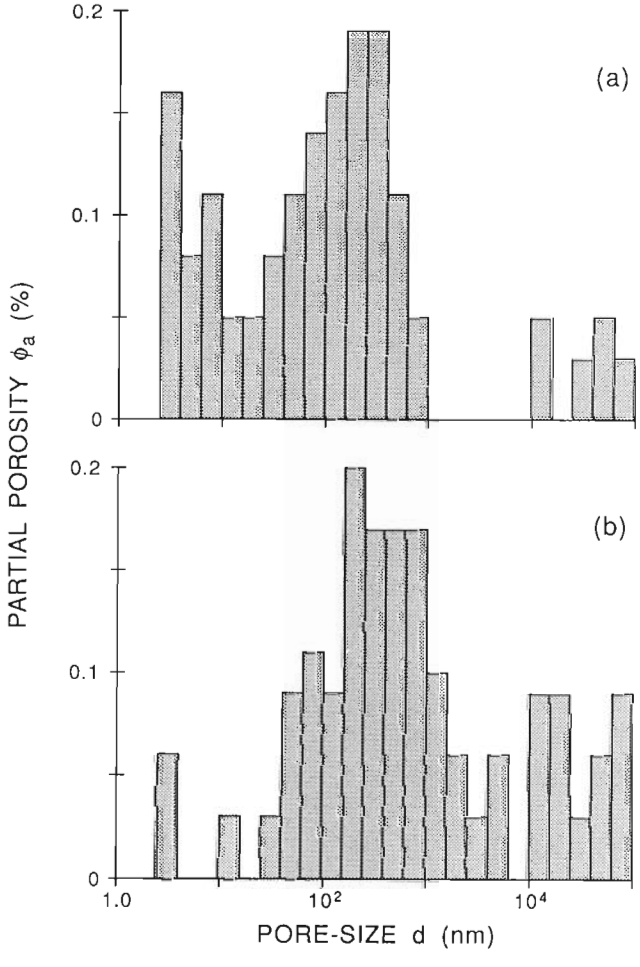


**Figure 8.** Pore-size distribution for samples (a) KP-1 [I.D. = PBA79-32], and (b) KP-4 [I.D. = 79-215].

**Table 10.** Pore-size distribution data for different pore-size ranges, d, obtained by mercury porosimetry for the 5 crystalline rock samples from the Kapuskasing Structural Zone

| Sample Number | KP-1 | KP-2 | KP-3 | KP-4 | KP-5 |
|---|---|---|---|---|---|
| d(nm) | | | $\phi_a$ (%) | | |
| 2.5-4.0 | 0.06 | 0.05 | 0.00 | 0.16 | 0.00 |
| 4.0-6.3 | 0.00 | 0.03 | 0.00 | 0.08 | 0.00 |
| 6.3-10 | 0.00 | 0.00 | 0.00 | 0.11 | 0.00 |
| 10- | 0.03 | 0.03 | 0.00 | 0.05 | 0.00 |
| 16- | 0.00 | 0.00 | 0.00 | 0.05 | 0.00 |
| 25- | 0.03 | 0.00 | 0.03 | 0.08 | 0.00 |
| 40- | 0.09 | 0.08 | 0.01 | 0.11 | 0.00 |
| 63- | 0.11 | 0.08 | 0.02 | 0.14 | 0.00 |
| 100- | 0.09 | 0.11 | 0.02 | 0.16 | 0.00 |
| 160- | 0.20 | 0.22 | 0.01 | 0.19 | 0.00 |
| 250- | 0.17 | 0.19 | 0.01 | 0.19 | 0.00 |
| 400- | 0.17 | 0.14 | 0.01 | 0.11 | 0.00 |
| 630- | 0.17 | 0.08 | 0.02 | 0.05 | 0.00 |
| 1000- | 0.11 | 0.00 | 0.03 | 0.00 | 0.06 |
| 1585- | 0.06 | 0.00 | 0.03 | 0.00 | 0.06 |
| 2512- | 0.03 | 0.00 | 0.02 | 0.00 | 0.06 |
| 3981- | 0.06 | 0.00 | 0.01 | 0.00 | 0.06 |
| 6310- | 0.00 | 0.03 | 0.03 | 0.00 | 0.08 |
| $\phi_{gm}$ | 1.71 | 1.40 | 0.47 | 1.71 | 0.62 |
| $d_{hg}$ | 766 | 489 | 2954 | 114 | 1296 |
| $\delta_D$ | 2.85 | 2.74 | 2.74 | 2.72 | 2.81 |

$\phi_a$ = Partial porosity (%)
d = Pore-size range (nm)
$\phi_{gm}$ = Total porosity measured by mercury porosimetry (%)
$d_{hg}$ = Mean (geometric) pore-size (nm)
$\delta_D$ = Density (g/cc)

where $\gamma$ is the surface tension of mercury, and $\Theta$ is the contact angle. Values of $\theta$ =30° and $\gamma$ =0.48 N/m have been used, with equilibration times of 10 and 30 seconds for low and high pressures, respectively. A good review of the technique is given in Rootare (1970). These measurements were made by ORTECH (Toronto, Ontario), using a Micromeretics, Auto Pore 9200, mercury porosimeter. The pressure range available is 0.14-420 MPa with an equivalent pore-size range of 10-0.003 $\mu$m.

## EXPERIMENTAL RESULTS

The results for $W_r$ at varying duration times of saturation ($t_s$), vacuum drying ($t_I$) and oven-drying ($t_D$) are listed in Tables 3, 4, and 5, respectively. Only the final results for saturation and oven-drying, that is $W_r$ at the maximum values of $t_s$ and $t_D$, are used to determine $W_W$ and $W_D$. The effective porosities ($\Phi_E$) derived from equations (2), using these values, and are listed in Table 6. The degree of saturation ($S_r$) calculated for the maximum value of $t_I$ is represented by the irreducible water saturation, $S_{ir}$, and is also listed in Table 6.

Two sets of complex resistivity measurements were carried out on each of the two to four specimens for all of the four samples. The results are listed in Table 7a. Typical examples of regular complex resistivity plots are shown in Figures 2 and 3. It was noticed that the complex resistivity plots for some of the specimens showed irregular shaped arcs deviating from semi-circles, as described in Figures 4a and 5a. These specimens coincided with those that showed extremely high impedance values, larger than $6 \times 10^5$ ohms, suggesting that the existence of interference from the leakage resistance ($10^7$ ohms) of the measuring system is the cause of these irregular shapes. In order to reduce the impedance of the specimens that showed high values and eliminate the interference, specimens that displayed irregular shaped arcs were cut to about half of their original thickness and

remeasured. The results are listed in Table 7b. As a result of this reduction in thickness, their complex resistivity plots showed regular arc shapes, as shown in Figures 4b and 5b. Sample/specimen KP-3/1 was cut into sample/specimens KP-3/5 and KP-3/6, the latter cut in a different direction. The thickness of KP-3/5 was reduced from that of KP-3/1 even though no irregular shaped arc was observed. This was to show that the normality of an arc does not change with reduction in thickness for a specimen initially displaying a normal shaped arc. The bulk resistivity values for specimens that displayed irregular shaped arcs were eliminated from the final analysis of the complex resistivity data, and therefore not included in the final results listed in Table 8.

Results of resistivity measurements used for formation factor determination by equation 7 are listed in Table 9. A good linear relationship exists between $1/F_a$ and $\rho_w$ (equation 7) for sample/specimens KP-3/5, KP-3/6, KP-4/2, KP-4/4, and KP-5/5, resulting in relatively small error ranges for formation factor (F) and surface resistivity ($\rho_c$) values of these samples. Typical examples of these results are shown in Figure 6. Poor linear relationships and relatively large error ranges for the formation factor (F) and surface resistivity ($\rho_c$) values are seen for sample/specimens KP-2/6, KP-2/7, and KP-5/2. A typical example is shown in Figure 7. Repeated measurements (see Table 9) for these sample/specimens did not result in significant improvements. Therefore, only a portion of each set of these measurements were used for formation factor determination. The data points above the "X's" in Table 9 were used for this purpose. The results of the final analysis of these measurements, including all other measurements, are listed in Table 10.

Preliminary results of the pore-size distribution measurements made by mercury porosimetry are presented in Table 10, for all 4 samples and an additional sample KP-1 used in Katsube et al. (1991). The partial porosity, $\Phi_a$, which is the porosity contributed by each pore-size range (e.g. 2.5-4.0 nm, 4.0-6.3 nm), is listed in the column under each sample. The total porosity measured by mercury porosimetry, $\Phi_{gm}$, listed near the bottom of the table, is the sum of the partial porosities ($\Phi_a$). The total porosity ($\Phi_{gm}$) is in the range of 0.47 to 1.7%, values similar to those of effective porosity ($\Phi_E$), except for sample KP-4 (Table 11) for which total porosity ($\Phi_{gm}$) is considerably larger than effective porosity ($\Phi_E$). Two examples of pore-size distributions shown in Figure 8 depict a rather complex distribution, similar to those previously reported for crystalline rocks (Agterberg et al., 1984; Katsube and Hume, 1987a). The pore-sizes (d) are in the range of 3 to 10 000 nm, values similar to those of crystalline rocks (Katsube and Hume, 1987a). The geometric mean ($d_{hg}$) of the pore-sizes are in the order of 100-3000 nm (Table 10 and 11), the maximum value being considerably larger than those previously reported for similar rocks (Katsube and Hume, 1987a; Katsube, 1991). This is because pore-sizes above $10^4$ nm have been included in the geometric mean ($d_{hg}$) determination, a pore-size range usually not included. If excluded, they are expected to produce results similar to those previously reported (Katsube, 1991).

**Table 11.** Summary of measurements

(a)

| Samples | $\delta$ (g/cm$^3$) | $S_{ir}$ (%) | $\phi_E$ (%) | $\phi_{gm}$ (%) | $d_{hg}$ (nm) |
|---|---|---|---|---|---|
| KP-2 | 2.91 | 5.2 | 1.21 | 1.40 | 489 |
| KP-3 | 2.93 | 49.5 | 0.42 | 0.47 | 2954 |
| KP-4 | 2.99 | 16.4 | 0.64 | 1.71 | 114 |
| KP-5 | 2.88 | 9.6 | 0.84 | 0.62 | 1296 |

(b)

| | $\rho_r$ ($10^3$ Ωm) | | F ($10^3$) | | $\rho_c$ ($10^3$ Ωm) | |
|---|---|---|---|---|---|---|
| Samples | V | P | V | P | V | P |
| KP-2 | 32.2 | 12.1 | 0.93 | 1.0 | 11.0 | 5.1 |
| KP-3 | 31.5 | 12.0 | 7.0 | 4.6 | 43.0 | 12.0 |
| KP-4 | 27.1 | 5.8 | 4.8 | 2.8 | 56.0 | 7.2 |
| KP-5* | 21.4 - 29.8 | | 0.84 - 1.4 | | 17.0 - 15.0 | |

V = Measurement made in the direction vertical to foliation.
P = Measurement made in the direction parallel to foliation.
$\phi_{gm}$ = Total porosity measured by mercury porosimetry.
$d_{hg}$ = Mean (geometric) pore-size (nm).
* = No foliation.

## DISCUSSION AND CONCLUSIONS

The effective porosities ($\Phi_E$, Tables 6 and 11) of these samples range from 0.64 to 1.21%, values common for crystalline rocks (Katsube et al., 1985; Katsube and Hume, 1987a). The irreducible water saturation ($S_{ir}$) shows a wide range of variation, 5.0 to 49.5%. In principle, the lower values indicate larger pores and smaller surface areas, and the higher values indicating smaller pores, larger surface areas, and the existence of alteration products. The pore-sizes obtained by mercury porosimetry are in the range of 3 to 10 000 nm. The geometric mean ($d_{hg}$) data determined from the preliminary analysis of the pore-size distribution data (Table 11) do not necessarily support the results of the irreducible water saturation ($S_{ir}$), suggesting further analysis of the data.

Bulk resistivities ($\rho_r$, Table 9) show strong directional effects, except for sample number KP-5 which is an anorthosite with no foliation. Bulk resistivities normal (vertical direction) to the plane of foliation range from $2 \times 10^4$ to $3 \times 10^4$ Ω·m, values which are similar to the sample that has no directional effect (sample KP-5), and which are slightly smaller than those commonly observed for these types of rocks (Katsube et al., 1991; Katsube et al., 1985; Katsube and Hume, 1987a, b, 1989). Bulk resistivities (Table 9) parallel to the foliation range from $6 \times 10^3$ to $1.2 \times 10^4$ Ω·m, 3 to 5 times smaller than those for the vertical direction. The values for the parallel direction are considerably smaller than those commonly observed for these types of rocks.

The formation factor (F) and surface resistivity ($\rho_c$) show clear directional effects for samples KP-3 and KP-4 (Table 11). Values for the parallel direction are about one half those of the vertical direction for the formation factor (F), and about one third to one seventh for the surface resistivity ($\rho_c$). No directional effects for formation factor (F) but a slight one for the surface resistivity ($\rho_c$) is seen for KP-2. There are indications that the lower surface resistivity ($\rho_c$) values for the parallel direction of these samples is the cause of their directional effect of the bulk resistivity ($\rho_r$). For example, although the formation factor (F) shows no directional effect for sample KP-2 (Table 11), its surface resistivity ($\rho_c$) is about half that of the parallel direction, a trend that agrees with the directional effect of its bulk resistivity ($\rho_r$).

## ACKNOWLEDGMENTS

The authors thank J.A. Percival (Geological Survey of Canada) for providing geological information regarding the samples used in this study. The authors are grateful to Dr. Q. Bristow (Geological Survey of Canada) for critically reviewing this paper and for his comments. The authors also thank J.P. Frechette (Geological Survey of Canada) for the assistance that he provided for the electrical measurements.

## REFERENCES

**Agterberg, F.P., Katsube, T.J., and Lew, S.N.**
1984: Statistical analysis of granite pore size distribution data, Lac du Bonnet batholith, eastern Manitoba; in Current Research, Part A; Geological Survey of Canada, Paper 84-1A, p. 29-38.

**API (American Petroleum Institute)**
1960: Recommended practices for core-analysis procedure; API Recommended Practice 40 (RP 40) First Edition, American Petroleum Institute, Washington, D.C., p. 55.

**Archie, G.E.**
1942: The electrical resistivity log as an aid in determining some reservoir characteristics; Transactions of the American Institute of Mining, Metallurgical and Petroleum Engineers, v. 146, p. 54-67.

**Bailey, R.C., Craven, J.A, Macnae, J., and Polzer, B.**
1989: Imaging deep fluids in Archean crust; Nature, v. 340, p. 136-138.

**Jones, A.G**
in press: Electrical properties of the continental lower crust; in The Lower Continental Crust, (ed.) D.M. Fountain, R.J. Arculus, and R.W. Kay; Elsevier.

**Katsube, T.J.**
1975: The electrical polarization mechanism model for moist rocks; Geological Survey of Canada, Paper 75-1C, p. 353-360.
1981: Pore structure and pore parameters that control the radionuclide transport in crystalline rocks; Proceedings of the Technical Program, International Powder and Bulk Solids Handling and Processing, Rosemont, Illinois, p. 394-409.
1991: Petrophysical characteristics of granites, shales and gabbros, and their significance in nuclear fuel waste containment; in Proceedings of "1991 Joint International Waste Management Conference, Vol. 2", Seoul, Korea, p. 313-320.

**Katsube, T.J. and Hume, J.P.**
1987a: Pore structure characteristics of granitic rock samples from Whiteshell Research Area; in Geotechnical Studies at Whiteshell Research Area (RA-3); CANMET, Report MRL 87-52, p. 111-158.
1987b: Electrical properties of granitic rocks in Lac du Bonnet batholith; in Geotechnical Studies at Whiteshell Research Area (RA-3); CANMET, Report MRL 87-52, p. 205-220.
1989: Electrical resistivity of rocks from Chalk River; in Workshop Proceedings on "Geophysical and Related Geoscientific Research at Chalk River, Ontario", Atomic Energy of Canada Limited, Report AECL-9085, p. 105-114.

**Katsube, T.J. and Mareschal, M.**
in press: Petrophysical model of deep electrical conductors in Precambrian crusts; graphite lining as a source and its disconnection due to uplift; Journal of Geophysical Research.

**Katsube, T.J. and Salisbury, M.**
1991: Petrophysical characteristics of surface core samples from the Sudbury structure; in Current Research, Part E; Geological Survey of Canada, Paper 91-1E, p. 265-271.

**Katsube, T.J. and Scromeda, N.**
1991: Effective porosity measuring procedure for low porosity rocks; in Current Research, Part E; Geological Survey of Canada, Paper 91-1E, p. 291-297.

**Katsube, T.J. and Walsh, J.B.**
1987: Effective aperture for fluid flow in microcracks; International Journal of Rock Mechanics and Mining Sciences and Geomechanics Abstracts, v. 24, p. 175-183.

**Katsube, T.J., Mareschal, M., and Aucoin, F.**
1991: Electrical characteristics of a graphitic rock from the Kapuskasing Structural Zone; in Current Research, Part E; Geological Survey of Canada, Paper 91-1E, p. 257-263.

**Katsube, T.J., Percival, J.B., and Hume, J.P.**
1985: Characterization of the rock mass by pore structure parameters; Atomic Energy of Canada Limited Technical Record, TP-299, p. 375-413.

**Katsube, T.J., Scromeda, N., and Williamson, M.**
1992: Effective porosity of tight shales from the Venture Gas Field, offshore Nova Scotia; in Current Research, Part D; Geological Survey of Canada, Paper 92-1D, p. 111-119.

**Kurtz, R.D., Craven, J.A., Niblett, E.R., and Stevens, R.A.**
in press: A magnetotelluric study of the Kapuskasing Structural Zone; An upthrust cross-section of the Archean crust; Geophysics Journal International.

**Kurtz, R.D., Macnae, J.C., and West, G.F.**
1989: A controlled source, time-domain electromagnetic survey over an upthrust section of Archean crust in the Kapuskasing Structural zone; Geophysics Journal International, p. 195-203.

**Mareschal, M.**
1990: Electrical conductivity: the story of an elusive parameter, and of how it possibly relates to the Kapuskasing uplift (Lithoprobe, Canada); Exposed Cross-Sections of the Continental Crust, (ed.) M.H. Salisbury and D.M. Fountain; Kluwer Academic Publishers, Netherland, p. 453-468.

**Mareschal, M., Fyfe, W.S., Percival, J., and Chan, T.**
in press: Auger scans of Kapuskasing gneisses to constrain the source of lower-crustal conductivity; Nature.

**Patnode, H.W. and Wyllie, M.R.J.**
1950: The presence of conductive solids in reservoir rocks as a factor in electric log interpretation; Transactions of the American Institute of Mining, Metallurgical and Petroleum Engineers, v. 189, p. 47-52.

**Percival, J.A. and Card, K.D.**
1983: Archean crust as revealed in the Kapuskasing uplift, Superior Province, Canada; Geology, v. 11, p. 323-326.
1985: Structure and evolution of Archean crust in central Superior Province, Canada; in Evolution of Archean Supercrustal Sequences, (ed.) L.D. Ayres, P.C. Thurston, K.D. Card, and W. Weber, Geological Association of Canada, Special Paper, v. 28, p. 179-192.

**Rootare, H.M.**
1970: A review of mercury porosimetry; Perspectives of Power Metallurgy, v. 5, p. 225-252.

**Wadden, M.M. and Katsube, T.J.**
1982: Radionuclide diffusion rates in crystalline rocks; Chemical Geology, v. 36, p. 191-214.

**Washburn, E.W.**
1921: Note on a method of determining the distribution of pore sizes in a porous material; Proceedings of the National Academy of Science, v. 7, p. 115-116.

---

Geological Survey of Canada Project 870057

# Eastern Canada and National and General Programs

# Est du Canada et programmes nationaux et généraux

# Stratigraphic, structural, and metamorphic relations along the eastern margin of the Humber Zone, Corner Brook Lake map area, western Newfoundland[1]

**Peter A. Cawood[2] and Jeroen A.M. van Gool[2]**
**Continental Geoscience Division**

*Cawood, P.A. and van Gool, J.A.M., 1992: Stratigraphic, structural, and metamorphic relations along the eastern margin of the Humber Zone, Corner Brook Lake map area, western Newfoundland; in Current Research, Part E; Geological Survey of Canada, Paper 92-1E, p. 239-247.*

***Abstract***

*This area of the eastern internal domain of the Appalachian Humber Zone, contains six units: gneissic basement (Corner Brook Lake complex); marble and pelite (Breeches Pond Formation); gneisses of the Caribou Lake complex; metaclastic and meta-igneous rocks (South Brook Formation and the Steady Brook member); and Matthews Brook serpentinite – an isolated slice. Three fault-bounded, structural domains from west to east are: an east-dipping thrust belt; a central regional antiform; and a 1-2 km wide strip of steeply dipping rocks of Caribou Lake complex. Tectonic events involved early thrusting and folding ($D_1$), followed by ductile folding ($F_2$, $F_3$), formation of kink bands ($F_4$), and development of the central antiform ($F_5$). Brittle faults ($D_6$) crosscut all previous structures. Metamorphic grade increases from greenschist facies in the west to amphibolite facies around Corner Brook Lake. Greenschist facies retrogression occurs along the shore of Grand Lake. Main deformation and metamorphism is probably of mid-Paleozoic age. Late faulting and retrogression may be as young as Carboniferous.*

***Résumé***

*Ce secteur du domaine oriental intérieur de la zone appalachienne de Humber contient six unités: un socle gneissique (complexe de Corner Brook Lake), un marbre et une pélite (Formation de Breeches Pond), les gneiss du complexe de Caribou Lake, des roches métaclastiques et méta-ignées (Formation de South Brook et Membre de Steady Brook) et la serpentinite de Matthews Brook, qui constitue une écaille isolée. D'ouest en est, trois domaines structuraux limités par des failles sont les suivants: une zone de charriage de pendage est; une antiforme régionale centrale; et une bande de 1 à 2 km de large, composée de roches de fort pendage, appartenant au complexe de Caribou Lake. Des événements tectoniques ont eu lieu successivement, à savoir un épisode initial de charriage et de plissement ($D_1$), suivi d'un épsode de plissement ductile ($F_2$, $F_3$), de la formation de «kink bands» ($F_4$) et du développement de l'antiforme centrale ($F_5$). Des failles cassantes ($D_6$) traversent toutes les structures antérieures. Le degré de métamorphisme augmente du faciès des schistes verts à l'ouest au faciès des amphibolites aux alentours du lac Corner Brook. On observe une régression du faciès des schistes verts sur les rives du lac Grand. Le principal épisode de déformation et de métamorphisme date probablement du Paléozoïque moyen. La formation de failles et le métamorphisme régressif tardifs sont peut-être aussi récents que le Carbonifère.*

[1] Contribution to Canada-Newfoundland Cooperation Agreement on Mineral Development, 1990-1994, a subsidiary agreement under the Economic and Regional Development Agreement. Project funded by the Geological Survey of Canada.

[2] Centre for Earth Resources Research, Memorial University of Newfoundland, St. John's, Newfoundland A1B 3X5

## INTRODUCTION

The Corner Brook map sheet (12A/13) lies along the eastern margin of the Appalachian Humber Zone (Fig. 1), at its boundary with the Dunnage Zone. The Humber Zone is divided into a western external domain and an eastern internal domain on the basis of increasing deformation and metamorphism towards the eastern orogenic hinterland of the Appalachian Orogen (Williams, in press). The external domain lies in the northwest corner of the map sheet and consists of the Humber Arm allochthon and a carbonate-dominated cover succession unconformably overlying Grenville basement. Polydeformed, greenschist- to amphibolite-facies sedimentary and igneous rocks of the internal domain of the Humber Zone form the dominant rock assemblage of the map sheet (Fig. 1, 2). This sequence extends from around Corner Brook Lake east to Grand Lake and the Northern Harbour road and north to the Trans-Canada Highway. Igneous and sedimentary rocks of the Dunnage Zone are exposed on Glover Island in Grand Lake, and east of the lake. Humber and Dunnage zone rocks are juxtaposed along the Cabot Fault system which in the map area runs along the western arm of Grand Lake (Fig. 1). Carboniferous rocks of the Deer Lake Basin unconformably overlie the juxtaposed segments of the Humber and Dunnage zones along the northeast segment of the map sheet (Fig. 1, 2; Hyde, 1982).

Previous work within the Corner Brook map sheet has focused on the eastern margin of the Humber Arm allochthon and its relationship with the carbonate succession (Walthier, 1949; Cawood and Williams, 1986), and on the younger successor basin sequence (Hyde, 1982). Mapping within the internal domain of the Humber Zone and the adjoining Dunnage Zone rocks has been restricted to reconnaissance scale work (Kennedy, 1982; Knapp, 1982; Knapp et al., 1979; see also Hibbard, 1983). This paper reports the results of the first detailed mapping of the polydeformed schists and gneisses of the eastern Humber Zone in the Corner Brook region.

## GENERAL GEOLOGY

The distribution and interrelationship of rock units in the internal domain of the Humber Zone in the Corner Brook region is shown in Figure 2. Six lithostratigraphic units are recognized in this region: gneissic basement of the Corner Brook Lake complex, marbles and pelites of the overlying Breeches Pond formation, gneisses of the Caribou Lake complex, metaclastic and meta-igneous lithologies of the South Brook Formation of the Mount Musgrave Group, and the constituent Steady Brook member of this formation, and an isolated slice of ultramafic rocks, the Matthews Brook serpentinite. The Corner Brook Lake complex, the Steady Brook member and the Matthews Brook serpentinite are new units informally defined below. The Mount Musgrave Group was originally introduced as the Mount Musgrave formation by McKillop (1963) and Lilly (1963) and mapped in the Corner Brook Lake region by Kennedy (1982). Williams et al. (1985) raised the unit to group status, divisible into the basal arkoses of the Little North Pond Formation and the overlying psammitic and pelitic schists of the South Brook Formation (cf. Lilly, 1963). The Caribou Lake unit was originally defined as a formation by Kennedy (1982) but is redefined herein as a complex to reflect the variety of schistose to gneissic sedimentary and igneous lithologies within the unit and their uncertain primary interrelationships. The Breeches Pond formation was originally introduced by Kennedy (1982) as the Twillick Brook formation but is herein redefined and renamed.

## DESCRIPTION AND CORRELATION OF ROCK UNITS

The **Corner Brook Lake complex** consists of banded amphibolite and granodioritic gneiss along with minor quartzite and quartz-feldspar-mica psammitic paragneiss. Banding is parallel to the regional $S_1$ schistosity. The unit is well exposed in a series of thrust slices in the hills north and south of the Corner Brook Lake. In addition, a small block of the complex, consisting largely of amphibolite occurs in Matthews Brook at the northern end of the map sheet.

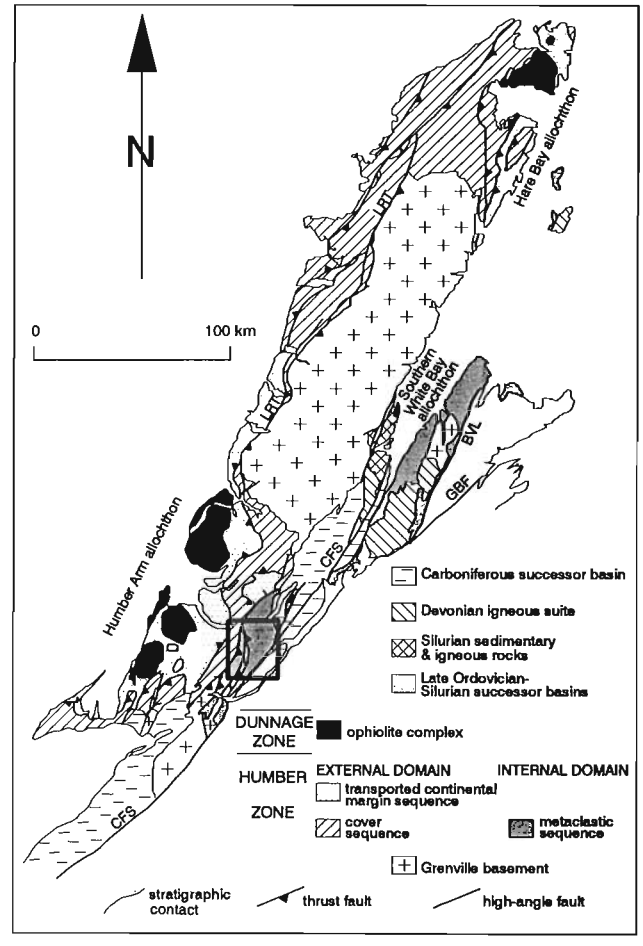


**Figure 1.** Simplified geological map of the Humber Zone in west Newfoundland. Box outlines location of Figure 2. Abbreviations: LRT - Long Range Thrust; BVL - Baie Verte Line; GBF - Green Bay Fault; CFS - Cabot Fault System.

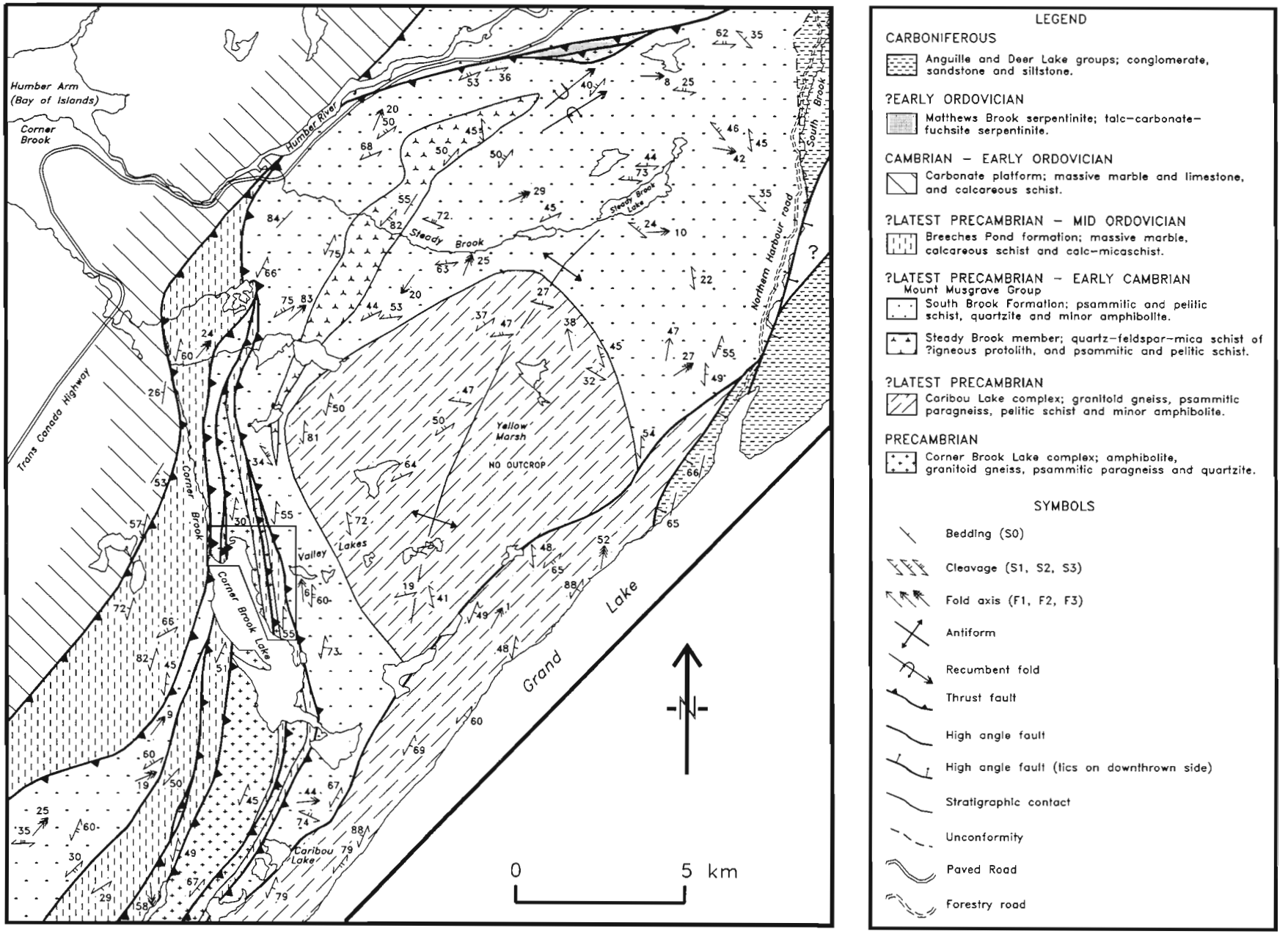


**Figure 2.** Geological map of the eastern Humber Zone in the Corner Brook Lake-Grand Lake region. Box at northeast end of Corner Brook Lake outlines area of Figure 3.

Amphibolite occurs in bands from several centimetres wide to, at least, 75 m thick. It consists of amphibole-plagioclase and amphibole-biotite schist locally with minor garnet. The granitoid gneiss consist of varying modal proportions of quartz, plagioclase, K-feldspar, amphibole, biotite, and minor muscovite, giving a compositional range from diorite to granodiorite to locally quartz monzonite. Small, centimetre-scale, pegmatitic sweats which predate the $S_1$ foliation occur within the gneiss. The relative proportions of amphibolite and granitoid gneiss are highly variable.

The Corner Brook Lake complex correlates with, and represents the along-strike extension of, the unnamed gneiss complex mapped south of Grand Lake by Currie (1987) and Piasecki (1991). The lithological character of the complex and its stratigraphic contact with the overlying the Breeches Pond formation, a deformed and metamorphosed equivalent of the carbonate sequence in the western Humber Zone, suggests that it constitutes part of the Grenville basement to the Appalachian Orogen.

The **Caribou Lake complex** lies in a belt along the western shore of Grand Lake and in a rectangular block extending north of Valley Lakes. It consists of massive to weakly banded granitoid gneiss, psammitic paragneiss, and pelitic schist, with minor amphibolite. The orthogneiss is of tonalitic to granodioritic composition consisting of quartz, plagioclase, biotite, and some muscovite. The gneiss is generally massive and ranges from equigranular to albite-porphyroblastic. It occurs in sheets parallel to the principal regional foliation ($S_1$) separated by pelitic and semipelitic schist. The schist consists of biotite, muscovite, quartz, and albite±garnet. The albite often occurs in porphyroblasts, locally up to 1 cm in diameter. Porphyroblasts are largest in the mica-rich pelitic lithologies. Amphibolite is a relatively minor phase and is best exposed along the shore of Grand Lake at the southern end of the map sheet, where it is interbanded with granitoid gneiss.

Northwestern outcrops of the Caribou Lake complex occupy the core of a regional dome, enveloped by psammitic schist of the Mount Musgrave Group. Although the contact between the two units is not exposed, the progressive increase in psammitic lithologies toward the contact and the absence of intense shearing suggests an original stratigraphic relationship between the two units. The latest Precambrian age for the Mount Musgrave Group (Williams et al., 1985) implies a similar or older age for the Caribou Lake complex. To the south, Currie (1987; see also Owen and Currie, 1991, Fig. 1) has correlated the along-strike extension of the Caribou Lake complex with the Hare Hill granite, dated at 617 ± 8 Ma (van Berkel and Currie, 1988). Alternatively, its similarity to the Corner Brook Lake complex may suggest that it represent part of Grenville basement (cf. Williams and St. Julian, 1978).

Carbonates, pelites and psammites of the **Breeches Pond formation** are restricted to a series of thrust slices along the western side of the map area. The unit is particularly well exposed in the hills and streams along the northeast side of Corner Brook Lake (Fig. 3). The unit is informally divided into a lower siliciclastic member and an upper carbonate dominated member.

The siliciclastic member of the Breeches Pond formation consists of granule to cobble conglomerate and psammitic to semipelitic schist. It occurs at the base of the formation, directly overlying the Corner Brook Lake complex. Although the basal contact is locally modified by faulting and shearing, clear stratigraphic contacts were observed in the thrust slices east of Corner Brook Lake which, combined with the presence of a localized basal conglomerate suggests an original unconformable contact. The conglomerate consists largely of quartz pebbles, occasionally up to 15 cm long, as well as minor feldspar and granitoid clasts in an arkosic matrix. The conglomerate is restricted to isolated exposures associated with the western-most slices of gneissic basement. It has a minimum thickness of about 10 m.

Psammitic and pelitic schists are the characteristic lithologies of the basal member of the Breeches Pond formation. In the amphibolite-facies thrust sheets east of Corner Brook Lake they occur in a 20-25 m thick band consisting of quartz-muscovite±biotite±garnet psammite

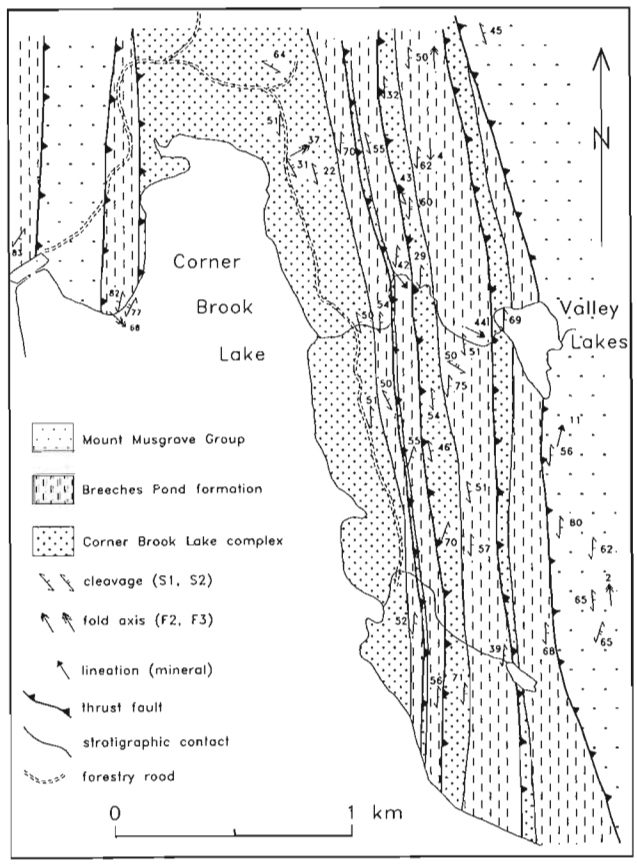


**Figure 3.** Detailed map of thrust belt along northeast side of Corner Brook Lake.

overlain by garnet-bearing quartz-muscovite schist which in turn passes up into a spectacular coarse grained and massive kyanite-garnet-staurolite-graphite-quartz-muscovite-graphite schist. Thin marble beds (<1 m) and amphibole-bearing mica schists, equivalents of calcareous pelites in the lower grade thrust sheets, are minor lithologies within this basal sequence.

The carbonate dominated member of the formation consists of marble, marble conglomerate, calcareous mica schist, mica-bearing carbonate, amphibole-bearing pelitic schist, minor graphitic schist and rare quartz-rich psammite. The ordering and proportion of the various carbonate and pelitic lithologies within this unit shows some variation both within and between thrust sheets. Outcrop is insufficient to resolve if this reflects primary facies variations and/or subsequent structural complexities. At the top of the Breeches Pond formation southeast of Corner Brook Lake, is an horizon of quartzite and quartz-bearing psammite at least 5 m thick.

The Breeches Pond formation corresponds with the Loon Pond metasediments (Martineau, 1980) and units CH1 and CH2 (Currie, 1987) recognized at the southern end of Grand Lake and farther south, and the Keystone schist on Glover Island (Knapp, 1982). The change from a lower siliciclastic dominated unit to a carbonate dominated unit within the Breeches Pond formation and related units probably corresponds with the rift-drift transition recognized in the western cover sequence (Williams and Hiscott, 1987).

The psammites and pelitic schist of the **Mount Musgrave Group** underlie the major portion of the high ground between Corner Brook Lake, the Northern Harbour road and the Trans-Canada Highway. In the map area, the majority of the rocks within the group belong to the **South Brook Formation** (Williams et al., 1985). These rocks are quartz-rich schists and are often characterized by a differentiated layering. They consist of quartz-muscovite±epidote schists, quartz-muscovite-albitebiotite± garnet psammitic and pelitic schists, quartzite and minor graphitic schist. Magnetite, tourmaline, and sphene are common accessory phases. A continuous horizon of quartzites was mapped along the high ridges south of the Trans-Canada Highway.

Immediately south of the quartzite horizon and extending southeast to Steady Brook and beyond towards Corner Brook Lake is a unit of massive quartz-feldspar-mica schist, interbanded with mica pelitic schist and quartz-feldspar psammite and granule metaconglomerate. This unit is herein informally referred to as the **Steady Brook member** of the South Brook Formation. The massive quartz-feldspar-mica schist is interpreted to represent a felsic igneous rock within the Mount Musgrave Group. At a number of localities it contains inclusions of amphibolitic composition which probably represent mafic igneous xenoliths. The member appears to pass gradationally into the surrounding lithologies of the South Brook Formation.

Williams et al. (1985) have shown that the Mount Musgrave Group in the Pasadena area to the northwest rests on late Precambrian granitoid dated by U/Pb zircon at 602 ± 10 Ma and mafic volcanic of the Hughes Lake Complex, implying a latest Precambrian or early Paleozoic age for the unit. The group is generally correlated with the latest Precambrian to early Cambrian rift facies lithologies in the western Humber Zone. The inferred igneous protolith for rocks of the Steady Brook member suggest these may be related to the Hughes Lake complex.

The **Matthews Brook serpentinite** lies at the northern end of the map sheet just east of the Trans-Canada highway. It is restricted to a narrow fault-bounded lens along, and immediately along strike from, the lower reaches of Matthews Brook (Fig. 2). The serpentinite is generally altered to an assemblage which includes talc, carbonate, magnesite, actinolite, chlorite, siderite, magnetite, fuchsite, and quartz. Asbestos fibres are locally present. The Matthews Brook serpentinite is juxtaposed against quartz-mica schist of the Mount Musgrave Group to the northwest and amphibolite with minor granitoid gneiss of the Corner Brook Lake complex to the southeast. Kennedy (1982) mapped a similar, but less altered lens of serpentinite, along a forestry track just south of the Corner Brook map sheet. This serpentinite occupies a similar structural position as the Matthews Brook serpentinite and is herein included within the unit.

## STRUCTURE

The eastern Humber Zone in the Corner Brook region constitutes a north-northeast striking belt of predominantly metaclastic rocks which can be subdivided into three fault-bounded structural domains (Fig. 4, inset). From west to east these are: an east dipping thrust belt; a central block deformed into a late regional antiform; and a 1-2 km wide strip of steeply dipping Caribou Lake complex along the shores of Grand Lake. The axis of the belt plunges slightly to the north-northeast, which is revealed in the map pattern of the central antiform (Fig. 2) and from the plunge of small scale and large scale fold axes (Fig. 4). The increase in exposure of basement rocks towards the south (cf. Currie, 1987) agrees with this observation.

The thrust belt in the western part of the map area (Fig. 2), named the Corner Brook Lake thrust belt, consists of a stack of thrust sheets which generally dip to the east. The thrust slices vary in width from less than 100 m to several kilometres. This variation in apparent thickness is partially caused by folding of the rocks in the horses and/or by an as yet unrecognized internal thrusting within the slices. The central antiformal structure plunges north-northeast and has massive rocks of the Caribou Lake complex in its core. The western limb of the antiform is overturned towards the thrust belt to the west. The structure is cut off to the southeast by the narrow belt of straight gneisses of the Caribou Lake complex.

### *Field relationships*

Structures of six different generations were recognized, which represent at least three tectonic events and can be correlated throughout the area. The sequence of events involves an early phase of thrusting and folding ($D_1$),

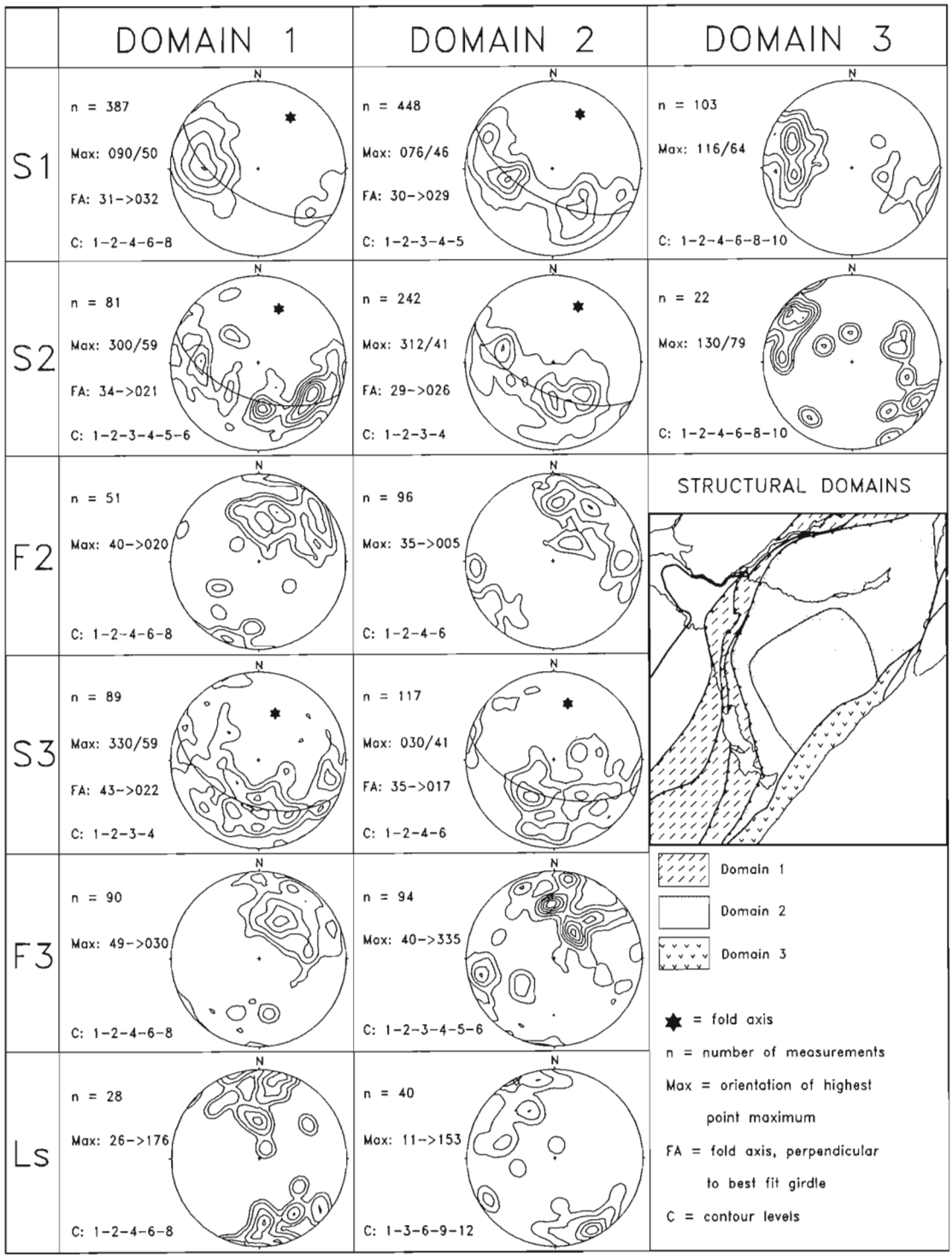


**Figure 4.** Stereographic plots of structural data from the Corner Brook Lake-Grand Lake region. Foliations ($S_1$, $S_2$, and $S_3$) are plotted as poles to planes and fold axes ($F_2$ and $F_3$) and elongation lineations ($L_s$) are plotted in lower hemisphere, equal area projection. Inset shows location of domains.

followed by a phase of ductile folding ($F_2$ and $F_3$) and formation of kink bands ($F_4$). The development of the central antiform does not appear to be related to any small scale structures and is tentatively interpreted as a separate event ($D_5$). The last event recognized in the area ($D_6$) is expressed in brittle faults and fractures, which crosscut all previous structures.

In a large part of the map area the **$S_1$** foliation and **$F_1$** folds are the oldest penetrative structures recognized (Fig. 5a). In massive quartzofeldspathic rocks and mica schists, $S_1$ is a penetrative schistosity of preferentially oriented micas and flattened quartz grains. In the quartz-muscovite schists of the Mount Musgrave Group, $S_1$ is generally a millimetre-scale differentiated layering, commonly subparallel to bedding, and isoclinal; rootless folds suggest that $S_0$ was transposed parallel to $S_1$. Most $F_1$ folds are isoclinal and have a well developed $S_1$ axial planar cleavage (Fig. 5a).

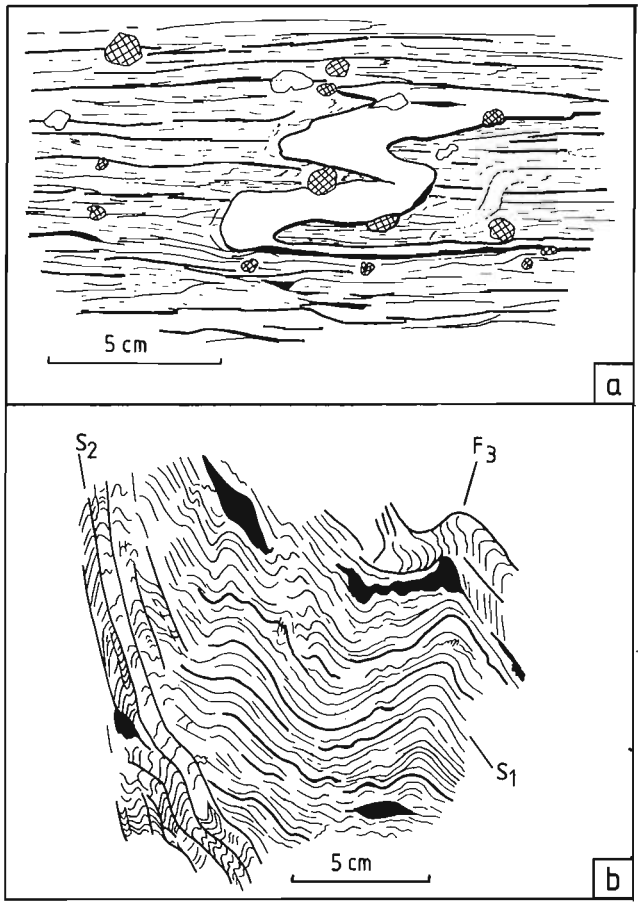


**Figure 5.** Sketches of small scale structures. a) $F_1$ isoclinal, rootless fold in a quartz vein in the South Brook Formation. The axial planar foliation is $S_1$. Garnet (cross-hatched) and plagioclase (white) porphyroblasts overgrow $S_1$. b) $S_1$ differentiated layering (throughout the figure), $S_2$ crenulation cleavage (left and top right) and $F_3$ folds (right hand half, steep axial plane) in quartz-muscovite schist of the South Brook Formation. Black areas are chorite-epidote schist.

During the second phase of deformation (**$D_2$**), $S_1$ was crenulated or folded, resulting in generally asymmetric folds with a wide range of interlimb angles and fold shapes. The axial planar cleavage ($S_2$) has characteristics similar to $S_1$ and forms either a new crenulation cleavage ($S_2$), which is a differentiated layering in quartz-muscovite schists (Fig. 5b), a second crosscutting schistosity of isolated micas, which locally crenulates the $S_1$, or a widely spaced fracture cleavage. On outcrop scale, $F_2$ folds are gentle to tight, mainly similar folds, with a well developed $S_2$ axial planar cleavage.

**$F_3$** folds are often spatially associated with $F_2$ crenulations and folds (Fig. 5b). The $S_2$ cleavage is locally overprinted by $F_3$ folds but $F_2$ - $F_3$ fold interference is rare. Fold styles of $F_2$ and $F_3$ are comparable, but $S_3$ cleavages are seldom developed. These observations suggest that these two fold generations are genetically associated.

Kink bands form a fourth generation of structures (**$F_4$**). They fold both $S_1$ and $S_2$, but overprinting relationships with $D_3$ structures are not observed. The association of $D_2$ and $D_3$ and the more brittle nature of the kink bands suggests that they are younger than $D_3$.

The large antiform (**$F_5$**) is interpreted as a structure formed in a separate event. It folds $S_1$, $S_2$, and $S_3$ foliations on a large scale and must be younger than these structures. No small scale folds are observed which can be related to the antiform. The age-relation with the $F_4$ kink bands is presently unknown.

The youngest structures are brittle fractures ($D_6$) and are observed throughout the area, but are most common in the eastern structural domain. The majority of these structures are high angle faults with offsets ranging from millimetres to tens of metres. The sense of movement, determined from slickensides, indicates either normal dip-slip or strike-slip displacement. Of the larger extensional faults, many are infilled by massive, coarse grained quartz, forming lenses up to several metres wide.

### *Orientation data*

Figure 4 shows the main structural elements plotted in lower hemisphere projection for each of the three structural domains. The data were contoured and, where applicable, best fit great circles were calculated by eigenvector-analysis. In spite of differences in structural setting, the data for domains 1 and 2 are similar. The data for domain 3 show a distinctly different distribution.

$S_1$, $S_2$ and $S_3$ planes in domains 1 and 2 all have a great circle distribution around a fold axis that plunges about 30 to 35° to the north-northwest, which is close to the orientation of the weakly defined point maxima of the $F_2$ and $F_3$ fold axes in the thrust belt. Orientations of $F_2$ and $F_3$ axes in domain 2 do not coincide very well with the calculated fold axes for $S_1$ and $S_2$ and have a larger spread than in domain 1. This is a result of refolding in the central antiform.

Elongation lineations ($L_s$), which are interpreted as being related to thrusting during $D_1$, were not commonly observed. Posttectonic recrystallization during metamorphism

destroyed the lineations in most of the belt. The few lineations that have been preserved indicate that the direction of elongation is oblique to the down-dip orientation of the $S_1$ planes, suggesting oblique thrusting or a rotation of the belt after the thrust event.

The orientation of foliations in domain 3 is fairly constant, steeply dipping towards the east-southeast. Few folds were observed and the most significant ones are large scale (hundreds of metres) gentle folds with subhorizontal fold axes and axial planes.

## METAMORPHISM

The eastern Humber Zone in the map area has been affected by at least one metamorphic event which ranged from greenschist to amphibolite facies and involved several phases of mineral growth. The metamorphic grade of the rocks in the adjoining carbonate cover sequence to the west is subgreenschist to lower greenschist facies. Through the thrust belt, the metamorphic grade increases rapidly eastward to amphibolite facies around Corner Brook Lake. In the central structural block and the strip of Caribou Lake complex along Grand Lake the metamorphic grade seems to be constant at amphibolite facies.

The variations in metamorphic grade across the map area are best expressed in the mineral assemblages in the pelitic and semi-pelitic beds of the Caribou Lake, Mount Musgrave and the Breeches Pond units. Figure 6 is a P-T diagram which shows an estimated metamorphic field gradient defined by these assemblages and a few of the relevant reaction curves. The structurally lowest, western thrust sheet, consisting of the Breeches Pond formation, contains a greenschist facies assemblage of co-existing muscovite-chlorite-biotite (Fig. 6, assemblage A). In the higher thrust sheets south and north of Corner Brook Lake, garnet and biotite (Fig. 6, assemblage B) are stable together, indicating upper greenschist to lower amphibolite facies. Pelites in the thrust sheets immediately east of Corner Brook Lake contain the assemblage garnet-kyanite-staurolite-muscovite (Fig. 6, assemblage C), typical for pelites in the medium pressure amphibolite facies. The assemblage garnet-staurolite-biotite-muscovite (Fig. 6, assemblage C) in pelites of the Caribou Lake complex in the central and eastern part of the area indicate similar metamorphic peak conditions in the remainder of the area. The curves for the formation and breakdown of staurolite within the kyanite field delimit the peak metamorphic conditions in the central and eastern part of the belt. These indicate a minimum pressure of about 3 kbar and a temperature of between 450 and 550°C.

Mineral assemblages in the calcareous schists in the western thrust belt show a similar variation in metamorphic conditions. In the lowest thrust sheets, quartz and carbonates co-exist in stable assemblages. In the higher thrust sheets, garbenschiefer occur in which late amphiboles replaced quartz and carbonate minerals.

Late growth of albite and/or biotite porphyroblasts occurred in most of the area in all silicate-dominated rock types. This late mineral growth is separated in time from the growth of the peak metamorphic minerals by a deformation event. Presently it is not clear whether these late phases represent a separate metamorphic event or a late pulse of mineral growth in one single event. Retrograde chloritization of the rocks occurs throughout the belt, but is most pervasive in the northwest near the floor thrust and along the shore of Grand Lake.

## TIMING OF METAMORPHISM AND DEFORMATION

Geometrical relationships between porphyroblasts and structural elements indicate that the peak of metamorphism in most of the belt occurred between $D_1$ and $D_2$. Garnet, kyanite, and staurolite, which roughly represent peak metamorphic conditions, have overgrown the $S_1$ foliation (Fig. 5a) and the $S_2$ foliation generally curves around these minerals. The albite porphyroblasts contain inclusions of the peak minerals and in some localities overgrow the $S_2$, but are also observed with $S_2$ wrapping around them. The albite porphyroblast growth postdates the peak of metamorphism but the timing with respect to $D_2$ varies due to variations throughout the area in timing of either the $D_2$ or the retrograde metamorphism. Late biotite porphyroblasts, which are up to several millimetres thick, overgrow all foliations in random orientations. They are a retrograde, post $D_3$ phenomenon.

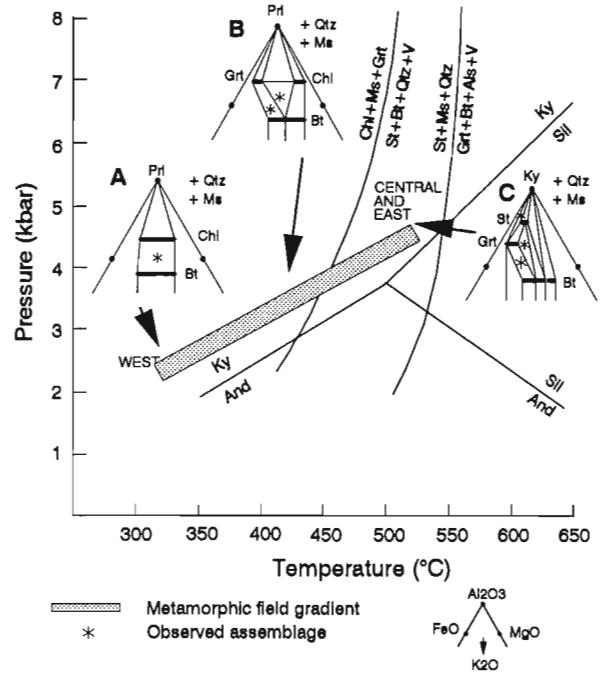


**Figure 6.** P-T diagram showing estimated metamorphic field gradient for the Corner Brook Lake-Grand Lake region. Schematic AFM diagrams with the observed assemblages and appropriate reaction curves are indicated for the different parts of the area at different conditions. Mineral name abbreviations according to Kretz (1983). Aluminum silicate stability fields from Holdaway (1971), staurolite-in and staurolite-out curves from Rivers (1983).

Absolute timing of metamorphism and deformation is poorly constrained. The continuity of metamorphic mineral facies and structural elements between the different lithological assemblages within the eastern Humber Zone requires metamorphism and deformation to postdate the youngest unit, the early Paleozoic Breeches Pond formation. An upper age limit is provided by the little deformed and generally unmetamorphosed Carboniferous lithologies of the Deer Lake basin. In addition, the greenschist facies retrogression of rock units along the shore of Grand Lake is probably related to Carboniferous movement on the Cabot Fault system implying a pre-Alleghanian age for peak metamorphism. K-Ar ages on muscovite from the Mount Musgrave Group near the Trans-Canada Highway give cooling ages of 437 ± 14 Ma and 420 ± 14 Ma (Wanless et al., 1973; recalculated to new constants). These ages, if correct, provide a Silurian upper age limit on metamorphism. Dunning et al. (1990) have recently shown the importance of the Silurian Salinic orogeny in southwest Newfoundland and the limited K-Ar data suggest this event may have also been important in the eastern Humber Zone.

## ACKNOWLEDGMENTS

We are indebted to Roger March and Jim Ryan for their assistance in the field work. Ken Currie, Greg Dunning, and Mark Piasecki visited the field area and provided stimulating discussion. We thank the city of Corner Brook and Corner Brook Pulp and Paper for permission to use private roads. Alvin Harris and Stuart Cochrane, Newfoundland Department of Mines gave access to Pasadena core storage library.

## REFERENCES

**Cawood, P.A. and Williams, H.**
1986: Northern extremity of the Humber Arm Allochthon in the Portland Creek area, western Newfoundland, and relationships to nearby groups: Current Research, Part A; Geological Survey of Canada, Paper 86-1A, p. 675-682.

**Currie, K.L.**
1987: A preliminary account of the geology of the Harry's River map-area, southern Long Range of Newfoundland; Geological Survey of Canada, Paper 87-1A, p. 653-662.

**Dunning, G.R., O'Brien, S.J., Colman-Sadd, S.P., Dickson, W.L., O'Neill, P.P., and Krogh, T.E.**
1990: Silurian Orogeny in the Newfoundland Appalachians; Journal of Geology, v. 98, p. 895-913.

**Hibbard, J.**
1983: Notes on the metamorphic rocks in the Corner Brook area (12A/13) and regional correlation of the Fleur de Lys Belt, western Newfoundland; Newfoundland Mineral Development Division, Current Research, Report 83-1, p. 41-50.

**Holdaway, M.J.**
1971: Stability of andalusite and the aluminum silicate phase diagram; American Journal of Science, v. 271, p. 97-131.

**Hyde, R.S.**
1982: Geology of the Carboniferous Deer Lake Basin; Mineral Development Division, Newfoundland Department of Mines and Energy, Map 82-7, scale 1:100 000.

**Kennedy, D.P.S.**
1982: Geology of the Corner Brook Lake area, western Newfoundland; MSc thesis, Memorial University of Newfoundland, St. John's, Newfoundland, 370 p.

**Knapp, D.**
1982: Ophiolite emplacement along the Baie Verte-Brompton Line at Glover Island, western Newfoundland; PhD thesis, Memorial University of Newfoundland, St. John's, Newfoundland, 338 p.

**Knapp, D., Kennedy, D., and Martineau, Y.**
1979: Stratigraphy, structure and regional correlation of rocks at Grand Lake, western Newfoundland; Geological Survey of Canada, Paper 79-1A, p. 317-325.

**Kretz, R.**
1983: Symbols for rock-forming minerals; American Mineralogist, v. 68, p. 277-279.

**Lilly, H.D.**
1963: Geology of the Hughes Brook-Goose Arm area, western Newfoundland; Memorial University of Newfoundland, Geology Report No. 2, 123 p.

**Martineau, Y.A.**
1980: The relationships among rock groups between the Grand Lake thrust and Cabot fault, western Newfoundland; MSc thesis, Memorial University of Newfoundland, St. John's, Newfoundland, 150 p.

**McKillop, J.H.**
1963: Geology of the Corner Brook area, Newfoundland, with emphasis on the carbonate deposits; Memorial University of Newfoundland, Geology Report No. 1, 102 p.

**Owen, J.V. and Currie, K.L.**
1991: The Disappointment Hill complex: Proterozoic granulites in southwestern Newfoundland; Transactions of the Royal Society of Edinburgh: Earth Sciences, v. 82, p. 55-63.

**Piasecki, M.A.J.**
1991: Geology of the southwest arm of Grand Lake, western Newfoundland; Current Research, Part D; Geological Survey of Canada, Paper 91-1D, p. 1-8.

**Rivers, T.**
1983: Progressive metamorphism of pelitic and quartzo-feldspathic rocks in the Grenville Province of western Labrador - tectonic implications of bathozone 6 assemblages; Canadian Journal of Earth Sciences, v. 20, p. 1791-1804.

**van Berkel, J.T. and Currie, K.L.**
1988: Geology of the Puddle Pond (12A/5) and Little Grand Lake map areas, southwestern Newfoundland; Newfoundland Department of Mines, Mineral Development Division, Report 88-1, p. 99-107.

**Walthier, T.N.,**
1949: Geology and mineral deposits of the area between Corner Brook and Stephenville, western newfoundland (Part I); Geology and mineral deposits of the area between Lewis Hills and Bay St. George, western Newfoundland (Part II); Newfoundland Geological Survey, Bulletin No. 35, 87 p.

**Wanless, R.K., Stevens, R.D., Lachance, G.R., and Delabio, R.N.**
1973: Age determinations and geological studies, K-Ar isotopic ages report 11; Geological Survey of Canada, Paper 73-2.

**Williams, H.**
in press: Temporal and spatial subdivisions of the rocks of the Canadian Appalachian Region; in Chapter 2 Geology of the Appalachian-Caledonian Orogen in Canada and Greenland, (ed.) H. Williams; Geological Survey of Canada, Geology of Canada, no. 6. (also Geological Society of America, Decade of North American Geology, v. F-1).

**Williams, H. and Hiscott, R.N.**
1987: Definition of the Iapetus rift- drift transition in western Newfoundland; Geology, v. 15, p. 1044-1047.

**Williams, H. and St. Julian, P.**
1978: The Baie Verte-Brompton Line in Newfoundland and regional correlations in the Canadian Appalachians; Current Research, Part A; Geological Survey of Canada, Paper 78-1A, p. 225-229.

**Williams, H., Gillespie, R.T., and van Breemen, O.**
1985: A late Precambrian rift-related igneous suite in western Newfoundland; Canadian Journal of Earth Sciences, v. 22, p. 1727-1735.

# The Noggin Cove Formation, Carmanville map area, northeast Newfoundland: a back-arc basin volcanic complex

**Dennis Johnston**[1]
**Continental Geoscience Division**

*Johnston, D., 1992: The Noggin Cove Formation, Carmanville map area, northeast Newfoundland: a back-arc basin volcanic complex; in Current Research, Part E; Geological Survey of Canada, Paper 92-1E, p. 249-257.*

***Abstract***

*The Noggin Cove Formation consists mainly of mafic volcanic conglomerates and coarse sandstones, with lesser amounts of medium-bedded tuffs, lapilli breccias, and subordinate pillowed basalt and black shale. The volume of fragmental rocks and the high proportion of fragmental volcanic rocks relative to primary volcanic rocks indicate an explosive volcanic source. Geochemical data strongly suggest a back-arc setting. Resedimented volcanic rocks were transported southward to form a marine volcaniclastic apron over pillowed basalt and mafic dykes.*

*The Carmanville Melange, and slumped to olistostromal shale and siltstone beds (Woody Island Sequence of Currie, 1992) are interpreted to overlie the Noggin Cove Formation. Slumping and olistostrome formation would be expected in the tectonic setting proposed, but it is possible that further disruption of the melanges records accretion of the back-arc basin to terranes farther east (Gander Zone).*

***Résumé***

*La Formation de Noggin Cove se compose principalement de conglomérats volcaniques mafiques et de grès grossiers, de quantités moindres de tufs à litage moyen, de brèches volcaniques à lapilli, et de quantités accessoires de basaltes en coussins et de shale noir. Le volume de roches détritiques et la forte proportion de roches volcaniques clastiques par rapport aux roches volcaniques primaires indique l'existence d'une source d'éruptions volcaniques explosives. Les données géochimiques indiquent nettement un contexte d'arrière-arc. Les roches volcaniques qui se sont redéposées ont été transportées vers le sud et forment une plaine d'épandage marine de type volcanoclastique au-dessus de basaltes en coussins et de dykes mafiques.*

*On considère que le mélange ophiolitique de Carmanville, et les couches de shale et de siltstone déformées ou formant des olistostromes (séquence de Woody Island telle que définie par Currie, 1992), recouvrent la Formation de Noggin Cove. On s'attend à des glissements et à la formation d'olistostromes dans le cadre tectonique proposé, mais il est possible que d'autres dérangements des mélanges ophiolitiques témoignent de l'accrétion du bassin d'arrière-arc à des terranes situés plus à l'est (zone de Gander).*

[1] Department of Earth Science, Memorial University of Newfoundland, St. John's, Newfoundland A1B 3X5

## INTRODUCTION

The Noggin Cove Formation (Williams et al., 1991), a sequence of mafic lavas and volcaniclastics, forms part of the Exploits Subzone of the Dunnage Zone (Williams et al., 1988). Detailed mapping of the Noggin Cove Formation was completed during the 1991 field season. Previous workers in this area considered the Noggin Cove Formation to be an allochthonous slice or raft in the Carmanville Ophiolitic Melange (Pajari et al., 1979) or a major structural slice whose emplacement may have controlled melange formation (Williams et al., 1991). This paper proposes that the Noggin Cove Formation is a portion of a back-arc basin volcanic complex that resulted from the rifting of an island arc. The spectacular debris flows of the Noggin Cove Formation record this rifting event as do the olistostromal Carmanville Melange and slumped and olistostromal beds of the Woody Island Sequence. The Carmanville melanges are interpreted as olistostromal based on their distribution, on the occurrence of bedding within the matrix, and on the interbedding and inter-folding of the melanges with volcanic rocks of the Noggin Cove Formation and with siltstones of the Woody Island Sequence. Relationships in the Beaver Cove area, and along the northern shorelines from Frederickton to Rocky Point, indicate the Carmanville melanges and Woody Island sequence form a stratigraphic succession above the Noggin Cove Formation.

## ROCK TYPES AND DISTRIBUTION

### *Noggin Cove Formation*

Volcanic conglomerates are volumetrically the most significant rock type of the Noggin Cove Formation. Vesicular to amygdaloidal basaltic clasts predominate; clasts are generally less than 30 cm but larger blocks, up to 60 cm in diameter occur. Rare, non-vesicular clasts in the conglomerates are presumed to be derived from the pillow lavas. Clasts are supported in a fine to coarse tuffaceous matrix; only rarely are conglomerates clast-supported. Thicknesses of the volcanic conglomerate beds range as high as 15 m, but generally are from 1 to 10 m. In many cases, large, vesicular, subrounded blocks are isolated in the fine to coarse tuffaceous matrix. The conglomerate beds are usually massive, but in some cases, the beds have a basal zone of crude reversed grading capped by a thicker upper zone of normal grading. In the thicker beds, a lower-central, very coarse zone of large, rounded vesicular blocks grades into an upper thicker section of very coarse- to coarse grained, volcanic sandstone. Rare intraclasts of medium bedded tuffs and massive conglomerate range to 4 m in size. The bottom contacts of the beds are generally non-erosive, even over very fine tuffs. Parallel lamination of coarse-grained volcanic sandstones occurs in the upper and lower parts of some conglomerate beds.

Collectively, the observations indicate that most of the volcanic conglomerates and coarse grained sandstones were deposited as debris flows. A very viscous matrix with plastic behavior is common for debris flows (Fisher, 1984) and explains the lack of sorting and common occurrence of large isolated blocks in conglomerates of the Noggin Cove Formation. The bed thicknesses are commonly 5 to 10 times the maximum fragment size for these debris flows, suggesting that the debris flows were subaqueous as opposed to subareal. Bed thicknesses of subareal debris flows are only 2 to 4 times the maximum fragment size (Fisher, 1984). Parallel laminated sandstones at the base and top of the debris flows indicate laminar flow. The massive central portions of the debris flows were likely transported largely intact (as a "plug") over basal laminar underflow. This could explain the occurence of large intraclasts in the conglomerates.

Debris flow conglomerates form almost all of the southern exposures of the Noggin Cove Formation. Minor, medium bedded, fine- to medium-grained tuffs found with the debris flows locally exhibit partial bouma sequences (a-c divisions) indicating deposition by turbidity currents. Reverse grading capped by normal grading in some beds suggests turbidity currents were highly concentrated, similar to the debris flows described above. Further north, the massive conglomerates are subordinate to mafic lavas and bedded tuffs.

Basaltic pillow lavas and flows, as well as mafic to ultramafic dykes are largely confined to the northern exposures of the Noggin Cove Formation (Fig. 1) although rare, small mafic dykes cut the massive conglomerates further south. Extensive outcrops of pillow lavas and mafic flows occur from Noggin Hill southward into Carmanville and southwest into Noggin Cove and trondhjemites intrude pillow lavas at Noggin Cove Head and in the town of Carmanville.

Minor lapilli breccias, consisting of angular basaltic clasts in a limestone matrix, and medium bedded, coarse grained, calcareous tuffs occur at Noggin Point, in Noggin Cove, and at Rocky Point. The tuffs have low to high angle cross-stratification. Interbedded with these rocks are black shales, siltstones, and a chaotic breccia of finely bedded siltstone clasts in a limestone matrix.

Small occurences of black shale are interbedded with volcanic conglomerates southwest of Carmanville, between Carmanville and the town of Noggin Cove, and along the east shoreline of Noggin Cove. This black shale resembles the matrix to the Carmanville Melange but does not contain any clasts and is not homogenized.

### *Melanges*

The Carmanville Melange that occur with the volcanic rocks of the Noggin Cove Formation have been described by previous workers (Pajari et al., 1979; Williams et al., 1991). The melanges occur only to the north of the volcanic rocks, except at Davidsville; they do not bound the southern contact of the Noggin Cove Formation. In some cases, the melanges are interbedded and inter-folded with the volcanics (e.g. Noggin Cove, Beaver Cove) or with siltstones and sandstones (e.g. Woody Island, Beaver Cove). In many cases, folded beds of siltstone can be seen within the black shale matrix of the melange (e.g. Davidsville, Noggin Cove, northeast of Frederickton); these beds within the matrix are commonly disrupted. Clasts of previously formed melange

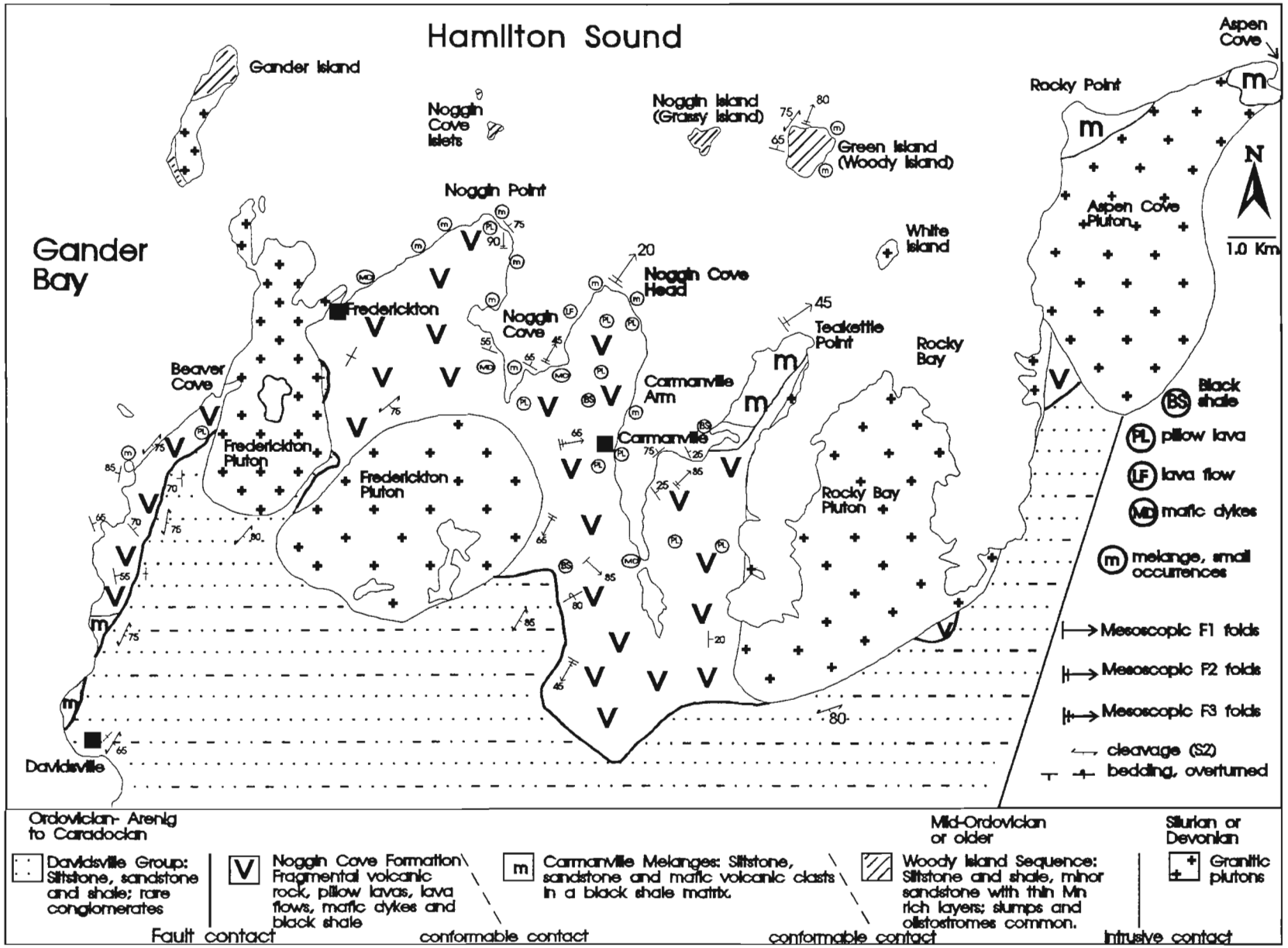


**Figure 1.** Geological map of the Noggin Cove Formation and surrounding units.

occur in melanges on the east side of Noggin Cove Head and on Woody Island. Along the east side of Noggin Point, melange with a homogenized green matrix is interbedded and gradational with a homogenized black shale matrix. A small occurrence of this green melange matrix is in contact with homogenized black shale on the east side of Noggin Cove Head. Blending occurs along the contacts and locally the black shale intrudes laterally into the green melange matrix. On the west side of Noggin Cove and on the east side of Noggin Cove Head, the black shale matrix locally pierces and appears to "bleed" through fragmental volcanic rock. A "melange dyke" cuts across bedding on Woody Island.

A salient feature of the melanges is the high proportion of siliceous siltstone and sandstone that occurs both blended into the matrix and as clasts. The proportions of volcanic, limestone, and trondhjemite clasts are much lower in comparison. Ultramafic rock occurs in slumped to olistostromal "beds" at Rocky Point and an ultamafic block occurs along strike of these "beds" at Aspen Cove.

## PROVENANCE

Southern exposures of the Noggin Cove Formation are almost exclusively massive debris flow conglomerates whereas in the northern exposures, the massive conglomerates are subordinate to pillow lavas and mafic dykes, medium bedded tuffs, lapilli breccias, and black shale. A southward flow direction is inferred from this distribution of debris flows. This is supported by a south-southwest flow direction obtained from imbricated clasts in bedded tuffs in Noggin Cove. The vesicular clasts of the debris flows indicate that the volcanic source to the north was subareal to shallow submarine (less than 200 m below water level, Fisher, 1984). Lapilli breccias, composed of very angular basaltic clasts in a calcite matrix, found only in the Noggin Cove area, were likely deposited in a shallow marine, relatively proximal setting to this eroding volcanic edifice. Similarly, medium bedded tuffs in Noggin Cove are predominantly angular and coarse grained, have low to high angle cross-stratification and are calcareous, suggesting shallow marine deposition. The following points provide further evidence in support of a northerly source. (1) Clast supported volcanic conglomerates occur only to the north (e.g. Noggin Cove). (2) Large intraclasts, up to 4 m in diameter, are more common in conglomerates to the north (e.g. Carmanville South, Noggin Cove). (3) A single occurence of large subrounded volcanic blocks, up to 0.6 m x 1.8 m in size, suspended in a fine grained, tuffaceous matrix, outcrops in the town of Noggin Cove; this "conglomerate" suggests mass wastage in a very proximal setting (Fig. 2).

## PETROLOGY/METAMORPHISM

Examination of thin sections of 35 samples from the Noggin Cove Formation reveals extensive greenschist facies metamorphism with little original mineralogy preserved. Fibrous amphibole (uralite) is very common, as is chlorite,

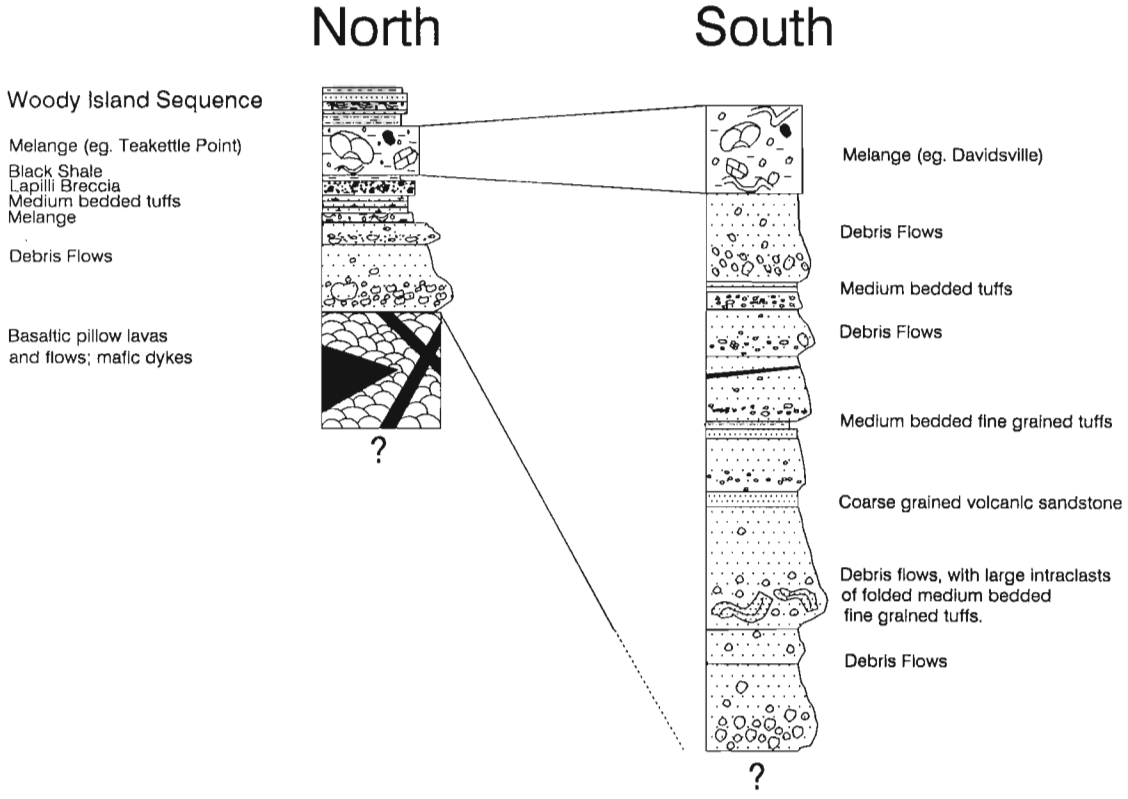


**Figure 2.** North versus south schematic stratigraphic sections of the Noggin Cove Formation, Carmanville melanges, and Woody Island Sequence.

calcite, and epidote. Secondary opaques are also very common and lesser amounts of sphene and biotite are present. In the fragmental volcanic rocks, secondary fibrous amphiboles are more common than chlorite in the clasts, whereas chlorite is more common in the matrix. Plagioclase is present in the pillow lavas, flows, and dykes but is sparse or absent in the fragmental volcanic rocks. In rare cases, original pyroxenes are preserved. Mafic intrusions in Noggin Cove and mafic blocks in a volcanic conglomerate from Carmanville South are highly serpentinized but rare ghost olivine crystals can be discerned. Bedded tuffs and lapilli breccias have abundant original calcite.

Electron microprobe, scanning electron microscope (SEM), and textural analyses of the pervasive secondary amphiboles indicate an earlier phase of greenschist facies metamorphism (tremolite/hornblende, amphibole classification, Currie, 1991) is overprinted by a later phase of contact metamorphism (edenite). These two phases can be distinquished on the SEM. The greenschist phase is irregular in outline and is overprinted by prismatic blades of edenite. Many amphiboles are zoned: cores of tremolite/hornblende compositions have rims of edenite composition.

## STRUCTURE

### *$F_1$ folds*

Mesoscopic $F_1$ folds are commonly tight to isoclinal, intrafolial, and in many cases are attenuated or disrupted in the strong northeast cleavage that crosscuts them. Several of these folds were identified in the Noggin Cove Formation with fold limbs ranging up to 15 m in length but commonly less than 1 m. The dominant structural feature of the Carmanville area is a regional northeast-trending, steep penetrative cleavage; $F_1$ folds are crosscut in a non-axial planar manner by this cleavage. A faint bed parallel cleavage associated with $F_1$ occurs only very rarely.

$F_1/F_2$ fold interference patterns (type III of Ramsay, 1967) occur in the Noggin Cove Formation along the shoreline from Frederickton to Noggin Point, in Noggin Cove, and in the crags overlooking the highway south of Carmanville; also, a well defined type III refold of a fine silt bed occurs within a black shale interbedded with the volcanics in Noggin Cove. These fold interference patterns indicate the $F_1$ axial planes were at a high angle to the $F_2$ axial plane before $F_2$ folding. Because $S_2$ is steep, the $F_1$ axial surface must have been horizontal to subhorizontal prior to $F_2$ folding, suggesting $F_1$ folds were recumbent.

A large, open, downward facing anticline, where the regional steep northeast-trending cleavage ($S_2$) crosscuts both limbs in a non-axial planar manner, occurs in volcanic conglomerates south of Carmanville in the rocky bluffs 1 km due west of the head of Carmanville Arm. Several examples of overturned beds cut by a steeper $S_2$, were identified in the volcanic rocks of the Noggin Cove Formation. These observations support $F_1$ recumbent folding.

### *$F_2$ folds*

These folds are defined as those for which the dominant regional northeast cleavage is axial planar. This cleavage predominantly dips steeply to the southeast (Fig. 3a). $F_2$ fold axes have variable plunges but collectively form a girdle that matches the average orientation of $S_2$ (Fig 3a&b); fold hinges could only be traced short distances and appear to die out parallel to $S_2$, suggesting the variable plunges are part of a tight system of doubly plunging en echelon folds (eg. Ramsay and Huber, 1987). Because of this tight en echelon folding of the Noggin Cove Formation volcanic rocks (with beds that have limited lateral continuity and lack marker horizons), macroscopic $F_2$ folds could not be delineated. Detailed structural analysis of rocks to the west, that have undergone a similar deformational history (eastern Notre Dame Bay area, Karlstrom et al., 1982), indicate a sub-horizontal enveloping surface for macroscopic $F_2$ folds. Mesoscopic $F_2$ folds are the most obvious and most common folds in the Noggin Cove Formation; these folds are open to isoclinal, although predominantly isoclinal with bedding commonly rotated into the strong $S_2$ cleavage.

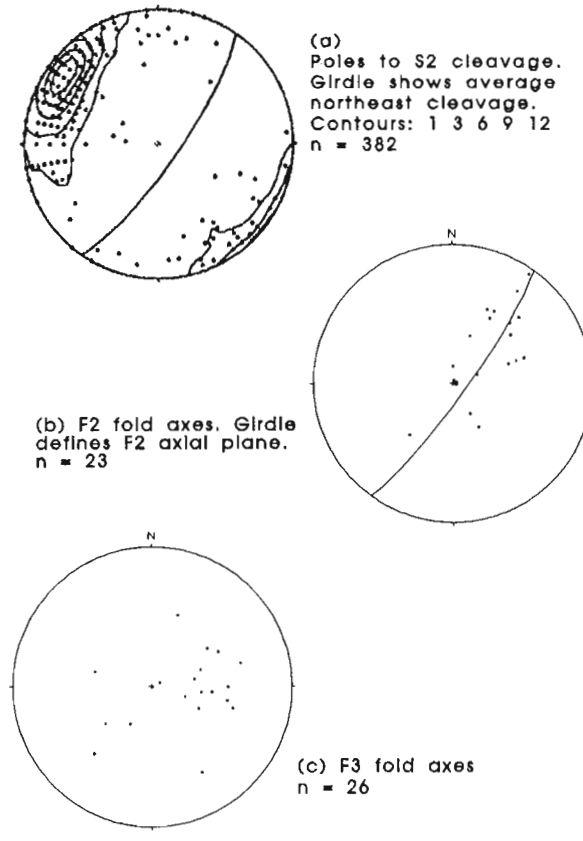


**Figure 3.** Structural data, Noggin Cove Formation.

### *$F_3$ folds*

These structures include the kinking and folding of the regional northeast ($S_2$) cleavage. Kinking of the cleavage is more common than folding. Gentle to tight folding about moderate to steep fold axes results in the $S_2$ cleavage varying substantially from its northeast trend (Fig. 3a). S,Z, and M folds occur; hinge interference of the folded $S_2$ cleavage with an axial planar weak $S_3$ cleavage occurs in an M fold of course grained, volcanic sandstone south of Carmanville. More than one generation of post $F_2$ folding may be present. In addition to a northeast-southwest trend, a more dominant east-west trend is suggested by the preponderance of $F_3$ fold axes with moderate to steep plunges to the east and west (Fig. 3c). This trend is likely associated with a late, east-west, weak, open fracture cleavage.

### *Faults*

The contact between volcanic rocks of the Noggin Cove Formation and the sandstones, siltstones, and shales of the Davidsville Group south of the Noggin Cove Formation is interpreted to be a fault based on the following observations. (1) The change from volcanic conglomerates and sandstones to siliceous shales, siltstones, and sandstones can be seen to be knife sharp 1 km south of Beaver Cove just west of the road. Southward the contact can be placed within 5 m in many locations and is linear. South of Frederickton, and south of the Carmanville to Musgrave Harbour road, the same abrupt transition occurs; (2) The siliceous sediments are invariably disrupted or sheared near the contact whereas the volcanic rocks seem unaffected; (3) Gravity data (Miller, 1988) suggests an east-west structural break along the southern margin of the Noggin Cove Formation. The sinuous trace of the contact suggests it is an early fault folded by $F_2$. The most likely scenario is that this is a thrust fault related to $F_1$ recumbent folding. Pillow lavas south of the Noggin Cove Formation at Round Pond closely resemble those of the Noggin Cove Formation. They could be a klippe emplaced by southward thrusting.

## RELATIONSHIP TO NEARBY GROUPS

The Noggin Cove Formation is in fault contact with siliceous sediments of the Davidsville Group to the south, is bounded to the west by Gander Bay and truncated to the east by the Rocky Bay and Aspen Cove plutons. The Frederickton, Rocky Bay, and Aspen Cove plutons intrude the Noggin Cove Formation in an approximate east-west belt. The high proportion of edenite revealed by microprobe analysis, in samples of the Noggin Cove Formation not in close proximity to these plutons, suggests that they are more extensive at depth.

To the north, the Noggin Cove Formation is interbedded with melanges, siliceous breccias (finely bedded angular siltstone clasts in a limestone matrix), black shales, and bedded siltstones. The best examples of this interbedding occur at Noggin Point and in Noggin Cove. $F_2$ folds with low to moderate northeast plunges and consistent north facings cut by $F_2$ cleavage along the northern shorelines indicate these units overlie the Noggin Cove Formation. This is supported by a predominance of north facings within beds of the Noggin Cove Formation. Siltstones along the Frederickton to Noggin Point shoreline and in Noggin Cove resemble those found on the islands to the north (Woody Island sequence of Currie, 1992). Coticules, common in the siltstone and sandstone beds of the Woody Island sequence, also occur in siltstones and sandstones interbedded with volcaniclastics of the Noggin Cove Formation at Beaver Cove. Bathymetric charts and gravity data (Miller, 1988) also suggest structural and stratigraphic continuity northward between the Noggin Cove Formation, melanges, and the Woody Island sequence.

The melange at Davidsville is interpreted here as olistrostromal and overlying the Noggin Cove Formation. The melange is very similar to the melanges north of the Noggin Cove Formation with respect to its matrix and clasts. Rare folded beds of siltstone occur within the black shale matrix of the melange and the predominance of siliceous clasts (versus mafic volcanic clasts) suggest a transition to a more siliceous source. Coticules in a medium bedded siltstone occur as a large block in black shale along the shoreline at Davidsville, indicating the same transition from the volcanic rocks to melange to the coticule-bearing siltstone and sandstone that occurs northward of the Noggin Cove Formation. The subhorizontal enveloping surface of $F_2$ folds suggests horizontal layering prior to $F_2$ folding. Because $F_2$ folds are doubly plunging (see also Wu, 1979), the melange at Davidsville may be equivalent to melanges north of the Noggin Cove Formation.

## GEOCHEMISTRY

Geochemical data was obtained from 27 samples of volcanic rocks in the Carmanville area. Of the 27 samples, 20 are from pillows, flows, dykes, and conglomerates of the Noggin Cove Formation, 6 are from pillow or gabbro blocks in the Carmanville melanges, and 1 sample is from pillow lavas at Round Pond.

Figure 4a shows the overlap of the geochemical signatures for samples from the Noggin Cove Formation and Carmanville melanges; this overlap suggests that all are from the same volcanic complex. The majority of samples plot within the E-MORB and N-MORB fields, indicating a back-arc basin paleotectonic setting. Arc signatures for some of the samples (field D) support this interpretation. Good grouping of the fragmental volcanic rocks in the E-MORB field reflects a consistent source.

From a comparison of the discrimination diagrams (Fig. 4a, b), it can be seen that the Noggin Cove Formation basalts have geochemical signatures very similar to those of the Lau Basin, Valu Fa Ridge, and Ata Island (Volpe, 1988; Vallier et al., 1991). There is an excellent match in the extended rau-earth element plots between arc basalts from the immediate Carmanville area and samples dredged from the Valu Fa Ridge (Fig. 4c). These geochemical results strongly suggest a back-arc basin paleotectonic setting for the Noggin Cove Formation. The spread in geochemical signatures for

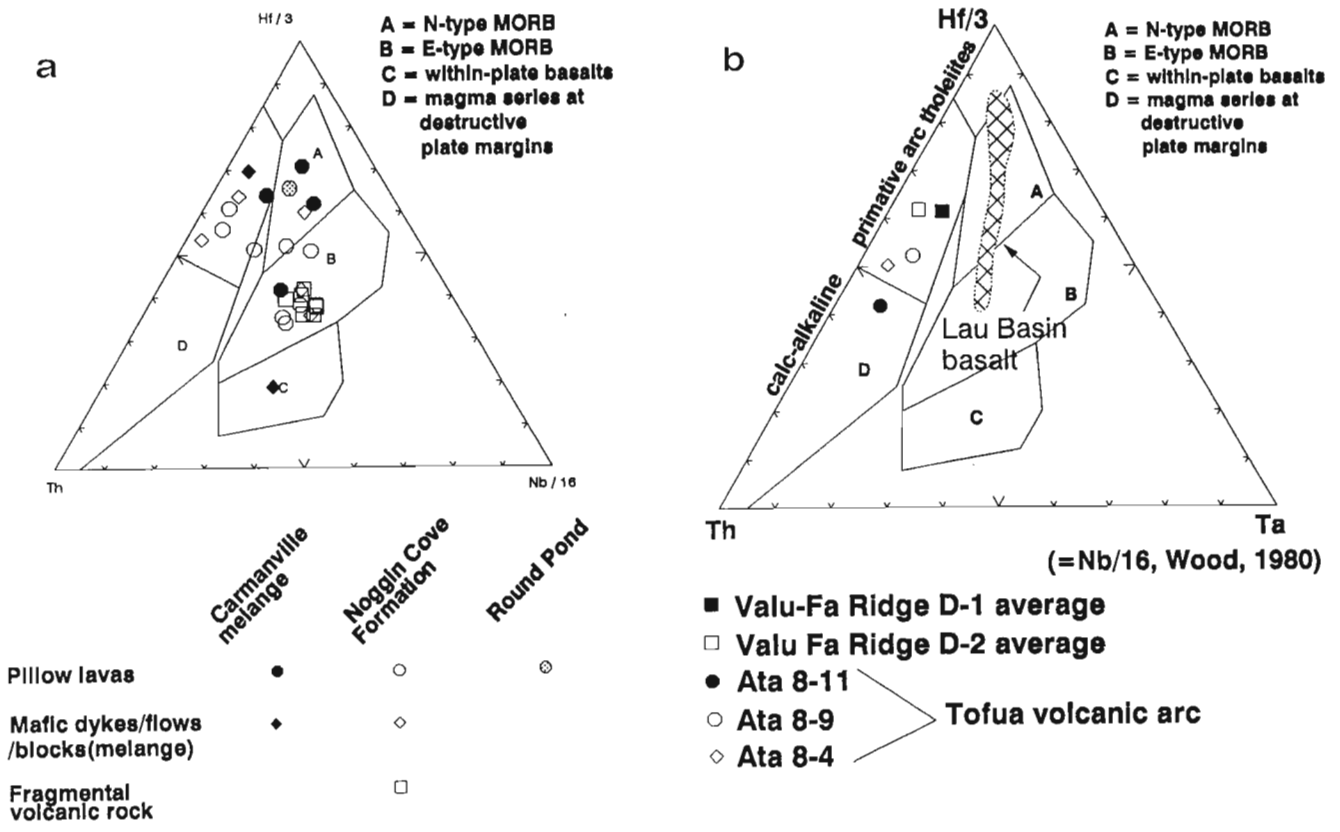


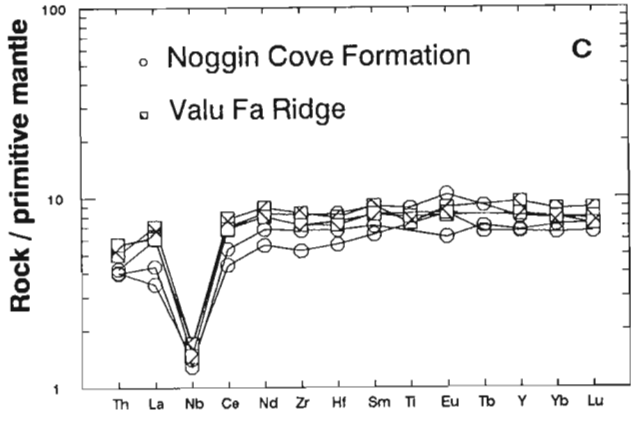


**Figure 4.** a) Th-Hf-Nb diagram (Wood, 1980) for samples from the Noggin Cove Formation and Carmanville melanges. b) Hf-Th-Nb diagram for samples from the Lau Basin, Valu Fa Ridge and the active Tofua volcanic arc (from Vallier et al., 1991). c) Extended REE plots for samples from the Valu Fa Ridge (Vallier et al., 1991) and from the Noggin Cove Formation that plot in field D of Figures 4a and 4b. Primitive mantle normalizing values from Swinden et al., 1990.

the pillows, dykes, and flows may represent the transition from arc- to mantle-derived magmas as an arc is rifted apart to form a back-arc basin (e.g. Swinden et al., 1990).

## AGE AND CORRELATION

The age of the Noggin Cove Formation is poorly constrained. Based on regional correlations, the melanges and coticule-bearing lithologies to the north are considered Middle Ordovician or earlier (Williams, 1992). The Noggin Cove Formation underlies these units and is interpreted here as Middle Ordovician or older. This age is supported by a proposed correlation of the Noggin Cove Formation with the Tea Arm Volcanics of the Exploits Group. The Tea Arm Volcanics are conformably overlain by the Strong Island Chert which contains early Llanvirn graptolites (Dec et al., 1992, Williams et al., 1992). Geochemical analyses of lavas from the Tea Arm Volcanics and from lavas interbedded with the Strong Island Chert indicate an arc to back-arc succession (Dec et al., 1992). The same arc to back-arc basin transition is strongly suggested from geochemical analysis of samples from the Noggin Cove Formation.

## Interpretation

The Noggin Cove Formation is interpreted as a volcaniclastic apron shed from a northern subareal to shallow marine explosive volcanic source; a large volume of fragmental volcanic rock was deposited onto and south of a band of basaltic pillow lavas, dykes, and flows, which presumably formed part of the pedestal of an island volcano. The fragmental rock is largely deposited as debris flows, some of which are spectacular in terms of their thickness and the size of blocks and folded intraclasts. Lesser amounts of medium bedded cross-stratified calcareous tuffs, and a lappili breccia

with a calcite matrix, are found only to the north; these are interpreted as shallow marine deposits more proximal to the volcanic source than the debris flows.

Coticules at the top of the Noggin Cove Formation and in beds of the overlying Woody Island sequence indicate high levels of Mn. Sediments from the Lau Basin are extremely enriched in manganese (Cronan et al., 1984), lending further support to the back-arc basin paleotectonic setting for the Noggin Cove Formation indicated by geochemical results. However, the high proportion of fragmental volcanic rocks relative to the primary volcanic rocks in the Noggin Cove Formation, the preponderance of vesicular clasts, and the sheer volume of the fragmental volcanic rock all suggest a highly explosive island arc origin (Garcia, 1978). The presence of slab influenced magmas is also indicated by the geochemical results. To reconcile these interpretations, I propose the Noggin Cove Formation represents a volcanic complex on the arc flank of a back-arc basin. Preferential preservation of this tectonic setting relative to the centre of the basin has been predicted from studies of similar back-arc basin volcanic assemblages (see Busby-Spera, 1988).

Slumping occurs more frequently on the arc flank of back-arc basins than in any other tectonic setting due to the combination of several factors: steep regional gradients, high seismicity, rapid sediment accumulation, unstable sediment structure (e.g. thixotropic properties of montmorillonite), and shallow level intrusions into sediments on steep slopes (Lonsdale, 1975; Busby-Spera, 1988). The thicknesses of many of these debris flows of the Noggin Cove Formation is likely the result of storage of the fragmental rock on the slopes of a volcano; the release of the stored debris is then triggered by earthquakes or gravitational instability. Bedded and massive intraclasts in the volcanic conglomerates attest to lithification prior to disruption. The same is true for a chaotic conglomerate that occurs at Noggin Point and in Noggin Cove; this conglomerate consists of angular clasts of finely bedded siltstone in a limestone matrix and is interbedded with the lapilli breccia. Strong earthquake activity is presumed necessary for disruption of the previously lithified rock incorporated in these conglomerates and is assumed responsible for olistrostrome formation and slumping in the Carmanville Melanges and "melange beds" of the Woody Island sequence; clasts of previously formed melange within these units indicates the same style of lithification followed by disruption. Strong earthquake activity could result from block faulting as an arc is rifted. The enhanced relief provided by the block faulting could explain the deposition of thick debris flows (Carey and Sigurdsson, 1984) and olistostromes. Block faulting may also expose ultramafic rock for incorporation into the melanges (e.g. Rocky Point, Aspen Cove) and may account for the intense deformation seen in some blocks in the melange ("recycled" blocks and matrix of Williams et al., 1991).

Bedded tuffs, volcanic conglomerates, and lappili breccia at the top of the Noggin Cove Formation grade into epiclastics of the Woody Island sequence at Beaver Cove and along the northern shoreline from Frederickton to Carmanville. This transition marks an abrupt cessation of volcanism but olistostromal melanges and slumped beds in the Woody Island Sequence indicate continued instability. The deeper water sediments of the Woody Island Sequence may represent deposition into the developing back-arc basin.

Disruption of bedding within the melanges, local intrusion and blending of the melanges into adjoining units, and melange dykes that cut across bedded sediments suggest these olistostromes and slumps were again disrupted; this event may be recording the subsequent accretion of this back-arc volcanic complex to a continent or continental fragment (i.e. Gander Zone). Ultramafic rocks, presumably associated with the Gander River Ultramafic Belt (GRUB Line), occur with Noggin Cove Formation volcanic rocks in slumped to olistostromal beds east of the Carmanville area at Rocky Point. The provenance of the ultramafic rocks may provide links to the GRUB Line.

## ACKNOWLEDGMENTS

Sincere thanks to Hank Williams, Ken Currie, and Mark Piasecki for logistical support of field work and for their continued academic guidance. A special thanks to the people of Carmanville, particularly Scott and Joan Hicks, and Gary, Ross, and Roy Collins, for their great hospitality and humour.

## REFERENCES

**Busby-Spera, C.J.**
1988: Evolution of a Middle Jurassic back-arc basin, Cedros Island, Baja California: Evidence from a marine volcaniclastic apron; Geological Society of America Bulletin, v. 100, p. 218-233.

**Carey, S. and Sigurdsson, H.**
1984: A model of volcanogenic sedimentation in marginal basins. in Marginal Basin Geology, (ed.) B.P. Kokelaar and M.F. Howells; Geological Society of London, Special Publication 16, p. 37-58.

**Cronan, D.S., Moorby, S.A., Glasby, G.P., Knedler, K., Thomson, J., and Hodkinson, R.**
1984: Hydrothermal and volcaniclastic sedimentation on the Tonga-Kermadec Ridge and in its adjacent marginal basins; in Marginal Basin Geology, (ed.) B.P. Kokelar and M.F. Howells; Geological Society Special Publication 16, Blackwell Scientific Publications, London, p. 137-149.

**Currie, K.L.**
1991: A simple quantitative calculation of mol fractions of amphibole end-members; Canadian Mineralogist, v. 29, p. 287-299.
1992: Carmanville map area (2E-8): - a new look at Gander-Dunnage relations in Newfoundland; in Current Research, Part D; Geological Survey of Canada, Paper-1D, p. 27-33.

**Dec, T., Swinden, S., and Floyd, J.D.**
1992: Sedimentological, geochemical and sediment-provenance constraints on stratigraphy and depositional setting of the Strong Island Chert (Exploits subzone, Notre Dame Bay); in Current Research, Newfoundland Department of Mines, Geological Survey of Newfoundland, Report 92-1, p. 85-96.

**Fisher, R.V.**
1984: Submarine Volcanoclastic Rocks; in Marginal Basin Geology, (ed.) B.P. Kokelar and M.F. Howells; Geological Society Special Publication 16, Blackwell Scientific Publications, London, p. 5-27.

**Garcia, M.O.**
1978: Criteria for the identification of ancient volcanic arcs; Earth Science Review v. 14, p. 147-65.

**Karlstrom, K.E., van der Pluijm, B.A., and Williams, P.F.**
1982: Structural interpretation of the eastern Notre Dame area, Newfoundland: regional post-Middle Silurian thrusting and asymetrical folding; Canadian Journal of Earth Sciences, v. 19, p. 2325-2341.

**Lonsdale, P.F.**
1975: Sedimentation and tectonic modification of the Samoan archipelagic apron; American Society of Petroleum Geologists Bulletin, v. 59, p. 780-798.
**Miller, H.G.**
1988: Geophysical interpretation of the geology of the northeast Gander Terrane, Newfoundland; Canadian Journal of Earth Sciences, v. 25, p. 1161-1174.
**Pajari, G.E., Pickerill, R.K., and Currie, K.L.**
1979: The nature, origin and significance of the Carmanville Ophiolitic Melange, Northeastern Newfoundland; Canadian Journal of Earth Sciences, v. 15, p. 1439-1451.
**Ramsay, J.G.**
1967: Folding and Fracturing of Rocks; McGraw-Hill Book Co., New York, 568 p.
**Ramsey, J.G. and Huber, M.I.**
1987: The techniques of modern structural geology; vol 2, Folds and fractures, Academic Press, London, p. 313.
**Swinden, H.C., Jenner, G.A., Fryer, B.J., Hertogen, J., and Roddick, J.C.**
1990: Petrogenesis and paleotectonic history of the Wild Bight Group, an Ordovician rifted island arc in central Newfoundland; Contributions to Mineral Petrology, v. 105, p. 219-241.
**Vallier, T.L., Jenner, G.A., Frey, F.A., Gill, J.B., Davis, A.S., Volpe, A.M., Hawkins, J.W., Morris, J.D., Cawood, P.A., Morton, J.L., Scholl, D.W., Rautensclein, M., White, W.M., Williams, R.W., Stevenson, A.J., and White, L.D.**
1991: Subalkaline andesite from Valu Fa Ridge, a back-arc spreading center in southern Lau Basin: petrogenesis, comparitive chemistry, and tectonic implications; Chemical Geology, v. 91, p. 227-256.
**Volpe, A.M.**
1988: PhD thesis, University of California, San Diego, California, U.S.A.
**Williams, H.**
1992: Melanges and coticule occurences in the northeast Exploits Subzone, Newfoundland; in Current Research, Part D; Geological Survey of Canada, Paper 92-1D, p. 121-127.
**Williams, H., Coleman-Sadd, S.P., and Swinden, H.S.**
1988: Tectonic-stratigraphic Subdivisions of Central Newfoundland; in Current Research, Part B; Geological Survey of Canada, Paper 88-1B, p. 91-98.
**Williams, H., Piasecki, M.A.J., and Johnston, D.**
1991: The Carmanville Melange and Dunnage-Gander relationships in northeast Newfoundland; in Current Research, Part D; Geological Survey of Canada, Paper 91-1D, p. 15-23.
**Williams, S.H., O'Brien, B.H., Coleman-Sadd, S.P., and O'Brien, F.H.C.**
1992: Dunnage Zone graptolites- an extension of the age range and distribution of certain Ordovician formations of the Exploits Subzone; in Current Research, Newfoundland Department of Mines, Geological Survey of Newfoundland, Report 92-1, p. 203-210.
**Wood, D.A., Joron, J-L., and Treuil, M.**
1979: A re-appraisal of the use of trace elements to classify and discriminate between magma series in different tectonic settings; Earth and Planetary Science Letters, v. 45, p. 326-336.
**Wood, D.A.**
1980: The application of a Th-Hf-Ta diagram to problems of tectonomagmatic classification and to establishing the nature of crustal contamination of basaltic lavas of the British Tertiary Volcanic Province; Earth and Planetary Science Letters, v. 50, p. 11-30.
**Wu, T.W.**
1979: Structural, stratigraphic and geochemical studies of the Horwood Peninsula - Gander Bay area, northeast Newfoundland; MSc thesis, Brock University, St. Catherines, Ontario 185 p.

# Tectonics across the Gander-Dunnage boundary in northeastern Newfoundland[1]

**M.A.J. Piasecki[2]**
**Continental Geoscience Division**

*Piasecki, M.A.J., 1992: Tectonics across the Gander-Dunnage boundary in northeastern Newfoundland; in Current Research, Part E; Geological Survey of Canada, Paper 92-1E, p. 259-268.*

***Abstract***

*Gander and Dunnage zones north of Gander Lake are separated by a major shear zone inclined steeply to the northwest, in which kinematic fabrics indicate a history of early and late ductile movements in a transpressional regime. An early, probably Silurian episode of sinistral translation was followed by a dextral back-movement. In gently inclined rocks, these movements correspond respectively to northeast-over-southwest and reversed motions, a sequence consistent with movements on the Gander-Dunnage boundary in central and southeastern Newfoundland.*

*Later sinistral reworking of the shear zone coincided in part with end-Silurian plutonism, metamorphism, and major curvilinear folding which particularly affected the Dunnage Zone. This phase may correspond with the sinistral transpressive movements and related plutonism in the Dover fault zone.*

*Sinistral and dextral shearing also affects boundaries between lithostratigraphical units within the Hamilton Sound sequence, and probably also between it and the Davidsville Group.*

***Résumé***

*Les zones de Gander et Dunnage situées au nord du lac Gander sont séparées par une grande zone de cisaillement, fortement inclinée vers le nord-ouest, dans laquelle les fabriques cinématiques traduisent une série d'épisodes initiaux et d'épisodes tardifs de mouvements ductiles dans un régime de transpression. Un épisode précoce de translation sénestre, probablement d'âge silurien, a été suivi d'un mouvement inverse dextre. Dans les roches légèrement inclinées, ces mouvements correspondent respectivement à des déplacements nord-est postérieurs à des déplacements sud-ouest, et à des déplacements inverses, séquence qui s'accorde avec des mouvements suivant la limite des zones de Gander et de Dunnage dans le centre et dans le sud-est de Terre-Neuve.*

*Le remaniement sénestre tardif de la zone de cisaillement coïncidait en partie avec les épisodes de plutonisme, de métamorphisme, et de plissement curviligne de la fin du Silurien qui ont tout particulièrement touché la zone de Dunnage. Cette phase correspond peut-être aux mouvements transpressifs sénestres et au plutonisme connexe qui ont eu lieu dans la zone de faille de Dover.*

*Le cisaillement sénestre et le cisaillement dextre ont aussi touché les limites entre les unités lithostratigraphiques de la séquence de Hamilton Sound, et probablement aussi entre celle-ci et le Groupe de Davidsville.*

[1] Contribution to Canada-Newfoundland. Cooperation Agreement on Mineral Development 1990-1994, a subsidiary agreement under the Economic and Regional Development Agreement. Project funded by the Geological Survey of Canada.

[2] Department of Geology, University of Keele, Keele, Staffordshire ST5 5GB, UK.

## INTRODUCTION

In northeastern Newfoundland, the Gander Zone and Dunnage Zone are separated by a belt of ophiolitic rocks, the Gander River Ultramafic Belt (GRUB of Blackwood, 1982) and also a major ductile shear zone in excess of 1 km thick (Fig. 1; Williams et al., 1991; Goodwin and O'Neill, 1991).

The Carmanville region is critical to studies of Gander-Dunnage relations, as in this area GRUB rocks become discontinuous, and, locally, Gander and Dunnage rocks are in direct contact. From southwest to northeast, Dunnage lithologies progressively terminate against GRUB rocks and the shear zone, until near Ragged Harbour, the Davidsville Group (Kennedy and McGonigal, 1972; O'Neill and Blackwood, 1989) gives way to a lithologically distinct sequence of metasediments which have been separated from the Davidsville Group and provisionally named the Hamilton Sound sequence by Currie (1992)

In the northeastern part of the Carmanville area (Fig. 1), Gander and Dunnage metasediments are encompassed by granites (Currie and Pajari, 1981), near which they are transformed from phyllites to garnet-andalusite-sillimanite schists, which has led Kennedy and McGonigal (1972) to postulate the presence of Gander rocks on both sides of the GRUB.

The Gander-Dunnage boundary has been interpreted as a stratigraphic and tectonic break (Kennedy and McGonigal, 1972; Williams et al., 1991; Goodwin and O'Neill, 1991), or a sedimentological passage (Pajari and Currie, 1978; Currie et al., 1980). This report, based on field re-examination of the Carmanville map-sheet and on a wider regional investigation, describes the nature of this boundary in greater detail than before, contrasts the structural sequences in the Gander and Davidsville groups across it, and describes, for the first time, the structural sequence in the rocks of the Hamilton Sound sequence.

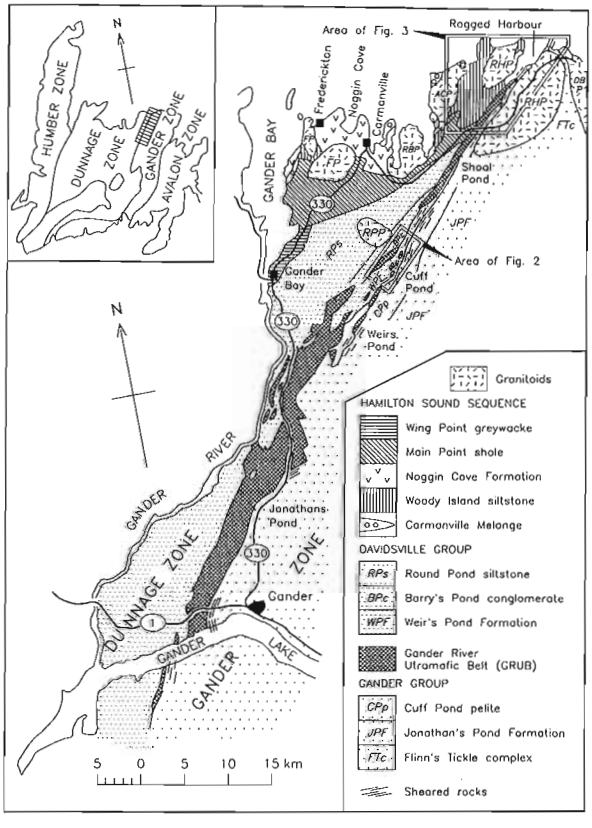


**Figure 1.** Simplified geology of the northeastern Gander-Dunnage boundary zone. Symbol for sheared rocks coincides with sectors of the boundary investigated in this study.

## GANDER – DUNNAGE RELATIONSHIPS

### *Lithologies across the Gander – Davidsville groups' boundary*

In the Carmanville area, as this boundary is approached from the east, the largely psammitic Gander Group (Jonathan's Pond Formation, O'Neill and Blackwood, 1989) passes stratigraphically upwards through a striped psammite-pelite transition into a unit of grey-green to black pelite with ribs of psammite that become progressively sparser towards the adjacent rocks of the GRUB. This unit is provisionally named the Cuff Pond pelite (Currie,

1992). It was once thought to represent a stratigraphical transition from the Gander Zone into the Dunnage, but present re-investigation shows that it forms the outermost flank of the Gander River Group in this area (Fig. 1, 2, 3; cf. Currie, 1992; Williams at al., 1991). A similar transition from the Jonathan's Pond Formation to a pelite closely resembling the Cuff Pond pelite appears to be also present on the north shore of Gander Lake, where, however, it is much thinner, probably as a result of protracted ductile and brittle tectonic movements.

In the region of Cuff Pond, where the GRUB takes the form of discontinuous lenses (Fig. 2), Raft Pond pelite-mylonite is in direct contact with a pelite-mylonite of the Weir's Pond Formation of the Davidsville Group. Both mylonitic pelites (phyllonites) have a similar colour and appearance, both contain thin psammitic bands, and the distinction between the two is difficult to make on the basis of lithologies alone. However, the Gander Group is structurally more complex than the Davidsville Group (as redefined by Currie, 1992), and criteria derived from this structural contrast can be used to separate mylonitic pelites derived from Gander and Dunnage protoliths.

### *Gander-Dunnage boundary shear zone*

The Gander-Dunnage boundary is marked by a subvertical to steeply inclined tectonic zone, locally in excess of 1 km in width, within which belts of blastomylonite, mylonite, and locally ultramylonite anastomose between protomylonites (nomenclature after White, 1982).

The sheared rocks are characterized by swarms of subconcordant quartz veins (Fig. 4), muscovitized matrices, and more rarely by small muscovite porphyroblasts, all typical products of ductile shearing in the presence of fluid (Piasecki, 1988b). Stretching lineations, which plunge gently to moderately steeply (50°) to the northeast and southwest (Fig. 2) are defined by rodded quartz veins, parallel alignment of minerals and trails of phyllosilicates. The mylonites exhibit kinematic (sense-of-shear) indicators, such as S-C and shear band foliations (Berthe et al., 1979), and asymmetric, syn-shearing folds.

The GRUB also contains zones of mylonites. At Gander Lake and the Trans-Canada Highway, its margin against Gander Group mylonites takes the form of a narrow belt of green mylonite-ultramylonite with carbonate lenticles, derived from a mafic to ultramafic protolith. In the Carmanville area, the Shoal Pond ultramafic is extensively sheared along its margins, and within internal anastomosing zones, to talc-tremolite/actinolite phyllonites.

Locally, as at Raft Pond, its margin contains green gabbro-diabase derived mylonites accompanied by lenses of carbonate and trondhjemite mylonite. Near Cuff Pond, the sheared Gander-Dunnage boundary contains a trail of lenses of serpentinite, many mylonitic. Many lenses of serpentinite and trondhjemite are enclosed by mylonitized pelites of the Weir's Pond Formation (Fig. 2). Most of these probably represent syndepositional olistoliths derived from the underlying GRUB (cf. Pajari et al., 1979), but others may result from tectonic imbrication.

**Early movements in the boundary shear zone**

The mylonite zone is a zone of complex low-angle transcurrent to oblique movements. Kinematic indicators in both Gander- and Davidsville-derived mylonites exhibit both sinistral and dextral senses of movements. Both may be present in the same exposure, adjacent foliation-parallel domains showing one sense of movement predominating over the other. Fabrics of sinistral movements are more common than those of dextral movements. The presence of serpentinite-mylonites in which dextral shear bands modify an earlier mylonitic (phyllonitic) foliation, indicate that sinistral shearing was succeeded by dextral shearing. Rarely, sinistral and dextral shear bands form conjugate sets, indicating that they are related to flattening strain(s).

## *Contrasts in early structural history of the Gander and Davidsville groups across the boundary shear zone*

The Gander and Davidsville groups and the Hamilton Sound sequence exhibit different deformation sequences. These are listed in Table 1, and are differentiated by the respective prefixes, G, D, and H.

Gander Group rocks along the western flank of the Gander Zone dip gently towards the northwest. Their earliest, G1 tectonic fabric is an approximately one centimetre-spaced pressure-solution cleavage, defined by discontinuous stringers of mica and chlorite best developed in psammites. It is axial-planar to megascopic near-recumbent, north-trending G1 isoclinal folds. Locally, an even older

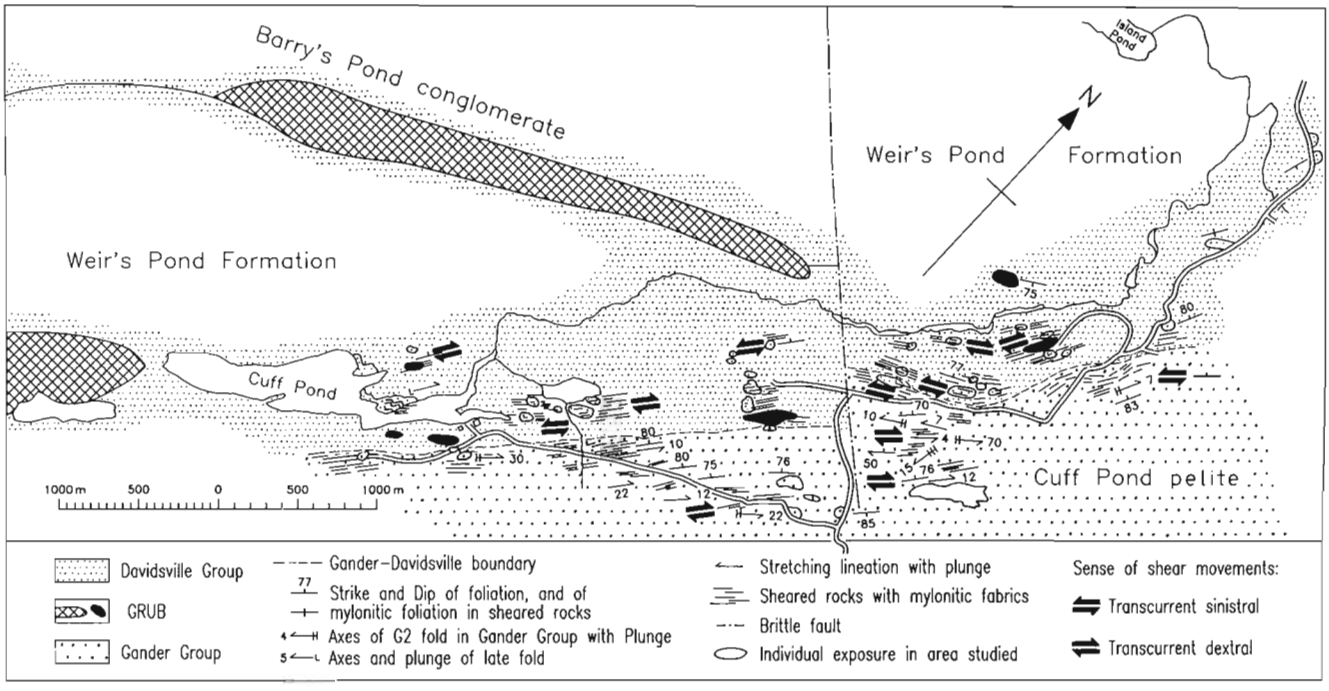


**Figure 2.** Geology along the Gander-Dunnage boundary at Cuff Pond.

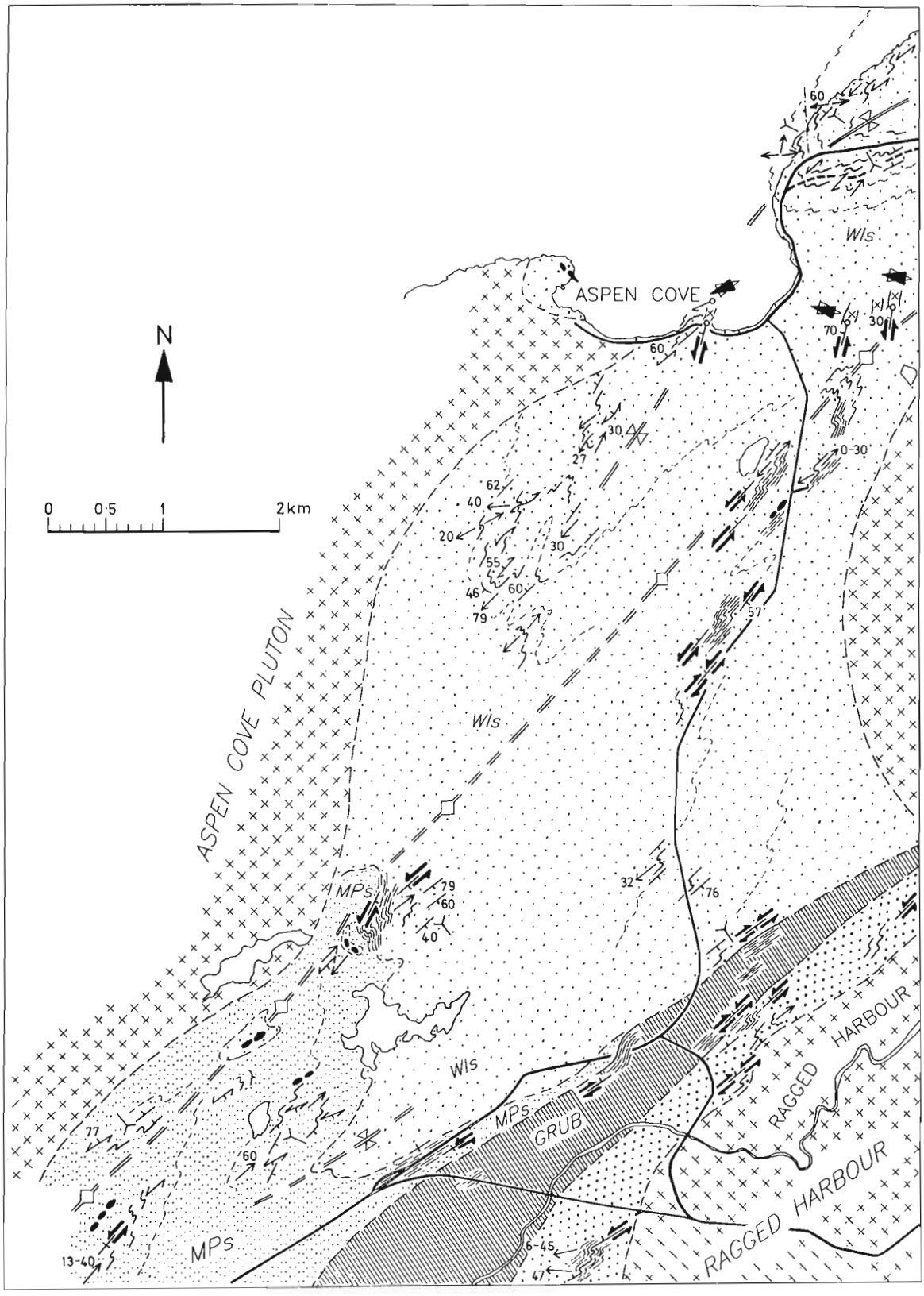


**Figure 3.** Geology across the Gander-Dunnage boundary in the northeastern sector of the Carmanville area. Explanation in text. Presence of symbols denotes areas investigated in detail.

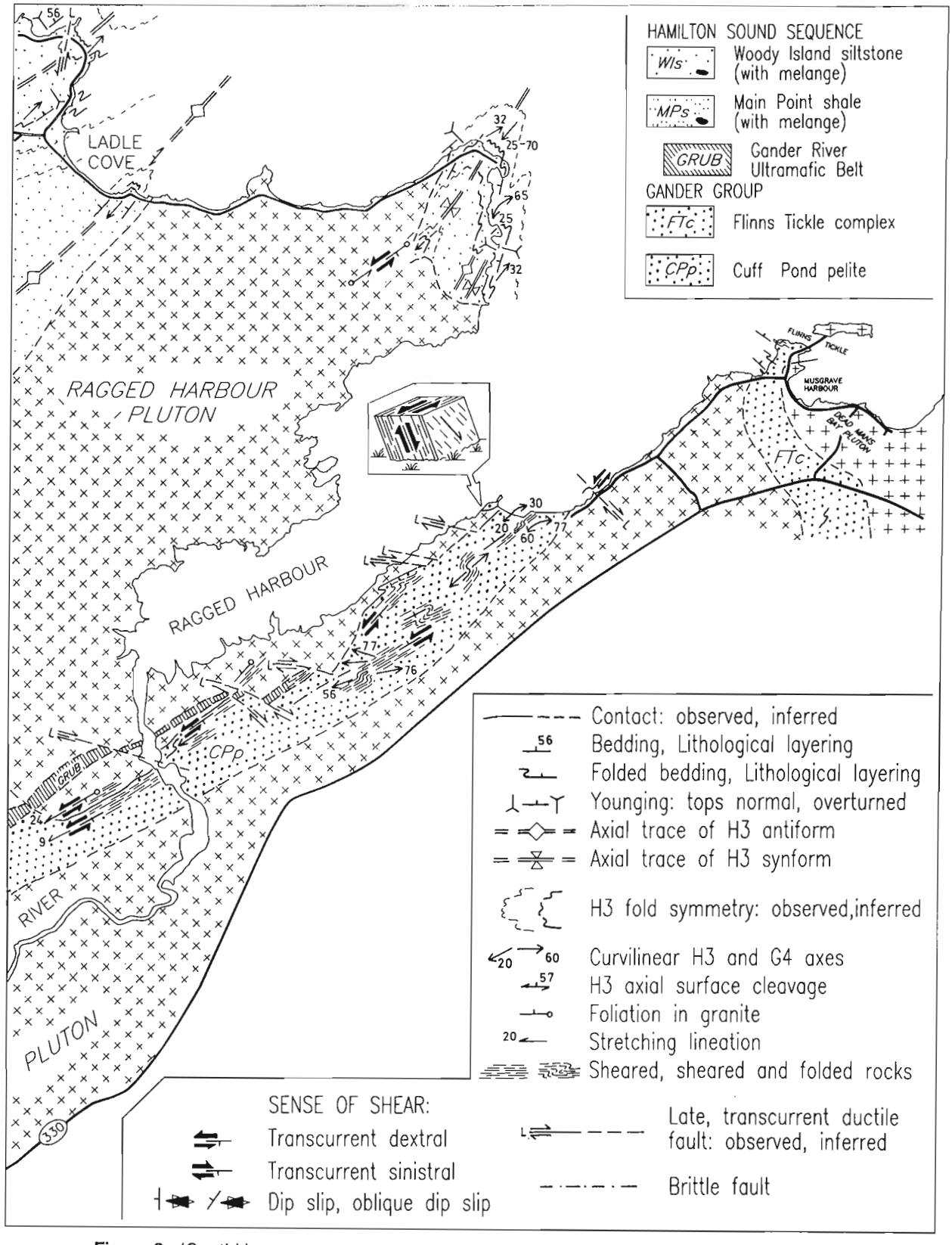


**Figure 3.** (Cont'd.)

**Table 1.** Comparison and correlation of deformational sequences in the Gander and Davidsville groups and the Hamilton Sound sequence (designated G, D, and H respectively).

| | GANDER GROUP | DAVIDSVILLE GROUP | HAMILTON SOUND SEQUENCE |
|---|---|---|---|
| **Non-penetrative deformation** | | | |
| | Brittle faults | Brittle faults | Brittle faults |
| | Dextral strike-slip faults | ? | Sinistral strike-slip faults |
| | Kink zones | ? | ? |
| | Open, near-recumbent folds | Open, near-recumbent folds | Open, near-recumbent folds |
| | | Open, inclined folds | |
| **Penetrative deformation** | | | |
| Late | G4 Small inclined curvilinear folds, weak G4 axial surface cleavage, plutonism | ? | H3 Large inclined curvilinear folds, strong H3 axial surface cleavage, plutonism |
| Late | G3 Layer-parallel mylonitic foliation, sinistral shearing, asymmetric folds, granite sheets | D2 Layer-parallel mylonitic foliation, sinistral shearing, asymmetric folds | H2 Asymmetric folds of H1 foliation with H2 axial planar schistosity, layer-parallel H2 mylonitic foliation, sinistral shearing, granite sheets |
| Early | G2 Isoclinal asymmetric folds of G1 cleavage with G2 axial planar cleavage, cleavage-parallel G2 mylonitic foliation, sinistral then dextral shearing | D1 Inclined folds of bedding, with axial-surface cleavage, cleavage-parallel mylonitic foliation, sinistral then dextral shearing | H1 Layer-parallel foliation, dextral shearing, and earlier sinistral shearing? Attitude of earliest folds unknown |
| Early | G1 Near-recumbent folds of bedding, axial surface cleavage | | |

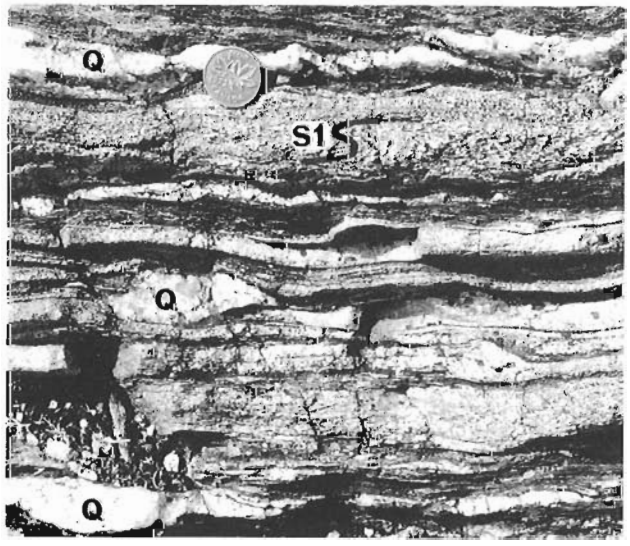


**Figure 4.** Mylonite from the Gander-Dunnage boundary with subconcordant quartz veinlets (Q). Under coin, a boudined psammitic rib which contains a G2 fold hinge with folded G1 cleavage (S1) indicates a Gander protolith for this mylonite. North of Ragged Harbour River.

tectonic fabric may be present (Dr. S.P. Colman-Sadd, pers. comm., 1991). As the sheared boundary of the Gander Zone is approached, G2 folds appear. They are small, isoclinal, asymmetric (west limb longer), and are inclined steeply to the northwest. Their hinges plunge gently to steeply (70°) to the southwest and northeast, as does the regional stretching lineation, and their axial surfaces coincide with the mylonitic C-foliation of the shear zone. These apparently syn-shearing folds seem to indicate a compressive component within a transpressive G2 shear regime.

The G2 folds transpose the wide-spaced G1 cleavage into a more closely spaced, steep G2 pressure solution cleavage, and, from east to west, the gentle northwesterly inclination of Gander rocks progressively steepens. Within the shear zone, G2 cleavage becomes a paper-thin mylonitic C-foliation dipping steeply towards the northwest, and psammitic bands within sheared pelite (phyllonite) become necked, boudined, and separated.

By way of contrast, in the Davidsville Group, both along the north shore of Gander Lake and in the Carmanville map area, the earliest tectonic structures are outcrop-size, open-limbed, D1 northeast-trending folds which fold bedding, locally with primary sedimentary structures. D1 folds are moderately to steeply inclined to the northwest, and have a penetrative axial-surface cleavage which refracts extensively, changing attitude from steep in sandstones to near bed-parallel in shales. Traced into the shear zone, the D1

folds progressively tighten, D1 cleavage intensifies and becomes the main, steeply northwest-inclined C-foliation in Davidsville-derived mylonites. Beds of metasiltstone attenuate, but rarely separate into boudins, indicating weaker shear deformation relative to that in the Gander Group, or alternatively, a lesser rheological contrast between the muddy siltstones and shales of the Davidsville protolith than that between the better differentiated siltstones and shales in the Gander protolith.

Thus, along the sheared Gander-Dunnage boundary, the mylonitic C-foliation common to both Gander and Davidsville mylonites, appears to be at least G2 in Gander-derived phyllonites, but D1 in Davidsville phyllonites (Table 1). Because of this contrast, sheared Gander pelites can be distinguished from the lithologically similar, sheared Davidsville pelites by the presence in some boudined psammitic bands of rootless G2 isoclinal folds still preserving folded G1 cleavage in their hinges (Fig. 4). This relict structure is so distinctive that it has been used in this study as a structural signature of Gander Group mylonites, allowing the Gander-Davidsville boundary to be located to within some 50 m in phyllonites in which neither assemblage can be otherwise recognized.

## *Late penetrative structures in the Gander Group*

### Late regional shearing

In the northeastern sector of the Carmanville area, the Cuff Pond pelite adjacent to the Ragged Harbour granite is a coarse, mylonitic schist with sinistral and dextral kinematic indicators. It is cut by discordant granite sheets, early marginal members of the Ragged Harbour granite. The sheets are themselves foliated parallel to the foliation in the host mylonitic schist, but they contain only sinistral S-C and shear band foliations. Many are separated into boudins that have slipped on sinistral shear bands, indicating that the sinistral shearing which affects these granite sheets is distinct from the earlier sinistral and dextral shearing. Stretching lineations related to this late shearing plunge variably and are broadly coaxial with those of the earlier shearing, but its shear bands tend to be less closely spaced and more steeply inclined than those of the earlier shearing. Syn-G3 shearing folds are small, asymmetric structures that fold the main mylonitic foliation with its early sinistral and dextral kinematic indicators, but are themselves enveloped by mylonitic schists with sinistral kinematics. The implication is that of a late reactivation of the main shear zone, coeval with the early stages of granite emplacement.

Along the south shore of Ragged Harbour (and also near Aspen and Ladle coves), subconcordant granite sheets exhibit a down-dip to oblique mineral stretching lineation, and two sets of S-C and shear band fabrics. In the horizontal plane, these fabrics indicate sinistral movement, and, in the plane of dip, a down-dip translation parallel to the lineation (inset within Ragged Harbour in Fig. 3). The two sets of kinematic fabrics do not mutually interfere. They are interpreted as transpressional fabrics indicating a transpressional regime for the late sinistral shearing.

In the absence of granite sheets, as in the region of Cuff Pond and Raft Pond, the presence of the late shearing in Gander- and also Davidsville-derived mylonites is indicated by late, crosscutting quartz veinlets deformed by sinistral shear bands.

### Late folding

Folds of the last regionally penetrative deformation, G4, fold Gander-derived mylonites and the sinistrally sheared early members of the granite suite. The G4 folds are small, open to close, inclined to near-upright, northeast-trending folds with a weak axial surface cleavage. They commonly pass into a decimetre-scale crenulation structure. They are curvilinear, with widely variable axial plunges and plunge directions (Fig. 3). They define numerous small scale culminations and depressions which steepen the plunges of G2 and G3 stretching lineations, and locally they take the form of sheath folds with steeply plunging direction of maximum extension.

G4 folds were succeeded by small, non-penetrative, minor, very open-limbed, sub-recumbent buckle folds without axial surface cleavage, and locally by conjugate kink bands, symmetrically inclined to the margin of the Deadmans Bay Pluton. They may be related to its emplacement.

### Late non-penetrative shearing and faulting

End-stage ductile deformation structures in the Gander Group are minor, subvertical, dextral, ductile strike-slip faults, 10 cm to 2 m thick. These minor shears affect the later phases of the Ragged Harbour Pluton, and, in combination with northeasterly-trending brittle strike-slip faults, they are responsible for northeasterly termination of the thinned-out extremity of the GRUB (Fig. 3).

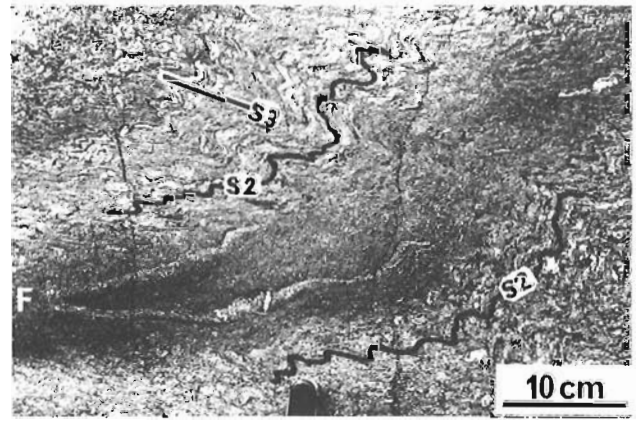


**Figure 5.** Anatomy of an H3 fold. Crenulation with axial surface S3 marks a H3 hinge zone. It folds an older schistosity (S2), axial-planar to an intrafolial H2 fold (centre), which in its hinge (F) folds bedding and an even earlier schistosity (H1, not visible in the photograph). Ladle Cove.

### *Late, non-penetrative ductile structures in the Davidsville Group*

In the Davidsville Group, D1 folds, D1 axial surface cleavage, and fabrics related to the early (sinistral and dextral) and late (sinistral) shearing are locally refolded by northeast-trending, open-limbed buckle folds without a related cleavage. Most of the late folds are variably inclined to the northwest or southeast, but some are near-recumbent.

## STRUCTURAL DEVELOPMENT OF THE HAMILTON SOUND SEQUENCE

The Hamilton Sound sequence has been recognized as a lithostratigraphical entity, separated from the Davidsville Group, and named by Currie (1992). This sequence contains spectacular olistostromal melanges within the Woody Island siltstone, the Main Point shale, and the fragmental volcanics of the Noggin Cove Formation. These melanges are depicted as the Carmanville Melange in Figure 1 (see Williams et al., 1991; Pajari et al., 1979), distinct from the belts of lenticular GRUB rocks within the Davidsville Group (Fig. 1, 2). The Woody Island siltstone is further characterized by the common presence thin bands and lenses of pink and black coticule (manganiferous garnet-quartz concentrations, for description see Williams, 1992).


**Figure 6.** Variable plunges in adjacent H3 fold hinges (centre) and curvilinear hinges (top right). Aspen Cove.

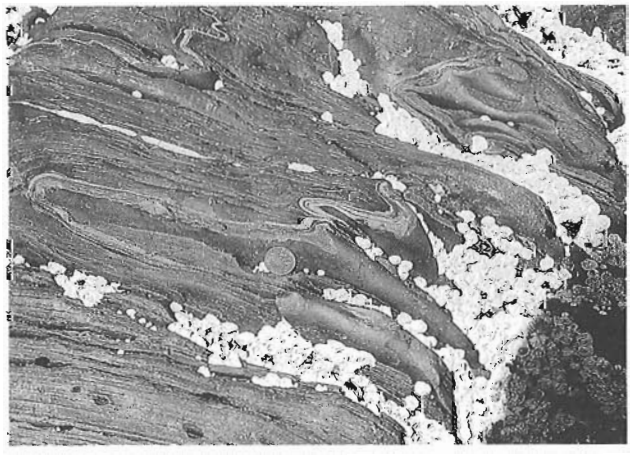

**Figure 7.** Curvilinear, small-scale H3 fold hinges (marked) in the Hamilton Sound sequence. Aspen Cove.

### *Early structures in the Hamilton Sound sequence*

Rocks of the Hamilton Sound sequence have a penetrative muscovite-chlorite or muscovite-biotite schistosity which is subparallel to bedding. In the area of Figure 3, this schistosity is axial planar to rare, rootless, intrafolial isoclinal folds. Their hinges fold an older mica schistosity. This oldest, folded schistosity is assigned to an H1 deformation event, the intrafolial folds and the regional, bedding-parallel schistosity to H2 (Table 1). Figure 5 depicts these structures, modified by late (H3) folding.

The H2 schistosity intensifies into a mylonitic foliation along the boundaries of the Main Point shale, and in belts of high strain within the Woody Island siltstone (Fig. 3). The mylonitic foliation exhibits asymmetric syn-shearing H2 folds which fold the early H1 schistosity, and a stretching lineation, which, where it is not affected by later folding, is coaxial with shear-related lineations in Gander Group mylonites. Mylonitic Hamilton Sound sequence contains both dextral and sinistral kinematic indicators. Adjacent to the Ragged Harbour and Aspen Cove plutons, the sinistral shearing also affects granite sheets, implying that it is equivalent to the late sinistral shearing in the Gander Group (G3 in Table 1); but it is uncertain whether it also contains an element of the earliest sinistral shear fabric (G2).

### *Late structures in the Hamilton Sound sequence*

In the area of Figure 3, the bedding-parallel H2 schistosity and the sheared granite sheets are folded by a regional, close-limbed, northeast-trending antiform of an H3 event, the axial trace of which extends for 9 km from Ladle Cove (Fig. 3). It is inclined to the northwest, as are large, 200 m to 500 m scale congruous (parasitic) folds in its northwestern limb, whereas in its southeastern limb, the congruous structures are inclined to the southeast. The latter in turn contain smaller congruous folds of all scales. These are strikingly curvilinear, resulting in common plunge culmination and depressions (Fig. 6), irregular plunges and/or trends of axes in small folds (Fig. 3, 7) and in incipient sheath folds with a steep to subvertical direction of maximum extension. H3 axial surface cleavage is a prominent foliation in the limbs of the H3 folds, but in their hinge zones it is very irregular and may refract for up to 40°. Near Ladle Cove, H3 folds are associated with approximately 1 m wide subvertical, sinistral shear zones trending east-by-northeast. The geometry and attitude of H3 folds corresponds with those of the small, late G4 folds in the Gander Group (Table 1). The H3 structures also appear to resemble "F2" folds (Karlstrom et al., 1982) from the Bay of Exploits region.

H3 folding was succeeded by minor, open, subrecumbent buckle folds without axial surface cleavage and irregular axial trends, and by steep, narrow zones of sinistral, north-trending strike-slip faults (Fig. 3), and in turn by brittle faulting.

## STRUCTURAL TIMING OF PLUTONIC ACTIVITY

Towards the Ragged Harbour and Aspen Cove granites (Currie and Pajari, 1981), Gander Group and Hamilton Sound sequence metasediments become progressively metamorphosed from phyllites (phyllonites where mylonitic) of low greenschist facies grade to medium- and locally coarse-grained amphibolite facies schists (and mylonitic schists), locally kyanite bearing. Significantly, the coarsened rocks maintain their regional foliar and linear fabrics, implying that much of the coarsening process was dynamothermal rather than static (contact metamorphic). These schists have been subsequently overprinted on the regional scale by at least two generations of static andalusite porphyroblasts which reach 2 cm in size, and by sillimanite (fibrolite). Locally they have been recrystallized to coarse, decussate hornfels.

The schists are cut by thin granite sheets, early marginal members of the Ragged Harbour and Aspen Cove plutons. Some such sheets in the Woody Island siltstone and in the Cuff Pond pelite share with their schistose hosts the S-C and shear band foliations of the late sinistral shearing (H2 and G3 in Table 1). They indicate emplacement of the marginal facies of the plutons during, or overlapping, the episode of late sinistral shearing, a relationship further supported by the correspondence of areas of coarsened, prograded schist (including mylonite schist) and of granite.

The coarsened schists and the sheared granite sheets are folded by the regional curvi-linear folds (H3 and G4). The relationship between the regional andalusite overprint and the folding is complex. In the Woody Island siltstone, andalusite overprints the axial surface cleavage of the folds. In mylonitic Cuff Pond pelite north of the Ragged Harbour River, small, centimetre-scale G4 folds fold the mylonitic fabric, bending, breaking, and separating 1 cm long porphyroblasts of pink, overprinting andalusite. In the same rock, some andalusite porphyroblasts are deformed by shear bands of the late episode of sinistral shearing. These relationships indicate that the onset of plutonism varied in time and place, overlapping both the late sinistral shearing and regional (H3/G4) folding.

At Musgrave Harbour, the Cuff Pond pelite adjacent to the boundary of the Deadman's Pluton is a coarse sillimanite-bearing schist extensively injected by agmatitic migmatite (the Flinn's Tickle complex), in which numerous mobile neosomes have segregated along sinistral shear bands (see also Goodwin and O'Neill, 1991), further indicating that a magma-related thermal peak accompanied the late shearing.

## DISCUSSION

### *Hamilton Sound sequence*

Structural studies complement Currie's (1992) conclusion that the Carmanville area contains not two, but three distinct, juxtaposed assemblages: the Gander Group of the Gander Zone, and the Davidsville Group and Hamilton Sound sequence of the Dunnage Zone. Structural contrasts (Table 1) and lithological contrasts between the redefined Davidsville Group and the Hamilton Sound sequence point to a tectonic boundary separating these assemblages, but this boundary may not be exposed. It is provisionally drawn at the structural base of the Wing Point greywacke (Fig. 1), which contains steeply inclined folds that face downwards, implying earlier recumbent folding for which there is, as yet, no evidence in the Davidsville Group. The lithologies of, and the deformation sequence in, the high-grade metasediments to the north of the GRUB, once assigned to the Gander Group (Kennedy and McGonigal, 1972), demonstrate their affinity with the Hamilton Sound sequence.

### *Tectonics along the Gander-Dunnage boundary*

In central Newfoundland, north-over-south sense of overriding by an allochthonous Dunnage Zone over flat-lying Gander rocks corresponds with transcurrent sense of motion in steepened rocks (Fig. 2 in Piasecki et al., 1990); and this movement was followed by a regional south-over-north "back-movement" along the same belts of shearing (Williams et al., 1989; Williams and Piasecki, 1990; Piasecki, 1988a; Piasecki et al., 1990).

North of Gander Lake, the steep northwesterly dip of the boundary shear zone results from progressive downturning towards the northwest of gently inclined Gander Group rocks, in which Hanmer (1981) recorded a north-over-south shear movement on a regional scale, but which also contain opposed (south-over-north) kinematic indicators (personal observation). Thus the early sinistral and dextral movements on this steepened boundary correspond with the sequence of shear movements on the Gander-Dunnage boundary in central Newfoundland. Correlation of the late sinistral shearing event is enigmatic, because in many areas it is uncertain whether fabrics of sinistral shearing are the product of only one phase of shearing, or of two.

The geophysical signature of the GRUB and of the adjacent Gander-Dunnage boundary does not appear to extend to depth; and gravity-magnetic anomalies suggest the presence of Dunnage-type rocks interlayered with Gander rocks, implying that the northern Gander Lake Subzone may represent a stack of allochthonous sheets (Miller, 1988). The suggested interpretation of the steep attitude of this boundary north of Gander Lake is that it may be related to a northeast-trending lateral ramp (cf. Currie, 1992) which constrained the eastern margin of a southwestward-moving ophiolitic-volcanic Dunnage Zone, or, as Miller's (1988) modelling would suggest, a lateral wall to a thrust stack (duplex) of Gander interlayered with Dunnage.

### *Temporal relationships*

Contrasts between the early structural sequences in the Gander and Dunnage zones clearly indicate that the Gander rocks were already foliated and folded at the time of emplacement of the GRUB and the deposition of the Davidsville Group. The magnitude of this temporal break remains uncertain. It may be a hiatus marking an orogeny (Kennedy and McGonigal, 1972; Williams et al., 1991), or an insignificant break, the first deformation in the Gander Group

being envisaged as related to the arrival of the GRUB (Pajari and Currie, 1978) in early Ordovician time (Dec and Coleman-Sadd, 1990; Williams and Piasecki, 1990). The latter would also account for the facies change from the psammitic Jonathan's Pond Formation to the Cuff Pond pelite. Kinematic fabrics related to this first juxtaposition of the Gander and Dunnage zones appear to have been overprinted by subsequent events. Movements recorded in the mylonitic fabrics (G2, D1, and H1(?) in Table 1) probably mark the beginning of a Silurian orogenic event of thrusting, crustal thickening, metamorphism, and plutonism (Currie and Piasecki, 1989).

### *Correlations with the Dover fault zone*

In the Dover fault zone, Holdsworth (1991) recorded an "early" phase of sinistral shearing with coeval plutonism and folding in a transpressional regime, and also the presence of still older movements. The author suggests that the late sinistral shearing, plutonism and curvilinear folding in the Carmanville region (G3/G4, D2/D3, and H2 events in Table 1) correspond with the early phase in the Dover zone, and the G1/G2, D1, and H1 events with the "older" events.

## ACKNOWLEDGMENTS

I thank the Geological Survey of Canada for financial support under Research Contract 23226-0-0543, my co-workers Drs. K.L. Currie and H. Williams for stimulating discussions and logistic assistance in the field, and Mrs. Helen Pennell of Noggin Cove for her excellent catering.

## REFERENCES

**Berthe, D., Choukroune, P., and Jegouzo, P.**
1979: Orthogneiss, mylonite and non coaxial deformation of granites: the example of the South Armorican Shear Zone; Journal of Structural Geology, v. 69, p. 31-42.

**Blackwood, R.F.**
1982: Geology of the Gander Lake (2D/15) and Gander River (2E/2) area; Newfoundland Department of Mines and Energy, Mineral Development Division, Report 82-4, 56 p.

**Currie, K.L.**
1992: Carmanville map-area (2E/8): a New Look at Gander-Dunnage relations in Newfoundland; in Current Research, Part D; Geological Survey of Canada, Paper 92-1D, p. 27-33.

**Currie, K.L. and Pajari, G.E.**
1981: Anatectic peraluminous granites from the Carmanville area, northeastern Newfoundland; Canadian Mineralogist, v. 19, p. 147-158.

**Currie, K.L. and Piasecki, M.A.J.**
1989: Kinematic model for southwestern Newfoundland based upon Silurian sinistral shearing; Geology, v. 17, p. 938-941.

**Currie, K.L., Pajari, G.E., and Pickerill, R.K.**
1980: Carmanville map-area, Newfoundland (12E/5); Geological Survey of Canada, Open File 776.

**Dec, T. and Colman-Sadd, S.P.**
1990: Timing of ophiolite emplacement onto the Gander Zone: evidence from provenance studies in the Mount Cormack Subzone; in Current Research, Newfoundland Department of Mines and Energy, Geological Survey Branch, Report 90-1, p. 289-303.

**Goodwin, L.B. and O'Neill, P.**
1991: The structural evolution of the northern segment of the Dunnage Zone – Gander Zone boundary, Newfoundland; in Current Research, Newfoundland Department of Mines and Energy, Geological Survey Branch, Report 91-1, p. 97-107.

**Hanmer, S.K.**
1981: Tectonic significance of the northeastern Gander Zone, Newfoundland: an Acadian ductile shear zone; Canadian Journal of Earth Sciences, v. 18, p. 120-135.

**Holdsworth, R.E.**
1991: The geology and structure of the Gander-Avalon boundary zone in northeastern Newfoundland; in Current Research, Newfoundland Department of Mines and Energy, Mineral Development Division, Report 91-1, p. 109-126.

**Karlstrom, K.E., van der Pluijm, B.A., and Williams, P.F.**
1982: Structural interpretation of the eastern Notre Dame Bay area, Newfoundland: regional post-Middle Silurian thrusting and asymmetrical folding; Canadian Journal of Earth Sciences, v. 19, p. 2325-2341.

**Kennedy, M.J. and McGonigal, M.H.**
1972: The Gander Lake and Davidsville Groups of northeastern Newfoundland: New data and geotectonic implications; Canadian Journal of Earth Sciences, v. 9, p. 452-459.

**Miller, H.G.**
1988: Geophysical interpretation of the geology of the northeast of the Gander Terrane, Newfoundland; Canadian Journal of Earth Sciences, v. 25, p. 1161-1174.

**O'Neill, P.P. and Blackwood, F.**
1989: A proposal for revised stratigraphical nomenclature of the Gander and Davidsville groups and the Gander River Ultrabasic Belt of Northeastern Newfoundland; in Current Research, Newfoundland Department of Mines and Energy, Mineral Development Division, Report 89-1, p. 165-176.

**Pajari, C.E and Currie, K.L.**
1978: The Gander Lake and Davidsville Groups of northeastern Newfoundland: a re-examination; Canadian Journal of Earth Sciences, v. 15, p. 708-714.

**Pajari, G.E., Pickerill, R.K., and Currie, K.L.**
1979: The nature, origin, and significance of the Carmanville ophiolitic melange, northeastern Newfoundland; Canadian Journal of Earth Sciences, v. 16, p. 1439-1451.

**Piasecki, M.A.J.**
1988a: A Major ductile shear zone in the Bay D'Espoir area, Gander Terrane, southeastern Newfoundland; in Current Research, Newfoundland Department of Mines and Energy, Mineral Development Division, Report 88-1, p. 135-144.
1988b: Strain-induced mineral growth in ductile shear zones, and a preliminary study of ductile shearing in western Newfoundland; Canadian Journal of Earth Sciences, v. 25, p. 2118-2129.

**Piasecki, M.A.J., Williams, H., and Colman-Sadd, S.P.**
1990: Tectonic relationships along the Meelpaeg, Burgeo and Burlington Lithoprobe Transects in Newfoundland; in Current Research, Newfoundland Department of Mines and Energy, Geological Survey Branch, Report 90-1, p. 327-339.

**White, S.**
1982: Fault rocks of the Moine Thrust Zone: a guide to their nomenclature; Textures and Microstructures, v. 4, p. 211-221.

**Williams, H.**
1992: Melanges and coticule occurrences in the northeast Exploits Subzone, Newfoundland; in Current Research, Part D; Geological Survey of Canada, Paper 92-1D, p. 121-127.

**Williams, H. and Piasecki, M.A.J.**
1990: The Cold Spring Melange and a possible model for Dunnage-Gander zone interaction in central Newfoundland; Canadian Journal of Earth Sciences, v. 27, p. 1126-1134.

**Williams, H., Piasecki, M.A.J., and Colman-Sadd, S.P.**
1989: Tectonic relationships along the proposed central Newfoundland Lithoprobe transect and regional correlations; in Current Research, Part B; Geological Survey of Canada, Paper 89-1B, p. 55-66.

**Williams, H., Piasecki, M.A.J., and Johnson, D.**
1991: The Carmanville Melange and Dunnage-Gander relationships in northeast Newfoundland; in Current Research, Part D; Geological Survey of Canada, Paper 91-1D, p. 15-23.

# Observations on coalbed methane potential, Prince Edward Island

**A.C. Grant and P.N. Moir**
**Atlantic Geoscience Centre, Dartmouth**

*Grant, A.C. and Moir, P.N., 1992: Observations on coalbed methane potential, Prince Edward Island; in Current Research, Part E; Geological Survey of Canada, Paper 92-1E, p. 269-278.*

***Abstract***

*Exploratory wells for oil and gas in the Gulf of St. Lawrence and on Prince Edward Island have intersected "coal measures", which coincide with a seismic horizon mappable over large areas (approximately 66 000 km$^2$) of the Gulf of St. Lawrence Basin and Sydney Basin. Measurements of coal thicknesses reported from the wells are not precise, but calculations using an "average" seam thickness and "typical" values for coal density and methane content indicate a large methane resource potential for the mapped coal measures. Although speculative, this result draws attention to central Prince Edward Island, where the coal measures are onshore and at depths from which methane is potentially exploitable.*

*Evaluation of available geophysical and geological data indicates that drilling and testing are required to further assess coalbed methane potential of Prince Edward Island.*

***Résumé***

*Dans le golfe du Saint-Laurent et dans l'Île du Prince-Édouard, les puits d'exploration des gisements de pétrole et de gaz ont recoupé les «couches houillères» qui coïncident avec un horizon sismique cartographiable sur de vastes étendues (approximativement 66 000 km$^2$) du bassin du golfe du Saint-Laurent et du bassin de Sydney. Les mesures des épaisseurs de houille faites à partir des puits ne sont pas précises, mais les calculs basés sur l'épaisseur «moyenne» d'un filon et sur les valeurs «typiques» de la densité du charbon et du contenu de méthane indiquent que les couches houillères cartographiées renferment de vastes ressources potentielles en méthane. Ce résultat relève de la spéculation, mais met en évidence l'importance de la région centrale de l'Île du Prince-Édouard, dans laquelle les couches houillères se trouvent sur terre, à des profondeurs où le méthane se prête possiblement à l'exploitation.*

*L'évaluation des données géophysiques et géologiques disponibles indique que des forages et des essais sont nécessaires pour une évaluation plus poussée des ressources potentielles en méthane de l'Île du Prince-Édouard.*

# INTRODUCTION

This paper examines geophysical and geological observations that bear upon assessing the methane potential of coal measures beneath Prince Edward Island.

## *Geological Background*

The Gulf of St. Lawrence Basin and Sydney Basin (Fig. 1) are Permo-Carboniferous successor basins on Lower Paleozoic rocks deformed by the Taconian (Ordovician) and Acadian (Devonian) orogenies. The rocks of these basins are mainly coarse- to fine-grained terrigenous clastics with subordinate marine clastics, carbonates, and evaporites (Sanford and Grant, 1990). Productive coal deposits occur in strata of Westphalian to Stephanian age (Fig. 2), and have been extensively mined in Nova Scotia and New Brunswick (Hacquebard, 1986).

In 1908 and 1909 the Geological Survey of Canada undertook a drilling program to determine whether coal deposits mined in Nova Scotia extended to Prince Edward Island (Brock, 1910). Five holes were drilled to depths approaching 2000 feet (610 m), the approximate limit for economic mining of coal. As none of the holes intersected significant showings of coal, these drilling results tended to discount Prince Edward Island as a coal "province". Later however, exploratory wells on the Island drilled for oil and gas encountered coal seams, and in 1975 a test hole (MacDougall 1A) was drilled to evaluate coal showings in the 1958 MacDougall No. 1 well (Howie, 1977). Unfavourable results from this test tended to discount coal potential.

Hacquebard (1986) examined coal zones penetrated by exploratory wells offshore in the Gulf of St. Lawrence (Fig. 1), and established correlations with coals of the Mabou

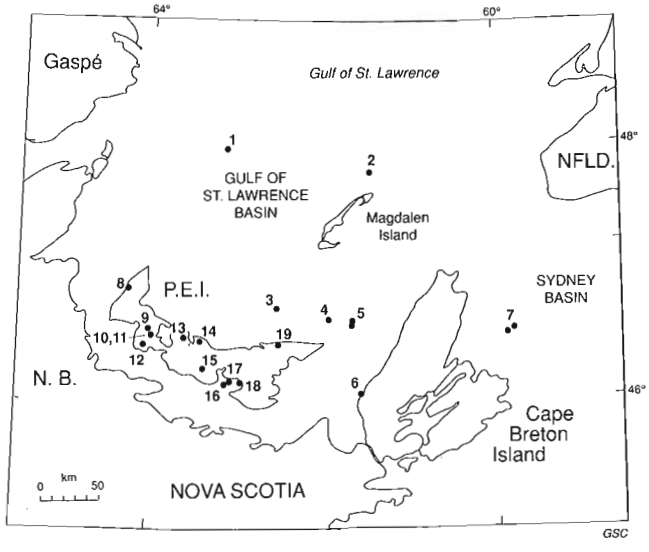


**Figure 1.** Map showing location of Gulf of St. Lawrence Basin and Sydney Basin. Numbered dots are sites of coal measure samples discussed in text (Table 2 and Figs. 6 and 7).

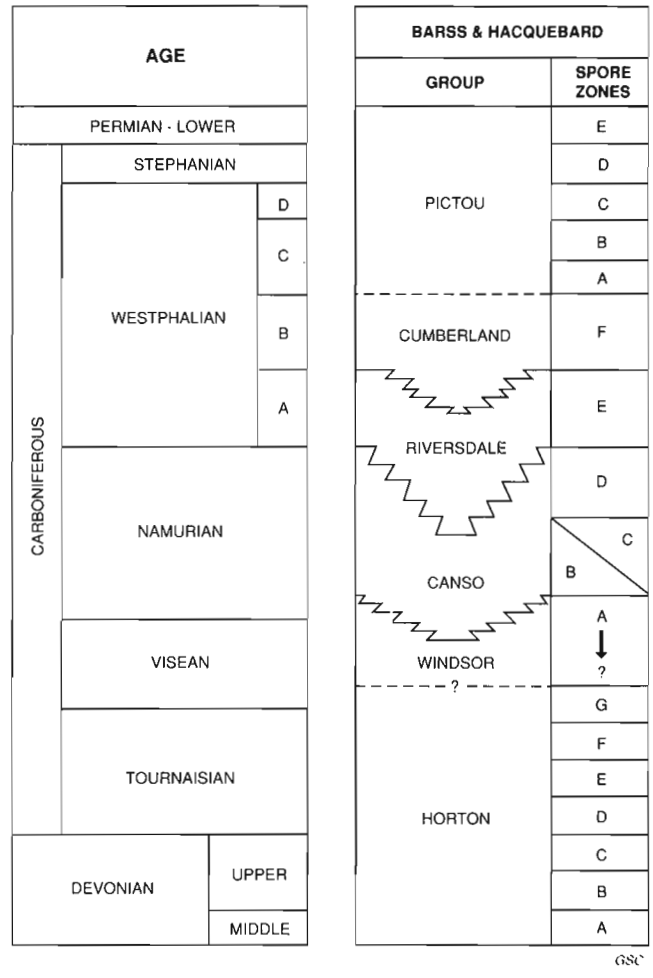


**Figure 2.** Stratigraphic diagram for Upper Paleozoic rocks in eastern Canada, after Hacquebard et al. (1989).

and Inverness coalfields on the west coast of Cape Breton Island. He concluded that this borehole evidence defines the Gulf of St. Lawrence Carboniferous Basin as the largest coalfield of eastern Canada. Analysis of seismic data from the Gulf of St. Lawrence region (Fig. 3), as reported in this paper, supports Hacquebard's interpretation and defines the extent of the coal zones offshore, and onshore beneath Prince Edward Island (Fig. 4).

## *Coalbed methane*

Methane is produced in the transformation of vegetable matter to coal; it is the main constituent of natural gas. Rightmire and Choate (1986) state that coalification to the rank of low volatile bituminous-semi-anthracite would have generated more than 5000 ft.$^3$ of methane per ton of coal (156 m$^3$ per tonne; Table 1). Up to half of this methane may remain in the coal, trapped in fractures and molecularly adsorbed onto the coal. The coal is thus both source and reservoir for the gas, with the capacity to hold two to three

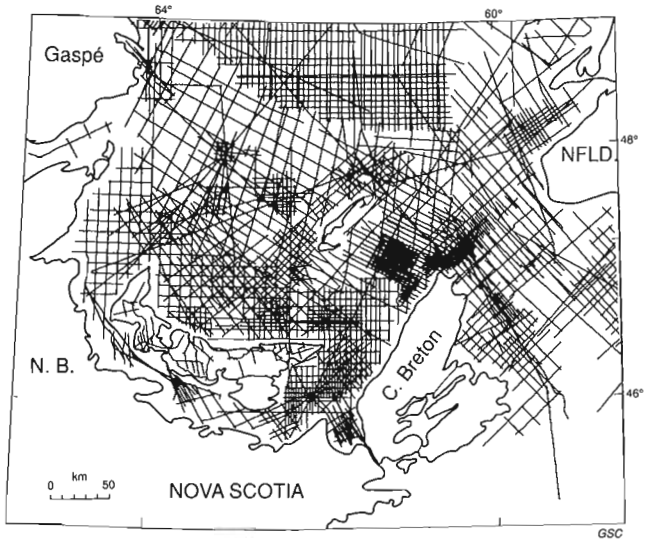


**Figure 3.** Map showing location of industry seismic lines in Gulf of St. Lawrence and on Prince Edward Island.

times as much gas as conventional reservoirs. Excess gas expelled during coalification may have charged adjacent reservoirs.

Creedy (1988) examined gas content versus depth in British coal seams, and found the most common relationship to be a linear increase with depth, ultimately reaching a constant value. He also demonstrated that methane content generally increases with coal rank, rank being a more important factor than petrographic composition. The quantity of gas adsorbed by the coal is influenced by a number of factors; it increases with a decrease in temperature, decrease in moisture content, and increase in rank. Gas present in excess of the adsorption capacity can only be accommodated by compression in open spaces within the coal. Creedy (1988) compared highest gas contents for British and United States coals; for high-volatile coal samples maximum gas contents were 15-16 $m^3/t$ (British) and 17-19 $m^3/t$ (U.S.); for anthracites from both countries the maximum methane content was 22 $m^3/t$.

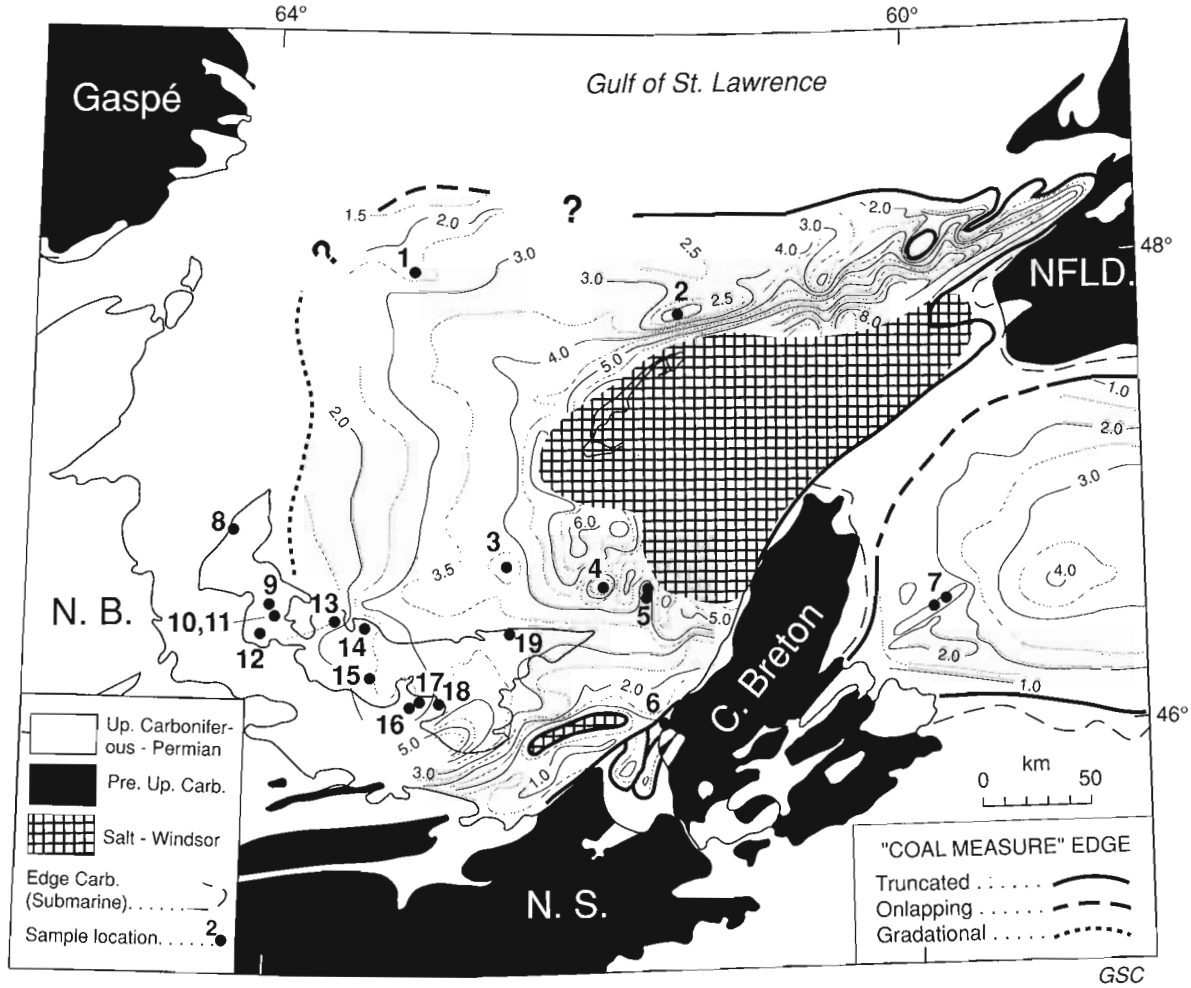


**Figure 4.** Map of "coal measures" seismic horizon, contours in km below sea level, derived from interpretation of seismic data (Fig. 3). Areas of salt diapirism are denoted by cross hatching.

**Table 1.** Methane Generation by Coal Rank, $m^3$/tonne (after Rightmire and Choate, 1986)

| RANK | METHANE | VITRINITE REFLECTANCE ($R_o$) |
|---|---|---|
| Lignite | -- | |
| Sub-bituminous | -- | |
| | | 0.50 |
| High-volatile Bituminous | 18 | |
| | | 1.20 |
| Medium-volatle Bituminous | 76 | |
| | | 1.63 |
| Low-volatile Bituminous | 62 | |
| | | 2.10 |
| Semi-anthracite | 22 | |
| | | 2.40 |
| Anthracite | 25 | |
| Total | 203 | |

Ulery (1988) examined geological factors influencing the gas content of Pennsylvanian and Permian coalbeds in southeastern Pennsylvania – coalbeds of essentially the same age as those in the Gulf of St. Lawrence Basin. This work showed that coalbed gas content is related primarily to rank and depth of the coalbed.

Exploitation of coalbed methane in the United States is subsidized as a non-conventional fuel, and extensive research on its development has been carried out in a number of sedimentary basins. The conventional gas industry recognizes this subsidized coal gas as a potential competitive threat (Natural Gas Exports Division, 1991).

Data bearing upon coal measures in the Gulf of St. Lawrence region – particularly beneath Prince Edward Island, are evaluated in this paper against the general characteristics of coalbed methane summarized above.

## METHODS OF STUDY

### *Seismic data*

Industrial multichannel seismic coverage (Fig. 3) is the basis for the map of "Coal Measures" (Fig. 4). The coal measures "horizon" comprises a band of several reflectors, which can be mapped regionally to tie with the level of coal occurrences as logged in the various exploratory wells offshore, and on Prince Edward Island. The character of the coal measures horizon is illustrated in Figure 5, which shows portions of marine seismic lines through (a) the Cable Head E-95 well and (b) the East Point E-49 well. Depths to this horizon have been converted from reflection time to kilometres using a regional velocity function.

Seismic expression of coal measures in the Gulf of St. Lawrence Basin dies out to the west, as indicated by the heavy dotted line in Figure 4. To the north, where marked by a dashed line, the coal measures horizon onlaps the "basement" seismic marker. A heavy solid line indicates the coal measures are truncated erosionally or structurally. Stuctural disturbance associated with salt diapirism prevents mapping southwest of Prince Edward Island, and northwest of Cape Breton Island.

The seismic data in some areas show development of shallower and deeper horizons with "coal measure" character, suggesting that shallower and deeper coal measures may occur, but geological control generally is not available to calibrate these observations.

### *Geological data*

Sources of sample information relevant to coal measures beneath the Gulf of St. Lawrence and Prince Edward Island are listed in Table 2. For the Gulf of St. Lawrence region the analyses of offshore wells and onshore mining areas by Hacquebard (1986) are summarized in Figure 6.

Bedrock unit boundaries in Figure 7 are from summaries of borehole logs by van de Poll (1983), who described Pictou Group "redbeds", "transition sequence" and "coal measures", and Pre-Pictou strata ranging from Horton Group to Cumberland Group (Fig. 2). The "coal measures" are grey sandstone to shale with "traces" (hole 8) to "common fragments" (hole 14) of coal. Van de Poll (1983) reported "coal fragments ..." and "a few coalified plant remains" in Pre-Pictou (Canso and Riversdale) strata in holes 14 and 16 respectively.

Figure 7 also shows specific depths and intervals of coal occurrence reported by Howie (1977), and levels at which coal samples have been taken for vitrinite reflectance measurements (Vonk and Avery, 1986b, c).

Indications of coal rank versus depth based on vitrinite reflectance measurements are summarized in Figure 8, by averaged curves for six wells and several point measurements from Mabou-Inverness and wells 10 and 17. Comparing Figure 8 and Table 1 indicates that coals sampled in the Gulf of St. Lawrence and on Prince Edward Island range in rank from high volatile C bituminous to semi-anthracite (from 0.6 to 2.0% Ro).

### *Gas shows*

"Mud logs" of gas detected in drilling mud and cuttings for wells 1-5 and 19 (Table 2) generally show pronounced peaks associated with coaly intervals (Fig. 9). The plots for these wells represent total gas; higher peaks sometimes include ethane and occasional propane components. Because the mud logs serve primarily to detect the presence or absence of gas, and the gas monitors were of several types, no attempt has been made to normalize the records to common units or scales.

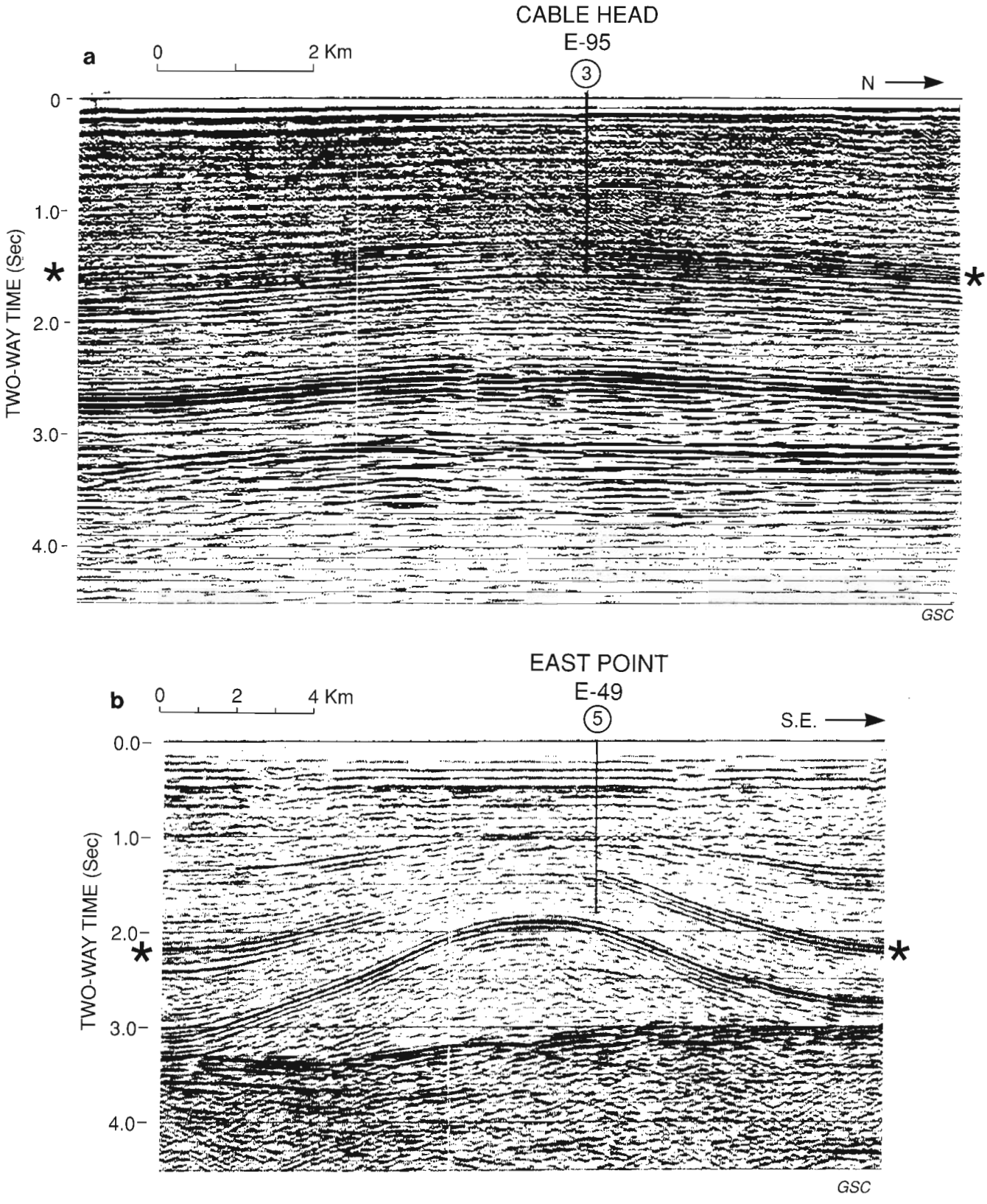


**Figure 5.** Seismic records through (**a**) Cable Head E-95 and (**b**) East Point E-49 well sites (wells 3 and 5 in Figs. 4 and 6). Asterisks indicate level of coal measures horizon.

**Table 2.** List of wells and coalfields providing subsurface information related to coal measures: see Figures 4, 6 and 7.

| | Well or Coalfield | Completion Year | Total Depth (M) |
|---|---|---|---|
| 1 | Shell-Soquip-Amoco Bradelle L-49 | 1973 | 4420.5 |
| 2 | Sarep H.Q Brion Island No. 1 | 1978 | 3206.2 |
| 3 | Irving-Chevron Texaco Cable Head E-95 | 1983 | 3235. |
| 4 | Hudson's Bay et al. Beaton Point F-70 | 1980 | 1734. |
| 5 | Hudson's Bay-Fina East Point E-49 | 1974 | 3526. |
| 6 | Mabou-Inverness Coalfield | | |
| 7 | Sydney Coalfield | | |
| 8 | Prince Edward Island Government Well No. 5 | 1909 | 509. |
| 9 | Imperial Port Hill No. 1 | 1958 | 1417. |
| 10 | Imperial MacDougall No. 1 | 958 | 2767.9 |
| 11 | MacDougall Core Hole 1A | 1975 | 712.8 |
| 12 | Imperial Wellington Station No. 1 | 1958 | 2960.8 |
| 13 | Hudson's Bay-Fina et al. Irishtown No. 1 | 1972 | 4107.8 |
| 14 | Hudson's Bay-Fina Green Gables No. 1 | 1972 | 3429.6 |
| 15 | Soquip et al. Tyrone No. 1 | 1975 | 4166.6 |
| 16 | Island Development Corp. Hillsborough No. 1 | 1944 | 4479.3 |
| 17 | Doherty Governor's Island No. 2 | 1926 | 1819.7 |
| 18 | Prince Edward Island Government Well No. 1 | 1910 | 582.2 |
| 19 | Soquip et al. Naufrage No. 1 | 1975 | 3105.3 |

References
Hacquebard (1986); 1-7
Howie (1977); 11
van de Poll (1983); 8-10, 12-19

The plot for well 15 (Fig. 9) shows methane content (ppm) measured from canned cuttings (Hardy and Jackson, 1980); the mud log from this well showed no trace of gas.

The East Point E-49 well (Fig. 9) is classed as a gas discovery (Hudson Bay Oil and Gas Co. Limited, 1970); a test at 1581.9-1591.4 m flowed gas at 152 910 $m^3/d$ (5.3 MMcf/d).

SOQUIP (1987) reported gas shows in The Green Gables well (Fig. 7; Table 2-14) at depths of approximately 2280 and 2360 m.

### *Data quality*

Discrepancies in coal descriptions for some wells indicate the sample evidence can be interpreted in different ways. Unless the wells were drilled and logged specifically for coal it is unlikely that accurate quantitative assessments can be made. Howie (1977) discussed problems inherent in evaluating reports of coal from cable tool drilling, noting that caving and pulverization of the coaly material make logging difficult. Hacquebard (1986) regards seam thicknesses recorded for the 5 offshore wells (Fig. 6) as approximate, because the downhole logging speed was too fast for accurate delineation of coaly intervals on the density logs.

The MacDougall 1A borehole (Howie, 1977) was drilled near the 1958 Macdougall No. 1 well site (Table 2) to check coal occurrences reported in that well. As mentioned in the introduction to this paper, this borehole did not encounter significant amounts of coal, which tended to discourage further exploration. Note, however, that the MacDougall bore hole is at the western, gradational edge of coal measures as defined by seismic data (Fig. 4).

The reported coal occurrences on Prince Edward Island (Howie, 1977) include a 3 foot (1 m) seam and a 10 foot seam (3 m) in wells 13 and 14 (asterisks, Fig. 7). In the 5 offshore wells (Fig. 6), Hacquebard (1986) records 20 seam intersections thicker than 2 m (6.6 feet), with 8 of these thicker than 3 m (9.8 feet). Despite inaccuracies in seam measurements, these reported thicknesses compare with seams known in mines on Cape Breton Island (Fig. 6); it is possible that seams of this thickness occur throughout the mapped area of the coal measures (Fig. 4.).

## METHANE RESOURCE CALCULATION

The seismic data, geological data and gas analyses reviewed above indicate that coal measures lie beneath Gulf of St. Lawrence and Prince Edward island, and that these coal measures contain methane. The data summarized in Figures 4, 6, and 7 are used below to estimate the amount of methane in these coal measures. Nikols (1991) stressed that coalbed methane calculations are "resource" estimates, a resource being a quantity known or believed to exist, calculated in place, and not constrained by economic or technological considerations.

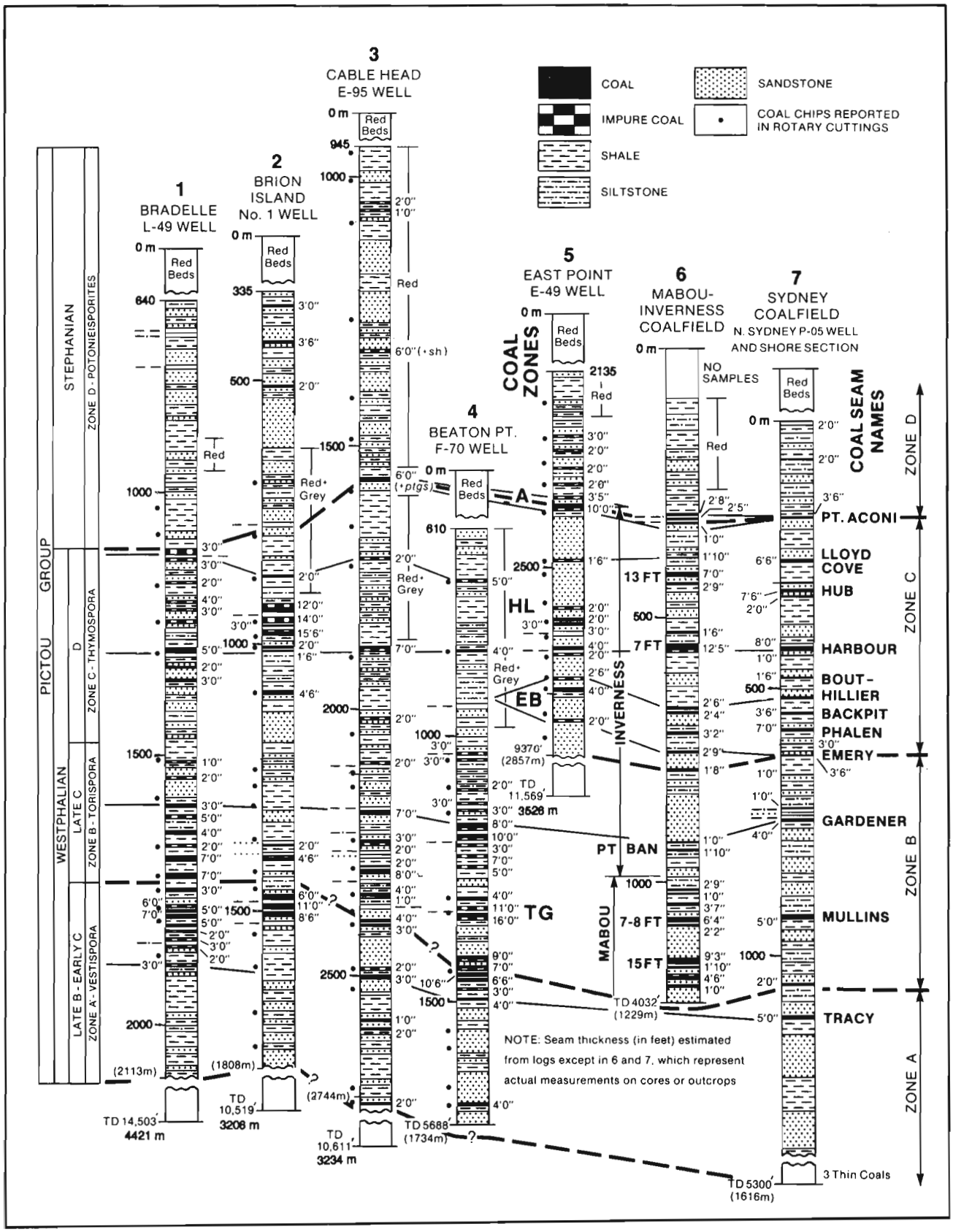


**Figure 6.** Logs of wells in Gulf of St. Lawrence region with correlations of coal bearing strata to coalfields on Cape Breton Island (locations in Figs. 1 and 4). After Hacquebard (1986).

Both offshore and onshore data (Fig. 6 and 7) support the probability that at least one 3 m seam persists over the area of coal measures mapped beneath Prince Edward Island and Gulf of St. Lawrence (Fig. 4; approx. 42 000 $km^2$, excluding Sydney Basin). A seam this thick yields a coal volume of 126 x $10^9$ $m^3$ for this area. Assigning the coal a specific gravity of 1.32 G/CC and applying a methane content of 13 $m^3$ per tonne (Nikols and Rottenfusser, 1991) yields a methane resource of 2.16 x $10^{12}$ $m^3$ (76.3 TCF).

The mapped area of coal measures beneath central and eastern Prince Edward Island (Fig. 4) is about 4,200 $km^2$, with a proportional methane resource of .216 x $10^{12}$ $m^3$ (7.6 TCF) for a 3 m coal seam over this area.

## DISCUSSION

The above calculations are speculative, but conservative assumptions yield a methane volume that prompts consideration of whether this resource can be exploited. Setting aside the offshore area because of higher drilling costs, attention shifts to prospective land areas. Within the Gulf of St. Lawrence Basin these include Brion Island, Mabou-Inverness, and Prince Edward Island (Fig. 4). The coal measures beneath these areas lie in a depth range from which coalbed methane is being exploited in some basins in the United States. The remainder of this paper focuses on Prince Edward Island.

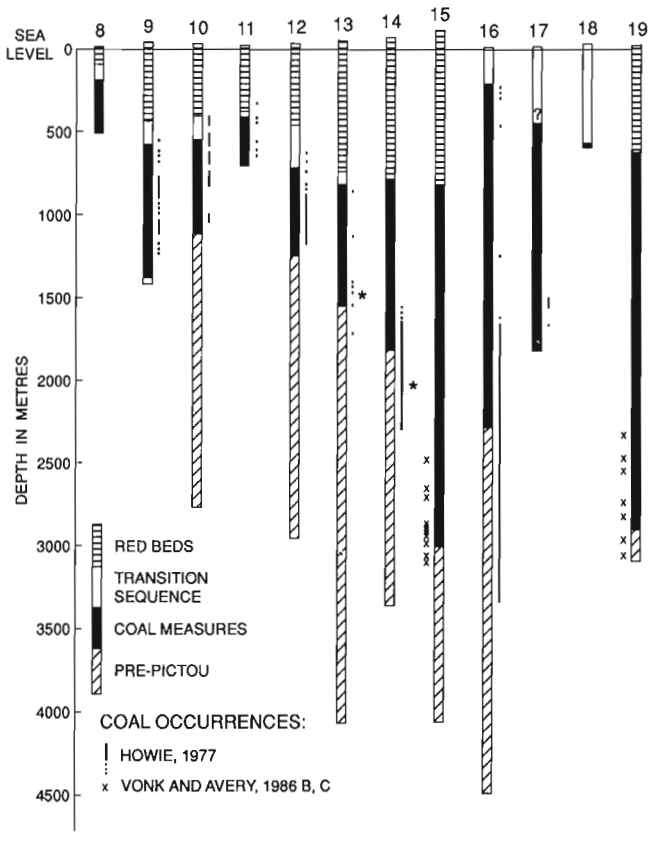


**Figure 7.** Logs of wells on Prince Edward Island (locations in Figs. 1 and 4). Bedrock units after van de Poll (1983).

Factors that determine the feasibility of coalbed methane development include 1) coal rank, 2) depth of overburden, 3) coal bed thickness, 4) favourable structure and fracture permeability, 5) permeability of adjacent strata, 6) water content, and 7) pressure stress relationships (Markowski, 1991).

Factors 4 - 7 from the list above cannot be addressed with existing data; these parameters can be evaluated only through drilling and testing. Coalbed permeability is considered the most critical parameter for production of coalbed methane.

It remains to consider whether rank, thickness, and depth of coal beds are such that drilling and testing may be warranted.

Measurements of coal rank reported for several wells (Fig. 8) are in the range favourable to generation of coalbed methane (e.g., Rightmire and Choate, 1986; Creedy, 1988).

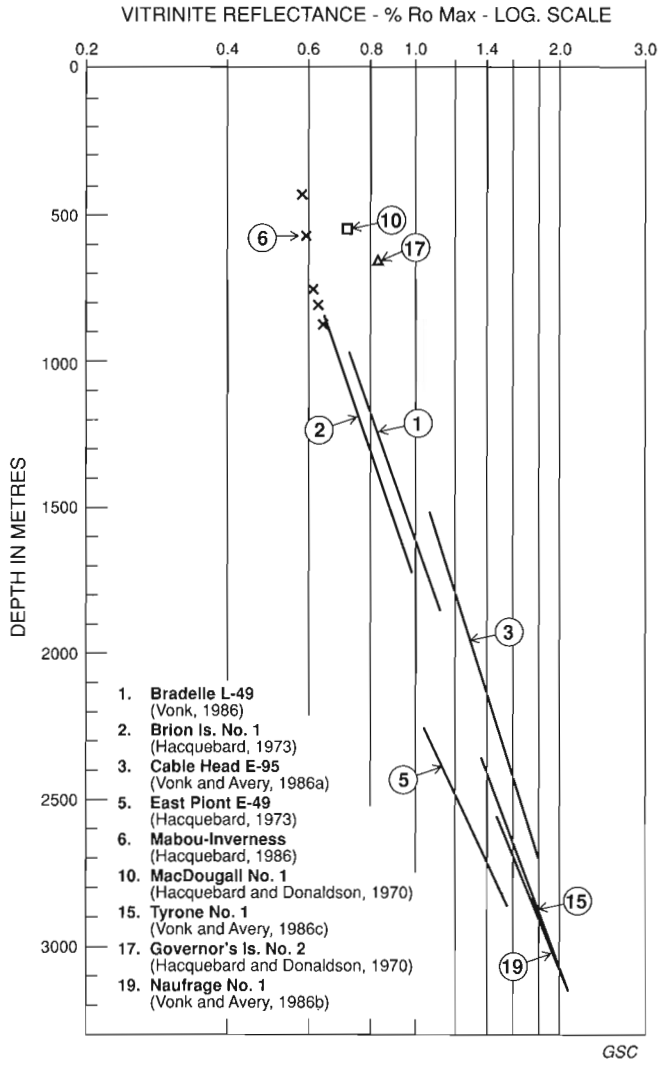


**Figure 8.** Plot of vitrinite reflectance measurements vs. depth. Numbered curves and data points correspond to Table 2.

As discussed, it is possible that seam numbers and thickness under Prince Edward Island (Fig. 4) are comparable to those encountered in coal mines on Cape Breton Island (Fig. 6 and 7). The resource calculation above shows that one 3 m seam can contain a large volume of methane; in the United States, coalbed methane operations frequently exploit several seams.

Calculated depths to the coal measures beneath Prince Edward Island range from one kilometre to more than 5 km (Fig. 4). If other factors are favourable, depth limitations may determine the area of the coal measures exploitable for methane.

Costs of recovering coalbed methane increase with depth, although at burial depths of less than several hundred metres methane may be lost by seepage (Rightmire and Choate, 1986). Holditch (1991) states that most methane produced in the United States will be from reservoirs less than 5000 feet (1524 m) deep, because of low-cost drilling to these shallow depths. O'Brien (1991) reports that the Piceance Basin in Colorado holds an estimated 84 TCF of gas in place, but because this gas lies between 6000 and 9000 feet (1829 and 2743 m) it is deemed too deep to be economical.

In contrast to these views, recent issues of "Quarterly Review of Methane from Coal Seams Technology", a publication of the (U.S) Gas Research Institute, report on various projects aimed at "deep" coalbed methane; several examples are recorded below:

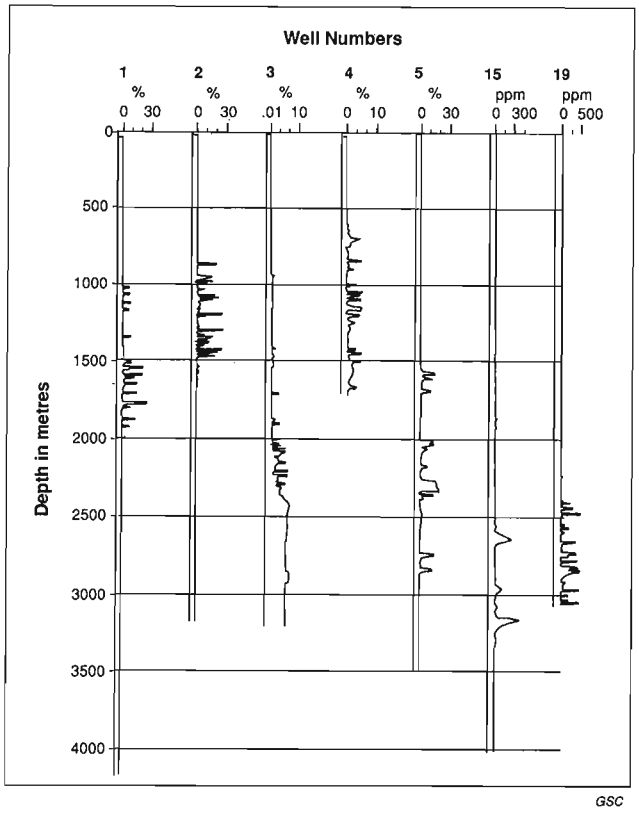


**Figure 9.** Gas shows for wells in the Gulf of St. Lawrence and on Prince Edward Island. Well numbers correspond to Table 2.

1. Western Washington; Meridian Oil permitted a 6000 foot (1829 m) test in northern Lewis County (1989, v. 7, no. 1, 2, p. 2)
2. Piceance Basin, Colorado; Chevron USA Inc. plans 5 wildcat tests to depths of 6500 to 7500 feet (1981 to 2286 m) (1989, v. 7, no. 1, 2, p. 5): Barrett Resources have completed wells producing to depths of 7000 feet (2134 m) in the Grand Valley field (1990, v. 7, no. 4, p. 7): Fuelco plans 5 tests in the Rulison Field to projected depths of 8000 to 9100 feet (2438 to 2774 m) (1991, v. 8, no. 2, p. 7)
3. Sand Wash Basin, Colorado: Meridian Oil Inc. completed 2 wells at 5700 and 6500 feet (1737 and 1981 m), and Chevron USA Inc. plans a 9500 foot (2896 m) test (1991, v. 8, no. 2, p. 5)
4. Washakie Basin, Wyoming; Pacific Gas and Electric Resources Company is reported to have drilled two wells to depths of about 9000 feet (2743 m) (1991, v. 8, no. 2, p. 6):
5. Wind River Basin, Wyoming; several operators are targeting methane wells to depths of 7000 to 10 600 feet (2134 to 3231 m). These deeper wells are directed at sand intervals in coal-bearing strata – "tight gas reservoirs" – (1991, v. 8, no. 4, p. 2).

The above examples document exploration for coalbed methane to depths below 3 km. "Tight gas reservoirs" include adjacent beds charged by the excess gas expelled during coalification. Rightmire and Choate (1986) propose that tight gas be included with coalbed methane in studies of overall resource potential, although the means of producing methane from coal seams as opposed to sands might differ. The potential for charging tight gas reservoirs presumably exists wherever coal measures occur (Fig. 4).

In the United States coalbed methane is produced from existing mines, and from vertical and horizontal boreholes. Technologies for exploiting coalbed methane, such as horizontal drilling, are advancing rapidly. In Canada – although not focused on coalbed methane – the drilling industry completed 157 horizontal holes in the first three quarters of 1991, compared to 57 over the same period in the previous year (Daily Oil Bulletin, 1991).

## CONCLUSIONS

Drilling has detected coal measures in the Gulf of St. Lawrence and beneath Prince Edward Island, and seismic data indicate continuity of these coal measures between and beyond the drill sites. Methane "shows" were reported from all wells where mud logs were run, or canned cuttings were analyzed for gas. The coal measures beneath Prince Edward Island undoubtedly contain a coalbed methane "resource"; they are of similar rank and thickness and within the depth range of coal deposits being exploited for methane in some basins in the United States.

Whether the coalbed methane resource beneath Prince Edward Island is economically exploitable can only be determined by a program of drilling and testing.

Coalbed methane might initially provide energy for electrical power generation, as Prince Edward Island is not served by a gas pipeline and depends mainly on imported oil for its energy needs.

## ACKNOWLEDGMENTS

It is a pleasure to acknowledge many fruitful discussions with colleagues C.E. Barss, P.A. Hacquebard, and B.V. Sanford, and with R.C. Boehner, Nova Scotia Department of Mines and Energy. A.E. Jackson is thanked for much help with geophysical data, and S.L. Grant and J.C.Y. Smith for large compilations. G.L. Cook and G.M. Grant prepared illustrations. R. Goh, Amoco Canada Petroleum Co. Ltd., lent valuable assistance with industry seismic data. Reviews by P.A. Hacquebard and M.A. Williamson are much appreciated.

## REFERENCES

**Brock, R.W.**
1910: Borings on Prince Edward Island; in Summary Report 1909, Geological Survey of Canada, Sessional Paper No. 26, p. 30-37.

**Creedy, D.P.**
1988: Geological controls on the formation and distribution of gas in British Coal Measure strata; International Journal of Coal Geology, v. 10, p. 1-31.

**Daily Oil Bulletin**
1991: Horizontal drilling steady through three quarters; October 28, p. 1.

**Hacquebard, P.A.**
1973: Pre- and postdeformational coalification and its significance for oil and gas exploration; C.N.R.S. Paris, 1973 International Colloquium on "Petrographie de la materiere organique des sediments, etc.", p. 225-241.
1986: The Gulf of St. Lawrence Carboniferous Basin: the largest coalfield of Eastern Canada; Bulletin of Canadian Institute of Mining and Metallurgy, v. 79, p. 67-78.

**Hacquebard, P.A. and Donaldson, J.R.**
1970: Coal metamorphism and Hydrocarbon potential in the Upper Paleozoic of the Atlantic Provinces, Canada; Canadian Journal of Earth Sciences, v. 7, p. 1139-1163.

**Hacquebard, P.A., Gillis, K.S., and Bromley, D.S.**
1989: Re-evaluation of the coal resources of Western Cape Breton Island; Nova Scotia Department of Mines and Energy, Paper 89-3, 47 p.

**Hardy, I.A. and Jackson, A.E.**
1980: A compilation of geochemical data: east coast exploratory wells; Geological Survey of Canada, Open File 694.

**Holditch, S.A.**
1991: Completion methods in coal seam reservoirs; abstract in Quarterly Review of Methane from Coal Seams Technology, v. 8, no. 3, p. 38.

**Howie, R.D.**
1977: Geological studies and evaluation of MacDougall core hole 1A, Western Prince Edward Island; Geological Survey of Canada, Paper 77-20, 26 p.

**Hudson Bay Oil and Gas Co. Limited**
1970: Well History, Hudson Bay Fina East Point E-49.

**Markowski, A.K.**
1991: Preliminary feasibility study of the coal-bed methane resource in Pennsylvania; abstract in Bulletin of American Association of Petroleum Geologists, v. 75, p. 1387.

**Natural Gas Exports Division, Oil and Gas Branch.**
1991: Coal seam gas development in the continental U.S.; Energy, Mines and Resources Canada, 20 p.

**Nikols, D.**
1991: Resources and reserves of coal bed methane in Canada; Canadian Gas Association Technical Meeting, Vancouver.

**Nikols, D.J. and Rottenfusser, B.A.**
1991: Coal bed methane – a Canadian Resource for the 90's; Canadian Gas Association Technical Meeting, Vancouver.

**O'Brien, R.**
1991: Tax credit, pipeline expansions will make U.S. coal seam gas a strong competitor; Daily Oil Bulletin, July 25, p. 1-2.

**Rightmire, C.T. and Choate, R.**
1986: Coal-bed methane and tight gas sands relationships; AAPG Studies in Geology No. 24, p. 87-110.

**Sanford, B.V. and Grant, A.C.**
1990: Bedrock geological mapping and basin studies in the Gulf of St. Lawrence; in Current Research, Part B; Geological Survey of Canada, Paper 90-1B, p. 33-42.

**SOQUIP**
1987: Estuary and Gulf of St. Lawrence; geological – geophysical geochemical data integration; Geological Survey of Canada, Open File 1721.

**Ulery, J.P.**
1988: Geologic factors influencing the gas content of coalbeds n Southwestern Pennsylvania; United States Department of the Interior, Bureau of Mines report of Investigations 9195, 26 p.

**van de Poll, H.W.**
1983: Geology of Prince Edward Island; Province of Prince Edward Island, Department of Energy and Forestry, Energy and Minerals Branch Report 83-1, 66 p.

**Vonk, A.M.**
1986: Vitrinite reflectance (Ro Max) of coal samples from Shell – Soquip - Amoco Bradelle L-49; Geological Survey of Canada, Open File 1924.

**Vonk, A.M. and Avery, M.P.**
1986a: Vitrinite reflectance (Ro Max) of coal samples from Irving Chevron-Texaco Cablehead E-95; Geological Survey of Canada, Open File 1620.
1986b: Vitrinite reflectance (Ro Max) of coal samples from Soquip et al. Naufrage No. 1; Geological Survey of Canada, Open File 1619.
1986c: Vitrinite reflectance (Ro Max) of coal samples from Soquip et al. Tyrone No. 1; Geological Survey of Canada, Open File 1618.

---

Geological Survey of Canada Project 870050

# A paleomagnetic analysis of the Tangier Dyke in Meguma Terrane of Nova Scotia

**E.I. Tanczyk**
**Continental Geoscience Division**

*Tanczyk, E.I., 1992: A paleomagnetic analysis of the Tangier Dyke in Meguma Terrane of Nova Scotia; in Current Research, Part E; Geological Survey of Canada, Paper 92-1E, p. 279-288.*

***Abstract***

*A detailed paleomagnetic study of a section across a 15m wide dyke and its host rock isolated two poles: one related to the intrusive event and the other to the regional metamorphism of the host. Remanence acquisition in the dyke is linked by a positive contact test to the 370 Ma radiometric age of the dyke swarm. A field reversal occurred during the time of intrusion. The older remanence related to Acadian metamorphism in the host rock is unlike any Devonian pole from North America. It is interpreted as a pre-accretionary signature characteristic of the Meguma Terrane. Tectonic models that stipulate a large dextral displacement of the terrane with respect to the continent in the Devonian account for the observed discrepancy.*

***Résumé***

*Une étude paléomagnetique détaillée d'une coupe transversale d'un dyke de 15m de large et des roches encaissantes a permis d'isoler deux pôles: l'un associé à l'événement intrusif, l'autre au métamorphisme régional de la roche encaissante. Après un essai positif de contrôle par contact, on a associé l'acquisition de la rémanence par le dyke à l'âge radiométrique (370 Ma) de l'essaim de dykes. Une inversion du champ s'est produite à l'époque de l'intrusion. La rémanence plus ancienne liée au métamorphisme d'âge acadien dans la roche encaissante est différente de celle de tout pôle d'âge dévonien en Amérique du Nord. On l'a interprétée comme une signature antérieure à l'épisode d'accrétion caractéristique du terrane de Meguma. Les modèles tectoniques qui impliquent un important déplacement dextre du terrane par rapport au continent au cours du Dévonien expliquent la contradiction observée.*

## INTRODUCTION

The paleomagnetic investigation of a lamprophyric dyke in the Tangier district of Nova Scotia forms part of a larger study of the Meguma Terrane with the objective of comparing paleomagnetic pole positions within the terrane to those of similar age on the other side of the suture. The comparison is aimed at establishing the time at which large-scale paleomagnetically-detectable, relative movements ceased along the Minas Geofracture, and possibly indicate the provenance of the terrane.

The Meguma Terrane is the most outboard displaced block of the Appalachian collage, and was the last to accrete to North America. On geological evidence, the final phase of the accretionary process was interpreted as a dextral transpression along the Minas Geofracture caused by oblique convergence (Keppie,1982, Fig.1a). $^{40}Ar$-$^{39}Ar$ mica cooling ages of 360-370 Ma date the upper limit of the cessation of this motion (Keppie and Dallmeyer, 1987). Meguma paleomagnetic poles as far back as the Early Carboniferous are similar to those from the Avalon Terrane across the suture, indicating that any displacement that may have occurred after the Devonian was minor (Scotese et al., 1984). Results from the ongoing study of the Meguma Terrane have extended the agreement across the suture back to the Late Devonian (Tanczyk, 1989). New data presented here provide a paleomagnetic contact test as an improvement of the age constraint on the earlier results. Evidence for a tectonic divergence between the Meguma Terrane and North America prior to 370Ma was discovered in the study of the Tangier dyke.

The dyke is part of the lamprophyric Weekend dyke swarm situated along the eastern shore of Nova Scotia (Ruffman and Greenhough, 1990) and dated by Kempster at al. (1989) at ca. 370 Ma by $^{40}Ar$-$^{39}Ar$. It was first mentioned in mapping by Faribault in 1901. Its possible composite intrusion history, abundance of xenoliths indicating a lower crustal origin, and well aligned crystals that facilitate studies on direction of magma flow, account for the recent interest by a number of researchers. (The Tangier dyke (Giles and Chatterjee, 1987) was subequently referred to as the "Popes Harbour dyke" by Greenhough et al.(1988), and Ruffman and Greenhough (1990). This study gives preference to the original name.)

The dyke intrudes the Goldenville Formation, a turbiditic sandy shale deposited during the Cambrian and metamorphosed to lower greenschist facies during the Acadian Orogeny. $^{40}Ar$-$^{39}Ar$ dating by Muecke et al.(1988) constrained the deformation in this area to the 405-390 Ma interval. Preservation of original sedimentary features in the Goldenville Formation suggests that no subsequent deformation occurred. The age of the Weekend dyke swarm coincides with the peak of granitic intrusive activity in the Meguma, an example of which is the emplacement of the South Mountain Batholith, dated at 373-361 Ma by Rb-Sr (Clarke and Halliday, 1980). A genetic relationship is possible between the Tangier dyke and nearby granitic intrusions of the same age (Chatterjee and Giles, 1988).

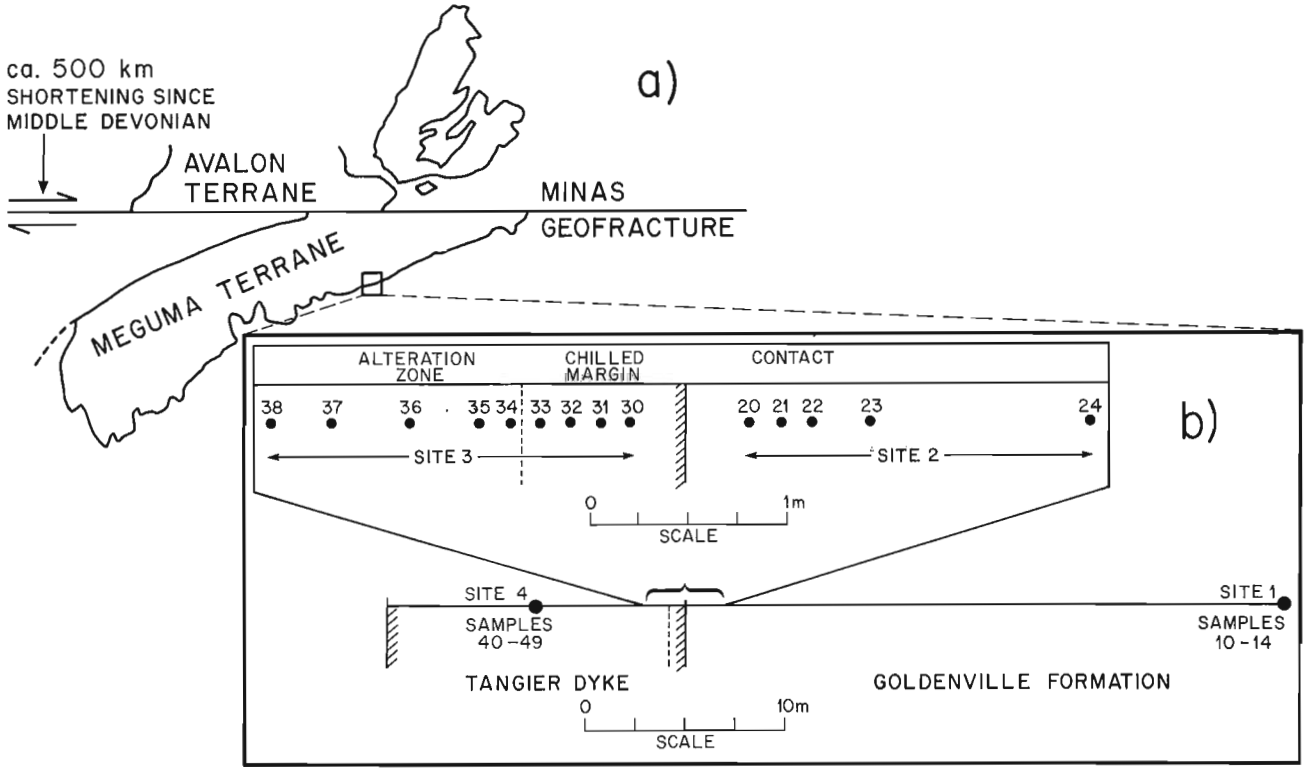


**Figure 1.** **a**) Tectonic setting of the Meguma Terrane in the Late Devonian (As proposed by Keppie, 1982). **b**) Schematic cross-section of the sampling locality.

## SAMPLING AND EXPERIMENTAL METHODS

Oriented drill core samples were obtained from four sites in the Tangier dyke and the host Goldenville Formation at a continuous exposure along the coast (Fig.1b). The samples constitute a cross-section spanning the dyke from its core into the host rock up to 30m from the dyke. On average, 7 cores were drilled at each site, from which 3 samples were cut. Half of the collection was demagnetized thermally up to 710°C in steps varying from 100° to 5°, depending on the resolution required in the proximity of unblocking temperatures ($T_{ub}$s). The remainder of the collection was treated in an alternating field (AF) demagnetizer up to 290 millitesla (mT), using a triaxial tumbling mechanism. As with thermal treatment, the spacing of the steps was varied as warranted from 10 to 1mT. The remanence directions and intensities were measured on a JR-4 spinner magnetometer, and all data processing was performed on the interactive SPIN database system (Parmelee and Garand, 1984).

## PALEOMAGNETIC RESULTS

The remanence vectors measured on the Tangier dyke and the surrounding Goldenville Formation can be subdivided into 5 distinct categories (Table 1).

### *Goldenville remanence (G)*

After removal of a viscous component, demagnetization of the Goldenville Formation at site 1 at 30m from the dyke, isolated a single stable remanence (Fig. 2a). The Goldenville remanence is carried predominantly by hematite with a high alternating field stability (Afs) range of 120-230 mT, and $T_{ub}$s in excess of 710°C. Hematite's theoretical Curie point of 680°C represents the unblocking of the spin-canted magnetic moment. A hard defect moment caused by lattice imperfections may also be present and can account for remanence stability up to the Neel point of 725°C (Smith and Fuller, 1967). The unusually high $T_{ub}$s observed in the present study are attributed to this property of hematite.

At site 1 the Goldenville remanence occurs in both polarities, sometimes mixed in the same sample (Fig.2b). At the contact site 2 the magnetization of one sample farthest from the dyke (2m) was resolved into a dyke overprint superimposed on the host remanence (Fig. 2c). The overprint unblocked at 500°C, but the $T_{ub}$ of the older remanence was not reached, and is greater than 710°C. The unblocking spectrum suggests that titanomagnetite carries the overprint, while hematite was not affected by the intrusion and preserved the characteristic Goldenville Formation signature. Thin section analysis supports this interpretation, because there is no recrystallization of chlorite into amphiboles, and therefore no evidence for the elevation of temperature above the greenschist isograd at this location. The Goldenville remanence, which occurs only at a distance from the dyke, is interpreted to be a remagnetization acquired during the Acadian Orogeny in the Devonian.

### *Tangier Normal remanence ($T_n$)*

A second remanence, $T_n$, is also present at site 1. Judging by magnetic mineralogy, its occurrence is governed by fluctuations in the titanomagnetite / hematite ratio. The reset samples have an Afs range of 45-80mT and a $T_{ub}$ of 300°C, while the alternating field stability of the Goldenville remanence is 120-230mT and its $T_{ub}$s exceed 710°C. Secondary titanomagnetite could have been introduced regionally at the time of emplacement of the dyke swarm, or existing titanomagnetite reset within the temperature confines of lower greenschist facies. Vector diagrams suggest that where Tangier Normal remanence occurs in the Goldenville Formation (Fig.2d), the remagnetization is complete, and results from site 1 can be treated as single components.

At site 2 the Tangier Normal remagnetization is the only component in all but the sample farthest from the intrusion, as discussed above. The principal magnetic carrier is titanomagnetite, with a $T_{ub}$ range of 500°-570°C, and an alternating field stability range of 50-130mT (Fig.3a). Hematite was also reset near the dyke, as manifested by the occurrence of a $T_{ub}$ of >640°C and an alternating field stability of 160mT in one core. The dyke rocks of the chilled margin (site 3, Fig.3b) carry a single component remanence whose average is statistically indistinguishable from the one in the contact (Table 2). Here the ranges of both the alternating field stability (120-200mT) and the $T_{ub}$ (540°-600°C) are higher than in site 2, indicating an additional presence of hematite. The agreement of remanences across the contact and the existence of a characteristic host rock remanence further from the dyke constitute a positive contact test. The Tangier remanence can be associated with the time of the dyke intrusion, and is pre-dated by the Goldenville remanence.

### *Tangier Reversed remanence ($T_r$)*

The mineralogy, grain size and magnetic properties of the core of the Tangier dyke (site 4) are radically different from that of the margin. Here the dominant opaque is coarse-grained pyrrhotite, whose primary igneous origin is indicated by quenched texture and minor exsolution lamellae of pyrite. Low $T_{ub}$s of 200-475°C, and a tendency for instability of the remanence under alternating field treatment in this site are both consistent with the magnetic behaviour of pyrrhotite. The tendency of this magnetic carrier to acquire spurious magnetizations under alternating field treatment has been noted by Thompson (1990). The pyrrhotite carries a single component remanence $T_r$ (Fig. 3c), which is incompletely reversed with respect to the one in the chilled margin. The inclination of the Tangier Reversed remanence in site 4 is about 30° steeper than the Tangier Normal average (Table 2). The opposite polarity of the core presumably represents a true field reversal, because the pyrrhotite is very pristine, and there is no evidence for overprinting in the demagnetization spectrum. Notably, the inclination of Tangier Normal remanence from the contact, while in statistical agreement with the margin, is somewhat steeper, suggesting it was blocked after the margin, at the onset of the

**Table 1.** Paleomagnetic remanence directions (stable samples only)

| S | Dist. | # | N | D | I | $\alpha_{95}$ | $T_{ub}$ or Afs |
|---|---|---|---|---|---|---|---|
| GOLDENVILLE REMANENCE (G) | | | | | | | |
| 1 | 30m | 10B | 17 | 49 | 12 | 9.1 | >710° |
| | | 10C | 21 | 60 | 27 | 7.8 | 210mT |
| | | 10D | 13 | 64 | 38 | 18.7 | 130mT |
| | | 12C | 14 | 42 | 17 | 8.2 | >675° |
| | | 13D | 9 | 246 | -23 | 6.8 | 230mT |
| | | 14A | 16 | 238 | -45 | 16.8 | 120mT |
| 2 | 2m | 24A | 11 | 67 | 40 | 14.4 | >710° |
| TANGIER NORMAL REMANENCE ($T_n$) | | | | | | | |
| 1 | 30m | 10A | 13 | 207 | 37 | 8.4 | 45mT |
| | | 11B | 11 | 196 | 18 | V | 80mT |
| | | 11D | 10 | 194 | 24 | 10.6 | 60mT |
| | | 13B | 12 | 227 | 15 | 15.9 | 50mT |
| | | 14C | 4 | 215 | 33 | 15.6 | 300° |
| 2 | .3m | 20A | 8 | 215 | 36 | 4.2 | 570° |
| | | 20B | 8 | 218 | 40 | 4.0 | 50mT |
| | | 21B | 20 | 231 | 31 | 8.9 | 130mT |
| | | 21C | 12 | 213 | 31 | 5.1 | 525° |
| | .9m | 23A | 5 | 204 | 52 | 13.9 | >640° |
| | | 23B | 9 | 221 | 29 | 12.0 | 160mT |
| | 2m | 24A | 9 | 227 | 49 | V | 500° |
| 3 | .3m | 30A | 21 | 222 | 11 | 9.3 | 170mT |
| | | 30B | 18 | 223 | 10 | 7.3 | 140mT |
| | | 30C | 10 | 201 | 28 | 7.8 | 600° |
| | .45m | 31A | 16 | 214 | 18 | 5.8 | 170mT |
| | | 31C | 24 | 201 | 35 | 8.8 | 190mT |
| | .6m | 32A | 7 | 214 | 2 | 10.2 | 80mT |
| | | 32B | 8 | 199 | 21 | 7.1 | 540° |
| | | 32C | 20 | 202 | 29 | 7.4 | 120mT |
| | | 32D | 11 | 202 | 17 | 6.7 | 550° |
| | .9m | 34A | 12 | 220 | 57 | 13.8 | 200mT |

| S | Dist. | # | N | D | I | $\alpha_{95}$ | $T_{ub}$ or Afs |
|---|---|---|---|---|---|---|---|
| TANGIER REVERSED REMANENCE ($T_r$) | | | | | | | |
| 4 | 7.5m | 40B | 9 | 32 | -68 | 2.7 | 475° |
| | | 41C | 9 | 37 | -65 | 3.0 | 200° |
| | | 42C | 5 | 97 | -44 | 17.8 | 35mT |
| | | 43A | 8 | 32 | -55 | 2.8 | 200° |
| | | 44C | 9 | 19 | -50 | 6.9 | 200° |
| | | 45A | 8 | 36 | -57 | 3.0 | 200° |
| | | 47A | 8 | 87 | -43 | 1.4 | 200° |
| | | 48B | 5 | 37 | -55 | 17.1 | >40mT |
| | | 49B | 8 | 48 | -56 | 3.6 | 200° |
| TANGIER ABERRANT REMANENCE ($T_a$) | | | | | | | |
| 1 | 30m | 11C | 11 | 25 | 71 | 6.4 | 60mT |
| | | 13A | 23 | 86 | 60 | 10. | 270mT |
| | | 14D | 10 | 12 | 88 | 8.5 | 90mT |
| 2 | .6m | 22A | 8 | 195 | 66 | 9.3 | 570° |
| | | 22B | 18 | 230 | 66 | 5.2 | 130mT |
| | .9m | 23B | 11 | 275 | 81 | V | 60mT |
| | 2m | 24B | 15 | 240 | 87 | 7.0 | 160mT |
| | | 24C | 9 | 217 | 72 | 14.9 | 570° |
| | | 24D | 9 | 199 | 83 | 10.5 | 45mT |
| 4 | 7.5m | 41A | 8 | 15 | 59 | 10.4 | 50mT |
| | | 41B | 8 | 151 | -71 | 11.5 | 500° |
| KIAMAN REMANENCE (K) | | | | | | | |
| 1 | 30m | 12B | 15 | 160 | -40 | 10.9 | 70mT |
| | | 13C | 10 | 189 | -16 | 6.2 | 35mT |
| 3 | .45m | 31B | 10 | 189 | 9 | 8.8 | 600° |
| | .9m | 34A | 7 | 177 | 12 | V | 30mT |
| | | 34B | 5 | 170 | -25 | 9.9 | 70mT |
| | 1.2m | 35C | 7 | 141 | 28 | 13.3 | >710° |
| | 1.8m | 37A | 6 | 186 | 4 | 9.4 | 500° |
| | 2.1m | 38C | 8 | 148 | 27 | 19.6 | >110mT |

S = site number; Dist. = distance to contact; # = sample number; N = number of measurements; D(°), I(°) = declination and inclination of remanence vectors with respect to horizontal; $\alpha_{95}$(°) = radius of the circle of confidence; V indicates result was refined by vector subtraction.

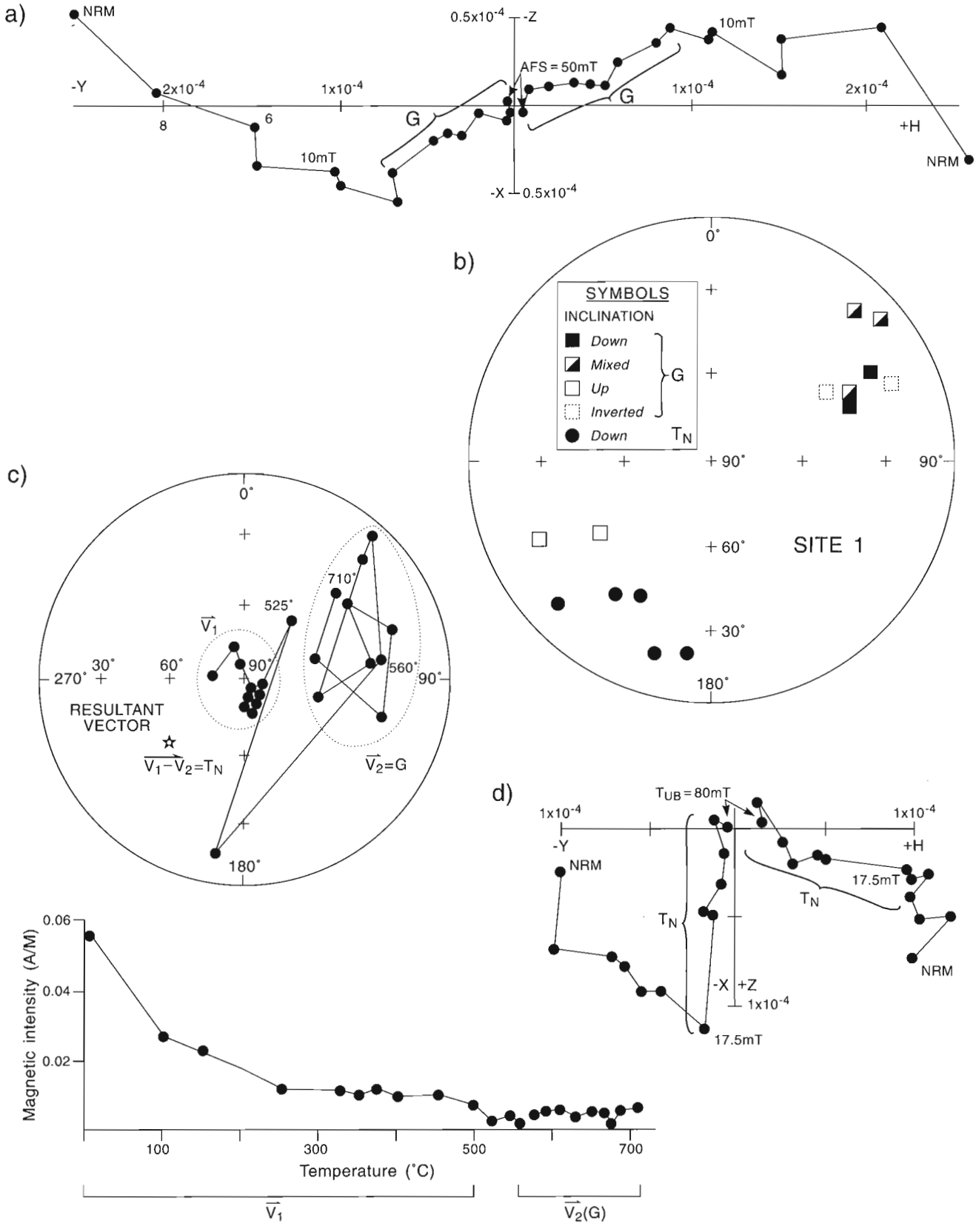


**Figure 2.** Goldenville Remanences. **a)** Single component after removal of viscous overprint at 10mT. **b)** Stable endpoints of Goldenville (**G**) and Tangier Normal ($\mathbf{T_n}$) demagnetization results from site 1. Two samples were inverted from the opposite quadrant for averaging. **c**) Resolution of Tangier Normal ($\mathbf{T_n}$) and Goldenville (**G**) at contact using subtraction of component vectors $V_1$ and $V_2$. **d**) Single component Tangier Normal ($\mathbf{T_n}$) remagnetization after removal of a viscous overprint at 17.5mT.

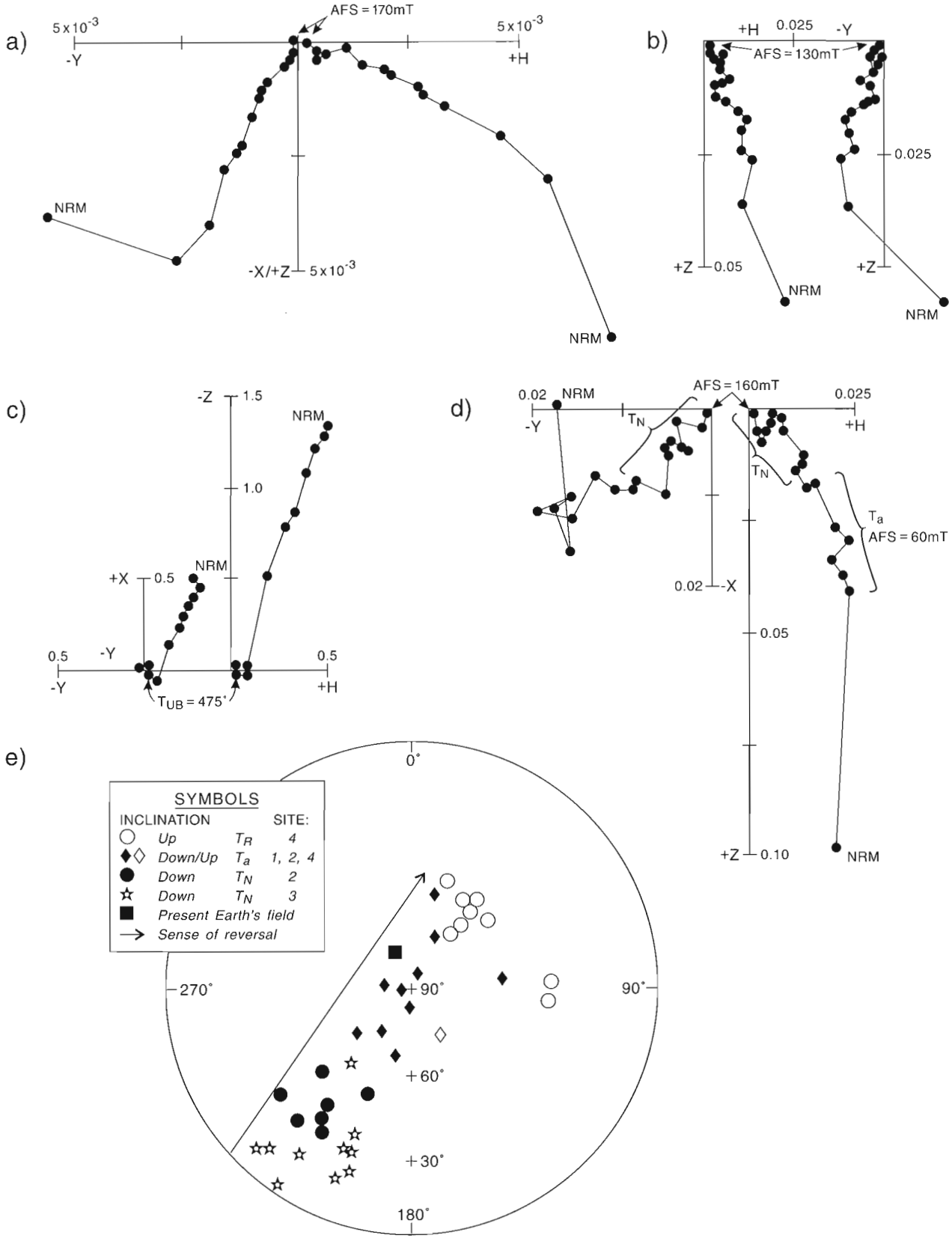


**Figure 3.** Tangier remanences. **a)** Single component Tangier Normal ($T_n$) remagnetization from contact rocks of the Goldenville Formation. **b)** Single component Tangier Normal ($T_n$) from dyke margin. **c)** Single component Tangier Reversal ($T_r$) from dyke core. **d)** Resolution of Tangier Aberrant ($T_a$) and Tangier Normal ($T_n$) in contact zone. Tangier Aberrant ($T_a$) is eliminated at 60mT. **e)** Stable endpoints of Tangier demagnetization results from sites 2,3, and 4 showing polarity reversal.

reversal. The explanation for the time lag lies in the magnetic mineralogy. Because hematite (Curie point 680°C) prevails in the chilled margin and magnetite (Curie point 580°C) in the contact, the margin passed through the blocking temperature earlier.

### *Tangier Aberrant remanence ($T_a$)*

An anomalous set of directions occurs sporadically in the studied area both inside and outside the dyke except in the margin, which is especially resistant to overprints by virtue of its mineralogy and fine grain size. The $T_{ub}$ and alternating field stability of the Tangier Aberrant remanence are characteristically in the titanomagnetite range (500°-570°C, 45-130mT), although some very hard magnetizations were found resembling the characteristics of hematite. The Tangier Aberrant remanence is a steep down-directed remanence, commonly found as a single component. The occurrence of one result in the opposite polarity is considered statistically insignificant. In site 2 the Tangier Aberrant remanence was resolved vectorially as an overprint on the Tangier Normal remanence (Fig. 3d). The overprint carried by titano-magnetite disappeared at 60mT, leaving the Tangier Normal remanence with a hematite alternating field stability of 160mT. Tangier Aberrant remanences fall on a great circle between the Tangier Normal and Reversed remanences (Fig. 3e) and may be related to the reversal process. The influence of a viscous component of the present Earth's field cannot be ruled out as a cause of the Tangier Aberrant remanence, but the former interpretation is favoured, as discussed below.

### *Kiaman remanence (K)*

Kiaman remagnetization (Late Carboniferous – Early Permian) is spatially restricted to a linear zone of alteration found in the dyke and to a localized alteration in the host rock. In the dyke an abrupt change in magnetic mineralogy occurs at 0.9m from the contact: the zone interpreted by Greenhough et al. (1988) as a second chilled margin. Here magnetic intensity increases by an order of magnitude over a distance of several centimeters. The change coincides with a destabilization of the original dyke remanence. Most samples in this zone yielded either no meaningful results, or a Kiaman overprint with variable alternating field stability and $T_{ubs}$. This suggests that the alteration has affected all magnetic minerals present. The association of the Kiaman overprint with the unstable zone implies that it is the youngest remanence in the area. Its agreement with the Kiaman reference pole for North America (Fig. 4) substantiates an age assignment of Late Carboniferous-Early Permian to this overprint.

**Table 2.** Average remanence vectors and poles

| Pole | Site | N(N) | D(°) | I(°) | $\alpha_{95}$ | Long. | Lat. | δp | δm |
|---|---|---|---|---|---|---|---|---|---|
| $T_n$ | 1 | 5 | 208 | 26 | 15.1 | 267E | 26S | 8.8 | 16.3 |
| | 2 | 7 | 219 | 39 | 8.6 | 261E | 15S | 6.0 | 10.2 |
| | 3 | 10 | 210 | 23 | 10.8 | 264E | 27S | 6.1 | 11.5 |
| $T_r$ | 4 | 9 | 50 | -58 | 11.7 | 261E | 4N | 12.7 | 17.2 |
| $T_a$ | 1 | 5 | 28 | 74 | 17.8 | 334E | 67N | 29.1 | 32.2 |
| | 2 | 6 | 219 | 77 | 9.1 | 281E | 24N | 15.9 | 17.0 |
| G | 1-2 | 7 | 57 | 29 | 11.3 | 40E | 34N | 6.9 | 12.5 |
| $T_n$ | 1-3 | **3** | 212 | 29 | 15.1 | 264E | 23S | 9.2 | 16.7 |
| $T_n$&$T_r$ | 1-4 | **4** | 215 | 37 | 20.2 | 263E | 17S | 13.8 | 23.7 |
| $T_a$ | 1,2,4 | 11 | 298 | 89 | 11.8 | 294E | 46N | 23.5 | 23.6 |
| K | 1,4 | 8 | 171 | 0 | 22.1 | 310E | 44S | 11.1 | 22.1 |

**N**(N) = Unit weight to **sites** (samples); Long., Lat. = coordinates of paleomagnetic pole position; δp, δm = semiaxes of the oval of confidence at probability level of 0.05. Remaining parameters are defined in Table 1.

## INTERPRETATION

The Goldenville remanence was imprinted on the Meguma Terrane prior to its accretion to the rest of the Appalachians, as implied by its disagreement with selected Devonian poles of North America used in the paleogeographic reconstruction by Van der Voo (1988), (Fig. 4). The upper age bracket for the Goldenville remanence is provided by the positive contact test on the Tangier dyke. Because the Goldenville remanence is carried by hematite stringers controlled by the axial plane cleavage, it is most likely of metamorphic (Acadian) origin. Polar wander from **G** to $\mathbf{T_n}$ is consistent with dextral displacement as proposed by Keppie (1982) for the Meguma Terrane.

The Tangier remanence, appearing in a normal ($\mathbf{T_n}$) and reversed ($\mathbf{T_r}$) mode, represents a post-accretionary Meguma pole position in agreement with two other Meguma poles, LC and MI, and with poles outside of the Meguma Terrane, MB and others in Figure 4. The Tangier Normal pole ($\mathbf{T_n}$) is

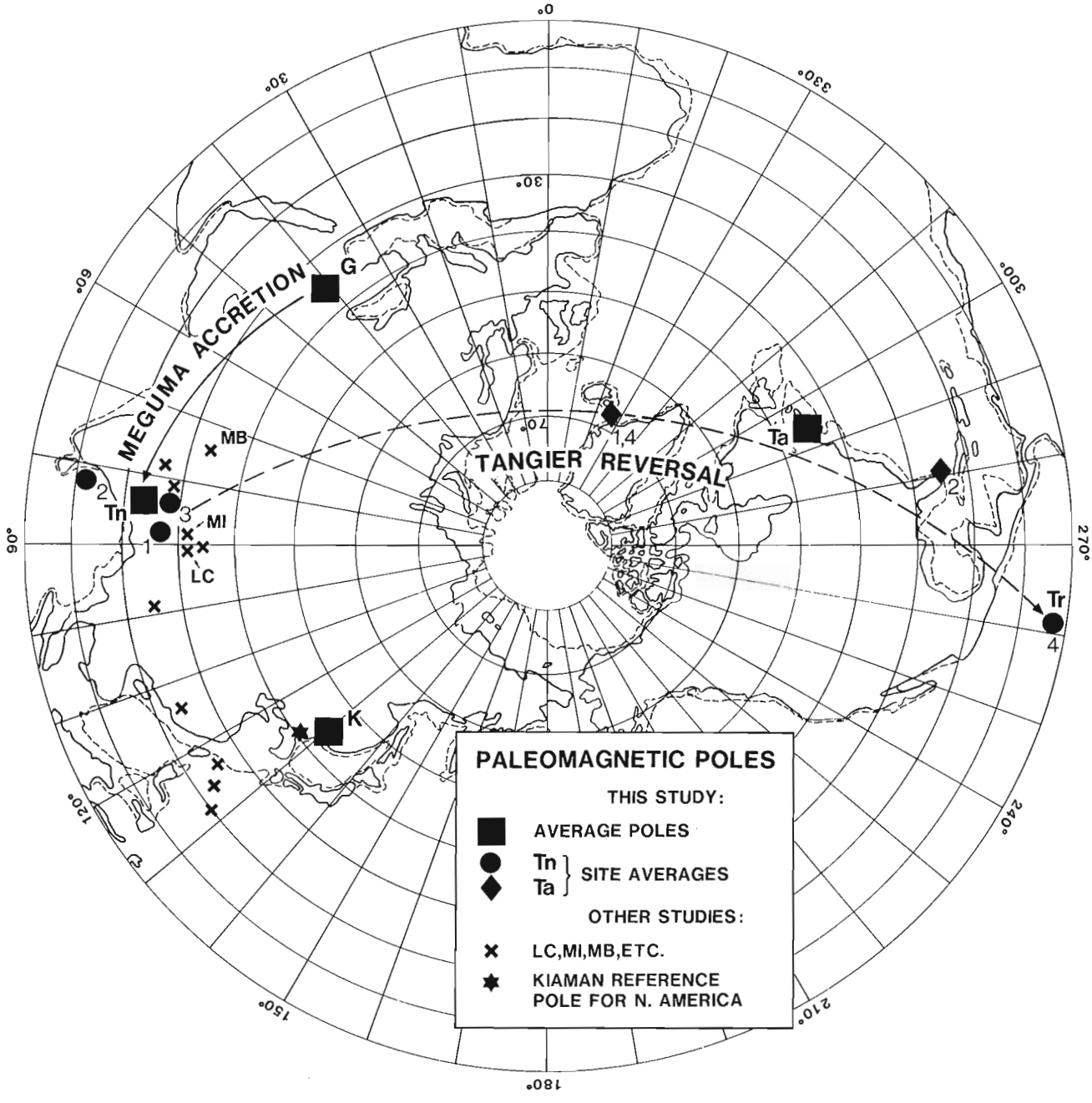


**Figure 4.** Poles from Table 2 (with exception of $\mathbf{T_n}$ and $\mathbf{T_r}$) projected on the northern hemisphere. Polar wander tracks the accretion of the Meguma Terrane to the Appalachians and the Tangier reversal. Other studies are: LC, MI = Liscomb Complex and Mavilette Intrusion from the Meguma Terrane (Tanczyk, 1989); MB = McAras Brook pole "a" from the Avalon Terrane (Stearns and Van der Voo, 1988), and other Devonian North American poles used in the reconstruction by Van der Voo (1988).

considered to pre-date the Tangier Reversed pole ($T_r$), because it is geologically implausible for the centre of the dyke to have cooled before the margins. There is also no mineralogical or magnetic evidence for a pervasive resetting at the contact zone. The recognition of a reversal is consistent with the Early Carboniferous paleomagnetic record of a frequently reversing field (Roy et al. 1983). Recent studies have also uncovered dual polarities in the Late Devonian (Stearns and Van der Voo, 1988).

Several findings of this study support a composite intrusion history for the Tangier dyke as proposed by Greenhough et al.(1988). Sufficient time for a reversal would be provided by such a scenario. The abrupt change in magnetic mineralogy at the altered zone could be due to a second pulse of magma of a slightly different composition. An initially narrower dyke width also explains why the Goldenville remanence survived closer to the contact than would normally be expected for a 15m wide dyke.

The best estimate of the Tangier pole is given by the Tangier Normal average of sites 1-3, because this remanence is supported by the contact test, and is carried by a diverse mineralogy. The identification of Tangier Reversed pole is based on one site and one magnetic mineral. Its divergence from a truly antipodal position with respect to the Tangier Normal pole may not be significant. Including Tangier Reversed results in the Tangier Normal average increases errors above acceptable limits (Table 2). Thus the average of sites 1-3 is preferred and plotted in Figure 4.

The Tangier pole is in agreement with previous findings of poles of similar ages in the Meguma Terrane (Tanczyk, 1989), and with the Upper Devonian McAras Brook result derived from the opposite side of the Minas Geofracture (Fig.4). Further agreement between the Tangier Normal pole and other Devonian poles for this time period shown in Figure 4 confirms the widely accepted view that the Meguma Terrane accreted to the Appalachians in the Late Devonian.

The origin of the Tangier Aberrant remanence remains uncertain. A later geological event, including the effect of the present Earth's field, is not the favoured explanation, because the Tangier Aberrant remanence occurs as a single component in unaltered rocks. The reversed Kiaman field is a well established worldwide feature and can be used as a paleomagnetic age bracket. In the Tangier dyke minor Kiaman overprinting is associated with the zone of greatest alteration. It seems unlikely, therefore, that the Tangier Aberrant remanence, being more widespread and stable than the Kiaman overprint, could have resulted from a petrographically undetectable alteration. The preferred hypothesis is that the $T_a$ result represents an aberrant pole position related to the Tangier reversal.

## ACKNOWLEDGMENTS

I would like to thank P.S. Giles, presently of the Atlantic Geoscience Centre, for his participation in the field work of this project, and for providing me with the geological background on the studied area. Contributions from my colleagues at the Geological Survey of Canada are greatly appreciated: O. Ijewliw provided assistance with petrographic analyses, and S.J. McEachern with the demagnetization. The manuscript was reviewed by K.L. Buchan, J.K. Park and A.L. Sangster.

## REFERENCES

**Chatterjee, A.K. and Giles, P.S.**
1988: Al-rich pyroxenes in granulite xenoliths from Tangier: Implications to lower continental crust, Eastern Meguma Zone, Nova Scotia; Maritime Sediments and Atlantic Geology, v. 24, p. 189.

**Clarke, D.B. and Halliday, A.N.**
1980: Strontium isotope geology of the South Mountain Batholith, Nova Scotia; Geochimica et Cosmochimica Acta, v. 44, p. 1045-1058.

**Faribault, E.R.**
1901: Tangier gold district. In "Work by Mr. E.R. Faribault. Report A, summary report on the operations of the Geological Survey for the year 1898 by the Director. Geological Survey of Canada, Annual Reports A, D, F, G, J, L, M, R, S, p. 157A-159A.

**Giles, P.S. and Chatterjee, A.K.**
1987: Lower crustal xenocrysts and xenoliths in the Tangier dyke, Eastern Meguma Zone, Nova Scotia; Nova Scotia Department of Mines and Energy, Report 87-5, p. 85-88.

**Greenhough, J.D., Ruffman, A., and Owen, J.V.**
1988: Magma injection directions inferred from a fabric study of the Popes Harbour dike, eastern shore, Nova Scotia, Canada; Geology, v. 16, p. 547-550.

**Kempster, R.M.F., Clarke, D.B., Reynolds, P.H. and Chatterjee, A.K.**
1989: Late Devonian lamprophyric dykes in the Meguma Zone of Nova Scotia; Canadian Journal of Earth Sciences, v. 26, p. 611-613.

**Keppie, J.D.**
1982: The Minas Geofracture; in Major structural zones and faults of the northern Appalachians; Geological Association of Canada, Special Paper 24, p. 263-280.

**Keppie, J.D. and Dallmeyer, R.D.**
1987: Dating transcurrent terrane accretion: an example from the Meguma and Avalon composite terranes in the Northern Appalachians; Tectonics, v. 6, p. 831-847.

**Muecke, G.K., Elias, P., and Reynolds, P.H.**
1988: Hercynian/Alleghanian overprinting of an Acadian Terrane: $^{40}Ar/^{39}Ar$ studies in the Meguma Zone, Nova Scotia, Canada; Chemical Geology (Isotope Geoscience Section), v. 73, p. 153-167.

**Parmelee, J.A. and Garand, R.**
1984: Spin system's user guide, Internal report 1984-4 (G), Division of Seismology and Geomagnetism, Earth Physics Branch, EMR. 107 pp.

**Roy, J.L., Tanczyk, E.I., and Lapointe, P.**
1983: The paleomagnetic record of the Appalachians; in Regional trends in the geology of the Appalachian-Caledonian-Hercynian-Mauritanide Orogen; (ed.) P.E. Schenk, Reidel Publishing, Dordrecht, Holland, p. 11-26.

**Ruffman, A. and Greenhough, J.D.**
1990: The Weekend dykes, a newly recognized mafic dyke swarm on the eastern shore of Nova Scotia, Canada; Canadian Journal of Earth Sciences, v. 27, p. 644-648.

**Scotese, C.R., Van der Voo, R., Johnson, R.E., and Giles, P.S.**
1984: Paleomagnetic results from the Carboniferous of Nova Scotia; in Plate reconstruction from Paleozoic paleomagnetism; American Geophysical Union, Geodynamic Series, v. 2, p. 63-81.

**Smith, R.W. and Fuller, M.**
1967: Alpha-hematite: Stable remanence and memory; Science, v. 156, p. 1130-1133.

**Stearns, C. and Van der Voo, R.**
1988: Dual polarity magnetizations from the Upper Devonian McAras Brook Formation, Nova Scotia, and their implications for the North American apparent polar wander path; Tectonophysics, v. 156, p. 179-191.

**Tanczyk, E.I.**
1989: Paleomagnetic investigations in the Meguma displaced terrain of Nova Scotia, Canada; in Tectonostratigraphic expression of terrane accretion in the circum-Atlantic Paleozoic Orogens; Abstracts and Program of IGCP Project 233, p. 111-114.

**Thomson, G.F.**
1990: The anomalous demagnetization of pyrrhotite; Geophysics Journal International, v. 103, p. 425-430.

**Van der Voo, R.**
1988: Paleozoic paleogeography of North America, Gondwana, and intervening displaced terranes: Comparisons of paleomagnetism with paleoclimatology and biogeographical patterns; Geological Society of America Bulletin, v. 100, p. 311-324.

Geological Survey of Canada Project 870002

# Diagenèse pré- et post-minéralisation : implications pour le dépôt de Gays River, Nouvelle-Écosse

**Martine M. Savard**
**Centre géoscientifique de Québec, Sainte-Foy**

*Savard, M.M., 1992 : Diagenèse pré- et post-minéralisation : implications pour le dépôt de Gays River, Nouvelle-Écosse; dans Recherches en cours, Partie E; Commission géologique du Canada, Étude 92-1E, p. 289-298.*

***Résumé***

*La pétrographie régionale autour du dépôt de Pb-Zn de Gays River montre que la minéralisation est postérieure à la dolomitisation des calcaires, chevauche dans le temps une cimentation calcitique zonée et la migration de bitume, et est antérieure à une cimentation calcitique uniforme. La géochimie ($\delta^{18}O$, $\delta^{13}C$, $^{87}Sr/^{86}Sr$) et la microthermométrie (Th, Tm) indiquent que (1) les dolomites ont été produites par des fluides émanant du bassin en milieu d'enfouissement peu profond et que (2) les deux calcites, comme les dolomites, ont précipité à partir de saumures radiogéniques devenant progressivement plus salines et plus chaudes avec le temps. Spatialement restreinte à la région immédiate du dépôt, la calcite zonée (syn-minéralisation) est significativement enrichie en carbone d'origine organique.*

*Les résultats suggèrent que des saumures de bassin ont circulé sur l'étendue des sous-bassins de Shubenacadie et de Musquodoboit, avant et après la minéralisation. Lors de la minéralisation, deux fluides, dont l'un riche en $^{12}C$, ont possiblement été impliqués.*

***Abstract***

*Regional petrography around the Gays River Pb-Zn deposit establishes that mineralization post-dates limestone dolomitization, overlaps with zoned-calcite cementation and hydrocarbon migration, and pre-dates uniform calcite cementation. Geochemistry ($\delta^{18}O$, $\delta^{13}C$, $^{87}Sr/^{86}Sr$) and microthermometry (Th, Tm) indicate that (1) dolomitization was produced by basinal brines in shallow burial environment; and that (2), the calcite, like the dolomite, precipitated from radiogenic brines that had progressively increased in salinity and temperature. Spatially restricted to the immediate area around the mine, the zoned calcite (syn-mineralization) is significantly enriched in organic carbon.*

*The results of this diagenetic study suggest that basinal brines were moving through the Shubenacadie and Musquodoboit sub-bassins before and after mineralization. Two fluids might have been involved during mineralization, one of which was a $^{12}C$-rich fluid.*

## INTRODUCTION

Le dépôt de Pb et Zn de Gays River a souvent été classifié comme étant de type «vallée du Mississippi» (Hannon, 1980) ou de type «Irish» (Akende et Zentilli, 1984; Kontak, communication personnelle) puisqu'il est de basse température, syndiagénétique et encaissé dans des dolomies. Sur la base de données géochimiques et microthermométriques venant du gîte même, Ravenhurst et al. (1989) ont proposé des saumures de bassin en provenance du nord-est comme fluides minéralisateurs. Pour étayer ce modèle, il faut connaître les processus diagénétiques d'arrière-plan, en d'autres termes le contexte diagénétique régional tel qu'enregistré par la formation encaissante. Pour la Formation de Gays River, des modèles de dolomitisation en surface, par évaporation (MacLeod, 1984) et par mélange d'eaux marines et météoriques (Schenk et Hatt, 1984), ont été avancés à partir d'études pétrographiques. Les ciments calcitiques n'ont été étudiés que très sommairement (Akende et Zentilli, 1984; MacLeod, 1984; Schenk et Hatt, 1984; Ravenhurst et al., 1989). Pour cette raison, une étude diagénétique régionale des carbonates, de la matière organique et des minéraux des argiles, couvrant les sous-bassins de Shubenacadie et de Musquodoboit ainsi que la région minière de Gays River, a été entreprise. Le présent rapport documente les résultats obtenus pour les carbonates. Bien que préliminaires, ces résultats permettent (1) de proposer un modèle de dolomitisation, (2) d'évaluer les liens entre les mécanismes de dolomitisation et de minéralisation, (3) de proposer un modèle de cimentation calcitique tardive, (4) de définir la nature des fluides qui se sont succédés régionalement, et, finalement, (5) de discuter des implications de ces résultats sur le modèle de mise en place du dépôt de Gays River.

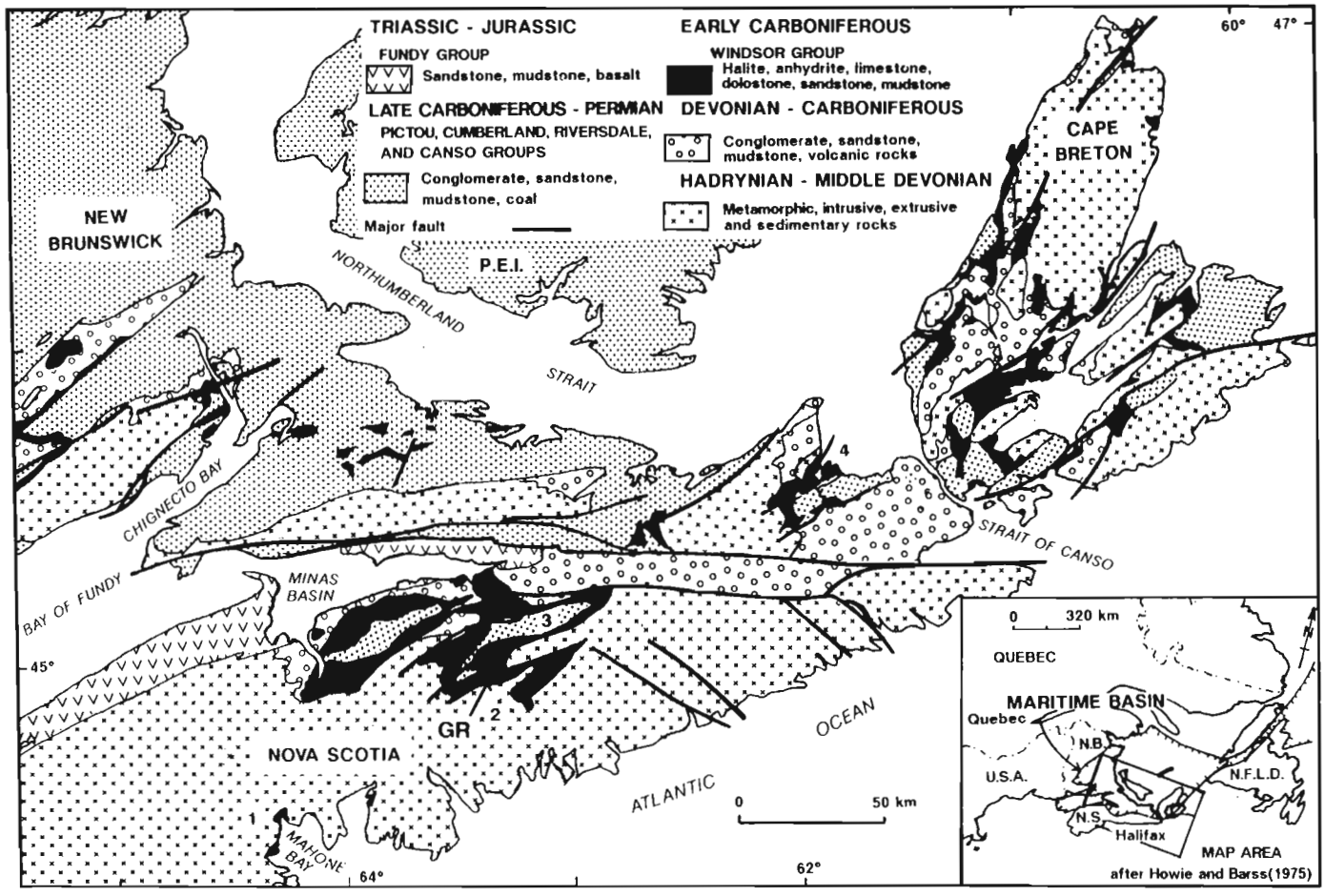


**Figure 1.** Carte de localisation et géologie régionale (d'après Boehner et al., 1989). La présente étude porte sur les sous-bassins de Shubenacadie (2) et de Musquodoboit (3) où se trouve la mine de Gays River (GR). Le Groupe de Windsor est représenté en noir, les roches métamorphiques du socle (Groupe de Meguma, etc.) sont représentées par des «x», les roches clastiques du Dévono-Carbonifère par des «o» et les roches clastiques du Permo-Carbonifère par des points. 1 : Région de Mahone Bay. 2 : Région d'Antigonish.

## ÉCHANTILLONNAGE ET TECHNIQUES ANALYTIQUES

L'échantillonnage de la Formation de Gays River a été effectué pendant les campagnes de terrain de 1990 et 1991. Les travaux ont eu lieu principalement à la carothèque de Stellarton en Nouvelle-Écosse, où sont entreposés les sondages néo-écossais, et à la carrière Mosher Bros., où affleure un monticule de la Formation de Gays River en contact discordant avec le Groupe de Meguma.

La pétrographie en cathodoluminescence (CL) a été effectuée avec un luminoscope de marque Nuclide ELM-2E. Les observations au microscope électronique à balayage (MEB) ont été faites sur des cassures fraîches avec un appareil JEOL JSM T330-A.

Toutes les poudres pour analyses isotopiques ont été séparées mécaniquement à l'aide d'une microforeuse Jensen. Les 165 analyses des isotopes stables du carbone et de l'oxygène ont été effectuées au Laboratoire Derry-Rust du Centre géoscientifique Ottawa/Carleton d'Ottawa. L'analyse des échantillons de dolomite et calcite intimement mélangées a été réalisée grâce à une extraction sélective lors de l'attaque acide (Al-Aasm et al., 1990). Les résultats sont exprimés en pour mille (‰), selon la notation habituelle (delta), relativement au standard PDB. La précision des valeurs est de ± 0,1 ‰.

Les 34 analyses du rapport $^{87}Sr/^{86}Sr$ ont été effectuées à l'Institut géologique de l'Université de la Ruhr de Bochum, en Allemagne, à l'aide d'un spectromètre de masse Fannigan Mat 262 à cinq récepteurs. Entre novembre 1991 et janvier 1992, les standards NBS 987 et USGS EN-1 ont respectivement donné des valeurs moyennes de 0,710230 ± 0,000013 et de 0,2709127 ± 0,000012 (2σ). Entre janvier et mars 1991, les mêmes standards étaient à 0,710193 ± 0,000012 et 0,709121 ± 0,000009 (2σ). Les échantillons étaient constitués de poudre monominérale obtenue par séparation mécanique et ayant aussi servi à l'analyse des isotopes stables. L'erreur sur les analyses individuelles des échantillons était généralement inférieure à ± 0,000015 (2σ).

La microthermométrie de 12 plaques minces a été effectuée au département de géologie et de géophysique de l'Université de Calgary par R. Spencer. Seules les inclusions primaires ou pseudo-secondaires ont été retenues. Pour l'étude des températures de précipitation, les inclusions fluides à deux phases ont été chauffées graduellement selon un incrément de 2 à 3 °C/min. La température de disparition des bulles de vapeur a été systématiquement notée et pour vérifier l'homogénéisation, un abaissement de température à intervalle de 5 °C était exercé.

Pour l'étude de la salinité, les échantillons étaient refroidis jusqu'à -125 °C ou jusqu'à l'obtention de solides. Leur température de fusion était notée lors du réchauffement graduel subséquent.

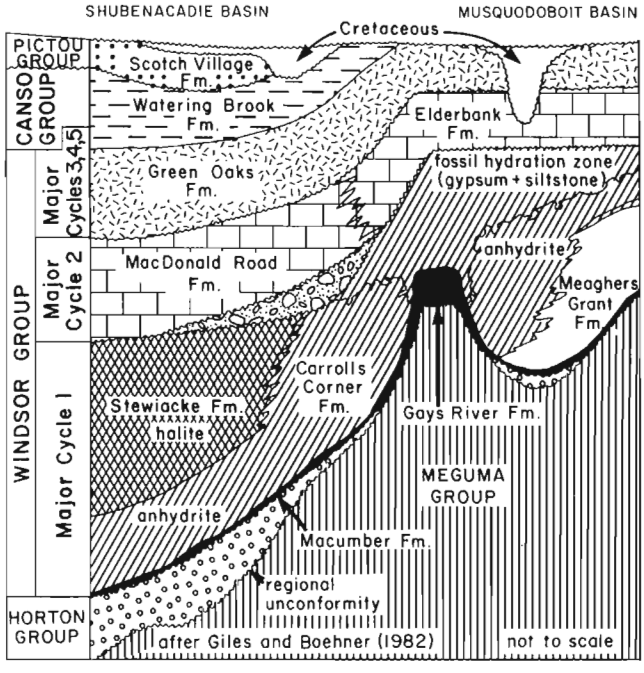


**Figure 2.** Représentation schématique de la stratigraphie du Groupe de Windsor dans les sous-bassins de Shubenacadie et de Musquodoboit (d'après Giles et Boehner, 1982).

## GÉOLOGIE

Les carbonates de base du Groupe de Windsor ont été déposés lors d'une incursion marine rapide survenue après le rifting intracontinental postacadien responsable de l'ouverture du bassin des Maritimes (Boehner, 1984; Schenk et Hatt, 1984; fig. 1). Ces carbonates appartiennent au premier cycle de transgression-régression majeur du Groupe de Windsor (Giles, 1981b). Les quatre cycles subséquents contiennent une très large proportion de sels et sulfates évaporitiques (fig. 2) car, au Dévono-Carbonifère, le bassin des Maritimes se situait à une paléolatitude approximative de 10-15°S sous un climat semi-aride et chaud (Hamblin et Rust, 1989).

Dans les sous-bassins de Shubenacadie et de Musquodoboit, les carbonates de base comprennent les formations de Macumber et de Gays River qui reposent respectivement sur les conglomérats et grès fluviatiles du Groupe de Horton (Viséen) et sur les métawackes du Groupe de Meguma (Cambro-Ordovicien; fig. 2). Les carbonates sont à leur tour recouverts par les évaporites des formations de Carrolls Corner et de Stewiacke (Giles et Boehner, 1982).

La Formation de Gays River est formée de quatre faciès principaux généralement distribués comme suit, de la base au sommet : (1) brèche de talus encroûtée par des ciments et des algues calcaires; (2) bafflestone à algues codiacées; (3) bafflestone et bindstone à bryozoaires et coraux; et (4) bindstone stromatolitique, wackestone et packstone à mollusques ainsi que bindstone à algues (affinité incertaine) et bryozoaires. Cette succession de faciès reflète une diminution progressive de la profondeur d'eau (Boehner et al., 1989). Dans la région étudiée, tous ces calcaires marins ont été entièrement dolomitisés. À Gays River, ils ont aussi été minéralisés. Le dépôt produit surplombe un haut-fond paléogéographique qui sépare les sous-bassins de Shubenacadie et de Musquodoboit.

## PARAGENÈSE

### *En région*

Dans les sous-bassins de Shubenacadie et de Musquodoboit, à l'extérieur d'un rayon de 4 km autour de la mine de Gays River, la séquence paragénétique est simple : cimentation marine précoce; remplacement dolomitique; microfracturation et cimentation dolomitique; début de cimentation calcitique et migration d'hydrocarbures; microfracturation, cimentation calcitique tardive et stylolitisation.

Le ciment marin précoce est formé de fibres isopaques, riches en inclusions, qui remplissent moins de 5% de la porosité primaire totale (fig. 3 et 4). Malgré la complète dolomitisation de ces cristaux marins, leur texture reste visible et s'apparente à celle de calcites hautement magnésiennes (Lohmann et Meyers, 1977; Sandberg, 1985). Les premières microfractures recoupent le ciment marin précoce et sont partiellement remplies par le ciment dolomitique. Dans le sous-bassin de Musquodoboit, les ciments calcitiques tardifs (voir plus bas) englobent souvent du bitume sous forme de goutte. Dans certain

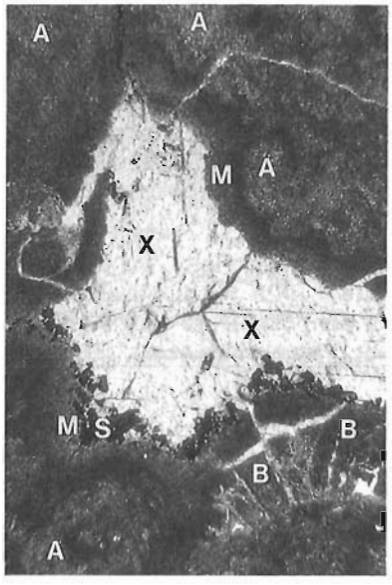


**Figure 3.** Cavité de croissance dans un bindstone algaire (A) dolomitisé. Le ciment marin (M) précoce a été dolomitisé, mais reste identifiable. Ce ciment et une boue dolomitisée (B) forment les fragments de la microbrèche à la base de la cavité. La sphalérite (S) apparaît par dessus ou entre les fragments de la brèche. Finalement, la calcite xénomorphe (X) enveloppe les fragments de la brèche et remplit le pore résiduel. Lumière transmise. Longueur de la photo : 3,5 mm.


**Figure 4.** Même cavité qu'à la figure 3. Microdolomite uniformément terne (D), même après le remplacement des algues et du ciment marin, des composés calcaires de différentes natures. La cavité est remplie par la calcite zonée. CL. Longueur de la photo : 2,4 mm.

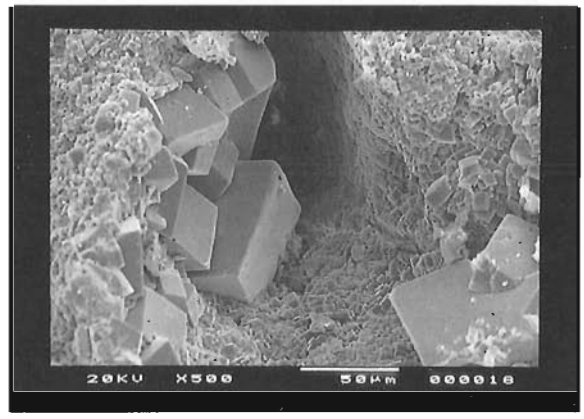


**Figure 5.** Dolomite de remplacement anédrique à automorphe, en petits cristaux, et ciment dolomitique autour d'une cavité de type fenestrae. MEB.

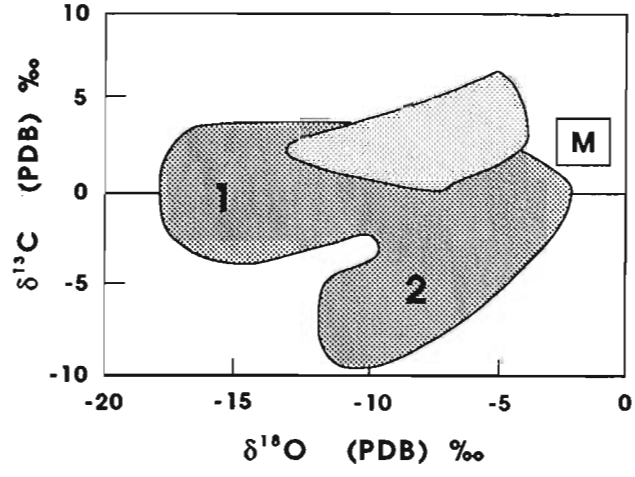


**Figure 6.** Diagramme des valeurs isotopiques pour le carbone et l'oxygène. Les résultats pour les dolomites sont compris dans la région pâle et ceux des calcites dans la région foncée. Deux populations se distinguent chez les calcites : (1) une population à $\delta^{13}C$ constant et (2) une autre à $\delta^{13}C$ très variable. Le champ identifié par le «M» représente une compilation des valeurs mondiales du Viséen inférieur d'après Lohmann et Walker (1989) et Popp et al. (1986).

cas, celui-ci remplit des pores résiduels après la cimentation dolomitique; une légère corrosion des dolomites est souvent associée à la présence du bitume.

### *À la mine*

À l'intérieur d'un rayon de 4 km autour de la mine, la séquence régionale est répétée. Y sont intercalés des épisodes : de microbréchification; de remplissage par un assemblage de sphalérite; galène, fluorite, anhydrite et barite; et de remplacement par de la sphalérite et de la galène (tabl. 1). Tous ces phénomènes sont probablement contemporains du début de la cimentation calcitique et de la migration d'hydrocarbures.

Le ciment de sphalérite est translucide et grossier, alors que la sphalérite de remplacement est microcristalline. La galène constitue généralement une phase de remplacement et est de dimension variable. La fluorite est très peu abondante; elle apparaît sous forme de gros cristaux isolés. La pétrographie détaillée et la microthermométrie de la minéralisation sont étudiées par Kontak (1991).

## PÉTROGRAPHIE DES DOLOMITES ET DES CALCITES

Les dolomites de remplacement sont des microrhomboèdres anédriques à automorphes (2 à 5 µm), rouges ou ternes en CL (fig. 5 et 4). Il n'y a pas de porosité interstitielle visible entre les microcristaux de remplacement. Le ciment dolomitique est formé de rhomboèdres parfaits (10 à 60 µm; fig. 5) et non-luminescents en CL. Localement, ce ciment peut obstruer jusqu'à 2 % des pores.

Les ciments calcitiques forment de grands cristaux xénomorphes et poecilitiques excédant souvent plusieurs millimètres (fig. 3). Dans ces cristaux, deux faciès reconnus en CL se succèdent : un faciès zoné où de multiples bandes luminescentes et ternes alternent (fig. 4); et un faciès uniformément luminescent ou terne (Savard, 1991). Les calcites uniformes sont distribuées sur toute l'étendue des deux sous-bassins, alors que les calcites zonées apparaissent surtout dans le sous-bassin de Musquodoboit et à la mine de Gays River.

## GÉOCHIMIE

### *Dolomites*

Les dolomites (phase de remplacement et ciment non différenciés) exhibent des valeurs de $\delta^{18}O$ allant de -4 à -13 ‰ (fig. 6). Cet intervalle est nettement inférieur aux signaux marins mondiaux tirés de calcites du Viséen inférieur («M», fig. 6). Des brachiopodes d'un âge correspondant provenant du bassin des Maritimes ont un signal variant entre -6,1 et -4,3 ‰ (Akende et Zentilli, 1984), ce qui est aussi plus élevé que la moyenne des dolomites étudiées. En théorie, des dolomites précipitées en concomitance avec ces calcites ne pourraient avoir été que plus lourdes (jusqu'à +3,8 ‰; Land, 1985).

Les isotopes du carbone des dolomites ont des valeurs se situant dans l'intervalle marin («M», fig. 6; et 3,6 à 4,6 ‰ de Akende et Zentilli, 1984). Les rapports obtenus pour les isotopes du strontium s'étalent du signal marin à des rapports légèrement plus radiogéniques (fig. 7).

**Tableau 1.** Paragenèse reconnue dans les sous-bassins de Shubenacadie et de Musquodoboit. La chronologie relative réfère aux événements pré-, syn- et post-minéralisation (sphalérite et galène).

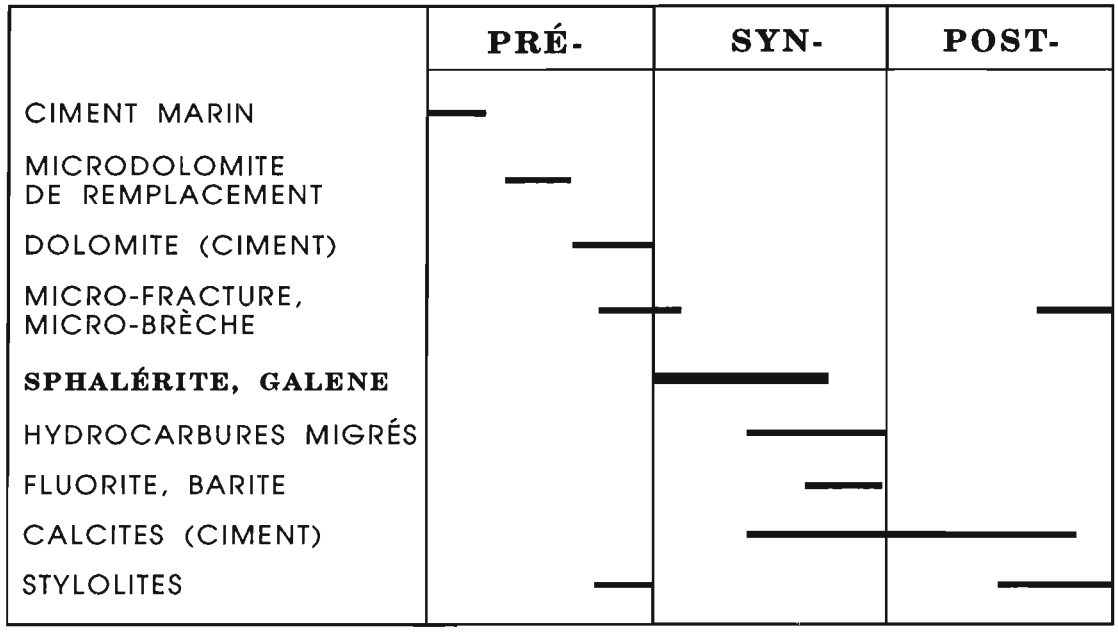

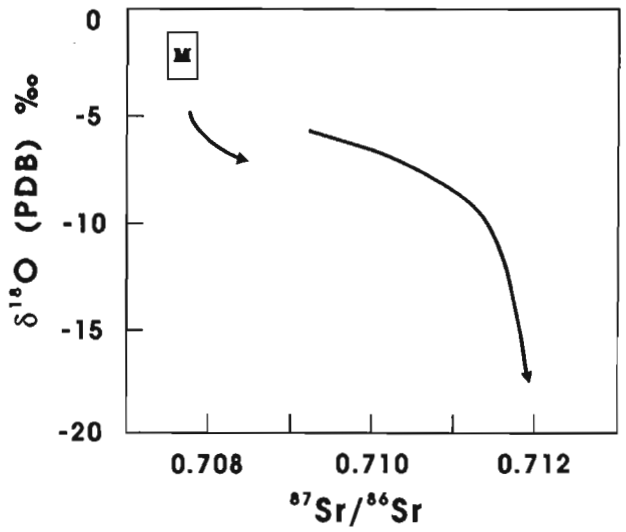


**Figure 7.** Diagramme des valeurs isotopiques pour l'oxygène et le strontium. Les résultats pour les dolomites et les calcites sont respectivement représentés par la flèche courte et la flèche longue. Le champ identifié par le «M» représente une compilation des valeurs mondiales du Viséen inférieur d'après Lohmann et Walker (1989), Popp et al. (1986), et Veizer (1989).

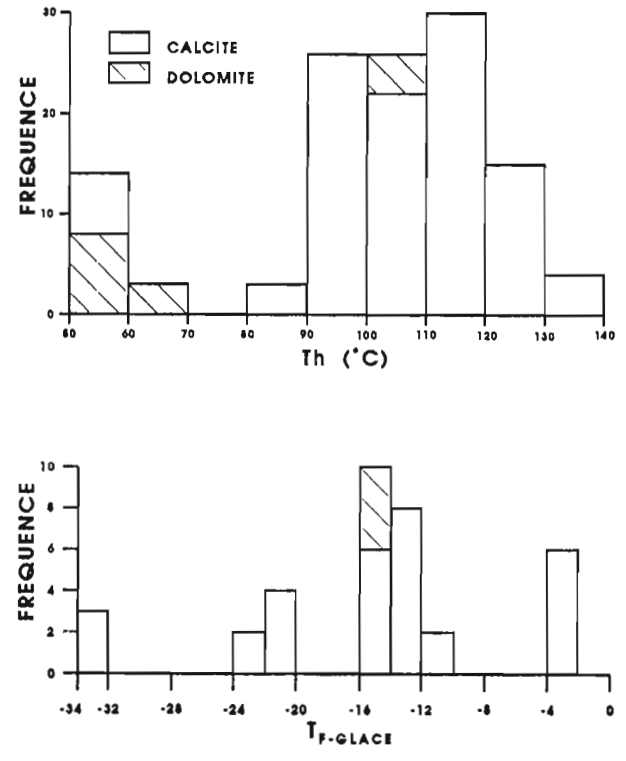


**Figure 8.** Histogrammes des résultats de microthermométrie pour des inclusions primaires (dolomites) et pseudo-secondaires (calcites) à deux phases. En haut : les températures d'homogénéisation (Th). En bas : les températures de fusion de la glace (Tf-glace).

### *Calcites*

Les calcites ont des valeurs de $\delta^{18}O$ très basses qui varient entre -17,5 et -3,1 ‰. Dans cet intervalle, les isotopes du carbone permettent de distinguer (1) une population à $\delta^{13}C$ relativement invariable et (2) une population à $\delta^{13}C$ significativement variable (fig. 6). Ces populations respectives correspondent grossièrement aux faciès pétrographiques uniforme et zoné reconnus en cathodoluminescence. La population 2 (calcite zonée) provient de la mine et du sous-bassin de Musquodoboit.

Les rapports isotopiques du strontium pour les calcites sont tous radiogéniques (fig. 7). Ceci est vrai pour les calcites des populations 1 et 2 définies ci-haut.

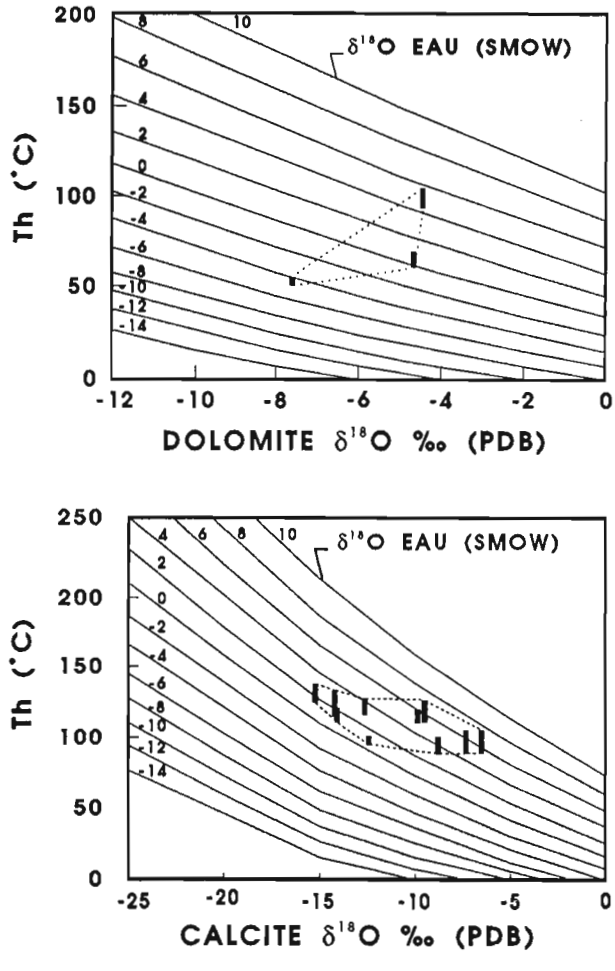


**Figure 9.** Graphiques mettant en relation la signature isotopique de l'oxygène des eaux parentes et celle des carbonates qu'elles précipitent d'après les équations de Craig (1965, calcite) et Land (1985, dolomite). Les températures de précipitation utilisées sont les températures d'homogénéisation obtenues par microthermométrie. Les signatures isotopiques des carbonates sont présentées au tableau 2.

**Tableau 2.** Compilation, par localité, des résultats de microthermométrie et d'analyses isotopiques provenant d'échantillons communs. Shu. : Shubenacadie; Reg. : région; G.R. : Gays River; Mus. : Musquodoboit; Éch. : échantillons; Cal. : calcite; Dol. : dolomite; T. : tardive; C. : ciment; (c) : centre du cristal; (b) : bordure du cristal.

| Localité | # Forage | # Éch. | Phase | $T_h$ (°C) | $T_{f\text{-glace}}$ (°C) | $\delta^{18}O$ ($^{o}/_{oo}$ - PDB) | $\delta^{13}C$ ($^{o}/_{oo}$ - PDB) | $^{87}Sr/^{86}Sr$ |
|---|---|---|---|---|---|---|---|---|
| Shu. ouest | NM-3 | 343 | Cal. T. | 80 à 90 (3)<br>91 à 100 (6) | -4 à -2 (3) | | | |
| | NM-8 | 332 | Cal. T. | 90 à 100 (6)<br>101 à 110 (2) | -24 à -22 (2) | -6.1 | 2.7 | |
| | DS-120 | 605 | Cal. T. | 111 à 120 (4) | (ne gèlent pas) | -9.7 | 2.5 | 0.71130 |
| | DS-26 | 525 | Cal. T. | 111 à 120 (8)<br>121 à 130 (1) | -14 à -10 (4) | | | |
| Reg. G.R. | GR-256 | 227 | C. Dol. | 60 à 70 (3) | Environ -18 | -4.6 | 2.6 | 0.70792 |
| Mine | U-635 | 895 | C. Dol. | 50 à 55 (8) | (trop petites) | -7.6 | 3.4 | |
| | | 895 | Cal. T. | 50-65 (6) | (ne gèlent pas) | | | |
| Mus. sud-ouest | MG-25 | 358 | Cal. T. | 111 à 120 (3)<br>121 à 130 (5) | -4 à -2 (3) | -14.0 | 1.7 | 0.71050 |
| | MG-71 | 123 | C. Dol. | 91 à 100 (3)<br>101 à 110 (4) | -16 à -12 (4) | -4.3 | 3.7 | |
| | | | Cal. T.[c] | 101 à 110 (20) | -16 à -12 (6) | -12.4 | 2.1 | 0.71016 |
| | | | Cal. T.[b] | 111 à 120 (8)<br>121 à 130 (4) | -24 à -20 (4) | | | |
| Mus. est | 208-13 | 90 | Cal. T. | 91 à 100 (7) | -4 à 0 (3) | -12.3 | 1.5 | 0.71173 |
| | | 92 | Cal. T. | 121 à 130 (2)<br>131 à 140 (4) | -36 à -32 (3) | -15.5 | 2.0 | |
| | 208-14 | 135 | Cal. T. | 111 à 120 (7) | environ -14 | -13.9 | 1.9 | 0.71160 |
| | 210-12 | 586 | Cal. T. | 91 à 100 (7) | -14 à -12 (6) | -8.6 | 2.6 | |

## MICROTHERMOMÉTRIE

Dans le ciment dolomitique, les inclusions fluides alignées selon les fronts de croissance des cristaux sont considérées comme primaires. Elles contiennent une phase liquide ainsi qu'une phase gazeuse. Les inclusions de la dolomite de remplacement sont trop petites pour avoir été étudiées.

Les températures d'homogénéisation des dolomites (50 à 110 °C) sont plus élevées que la température des eaux de surface. Les températures de fusion obtenues indiquent que la salinité des fluides parents était vraisemblablement de 16 à 19 %, au poids, en équivalent de NaCl (tabl. 2; fig. 8). Cette salinité est nettement supérieure à celle d'eaux marines normales (3,5 %). Au stade actuel de l'étude, il semble que les dolomites du sud-ouest du sous-bassin de Musquodoboit aient des températures d'homogénéisation plus élevées (90 à 110 °C) qu'à la mine (50 à 70 °C; tabl. 2).

Dans les calcites, plusieurs populations d'inclusions fluides sont secondaires. Elles ont toutes été ignorées pour l'étude microthermométrique systématique. Certaines inclusions sont possiblement d'origine primaire, bien qu'elles n'en montrent pas toutes les caractéristiques de base. Ces quelques inclusions ont donné des résultats de températures d'homogénéisation relativement constantes et ont été retenues pour l'interprétation finale (tabl. 2 et fig. 8).

La répartition des échantillons étudiés couvre l'ensemble de la région d'intérêt. Puisque les travaux au luminoscope affectent les propriétés des inclusions, la CL des calcites étudiées (uniforme ou zonée) n'a pas encore été vérifiée.

Il semble qu'il n'y ait pas de variation systématique de la température de précipitation, cette dernière jouant généralement entre 90 et 130 °C. La salinité par contre est très variable. Elle passe d'un peu plus saline que l'eau de mer (-4 à -2 °C; 6,4 à 3,3 % en équivalent de NaCl), à très saline (-36 à -10 °C; 14 à plus de 30 %).

## DISCUSSION

### *Dolomitisation - Diagenèse pré-minéralisation*

Puisque la texture des calcaires est bien préservée, le changement de la calcite à la dolomite s'est effectué par remplacement volume par volume. L'apport de $Mg^{2+}$ et de $CO^{2-}_3$ a apparemment compensé le gain de porosité qui doit accompagner un remplacement molécule par molécule. La réaction décrivant ce phénomène est la suivante (Morrow, 1990) :

$$(2\text{-}x)CaCO_3 + Mg^{2+} + xCO_3 = CaMg(CO_3)_2 + (1\text{-}x)Ca^{2+}.$$

Le ciment dolomitique résulte possiblement d'un apport supplémentaire de $Mg^{2+}$ et de $CO^{2-}_3$ qui a fait basculer le volume produit dans le sens d'une légère perte de porosité (Lucia et Major, 1991).

La dolomitisation s'est produite avant qu'il n'y ait eu précipitation de calcite non magnésienne (pauvre en inclusions et postérieure au ciment marin) qui accompagne normalement la stabilisation des phases marines métastables. La dernière étape de dolomitisation (ciment dolomitique) est contemporaine de la microbréchification, un indice vraisemblable de compaction mécanique. Ainsi, sur une base pétrographique, il semble que les dolomites soient apparues en enfouissement peu profond.

L'écart est grand entre les valeurs de $\delta^{18}O$ que devraient théoriquement montrer les dolomites marines viséennes et que révèlent effectivement les dolomites de la Formation de Gays River (fig. 6 et 9). Il existe aussi un léger écart entre le signal marin mondial et les valeurs des rapports isotopiques du strontium des dolomites (fig. 7). La préservation texturale après la dolomitisation suggère que le strontium présent dans le réseau cristallin des dolomites est majoritairement hérité des calcaires marins. Puisque les signatures géochimiques des dolomites sont quand même radiogéniques, il faut que les fluides responsables de la dolomitisation aient été significativement radiogéniques, car seuls des fluides radiogéniques hautement salins peuvent laisser leur empreinte dans un système diagénétique à faible rapport eau/roche (Banner et Hanson, 1990).

Les résultats de microthermométrie indiquent des salinités élevées et des températures de précipitation supérieures aux températures de surface. Ces températures de précipitation, combinées aux valeurs de $\delta^{18}O$, révèlent que les eaux de précipitation étaient beaucoup plus lourdes que l'eau de mer (fig. 9).

Les attributs pétrographiques, géochimiques et microthermométriques indiquent donc que la dolomitisation massive dans la région de Shubenacadie-Musquodoboit résulte de l'expulsion par compaction de saumures en milieu d'enfouissement peu profond (quelques centaines de mètres). Ceci constitue pour l'instant une hypothèse de travail. Le modèle à vérifier est le suivant : (1) les fluides ayant produit la dolomitisation consistaient en eaux d'origine marine évaporées, très salines, denses, à rapport Mg/Ca favorable à la dolomitisation; (2) ces eaux sont descendues par gravité vers le fond du bassin des Maritimes; (3) en milieu d'enfouissement, elles se sont réchauffées; (4) lors de leur remontée par compaction ou pression tectonique, elles se sont enrichies en $^{87}Sr$ par réaction avec les sédiments clastiques suite à leur circulation à travers le Groupe de Horton qui agissait comme un aquifère entre les évaporites et les roches métamorphiques du Groupe de Meguma; (5) elles ont atteint les calcaires métastables de la Formation de Gays River qu'elles ont dolomitisés. Les variations des températures de précipitation et des signatures isotopiques reflètent l'évolution graduelle du système passant de marin, peu radiogénique, peu salin et moins chaud, à enfoui, plus radiogénique, très salin et plus chaud (fig. 6, 7 et 9).

### *Cimentation calcitique - Diagenèse syn- et post-minéralisation*

Au stade actuel de l'étude, les attributs géochimiques indiquent que les fluides responsables de la cimentation calcitique étaient salins, radiogéniques et chauds, tout comme ceux qui ont produit la dolomitisation (population 1, fig. 6). Ces fluides, pendant la période de précipitation des calcites, étaient par endroits plus chauds et plus salins que lors de la dolomitisation (tabl. 2, fig. 6 et 8). Ce fait a été reconnu dans l'ensemble des inclusions fluides de dolomite et de calcite étudiées, et à l'échelle de l'échantillon 123 (tabl. 2). Selon la chronologie relative, le système a eu une salinité et une température croissantes de la précipitation de la dolomite à la précipitation du coeur de la calcite et jusqu'à sa bordure. Les rapports hautement radiogéniques des calcites reflètent la précipitation directe à partir des fluides parents radiogéniques à des rapports eau/roche progressivement plus élevés (fig. 7).

Les calcites zonées sont généralement contemporaines de la minéralisation, contrairement aux calcites uniformes qui y sont postérieures très souvent. Les $\delta^{13}C$ des calcites zonées suggèrent qu'au moins un autre type de fluide salin a circulé dans le bassin de Musquodoboit. Celui-là contenait du carbone léger ($^{12}C$), vraisemblablement dérivé de composés organiques (population 2 de la figure 6). Les fluides pouvaient être des eaux de formation associées à des hydrocarbures.

### *Mise en place du gîte*

L'étude des dolomites et calcites suggère que des saumures de bassin circulaient dans les sous-bassins de Musquodoboit et de Shubenacadie avant, après et vraisemblablement pendant la mise en place du dépôt de Gays River. Ces saumures se seraient écoulées dans les sédiments clastiques du Groupe de Horton et les calcaires de base du Groupe de Windsor, car, pendant la diagenèse d'enfouissement, ils représentaient un milieu perméable situé entre des roches clastiques plissées et métamorphisées et des évaporites.

Dans la zone hautement minéralisée, la sphalérite et la galène remplacent les faciès sans discrimination et il n'y a pas eu de contrôle exercé par les différences internes de perméabilité. Les carbonates libérés ont possiblement participé à la précipitation de la calcite syn-minéralisation dont une large portion contient du carbone dérivé de composés organiques. Ce contexte suggère que la réduction thermique de sulfates provoquée par des réducteurs tels que des hydrocarbures était possiblement impliquée lors de la minéralisation. Dans les zones à basse teneur du pourtour de la mine, la minéralisation cimente les carbonates et obstrue la porosité primaire.

La Formation de Gays River est totalement dolomitisée dans les sous-bassins de Musquodoboit et de Shubenacadie, ne l'est qu'à sa base dans la région de Mahone Bay et ne l'est pratiquement pas dans la région d'Antigonish (fig. 1). De plus, les calcites tardives ont les attributs géochimiques de systèmes météoriques dans ces deux dernières régions (Savard, données non publiées). Le système salin n'y a pas existé (ou duré). La mise en place du dépôt, comme la

dolomitisation, semble donc intimement liée à la pérennité de fluides salins et hypersalins. Conséquemment, sur une très large échelle, il semble que les dolomites puissent représenter un métallotecte. À l'intérieur de régions entièrement dolomitisées, des traceurs diagénétiques tels que la calcite zonée et ses valeurs basses de $\delta^{13}C$, la baisse de la réflectance de la matière organique (Rh), la diminution des teneurs en smectite et la présence de kaolinite peuvent servir de guide d'exploration (Héroux et al., données inédites).

Les dolomites produites à température élevée correspondent à un axe d'anomalie thermique décelé par l'altération de la matière organique et des smectites (Héroux et al., données inédites). Cet axe pourrait indiquer que des fluides impliqués lors de la minéralisation provenaient du sud du dépôt de Gays River. Des travaux en cours serviront à décrire avec plus de précision l'étendue et la nature de l'anomalie thermique.

## CONCLUSIONS

L'étude diagénétique régionale des carbonates entourant la mine de Gays River suggère que :

1. la dolomitisation (pré-minéralisation) est le produit d'un système salin diagénétique en enfouissement peu profond;
2. la précipitation des calcites syn-minéralisation (dont plusieurs zonées en CL) est le produit de fluides salins contenant des composés organiques;
3. la précipitation des calcites syn- et post-minéralisation (uniformes en CL) résulte d'un système identique à celui des dolomites;
4. un système de fluides salins, chauds et radiogéniques a été actif avant, après et pendant la minéralisation à Gays River;
5. la mise en place du dépôt implique possiblement le mélange de deux fluides et la réduction thermique de sulfates en présence de composés organiques.

## REMERCIEMENTS

L'auteure remercie Normand Tassé de l'INRS pour tous les commentaires enrichissants qu'il a fait lors de la révision du manuscrit. L'échantillonnage à Gays River a été rendu possible grâce à l'assistance de P. St-Antoine et à l'aimable collaboration de la compagnie Westminer Canada Inc. (merci à M. Cullen et J. Campbell pour leur collaboration). A la carothèque de Stellarton, Jim Langille, John McMullin et Bill Palmer ont fourni encore cette année une aide appréciable et ont réservé à l'auteure le même accueil chaleureux. L'échantillonnage dans les carrières de l'est a été autorisé par les frères Mosher. Les lames minces ont été préparées par Jean-Claude Bérubé de l'INRS-Géoressources. Un grand merci à Yvon Houde, Marco Boutin et Lise Michard pour les illustrations qu'ils ont effectuées.

## RÉFÉRENCES

**Akande, S.O., and Zentilli, M.,**
1984: Geologic, fluid inclusion, and stable isotope studies of the Gays River lead-zinc Deposit, Nova Scotia; Economic Geology, v. 79, p. 1187-1211.

**Al-Aasm, I., Taylor, B.E., and South, B.**
1990: Stable isotope analysis of multiple carbonate samples using selective acid extraction; Chemical Geology, v. 80, p. 199-125.

**Anderson, G.M., and Macqueen, R.W.**
1982: Ore deposit models-6. Mississippi valley-type lead-zinc deposits; Geological Association of Canada, v. 9, p. 108-117.

**Banner, J.L., and Hanson, G.H.**
1990: Calculation of simultaneous isotopic trace element variations during water-rock interaction with applications to carbonate diagenesis; Geochimica et Cosmochimica Acta, v. 54, p. 3123-3137.

**Boehner, R.C.**
1980: Preliminary Report on the Carboniferous Geology of the Antigonish Structural Basin, Antigonish County, Nova Scotia; Report of Activities, Department of Mines and Energy, Halifax, Nova Scotia, Report 80-1, p. 147-164.
1984: Stratigraphy and depositional history of marine evaporites in the Lower Carboniferous Windsor Group, Shubenacadie and Musquodoboit Structural Basins, Nova Scotia, Canada; Ninth International Congress of Carboniferous Stratigraphy and Geology, Urbana, Illinois, 1979; Proceedings, v. 3, p. 163-178.

**Boehner, R.C., Giles, P.S., Murray, D.A., and Ryan, R.J.**
1989: Carbonate buildups of the Gays River Formation, Lower Carboniferous Windsor Group, Nova Scotia; in Reefs, Canada and adjacent area, edited by H.H.J. Geldstzer, N.P. James and G.E. Tebbutt, Canadian Society of Petroleum Geologists, Memoir 13, p. 609-621.

**Craig, H.**
1965: The measurement of oxygen isotope paleotemperatures; in Stable isotopes in oceanographic studies and paleotemperatures, edited by E. Tongiogi, Consiglio Nazionale delle Richerche, Laboratorio di Geologia Nucleare, Pisa, Italy, p. 161-182.

**Giles, P.S.**
1981a: The Windsor Group of the Mahone Bay Area, Nova Scotia; Department of Mines and Energy of Nova Scotia, Paper 81-3, 51p.
1981b: Major transgressive-regressive cycles in the Middle to Late Visean rocks of Nova Scotia; Department of Mines and Energy of Nova Scotia, Paper 81-2, 27 p.

**Giles, P.S., and Boehner, R.C.**
1982: Geological map of the Shubenacadie and Musquodoboit Basins, central Nova Scotia; Department of Mines and Energy of Nova Scotia, Map 82-4.

**Giles, P.S., Boehner, R.C., and Ryan, R.J.**
1979: Carbonate banks of the Gays River Formation in central Nova Scotia; Department of Mines, Province of Nova Scotia, Paper 79-7, 57 p.

**Hamblin, T., and Rust, B.R.**
1989: Tectono-sedimentary analysis of alternate-polarity half-graben basin-fill successions: Late Devonian-Early Carboniferous Horton Group, Cape Breton Island, Nova Scotia; Basin Research, v. 2, p. 239-255.

**Hannon, P.**
1980: Gays River Lead-Zinc deposit; in Trip 6. Mineral deposits and mineralogenic provinces of Nova Scotia, Geological Association Canada-Mineralogical Association of Canada, Annual Meeting, Halifax, Field Trip Guidebook, p. 74-79.

**Howie, R.D., and Barss, M.S.**
1976: Upper Paleozoic rocks of the Atlantic Provinces, Gulf of St.Lawrence, and adjacent continental shelf; in Offshore Geology of Eastern Canada, Geological Survey of Canada, Paper 74-30, p. 35-50.

**Kontak, D.J.**
1991: Preliminary results of geological studies at the Gays River Deposit, southern Nova Scotia: a carbonate-hosted Pb-Zn deposit of Permo-Carboniferous age; Nova Scotia Department of Natural Resources, Report 91-5, Program and Summaries, Fifteenth Annual Open House and Review of Activities, p. 26.

**Land, L.**
1985: The origin of massive dolomite; Journal of Geological Education, v. 33, p. 112-125.

**Lohmann, K.C., and Meyers, W.J.**
1977: Microdolomite inclusions in cloudy prismatic calcites: a proposed criterion for former high-magnesium calcites; Journal of Sedimentary Petrology, v. 47, p. 1075-1088.

**Lucia, F.J., and Major, R.P.**
1991: Porosity occlusion by hypersaline reflux dolomitisation; Dolomieu Conference on Carbonate Platforms and Dolomitization, Abstracts, edited by A. Bosellini, R. Brandner, E. Flugel, B. Purser, W. Schlager, M. Tucker and D. Zenger, Ortisei/St-Ulrich, The Dolomites, Italy, 16-21 september, p. 156.

**MacLeod, J.L.**
1984: Diagenesis and its effects on base metal mineralisation within a Mississippian carbonate complex, Gays River, Nova Scotia, Canada; International Congress of Carboniferous Stratigraphy and Geology, v. 3, p. 193-204.

**Morrow, D.**
1990: Dolomite - Part 2: Dolomitization models and ancient dolostones; in Diagenesis, edited by I.A. McIlreath and D.W. Morrow, Geoscience Canada, Reprint Series no. 4, p. 125-140.

**Popp, B., Anderson, T.F., and Sandberg, P.A.**
1986: Brachiopods as indicators of original isotopic compositions in some Paleozoic limestones; Geological Society of America Bulletin, v. 97, p. 1262-1269.

**Ravenhurst, C.E., Reynolds, P.H., Zentill, M., Krueger, H.W., and Blenkinsop, J.**
1989: Formation of Carboniferous Pb-Zn and barite mineralization from basin-derived fluids, Nova Scotia, Canada; Economic Geology, v. 84, p. 1471-1488.

**Sandberg, P.A.**
1985: Aragonite cements and their occurrence in ancient limestone; in Carbonate cements, edited by N. Schneidermann and P.M. Harris, Society of Economic Paleontologists and Mineralogists, Special Publication no. 36, p. 33-58.

**Savard, M.M.**
1991: A preliminary report on the relationship between mineralization and carbonate diagenesis in the Gays River Formation, Nova Scotia; in Current Research, Part D, Geological Survey of Canada, Paper 91-1D, p. 147-156.

**Schenk, P.E., and Hatt, B.L.**
1984: Depositional environment of the Gays River Reef, Nova Scotia, Canada; International Congress of Carboniferous Stratigraphy and Geology, v. 3, p. 117-130.

**Veizer, J.**
1989: Strontium isotopes in Seawater through time; Annual Reviews of Earth and Planetary Sciences, v. 17, p. 141-167.

Projet 90017 de la Commission géologique du Canada

*Manuscript withdrawn at press time*
*Manuscrit rétiré au moment d'aller à l'impression*

*p. 299-308*

# Digital cartography with the Macintosh computer, in and out of the field

**T.D. Peterson and S. Hanmer**
**Continental Geoscience Division**

*Peterson, T.D. and Hanmer, S., 1992: Digital cartography with the Macintosh computer, in and out of the field; in Current Research, Part E; Geological Survey of Canada, Paper 92-1E, p. 309-314.*

***Abstract***

*A system is described to archive geological field data, and draft geological maps, using a proprietary CAD program for the Macintosh computer. The system complements existing software for DOS-based microcomputers, also in use at the GSC, and produces files which can be placed directly on-stream for publication. Hard copy can be obtained from a wide variety of output devices.*

***Résumé***

*On décrit ici un système permettant l'archivage des données géologiques de terrain et des cartes géologiques provisoires, à l'aide d'un programme exclusif CAO adapté à l'ordinateur Macintosh. Ce système complète le logiciel existant pour les microordinateurs employant le DOS, également utilisés à la CGC, et produit des fichiers qui peuvent directement servir à la publication. On peut obtenir une copie papier à partir d'une grande variété d'unités périphériques de sortie.*

## INTRODUCTION

The explosion in the capability of portable microcomputers in recent years now makes it possible for a geologist to digitally record the day's field work in less time, and with greater accuracy, than was ever feasible by direct plotting on hardcopy base maps. A major consideration is the ease of use and reliability of computer systems (there being no technical or software support in the field) and how readily the data so stored can be transferred into other formats. For many geoscientists, mapping, and the representation of geological data, are highly individualistic activities; one frequently hears that a geological map is as much a work of art as a technical product (an attitude we heartily agree with). A problem common to all computer programs is that the user is constrained to follow the train of thought of the programmer.

Many scientists and students prefer graphical user interfaces (GUIs). We consider GUIs (initially developed for microcomputers on, but no longer unique to, the Macintosh) to be appropriate for scientists routinely dealing with geographically oriented data. This report outlines a Macintosh-based system for archiving geological field data, and drafting geological maps. Our system complements the more database-oriented program FIELDLOG (v. 1.8, Brodaric and Fyon, 1989) (v. 2.82 in prep.: B. Brodaric, CGD) used by some scientists in Continental Geoscience Division with IBM-compatible microcomputers; transfer of data between the two systems presents no difficulties. The principal difference between our system and FIELDLOG (which uses AutoCad®)is that FIELDLOG permits the user to conduct more sophisticated relational database searches and stores the data in an external database linked to the map; it bears some resemblances to Geographic Information

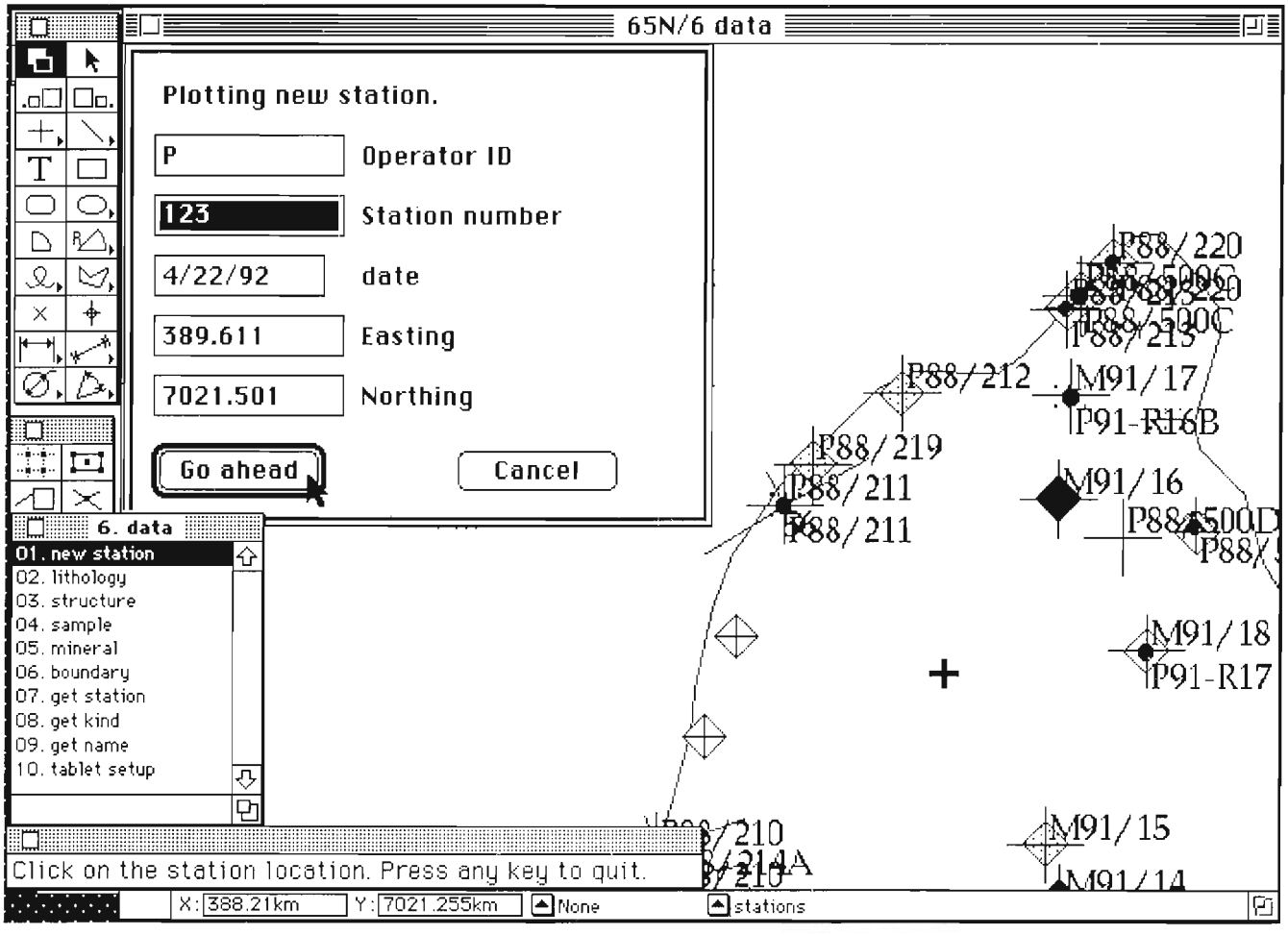


**Figure 1.** Example of plotting a new station location. The computer is waiting for the user to click on the location (the fat-cross cursor), after which a dialog window appears. This window (overlain near the top left corner of this figure) suggests the date (default is the current date in the computer's clock); indicates the co-ordinates where the user clicked (which can be edited at this point); requests the geologist ID (up to 256 characters, though only one character is used in this example) (default is the last ID entered); and requests a station number. Duplicate station numbers are rejected by the program. Note that the figure is a bit-map screen capture, not a printout of the vector file.

Systems (GIS). In our system, the map *is* the database (in keeping with the object-oriented philosophy of Macintosh software), and the emphasis is on streamlining the path from data collection to final map drafting.

We are using MiniCad+ version 3.1.x (Graphsoft, 1992), a popular CAD (Computer Assisted Design) program. Although primarily a drafting program, MiniCad+ also permits the storage of data in a database-type format, which requires no other program to access or edit. We prefer MiniCad+ because: (1) it is inexpensive for software of this type, and (2) its interface is easy to learn and similar to that of MacDraw, a well-known, standard-setting early drafting program for the Macintosh. We have successfully used Mac SE30s (16 MHz clock speed with a built-in black-and-white monitor) in the field to acquire systematic mapping data in two major field projects, during the field seasons of 1990 and 1991. Drafting of maps is feasible with this platform, but is better performed using faster (30+ MHz clock speeds) machines with colour monitors.

Copies of the routines we have developed and a manual describing their use, may be obtained from the first author by sending a 3.5" floppy disk. We emphasize that this paper is not intended as an endorsement of any company.

## ORGANIZATION OF THE DATA AND BASE MAP

Symbolic point data such as station locations, lithological and mineral occurrences, and structural measurements are stored on standard "layers" separate from the base map (digitized versions of 1:250 000 topographic maps suitable for base maps are available from the Surveys, Mapping and Cartographic Information Centres, Ottawa). A file may contain any number of layers. Each symbol instance is associated with a record instance, in which is stored the station name (if applicable), the spatial co-ordinates, and the value of the datum (lithology type, strike and dip, etc.). These are readily observed for any symbol by selecting it, and opening a window which lists all of the variables. Variables appearing in the window can be edited and the changes quickly updated on the map itself. The user creates and edits symbols, stored in a symbol library with each file, as needed. We find that completed, single 1:50 000 scale maps consume anywhere from 300 KB to 1.2 MB of storage space, depending on the density of data and whether or not the base map contains topographic contours.

All locations are referred to a user-defined orthogonal co-ordinate system; we use UTM co-ordinates. At present, non-orthogonal map projections cannot be recommended with this software because co-ordinate transformations would have to be performed outside the MiniCad+ environment.

## SUMMARY OF ROUTINES

T.D. Peterson has written approximately 4500 lines of code since January 1990 in MiniPascal, which has the syntax and vocabulary of standard Pascal but includes hundreds of additional commands for the creation and manipulation of graphical objects. The routines are run by double-clicking on the name of the routine in a dedicated window ("palette") (c.f. Fig. 1). There are several palettes, each of which combines routines with related functions. Space precludes us from describing each of these, however, they are listed in Table 1 and some of the drafting routines are described in a later section. We have striven to provide the user with typical Macintosh dialog windows whenever possible.

**Table 1.** List of data entry and drafting routines for the mapping system

| 1. Drafting | 2. Polygons | 3. Coloring |
|---|---|---|
| add to class | chain | color by class |
| boundary | contours to 3D | file colors |
| cut out | genchain | file fillfore |
| pattern | genmultichain | getfillback |
| tag regions | label contours | getfillfore |
| text on circle | multichain | getpenback |
| | polyarea | getpenfore |
| | polylength | recolor map |
| **4. Miscellaneous** | **5. Selecting** | **6. Data** |
| change classes | get class | new station |
| change class | get kind | lithology |
| lat/long arcs | get name | structure |
| lat/long mesh | min textsize | sample |
| lat/long ticks | pick out | mineral |
| set UTM | polyselect | get station |
| | | tablet setup |
| **7. Updates** | **8. Dbase functions** | **9. ArcInfo** |
| update lithologies | export structures | object dump |
| update minerals | import lithologies | structure dump |
| update samples | import minerals | text dump |
| update stations | import samples | |
| update structures | import stations | |
| | import structures | |

## USING THE SYSTEM

### *Data entry and transfer*

Data is entered "by eye" by clicking on the screen using lakes, streams, and contour lines for reference (Fig. 1, 2) or, alternatively, with a digitizing tablet and an airphoto (data may also be imported from a properly formatted ASCII text file). Once one datum associated with any location has been plotted, additional data may be entered without further input of the location. If several stations are selected, a datum common to all of them may be plotted simultaneously. We prefer in most cases to have a numbered station for all data points, because this is the simplest way to ensure that data at a specific location can be "connected" when exported to relational database formats. However, this is not a necessity and when (for example) a large area yields few data (such as a homogeneous plutonic body), it is more convenient to sprinkle an area with lithological symbols, to serve as markers for later drafting of contacts, and have no stations in the area. Structural and mineral data may also be plotted without stations, but samples must be plotted at named stations. Figure 2 gives an example from one of our projects.

Data can be moved from one map file to another by: (1) copying and pasting via the standard Macintosh clipboard, (2) using our routines for exporting and importing, or (3)

exporting and importing using MiniCad+'s built-in functions. Method (2), sometimes in combination with (3), is preferable because the routines check for duplication of station names, and guarantee correct spatial placement and layer organization of all data.

Structural data can be exported to tab-delimited text files (e.g., for making stereonets with other programs) in a number of ways (Fig. 3). The user can export all structures of a given type, or only those data which are selected, or those associated with named stations, or those lying within a specified polygon, or any combination of the above. At present, other types of data (e.g., sample locations) must be exported in their entirety. We have successfully exported the field-acquired data from approximately six 1:50 000 map sheets from one of our projects into a relational database program external to MiniCad+ where it can be queried and added to as appropriate (e.g. petrographic observations) in the normal manner. As indicated above, if the user has an existing database, it can be imported into a map with minor alterations.

### *Drafting maps*

It is feasible to draft geological maps with MiniCad+ without using any of our routines. However, the routines make it much simpler to organize map units and ensure consistent colouring, to draft special linework (e.g., faults), and to correct imperfections in the base map, etc.

Each occurrence of a geological unit (a *region*) is represented as a closed polygon, whose boundaries are perfectly matched with contiguous regions and with shorelines. These are created using a combination of polygon-drawing, surface intersection/addition, and surface clipping tools native to MiniCad+. We find the surface functions in MiniCad+ to be extremely useful; in general, with other CAD packages such routines are third-party and external to the program. Each region is assigned to a user-determined class, whereupon it is automatically given the correct colour and pattern according to an assignment file. The files are created by the user, by selecting any object with the desired colour assignments, and running the "file colours" routine.

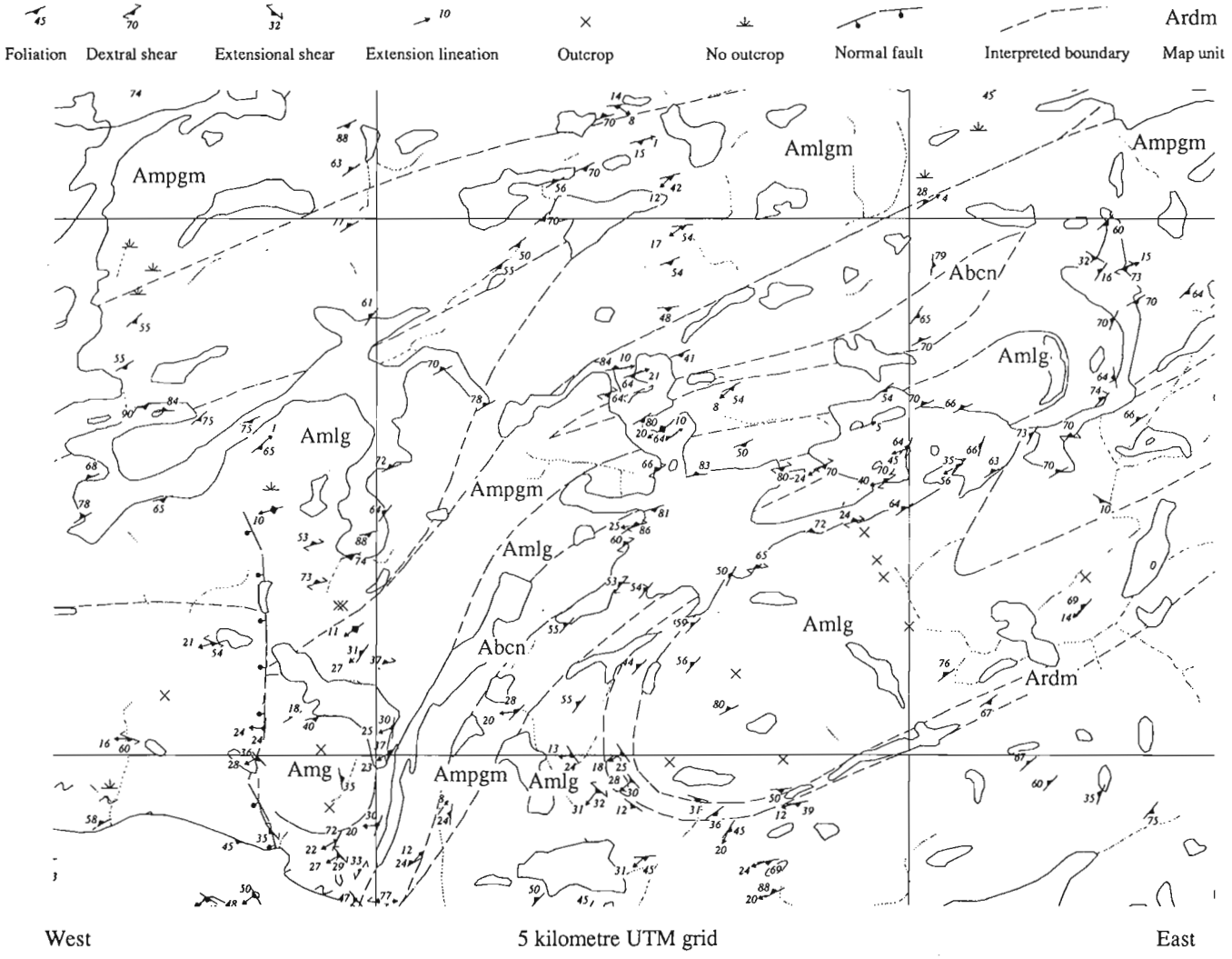


**Figure 2.** Example of a field data file, showing selected structural data. The layers containing station markers, lithological symbols, and sample locations have been made invisible (see Fig. 1, where all layers are visible, and hence symbols are 'stacked' on top of the station location). The map is a portion of the Clut Lake sheet (NTS 74P/5).

| Foln | Azim | Dip | Stn | UTM (E) | UTM (N) | | Lin | Azim | Plunge | Stn | UTM (E) | UTM (N) |
|---|---|---|---|---|---|---|---|---|---|---|---|---|
| foln | 50 | 65 | S183 | 458.924 | 6587.869 | | lin | 50 | 1 | S183 | 458.939 | 6587.942 |
| foln | 214 | 31 | S179 | 459.830 | 6585.964 | | lin | 230 | 27 | S179 | 459.802 | 6585.917 |
| folnS | 210 | 37 | S177 | 460.126 | 6585.024 | | lin | 240 | 23 | S177 | 460.076 | 6584.997 |
| foln | 139 | 47 | S175 | 459.795 | 6583.640 | | lin | 217 | 42 | S175 | 459.775 | 6583.620 |
| foln | 202 | 30 | none | 459.982 | 6584.354 | | lin | 266 | 20 | none | 459.954 | 6584.353 |
| foln | 185 | 30 | none | 460.123 | 6585.249 | | lin | 250 | 25 | none | 460.092 | 6585.237 |
| folnV | 235 | 90 | none | 459.781 | 6586.187 | | lin | 235 | 11 | none | 459.757 | 6586.154 |
| folnV | 254 | 90 | none | 459.011 | 6587.307 | | lin | 254 | 10 | none | 458.958 | 6587.279 |
| folnS | 110 | 60 | M134 | 457.678 | 6585.148 | | lin | 270 | 16 | M134 | 457.600 | 6585.155 |
| folnS | 110 | 54 | M135 | 458.466 | 6586.040 | | lin | 255 | 21 | M135 | 458.391 | 6586.028 |
| foln | 150 | 50 | J221 | 458.836 | 6583.684 | | lin | 235 | 48 | J221 | 458.800 | 6583.671 |
| foln | 121 | 42 | J234 | 458.410 | 6583.641 | | lin | 242 | 34 | J234 | 458.357 | 6583.644 |
| folnN | 138 | 29 | none | 459.656 | 6584.066 | | lin | 240 | 27 | none | 459.597 | 6584.043 |
| foln | 205 | 72 | M160 | 459.592 | 6584.216 | | lin | 241 | 22 | M160 | 459.572 | 6584.172 |
| foln | 135 | 36 | M166 | 458.869 | 6584.948 | | lin | 244 | 28 | M166 | 458.826 | 6584.955 |
| foln | 75 | 42 | C179 | 462.778 | 6590.367 | | lin | 225 | 12 | C179 | 462.721 | 6590.347 |
| foln | 84 | 54 | C180 | 462.888 | 6589.904 | | lin | 235 | 17 | C180 | 462.815 | 6589.885 |
| foln | 240 | 24 | C166 | 460.306 | 6584.024 | | lin | 42 | 12 | C166 | 460.385 | 6584.053 |
| foln | 187 | 24 | C167 | 460.666 | 6584.450 | | lin | 35 | 8 | C167 | 460.628 | 6584.521 |
| foln | 145 | 24 | C169 | 461.826 | 6584.981 | | lin | 264 | 13 | C169 | 461.791 | 6584.998 |
| foln | 145 | 25 | C170 | 462.303 | 6584.993 | | lin | 240 | 18 | C170 | 462.257 | 6584.986 |
| foln | 85 | 45 | C172 | 462.544 | 6584.029 | | lin | 230 | 31 | C172 | 462.477 | 6584.016 |
| folnS | 278 | 77 | C165 | 460.009 | 6583.657 | | lin | 85 | 48 | C165 | 460.124 | 6583.649 |
| foln | 140 | 30 | none | 462.390 | 6584.745 | | lin | 229 | 28 | none | 462.351 | 6584.720 |
| foln | 239 | 28 | C533 | 465.128 | 6590.172 | | lin | 59 | 4 | C533 | 465.217 | 6590.187 |

**Figure 3.** Example of a flat-file table of structural data obtained from the file of Figure 2. The table can be incorporated into relational databases, or imported into a stereonet program. UTM co-ordinates are in kilometres, not metres.

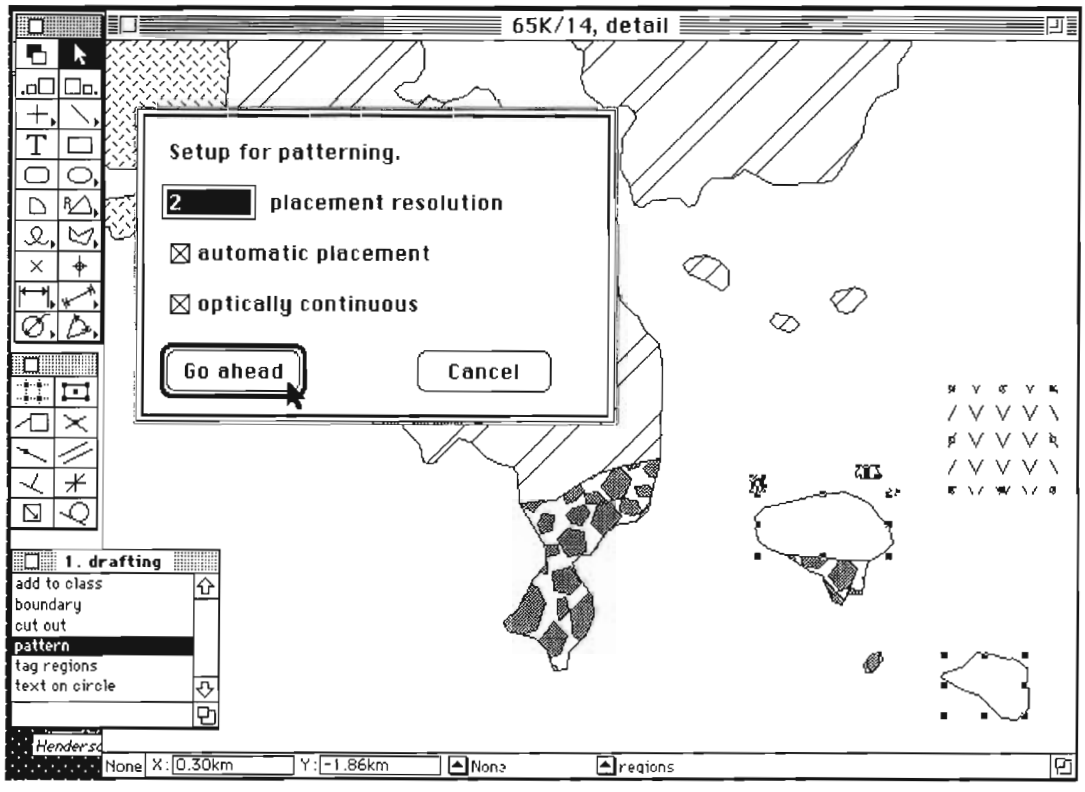


**Figure 4.** Example of a patterning task. The user selects the pattern cell (visible at center right), and the polygons to be patterned. The user has the option of specifying the origin of the pattern (i.e., the corner of a pattern cell) by clicking on-screen or by keyboard entry, or allowing the routine to automatically select an origin; and of having multiple polygons patterned in an optically continuous fashion (i.e., all patterns share a common origin). "Placement resolution" determines the number of points within the pattern cell (and entities contained in the cell) which are checked to determine if they lie within the polygon(s) (Bit-map screen capture).

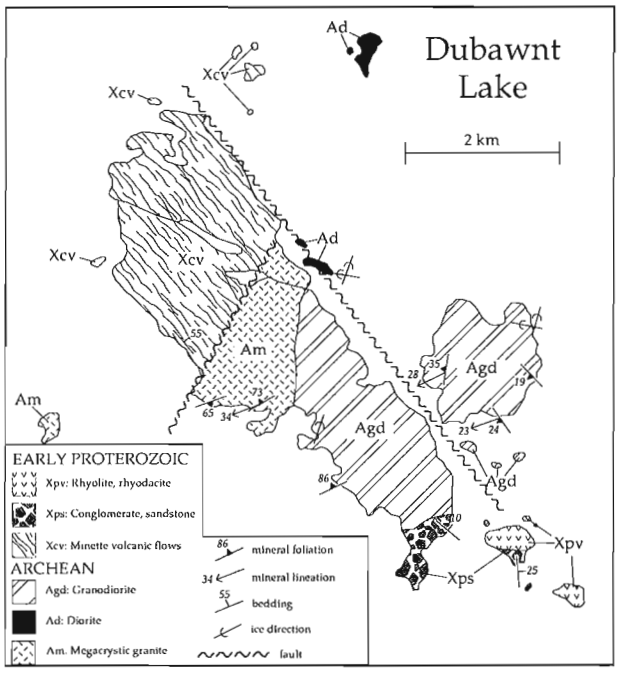


**Figure 5.** Example of a completed map. The figure is a portion of NTS 65K/14 (Dubawnt Lake, NWT) mapped by one of the authors in 1990. The published version would use solid color, rather than pattern fills. Units Xcv, Xps, and Xpv patterned using our patterning routine; unit Agd patterned with MiniCad+'s hatching routine; and units Am and Ad patterned with Macintosh bit-map fills.

Geological boundaries (contacts, faults) should be kept on separate layers, and may correspond to all or part of the edge of a region. A user-defined polygon can be overlain along its length by any symbol (e.g., fault squiggles, mineral isograd symbols) to provide contacts or other linear phenomena which cannot be adequately represented by simple solid, dashed, or dotted lines. Note that this system does not follow the topological "arc-node" basis for defining regions and contacts typical of GIS packages; rather, a Mac-type object-oriented approach is used. This results in duplication of all region boundaries by sets of contacts and shorelines, but the price in extra storage space is relatively small compared to the advantages in the ease of drafting, and control of display, that are achieved.

We prefer to draft in colour. However, for black-and-white figures regions may also be patterned using: (1) the common Mac bit-map patterns. These are of limited utility; (2) MiniCad+'s hatching feature, allowing for patterns made of lines at any spacing or angle; (3) our own pattern routine, which permits patterning with any rectangular "unit cell" composed of lines, polygons, rectangles, and arcs/circles. Figure 4 shows an example of a patterning task, and Figure 5 shows examples of all three pattern types.

A number of routines are also provided for cleaning up digital base maps. We find that long shorelines or contours are often obtained in two or more polygons, which match perfectly end-to-end but cannot be used together to define a region (such as a lake). The "chain" routines correct this common defect and also provide for generalizing the polygons, in case the degree of detail in the originals is greater than required (this can be an issue for very large maps or for slow computers). Of course, original base maps should never be altered by generalizing.

Additional routines useful for map drafting include three types of latitude/longitude mesh drawings, labeling contour polygons and converting them to 3D, drawing text on arcs, and various selection routines. Although we have not incorporated GIS routines, it is a simple matter with MiniCad+ to extract some data of this type (e.g., the total area of a geological unit within a map area, the length of a traverse line, etc.). A representative portion of one of our maps is given in Figure 5.

## OBTAINING OUTPUT

Output may be obtained from any Postscript-driven device; we have experience with black-and-white and color laser printers, and large-format plotters. Plotter drivers for other devices (e.g., Tectronix plotters) can be obtained through Graphsoft. A MiniCad+ file may also be translated into DXF, a standard ASCII text format which can be read by most other CAD prgrams and GIS packages; DXF is an industry-wide standard and is widely used within the Continental Geoscience Division for transfer of graphics across platforms.

We are currently producing maps for publication with this system. Our preferred route at present is to export the base map, contacts, etc. into a DXF file and all point data (structure symbol occurrences, etc.) into an ASCII table format, both of which can be imported into ArcInfo (used by Digital Cartography, CGD, for drafting of maps) for final production. The exportation of nine 1:50 000 maps has been accomplished without difficulty.

## ACKNOWLEDGMENTS

We thank Graphsoft, Inc. for permission to reproduce examples of the MiniCad+ interface. The manuscript was critically reviewed by Mikkel Schau, with additional comments from Boyan Brodaric. Autocad is a registered trademark of Autodesk, Inc.

## REFERENCES

**Brodaric, B. and Fyon, J.A.**
1989: OGS FIELDLOG: A microcomputer-based methodology to store, process, and display map-related data; Ontario Geological Survey, Open File Report 5709.

**Graphsoft**
1992: MiniCad+, Computer Aided Design System; Graphsoft, Inc., 8370 Court Ave., Suite 202, Ellicott City, Maryland 21043.

Geological Survey of Canada Project 880012

# Is Ni in chrome pyrope garnet a valid diamond exploration tool?[1]

**B.A. Kjarsgaard**
**Continental Geoscience and Mineral Resources divisions**

*Kjarsgaard, B.A., 1992: Is Ni in chrome pyrope garnet a valid diamond exploration tool?; in Current Research, Part E; Geological Survey of Canada, Paper 92-1E, p. 315-322.*

***Abstract***

*Calibration of the Ni thermometer has been independently tested by comparing equilibration temperatures of peridotite xenoliths from Somerset Island, Northwest Territories with Ni temperatures derived from analysis of garnets by proton microprobe from the same xenoliths. Results agree with the original observation that Ni content of garnet is strongly temperature dependant. Large (up to 238°C) temperature differences exist between the Ni thermometer and the two pyroxene thermometer of Finnerty and Boyd which was used as the reference (or 'true') temperature. However, Ni temperature correlates quite well (± 80°C) with the two pyroxene thermometer of Brey, Köhler, and Nickel, suggesting that a revision of the current calibration of the Ni thermometer is feasible. Inherent assumptions implicit in the use of Ni thermometry in diamond exploration are examined; these assumptions produce major drawbacks to the reliable application of the Ni thermometer.*

***Résumé***

*On a indépendamment procédé à des essais de l'étalonnage du géothermomètre Ni en comparant les températures d'équilibre de xénolites de péridotite provenant de l'île Somerset (Territoires du Nord-Ouest) avec les températures Ni dérivées de l'analyse de grenats provenant des mêmes xénolites, par microsonde protonique. Les résultats concordent avec l'observation initiale, selon laquelle le contenu en Ni du grenat est fortement fonction de la température. Il existe de grandes différences de température (jusqu'à 238 °C) entre le géothermomètre Ni et le géothermomètre à deux pyroxènes, tel que décrit par Finnerty et Boyd, qui a servi à déterminer la température de référence (ou température vraie). Cependant, la température Ni présente une bonne corrélation (± 80 °C) avec le géothermomètre à deux pyroxènes décrit par Brey, Köhler et Nickel, ce qui semble indiquer qu'une révision de l'étalonnage actuel du géothermomètre Ni est réalisable. On examine les hypothèses implicites concernant l'emploi de la géothermométrie Ni dans la prospection diamantifère; ces hypothèses indiquent d'importants obstacles à l'application fiable du géothermomètre Ni.*

[1] Contribution to the Canada-Northwest Territories Mineral Initiative 1991-1996 and Canada-Saskatchewan Partnership Agreement on Mineral Development 1990-1995.

## INTRODUCTION

The strongly temperature dependant partitioning of Ni between chrome pyrope garnet and olivine has been used to construct a geothermometer (Griffin et al., 1989a). The Ni thermometer is envisaged as an important diamond exploration tool, able to provide semi-quantitative estimates of potential diamond grade (Griffin, 1990). This contribution reviews the calibration of the Ni thermometer as well as its use as a guide to diamond exploration. Ni temperature estimates from garnets separated from previously studied peridotite xenoliths from Somerset Island kimberlites (Kjarsgaard and Peterson, 1992) are used as an independent test of the thermometer. The application of the thermometer with respect to diamond grade is also tested by use of these garnet temperatures since bulk sampling (Davies, 1975) has established these kimberlites grades <1 c/100 t.

## THE Ni THERMOMETER

Griffin et al. (1989a) calibrated a thermometer based on nickel exchange between chrome pyrope garnet and olivine in garnet peridotite xenoliths, and assumed it to be independant of garnet major element composition. The reference temperature for the calibration is based on thermobarometry using the two pyroxene thermometer and opx-garnet barometer of Finnerty and Boyd (1987: $T_{FB86}$ and $P_{MC74}$), or the olivine-garnet Fe/Mg exchange thermometer of O'Neill and Wood (1979; corrected in O'Neill, 1980:$T_{OW80}$) at an assumed pressure. Griffin et al. (1989a) illustrated that Ni partitioning is strongly temperature dependant, with garnet accepting more Ni (<10 to 120 ppm) with increasing T and derived the following equation

$$1000/K = -0.428 \log_{10}(100K_D) + 0.84 \qquad (r = -0.98) \quad (I)$$

where $K_D = Ni_{garnet}/Ni_{olivine}$. Based on the observation that olivine has a restricted Ni content (2400 - 3200 ppm) and is the dominant modal mineral in peridotite xenoliths (60 - 80%) as compared to garnet (%), Griffin et al. (1989a) suggested that olivine represents an "essentially infinite reservoir of fixed composition relative to garnet". By assuming $Ni_{olivine}$ = 3000 ppm, Griffin et al., (1989a) derived the following equation

$$1000/K = -0.435 \log_{10}(Ni_{garnet}/30) + 0.83 \qquad (r = -0.98) \quad (II)$$

which reproduces the estimated temperatures from equation (I) with an error of ± 4% (or ± 50°C). A pressure correction was not built into either version of the Ni thermometer. However, they do suggest P effects are probably in the order of a few degrees/kilometre, and note that further quantification of the pressure effect would be useful.

## APPLICATIONS OF THE Ni THERMOMETER

The main suggested applications of the Ni in chrome pyrope thermometer are to problems related to the genesis of diamond (Griffin et al., 1989b) and as a diamond exploration tool (Griffin, 1990). The latter application is of great interest to the exploration industry; any technique which can assist in differentiating a diamond-rich kimberlite from one poor or barren of diamonds at an early stage in the evaluation process (before extensive and expensive bulk sampling) is exceptionally useful. In this respect, Griffin (1990) has suggested that the Ni thermometer is a "rapid, cheap and powerful tool for evaluating diamond prospects" and furthermore, is a more robust and reliable indicator of potential diamond grade than established techniques which use the presence or absence of 'G10' (high-Cr, low-Ca) garnets.

The use of the Ni thermometer in assessing diamond potential relies on converting a temperature estimate to a depth estimate. This is accomplished by obtaining a pressure from the intersection of the geothermal gradient with the temperature obtained by Ni thermometry (Fig. 1). Griffin (1990) suggested use of the theoretical 40 $mW/m^2$ geotherm since Finnerty and Boyd (1987) illustrated that xenoliths from South African kimberlites cluster near this theoretical 'cratonic' geotherm. By this temperature/geotherm intersection method, garnets with estimated temperatures of 1000°C or higher are inferred to have equilibrated in the diamond stability field. Based on the analysis of garnets from concentrate and inclusions in diamond from 50 kimberlites and lamproites, Griffin (1990) stated that in areas with 'cratonic' geotherms, high proportions of these garnets have Ni temperatures between 950 and 1250°C (the 'diamond window'). Furthermore, diamond-poor host rocks contained mainly garnets with Ni temperatures < 950°C (suggesting equilibration in the graphite stability field) or >1250°C (diamonds suggested to be resorbed at these high temperatures).

## INHERENT ASSUMPTIONS IN THE CALIBRATION OF THE Ni THERMOMETER

Calibration of a new thermometer (or barometer) is usually constrained by experiments and/or thermodynamic theory. In the case of equation (I), the thermometer utilizes an exchange reaction and the calibration is constrained by reference to the FB86 thermometer with the MC74 barometer or OW80 thermometer with assumed pressure. While the OW80 thermometer is believed to provide reasonable temperature estimates (Brey and Köhler, 1990), it is pressure dependant and assuming an equilibration pressure introduces uncertainties to the temperature determination. The FB86 thermometer and MC74 barometer have undergone much

scrutiny and it has been suggested that this thermometer/barometer combination does not produce reliable P-T estimates (Carswell and Gibb, 1987; Brey and Köhler, 1990; Carswell, 1991; Brey, 1991). Because of uncertainties as to the validity of the reference temperatures used in calibrating the Ni thermometer, caution must be exercised in its application. It should also be noted that the assumption of constant olivine Ni content is a serious simplification which may compomise results. In particular, peridotite xenoliths have varying modal mineralogies (e.g. lherzolite, harzburgite, wehrlite) and contain other Ni-bearing phases such as orthopyroxene (up to 1100 ppm Ni) or clinopyroxene (up to 400 ppm Ni). The presence or absence of these phases will affect the Ni content of olivine and thereby introduce further uncertainties into use of equation (II).

## LIMITATIONS IN THE APPLICATION OF THE Ni THERMOMETER

The application of the Ni thermometer as a diamond exploration tool is problematic. Converting a Ni temperature estimate to a depth estimate by means of intersection with a geotherm requires knowledge of the geothermal gradient. Griffin (1990) suggested utilizing the theoretical 40 $mW/m^2$ 'cratonic' geotherm. However, one cannot assume that every craton worldwide has a similar geotherm. Furthermore, it is not clear as to what a typical 'cratonic' geotherm is. Brey (1991) considered the supposed 40 $mW/m^2$ inflected geotherm of the Kaapvaal craton to be fictive (an artifact of using the FB86/MC74 thermobarometer), and presents new data consistent with the geothermal gradient being slightly cooler than a theoretical 44 $mW/m^2$ geotherm. Without knowledge of the geotherm, depth estimation is problematic, i.e. the intersection of the 44 $mW/m^2$ geotherm and the graphite/diamond transition occurs at a temperature approximately 140°C higher compared to the 40 $mW/m^2$ geotherm (Fig. 1). For example, garnets with Ni temperature estimates between 1000 and 1150°C could be inferred to have equilibrated in either the diamond or graphite stability field depending on whether the geothermal gradient was 40 $mW/m^2$ or 44 $mW/m^2$.

Another important problem in applying the Ni thermometer to diamond exploration regards diamond grade assessment. Griffin (1990) suggested data derived from Ni thermometry can give a semi-quantitative estimate of potential diamond grade, however, this is an over-simplification. The Ni thermometer can assess only diamonds of garnet-bearing peridotitic paragenesis. On the basis of inclusions of high Mg-chromites in diamonds, chromite-bearing peridotitic assemblages are considered an important diamond-bearing mantle lithology (Gurney, 1989). Furthermore, in some kimberlites (Premier, Orapa, Monastery), 60 - 90 per cent of all diamonds are of eclogitic paragenesis (Gurney et al., 1991), and the Ni thermometer cannot evaluate the contribution of eclogitic paragenesis diamonds to the total

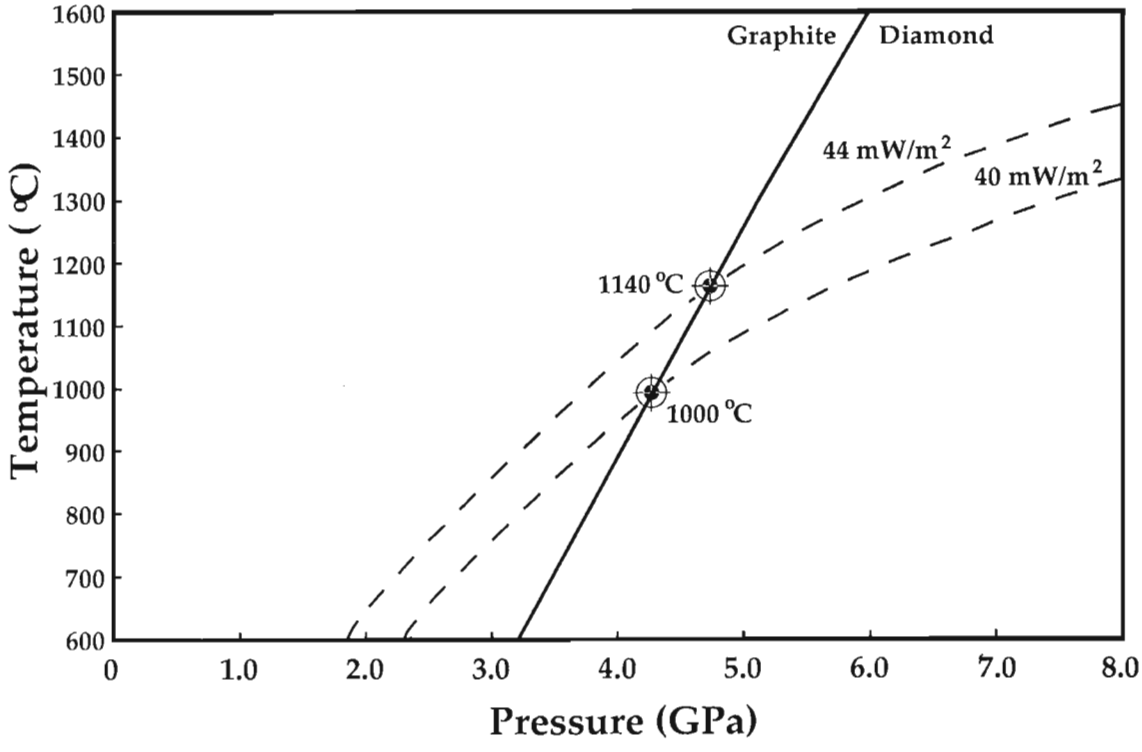


**Figure 1.** An illustration of the inherent problem of converting a Ni temperature to a depth estimate using the intersection of the temperature estimate with an unknown paleogeotherm. Note that the graphite/diamond transition occurs at approximately 1140°C on a 44 $mW/m^2$ geotherm compared to 1000°C on a 40$mW/m^2$ geotherm. The theoretical 40$mW/m^2$ and 44$mW/m^2$ geotherms are after Pollack and Chapman (1977). The graphite/diamond transition is from Kennedy and Kennedy (1976).

diamond grade. Finally, there is the suggestion that Ni temperature estimates >1250°C are associated with the destruction of diamond (Griffin, 1990). Diamond resorption is usually quantified by considering that ilmenite composition reflects oxygen fugacity (Mitchell, 1986). Again, Ni thermometry gives no indication of $f_{O_2}$, and high temperature does not necessarily imply high $f_{O_2}$ (and resorption).

## ASSESSMENT OF THE Ni THERMOMETER

### *Method*

Garnets (typically 0.5 - 2.0 mm dia.) were separated from lherzolite xenoliths collected from Somerset Island, N.W.T. (Kjarsgaard and Peterson, 1992), mounted in resin blocks and polished. Proton microprobe analyses were performed at the University of Guelph. Analytical conditions were as follows: beam current, 1.57 to 2.48 nA at 3.0 MeV; beam size, 8 X 10 μm in spot mode or 80 $\mu m^2$ in raster mode; accumulated proton charge, 0.5 μC. X-rays were detected with a Link Si(Li) detector for counting times varying between four and five minutes. The proton beam passed through a 125 μm thick mylar absorber and a 106 mm thick aluminum X-ray filter. Data reduction was performed with the GUPIX software program developed at the University of Guelph (Maxwell et al., 1989). Further details of the analytical techniques and data reduction are given in Campbell et al. (1990). Two to four analyses were done on each garnet (core, near rim or core, middle, near rim). Seven of the thirty samples included multiple (2 - 3) garnets from the same sample. Analyses in the spot or raster mode produced comparable results.

**Table 1.** Nickel content of garnet (as determined by proton microprobe) and olivine (as determined by electron microprobe) from lherzolite xenoliths from Somerset Island

| Sample | Ni garnet avg, ppm | # of analyses | Ni garnet range, ppm | Ni olivine ppm (X $10^3$) | T(Ni#1) °C | T(Ni#2) °C | T(BKN) °C | T(FB86) °C |
|---|---|---|---|---|---|---|---|---|
| K11A1 | 80 | 7 | 76 - 87 | 3.14 | 1227 | 1278 | 1146 | 1043 |
| K11A3 | 55 | 4 | 52 - 61 | 2.67 | 1145 | 1126 | 1121 | 994 |
| K11A4 | 78 | 6 | 74 - 83 | 2.83 | 1260 | 1264 | 1234 | 1129 |
| K11A5 | 63 | 4 | 61 - 66 | 3.22 | 1123 | 1175 | 1127 | 1012 |
| K11A6 | 82 | 4 | 79 - 84 | 2.83 | 1284 | 1290 | | |
| K11A7 | 64 | 4 | 60 - 66 | 2.91 | 1167 | 1181 | 1156 | 1054 |
| K11A9 | 66 | 4 | 63 - 69 | 2.83 | 1189 | 1192 | 1192 | 1088 |
| K11A14 | 51 | 6 | 46 - 54 | 2.59 | 1128 | 1098 | 1123 | 997 |
| K11A15 | 64 | 4 | 60 - 68 | 2.59 | 1215 | 1183 | 1152 | 1052 |
| K11A16 | 63 | 4 | 59 - 67 | 3.07 | 1144 | 1178 | 1158 | 1063 |
| K11A17 | 52 | 3 | 48 - 58 | 3.62 | 1019 | 1102 | | |
| K12A2 | 76 | 4 | 74 - 80 | 2.83 | 1252 | 1256 | 1218 | 1142 |
| K12A3 | 80 | 3 | 75 - 83 | 2.91 | 1259 | 1276 | 1206 | 1119 |
| K12A6 | 66 | 4 | 66 - 71 | 3.30 | 1133 | 1195 | | |
| K12A7 | 81 | 3 | 77 - 85 | 2.83 | 1280 | 1285 | 1214 | 1132 |
| K12A8 | 77 | 3 | 70 - 83 | 3.14 | 1212 | 1261 | 1246 | 1130 |
| K13B1 | 72 | 4 | 66 - 81 | 3.54 | 1138 | 1230 | | |
| K13B3 | 6 | 3 | 4 - 8 | 3.22 | 602 | 616 | 859 | 708 |
| K13B4 | 61 | 4 | 57 - 66 | 3.14 | 1123 | 1165 | | |
| K13B5 | 48 | 4 | 47 - 51 | 3.54 | 1005 | 1078 | 1083 | 941 |
| K15A2 | 71 | 3 | 69 - 73 | 2.99 | 1199 | 1225 | 1140 | 1057 |
| K15A6 | 14 | 4 | 11 - 18 | 3.14 | 733 | 750 | | |
| K15A7 | 76 | 4 | 73 - 77 | 2.75 | 1261 | 1253 | 1227 | 1131 |
| K15A9 | 59 | 4 | 52 - 64 | 3.38 | 1083 | 1149 | | |
| K15A10 | 66 | 6 | 62 - 69 | 3.30 | 1130 | 1192 | | |
| K16A1 | 58 | 5 | 55 - 64 | 3.69 | 1050 | 1146 | | |
| K16A2 | 51 | 6 | 48 - 55 | 2.91 | 1083 | 1094 | 999 | 856 |
| K16A3 | 53 | 8 | 47 - 58 | 3.46 | 1041 | 1110 | 1046 | 927 |
| K24KK | 46 | 4 | 43 - 48 | 2.99 | 1043 | 1061 | 1120 | 1025 |
| N2B | 70 | 1 | 70 | 3.14 | 1174 | 1219 | | |

Limit of detection for Ni for proton microprobe analyses ranged from 5 to 7 ppm Ni, with a one sigma error of 4 to 5 ppm. T(Ni#1) and T(Ni#2) are temperatures calculated by the Ni thermometer as per equation (I) and (II) respectively; T(BKN) and T(FB86) are reference temperatures calculated for the same xenoliths from the thermobarometer combinations of Brey et al. (1990: $T_{BKN}$ vs $P_{BKN}$) and Finnerty and Boyd (1987: $T_{FB86}$ vs $P_{MC74}$).

### *Results*

Analytical data of nickel content in chrome pyrope garnets from garnet lherzolite xenoliths are listed in Table 1. Nickel content ranged from 4 to 87 ppm. Range in Ni content for a single sample was 4 - 11 ppm. This is similar to the range of values previously reported from detailed traverses across garnets (excluding the enriched rim area) from porphyroclastic garnet lherzolites (Fig. 1 of Griffin et al., 1989c). No zoning was noted from the core to near the rim, and it is concluded that the Somerset Island garnets are homogenous with respect to their Ni content (excluding the possibility of Ni enriched rims; detailed traverses were not undertaken in this study). The Ni contents of olivine coexisting with garnet are listed in Table 1 (electron microprobe analysis by wavelength dispersive methods with a 200 second count time; further details are provided in Kjarsgaard and Peterson, 1992) and are homogenous with respect to Ni.

Temperatures obtained by Ni thermometry are listed in Table 1, representing the two different calibrations of Griffin et al. (1989a). T(Ni#1) uses the measured Ni content of olivine ($D_{garnet/olivine}$; equation I), whereas T(Ni#2) assumes 3000 ppm Ni in olivine (equation II). A comparison of the two Ni temperature estimates shows that 24 of 30 samples have similar temperatures to ± 52°C, although in 26 of 30 samples T(Ni#2) produces higher temperatures. Note that data for xenolith K13B3 is not considered further since Ni was below the limit of detection. An assessment of Ni thermometer calibrations I and II has been made by

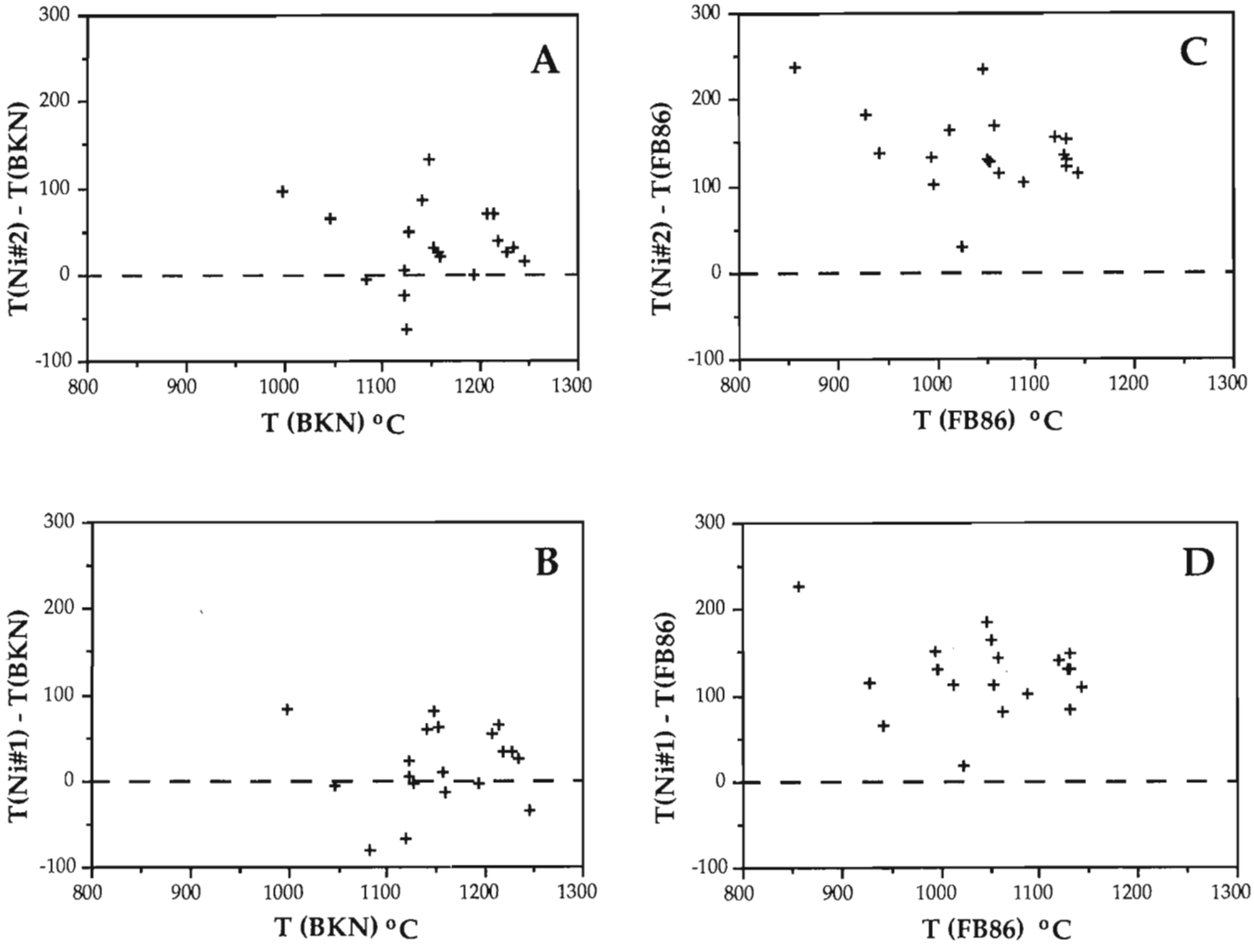


**Figure 2.** Comparison of the difference between Ni temperature and reference temperature plotted against reference temperature. Ni temperatures calculated by equation II (A, C) in general overestimate the temperature as compared to temperatures calculated by equation I (B, D). Note large T overestimates in (D) suggest the thermometer needs recalibration as the FB86 thermometer was utilized as the reference temperature in the original calibration. T(Ni#1) and T(Ni#2) are temperatures calculated by the Ni thermometer as per equations I and II respectively; T(BKN) and T(FB86) are temperatures calculated from the thermobarometer combinations of Brey et al. (1990: $T_{BKN}$ vs $P_{BKN}$) and Finnerty and Boyd (1987:$T_{FB86}$ vs $P_{MC74}$).

comparing Ni temperature with T estimates derived using the conventional two-pyroxene/opx-garnet thermobarometers of Brey et al. (1990) and Finnerty and Boyd (1987). Equilibration temperatures of twenty of the thirty samples are listed in Table 1 (data from Kjarsgaard and Peterson, 1992 and unpublished). In Figure 2(A - D), the difference between the estimated Ni temperature T(Ni#1) or T(Ni#2) and the reference temperature $T_{BKN}$ or $T_{FB86}$ is plotted against the reference temperature. Comparing Figures 2B and 2D with 2A and 2C illustrates that better temperature estimates are produced by T(Ni#1) as compared to T(Ni#2). Figures 2C and 2D versus 2A and 2B show the relationship between Ni temperature and reference temperature ($T_{FB86}$ versus $T_{BKN}$, respectively). With the FB86 thermometer as a reference, T(Ni#2) overestimates temperature by 36 - 238°C (Fig. 2C) and T(Ni#1) overestimates temperature by 18 - 227°C (Fig. 2D). In contrast, with the BKN thermometer as a reference, Ni temperature estimates range from +140 to -25°C for T(Ni#2) or from + 81 to - 77°C for T(Ni#1).

## DISCUSSION

The Somerset Island kimberlites provide a good null test for any diamond exploration guide since they grade < 1c/100t (Davies, 1975). Heavy mineral concentrates from these kimberlites are consistent with them being almost barren. Only rare G10 garnets and high-Mg, Cr chromites have been identified, and no eclogitic garnets (Jago and Mitchell, 1989; Fipke, 1990; unpublished data). Therefore, application of the Ni thermometer as an indicator of diamond grade should produce a negative result. Comparing Somerset Island to barren and diamondiferous kimberlites from W. Tanzania (Fig. 3) shows that Ni temperatures from Somerset Island produce a frequency peak between 1000 - 1300°C, that is, similar to the suggested frequency peak of 950 - 1250°C for diamondiferous kimberlites (Griffin, 1990).

Figure 4 shows depths estimated via the intersection of the geotherm with the Ni temperature and illustrates the problem of assuming a theoretical 40 mW/m$^2$ 'cratonic' paleogeotherm (Griffin, 1990). Utilizing the Somerset Island results and assuming a 40 mW/m$^2$ paleogeotherm suggests these kimberlites are a favourable exploration target. In contrast, recognizing that the paleogeotherm is approximately 44 mW/m$^2$ (Kjarsgaard and Peterson, 1992), combined with evidence from heavy mineral concentrates (scarce or absent G10 and eclogitic garnets, high-Mg, Cr chromites) is consistent with these kimberlites having a low diamond tenor.

## SUMMARY

At present, use of the Ni thermometer as a valid diamond exploration tool appears limited. Without knowledge of the regional paleogeotherm, Ni temperature estimates cannot be converted to the depth estimates required to infer whether the garnets equilibrated in the graphite or diamond stability field. In addition, this technique only assesses a host rock's potential in terms of containing diamonds of garnet-bearing peridotitic paragenesis. Furthermore, the calibration of the Ni thermometer is suspect. There appears to be good evidence that Ni in garnet is strongly temperature dependant (Griffin et al., 1989a, c; this study). However, results from this study illustrate that the Ni thermometer overestimates temperatures by up to 238°C as compared to $T_{FB86}$ (which was used initially as a reference calibration standard), but produces results to ± 81°C compared to $T_{BKN}$. The Ni temperature overestimates as compared to the FB86 thermometer must be related to the calibration since the Ni contents of both garnet and olivine from the Somerset Island lherzolites are within the range of those used in the original calibration.

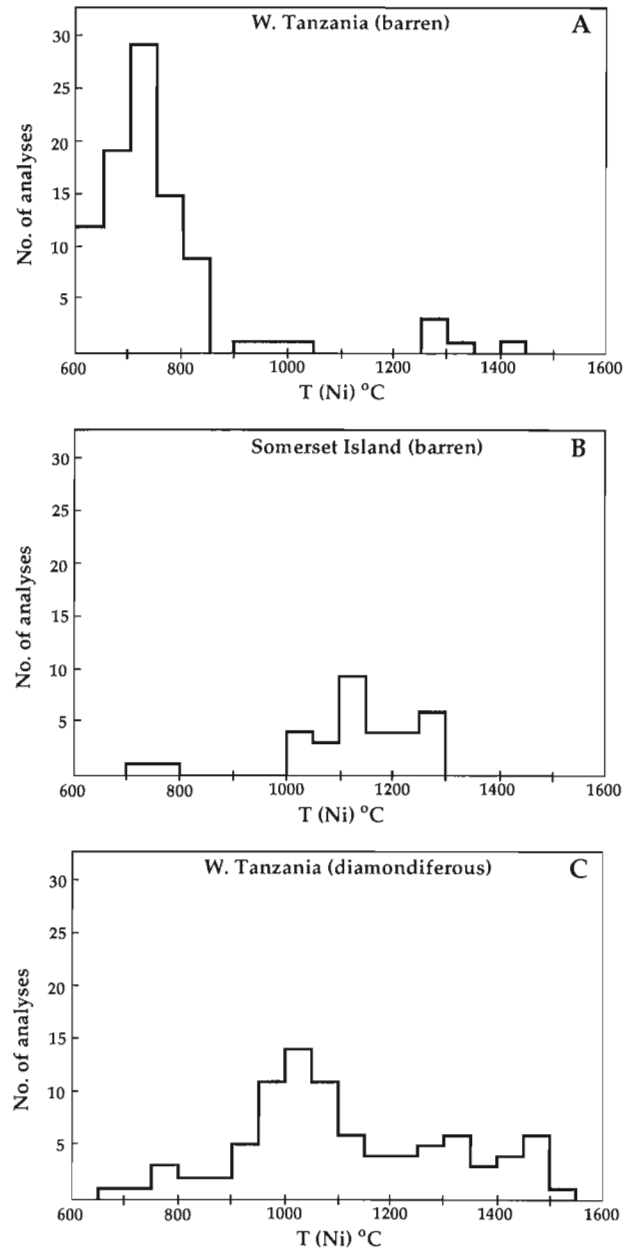


**Figure 3.** Plots of frequency versus Ni temperature for garnets from kimberlites from Somerset Island (this study) and W. Tanzania (data from Griffin et al., 1991). See text for discussion.

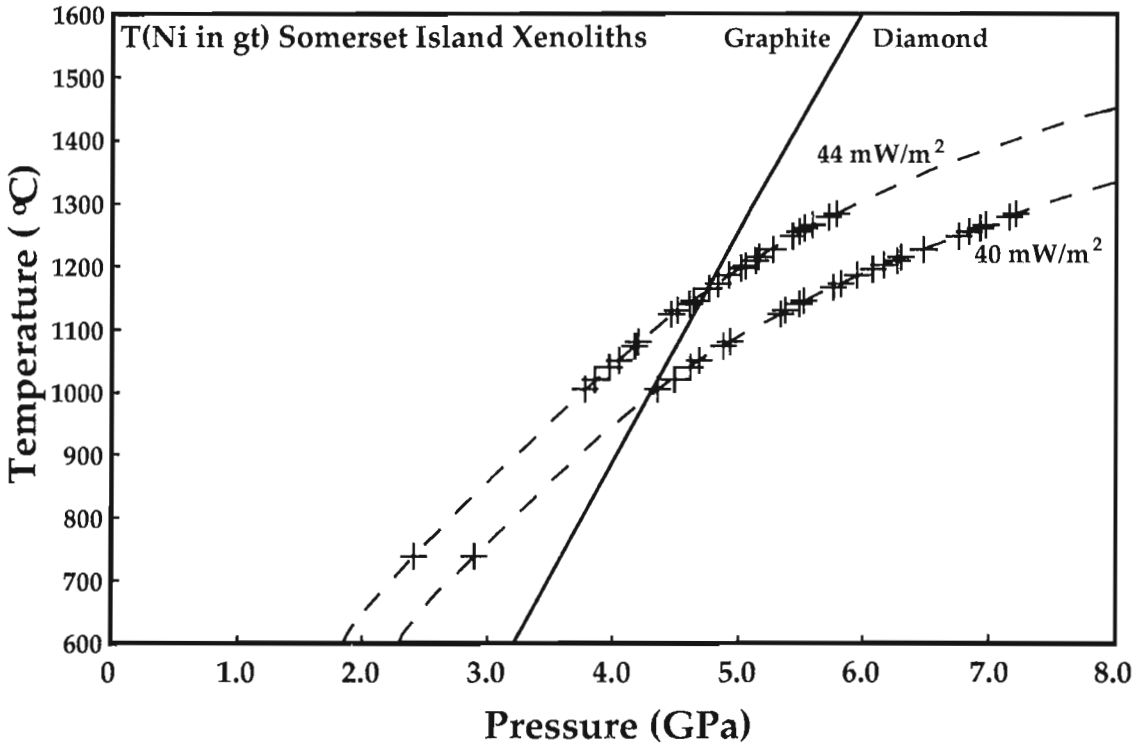


**Figure 4.** Intersection of Ni temperatures from Somerset Island garnets with a theoretical 40mW/m$^2$ geotherm (Pollack and Chapman, 1977; Finnerty and Boyd, 1987) versus the measured 44mW/m$^2$ paleogeotherm (Kjarsgaard and Peterson, 1992) . See text for discussion. Geotherms and graphite/diamond transition as per Figure 1 and Kjarsgaard and Peterson (1992).

Brey and Köhler (1990) have noted that in the temperature range 900 - 1150°C (their Fig. 3c), the FB86 thermometer underestimates temperatures by 90 - 300°C in comparison to the BKN thermometer. Interestingly, if this temperature underestimate is added to the FB86 thermometer, it would essentially eliminate the temperature differences shown in Figures 2C and 2D. This suggests it may prove worthwhile to recalibrate the Ni thermometer utilizing the BKN thermometer as the reference standard. Useful depth estimates could then be obtained from single garnet grains if the paleogeotherm has been established by other methods.

## ACKNOWLEDGMENTS

Polar Continental Shelf Project is thanked for helicopter and fixed wing support and accomadation at Resolute Bay during sampling of the Somerset Island kimberlites. Bill Teesdale, University of Guelph provided expert assistance with the proton microprobe analyses. Contribution to the Canada-NWT Mineral Initiative 1991-1996 and Canada-Saskatchewan Mineral Development Agreement 1990-1995. Comments from A.N. LeCheminant and T. Peterson as well as critical review by R. Berman greatly improved the manuscript.

## REFERENCES

**Brey, G.P.**
1991: Fictive conductive geotherms beneath the Kaapvaal Craton; Extended Abstracts, Fifth International Kimberlite Conference, Araxá, Brazil. CPRM Special Publication 2/91, Brasilia, p. 23-25.

**Brey, G.P. and Köhler, T.**
1990: Geothermobarometry in Four-phase Lherzolites II. New thermobarometers, and Practical Assessment of Existing Thermobarometers; Journal of Petrology, v. 31, p. 1353-1378.

**Brey, G.P., Köhler, T., and Nickel, K.G.**
1990: Geothermobarometry in Four-phase Lherzolites I. Experimental results from 10 to 60 kb; Journal of Petrology, v. 31, p. 1313-1352.

**Campbell, J.L., Maxwell, J.A., Teesdale, W.J., Wang, J.-X. and Cabri, L.J.**
1990: MICRO-PIXIE as a complement to electron probe microanalysis in mineralogy; Nuclear Instruments and Methods in Physics Research, B44, p. 347-356.

**Carswell, D.A.**
1991: The garnet-orthopyroxene Al barometer: problematic application to natural garnet lherzolite assemblages; Mineralogical Magazine, v. 55, p. 19-31.

**Carswell, D.A. and Gibb, F.G.F.**
1987: Evaluation of mineral thermometers and barometers applicable to garnet lherzolite assemblages; Contributions to Mineralogy and Petrology, v. 95, p. 473-487.

**Finnerty, A.A. and Boyd, F.R.**
1987: Thermobarometry for garnet peridotites: basis for the determination of thermal and compositional structure of the upper mantle; in Mantle Xenoliths, P.H. Nixon (ed.); J. Wiley and Sons, Toronto, p. 381-402.

**Fipke, C.**
1990: The development of advanced technology to distinguish between diamondiferous and barren diatremes; Geological Survey of Canada, Open File 2124, 603p.

**Griffin, W.L.**
1990: The nickel thermometer: a new tool for diamond exploration; Exploration Research News, v. 4, p. 3-4.

**Griffin, W.L., Cousens, D.R., Ryan, G.C., Sie, S.H., and Suter, G.F.**
1989a: Ni in chrome pyrope garnets: A new geothermometer; Contributions to Mineralogy and Petrology, v. 103, p. 199-202.

**Griffin, W.L., Gurney, J.J., Ryan, G.C., Cousens, D.R., Sie, S.H., and Suter, G.F.**
1989b: Trapping temperatures and and trace elements in P-type garnets in diamonds: A proton microprobe study (extended abstract); 28th International Geological Congress, Workshop on Diamonds, p. 23-25.

**Griffin, W.L., Smith, D., Boyd, .R., Cousens, D.R., Ryan, G.C., Sie, S.H., and Suter, G.F.**
1989c: Trace-element zoning in garnets from sheared mantle xenoliths; Geochimica et Cosmochimica Acta, v. 53, p. 561-567.

**Griffin, W.L., Ryan, G.C., O'Reilly, S.Y., Nixon, P.H. and Win, T.T.**
1991: Trace elements in garnets from Tanzanian kimberlites: Relation to diamond content and tectonic setting (extended abstracts); Fifth International Kimberlite Conference, Araxá, Brazil. CPRM Special Publication 2/91, Brasilia, p. 145-147.

**Gurney, J.J.**
1989: Diamonds; in Kimberlites and related rocks, Volume 2, Their Mantle/Crust Setting, Diamonds and Diamond Exploration, J. Ross (ed.); Proceedings of the Fourth International Kimberlite Conference, Perth, 1986, Geological Society of Australia Special Publication 14, Blackwell Scientific Publications, Oxford, p. 935-965.

**Gurney, J.J., Moore, R.O., Otter, M.L., Kirkley, M.B., Hops, J.J., and McCandless, T.E.**
1991: Southern African Kimberlites and their Xenoliths; in Magmatism in Extensional Structural Settings - The Phanerozoic African Plate, A.B. Kampunzu and R.T. Lubala (ed.); Springer, Berlin, p. 495-536.

**Jago, B.C. and Mitchell, R.H.**
1989: A new garnet classification technique: divisive cluster analysis applied to garnet populations from Somerset Island; in Kimberlites and related rocks, Volume 1, Their Composition, Occurrence, Origin and Emplacement, J. Ross (ed.); Proceedings of the Fourth International Kimberlite Conference, Perth, 1986, Geological Society of Australia Special Publication 14, Blackwell Scientific Publications, Oxford, p. 298-310.

**Kennedy, C.S. and Kennedy, G.C.**
1976: The equilibrium boundary between graphite and diamond; Journal of Geophysical Research, v. 81, p. 2467-2470.

**Kjarsgaard, B.A. and Peterson, T.D.**
1992: Kimberlite-derived ultramafic xenoliths from the diamond stability field: A new Cretaceous geotherm for Somerset Island, Northwest Territories; in Current Research, Part B; Geological Survey of Canada, Paper 92-1B, p. 1-6.

**Maxwell, J.A., Campbell, J.L. and Teesdale, W.J.**
1989: The Guelph PIXIE software package; Nuclear Instruments and Methods in Physics Research, B43, p. 218-230.

**Mitchell, R.H.**
1986: Kimberlites, Plenum Press, New York, 442 p.

**O'Neill, H. St. C.**
1980: An experimental study of Fe-Mg partitioning between garnet and olivine and its calibration as a geothermometer: corrections; Contributions to Mineralogy and Petrology, v. 72, p. 337.

**O'Neill, H. St. C. and Wood, B.J.**
1979: An experimental study of Fe-Mg partitioning between garnet and olivine and its calibration as a geothermometer; Contributions to Mineralogy and Petrology, v. 70, p. 59-70.

**Pollack, H. N. and Chapman, D. S.**
1977: On the regional variation of heat flow, geotherms and lithospheric thickness; Tectonophysics, v. 38, p. 279 - 296.

Geological Survey of Canada Project 680071

# Clay-size minerals and near-surface stratigraphy on the northeastern Grand Banks of Newfoundland

**P. Stoffyn-Egli[1], G.V. Sonnichsen, and A. Zawadski**
**Atlantic Geoscience Centre, Dartmouth**

*Stoffyn-Egli, P., Sonnichsen, G.V., and Zawadski, A., 1992: Clay-size minerals and near-surface stratigraphy on the northeastern Grand Banks of Newfoundland; in Current Research, Part E; Geological Survey of Canada, Paper 92-1E, p. 323-331.*

***Abstract***

*The mineralogy of the less than 2 μm size fraction of 49 samples was determined in three boreholes from the northeastern Grand Banks by X-ray diffraction. Semi-quantitative analysis using talc as an internal standard gives more accurate trends versus depth than traditional methods. A generally consistent clay mineral assemblage consisting of smectite, mica, kaolinite and minor amounts of chlorite was present throughout the 110 m of sediment sampled. Horizons rich in iron hydroxides were identified. Two horizons correlate with angular seismostratigraphic unconformities at top and bottom of a proposed deltaic sequence.*

***Résumé***

*On a déterminé, au moyen de la diffraction des rayons x, la minéralogie de la fraction inférieure à 2 μm de 49 échantillons dans trois sondages forés au nord-est des Grands Bancs. L'analyse semi-quantitative des échantillons par l'addition d'un minéral standard (talc) donne des variations de concentration en fonction de la profondeur plus exactes que celles mesurées à l'aide des méthodes traditionnelles. Un assemblage d'argiles raisonnablement constant composé de smectite, mica, kaolinite et une petite quantité de chlorite se retrouve dans la totalité des 110 m de sédiments échantillonnés. Des horizons riches en hydroxides de fer ont étés identifiés. Deux horizons peuvent êtres corrélés à des discordances angulaires sismostratigraphiques relevées aux limites supérieure et inférieure d'une séquence deltaïque proposée.*

[1] MICROCHEM, Geochemistry Consultants, Oyster Ponds, Nova Scotia B0J 1W0

## INTRODUCTION

Development of the oil fields on the northeastern Grand Banks (Fig. 1) requires an understanding of both the regional geology and the site specific physical properties of near-surface sediments to ensure safe and economic design of seabed facilities. The upper 100 m of sediment have been studied from over 4000 km of high resolution single channel seismic reflection data collected across the northeastern Grand Banks (Fader and King, 1981; Fader and Miller, 1986; Parrott et al., 1988; Lewis et al., 1987). Borehole investigations at sites of proposed oil production have provided sediment samples and in situ measurements of physical properties. Between 1979 and 1983, 7 boreholes, to a maximum depth of 130 m, were completed by Mobil Oil Canada Ltd. and Petro Canada on the northeastern Grand Banks (Barrie et al., unpublished report, 1983, Collins and Christian, 1984). Clay-sized mineral analyses (Segall et al., 1985; Segall, 1986; Segall et al., 1987) were conducted on a limited number of samples from the boreholes. A higher kaolinite content in 5 samples directly below a regional unconformity which underlies the reworked Quaternary sediments were interpreted by Segall and coworkers as evidence for subaerial weathering.

In 1988, as part of a joint program with Mobil Oil Canada Ltd., the Atlantic Geoscience Centre (AGC) collected a near-continuous 88 m borehole (BH6), approximately 14 km from the Hibernia discovery site (Moran and Mosher, AGC Cruise Report, 88400, 1988; Fig. 1). Additional samples were also provided to the Atlantic Geoscience Centre from a 120 m borehole (G1A; Moran et al., 1988; Mosher, unpublished report, 1990) and an adjacent (<50 m distant) 25 m borehole (S1A) near the Hibernia area. The samples provide an opportunity to correlate the regional seismostratigraphy with the composition of the near-surface sediments and to identify processes which may have altered them.

This paper describes the seismostratigraphy of the upper 100 m of the northeastern Grand Banks and presents preliminary mineralogical analyses of the clay fraction from selected borehole samples. Mineralogical assemblages identified in the boreholes are related to possible sediment sources. Variations in mineral concentrations versus depth are identified and correlated with regional seismostratigraphic units.

## REGIONAL SETTING

The continental shelf off Newfoundland consists of several broad shallow bank tops, separated by transverse saddles. Grand Bank is the largest of the banks with an area of more than 100 000 km$^2$. The surface slopes gently from shallow water (<5 m) near the centre of the bank to about 100 m along the perimeter (Fig. 1). Avalon Channel, locally up to 200 m deep, separates Grand Bank from the island of Newfoundland.

The surface of Grand Bank is covered with a veneer of sand and gravel, typically less than 1 m thick. The surficial sediments are separated from the underlying strata by a regional angular unconformity which is interpreted to mark a marine transgression related to the last glacial sea level minimum. In the area addressed by this paper, the sands and gravels directly overlie marine silts and clays of the Banquereau Formation (Fader and King, 1981). The Banquereau Formation and underlying Cretaceous bedrock, which outcrops to the west, are part of a seaward-dipping wedge of shelf-progradational sediments deposited as the adjacent oceans deepened and widened. The Banquereau Formation, although usually considered Tertiary, may also contain Quaternary sediments (C.F.M. Lewis, pers. comm., 1992). Nearer to Newfoundland, Cambrian to Devonian shelf-deposited siltstone outcrop on the seafloor (King et al., 1986), whereas late Proterozoic sedimentary and volcanic rocks are found on the Avalon Peninsula (Fig. 1).

## NEAR-SURFACE SEISMOSTRATIGRAPHY AND LITHOLOGY

Five regional seismic units are identified on shallow reflection profiles from the northeastern Grand Banks (C.F.M. Lewis, pers. comm., 1992; Fig. 2). They are separated from each other by angular unconformities.

### *Unit 1 – Surficial unit*

This is a thin unit of sand and gravel with bedforms found in water depths less than 110 m. It overlies a regional unconformity interpreted to represent a late

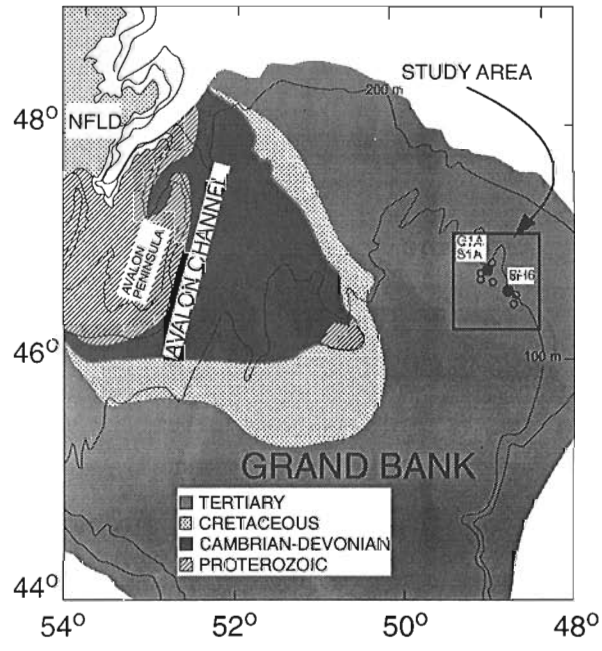


**Figure 1.** Location map showing the regional surficial bedrock on the Grand Banks and the location of boreholes described in this report. The open circles denote boreholes analyzed by Segall et al. (1986,1987). Bedrock geology modified after Fader et al. (1989).

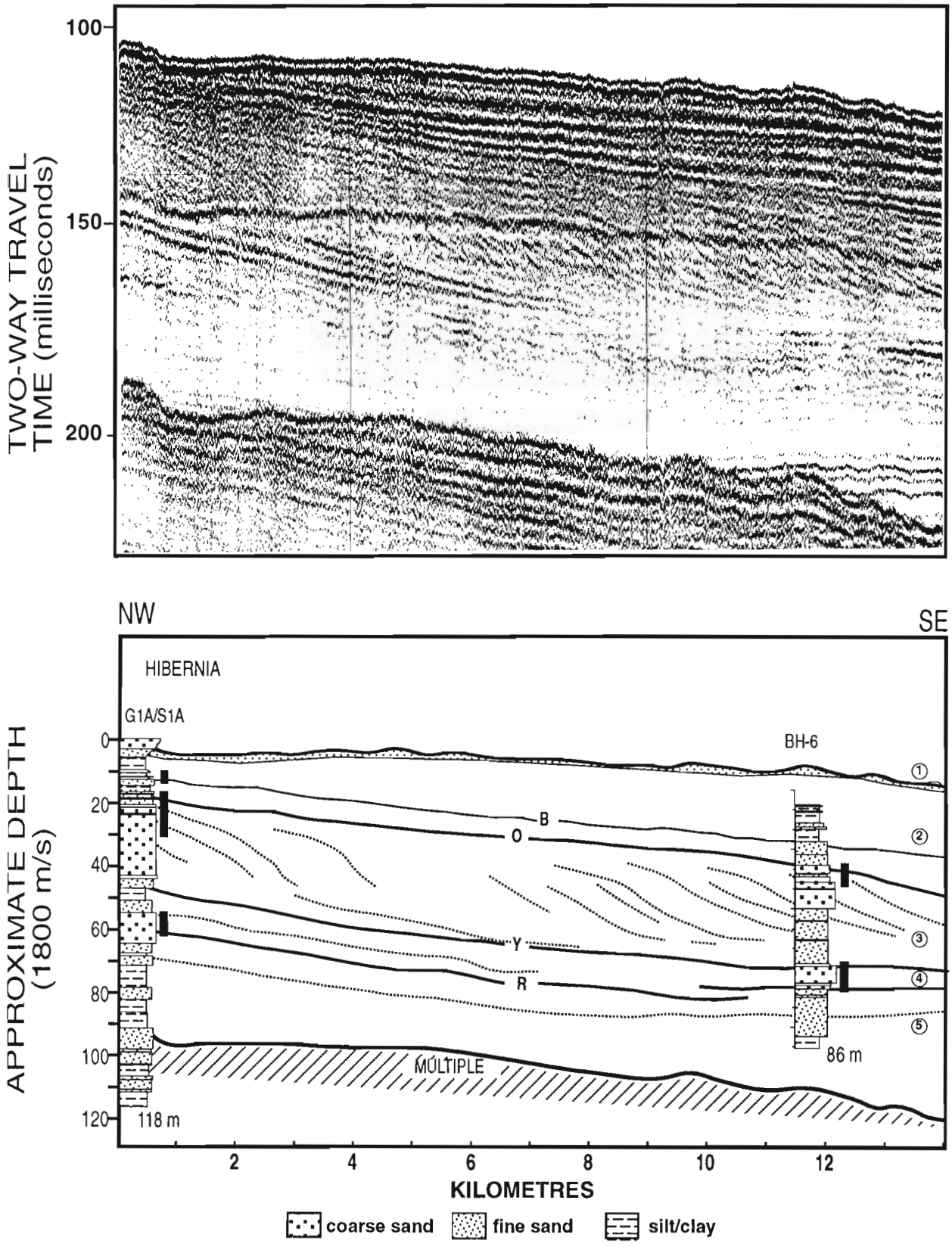


**Figure 2.** A 10 cubic inch airgun profile and accompanying line interpretation between G1A and BH6. The lithological logs are adapted from Mosher (unpublished report, 1990). The thickness of the Grand Banks sand and gravel unit is approximate. Numbers signify the unit numbers assigned in the text. The solid bars depict zones of iron-stained sand particles which coincide with the goethite peaks identified by clay-sized mineral analysis.

Pleistocene-Holocene low sea level stand and a subsequent marine transgression which reworked and redeposited the sediment cover (Fader and King, 1981).

### *Unit 2 -- Upper parallel reflection sequence*

Medium to high amplitude continuous parallel reflections, which generally dip east-northeastward at less than 0.5° are the predominant reflection pattern on the northeastern Grand Banks. Borehole samples (Barrie et al., unpublished report, 1983; Segall, 1986; Mosher, unpublished report, 1990) show that sediments consist of semi-consolidated, bedded, silt and clay (40-45 % each). The upper parallel reflection sequence is interpreted to represent depositional aggradation and progradation in a marine shelf environment on the basis of the conformable, gently dipping nature and of a seaward increase in dip angle and sequence thickness (C.F.M. Lewis, pers. comm., 1992).

### *Unit 3 -- Zone of clinoform reflections*

This unit is identified as a wedge of strata beneath unit 1 with internal clinoform (s-shaped) reflections. It thickens eastward to a maximum of approximately 48 m and can be traced north and south for more than 100 km. Angular unconformities (reflections "O" and "Y" in Fig. 2) appear to bound this unit of clinoform reflections. Boreholes through the clinoform reflection unit document a near continuous sequence of fine, medium and coarse sands (70-90%), small percentages of gravel, and equal proportions of silt and clay (5-10%; Mosher, unpublished report, 1990). As the clinoform sequence thickens eastward, it contains a greater proportion of silt and clay (Barrie et al., unpublished report, 1983). Based on seismic character and sedimentology, the unit has been described as a progradational delta related to a former sea level low-stand (C.F.M. Lewis, pers. comm., 1992; Mosher, unpublished report, 1990).

### *Unit 4 -- Diffuse unit*

In places, a diffuse, chaotic zone up to 12 m thick, can be seen beneath the "Y" reflection unconformity. The lower boundary of the unit is an unconformity with an often irregular surface (reflection "R" in Fig. 2). Clinoform reflections are occasionally evident but are very poorly organized. The grain size in the diffuse unit is similar to the overlying clinoform sequence being predominantly sand with a coarse interval between 55 and 70 m. It is tentatively interpreted to be a remnant of an earlier deltaic deposit eroded prior to deposition of the overlying progradational unit.

### *Unit 5 -- Lower parallel reflection sequence*

Beneath the diffuse zone, there is a return to the high amplitude, continuous parallel reflections described in unit 2. Borehole samples show that the sediments are similar in grain size to the overlying silts and clays of unit 2. Seaward of the deltaic units (3 and 4), unit 2 directly overlies unit 5 and they are seismically very similar. Unit 5 is considered distinct from unit 2 because it is possible that they are separated by a disconformity which may represent a significant time gap.

## CLAY-SIZED MINERAL ANALYSIS

Forty-nine samples were analyzed for clay mineral concentrations using X-ray diffraction: 25 from BH6, 12 from G1A and 12 from S1A. Most samples were evenly spaced throughout the boreholes to ensure relatively unbiased sampling. The remainder were selected on the basis of grain size distribution and/or pebble lithology. An orienting internal standard (talc) was used for semi-quantitative analysis of the less than 2μm particle size fraction of the samples. The methods used in this study are based on Moore and Reynolds (1989) with significant modifications as described below.

### *Sample preparation*

Size fractionation was done by centrifuging the sample suspended in a 0.5% solution of sodium metaphosphate in distilled water. Stokes' law was used to calculate the centrifuge time and speed so that only particles smaller than 2μm remained in suspension. The suspension was then further concentrated in the centrifuge.

There was no chemical treatment of the samples to remove specific phases (e.g. organic matter, iron oxides, carbonates), to avoid possible changes in the clay minerals. Moreover, detection of carbonate phases or iron oxides is of interest in this study. Differences in matrix effects between samples, for example owing to variable iron oxides content, are compensated for by the use of an internal standard.

### *Sample mounting*

#### Qualitative mount

Semi-quantitative analysis requires that the particle concentration of each centrifuged sample suspension be known. One millilitre of suspension was air dried on a pre-weighed glass slide, then reweighed to calculate the concentration. This oriented sample mount could then be used for qualitative analysis without interference from the internal standard. This method, which requires a minimum amount of sample, was used because of the low clay content of many samples.

#### Semi-quantitative mount

Talc (Aldrich Chemical Company) was used as the internal standard. It was added to the sample as a suspension of less than 2μm particles of known concentration. The sample was then mounted by the filtration method. Quick filtration of the sample avoids segregation of minerals owing to differential settling, which happens in the case of the air dried mount. The samples were very slow to filter, probably due to the high smectite content. To speed up filtration, flocculation was induced by adding a solution of magnesium chloride to the sample plus talc (final Mg concentration: 0.1N). Although

deflocculation is recommended before filtration (Moore and Reynolds, 1989), flocculation did not seem to measurably affect the diffractograms. Moreover, saturating smectite with Mg has the advantage of producing sharper peaks at a consistent 2θ value.

The filter (0.4μm pore size Nuclepore membrane, 45 mm in diameter) was rinsed with a few millilitres of deionized water, laid gently sample face down on a glass slide (2.5 cm square) and peeled off after two minutes. The amount of sample plus talc filtered was calculated to give approximately 5 mg/cm$^2$ of dry sample on the slide and a concentration of 5.6% talc. This was the minimum amount of sample required to assume infinite thickness with the geometry of the diffractometer used (Moore and Reynolds, 1989).

### *Sample analysis*

The samples were analyzed with an automated Siemens D500 X-ray diffraction system using a copper lamp. After data acquisition, a peak finding routine based on the second derivative method was used to calculate peak position, intensity and area after background and $K\alpha_2$ corrections.

#### Qualitative analysis

Because many samples were similar in mineral composition, only selected qualitative mounts were run. Peak identifications were aided by computer search of the Joint Committee on Powder Diffraction Standard mineral file. The minerals detected in all samples were expandable clay minerals (hereafter called smectite), mica (including illite), kaolinite, chlorite and quartz. Some samples also contained goethite and/or gibbsite. In this preliminary work, no attempt was made to identify clay mineral types beyond these general categories.

#### Semi-quantitative analysis

Three runs were done for semi-quantitative analysis:

1. normal run: 2-35° 2θ;
2. short run: 24-26° 2θ; higher resolution
3. glycolated run: 2-14° 2θ after glycolation overnight under partial vacuum in a chamber containing ethylene glycol.

In most cases a peak deconvolution program was used to calculate the peak area representative of each mineral; one of three peak shapes (Gaussian, Cauchy or pseudo-Voight) was used depending on which best fit the data.

- Smectite: the peak was measured on the glycolated run at d=1.69 nm. This peak was usually overlapping the 1.42 nm peak of chlorite and deconvolution by Gaussian approximation was used to calculate the smectite peak area.
- Mica and talc: the peaks of these two minerals (d=1.01 nm and 0.94 nm respectively) also overlapped and were deconvoluted using a Cauchy approximation. The glycolated run was used because the smectite peak was often large enough to interfere with these peaks in the normal run.
- Kaolinite and chlorite: the peak at d=0.71 nm in the normal run was used to quantify these minerals. The proportion assigned to either one was calculated by deconvoluting the peaks at d=0.354 and 0.357 nm, respectively, using a pseudo-Voight approximation on the short run.
- Quartz and goethite: the quartz peak at d=0.426 nm in the normal run was used to measure quartz. When goethite was present in sufficient amounts, deconvolution using a Gaussian approximation was necessary because the goethite peak (d=0.418 nm) overlaps the quartz peak.

The results are expressed in ratio of peak area of mineral over peak area of talc. For each mineral, these ratios are directly comparable between samples.

**Table 1.** Peak intensity ratios of various standard minerals using talc as the internal standard. See text for calculation. Weighing factors are the inverse of peak intensity ratio. The published factors are the most commonly used (Segall et al., 1987 and references therein).

| | PIR | PIR selected | Weighing factors | Published factors |
|---|---|---|---|---|
| MONTMORILLONITE #22 | 0.72 | 0.75 | 1.3 | 1.0 |
| SMECTITE | 1.46 | | | |
| MONTMORILLONITE #25 | 1.38 | | | |
| MUSCOVITE | 0.34 | 0.33 | 3.0 | 4.0 |
| BIOTITE | 0.70 | | | |
| KAOLINITE A | 0.49 | 0.50 | 2.0 | 2.0 |
| KAOLINITE B | 0.99 | | | |
| CLINICHLORE | 0.48 | 0.50 | 2.0 | 2.0 |
| CHLORITE | 0.30 | | | |
| QUARTZ | 0.03 | 0.03 | | |

### *Calculation of concentrations*

In this study, at least two standards of each clay type and quartz (from the Ward Natural Science Establishment) were ground, then prepared and analyzed using the same methods. The only difference is that the talc concentration used in this case was approximately 50 per cent.

A peak intensity ratio (PIR) for each standard was calculated as follow:

PIR = (min. peak area/talc peak area) x(talc conc./min. conc.)

The results are listed in Table 1 and show that the peak intensity ratio for a given clay mineral can vary by a factor of two. This is even true for kaolinite, a mineral with well defined chemical composition and crystallinity. Mixtures of equal amounts of standard smectite, biotite, kaolinite and chlorite and varying amounts of talc were also analyzed to evaluate matrix effects on the value of the peak intensity ratio.

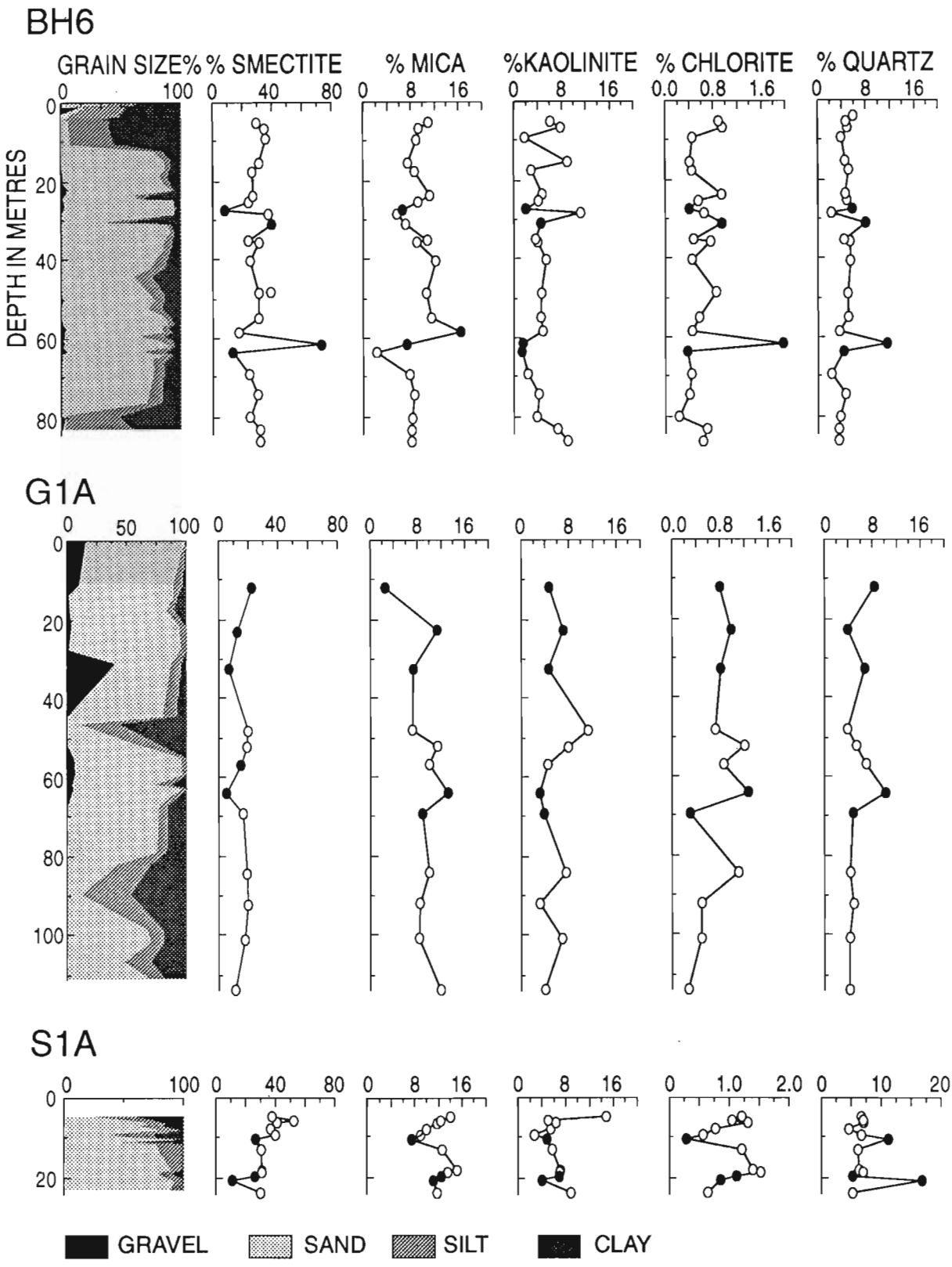


**Figure 3.** Plots of clay-sized mineral concentration versus depth are shown alongside grain size logs adapted from Mosher (unpublished report, 1990). The solid dots denote samples which contain goethite in the clay-sized fraction.

The variations were much smaller than the variations between equivalent clay minerals shown in Table 1. The peak intensity ratio used to calculate concentrations was chosen as follows:

- smectite: 0.75 because the montmorillonite #22 had approximately the same peak width at half maximum as the smectite in the samples;
- Mica: 0.33 was chosen because muscovite is more similar in chemical composition and crystal structure to illite than biotite. The available illite #35 standard was too poorly crystallized and contaminated to be used here.
- chlorite and kaolinite: 0.5 to keep consistent with other studies where factors are the same for both minerals. This is not necessarily the case but aids in comparing our data set with published values.
- Quartz: 0.03. Because quartz is not an orienting mineral, talc is not an appropriate internal standard for this mineral. However, quartz being the only non-clay mineral and present in minor amounts in all samples, it did not seem warranted to do a different mount and use a different internal standard for quartz only.

Goethite and gibbsite, found in some samples were not quantified because of lack of a suitable standard. Abundances are discussed qualitatively on the basis of peak area.

Mineral concentrations were calculated as follow:

Cmin. = (min. peak area/talc peak area) x (talc conc./PIR)

Semi-quantitative results are plotted versus depth in Figure 3.

### *Precision*

Two samples were mounted four times and analyzed using the same methods to estimate reproducibility. For the three major minerals (smectite, mica and kaolinite) the precision is better than ±8% (2σ/mean) whereas for the minor components (chlorite and quartz) precision is ±25%.

## RESULTS

On average, the mineral concentrations measured in each sample amount to only 50% of the less than 2μm fraction. Such high residual values have been reported by other investigators using internal standard methods (Heath and Pisias, 1979; Segall et al., 1987). One reason for the residual value may be that the internal standards do not accurately represent minerals in the sample. The residual value is also partly accounted for by the presence of goethite and gibbsite which were not quantified. Another contribution is the amorphous phases not detected by X-ray diffraction but almost always present in significant amounts in marine sediments.

Traditionally, mineral concentrations have been calculated by multiplying peak areas by weighing factors and normalizing the results to 100% (McManus, 1991, and references therein; Segall et al., 1987). Weighing factors depend on instrumental conditions, sample composition and the standard minerals used to determine them. Indiscriminate use of published factors is therefore questionable. By contrast, the use of an internal standard helps compensate for different instrumental parameters and matrix effects. Table 1 shows the inverse of the peak intensity ratio used, which is more comparable to the weighing factors commonly used in the literature.

Normalization to 100% should be avoided because an error in the measurement of one mineral or a considerable change in its concentration (or that of amorphous material) will affect the values for the other minerals and give a false impression of covariance. This will change trends versus depth and, in some cases, mineral ratios. Even if absolute concentrations calculated on the basis of an internal standard, as in this study, are not very accurate (depending mostly on standards chosen), down core trends are more accurate than in the traditional method and residual values provide useful information. Moreover, ratios of mineral peak/talc peak (provided talc concentration is kept constant) are directly comparable between samples, thus relative changes such as trends versus depth and differences between boreholes can be detected without the need for standard minerals.

In the samples analyzed, smectite is the most abundant mineral (mean=27%), followed by mica (mean=10%), kaolinite (mean=5.5%) and quartz (mean=5.9%). These concentrations are in general agreement with the results of Segall et al. (1987), especially when the different methods in calculating concentrations are taken into account.

Much less chlorite (usually less than 1%) was detected in comparison to the results of Segall et al. (1987). The reasons for this discrepancy are not clear; both studies used the same kaolinite/chlorite peak doublet and equal weighting factors. It seems unlikely that such a large difference would occur over the limited study area. Feldspars, amphiboles and pyroxenes, found in minor quantities by Segall et al. (1987) were not detected in the present study. Differences in size fractionation methods and in speed of filtration during sample preparation could cause this discrepancy.

Calcite and dolomite were not present in any of the three boreholes but small amounts of gibbsite were present in many samples and its abundance correlates with that of kaolinite, especially in BH6.

Several samples were characterized by the presence of goethite. Because detection of iron minerals is very poor with copper X-radiation, a measurable goethite peak suggests significant amounts of this mineral. The iron-rich horizons were present in all three boreholes: BH6 at 27 and 61 m; G1A at 12, 23, 32 m and 60 m, and S1A at 10 and 21 m (Fig. 3).

With the exception of one sample at 61.6 m depth in BH6, which contains over 70% smectite and is the only one to have more chlorite than kaolinite, mineral concentrations do not show drastic changes with depth. G1A contains on average half the amount of smectite compared to the other boreholes. The difference in sampling intervals may explain this discrepancy between G1A and the adjacent S1A.

## DISCUSSION

Initial studies of the mineralogy of marine sediments offshore Newfoundland were conducted primarily on surficial samples and shallow core samples from the reworked surficial sediments (seismostratigraphic unit 1). Piper and Slatt (1977) found the presence of montmorillonite and kaolinite (<2μm size fraction) in bank sediments and suggested the source was underlying coastal plain sediments; on northeastern Grand Bank the absence of kaolinite implied a Tertiary rather than a more westerly Cretaceous source for the surficial sediments. They also identified a diluted chlorite signal on the Grand Bank derived from igneous and metamorphosed bedrock eroded from nearshore and mainland Newfoundland. Our samples from the subsurface have a mineralogy consistent with a Tertiary source (smectite and illite) with an admixture of Cretaceous formation (kaolinite). No reference could be found to the possible source of gibbsite which seems to be associated with kaolinite in our samples. The scarcity of chlorite and absence of feldspars, amphiboles and pyroxenes in the less than 2μm fraction indicate the paucity of land-derived sediment in this fraction.

The most conspicuous feature of the three boreholes analyzed is the presence of discrete depth intervals with abundant goethite. These iron-rich horizons do not exhibit consistent differences in clay mineral concentration. Based on the samples analyzed, the iron-rich horizons occur where the gravel content is maximum and/or where the sand-sized fraction represents more than 90% of the sample (Mosher, unpublished report, 1990). Quartz grains within the horizons exhibit pronounced iron oxide staining (Fig. 2). Chemical analysis of samples from BH6 confirmed that at 27 m there is a high concentration of oxidized iron but low concentration of oxidized manganese. This suggests that the sediment was at one time exposed to oxidizing conditions but has subsequently undergone some reduction (D. E. Buckley, pers. comm., 1992). A presently reducing environment is supported by the dark colour of the sediment and the presence of pyrite (Mosher, unpublished report, 1990).

None of the three boreholes show evidence of the increased kaolinite and decreased smectite abundance detected in samples of Segall et al. (1987) and interpreted to indicate a weathered zone formed in an acidic leaching environment. In fact, it is more likely that the clay mineral assemblages reflect detrital deposition rather than in situ mineralogical changes (Chamley, 1989). However, the iron-rich horizons could have formed in well oxygenated conditions, such as a near shore high energy environment which is consistent with the coarse grain size.

Based on an estimated seismic velocity of 1800 m/s, a close correlation can be seen between the regional seismostratigraphy and the iron-rich zones (Fig. 2). In all three boreholes, an iron-rich zone occurs at the unconformity surface ("O") at the top of unit 3. BH6 and G1A both have iron enrichment in a coarse sand body within unit 4. It has been suggested that the clinoform reflection sequence and the diffuse unit were deposited in a deltaic environment related to former lower sea level(s) (C.F.M. Lewis, pers. comm., 1992). The presence of iron-rich zones associated with erosional unconformities would appear to support such an hypothesis. S1A and G1A indicate an additional iron-rich zone which ties very well to a strong reflection (labelled "B" in Figure 2) immediately above unit 2. The horizon deserves further examination as it implies an event not detected at BH6, 14 km away; additional samples from BH6 may confirm the presence or absence of the horizon. The higher concentration of smectite in BH6 as compared to G1A may reflect the more distal position of BH6 within the delta units.

## SUMMARY AND CONCLUSIONS

To obtain accurate down core trends of mineral concentration it is essential to use an internal standard method. This eliminates the need to normalize results to 100% and does not greatly complicate the analysis.

Accurate concentrations may not be achievable due to difficulty in choosing appropriate standards. However, the proportion of sample not accounted for by the total of the minerals measured (residual value) is a useful indicator of accuracy, change in mineral type and variation in amorphous material content.

The clay-sized mineral analyses allowed correlation among boreholes and provided strong supporting evidence to the regional seismostratigraphy.

Iron enriched zones occur in sand units at or near the top of progradational units identified on seismic reflection profiles. The zones coincide with unconformities and indicate changes in depositional conditions, such as a near-shore high energy environment. However, short spells of subaerial exposure cannot be ruled out as the resulting mineralogical changes may have been diluted or erased during subsequent reworking or erosion of sediments at these horizons.

There is no major change in the clay-sized mineral assemblage to suggest that the various seismostratigraphic units recognized in the area have different sediment sources. They appear to have been locally derived from eroded Tertiary and Cretaceous coastal plain sediments.

## ACKNOWLEDGMENTS

Funding for this research was provided by the Panel for Energy Research and Development (PERD). The authors wish to thank D.J.W. Piper, D.R. Parrott, and K. Moran for helpful comments and suggestions. D. E. Buckley provided the chemical analyses of samples from BH6 and many useful suggestions. We wish to thank Mobil Oil Canada Ltd. for the samples provided from G1A and Brian Rogers of Gulf Canada for providing samples from S1A.

# REFERENCES


**Chamley, H.**
1989: Clay Sedimentology. Springer-Verlag, Berlin, 623 p.

**Collins, W.T. and Christian, D.**
1984: Petro-Canada Borehole Investigation. Contract report by C-CORE, Memorial University of Newfoundland. Geological Survey of Canada, Open File, 26 p.

**Fader, G.B. and King, L.H.**
1981: A reconnaissance survey of the surficial geology of the Grand Banks of Newfoundland; in Current Research, Part A; Geological Survey of Canada, Paper 81-1A, p. 45-56.

**Fader, G.B.J. and Miller, R.O.**
1986: A reconnaissance of the surficial and shallow bedrock geology of the southeastern Grand Banks of Newfoundland; in Current Research, Part B; Geological Survey of Canada, Paper 86-1B, p. 591-604.

**Fader, G.B., Cameron, G.D.M., and Best, M.A.**
1989: Geology of the Continental Margin of Eastern Canada; Geological Survey of Canada; Map 1705A, scale 1:5 000 000.

**Heath, G.R. and Pisias, N.G.**
1979: A method for the quantitative estimation of clay minerals in the North Pacific deep-sea sediments; Clays and Clay Minerals, v. 27, p. 175-184.

**King, L.H., Fader, G.B.J., Jenkins, W.A.M., and King, E.L.**
1986: Occurrence and regional geological setting of Paleozoic rocks on the Grand Banks of Newfoundland; Canadian Journal of Earth Sciences, v. 23, p. 504-526.

**Lewis, C.F.M., Parrott, D.R, and Durling, P.**
1987: Shallow Tertiary seismostratigraphy and engineering geology of the northeastern Grand Banks of Newfoundland; Geological Survey of Canada Open File 1437, 22 p.

**McManus, D.A.**
1991: Suggestions for authors whose manuscripts include quantitative clay mineral analysis by X-ray diffraction; Marine Geology, v, 98, p. 1-5.

**Moore, D.M. and Reynolds, R.C., Jr.**
1989: X-Ray Diffraction and the Identification and Analysis of Clay Minerals; Oxford University Press, New York, 332p.

**Moran, K., Mosher, D.C., Gillespie, D., Jarrett, K., and Courtney, R.C.**
1988: Cruise report M/V Pholas 88401; Geological Survey of Canada, Open File 2297, 63 p.

**Parrott, D.R., Lewis, C.F.M., Sonnichsen, G.V., Mosher, D.C., Douma, M., Lewis J., Stewart, J. and Kimbal, D.**
1988: Near surface seismic reflection studies of the Jeanne d'Arc Basin area, northeastern Grand Banks of Newfoundland; in Current Research, Part B; Geological Survey of Canada, Paper 89-1B, p. 67-73.

**Piper, D.J.W. and Slatt, R.M.**
1977: Late Quaternary clay mineral distribution on the eastern continental margin of Canada; Geological Society of America Bulletin, v. 88, p. 267-272.

**Segall, M. P.**
1986: Geological and mineralogical interpretation of shallow sediments from the northeastern Grand Banks of Newfoundland; Geological Survey of Canada, Open File 1439, 102 p.

**Segall, M.P., Barrie, J.V., Lewis, C.F.M., and Maher, M.L.J.**
1985: Clay minerals across the Tertiary-Quaternary boundary, northeastern Grand Banks of Newfoundland: preliminary results; in Current Research, Part B; Geological Survey of Canada, Paper 85-1B, p. 63-68.

**Segall, M.P., Buckley, D.E., and Lewis, C.F.M.**
1987: Clay mineral indicators of geological and geochemical modification of near surface Tertiary and Quaternary sediments on the northeastern Grand Banks of Newfoundland; Canadian Journal of Earth Sciences, v. 24, p. 2172-2187.


---

Geological Survey of Canada Project 830056

# Re-evaluation of the petrology and depositional environment of felsic volcanic and related rocks in the vicinity of the Brunswick No. 12 massive sulphide deposit, Bathurst Mining Camp, New Brunswick[1]

**D. Lentz[2] and W. Goodfellow**
**Mineral Resources Division**

*Lentz, D. and Goodfellow, W., 1992: Re-evaluation of the petrology and depositional environment of felsic volcanic and related rocks in the vicinity of the Brunswick No. 12 massive sulphide deposit, Bathurst Mining Camp, New Brunswick; in Current Research, Part E; Geological Survey of Canada, Paper 92-1E, p. 333-342.*

***Abstract***

*The Nepisiguit Falls Formation (NF; QFAS, QAS, and CT) that immediately underlies the Brunswick No. 12 deposit consists of relatively homogeneous, quartz and alkali feldspar porphyritic, crystal-rich and matrix-supported rocks with a dense cryptocrystalline ("glassy") to granular, microcrystalline groundmass. The quartz-feldspar augen schist represents a coarse grained, crystal-rich, laterally-ejected, subaqueous pyroclastic deposit that is thickest (<500 m) beneath the massive sulphide deposit. The fine grained, crystal-rich tuffs (CT) consist dominantly of reworked pyroclastic material that is laterally extensive. Fine grained sedimentary rocks (FW) with lenses of crystal tuff occur in the immediate footwall to the deposit and pinch out north and south of the deposit into crystal tuff. This rapid thickness change coincides with stringer mineralization and associated hydrothermal alteration. This suggests that the deposit is hosted in a fault-bounded sedimentary basin. A thick succession of intercalated rhyolite flows, tuffs, tuffites, and hyalotuffs (Flat Landing Brook Formation) overlies the massive sulphides and Algoma-type iron-formation.*

***Résumé***

*La Formation de Nepisiguit Falls (NF; QFAS, QAS, et CT) immédiatement sous-jacente au gisement Brunswick No. 12, se compose de roches porphyriques relativement homogènes, contenant du quartz et des feldspaths alcalins, riches en cristaux contenus dans une pâte cryptocrystalline dense («vitreuse») ou microgrenue. Le schiste oeillé quartzo-feldspathique représente un dépôt pyroclastique subaquatique de granulométrie grossière, riche en cristaux, produit par projection latérale de laves, qui atteint son épaisseur maximale (<500 m) au-dessous du gisement de sulfures massifs. Les tufs de granulométrie fine, riches en cristaux (CT), se composent principalement de matériaux pyroclastiques remaniés qui accusent une importante extension latérale. Des roches sédimentaires de granulométrie fine (FW) comportant des lentilles de tufs à cristaux apparaissent immédiatement au mur du gisement et se terminent en biseau au nord et au sud du gisement dans des tufs CT. Cette rapide variation d'épaisseur coïncide avec une minéralisation en filonnets et avec l'altération hydrothermale connexe. Ceci semble indiquer que le gisement est logé dans un bassin sédimentaire limité par des failles. Une épaisse succession de couches interstratifiées composées de coulées rhyolitiques, de tufs, de tuffites et de hyaloclastites (Formation de Flat Landing Brook) recouvre les sulfures massifs ainsi que la formation ferrifère du type de la Formation d'Algoma.*

---

[1] Contribution to Canada-New Brunswick Cooperation Agreement on Mineral Development 1990-1995, a subsidiary agreement under the Economic and Regional Development Agreement. Project funded by the Geological Survey of Canada.

[2] Geological Survey of Canada, P.O. Box 50, Bathurst, New Brunswick E2A 3Z1

## INTRODUCTION

Felsic volcanic and volcaniclastic rocks in the Bathurst Mining Camp are subdivided into the lower Nepisiguit Falls (NF) and the upper Flat Landing Brook (FLB) formations of the Ordovician Tetagouche Group (van Staal and Fyffe, 1991). The Brunswick No. 6 and No. 12 deposits occur within fine grained sedimentary rocks near the top of the Nepisiguit Falls Formation. The chemical composition of these felsic rocks suggests that massive sulphide deposits of the Bathurst area formed in a rift-related tectonic environment (van Staal, 1987; Dostal, 1989; van Staal et al., 1991).

This paper describes the lithotypes that comprise the Nepisiguit Falls Formation in the vicinity of the Brunswick deposits, and re-evaluates their depositional environments. This work constitutes the initial phase of a Canada-New Brunswick Agreement on Mineral Development project, the objective of which is to characterize hydrothermal alteration associated with the Bathurst massive sulphide deposits and to better understand how they formed. In order to identify alteration effects related to ore formation, however, primary volcanic and sedimentary textures and overprinting secondary features formed by deformational processes must be documented.

## GEOLOGICAL SETTING

The rocks of the Bathurst Mining Camp (Fig. 1) in northeastern New Brunswick comprise a Cambro-Ordovician sequence of sedimentary and bimodal volcanic rocks that were intruded by mafic to felsic plutons (Skinner, 1974). The sequence was subsequently deformed and metamorphosed (greenschist facies) during Late Ordovician (Caradocian) to Late Silurian (Ludlovian) time (van Staal and Fyffe, 1991). The stratigraphic sequence consists of phyllite, greywacke, quartzite, and carbonaceous pelite of the Miramichi Group (unit $O_{M2}$; Fig. 2) and conformably overlie rocks of the Tetagouche Group. The Tetagouche Group is subdivided into (1) volcanic, volcaniclastic, and sedimentary rocks of the Nepisiguit Falls Formation (unit $O_{T1}$; Fig. 2), (2) an overlying rhyolite-dominated sequence called the Flat Landing Brook Formation (FLB; unit $O_{T4}$; Fig. 2, 3), and (3) an upper sequence composed of sedimentary rocks (units $O_{T7}$ and $O_{T12}$) intercalated with transitional tholeiitic to alkaline mafic volcanic rocks of the Boucher Brook Formation (BB) (Fig. 2, 3; van Staal and Fyffe, 1991; van Staal et al., 1991).

At least six generations of folds have been identified in the Bathurst Mining Camp (van Staal, 1985, 1987). The $S_1$ foliation is particularly well developed and is commonly transposed parallel to bedding. $F_1$ folds and $S_1$ foliations are associated with early thrusts and high strain zones within the Tetagouche Group. Alkaline mafic rocks of the Tetagouche Group are separated from the tholeiitic mafic volcanic rocks of the contemporaneous Fournier Group by a blueschist-bearing, high-strain zone related to $D_1$ fabric development (van Staal et al., 1990). $F_2$ folds are tight to isoclinal with a strongly developed $S_2$ fabric within the hinge zones. In the Brunswick Mines area, the $F_2$ axial trace is steeply dipping with shallow, doubly-plunging axes. The interference between the $F_2$ folds and large northeast-trending $F_5$ folds (previously $F_3$ folds) is responsible for the distribution of map units (van Staal and Williams, 1984; van Staal, 1987). Other generations of folds and foliations overprint the dominant $D_1$ structures are also developed.

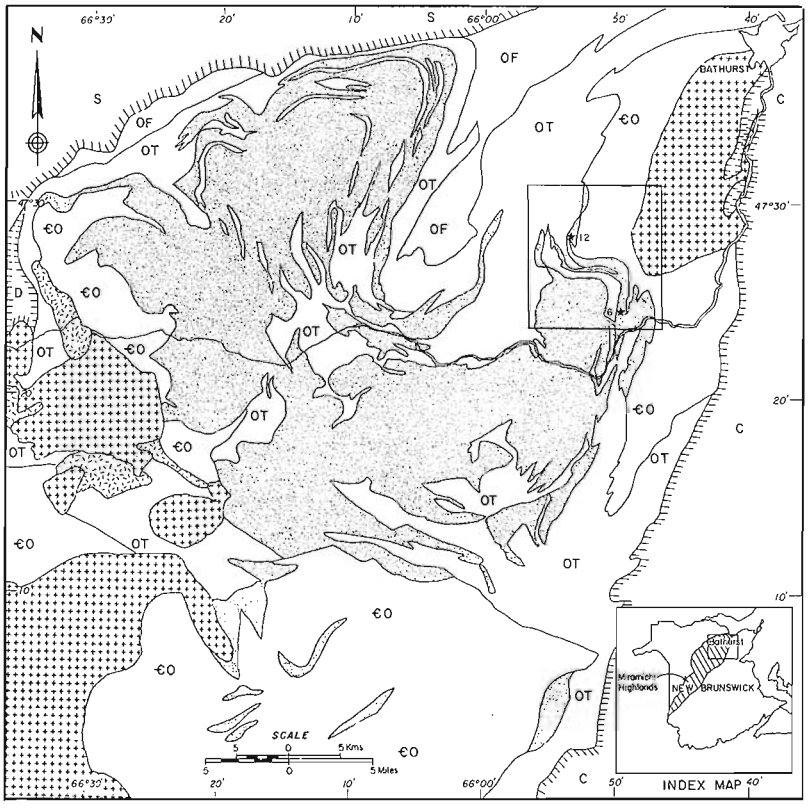


**Figure 1.**

Regional geology of the northeastern Miramichi Highlands of New Brunswick illustrating the distribution of felsic volcanic and volcaniclastic rocks of the Tetagouche Group (modified after McCutcheon, 1990). Legend: C = Carboniferous sedimentary rocks; + = Devonian granitoid intrusions; D = Devonian volcanic and sedimentary rocks; S = Silurian Sedimentary rocks; OF = Middle Ordovician Fournier Group; OT = Middle Ordovician Tetagouche Group; Stippled = Middle Ordovician felsic volcanic and volcaniclastic sedimentary rocks; H = Miramichi Group, Cambro-Ordovician sedimentary rocks. Inset is the authors' current study area (see Fig. 2).

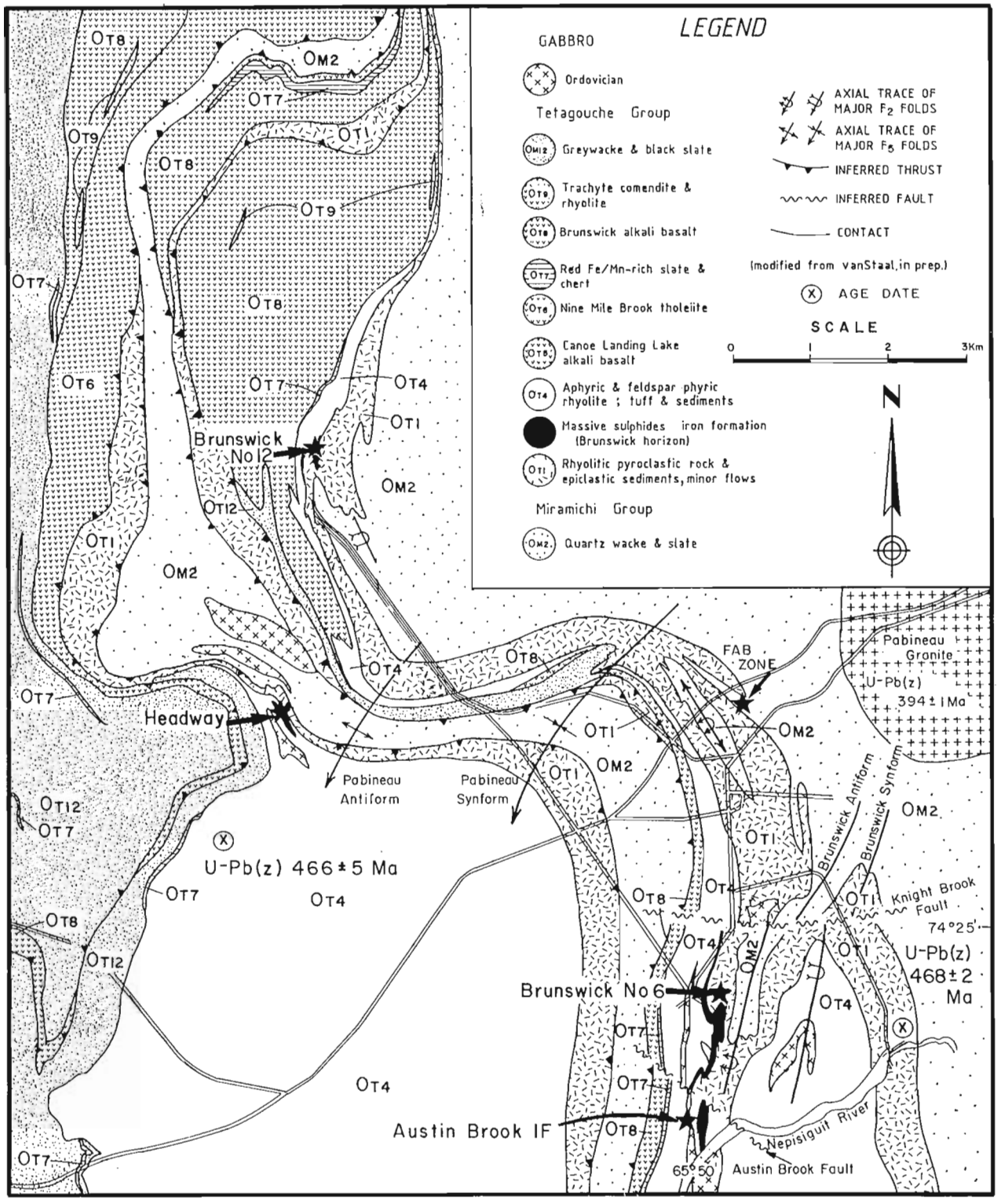


**Figure 2.** Geological map of the Brunswick No. 6 and No. 12 areas based on recent geological mapping of the area (modified after van Staal, pers. comm. 1992).

The Brunswick massive sulphide deposits and associated iron formations occur within the upper part of the Nepisiguit Falls Formation, a unit that overlies graphitic sedimentary rocks of the Miramichi Group. The sulphide deposits are overlain by rhyolitic volcanic rocks and associated sedimentary rocks of the Flat Landing Brook Formation that generally coincide with the transition from rift-related felsic to mafic volcanism within the back-arc basin (Whitehead and Goodfellow, 1978; van Staal, 1987; Fyffe et al., 1990).

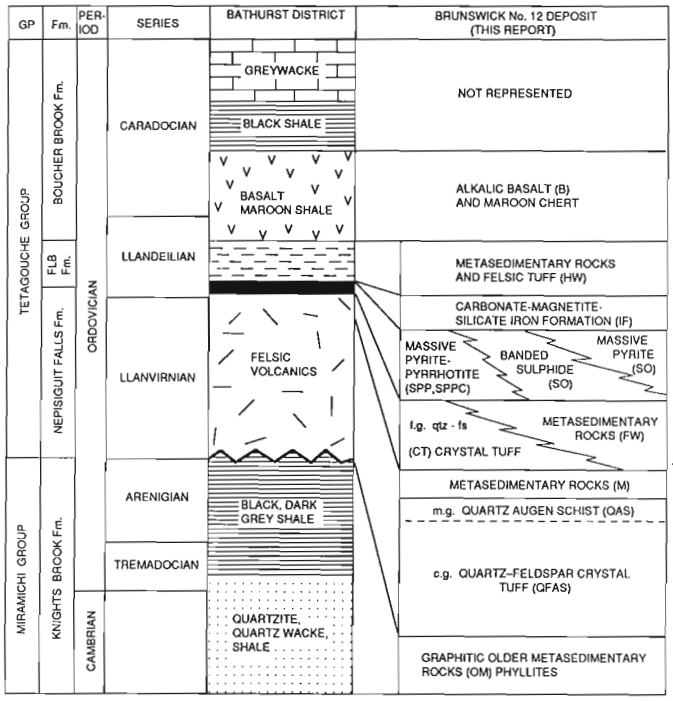


**Figure 3.** Stratigraphic section in the Brunswick No. 12 deposit compared to previously published stratigraphic sections by van Staal and Fyffe (1991) (modified after Luff et al., 1992).

# LITHOTYPES

## *Introduction*

The Brunswick No. 6 and No. 12 massive sulphide deposits are hosted by fine- to coarse-grained, quartz and feldspar, crystal-rich tuffs, porphyritic intrusions, and reworked pyroclastic and volcaniclastic rocks of the Nepisiguit Falls Formation. In the vicinity of Brunswick No. 12 deposit, weak to strong $S_1$ and $S_2$ fabrics have transformed the crystal-rich tuffs and sedimentary rocks into augen schists (Fig. 3, 4). The distribution of the crystals, fragments, and matrix (glass shards) in these rocks has been variably modified by sedimentary reworking. Textural and structural features in rocks at the Brunswick No. 12 deposit are illustrated in Figures 5A to 5H.

## *Nepisiguit Falls Formation*

The Nepisiguit Falls Formation (Nepisiguit Falls) consists of quartz-feldspar augen schist (QFAS), quartz augen schist (QAS or QES), quartz-feldspar crystal tuff (CT) and sedimentary rocks (M, FW, HW). These are descriptive terms that have been used by geologists at Brunswick Mines for many years (Fig. 3). The nomenclature has been revised in order to reflect our current understanding of the origin of these rock types.

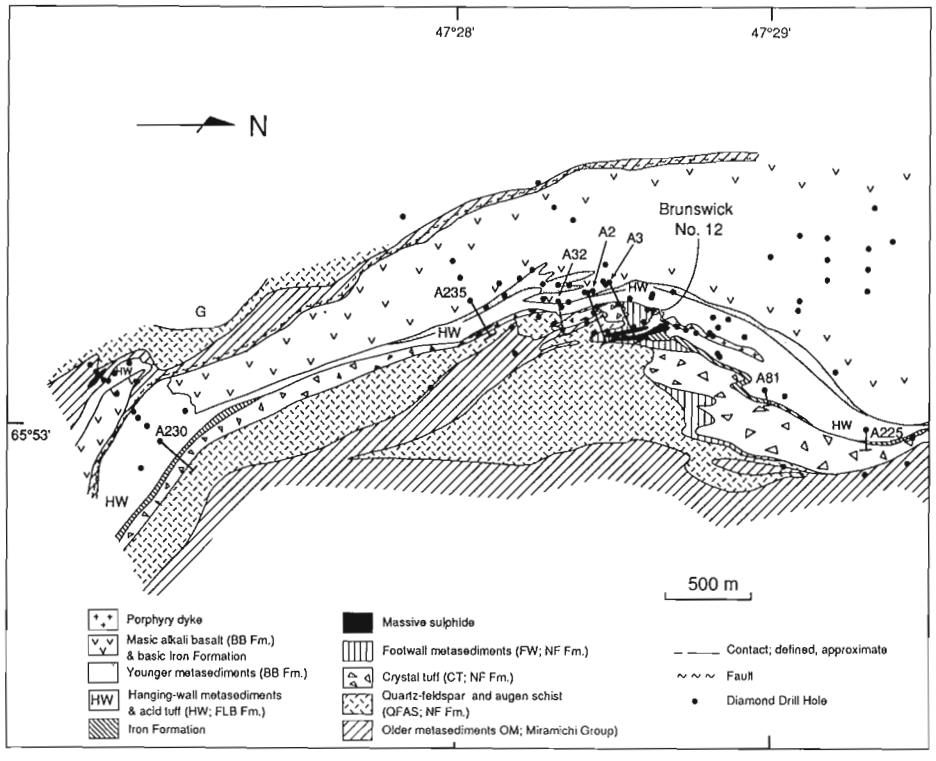


**Figure 4.**

Geological plan of the Brunswick No. 12 deposit compiled by Bill Luff and the staff at Brunswick Mining and Smelting Corporation with selected diamond drill holes examined thus far in this study.

### Quartz-feldspar augen schist (QFAS)

Feldspar phenocrysts within the quartz-feldspar augen schist are subhedral to euhedral and generally twice the size of quartz grains. The feldspar crystals comprise 10 to 20 vol.% of the rock and are also matrix supported in most areas (Fig. 5A). The content of feldspar (10-20 vol.%) and quartz (20-30 vol.%) phenocrysts is very consistent throughout the quartz-feldspar augen schist. Discontinuous colour wisps, distinguished by grey to green hues, are similar to relic pumice fragments and possibly lithic fragments that have been observed in a few relatively undeformed coarse grained crystal tuff units. Although not common, small dark wisps (0.5 to 1 cm; 10 vol.%) that resemble lithic fragments of metapelite were identified in the quartz augen schist and quartz-feldspar augen schist in the north zone of the deposit. Betaform quartz was observed in the quartz-feldspar augen schist near the gradational contact with the quartz augen schist (QAS) (Fig. 6C). Rare graded sequences and channel fills at Nepisiguit Falls (McCutcheon, 1990) are consistent with a submarine pyroclastic origin for the quartz-feldspar augen schist (Nelson, 1983).

Alkali feldspar phenocrysts are cut and partly replaced by microcrystalline quartz-albite-chlorite-sericite veinlets, although these rocks remain recognizable as quartz-feldspar augen schist.

### Quartz augen schist (QAS)

The medium-grained, quartz crystal tuff/tuffite, which is better known as quartz augen schist, is composed of subrounded to subangular quartz grains (20 to 30 vol.%) hosted in a dominantly sericitic matrix (Fig. 5B). Quartz grains vary from 0.1 to 1 cm in diameter, and are matrix supported and uniformly distributed. Small, ragged feldspar grains that are variably altered to fine grained mica or albite occur near the base of the quartz augen schist. The alkali feldspar phenocrysts increase in abundance and size (0.2 to 2 cm) in the transition zone between quartz-feldspar augen schist and quartz augen schist. The stratigraphic thickness of the quartz augen schist is variable (0 to >300 m) with both abrupt (50 cm) and gradational (>50 m) transitions into quartz-feldspar augen schist. Within the vicinity of the Brunswick No. 12 deposit, petrographic evidence indicates that the quartz augen schist is an alteration product of the quartz-feldspar augen schist with granoblastic quartz, albite, sericite, and chlorite pseudomorphs after large alkali feldspar phenocrysts (Goodfellow, 1975a; Juras, 1981; Nelson, 1983; Lentz and Goodfellow, 1992; Luff et al., 1992; Fig. 6E). In addition, primary or secondary albite is partially to completely replaced by phyllosilicates.

### Fine grained, quartz-feldspar crystal tuff (CT)

In the vicinity of the Brunswick deposits, fine grained, quartz-feldspar, crystal-rich tuff/tuffite is laterally continuous but of variable thickness. The crystals are locally graded and homogeneously distributed in a glassy to granular matrix. Juras (1981), Nelson (1983), and Luff et al. (1992) have described fragmented crystals, relict fiamme, lithic fragments (0 to 20%), pumice clasts (10 to 20%), and granophyric textures in the crystal tuff. The absence of these textures in the stratigraphically lower quartz-feldspar augen schist is evidence against a reworking of the quartz-feldspar augen schist and quartz augen schist to form the crystal tuff (Nelson, 1983). This suggests that, in places, the crystal tuff represents reworked, distal pyroclastic fall deposit. The crystal tuff probably originated, therefore, as a subaqueous, vertically-ejected, unwelded, pyroclastic fall deposit (Stix, 1991).

### Sedimentary rocks (M, FW)

There are several very fine-grained, moderately to poorly-layered, leucocratic sedimentary rocks (M, FW) that occur in the footwall sequence of the Brunswick No. 12 deposit (Fig. 5D). The FW sedimentary rocks occur directly beneath most of the deposit and pinch out laterally into crystal tuff north and south of the deposit. The transition is quite sharp possibly representing onlaping onto the crystal tuff or a lateral facies change and coincides with the zones of stringer-sulphide mineralization and associated intense hydrothermal alteration (Luff et al., 1992). Within the footwall rocks, scattered quartz and feldspar crystals and intercalated crystal tuff indicate variable pyroclastic components. High chlorite abundances near the deposit has been attributed to either hydrothermal sedimentation during a pre-ore hydrothermal stage (McCutcheon, 1990, 1992) or to pervasive chloritic alteration (melanocratic) by hydrothermal fluids that have migrated laterally from the stringer sulphide zone (Goodfellow, 1975a, b; Jambor, 1979; Juras, 1981; Nelson, 1983; Luff et al., 1992). The later process may have chloritized and sericitized the footwall sediments (Fig. 5D).

## *Flat Landing Brook Formation*

The Flat Landing Brook Formation (FLB) comprises crystal-poor (<20%) to aphyric rhyolite, fragmental rhyolites, and hyalotuffs or felsic tuffs with intercalated reworked volcaniclastic debris that is texturally similar to the rocks of the Nepisiguit Falls Formation.

### Aphyric to porphyritic rhyolites (R)

Aphyric and quartz-feldspar phyric rhyolites of the Flat Landing Brook Formation (Fig. 5F, G, and H) discontinuously overlie pyroclastic and volcaniclastic rocks of the Nepisiguit Falls Formation and in several areas they are in contact with iron-formation, e.g., at the Narrows in the Nepisiguit River. At the Narrows, the rhyolites contain white to grey, fine- to medium-grained clasts within a highly foliated glassy matrix. These rocks were previously described as crystal tuffs but are presently interpreted as fragmental rhyolite with pseudopyroclastic textures (Langton and McCutcheon, 1990). The aphanitic to weakly porphyritic Flat Landing Brook rhyolites (Fig. 5G and 5F, respectively) have textures reminiscent of flow banding and flow top breccias. Pebble-sized lithophysae with quartz, calcite, and

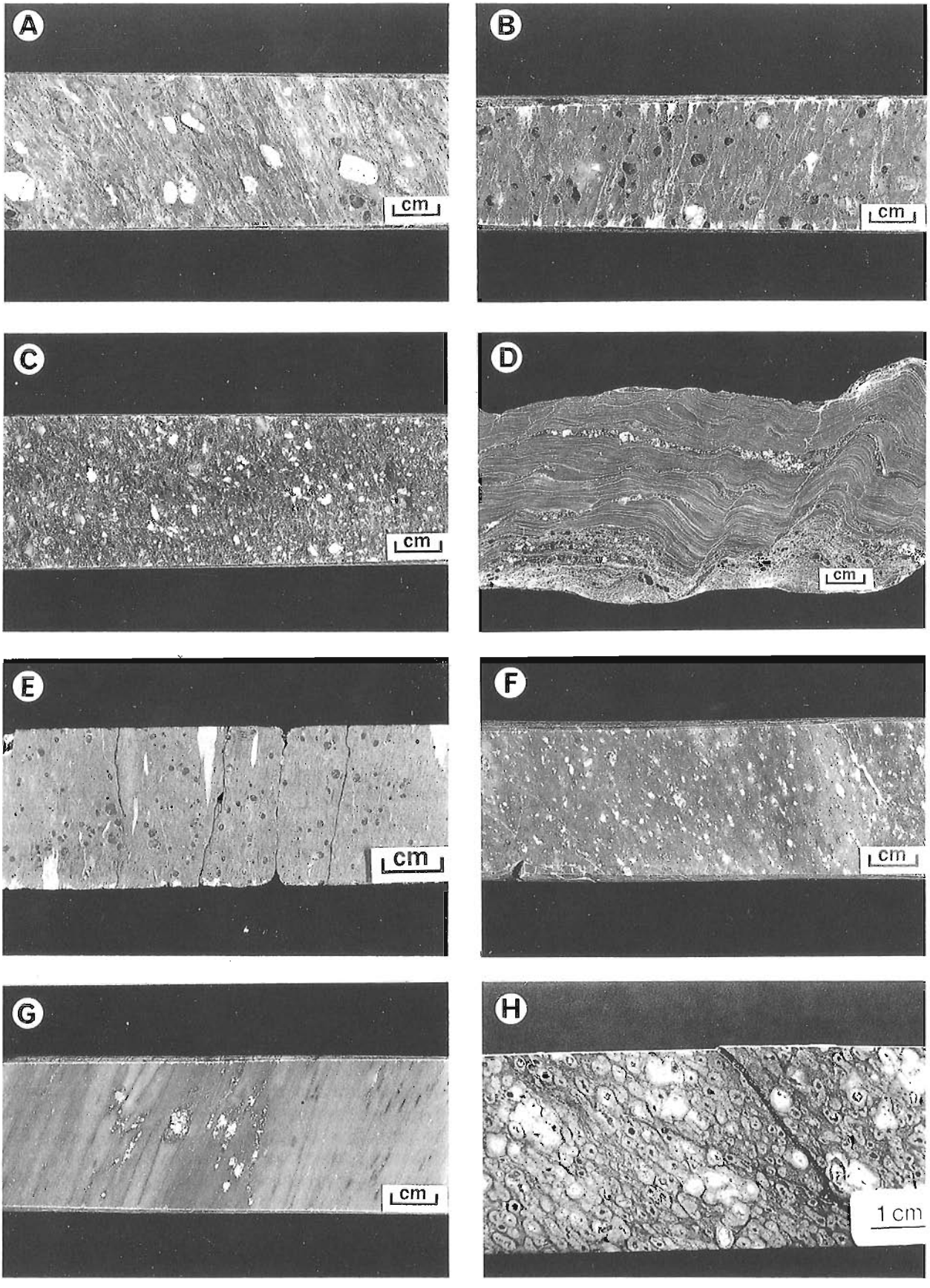
A
cm
B
cm
C
cm
D
cm
E
cm
F
cm
G
cm
H
1 cm

magnetite cores have also been found within these rhyolites (Fig. 6F). They commonly have a crackled appearance with selvages that are bleached and variably altered.

### Sedimentary rocks (HW)

Aphyric to feldspar-phyric felsic tuff (or hyalotuff) may be considered a facies equivalent of the Flat Landing Brook Formation and the first appearance of these rocks defines the base of the Flat Landing Brook Formation. These sedimentary rocks are intercalated with the rhyolites (FLB) near the Brunswick No. 6 deposit. Volcaniclastic rocks derived from reworked Nepisiguit Falls rocks may be intercalated with rhyolites and hyalotuffs. Within the hanging wall rocks to the Brunswick No. 12 deposit, crystal tuff (Fig. 5E) is intercalated with very fine grained, thinly-bedded sedimentary rocks. These fine grained, crystal-rich tuffs and sedimentary rocks are very similar to those directly below the Brunswick No. 12 massive sulphide although they are more leucocratic (sericite-rich) and contain less than a few per cent disseminated sulphide even in the hinge of the $F_2$ fold in the West ore zone (Luff et al.1992; Fig. 4). A reworked pyroclastic origin is also favoured for these units. Saif (1977) proposed that these sedimentary rocks be grouped together into a new formation (Austin Brook Formation) because of their stratigraphic continuity and close association with the rocks of the "Brunswick horizon". These hanging-wall crystal tuffs, tuffites, and hyalotuffs should be considered as part of the Flat Landing Brook Formation with reworked components of Nepisiguit Falls volcanic rocks.

**Figure 5.** Macroscopic features of the pyroclastic and volcaniclastic rocks in the vicinity of the Brunswick No. 6 and No. 12 massive sulphide deposits.

**A.** QFAS (m.g. to c.g. quartz-alkali feldspar crystal-rich tuff)(LPA-122, DDH A230-1012')

**B.** QAS (m.g. quartz (feldspar) crystal-rich tuff)(LPA-103, DDH A32-1043')

**C.** crystal tuff (f.g. quartz-feldspar crystal-rich tuff) (LPA-173, DDH B352-1664')

**D.** FW (v.f.g. sedimentary rock (reworked tuff/tuffite) with layer parallel and discordant pyrite-pyrrhotite) (LPA-003A; 850 level 3 shaft).

**E.** HW (f.g. quartz crystal tuff with fiamme)(LPA-018, DDH A1-307').

**F.** Rhyolite (f.g. feldspar crystal rhyolite) (LPA-164, DDH B352-1010').

**G.** Rhyolite (weakly banded rhyolite with sulphide disseminations (LPA-106, DDH A235-615').

**H.** Lithophysae-rich rhyolite (LPA-112, A230-375').

### Younger sedimentary rocks

Just to the west of the Brunswick No. 12 deposit, maroon hematitic and manganiferous slates and cherts ($O_{T7}$; Fig. 2) underlie the basalt (Davies, 1981; Fig. 3, 4). These sedimentary rocks referred to as Boucher Brook Formation and similar type sedimentary rocks are also intercalated with the overlying alkali mafic volcanic rocks and differ mineralogically and texturally from the underlying leucocratic volcaniclastic sedimentary rocks that characterize the Flat Landing Brook Formation.

## DISCUSSION

The petrogenesis of many rocks in the Nepisiguit Falls Formation is equivocal. Part of the quartz-feldspar augen schist, for example, may be pyroclastic or epiclastic, whereas other parts may be lava flows or porphyritic intrusions (Loudon, 1960; Skinner, 1974; Fyffe and Davies, 1982; McCutcheon, 1990; van Staal et al., 1992). Within the immediate vicinity of the Brunswick No. 12 deposit, the lack of bedding, the paucity of crystal grading and crystal fragmentation, and a glassy cryptocrystalline groundmass (cf. van Staal et al., in press) in quartz augen schist and quartz-feldspar augen schist indicate that these rocks probably represent laterally-ejected, pyroclastic flows (cf. Stix, 1991). Although many of these features are also common in subaqueous lava flows, the absence of fragmental crystal-rich rhyolites near the top of the unit supports a pyroclastic origin.

The composite $S_1$ and $S_2$ fabric is highly heterogeneous within pyroclastic and sedimentary rocks. Whether the observed grain size and textural features are mechanically produced by submarine reworking or by cataclasis during $S_1$ fabric development is important to ascertain. Although not always the case, the elongation of rounded quartz in some quartz augen schist samples compared to subangular to euhedral quartz in the quartz-feldspar augen schist indicates that this is a structural phenomenon. This is consistent with the preferred development of schistosity in the matrix of the quartz augen schist because of its high mica content. Van Staal (1985) has shown that cataclastic fragmentation of the crystals may account for a decrease in grain size and pseudopyroclastic texture in some areas. However, there are preserved euhedral alkali feldspar and betaform quartz phenocrysts that give an estimate of the primary grain size variation within these units. Other pseudopyroclastic features that have been altered include perlitic fractures which resemble glass shards (cf. Juras, 1981; Fig. 6D). Because the petrographic discrimination of pseudopyroclastic features from primary pyroclastic features is very difficult, greater emphasis has been placed on facies relationships within the rocks of the Nepisiguit Falls Formation.

Cas (1978) has suggested that subaqueous felsic pyroclastic flows may remain highly fluid because high water pressure (deep water conditions) inhibits degassing of the erupting material. This may explain the laterally-extensive character of these rocks, as well as the large crystals, negligible crystal fragmentation, and rare presence of

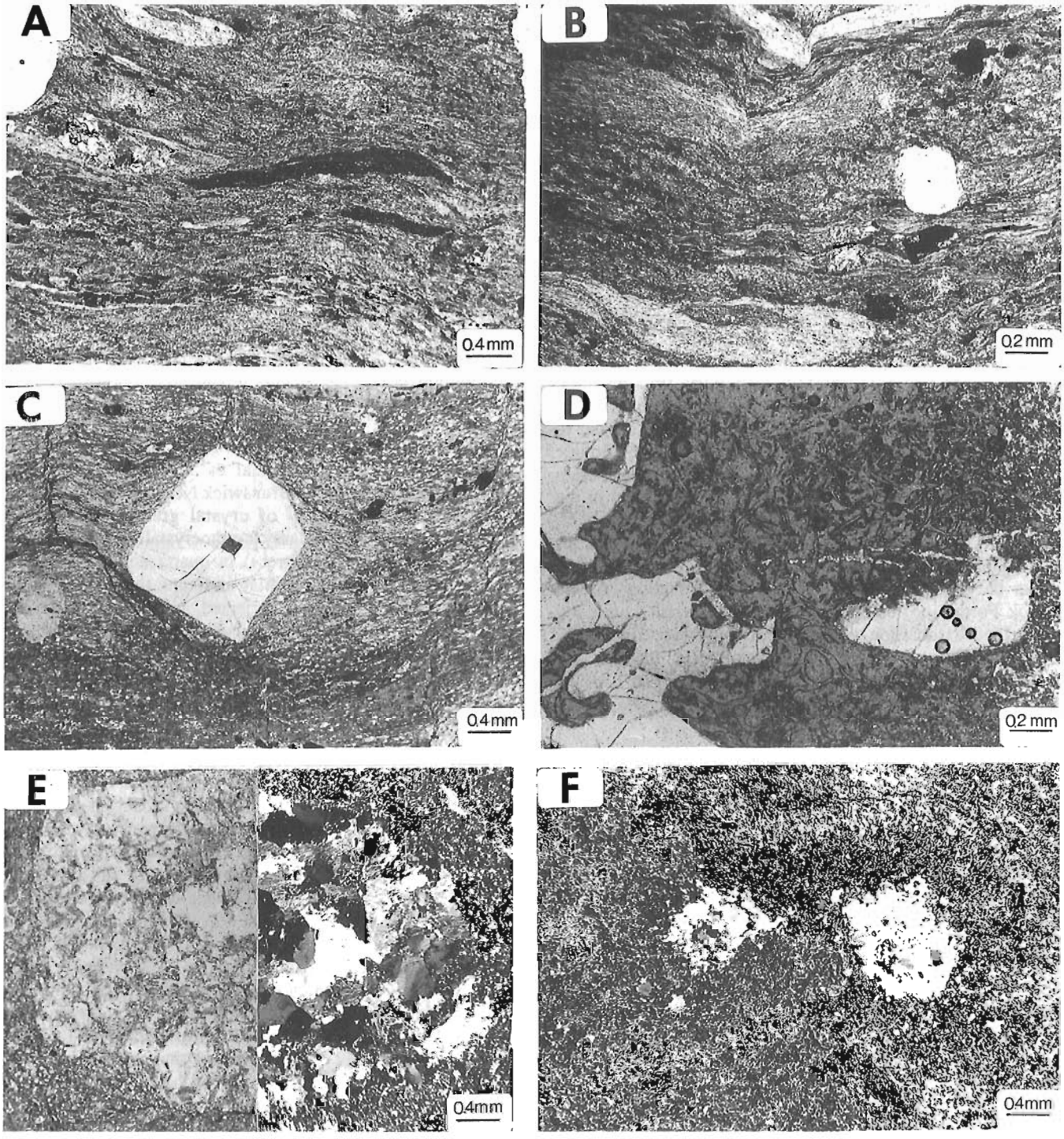


**A.** Relict lithic fragment (black) and fiamme (light) in a very fine grained mica-feldspar-quartz matrix (tuff) (LPA-018, Fig. 5E) (CP).

**B.** Betaform quartz- and fiamme-hosted in very fine-grained tuffaceous matrix (LPA-018, Fig. 5E) (CP).

**C.** Betaform quartz hosted in weakly altered, quartz-feldspar augen schist (LPA-012, 850 m level 3 shaft) (PP).

**D.** Pseudopyroclastic alteration product of perlitic glass, which resemble relict glass shards in UMP (CT)

**E.** Granular intergrowth of quartz, albite, and minor chlorite pseudomorphically replacing alkali feldspar phenocryst in transitional zone between quartz-feldspar augen schist and quartz-augen schist (LPA-009; 750 level) (PP and CP).

**F.** Lithophysae with quartz-calcite-magnetite core in chlorite-sericite-biotite assemblage in rhyolite (LPA-112; DDH A230-375')(CP).

**Figure 6.** Photomicrographs of pyroclastic and related textures from the felsic volcanic and volcaniclastic rocks in the vicinity of the Brunswick No. 6 and No. 12 massive sulphide deposits. (CP-cross polarized light; PP-plane polarized light).

recognizable fiamme. The lower portion of Nepisiguit Falls Formation may represent the entire spectrum of vent-proximal, hot pyroclastic flows, and distal, cold volcaniclastic debris flows (cf. Stix, 1991; Cole and deCelles, 1991), accounting for the extreme textural variability along strike (Fig. 7). The crystal tuff unit within the upper portion of the Nepisiguit Falls Formation represents a later eruption that is separated from the underlying volcanic rocks by a thin, discontinuous unit of fine-grained sedimentary rocks (M). As mentioned previously, evidence of explosive activity and reworking of the crystal tuff is consistent with a pyroclastic fall origin (Fig. 7).

There are two dominant hypotheses for the origin of the quartz augen schist. These are: 1) an epiclastic origin involving subaerial weathering of feldspar, and 2) hydrothermal alteration of feldspar in quartz-feldspar augen schist in a submarine environment. The evidence presented by McCutcheon (1992) for an epiclastic origin for the quartz augen schist and some of the quartz-feldspar augen schist include: 1) the occurrence of interbedded, fine grained sedimentary rocks, size grading, crossbedding, and channels; 2) the presence of rounded quartz; and 3) the major-element composition of the quartz augen schist is variable and similar to world-wide averages for sandstones. Alternatively, the chlorite- and sericite-bearing, quartz augen schist, which forms part of the footwall sequence at the Brunswick No. 12 deposit, has been interpreted as a product of hydrothermal alteration of quartz-feldspar augen schist related to the formation of the massive sulphide deposits or to seafloor alteration (Goodfellow, 1975a, b; Juras, 1981; Nelson, 1983; Lentz and Goodfellow, 1992; Luff et al., 1992). The evidence for this interpretation includes: 1) a spatial association of the quartz augen schist with the sulphide stringer zone below the deposit; 2) an increase in the Mg and Fe content and a decrease in Ca and Na content of the quartz augen schist toward the center of the hydrothermal fluid discharge conduit; and 3) a gradational contact between the quartz augen schist and quartz-feldspar augen schist at the Brunswick No. 12 deposit manifested by gradual alteration of feldspar towards the center of the stringer zone.

The occurrence of relict pumice fragments and homogeneously-distributed, matrix-supported, cataclastic to euhedral quartz (2 to 4 mm diameter) that is smaller than in the quartz-feldspar augen schist (5 to 10 mm), the lower abundance of quartz (15 to 25 vol.%) compared to the quartz-feldspar augen schist (20 to 30 vol.%), and the absence of grading or bedding features at the Brunswick No. 12 deposit does not favor an epiclastic origin for the quartz augen schist. The presence of sedimentary rocks (M) overlying the quartz augen schist shows that there is a time break between the quartz augen schist and the crystal tuff (Fig. 3).

Van Staal et al. (1992) have discussed the various attributes and limitations of a caldera setting for the felsic volcanic rocks of the Bathurst Camp. There is insufficient evidence recognizable for a single, mineralized resurgent caldera complex (Harley, 1979); therefore, this hypothesis is considered an oversimplification.

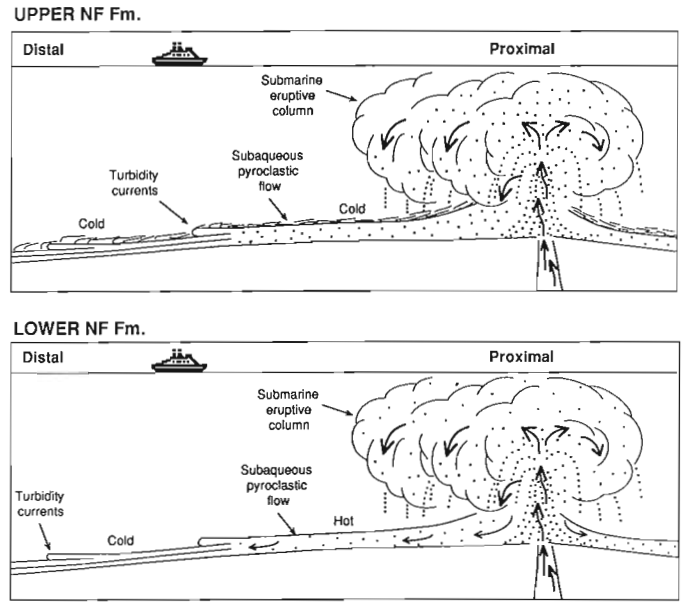


**Figure 7.** Schematic model for the evolution of proximal-distal volcanic relationships within in the Nepisiguit Falls Formation.

## CONCLUSIONS

Within the vicinity of the Brunswick No. 12 deposit, the felsic volcanic and volcaniclastic rocks of the Nepisiguit Falls Formation have petrographic features consistent with a pyroclastic and a reworked pyroclastic origin. The lack of crystal fragmentation, large crystal size, and discontinuous colour wisps that resemble relict pumice fragments is compatible with a deep water, laterally-ejected pyroclastic flow. Most of the quartz augen schist probably formed by alteration of feldspar in quartz-feldspar augen schist, either by high-temperature hydrothermal fluids in discharge conduits, and/or by reacting with heated seawater within cooling volcanic units. The close spatial association of quartz augen schist with the sulphide stringer zone at the Brunswick No. 12 deposit supports this interpretation.

The fine grained, quartz-feldspar crystal tuffs (CT) that overlie the quartz augen schist and quartz-feldspar augen schist contain fiamme and crystal shards that are indicative of a pyroclastic origin but also are texturally heterogeneous, with crystal grading indicative of local reworking of pyroclastic rocks. The footwall sedimentary rocks (FW) have a matrix similar to that of the underlying and interlayered crystal tuff units. Most of the chlorite within this unit reflects a chemical modification of the sediment during either sedimentation or hydrothermal alteration (Luff et al. 1992). The coincidental thickening of pyroclastic (QFAS) and footwall sedimentary rocks (FW) beneath the Brunswick No. 12 deposits indicates that the Brunswick No. 12 deposit formed in a local basin. A thick succession of intercalated volcaniclastic rocks, tuffs, tuffites, and rhyolite flows of the Flat Landing Brook Formation overlie the "Brunswick horizon".

## ACKNOWLEDGMENTS

We would like to thank Bill Luff of Brunswick Mining and Smelting Limited for his co-operation and encouragement with this study and continuing studies in the area. Extensive discussions with Gordon Clark, John Langton, Steve McCutcheon, Jan Peter, and Cees van Staal were greatly appreciated. A comprehensive review by Steve McCutcheon greatly improved the manuscript. This project is funded by the Canada-New Brunswick Cooperation Agreement on Mineral Development.

## REFERENCES

**Cas, R.**
1978: Silicic lavas in Paleozoic flyschlike deposits in New South Wales, Australia: behavior of deep subaqueous silicic flows; Geological Society of America Bulletin, v. 89, p. 1708-1714.

**Cole, R.B. and deCelles, P.G.**
1991: Subaerial to submarine transitions in early Miocene pyroclastic flow deposits, southern San Joaquin basin, California; Geological Society of America Bulletin, v. 103, p. 221-235.

**Davies, J.L.**
1981: Geological map of upper parts of Pabineau and Little Rivers areas, New Brunswick; New Brunswick Department of Natural Resources, Mineral Resouces Branch, Map P-7.

**Dostal J.**
1989: Geochemistry of Ordovician volcanic rocks of the Tetagouche Group of southwestern New Brunswick; Atlantic Geology, v. 25, p. 199-209.

**Fyffe, L.R. and Davies, J.L.**
1982: Sulphide deposits of the Bathurst area, New Brunswick; in Regional trends in the geology of the Appalachian- Caledonian-Hercynian-Laurentide Orogen, Field Trip guidebook B, NATO Advanced Study Institute, Atlantic Canada.

**Fyffe, L.R., van Staal, C.R., and Winchester, J.A.**
1990: Late Precambrian-Early Paleozoic volcanic regimes and associated massive sulphide deposits in the northeastern mainland Appalachians; Canadian Institute of Mining and Metallurgy, v. 83, p. 70-78.

**Goodfellow, W.D.**
1975a: Rock geochemical exploration and ore genesis at Brunswick No. 12 deposit; Ph.D. thesis, University of New Brunswick, Fredericton, New Brunswick.

**Harley, D.N.**
1979: A mineralized resurgent caldera complex in the Bathurst-Newcastle mining district, New Brunswick, Canada; Economic Geology, v. 74, p. 786-796.

**Jambor, J.L.**
1979: Mineralogical evolution of proximal distal features in New Brunswick massive sulphide deposits; Canadian Mineralogist, v. 17, p. 79-87.

**Juras, S.J.**
1981: Alteration and sulphide mineralization in footwall felsic and sedimentary rocks, Brunswick No. 12 deposit, Bathurst, New Brunswick, Canada; M.Sc. thesis, University of New Brunswick, Fredericton, New Brunswick.

**Langton, J.P. and McCutcheon, S.R.**
1990: Brunswick Project, Gloucester County, New Brunswick; in Project Summaries for 1990, Fifteenth Annual Review of Activities, (ed.) S.A. Abbott, New Brunswick Department of Natural Resources and Energy, Minerals and Energy Division, Information Circular 90-2, p. 121-128.

**Lentz, D.R. and Goodfellow, W.D.**
1992: Origin of quartz-augen schist in light of recent investigations at the Brunswick No. 12 sulphide deposit, Bathurst, New Brunswick; Geological Association of Canada/Mineralogical Association of Canada Program with abstracts, Wolfville '92.

**Loudon, J.R.**
1960: The origin of the porphyry and porphyry-like rocks of the Elbow, New Brunswick; Ph.D. thesis, University of Toronto, Toronto, Ontario, 173 p.

**Luff, W., Goodfellow, W.D., and Juras, S.**
1992: Evidence for a feeder pipe and associated alteration at the Brunswick No. 12 massive sulphide deposit; Exploration and Mining Geology, v. 1, no. 2, p. 167-185.

**McCutcheon, S.R.**
1990: Base-metal deposits of the Bathurst-Newcastle district; in Field guide to massive sulphide deposits in northern New Brunswick, (ed.) L.R. Fyffe; Base metal Symposium 1990, Minerals and Energy Division, Department of Natural Resources and Energy, New Brunswick, p. 42-71.
1992: Base-metal deposits of the Bathurst-Newcastle district: characteristics and depositional models; Exploration and Mining Geology, v. 1, no. 2, p. 105-119.

**Nelson, G.A.**
1983: Alteration of footwall rocks at Brunswick No. 6 and Austin Brook deposits, Bathurst, New Brunswick, Canada; M.Sc. thesis, University of New Brunswick, Fredericton, New Brunswick.

**Saif, S.I.**
1977: Identification, correlation and origin of the Key Anacon-Brunswick mines ore horizon, Bathurst, New Brunswick; Ph.D. thesis, University of New Brunswick, Fredericton, New Brunswick, 292 p.

**Skinner, R.**
1974: Geology of Tetagouche Lakes, Bathurst, and Nepisiguit Falls map-areas, New Brunswick with emphasis on the Tetagouche Group; Geological Survey of Canada, Memoir 371, 133 p.

**Stix, J.**
1991: Subaqueous, intermediate to silicic-composition explosive volcanism: a review; Earth-Science Reviews, v. 31, p. 21-53.

**van Staal, C.R.**
1985: The structure and metamorphism of the Brunswick Mines area, Bathurst, New Brunswick, Canada; Ph.D. thesis, University of New Brunswick, Fredericton, New Brunswick.
1987: Tectonic setting of the Tetagouche Group in northern New Brunswick: implications for plate tectonic models in the northern Appalachians; Canadian Journal of Earth Sciences, v. 24, p. 1329-1351.

**van Staal, C.R. and Fyffe, L.R.**
1991: The New Brunswick Dunnage and Gander Zones; in The Appalachian-Caledonian Orogen in Canada and Greenland, (ed.) H. Williams; Geological Survey of Canada, Geology of Canada, No. 6, (also the Geology of North America, v. F-1).

**van Staal, C.R. and Williams, P.F.**
1984: Structure, origin and concentration of the Brunswick No. 12 and 6 orebodies; Economic Geology, v. 79, p. 1669-1692.

**van Staal, C.R., Fyffe, L.R., Langton, J.P., and McCutcheon, S.R.**
1991: Dunnage and Gander Zones, New Brunswick: Canadian Appalachian Region; New Brunswick Department of Natural Resources and Energy, Mineral resources, Geoscience Report 91-2, 39 p.

**van Staal, C.R., Fyffe, L., Langton, J.P., and McCutcheon, S.R.**
1992: The Ordovician Tetagouche Group, Bathurst Camp, northern New Brunswick, Canada: History, tectonic setting and distribution of massive sulphide deposits; Exploration and Mining Geology, v. 1, no. 2, p. 93-103.

**van Staal, C.R., Langton, J.P., and McCutcheon, S.R.**
in press: Geology and tectonic setting of the Bathurst Camp, northern New Brunswick; in Massive sulphide deposits and geology in northern New Brunswick, Geological Association of Canada, Field Trip Guidebook C-6.

**van Staal, C.R., Ravenhurst, C.E., Winchester, J.A., Roddick, J.C., and Langton, J.P.**
1990: Evidence for a post-Taconic blueschist suture in northern New Brunswick, Canada; Geology, v. 18, p. 1073-1077.

**Whitehead, R.E.S. and Goodfellow, W.D.**
1978: Geochemistry of volcanic rocks from the Tetagouche Group, Bathurst, New Brunswick, Canada; Canadian Journal of Earth Sciences, v. 15, p. 207-219.

Geological Survey of Canada Project 790033

# Re-evaluation of the petrochemistry of felsic volcanic and volcaniclastic rocks near the Brunswick No. 6 and 12 massive sulphide deposits, Bathurst Mining Camp, New Brunswick[1]

**D. Lentz[2] and W. Goodfellow**
**Mineral Resources Division**

*Lentz, D. and Goodfellow, W., 1992: Re-evaluation of the petrochemistry of felsic volcanic and volcaniclastic rocks near the Brunswick No. 6 and 12 massive sulphide deposits, Bathurst Mining Camp, New Brunswick; in Current Research, Part E; Geological Survey of Canada, Paper 92-1E, p. 343-350.*

***Abstract***

*The "Brunswick horizon" massive sulphide deposits and associated Algoma-type iron-formation formed after the period of felsic pyroclastic volcanism (Nepisiguit Falls Formation) and before the onset of rhyolitic volcanism (Flat Landing Brook Formation). Immobile trace-element systematics of the pyroclastic and intrusive rocks (Nepisiguit Falls Formation) and rhyolites and tuffs (Flat Landing Brook Formation) are indistinguishable on a regional scale, although the latter have slightly higher HREE, Zr, Nb, Y, and Th contents within individual areas. These compositional features are interpreted as progressive partial melting of lower crust resulting in higher abundance of high-field-strength elements in the Flat Landing Brook Formation compared to the Nepisiguit Falls Formation. This is potentially useful in evaluating the stratigraphic position where petrographic features are ambiguous or have been destroyed by intense deformation and metamorphism.*

***Résumé***

*Les gisements de sulfures massifs de l'«horizon de Brunswick» et la formation ferrifère associée du type Algoma, se sont constitués après la période de volcanisme felsique pyroclastique (Formation de Nepisiguit Falls) et avant le début du volcanisme rhyolitique (Formation de Flat Landing Brook). On ne peut distinguer à l'échelle régionale la distribution systématique des éléments à l'état de traces que contiennent les roches pyroclastiques et intrusives (Formation de Nepisiguit Falls) et les rhyolites et tufs (Formation de Flat Landing Brook), bien que dans certains secteurs, ces derniers aient un contenu légèrement plus élevé en terres rares lourdes, Zr, Nb, Y, et Th. Ces caractéristiques de composition sont sans doute le résultat de la fusion partielle progressive de la portion inférieure de la croûte, qui a permis une plus grande abondance des éléments générant une forte intensité de champ dans la Formation de Flat Landing Brook que dans la Formation de Nepisiguit Falls. Ceci pourrait servir à évaluer la position stratigraphique des roches dont les détails pétrographiques sont ambigus ou ont été détruits par des épisodes de déformation et de métamorphisme intenses.*

[1] Contribution to Canada-New Brunswick Cooperation Agreement on Mineral Development 1990-1995, a subsidiary agreement under the Economic and Regional Development Agreement. Project funded by the Geological Survey of Canada.

[2] Geological Survey of Canada, P.O. Box 50, Bathurst, N.B. E2A 3Z1

# INTRODUCTION

The chemical compositions of the mafic and felsic volcanic rocks in the Bathurst Camp suggest that the massive sulphide deposits formed in a rift-related tectonic environment (van Staal 1987; Dostal 1989; Fyffe et al., 1990; van Staal et al., 1991). Lentz and Goodfellow (1992) described the lithotypes that characterize the Brunswick deposits and re-evaluated their depositional environments. This report, which presents new chemical data and re-evaluates existing data on felsic volcanic rocks, is the initial phase of a project to characterize the hydrothermal alteration associated with massive sulphides in the Bathurst Camp and to better understand processes of ore formation. In order to identify alteration effects related to ore formation, however, compositional variations related to magmatic, depositional processes, and deformational processes must first be documented. Important chemical contrasts that have been identified below for volcanic rocks in the Nepisiguit Falls Formation (Nepisiguit Falls Formation) and the Flat Landing Brook Formation (Flat Landing Brook Formation) relate to differences in their depositional conditions, petrogenesis, and tectonic setting.

# LITHOGEOCHEMISTRY

## *Introduction*

The major- and trace-element composition of 122 felsic volcanic and volcaniclastic rock samples from the Brunswick No. 6 and No. 12 massive sulphide deposits and the surrounding area have been determined. The felsic volcanic rocks have been subdivided into quartz augen schist (QAS), quartz-feldspar augen schist (QFAS or QFP), and crystal tuff (CT) of the Nepisiguit Falls Formation and hanging-wall felsic tuff/tuffite (FT) and massive to flow-banded rhyolite (R) of the Flat Landing Brook Formation on the basis of texture, phenocryst assemblage, lithic fragments, and fiamme and stratigraphic position. Chemical data for several rock suites collected by Dr. Wayne Goodfellow between 1975 and 1988 are considered in this study. Table 1 presents selected new chemical data for felsic volcanic rocks distributed regionally throughout the Bathurst Camp and around Brunswick Mines. A compilation of average compositions of regional felsic volcanic rocks from the Tetagouche Group is also given for comparative purposes (Table 2).

The felsic volcanic rocks have been altered by various processes (van Staal, 1987). In general, albitization, silicification, chloritization, and sericitization of felsic volcanic rocks associated with seawater alteration or coincident with hydrothermal discharge zones (feeder pipes) strongly affect the major-element compositions of these rocks (Luff et al., 1992). Metamorphic reactions and associated fabric development may account for some chemical modification of these volcanic rocks (van Staal, 1987). Mobility of silica, alkaline and alkaline-earth elements, and some transition elements within felsic volcanic rocks precludes their use as petrogenetic indicators. Instead, less mobile high-field-strength elements (HFSE) such as Al, Ti, Zr, Y, Nb, Th, and REE and their ratios are used to determine the chemical evolution and petrogenesis of the felsic volcanic rocks (cf. Winchester and Floyd, 1977; Ludden and Thompson, 1978; Humphris, 1984). As Finlow-Bates and Stumpfl (1981) found, that within the immediate vicinity of two volcanogenic massive sulphide deposits in the Bathurst Camp, there was some evidence of La, Ce, Y, and Nb mobility, caution should be used in their interpretation.

## *Analytical methods*

Most of the common major elements and some trace elements were analyzed by X-ray fluorescence spectroscopy although the high sulphide samples (>5 wt.% sulfur) from the vicinity of the mine were analyzed by inductively-coupled plasma emission spectroscopy (ICP-ES) at the Geological Survey of Canada. Most of the trace elements were determined using atomic absorption and ICP-E spectroscopy. The REE were pre-concentrated by ion exchange and determined by ICP-ES. In general, there was good agreement between methods, but element analysis by ICP is presented because of high precision on duplicate analyses. Water, carbon dioxide, and sulphur were determined by wet chemical methods. Ferric/ferrous determinations were done at the Geological Survey of Canada using the standard ammonium metavanadate titration.

## *Immobile-element systematics*

On a regional scale there are no obvious compositional differences between the different types of felsic volcanic rocks (Table 1 and 2). Furthermore, the composition of the weakly- to moderately-altered felsic volcanic rocks at the Brunswick No. 12 deposit (crystal tuff and quartz augen schist) do not differ significantly from the quartz-feldspar augen schist, regionally (Table 1). The quartz-feldspar augen schist and quartz augen schist at the Brunswick No. 12 deposit (this study) and No. 6 deposit (McCutcheon, 1990) are quite similar. The compositional homogeneity of the quartz augen schist (Table 2) and similarity to quartz-feldspar augen schist points to a cogenetic relationship between the two lithotypes. The average composition of Kuroko footwall rhyolite (Dudás et al., 1983) is included for comparative purposes only.

A spectrum of rare-earth elements (REE) (n = 8) were determined on eight regional felsic volcanic rocks and five felsic volcanic rocks from the Brunswick No. 12 deposit (Table 1). Regional felsic volcanic rocks from this study have moderate to high ΣREE (182.6 ± 64.4 ppm) and ΣLREE (153.6 ± 59.2 ppm) which overlap with the quartz augen schists from the Brunswick Mines area. The rhyolites and associated felsic volcanic rocks (Flat Landing Brook Formation) have slightly higher HREE contents than felsic pyroclastic rocks (Nepisiguit Falls Formation). Within the regional suite, there are more pronounced europium anomalies associated with quartz-feldspar augen schist ($Eu/Eu^* = 0.1$ to 0.5; Fig. 1A) than undivided regional felsic volcanic rocks ($Eu/Eu^* = 0.3$ to 0.7)(Fig. 1A). Extended-REE spider diagrams illustrate the compositional similarity between the quartz-feldspar augen schist (GW 20, 28, 30, and 66; Nepisiguit Falls Formation), felsic tuff (schist)

**Table 1.** Selected major- and trace-element compositional data on regional and Brunswick No. 12 felsic volcanic rocks in the Bathurst Camp

| Sample | GW20 | GW21 | GW28 | GW30 | GW33 | GW38 | GW40 | GW66 | 1 | 2 | 3 | 4 | 5 | 6 | 7 | 8 |
|---|---|---|---|---|---|---|---|---|---|---|---|---|---|---|---|---|
| Type | QFAS | FV | QFAS | QFAS | FV | RT | FV | QFAS | QAS | QAS | QAS | QAS | QAS | CT | CT | TS |
| $SiO_2$ wt.% | 67.1 | 76.4 | 72.3 | 74.6 | 66.9 | 70.6 | 74.6 | 70.0 | 50.0 | 68.7 | 65.1 | 71.1 | 71.5 | 61.8 | 66.8 | 73.0 |
| $TiO_2$ | 0.79 | 0.31 | 0.22 | 0.32 | 0.50 | 0.63 | 0.79 | 0.23 | - | 0.62 | 0.54 | 0.51 | 0.53 | 0.71 | 0.56 | 0.25 |
| $Al_2O_3$ | 15.3 | 11.4 | 14.0 | 12.8 | 13.8 | 12.4 | 10.2 | 16.3 | 11.0 | 13.0 | 13.6 | 13.6 | 13.2 | 17.3 | 12.8 | 12.7 |
| $Fe_2O_{3T}$ | 5.45 | 2.86 | 1.91 | 2.51 | 3.65 | 4.52 | 5.12 | 2.34 | 26.0 | 10.1 | 7.9 | 4.11 | 3.61 | 6.52 | 10.1 | 4.43 |
| $Fe_2O_3$ | - | - | - | - | - | - | - | - | - | - | - | 1.33 | 0.50 | 1.3 | - | 1.1 |
| FeO | - | - | - | - | - | - | - | - | - | - | - | 2.5 | 2.8 | 4.7 | - | 3.0 |
| MgO | 1.88 | 1.21 | 0.43 | 1.05 | 0.80 | 1.58 | 1.28 | 1.57 | 2.0 | 1.22 | 0.46 | 2.14 | 2.14 | 3.94 | 1.96 | 2.22 |
| MnO | 0.09 | 0.06 | 0.02 | 0.03 | 0.07 | 0.06 | 0.09 | 0.03 | - | 0.05 | 0.02 | 0.04 | 0.04 | 0.20 | 0.15 | 0.16 |
| CaO | 0.82 | 0.62 | 0.35 | 0.34 | 0.89 | 0.98 | 0.46 | 1.12 | - | 0.24 | 0.34 | 0.32 | 0.25 | 0.45 | 0.37 | 0.37 |
| $Na_2O$ | 3.22 | 2.05 | 2.49 | 4.84 | 6.24 | 3.94 | 0.27 | 2.61 | - | 0.0 | 0.2 | 1.0 | 1.0 | 1.9 | 0.1 | 0.1 |
| $K_2O$ | 2.99 | 3.00 | 6.8 | 2.6 | 1.99 | 2.05 | 3.20 | 5.02 | 2.0 | 2.60 | 3.74 | 3.89 | 4.08 | 3.74 | 2.65 | 3.57 |
| $P_2O_5$ | 0.19 | 0.22 | 0.25 | 0.15 | 0.19 | 0.19 | 0.15 | 0.32 | - | 0.17 | 0.18 | 0.16 | 0.17 | 0.14 | 0.17 | 0.03 |
| $H_2O$ | 2.4 | 1.7 | 1.0 | 1.3 | 1.3 | 1.8 | 2.5 | 2.2 | 3.7 | 2.5 | 2.2 | - | 2.2 | 3.5 | - | 2.8 |
| $CO_2$ | 0.0 | 0.2 | 0.1 | 0.1 | 0.0 | 0.2 | 0.0 | 0.0 | 0.3 | 0.2 | 0.4 | 0.2 | 0.1 | 0.2 | 0.8 | 0.8 |
| S | 0.7 | 0.6 | 0.0 | 0.0 | 0.0 | 0.3 | 0.0 | 0.0 | 9.0 | 1.02 | 4.91 | 0.54 | 0.61 | 0.5 | 1.7 | 0.0 |
| Total | 100.9 | 100.7 | 99.9 | 100.7 | 96.4 | 99.3 | 97.7 | 101.8 | 101.4* | 100.4 | 99.6 | 97.3 | 99.1 | 100.4 | 98.2 | 100.1 |
| Zr ppm | 360 | 170 | 180 | 190 | 520 | 360 | 380 | 190 | - | 230 | 250 | 230 | 250 | 330 | 250 | 340 |
| Ba | 970 | 830 | 400 | 350 | 320 | 320 | 240 | 380 | - | 330 | 650 | 500 | 630 | 600 | 420 | 2300 |
| Rb | 100 | 120 | 230 | 100 | 76 | 74 | 140 | 220 | - | 110 | 170 | 110 | 110 | 120 | 130 | 140 |
| Sr | 180 | 88 | 28 | 27 | 66 | 140 | 10 | 57 | - | 40 | 50 | 40 | 50 | 34 | 15 | 47 |
| Y | 41 | 42 | 68 | 27 | 76 | 74 | 36 | 83 | - | 32 | 33 | 37 | 35 | 31 | 30 | 53 |
| Nb | 18 | 11 | 13 | 13 | 22 | 18 | 18 | 15 | - | - | - | - | - | 24 | 13 | 26 |
| Th | 9 | 2 | 2 | 1 | 8 | 4 | 0 | 11 | - | - | - | - | - | - | - | - |
| Be | 2.9 | 2.8 | 1.7 | 1.5 | 2.2 | 2.6 | 2 | 3.7 | - | - | - | - | - | 2.1 | 1.6 | 3.4 |
| B | 20 | 17 | 11 | 4.6 | 3.6 | 8.8 | 48 | 16 | - | - | - | - | - | - | - | - |
| Cu | 22 | 12 | 8 | 5 | 6 | 12 | 17 | 9 | - | - | - | - | - | 13 | 29 | 4 |
| Pb | 20 | 24 | 10 | 17 | 26 | 18 | 4 | 28 | - | - | - | - | - | 11 | 12 | 9 |
| Zn | 45 | 58 | 39 | 17 | 65 | 67 | 67 | 58 | - | 30 | 90 | 100 | 70 | 63 | 20 | 62 |
| Cd | 0.5 | 0.7 | 0.4 | 0.3 | 0.4 | 0.1 | 0.2 | - | - | - | - | - | - | - | - | - |
| Ni | 48 | 300 | 17 | 23 | 16 | 19 | 42 | 20 | - | 10 | 50 | 20 | 0 | 12 | 7 | 0 |
| Cr | 54 | 22 | 11 | 14 | 14 | 25 | 56 | 26 | - | - | - | - | - | 36 | 34 | 13 |
| V | 76 | 20 | 13 | 24 | 21 | 52 | 87 | 9 | - | - | - | - | - | 87 | 59 | 17 |
| As | 3 | 19 | 1 | 41 | 22 | 11 | 25 | 12 | - | - | - | - | - | 3.1 | 10.6 | 0.2 |
| Sb | 0.9 | 0.6 | 2.8 | 0.2 | 0.2 | 0.2 | 0.7 | 0.8 | - | - | - | - | - | 2.3 | 1.4 | 0.2 |
| La | 58 | 24 | 31 | 31 | 49 | 52 | 25 | 17 | 37 | 41 | 37 | 35 | 39 | 32 | 29 | 47 |
| Ce | 120 | 51 | 72 | 63 | 110 | 90 | 53 | 45 | 75 | 86 | 77 | 74 | 81 | - | - | - |
| Nd | 62 | 26 | 39 | 33 | 60 | 56 | 30 | 23 | 38 | 46 | 40 | 40 | 42 | - | - | - |
| Sm | 10.0 | 4.7 | 8.1 | 6.3 | 11.0 | 10.0 | 5.8 | 5.2 | 7.0 | 8.0 | 7.2 | 7.1 | 7.5 | - | - | - |
| Eu | 1.5 | 0.6 | 0.4 | 0.8 | 1.9 | 1.7 | 1.2 | 0.3 | 3.2 | 2.6 | 2.2 | 1.1 | 1.2 | - | - | - |
| Gd | 9.6 | 5.8 | 9.2 | 6.9 | 12.0 | 11.0 | 6.1 | 6.9 | 6.6 | 7.5 | 6.9 | 7.0 | 7.1 | - | - | - |
| Dy | 7.1 | 6.2 | 9.6 | 6.9 | 11.0 | 11.0 | 6.0 | 11.0 | 5.3 | 5.7 | 5.8 | 6.2 | 6.1 | - | - | - |
| Yb | 3.2 | 3.2 | 4.5 | 3.4 | 5.9 | 5.0 | 3.0 | 6.8 | 2.4 | 2.6 | 2.8 | 3.0 | 2.9 | 2.7 | 2.7 | 4.0 |
| REE | 271.4 | 121.5 | 173.8 | 151.3 | 260.8 | 236.7 | 130.1 | 115.2 | 174.5 | 199.4 | 178.9 | 173.4 | 186.8 | - | - | - |

NOTES: FV - undivided felsic volcanic rock, QFAS - quartz-feldspar-augen schist, QAS - quartz-(feldspar) augen schist, CT - crystal tuff, TS - tuffaceous sediment, RT - rhyolite tuff. * sample total corrected from $Fe_2O_{3T}$ to FeO; - denotes no analysis. Brunswick No. 12 samples: 1 - A32-100, 2 - A32-400, 3 - 12-1, 4 - 19-7, 5 - A5-780, 6 - 8147-3021, 7 - 8037-2609, & 8 - 8037-2265.

(GW 38; Flat Landing Brook Formation), and rhyolites (GW 21, 33, 40; Flat Landing Brook Formation) (Fig. 1A) suggesting a common source area or operation of similar processes with their evolution. These extended REE patterns mimic those from previous studies (Fig. 1B). A detailed compositional examination of Brunswick No. 6 stratigraphy revealed that hanging-wall tuffites (Flat Landing Brook Formation) that overlie the massive sulphide deposit were higher in Zr, Nb, Y, and HREE than both altered and unaltered footwall sequences of the Nepisiguit Falls Formation (McCutcheon, 1990, 1992; Table 2; Fig. 1B). Langton (1991) also noted a higher Zr, Nb, Th, and HREE contents in rhyolites (Flat Landing Brook Formation) and related rocks than in quartz-feldspar augen schist (Nepisiguit Falls Formation) in the map area south of the Brunswick No. 6 deposit (south of the Nepisiguit River). van Staal et al. (1991) noted that average dacite and rhyolite compositions (Flat Landing Brook Formation) have high HREE contents (Table 2; Fig. 1B).

Empirical discrimination diagrams of Winchester and Floyd (1977) indicate that the felsic volcanic rocks are subalkaline in nature and vary in composition from dacites to rhyolites (Fig. 2A, 2B). There is, however, considerable compositional overlap between the various subdivisions of felsic volcanic rocks.

Zirconium contents, that average 300 ppm (and range between 100 and 500 ppm) indicate a subalkaline composition (Leat et al., 1986; Fig. 2C,D). The uniformly low Zr/Nb ratio (<10) is compatible with a continental-rift setting for Tetagouche Group felsic volcanic rocks. On a regional scale there is considerable overlap between felsic volcanic rocks of the Nepisiguit Falls Formation and Flat Landing Brook formations. Within individual areas, however, Zr and Nb contents are significantly different between these formations (cf. Whitehead and Goodfellow, 1978; McCutcheon, 1990; Langton, 1991; Table 2; Fig. 2D).

The Nb-Y empirical discrimination diagram derived for granitic rocks (Pearce et al., 1984) was applied to the felsic volcanic rocks. The trace-element systematics of Nb and Y are compatible with the felsic volcanic rocks being transitional between a volcanic-arc/syn-collisional and a within-plate environment (Fig. 3A,B) compatible with previous interpretations (Whitehead and Goodfellow, 1978;

**Table 2.** Previous major- and trace-element data on felsic volcanic rocks from the Bathurst Camp, Bathurst, New Brunswick

| Sample | QFAS 1 | | QAS 2 | | HWTS 3 | | Rhyolite 4 | | Dacite 5 | | Felsic 6 | | QFAS 7 | | Rhyolite 8 | |
|---|---|---|---|---|---|---|---|---|---|---|---|---|---|---|---|---|
| n | 6 | | 16 | | 7 | | 13 | | 11 | | 7 | | 11 | | 12 | |
| $SiO_2$ wt.% | 71.5 | ± 0.4 | 68.4 | ± 2.5 | 73.9 | ± 2.5 | 74.9 | ± 1.4 | 70.0 | ± 2.0 | 77.3 | ± 2.8 | 73.0 | ± 2.7 | 74.6 | 2.6 |
| $TiO_2$ | 0.52 | 0.02 | 0.62 | 0.09 | 0.40 | 0.18 | 0.28 | 0.07 | 0.45 | 0.14 | 0.21 | 0.03 | 0.37 | 0.10 | 0.34 | 0.12 |
| $Al_2O_3$ | 13.47 | 0.41 | 12.84 | 1.05 | 12.73 | 0.86 | 12.61 | 1.13 | 14.28 | 0.74 | 10.14 | 1.19 | 13.25 | 0.93 | 12.81 | 1.97 |
| $Fe_2O_{3T}$ | 3.45 | 0.43 | 9.91 | 2.38 | 2.95 | 1.09 | 1.85 | 0.07 | 3.53 | 1.19 | 3.54 | 2.91 | 4.26 | 0.81 | 4.49 | 0.84 |
| MgO | 1.81 | 1.17 | 1.72 | 0.36 | 1.01 | 0.35 | 0.64 | 0.50 | 1.04 | 0.42 | 0.48 | 0.57 | 1.29 | 0.65 | 1.22 | 0.50 |
| MnO | 0.06 | 0.01 | 0.06 | 0.02 | 0.08 | 0.05 | 0.01 | 0.01 | 0.05 | 0.02 | 0.07 | 0.10 | 0.01 | 0.02 | 0.05 | 0.04 |
| CaO | 0.45 | 0.19 | 0.18 | 0.03 | 0.72 | 0.77 | 0.27 | 0.11 | 1.27 | 0.69 | 0.75 | 0.86 | 0.43 | 0.58 | 0.31 | 0.28 |
| $Na_2O$ | 2.61 | 0.35 | 0.30 | 0.76 | 3.41 | 1.20 | 1.97 | 0.69 | 3.38 | 1.55 | 1.98 | 1.44 | 2.41 | 0.77 | 1.66 | 0.98 |
| $K_2O$ | 4.11 | 0.15 | 2.25 | 0.30 | 3.34 | 2.11 | 5.73 | 1.74 | 3.31 | 1.61 | 3.42 | 1.55 | 3.94 | 1.03 | 4.19 | 1.32 |
| $P_2O_5$ | 0.17 | 0.01 | 0.17 | 0.01 | 0.10 | 0.05 | 0.11 | 0.04 | 0.18 | 0.05 | 0.06 | 0.03 | 0.09 | 0.05 | 0.06 | 0.05 |
| $H_2O$ | 1.4 | 0.1 | 3.2 | 0.45 | 1.2 | 0.5 | 1.20 | 0.49 | 1.99 | 0.65 | 0.86 | 0.50 | 1.40 | 0.45 | 1.24 | 0.36 |
| $CO_2$ | – | – | – | – | – | – | – | – | – | – | 0.51 | 0.77 | 0.02 | 0.03 | 0.13 | 0.20 |
| S | – | – | – | – | – | – | 0.03 | 0.03 | 0.01 | 0.01 | 1.40 | 1.26 | – | – | – | – |
| Total | 99.6 | | 99.7 | | 99.8 | | 99.6 | | 99.5 | | 100.8 | | 100.5 | | 101.1 | |
| Zr ppm | 203 | ± 22 | 249 | ± 43 | 314 | ± 53 | 191 | ± 23 | 227 | ± 70 | 220 | ± 98 | 163 | ± 31 | 293 | 105 |
| Ba | 808 | 53 | 396 | 60 | 892 | 588 | 681 | 131 | 544 | 158 | 730 | 423 | 756 | 201 | 814 | 390 |
| Rb | 145 | 14 | 122 | 12 | 128 | 70 | 162 | 41 | 129 | 50 | 151 | 53 | 129 | 23 | 145 | 34 |
| Sr | 70 | 19 | 46 | 69 | 117 | 80 | 47 | 10 | 124 | 64 | 46 | 35 | 62 | 34 | 29 | 17 |
| Y | 16 | 2 | 7 | 2 | 54 | 25 | 51 | 7 | 60 | 19 | 42 | 27 | 45 | 11 | 50 | 17 |
| Nb | 14 | 5 | 14 | 6 | 26 | 7 | 14 | 3 | 14 | 3 | 17 | 7 | 11 | 5 | 26 | 12 |
| Th | 14.2 | 0.7 | 14.9 | 1.9 | 19.7 | 1.8 | 15.4 | 5.8 | 13.0 | 6.0 | 13 | 5 | 12.3 | 1.7 | 16.5 | 2.6 |
| Cu | 14 | ± 2 | 7 | ± 8 | 7 | ± 3 | 11 | ± 12 | 42 | ± 27 | 24 | ± 39 | 3 | ± 3 | 4 | 5 |
| Pb | 27 | 8 | 14 | 18 | 19 | 9 | 19 | 8 | 20 | 11 | 87 | 98 | 17 | 20 | 27 | 39 |
| Zn | 68 | 10 | 53 | 31 | 88 | 18 | 41 | 10 | 59 | 16 | 100 | 98 | 26 | 17 | 159 | 244 |
| Ni | 11 | 1 | 9 | 3 | 9 | 6 | 7 | 8 | 5 | 2 | 3.7 | 1.2 | 8 | 4 | 3 | 2 |
| Cr | 16 | 2 | 13 | 62 | 13 | 6 | 19 | 10 | 21 | 12 | 34 | 5 | 17 | 4 | 11 | 4 |
| V | 44 | 9 | 57 | 14 | 23 | 18 | 24 | 17 | 42 | 27 | 14 | 4 | 41 | 16 | 32 | 18 |
| Sb | 0.3 | 0.2 | 1.0 | 0.4 | 0.9 | 0.6 | – | – | – | – | 4.7 | 5.6 | 0.6 | 0.2 | 0.8 | 0.6 |
| La | 38.0 | 3.4 | 44.4 | ± 8.9 | 49.1 | ± 10.9 | 35.5 | ± 10.4 | 31.5 | ± 10.9 | – | – | 29.6 | ± 11.3 | 47.2 | 16.2 |
| Ce | 80.0 | 7.2 | 90.8 | 13.6 | 101.5 | 23.0 | 64.5 | 14.1 | 65.2 | 22.7 | – | – | 62.5 | 16.0 | 98.9 | 25.8 |
| Nd | 37.6 | 2.4 | 43.6 | 7.6 | 47.9 | 11.4 | 47.1 | 8.4 | 42.2 | 12.8 | – | – | 28.6 | 9.5 | 45.3 | 14.3 |
| Sm | 6.6 | 0.4 | 7.7 | 1.4 | 9.7 | 2.9 | 8.9 | – | 15.7 | – | – | – | 5.64 | 1.52 | 9.0 | 2.9 |
| Eu | 1.03 | 0.07 | 1.07 | 0.1 | 1.19 | 0.35 | 1.0 | – | 0.4 | 0.9 | – | – | 0.84 | 0.30 | 1.47 | 0.63 |
| Gd | 5.4 | 0.3 | 5.8 | 1.1 | 1.37 | 0.54 | 8.9 | – | 17.4 | – | – | – | 5.0 | 1.3 | 8.1 | 2.6 |
| Dy | 4.2 | 0.3 | 3.6 | 0.6 | 8.0 | 3.0 | 8.4 | – | 18.6 | – | – | – | 4.7 | 1.0 | 7.8 | 2.2 |
| Yb | 1.6 | 0.2 | 2.2 | 2.1 | 4.7 | 1.6 | 4.4 | – | 11.3 | – | – | – | 2.21 | 0.44 | 4.72 | 1.12 |
| Lu | 0.28 | 0.04 | 0.22 | 0.03 | 0.70 | 0.24 | – | – | – | – | – | – | 0.35 | 0.07 | 0.75 | 0.17 |

NOTES: $Fe_2O_{3T}$ denotes total Fe reported as $Fe_2O_3$; references; 1, 2, & 3 – Brunswick No. 6 footwall (QFAS, QAS) and hanging-wall felsic rocks McCutcheon (1990), 4 & 5 – van Staal et al. (1991), 6 – Connell & Hattie (1990); 7 – QFAS, Langton (in press); 8 – rhyolite, Langton (in press); n = number of samples; – no analysis; ± = $t_{0.25}s/\sqrt{n}$ is a 95% confidence interval (Le Maitre, 1982).

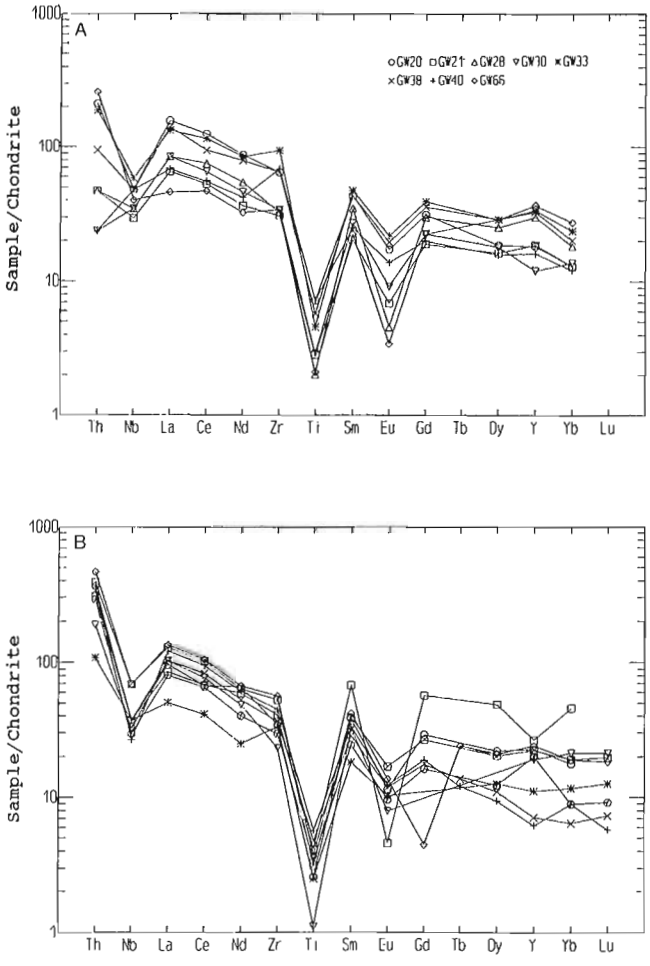


**Figure 1.**

**A**) Extended REE plot for regional felsic volcanic rocks (W. Goodfellow, unpub. data, 1992; Table 1). **B**) averaged samples of previously published regional felsic volcanic and volcaniclastic rocks from the Tetagouche Group, Bathurst, New Brunswick (Table 2). Symbols: x - quartz-feldspar augen schist, + - quartz augen schist, and ◊ - hanging wall tuffite?, McCutcheon (1990); O - rhyolite and ❑ - dacite, van Staal et al. (1991); ▽ - rhyolite, Dostal et al. (1989); ● - quartz-feldspar augen schist and ■ - rhyolite, Langton (in press); * - pre-ore rhyolite Kuroko deposits Dudás et al. (1983). Samples normalized to chondrite (Andrews and Ebihara, 1982).

van Staal, 1987; Dostal, 1989). The Nb and Y contents are considerably more coherent, even in the most altered rocks (quartz augen schist and crystal tuff), than was found by Finlow-Bates and Stumpfl (1981). The ubiquitously low Rb contents (<200 ppm) precludes a syn-collisional origin for the felsic volcanic rocks although hydrothermal alteration may have decreased the Rb contents. No significant differences were identified in this regional study, although higher Nb and/or Y were associated with the rocks of the Flat Landing Brook Formation compared to the Nepisiguit Falls Formation within individual areas (cf. McCutcheon, 1990; Langton, 1991; Table 2; Fig. 3B,D).

The abundances of Zn, Pb, Cu, Mn, and Ba in the Tetagouche Group felsic volcanic rocks are similar to the felsic volcanic rocks of the Kuroko deposits (Dudás et al., 1983). The regional felsic volcanic rocks from this study (Table 1) have a Cu/(Zn+Pb+Cu) ratio of 0.14, a Pb/(Zn+Pb+Cu) ratio of 0.22, and a Zn/(Zn+Pb+Cu) ratio of

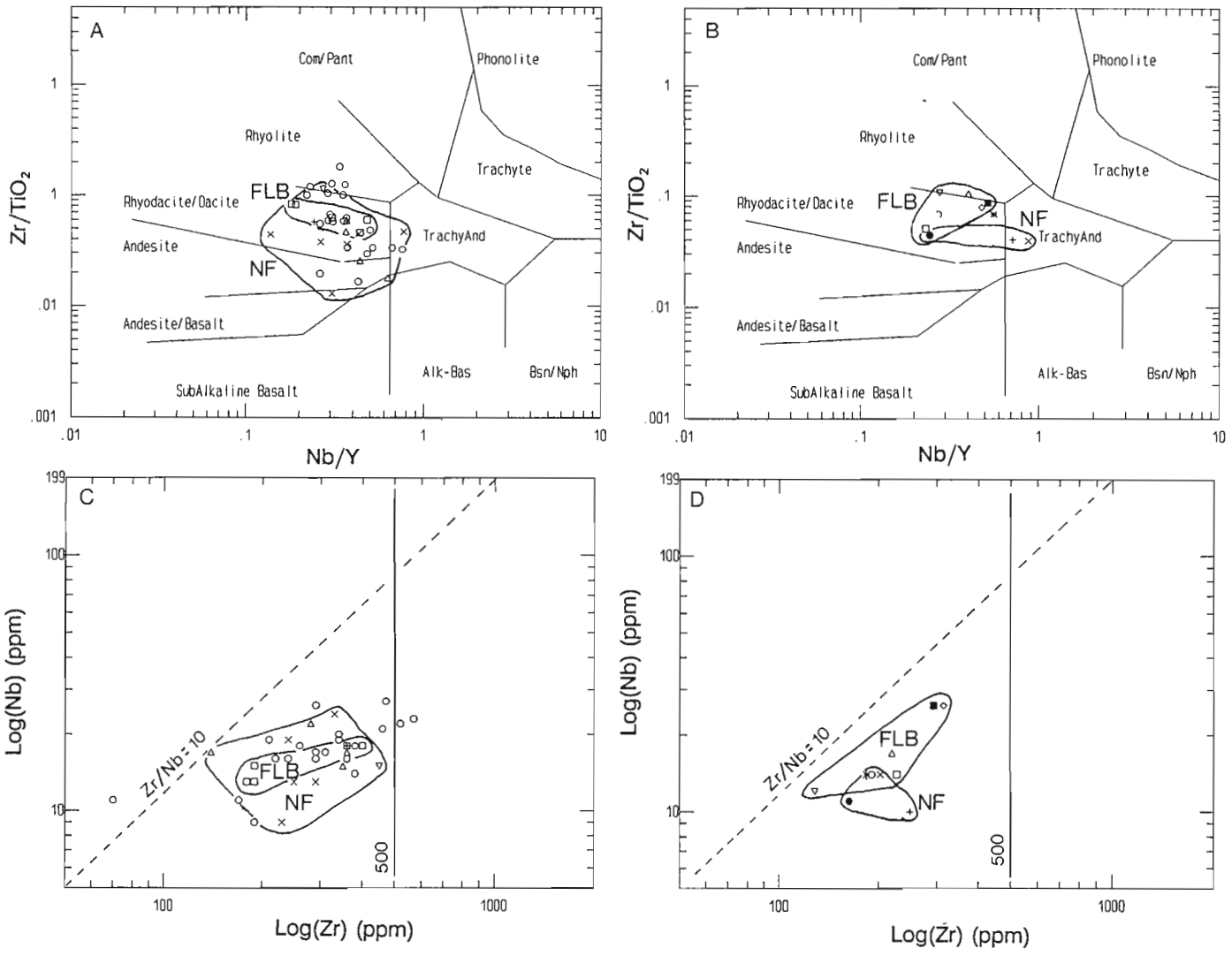


**Figure 2.** **A**) Plot of $Zr/TiO_2$ versus Nb/Y ratio discrimination diagram of Winchester and Floyd (1977) for regional Brunswick Mines felsic volcanic rocks. Symbols: ❑ = rhyolite, ▵ = quartz-feldspar augen schist, O = acid volcanic (undivided), ▽ = quartz augen schist, x = crystal tuff, + = felsic tuff. **B**) Plot of $Zr/TiO_2$ versus Nb/Y ratio discrimination diagram of Winchester and Floyd (1977) for average compositions of previously published, regional felsic volcanic rock data. Symbols: x - quartz-feldspar augen schist, + - quartz augen schist, and ◊ - hanging-wall tuffite?, McCutcheon (1990); O - rhyolite and ❑ -dacite, van Staal et al. (1991); ▽ - rhyolite, Dostal (1989); ▵ - rhyolite, Connell and Hattie (1990); ● - quartz-feldspar augen schist and ■ - rhyolite, Langton (in press); * - pre-ore rhyolite Kuroko deposits Dudás et al. (1983). **C**) Plot of Zr versus Nb (Leat et al., 1986) of regional and Brunswick Mines felsic volcanic rocks (this study; symbols as in Fig. 2A). **D**) Plot of Zr versus Nb (Leat et al. 1986) average compositions of previously published, regional felsic volcanic rock data. Ocean-island and continental-rift felsic volcanic rocks have (Zr/Nb) <10 and subduction-related felsic volcanic rocks have (Zr/Nb) >10. See Figure 2B for symbols; Nepisiguit Falls Formation (Nepisiguit Falls Formation) and Flat Landing Brook Formation (Flat Landing Brook Formation). The field only outline the rock symbols and do not represent compositional ranges.

0.64, which are comparable to previous felsic volcanic data from the region (Table 2), and the ratios from massive sulphide deposits themselves (McCutcheon, 1990).

## DISCUSSION

The origin of many rocks in the Nepisiguit Falls Formation is equivocal. For example, the quartz augen schist has been interpreted as an epiclastic rock (cf. McCutcheon, in press, 1992) and the product of hydrothermal alteration of quartz-feldspar augen schist (cf. Goodfellow, 1975a,b; Juras, 1981; Nelson 1983; Luff et al., 1992). The quartz-feldspar augen schist represents a range of different rock types including pyroclastic, epiclastic, lava or porphyritic intrusion (Skinner, 1974; McCutcheon, 1990; van Staal et al., 1992). In each instance, the origins must be assessed in order to interpret the chemical composition of these rocks. Sedimentary reworking may have altered the primary chemical composition of some volcaniclastic rocks.

The composition of these rocks may be used to characterize the evolution of felsic magmatism before and after formation of massive sulphide deposits. Felsic pyroclastic rocks (QFAS, QAS, CT; NF Fm) and rhyolites (R, RT; Flat Landing Brook Formation) have trace-element compositions indicative of transition between volcanic-arc and within-plate environments. Slight compositional differences between pre-ore and post-ore felsic volcanic rocks (cf. McCutcheon, 1990; Langton, 1991) suggests that these rocks were derived from a common source area or product of similar processes, possibly originating in the lower crust. However, significantly higher HREE, Zr, Nb, Th, and Y abundances in rhyolites and tuffs of the Flat Landing Brook Formation compared to the crystal tuffs of the Nepisiguit Falls Formation can be identified within individual areas, where petrographic evidence is not present or destroyed by intense deformation and metamorphism. These compositional differences are potentially a useful chemo-stratigraphic tool in assessing stratigraphic position above (Flat Landing Brook Formation) or below (Nepisiguit Falls Formation) the "Brunswick horizon".

The REE composition of felsic volcanic rocks in this study are virtually identical to compositions determined by previous workers (McCutcheon, 1990, 1992; Dostal, 1989; Connell and Hattie, 1990; van Staal et al., 1991) (Table 2). Quartz-feldspar augen schist regionally has a pronounced negative europium anomaly related to feldspar fractionation and/or alteration of calcic plagioclase. McCutcheon (1990) found that the quartz augen schist had uniformly negative europium anomalies, similar to the quartz-feldspar augen schist and the undivided felsic volcanic rocks in this study. Such consistent pronounced negative europium anomalies are in keeping with feldspar fractionation. The stability of secondary Ca-bearing phases may be responsible for the apparent immobility of Eu even in regional volcanic rocks except the small negative to positive $Eu/Eu^*$ in the altered footwall felsic volcanics at the Brunswick deposit (Table 1). As previously mentioned, Finlow-Bates and Stumpfl (1981) documented La, Ce, and Y depletion in the most mineralized felsic volcanics associated with several massive sulphide deposits. Previous research has documented LREE and Eu mobilization in hydrothermally-altered footwall rocks in the immediate vicinity of the massive sulphide deposits (Graf, 1977; Finlow-Bates and Stumpfl, 1981). However, this could not be discerned in the few altered footwall rocks (QAS and CT; Table 1) from the Brunswick No. 12 deposit examined in this study.

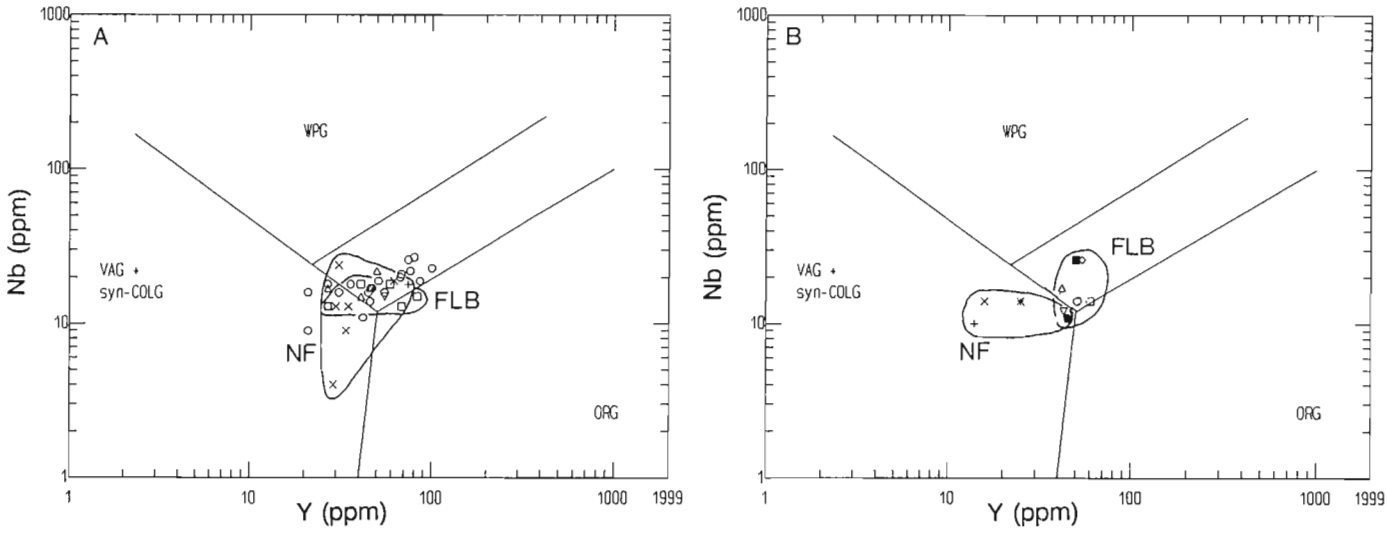


**Figure 3.** **A**) Discriminant plot of Nb versus Y (Pearce et al., 1984) for regional and Brunswick Mines felsic volcanic rocks (this study; symbols as in Fig. 2A). **B**) Discriminant plot of Nb versus Y (Pearce et al., 1984) for average compositions of previously published, regional felsic volcanic rock data. Fields: WPG = within-plate granitoid, ORG = ocean-ridge granitoid, VAG = volcanic-arc granitoid, and syn-COLG = syn-collisional granitoid. See Figure 2B for symbols; Nepisiguit Falls Formation (Nepisiguit Falls Formation) and Flat Landing Brook Formation (Flat Landing Brook Formation). The field only outline the rock symbols and do not represent compositional ranges.

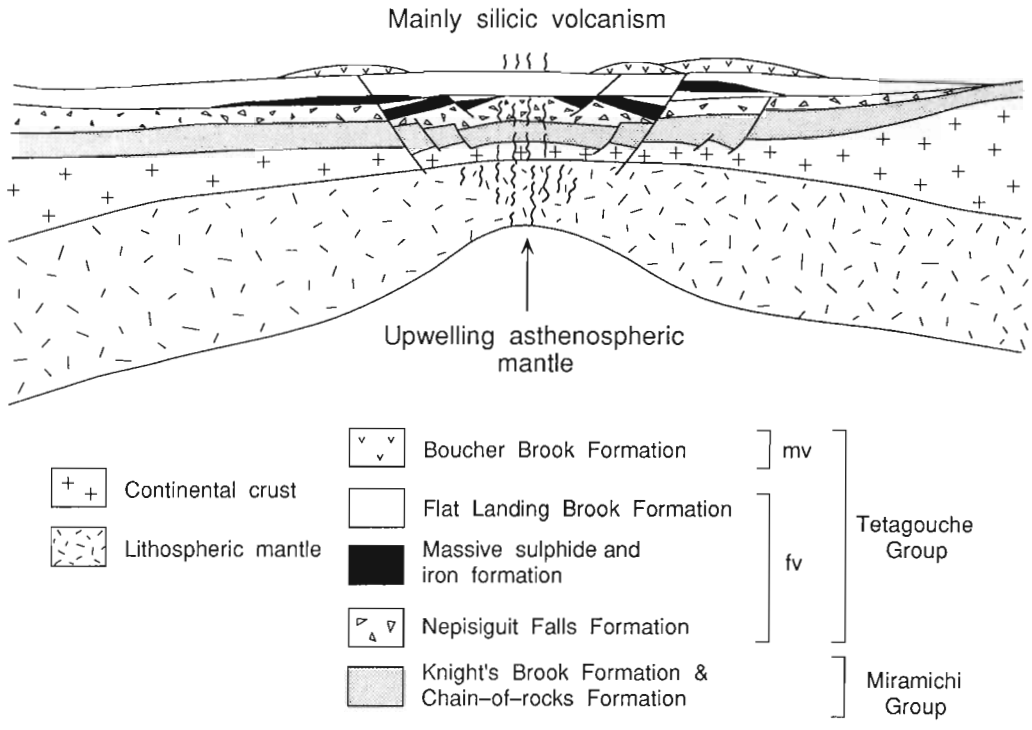


**Figure 4.** Schematic model of a continentally-situated, back-arc rift environment. The Nepisiguit Falls and Flat Landing Brook felsic volcanic and volcaniclastic rocks are formed above a thinning continental crust and undepleted lithospheric upper mantle. fv = felsic volcanic and mv = mafic volcanic (modified after John Langton, pers. comm., 1992).

Pearce et al. (1984) noted that within-plate granitoid magmas inherit the underlying crustal signature to a much greater extent in weakly attenuated crust (anorogenic). The HFSE poor Nepisiguit Falls Formation volcanic rocks rocks may represent first stage partial melts of an amphibolite-grade, lower crust. Second stage partial melts from this source would contain higher incompatible and HFS elements, including REE (Cullers and Graf, 1984), contents. Although somewhat speculative, earlier partial melts may have formed at a lower temperature and higher water fugacities (amphibolite grade) than second stage melts (granulite grade) which probably formed at higher temperatures and lower water fugacities. This interpretation is consistent with the numerous, coarse grained crystals and pyroclastic features in rock of the Nepisiguit Falls Formation (Lentz and Goodfellow, 1992). Interestingly, the high abundance of quartz crystals and the presence of quartz-only pyroclastic rocks might suggest that these melts were generated at considerable depth where the quartz saturation field is largest. In addition, the change from crystal-rich to crystal-poor melts within the felsic volcanic sequence is consistent with evolution from low to high temperature melts and could account for voluminous rhyolitic flows. This interpretation is also consistent with the tectonic model proposed by Whitehead and Goodfellow (1978), van Staal (1987), Dostal (1989), and van Staal et al. (1991) who hypothesize that the felsic magmas were generated by partial melting within an attenuated crust above upwelling mantle which eventually gave rise to alkaline mafic volcanism (Fig. 4).

Further detailed examination of the compositional differences between the Nepisiguit Falls and Flat Landing Brook volcanic and related sedimentary rocks is essential to help unravel the complex stratigraphy in the vicinity of the Brunswick deposits.

## CONCLUSIONS

The immobile-element composition of the felsic volcanic rocks is variable from dacite to rhyolite. There is considerable overlap in the composition of these felsic volcanic rocks on a regional scale. Their compositions are compatible with their generation in a continental-rift setting and with lower crustal origin for the melts. The slightly higher abundance of HREE, Zr, Nb, and Y in rhyolites (Flat Landing Brook Formation) compared to quartz-feldspar augen schist, quartz augen schist, and crystal tuff (Nepisiguit Falls Formation) that precede them is interpreted as progressive partial melting of lower crust with break-down of resistent phases (garnet) contributing to slightly higher abundance of HFSE. More detailed work is needed near the Brunswick No. 6 and No. 12 deposits to help chemically distinguish the two formations enveloping the "Brunswick ore horizon" and characterize the chemostratigraphy of these units.

## ACKNOWLEDGMENTS

We would like to thank Bill Luff of Brunswick Mining and Smelting Limited for his co-operation and encouragement with this study and continuing studies in the area. Extensive discussions with Gordon Clark, John Langton, Steve McCutcheon, Cees van Staal, and Joseph Whalen were greatly appreciated. This project is funded by the Canada-New Brunswick Cooperation Agreement on Mineral Development (1990-1995).

## REFERENCES

**Andrews, E. and Ebihara, M.**
1982: Solar-system abundances of the elements; Geochimica et Cosmochimica Acta, v. 46, p. 2363-2380.

**Connell, M.D. and Hattie, D.W.**
1990: Preliminary report on whole-rock analyses from lithogeochemical study of red manganiferous slate and black slate-chert in the Miramichi Terrane, New Brunswick; (comp.) G.P. Watson, Geological Survey of Canada, Open File 2171, 43 p.

**Cullers, R.L. and Graf, J.L.**
1984: Rare earth elements in igneous rocks of the Continental Crust: intermediate and silicic rocks - ore petrogenesis; in Rare earth element geochemistry, (ed.) P. Henderson, Developments in Geochemistry 2, Elsevier, N.Y., p. 275-316.

**Dostal, J.**
1989: Geochemistry of Ordovician volcanic rocks of the Tetagouche Group of southwestern New Brunswick; Atlantic Geology, v. 25, p. 199-209.

**Dudás, F.Ö., Campbell, I.H., and Gorton, M.P.**
1983: Geochemistry of igneous rocks in the Hokuroku District, northern Japan; Economic Geology, Monograph 5, p. 115-133.

**Finlow-Bates, T. and Stumpfl, E.F.**
1981: The behavior of so-called immobile elements in hydrothermally altered rocks associated with volcanogenic submarine-exhalative ore deposits; Mineralium Deposita, v. 16, p. 319-328.

**Fyffe, L.R., van Staal, C.R., and Winchester, J.A.**
1990: Late Precambrian-Early Paleozoic volcanic regimes and associated massive sulphide deposits in the northeastern mainland Appalachians; Canadian Institute of Mining and Metallurgy, v. 83, p. 70-78.

**Goodfellow, W.D.**
1975a: Rock geochemical exploration and ore genesis at Brunswick No. 12 deposit; Ph.D. thesis, University of New Brunswick, Fredericton, New Brunswick.
1975b: Major and minor element halos in volcanic rocks at Brunswick no. 12 sulphide deposit, N.B., Canada; in Geochemical Exploration 1974. (ed.) I.L. Elliot and W.K. Fletcher; Elsevier Amsterdam, p. 279-295.

**Graf, J.L.**
1977: Rare Earth Elements as hydrothermal tracers during the formation of massive sulfide deposits in volcanic rocks; Economic Geology, v. 72, p. 527-548.

**Humphris, S.E.**
1984: The mobility of rare earth elements in the crust; in Rare earth element geochemistry, (ed.) P. Henderson; Developments in Geochemistry 2, Elsevier, N.Y., p. 317-342.

**Juras, S.J.**
1981: Alteration and sulphide mineralization infootwall felsic and sedimentary rocks, Brunswick No. 12 deposit, Bathurst, New Brunswick, Canada; M.Sc. thesis, University of New Brunswick, Fredericton, New Brunswick.

**Langton, J.P.**
1991: Brunswick Project, Gloucester County, New Brunswick; in Project Summaries for 1991. Sixteenth Annual Review of Activities, (ed.) A.A. Abbott; New Brunswick Department of Natural Resources and Energy, Minerals and Energy Division, Information Circular 91.

**Le Maitre, R.W.**
1982: Numerical Petrology; Elsevier Publishing Co. N.Y.,N.Y., 281 p.

**Leat, P.T., Jackson, S.E., Thorpe, R.S., and Stillman, C.J.**
1986: Geochemistry of bimodal basalt-subalkaline/peralkaline rhyolite provinces within the southern British Caledonides; Journal of the Geological Society, London, v. 143, p. 259-273.

**Lentz, D.R. and Goodfellow, W.D.**
1992: Re-evaluation of the petrology and depositional environment of felsic volcanic and related rocks in the vicinity of the Brunswick No. 12 massive sulphide deposit, Bathurst Camp, New Brunswick; in Current Research, Part E; Geological Survey of Canada, Paper 92-1E.

**Ludden, J.N. and Thompson, G.**
1978: Behavior of rare-earth elements during submarine hydrothermal weathering of sea floor basalt; Earth and Planetary Science Letters, v. 43, p. 85-92.

**Luff, W., Goodfellow, W.D., and Juras, S.**
1992: Evidence for a feeder pipe and associated alteration at the Brunswick No. 12 massive sulphide deposit; Exploration and Mining Geology, v. 1, no. 2, p. 167-185.

**McCutcheon, S.R.**
1990: Base-metal deposits of the Bathurst-Newcastle district; in Field guide to massive sulphide deposits in northern New Brunswick, (ed.) L.R. Fyffe; Base metal Symposium 1990, Minerals and Energy Division, Department of Natural Resources and Energy, New Brunswick, p. 42-71.
1992: Base-metal deposits of the Bathurst-Newcastle district: characteristics and depositional models; Exploration and Mining Geology, v. 1, no. 2, p. 105-119.

**Nelson, G.A.**
1983: Alteration of footwall rocks at Brunswick No.6 and Austin Brook deposits, Bathurst, New Brunswick, Canada; M.Sc. thesis, University of New Brunswick, Fredericton, New Brunswick.

**Pearce, J.A., Harris, N.B., and Tindle, A.G.**
1984: Trace element discrimination diagrams for the tectonic interpretation of granitic rocks; Journal of Petrology, v. 25, p. 956-983.

**Skinner, R.**
1974: Geology of Tetagouche Lakes, Bathurst, and Nepisiguit Falls map-areas, New Brunswick with emphasis on the Tetagouche Group; Geological Survey of Canada, Memoir 371, 133 p.

**van Staal, C.R.**
1987: Tectonic setting of the Tetagouche Group in Northern New Brunswick: implications for plate tectonic models in the northern Appalachians; Canadian Journal of Earth Sciences, v. 24, p. 1329-1351.

**van Staal, C.R., Winchester, J.A., and Bedard, J.H.**
1991: Geochemical variations in Middle Ordovician volcanic rocks of the northern Miramichi Highlands and their tectonic significance; Canadian Journal of Earth Sciences, v. 28, p. 1031-1049.

**van Staal, C.R., Fyffe, L., McCutcheon, S.R., and Langton, J.P.**
1992 The Ordovician Tetagouche Group, Bathurst Camp, northern New Brunswick, Canada: History, tectonic setting and distribution of massive sulphide deposits; Exploration and Mining Geology, v. 1, no. 2, p. 93-103.

**Whitehead, R.E.S. and Goodfellow, W.D.**
1978: Geochemistry of volcanic rocks from the Tetagouche Group, Bathurst, New Brunswick, Canada; Canadian Journal of Earth Sciences, v. 15, p. 207-219.

**Winchester, J.A. and Floyd, P.A.**
1977: Geochemical discrimination of different magma series and their differentiation products using immobile elements; Chemical Geology, v. 20, p. 325-343.

---

Geological Survey of Canada Project 790033

# A geological perspective on global warming and the possibility of refossilizing carbon dioxide from fossil fuels as calcium carbonate minerals

**H.E. Dunsmore**
**Mineral Resources Division**

*Dunsmore, H.E., 1992: A geological perspective on global warming and the possibility of refossilizing carbon dioxide from fossil fuels as calcium carbonate minerals; in Current Research, Part E; Geological Survey of Canada, Paper 92-1E, p. 351-356.*

***Abstract***

*Nature removes carbon dioxide from the atmosphere and returns it to the safety of the lithosphere using photosynthesis, and by forming calcium and calcium-magnesium carbonate minerals. Highly concentrated, calcium-rich brines are commonly found associated with subsurface salt deposits. By bringing together the energy and chemical industries, it may be possible to use these brines to lock up carbon dioxide produced by burning fossil fuels while at the same time producing calcium carbonate, hydrochloric acid and a variety of other chemical-industrial commodities. Thus, following Nature's example, carbon dioxide should begin to be thought of not as a waste to be disposed of, but as a resource from which useful products may be made.*

***Résumé***

*Dans la nature, le gaz carbonique est éliminé de l'atmosphère et recyclé dans la lithosphère par la photosynthèse et par la formation de carbonates (de calcium ainsi que de calcium et magnésium). Les saumures fortement concentrées et riches en calcium s'observent souvent en association avec des dépôts salifères de subsurface. En réunissant les industries énergétiques et chimiques, il serait possible d'utiliser ces saumures pour capter le gaz carbonique produit par l'utilisation des combustibles fossiles et en même temps obtenir des carbonates de calcium, de l'acide chlorhydrique et divers autres produits destinés à l'industrie chimique. Ainsi, en suivant l'exemple de la nature, le gaz carbonique devrait enfin être considéré non comme un résidu à éliminer, mais comme une ressource pouvant servir à fabriquer des produits utiles.*

## INTRODUCTION

Of the many environmental issues facing industrial society today, the gravest of all is the prospect of global warming. This change will be caused in large part by the release of $CO_2$ to the atmosphere from the burning of fossil fuels. If, as seems likely, steps must be taken to moderate this enhanced greenhouse effect, it is crucial that the nature of the problem be clearly and fully understood so that appropriate solutions are put in place.

This paper addresses two main issues. The causes and consequences of possible anthropogenic global warming will be discussed from a geological perspective, emphasizing how the Earth's atmothermal balance has been maintained throughout geological time. Based on this evidence, a technique for capturing $CO_2$ is presented, one which should be applicable in many parts of the world.

## UNDERSTANDING THE PROBLEM

Life continues to flourish on Earth because surface temperatures have always been maintained within tolerable limits. This is accomplished by controlling the atmospheric content of greenhouse gases, including carbon dioxide. We shall begin this discussion by considering how carbon is distributed on the planet.

### *Distribution of carbon*

The Earth's carbon can be divided into two reservoirs of quite unequal size (Fig. 1). The larger of the two, containing something like 99.94% of the total, is made up of "dead" carbon locked away in the lithosphere, that is, in the rocks of the Earth's crust. Some 80% of this fossil carbon is fixed in the oxidized state as geochemically stable carbonate minerals in limestone and dolomite deposits (Fig. 1). The remaining 20%, consisting of the altered remains of organisms, occurs as kerogen and graphite disseminated throughout

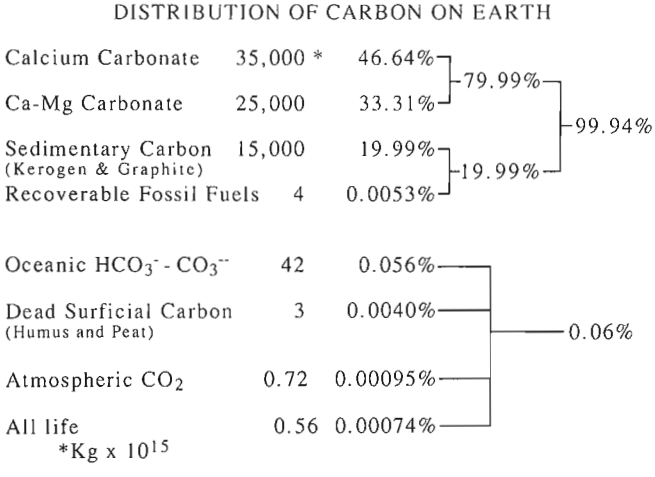


**Figure 1.** Estimates of the relative distribution of carbon on Earth, in kilograms and per cent (after Berner and Lasaga, 1989).

sedimentary and metasedimentary rocks. A very tiny fraction of this carbon has been maturated and concentrated as recoverable fossil fuels.

The smaller of the two reservoirs, containing a mere 0.06% of the global total, is made up of the "live" carbon actively being cycled within the atmosphere-hydrosphere-biosphere. Over 90% of this carbon is in solution in the world's oceans. The remainder, in decreasing order of abundance, is found in dead surficial material, the atmosphere, and living organisms (Fig. 1).

One is struck by the overwhelming dominance of the lithosphere as a store of carbon and the comparative insignificance, and implied fragility, of the atmosphere and life systems. Within the lithosphere, four times more carbon is held in the oxidized form, as carbonate minerals, than in the reduced form, as organic remains.

### *Earth's biogeochemical thermostat*

The basic configuration of the Earth's carbon-based, biogeochemical thermostat is illustrated in Figure 2. Two versions are shown, one depicting the situation prior to industrialization in the early 1800s, and the other after industrialization. Both consist of the "live" and "dead" reservoirs linked by various fluxes.

Throughout geological time, carbon has been continuously cycled back and forth between the two reservoirs (Fig. 2A). It is released from the lithosphere by geological processes powered by plate tectonics; these include the emission of $CO_2$-rich volcanic fluids, and the weathering and erosion of carbon-bearing rocks following uplift. The return flux combines both biological and geological processes; organisms produce the carbonate minerals and organic matter, primarily within the surface layers and on the margins of the world's oceans, but geological processes are responsible for ensuring that this material is successfully transferred back into the "dead" carbon reservoir, that is, buried.

Carbonate minerals are stable in the surficial environment, so in most instances the transition is complete when the mineral is formed. Organic carbon, on the other hand, can only be judged to have crossed the line when the host sediment has been buried and lithified.

To maintain atmothermal balance, changes in flux on the left side of the loop (Fig. 2A) must be matched by a corresponding change on the right. If not, carbon will either accumulate or become depleted in the minute "live" carbon reservoir, including the atmosphere. For example, if the left side becomes dominant, $CO_2$ will build up in the atmosphere and a permanent, runaway greenhouse effect will result, as on our sister planet Venus. On the other hand, if plate tectonics and associated volcanic activity ceases, carbon can no longer be cycled out of the lithosphere. In this instance, the right side of the loop becomes dominant, the atmosphere will lose most of its $CO_2$ and the planet will freeze up, as occurred on Mars. Over time and within limits, a balance

must be maintained between these two fluxes; otherwise, liquid water will disappear from the Earth's surface, and with it life as we know it.

Since the early 1800s, our industrial society has been effectively short-circuiting the thermostat (Fig. 2B). We have been digging up "dead" carbon as quickly as we can find it-carbon which Nature thought had been safely locked away-and, after use, have simply been dumping it into the "live" reservoir. This $CO_2$ is not only coming from fossil fuels, but also from the use of limestone for cement production, the smelting of metals, and so on. Because we have not provided a mechanism to refossilize this carbon, it is accumulating in the atmosphere-hydrosphere-biosphere, a system which already has its own anthropogenic problems and its own pool of carbon to content with.

Conceptually at least, the solution to the $CO_2$ problem is straightforward: any anthropogenic release of carbon from the lithosphere must be matched by an equal and opposite return. In other words, we must either eliminate the anthropogenic flux depicted in Figure 2b, or generate a flux of equal magnitude in the opposite direction.

The amount of carbon that our civilization is defossilizing has reached astounding proportions. Estimates put it at 10 to 15 times the natural flux of carbon out of the lithosphere (Turner, 1981, Francois and Walker, 1992). This may be hard to believe, until one visualizes the amount of fossil fuel consumed each day. Recently, the world's oil industry has been producing and burning about sixty-six million barrels of petroleum daily. If that number of oil drums was stood side by side in a row, the line would stretch for one complete revolution around the circumference of the Earth. To this must be added the oil equivalent of the natural gas and coal consumed each day, as well as the $CO_2$ produced from calcining limestone.

The anthropogenic flux of carbon out of the lithosphere is still very small compared to the magnitude of the annual organic production and decay cycles, that is, the massive and rapid cycling of carbon within the "live" reservoir. Perhaps it is this fact which has made the problem seem less urgent than it may well be. If the analysis depicted in Figure 2 is correct, it is imbalances in the rates of defossilization-refossilization of carbon which, in the long term, will determine whether the planet's surface warms or cools.

It is crucial to our understanding of the $CO_2$ problem to appreciate that the various carbon fluxes operate on very different time scales. Carbon within the atmosphere-hydrosphere-biosphere is cycled relatively quickly, anywhere from minutes to several centuries. The same is true of our exploitation of fossil carbon as an energy source and industrial commodity. On the other hand, geological and biogeological processes are very much more ponderous, operating within time frames of hundreds of thousands or even millions of years. Thus, the processes responsible for returning carbon to the safety of the lithosphere simply cannot respond quickly enough to our sudden interference to avoid a buildup of atmospheric $CO_2$.

Since the industrial revolution two centuries ago, the $CO_2$ content of the atmosphere has been rising exponentially. About half of the anthropogenic carbon remains in the atmosphere (Holland, 1978); the remainder, for now at least, has been cycled into biomass and the oceans. There has simply not been enough time for much of this excess carbon to have been transferred back into the lithosphere.

Given geological time, natural processes will restore the $CO_2$ balance, as they always have done, but the lengths of time involved are daunting. Some 57 million years ago, a $CO_2$-induced greenhouse warming event took place due to

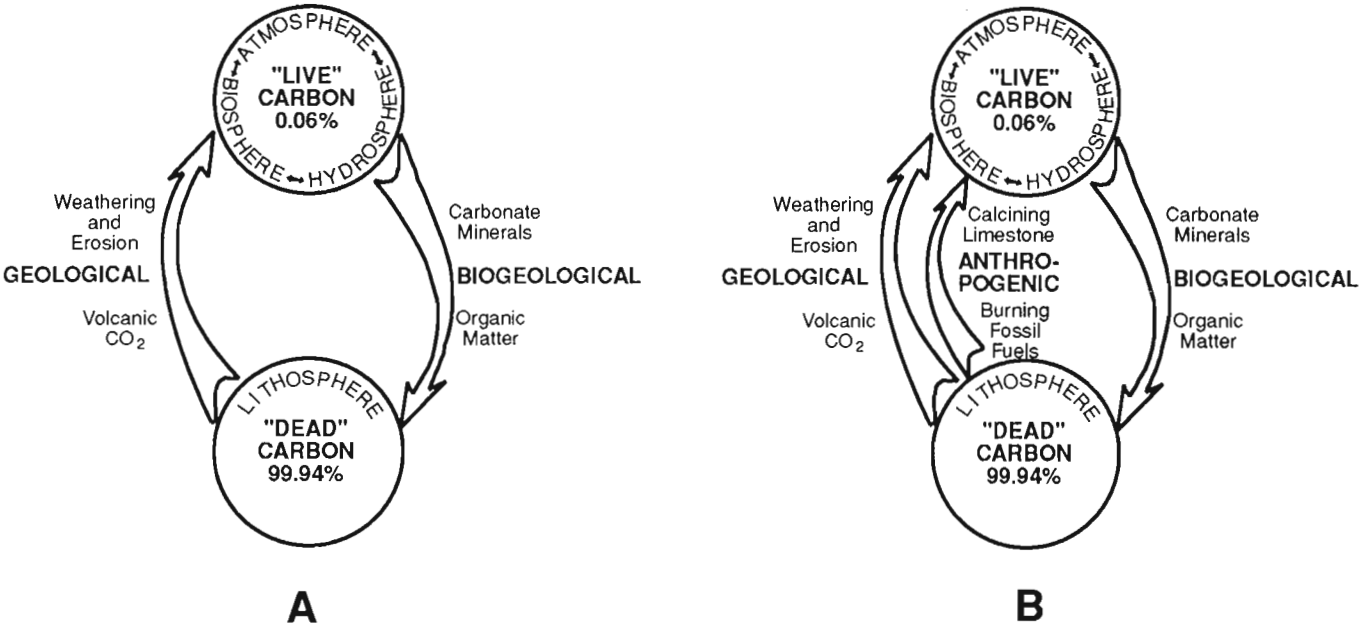


**Figure 2.** Schematic representation of Earth's carbon-based biogeochemical thermostat, prior to industrialization in the early 1800s (2A), and post-industrialization (2B).

the abrupt release of volcanic gases accompanying reorganization of tectonic plates in the North Atlantic; the geological record indicates that four million years were required for the climate to return to normal (McGowran, 1989). Putting this in perspective, our species has only been in existence for a few hundred thousand years.

## FOLLOWING NATURE'S EXAMPLE

When it comes to removing $CO_2$ from the atmosphere and disposing of it safely, we can probably do no better than attempt to duplicate the approach and processes which Nature has used for billions of years. Carbon control and disposal has been so crucial to life on Earth that all options have no doubt been tried, and only the most effective and efficient retained.

### *$CO_2$ is a resource, not a waste*

Before returning carbon to the lithosphere, the natural world uses it to make things, such as living organisms and carbonate shells, spines and skeletons. Thus, $CO_2$ quickly became an essential resource, not a waste to be disposed of. We too should begin to think of $CO_2$ in terms of the useful products that might be made from it.

This approach is analogous to energy-from-waste and recycling programs for our municipal and industrial garbage. The advantage is that a financial return is realized while at the same time the environmental impact is reduced.

### *Carbonate minerals, the preferred disposal medium*

Four times out of five, Nature refossilizes carbon as calcium or calcium-magnesium carbonates (Fig. 1). Because these materials are stable in most surficial and geological environments, $CO_2$ is effectively stored for periods of time that are measured in millennia, not minutes, months or years. Only one time out of five is the organic carbon route chosen.

The problem with the organic option is clearly one of preservation. Highly unstable organic matter must be prevented from releasing greenhouse gases, methane as well as $CO_2$, for hundreds of thousands of years. Attempts to refossilize carbon by artificially increasing the organic productivity of the oceans, or with massive afforestation programs on land, will only achieve their intended objective if the material produced is successfully transferred from the biosphere to the lithosphere. Using coal as an example, we would have to bury, at least as securely as radioactive wastes, a quantity of plant material which will, in time, generate coal deposits equivalent in carbon content to the ones we are currently exploiting. It would make more sense to go back to burning wood and leave the coal in the ground.

There are many valid reasons for planting trees, but doing so to justify the continued use of fossil fuels does not appear to be one of them. Reforestation is an excellent solution to deforestation. Enhancing organic productivity in one region of the ocean is the best way to compensate for reduced productivity somewhere else. These are biological solutions to biological problems, but a geological source of carbon

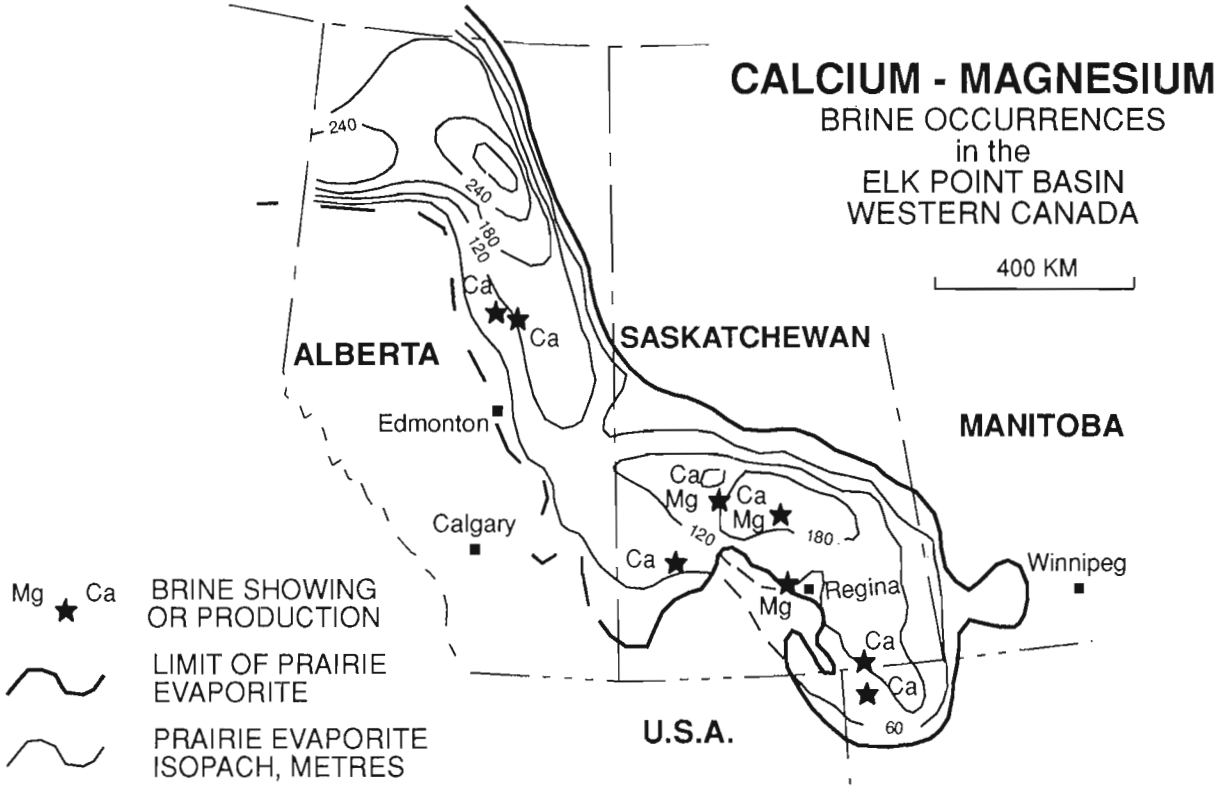


**Figure 3.** Distribution of subsurface brine occurrences in western Canada.

must be matched by a geological sink. Following Nature's example, the best geological solution appears to be the precipitation of stable carbonate minerals.

## SOURCE OF CALCIUM AND MAGNESIUM

To remove $CO_2$ as carbonate minerals would require a massive supply of easily obtained calcium and magnesium in close proximity to the deposits of fossil fuels. The traditional source of these metals has been carbonate rocks, but that's part of the problem. Obtaining them from other types of rocks, such as calcium sulphates or silicates, or from sea water would be prohibitively expensive. There is, however, another source which should be able to meet the requirements.

### *Subsurface evaporitic brines*

Sedimentary basins not only host coal, oil and natural gas, but also extensive deposits of evaporitic salts and brines. These were produced by solar evaporation of sea water in a restricted environment, resulting in the orderly precipitation of carbonate, sulphate and chloride salts. As well, large volumes of highly concentrated sea water in the form of residual brines were also generated. These reactive solutions can be preserved in the subsurface and are today highly enriched in a variety of elements, including calcium, magnesium, bromine, iodine, boron and lithium.

Like fossil fuels, salts and brines represent fossilized solar energy in chemical form; one is the end-product of photosynthesis, the other of evaporitic differentiation. This fact was not lost on the inorganic chemical industry which for many years has consumed large amounts of salts and brines as feedstock for a worldwide industry. In cold climates, we exploit this chemical potential energy in a small way when we spread sodium chloride on our streets and walks to melt the ice.

A number of evaporite deposits and associated brines are found within the large sedimentary basin underlying the western Canadian provinces of Alberta, Saskatchewan and Manitoba. This basin also contains most of Canada's oil and gas, a major share of its coal as well as the vast tar sands deposits. One of the best developed evaporite deposits is the Prairie Evaporite of Middle Devonian age within the Elk Point Basin (Fig. 3). In the Saskatchewan portion of the basin, this unit hosts one of the richest and most extensive potash (KCl) deposits in the world.

The distribution of known brine occurrences in the Elk Point Basin, both calcium- and magnesium-rich, are illustrated in Figure 3. Some of these brines are being produced commercially, some are seeping into potash mines, and some were recovered during exploration for oil and gas. Both types are chloride solutions with specific gravities as high as 1.36. The magnesium brines contain up to 7% magnesium by weight and appear to be restricted to the potash horizons, both being the product of extreme evaporitic differentiation. The calcium-rich brines typically contain 10% calcium, 25% chloride and 39% total dissolved solids. They are much more widely distributed and are hosted by several different formations. There has been no systematic search for these brines, most known occurrences having been discovered by chance, but indications are that the resource is very large indeed.

Brines of these types are, of course, not restricted to western Canada. Sedimentary basins in central and eastern Canada also contain evaporites and similar calcium solutions. Calcium and magnesium brines associated with evaporitic settings have been exploited commercially in other countries for many years.

In summary, subsurface brines are the only source of calcium and magnesium which could be extracted from the crust at a cost and on a scale to match the withdrawal of fossil fuels. Fortunately, the pollutant and potential antidote are spatially correlated, both being found within major sedimentary basins around the world.

## HOW COULD $CO_2$ REMOVAL BE ACHIEVED?

### *The concept*

Capturing $CO_2$ as stable carbonate minerals would require a merging of the resource, energy and chemical industries in a relationship analogous to symbiosis in biology.

Carbon dioxide produced from the combustion of fossil fuels would be passed from the power plant, oil refinery or cement kiln to the chemical plant. Here calcium-rich brine from the subsurface would be used to produce calcium carbonate and hydrochloric acid, which would in turn be passed to secondary industries. Waste brine and spent acid would be injected back into the subsurface. Calcium carbonate surplus to the needs of industry could be returned to the pit from which the coal, for example, was taken; the space formerly occupied by the coal could accommodate about 70% of the total volume of calcium carbonate produced. The chemical plant would also be expected to manufacture a variety of other more traditional chemical commodities from the brine feedstock.

CALCIUM CARBONATE PRECIPITATION

Overall Reaction:

$$Ca^{++}_{(aq)} + CO_{2(g)} + H_2O \rightleftharpoons CaCO_{3(s)} + 2H^+_{(aq)}$$

Four Simultaneous Equilibria:

1. $CO_{2(g)} \longrightarrow CO_{2(aq)}$
2. $CO_{2(aq)} + H_2O \longrightarrow H^+_{(aq)} + HCO_3^-{}_{(aq)}$
3. $HCO_3^-{}_{(aq)} \longrightarrow H^+_{(aq)} + CO_3^{--}{}_{(aq)}$
4. $Ca^{++}_{(aq)} + CO_3^{--}{}_{(aq)} \longrightarrow CaCO_{3(s)}$

**Figure 4.** Hydration of carbon dioxide and precipitation of calcium carbonate.

The concept is, of course, not without its share of problems. The two principal difficulties are that precipitation of calcium carbonate does not proceed on its own accord, and that enormous amounts of hydrochloric acid would be produced.

As can be seen in Figure 4, calcium carbonate precipitation is the result of four simultaneous equilibria. The rate limiting step is apparently the second of the four reactions. Organisms long ago got over this obstacle by inventing a powerful enzyme, carbonic anhydrase, which increases the reaction rate by 100 000 times. As a result, an aqueous solution such as our blood becomes a highly efficient $CO_2$ absorber and transfer medium. It can also be seen that acid would have to be removed from the system at the second and third steps.

The amount of acid produced would seem an even more insurmountable problem at this time. A simple calculation shows that two tonnes of HCl would be produced for each tonne of coal (33° C) burned. The question is immediately asked why the oceans are not acidic considering the amounts of limestone that has been precipitated and buried throughout geological time. It may be that clay minerals carried to the oceans from the continents have neutralized the acid (H.J. Abercrombie, pers. comm.). If so, nonmarine clays and other silicate minerals might be used to consume acid while at the same time extracting useful resources from rocks and minerals. If the chemical route to advanced ceramics dominates the next century, large amounts of acid might be required.

### *Possible methods*

Technology to precipitate calcium carbonate using $CO_2$ and calcium chloride solutions has never been developed. This may be because the problem has not been given much thought. As long as naturally occurring limestone could be used, there was no incentive to do so.

The most exotic route would be to duplicate biological processes, using membranes and powerful organic catalysts like carbonic anhydrase. Some of the most primitive organisms perfected the process over three billions years ago. Recent advances in biotechnology make this less far-fetched than it once was.

It would be technically feasible to capture $CO_2$ as sodium or potassium carbonate using the Solvay process. These materials could then be combined in solution with calcium chloride to precipitate calcium carbonate. It may be technically feasible, but is unlikely to be economically viable.

Another method which has been suggested uses heat to produce magnesium oxide and hydrochloric acid from magnesium chloride and water (Lipinsky, unpublished report, 1991). The magnesium oxide would then be reacted with $CO_2$ to generate magnesium carbonate.

Spray technology has also been proposed. Calcium chloride brine would be atomized in a stream of hot $CO_2$, and the hydrochloric acid separated as a gas on the basis of differential boiling points.

## CONCLUSIONS

If our industrial society wishes to continue to burn fossil fuels in ever-increasing amounts, it must also be prepared to take the steps necessary to clean up the resulting pollution. From a geological perspective, the only secure and lasting solution is to return the $CO_2$ to the lithosphere. It must not simply be dumped into the atmosphere, hydrosphere or biosphere.

Nature's preferred solution is to form carbonate minerals using the calcium and magnesium present in the world's oceans. The organisms that carry out this biomineralization are repaid for their considerable efforts by the useful commodities they have learned to produce, such as shells and skeletons. We can do no better than follow Nature's example.

Nature has not only shown us the way, but has also done the work of concentrating the required calcium and magnesium. These elements are conveniently stored in brines in close proximity to many of the world's fossil fuel deposits. By merging the energy and chemical industries, it should be possible to harness the full chemical potential of both the fossil fuels and the brines and salts.

What today appears to be a serious problem may in fact represent an opportunity. Clearly, it is possible to lock up $CO_2$ by synthesizing calcium carbonate because organisms do it all the time. We only have to figure out how they do it.

## ACKNOWLEDGMENTS

This paper was presented at the First International Conference on Carbon Dioxide Removal held in Amsterdam in March 1992. R.T. Bell is thanked for his constructive comments on the first version of this manuscript.

## REFERENCES

**Berner, R.A. and Lasaga, A.C.**
1989: Modeling the geochemical carbon cycle; Scientific American, March 1989, p. 74-81.

**Francois, L.M. and Walker, J.C.G.**
1992: Modelling the Phanerozoic carbon cycle and climate: constraints from the $^{87}Sr/^{86}Sr$ isotopic ratio of seawater; American Journal of Science, v. 292, p. 81-135.

**Holland, H.D.**
1978: The Chemistry of the Atmosphere and Oceans; Wiley, New York.

**McGowran, B.**
1989: Silica burp in the Eocene ocean; Geology, v. 17, p. 857-860.

**Turner, G.**
1981: The development of the atmosphere; The Evolving Earth, L.R.M. Cocks, (ed.); British Museum and Cambridge Press, London and Cambridge, p. 121-136.

# Laboratory physical property measurements on kimberlites

**T.J. Katsube, N. Scromeda, G. Bernius, and B.A. Kjarsgaard**
**Mineral Resources Division**

*Katsube, T.J., Scromeda, N., Bernius, G., and Kjarsgaard, B.A., 1992: Laboratory physical property measurements on kimberlites; in Current Research, Part E; Geological Survey of Canada, Paper 92-1E, p. 357-364.*

***Abstract***

*Search for kimberlite-hosted diamond deposits in Canada has become a subject of interest, with continuing and new exploration activity in Saskatchewan, Alberta, Ontario and the Northwest Territories. Physical property measurements were made on 23 Canadian kimberlite samples to obtain information that might lead to further development of geophysical methods to effectively detect kimberlites below overburden.*

*Results show that physical properties may be related to mineralogy (primary and secondary) and petrographic textural type (crater, diatreme or hypabyssal facies). Crater and diatreme facies rocks appear relatively porous compared to the hypabyssal facies, tending to be more susceptible to alteration. Altered kimberlites appear to have higher porosity, lower electrical resistivity and lower density compared to fresh kimberlites. Magnetic susceptibility varies among samples representing different kimberlite fields, and among samples taken within single fields. The magnetic susceptibility values in this paper are within previously reported values for kimberlites.*

***Résumé***

*Au Canada, les gisements diamantifères contenus dans des kimberlites sont devenus une cible intéressante; des travaux d'exploration (anciens projets qui se poursuivent ou nouveaux entrepris) sont effectués en Saskatchewan, en Alberta, en Ontario et dans les territoires du Nord-Ouest. Les propriétés physiques de 23 échantillons de kimberlites canadiennes ont été mesurées pour obtenir de l'information qui pourrait aider à la mise au point de méthodes géophysiques efficaces de détection des kimberlites recouvertes de morts-terrains.*

*Les résultats montrent que les propriétés géophysiques peuvent être associées à la minéralogie (primaire et secondaire) et au type de texture pétrographique (cratère, diatrème ou faciès hypovolcanique) des lithologies. Les roches des faciès de cratère et de diatrème sont relativement poreuses par rapport à celles du faciès hypovolcanique, qui tendent à être plus sensibles à l'altération. Les kimberlites altérées semblent posséder une porosité plus élevée mais une résistivité électrique et une densité plus faibles que les kimberlites fraîches. La susceptibilité magnétique est variable, que les échantillons proviennent de différents domaines kimberlitiques ou d'un seul d'entre eux. Les valeurs de susceptibilité magnétique citées dans cet article se situent dans la gamme de celles antérieurement citées pour les kimberlites.*

[1] Contribution to Canada-Northwest Territories Economic Development Agreement Minerals Initiative, 1991-1996 and Canada-Saskatchewan Partnership Agreement on Mineral Development 1990-1995. Funded by Geological Survey of Canada

## INTRODUCTION

The search for kimberlite-hosted diamond deposits in Canada has recently become a subject of great interest, with continuing and new exploration activity in Saskatchewan, Alberta, Ontario and the Northwest Territories (Kjarsgaard and Peterson, 1992; Northern Miner, March 30, 1992). The use of airborne magnetics and electromagnetics as a viable exploration tool for kimberlites has been demonstrated in Siberia, Botswana and Australia (summarized in Atkinson, 1989). To obtain basic physical property information that might lead to further development of geophysical methods to effectively detect kimberlites below overburden and distinguish them from surrounding country rocks, electrical resistivity, formation factor, magnetic susceptibility, density and porosity measurements have been carried out on kimberlite samples. The sample suite includes kimberlites from Somerset Island (Northwest Territories) and Sturgeon Lake (Saskatchewan), as shown in Figure 1.

**Table 1.** Sample identification

| Sample Number | Sampling Location | Sample I.D. |
|---|---|---|
| SI-1 | Somerset Island, N.W.T. | PHA90-HD |
| SI-2 | Somerset Island, N.W.T. | PHA90-K4A |
| SI-3 | Somerset Island, N.W.T. | PHA90-K10D |
| SI-4 | Somerset Island, N.W.T. | PHA90-K10E |
| SI-5 | Somerset Island, N.W.T. | PHA90-K15B |
| SI-6 | Somerset Island, N.W.T. | PHA90-K22A |
| SI-7 | Somerset Island, N.W.T. | PHA90-K23A |
| SI-8 | Somerset Island, N.W.T. | PHA90-PC-1 |
| SI-9 | Somerset Island, N.W.T. | PHA90-J1A |
| SL-1 | Sturgeon Lake, Saskatchewan | SEM-KIM-2 |
| SL-2 | Sturgeon Lake, Saskatchewan | KIA91-MP-SLPJ2 |
| SL-3 | Sturgeon Lake, Saskatchewan | SEM-KIM-3 |
| SL-4 | Sturgeon Lake, Saskatchewan | SEM-KIM-4 |
| SL-5 | Sturgeon Lake, Saskatchewan | SEM-KIM-5 |
| SL-6 | Sturgeon Lake, Saskatchewan | SEM-KIM-6 |
| SL-7 | Sturgeon Lake, Saskatchewan | SEM-KIM-7 |
| SL-9 | Sturgeon Lake, Saskatchewan | SEM-KIM-9 |
| SL-10 | Sturgeon Lake, Saskatchewan | HDB-89-2 |
| SL-11 | Sturgeon Lake, Saskatchewan | HDB-89-3a |
| SL-12 | Sturgeon Lake, Saskatchewan | HDB-89-3b |
| SL-13 | Sturgeon Lake, Saskatchewan | HDB-89-8 |
| SL-14 | Sturgeon Lake, Saskatchewan | HDB-89-10 |
| SL-15 | Sturgeon Lake, Saskatchewan | HDB-89-11b |

## METHOD OF INVESTIGATION

### *Samples and sample preparation*

Twenty three (23) drill core and hand kimberlite samples were collected from the two areas in Canada for this study. The sample numbers, sampling locations and identification numbers are listed in Table 1. Measurement of magnetic susceptibility and bulk density were made for all 23 samples, electrical resistivity and porosity for 15 samples and formation factor for 3 samples.

Most of the hand samples had at least one flat surface. Magnetic susceptibility and one set of bulk density (buoyancy method) measurements were made on these hand and core samples. Then, rectangular specimens were cut out from these core and hand samples for electrical resistivity, formation factor, porosity and another set of bulk density (caliper method) measurements. The geometric characteristics of the rectangular specimens used for electrical measurements and the second set of bulk density measurements are listed in Table 2. Their dimensions are in the order of (1.3-2.2)x(1.5-2.4) cm for the cross-section, and 0.3-1.2 cm for thickness. Remaining chips, instead of the

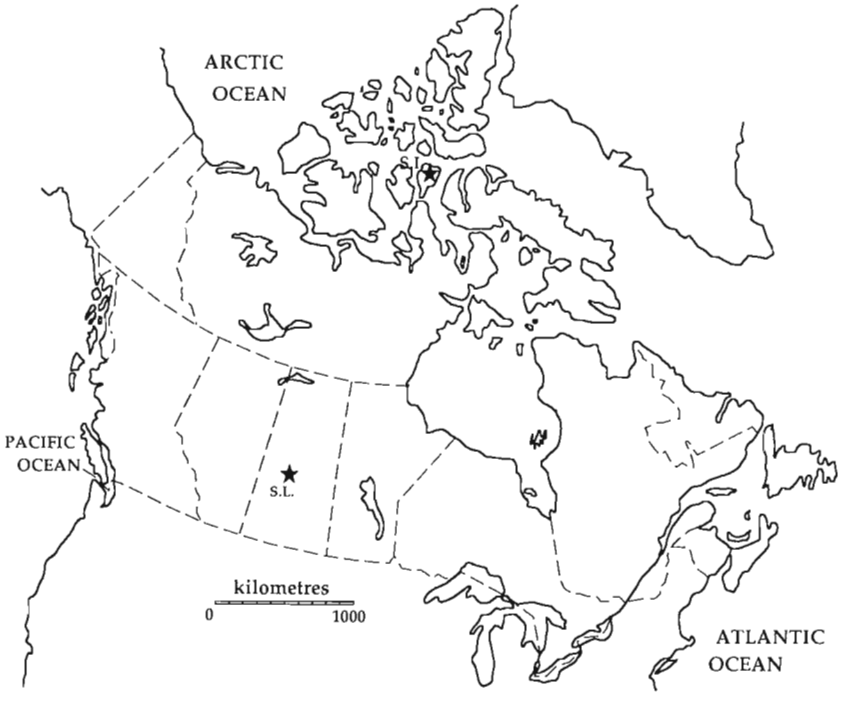


**Figure 1.**

Locations of the sites from which the two sample suites have been obtained. Detailed map of the sampled sites for the Somerset Island suite can be found in Kjarsgaard and Peterson (1992). S.I. and S.L. on the map represent the Somerset Island (Northwest Territories) and Sturgeon Lake (Saskatchewan) sites.

**Table 2.** Dimensions of specimens cut out from the kimberlite samples for electrical measurements

| Sample No. | $a_1$ (cm) | $a_2$ (cm) | $\ell$ (cm) | W (g) | $K_G$ ($10^{-2}$ m) | $\delta_E$ (g/mL) |
|---|---|---|---|---|---|---|
| SI-1/1 | 1.741 | 2.203 | 0.844 | 8.6838 | 4.54 | 2.68 |
| SL-1/1 | 1.475 | 1.786 | 1.001 | 8.1847 | 2.63 | 3.11 |
| SL-1/3 | 1.444 | 1.786 | 0.346 | 2.9741 | 7.45 | 3.11 |
| SL-2/1 | 1.600 | 1.688 | 0.914 | 6.0620 | 2.96 | 2.46 |
| SL-3/1 | 2.015 | 2.166 | 1.183 | 12.2388 | 3.69 | 2.37 |
| SL-4/1 | 2.230 | 2.197 | 1.094 | 13.3356 | 4.48 | 2.49 |
| SL-5/1 | 1.440 | 1.702 | 0.518 | 4.0640 | 4.73 | 3.08 |
| SL-6/1 | 1.630 | 1.731 | 0.535 | 3.9278 | 5.28 | 2.60 |
| SL-7/1 | 1.849 | 1.550 | 0.428 | 3.3181 | 6.70 | 2.64 |
| SL-9/1 | 1.373 | 1.929 | 0.900 | 6.1444 | 2.94 | 2.53 |
| SL-10/1 | 1.049 | 1.589 | 0.628 | 3.3561 | 2.65 | 3.09 |
| SL-11/1 | 1.319 | 2.270 | 1.083 | 9.2596 | 2.77 | 2.86 |
| SL-11/2 | 1.313 | 2.259 | 0.378 | 3.3608 | 7.85 | 2.86 |
| SL-12/1 | 1.475 | 2.416 | 0.552 | 5.4855 | 6.83 | 2.95 |
| SL-13/1 | 1.519 | 1.635 | 0.665 | 5.0644 | 3.74 | 3.01 |
| SL-14/1 | 1.294 | 1.768 | 0.466 | 3.4660 | 4.91 | 3.23 |
| SL-15/1 | 1.868 | 2.199 | 0.899 | 11.0615 | 4.57 | 3.00 |
| SL-15/3 | 1.872 | 2.194 | 0.354 | 4.5994 | 11.60 | 3.00 |

$a_1$, $a_2$: Length of the two sides of the rectangular specimen.
$\ell$: Thickness of specimen.
W: Weight of specimen under room dry conditions.
$K_G$: Geometric factor.
$\delta_E$: Specific density (equation 2)

rectangular specimens, were used for effective porosity measurements for some of the samples. Two or more rectangular specimens were cut out from some samples.

The geometric factor, $K_G$, which is used in the electrical measurements was determined for all of the rectangular specimens by the following equation:

$$K_G = A/\ell \qquad (1)$$

$$A = a_1 a_2,$$

where $a_1$ and $a_2$ are the lengths of the two sides of the rectangular specimen, and $\ell$ is its thickness.

### *Bulk density measurements*

Two methods, caliper and buoyancy methods, have been used to determine the bulk density, $\delta$, of the samples. One, the caliper method, requires measurement of dimensions and weight of the specimens and is derived from

$$\delta_E = A\ell / W, \qquad (2)$$

where $\delta_E$ in the bulk density determined by this method and W is the weight of the room-dry (humidity 40%) specimen. This measurement constitutes part of the porosity determining procedure. The other, the buoyancy method, requires measurement of the specimen weight in air and submerged in water and is derived from

$$\delta_M = W_a \delta_w / (W_a - W_w), \qquad (3)$$

where $\delta_M$ is the bulk density determined by this method, $\delta_w$ is the density of the water, and $W_a$ and $W_w$ are the weights of the specimen in air and in water (White, 1956).

### *Effective porosity measurements*

Effective porosity, $\Phi_E$, in principle represents the pore volume of all interconnected pores, and is determined from the difference in weight between the oven-dried and water-saturated rock specimen (Katsube and Scromeda, 1991):

$$\Phi_E = \delta_E(W_w - W_D) / (\delta_w W_D) \qquad (4)$$

where $W_w$ and $W_D$ are the wet and dry weight of the rock specimen. A separate study showed the porosity variation within a sample to be 10 per cent for gneisses (Wadden and Katsube, 1982). Long duration times for saturating and oven drying have been used to determine $W_w$ and $W_D$, following the recommended practices for tight rocks described in Katsube and Scromeda (1991). The API Recommended Practice for Core-Analysis Procedures (API, 1960) has generally been followed in these recommendations. Further details of the technique, including its advantages and limitations are described in these papers (API, 1960; Katsube et al., 1992a).

The irreducible water saturation, $S_{ir}$, represents the water content remaining in the sample after a long vacuum drying time, and is defined as follows:

$$S_r = (W_r - W_D) / (W_W - W_D), \qquad (5)$$

where $W_r$ is the weight of the sample after the long vacuum drying time at 25°C. Details of this measuring procedure is described in Katsube et al. (1992a).

### *Complex electrical resistivity and formation factor*

The method used for the complex electrical resistivity and formation-factor measurement of these samples has been described previously (Katsube, 1981; Katsube and Walsh, 1987), and recently in Katsube et al. (1991a,b) and Katsube and Salisbury (1991).

The complex resistivity, $\rho^*$ (Katsube and Collett, 1975; Katsube 1975):

$$\rho^* = \rho_R + i\rho_I, \qquad (6)$$

where $\rho_R$ is the real resistivity and $\rho_I$ is the imaginary resistivity, is derived from the impedance $Z(\theta)$ measurements by

$$\rho^* = K_G Z(\theta), \quad (7)$$

**Table 3.** Magnetic susceptibility (MS) and density ($\delta_M$) of the kimberlite samples

| Sample | $\delta_E$ (g/c) | $\delta_M$ (g/mL) | MS (in $10^{-3}$ S.I. units) | Mean MS |
|---|---|---|---|---|
| SI-1 | 2.68 | 2.68 | | 20. |
| SI-2 | | 2.83 | 6.0 - 10.5 | 8.0 |
| SI-3 | | 2.53 | 18. - 27. | 25. |
| SI-4 | | 2.78 | 3.2 - 4.1 | 4.0 |
| SI-5 | | 2.64 | 18. - 36. | 24. |
| SI-6 | | 2.77 | 3.5 - 5.3 | 5.0 |
| SI-7 | | 2.86 | 8.0 - 13. | 12. |
| SI-8 | | 2.77 | 2.5 - 3.6 | 3.0 |
| SI-9 | | 3.00 | 10. - 15. | 15. |
| SL-1 | 3.11 | 2.87 | 2.0 - 3.7 | 2.6 |
| SL-2 | 2.46 | 2.43 | 0.8 - 1.3 | 1.5 |
| SL-3 | 2.37 | 2.33 | | 0.9 |
| SL-4 | 2.49 | 2.34 | 1.2 - 2.5 | 1.7 |
| SL-5 | 3.08 | 2.94 | | 1.9 |
| SL-6 | 2.60 | 2.40 | 1.5 - 2.0 | 1.8 |
| SL-7 | 2.64 | 2.44 | | 1.6 |
| SL-9 | 2.53 | 2.43 | | 1.5 |
| SL-10 | 3.09 | 2.86 | | 2.5 |
| SL-11 | 2.86 | 2.71 | | 2.0 |
| SL-12 | 2.95 | 2.74 | | 2.1 |
| SL-13 | 3.01 | 2.85 | 1.4 - 2.9 | 1.7 |
| SL-14 | 3.23 | 2.76 | | 2.4 |
| SL-15 | 3.00 | 2.85 | | 1.7 |

$\delta_E$ = Density determined using Equation (2).
$\delta_M$ = Density determined using Equation (3).
MS = Magnetic susceptibility.

**Table 4.** Results of the effective porosity measurements

| Sample | $\delta_E$ (g/mL) | $W_W$ (g) | $W_D$ (g) | $S_{ir}$ (%) | $0_E$ (%) |
|---|---|---|---|---|---|
| SI-1 | 2.68 | 5.8884 | 5.8205 | 25.9 | 3.13 |
| SL-1 | 3.11 | 12.8458 | 12.7726 | 65.6 | 1.78 |
| SL-2 | 2.46 | 6.2678 | 5.8157 | 6.9 | 19.12 |
| SL-3 | 2.37 | 5.4166 | 5.0342 | 17.3 | 18.00 |
| SL-4 | 2.49 | 8.3267 | 7.8304 | 17.6 | 15.78 |
| SL-5 | 3.08 | 6.1865 | 6.1466 | 45.1 | 2.00 |
| SL-6 | 2.60 | 11.7986 | 11.1816 | 25.5 | 124.35 |
| SL-7 | 2.64 | 6.3006 | 6.0553 | 9.2 | 10.69 |
| SL-9 | 2.53 | 11.9724 | 11.3420 | 23.3 | 14.06 |
| SL-10 | 3.09 | 4.6350 | 4.5535 | 30.9 | 5.53 |
| SL-11 | 2.86 | 9.4062 | 9.2725 | 68.8 | 4.12 |
| SL-12 | 2.95 | 3.3936 | 3.3482 | 56.0 | 4.00 |
| SL-13 | 3.01 | 3.1139 | 3.0811 | 51.2 | 3.20 |
| SL-14 | 3.23 | 7.3168 | 7.2755 | 60.1 | 1.83 |
| SL-15 | 3.00 | 9.4660 | 9.3576 | 75.5 | 3.48 |

$W_w$ = wet weight
$W_D$ = dry weight
$S_{ir}$= irreducible water saturation
$\delta_E$ = bulk density (equation 2)
$\phi_E$ = effective porosity

where $\theta$ is the phase angle. The bulk rock resistivity, $\rho_r$, is determined from the complex resistivity ($\rho^*$), by the method described in Katsube (1975) and Katsube and Walsh (1987), or in more recent publications (e.g., Katsube et al., 1991a; Katsube and Salisbury, 1991).

The formation factor, F, is determined by taking the ratio of the bulk rock resistivity ($\rho_r$) over the pore fluid resistivity, $\rho_w$ (Archie, 1942), and is a parameter representing one of the pore structure characteristics of the rock. To eliminate the pore surface electrical conductivity effect (Patnode and Wyllie, 1950), F is actually derived by measuring the bulk resistivity ($\rho_r$) of the rock for solutions of different salinities (NaCl: 0.02, 0.05, 0.10, 0.20 and 0.50 N), and then inserting the results into an equation derived from the Patnode and Wyllie (1950, Equation 1) equation:

$$1/F_a = 1/F + \rho_w/\rho_c \quad (8)$$

where

$F_a = \rho_r/\rho_w$

$\rho_c = F\rho_s d$

$F_a$ = apparent formation factor

$\rho_c$ = bulk surface resistivity

$\rho_s$ = surface resistivity

d = pore aperture.

Complex resistivity and formation-factor were determined at room temperature conditions. The measurement errors for these samples are estimated to be in the ranges of 10-20 per cent and 20-40 per cent, respectively (Wadden and Katsube, 1982; Katsube, 1981). Further details of the measuring procedures used for these samples can be found elsewhere (Katsube, 1981; Katsube and Walsh, 1987; Katsube, et al., 1991a; Katsube and Salisbury, 1991).

### *Magnetic susceptibility measurements*

Magnetic susceptibility measurements were made on the hand samples using the hand-held JH-8 manufactured by Geoinstruments (Finland). This instrument is an analog type which is used to scan the surface of a sample to determine the range of magnetic susceptibility, MS, values. As a parameter which indicates the ease at which a rock becomes magnetized in a low magnetic field, magnetic susceptibility (MS) is a function, in the first instance, of the concentration of magnetic minerals such as magnetite (Grant and West, 1965; Latham et al., 1987) in a sample. Weathering of magnetite usually results in a change of magnetic susceptibility (MS) values. Weathering of magnetite to a mineral with lower susceptibilities, such as to hematite which has a magnetic susceptibility (MS) of about a factor of 1000 times lower than magnetite (Telford et al., 1976), has allowed low magnetic susceptibility (MS) values to be related to alteration (e.g., Latham et al., 1987).

**Table 5.** Results of electrical resistivity measurements

| Sample/ Specimen | Bulk Electrical Resistivity, $\rho_r$, ($10^3$ Ωm) Measurement (#1) | Measurement (#2) | Mean |
|---|---|---|---|
| SI-1/1 | 36.8 | 39.1 | 37.9 |
| SL-1/1* | 26.9 | 27.0 | 27.0 |
| SL-1/3 | 40.9 | 50.3 | 45.6 |
| SL-2/1 | 0.53 | 0.60 | 0.56 |
| SL-3/1 | 0.35 | 0.35 | 0.35 |
| SL-4/1 | 0.94 | 0.95 | 0.95 |
| SL-5/1* | 53.7 | 49.3 | 51.5 |
| SL-6/1 | 0.41 | 0.43 | 0.42 |
| SL-7/1 | 0.37 | 0.40 | 0.39 |
| SL-9/1 | 1.51 | 1.49 | 1.50 |
| SL-10/1* | 34.1 | 30.4 | 32.3 |
| SL-11/1* | 31.5 | 32.2 | 31.9 |
| SL-11/2 | 58.1 | 54.2 | 56.4 |
| SL-12/1 | 59.2 | 65.1 | 62.1 |
| SL-13/1 | 25.2 | 29.3 | 27.3 |
| SL-14/1* | 58.9 | 58.3 | 58.6 |
| SL-15/1* | 41.1 | 35.0 | 38.1 |
| SL-15/3 | 51.8 | 51.0 | 51.8 |

Measurement (#1) : Measurement after 24 hours of saturation.
Measurement (#2) : Measurement after 48 hours of saturation.

* High resistivity interferences detected by complex resistivity plots (Katsube et al., 1992b).

## EXPERIMENTAL RESULTS

The results of bulk density determination ($\delta_E$) using equation (2) are listed in Tables 2 and 3. The dimensions of the specimens used for electrical measurements are also listed in Table 2. The results of the magnetic susceptibility and bulk density ($\delta_M$) measurements using equation (3) are listed in Table 3. A slight difference between the two bulk densities are seen. The bulk density values are in the range of 2.4 - 3.2 g/mL. The larger values are in the larger end of bulk densities for rocks (Daly et al., 1966), resembling those of basic rocks. The smaller values are in the lower end of the reported values for rocks (Daly et al., 1966), resembling those for sedimentary rocks.

The results of the magnetic susceptibility measurements are listed in Table 3. Magnetic susceptibilities are in the range of $(2.5 - 36)\times10^{-3}$ S.I. units for the Somerset Island and $(0.8 - 3.7)\times10^{-3}$ S.I. units for the Sturgeon Lake samples. The larger values are within the range of those for ultramafic intrusive rocks (Grant and West, 1965).

The results of the effective porosity ($\Phi_E$) measurements are listed in Table 4, their values being in the range of 1.8 - 19.1 per cent (%). These values resemble those of sedimentary rocks (Daly et al., 1966), the larger ones being similar to those of sandstones, while the smaller ones resemble those of shales and carbonates.

The results of the electrical resistivity ($\rho_r$) measurements are listed in Table 5, the values being in the range of 350 - $6.2\times10^4$ Ω-m for the samples from Somerset Island and Sturgeon Lake. This is a wide range of variation, the smaller values resembling those of Paleozoic and Precambrian

**Table 6.** Formation-factor, surface resistivity and bulk resistivities for different NaCl solutions for kimberlite samples

| Samples | $\rho_{rn}$ ($\times10^3$ Ω· m) | | | | | F ±% ($\times10^2$) | $\rho_c$ ±% ($\times10^3$) (Ω· m) |
|---|---|---|---|---|---|---|---|
| $\rho_w$ (Ω· m) NaCl (N) | 0.32 ±0.02 0.5 | 0.70 ±0.03 0.2 | 1.25 ±0.05 0.1 | 2.09 ±0.09 0.05 | 4.75 ±0.23 0.02 | | |
| SL-1/3 | 0.75 X | 1.10 | 2.6 X | 3.8 X | 9.6 X | 16.7 23.1±18. | - 37.6±120 |
| SL-4/1 | 0.21 | 0.39 | 0.55 | 0.66 | 1.3 | 6.46± 4.8 | 1.95± 7.6 |
| SL-7/1 | 0.021 | 0.042 | 0.075 | 0.11 | 0.17 | 0.72± 0.4 | 0.35± 1.2 |

$\rho_w$ = pore fluid resistivity
$\rho_{rn}$ = bulk resistivity of the rock for solutions of different salinities
F = formation-factor
$\rho_c$ = surface resistivity
X = data points used for formation factor determination

sedimentary and volcanic rocks (Keller, 1966), and the larger ones resembling those of crystalline rocks (Katsube and Hume, 1987a, 1989).

Besides the electrical resistivity measurement errors that were previously described, there are errors caused by measurement limitations (Gauvreau and Katsube, 1975). Examples of high resistivity interferences are given in Katsube et al. (1992b), which result in measured resistivities being smaller than the true values. These effects can be detected from the complex resistivity plots, as described in Katsube et al. (1992b). Most specimens that showed such effects were reduced in thickness and remeasured with improved accuracy. Measurements that showed indications of error due to high resistivity interference are noted in Table 5. They are considered to be about 30-40% smaller than the true values.

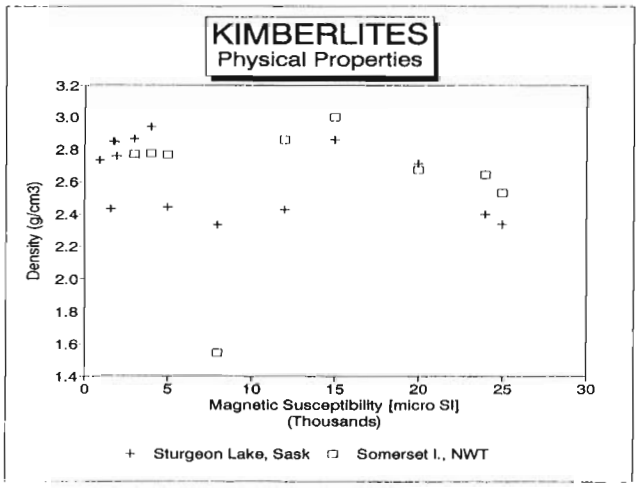


**Figure 2.** The relationship between magnetic susceptibility (MS) and bulk density ($\delta_M$), for all of the 23 kimberlite samples.

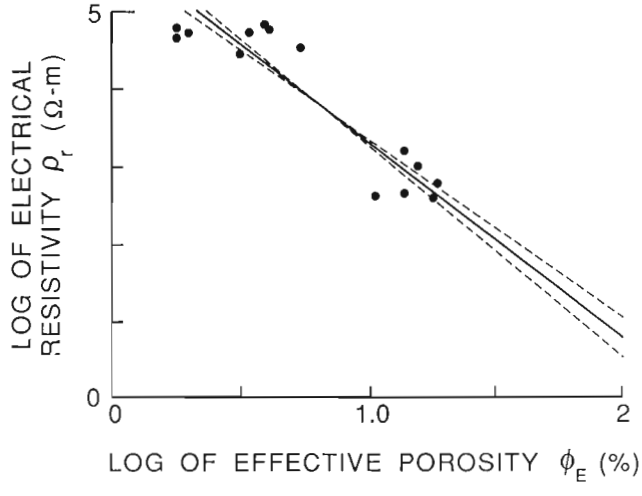


**Figure 3.** The relationship between effective porosity ($\Phi_E$) and bulk electrical resistivity ($\rho_r$) for Sturgeon Lake (Saskatchewan) samples.

Results of resistivity measurements for the formation factor determinations of the 3 samples are listed in Table 6. The quality of the data for sample/specimens SL-4/1 and SL-7/1 is good, with error ranges for both formation factor (F) and bulk surface resistivity ($\rho_c$) below 8%. Measurement for sample/specimens SL-1/3 did not show a good result with large error ranges. Repeated data analysis to determine the two parameters for this sample/specimens resulted in a slight improvement, with the errors below 18 and 120 % for the two parameters. The data points above the "X's" in Table 6 were used in the repeated analysis for this purpose. The formation factor value of $2.3 \times 10^3$ for sample/specimen SL-1/3 resembles that of a crystalline rock (Katsube and Hume, 1987b, 1989), and the values for the other two sample/specimens resemble those of sedimentary rocks (Keller, 1966).

## DISCUSSION AND CONCLUSIONS

The bulk density ($\delta_E$) determined using the caliper method is generally larger than that ($\delta_M$) measured by the buoyancy method (Table 3). The bulk density, $\delta_M$, is likely to be smaller than the true value in many cases, because of water penetrating the sample when measuring $W_W$ in the water (equation 3). That is:

$$W_W = V\delta_M - (V - \Delta V)\delta_w \qquad (9)$$

where V is the volume of the specimen and $\Delta V$ is the volume of water that penetrated the specimen. From this equation,

$$\delta_M = \{(V - \Delta V)/V\}\{\delta_w W_a/(W_a - W_w)\}. \qquad (10)$$

When compared with equation (3), equation (10) shows that $\delta_M$ is smaller than the true values for values of $\Delta V$ larger than zero. However, the samples with the larger difference between $\delta_E$ and $\delta_M$ (Table 3) are not necessarily the ones with larger porosities (Table 4). Therefore, this explanation alone is not conclusive. Future pore-size distribution measurements are likely to provide further explanation.

The results of the physical property measurements (Tables 3-5, Fig. 2) show a range of values which may be related to the variation in mineralogy (primary and secondary) and petrographic textural type (crater, diatreme or hypabyssal facies), using the classification system outlined by Clement and Skinner (1979). Generally, crater and diatreme facies rocks appear to be relatively porous as compared to the hypabyssal facies, and as a result probably tend to be more susceptible to alteration (secondary clay minerals and carbonates). The lack of good correlation between the bulk density and magnetic susceptibility (Fig. 2) will likely provide interesting information on the mineralogical characteristics of these samples.

At a first approximation, there is a relatively good correlation between the degree of alteration of the kimberlites and the physical properties (Tables 3-5). Altered kimberlites appear to have high porosity, low electrical resistivity and low density, whereas fresh kimberlites have lower porosities, higher resistivities and higher densities, as shown by the Sturgeon Lake samples. The relationship between porosity and electrical resistivity is shown in Figure 3. Further studies are underway to determine the quantitative relationship

between the mineralogy and the physical properties. For example, the possibility of distinguishing between fresh porous rocks and altered porous rocks by a combination of physical property measurements is being investigated.

Variation in magnetic susceptibility ($5x10^{-4}$ - $7x10^{-2}$ S.I. units) is seen between samples representing different kimberlite fields, and also between samples taken within a kimberlite field. Previously reported kimberlite magnetic susceptibilities (MS) are $(1.26\text{-}75.4)x10^{-3}$ S.I. units for Yakutian (Siberia) kimberlites (Gerryts, 1970), and $(0.63\text{-}75.4)x10^{-3}$ S.I. units for Lesotho (Africa) kimberlites (Nixon, 1973). Therefore, our magnetic susceptibility values fall within these reported ranges of values.

## ACKNOWLEDGMENTS

The authors acknowledge support from the Canada-Northwest Territories 1991-1996 Mineral Initiative, and from the Canada-Saskatchewan Mineral Development Agreement for Kimberlite Studies (1990-1995) for this study. The authors are grateful to the mining companies that provided the Sturgeon Lake (Saskatchewan) samples used in this study. K.A. Richardson (Geological Survey of Canada) critically reviewed this paper and K.L. Buchan (Geological Survey of Canada) provided advice and suggestions regarding some of the measurements. The authors also thank C. Gauvreau (Geological Survey of Canada) for reviewing the text on the electrical measuring system.

## REFERENCES

**API (American Petroleum Institute)**
1960: Recommended practices for core-analysis procedure: API Recommended Practice 40 (RP 40) First Edition, American Petroleum Institute, Washington, D.C., p. 55.

**Archie, G.E.**
1942: The electrical resistivity log as an aid in determining some reservoir characteristics; Transactions of the American Institute of Mining, Metallurgical and Petroleum Engineers, v. 146, p. 54-67.

**Atkinson, W.J.**
1989: Diamond exploration philosophy, practice and promises; a review; in Proceedings of the Forth International Kimberlite Conference, Kimberlites and Related Rocks, Volume 2, J. Ross (ed.); Geological Society of Australia, Special Publication 14, p. 1075-1107.

**Clement, C.R. and Skinner, E.M.W.**
1979: A textural genetic classification of kimberlite rocks (Extended Abstract); in Proceedings of the Kimberlite Symposium II, Cambridge, p.14.

**Daly, R.A., Manger, E.G., and Clark, S.P., Jr.**
1966: Density of rocks: Section 4; in Handbook of Physical Constants; Geological Society of America, Inc. Mem. 97, p. 19-26.

**Gauvreau, C. and Katsube, T.J.**
1975: Automation in electrical rock property measurements; in Report of Activities, Part A; Geological Survey of Canada, Paper 75-1A, p. 83-86.

**Grant, F.S. and West, G.F.**
1965: Interpretation Theory in Applied Geophysics; McGraw-Hill, p. 355-381.

**Gerryts, E.**
1970: Diamond prospecting by geophysical methods; a review; in Mining and Ground Water Geophysics, L.W. Morley (ed.); Geological Survey of Canada Economic Geology Report 26, p. 439-446.

**Katsube, T.J.**
1975: The electrical polarization mechanism model for moist rocks; in Report of Activities, Part C; Geological Survey of Canada, Paper 75-1C, p. 353-360.
1981: Pore structure and pore parameters that control the radionuclide transport in crystalline rocks; Proceedings of the Technical Program, International Powder and Bulk Solids Handling and Processing, Rosemont, Illinois, p. 394-409.

**Katsube, T.J. and Collett, L.S.**
1975: Electromagnetic propagation characteristics of rocks; in "The Physics and Chemistry of Rocks and Minerals", R.G.J. Strens (ed.); John Wiley & Sons Ltd., p. 279-295.

**Katsube, T.J. and Hume, J.P.**
1987a: Electrical properties of granitic rocks in Lac du Bonnet batholith; in Geotechnical Studies at Whiteshell Research Area (RA-3); CANMET Report MRL 87-52, p. 205-220.
1987b: Pore structure characteristics of granitic rock samples from Whiteshell Research Area; in Geotechnical Studies at Whiteshell Research Area (RA-3); CANMET Report MRL 87-52, p. 111-158.
1989: Electrical resistivity of rocks from Chalk River; in Workshop Proceedings on "Geophysical and Related Geoscientific Research at Chalk River, Ontario"; Atomic Energy of Canada Limited Report AECL-9085, p. 105-114.

**Katsube, T.J. and Salisbury, M.**
1991: Petrophysical characteristics of surface core samples from the Sudbury structure; in Current Research, Part E; Geological Survey of Canada, Paper 91-1E, p. 265-271.

**Katsube, T.J. and Scromeda, N.**
1991: Effective porosity measuring procedure for low porosity rocks; in Current Research, Part E; Geological Survey of Canada, Paper 91-1E, p. 291-297.

**Katsube, T.J. and Walsh, J.B.**
1987: Effective aperture for fluid flow in microcracks; International Journal of Rock Mechanics and Mining Sciences and Geomechanics Abstracts, v. 24, p. 175-183.

**Katsube, T.J., Best, M.E., and Mudford, B.S.**
1991a: Petrophysical characteristics of shales from the Scotian shelf: Geophysics, v. 56, p. 1681-1689.

**Katsube, T.J., Mareschal, M., and Aucoin, F.**
1991b: Electrical characteristics of a graphitic rock from the Kapuskasing Structural Zone; in Current Research, Part E; Geological Survey of Canada, Paper 91-1E, p. 257-263.

**Katsube, T.J., Scromeda, N., and Williamson, M.**
1992a: Effective porosity of tight shales from the Venture Gas Field, offshore Nova Scotia; in Current Research, Part D; Geological Survey of Canada, Paper 92-1D, p. 111-119.

**Katsube, T.J., Scromeda, N., Mareschal, M., and Bailey, R.C.**
1992b Electrical resistivity and porosity of crystalline rock samples from the Kapuskasing Structural Zone, Ontario; Geological Survey of Canada, Paper 92-1E, p. 257-263.

**Keller, G.V. and Frischknecht, F.C.**
1966: Electrical Methods in Geophysical Prospecting; Pergamon Press, New York, 517 p.

**Kjarsgaard, B.A. and Peterson, T.D.**
1992: Kimberlite-derived ultramafic xenoliths from the diamond stability field; a new Cretaceous geotherm for Somerset Island, North West Territories; in Current Research, Part B, Geological Survey of Canada, Paper 92-1B, p. 1-6.

**Latham, A.G., Morris, W.A., and Lapointe, P.**
1987 Magnetic properties of Lac du Bonnet borecores, Manitoba; in Geotechnical Studies at Whiteshell Research Area (RA-3); CANMET Report MRL 87-52, p. 187-202.

**Nixon, P.H. (Ed.)**
1973: Lesotho Kimberlites: Lesotho National Development Corporation, Mesuru, 350 p.

**Patnode, H.W. and Wyllie, M.R.J.**
1950: The presence of conductive solids in reservoir rocks as a factor in electric log interpretation: Transactions of the American Institute of Mining, Metallurgical and Petroleum Engineers, v. 189, p. 47-52.

**Sheriff, R.E.**
1974: Encyclopedic Dictionary of Exploration Geophysics; Society of Exploration Geophysics.
**Telford, W.M., Geldart, L.P., Sheriff, R.E., and Keys, D.A.**
1976: Magnetic susceptibilities of various minerals, Table 3; in Applied Geophysics, Cambridge University Press, p. 860.
**Wadden, M.M. and Katsube, T.J.**
1982: Radionuclide diffusion rates in crystalline rocks; Chemical Geology, v. 36, p. 191-214.
**White, Harvey E.**
1956: Modern Collage Physics; D. van Norstrand Company, 2nd Ed., p. 216.

---

Geological Survey of Canada Project 870057

# Statistical analysis of pore-size distribution data for tight shales from the Scotian Shelf

**T.J. Katsube**
**Mineral Resources Division**

*Katsube, T.J., 1992: Statistical analysis of pore-size distribution data for tight shales from the Scotian Shelf; in Current Research, Part E; Geological Survey of Canada, Paper 92-1E, p. 365-372.*

***Abstract***

*Shale pore-size distribution data have been analyzed to obtain information on the nano-pore (pore-size range 2.5-60 nm) characteristics, because they play an important role in determining the shale petrophysical properties and significantly influence the hydrocarbon distribution in sedimentary basins.*

*A significant amount of porosity appears to exist below the smallest pores that can be measured (2.5 nm). The missing porosity was determined by fitting a normal distribution curve to the pore-size distribution data.*

*Results show missing porosity values in the range of 0.2-4.0 % for a suite of tight shales. This is about 12-36% of the nano-pore porosity, which occupies 83 ± 4% of the effective porosity, i.e. the porosity of all interconnected pores in the shales. Therefore, missing porosity determination significantly improves effective porosity measurement accuracy. Results also show that mean pore-sizes of the nano-pores are in the range of 2.7-11.5 nm, the smallest known values for rocks, and that water penetrates all nano-pores.*

***Résumé***

*Les données relatives à la distribution des pores ont été analysées afin d'obtenir de l'information sur les caractéristiques des nanopores (dimensions de 2,5 à 60 nm), parce qu'elles sont importantes dans la détermination des propriétés pétrophysiques des shales et influencent de façon significative la répartition des hydrocarbures dans les bassins sédimentaires.*

*Il semble qu'une part relativement importante de la porosité puisse être associée aux pores trop petits pour être mesurés (sous la limite de 2,5 nm). La fraction de porosité manquante a donc été déterminée en ajustant une courbe de distribution normale aux données sur la distribution de la dimension des pores.*

*Les résultats indiquent que dans le cas d'une suite de shales peu perméables, les valeurs de porosité manquantes se trouvent dans l'intervalle 0,2 à 4 %. Ceci représente environ 12 à 36 % de la porosité des nanopores, qui constitue 83 ± 4 % de la porosité efficace, c'est-à-dire de la porosité de tous les pores interreliés présents dans les shales. Par conséquent, la détermination de la fraction de porosité manquante améliore nettement la précision des mesures de porosité efficace. Les résultats montrent également que la dimension moyenne des nanopores se situe entre 2,7 et 11,5 nm (plus petites valeurs jamais signalées) et que l'eau pénètre dans tous les nanopores.*

## INTRODUCTION

Hydrocarbon distribution in sedimentary basins is influenced by shale petrophysical properties. That is, shales play a dominant role in the development of fluid migration pathways during the geological evolution of sedimentary basins. Therefore, the knowladge of petrophysical data for shales, especially tight shales at depth, is essential (Mudford and Best, 1989) to help describe the hydrocarbon generation, migration and accumulation history in sedimentary basins (Williamson, 1992). As part of a program designed to obtain such information, a study to determine why permeabilities of tight shales are extremely low, often less than $10^{-20}$ $m^2$ (Luffel and Guidry, 1989; Brace, 1980; Morrow et al., 1984; Mudford and Best, 1989), has been carried out on 10 tight shale and shaly samples from the Scotian Shelf. As a result, Katsube et al. (1991) have suggested that the low permeability of tight shales is due to the interconnected pore network consisting of extremely small pores, their pore-size being in the order of 10 nm. These pores exhibit a unimodal distribution of pore-sizes in the 2.5-60 nm range (Figure 1), with a mean pore-sizes for the samples of the range of 8-16 nm (Katsube et al., 1991). As these small pores play a significant role in determining the petrophysical properties of the shales, a study has been carried out to obtain a better understanding of the characteristics of these pores. This paper discusses the results of the study.

The minimum pore-size measured by mercury porosimetry used in these studies (Katsube et al., 1991) was 3.0 nm. However, the pore-size distributions shown in Figure 1 suggest that pores exist below that limit. If that is true, the effect of the porosity for pores smaller than 3.0 nm could be significant, as they are likely to be part of the unimodal pore-size distribution of the nano-pores which constitutes a large portion of the total effective porosity of these shale samples. That is, the effective porosity determined by mercury porosimetry could be inaccurate, because of the missing porosity contained in the pores smaller than the 3.0 nm. A statistical method has been applied to estimate the porosity contained in these pores, with the assumption that they constitute part of a unimodal pore-size distribution (Figure 1). This paper discusses the results of this analysis.

## ANALYTICAL PROGRAM

### *The experimental data*

The pore-size distributions of the 10 samples were determined by mercury intrusion porosimetry. The mercury porosimeter used for these measurements is capable of generating pressures of 420 MPa which is high enough to force mercury into pores as small as 3.0 nm in diameter. A general review of the technique is given in Rootare (1970), and specifics of the method used in these measurements, such as the pressure steps between 0 and 420 MPa and equilibration times, are described in Katsube and Walsh (1987) and Katsube et al. (1991).

The pore-size distribution data resulting from mercury porosimetry measurements for all 10 samples have been published in Katsube et al. (1990, 1991), and are listed in Table 1. The partial porosity, $\phi_a$, which is the porosity contributed by each pore-size range (e.g. 2.5-4.0 nm, 4.0-6.3 nm or 0.4-0.6, 0.6-0.8 on the logarithmic scale), is listed in the column under each sample. The total porosity measured by mercury porosimetry, $\phi_{gm}$, listed near the bottom of the table, is the sum of the partial porosities ($\phi_a$):

$$\phi_{gm} = \Sigma\phi_{ai},\ i = 1\text{ -n}, \qquad (1)$$

where n is the number of pore-size ranges. Typical pore-size distributions shown in Figure 1 depict a relatively simple unimodal population concentrated in the 2.5-25 nm range. The geometric means, $d_{hg}$, of the pore-sizes are of the order of 8.7-16.2 nm (Table 1). These are extremely small values (Katsube and Walsh, 1987), and to our knowledge, some of the smallest ever reported for rocks (Katsube et al., 1991). Two types of pore-size distribution patterns have been identified for these rocks. One, typified by Figure 1a has scarcely any pore throats above 120 nm, the other typified by Figure 1b has a pore-size distribution continuing above 1000 nm.

Although the minimum measurable pore-size by the mercury porosimeter used for these measurements is 3.0 nm, the lower limit of the smallest pore-size ranges (2.5 - 4.0)

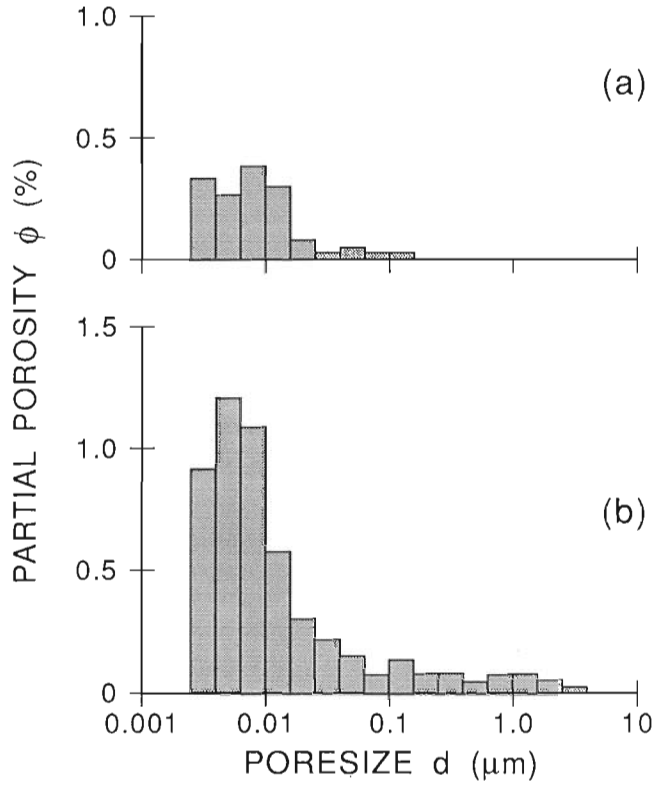


**Figure 1.** Typical pore-size distributions in terms of partial porosity ($\phi_a$) for (**a**) Sample number 6 (5131.5 m), and (**b**) Sample number 10 (5557.0 m), (after Katsube et al., 1991). Partial porosity ($\phi_a$) is the porosity contributed by each pore-size range (e.g. 2.5-4.0 nm, 4.0-6.3 nm).

adopted in this analysis is 2.5 nm. Thus, the minimum pore-size and its log will be represented by $d_{min}$ = 2.5 nm, and $\ell_{min}$ = 0.4, respectively.

### *Effective porosity concepts*

Effective porosity, $\phi_E$, represents the porosity of all interconnected pores in the rock, including the blind and pocket pores. It is not necessarily equal to the total porosity ($\phi_{gm}$), because of the missing porosity, $\Delta\phi$, contained in the pores smaller than 2.5 nm. The relationship between these porosities is as follows:

$$\phi_{Eg} = \phi_{gm} + \Delta\phi, \qquad (2)$$

where $\phi_{Eg}$ is the estimated effective porosity. The parameter $\phi_{Eg}$ is used instead of $\phi_E$ in this equation, because it is obtained from actual measurements of $\phi_{gm}$ and estimations of $\Delta\phi$, which is not necessarily equivalent to the conceptual parameter of effective porosity ($\phi_E$). One of the objectives of this study is to determine the values of $\phi_{Eg}$ from the mercury porosimetry measurements. Actually, that is to obtain the values of $\Delta\phi$.

### *Analytical Method*

The nano-pores (2.5 - 25 nm) form the most outstanding body of pores in the pore-size distributions of these 10 samples. The normal distribution curve, usually expressed by

$$f(x) = 1/[\sigma\sqrt{(2\pi)}]\exp[-(x-a)^2/(2\sigma^2)], \qquad (3)$$

where $\sigma$ is the standard deviation, a is the mean, and x is the variable, has been slightly modified and adjusted to fit the nano-pore data:

$$h(\ell) = \phi_{max}\exp[-(\ell-\ell_{np})^2/(2\sigma^2)], \qquad (4)$$

where $\ell$ is a variable representing the log of pore-size d:

**Table 1.** Pore-size distribution data for different pore-size ranges, d, obtained by mercury porosimetry for the 10 shale samples (after Katsube et al., 1990, 1991)

| Sample Number | V-1 | V-2 | V-3 | V-4 | V-5 | V-6 | V-7 | V-8 | V-9 | V10 |
|---|---|---|---|---|---|---|---|---|---|---|
| d(nm) | | | | | $\phi_a$ | (%) | | | | |
| 2.5-4.0 | 0.86 | 0.57 | 0.76 | 1.43 | 0.66 | 0.33 | 1.03 | 1.16 | 0.43 | 0.82 |
| 4.0-6.3 | 1.14 | 0.64 | 1.15 | 1.43 | 0.63 | 0.27 | 1.06 | 1.54 | 0.35 | 1.23 |
| 6.3-10 | 1.00 | 1.03 | 1.15 | 1.21 | 0.58 | 0.38 | 1.11 | 1.83 | 0.46 | 1.10 |
| 10- | 0.47 | 1.24 | 0.79 | 0.84 | 0.21 | 0.30 | 0.87 | 1.85 | 0.35 | 0.58 |
| 16- | 0.28 | 2.06 | 0.52 | 0.48 | 0.18 | 0.08 | 0.42 | 0.72 | 0.22 | 0.30 |
| 25- | 0.14 | 0.49 | 0.37 | 0.28 | 0.13 | 0.03 | 0.21 | 0.31 | 0.11 | 0.22 |
| 40- | 0.11 | 0.28 | 0.26 | 0.28 | 0.08 | 0.05 | 0.19 | 0.23 | 0.11 | 0.16 |
| 63- | 0.08 | 0.18 | 0.13 | 0.22 | 0.08 | 0.03 | 0.08 | 0.13 | 0.05 | 0.08 |
| 100- | 0.11 | 0.34 | 0.13 | 0.20 | 0.11 | 0.03 | 0.13 | 0.18 | 0.05 | 0.14 |
| 160- | 0.06 | 0.21 | 0.05 | 0.11 | 0.05 | 0.00 | 0.05 | 0.08 | 0.00 | 0.08 |
| 250- | 0.06 | 0.00 | 0.08 | 0.08 | 0.03 | 0.00 | 0.03 | 0.08 | 0.00 | 0.08 |
| 400- | 0.06 | 0.00 | 0.03 | 0.11 | 0.11 | 0.00 | 0.00 | 0.08 | 0.00 | 0.05 |
| 630- | 0.03 | 0.00 | 0.05 | 0.03 | 0.03 | 0.00 | 0.00 | 0.03 | 0.00 | 0.08 |
| 1000- | 0.03 | 0.00 | 0.05 | 0.00 | 0.05 | 0.00 | 0.00 | 0.10 | 0.00 | 0.08 |
| 1585- | 0.00 | 0.00 | 0.05 | 0.00 | 0.05 | 0.00 | 0.00 | 0.05 | 0.00 | 0.05 |
| 2512- | 0.00 | 0.00 | 0.03 | 0.00 | 0.00 | 0.00 | 0.00 | 0.00 | 0.00 | 0.03 |
| $\phi_{gm}$ | 4.9 | 7.7 | 6.3 | 7.6 | 3.7 | 1.6 | 5.9 | 9.1 | 2.3 | 5.8 |
| $d_{hg}$ | 10.0 | 16.2 | 13.3 | 11.1 | 13.6 | 8.7 | 9.5 | 11.9 | 10.0 | 13.1 |
| $\delta_D$ | 2.77 | 2.58 | 2.62 | 2.80 | 2.64 | 2.73 | 2.65 | 2.57 | 2.69 | 2.74 |

$\phi_a$ = Partial porosity (%).
d = Pore-size range (nm).
$\phi_{gm}$ = Total porosity measured by mercury porosimetry (%).
$d_{hg}$ = Mean (geometric) pore-size (nm).
$\delta_D$ = Density (g/cc).

$$\ell = \log(d), \quad (5)$$

and $\ell_{np}$ is the log of the mean pore-size or mode of the nano-pores ($d_{np}$). Both mean pore-size and the mode are equal, since this curve is symmetrical.

The pore-size, generally represented by d, is always displayed on a logarithmic scale in this study, as shown in Figure 1. Each decade of the pore-size scale (X-axis) is divided into five ranges on a logarithmic scale, that is $10^{-1}$ to $10^{3}$ times the ranges of 0-1.6, 1.6-2.5, 2.5-4.0, 4.0-6.3, and 6.3-10, in nm. On the logarithmic scale (X-axis), these ranges have a width of 0.2. Equation (4) is based on the log of the pore-sizes.

To simplify the curve fitting process, the log of equation (4) has been taken:

$$\log[f(\ell)] = \log(\phi_{max}) - (\ell-\ell_{np})^2\log(e)/(2\sigma^2). \quad (6)$$

**Table 2.** Values of the coefficients $B_0$, $B_1$ and $B_2$ obtained from curve fitting (equation 7). ($d_{min}$ - d) indicates the pore-size range used for curve fitting

| Sample | $d_{min}$ - d | $B_0$ | $B_1$ | $B_2$ |
|---|---|---|---|---|
| V-1 | 2.5 - 25 | - 2.34 | 1.36 | - 1.25 |
| V-2 | 2.5 - 63 | - 3.11 | 2.52 | - 1.31 |
| V-3 | 2.5 - 63 | - 2.29 | 0.87 | - 0.67 |
| V-4 | 2.5 - 25 | - 1.97 | 0.73 | - 0.82 |
| V-5 | 2.5 - 16 | - 2.24 | 0.58 | - 0.86 |
| V-6 | 2.5 - 25 | - 2.03 | 2.89 | - 2.16 |
| V-7 | 2.5 - 25 | - 2.49 | 1.68 | - 1.30 |
| V-8 | 2.5 - 40 | - 2.48 | 1.88 | - 1.28 |
| V-9 | 2.5 - 25 | - 2.83 | 1.39 | - 1.06 |
| V-10 | 2.5 - 25 | - 2.35 | 1.28 | - 1.11 |
| Units | nm | | | |

**Table 3.** Values of nano-pore mode ($d_{np}$), standard deviation ($\sigma^2$), nano-pore porosity ($\phi_{np}$) and maximum nano-pore partial porosity ($\phi_{max}$). These were derived from the coefficients in Table 2

| Sample | $\ell_{np}$ | $d_{np}$ | $\sigma$ | b | $\phi_{np1}$ | $\phi_{max}$ |
|---|---|---|---|---|---|---|
| V-1 | 0.644 | 4.41 | 0.412 | 5.16 | 5.53 | 1.07 |
| V-2 | 1.062 | 11.5 | 0.412 | 5.16 | 6.51 | 1.26 |
| V-3 | 0.749 | 5.61 | 0.566 | 7.09 | 6.97 | 0.983 |
| V-4 | 0.545 | 3.51 | 0.520 | 6.52 | 10.2 | 1.56 |
| V-5 | 0.437 | 2.73 | 0.500 | 6.27 | 4.51 | 0.721 |
| V-6 | 0.769 | 5.88 | 0.316 | 3.96 | 1.53 | 0.386 |
| V-7 | 0.746 | 5.58 | 0.412 | 5.16 | 5.84 | 1.13 |
| V-8 | 0.834 | 6.82 | 0.412 | 5.16 | 8.37 | 1.62 |
| V-9 | 0.756 | 5.70 | 0.447 | 5.60 | 2.35 | 0.42 |
| V-10 | 0.677 | 4.75 | 0.447 | 5.60 | 5.83 | 1.04 |
| Units | | nm | | | % | % |

$\ell_{np} = -B_1/(2B_2) + 0.1$
$\ell_{np} = \log(d_{np})$
$\sigma = \sqrt{(1.36/B_2)}$
$\phi_{max} = h(\ell_{np}) = 10^m$
$m = [B_0 - B_1^2/(4B_2)]$
$\phi_{np1} = b\phi_{max}$
$b = 12.5\sigma$

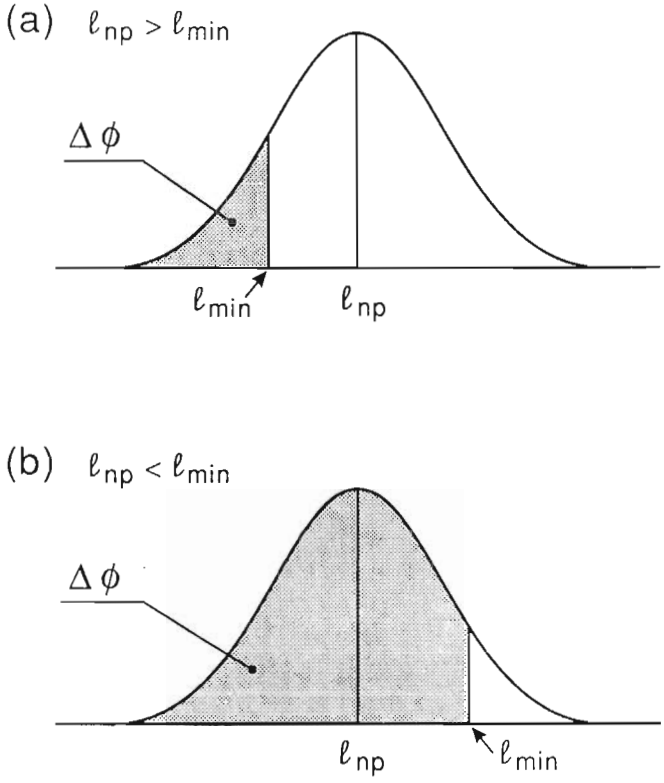


**Figure 2.** Normal distribution curve used to represent the body of nano-pores and the missing porosity ($\Delta\phi$).

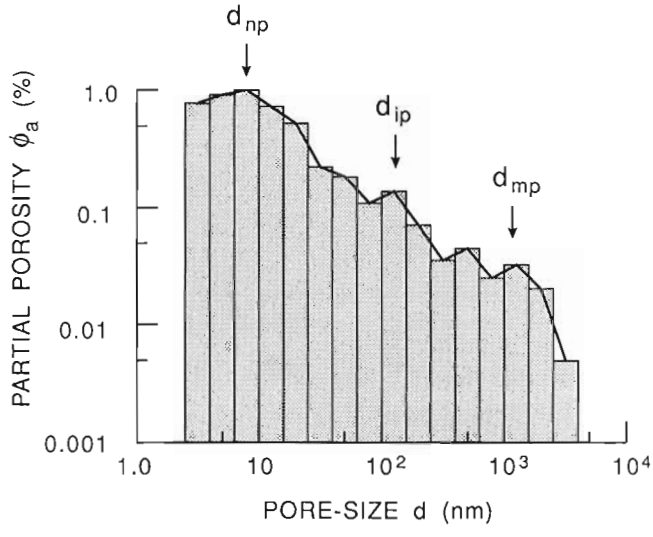


**Figure 3.** Average pore-size distribution for all 10 samples. The parameters $d_{np}$, $d_{ip}$ and $d_{mp}$ are the modes of the nano-pores, intermediate pores and micro-pores, respectively.

This equation takes the form of a polynomial equation:

$$g(\ell) = B_0 + B_1\ell + B_2\ell^2, \qquad (7)$$

where

$g(\ell) = \log[h(\ell)]$,
$B_0 = \log(\phi_{max}) - [\ell_{np}2\log(e)]/(2\sigma^2)$,
$B_1 = \ell_{np}[\log(e)]/\sigma^2$,
$B_2 = -\log(e)/(2\sigma^2)$.

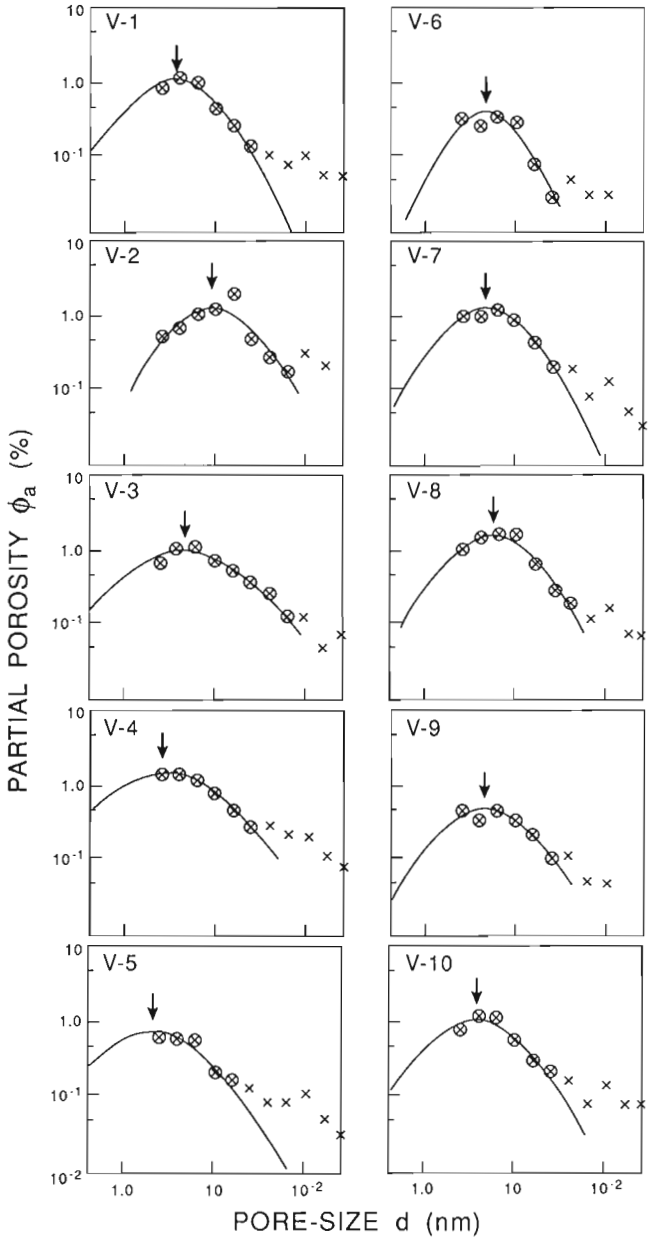


**Figure 4.** Plots of the pore-size distribution in the range of 2.5 to 250 nm for all 10 shale samples, V-1 to V-10. Circled crosses indicate data points used for curve fitting.

Equation (7) is actually used to fit the log of the pore-size distribution data. Subsequent to the curve fitting, and the determining of the coefficients $B_0$, $B_1$ and $B_2$ in equation (7), nano-pore mode ($\ell_{np}$), standard deviation ($\sigma$), and peak nano-pore porosity ($\phi_{max}$) at $\ell = \ell_{np}$ are derived from

$$\ell_{np} = -B_1/(2B_2) + 0.1 \qquad (8)$$

$$\sigma^2 = -\log(e)/(2B_2) \qquad (9)$$

$$\phi_{max} = h(\ell_{np}) = 10^m \qquad (10)$$
$$m = [B_0 - B_1 2/(4B_2)].$$

A value of 0.1 is added in equation (8) so that $\ell_{np}$ represents the true mode. This is necessary because all data points used in this study are represented by the left end of their interval (width of 0.2 on a logarithmic scale) on the X-axis (see Fig. 1) rather than the centre, and because the curves are fitted to these left-end points.

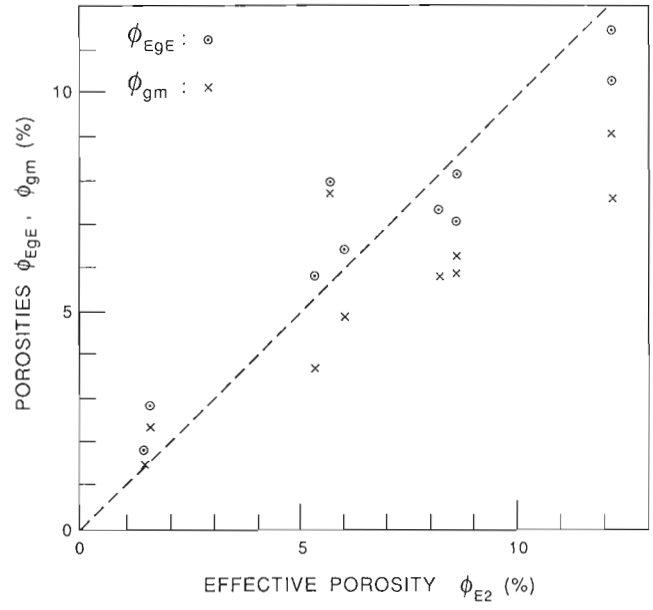


**Figure 5.** Estimated effective porosity ($\phi_{Eg}$) and total porosity ($\phi_{gm}$) as a function of effective porosity ($\phi_{El}$) for the 10 shale samples. The functional relationships between $\phi_{Eg}$ versus $\phi_{El}$, and $\phi_{gm}$ versus $\phi_{El}$ are as follows:

$\phi_{Eg} = (0.80 \pm 0.04)\phi_{El} + (1.0 \pm 0.3)$, r=0.96,
$\phi_{gm} = (0.64 \pm 0.08)\phi_{El} + (1.0 \pm 1.4)$, r=0.88,

where r is the correlation coefficient. The one-point broken line represents $\phi_{Eg} = \phi_{El}$.

### *Nano-Pore and Missing Porosities* ($\phi_{np}$, $\Delta\phi$)

It is assumed that the missing porosity ($\Delta\phi$) is part of the nano-pore population, for all 10 samples, as shown in Figure 2. The nano-pore porosity ($\phi_{np}$) and missing porosity ($\Delta\phi$) are determined by integrating the partial porosity ($\phi_a$), represented by Equation (4), as follows:

$$\Delta\phi = \Sigma\phi_a = \Sigma h(\ell), \quad \text{for } \ell = \ell_{np} - 3\sigma \text{ to } \ell = \ell_{min}, \tag{11}$$

and

$$\phi_{np} = \Sigma\phi_a = \Sigma h(\ell), \quad \text{for } \ell = \ell_{np} - 3\sigma \text{ to } \ell = \ell_{np} + 3\sigma. \tag{12}$$

The nano-pore porosity ($\phi_{np}$) can also be determined by using the following equation, which is derived by comparing equation (4) to (3):

$$\phi_{np} = \{q\sigma\sqrt{(2\pi)}\}\phi_{max} = 12.5\sigma\,\phi_{max}, \tag{13}$$

**Table 4.** Partial porosity of nano-pores, $\phi_{anp}$, calculated for $\ell$=-1 to $\ell$=3 by inserting the values of $\ell_{np}$, $\sigma$ and $\phi_{max}$ (Table 3) into $h(\ell)$ of Equation (4)

| Sample Number | V-1 | V-2 | V-3 | V-4 | V-5 | V-6 | V-7 | V-8 | V-9 | V10 |
|---|---|---|---|---|---|---|---|---|---|---|
| d(nm) | | | | | $\phi_{anp}$ | (%) | | | | |
| 0.1- | 0.00 | 0.00 | 0.01 | 0.03 | 0.02 | 0.00 | 0.00 | 0.00 | 0.00 | 0.00 |
| 0.16- | 0.01 | 0.00 | 0.04 | 0.09 | 0.05 | 0.00 | 0.00 | 0.00 | 0.00 | 0.01 |
| 0.25- | 0.02 | 0.00 | 0.09 | 0.21 | 0.12 | 0.00 | 0.01 | 0.01 | 0.01 | 0.03 |
| 0.40- | 0.08 | 0.01 | 0.18 | 0.42 | 0.24 | 0.00 | 0.05 | 0.04 | 0.03 | 0.10 |
| 0.63- | 0.21 | 0.02 | 0.32 | 0.72 | 0.41 | 0.01 | 0.14 | 0.12 | 0.07 | 0.23 |
| 1.0-1.6 | 0.45 | 0.08 | 0.51 | 1.08 | 0.57 | 0.04 | 0.33 | 0.33 | 0.14 | 0.45 |
| 1.6-2.5 | 0.76 | 0.23 | 0.72 | 1.40 | 0.69 | 0.13 | 0.63 | 0.70 | 0.25 | 0.73 |
| 2.5-4.0 | 1.01 | 0.50 | 0.89 | 1.55 | 0.72 | 0.27 | 0.95 | 1.17 | 0.36 | 0.96 |
| 4.0-6.3 | 1.06 | 0.86 | 0.98 | 1.49 | 0.63 | 0.38 | 1.12 | 1.54 | 0.42 | 1.04 |
| 6.3-10. | 0.88 | 1.17 | 0.95 | 1.23 | 0.47 | 0.35 | 1.05 | 1.60 | 0.40 | 0.92 |
| 10-16 | 0.58 | 1.25 | 0.81 | 0.88 | 0.30 | 0.22 | 0.78 | 1.32 | 0.31 | 0.66 |
| 16-25 | 0.30 | 1.07 | 0.61 | 0.54 | 0.16 | 0.09 | 0.46 | 0.85 | 0.20 | 0.39 |
| 25-40 | 0.12 | 0.72 | 0.41 | 0.29 | 0.08 | 0.03 | 0.21 | 0.44 | 0.11 | 0.19 |
| 40-63 | 0.04 | 0.38 | 0.24 | 0.13 | 0.03 | 0.01 | 0.08 | 0.18 | 0.05 | 0.08 |
| 63- | 0.01 | 0.16 | 0.12 | 0.05 | 0.01 | 0.00 | 0.02 | 0.06 | 0.01 | 0.02 |
| 100- | 0.00 | 0.05 | 0.06 | 0.02 | 0.00 | 0.00 | 0.01 | 0.01 | 0.00 | 0.01 |
| 160- | 0.00 | 0.01 | 0.02 | 0.01 | 0.00 | 0.00 | 0.00 | 0.00 | 0.00 | 0.00 |
| 250- | 0.00 | 0.00 | 0.01 | 0.00 | 0.00 | 0.00 | 0.00 | 0.00 | 0.00 | 0.00 |
| 400- | 0.00 | 0.00 | 0.00 | 0.00 | 0.00 | 0.00 | 0.00 | 0.00 | 0.00 | 0.00 |
| $\ell_{np}$ | 0.64 | 1.06 | 0.75 | 0.55 | 0.44 | 0.77 | 0.75 | 0.83 | 0.76 | 0.68 |
| $d_{np}$ | 4.41 | 11.5 | 5.61 | 3.51 | 2.73 | 5.88 | 5.58 | 6.82 | 5.70 | 4.75 |
| $\sigma$ | 0.41 | 0.41 | 0.57 | 0.52 | 0.50 | 0.32 | 0.41 | 0.41 | 0.45 | 0.45 |
| $\phi_{max}$ | 1.07 | 1.26 | 0.98 | 1.56 | 0.72 | 0.39 | 1.13 | 1.62 | 0.42 | 1.04 |
| $\ell\phi$ | 1.52 | 0.34 | 1.86 | 3.95 | 2.12 | 0.18 | 1.16 | 1.20 | 0.50 | 1.55 |
| $\phi_{np1}$ | 5.53 | 6.51 | 6.97 | 10.5 | 4.51 | 1.53 | 5.84 | 8.37 | 2.35 | 5.83 |

d = Pore-size range (nm).
$\phi_{anp}$ = Nano-pore partial porosity (%).
$\ell_{np}$ = log($d_{np}$).
$d_{np}$ = Nano-pore mode.
$\sigma$ = Standard deviation.
$\phi_{max}$ = Maximum nano-pore porosity.
$\Delta\phi$ = Estimated missing porosity.
$\phi_{np1}$ = Nano-pore porosity using Equation (12).

**Table 5.** List of porosities. The missing porosity ($\Delta\phi$) was determined using equations 8-12. The estimated effective porosity ($\phi_{Eg}$) values were derived from $\Delta\phi$ and $\phi_{gm}$ using Equation (2)

| Sample | $\phi_{np1}$ | $\phi_{np2}$ | $\phi_{gm}$ | $\Delta\phi$ | $\phi_{Eg}$ | $\phi_{EI}$ |
|---|---|---|---|---|---|---|
| V-1 | 5.53 | 5.53 | 4.9 | 1.52 | 6.42 | 6.0 |
| V-2 | 6.51 | 6.61 | 7.7 | 0.34 | 8.04 | 5.7 |
| V-3 | 6.97 | 6.97 | 6.3 | 1.86 | 8.16 | 8.6 |
| V-4 | 10.15 | 10.17 | 7.6 | 3.95 | 11.5 | 12.1 |
| V-5 | 4.51 | 4.52 | 3.7 | 2.12 | 5.82 | 5.3 |
| V-6 | 1.53 | 1.53 | 1.6 | 0.18 | 1.78 | 1.4 |
| V-7 | 5.84 | 5.83 | 5.9 | 1.16 | 7.1 | 8.6 |
| V-8 | 8.37 | 8.37 | 9.1 | 1.20 | 10.3 | 12.1 |
| V-9 | 2.35 | 2.35 | 2.3 | 0.50 | 2.8 | 1.5 |
| V-10 | 5.83 | 5.83 | 5.8 | 1.55 | 7.35 | 8.2 |
| units | % | % | % | % | % | % |

$\phi_{np1}$ = Nano-pore porosity using Equation (12).
$\phi_{np2}$ = Nano-pore porosity using Equation (13).
$\phi_{gm}$ = Total porosity measured by mercury porosimetry.
$\Delta\phi$ = Estimated missing porosity.
$\phi_{Eg}$ = Estimated effective porosity by mercury porosimetry.
$\phi_{EI}$ = Effective porosity measured by immersion technique using longer oven drying time (from Katsube et al., 1992).

where q is 5 in this case. This is because, the total area bounded by equation (3) and the X-axis is equal to 1.0, and that by equation (4) is $\{\sigma\sqrt{(2\pi)}\}\phi_{max}$, with the number of data points (intervals or cells), q, per decade (equal to 1.0 on a logarithmic scale) along the X-axis being equal to 5 in this case (see Fig. 1).

## RESULTS OF ANALYSIS

### *Curve fitting*

Following the procedure adopted by Agterberg et al. (1984), the average pore-size distribution is obtained (Fig. 3) by taking the average partial porosity, $\Phi_a$, for each pore-size range:

$$\Phi_{aij} = (1/10)\Sigma\phi_{aij}, \quad i=1\text{-}10, \qquad (14)$$

where i is the sample number, 1-10, and j is the number of the pore-size range, 1-16, starting at d=2.5-4.0 nm and ending at d=2500-4000 nm. In Figure 3, three populations of pores are identified by their modes, $\ell_{np}$, $\ell_{ip}$ and $\ell_{mp}$, representing nano-pores, intermediate-pores and micro-pores, respectively. The two peaks in the 400-1000 nm range are considered to represent the single mode of $\ell_{mp}$.

The plots for the pore-size distribution of all 10 samples in the range of 2.5 - 250 nm are illustrated in Figure 4. It is clear from Figures 3 and 4, that the nano-pores are the most significant population of pores in this suite of samples, as indicated by Katsube et al. (1991). The effect of the intermediate pores begin to be seen from about 25-100 nm. The curve expressed by equation (7) has been fitted to the data of all 10 samples. Curve fitting has been easy for samples such as V-3 (Fig. 4), because the effects of the intermediate-pores do not enter until about d=100 nm, thus leaving a wide range (2.5-63 nm) of pore-size data available the fitting. Curve fitting has been difficult for data such as those of Samples V-5 and V-10, because the effect of intermediate-pores enter from about 16-25 nm, thus leaving little data available for fitting. In the case of Sample V-6 (Fig. 4), not only is there a scatter of the data, but it was not clear whether the data point of 40 nm should belong to the nano- or intermediate-pores. As a result of various curve-fitting tests, the pore-size ranges listed in the second column of Table 2 were considered to produce the most reasonable results. Values of the coefficients determined as a result of this curve fitting are listed in the same table. That is, the values of coefficients $B_0$, $B_1$ and $B_2$, are listed in Table 2.

### *Determination of $\phi_{np}$ and $\Delta\phi$*

The results of deriving the parameters $d_{np}$, $\sigma^2$ and $\phi_{max}$ from the coefficients in Table 2, using equations (8) to (10), are listed in Table 3. The partial porosity of the nano-pores, $\phi_{anp}$, has been calculated for $\ell$=-1 to $\ell$=3 by inserting the values of $\ell_{np}$, $\sigma$ and $\phi_{max}$ (Table 3) into $h(\ell)$ of equation (4). The results are listed in Table 4. The nano-pore porosity ($\phi_{np}$) derived using equation (12) is represented by $\phi_{np1}$ and is listed in Tables 3 and 4. The missing porosity ($\Delta\phi$) was determined using equation (11) and is listed in Table 5, together with the nano-pore porosity ($\phi_{np}$) derived using equation (13) which is represented by $\phi_{np2}$. The estimated effective porosity ($\phi_{Eg}$) values were derived from $\Delta\phi$ and $\phi_{gm}$ using equation (2). These results are also listed in Table 5.

## DISCUSSION AND CONCLUSIONS

The two nano-pore porosities, $\phi_{np1}$ and $\phi_{np2}$, show very similar values (Table 5), although the curve fitting procedures by which they were derived are slightly different, one derived using equation (12) and the other using Equation (13). In addition, the nano-pore partial porosity ($\phi_{anp}$) values, derived by using Equation (4) and listed in Table 4, are very similar to the original data (Table 1) in the vicinity ($d_{np}\pm\sigma$) of the modes ($d_{np}$). Therefore, the nano-pore porosity ($\phi_{np}$) obtained by this curve fitting method is considered representative of the true nano-pore porosity of these samples.

The nano-pore porosity ($\phi_{np}$) occupies a significant portion (83±4 %) of the estimated effective porosity ($\phi_{Eg}$), as is clear from Table 5. The estimated effective porosity ($\phi_{Eg}$) is considered to be equivalent to the effective porosity ($\phi_E$), that is the total porosity of all interconnected pores, of these samples. The nano-pore mode ($d_{np}$) is in the range of 2.7 to 11.5 nm with an average of 5.0 nm (5.0±1.2), and the standard deviation ($\sigma$) in the range of 0.41 to 0.5 on the logarithmic scale.

The estimated effective porosity ($\phi_{Eg}$) values (Table 5) show a relatively good correlation with the reported values of effective porosity, $\phi_{EI}$, measured by the immersion technique (Katsube et al., 1992), as shown in Figure 5. The fact that this correlation is a considerable improvement over the correlation between $\phi_{gm}$ and $\phi_{EI}$ (Figure 5), indicates that the inclusion of the missing porosity ($\Delta\phi$) in the estimated effective porosity ($\phi_{Eg}$) calculations, has considerably improved the accuracy of the porosity measurements by mercury porosimetry. That is, a significant amount of porosity does exist below the smallest pores measured by the mercury porosimetry method used in these studies. Therefore, it is necessary to determine the missing porosity ($\Delta\phi$) in order to obtain accurate measurements of effective porosity ($\phi_E$), when using mercury porosimetry. The missing porosity ($\Delta\phi$) for these samples is in the range of 0.2-4.0 %. On average, this is about 20 % (4-36 %) of the estimated effective porosity ($\phi_{Eg}$) of these samples.

The effective porosity ($\phi_{EI}$) obtained by the immersion technique was determined by taking the difference in mass between an oven-dried rock specimen and the same specimen saturated with distilled water (Katsube and Scromeda, 1991; Katsube et al., 1992). The fact that the two porosities, $\phi_{Eg}$ and $\phi_{EI}$, show a good correlation, suggests that water penetrates and can be evacuated from all of the nano-pores.

## ACKNOWLEDGMENTS

The author expresses his appreciation to M.E. Best (Pacific Geoscience Centre, Sidney, British Columbia) and M. Williamson (Atlantic Geoscience Centre, Dartmouth, Nova Scotia) for their support of this study. The author is very grateful to F.P. Agterberg (Mineral Resources Division, Ottawa) for his comments and for critically reviewing this paper.

## REFERENCES

**Agterberg, F.P., Katsube, T.J., and Lew, S.N.**
1984: Statistical analysis of granite pore size distribution data, Lac du Bonnet batholith, eastern Manitoba; in Current Research, Part A; Geological Survey of Canada, Paper 84-1A, p. 29-38.

**Brace, W.F.**
1980: Permeability of crystalline and argillacious rocks; International Journal of Rock Mechanics and Mining Sciences and Geomechanics Abstracts, v. 17, p. 241-251.

**Katsube, T.J. and Scromeda, N.**
1991: Effective porosity measuring procedure for low porosity rocks; in Current Research, Part E; Geological Survey of Canada, Paper 91-1E, p. 291-297.

**Katsube, T.J. and Walsh, J.B.**
1987: Effective aperture for fluid flow in microcracks; International Journal of Rock Mechanics and Mining Sciences and Geomechanics Abstracts, v. 24, p. 175-183.

**Katsube, T.J., Murphy, T.B., Best, M.E., and Mudford, B.S.**
1990: Pore structure characteristics of low permeability shales from deep formations; in Proceedings of the 1990 SCA (Society of Core Analysts) 4th Annual Technical Conference, August, 1990, Dallas, Texas, SCA-9010, p.1-21.

**Katsube, T.J., Best, M.E., and Mudford, B.S.**
1991: Petrophysical characteristics of shales from the Scotian shelf: Geophysics, v. 56, p. 1681-1689.

**Katsube, T.J., Scromeda, N., and Williamson, M.**
1992: Effective porosity of tight shales from the Venture Gas Field, offshore Nova Scotia; in Current Research, Part D; Geological Survey of Canada, Paper 92-1D, p. 111-119.

**Luffel, D.L. and Guidry, F.K.**
1989: Reservoir rock properties of Devonian shale from core and log analysis; The Society of Core Analysts, Annual Technical Conference Preprints, Volume I, Aug. 2-3, Paper 8910.

**Morrow, C., Shi, L., and Byerlee, J.**
1984: Permeability of fault gauge under confining pressure and shear stress; Journal of Geophysical Research, v. 89, p. 3193-3200.

**Mudford, B.S. and Best, M.E.**
1989: Venture Gas Field, offshore Nova Scotia; case study of overpressuring in region of low sedimentation rate; American Association of Petroleum Geologists Bulletin, v. 73, p. 1383-1396.

**Rootare, H.M.**
1970: A review of mercury porosimetry; Perspectives of Power Metallurgy, v. 5, p. 225-252.

**Williamson, M.A.**
1992: Hydrocarbon resource study of east coast frontier basins; past present and future (Abstract); in Current Activity Forum 1992; Geological Survey of Canada, Program with Abstracts, p. 4.

Geological Survey of Canada Project 870057

# Arsenopyrite and loellingite in the Fire Tower Zone porphyry tungsten-molybdenum deposit, Mount Pleasant, New Brunswick

**Kyle E. Durocher[1], W. David Sinclair, Jeanne B. Percival, and Richard P. Taylor[1]**
**Mineral Resources Division**

*Durocher, K.E., Sinclair, W.D., Percival, J.B., and Taylor, R.P., 1992: Arsenopyrite and loellingite in the Fire Tower Zone porphyry tungsten-molybdenum deposit, Mount Pleasant, New Brunswick; in Current Research, Part E; Geological Survey of Canada, Paper 92-1E, p. 373-380.*

***Abstract***

*X-ray diffraction analyses were used to outline the distribution of arsenopyrite and loellingite within the Fire Tower Zone porphyry-type tungsten-molybdenum deposit at Mount Pleasant. Arsenopyrite is widespread, occurring both within the tungsten-molybdenum deposit and in surrounding country rocks. Loellingite is more restricted in its distribution; it is associated mainly with zones of high-grade tungsten in the upper part of the deposit. The weight proportion of loellingite relative to arsenopyrite in samples containing both minerals ranges from <0.05 to 0.95.*

*Electron-microprobe analyses of arsenopyrite show no evidence of compositional zoning either within individual grains or throughout the Fire Tower Zone. Arsenopyrite is arsenic-rich (33.5 to 35.7 atomic % As), reflecting formation under low confining pressures (<1 kbar). Assuming equilibrium between arsenopyrite and loellingite, the average composition of arsenopyrite (34.6 atomic % As) indicates temperatures of formation of the arsenopyrite in the range of 370 to 470°C.*

***Résumé***

*L'analyse par diffraction des rayons X a été utilisée pour délimiter la répartition de l'arsénopyrite et de la loellingite dans le gisement de tungstène et molybdène de type porphyrique de la zone de Fire Tower, à Mount Pleasant. L'arsénopyrite est répandue; elle s'observe dans le gisement de tungstène et molybdène tout comme dans les roches encaissantes environnantes. La loellingite a une répartition plus restreinte; elle est principalement associée à des zones très riches en tungstène dans la partie supérieure du gisement. Le proportion pondérale de la loellingite par rapport à l'arsénopyrite dans les échantillons contenant les deux minéraux se situe entre < 0,05 et 0,95.*

*L'analyse de l'arsénopyrite par microsonde électronique n'indique aucune zonation de composition, ni dans les grains individuels ni dans l'ensemble de la zone de Fire Tower. L'arsénopyrite est riche en arsenic (33,5 à 35,7 % d'As élémentaire), ce qui signifie qu'elle est apparue à des pressions de confinement faibles (< 1 kb). En admettant qu'il y ait un équilibre entre l'arsénopyrite et la loellingite, la composition moyenne de l'arsénopyrite (34,6 % d'As élémentaire) indique que les températures de formation de l'arsénopyrite sont comprises entre 370 et 470 °C.*

[1] Department of Earth Sciences, Carleton University, Ottawa, Ontario K1S 5B6

## INTRODUCTION

Although arsenopyrite (FeAsS) and loellingite ($FeAs_2$) have been recognized in previous studies of the tungsten-molybdenum deposits of the Fire Tower Zone at Mount Pleasant (e.g., Dagger, 1972; Petruk, 1973), their distribution was not documented in detail. The distribution and relative abundances of these two As-rich minerals have important metallurgical as well as mineralogical implications. Specifically, difficulties in separating loellingite from wolframite during tungsten mining operations from 1983-1985 were problematic in maintaining a low, acceptable As content of the tungsten concentrate (G.J.A. Kooiman, pers. comm., 1991).

In this study, X-ray diffraction analyses of heavy-mineral concentrates of samples from the tungsten-molybdenum deposit and surrounding rocks in the Fire Tower Zone were used to estimate weight proportions of loellingite relative to arsenopyrite. This was done by comparing ratios of peak heights for these two minerals on diffractometer traces of the concentrates to peak-height ratios of these minerals determined from prepared standards. Quantitative data on the compositions of arsenopyrite obtained by electron-microprobe analysis of polished thin sections have been used to assess the pressure and temperature of formation of the arsenopyrite.

## GEOLOGICAL SETTING

Tungsten-molybdenum and tin deposits at Mount Pleasant occur within the Mount Pleasant caldera near its southwestern margin, in southwestern New Brunswick (Fig.1). Rocks within the caldera consist mainly of volcanic and sedimentary rocks of the Late Devonian Piskahegan Group (McCutcheon, 1990a, b). To the west of Mount Pleasant, the caldera is bounded by Ordovician to Silurian metasedimentary rocks of the Digdeguash Formation in the St. Croix terrane (Fyffe, 1991).

At Mount Pleasant, tungsten-molybdenum and tin deposits are associated with hydrothermal breccias and different phases of highly differentiated, fluorine-rich granite that were emplaced in volcanic rocks of the Piskahegan Group. At least three centres of granitic intrusion and related mineralization have been recognized: the Fire Tower Zone, the North Zone, and the Saddle Zone (Kooiman et al., 1986; Sinclair et al., 1988; Sinclair and Kooiman, 1992). In the Fire Tower Zone, hydrothermal breccias (referred to as Fire Tower breccia and granite breccia) and intrusive rocks form a roughly vertical, pipe-like complex (Fig. 2).

Three phases of granite have been recognized in the Fire Tower Zone; fine grained granite is the oldest phase, granite porphyry is intermediate, and porphyritic granite is the youngest phase. Radiometric ages of the different

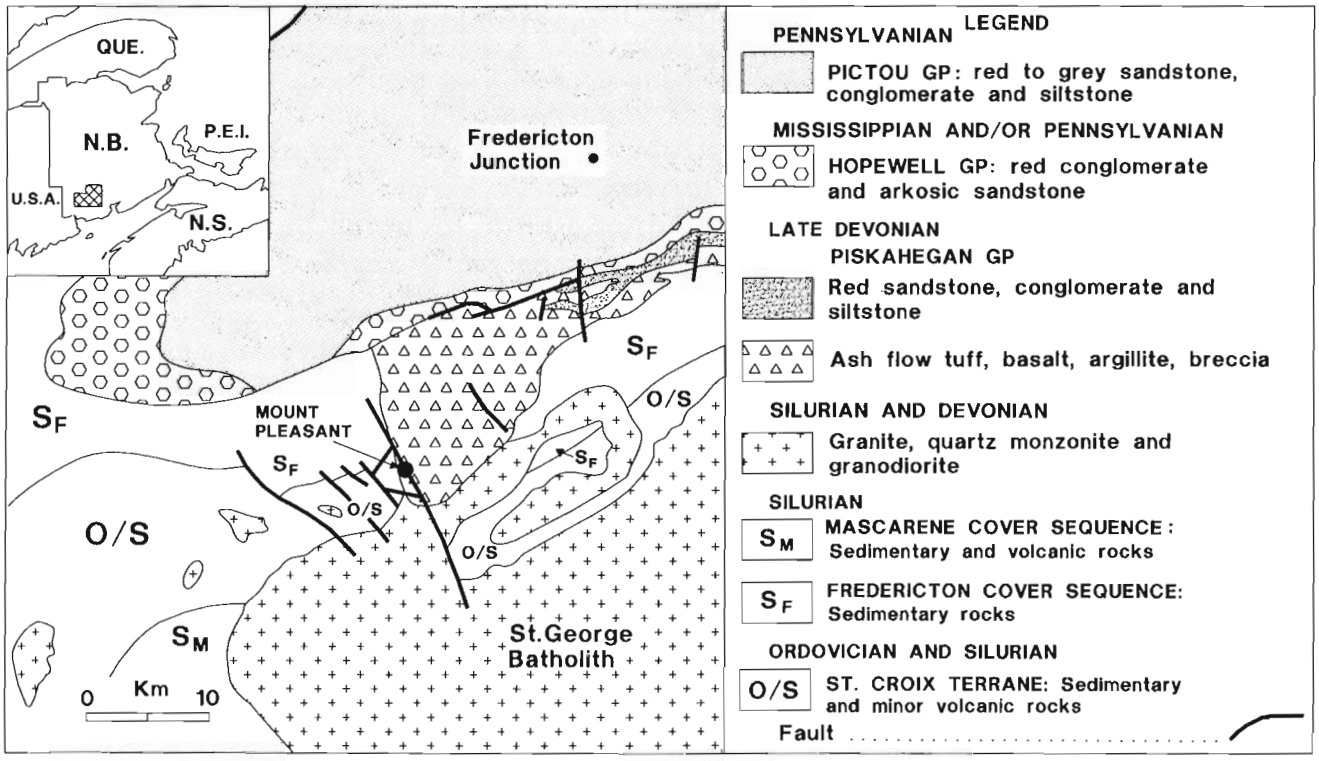


**Figure 1.** Location and geological setting of Mount Pleasant, New Brunswick (modified from Kooiman et al., 1986).

phases and associated biotite hornfels range from 361 to 330 Ma (Late Devonian to early Mississippian) (Sinclair and Kooiman, 1990).

The tungsten-molybdenum deposit in the Fire Tower Zone is related to the emplacement of the fine grained granite phase. Both the fine-grained granite and the associated tungsten-molybdenum deposit are crosscut by irregular, dyke-like bodies of granite porphyry. Tin-bearing veins and replacement zones are associated with the emplacement of porphyritic granite and, in places, are superimposed on the tungsten-molybdenum deposit (Kooiman et al., 1986). At depth, granite porphyry grades into porphyritic granite.

## THE FIRE TOWER ZONE TUNGSTEN-MOLYBDENUM DEPOSIT

The Fire Tower Zone tungsten-molybdenum deposit is a large, low-grade, porphyry-type deposit. Reserves in the Fire Tower Zone prior to mining totalled 22.5 million tonnes grading 0.21% W, 0.1% Mo and 0.08% Bi (Parrish and Tully, 1978), and included a higher grade deposit of 9.4 million tonnes grading 0.39% $WO_3$ and 0.20% $MoS_2$ (Kooiman et al., 1986). From 1983 to 1985, about 1 million tonnes of ore were mined, from which more than 2000 tonnes of concentrate grading 70% $WO_3$ were produced.

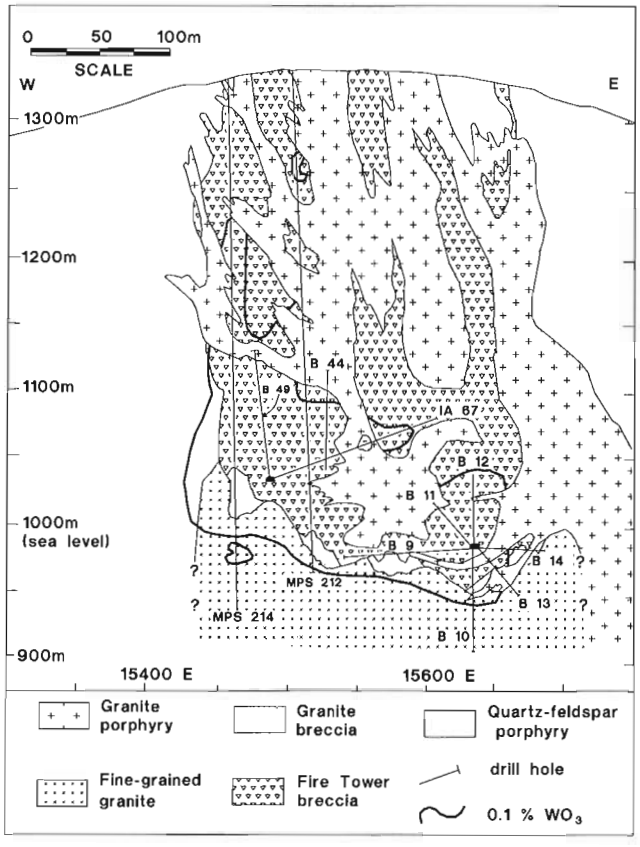


**Figure 2.** Geology of the Fire Tower Zone, section 12405N, and the outline of the tungsten-molybdenum deposit (after Kooiman et al., 1986).

The following description of the Fire Tower Zone tungsten-molybdenum deposit is based on previous descriptions (Dagger, 1972; Petruk, 1973; Parrish and Tully, 1978; Pouliot et al., 1978; Kooiman et al., 1986), supplemented by hand specimen and thin section examination of samples used in this study. The deposit consists of wolframite and molybdenite which occur as disseminated grains in Fire Tower breccia, and in fractures and quartz veinlets that cut Fire Tower breccia, granite breccia, underlying fine grained granite, and associated volcanic rocks of the Piskahegan Group (quartz-feldspar porphyry in Fig. 2). Minor amounts of bismuth and bismuthinite are also present; associated alteration and gangue minerals are mainly topaz, fluorite, chlorite, biotite, arsenopyrite, and loellingite. The average modal mineralogy, based on samples used in this study, is approximately 70% quartz, 10% topaz, 8% chlorite, 5% fluorite, 5% micas and clays, and 2% opaques.

A close association of arsenopyrite and loellingite with the principal ore minerals, wolframite and molybdenite, is reflected in their paragenesis (Fig. 3). Arsenopyrite commonly occurs with wolframite and molybdenite in veins and fractures, and, in many cases, is in direct contact with them (Fig. 4). Arsenopyrite is also characterized by inclusions of bismuthinite, bismuth, loellingite, and chalcopyrite. Early deposition of loellingite is suggested by the fact that it is typically inclusion-free, except for topaz in a few places. Some loellingite grains are rimmed by arsenopyrite (Fig. 5), indicating either that deposition of arsenopyrite continued after that of loellingite, or that re-equilibration of loellingite has occurred. Arsenopyrite and loellingite thus are closely associated spatially, although clear textural evidence that the two minerals were in equilibrium when they were deposited is lacking.

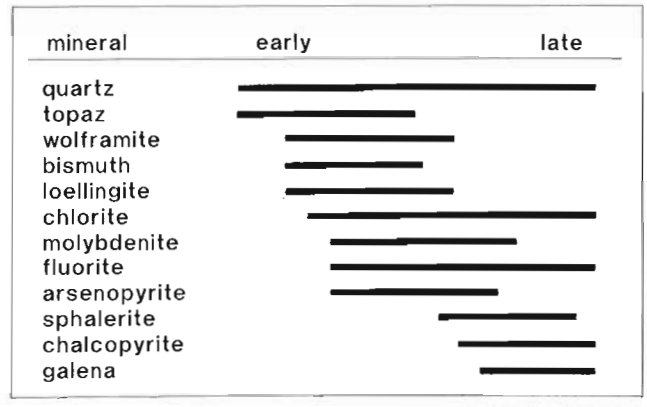


**Figure 3.** Paragenetic sequence of mineralization in the Fire Tower Zone.

## X-RAY DIFFRACTION ANALYSIS: SAMPLE PREPARATION AND ANALYTICAL METHOD

For this study, 68 representative samples from 3 metre sections of drill core were collected from the 12405N section of the Fire Tower Zone. Smear mounts of heavy-mineral separates from each sample were prepared in the following way: the samples were crushed and ground to -60/+115 mesh, and the heavy minerals separated using heavy liquids; 50 mg of each separate were then thoroughly ground in methanol, pipetted onto a round glass slide, and allowed to air dry.

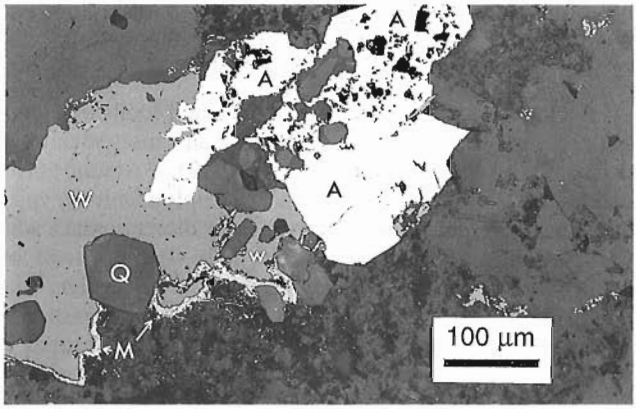


**Figure 4.** Photomicrograph of arsenopyrite (A), wolframite (W), molybdenite (M) and quartz (Q) from a mineralized vein, Fire Tower Zone tungsten-molybdenum deposit.

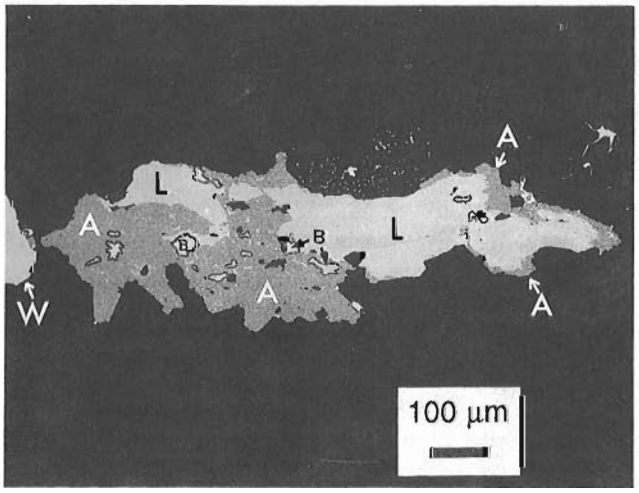


**Figure 5.** Scanning electron microscope image of arsenopyrite (A), loellingite (L), bismuth (B), and wolframite (W) in a mineralized vein, Fire Tower Zone tungsten-molybdenum deposit. Numerous bismuth inclusions (outlined in black) are present in arsenopyrite, compared to relatively few in loellingite. Loellingite is rimmed and possibly replaced in part by arsenopyrite.

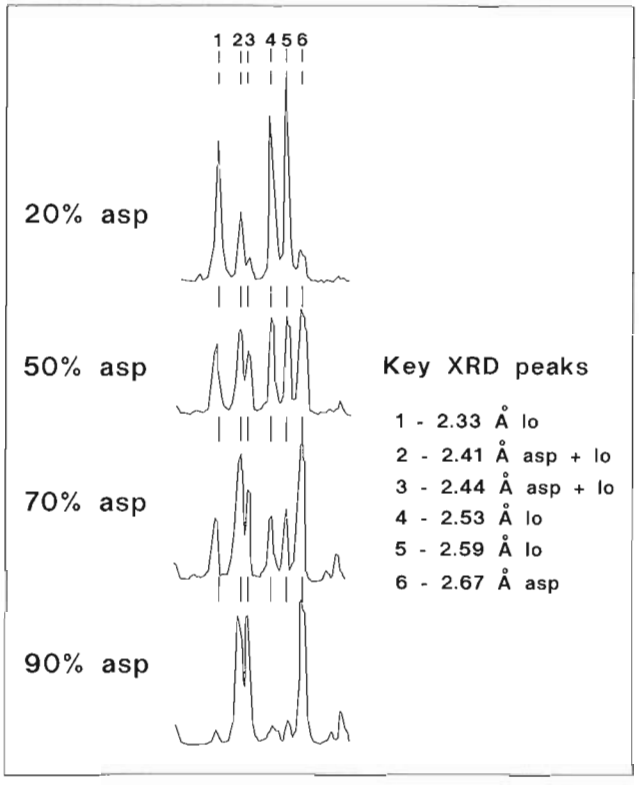


**Figure 6.** Variations in peak heights of loellingite (lo) and arsenopyrite (asp) on diffractometer traces relative to arsenopyrite content in the loellingite-arsenopyrite standards.

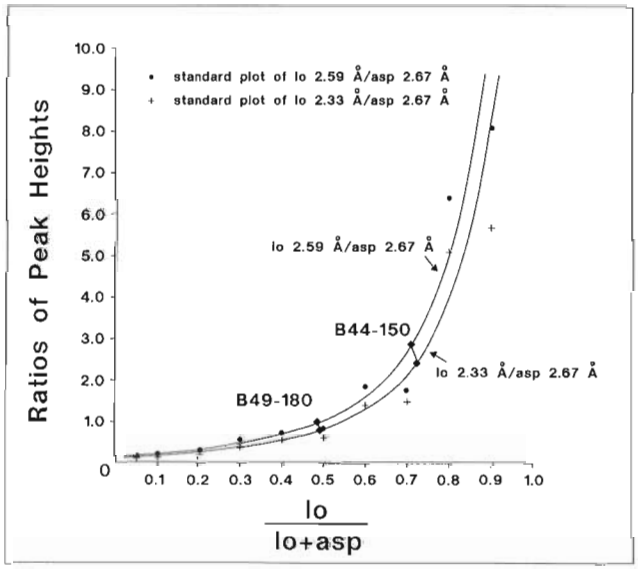


**Figure 7.** Standard curves and representative sample plots (tie-lines join points that represent the same sample on the two curves).

Smear mounts of standards were prepared in a similar way from mixtures of relatively pure arsenopyrite and loellingite (from Mount Pleasant) in the following weight proportions of loellingite: 0.1, 0.2, 0.3, 0.4, 0.5, 0.6, 0.7, 0.8, 0.9, and 0.95.

X-ray diffraction analyses of the smear mounts were made with a Phillips PW 1710 diffractometer equipped with a graphite monochromater, CuKα radiation and a Ni filter. Details of the operating procedures were described by Durocher (1991). The standards were analyzed on two occasions, 6 months apart. The heights of selected arsenopyrite and loellingite X-ray peaks measured on the diffractometer traces from both runs were typically within ±10% of each other.

In addition to arsenopyrite and loellingite, other minerals identified in the heavy-mineral concentrates included major to minor amounts of wolframite, molybdenite, sphalerite, topaz and quartz, and minor to trace amounts of chlorite, fluorite and bismuth; pyrite, bismuthinite and cassiterite were also detected in some samples.

For the determination of peak-height ratios of loellingite to arsenopyrite on the diffractometer traces, two loellingite (lo) peaks, lo 2.59 Å and lo 2.33 Å, and one arsenopyrite (asp) peak, asp 2.67 Å, were chosen. These peaks consistently showed little or no interference with other peaks in either the standard, or the sample concentrates (Fig. 6). Two ratios were measured for each sample and standard: 1) lo 2.59 Å/asp 2.67 Å and 2) lo 2.33 Å/asp 2.67 Å. For the standards, these ratios were plotted against the weight proportion of loellingite; the resulting calibration curves (Fig. 7) were then used to estimate the proportion of loellingite relative to arsenopyrite + loellingite in the samples.

Several sources of error are inherent in this method. Slight discrepancies of peak intensities between the Powder Diffraction Files and the monomineralic standards are due to the use of smear mounts. For example, variation in grain size and preferred orientation of grains on the smear mounts can affect the intensity of the X-ray peaks. Packed powder, randomly-oriented mounts give peak intensities similar to those on the Powder Diffraction Files; smear mounts, however, were used in this study because there was insufficient material for packed powder mounts. Some error may have been introduced in the standard curves, which were hand-drawn to obtain a best-fit curve from the points obtained for peak-height ratios.

Because of the difficulty in quantifying errors inherent in these procedures, the results obtained are considered only semi-quantitative. At either end of each calibration curve, the error in the estimated weight proportion of loellingite increases markedly as the content of loellingite or arsenopyrite approaches zero; error for such samples is probably on the order of 20-25%. Samples that plot in the middle portions of the curves have the least error (5-10%).

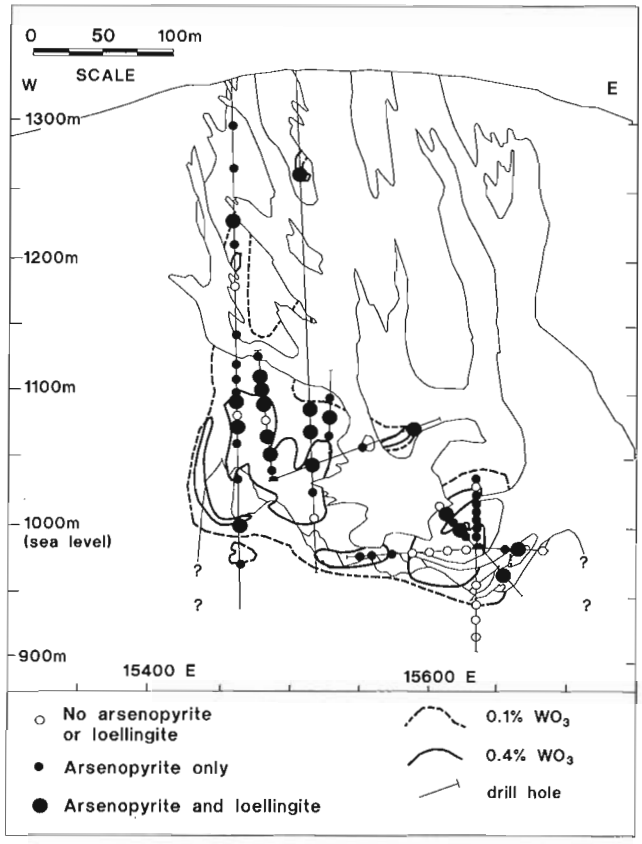


**Figure 8.** Location of samples on section 12405N, and distibution of arsenopyrite and loellingite.

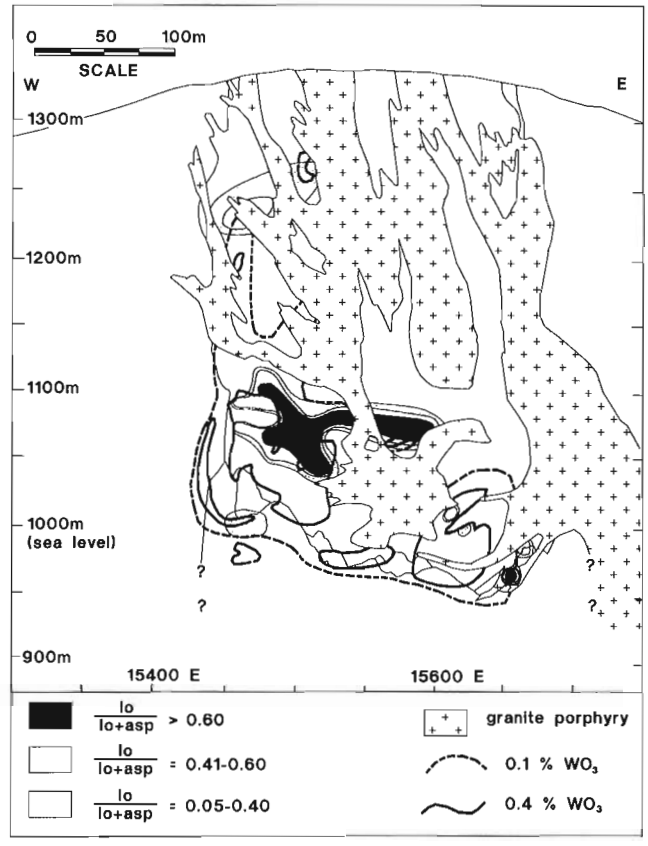


**Figure 9.** Contoured values of the weight proportion of loellingite relative to loellingite + arsenopyrite on section 12405N.

## DISTRIBUTION OF ARSENOPYRITE AND LOELLINGITE

Of the 68 samples analyzed, 53 contained arsenopyrite, and 19 of these contained detectable amounts of loellingite. The weight proportion of loellingite relative to arsenopyrite + loellingite in 16 of these samples ranged from 0.05 to 0.95 (Table 1; 3 samples not listed contained only trace amounts of loellingite). The results determined from the two standard curves for each sample agree within 5-10%, which is within the estimated analytical error.

Distribution of the arsenopyrite and loellingite is shown in Figures 8 and 9. Arsenopyrite is widespread and occurs throughout much of the Fire Tower Zone, both within and outside the tungsten-molybdenum deposit. It is, however, less abundant or absent in samples from the lower part of the deposit in Fire Tower breccia, granite breccia, and underlying fine grained granite. Loellingite, on the other hand, is more restricted in its distribution. All samples containing loellingite occur within the deposit (as outlined by the 0.1% $WO_3$ contour), and samples containing the highest proportions of loellingite generally occur in or near high-grade tungsten zones (>0.4% $WO_3$). Loellingite is particularly concentrated in the upper western part of the deposit, above and in the upper part of a high-grade tungsten zone (Fig. 9). The association of loellingite with other high-grade tungsten zones is more erratic. One of the samples containing detectable amounts of loellingite (B13-95, Table 1) is from altered and slightly mineralized granite porphyry in the lower, eastern part of the Fire Tower Zone, and is not part of the tungsten-molybdenum stage of mineralization.

**Table 1.** Peak-height ratios of loellingite to arsenopyrite measured from X-ray diffraction traces of heavy-mineral separates from the Fire Tower Zone, Mount Pleasant, and the weight proportion of loellingite (lo) relative to arsenopyrite (asp)

| Sample No. | 1<br>lo 2.59 Å / asp 2.67 Å | 2<br>lo 2.33 Å / asp 2.67 Å | lo / lo + asp (1/2) |
|---|---|---|---|
| MPS212-880 | 17.54 | 13.16 | 0.95/0.95 |
| 1A67-350 | 9.17 | 6.90 | 0.85/0.90 |
| MPS212-980 | 6.06 | 4.26 | 0.81/0.82 |
| B49-200 | 4.42 | 3.82 | 0.77/0.80 |
| B13-95 | 3.70 | 2.65 | 0.73/0.72 |
| B44-150* | 2.94 | 2.45 | 0.73/0.71 |
| B49-100 | 2.09 | 1.34 | 0.62/0.58 |
| B49-230* | 0.74 | 0.59 | 0.56/0.52 |
| MPS214-850 | 1.22 | 0.95 | 0.51/0.51 |
| B49-180* | 0.96 | 0.72 | 0.49/0.48 |
| B11-100 | 1.01 | 0.58 | 0.46/0.41 |
| B49-35 | 0.77 | 0.56 | 0.40/0.38 |
| MPS214-1100 | 0.44 | 0.33 | 0.28/0.29 |
| B11-50 | 0.31 | 0.30 | 0.21/0.25 |
| MPS212-840 | 0.27 | 0.19 | 0.21/0.23 |
| MPS214-835 | 0.17 | 0.0 | 0.05/0.0 |

*Samples (and standards) analyzed 6 months later than the rest of the samples.

**Table 2.** Chemical composition of representative arsenopyrite grains from the Fire Tower Zone, Mount Pleasant

| | 1 | 2 | 3 | 4 |
|---|---|---|---|---|
| | **Weight %** | | | |
| Fe | 33.28 | 34.10 | 33.63 | 32.98 |
| As | 46.84 | 47.69 | 47.09 | 47.53 |
| Co | 0.17 | 0.18 | 0.16 | 0.09 |
| Ni | 0.00 | 0.02 | 0.00 | 0.00 |
| Sb | 0.01 | 0.00 | 0.00 | 0.05 |
| S | 18.73 | 18.93 | 19.36 | 18.35 |
| total | 99.03 | 100.92 | 100.24 | 99.00 |
| | **Atomic %** | | | |
| Fe | 32.95 | 33.17 | 32.77 | 32.82 |
| As | 34.58 | 34.58 | 34.22 | 35.26 |
| Co | 0.16 | 0.17 | 0.14 | 0.09 |
| Ni | 0.00 | 0.02 | 0.00 | 0.00 |
| Sb | 0.00 | 0.00 | 0.00 | 0.02 |
| S | 32.30 | 32.07 | 32.87 | 31.81 |

Location of samples:
1. Drillhole MPS214 at 793 ft.
2. Drillhole MPS214 at 900 ft.
3. Drillhole MPS214 at 1200 ft.
4. Drillhole B49 at 100 ft.

## ARSENOPYRITE COMPOSITIONS AND APPLICATION OF THE ARSENOPYRITE GEOTHERMOMETER

Electron-microprobe analysis was carried out to determine the composition of the arsenopyrite, and whether or not any compositional zonation exists either within individual grains or throughout the Fire Tower Zone. The analysis was done using a Cambridge Microscan 5 electron-microprobe operated at 25 kV, with a beam current of 30 nA (measured on pyrite), by the WDS method using the following standards: pyrite, safflorite, millerite, tetrahedrite, arsenopyrite, chalcopyrite, sphalerite, bismuth, and nickel.

The chemical composition of representative samples of arsenopyrite are presented in Table 2 and Figure 10. The arsenopyrite compositions of all samples analyzed range from 33.5 to 35.5 atomic % As, 32.5 to 33.5 atomic % Fe, and 31.0 to 34.0 atomic % S. Compared to stoichiometric FeAsS, the Fire Tower Zone arsenopyrite compositions are slightly arsenic-rich (Fig.10). The contents of trace elements such as Co, Ni, and Sb are low, and cumulatively amount to 0.2 wt.% or less. The arsenopyrite compositions are relatively

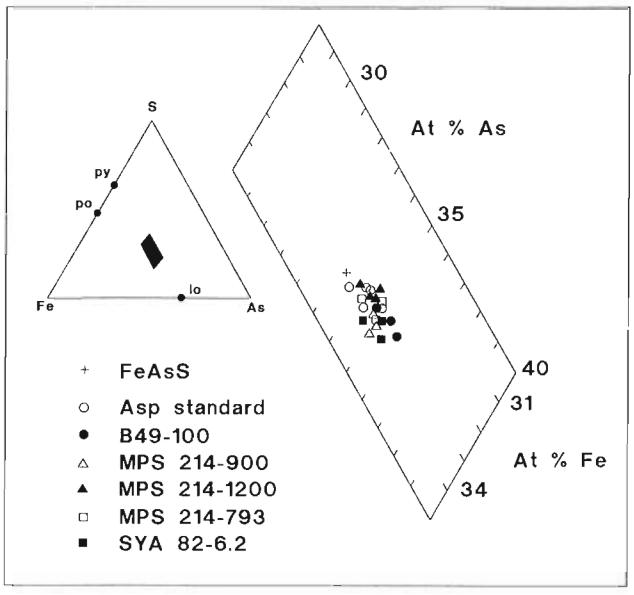


**Figure 10.** Plot of Fire Tower Zone arsenopyrite compositions on an Fe-As-S ternary diagram (py = pyrite, po = pyrrhotite, asp = arsenopyrite, lo = loellingite).

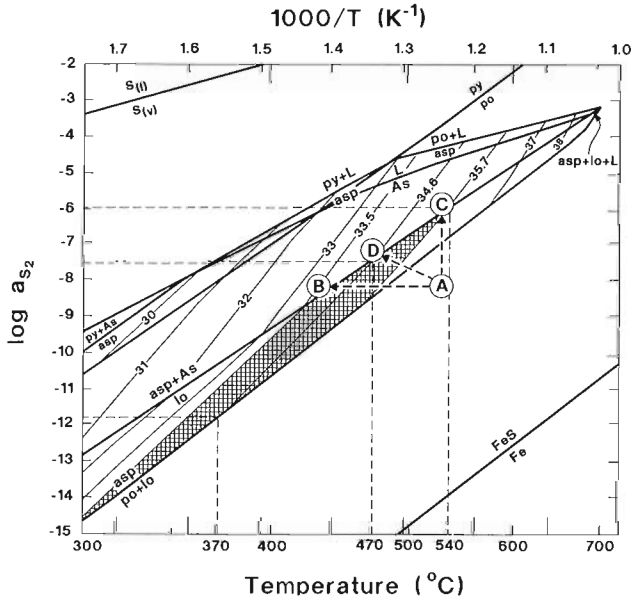


**Figure 11.** Stability relations of arsenopyrite on a projection of the activity of $S_2$ versus temperature; arsenopyrite compositions are contoured in atomic % As (after Kretschmar and Scott, 1976). Compositional range of Fire Tower Zone samples is represented by the hatched area; paths AB, AC, and AD represent different changes in temperature and/or activity of $S_2$ that possibly affected deposition of loellingite and arsenopyrite (see text for discussion)(asp = arsenopyrite, lo = loellingite, py = pyrite, As = arsenic, po = pyrrhotite, S = solid, L = liquid, and V = vapour).

restricted; although some variation in arsenopyrite composition from different parts of the Fire Tower Zone is evident, the differences are within analytical error. Similarly, no evidence of compositional zoning within individual arsenopyrite grains was observed.

Arsenopyrite compositions reflect the conditions under which the arsenopyrite and associated minerals formed. Kretschmar and Scott (1976) constructed a log $a_{S_2}$ - temperature diagram for the Fe-As-S system in which synthetic arsenopyrite compositions are contoured in atomic % As (Fig. 11). The application of this diagram to natural systems requires that equilibrium existed between arsenopyrite and loellingite at the time of their deposition. Once deposited, however, arsenopyrite is unlikely to re-equilibrate and change in composition in response to changing conditions, due to its refractory nature. Assuming equilibrium or near-equilibrium between arsenopyrite and loellingite in the Fire Tower Zone, application of the full range of Fire Tower Zone arsenopyrite compositions to this diagram indicates a temperature range of about 300 to 535°C and a range in log $a_{S2}$ of -6 to -15 (Fig. 11). The average As content of the arsenopyrite (34.6 atomic % As), corresponds to a more restricted temperature range of 370 to 470°C and log $a_{S_2}$ range of -7.6 to -11.8.

## DISCUSSION

Arsenopyrite is present throughout most of the Fire Tower tungsten-molybdenum deposit and surrounding rocks, except in samples from the lowermost part of the deposit. Loellingite is more restricted in its distribution; it occurs mainly in the central and upper parts of the deposit, particularly in the upper, higher grade parts of the tungsten zones. Loellingite was not detected in samples from outside the deposit.

Application of the Kretschmar and Scott (1976) arsenopyrite geothermometer to the average composition of the arsenopyrite indicates a temperature of formation between 370 and 470°C. In comparison, studies of fluid inclusions in associated gangue minerals from the Fire Tower Zone tungsten-molybdenum deposit gave homogenization temperatures ranging from 55 to 492°C (Samson, 1990). The higher temperatures in this range are in general accord with the temperatures indicated by the arsenopyrite geothermometer. The lower temperatures are probably due to cooling of the mineralizing fluids prior to entrapment (Samson, 1990); this cooling likely occurred after deposition of arsenopyrite.

Arsenopyrite is not considered to be a good geobarometer (Kretschmar and Scott, 1976), but Morimoto and Clark (1961) and Sharp et al. (1985) showed that S-rich arsenopyrite possesses a lower molar volume than As-rich arsenopyrite, and therefore is favoured at high pressures, whereas the As-rich member is favoured at low pressures. The As-rich composition of the arsenopyrite in the Fire Tower Zone thus is consistent with a relatively shallow

emplacement (<1 km) of granitic intrusions and associated tungsten-molybdenum and tin deposits at Mount Pleasant as suggested by Sinclair et al. (1988).

Paragenetic relationships indicate that deposition of loellingite began early and arsenopyrite continued later, although considerable overlap in the deposition of the two minerals is evident. These relationships may be due, at least in part, to changing conditions depicted schematically by paths AB, AC and AD in Figure 11. Point A represents approximately the initial conditions for deposition of loellingite in the loellingite + pyrrhotite stability field (although pyrrhotite does not occur with loellingite at Mount Pleasant). Points B, C, and D represent compositions of arsenopyrite that fall within the range observed from the electron-microprobe analyses. Increasing deposition of arsenopyrite relative to loellingite may have been due to decreasing temperature (path AB), increasing activity of $S_2$ (path AC), or some combination of the two (e.g., path AD). The close association of loellingite with high-grade tungsten zones suggests that the same factors have played a role in the formation of the Fire Tower Zone tungsten-molybdenum deposit. Other factors, such as changes in pressure and mixing of meteoric water with the mineralizing fluids, may also have been important but have not been considered here.

## ACKNOWLEDGMENTS

The authors gratefully acknowledge NovaGold Resources Ltd. for permission to carry out this study and to publish the results. G.J.A. Kooiman provided background information and encouragement for the study. Guy Darcy assisted with the heavy mineral separations, and Peter Jones and Don Harris provided electron-microprobe analyses. Jan Peter reviewed the paper and offered many constructive comments.

## REFERENCES

**Dagger, G.W.**
1972: Genesis of the Mount Pleasant tungsten-molybdenum-bismuth deposit, New Brunswick, Canada; Institution of Mining and Metallurgy, Transactions, v. 81, section B, p. 73-102.

**Durocher, K.E.**
1991: A study of the composition and distribution of arsenopyrite and loellingite in the Fire Tower tungsten-molybdenum deposit, Mt. Pleasant, New Brunswick; B.Sc. thesis, Carleton University, Ottawa, Ontario, 62 p.

**Fyffe, L.R.**
1991: Geology of the Flume Ridge - Kedron Stream map areas, Charlotte County, New Brunswick; in Project Summaries for 1991, Sixteenth Annual Review of Activities, (ed.) S. Abbott; New Brunswick Department of Natural Resources and Energy, Information Circular 91-2, p. 12-20.

**Kooiman, G.J.A., McLeod, M.J., and Sinclair, W.D.**
1986: Porphyry tungsten-molybdenum orebodies, polymetallic veins and replacement bodies, and tin-bearing greisen zones in the Fire Tower Zone, Mount Pleasant, New Brunswick; Economic Geology, v. 81, p. 1356-1373.

**Kretschmar, U. and Scott, S.D.**
1976: Phase relations involving arsenopyrite in the system Fe-As-S and their application; Canadian Mineralogist, v. 14, p. 364-386.

**McCutcheon, S.R.**
1990a: The Late Devonian Mount Pleasant caldera complex: stratigraphy, mineralogy, geochemistry and the geologic setting of a Sn-W deposit in southwestern New Brunswick; Ph.D. thesis, Dalhousie University, Halifax, Nova Scotia, 609 p.
1990b: The Mount Pleasant caldera: geological setting of associated tungsten-molybdenum and tin deposits; in Mineral Deposits of New Brunswick and Nova Scotia, (ed.) D.R. Boyle; Guidebook for field trip associated with the 8th IAGOD Symposium, August, 1990; Geological Survey of Canada, Open File 2157, p. 73-77.

**Morimoto, N. and Clark, L.A.**
1961: Arsenopyrite crystal-chemical relations; American Mineralogist, v. 15, p. 121-126.

**Parrish, I.S. and Tully, J.V.**
1978: Porphyry tungsten zones at Mt. Pleasant, N.B.; The Canadian Institute of Mining and Metallurgy, Bulletin, v. 71, no. 794, p. 93-100.

**Petruk, W.**
1973: The tungsten-molybdenum-bismuth deposit of Brunswick Tin Mines Limited; its mode of occurrence, mineralogy, and amenability to mineral beneficration; The Canadian Institute of Mining and Metallurgy, Bulletin, v. 66, no. 732, p. 113-130.

**Pouliot, G., Barondeau, B., Sauve, P., and Davis, M.**
1978: Distribution of alteration minerals and metals in the Fire Tower Zone at Brunswick Tin Mines Limited, Mount Pleasant area, New Brunswick; Canadian Mineralogist, v. 16, p. 223-237.

**Samson, I.M.**
1990: Fluid evolution and mineralization in a subvolcanic granite stock: the Mount Pleasant W-Mo-Sn deposits, New Brunswick, Canada; Economic Geology, v. 85, p. 145-163.

**Sharp, Z.D., Essene, E.J., and Kelly, W.C.**
1985: A re-examination of the arsenopyrite geothermometer: pressure considerations and applications to natural assemblages; Canadian Mineralogist, v. 23, p. 517-534.

**Sinclair, W.D. and Kooiman, G.J.A.**
1990: The Mount Pleasant tungsten-molybdenum and tin deposits; in Mineral Deposits of New Brunswick and Nova Scotia, (ed.) D.R. Boyle; Guidebook for field trip associated with the 8th IAGOD Symposium, August, 1990; Geological Survey of Canada, Open File 2157, p. 78-87.
1992: The Saddle Zone tin deposit, Mount Pleasant, New Brunswick: in situ concentration of ore fluids in a granitic magma; Geological Association of Canada/Mineralogical Association of Canada, Abstracts Volume, v. 17, p. A101.

**Sinclair, W.D., Kooiman, G.J.A., and Martin, D.A.**
1988: Geological setting of granites and related tin deposits in the North Zone, Mount Pleasant, New Brunswick: in Current Research, Part B; Geological Survey of Canada, Paper 88-1B, p. 201-208.

Geological Survey of Canada projects 770071, 680023

# Cambro-Ordovician stratigraphy in the Québec Reentrant, Grosses-Roches-Les Méchins area, Gaspésie, Quebec

**Lawrence Bernstein[1], Noel P. James[1] and Denis Lavoie**
**Quebec Geoscience Centre, Sainte-Foy**

*Bernstein, L., James, N.P., and Lavoie, D., 1992: Cambro-Ordovician stratigraphy in the Québec Reentrant, Grosses-Roches-Les Méchins area, Gaspésie, Quebec; in Current Research, Part E; Geological Survey of Canada, Paper 92-1E, p. 381-392.*

***Abstract***

*Cambro-Ordovician deep-water sediments in the Grosses-Roches-Les Méchins area comprise three formations: Orignal, Grosses-Roches (new), and Anse du Crapaud (new). The Orignal is Lower? to early Upper Cambrian red, green, and grey shale. It is sharply overlain by the Grosses-Roches, a thick succession of Upper Cambrian arenite and polymict- and oligomict conglomerate. The Anse du Crapaud gradationally overlies the Grosses-Roches and includes four informal members, in ascending order, A-D: 'A' is black and greenish black shale with minor limestone and sandstone; 'B' is limestone and sandstone in olive, brown, and black mudstone; 'C' is mostly olive and brown mudstone; and 'D' includes limestone and lesser sandstone, siltstone, and brown and black mudstone and shale. Lower Tremadocian to uppermost Arenigian-lower Llanvirnian trilobites and graptolites are in members B-D. The Cambrian-Ordovician boundary is most likely near the base of member A.*

***Résumé***

*Les sédiments d'eau profonde cambro-ordoviciens de la région de Grosses-Roches-Les Méchins comprennent trois formations, soit celles d'Orignal, de Grosses-Roches (nouvelle) et d'Anse du Crapaud (nouvelle). La Formation d'Orignal du Cambrien inférieur ? au début du Cambrien tardif est composée de shale rouge, vert et gris. Elle est en contact direct avec la formation sus-jacente de Grosses-Roches, une épaisse succession du Cambrien supérieur d'arénite et de conglomérat tant polygénique qu'oligogénique. La Formation de Grosses-Roches passe graduellement à celle d'Anse du Crapaud, laquelle est divisée en quatre membres informels qui, de la base au sommet (A-D), sont les suivants : le membre A est formé de shale noir et noir verdâtre avec des quantités mineures de calcaire et de grès; le membre B consiste en du calcaire et du grès, interstratifiés avec du mudstone olive, brun et noir; le membre C est principalement constitué de mudstone olive et brun; quant au membre D, il comprend du calcaire avec des quantités moindres de grès, de siltstone ainsi que de mudstone et de shale bruns et noirs. Les membres B et D contiennent des trilobites et des graptolites s'échelomant du Trémadocien inférieur à l'Arénigien terminal – Llanvirnien inférieur. La limite cambro-ordovicienne est probablement localisée près de la base du membre A.*

[1] Department of Geological Sciences, Queen's University, Kingston, Ontario K7L 3N6

## INTRODUCTION

Cambro-Ordovician continental slope sedimentary rocks outcrop for some 300 km along the south shore of the St. Lawrence River in eastern Quebec (Fig. 1). The allochthonous succession consists of siliciclastic-dominated Cambrian, and mixed siliciclastic and carbonate Lower Ordovician strata. This paper describes Cambro-Ordovician strata extensively exposed between Grosses-Roches and Les Méchins in Gaspésie (Fig. 1, 2). These are the best preserved, most contiguous sections in the region. This new information is the result of field work during the summer of 1991, three weeks of which were spent in the Grosses-Roches-Les Méchins area as part of a regional investigation of Cambro-Ordovician event stratigraphy in eastern Quebec. The tripartite succession includes two Cambrian units, a lower *Orignal Formation* and an upper *Grosses-Roches Formation* (new), overlain by a Lower- lower Middle Ordovician *Anse du Crapaud Formation* (new). The Anse du Crapaud Formation is the main focus of this paper.

## GEOLOGICAL SETTING

Cambro-Ordovician slope deposits of the Québec Supergroup, Lower St. Lawrence-Gaspésie region, were deposited in the Québec Reentrant of the Humber tectonostratigraphic zone (Williams, 1979) (Fig. 1). Strata are preserved in southeasterly-dipping thrust slices emplaced during the Middle Ordovician Taconian orogeny and comprise part of the inner belt of the Québec Appalachians external tectonic domain (St-Julien and Hubert, 1975). They have also been displaced by dextral and sinistral transcurrent faults related to Acadian orogenesis (Slivitzky et al., 1991). Strata in the study area generally dip to the southeast (30-60°) and are cut by numerous south-trending, steep normal and reverse faults with displacements of tens to hundreds of metres.

## STRATIGRAPHY: LOWER ST. LAWRENCE-GASPÉSIE

There are many reasons for the lack of a well defined stratigraphy in the Lower St. Lawrence - Gaspésie; the region is structurally complex, fossils are rare, good exposure is generally limited to the rocky coast, and strata consist overwhelmingly of schists, shales, and siltstones with few marker horizons. The present stratigraphy, based on large-scale mapping (e.g., Béland, 1957; Hubert, 1973; Biron, 1971, 1974; Liard, 1973; Lajoie, 1972; Vallières, 1984; Slivitzky et al., 1991; and others), is suitable for broad, regional correlations (Fig. 3), but proved to be inadequate at finer scales.

The lithostratigraphy and stratigraphic nomenclature of Vallières (1984) in the Rivière-du-Loup-Trois-Pistoles region has recently been extended into Gaspésie (Slivitzky et

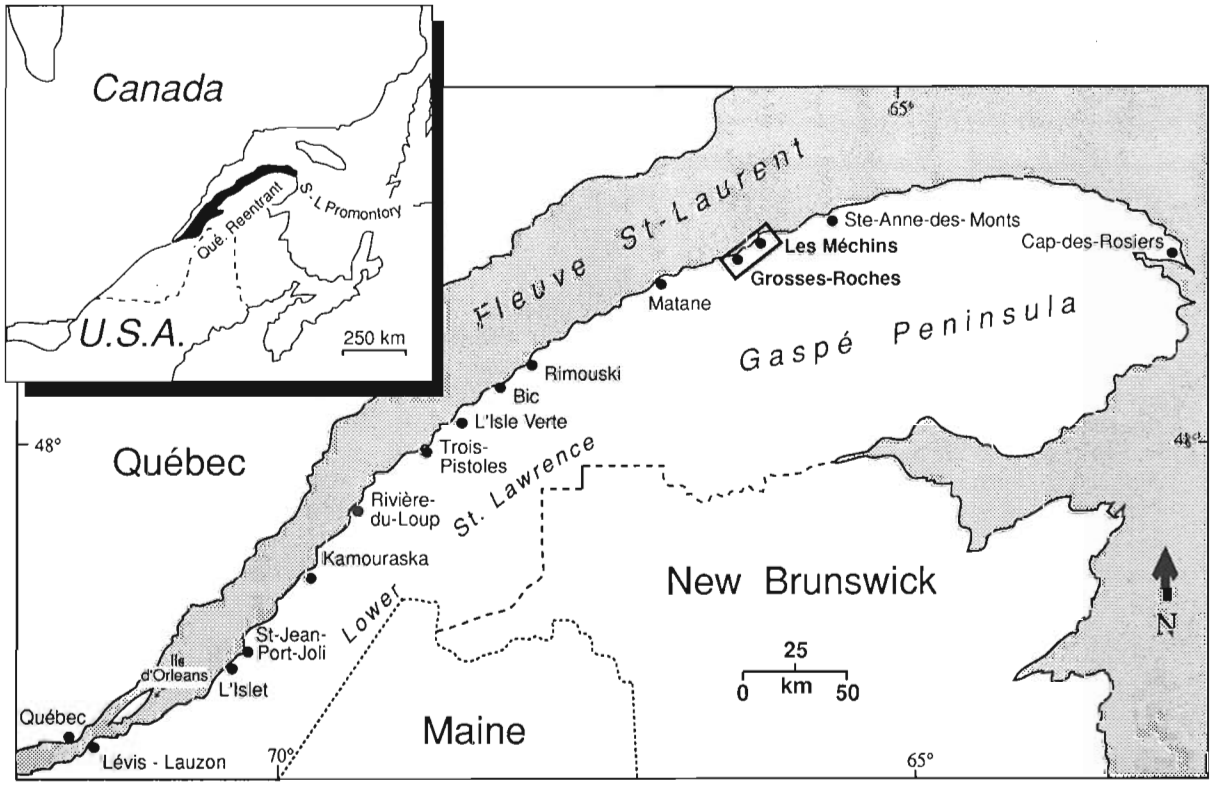


**Figure 1.** Location map for eastern Quebec with inset map showing distribution of allochthonous Cambro-Ordovician slope sediments in black; S-L = St. Lawrence. Box highlights field area for this contribution.

al., 1991) (Fig. 3). Evidence presented later, however, indicates that there are significant lithological differences that warrant alternate nomenclatures in the Grosses-Roches-Les Méchins area.

## STRATIGRAPHY: GROSSES-ROCHES-LES MÉCHINS

Cambrian-Ordovician slope facies crop out almost continuously between Grosses-Roches and Les Méchins (Fig. 1, 4) in foreshore flats, road- and rivercuts, and quarries. The succession is divided into three formations: a lower, fine grained Orignal, a middle, coarse grained Grosses-Roches (new), and an upper heterolithic Anse du Crapaud (new) (Fig. 2, 5).

### *The Orignal Formation*

This formation is dominated by greyish red, dark greenish grey, and dark gray mudstone and shale (10 R 5/4, 5 GY 4/1, and N3; Geological Society of America colour chart) with numerous laminations and thin beds of siltstone, and rare, thick bedded, greenish black (5 GY 2/1), coarse grained, subarkosic arenite and wackestone (Fig. 2 and 6a). The formation is more than 200 m thick; the base is covered.

#### Age of the Orignal Formation

No fossils are known from the Orignal Formation in Gaspésie. In similar facies at L'Islet and Kamouraska (St-Roch Formation, Fig. 3), a Lower Cambrian age is indicated by the brachiopod *Botsfordia pretiosa* (Hubert, 1973; and this study) (Fig. 7). Fossils have not been found in-place in the upper part of the formation. Lower Cambrian *Salterella* is found in platform-derived limestone clasts at St-Jean-Port-Joli (Strong and Walker, 1981). Upper strata lie just below Middle to early Late Cambrian Grosses-Roches conglomerate in the study area (see below).

### *The Grosses-Roches Formation (new)*

The Grosses-Roches Formation is a 300-400 m thick succession dominated by resedimented polymict and intraformational conglomerate and very coarse grained sandstone (mostly quartz arenite) (Fig. 2). At the base, coarse grained quartz arenite or polymict conglomerate directly overlies the Orignal Formation, locally filling channel-shaped scours apparently many tens of metres wide and deep (Fig. 2 and 6a).

McGerrigle (1950) and Béland (1957) thought that this coarse grained succession was Lower Ordovician in age because it contains Upper Cambrian boulders (Rasetti, 1946) and is overlain by Lower Ordovician beds. For this reason they placed it at the base of the Lower Ordovician Cap-des-Rosiers Formation. This is incorrect lithostratigraphic procedure. Moreover, similar coarse grained siliciclastics and conglomerates are not exposed at Cap-des-Rosiers.

Southwest of the study area, Vallières (1984) introduced the Trois Pistoles Group for the succession overlying the Orignal Formation. The group includes three formations: a lower coarse grained Saint-Damase, a middle finer grained Rivière-du-Loup, and an upper coarse grained Kamouraska (Fig. 3). This lithostratigraphic framework was extended farther northeast and expanded to include, at the top, the Romieu Formation (Slivitzky et al., 1991) (Fig. 3). Generally, the coarse grained Sainte-Damase and Kamouraska formations can only be distinguished where they are separated by finer grained Rivière-du-Loup beds. Such fine grained strata are not well developed in the Grosses-Roches-Les Méchins area (see Fig. 2) and Slivitzky et al. (1991, maps 2093-B, D) mapped the Saint-Damase and Kamouraska formations as a single unit. Our observations suggest that the entire siliciclastic-dominated, coarse grained succession is best encompassed by one formation. The name is used for well known exposures located near the town of Grosses-Roches. Importantly, the presence or absence of fine grained Rivière-du-Loup strata may reflect relative 'distal' and 'proximal' positions on the paleocontinental slope.

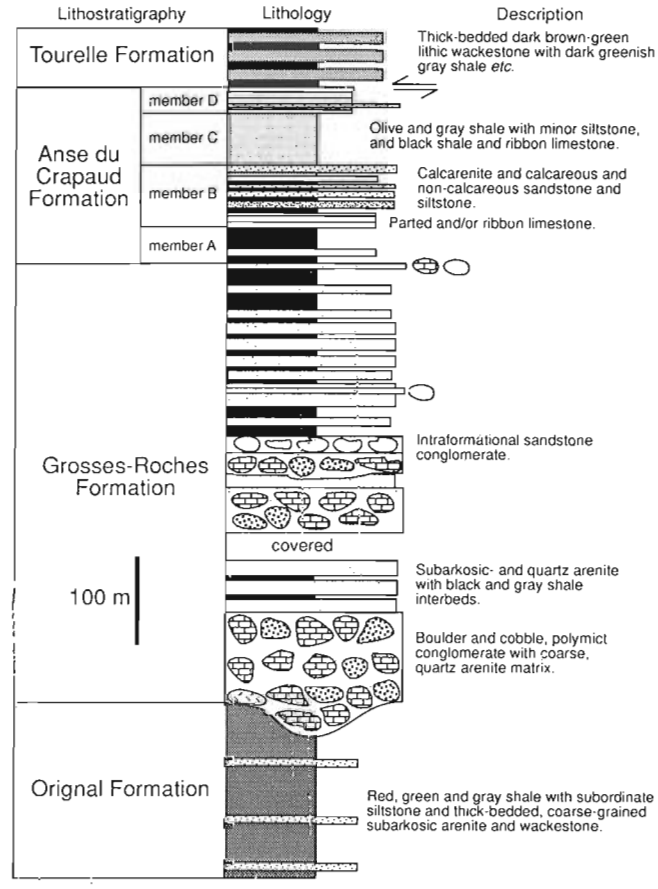


**Figure 2.** Generalized Cambro-Ordovician lithostratigraphic column in the Grosses-Roches-Les Méchins area. Description of Grosses-Roches Formation adapted from Hendry (1978).

Slivitzky et al. (1991) also proposed the Romieu Formation for a thick succession of mostly dolomitic mudstone and calcilutite between their Kamouraska and Rivière Ouelle formations (Fig. 3); they did not map the formation in the Grosses-Roches-Les Méchins area (their maps 2093B, D). Likewise, we did not recognize Romieu Formation strata, however, the formation is poorly constrained lithostratigraphically and difficult to apply in the field. Slivitzky et al. (1991) did not define its lower and upper bounding surfaces or describe a type section. In addition, the reference section is bounded by faults, highly faulted internally, and diagenetically altered. The age-range of the formation is also poorly constrained: Middle Cambrian, Late Cambrian, and Arenigian fossils have been attributed to the formation (Slivitzky et al., 1991, p. 13).

Grosses-Roches Formation sediments are organized in fining-upward metre to decametre scale packages with basal conglomerate successively overlain by sandstone and shaly sandstone or shale (Hendry, 1978). Intraformational oligomict conglomerate (sandstone clasts in sandstone matrix) is common in the upper half of the formation. Fine grained interbeds of black shale, light grey siltstone, and fine grained sandstone are common throughout. Ribbon calcisiltites occur occasionally in the upper part of the formation.

Polymict quartzose conglomerates contain sandstone and carbonate clasts; the former are more common than the latter. Abundant round boulders and cobbles of coarse grained sandstone and tan weathering, cherty dololutite and dolomitic siltstone are probably derived from the underlying Orignal Formation where there are identical sandstone and dolomitic beds. A similar origin is suggested for metre-size rafts of red and green shale in the basal part of the formation. Platform-derived carbonate clasts are common, usually composed of limestone and include, in relative decreasing order of abundance, oolite, bioclastic- grainstone, packstone and wackestone, thrombolite, and stromatolite (Fig. 6b). They are usually rounded and up to 2 m in diameter. In contrast, slope-derived limestone clasts are tabular and consist of calcilutite and calcisiltite. They are usually massive, but can be laminated and ripple cross-laminated, and are quite variable in length (up to 1 m). In the basal part of the formation platform clasts are more common than slope-derived clasts whereas in its upper part it is the reverse. Boulders and cobbles of polymict conglomerate, although less abundant than other clast types, are significant because they reflect at least two phases of resedimentation and lithification. Occasional crystalline basement boulders are also present.

The upper part of the formation is gradational with the overlying Anse du Crapaud Formation (Fig. 5). The 60-70 m thick interval is mostly black, grey, and dark greenish grey (5 G 4/1) shale, ribbon and parted siltstone (calcareous and non-calcareous), and minor ribbon calcisiltite/calcilutite. Subordinate coarser lithologies are laterally impersistent, very thick-bedded, quartzose polymict conglomerate, intraformational conglomerate and thinner bedded, coarse grained sandstone.

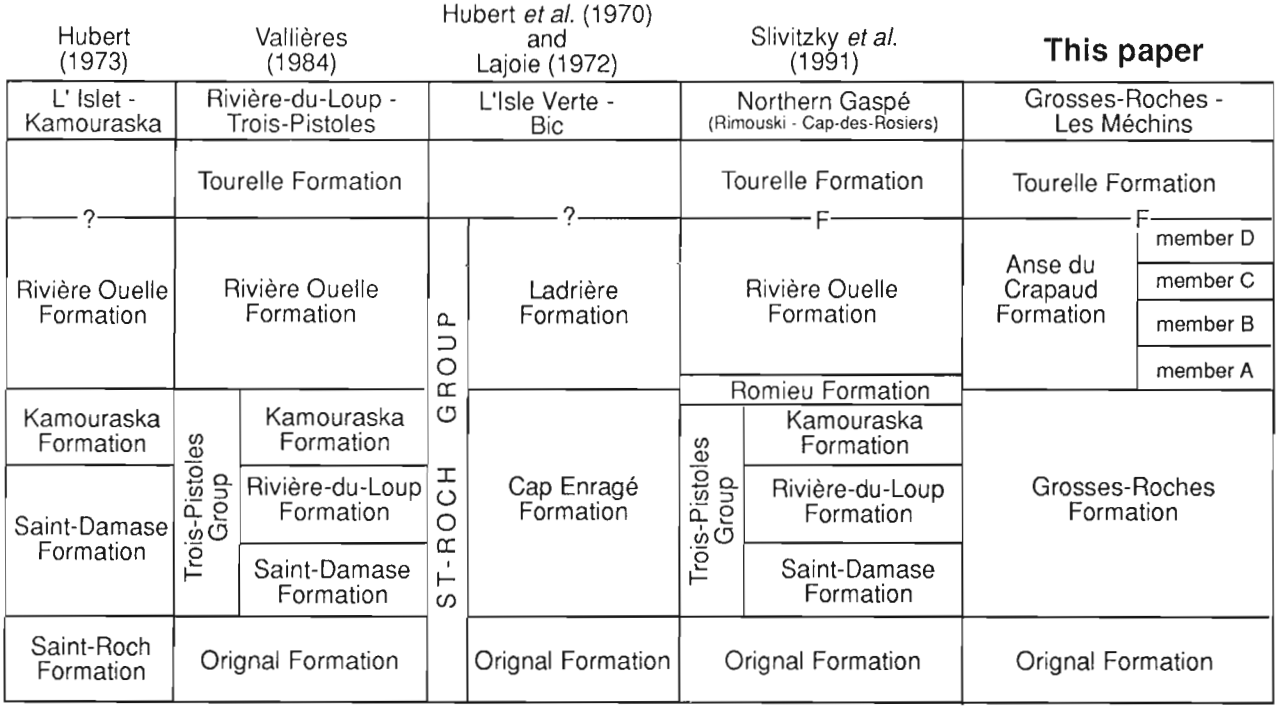


**Figure 3.** Correlation of Cambrian to early Middle Ordovician lithostratigraphic units in eastern Quebec (Lower St. Lawrence-Gaspésie) along the south shore of the St. Lawrence River. F – fault contact; ? – contact covered or section incomplete. For localities, see Figure 1.

### Age of the Grosses-Roches Formation

Rasetti (1945, 1946, 1948a, b) extracted Lower to early Upper Cambrian (upper? Marjuman stage (Ludvigsen and Westrop, 1985)) trilobites from limestone boulders in polymict conglomerates, indicative of deposition not older than early Upper Cambrian (Fig. 5). A Tremadoc age for the basal part of the overlying formation suggests that Grosses-Roches deposition probably ceased near the end of the Cambrian.

## *Anse du Crapaud Formation (new)*

The Anse du Crapaud Formation is a 235-270 m thick succession of shale, siltstone, limestone, sandstone, and subordinate limestone conglomerate (Fig. 2, 5, 8). The base rests conformably on the uppermost quartzose conglomerate or coarse grained arenite of the Grosses-Roches Formation. The top is in fault contact with overlying Middle Ordovician Tourelle Formation sandstones. Correlative facies in the Rivière-du-Loup region are gradationally overlain by the Tourelle (Vallières, 1984); elsewhere they are usually covered by the fault-bounded Cap-Chat Melange (Biron, 1971, 1974; Slivitzky et al. 1991).

Slivitzky et al. (1991) applied the term Rivière Ouelle to strata overlying our Grosses-Roches Formation (Fig. 3). This term was originally defined in the L'Islet-Kamouraska region for a succession of greyish red (10 R 4/2), greenish grey (5 GY 6/1) and grey shale with olive-grey siltstone (5 Y 4/1) (Hubert, 1973) (Fig. 3). Strata in the Grosses-Roches-Les Méchins region, however, are significantly different, having abundant limestone and sand-size siliciclastic units and very few reddish mudstone beds. It is suggested, therefore, that a new and locally derived name is appropriate and neccessary in order to reflect these mappable lithological differences (see below). Although the term Gros Méchins is preferable, it is in use (Biron 1974; Slivitzky et al., 1991). Anse du Crapaud is instead proposed as it is near exposures of the type section.

The Anse du Crapaud Formation is informally divided on the basis of detailed observations and measured sections into four members that are, in ascending order, A-D. Members A-C are apparently mappable southwest to Matane; members B and C are exposed and well developed at Cap-des-Rosiers.

### Member A

Member A is dominated by variegated shale and mudstone that is black, greenish black (5 GY 2/1), greenish grey (5 GY 6/1), dark grey (N3) and interlaminated black-dark greenish grey (Fig. 5, 6c). In the upper part of the member shale is calcareous and has rare horizontal burrows. Subordinate lithologies are nodular and thin-bedded parted and ribbon calcisiltite/calcilutite, quartzose and non-quartzose calcarenite, and fine grained, dolomitic or calcareous sandstone. Calcisiltite, calcarenite, and sandstone beds and lenses generally display ripple-lamination and locally are crossbedded. Thick layers of displasive fibrous calcite, occasionally with cone-in-cone structure (see Coniglio, 1985; Franks, 1969), are locally developed near the top of the member. Clastic dykes and synsedimentary slumped beds are present. The variable thickness of member A (25-60 m) mostly reflects tectonic thickening and shortening.

*Age of member A*

Unidentified graptoloid fragments, possibly including *Rhabdinopora* sp. (identified by L. Bernstein; see Williams and Stevens, 1991) are found in the upper part, suggesting a Tremadocian age (Fig.7).

### Member B

This 90 m-thick succession of limestone, sandstone, siltstone, shale, and mudstone rests sharply and conformably on member A. It is divided into limestone-dominated lower (1) and siliciclastic-dominated upper (2) units (Fig. 5, 8).

*Unit 1*

This 25-30 m-thick interval consists of thick- and thin-bedded, parted and ribbon calcilutite/calcisiltite with subordinate calcarenite. Limestones are quartzose in the uppermost part. Rare lenses and thin and thick beds of limestone conglomerate are also present (Fig. 6d). Limestones weather to a very pale orange (10 YR 8/2), but are light grey on fresh surfaces. Some thin beds are ripple-laminated; thicker strata are sharp-based and commonly have graded lower, and ripple-laminated upper parts. Shales and mudstones are black or brown and contain burrows (*Chondrites*).

*Unit 2*

Unit 2 includes thin- and medium-bedded fine-grained sandstone, and thick-bedded, coarse grained, calcareous quartz arenite, and peloid calcarenite (locally quartzose) (Fig. 6c). Thin and thick interbeds contain ribbon and parted calcarenite and calcisiltite, and rare intraformational

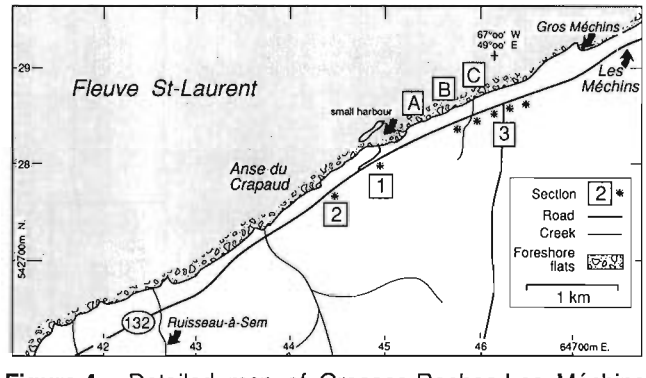


**Figure 4.** Detailed map of Grosses-Roches-Les Méchins study area shown in Figure 1. Sections illustrated on Figures 5 and 8.

(slope-derived) limestone conglomerate. Subordinate shale and mudstone are typically well burrowed and pale olive (10 Y 6/2), olive grey (5 Y 4/1), or brownish black (5 YR 2/1).

Peloid calcarenites and coarse grained sandstones are laterally impersistent, generally have erosive bases, and usually are cross bedded (Fig. 6e, f). Paleocurrents indicate south and westerly sediment transport directions; rarely developed flutes indicate southerly flow. Siltstones/fine grained sandstones are yellowish grey to dusky yellow weathering (5 Y 7/2 to 5Y 6/4), grey on fresh surfaces and commonly dolomitic or calcareous. They are sharp-based and display grading, lamination, and ripple crosslamination; bases commonly have vertical and horizontal burrows and traces.

*Age of member B: unit 1.* Unit 1 is Tremadocian to lower Arenigian in age (Fig. 7). It contains unidentified graptoloid fragments (*Rhabdinopora*? sp.) that suggest Tremadoc deposition. Correlative ribbon and parted limestone and black shale sediments at Matane and Cap-des-Rosiers yield early? and middle Tremadoc graptolites (Landing et al., 1986, 1992; Bernstein, this study). A trilobite found near the base of the

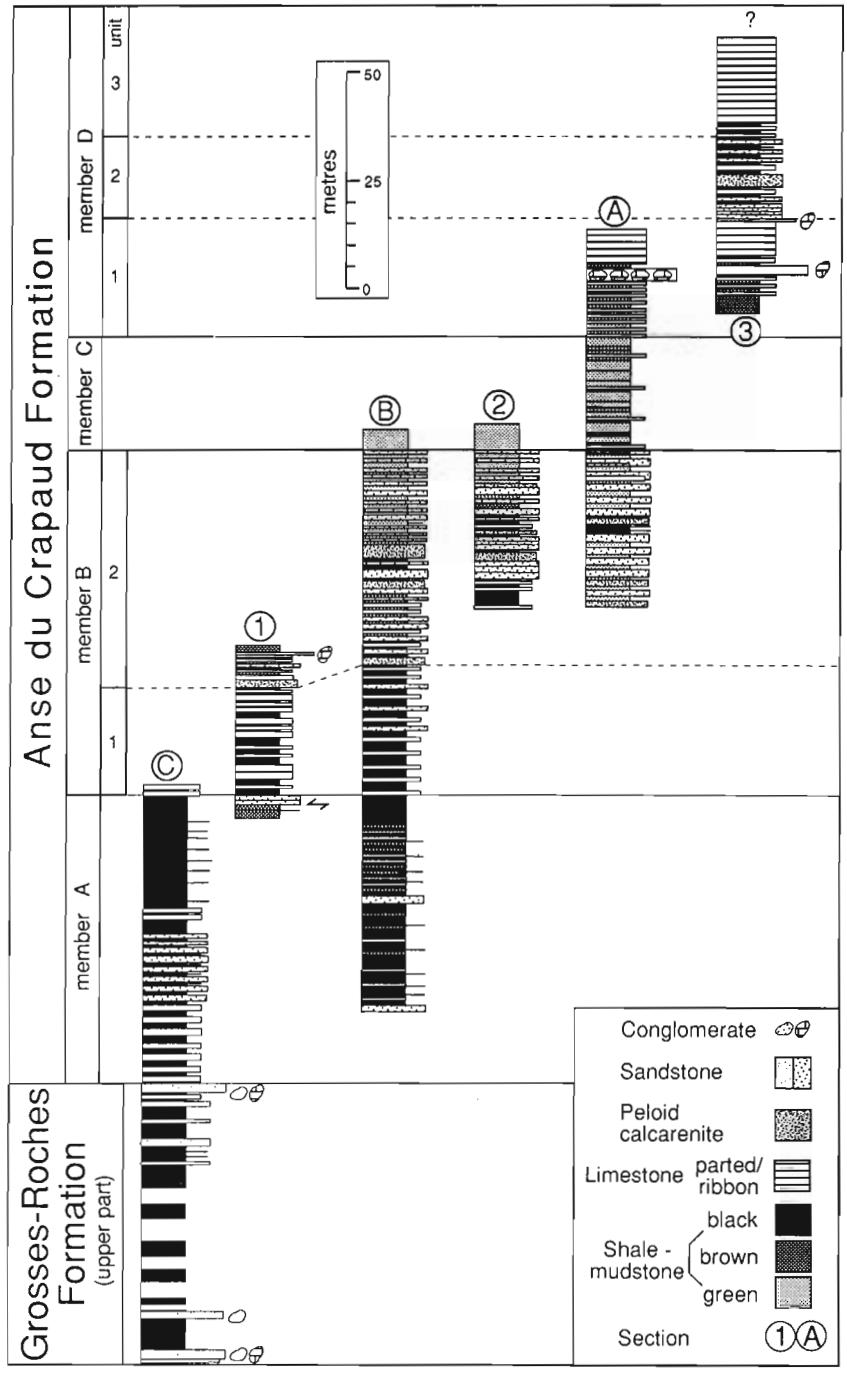


**Figure 5.**

Stratigraphic columns illustrating Cambro-Ordovician stratigraphy in Grosses-Roches-Les Méchins area. Section locations are shown in Figure 4. Sections 1, 2, and 3 are detailed in Figure 8. Note that only the upper part of the Grosses-Roches Formation is shown (see text for detailed description).

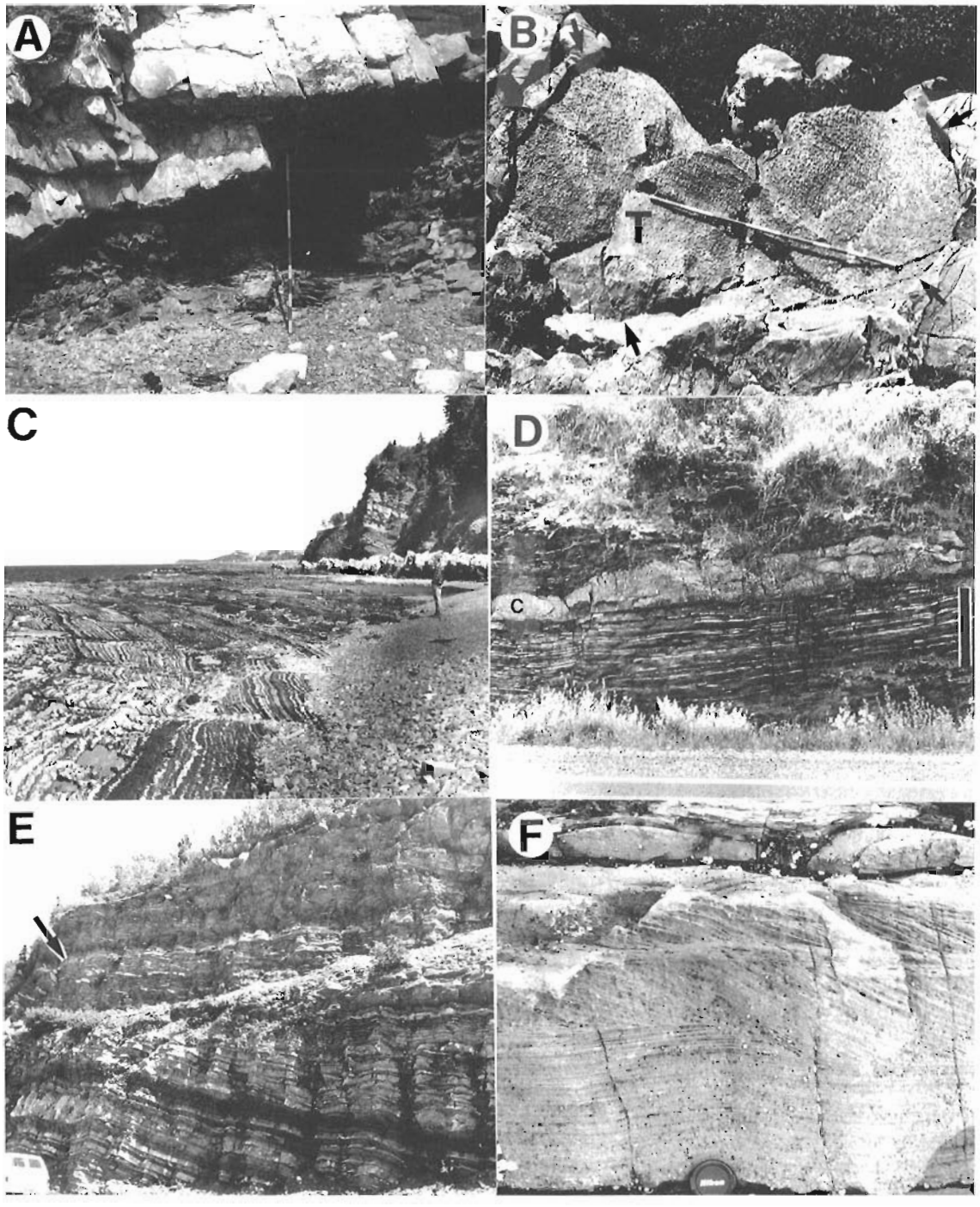


**Figure 6.** Field photographs of Orignal and Grosses-Roches formations and Anse du Crapaud Formation, members A-C. Way up is at top of page unless otherwise noted. **A**) Contact between Orignal Formation shale and mudstone and overlying Grosses-Roches Formation sandstone, near Grosses-Roches. Staff = 1.5 m. **B**) Plan view of large thromobolite boulder (T) near base of Grosses-Roches Formation, Anse du Crapaud. Arrows indicate edge of boulder. Staff = 1.5 m. **C**) Member A, Anse du Crapaud Formation, exposed in foreshore flats at low tide, north of small harbour (see Fig. 4), looking north. Resistant beds on right are quartzose peloid calcarenites of member B. Cliff in background is made up of members B and C. Geologist on right for scale = 1.9 m. **D**) Ribbon limestone and a thick, slope-derived limestone conglomerate (C) in brown and black mudstone of unit 1, member B, Anse du Crapaud Formation, in roadcut on route #132 east of Grosses-Roches at Ruisseau-à-la-Loutre. Bar = 1.5 m. **E**) Contact between members B and C (arrow), Anse du Crapaud Formation, in roadcut, section 2. Truck for scale. **F**) Peloid calcarenite with erosive base, lower laminated and upper compound cross-stratified parts, unit 2, member B, Anse du Crapaud Formation, foreshore flats section C. Note erosive base of lower cross-stratified set. Lens cap diameter = 4 cm.

Cap-des-Rosiers section tentatively identified as *Myindella* (R.A. Fortey, pers. comm., 1992) confirms early Tremadoc deposition. *Tetragraptus* cf. *serra serra*, a lower Arenigian graptolite (Williams and Stevens, 1988), is tentatively identified in float from the base of a thick ribbon and parted limestone and black shale interval correlative to unit 1 exposed along the wharf road at Gros Méchins (Fig. 4). A basal Ordovician trilobite tentatively identified as *Shumardia* (*Conophyrs*) (R.A. Fortey, pers. comm., 1992) was found near the base of a small roadcut on highway #132, 1.2 km east of Grosses-Roches (Fig. 6d). The section is isolated and stratigraphically out of context; it is probably correlative with the base of unit 1 near Les Méchins and Gros Méchins.

*Age of Member B: unit 2.* Except for graptoloid fragments, no biostratigraphically significant fossils have been recovered. Calcarenites sampled for conodont analysis are being processed.

The change in shale and mudstone colour near the base of unit 2 from black to green may be chronologically significant. Landing et al. (1992) documented a similar colour change in slope deposits elsewhere in Gaspésie, central New York State and western Vermont, as have James and Stevens (1986) in western Newfoundland, and proposed that it is coincident with the Tremadoc/Arenig boundary. In both studies, biostratigraphic control is relatively good. This suggests that most of unit 2 may be lower Arenigian in age.

## Member C

Member C gradationally overlies member B. It is about 45 m thick and consists almost entirely of variably burrowed, dusky brown (5 YR 2/2) weathered mudstone and shale (Fig. 6e). Some brown and dark reddish brown (10R 3/4) mudstone is found near the base of the member. Minor black shale beds and siltstone laminae and thin beds weathered greyish yellow (5 Y 8/4) are developed in the lower 17 m. The upper 28 m contains sporadic black shale and ribbon calcilutite intervals 1-2 m thick.

*Age of member C*

No fossils to date have been recovered. A middle? Arenigian age is suggested by late Arenig graptolites and trilobites in the basal part of the overlying member (see below) and the tentative position of the Tremadoc/Arenig boundary in member B (Fig. 7).

## Member D

This member is heterolithic assemblage of ribbon and parted limestone, quartz arenite, intraformational limestone conglomerate, and mudstone and shale that gradationally overlies member C. It is at least 80 m thick and includes, in ascending order: a limestone-rich unit (1), a sandstone/siltstone and limestone unit (2), and a limestone-dominated unit (3).

*Unit 1*

This 30 m thick interval is mostly ribbon and parted limestone. Nodular and thin-bedded ribbon calcilutite in bioturbated(?) moderate olive brown (5 Y 4/4) to olive black (5 Y 2/1) mudstone and shale at the base are erosively overlain by a laterally persistent 1-2.5 m thick, intraformational, clast-supported limestone conglomerate (Fig. 9a). Clasts are slope-derived calcisiltite, rarely calcilutite or resedimented displasive fibrous calcite layers. They are usually elongate, up to 7 cm long, poorly sorted, and moderately imbricated. The conglomerate is characterized by a pervasive stylolitic 'fitted' fabric; the matrix is black shale.

Above the conglomerate are ribbon and parted calcilutite/calcisiltite and subordinate calcarenite (Fig. 9b). Beds average 4 cm thick, weather to a very pale orange (10 YR 8/2) and are light grey on fresh surfaces. They rarely contain small burrows (*Chondrites*?). Interbeds and laminae are 'sooty', moderate brown (5 YR 3/4) weathering, silty mudstone and calcareous, fine grained sandstone/siltstone. Strata contain rare graptolites and trilobites.

*Unit 2*

The lower surface of unit 2 is a very low angle, erosion surface (Fig. 9b). The overlying rocks are a lower succession of limestone conglomerate and sandstone (6 m), a middle interval of mainly limestone (7 m), and an upper package of ribbon sandstone (5 m thick).

A westward thickening (0-75 cm), laterally impersistent, clast-supported limestone conglomerate overlies the basal erosive surface (Fig. 9c). A similar eastward-thickening conglomerate lies 2 m higher in the section. Clasts are

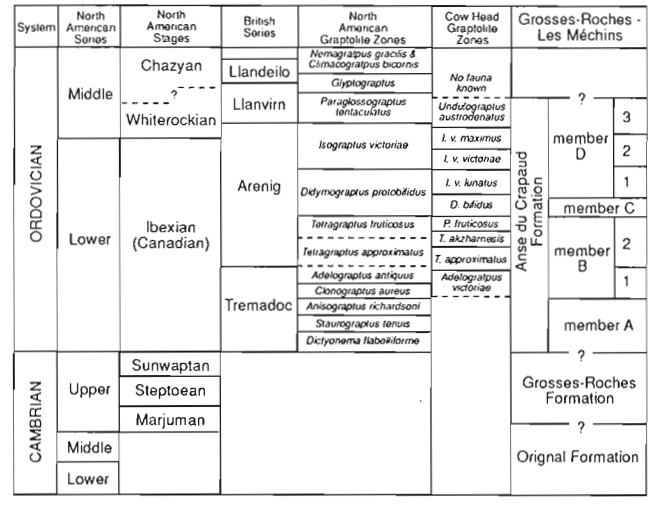


**Figure 7.** Cambrian-early Middle Ordovician biostratigraphy in Grosses-Roches-Les Méchins region. System, Series, Ordovician Stage boundaries and North American graptolite zones from Barnes et al. (1981). Upper Cambrian stages from Ludvigsen and Westrop (1985). Cow Head graptolite zones from Williams and Stevens (1988, 1991).

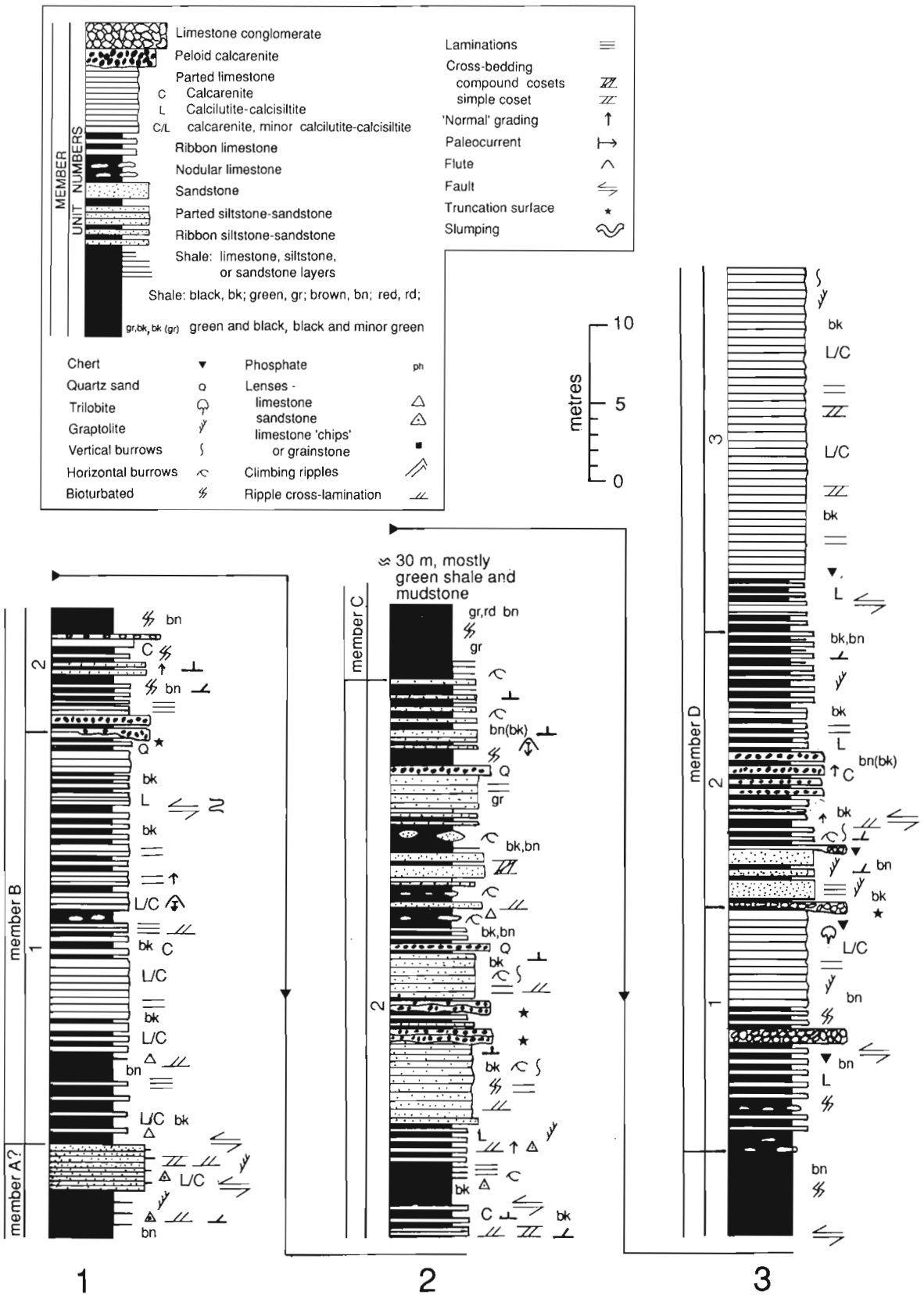


**Figure 8.** Detailed stratigraphic columns for sections 1-3. (See inset key for symbols and Fig. 4 for section location).

slope-derived calcilutite/calcisiltite and calcarenite, poorly sorted (up to 1 m long, 3 cm average), and typically elongate and flat-lying. Underlying beds of unit 1 are locally partly eroded and incorporated into the base of the conglomerate. Other clasts are black, chertified shale pebbles and uncommon large boulders of burrowed, pale olive and olive grey mudstone/shale. The sparse matrix is mostly dark greenish grey (5 GY 4/1) and black shale.

The basal conglomerate is followed by about 5 m of dolomitic, fine grained sandstone and siltstone separated by dark yellowish brown (10 YR 4/2) shale. Some of the sandstone and shale beds are graptolite-rich. Strata immediately overlying the lower conglomerate grade laterally into yellowish brown mudstone.

The middle succession is characterized by thin- to very thick-bedded, sharp-based, very pale orange weathering calcisiltite and calcarenite. Variably thick interbeds occur in these sediments and are moderate brown to brownish black, burrowed shale and mudstone and minor fine grained sandstone. Limestone beds commonly display, in ascending order, grading, horizontal lamination, and ripple crosslamination. Lenses of pebble-granule conglomerate

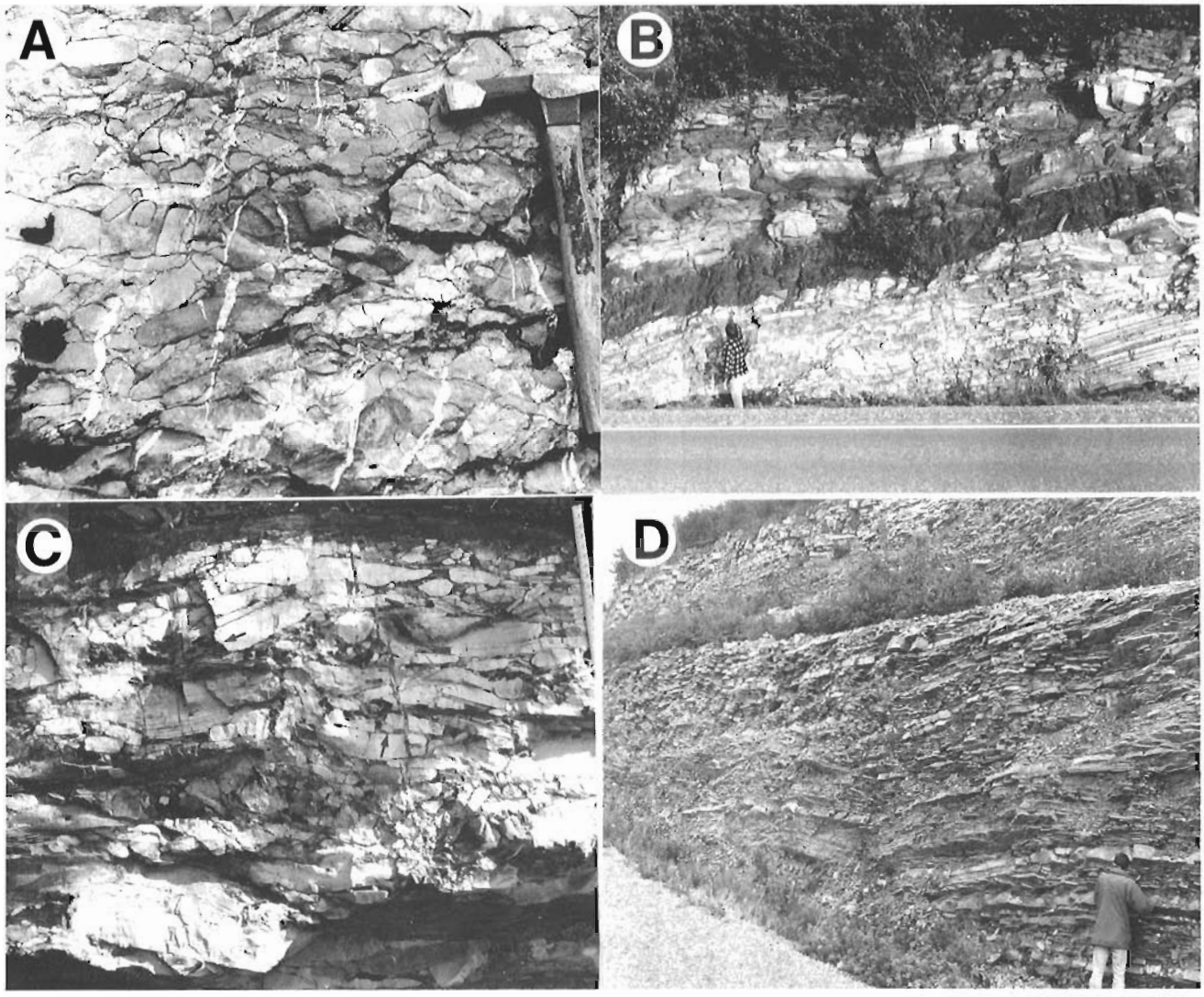


**Figure 9.** Field photographs of Anse du Crapaud Formation, member D. **A**) Slope-derived, clast-supported limestone conglomerate with fitted fabric near base of unit 1, exposed in foreshore cliff, section C. Hammer for scale. **B**) Parted limestone of unit 1 overlain by dark mudstone and lighter, dolomitic, fine grained sandstone and siltstone of unit 2, roadcut, section 3. Geologist points at contact between units. Note normal fault at left (north) end of roadcut and absence of limestone conglomerate at base of unit 2. **C**) Close-up of slope-derived limestone conglomerate at base of unit 1, roadcut, section 3. Black clasts (arrow) are chertified shale. Ruler = 15 cm. **D**) Parted and ribbon limestone of unit 3, section 3, in roadcut southwest of Les Méchins. Uppermost Arenigian - lower Llanvirnian graptolites were collected from second level above bench. Geologist for scale.

(chertified black shale and limestone clasts) are regularly developed in the graded basal parts. Trace fossils are commonly preserved on the base of beds and, rarely, poorly preserved graptolites are found in the finer grained beds. The upper sequence includes ribbon dolomitic fine grained sandstone in burrowed brownish black to moderate brown shale and mudstone. The upper 3 m contain thin calcilutite beds with poorly preserved graptolites.

*Unit 3*

This unit is compositionally very similar to unit 1, member D. It encompasses about 23 m of medium-bedded, parted and ribbon calcilutite/siltstone and minor calcarenite. The latter are often crossbedded. Interbeds are brownish grey (5 YR 4/1) to brownish black weathering mudstone, commonly burrowed, and laminated, calcareous, fine grained sandstone. Well preserved graptolites are dispersed in the upper part of the unit.

*Age of member D.* The age-range is relatively well constrained (Fig. 7). Graptolites in units 1 and 2 (tentatively identified by the author) and trilobites, probably *Illaenopsis* (R.A. Fortey, pers. comm., 1992), are mid- to late Arenig and possibly younger. Graptolites indicate *Didymograptus protobifidus* to *Isograptus victoriae* zones, (Cow Head graptolite zones, western Newfoundland; Williams and Stevens, 1988). Slivitzky et al. (1991) collected graptolites in dolomitic siltstones and sandstones (most likely from the middle interval of unit 2) that indicate basal *Didymograptus* to *Isograptus* zones (North American) (Riva, pers. comm. 1982, in Slivitzky et al., 1991). Graptolites tentatively identified as *Paraglossograptus* sp. and possibly *Undulograptus* sp. from the top of unit 3 are uppermost Arenigian-lowermost Llanvirnian (*Undulograptus austrodenatus* zone, Cow Head; Williams and Stevens, 1988).

## CONCLUSIONS

1. Slope facies in the Grosses-Roches-Les Méchins area include Cambrian siliciclastic and Lower-lower Middle Ordovician carbonate/siliciclastic sediments. Three formations are recognized: a lower Orignal, a middle Grosses-Roches (new), and an upper Anse du Crapaud (new). This lithostratigraphy is intended to be used on a local scale and not to replace the 'regional' scheme proposed by Slivitzky et al. (1991).
2. The Middle? to early Upper Cambrian Orignal Formation is dominated by red, green and grey shale and mudstone with subordinate thin siltstone laminae and beds, and minor thick-bedded coarse grained subarkosic arenite.
3. The Saint-Damase, Rivière-du-Loup, and Kamouraska formations are not useable for the coarse grained Cambrian interval in the Grosses-Roches-Les Méchins area. A single formation termed Grosses-Roches is instead proposed. The Romieu Formation is not recognized in the study area.
4. The early to late Upper Cambrian Grosses-Roches Formation sharply overlies the Orignal Formation. It is mostly coarse grained arenite, polymict quartzose conglomerate, and oligomict conglomerate. Limestone clasts are slope- and platform-derived; arenaceous clasts are slope-derived.
5. The term Rivière Ouelle Formation for strata overlying the Grosses-Roches Formation is not applicable in the study area. The term Anse du Crapaud Formation is instead proposed.
6. The Anse du Crapaud Formation gradationally overlies the Grosses-Roches Formation. It is a succession of variegated shale, mudstone and siltstone, and limestone, sandstone, and slope-derived limestone conglomerate. Sediment transport direction was south and west. The formation is divided into four informally defined members that are, in ascending order, A-D. Preliminary observations indicate that members A-C are well developed at Matane and Cap-des-Rosiers.
7. Newly discovered trilobites and graptolites indicate a Tremadocian to Upper Arenigian-lower Llanvirnian age-range for members B-D. The Cambrian-Ordovician boundary is most likely near the base of member A.

## ACKNOWLEDGMENTS

L. Bernstein thanks J. Wiebe for his enthusiastic assistance in the field. His keen eye for fossils and climbing skills were also much appreciated. We thank M. Malo for reviewing an earlier version of this contribution and R.A. Fortey for trilobite identifications. L. Bernstein also thanks G. Narbonne for discussions pertaining to stratigraphy. Field work was partly funded by the Geological Survey of Canada. N.P. James acknowledges the continued support of the National Research and Engineering Council of Canada.

## REFERENCES

**Barnes, C.R., Norford, B.S., and Skevington, D.**
1981: The Ordovician System in Canada; International Union of Geological Sciences, Publication 8, 27 p., 2 charts.

**Béland, J.**
1957: Région de Sainte-Félécité - Grosses-Roches; Ministère des Mines, Québec, RP 339.

**Biron, S.**
1971: Géologie de la rive du Saint-Laurent de Cap-Chat à Gros-Morne; Ministère des Richesses naturelles, Québec, DP-240.
1974: Géologie de la région des Méchins; Ministère des Richesses naturelles, Québec, DP-299.

**Coniglio, M.**
1985: Origin and diagenesis of fine-grained slope sediments: Cow head Group (Cambro-Ordovician), western Newfoundland; Ph.D. thesis, Memorial University of Newfoundland, St. John's Newfoundland, 684 p.

**Franks, P.C.**
1969: Nature, origin, and significance of cone-in-cone structures in the Kiowa Formation (Early Cretaceous), north-central Kansas; Journal of Sedimentary Petrology, v. 39, p. 1438-1454.

**Hendry, H.E.**
1978: Cap des Rosiers Formation at Grosses Roches, Quebec- deposits of the midfan region on an Ordovician submarine fan; Canadian Journal of Earth Sciences, v. 15, p. 1472-148.

**Hubert, C.**
1973: Kamouraska, La Pocatière, and Saint-Jean-Port-Joli area; Ministère des Richesses naturelles, Québec, Geological Exploration Service, Geological Report 151, 205 p.
**Hubert, C., Lajoie, J., and Léonard, M.A.**
1970: Deep sea sediments in the lower Paleozoic Québec Supergroup; in Flysch sedimentation in North America, (ed.) J. Lajoie; Geological Association of Canada, Special Paper No. 7, p. 103-126.
**James, N.P. and Stevens, R.H.**
1986: Stratigraphy and correlation of the Cambro-Ordovician Cow Head Group, western Newfoundland; Geological Survey of Canada, Bulletin 366, 143 p.
**Lajoie, J.**
1972: Géologie des régions de Rimouski et de Lac-des-Baies (moitié ouest), Comtés de Rimouski et Rivière-du-Loup; Ministère des Richesses naturelles, Québec, DP-64, 40 p.
**Landing, E., Barnes, C.R., and Stevens, R.K.**
1986: Tempo of earliest Ordovician graptolite faunal succession: conodont-based correlations from the Tremadocian of Quebec; Canadian Journal of Earth Sciences, v. 23, p. 1928-1949.
**Landing, E., Benus, A.P., and Whitney, P.R.**
1992: Early and early Middle Ordovician continental slope deposition: shale cycles and sandstones in the New York Promontory and Quebec Reentrant region; New York State Museum Bulletin, no. 474, 40 p.
**Liard, P.**
1973: Cartes supplémentaires pour la région de Mont-Joli - Matane; Ministère des Richesses naturelles, Québec, DP-290.
**Ludvigsen, R. and Westrop, S.R.**
1985: Three new Upper Cambrian stages for North America; Geology, v. 13, p. 139-143.
**McGerrigle, H.W.**
1950: The geology of Eastern Gaspé. Québec Department of natural Resources, Geological Report No. 35, 174 p.
**Rasetti, F.**
1945. Faunes cambriennes de conglomérats de la formation de Sillery; Naturaliste Canadien, v. 72, p. 53-67.
1946: Early Upper Cambrian trilobites from western Gaspé; Journal of Paleontology, v. 20, p. 442-462.
1948a: Lower Cambrian trilobites from the conglomerates of Quebec (*Ptychopariidea*); Journal of Paleontology, v. 22, p. 1-24.
1948b: Middle Cambrian trilobites from the conglomerates of Quebec (exclusive of *Ptychopariidea*); Journal of Paleontology, v. 22, p. 315-339.
**Slivitzky, A., St-Julien, P., and Lachambre, G.**
1991: Synthèse géologique du Cambro-Ordovician du nord de la Gaspésie; Ministère de l'Energie et des Ressources, Québec, ET 88-14, 61 p.
**St-Julien, P. and Hubert, C.**
1975: Evolution of the Taconian Orogen in the Quebec Appalachians; American Journal of Science, v. 275-A, p. 337-362.
**Strong, P.G. and Walker, R.G.**
1981: Deposition on the Cambrian continental rise: the St. Roch Formation near St-Jean-Port-Joli, Québec; Canadian Journal of Earth Sciences, v. 18, p. 1320-1335.
**Vallières, A.**
1984: Stratigraphie et structure de l'orogénie taconique de la région de Rivière-du-Loup; Ph.D. thesis, Université Laval, Quebec, 302 p.
**Williams, H.**
1979: Appalachian Orogen in Canada; Canadian Journal of Earth Sciences, v. 16, p. 792-807.
**Williams, S.H. and Stevens, R.K.**
1988: Early Ordovician (Arenig) graptolites of the Cow Head Group, western Newfoundland, Canada; Palaeontographica Canadiana No. 5, University of Toronto Press, 167 p.
1991: Late Tremadoc graptolites from western Newfoundland; Palaeontology, v. 34, p. 1-47.

---

Geological Survey of Canada Project 920001ML

# Amphibole thermobarometry: a thermodynamic approach

**Urs K. Mäder and Robert G. Berman**
**Continental Geoscience Division**

*Mäder, U.K. and Berman, R.G., 1992: Amphibole thermobarometry: a thermodynamic approach; in Current Research, Part E; Geological Survey of Canada, Paper 92-1E, p. 393-400.*

***Abstract***

*Preliminary amphibole mixing properties and standard state properties for the end-members tschermakite, pargasite, ferrotremolite, ferrotschermakite, and ferropargasite have been derived from an analysis of relevant phase equilibrium experiments, coexisting cummingtonite-hornblende pairs, and natural mineral parageneses recording pressures and temperatures established independently. When merged with other mineral properties given by Berman (1988, 1990), these amphibole properties allow the calculation of numerous equilibria suitable for thermobarometric purposes in a wide range of different parageneses. The model parameters are best constrained in amphibolite-granulite grade hornblende-garnet-plagioclase-quartz and hornblende-clinopyroxene-plagioclase-quartz assemblages. Applications also include garnet-amphibole thermometry and hygrometry.*

***Résumé***

*Les propriétés préliminaires de mélanges amphiboliques ainsi que les propriétés à l'état stable de membres extrêmes (tschermakite, pargasite, ferrotrémolite, ferrotschermakite et ferropargasite) ont été établies à partir d'une analyse des expériences pertinentes sur les équilibres de phases, des associations cummingtonite-hornblende et des paragenèses de minéraux naturels témoignant des pressions et températures de formation, établies indépendamment. Ces propriétés des amphiboles, une fois fusionnées avec d'autres propriétés minérales signalées par Berman (1988; 1990), permettent de calculer les nombreux équilibres correspondant aux conditions thermobarométriques d'une vaste gamme de paragenèses. Les paramètres du modèle sont au mieux définis dans les assemblages hornblende-grenat-plagioclase-quartz et hornblende-clinopyroxène-plagioclase-quartz associés aux faciès des amphibolites et des granulites. Les applications comprennent aussi l'hygrométrie et la thermométrie basées sur l'association grenat-amphibole.*

## INTRODUCTION

In spite of the common occurrence of amphiboles in a wide range of rock compositions from greenschist to granulite metamorphic grade, their use in quantitative petrologic modelling has been quite limited. This paradox reflects the mineralogical and crystal chemical complexity of amphiboles, a complexity which complicates both the interpretation of paragenetic data and the implementation and interpretation of phase equilibrium experiments involving amphiboles. In the past few years several "aluminum-in-hornblende" barometers applicable to granitoid compositions have been calibrated (e.g. Johnson and Rutherford, 1989); their shortcomings have been summarized by Blundy and Holland (1990). Several specific equilibria have also been calibrated, including the barometers of Kohn and Spear (1989, 1990) and the thermometers of Graham and Powell (1984) and Blundy and Holland (1990).

In this contribution, we utilize several key experimental studies performed recently on amphibole end-members and binaries together with well-constrained paragenetic data to calibrate preliminary amphibole mixing properties as well as standard state thermodynamic properties for several amphibole end-members. These data are then used in conjunction with already established properties for other minerals (Berman, 1988) to perform geothermobarometric calculations. A major advantage of this approach is that thermobarometric calculations can be made for a wide variety of different amphibole-bearing mineral assemblages in a range of different rock compositions. Table 2 lists the main assemblages that we have focused on in this study, and some of the equilibria that apply in these assemblages. Figures 1a and 1b illustrate some of the more important equilibria as a function of pressure (P) and temperature (T). Calculations are most conveniently performed using the TWEEQU (version 1.1) software package (Berman, 1991) which computes all possible equilibria among a given set of mineral end-members thought to have equilibrated under the same P-T conditions.

**Table 1.** Abbreviations

| | |
|---|---|
| Minerals: | |
| gar, cpx | garnet, clinopyroxene |
| hbl, amp | hornblende, amphibole |
| bio, qtz | biotite, quartz |
| plg, akf | plagioclase, alkalifeldspar |
| Mineral end-members (species): | |
| Tr, Ftr | tremolite, ferrotremolite |
| Ts, Fts | tschermakite, ferrotschermakite |
| Pa, Fpa | pargasite, ferropargasite |
| Pyr, Gro, Alm | pyrope, grossular, almandine |
| Di, Hd | diopside, hedenbergite |
| Phl, Ann | phlogopite, annite |
| An, Ab, Ksp | anorthite, albite, K-feldspar |
| Fo, Sp | forsterite, spinel |
| En, Fa | enstatite, fayalite |

## FORMALISM

For any balanced chemical reaction among j species, the equilibrium condition is:

$$\Delta_r G^{P,T} = -RT\ln K \quad (1)$$

The Gibbs free energy of reaction, $\Delta_r G^{P,T}$, is given by

$$\Delta_r G^{P,T} = \sum_j \nu_j \Delta_a G_j^{(P,T)} \quad (2)$$

with $\nu_j$ being the stoichiometric reaction coefficient and $\Delta_a G^{P,T}$, the apparent Gibbs free energy of formation (Berman, 1988), which is computed from

$$\Delta_a G^{P,T} = \Delta_f H^{1,298} + \int_{298}^{T} C_p dT - T\left[S^{1,298} + \int_{298}^{T} (C_{p/T}) dT\right] + \int_{1}^{P} V dP \quad (3)$$

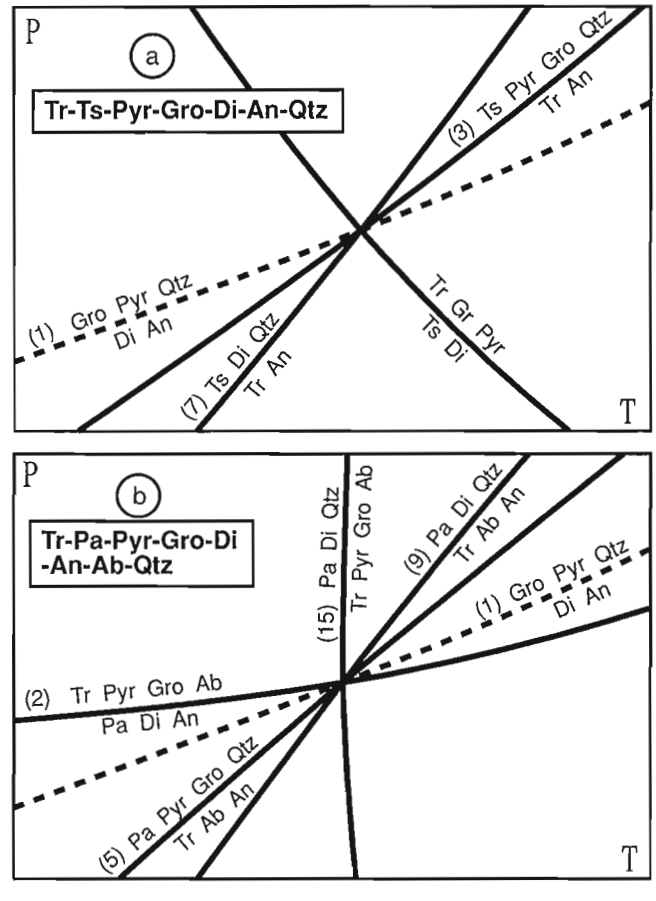


**Figure 1.** Schematic pressure-temperature diagram of some barometers and thermometers. Numbers are keyed to Table 2. See Table 1 for abbreviations of minerals.

The equilibrium constant can be written as

$$K = \prod_j a_j^{\nu_j} \quad (4)$$

The activity $a_j$ of species j is the product of an activity coefficient, $\gamma_j$, summing the nonideal interactions, times the ideal contribution to the free energy of mixing (Price, 1985):

$$a_j = \gamma_j \cdot \prod_s \prod_m (f_m x_m)^{r_m} \quad (5)$$

where $n_s$ is the multiplicity of site s, $x_m$ is the mole fraction of cation m on site s, and $f_m$ is a normalization factor equal to $n_s/r_m$, with $r_m$ being the number of m cations on site s. The activity coefficient of species j, $\gamma_j$, is given by

$$\gamma_j = \prod_s \cdot \prod_m \gamma_m \quad (6)$$

where $\gamma_m$ is the activity coefficient of cation m on site s, and the product is taken for all m cations on all s sites in species j. For the symmetric interactions assumed in this study, $\gamma_m$ is computed from

$$n_s RT \ln\gamma_m = \sum W_{ij} x_i x_j \left[\frac{Q_m}{f_m x_m} - 1\right] \quad (7)$$

In (7), the summation is for all Margules parameters, $W_{ij}$, and $Q_m$ is the number of i,j subscripts that are equal to m.

**Table 2.** Selected amphibole barometers and thermometers

Barometers:
gar-cpx-plg-qtz
1 12 Gro + Pyr + 3 Qtz = 3 Di + 3 An
amp-gar-cpx-plg
2 3 Tr + 5 Pyr + 10 Gro + 3 Ab = 3 Pa + 12 An + 18 Di
amp-gar-plg-qtz
3 3 Ts + 2 Pyr + 4 Gro + 12 Qtz = 3 Tr + 12 An
4 3 Fts + 2 Alm + 4 Gro + 12 Qtz = 3 Ftr + 12 An
5 3 Pa + Pyr + 2 Gro + 18 Qtz = 3 Tr + 6 An + 3 Ab
6 3 Fpa + Alm + 2 Gro + 18 Qtz = 3 Ftr + 6 An + 3 Ab
amp-cpx-plg-qtz
7 Ts + 2 Di + 2 Qtz = Tr + 2 An
8 Fts + 2 Hd + 2 Qtz = Ftr + 2 An
9 Pa + Di + 5 Qtz = Tr + Ab + An
10 Fpa + Hd + 5 Qtz = Ftr + Ab + An

Thermometers:
11 Alm + 3 Di = Pyr + 3 Hd
12 3 Tr + 5 Alm = 3 Ftr + 5 Pyr
13 Ts + Alm = Fts + Pyr
14 3 Pa + 4 Alm = 3 Fpa + 4 Pyr
15 3 Pa + 6 Di + 2 Qtz = 3 Tr + Pyr + 2 Gro + 3 Ab

Other equilibria:
16 Tr + 2 Sp = Ts + Fo
17 2 Ftr = 3 Fa + 4 Hd + 5 Qta + 2 H2O
18 Pa + 5 En = Di + 4 Fo + An + Ab + H2O

## MODEL CALIBRATION

The position of any equilibrium may be computed from equation (1). In the case of thermobarometry, measured mineral compositions are combined with known thermodynamic parameters to solve equation 1 for P (T) at a given T (P). In the case of calibrating thermodynamic parameters, assumed P and T (experimentally measured or independently calculated for natural samples) are combined with known mineral compositions to compute any unknown thermodynamic parameters. In this study we have derived amphibole mixing properties and end-member properties from simultaneous analysis of experimental phase equilibrium data, paragenetic data including constraints from coexisting cummingtonite-hornblende pairs, and calorimetric data. Attempts to include actinolite-hornblende pairs along with the above data proved unsuccessful, and further work is needed to resolve the source of this discrepancy. For the analysis we used linear programming to solve inequality constraints derived from equation 1 through consideration of (a) the direction from which equilibrium was approached in phase equilibrium data, and (b) estimated uncertainties in P, T, and mineral compositions of natural data sets. Inequality constraints for coexisting amphibole pairs are incorporated as discussed by Berman and Brown (1984).

Table 3 lists the data used as well as the equilibria that were applied for each assemblage. The natural data were selected on the basis of (1) assemblages containing amphibole in addition to other minerals that allow an independent P/T determination, (2) textural and chemical evidence of equilibrium among all relevant minerals, and (3) availability of full chemical analyses of all relevant minerals. Pressures and temperatures for the natural samples were computed with fluid- and amphibole-absent equilibria 1 and 11 (Table 2). All calculations used the thermodynamic data of Berman (1988, 1990) combined with the solution models of Berman (1990) for garnet, Furhman and Lindsley (1988) for plagioclase, and Newton (1983) for clinopyroxene.

For amphibole end-members, standard state volumes were estimated from X-ray data of synthetic and natural end-members except for tschermakite and ferrotschermakite where volumes had to be extrapolated (D.M. Jenkins, written comm., 1991). We assumed thermal expansivities and

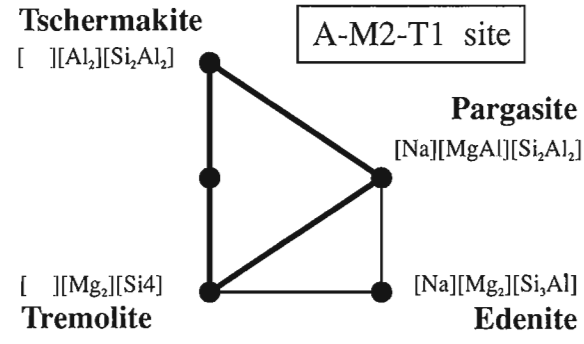


**Figure 2.** Composition space of tremolite-tschermakite-pargasite amphibole solutions.

**Table 3.** Calibrant data

| Equilibrium | P[kb] | T[°C] | Type | Reference |
|---|---|---|---|---|
| 7 | 2-7 | 640-950 | exp | Jenkins, p.c. |
| 16 | 6-8 | 780-820 | exp | Jenkins, p.c. |
| 9 | 2-6 | 590-710 | exp | Sharma & Jenkins, 1991 |
| 18 | 0.5-1.5 | 755-915 | exp | Lykins & Jenkins, 1987, in press |
| 17 | 0.5-3 | 400-750 | exp | Ernst, 1966 |
| 3-10, 12-14 | 8-10.5 | 670-800 | nat | Percival, 1983, and p.c. |
| 3-10, 12-14 | 10-11 | 700-800 | nat | Coolen, 1980 |
| 3-10, 12-14 | 6-8 | 670-720 | nat | Glassley & Sorensen, 1980 |
| 7-10 | 3.5 | 500-560 | nat | Ferry, 1988 |
| 3-6, 12-14 | 3.5 | 530 | nat | Leger & Ferry, 1991 |
| 3-6, 12-14 | 3 | 600-630 | nat | Labotka, 1987 |
| - | 2-3 | 690-770 | solv | Powell, 1975 |

Note: equilibrium number refers to Table 1; exp = experimental; nat = natural assemblage; solv = coexisting hornblende-cummingtonite; p.c. = personal communication.

**Table 4.** Margules parameters (Joules/22 oxygen formula)

| Site | Interaction | Margules parameter |
|---|---|---|
| A | Na-v | 5236 |
| | K-v | 5236 |
| M2 | Mg-Fe | 3102 |
| | Mg-Al | 21762 |
| | Mg-Fe3 | 3102 |
| | Mg-Ti | 696 |
| | Fe-Al | -11809 |
| | Fe-Ti | -70000 |
| | Al-Ti | -31064 |
| M4 | Ca-Mg | 43913 |
| | Ca-Fe | 42621 |
| | Mg-Fe | 3102 |
| M13 | Mg-Fe | 3102 |

compressibilities to be equal to those of tremolite except that pargasite and ferropargasite compressibilities were derived from measurements by Comodi et al. (1991). Third law entropies were estimated using the model of Holland (1989) correcting for configurational contributions (Westrich and Holloway, 1981). Entropies were optimized but kept within specified bounds. Heat capacities were estimated from tremolite properties using additive oxide components of Berman and Brown (1985). Enthalpies of formation were derived solely from optimization.

## AMPHIBOLE SOLUTION MODEL

Most calcic amphiboles can be approximated within the system tremolite-tschermakite pargasite and their ferrous analogs (Fig. 2). Our philosophy was to let the data guide us towards a solution model of minimal complexity able to satisfy the constraints within their estimated uncertainties. A 4-site mixing model with symmetric, P- and T-independent Margules parameters was adopted considering the sites A, M2, M4, and M13 (=M1+M3). Aluminum on tetrahedral sites is assumed to be fully coupled to aluminum on octahedral sites (tschermaks substitution) and/or sodium on the A-site (pargasite or edenite substitution) and therefore the tetrahedral site is omitted from the mixing model. In addition, lack of sufficient data on fluorine, chlorine, or oxygen content of the hydroxyl site forced us to omit this site altogether. This latter assumption may compromise some of the natural data employed in this study as well as applications of the derived model.

A variety of schemes that compute cation distributions for amphiboles from microprobe analysis can be rationalized (e.g. Robinson et al., 1982; Spear and Kimball, 1984). We have chosen the following assumptions and procedures:

1. M4+M2+M13+T sum to 15 cations (Na is excluded from M4-site);
2. Ti, $Fe^{3+}$ and octahedrally coordinated Al are allocated to M2;
3. Mn is assigned to M4 for Fe-Mg amphiboles, to M13 for Ca-amphiboles;
4. Ti is coupled with an OH=O substitution;
5. $Fe^{3+}$ is computed from total anion charges;
6. Mg/Fe is distributed across M-sites according to constant distribution coefficients, based on Mossbauer data (Makino and Tomita, 1989; Bancroft et al., 1967):

$$\left(\frac{Mg}{Fe}\right)_{M2} \cdot \left(\frac{Fe}{Mg}\right)_{M4} = 35.96; \quad \left(\frac{Mg}{Fe}\right)_{M2} \cdot \left(\frac{Fe}{Mg}\right)_{M13} = 3.33$$

The model is not very sensitive to the assumed values of these distribution coefficients. Banning Na from the M4-site provides the simplest scheme of placing some Mg and Fe onto M4 in order to define cummingtonite and grunerite activities

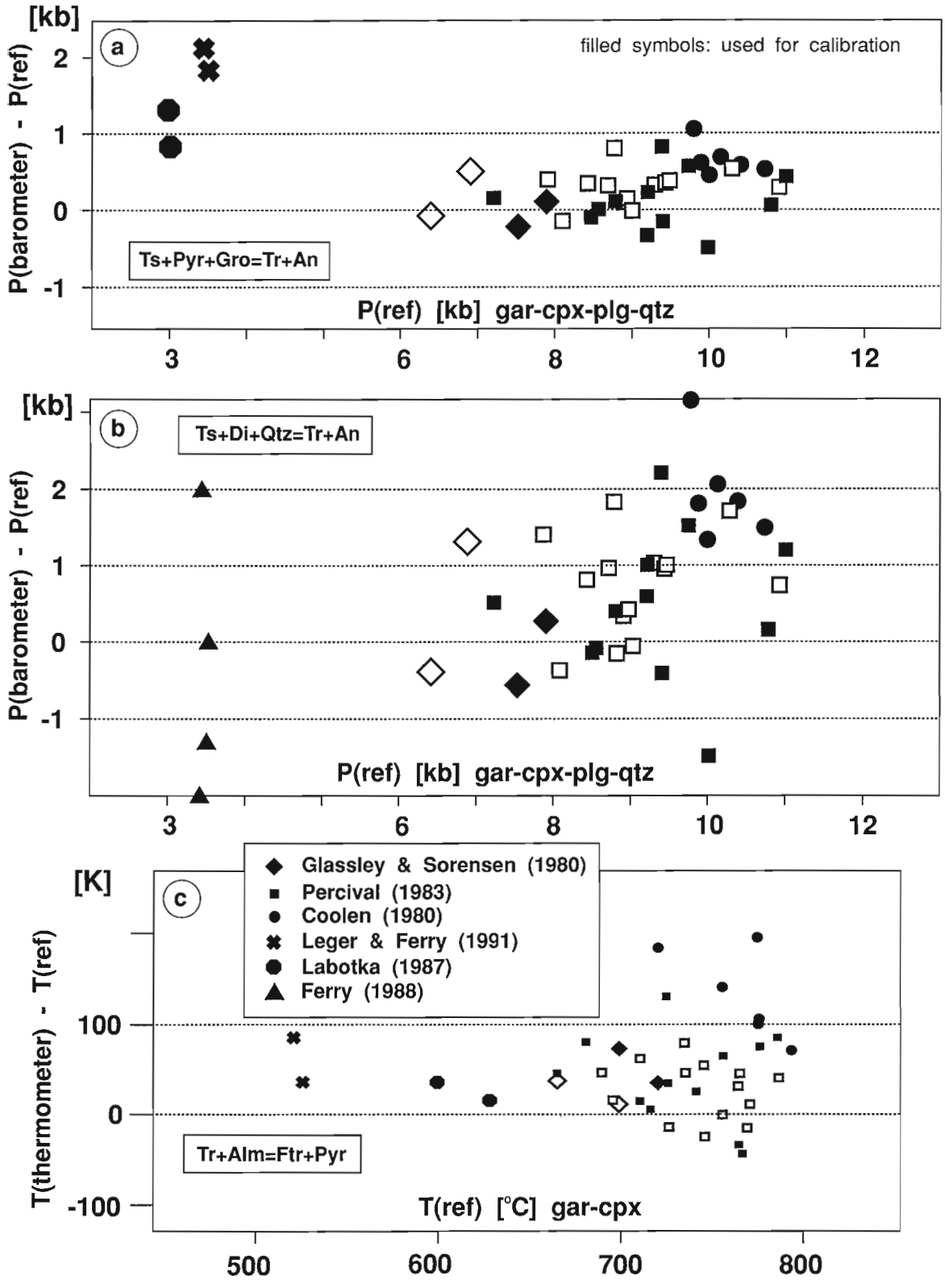


**Figure 3.** Pressure-pressure difference diagrams for calibrant data sets. Filled symbols represent rocks that were used in the calibration. Reference pressure was calculated with equilibrium 1 (Table 2) or estimated for rocks at 3-3.5 kbar. Reference temperatures were obtained from garnet-clinopyroxene thermometry (11, Table 2) or estimated for garnet-absent rocks. Estimates are those of the original authors.

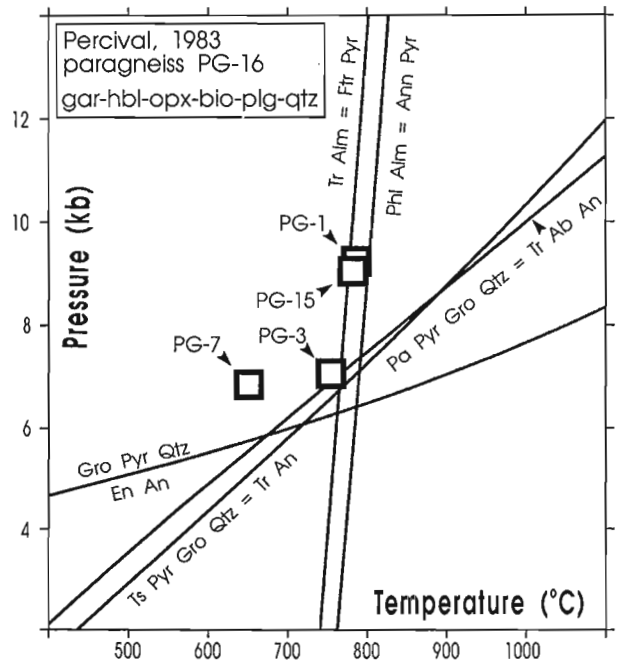


**Figure 4.** Pressure-temperature diagram for paragneisses from the Kapuskasing area. See text for discussion and Table 1 for mineral abbreviations.

in Ca-amphiboles. The introduction of an oxy-component coupled to Ti content is based on compositional trends observed within data sets of complete amphibole analyses (e.g. Cosca, 1991).

## RESULTS

The final optimization included 32 constraints from experimental data and some 600 constraints derived from 48 natural paragenesis. The resulting Margules parameters and standard state properties are presented in Tables 4 and 5. While the phase equilibrium data place rather stingent constraints on the standard state properties of all Mg amphibole end-members except Ts, the Fe end-members are poorly constrained or unconstrained by these data (except Ftr). The natural data place the most constraints on the amphibole mixing properties. The M4 site interactions are derived solely from the coexisting cummingtonite- hornblende pairs, as these site interactions cancel in all other equilibria listed in Table 2. The M4 site interactions are important, however, in applications using other equilibria in which only one of the amphibole end-members occur. In the final stage of analysis, we assumed $Fe^{3+}$ to have the same interaction with Mg as $Fe^{2+}$, and Fe-Mg interactions on all sites to be equal. It is particularly encouraging that derived Mg-Al and Fe-Al interaction parameters are similar in sign and magnitude to values found in other chain silicates (e.g. orthopyroxene, Aranovich, 1991). Further work is needed to refine the Ti interactions, which are poorly constrained by the present data set.

Figures 3a and 3b demonstrate the ability of the model to fit the calibrant data within acceptable uncertainties. It appears that the hornblende-garnet-plagioclase-quartz

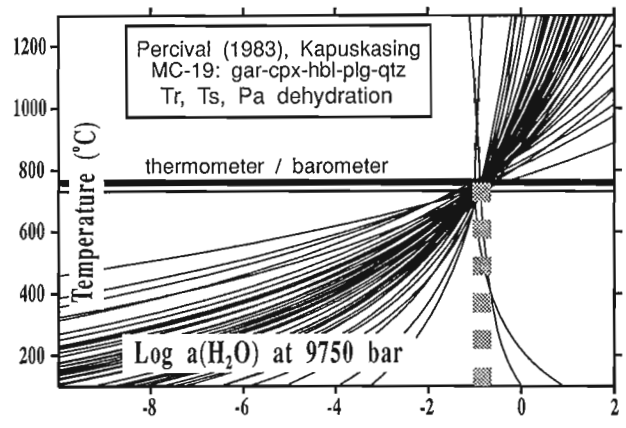


**Figure 5.** Temperature-water activity diagram for a mafic gneiss from the Kapuskasing area. See text for discussion and Table 1 for mineral abbreviations.

equilibrium (Fig. 3a) is the most robust barometer. The garnet-amphibole Fe-Mg exchange thermometers (12-14, Table 2) form a set of parallel P-T curves that in most cases differ by less than 40 degrees. These thermometers are susceptible to retrogradation like other Fe-Mg exchange thermometers, and display more scatter and are shifted to higher temperatures compared to the garnet-pyroxene thermometer that forms the basis of comparison in Figure 3c.

## APPLICATIONS

Two of the data sets were split into calibrant data and rocks used as a monitor for quality of fit. The latter are depicted as open symbols in Figure 3 and show deviations comparable to the calibrant data despite the compositional range encompassed by these mafic gneisses.

In Figure 4 we present results for hornblende-bearing garnet-biotite gneisses from the same area as the mafic gneisses of Percival (1983) used for calibration. The assemblage garnet-hornblende-biotite-plagioclase-quartz allows us to apply four garnet-hornblende barometers (no. 3-6, Table 2), the garnet-biotite thermometer, and the amphibole-garnet thermometers (12-14, Table 2). Several of these equilibria are illustrated in Figure 4, and yield a pressure-tempearture estimate of 7 kbar and 770°C. This rock also contains orthopyroxene and therfore permits an independent pressure check applying the garnet- orthopyroxene-plagioclase-quartz barometer. Results for four other gneisses that do not contain orthopyroxene are in general agreement with results obtained for the mafic gneisses (Fig. 4a).

Because of the strong dependence of amphibole dehydration equilibria on water activity one can use the derived amphibole properties to estimate water activity from rocks that yield tight constraints on pressure and temperature. In Figure 5 we have computed all possible dehydration equilibria (4 are lineraly independent) among Mg-components for a garnet-clinopyroxene-hornblende-plagioclase-quartz rock from the Kapuskasing area

**Table 5.** Thermodynamic properties of amphibole end-members

| | $\Delta_f H^{1,298}$[J/mole] | | $S^{1,298}$[J/mole/K] | $V^{1,298}$[J/bar] |
|---|---|---|---|---|
| Tr | -12305577.6 | | 551.150 | 2.7268 |
| Ts | -12578949.2 | | 514.687 | 2.7090 |
| Pa | -12723471.3 | | 590.500 | 2.7090 |
| Ftr | -10484188.5 | | 725.000 | 2.8170 |
| Fts | -11504426.4 | | 622.397 | 2.7590 |
| Fpa | -11279595.2 | | 738.000 | 2.7860 |
| Cp: | $k_0$ | $k_1$ | $k_2$ | $k_3$ |
| Tr | 1229.36 | -6401.900 | -32089890. | 4208807760. |
| Ts | 1248.18 | -6779.026 | -33606240. | 4536217000. |
| Pa | 1276.26 | -6514.016 | -35217190. | 4745671000. |
| Ftr | 1323.56 | -8519.785 | -25067000. | 3673229000. |
| Fts | 1304.70 | -8049.757 | -29392510. | 4214870000. |
| Fpa | 1351.62 | -8208.323 | -29598880. | 4317209000. |
| $\alpha$, $\beta$: | $v_3(x10^5)$ | $v_4(x10^5)$ | $v_1(x10^5)$ | $v_2(x10^8)$ |
| Tr | 2.43738877 | 0.00098338 | -0.13917727 | 0.00034809 |
| Ts | 2.43738877 | 0.00098338 | -0.13917727 | 0.00034809 |
| Pa | 3.08710000 | 0.0 | -0.11025400 | 0.0 |
| Ftr | 2.43738877 | 0.00098338 | -0.13917727 | 0.00034809 |
| Fts | 2.43738877 | 0.00098338 | -0.13917727 | 0.00034809 |
| Fpa | 3.08710000 | 0.0 | -0.11025400 | 0.0 |

Note: Cp and $\alpha$, $\beta$ coefficients using equations 4 and 5, respectively, of Berman (1988)

(Percival, 1983, sample MC-19). Equilibria that are independent of water activity (thermometers and barometers) plot as horizontal lines in this diagram. The bundle of curves at 770°C suggest a water activity of -0.7 to -1 log unit ($a_{H2O}$ =0.2 to 0.1). Only rocks that yield tightly constrained P-T estimates are suitable for computation of water activity. An independent test would be to utilize mica dehydration equilibria in rocks with apropriate mineral parageneses.

## DISCUSSION AND LIMITATIONS

Thermodynamic data derived in this study must be combined with the solution models and data base of Berman (1988, 1990) in order to perform thermobarometric calculations, most conveniently with software described by Berman (1991).The user should beware that the results, including standard state properties of end-member components, are dependent on the choice of model, and cannot be used or interpreted out-of-context (e.g. combined with other thermodynamic data bases or applied with a different cation distribution scheme for amphiboles). This is particularly true in a system where stringent constraints on some end-members are lacking, and compositional uncertainties stemming from incomplete amphibole analyses are significant.

Because of the large number of amphibole equilibria that can be written for different mineral parageneses, there are a number of "new" equilibria with good thermobarometry potential. For example, the tremolite-pargasite-garnet-clinopyroxene equilibrium 2 (Table 2) is always in good agreement with the garnet-clinopyroxene barometer (1) but can be applied to mafic rocks that are not saturated with respect to quartz. The hornblende-garnet-clinopyroxene-plagioclase thermometer 15 (Table 2) is independent of Fe end-members, and may prove useful in cases where retrogression has displaced Fe-Mg exchange thermometers to lower temperatures. Although it has a significant P-T slope, the equilibrium 2 Pa + Kfs + 6 Qtz = Tr + Phl + 2 An + 2 Ab yields pressures that are in encouraging agreement with those based on other equilibria for felsic granulites from the Furua Complex, and may provide useful barometric information for very common hornblende-biotite-plagioclase- alkali feldspar-quartz rocks. Further work to define other useful equilibria is ongoing.

For some data sets, particularly that of the Furua Complex, garnet-hornblende thermometers give systematically high temperatures. These discrepancies may be due to greater $Fe^{3+}$ in these samples than assumed with our cation distribution scheme, and further work will examine the effects of alternate schemes for assigning amphibole cation distribution.

The preliminary calibration presented here is best suited to amphibolite to granulite grade rocks and its performance in rocks of lower grade is not yet satisfactory. The calibrant data base is presently being expanded to allow for testing of more complex solution models that may be expected to

increase the range of applicability. We welcome any contributions that will expand the data base used in the development of this model.

## ACKNOWLEDGMENTS

We would like to thank particularly Dave Jenkins whose unlimited willingness to share unpublished data and experience contributed greatly to this project. John Percival shared unpublished probe data, providing us with one of the best petrologic data sets available. Leonya Aranovich has enlightened us with many discussions and Ken Currie improved the manuscript. Dugald Carmichel and John Ferry kindly provided probe data prior to publication. Mike Genkin assisted with assembling the data base.

## REFERENCES

**Aranovich, L. Ya.**
1991: Mineral Equilibria of Multicomponent Solid Solutions; Nauka Press, Moscow, 253 p. (in Russian).

**Bancroft, G.M., Burns, R.G., and Maddock, A.G.**
1967: Determination of cation distribution in the cummingtonite-grunerite series by Mossbauer spectra; American Mineralogist, v. 52, p. 1009-1026.

**Berman, R.G.**
1988: Internally-consistent thermodynamic data for minerals in the system $Na_2O$-$K_2O$-CaO-MgO-FeO-$Fe_2O_3$-$Al_2O_3$-$SiO_2$-$TiO_2$-$H_2O$-$CO_2$; Journal of Petrology, v. 29, p. 445-522.
1990: Mixing properties of Ca-Mg-Fe-Mn garnets; American Mineralogist, v. 75, p. 328-344
1991: Thermobarometry using multi-equilibrium calculations: a new technique, with petrological applications; Canadian Mineralogist, v. 29, p. 833-855.

**Berman, R.G. and Brown, T.H.**
1984: A thermodynamic model for multicomponent melts, with application to the system CaO-$Al_2O_3$-$SiO_2$; Geochimica et Cosmochimica Acta, v. 48, p. 661-678.
1985: Heat capacity of minerals in the system $Na_2O$-$K_2O$-CaO-MgO-$Fe_2O_3$-$Al_2O_3$-$SiO_2$-$TiO_2$-$H_2O$-$CO_2$: representation, estimation, and high temperature extrapolation; Contributions to Mineralogy and Petrology, v. 89, p. 168-183.

**Blundy, J.D. and Holland, T.J.B.**
1990: Calcic amphibole equilibria and a new amphibole-plagioclase geothermometer; Contributions to Mineralogy and Petrology, v. 104, p. 208-224.

**Coolen, J.J.M.M.M.**
1980: Chemical petrology of the Furua granulite complex, Southern Tanzania; GUA Papers of Geology, Series 1, no. 13, 257 p.

**Comodi, P., Mellini, M., Ungaretti, L., and Zanazzi, P.F.**
1991: Compressibility and high pressure structure refinement of tremolite, pargasite and glaucophane; European Journal of Mineralogy, v. 3, p. 485-499.

**Cosca, M.A., Essene, E.J., and Bowman, J.R.**
1991: Complete chemical analyses of metamorphic hornblendes: implications for normalizations, calculated $H_2O$ activities, and thermobarometry; Contributions to Mineralogy and Petrology, v. 108, p. 472-484.

**Ernst, W.G.**
1966: Synthesis and stability relations of ferropargasit; American Journal of Science, v. 264, p. 37-65.

**Ferry, J.M.**
1988: Contrasting mechanisms of fluid flow through adjacent stratigraphic units during regional metamorphism, south-central Maine, USA; Contributions to Mineralogy and Petrology, v. 98, p. 1-12.

**Fuhrman, M.L. and Lindsley, D.H.**
1988: Ternary-feldspar modeling and thermometry; American Mineralogist, v. 73, p. 201-216.

**Glassley, W.E. and Sorensen, K.**
1980: Constant Ps-T amphibolite to granulite facies transition in Agto (West Greenland) metadolerites: implications and applications; Journal of Petrology , v. 21, p. 69-105.

**Graham, C.M. and Powell, R.**
1984: A garnet-hornblende geothermometer: calibration, testing, and application the Pelona Schist, Southern California; Earth and Planetary Science Letters, v. 31, p. 142-152.

**Holland, T.J.B.**
1989: Dependence of entropy on volume for silicate and oxide minerals: A review and a predictive model; American Mineralogist, v. 74, p. 5-13.

**Johnson, M.C. and Rutherford, M.J.**
1989: Experimental calibration of the aliminum-in-hornblende geobarometer with application to Long Valley caldera (California) volcanic rocks; Geology, v. 17, p. 837-841.

**Kohn, M.J. and Spear, F.S.**
1989: Empirical calibration of geobarometers for the assemblage garnet+hornblende+plagioclase+quartz; American Mineralogist, v. 74, p. 77-84.
1990: Two new geobarometers for garnet amphibolites, with applications to southeastern Vermont; American Mineralogist, v. 75, p. 89-96.

**Labotka, T.C.**
1987: The garnet+hornblende isograd in calcic schists from an andalusite-type regional metamorphic terraine, Panamint Mountains, California; Journal of Petrology, v. 28, p. 323-354.

**Leger, A. and Ferry, J.M.**
1991: Highly aluminous hornblende from low-pressure metacarbonates and a preliminary thermodynamic model for the Al content of calcic amphibole; American Mineralogist, v. 76, p. 1002-1017.

**Lykins, R.W. and Jenkins, D.M.**
1987: Experimental determination of pargasite stability in the presence of orthopyroxene; Geological Society of America, Abstracts with Programs, v. 19, p. 752.
in press: Experimental determination of pargasite stability in the presence of orthopyroxene; Contributions to Mineralogy and Petrology.

**Makino, K. and Tomita, K.**
1989: Cation distribution in the octahedral sites of hornblendes; American Mineralogist, v. 74, p. 1097-1105.

**Newton, R.C.**
1983: Geobarometry of high-grade metamorphic rocks; American Journal of Science, v. 283-A, p. 1-28.

**Percival, J.A.**
1983: High-grade metamorphism in the Chapleau-Foleyet Area, Ontario; American Mineralogist, v. 68, p. 667-686.

**Powell, R.**
1975: Thermodynamics of coexisting cummingtonite-hornblende pairs; Contributions to Mineralogy and Petrology, v. 51, p. 29-37.

**Price, J.G.**
1985: Ideal site mixing is solid solution, with an application to two-feldspar geothermometry; American Mineralogist, v. 70, p. 696-701.

**Robinson, P., Spear, F.S., Schumacher, J.C., Laird, J., Klein, C., Evans, B.W., and Doolan, B.L.**
1982: Phase relations of metamorphic amphiboles: natural occurrence and theory; in Amphiboles: Petrology and Experimental Phase Relations, (ed.) P.H. Ribbe; Reviews in Mineralogy, v. 9B, p. 1-228.

**Sharma, A. and Jenkins, D.M.**
1991: Experimental reversals for the Al-content in pargasitic amphiboles coexisting with plagioclase, diopside, and quartz; Geological Society of America, Abstracts with Programs, v. 23, p. 94.

**Spear, F.S. and Kimball, K.**
1984: RECAMP- A FORTRAN IV program for estimating $Fe^{3+}$ contents in amphiboles; Computers and Geosciences, v. 10, p. 317-325.

**Westrich, H.R. and Holloway, J.R.**
1981: Experimental dehydration of pargasite and calculation of its entropy and Gibbs energy; American Journal of Science, v. 281, p. 922-934.

Geological Survey of Canada Project 880014

# AUTHOR INDEX

## NOTICE TO LIBRARIANS AND INDEXERS

The Geological Survey's Current Research series contains many reports comparable in scope and subject matter to those appearing in scientific journals and other serials. Most contributions to Current Research include an abstract and bibliographic citation. It is hoped that these will assist you in cataloguing and indexing these reports and that this will result in a still wider dissemination of the results of the Geological Survey's research activities.

## AVIS AUX BIBLIOTHÉCAIRES ET PRÉPARATEURS D'INDEX

La série Recherches en cours de la Commission géologique contient plusieurs rapports dont la portée et la nature sont comparables à ceux qui paraissent dans les revues scientifiques et autres périodiques. La plupart des articles publiés dans Recherches en cours sont accompagnés d'un résumé et d'une bibliographie, ce qui vous permettra, on l'espère, de cataloguer et d'indexer ces rapports, d'où une meilleure diffusion des résultats de recherche de la Commission géologique.

Geological Survey of Canada Current Research, is released twice a year. Paper 92-1, parts A to D were published in January 1992 and Paper 92-1 Part E (this volume) was published in July 1992.

Recherches en cours, une publication de la Commission géologique du Canada, est publiée deux fois par année. Les parties A à D de l'Étude 92-1 ont été publiées en janvier 1992 tandis que le partie E de l'Étude 92-1 (le présent volume) l'a été en juillet 1992.

Part A, Cordillera and Pacific Margin
Partie A, Cordillère et marge du Pacifique

Part B, Interior Plains and Arctic Canada
Partie B, Plaines intérieures et région arctique du Canada

Part C, Canadian Shield
Partie C, Bouclier canadien

Part D, Eastern Canada and national and general programs
Partie D, Est du Canada et programmes nationaux et généraux

Part E (this volume)
Partie E (ce volume)